FUSION ENERGY 1996

SIXTEENTH
CONFERENCE PROCEEDINGS
MONTREAL, CANADA
7-11 OCTOBER 1996

IAEA

Vol.1

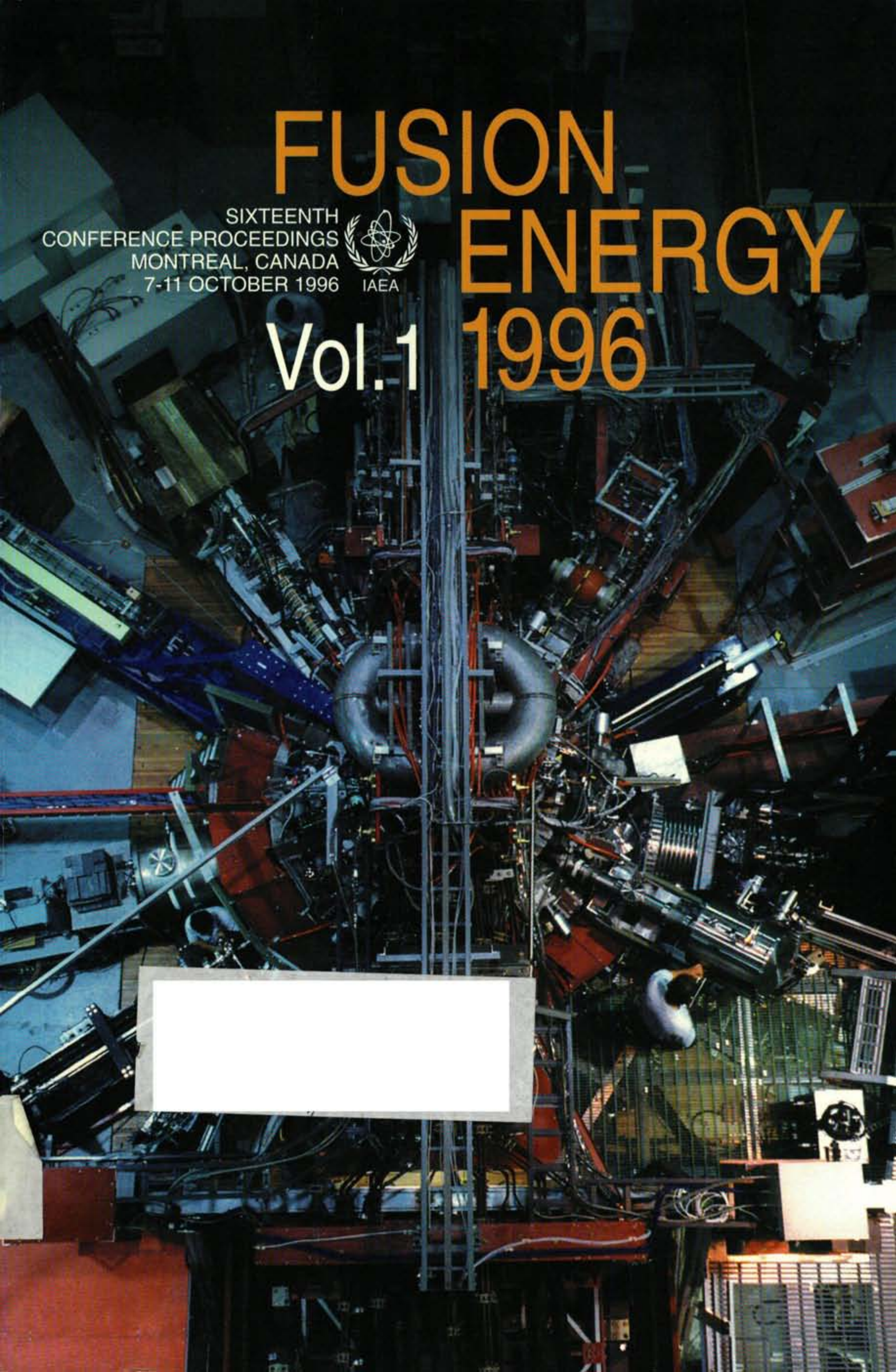

The cover picture shows the top view of the Tokamak de Varennes (TdeV) and its diagnostics. By courtesy of the Centre canadien de fusion magnétique (CCFM), Varennes, Quebec, Canada.

FUSION ENERGY 1996

VOLUME 1

The following States are Members of the International Atomic Energy Agency:

AFGHANISTAN	HOLY SEE	PERU
ALBANIA	HUNGARY	PHILIPPINES
ALGERIA	ICELAND	POLAND
ARGENTINA	INDIA	PORTUGAL
AUSTRALIA	INDONESIA	QATAR
ARMENIA	IRAN, ISLAMIC REPUBLIC OF	ROMANIA
AUSTRIA	IRAQ	RUSSIAN FEDERATION
BANGLADESH	IRELAND	SAUDI ARABIA
BELARUS	ISRAEL	SENEGAL
BELGIUM	ITALY	SIERRA LEONE
BOLIVIA	JAMAICA	SINGAPORE
BOSNIA AND HERZEGOVINA	JAPAN	SLOVAKIA
BRAZIL	JORDAN	SLOVENIA
BULGARIA	KAZAKSTAN	SOUTH AFRICA
CAMBODIA	KENYA	SPAIN
CAMEROON	KOREA, REPUBLIC OF	SRI LANKA
CANADA	KUWAIT	SUDAN
CHILE	LEBANON	SWEDEN
CHINA	LIBERIA	SWITZERLAND
COLOMBIA	LIBYAN ARAB JAMAHIRIYA	SYRIAN ARAB REPUBLIC
COSTA RICA	LIECHTENSTEIN	THAILAND
COTE D'IVOIRE	LITHUANIA, REPUBLIC OF	THE FORMER YUGOSLAV REPUBLIC OF MACEDONIA
CROATIA	LUXEMBOURG	TUNISIA
CUBA	MADAGASCAR	TURKEY
CYPRUS	MALAYSIA	UGANDA
CZECH REPUBLIC	MALI	UKRAINE
DENMARK	MARSHALL ISLANDS	UNITED ARAB EMIRATES
DOMINICAN REPUBLIC	MAURITIUS	UNITED KINGDOM OF GREAT BRITAIN AND NORTHERN IRELAND
ECUADOR	MEXICO	UNITED REPUBLIC OF TANZANIA
EGYPT	MONACO	UNITED STATES OF AMERICA
EL SALVADOR	MONGOLIA	URUGUAY
ESTONIA	MOROCCO	UZBEKISTAN
ETHIOPIA	MYANMAR	VENEZUELA
FINLAND	NAMIBIA	VIET NAM
FRANCE	NETHERLANDS	YEMEN
GABON	NEW ZEALAND	YUGOSLAVIA
GEORGIA	NICARAGUA	ZAIRE
GERMANY	NIGER	ZAMBIA
GHANA	NIGERIA	ZIMBABWE
GREECE	NORWAY	
GUATEMALA	PAKISTAN	
HAITI	PANAMA	
	PARAGUAY	

The Agency's Statute was approved on 23 October 1956 by the Conference on the Statute of the IAEA held at United Nations Headquarters, New York; it entered into force on 29 July 1957. The Headquarters of the Agency are situated in Vienna. Its principal objective is "to accelerate and enlarge the contribution of atomic energy to peace, health and prosperity throughout the world".

Printed by the IAEA in Austria
May 1997
STI/PUB/1004

PROCEEDINGS SERIES

FUSION ENERGY 1996

PROCEEDINGS OF THE
SIXTEENTH INTERNATIONAL CONFERENCE
ON FUSION ENERGY
ORGANIZED BY THE
INTERNATIONAL ATOMIC ENERGY AGENCY
AND HELD IN MONTREAL, 7–11 OCTOBER 1996

In three volumes

VOLUME 1

INTERNATIONAL ATOMIC ENERGY AGENCY
VIENNA, 1997

VIC Library Cataloguing in Publication Data

International Conference on Fusion Energy (16th : 1996 : Montreal, Canada)
Fusion energy 1996 : proceedings of the sixteenth International Conference on Fusion Energy / organized by the International Atomic Energy Agency and held in Montreal, 7–11 October 1996. — Vienna : The Agency, 1997.
3 v. ; 24 cm. — (Proceedings series, ISSN 0074–1884)
Contents: v.1.
STI/PUB/1004
ISBN 92–0–100797–3
"Formerly called the International Conference on Plasma Physics and Controlled Nuclear Fusion Research."
Includes bibliographical references.

1. Nuclear fusion—Congresses. 2. Controlled fusion—Congresses. 3. Plasma (Ionized gases)—Congresses. I. International Atomic Energy Agency. II. Title. III. Title: International Conference on Plasma Physics and Controlled Nuclear Fusion Research. IV. Series: Proceedings series (International Atomic Energy Agency).

VICL 97-00168

FOREWORD

The 16th International Atomic Energy Agency Fusion Energy Conference (formerly called the International Conference on Plasma Physics and Controlled Nuclear Fusion Research) was held in Montreal, Canada, from 7 to 11 October 1996. This series of meetings, which began in 1961, has been held biennially since 1974.

In addition to these biennial conferences, the IAEA organizes co-ordinated research projects, technical committee meetings, advisory group meetings and consultants meetings on fusion research topics. The objectives of the IAEA activities related to fusion research are to:

—Promote fusion energy development and worldwide collaboration;
—Support developing Member State activities in fusion research;
—Emphasize the safety and environmental advantages of fusion energy;
—Encourage the utilization of plasmas and fusion technology in industry;
—Provide auspices for the International Thermonuclear Experimental Reactor (ITER).

This conference, which was attended by some 500 participants from over thirty countries and two international organizations, was organized by the IAEA in co-operation with the Centre canadien de fusion magnétique and the Canadian National Fusion Program, to which the IAEA wishes to express its gratitude. Some 270 papers were presented in 19 oral and 8 poster sessions on magnetic and inertial confinement systems, plasma theory, computer modelling, alternative confinement approaches, fusion technology and future experiments. The opening session was designated the Artsimovich Memorial Session, in honour of Academician Lev Andreevich Artsimovich.

Fusion research is continuing to make excellent progress. Since the previous conference (Seville, 1994) over 10 MW of fusion power has been produced in the Tokamak Fusion Test Reactor, plasma conditions equivalent to breakeven have been demonstrated in the JT-60U experiment, the reversed shear mode has been demonstrated, low aspect ratio tokamaks have produced promising results and plans have been drawn up for powerful new inertial confinement fusion experiments. We can look forward to further encouraging results at the next conference (Yokohama, 1998), when the Joint European Torus will have employed a 50:50 mix of deuterium–tritium fuel, the Large Helical Device will be operating and the ITER Engineering Design Activities will be complete.

CONTENTS OF VOLUME 1

OVERVIEWS 1 (Session O1)

The ITER project: A physics and technology experiment
(IAEA-CN-64/O1-1) 3
R. Aymar et al.
Physics of high performance deuterium–tritium plasmas in TFTR
(IAEA-CN-64/O1-2) 19
K.M. McGuire et al.
Steady state operation research in JT-60U (IAEA-CN-64/O1-3) 37
K. Ushigusa, JT-60 Team
Features of JET plasma behaviour in two different divertor configurations
(IAEA-CN-64/O1-4) 57
JET Team
Overview of ASDEX Upgrade results (IAEA-CN-64/O1-5) 79
M. Kaufmann et al.
DIII-D tokamak concept improvement research
(IAEA-CN-64/O1-6) 95
V.S. Chan, DIII-D Team
Overview of helical systems (IAEA-CN-64/O1-7) 113
A. Iiyoshi

OVERVIEWS 2 (Session O2)

Divertor detachment, He exhaust and compact toroid injection on TdeV
(IAEA-CN-64/O2-1) 129
R. Décoste et al.
Progress towards enhanced confinement, long duration discharges
on Tore Supra (IAEA-CN-64/O2-2) 141
Equipe Tore Supra
High-field compact divertor tokamak research on Alcator C-Mod
(IAEA-CN-64/O2-3) 155
I.H. Hutchinson et al.
Divertor biasing effects to reduce the L–H power threshold
in the JFT-2M tokamak (IAEA-CN-64/O2-4) 167
Y. Miura et al.
Quasi-stationary ELM free high confinement with edge radiative
cooling in TEXTOR-94 (IAEA-CN-64/O2-5) 177
G.H. Wolf et al.

CONCEPT OPTIMIZATION 1 (Session A1)

Optimisation of JET steady-state ELMy discharges with ITER-relevant divertor conditions (IAEA-CN-64/A1-1) 189
JET Team

Stability in high gain plasmas in DIII-D (IAEA-CN-64/A1-2) 199
E.A. Lazarus et al.

Transport physics in reversed shear plasmas (IAEA-CN-64/A1-3) 211
F.M. Levinton et al.

Enhanced core confinement in JT-60U reversed shear discharges (IAEA-CN-64/A1-4) 227
T. Fujita et al.

High fusion performance ELM free H-modes and the approach to steady operation (IAEA-CN-64/A1-5) 239
JET Team

High triangularity discharges with improved stability and confinement in JT-60U (IAEA-CN-64/A1-6) 247
Y. Kamada et al.

CONFINEMENT AND α PARTICLES (Session A2)

Sawtooth mixing of alpha particles in TFTR D–T plasmas (IAEA-CN-64/A2-2) 261
M.P. Petrov et al.

Prospects for alpha channeling: Initial results from TFTR (IAEA-CN-64/A2-3) 271
N.J. Fisch et al.

Observation of alpha particle driven toroidal Alfvén eigenmodes in TFTR DT plasmas (IAEA-CN-64/A2-4) 281
R. Nazikian et al.

Study of TFTR DT neutron spectra using natural diamond detectors (IAEA-CN-64/A2-5) 293
A.V. Krasilnikov et al.

Alfvén eigenmodes and fast particle physics in JET reactor relevant plasmas (IAEA-CN-64/A2-6) 303
JET Team

OPERATIONAL LIMITS AND DISRUPTIONS (Session A3)

High performance experiments in JT-60U high current divertor discharges (IAEA-CN-64/A3-1) 315
S. Ishida et al.

Performance limitations in JET hot ion H-modes (IAEA-CN-64/A3-2) 331
JET Team
Fast current shutdown scenario for major disruption softening in JT-60U
(IAEA-CN-64/A3-4) 345
Y. Kawano et al.
MHD stability and disruption studies in ASDEX Upgrade
(IAEA-CN-64/A3-5) 359
O. Gruber et al.

DIVERTOR EXPERIMENTS (Session A4)

Effect of divertor configuration on plasma performance in JET
(IAEA-CN-64/A4-1) 371
JET Team
Radiative divertor with improved core plasma confinement in JT-60U
(IAEA-CN-64/A4-2) 385
K. Itami et al.
Divertor plasma physics experiments on the DIII-D tokamak
(IAEA-CN-64/A4-3) 397
M.A. Mahdavi et al.
Edge and divertor physics in ASDEX Upgrade with emphasis on
density limit characteristics (IAEA-CN-64/A4-4) 413
V. Mertens et al.
Variation of the divertor geometry in Alcator C-Mod
(IAEA-CN-64/A4-5) 425
B. Lipschultz et al.

CONCEPT OPTIMIZATION 2 (Session A5)

Study of H-mode physics in ASDEX Upgrade (IAEA-CN-64/A5-1) 439
H. Zohm et al.
MHD stability studies in reversed shear plasmas in TFTR
(IAEA-CN-64/A5-2) 453
J. Manickam et al.
Local analysis of confinement and transport in neutral beam heated
DIII-D discharges with negative magnetic shear
(IAEA-CN-64/A5-3) 463
D.P. Schissel et al.
High power density H-modes in Alcator C-Mod (IAEA-CN-64/A5-4) 475
Y. Takase et al.

Optimisation of JET plasmas with current profile control
(IAEA-CN-64/A5-5) 487
JET Team
Transport and loss of energetic ions in JT-60U (IAEA-CN-64/A5-6) 497
K. Tobita et al.

TRANSPORT EXPERIMENTS (Session A6)

Transport and fluctuations: More evidence on TEXT
(IAEA-CN-64/A6-1) 509
G. Cima et al.
Dependence of core turbulence on the discharge parameters in T-10
and its correlation with transport (IAEA-CN-64/A6-2) 519
V.A. Vershkov et al.
Local analysis of transport and turbulence in Tore Supra
(IAEA-CN-64/A6-3) 535
C. Laviron et al.
Physics of turbulence control and transport barrier formation in DIII-D
(IAEA-CN-64/A6-4) 547
E.J. Doyle et al.
Studies of perturbative plasma transport, ice pellet ablation and sawtooth
phenomena in the JIPPT-IIU tokamak (IAEA-CN-64/A6-5) 559
K. Toi et al.
Isotope scaling of heating and confinement in multiple regimes of TFTR
(IAEA-CN-64/A6-6) 573
S.D. Scott et al.

CONFINEMENT AND WAVES, DISRUPTIONS AND INSTABILITIES (Poster Session AP1)

Tangential CT injection and 1.5 cycle AC operation experiments
on STOR-M (IAEA-CN-64/AP1-1) 595
C. Xiao et al.
Energy confinement and H-mode power threshold scaling in JET with
ITER dimensionless parameters (IAEA-CN-64/AP1-2) 603
JET Team
Implications from dimensionless parameter scaling experiments
(IAEA-CN-64/AP1-3) 611
T.C. Luce et al.
Statistical properties of turbulent transport and fluctuations in
tokamak and stellarator devices (IAEA-CN-64/AP1-4) 617
C. Hidalgo et al.

Confinement and transport studies in ASDEX Upgrade
(IAEA-CN-64/AP1-5) 625
F. Ryter et al.
ICRF assisted low voltage start-up in TEXTOR-94
(IAEA-CN-64/AP1-6) 633
R. Koch et al.
Influence of the shape on TCV plasma properties
(IAEA-CN-64/AP1-7) 643
J.-M. Moret et al.
Modelling an RLC circuit for the investigation of disruption
instabilities in tokamaks (IAEA-CN-64/AP1-8) 649
R. Amrollahi, E. Farshi
Heat transport in the RTP tokamak (IAEA-CN-64/AP1-9) 655
G.M.D. Hogeweij et al.
Ware pinch effect in Tore Supra (IAEA-CN-64/AP1-10) 663
H. Capes, P. Laporte
Modeling of Tore Supra experiments and implications for the control
of an 'advanced' steady state reactor (IAEA-CN-64/AP1-11) 669
X. Litaudon et al.
Transient density fluctuations related to the sawtooth crash in the
Tore Supra tokamak (IAEA-CN-64/AP1-12) 677
P. Hennequin et al.
HT-7 superconducting tokamak and its operation (IAEA-CN-64/AP1-13) 685
HT-7 Group
Recent experiments and confinement studies on the HL-1M tokamak
(IAEA-CN-64/AP1-14) 693
HL-1M Team
Ion cyclotron emission: A collective alpha-particle effect in deuterium–
tritium plasmas in TFTR and JET (IAEA-CN-64/AP1-15) 699
R.O. Dendy et al.
Halo currents and VDEs in COMPASS-D (IAEA-CN-64/AP1-16) 707
G.G. Castle et al.
Beta limit studies and the effect of error fields at low collisionality
on COMPASS-D (IAEA-CN-64/AP1-17) 715
D.A. Gates et al.
Disruptions and vertical displacement events in JET
(IAEA-CN-64/AP1-18) 723
JET Team
Eddy-current characterization and plasma rotation control in wall-
stabilized tokamak discharges (IAEA-CN-64/AP1-19) 731
M.E. Mauel et al.
Disruption studies in DIII-D (IAEA-CN-64/AP1-20) 739
A.G. Kellman et al.

Practical beta limit in ITER shaped discharges in DIII-D and its increase by higher collisionality (IAEA-CN-64/AP1-21) 747
R.J. La Haye et al.
Disruptions, halo currents and killer pellets in Alcator C-Mod (IAEA-CN-64/AP1-22) 757
R.S. Granetz et al.
Positive current spike generation during major disruptions and ICRF heating experiments under conditions of L–H transition on the T-11M tokamak (IAEA-CN-64/AP1-23) 763
S.V. Mirnov et al.
Evolution of the tearing mode during LHCD induced mode locking in WT-3 (IAEA-CN-64/AP1-24) 771
T. Maekawa et al.
An attempt to mitigate disruptive plasma current decay in relation to vacuum vessel electrical aspects (IAEA-CN-64/AP1-25) 777
M. Abe et al.

DIVERTOR EXPERIMENTS AND TOKAMAK CONCEPT OPTIMIZATION (Poster Session AP2)

Active control of helium ash exhaust and transport characteristics in JT-60U (IAEA-CN-64/AP2-1) 789
A. Sakasai et al.
Experimental evidence for the suitability of ELMing H-mode operation in ITER with regard to core transport of helium (IAEA-CN-64/AP2-2) 801
M.R. Wade et al.
Impurity transport and exhaust in radiative edge experiments in ASDEX Upgrade (IAEA-CN-64/AP2-3) 809
H.-S. Bosch et al.
Erosion and transport of tungsten in ASDEX Upgrade (IAEA-CN-64/AP2-4) 817
K. Krieger et al.
Transport studies in the scrape-off layer and divertor of Alcator C-Mod (IAEA-CN-64/AP2-5) 825
B. LaBombard et al.
Impurity screening studies in the Alcator C-Mod tokamak (IAEA-CN-64/AP2-6) 833
G.M. McCracken et al.
Control of boundary power flux with ergodic divertor on Tore Supra (IAEA-CN-64/AP2-7) 839
P. Ghendrih et al.

Influence of limiter biasing on confinement and stability of ISTTOK plasma (IAEA-CN-64/AP2-8) 849
J.A.C. Cabral et al.
H mode transition and power threshold in JT-60U (IAEA-CN-64/AP2-9) 857
T. Fukuda et al.
Study of H-mode threshold conditions in DIII-D (IAEA-CN-64/AP2-10) 867
R.J. Groebner et al.
Local plasma parameters and H-mode threshold in Alcator C-Mod (IAEA-CN-64/AP2-11) 875
A.E. Hubbard et al.
Investigation of causality in the H–L transition on the JFT-2M tokamak (IAEA-CN-64/AP2-12) 885
K. Hanada et al.
Improved plasma confinement in the TUMAN-3M and FT-2 tokamaks (IAEA-CN-64/AP2-13) 891
M.V. Andrejko et al.
New features of the L–H transition in H modes in HT-6M (IAEA-CN-64/AP2-14) 899
B.N. Wan et al.
Formation and evolution of internal transport barriers in Alcator C-Mod (IAEA-CN-64/AP2-15) 907
D.T. Garnier et al.
Turbulent fluctuations in the main core of TFTR plasmas with negative magnetic shear (IAEA-CN-64/AP2-16) 913
E. Mazzucato et al.
Deuterium–tritium TFTR plasmas with high internal inductance (IAEA-CN-64/AP2-17) 921
S.A. Sabbagh et al.

Chairpersons of Sessions and Secretariat of the Conference 931

OVERVIEWS 1

(Session O1)

Chairperson

A. GIBSON
European Community

THE ITER PROJECT: A PHYSICS AND TECHNOLOGY EXPERIMENT

R. AYMAR, V. CHUYANOV, M. HUGUET,
R. PARKER, Y. SHIMOMURA and the
ITER JOINT CENTRAL TEAM and HOME TEAMS*

Abstract

THE ITER PROJECT: A PHYSICS AND TECHNOLOGY EXPERIMENT.

Recent progress in the collaborative work on the ITER Engineering Design Activities is summarized. ITER's position in relation to the overall fusion energy development programme, the latest physics assessments for ITER, and the development and status of work on the ITER design and safety characterisation are discussed. Major collaborative projects on key aspects of ITER technology are introduced. Conclusions refer to the outlook for future work and further progress towards ITER's programmatic goal.

1. ITER IN THE WORLDWIDE FUSION DEVELOPMENT PROGRAMME

The two years since the IAEA conference in Seville have witnessed extensive progress in all aspects of the ITER Engineering Design Activities [1], due principally to efficient collaboration between the ITER Joint Central Team (JCT) and the fusion community in the four ITER Parties and their associates. Successful collaboration has continued with the Home Teams in the areas of technology R&D, detailed design, and manufacturing process and costs. At the same time there has been an impressive development and convergence of the Parties' voluntary contributions in the physics area; the important physics issues have been identified and all the major physics experiments in magnetic controlled fusion are providing high quality, relevant results in a coordinated fashion for consideration through the ITER Physics Expert Groups.

These dedicated joint efforts have borne fruit. A major development to report is the ITER Council's acceptance in July 1995 of the ITER Interim Design Report (IDR) Package [2],[3] and its approval of the Package in December 1995 following domestic reviews by the ITER Parties. Against this background, the ITER Parties have entered explorations aimed at identifying issues for subsequent negotiations towards a possible agreement on ITER construction, operation, exploitation and decommissioning.

---

* This paper is an account of work undertaken within the framework of the ITER EDA Agreement. Neither the ITER Director, the parties to the ITER EDA Agreement, the IAEA or any agency thereof, or any of their employees, makes any warranty, express or implied, or assumes any legal liability or responsibility for the accuracy, completeness, or usefulness of any information, apparatus, product, or process disclosed, or represents that its use would not infringe privately owned rights. Reference herein to any specific commercial product, process or service by tradename, trademark, manufacturer, or otherwise, does not necessarily constitute its endorsement, recommendation, or favouring by the parties to the ITER EDA Agreement, the IAEA or any agency thereof. The views and opinions expressed herein do not necessarily reflect those of the parties to the ITER EDA Agreement, the IAEA or any agency thereof.

With the passing of this major milestone in the EDA work programme, it has been possible to freeze the main concepts and system approaches and to make the transition to the detailed design process in preparation for the Detailed Design Report which is due to be submitted to the ITER Council in December 1996.

The JCT and Home Teams have also succeeded in fully defining seven large integrated joint programmes in the key areas of technology R&D. The work is now proceeding according to agreed schedules and targets.

ITER is a central feature of the fusion development programmes of the four Parties and is strongly linked to their base programmes, both in physics and technology. ITER's future depends critically on the physics and technology results that are flowing from the base programmes. In physics particularly ITER needs a vigorous base research programme to build confidence and credibility in predictions and to reduce uncertainties in plasma performance. Voluntary physics research, with coordinated experiments in tokamaks of various sizes, is essential to increase the precision of performance projections. The technology programme has to support and validate system designs which drive a range of leading edge technologies into new domains in terms of, for instance, the size of superconducting magnets and structures; remote handling systems; materials to cope with the extreme heat flux in the divertor, and the high heat and neutron flux demands on all plasma facing components; and tritium breeding blanket modules.

At the same time ITER is stimulating efficient interactions which support a vigorous base programme in the Parties. ITER is helping to focus the base programme towards concrete, reactor-relevant issues and is injecting an additional degree of dynamism conducive to efficiency throughout the Parties' programmes. ITER is instrumental in providing a focus for coordination of scientific and technical contributions and convergence of opinion.

At this conference a large number of papers and posters from the ITER Joint Central Team, the Home Teams and other physics participants provide a representative sample of the results of recent collaborative work in the ITER EDA frame. The present paper can offer only an overview and reference some key features of that work. However, the contributions of all ITER personnel, including those who are not represented or cited here, are recognized and warmly acknowledged.

2. ITER PROGRAMMATIC AND TECHNICAL OBJECTIVES

The overall programmatic objective of ITER, as defined in the ITER EDA Agreement [1], is to demonstrate the scientific and technological feasibility of fusion energy for peaceful purposes. ITER would accomplish this by demonstrating controlled ignition and extended burn of deuterium-tritium plasmas, with steady state as an ultimate goal, by demonstrating technologies essential to a reactor in an integrated system, and by performing integrated testing of the high-heat-flux and nuclear components required to utilize fusion energy for practical purposes.

Detailed technical objectives along with the technical approaches to determine the best practicable way to achieve the programmatic objective of ITER have been established and were adopted by the ITER Council in December 1992 [4] and acknowledged in Protocol 2 of the ITER EDA Agreement. These objectives have been translated into a General Design Requirements Document [3], adopted within the project, which provides a more specific statement at the system and component level of the performance, safety, and configuration requirements to be met by the design.

In terms of plasma performance ITER has to meet the objective of demonstrating controlled ignition and extended burn, in inductive pulses with a flat-top duration of approximately 1000 s and an average neutron wall loading of about $1 MW/m^2$. ITER should also aim to demonstrate steady state operation using non-inductive current in reactor-relevant plasmas. For purposes of engineering performance and testing ITER should demonstrate the availability of technologies essential for a fusion reactor, test components for a reactor and test design concepts of tritium blankets relevant to a reactor. An important assumption underlying the detailed technical objectives is that there will be an adequate supply of tritium from external sources. A decision on incorporating breeding in ITER for the later phase of operation (Enhanced Performance Phase) should be decided on the basis of the availability of tritium from external sources, the results of breeder blanket testing during initial ITER operation and experience with ITER plasma and machine performance.

Recognising the objective that ITER should be designed to operate safely and to demonstrate the safety and environmental potential of fusion power, the following general safety principles underly the development of the ITER design with regard to safety and environmental characteristics:

- to ensure that ITER is potentially acceptable in any Party's territory;
- to maximise use of the inherent favorable safety characteristics of fusion;
- to meet dose/release limits based on recommendations of the International Commission on Radiological Protection (ICRP) and International Atomic Energy Agency (IAEA), and further reduce releases and doses to the public and site personnel to levels as low as reasonably achievable (ALARA); and
- to minimize the safety role of and dependence in safety assessments on uncertain plasma physics and experimental in-vessel components.

These principles give rise to specific functional requirements for the safety aspects of the ITER design.

The main characteristics and parameters of the ITER design follow from the above programmatic and detailed technical objectives which establish dual roles for ITER. It must provide a full-scale experimental working model of the core of a future fusion reactor in terms of its size, energy and neutron flux, expected activation and active intervention capacity, and overall safety characteristics. On the other hand there are important physics questions which will inevitably remain open, to be resolved only during ITER operations. ITER must therefore also serve as an experimental facility permitting the fusion community to explore a wide range of fusion physics phenomena and operational domains. Flexibility is required in the design to allow access for introducing advanced features and new capabilities and to permit optimization of plasma performance during operation. There must also be capacity for intervention and repair by remote handling, making it necessary to have modularity in major systems where possible.

3. ITER PARAMETERS, PLASMA PERFORMANCE, AND OPERATIONAL SCENARIOS

3.1 Main Parameters and Overall Performance

The major engineering design parameters for ITER are given in Table 1.

TABLE 1. MAJOR ENGINEERING DESIGN PARAMETERS FOR ITER

Major/minor radius R/a	8.14 m/2.80 m
Plasma configuration	Single-null divertor[a]
Nominal plasma volume V(plasma)	$\sim$2000 m^3
Plasma separatrix surface area A_S	$\sim$ 1200 m^3
Nominal plasma current I	21 MA
Toroidal field B	5.68 T (at R = 8.14 m)
MHD safety factor q_{95}	$\sim$3.0 (at I = 21 MA)
Fusion power (nominal) P_{fus}	1.5 GW
Average wall loading Γ_n	$\sim$ 1 MW/m^2 (at 1.5 GW)
PF flux swing $\Delta\phi_{PF}$	530 Wb
Flux swing for burn $\Delta\phi_{burn}$	>80 Wb
Burn duration (ignited) t_{burn}	≥ 1000 s
TF ripple δ_{ripple}	≤2% at plasma separatrix
Auxiliary heating power	100 MW

[a] With its channel poloidal extension ≥2 m.

These parameters are such that the most likely projections of ITER plasma performance indicate that the goal of achieving "controlled ignition" will be met with finite but modest margins, but that high fusion power extended burn to produce about 1 MW/m^2 of 14 Mev neutrons will be surely and safely achieved in a driven-burn mode using the planned auxiliary heating power of up to 100 MW.

This strategy calls for a range of operational scenarios. Thus a necessary flexibility in the capabilities of the systems/components which deal with the plasma environment should be built in, even at the expense of a limited increase in cost. The accommodation of advanced tokamak discharges aimed at true steady state reversed-shear operation is an element of this flexibility, fully in line with the agreed ITER objectives.

3.2 Performance Issues

The principal issues that directly determine the performance of the ITER plasma include:

- energy confinement at small normalized gyro-radius, $\rho*$
- long-pulse beta-limit at low normalized collisionality, $\nu*$ (non-ideal MHD effects),
- particle and energy confinement and fueling/exhaust efficacy for hydrogen isotopes and helium ash, in particular in high-density plasmas near the Greenwald density limit, and
- fusion reactivity reduction owing to the need to add medium- or high- Z impurities to facilitate radiative power dispersal.

Other issues concern the operation reliability, mainly in relation to the lifetime of plasma facing components.

The projections for plasma core energy confinement basically depend on a global scaling of ELMy H mode, observed in present experiments, the results from which have been included in a large, critically analysed database. This approach relies conceptually on the assumption that the tokamak confinement physics is governed by a number of non dimensional parameters and that a simple power law relation suffices to represent the energy confinement time for those non dimensional parameters that require extrapolation for ITER. The uncertainties in the functional forms to be assumed in (1) below have led to the concept of "ITER Demonstration Discharges" [5], in which experiments are done in present machines with all non dimensional quantities, except the normalised $\rho*$ ($\rho* = (2TM)^{1/2} (eBa)^{-1}$), having values envisaged for ITER. These Demonstration Discharges should provide the most reliable approach to scaling confinement, in the form of:

$$\Omega_i . \tau_E = (\rho *)^y . F(\beta, \nu*, q, R/a, k...) \qquad (1)$$

Completion of this ongoing experimental campaign lies in the future, but this expansion of current tokamak operations is expected to generate high confidence in ITER projections.

Presently, following recommendation from the Confinement Modeling and Database Expert Group [6], the reference global energy confinement time is given by 0.85 x ITERH93P. An enhancement factor, H_H, is introduced in this scaling:

$$\tau_E = H_H \mathrm{x} 0.85 \tau_E \,(\mathrm{ITERH93P}) \qquad (2)$$

An uncertainty of +/- 30% in confinement for the 95% confidence interval results from the database analysis. This corresponds to H_H factor typically between 0.7 and 1.3. It is worth noting that the lower limit of this uncertainty range corresponds to the confinement that one would expect from Bohm extrapolation of the present experiments.

The recommended scaling by the same Expert Group for the L- to H-mode transition is given by:

$$P_{th} = 0.080\, n_e^{0.75} B\, R^2 \;(\mathrm{MW},\, 10^{19}\mathrm{m}^{-3},\, \mathrm{T},\, \mathrm{m}) \qquad (3)$$

This formula does not reflect the present uncertainty in extrapolation from present experiments. Efforts are ongoing to include explicitly edge plasma and neutral densities in the database, in order to consider the possible important role of edge radiation losses.

The ideal MHD limit for ITER lies at β_N=3.5, and thus is not a constraint on operation. However, a common feature of long duration experiments on present machines, at ITER-like collisionality values, is the spontaneous creation of magnetic islands and confinement degradation at values of $\beta_N \simeq 2.5$, close to the value needed for ITER. Theoretical understanding of the occurring phenomena might lead to countermeasures [7], which can overcome what does not appear to be a strong constraint for ITER operation.

The maximum density achieved in most tokamak experiments is consistent with the empirical Greenwald limit $n_G = I/\pi a^2 (10^{20} m^{-3}$, MA, m), which in the case of ohmically-heated plasmas can be understood as a radiation limit. However, there is presently no generally accepted physics-based scaling for this limit. Auxiliary-heated experiments dedicated to transcending this limit have been successful, indicating that this limit is not fundamental [7]. A consistent interpretation is that a limit on edge density inside the transport barrier does exist, and that peaked density profiles, made possible by pellet injection fueling, are needed to surpass the simple Greenwald limit on line-average density.

It is not acceptable to plan for the ITER divertor targets to handle the total steady state alpha power of 300 MW, concentrated onto the target "wetted" area of $\simeq$ 10 m^2. The development of an acceptable engineering design requires a reduction of the peak heat flux to 5-10 MW/m^2. The strategy of using atomic processes to spread out the deposition of the power over the first wall and the divertor chamber wall (1200 m^2 and 400 m^2 respectively in ITER) has been effectively and successfully addressed in present experiments by a combination of impurity seeding (N, Ne, Ar) and gas puffing.

Modelling of the complex physics occurring has made enough progress to date to check basic assumptions with present experiments and to identify pertinent tendencies, not yet absolute predictions, for "detached" or "semidetached" regimes in ITER [8],[9]. It therefore appears likely that these regimes can be achieved with impurity seeding in ITER at reasonable up stream densities (5.10^{19} m^{-3}) and powers (~ 200 MW), reducing the target heat load to acceptable values. However, both core contamination and H mode power threshold will put limits on the allowable impurity concentration; the optimal solution will thus require compromise.

3.3 Operational Scenarios

In the area of physics design, a substantial effort has been devoted to developing [10] a simplified SOL/divertor model to provide self-consistent boundary conditions and to connect central He impurity concentration with fueling and pumping rates. The transport codes (PRETOR, ASTRA, TRANSP) have been used to develop and refine the ITER operational scenarios including reference ignited scenarios, long pulse non-inductively driven, and steady state scenarios based on the reversed shear plasma configuration. The main emphasis was on the following issues: a) a self-consistent simulation of the core and divertor; b) modeling of the effect of impurity seeding on the ignited plasma performance; c) ITER operation below the Greenwald density limit; and d) steady state and driven scenarios under constraints of ITER auxiliary systems.

Modelling, using the recommended global scaling laws, has shown that ignition at constant power can be sustained if impurity fueling, DT fueling and auxiliary heating have feedback control loops which keep fusion power, divertor heat loads and plasma density at the required level.

Two results are worth noting:

- 0.2% of argon at the flat-top allows the power to the divertor target to remain at the required level of 50 MW, when 1.5 GW of fusion power is achieved in ignited mode and the helium content corresponds to τ_{He}/τ_E= 3.5 -7, a lower value than assumed previously;
- the effect of plasma confinement on ITER performance is illustrated in Fig. 1, where the main plasma parameters are presented as function of enhancement factor.

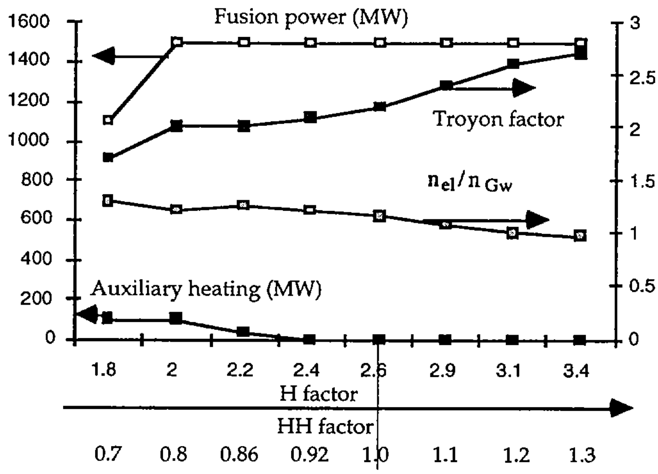

FIG. 1. Fusion power, auxiliary heating power, normalized density relative to the Greenwald limit and Troyon factor for a range of confinement from −30% to +30% of the reference value.

In driven burn operation of ITER, auxiliary heating power of 100 MW allows extension of pulse lengths and maintenance of high neutron wall load, providing high fluence for testing. At about 1 GW of fusion power, the pulse length can be extended to 8000 s with a plasma current of 16 MA.

True steady state operation can be met by a reversed shear scenario with a large bootstrap current fraction (>70%), requiring on axis and off axis current drive which can be provided by two different methods among those planned and developed for ITER. The present poloidal field system appears adequate to support the required magnetic configuration; nevertheless a reduction by a factor ~ 2 of the amount of toroidal field ripple will provide more flexibility. However, understanding and experimental knowledge of power and particle confinement scaling and of operational limits in this scenario are obviously needed to a similar level as are available for the reference pulsed operation. This presents a necessary goal for present and future experiments.

Besides plasma performance, operational scenarios should be looked at from the reliability point of view. This issue concerns most of the auxiliary subsystems, which provide the tokamak environment. But the most important issue relates to the question of what fraction of the overall ITER operational cycle must be allocated to maintenance or replacement of the critical plasma facing components (limiters, first wall and divertor targets) that are eroded or otherwise damaged by normal plasma operation, including disruptions and Vertical Displacement Events (VDE).

It appears that the last two phenomena are the determining factors. In order to mitigate the divertor target erosion during a disruption and the thermal (and electromagnetic) loads from VDE, a fast shutdown system must be able to terminate the fusion power and to remove the plasma thermal and magnetic energy in less than 3 seconds.

Injection of impurities, in the form of a "killer pellet", was proposed and even tested in present experiments. Ongoing studies [11] show that after injection of a given amount of impurities, radiation can consume the thermal stored energy in much less than 1 s and distribute it evenly. However, this amount of impurities cannot dissipate rapidly the magnetic energy and, in ITER, inevitably causes production of runaway electrons which carry a substantial part of the plasma current (10 MA). This runaway current, due specifically to the large magnetic flux available in ITER, cannot be controlled by the PF system and will be lost on the walls. Only a massive injection of deuterium (or helium perhaps) of more than 50 g seems capable of dissipating the stored magnetic energy in less than 1 s without leading simultaneously to a large runaway current. One of the results from this study is to question the possibility to observe, in any disruption, a fast current quench.

In addition, besides the large thermal loads applied to the first wall, VDE halo currents produce large mechanical loads on in-vessel components. Substantial progress has been made in collecting an empirical database on halo currents from present machines, but a good theoretical model (3D) is urgently needed for a reliable extrapolation of halo current magnitude and toroidal asymmetries in ITER.

3.4 Conclusion

Thanks to contributions from the world fusion community expressed comprehensively through the ITER Physics Expert Groups, significant progress has been made in the integration of the different aspects of ITER performance and operational scenarios. The physics assessments for ITER are now broadly based on the collated results of the current generation of fusion experiments and benefit from continuous interaction between members of their teams. Even with such a foundation, extrapolation from present plasmas to the ITER size and parameters cannot be predicted with certainty. Nevertheless, the wide-ranging reviews have not so far found any limitations in principal which could preclude achieving the required ITER performance and objectives.

Under the nominal plasma parameters, ignition in ITER is highly probable. Furthermore, even taking into account a wide range of uncertainties, 1.5 GW of fusion power can be achieved with up to 100 MW of auxiliary heating power, while simultaneously satisfying divertor heat load and H-mode power threshold requirements. Even with the combination of the most pessimistic assumptions (lower range of confinement and limited density), large Q ($\simeq$ 10) driven burn can still be produced in ITER.

A range of operational scenarios have been shown possible, from minimal 1000 s inductive pulse, to true steady state current driven reversed shear operations.

4. ITER DESIGN

4.1 Overall Status of the Design

The ITER design has evolved along the following lines, in relation to what was presented in the Interim Design Package [2],[3]:

- the essential features of ITER – its tokamak core and the overall facility – have been maintained and frozen, allowing transition from conceptual to detailed design for most of the components/subsystems;
- improvements have been introduced in coverage of variation in external conditions (seismic regime, site characteristics) and in relation to possible or hypothetical accident conditions;
- emphasis on the practicability of assembly, and timely maintenance through an appropriate combination of hands-on assisted and remote handling (RH) techniques.

4.2 Essential Features of the Tokamak

As Figures 2 and 3 indicate, the essential features of the ITER design remain :

- a very strong toroidal mechanical structure is built with 20 encased superconducting toroidal field (TF) coils, linked together by the upper and lower crowns and bolted inter-coil structures;

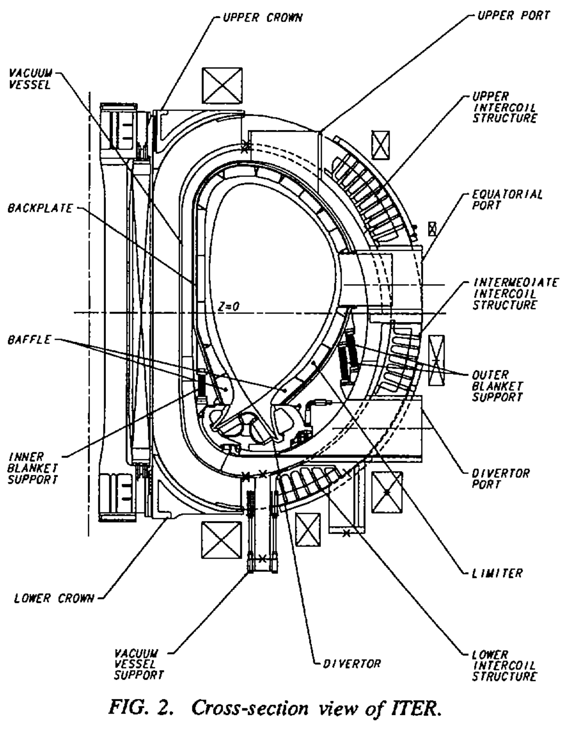

FIG. 2. Cross-section view of ITER.

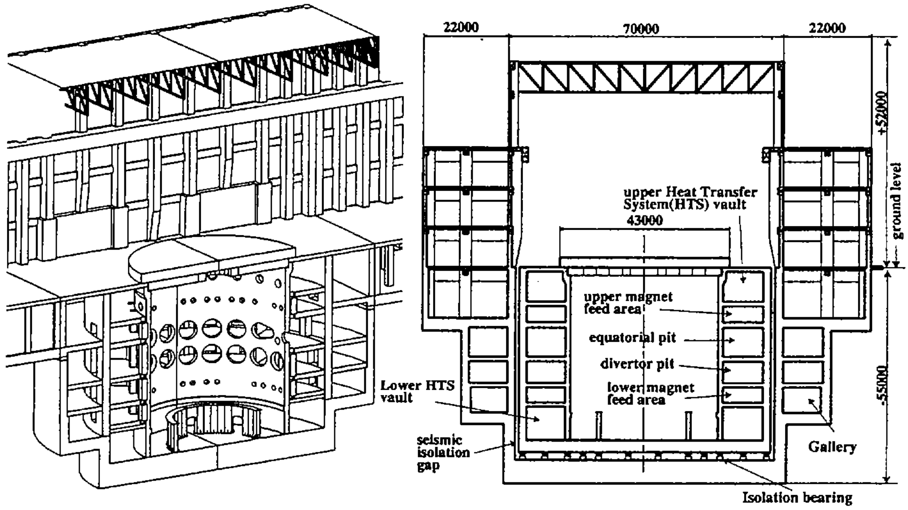

FIG. 3. Tokamak building and pit. Left: north-south cutaway view; right: east-west cross-section view (in case of seismic isolation).

- the seven superconducting poloidal field (PF) coils are attached to the TF coil cases, and the central solenoid (CS) supports a significant fraction of the TF coil centering forces;
- the double-walled vacuum vessel (VV) is directly attached to the TF coil cases, restraining vertical and horizontal forces and limiting their relative displacements inside a safe limit, during a possible earthquake or VDE.
  This arrangement of coils and vacuum vessel provides an integrated overall assembly which simplifies the equilibrium of electromagnetic loads in all conditions, relying mainly on the robustness of the TF coil cases;
- the in-vessel components (blanket and divertor) maintenance is made possible with practical remote handling tools, thanks to design which puts emphasis on their modularity;
- the machine core, inside its large cryostat, is put in an underground pit, inside a building of minimum height.

4.3 Buildings and Cryostat

The tokamak building configuration and the pit arrangement have been revised in relation to the possible need for seismic isolation. The goal was to minimize the design changes, which could be necessary if the site selected for construction has a peak ground acceleration larger (0.4 g) than the 0.2 g value assumed for the present design.

The key changes made in the 60 m diameter pit layout are the following:

- relocation of the primary heat transfer systems in two vaults, upper and lower;
- creation of upper and lower magnet feed areas, relocation of the cold terminal boxes and magnet switchgear inside the pit;
- creation of space below the cryostat for the vacuum vessel pressure suppression tank and drain tanks (also used in case of trapped PF coil in-situ repair);
- creation of service galleries to be used for remote handling and service routing.

The structural configuration of the tokamak building is depicted in Fig. 3. If the seismic ground peak acceleration is larger than 0.2 g, isolation will be added, placing a seismic gap at the pit wall, creating an isolated (64 m diameter) "tokamak pit" supported by flexible bearings, stiff vertically but allowing large horizontal movement ($\simeq$ 200 mm).

The new pit dimensions have led to a new design for the cryostat with higher cylindrical part and flat bottom and lid. The primary heat transport systems have been segregated in a large number of loops, all similar in power handling, pressure and water inventory: 10 for the blanket shielding modules, 4 for the outboard limiter and baffle modules, and 4 for the divertor cassettes. This segregation, besides providing smaller sized loop components to be fitted in the pit vaults, makes it possible to limit the water inventory to be dealt with in case of a mild breach in the vacuum vessel and to allow complete containment inside the pressurized vaults in case of a large breach in the components outside the vacuum vessel. This arrangement successfully addresses most safety concerns with tritium or activated corrosion products possibly present in the cooling water.

4.4 Tokamak Assembly

The assembly plan developed for the tokamak core meets compulsory constraints of accurate location of components, and provides necessary testing and control procedures, while making use of parallel operations in order to meet schedule requirements. The main procedure is as follows:

- one TF coil and two VV half-sectors with thermal shield are preassembled into one segment using poloidal welds on the two VV shells, which are tested for leaks;
- Backplate (BP) assembly is started in parallel with TF/VV segments assembly. Large BP sectors are welded from both sides to reduce and control distortion, and introduced by rotation into the VV. They are equipped with blanket modules already leak tested;
- Welding of VV segments together progresses in parallel with the backplate sector welding. The final closure of the vessel torus is made through two welds 180° apart toroidally, with access provided by a sector of 36° of the backplate, poloidally segmented, being nested into an adjacent segment. The backplate is then closed by welding the nested parts from inside only, finishing two poloidal welds 180° apart toroidally.

4.5 Maintenance and Intervention

Maintenance concepts for ITER have made major progress towards defining practical procedures [12]. Two large R&D projects have been launched to develop specific equipment and prototype tools (see below § 6) and to test their operation, and assess the required intervention times.

The general approach is to make ex-vessel interventions very unlikely by providing component redundancy where practical, but nevertheless to develop a concept for a coil replacement; this has led to design constraints for the building and the cryostat.

On the other hand, maintenance of in-vessel components (blanket modules and divertor cassettes) involves the very likely replacement of faulty components. The removed components are transported to the hot cell in sealed casks, on a railway system in the galleries around the pit. Double-door devices are used to avoid the release of radioactivity during docking and undocking of the casks on the cryostat flanges at the equatorial and divertor levels. The procedure makes use of large RH transporters and telemanipulators, being developed, and relies on an optimisation of hands-on or hands-on assisted operations in support of the fully remote activities. This is achieved in ITER:

- by surrounding the frequently used RH maintenance ports with shielding walls so that hands-on operation can be carried out in parallel in adjacent locations, and
- by using hands-on procedures for preparatory operations before removing all shielding from port ducts and for finishing operations after reinstallation of shielding.

4.6 Conclusion

In conclusion, the design of the ITER tokamak core and overall facility has made such progress that the present work plan can envisage realistically how to organise detailed studies to prepare for documenting technical specifications for components/subsystems procurement. The freezing of the main features and the transition into detailed design activities with significant industrial content provide the necessary conditions for deriving well-founded, robust cost estimates.

The ongoing detailed design studies are directly linked to R&D progress in order to include their results; the design of auxiliary heating systems and of diagnostics for ITER are some obvious examples [13],[14].

Only a very small number of design issues yet remain at the conceptual level and task forces are at work to finalise options and recommend a choice. They concern:

- the possible improvement to the CS reference design by splitting the coil into separated modules;
- the blanket module attachment to the backplate, including its water cooling connection;
- the possible introduction of ferritic inserts in the VV to reduce the TF ripple;
- the control of cooling systems (primary water heat transfer and cryogenic plant) to cope with the consequences of the tokamak pulsed operation.

5. SAFETY

The ultimate objectives of developing fusion as a practical and successful energy source must certainly involve realising its potential to be safe and environmentally benign. ITER, as the first experimental fusion reactor with a reactor relevant neutron flux and radioactive inventories, must demonstrate a fully safe operation, with a high level of protection of the health and safety of the work force and the general public and without significant environmental impacts.

The ITER EDA include a vigorous design and assessment activity to ensure the safety and environmental attractiveness of ITER so that it can be sited in any of the ITER Parties with a minimum of site-specific redesign. In this activity, detailed safety-related design requirements have been established based on internationally recognized safety criteria and limits.

A comprehensive safety and environmental assessment has recently been completed for the ITER Design, documented in detail in the Non-Site Specific Safety Report (NSSR-1) and reported in [15]. It was concluded that the ITER design meets successfully all the safety-related requirements that were established.

However, as a research facility, ITER requires flexibility in operation and acceptance of inevitable uncertainties in plasma behaviour, and should be prepared for possible changes of components and scenarios during its lifetime. This means that some safety issues are specific to the design choice of ITER as an experimental machine, e.g. relatively high activation of in-vessel components made of SS316LN, and not necessarily representative of a future fusion reactor. Even so, the safety analysis shows that the design can provide a robust safety envelope, by using well-established concepts of defence in depth and multiple lines of defence against postulated accidents. This achievement relies heavily on the basic favourable safety characteristics of magnetic fusion, mainly intrinsic fail-safe termination of fusion power with off-normal conditions from the auxiliary environment and low decay heat density which cannot melt the structure in case of any loss of coolant. Even more important, mobilizable inventories of radioactive materials in ITER, tritium and activated metallic dust from plasma-wall interaction or from corrosion by water coolant, are such that effluents and emissions during normal operation and envisaged accident sequences are low. Even for the ultimate case of a hypothetical "worst event" accident, the ground-level emission from "at risk" radioactive inventories will result in an early dose lower than 50 mSv under average weather conditions: the objective of no off-site evacuation is met.

6. TECHNOLOGY RESEARCH AND DEVELOPMENT

Technology R&D for ITER is now focused on seven critical areas, each the subject of a large project aimed at validating key aspects of the ITER design, including development and verification of industrial level manufacturing techniques.

The so-called "Seven Large Projects" share certain common features. They are typically multi-stage activities involving multiple Party contributions and cross-dependencies, and high industrial content. Each has a unified management structure and organization in which Project responsibility is shared between the JCT and the Home Teams, with one (or, in one case, two) Home Team(s) designated to take a lead role in overall coordination of the project.

Two of the Projects are directed towards developing superconducting magnet technology to a level that will allow the various ITER magnets to be built with confidence. The Central Solenoid Model Coil Project [16] and the Toroidal Field Model Coil Project [17] are intended to drive the development of the ITER full-scale conductor including strand, cable, conduit and terminations, and to integrate the supporting R&D programmes on insulators; joints; conductor ac losses and stability; Nb_3Sn conductor wind, react and transfer processes; and quality assurance. In each case the Home Teams concerned are collaborating to produce relevant scale model coils and associated mechanical structures for installation and testing in dedicated facilities – the CS Model Coil in Japan and the TF Model Coil in the EU.

Three Projects focus on key in-vessel components, including development and demonstration of necessary fabrication technologies and initial testing for performance and assembly/integration into the tokamak system. In the Vacuum Vessel Sector Project [18] , the main objective is to produce a full scale sector of the ITER vacuum vessel, and to undertake initial testing of mechanical and hydraulic performance. The Blanket Module Project [19] is aimed at producing and testing full scale modules of primary wall, limiter, and baffle type, and full scale, partial prototypes of coolant manifolds and backplate, and at demonstrating prototype integration in a model segment. The Divertor Cassette Project [20] aims to demonstrate that a divertor can be built within tolerances and to withstand the thermal and mechanical loads imposed on it during normal operation and during transients such as ELM's and disruptions. To this end, a full size prototype is being built and tested. Because of the consequences of erosion of the plasma facing materials, the project also includes tasks to understand erosion mechanisms, to develop methods of dust removal and of outgassing tritium codeposited with Be or C, and to demonstrate the feasibility of plasma spray as a possible means for in-vessel repair of armour.

The last two of the Large Projects focus on ensuring the availability of appropriate remote handling technologies which allow intervention on reasonable timescales so as to provide the flexibility needed for ITER to pursue its scientific and technical goals. The Blanket Module Remote Handling Project [21] is aimed at demonstrating that the ITER Blanket modules can be replaced remotely. This involves proof of principle and related tests of remote handling transport scenarios including opening and closing of the vacuum vessel and of the use of a transport vehicle on a monorail for the installation and removal of blanket modules. In the Divertor Remote Handling Development [22] the main objective is to demonstrate that the ITER divertor can be maintained and replaced remotely and that divertor cassettes can be remotely refurbished in a Hot Cell. This involves the design and manufacture of full scale prototype remote handling equipment and tools and their testing in a Divertor Test Platform (to simulate a portion of the divertor area of the tokamak) and a Divertor Refurbishment Platform to simulate the refurbishment facility.

In view of ITER's mission to test DEMO-relevant fusion blanket modules, the Parties are developing their own plans for breeding blanket module design and construction for test in ITER [23]. In addition, it is expected that ITER will itself require a breeding blanket to ensure an adequate supply of tritium fuel during the later (Enhanced Performance) Phase of operations. The planning for breeding blanket development and of testing programmes in ITER is proceeding in a coordinated way with the oversight of a Test Blanket Working Group in which the Parties and the JCT are represented.

The technical output from the Seven Large R&D Projects has direct importance in the validation of the ITER Design and in supporting the manufacturing cost estimates for some key cost drivers. But the Projects also have a more general importance as exemplars of cross-Party complex ventures and hence as precursors to possible joint construction activities. Already they have provided valuable organizational experience especially in achieving clear project management arrangements in terms of responsibilities, authority and liaison across the JCT, Home Teams and industries involved. Successful performance of the Large Projects within such an organizational framework will provide lessons for, and increase confidence in, proposals for construction.

7. CONCLUDING REMARKS

For planning purposes it is assumed that the ITER EDA is taking place with a view to construction starting as soon as practicably possible after the end of the EDA. The Work Programme and Schedule for the EDA is therefore a time-limited subset of a more extensive technical schedule for the Project which sets timetable, resources and related logic for all the design, engineering and R&D activities necessary to carry ITER through procurement and construction and to reach first plasma by the end of 2008.

The deliverables expected at the end of the EDA are set to serve this schedule, allowing a transition directly into a "just in time" construction procurement process in which the longest lead time items should be ready for call for tender by the end of the EDA. The other time critical element in the first phases of construction will be the site-specific design detailing and modifications and the site-specific safety and environmental analyses needed to support host regulatory procedures.

It follows that much of the technical work undertaken during the EDA is expected to continue without interruption after July 1998. In particular, the continuation of the key technology testing programmes and the further refinement of the physics understanding will be essential features of post-EDA activities.

In December 1995, after approving the IDR Package the ITER Council reaffirmed its position "that a next step such as ITER is a necessary step in the progress towards fusion energy, that its objectives are valid and timely; that the quadripartite cooperation has shown to be an efficient frame to achieve the ITER objectives, and that the right time for such a step is now".

The recent progress reported to this Conference reinforces this position. Given the well-founded plans for continued collaborative work over the remainder of the EDA, there is every reason to be confident that the potential participants in construction will indeed be in a position to take a positive construction decision with full assurance in the engineering design and parameters and the cost estimate of ITER.

REFERENCES

[1] ITER EDA Agreement and Protocol 2, ITER EDA Documentation Series No. 5, IAEA, Vienna (1994).
[2] ITER Interim Design Report Package Documents, ITER EDA Documentation Series No. 10, IAEA, Vienna (1996).
[3] Technical Basis for the ITER Interim Design Report, Cost Review and Safety Analysis, ITER EDA Documentation Series No. 7, IAEA, Vienna (1996).
[4] ITER Council Proceedings: 1992, ITER EDA Documentation Series No. 3, IAEA, Vienna (1994).
[5] PUTVINSKI, S., et al., IAEA-CN-64/F-1, these Proceedings, Vol. 2.
[6] TAKIZUKA, T., et al., IAEA-CN-64/F-5, ibid.
[7] PERKINS, F.W., et al., IAEA-CN-64/FP-24, ibid.
[8] JANESCHITZ, G., et al., IAEA-CN-64/F-2, ibid.
[9] KUKUSHKIN, A., et al., IAEA-CN-64/FP-27, ibid.
[10] BOUCHER, D., et al., IAEA-CN-64/FP-22, ibid.
[11] ROSENBLUTH, M., et al., IAEA-CN-64/FP-26, ibid.
[12] HAANGE, R., et al., IAEA-CN-64/FP-14, ibid.
[13] BOSIA, G., et al., IAEA-CN-64/FP-17, ibid;
HEMSWORTH, R., et al., IAEA-CN-64/FP-18, ibid.
[14] COSTLEY, A., et al., IAEA-CN-64/FP-28, ibid.
[15] SHIMOMURA, Y., et al., IAEA-CN-64/F-3, ibid.
[16] JAYAKUMAR, R., et al., IAEA-CN-64/FP-12, ibid.
[17] SALPIETRO, E., et al., IAEA-CN-64/FP-13, ibid.
[18] KOIZUMI, K., et al., IAEA-CN-64/FP-8, ibid.
[19] DÄNNER, W., et al., IAEA-CN-64/FP-9, ibid.
[20] ULRICKSON, M.A., et al., IAEA-CN-64/FP-4, ibid.
[21] KAKUDATE, S., et al., IAEA-CN-64/FP-15, ibid.
[22] MAISONNIER, D., et al., IAEA-CN-64/FP-16, ibid.
[23] GOHAR, Y., et al., IAEA-CN-64/FP-10, ibid.

PHYSICS OF HIGH PERFORMANCE DEUTERIUM–TRITIUM PLASMAS IN TFTR*

K.M. McGUIRE, C.W. BARNES[1], S.H. BATHA[2], M.A. BEER, M.G. BELL, R.E. BELL, A. BELOV[3], H.L. BERK[4], S. BERNABEI, M. BITTER, B.N. BREIZMAN[4], N.L. BRETZ, R.V. BUDNY, C.E. BUSH[5], J.D. CALLEN[6], S. CAUFFMAN, C.S. CHANG[7], Z. CHANG, C.Z. CHENG, G.A. COTTRELL[8], D.S. DARROW, R.O. DENDY[9], W. DORLAND[4], H. DUONG[10], P.C. EFTHIMION, D. ERNST[11], H. EVENSON[6], N.J. FISCH, R. FISHER[10], R.J. FONCK[6], C.B. FOREST[10], E.D. FREDRICKSON, G.Y. FU, H.P. FURTH, V.Ya. GOLOBOROD'KO[12], N.N. GORELENKOV[3], B. GREK, L.R. GRISHAM, G.W. HAMMETT, G.R. HANSON[5], R.J. HAWRYLUK, W.W. HEIDBRINK[13], H.W. HERRMANN, M. HERRMANN[5], K.W. HILL, J. HOGAN[5], B. HOOPER[14], J.C. HOSEA, W.A. HOULBERG[5], M. HUGHES[15], R.A. HULSE, D.L. JASSBY, F.C. JOBES, D.W. JOHNSON, R. KAITA, S.M. KAYE, J. KESNER[11], J.S. KIM[7], M. KISSICK[6], A.V. KRASILNIKOV[3], H.W. KUGEL, A. KUMAR[16], N.T. LAM[7], P. LaMARCHE, B. LeBLANC, F.M. LEVINTON[2], C. LUDESCHER, J. MACHUZAK[11], R. MAJESKI, J. MANICKAM, D.K. MANSFIELD, M.E. MAUEL[17], E. MAZZUCATO, J. McCHESNEY[11], D.C. McCUNE, G. McKEE[6], D.M. MEADE, S.S. MEDLEY, R. MIKA, D.R. MIKKELSEN, S.V. MIRNOV[3], D. MUELLER, Y. NAGAYAMA[18], G.A. NAVRATIL[17], R. NAZIKIAN, M. OKABAYASHI, D.K. OWENS, H.K. PARK, W. PARK, P. PARKS[10], S.F. PAUL, M.P. PETROV[19], C.K. PHILLIPS, M. PHILLIPS[15], P. PHILLIPS[4], A.T. RAMSEY, M.H. REDI, G. REWOLDT, S. REZNIK[12], J.H. ROGERS, A.L. ROQUEMORE, E. RUSKOV[13], S.A. SABBAGH[17], M. SASAO[18], G. SCHILLING, J. SCHIVELL, G.L. SCHMIDT, S.D. SCOTT, I.B. SEMENOV[3], T. SENKO, S. SESNIC, C.H. SKINNER, T. STEVENSON, W. STODIEK, J.D. STRACHAN, E.J. STRAIT[10], B.C. STRATTON, E.J. SYNAKOWSKI, H. TAKAHASHI, W.M. TANG, G. TAYLOR, J.L. TERRY[11], M.E. THOMPSON, S. VON GOELER, A. VON HALLE, R.T. WALTERS, S. WANG[20], R.B. WHITE, R.M. WIELAND, M. WILLIAMS, J.R. WILSON, K.L. WONG, G.A. WURDEN[1], M. YAMADA, V. YAVORSKI[12], K.M. YOUNG, L.E. ZAKHAROV, M.C. ZARNSTORFF, S.J. ZWEBEN

Plasma Physics Laboratory,
Princeton University,
Princeton, New Jersey,
United States of America

Abstract

PHYSICS OF HIGH PERFORMANCE DEUTERIUM–TRITIUM PLASMAS IN TFTR.

During the past two years, deuterium–tritium (D–T) plasmas in the Tokamak Fusion Test Reactor (TFTR) have been used to study fusion power production, isotope effects associated with tritium fueling, and alpha-particle physics in several operational regimes. The peak fusion power has been increased to 10.7 MW in the supershot mode through the use of increased plasma current and toroidal magnetic field and extensive lithium wall conditioning. The high internal inductance (high-l_i) regime in TFTR has been extended in plasma current and has achieved 8.7 MW of fusion power. Studies of the effects of tritium on confinement have now been carried out in ohmic, NBI- and ICRF-heated L-mode and reversed shear plasmas. In general, there is an enhancement in confinement time in D–T plasmas which is most pronounced in supershot and high-l_i discharges, weaker in L-mode plasmas with NBI and ICRF heating and smaller still in ohmic plasmas. In reversed shear discharges with sufficient deuterium NBI heating power, internal transport barriers have been observed to form, leading to enhanced confinement. Large decreases in the ion heat conductivity and particle transport are inferred within the transport barrier. It appears that higher heating power is required to trigger the formation of a transport barrier with D–T NBI and the isotope effect on energy confinement is nearly absent in these enhanced reversed shear plasmas. Many alpha-particle physics issues have been studied in the various operating regimes, including confinement of the alpha particles, their redistribution by sawteeth, and their loss due to MHD instabilities with low toroidal mode numbers. In weak shear plasmas, alpha-particle destabilization of a toroidal Alfvén eigenmode has been observed.

---

* Supported by US Department of Energy contract DE-AC02-76CHO-3073.

[1] Los Alamos National Laboratory, Los Alamos, New Mexico, USA.
[2] Fusion Physics and Technology, Torrance, California, USA.
[3] Troitsk Institute of Innovative and Thermonuclear Research, Moscow, Russian Federation.
[4] Institute for Fusion Studies, University of Texas, Austin, Texas, USA.
[5] Oak Ridge National Laboratory, Oak Ridge, Tennessee, USA.
[6] University of Wisconsin, Madison, Wisconsin, USA.
[7] Courant Institute, New York University, New York, N.Y., USA.
[8] JET Joint Undertaking, Abingdon, Oxfordshire, UK.
[9] Culham Laboratory, Abingdon, Oxfordshire, UK.
[10] General Atomics, San Diego, California, USA.
[11] Massachusetts Institute of Technology, Cambridge, Massachusetts, USA.
[12] Ukrainian Institute of Nuclear Research, Kiev, Ukraine.
[13] University of California, Irvine, California, USA.
[14] Lawrence Livermore National Laboratory, Livermore, California, USA.
[15] Northrop–Grumman Corporation, Princeton, New Jersey, USA.
[16] University of California, Los Angeles, California, USA.
[17] Columbia University, New York, N.Y., USA.
[18] National Institute for Fusion Science, Nagoya, Japan.
[19] A.F. Ioffe Physico-Technical Institute, St. Petersburg, Russian Federation.
[20] Institute of Plasma Physics, Academia Sinica, Hefei, Anhui, China.

1. INTRODUCTION

The primary objective of TFTR has been to explore and understand the physics governing plasma confinement and stability under conditions approaching those in the core of a fusion power reactor. Since operation with deuterium-tritium (D-T) fuel began in 1993, over 841 D-T discharges producing 1.2 GJ of fusion energy have been made for systematic investigations of fusion performance, effects associated with the use of tritium, and alpha-particle physics in a variety of operating regimes. These range from L-mode to enhanced performance regimes, including supershots, the high internal inductance (high-l_i) regime, the H-mode and the new enhanced reverse shear regime. These experiments have revealed important effects associated with the use of tritium and the behavior of alpha particles.

We begin by describing the confinement and stability properties of the high-performance operational regimes used in the D-T campaigns on TFTR. This will be followed by discussions of the effects due to the tritium fuel and the physics of alpha particles.

The plasmas in these experiments were run at a major radius of 2.45 – 2.62 m, minor radius 0.80 – 0.97 m, toroidal field at the plasma center 4.0 – 6.0 Tesla, and plasma current 0.6 – 2.7 MA. The plasma boundary is defined by a large-area toroidal limiter composed of carbon-composite tiles in high heat flux regions and graphite tiles elsewhere. Deuterium and tritium neutral beams with energies up to 115 keV were injected to heat and fuel the plasma with a total injected power up to 39.5 MW. ICRF power up to 8 MW has been used. A description of TFTR and of the tritium processing systems is given in [1] and references therein.

2. FUSION POWER PRODUCTION

2.1 Regimes of operation

The D-T experimental program in TFTR has focused on operating conditions which produce substantial fusion power, and hence can be used to study alpha-particle and other D-T related issues in reactor relevant conditions.

The first high-power D-T experiments were performed in supershot discharges [2]. Since then, the peak fusion power in TFTR has been extended to 10.7 MW in supershot discharges [3], as shown in Fig. 1. In other discharges designed to extend the duration of the fusion pulse, 6.5 MJ of fusion energy per pulse has been obtained. The most significant change responsible for the increase in peak fusion power has been increasing the toroidal magnetic field to 5.6 T and the plasma current to 2.7 MA in order to increase plasma stability [4]. To obtain supershots at this high current requires coating the inner limiter with lithium to suppress recycling. New techniques of lithium deposition *in situ* have been developed [5]. Lithium pellet conditioning of the limiter has now produced a confinement time τ_E = 0.33 s in a supershot with 17 MW of tritium neutral

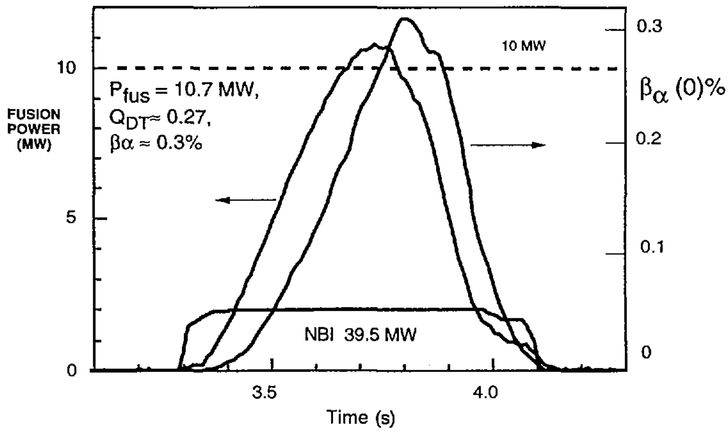

FIG. 1. Time evolution of the D-T fusion power and β_α from a shot producing the highest instantaneous power of 10.7 MW at 39.5 MW of input power for an instantaneous Q of 0.27.

beam heating, resulting in a record fusion triple product $n_i \cdot T_i \cdot \tau_E^* = 8.3 \times 10^{20}\,m^{-3} \cdot keV \cdot s$, where $\tau_E^* = W_{tot}/P_{heat}$. A similar plasma with D-T neutral beam heating achieved a global Q (= P_{fus}/P_{heat}) of 0.27 and a central Q of 0.6 – 0.7 with 21 MW of neutral beam heating.

As will be discussed below, the maximum stored energy and hence fusion power in supershot discharges is limited by the onset of MHD instabilities. This has motivated the development of other advanced tokamak regimes, in particular the high-l_i and reverse shear regimes, in which the current and pressure profile are modified to improve MHD stability limits[6,7].

Previously, Sabbagh *et al.* [8] reported the achievement of high values of normalized-β, β_n, and fusion power at high l_i produced by ramping down the plasma current, demonstrating the potential for increased stability. A new technique has been pioneered on TFTR [9] for generating high-l_i plasmas at high current, up to 2.3 MA, by forming a plasma at low edge-q, < 2.5, increasing the current at constant q and then rapidly expanding the cross section at essentially constant current to produce a final edge q of 4 - 4.5 at the start of high power NBI heating. With extensive limiter conditioning by lithium pellet injection, confinement has been improved in these plasmas such that P_{fus} = 8.7 MW has been attained at modest parameters (2 MA, 4.8 T).

Plasmas with reversed magnetic shear ($\partial q/\partial r < 0$) over the inner half of the minor radius have been produced in TFTR by rapidly ramping up the plasma current at maximum plasma cross-section while heating with NBI at power levels up to about 10 MW to inhibit resistive penetration of the current[10,11]. The co- and counter- tangential NBI during this "prelude" phase also provides current drive for control of the final q-profile. After forming a reversed shear plasma, the NBI heating power is generally increased to study the confinement and stability properties. In this high-power phase, spontaneous transitions to a new enhanced confinement regime, the Enhanced Reverse Shear (ERS) regime, have been observed when the NBI exceeds a power threshold, typically 18 - 20 MW for deuterium NBI in 1.6 MA plasmas. The ERS transition generally occurs after 0.2 – 0.3 s of high-power NBI. ERS plasmas exhibit a very rapid density increase in the shear-reversed region, achieving $n_e(0) = 1.2 \times 10^{20}\,m^{-3}$ with $T_i(0) \approx 24$ keV, $T_e(0) \approx 8$ keV, and a pressure peaking factor, $p(0)/\langle p\rangle \approx 7$, where $\langle p\rangle$ is the volume-average pressure. In recent experiments, very steep electron temperature gradients ($\partial T_e/\partial r > 50$ keV/m) have also been observed in the region of the transport barrier in some conditions. The ERS plasmas have been brought to nearly steady-state conditions by reducing the NBI power to a low level, typically 5 – 10 MW, for up to 0.5 s in what is termed the "postlude" NBI phase.

Two interesting observations have been made concerning the threshold power for the ERS transition. The first is that injection of a lithium pellet before or coincidentally with the high-power NBI can trigger an ERS transition at lower power. This technique has been used to trigger transitions in high-current, 2.2 MA, reverse-shear discharges where the intrinsic threshold power appears to be higher. The second is that the ERS threshold power for 1.6 MA plasmas appears to be much higher for tritium NBI than deuterium. This has so far limited the range of D:T mixture accessible for studying fusion power production in ERS plasmas, because of lithium dilution of the hydrogenic species in the plasma core. The profiles of q and plasma β for supershots, high-l_i and reverse shear modes are compared in Fig. 2. Table 1 gives a summary of a set of high performance TFTR shots which include a supershot, lithium assisted supershot, high-li shot and an enhanced reversed shear plasma.

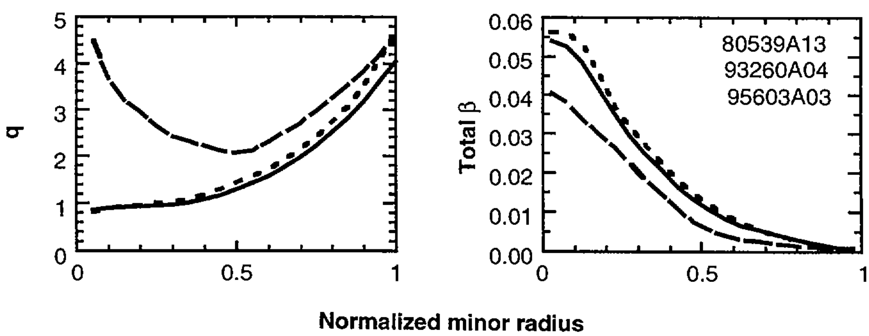

FIG. 2. Experiments in 1995–1996 have explored three high-confinement regimes. The solid curves are for supershots with $\beta_{n max} \leq 2$ which resulted in 10.7 MW of fusion power. The short dashed curves are for high l_i discharges with $\beta_{n max} \geq 2.3$ and P_{DT} = 8.7 MW, and the long dashed curves are for an enhanced reversed shear discharge with $\beta_{n max} < 2.0$.

TABLE I. SUMMARY OF HIGH PERFORMANCE TFTR SHOTS

	Supershot 80539A12	Li assisted 83546A15	High-l_i 95603A02	ERS 88170A51
I_p (MA)	2.7	2.3	2.0	1.6
B_t (T)	5.6	5.5	4.8	4.6
P_{NB} (MW)	39.6 (D–T)	17.4 (T only)	35.5 (D–T)	28.1 (D only)
$n_T/(n_D + n_T)(0)$	0.47	0.58	0.42	0
$n_e(0)$ ($10^{19}/m^3$)	10.2	8.5	6.9	9.0
$n_{hyd}(0)$ ($10^{19}/m^3$)	6.7	6.6	6.0	7.0
$Z_{eff}(0)$	2.4	2.0	1.6	2.1
$T_e(0)$ (keV)	13.0	12.0	8.0	8.0
$T_i(0)$ (keV)	36	43	45	25
W (MJ)	6.9	4.9	5.7	3.9
dW/dt (MW)	0.0	3.0	8.5	3.0
τ_E (s)	0.180	0.340	0.165	0.150
$\tau_E^* = W/P_{NB}$ (s)	0.174	0.28	0.161	0.139
$\tau_{ITER\text{-}89P}$ (s)	0.095	0.119	0.074	0.073
$\tau_E/\tau_{ITER\text{-}89P}$	1.89	2.86	2.23	2.05
$n_{hyd}(0)T_i(0)\tau_E$ (10^{20} m^{-3}·keV·s)	4.3	9.6	4.5	2.6
$n_{hyd}(0)T_i(0)\tau_E^*$ (10^{20} m^{-3}·keV·s)	4.2	8.0	4.4	2.4
P_{fus} (MW)	10.7	2.8	8.7	0
P_{fus}/P_{NB}	0.27	0.16	0.25	0
β_{norm}(mag) (%mT/MA)	1.83	1.35	2.50	1.95
β_{norm}(TRANSP)	1.83	1.5	2.40	1.95
β^*_{norm}(TRANSP)	2.99	3.0	3.9	3.7
κ	1.1	1.1	0.975	0.978
q_{cycl}	3.07	3.61	3.57	5.0
q^*	3.22	3.79	3.47	5.0

2.2 Confinement

2.2.1 Confinement in supershots and high-l_i plasmas

The supershot regime is characterized by peaked density and pressure profiles, and confinement enhancements up to ~3 times ITER-89P scaling. To obtain supershot confinement, it is essential to maintain low edge recycling and neutral beam deposition in the plasma center. In the core of supershots, the apparent thermal diffusivity is reduced and thermal transport becomes dominated by convective losses due to the radial particle flux which remains significantly larger than neoclassical theory. [12]

The confinement characteristics of the high-l_i plasmas are quite similar to those of supershots. In particular, it is necessary to control recycling to achieve good confinement in this regime also. In the 1996 experiments, attempts to extend the fusion performance further were constrained by the power handling capability of the bumper limiter. With the level of limiter conditioning achieved in 1996, at NBI powers in excess of 30 MW and stored energies above about 6 MJ the recycling of hydrogen isotopes increased dramatically during the NBI heating pulse, causing a reversion to L-mode confinement. We have begun to explore the use of krypton or xenon puffing to form a radiating layer at boundary in order to distribute the heat load on the limiter, thereby increasing its power handling ability.

2.2.2 Confinement in reverse shear

The confinement characteristics of reversed shear plasmas with modest heating power also resemble supershots with the same machine parameters. In ERS plasmas, however, the inferred electron particle diffusivity in the region of the steepest gradient drops by a factor of 10 - 50 to near-neoclassical levels, while the ion thermal diffusivity falls to levels well below predictions from conventional neoclassical theory [10,13]. The likely explanation for the inferred sub-neoclassical ion thermal diffusivity is the violation of the assumptions of standard neoclassical theory. Recent calculations by Lin *et al.* [14] indicate that a more comprehensive analysis of neoclassical transport which considers orbit dimensions comparable with pressure scale lengths is in better agreement with the data in the enhanced confinement regime. In addition, ion orbit squeezing, due to the large inferred radial electric fields, has recently been calculated to reduce the neoclassical ion transport.[15] Inasmuch as neoclassical transport is usually considered to be the minimum transport possible in a tokamak, these results represent a dramatic improvement in confinement and performance.

The present necessity of injecting lithium pellets at the start of high-power NBI in order to produce ERS transitions in high-current reverse-shear plasmas, coupled with the excellent particle confinement following the transition, has caused significant dilution of the hydrogenic species in 2.2MA ERS plasmas. As a result, the DD neutron rate for these plasmas is significantly depressed compared to supershots at similar parameters. Consequently, tritium NBI has not yet been used in high-current (2.2MA) ERS plasmas.

2.3 Stability

2.3.1 Stability in Supershot plasmas

The D-T fusion power in TFTR supershots is limited by pressure driven instabilities which can cause major or minor disruptions. At high plasma currents, > 2 MA, and toroidal magnetic field, >5 T, the limiting value of β_n is ~1.9. A weak inverse scaling of this limit with toroidal field is seen; $\beta_n \propto B_{tor}^{-(0.2-0.4)}$. The neoclassical tearing modes which limited operation at lower current [16] have been largely absent at higher current, and are thus not responsible for this dependence of the beta limit on the toroidal field. The stability limit in supershot plasmas appears to be set by a combination of global kink modes which may be coupled to toroidally localized ballooning modes [17,18,19]. The kink mode can locally decrease the magnetic shear and increase the local pressure gradient so that the ballooning mode becomes destabilized. While this phase can be well modeled by a 3-dimensional MHD code, MH3D, the stability of the n=1 ideal kink with q(0)<1 is still not understood.

2.3.2 Stability in High-l_i (internal inductance) plasmas

The high-l_i plasma producing 8.7 MW of fusion power disrupted at β_N = 2.35, significantly higher than in supershots at similar parameters. This limit is in good agreement with PEST modeling. The stability of these plasmas is discussed in papers by Sabbagh [9] and Manickam [20]. If the influx from the limiter can be controlled and adequate confinement maintained, it should be possible to increase the fusion performance of the 2.3MA, high-l_i plasmas substantially.

2.3.3 Stability in Reversed Shear plasmas

The investigation of reversed shear plasmas was originally motivated in part by theoretical predictions that such plasmas would have improved stability [21]. In these experiments, a new regime of improved confinement was discovered. Reversed shear plasmas at a moderate plasma current, 1.6MA, have been studied to test the theoretical modeling of stability. The core region of these plasmas does appear to be robustly stable to pressure driven modes. However, performance is still limited by pressure driven modes in the weak shear region. This is particularly a problem in the Enhanced Reverse Shear (ERS) discharges where the strong transport barrier creates a steep pressure gradient. This pressure gradient typically forms near the minimum in q, but during the evolution of the plasma the pressure gradient tends to propagate outwards while the low-shear region moves inwards as the current profile evolves on a resistive timescale. In these circumstances, pressure driven modes can develop. These are believed to be infernal modes [20], but in at least one case the infernal mode was coupled to a moderate n, toroidally localized ballooning mode, similar to what occurs in supershot disruptions [22]. Theoretical modeling of the stability with the PEST code has suggested various approaches towards extending this regime to higher currents and higher performance. The capability to control simultaneously the evolution of the q profile (through current drive) and the pressure profile (through manipulation of the transport barrier) will be necessary to develop the full potential of this regime.

2.4 Projection of D-T performance

The expected fusion reactivity enhancement in D-T plasmas over their deuterium counterparts can be estimated from the ratio of the velocity-weighted fusion cross-sections for DT and DD reactions. For fixed fuel density and temperatures the fusion power ratio, P_{D-T}/P_{D-D}, of purely thermal reactions reaches an idealized maximum of ~225 for T_i ~ 12 keV but the ratio falls to 150 at T_i = 30 keV. In plasmas with a significant population of non-thermal fuel ions from neutral beam injection, the beam-target reactivity enhancement also drops for T_i above 15 keV. The measured ratio of fusion power in TFTR supershots is ~115 if plasmas with the same stored energy are compared. When comparing plasmas with the same heating power, the isotope effect on confinement (Sec. 3.2) raises the DT fusion power and the fusion power ratio is ~140. Furthermore, the highest neutral beam power can be achieved with D-T operation due to the higher neutralization efficiency of tritium. As a result of this increase in power, the highest DT fusion power is actually 165 times the highest DD fusion power achieved in TFTR. However, it should be noted that to achieve this power ratio, the plasma energy increased from 5.6 MJ in the D plasma to 7.0 MJ in the D-T plasma. This emphasizes the importance of improving stability limits to achieving high fusion performance and demonstrates that the extrapolation of the highest performance D-only results, which are often stability or power handling limited, to D-T plasmas is not a simple matter of species substitution in numerical simulation codes.

3. EFFECTS DUE TO TRITIUM

3.1 Tritium transport

Tritium operation on TFTR has allowed the measurement of the local tritium density from the 14 MeV t(d,n)α neutron emissivity profile measured with collimated neutron detectors [23,24]. Tritium transport has been studied with this diagnostic technique by puffing a small amount of tritium gas into plasmas heated by deuterium NBI. Initially, tritium and helium transport were studied in low-recycling, high-performance supershots [25]. The diffusivity profiles of helium, tritium and heat were observed to be of similar magnitude and shape. This is a prominent characteristic of transport due to drift-like microinstabilities. The same helium transport coefficients successfully modeled the helium ash density in deuterium-tritium plasmas [26]. This similarity in diffusivities would allow helium ash removal in future reactors, such as ITER. Recently, helium and tritium transport measurements were performed in the steady-state "postlude" phase of ERS plasmas. The tritium profile remains hollow for a long time, > 0.15 s, and does not peak on axis. A transport barrier can be clearly observed that impedes tritium transport to the core. Helium has a similar density evolution.

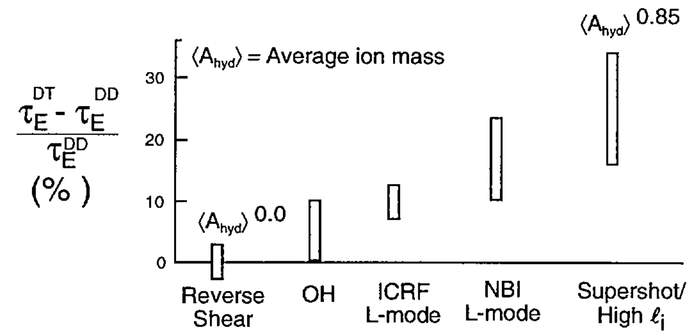

FIG. 3. Comparison of the percentage increase, in comparable D and D–T plasmas, for the confinement time in reverse shear, ICRF, OH L-mode, supershot and high-l_i regimes. The results are shown for an average mass of the hydrogenic ion of 2.5.

3.2 Isotope effect on confinement

The first D-T experiments in TFTR showed that the overall energy confinement in D-T supershots was significantly better than in comparable D-only plasmas.[27,28] This improvement is manifested by increased central ion and electron temperatures. In order to quantify the improvement and determine its origins, experiments with different D:T ratios have been carried out. The improvement in confinement, which is found to be primarily in the ion channel [12, 29], is associated with a reduction in the calculated ion thermal diffusivity by as much as a factor two.

Studies of the isotope effect have now also been carried out in ohmic, L-mode, reversed shear, and ICRF-heated plasmas.[30] The enhancement is most pronounced in supershot and high-l_i discharges, $\tau_E \propto \langle A\rangle^{0.85}$, where $\langle A\rangle$ is the average isotope mass of the plasma. NBI and ICRF heated L-mode plasmas show similar, weaker scaling: $\tau_E \propto \langle A\rangle^{0.3-0.5}$. In ohmic plasmas, the scaling is weak, $\tau_E \propto \langle A\rangle^{0.0-0.3}$, and it is essentially absent in ERS plasmas. Figure 3 shows a comparison of the isotope scaling in these TFTR regimes. Because of wall recycling, which is predominantly deuterium, the maximum value of $\langle A\rangle$ in these studies is 2.5. These results validate the assumed $\tau_E \propto \langle A\rangle^{0.5}$ scaling in regimes closest to proposed ITER operation ($T_i \sim T_e$, broad n_e, and significant heating to the electrons). However, these results are not consistent with gyro-Bohm scaling which remains an outstanding issue.

3.3 ICRF experiments

Ion cyclotron heating at the tritium second-harmonic frequency has potential applications for ITER. This scenario has been used previously to heat D-T supershots on TFTR [31,32,33,34]. Its effectiveness for heating an ohmic D-T target plasma, containing only thermal tritium, in the L-mode regime has now been demonstrated [33]. Heating efficiency was comparable to that obtained with neutral beam injection. This result indicates that good second-harmonic tritium heating should occur during the startup phase of ITER. In L-mode plasmas with T_i and T_e approximately equal, a favorable isotope scaling $\langle A \rangle^{0.5}$ was demonstrated going from D to D-T plasmas.

Fast wave direct electron heating of the postlude phase of ERS discharges has also been demonstrated [35]. ICRF power of 2 MW increased the central electron temperature by 2 keV. ICRF heating also sustained the highly peaked density and temperature profiles characteristic of ERS, delaying the transition out of ERS mode by approximately 100 ms.

Electron heating and current drive have also been demonstrated using the mode-converted ion Bernstein wave (IBW) in a mixed-species plasma [36]. This technique has been used to drive 125 kA on axis with 2 MW, and 100 kA off axis with 4 MW of RF power in D-^{4}He-^{3}He plasmas. Mode conversion heating in a D-T plasma has been demonstrated for the first time on TFTR. However, parasitic minority-ion absorption by a dilute ^{7}Li impurity introduced by wall coatings was significant, reducing the power coupled to electrons to 20 - 30% of the input level, in agreement with modeling. This poses a potential problem in ITER and other devices which use ^{9}Be wall facing materials.

Experiments in alpha channeling have indicated coupling of the mode converted IBW to fast-ions in D-T-^{3}He plasmas. Investigations which utilize coupling of the IBW to beam injected deuterons have verified essential details of the wave propagation physics, including the first evidence that the parallel propagation of the wave reverses away from the mode conversion surface. Inferred velocity space diffusion coefficients are of the order needed to achieve cooling of alpha particles [37].

4. PHYSICS OF ALPHA PARTICLES

4.1 Classical alpha confinement and thermalization

In an ignited D-T plasma, the alpha-particle power must be transferred to the thermal plasma before it is lost to the vacuum vessel wall. Alpha-particle confinement and loss has been measured in TFTR using several unique and novel alpha-particle diagnostics developed and implemented on TFTR [38].

The energy distribution of the alpha particles confined in the plasma has been measured in TFTR [39]. Alphas in the energy range 0.5 – 3.5 MeV have been detected through conversion to neutral helium by double charge-exchange in the high-density neutral cloud surrounding an ablating lithium pellet [40]. The pellet was injected after the end of NBI, to improve its penetration, but before the alpha population had decayed. The measured spectrum is compared with the TRANSP calculation in Fig. 4 and found to be in good agreement. The alpha spectrum in the lower energy range, 0.1 – 0.6 MeV, has been detected by absolutely calibrated spectrometry of charge-exchange recombination emission [41]. The intensities of the detected signals are within a factor 2 of calculations by TRANSP, based on purely classical slowing down processes.

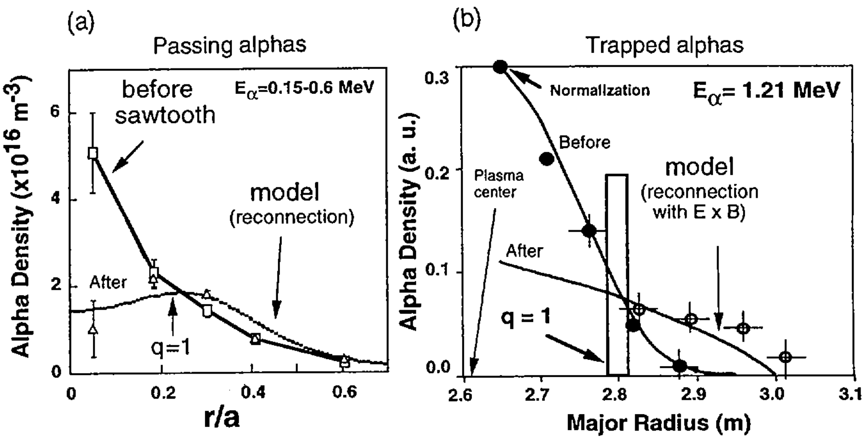

FIG. 4. Radial profiles of confined alphas near the center of TFTR as measured by (a) the Alpha-CHERS system for passing particles and (b) the pellet charge exchange (PCX) diagnostic. The profile just before the sawtooth crash is very peaked. The sawtooth crash significantly redistributes the alphas from inside to outside the $q = 1$ sawtooth inversion radius.

4.2 Effects of sawteeth

Measurements of the confined alpha distribution before and after a sawtooth crash were made with both confined alpha diagnostics, and the results are shown in Fig. 4. The alpha density on axis was reduced by as much as a factor 5 after the sawtooth crash [42]. The redistribution of the passing α-particles at the sawtooth as measured by the alpha-CHERS diagnostic with energies up to 0.6 MeV in a D-T plasma (Fig. 4a) was shown to be consistent with a relatively simple sawtooth mixing model which takes into account the reconnection of the magnetic flux which is presumed to occur at the sawtooth crash. Comparison of pellet charge exchange (PCX) measurements in the presence and absence of sawteeth in the period following the D-T heating phase indicate that the sawtooth activity transports trapped fast alphas radially outward as shown in Fig. 4b. This result cannot be explained by the conventional magnetic reconnection model for sawtooth mixing. Only the introduction of a helical electric field produced by the crash can explain the experimentally observed alpha redistribution [40].

4.3 Effects of MHD modes on the alpha particles

The first direct evidence of alpha particle loss induced by an MHD mode was due to a kinetic ballooning mode (KBM) in TFTR D-T experiments. The kinetic ballooning modes are driven by the sharp gradients in the plasma pressure profile and have localized ballooning characteristics. A significant enhancement, $\times$ 1.3 – 2, in alpha particle loss has been observed in some high-β D-T discharges. The loss enhancement correlates well with the appearance of high frequency (f $\approx$ 100 - 250 kHz), high-n ($\approx$ 6) KBM's driven by the plasma

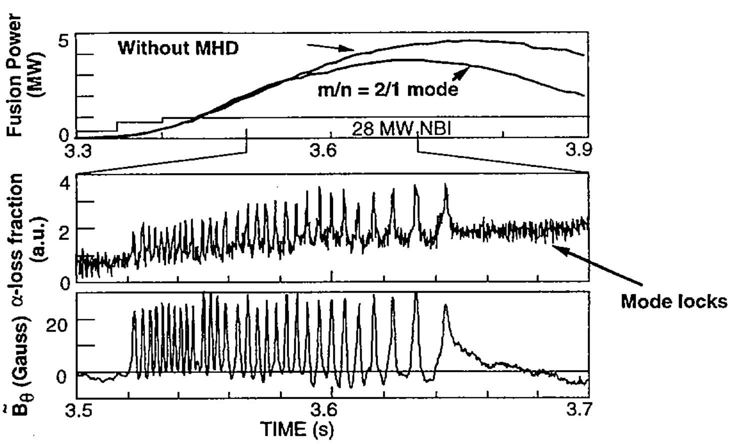

FIG. 5. With D–T operations, it is found that the alpha particle loss can be significant because of the presence of the neo-classical MHD modes.

pressure gradient [43]. Particle simulation shows that the observed alpha loss is induced by the wave-particle resonance. Similar KBM's are observed in D discharges, so the modes are not themselves driven by the alpha particles but by the pressure gradients in the plasma.

Enhancement in the loss of fusion alphas has been observed in high power D-T operation of TFTR in the presence of MHD activity. Sawteeth cause a strong, transient enhancement in the alpha loss at the time of the central crash. While the loss rate is transiently high, the net loss is small due to the short period of enhancement. Neoclassical tearing modes, as shown in Fig. 5, are also seen to enhance the alpha loss-rate. On the 60° alpha detector the loss may roughly double the first orbit loss. The detector signal itself is modulated at the frequency of the MHD mode, demonstrating that the loss is not toroidally symmetric; this may be important to ITER in designing plasma facing components. Stationary Magnetic Perturbations (SMP's), which are similar to locked modes, enhance the loss in a similar fashion to neoclassical tearing modes. The fusion alpha losses appear qualitatively similar to the fusion triton losses reported earlier. It is hoped to develop a quantitative understanding of these phenomena which could be applied to ITER.

4.4 Alpha driven TAE mode

The alpha-driven Toroidal Alfvén Eigenmode (TAE) had not been previously observed in supershot discharges at the highest fusion power and alpha concentration, consistent with theory. Recent theoretical calculations have shown that the predicted alpha-driven TAE threshold is sensitive to the q-profile and to the plasma β. This is potentially important in advanced tokamak regimes in which the core current profile is being modified to achieve higher stability. In

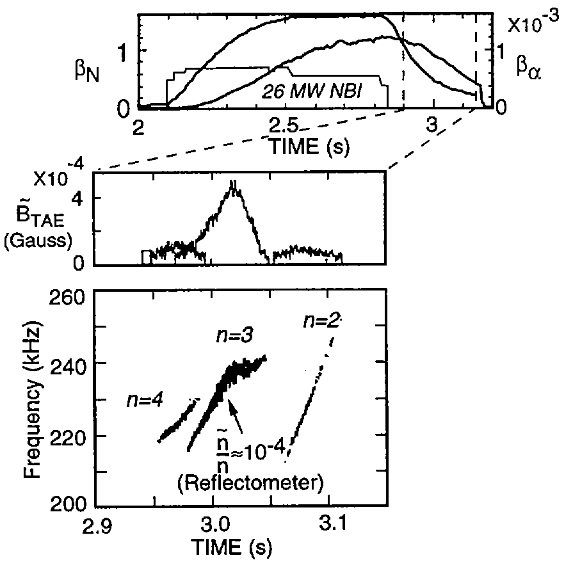

FIG. 6. Alpha-driven TAE in TFTR occurring ≈0.1 s after neutral beam injection in a D–T discharge with weak central magnetic shear. The frequency is consistent with the density-dependence TAE frequency, and mode timing is roughly consistent with theoretical predictions based on the beam ion damping.

recent experiments with weak magnetic shear, TAE's driven by energetic alpha-particles have been observed in TFTR D-T plasmas [44]. In Fig. 6, it is shown that these modes occur 100 – 300 ms following the end of NBI in plasmas with elevated central safety factor, q(0) = 1.1 – 2.5, and reduced central magnetic shear. The fusion power threshold is ~1.5 MW for q(0) ≈ 2.4 which corresponds to ~300 kW peak alpha power and $\beta_\alpha(0) \approx 10^{-4}$. Modes appear in the range 150 – 250 kHz with toroidal mode numbers n = 2, 3, 4, which are observed to propagate toroidally in the direction of the plasma current. From core reflectometer measurements, the dominant n = 3 mode is localized near r/a ≈ 0.3 – 0.4, which also coincides with the region of peak $\nabla\beta_\alpha$. The central β_α for the onset of mode activity is consistent with NOVA-K linear stability calculations [45] for alpha-driven TAE's in discharges with elevated q(0), low ion temperature (10 – 15 keV) and low beam-ion damping following the termination of neutral beam injection.

5. SUMMARY

TFTR has explored a wide range of physics issues in plasmas with high concentrations of tritium. Several possible advanced confinement regimes, supershot, high-l_i, and reversed shear, have been investigated using D-T and shown to have significant potential for reactors. In general, D-T plasmas have shown improved confinement compared to similar deuterium plasmas.

The fusion performance in TFTR supershots has been extended to 10.7 MW of peak power and 6.5 MJ of fusion energy per pulse. The most significant change responsible for the increase in fusion power has been operation at increased toroidal magnetic field, up to 5.5 T, and plasma current, up to 2.7 MA, and neutral beam heating power of 40 MW. Conditioning of the inner wall with lithium has improved the confinement to take advantage of the increased stability at higher field.

The high-current high-l_i regime has demonstrated good energy confinement and favorable MHD stability enabling the achievement of fusion power production comparable to that achieved in supershots at similar heating powers. The proven ability to achieve high values of β_N offers the potential of still higher values of fusion power in TFTR.

The formation of an internal transport barrier in the enhanced reverse shear regime has dramatically reduced the ion heat and particle flux from the core. This is accompanied by a substantial reduction in core plasma fluctuations and a steepening of the plasma pressure gradients. Future experiments will concentrate on understanding the physics of the barrier formation and on controlling the evolution of the barrier and the current profile to maintain stability.

ICRF heating schemes of importance to ITER have been validated and a new scheme for RF current drive through mode-conversion in a mixed-species plasma has been demonstrated. ICRF heating has been shown to sustain the ERS mode without particle fueling, which is important to the development of this operational regime. The interactions of energetic ions, including fusion alphas, with ICRF waves have been investigated and support the development of the alpha-channeling concept.

Fusion alpha particles have behaved classically for quiescent MHD plasmas. Sawteeth have been shown to redistribute fusion alphas near the plasma core. In discharges with weak magnetic shear, toroidal Alfvén eigenmodes driven by fusion alpha-particles have now been observed and found to be in accord with theoretical predictions.

ACKNOWLEDGEMENTS

TFTR has had many contributions from scientists and engineers both nationally and internationally. The authors express their appreciation to the technical, engineering and scientific staff who enabled the execution of these important D-T experiments on TFTR, and to R. C. Davidson for his support and encouragement.

This work is supported by US Department of Energy Contract DE-AC02-76-CH03073.

REFERENCES

[1] HAWRYLUK, R.J., et al., in Proc. 12th ANS Topical Mtg on the Technology of Fusion Energy, Reno, NV, 1996, and references therein.

[2] STRACHAN, J.D., et al., Phys. Rev. Lett. **72** (1994) 3526.
[3] McGUIRE, K.M., et al., Phys. Plasmas **2** (1995) 2176.
[4] BELL, M.G., et al., Nucl. Fusion **35** (1995) 1429.
[5] MANSFIELD, D.K., et al., Phys. Plasmas **3** (1995) 4252.
[6] JT-60 TEAM, in Plasma Physics and Controlled Nuclear Fusion Research 1994 (Proc. 15th Int. Conf. Seville, 1994), Vol. 1, IAEA, Vienna (1995) 31.
[7] JET TEAM, ibid., p. 51.
[8] SABBAGH, S.A., et al., ibid., p. 663.
[9] SABBAGH, S.A., et al., IAEA-CN-64/AP2-17, this volume.
[10] LEVINTON, F.M., et al., Phys. Rev. Lett. **75** (1995) 4417.
[11] NAVRATIL, G., in Controlled Fusion and Plasma Physics (Proc. 23rd Eur. Conf. Kiev, 1996), Vol. 20C, European Physical Society, Geneva (1996).
[12] ZARNSTORFF, M.C., et al., in Plasma Physics and Controlled Nuclear Fusion Research 1994 (Proc. 15th Int. Conf. Seville, 1994), Vol. 1, IAEA, Vienna (1995) 183.
[13] STRAIT, E.J., et al., Phys. Rev. Lett. **75** (1996) 4421.
[14] LIN, Z., et al., Phys. Rev. Lett. **78** (1997) 456.
[15] SHAING, K.C., Phys. Plasmas **1** (1994) 3365.
[16] CHANG, Z., et al., Phys. Rev. Lett. **74** (1995) 4663.
[17] FREDRICKSON, E.D., et al., Phys. Plasmas **2** (1995) 4216.
[18] PARK, W., et al., Phys. Rev. Lett. **75** (1995) 1763.
[19] FREDRICKSON, E.D., et al., Phys. Plasmas **3** (1996) 2620.
[20] MANICKAM, J., et al., IAEA-CN-64/A5-2, this volume.
[21] KESSEL, C., et al., Phys. Rev. Lett. **72** (1994) 1212.
[22] PARK, W., et al., IAEA-CN-64/D2-2, these Proceedings, Vol. 2.
[23] EFTHIMION, P.C., et al., Phys. Rev. Lett. **27** (1995) 85.
[24] EFTHIMION, P.C., et al., in Plasma Physics and Controlled Nuclear Fusion Research 1994 (Proc. 15th Int. Conf. Seville, 1994), Vol. 1, IAEA, Vienna (1995) 289.
[25] SYNAKOWSKI, E.J., et al., Phys. Fluids B **5** (1993) 2215.
[26] SYNAKOWSKI, E.J., et al., Phys. Rev. Lett. **75** (1995) 3689.
[27] HAWRYLUK, R.J., et al., Phys. Rev. Lett. **72** (1994) 3530.
[28] BUSH, C.E., et al., Phys. Plasmas **2** (1995) 2366.
[29] SCOTT, S.D., et al., Phys. Plasmas **2** (1995) 2299.
[30] SCOTT, S.D., et al., IAEA-CN-64/A6-6, this volume.
[31] TAYLOR, G., et al., in Plasma Physics and Controlled Nuclear Fusion Research 1994 (Proc. 15th Int. Conf. Seville, 1994), Vol. 1, IAEA, Vienna (1995) 431.
[32] MAJESKI, R., et al., ibid., p. 443.
[33] PHILLIPS, C.K., et al., Phys. Plasmas **2** (1995) 2427.
[34] MAJESKI, R.P., et al., Phys. Rev. Lett. **76** (1996) 764.
[35] ROGERS, J.H., et al., IAEA-CN-64/EP-2, these Proceedings, Vol. 3.
[36] MAJESKI, R.P., et al., Phys. Rev. Lett. **74** (1994) 2204.
[37] FISCH, N.J., et al., IAEA-CN-64/A2-3, this volume.
[38] ZWEBEN, S., et al., in Proc. 8th Int. Conf. on Plasma Physics, Nagoya, 1996, Plasma Phys. Control. Fusion (in press).
[39] FISHER, R.K., et al., Phys. Rev. Lett. **75** (1995) 846.
[40] PETROV, M.P., et al., IAEA-CN-64/A2-2, this volume.
[41] McKEE, G.R., et al., Phys. Rev. Lett. **75** (1995) 649.
[42] STRATTON, B., et al., Nucl. Fusion (in press).
[43] CHANG, Z., et al., Phys. Rev. Lett. **76** (1996) 1071.
[44] NAZIKIAN, R., et al., IAEA-CN-64/A2-4, this volume.
[45] FU, G.Y., et al., IAEA-CN-64/D2-6, these Proceedings, Vol. 2.

DISCUSSION

J. JACQUINOT: You have shown a strong density increase during discharges with internal confinement barriers. Can this be explained entirely by fuelling from the neutral beams?

K.M. McGUIRE: Yes, if we look at the TRANSP modelling, the beam fuelling in the centre is consistent with the density rise observed in the experiment.

S.I. ITOH: With respect to the ERS relaxation, you have reported that the back-transition coincides with the sudden growth of fluctuations. Supposing that the transition is triggered by the fluctuations, what is the time-scale for the increase of fluctuations?

K.M. McGUIRE: The time-scale for the increase of the fluctuations at the back-transition is approximately 40–60 ms.

S.I. ITOH: I have a question concerning the irreversibility of the back-transition, which relates to the controllability. Does the plasma recover the original high performance after the ERS relaxation?

K.M. McGUIRE: We do have examples where the plasma switches back and forth between the reverse shear mode and the enhanced reverse shear mode. Details can be found in the paper by E. Mazzucato et al. (IAEA-CN-64/AP2-16).

J.F. DRAKE: Since the ERS transport barrier tends to evolve into regions of either weak or positive magnetic shear, at the back-transition, how close is the plasma in the region of the barrier to the ideal MHD stability boundary?

K.M. McGUIRE: We find that at the back-transition the plasma is about 20–40% below the ideal boundary for low n kink modes and is moving away from the boundary because the plasma β is decreasing. We will check the stability for high n ballooning at the barrier location. Sometimes we do see double tearing modes later in time; these are associated with the shape of the q profile.

M. KEILHACKER: Could you elaborate a bit more on the power threshold for the ERS regime, its parameter dependence and the fact that it is higher in DT than in D plasmas.

K.M. McGUIRE: It takes at least 20% more neutral beam power to obtain ERS in DT than in D plasmas.

M. KEILHACKER: Do you have a physics picture of the processes underlying this threshold?

K.M. McGUIRE: At present, we do not have a good physics picture of the threshold in DT plasmas. However, we are studying the $\mathbf{E} \times \mathbf{B}$ shear flow in these plasmas (see the paper by S.D. Scott et al. (IAEA-CN-64/A6-6) for further details).

STEADY STATE OPERATION RESEARCH IN JT-60U

K. USHIGUSA, JT-60 TEAM[1]
Naka Fusion Research Establishment,
Japan Atomic Energy Research Institute,
Naka-machi, Naka-gun, Ibaraki-ken,
Japan

Abstract

STEADY STATE OPERATION RESEARCH IN JT-60U.

Significant progress in steady state operation research has been made in JT-60U. The highest fusion triple product $n_D(0)\tau_E T_i(0) = 1.5 \times 10^{21}$ keV·s·m^{-3} has been recorded in the high β_p H mode at $T_i(0) = 45$ keV. A fusion triple product of $n_D(0)\tau_E T_i(0) = 0.51 \times 10^{21}$ keV·s·m^{-3} with $W_{dia} = 9.32$ MJ was sustained for 0.5 s ($\sim 1.5\tau_E$) with ELM activity. It was found that the triangularity of the plasma shape has an important role in sustainment of current drive performance with high confinement and high fusion performance. The edge stability of high β_p H mode plasmas was significantly improved and giant ELMs were suppressed with an increase of the triangularity. With high triangularity operation ($\delta = 0.35$), $\beta_N \approx 2.5$ and H factor ($= \tau_E/\tau_E^{\mathrm{ITER89P}}$) ≈ 2.3, with a peak fusion performance of $n_D(0)\tau_E T_i(0) = 0.32 \times 10^{21}$ keV·s·m^{-3} and $Q_{DT} = 0.27$, were sustained for around 2.5 s. Highly improved core confinement with an equivalent $Q_{DT} \approx 0.83$ has been obtained in reversed shear discharges. Sustainment and control of a reversed shear configuration were successfully performed by LHCD, emphasizing the importance of current profile control in reversed shear discharges. The results observed have indicated that the reversed shear configuration is one of the attractive candidates for an advanced steady state operation scenario. The first demonstration of heating and current drive by negative ion based NBI has indicated the effectiveness of this method for core heating and current drive in reactor relevant plasmas.

1. INTRODUCTION

The objectives of JT-60 research are to establish the physics basis for a steady state tokamak fusion reactor and to contribute to the ITER physics R&D. Significant progress in key physics issues such as improved confinement, a radiative divertor, non-inductive current drive, profile control, stable high normalized β and fast particle physics was achieved in JT-60U in recent years. A high fusion triple product of $n_D(0)\tau_E T_i(0) = 1.2 \times 10^{21}$ keV·s·m^{-3} with a large bootstrap current fraction ($I_{BS}/I_p \approx 50\%$) was achieved in the high β_p H mode regime in 1993 [1]. Quasi-steady-state high fusion performance with $n_D(0)\tau_E T_i(0) = 0.44 \times 10^{21}$ keV·s·m^{-3} was also demonstrated in the high β_p ELMy H mode. In a low current regime ($I_p = 1$ MA), fully non-inductive discharges with NBCD and high bootstrap

[1] See the Appendix.

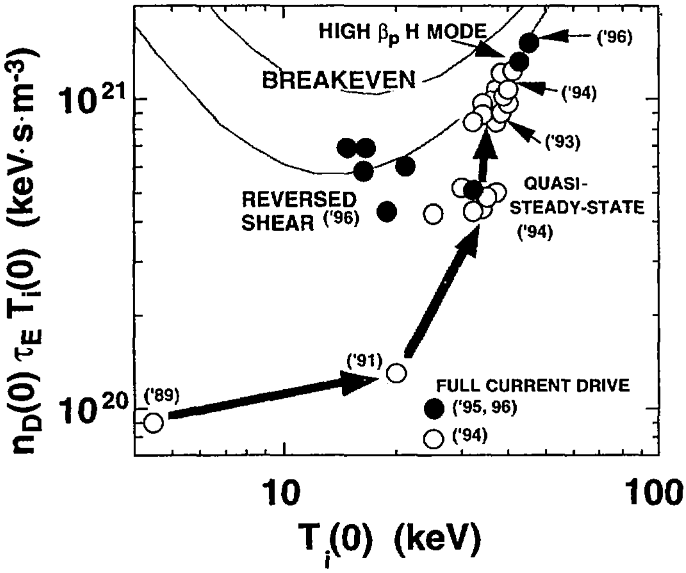

FIG. 1. Fusion triple product $n_D(0)\tau_E T_i(0)$ plotted against central ion temperature $T_i(0)$ for various improved confinement modes.

current (74%) were demonstrated at normalized beta $\beta_N = 2.9$, H factor $(= \tau_E/\tau_E^{ITER89P}) = 2.5$ and $q_{95} = 5.2$. The high β_p H mode regime is one of the targets for establishing the physics basis for a steady state tokamak reactor.

During the past two years, the high β_p H mode regime has been extended with a higher current of up to 2.7 MA ($q_{95} = 2.53$) with higher power neutral beam heating of up to 40.9 MW. Experiments with a reversed shear magnetic configuration have also been performed to develop an advanced steady state operation scenario. The fusion triple products achieved in these improved modes are shown in Fig. 1 and their major parameters are given in Table I. This paper describes recent progress in steady state operation research in JT-60U. The machine modification during these two years is described in Section 2. The progress of steady state operation research with the high β_p H mode regime and with the reversed shear configuration is presented in Sections 3 and 4. The first report on experimental results from negative ion based neutral beam injection (N-NBI) is given in Section 5. Section 6 describes other key issues, and the modification of the divertor configuration planned for February 1997 is introduced in Section 7. The paper is summarized in Section 8.

TABLE I. MAJOR PARAMETERS OF TYPICAL IMPROVED CONFINEMENT DISCHARGES

	E26939, high β_p H mode, ELM free	E26949, high β_p H mode, ELMy	E27411, high δ, ELMy	E24621, high δ, full CD	E27302, reversed shear
I_p (MA)	2.4	2.5	1.5	1.0	2.4
B (T)	4.32	4.3	3.6	3.0	4.28
q_{95}	3.9	3.0	4.07	5.56	3.46
κ	1.74	1.77	1.48	1.48	1.83
δ	0.08	0.07	0.36	0.325	0.06
P_{NB} (MW)	32.7	32.9	22.9	25.8	12.9
W_{dia} (MJ)	8.55	9.32	6.26	3.83	9.42
dW/dt (MW)	16.9	2.3	4.33	0.0	3.35
τ_E (s)	0.75	0.33	0.39	0.20	1.01
H factor	3.3	2.05	3.04	2.59	3.35
n_{e0} (10^{19} m^{-3})	6.0	5.85	4.7	3.6	10.1
n_{D0} (10^{19} m^{-3})	4.35	4.30	3.4	1.9	4.49
Z_{eff}	2.2	2.32	2.4	3.4	3.77
T_{i0} (keV)	45.0	35.5	24	27	15.1
T_{e0} (keV)	10.6	11.0	7.5	9.0	8.10
$n_{D0}\tau_E T_{i0}$ (10^{21} keV·s·m^{-3})	1.53	0.51	0.32	0.1	0.68
S_n (10^{16} s^{-1})	5.16	4.91	2.41	0.78	2.97
β_N	2.0	1.98	2.8	3.05	1.84
β_p	1.15	1.18	2.0	2.80	1.22
Q_{DD} (10^{-3})	3.5	1.78	1.53	—	3.73
Q_{DT}	0.43	0.28	0.27	—	0.82

2. MODIFICATION OF THE MACHINE

Two important systems have been newly installed in JT-60U. The first is the triangularity control system and the other is the N-NBI system [2, 3].

2.1. High triangularity configuration

The previous JT-60U plasmas had a cross-section with a low triangularity δ. High fusion performance in the high β_p H mode regime was obtained with $\delta < 0.1$ and was terminated by the appearance of giant ELMs. Obtaining high fusion performance in a higher density regime was difficult because ELMs appeared at relatively

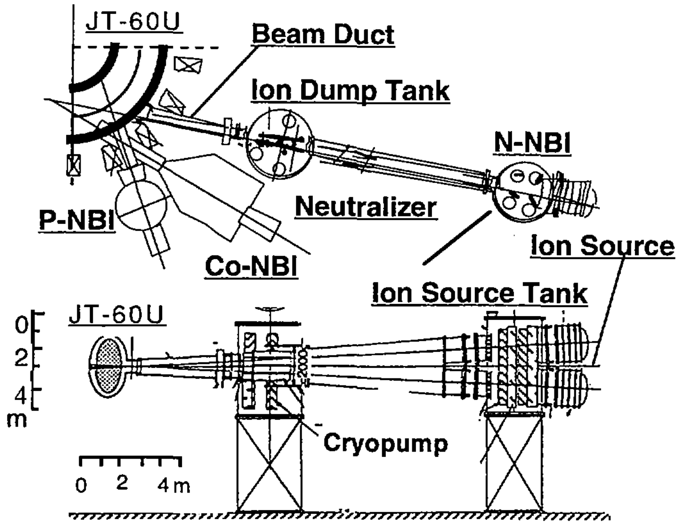

FIG. 2. JT-60U N-NBI system: beam energy 0.5 MeV, beam power 10 MW, pulse length 10 s, beam species D/H, two ion sources.

low density. To improve the stability at the plasma edge and to allow high fusion performance in a higher density regime, a triangularity control system has been installed in JT-60U. The triangularity δ can be controlled from -0.06 to 0.6 at $I_p = 1$ MA, and from -0.03 to 0.3 at $I_p = 2$ MA, with no large change of the plasma volume.

2.2. N-NBI system

For heating and current drive in a steady state tokamak reactor such as SSTR [4], effective heating to the desired ignition point and efficient current drive are required without depending on the edge plasma parameters. N-NBI is one of the most promising candidates for heating and current drive of high density, high temperature plasmas in a tokamak reactor. An N-NBI system with a beam energy of 0.5 MeV has been developed, and the system was installed in JT-60U at the beginning of 1996.

A schematic drawing of the JT-60U N-NBI system is shown in Fig. 2. A beam energy of 0.5 MeV is adopted for a good central penetration in high density operation, with shine-through below 5% in the density range (0.5–1) $\times 10^{20}$ m^{-3}. An injection power of 10 MW is determined to obtain clear N-NBI effects on heating and current drive performance in high density and improved confinement modes produced by high power positive ion based NBI (P-NBI). The total N-NBI system efficiency is estimated to be 40% including power supply losses, neutralization efficiency (60%), geometrical efficiency (90%) and reionization loss (2%).

2.3. Other modifications

The P-NBI system was modified to increase the injection power and the beam fuelling rate. A beam power of 40.9 MW at a beam energy of 90–95 keV was injected into high β_p H mode discharges. In order to measure the current profile, a 14 channel motional Stark effect (MSE) measurement system has been installed.

3. PERFORMANCE OF THE HIGH β_p H MODE REGIME

Efficient steady state operation with high performance is possible in the high β_p H mode regime because good quasi-steady-state confinement with a high bootstrap current fraction is produced with continuous ELMs. With an intensive core current driver such as the N-NBI system in JT-60U, fully non-inductive discharges with reactor core parameters can be expected in the high β_p H mode discharges. Therefore this regime is one of the most important scenarios for steady state operation research in JT-60U.

3.1. High β_p H mode at low q

With careful control of MHD activity during the current ramp-up phase at low density, the high β_p H mode was realized at a high current of up to 2.7 MA (q_{95} = 2.53). This made it possible to systematically study the safety factor dependence of high β_p H mode performance [5]. In Fig. 3 the ratio of the H factor to the safety factor at the 95% flux surface q_{95} is plotted against q_{95}. The quantity H/q_{95} is a useful figure of merit for the ignition margin since $(H/q_{95})^2$ is proportional to the

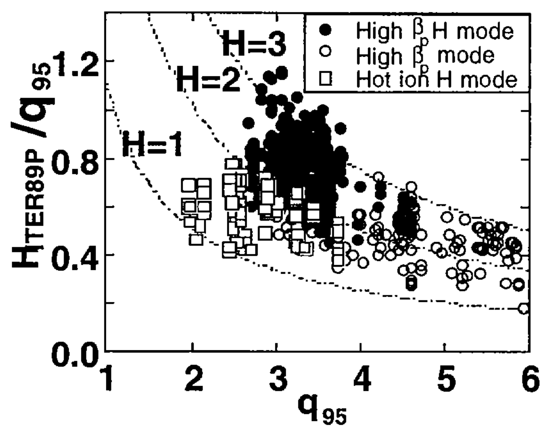

FIG. 3. Ratio of H factor to 95% safety factor, H/q_{95}, against q_{95}.

fusion triple product. The margin $H/q_{95} > 0.6$ is required in ITER for sustainment of ignition [6]. Experimental results indicate that the quantity H/q_{95} has a peak at around $q_{95} = 3$ in the high β_p H mode, which suggests that the maximum ignition margin would be expected at $q_{95} \approx 3$. The high β_p H mode in JT-60U is approaching the required domain in ITER ($H/q_{95} \approx 1$ at $q_{95} \approx 3$). A fusion triple product of $n_D(0)\tau_E T_i(0) = 1.53 \times 10^{21}$ keV·s·m^{-3} with H factor ≈ 3.3, $H/q_{95} \approx 0.85$ was achieved at $I_p = 2.4$ MA ($q_{95} = 3.9$) (E26939 in Table I). This is the record value of the fusion triple product in JT-60U. A quasi-steady-state high β_p ELMy H mode with a fusion triple product of $n_D(0)\tau_E T_i(0) = 0.51 \times 10^{21}$ keV·s·m^{-3} ($W_{dia} \approx 9.3$ MJ, H factor = 2.05, $H/q_{95} \approx 0.68$ and $\beta_N \approx 2.0$) was sustained for a duration of around $1.5\tau_E$ (E26949 in Table I).

3.2. Improved performance through increased triangularity

In the quasi-steady-state high β_p ELMy H mode with high fusion performance, a gradual increase in the temperature of the divertor tiles has been observed, and the performance was sometimes reduced with a large influx of carbon impurity from the divertor plates [7]. Higher density operation to reduce the divertor heat load is required to sustain high performance for a longer time. However, high performance plasmas in the high β_p H mode were not obtained in the high density regime because confinement improvement and density increase were terminated by an occurrence of giant ELMs, which appeared at a relatively low density in JT-60U. The effect of the triangularity of the plasma shape has been studied with the aim of improving the edge stability and enlarging the operational region of the high β_p H mode to a higher density regime.

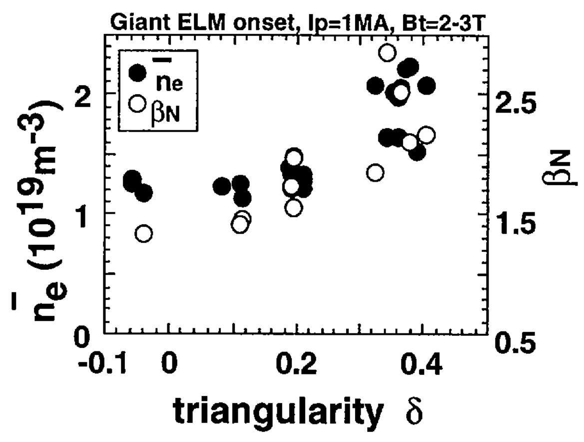

FIG. 4. Electron density and normalized β at giant ELM onset versus triangularity δ.

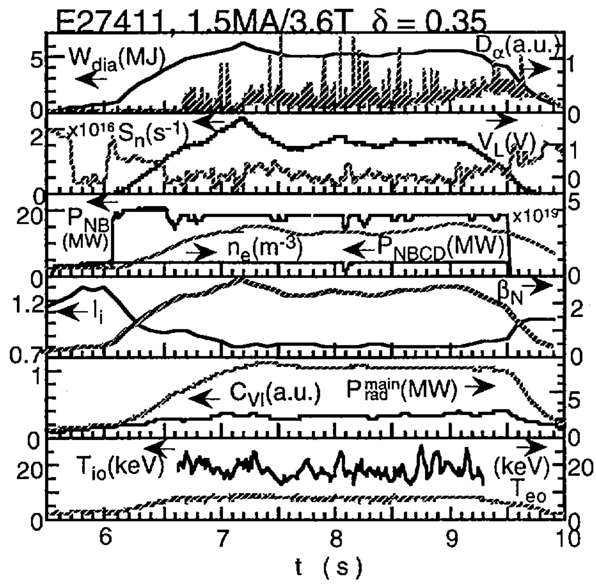

FIG. 5. Quasi-steady-state high β_p ELMy H mode with high triangularity, $n_D(0)\tau_E T_i(0)$ = 0.3×10^{21} keV·s·m^{-3} and $Q_{DT} = 0.25$.

The onset density of the giant ELMs and the normalized β at the ELM onset are plotted against the triangularity in Fig. 4, where other configuration parameters are fixed. Previous high β_p H mode experiments were performed with a triangularity δ of 0.08. The ELM onset density increases with δ. A similar dependence on the triangularity has been observed in the edge temperatures at the ELM onset [8]. Consequently, the normalized edge pressure gradient and the normalized β at the giant ELM onset increased by a factor of greater than 2 with increasing δ from 0.08 to 0.34, as shown in Fig. 4. The H factor also increased with δ for a fixed major radius. The maximum electron density with an H factor larger than 2.0 increased by a factor of 2 in the high δ discharges. This suggests that high δ discharges are favourable for realizing a cold dense divertor plasma with high confinement. ELM activity was also affected significantly by δ. Giant ELMs appearing in low δ discharges were suppressed completely and frequent ELMs with very small amplitudes appeared in high δ cases. This is also favourable for the divertor because of low pulsed heat loads. The impact of higher triangularity is highlighted in Fig. 5, where $\beta_N \approx 2.5$ and H factor $\approx$ 2.3 were sustained for 2.5 s in high δ discharges ($\delta = 0.35$). The fusion triple product $n_D(0)\tau_E T_i(0) = 0.32 \times 10^{21}$ keV·s·m^{-3} and the equivalent Q_{DT} = 0.27 were achieved at t = 7.1 s. It should be emphasized that this high performance is sustained without causing any large impurity influx from the divertor during high power neutral beam pulses.

With the increase of δ up to 0.33 from 0.08, a fully non-inductive discharge with high performance, high bootstrap current fraction ($I_{BS}/I_p \approx 60\%$), H factor = 2.0–2.5, β_N = 2.6–3 and $n_D(0)\tau_E T_i(0) = 0.1 \times 10^{21}$ keV·s·m^{-3} was sustained for 2 s ($10\tau_E$). The duration of the full current drive condition in similar discharges with a low δ (δ = 0.08) was limited to 0.6 s owing to the growth of low n modes or to carbon impurity influx from the divertor plates.

4. CHARACTERISTICS OF REVERSED SHEAR DISCHARGES

A reversed shear magnetic configuration is expected to provide an advanced steady state operation scenario with a high bootstrap current fraction for ITER and SSTR [4]. Various studies were performed in a reversed shear configuration to examine its potential as another scenario for steady state operation research in JT-60U. The reversed shear in JT-60U was formed by NBI or LHCD in the current ramp-up phase.

4.1. Reversed shear performance

A typical high performance discharge with reversed shear is shown in Fig. 6 [9]. The neutral beam power is injected during the current ramp-up phase to

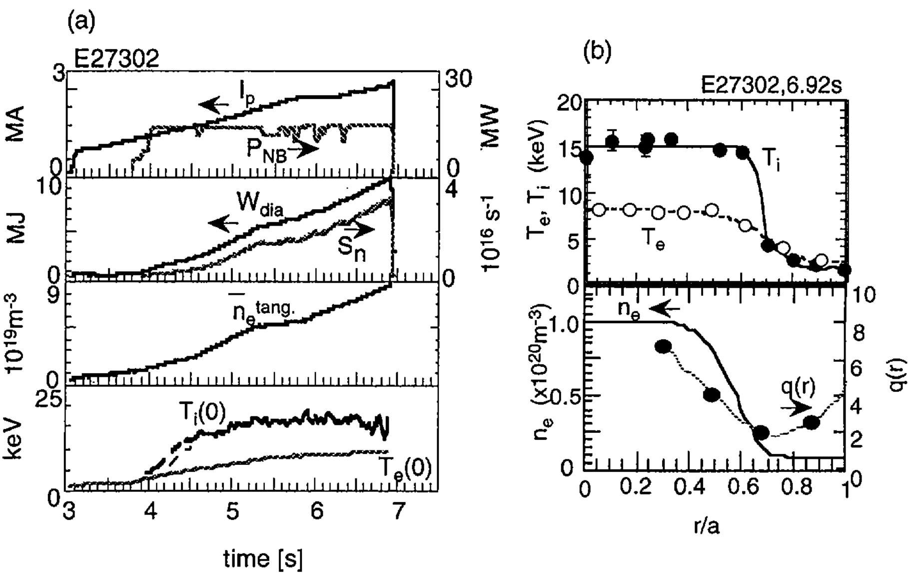

FIG. 6. (a) Time evolution of reversed shear high performance discharge; (b) radial profiles of temperatures, density and q at t = 6.92 s.

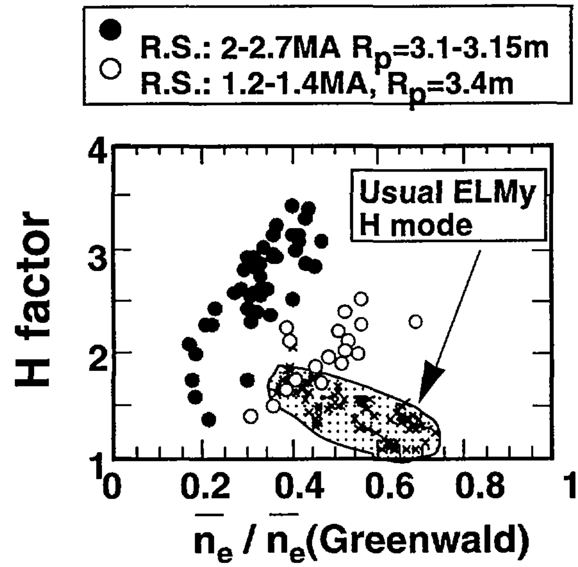

FIG. 7. H factor versus the electron density normalized by the Greenwald density limit (n_e(Greenwald) = $I_p/\pi a^2$) for the reversed and the normal shear discharges.

create a hollow current profile. The radial profile of the safety factor is reconstructed by using the data from the MSE measurement. A wide negative shear region (r/a < 0.6) is formed with careful control of MHD activity. The steep gradient in temperature and density at around q_{min} indicates the formation of an internal transport barrier (ITB). The fusion triple product $n_D(0)\tau_E T_i(0) = 0.68 \times 10^{21}$ keV·s·m^{-3} was attained in this discharge. A record value of the stored energy (9.56 MJ) in JT-60U was also obtained in the reversed shear discharges. Plasma parameters for the shot with the maximum stored energy are summarized in Table I. The Z_{eff} was around 3.77 and the impurity concentration in the reversed shear plasmas was rather high. The equivalent DT fusion power gain Q_{DT} was 0.82 in this shot (Q_{DT} = 0.83 was also obtained in a similar shot). Transport analysis in the reversed shear plasma indicated that the effective electron thermal diffusivity χ_e^{eff} decreased by a factor of ~20 near the position of the ITB. The effective ion thermal diffusivity χ_i^{eff} inside the ITB was smaller than the neoclassical value.

The H factor is plotted against the line average density normalized by the Greenwald density in Fig. 7. The H factor for reversed shear plasmas increases with the electron density while the H factor of the normal shear discharges degrades with increasing density. At n_e/n_e(Greenwald) ≈ 0.7, an H factor of 2.3 was obtained in the reversed shear discharges. For the reversed shear plasmas, the density increases inside the ITB without gas puffing, while strong gas puffing is required in the normal shear discharges because ELM activity limits the density increase.

The reversed shear discharges with high performance were often terminated by disruptions due to the β collapse. Before the collapse, the m/n = 3/1 mode localized near the ITB with an asymmetric mode structure and a growth rate of ~160 μs appeared. MHD stability analysis indicates that the observed β limit is consistent with stability of the n = 1 kink mode.

Helium transport was studied in reversed shear plasmas with the injection of a He beam and He gas [10]. The particle confinement of He was enhanced inside the ITB and the He density profile was determined by the strength of the ITB. Helium particles inside the ITB were expelled by a partial collapse. Further studies should be carried out with the aim of minimizing the concentration of He ash and impurities in the reversed shear core plasma.

4.2. Sustainment of the reversed shear configuration

In order to sustain a reversed shear configuration, which is produced transiently by a current ramp-up, active current profile control was investigated by using LHCD, as shown in Fig. 8 [11]. A reversed shear was produced by NBI into the current

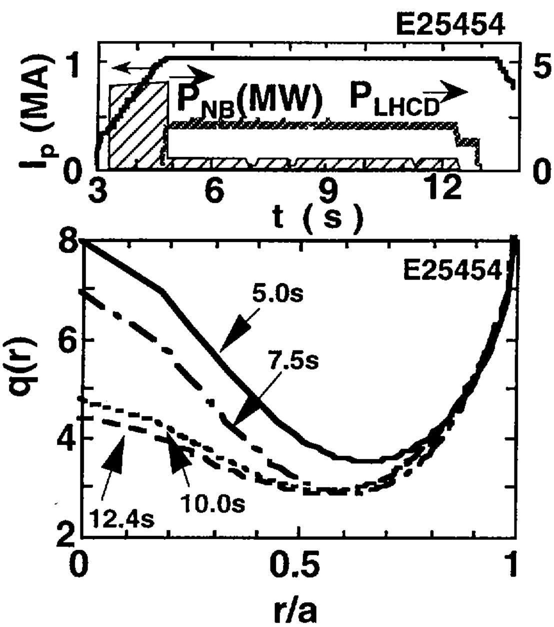

FIG. 8. Sustainment of reversed shear by LHCD and change in q profile during LHCD (n_e = 10^{19} m^{-3}, B_t = 3 T, hydrogen).

ramp-up phase. After a current flat-top was reached, the neutral beam power was switched off except for the probe beam for the MSE measurements, and the current profile was controlled by LH non-inductive current drive. A non-inductive hollow current was produced with careful control of multipeaked wave spectra excited by two multijunction launchers. The MSE measurements indicate that q_0 decreases gradually during LHCD, but the reversed shear is kept until the end of the LH pulse. Much faster current penetration was observed without LHCD. It has been found that the magnetic shear can be modified and the core confinement of high power neutral beam heated plasmas can be controlled by changing the launched wave spectra. The reversed shear configuration has also been produced by LHCD alone where the LH power is injected during the current ramp-up phase.

4.3. Radiative divertor

With successive neon and deuterium gas injection into a low recycling ELMy H mode, a radiative divertor plasma with a high recycling rate and an H factor of 1.5 was realized. Then the detached plasma was maintained for 2 s. By using a similar technique, radiative divertor experiments were also performed in reversed shear discharges with hydrogen, as shown in Fig. 9 [12]. Neon was injected at t = 5.5 s after the formation of the ITB (t = 4.95 s). The density increased to 3.3×10^{19} m^{-3} and was sustained until the end of the beam heating by feedback control. Additional hydrogen puffing during the density feedback control efficiently enhanced the recycling and the radiation cooling at the divertor. The divertor radiation increased to 7.6 MW, while the radiation power from the main plasma was

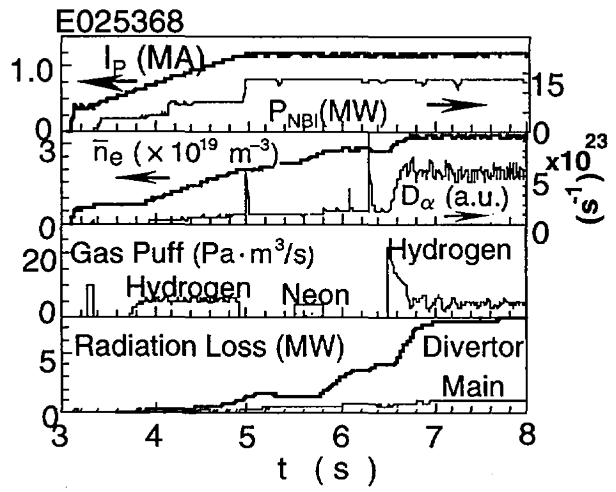

FIG. 9. Formation of radiative divertor in reversed shear discharges (hydrogen).

around 1 MW. The total radiated power was approximately 70% of the total absorbed beam power. The increase in Z_{eff} was also modest ($\Delta Z_{eff} \approx 0.3$). The density and temperature profiles before and during the radiative divertor phase showed that the ITB was sustained in the radiative divertor phase and moved inwards from $\rho/a = 0.3$ to 0.25. The establishment of a detached plasma was confirmed by a measurement of the heat flux on the divertor plates with an infrared camera. These experimental results suggest a robustness of the ITB in the reversed shear against the formation of the radiative divertor.

4.4. Fast particle behaviour in reversed shear

In reversed shear plasmas, confinement of energetic ions such as α particles may possibly be degraded because of the low poloidal magnetic field at the core plasma. Triton burnup deduced from the 14 MeV neutron yield has been investigated in a reversed shear configuration [13]. It was found that the triton loss in the reversed shear is larger than that in the normal shear owing to a large ripple stochastic domain formed in the reversed shear configuration. The experimental results agreed well with the orbit following Monte Carlo calculation [14]. These experimental results suggest that optimization of the q profile in the reversed shear configuration is required to obtain good confinement of both thermal plasma and energetic ions.

Second harmonic ICRF heating was investigated in the reversed shear discharges [15] heated by NBI. Strong central heating by ICRF was observed. The pressure gradient at the ITB increased during ICRF heating with the decrease of the ITB radius due to partial collapses and current penetration. The toroidal Alfvén eigenmodes (TAEs) were stable in the reversed shear with a strong transport barrier. Small amplitude TAEs with toroidal mode number n = 5–8 were observed only after the density gradient near the ITB became small owing to the sequential partial collapses.

5. HEATING AND CURRENT DRIVE PERFORMANCE BY N-NBI

The JT-60U N-NBI system was completed in March 1996. After subsequent beam conditioning, N-NBI power of 2.5 MW at a beam energy of 350 keV was injected into JT-60 plasmas.

Within the uncertainty of the measured shine-through and Z_{eff}, the shine-through power could be explained by the theoretical prediction based on both a single step and a multistep ionization cross-section. The characteristic time of the neutron decay after switch-off of the neutral beam pulse was investigated by changing the electron density ($n_e = (0.5–2.8) \times 10^{19}$ m^{-3}) and the injected beam energy (E_B = 200–350 keV). The experimental neutron decay time is plotted against the calculated neutron decay time in Fig. 10, where the calculations for the neutron signal were made by using a Fokker–Planck code with the classical slowing down process. Figure 10 indicates that the neutron decay time can be explained well by the

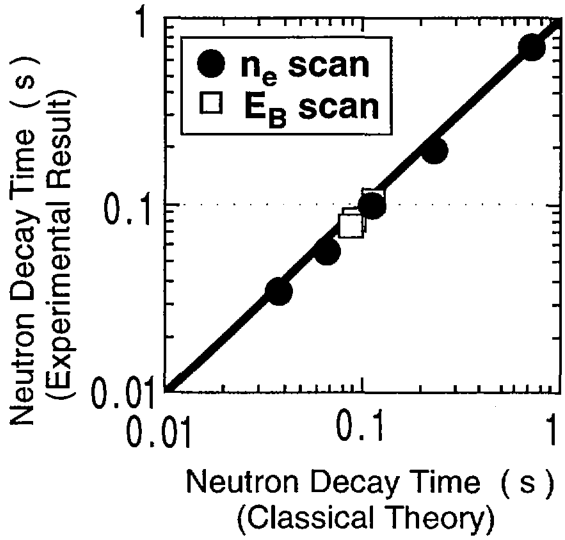

FIG. 10. Neutron decay time: experiments versus classical theory.

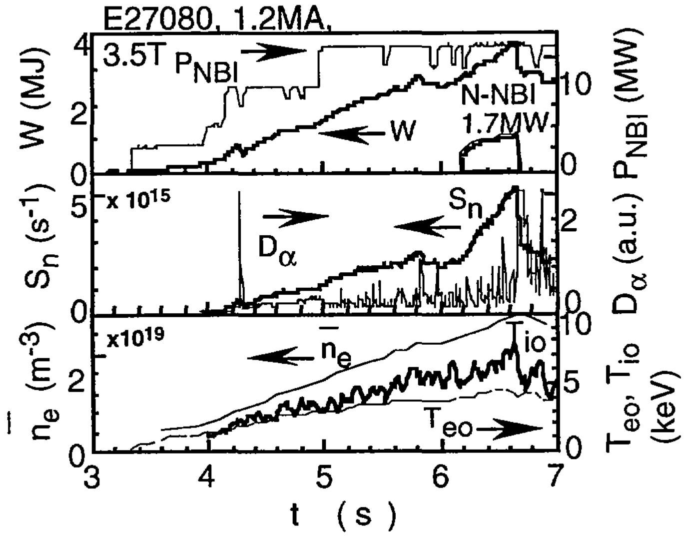

FIG. 11. N-NBI (350 keV) into a reversed shear plasma. A β_p collapse occurs during N-NBI (t = 6.65 s).

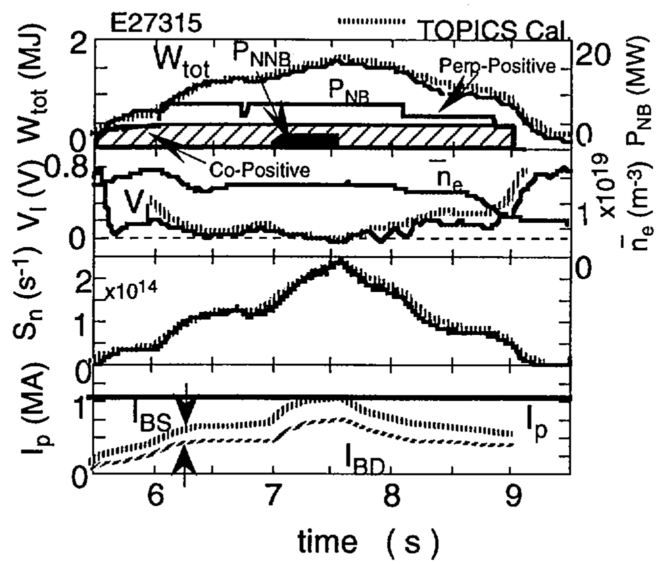

FIG. 12. Time evolution of full current drive discharge with NBCD by P-NBI and N-NBI.

theoretical prediction based on the classical slowing down process. Central electron heating by N-NBI has been confirmed experimentally. Giant sawteeth appeared during N-NBI and a peaked electron temperature profile was observed. Strongly anisotropic pressure ($\Delta\beta_{p\parallel}/\Delta\beta_{p\perp} > 3$ at $n_e \approx 10^{19}\,m^{-3}$) and a longer total incremental energy confinement time ($\tau_{Einc} = \Delta W_{tot}/\Delta P_{abs}$) compared with P-NBI at $E_B = 80$ keV ($\tau_{Einc}(NNB)/\tau_{Einc}(PNB) \approx 1.6$ at $n_e \approx 10^{19}\,m^{-3}$) were observed, which indicated the contribution from energetic parallel beam ions.

In Fig. 11, 1.73 MW of N-NBI power at $E_B = 350$ keV was injected into the reversed shear plasma, which was heated by P-NBI of 13 MW. A significant increase in the stored energy indicates that the confinement in the reversed shear discharge was enhanced by N-NBI. The increase in thermal energy content during N-NBI was 0.76 MJ, which corresponded to 90% of the diamagnetic energy increase during N-NBI. This improved confinement was terminated by a β_p collapse during the N-NBI pulse. The neutron emission rate increased by a factor of $\sim$2.5, which was mainly due to the beam–thermal D–D reaction. This result indicates the effectiveness of core heating by N-NBI in high density plasmas such as reversed shear discharges in JT-60U.

Current drive performance by N-NBI is shown in Fig. 12, where the beam was injected into a partially ($\sim$70%) current driven discharge by P-NBI (4 MW of co-tangential beams and 4 MW of perpendicular beams). During the N-NBI pulse, the surface loop voltage becomes negative, indicating fully non-inductive current drive.

The neutron emission increases by a factor of 2. The surface voltage, the total stored energy and the neutron emission rate were reproduced by a 1.5-D transport code (TOPICS [16]) and the ACCOME code [17]. The code simulation predicts that 0.28 MA is driven by N-NBI, which corresponds to a current drive efficiency of $\eta_{CD} \approx 0.8 \times 10^{19}$ m$^{-2}\cdot$A/W with 27% of the shine-through power, while $\eta_{CD} \approx 0.48 \times 10^{19}$ m$^{-2}\cdot$A/W for P-NBI.

Up to now, no N-NBI induced TAE has been observed over a parameter range of $P_{NNB} \leq 2.3$ MW, $E_B < 350$ keV, $I_p = 1$–1.5 MA, $B_t \geq 2$ T and $n_e \leq 2 \times 10^{19}$ m^{-3}.

6. OTHER KEY ISSUES

6.1. H mode threshold

In order to refine the understanding of the density dependence of the H mode power threshold scaling and to investigate the impact of the neutral density at the plasma edge on the power threshold, investigations have been made over a wide range of parameter scans such as I_p (0.9–2.4 MA), q_{eff} (3–11), B_t (1.5–4.1 T) and n_e ((0.7–3) $\times 10^{19}$ m^{-3}) with a fixed plasma configuration [18]. Experiments indicated that for $n_e > 1.2 \times 10^{19}$ m^{-3}, the threshold power could be written as $P_{th} = 1.1 n_e^{0.5} B_t$ (MW, 10^{19} m^{-3}, T). The non-dimensional constraint for a size scaling predicts that this power threshold can be modified to $P_{th} = 0.18 n_e^{0.5} B_t R^{1.5}$ (MW, 10^{19} m^{-3}, T, m). Extrapolating the threshold power to the ITER design parameter, this scaling suggests that $P_{th} = 53$ MW at 5×10^{19} m^{-3}.

Experiments on JT-60U have shown that the power threshold increases with a decrease of the density to below 1.2×10^{19} m^{-3}. Lower ion collisionality was required for the transition at a density below 1.2×10^{19} m^{-3}. In order to understand the density dependence of the power threshold, the effect of the neutral density at the plasma edge was investigated by using the DEGAS code. It was found that a low ion collisionality (high ion temperature) is required for the transition at a high neutral density at the plasma edge. The results suggest that the density dependence of the power threshold is caused by the neutral density dependence.

6.2. Disruption

By inducing a major disruption with a fast current ramp-down (high ℓ_i disruption), a regime of runaway electron production during disruptions was identified [19]; runaway electrons were observed at $|dI_p/dt| > 80$ kA/s and $B_t > 2.7$ T. These results suggest the importance of the amplitude of magnetic fluctuations relative to the magnetic field in the confinement of runaway electrons. The production of runaway electrons was suppressed even in a high magnetic field when a helical magnetic field was applied by local helical winding coils during the disruption. Fast current shutdown has been realized without producing runaway electrons by injecting a neon ice pellet.

6.3. Control of TAEs induced by ICRF heating

Edge current profile modification by LHCD or a current ramp method has been attempted for the control of TAEs in JT-60U [20]. The effect of plasma rotation on TAEs excited by ICRF heating was also investigated recently [15]. TAEs disappeared when co-tangential beams were injected, where a large velocity shear was formed during the beam injection. In the counter beam injection the velocity shear is low, and TAEs were not suppressed. These results suggest the feasibility of TAE suppression by plasma rotation profile control.

7. DIVERTOR MODIFICATION FOR STEADY STATE RESEARCH

In order to realize a radiative divertor plasma easily in improved confinement plasmas, the JT-60U divertor configuration will be modified. A W shaped divertor with inclined divertor plates and a dome on the private region is adopted for the new divertor configuration [21]. Three units of NBI cryopumps will be converted for divertor pumping. The pumping speed can be controlled by fast shutter valves. Numerical simulations indicate that the neutral backflow can be suppressed effectively by the baffling effect of the inclined divertor plates. The dome can increase the neutral pressure in the exhaust region and enhances divertor pumping efficiency. The dome also plays an important role in the methane impurity influx from the private region and prevents impurity concentration near the X point.

8. SUMMARY

Significant progress in steady state operation research has been made in JT-60U.

(1) The highest fusion triple product $n_D(0)\tau_E T_i(0) = 1.5 \times 10^{21}$ keV·s·m^{-3} was achieved in high β_p H mode at $I_p = 2.4$ MA.
(2) Sustainment for around 2.5 s of $\beta_N \approx 2.5$ and H factor ≈ 2.3 with a peak fusion performance of $n_D(0)\tau_E T_i(0) = 0.32 \times 10^{21}$ keV·s·m^{-3} and $Q_{DT} = 0.27$ was achieved by increasing the triangularity ($\delta = 0.35$). A fully non-inductive discharge with H factor = 2.0–2.6 and a large bootstrap current fraction ($I_{BS}/I_p = 0.6$) was sustained for 2 s in high δ operation.
(3) Improved core confinement with the equivalent $Q_{DT} \approx 0.83$ was obtained in reversed shear discharges.
(4) Sustainment and control of the reversed shear configuration were demonstrated by use of LHCD. A radiative divertor plasma with an ITB was produced by

neon gas injection into a reversed shear plasma. Studies on helium transport, fast particle behaviour, ICRF heating and TAEs in reversed shear plasmas showed that the reversed shear is one of the most attractive candidates for an advanced steady state operation scenario.

(5) The first demonstration of heating and current drive by N-NBI was performed. N-NBI power of 2.5 MW at a beam energy of 400 keV has been injected into JT-60U and has demonstrated the effectiveness of N-NBI as a core heating and current drive method in reactor relevant plasmas.

Steady state operation research in JT-60U will be continued by modifying the divertor configuration to a W shaped divertor, aiming at the simultaneous achievement of high fusion performance with improved confinement, non-inductive current drive and radiative divertor.

ACKNOWLEDGEMENTS

The authors would like to acknowledge all the institutes, universities and industries in Japan which have contributed to the JT-60 programme. The authors also express their appreciation to the worldwide international collaboration including DIII-D, TFTR and JET.

REFERENCES

[1] JT-60 TEAM, in Plasma Physics and Controlled Nuclear Fusion Research 1994 (Proc. 15th Int. Conf. Seville, 1994), Vol. 1, IAEA, Vienna (1995) 31.
[2] KURIYAMA, M., et al., in Proc. 16th Symp. on Fusion Engineering, Champaign, IL, 1995.
[3] MIYAMOTO, K., et al., IAEA-CN-64/GP-10, these Proceedings, Vol. 3.
[4] SEKI, Y., et al., in Plasma Physics and Controlled Nuclear Fusion Research 1990 (Proc. 13th Int. Conf. Washington, DC, 1990), Vol. 3, IAEA, Vienna (1991) 473.
[5] ISHIDA, S., et al., IAEA-CN-64/A3-1, this volume.
[6] PERKINS, F., et al., in Plasma Physics and Controlled Nuclear Fusion Research 1994 (Proc. 15th Int. Conf. Seville, 1994), Vol. 2, IAEA, Vienna (1995) 477.
[7] KAMADA, Y., et al., ibid., Vol. 1, p. 651.
[8] KAMADA, Y., et al., IAEA-CN-64/A1-6, this volume.
[9] FUJITA, T., et al., IAEA-CN-64/A1-4, ibid.
[10] SAKASAI, A., et al., IAEA-CN-64/AP2-1, ibid.
[11] IDE, S., et al., IAEA-CN-64/E-3, these Proceedings, Vol. 3.
[12] ITAMI, K., et al., IAEA-CN-64/A4-2, this volume.
[13] TOBITA, K., et al., IAEA-CN-64/A5-6, ibid.
[14] TANI, K., et al., J. Phys. Soc. Jpn. **50** (1981) 1726.
[15] KIMURA, H., et al., IAEA-CN-64/E-6, these Proceedings, Vol. 3.
[16] NAKA FUSION RESEARCH ESTABLISHMENT, Annual Report of the Naka Fusion Research Establishment for the Period of April 1, 1990, to March 31, 1991, Rep. JAERI-M-91-159, Japan Atomic Energy Research Inst., Ibaraki (1991) 59.
[17] TANI, K., et al., J. Comput. Phys. **98** (1992) 332.

[18] FUKUDA, T., et al., IAEA-CN-64/AP2-9, this volume.
[19] KAWANO, Y., et al., IAEA-CN-64/A3-4, ibid.
[20] KIMURA, H., et al., J. Plasmas Fusion Res. 71 (1995) 1147.
[21] HOSOGANE, N., et al., IAEA-CN-64/GP-11, these Proceedings, Vol. 3.

Appendix

THE JT-60 TEAM

V. Afnassiev[1), H. Akasaka, K. Akiba[2), N. Akino, K. Annou, T. Aoyagi, T. Arai, K. Arakawa, N. Asakura, M. Azumi, B.M. Bernholz[24), J. Cao[3), C.Z. Chen[6), Z. Chang[6), S. Chiba, O. Da Costa[4), N. Ebisawa, Y. Fang[5), G.Y. Fu[6), T. Fujii, T. Fujita, H. Fukuda[2), T. Fukuda, A. Funahashi, L. Grisham[6), S. Gunji, H. Haginoya[2), K. Hamamatsu, Y. Hasegawa, T. Hatae, S. Higashijima, H. Hiratsuka, S. Hirauchi, T. Hirayama, A. Hirose[22), A. Honda, M. Honda, B.G. Hong[7), R.M. Hong[17) N. Hosogane, C.K. Hwang[7), H. Ichige, S. Ide, Y. Ikeda, M. Isaka, A. Isayama, N. Isei, S. Ishida, Y. Ishii, M. Isobe[8), N. Isozaki, K. Itami, T. Itoh, T. Iwahashi, R. Jimbou[2),K. Lackner[20), Y. Kamada, A. Kaminaga, T. Kashiwabara, M. Kawai, Y. Kawamata, Y. Kawano, M. Kawanobe[2), D. Kazama, M. Kazawa, M. Kikuchi, J.Y. Kim[9), H. Kimura, T. Kimura, H. Kishimoto, Y. Kishimoto, S. Kitamura, K. Kiyono, K. Kodama, J. Koga[10), Y. Koide, S. Kokusen, K. Komuro[2), T. Kondoh, S. Konoshima, J. Koog[8), G.J. Kramer[11), A.V. Krasilnikov[12), H. Kubo, A. Kumagai[13), K. Kurihara, G. Kurita, M. Kuriyama, M. Kusaka[2), Y. Kusama, L. Lao[17), C. Liu[3), K. Masaki, T. Matsuda, T. Matsumoto, M. Matukawa, V.G. Merezhkin[14), B.E. Mills[21) T. Miura, N. Miya, K. Miyachi, H. Miyata, Y. Miyo, K. Mogaki, M. Mori, M. Morimoto, A. Morioka, S. Moriyama, M. Nagami, A. Nagashima, K. Nagashima, S. Nagaya, O. Naito, Y. Nakamura, R. Nazikian[6), M. Nemoto, S.V. Neudatchin[14), Y. Neyatani, T. Nishitani, H. Nobuska[2), N. Ogiwara, T. Ohga, M. Ohsawa[15), K. Ohshima[2), T. Ohshima, T. Oikawa, T. Okabe, J. Okano, K. Omori, S. Omori, Y. Omori, Y. Onose, T. Ooba[2), H. Oohara, T. Ozeki, R. Ramakrishnan[6), G. Rewoldt[6), M. Saidoh, M. Saigusa, N. Saito, A. Sakasai, S. Sakata, S. Sakurai, T. Sasajima, N. Sasaki[2), M. Sato, T. Sato[2), G. Schilling[6), S.D. Scott[6),M. Seimiya, H. Seki, M. Seki, M. Shibayama[2), M. Shimada, K. Shimizu, K. Shimizu[2), M. Shimizu, M. Shimono, S. Shinozaki, H. Shirai, M. Shitomi, F.X Söldner[18), K. Suganuma, T. Sugie, H. Sunaoshi, M. Takahashi, S. Takahashi, S. Takahashi[2), S. Takeji, H. Takenaga, T. Takenouchi[2), T. Takizuka, H. Tamai, T.S. Taylor[17), F.V. Tchernychev[16), M. Terakado, T. Terakado, K. Tobita, S. Tokuda, T. Totsuka, Y. Toyokawa, N. Toyoshima, K. Tsuchiya, T. Tsugita, Y. Tsukahara, S. Tsurumi[2), T. Tsuruoka[2), T. Tuda, Y. Uramoto, H. Usami[2), K. Ushigusa, K. Usui, J. Van Dam[19), K.A. Vladimirovich[16), J. Von Seggern[23), T.F. Vsevolodovich[16), M. Vitali[14), J. Yagyu, M. Yamagiwa, M. Yamamoto, T. Yamamoto, O. Yamashita, K. Yokokura, H. Yoshida, M. Yoshida, R. Yoshino

[1)STA fellow, Ioffe Inst., RF, [2)Staff on loan, [3)STA scientist exchange program, SWIP, China, [4)STA fellow, Ecole Polytech., France, [5)JAERI fellow, ASIPP, China, [6)PPPL, USA, [7)KAERI, Korea, [8)NIFS, Japan, [9)STA fellow, Univ. Texas, USA, [10)JAERI fellow, Univ. Texas, USA, [11)STA fellow, Netherlands, [12)TRINITI, RF, [13)Tsukuba Univ., Japan, [14)Kurchatov Inst., RF, [15)Kyushu Univ., Japan, [16)Ioffe Inst., RF, [17)GA, USA, [18)JET Joint Undertaking, UK, [19)Univ. Texas, USA, [20)IPP, Germany, [21)SNL, USA, [22)Univ. Saskatchewan, Canada, [23)ISSVP, Germany, [24)ENSGI, France

DISCUSSION

C. GORMEZANO: Why is Z_{eff} much higher in reversed shear plasmas than in high β_p plasmas?

K. USHIGUSA: In reversed shear plasmas, the particle confinement is improved after formation of the internal transport barrier. At the same time, the particle confinement time for impurities is also enhanced. This may be the reason why Z_{eff} in reversed shear plasmas is higher than in high β_p H mode plasmas.

S.A. SABBAGH: What was the highest neutron rate achieved in a reversed shear plasma? Also, at the same injected neutral beam power, how does the neutron production in high β_p H mode plasmas compare?

K. USHIGUSA: The highest neutron emission rate in reversed shear plasmas is 4×10^{16} s^{-1}. Compared with the high β_p H mode, the neutron emission rate in reversed shear plasmas is lower for the same injection power.

Y. SHIMOMURA: In your neon injection experiment, you had a result with 12 MW. What do you observe if you increase heating power up to 20 or 30 MW?

K. USHIGUSA: A disruptive β_p collapse appears in a high power beam heated reversed shear discharge before the formation of a radiative divertor with a neon and hydrogen/deuterium puff. At least ~1 s of steady reversed shear high performance plasma is required for production of a radiative divertor, and we have not yet obtained that. Only a short pulse radiative divertor with a neon puff was achieved in JT-60U.

FEATURES OF JET PLASMA BEHAVIOUR IN TWO DIFFERENT DIVERTOR CONFIGURATIONS

JET TEAM[1]
(Presented by J. Jacquinot)

JET Joint Undertaking,
Abingdon, Oxfordshire,
United Kingdom

Abstract

FEATURES OF JET PLASMA BEHAVIOUR IN TWO DIFFERENT DIVERTOR CONFIGURATIONS.

Two pumped divertors have been installed and tested in JET under ITER relevant conditions. A closed divertor is found to increase the particle and impurity exhaust rate in agreement with code modelling. Excellent power handling is demonstrated, allowing high current discharges with record stored energy (15 MJ) and quasi-steady-state discharges with high fusion triple product (4×10^{20} m^{-3} s keV). The ITERH93-P confinement scaling law is confirmed over a broad range and a more favourable β scaling is found. No hysteresis is found in the H-mode power threshold. A data base of highly radiating discharges including impurity seeding describes the relationship between radiated power, impurity concentration and density. First results of high performance with optimised magnetic shear are presented. Strong internal confinement barriers develop despite the relatively small input of toroidal momentum and particle fuelling from ICRH and NBI.

1. INTRODUCTION - JET, A FLEXIBLE FACILITY

The JET Joint Undertaking is an organisation involving the participation of 15 European countries with central funding from EURATOM. The JET machine [1] was designed with the essential objectives of obtaining and studying plasmas in conditions and dimensions approaching those required in a fusion power plant. In order to pursue new objectives, JET has been extended to the end of 1999 to make essential contributions to a viable divertor concept for ITER and carry out D/T experiments in an ITER-like configuration.

JET has considerable flexibility that allows the study of many different modes of operation. It can match ITER geometry and dimensionless parameters (except the normalised Larmor radius, ρ^*) and can study the effect of large variations around the ITER values. JET has operated at 6 MA in H-mode [2]. D/T plasmas were studied for the first time in 1991 [3]. In preparing for the forthcoming D/T phase (DTE1) to be carried out in early 1997, a closed circuit gas handling system is being commissioned with 3 g of tritium which will be increased to 10 g for the experiments. Remote handling of in-vessel components is an integral part of the programme and will be used for a divertor target exchange after DTE1.

JET has a coherent divertor programme which includes divertor model validation. The main thrust of the programme is to operate successively a series of single-null divertor configurations (Section 2) with increasing "closure", ie the fraction of recycled neutrals escaping from the divertor region is increasingly

[1] See Appendix.

smaller. Retaining the neutrals in the divertor region leads to a higher density and lower temperature divertor plasma for a given scrape-off layer (SOL) power and mid-plane separatrix density. The pumping in the divertor region is therefore made easier. Target sputtering could be reduced (unless chemical sputtering is dominant) and the retention of impurities could be enhanced [4]. However, ELMs (Edge Localised Modes) could defeat some of the favourable features of closed divertors by producing strong interactions with plasma facing components outside the target plates.

The divertor programme includes the successive testing of three pumped divertors between 1994 and 1998 with the following sequence :

- in 1994-1995, Mk I: an open divertor requiring sweeping the heat load in the divertor region;
- in 1996-1997, Mk IIA: a moderately closed divertor with a large wetted area. This divertor can accommodate up to 40MW for 8s without sweeping. In Mk IIA, operation is possible on both the horizontal and vertical target plates. Mk IIA is compared with Mk I in Fig. 1; and
- in 1997-1998, Mk II GB: a closed gas box divertor configuration to be installed by remote handling after DTE1.

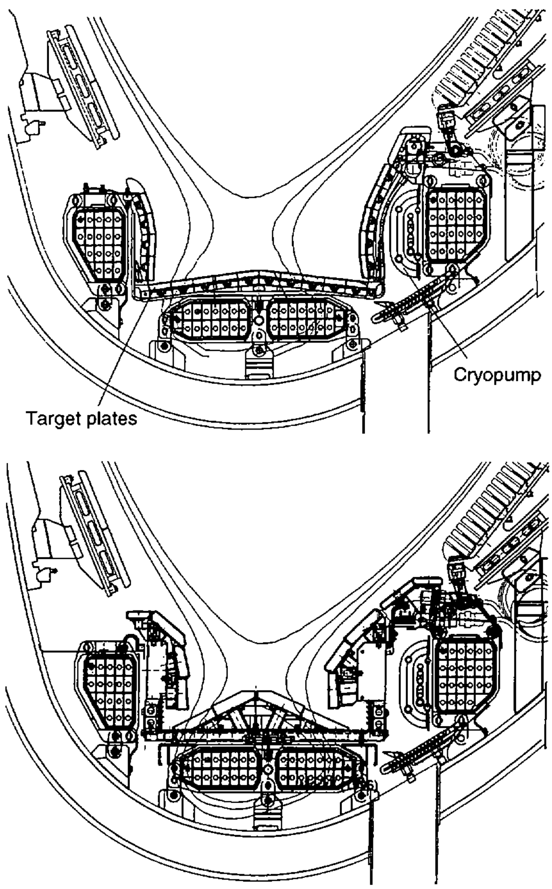

FIG. 1. View of the poloidal cross-section of the Mk I (top) and Mk IIA (bottom) pumped divertors.

TABLE I. JET PARAMETERS FOR Mk I AND Mk II DIVERTOR EXPERIMENTS

Plasma minor radius, a	0.95 m
Plasma half-height, b	1.75 m
Plasma major radius, geometrical centre, R_0	2.85 m
Plasma volume	85 m^3
Plasma aspect ratio, R_0/a	3.0
Plasma elongation, b/a	1.85
Toroidal magnetic field (at R_0), B_{T0}	3.6 T
Flat top pulse length, t	10-25 s
Plasma current, I_p	6.0 MA
Transformer flux, f	42 Wb
Neutral beam power at 80 keV and 140 keV	21 MW
Ion cyclotron power at 25-55 MHz	17 MW
Lower hybrid power at 3.7 GHz	7 MW

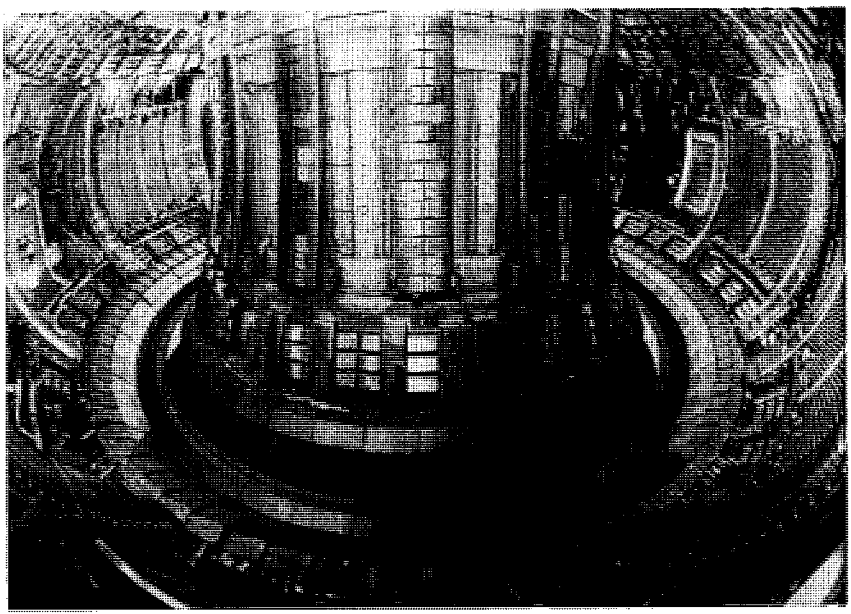

FIG. 2. Interior of the modified JET in 1996 showing several important in-vessel components: four ICRH antennas each on the right and left, adjacent lower hybrid launcher on the right, a part of the saddle coils on the inner wall and the Mk IIA divertor on the floor.

The parameters of the JET tokamak are given in Table I. A view of the in-vessel components of JET at the restart of operation in 1996 is given in Fig.2 where some of the components such as the divertor target plates, ion cyclotron resonance heating (ICRH) antennas and lower hybrid current drive (LHCD) launcher can be seen. The core and divertor plasma parameters are measured with an extensive set of instruments [5]. Specific Toroidal Alfvén Eigenmode (TAE) studies have been carried out [6] by exciting these modes using either in-vessel saddle coils or ICRF beat waves created by energising two antennas with a precisely controlled frequency difference. A new and entirely digital real time plasma position and shape control system [7] has been implemented providing greatly increased flexibility and accuracy. The JET control and data acquisition system is based on a network of dedicated minicomputers (in UNIX environment) which provide centralised control, monitoring and data acquisition on CAMAC and VME standards.

The support of the Vacuum Vessel has been fitted with hydraulic restraints in order to limit vessel displacements, in particular with regard to large sideways forces [8]. New instrumentation is available for measuring halo currents, forces applied to the vessel and the corresponding displacements.

Long pulse operation and scenario optimisation rely on the continuous development of the non-inductive current drive capability of JET which is based mainly on the LHCD system (3 MA has been driven) but also on the fast waves launched from the phased 4-strap ICRH antennas and the quasi-tangential neutral beam lines.

2. DIVERTOR PHYSICS ASPECTS

2.1 JET divertor configurations

X-point tiles fixed directly to the vacuum vessel were used in 1989-91 for H-mode studies in which the target to X-point distance was very small (< 10 cm). As a result, the screening effect of the divertor was mediocre at low divertor densities and a fraction of the impurity atoms sputtered from the target plates could go directly into the main plasma. Furthermore, the divertor plasma was not fully opaque to impurity and hydrogenic neutrals. This was partly beneficial since neutrals could re-enter the SOL well upstream and increase the flow over a significant part of the SOL [2]. However, these neutrals also led to increased impurity influxes by charge exchanged neutral sputtering. The duration of high performance discharges was often limited, ultimately, by a strong influx of carbon impurities, the so-called "carbon bloom". Energies of only about 15 MJ could be conducted to the target plates.

The relatively open Mk I divertor and in-vessel cryopump were installed for JET operation during 1994-95 (Fig.1). For high power handling, the magnetic configuration was swept (4 Hz) horizontally with the help of the in-vessel divertor coils. This allowed energies in excess of 180 MJ (CFC-tiles) and 120 MJ (beryllium tiles) to be conducted to the tiles without significant sublimation or melting occurring [2]. The carbon blooms which previously terminated high performance discharges were avoided. Operation with plasma currents up to 6 MA was possible, the plasma stored energy reached 13.5 MJ and the maximum D-D neutron rate was 4.7×10^{16}/s. A range of divertor physics experiments was conducted with high power (up to 32 MW) and steady-state H-mode plasmas with a radiative divertor using N_2 as the seeded impurity were studied.

The Mk IIA divertor presently used in JET is a moderately closed divertor consisting of a continuous water-cooled divertor structure about 6 m in diameter and weighing about 7 tonnes. It was installed to an alignment accuracy of 1 mm and its replacement is compatible with remote handling. The increased wetted area leads to a power handling capability which is a factor of 3 - 5 better than Mk I. Operation is carried out on both the horizontal and vertical target plates, permitting a comparison of results on impurity retention and neutral recycling, and on the orientation of the target plates both with and without pumping provided by the cryogenic pump. An extensive experimental campaign has been carried out with this divertor with plasma currents up to 5 MA and energies up to

150 MJ have been accommodated by Mk IIA without producing excessive impurity influxes. A number of configurations such as Standard Fat, Super Fat, High Flux Expansion, Vertical Plate and High X-point (to simulate Gas-Box type) configurations have been used with low (0.18) and high (0.32) triangularity plasmas.

2.2 Regimes of divertor operation

2.2.1 The low recycling regime is characterised by a low temperature gradient (target-upstream), reduced particle flows to the target and low density in the divertor and is required by scenarios providing the highest fusion performance (albeit transiently). The performance increases as the duration of the ELM-free period is increased by reducing the recycling (extensive wall conditioning, use of the cryopump, and use of target plate material such as beryllium and/or beryllium evaporation).

2.2.2 The high recycling regime is characterised by a high density at the target and a high parallel flow of ions to the target helps to retain impurities in the divertor by friction. The radiated power fraction is moderate and it is mostly confined to a narrow region close to the target. This could lead to a high power density at the target and excessive erosion. ITER has therefore also considered a "gas box" design [9] in which the radiation losses in the divertor are enhanced and the exhaust power is distributed over a larger sidewall area of a deep divertor via charge exchange and radiation losses. The target geometry is tailored to enhance this effect and the divertor is relatively closed. Hydrogenic and impurity neutrals are required to recirculate within the divertor region and the loss of these neutrals to the main chamber is minimised with the help of the divertor cryopump. However, flows from the main plasma to the X-point are reduced and this may adversely affect impurity control.

Code calculations at JET and elsewhere show that hydrogenic plasmas cannot radiate sufficiently for the plasma to be extinguished before reaching the target. To achieve this "fully detached" regime, in which the energy reaching the target is negligible, impurity seeding is needed to increase the radiative losses. In experiments at JET with Mk I and Mk IIA, detached plasmas obtained by seeding N_2 in the divertor region have been obtained with up to 80 % of the power being radiated [10]. The plasma then becomes detached as evidenced from the ion saturation current characteristics measured by Langmuir probes in the divertor region. The plasma remains stable, but the continued increase in radiation causes the radiation peak to move from the target plates to the X-point and leads ultimately to a radiative collapse in which the whole plasma surface radiates.

2.3 Differences in performance of Mk I and Mk IIA

2.3.1 Detachment is defined to occur when the ion flux (ion saturation current measured by Langmuir probes) to the target starts to decrease when the density is increased by gas fuelling. In agreement with code calculations, it is found [11] that detachment in L-mode occurs at a factor of 2 lower density in Mk IIA than in Mk I because the increased closure in Mk IIA permits a higher divertor density for the same mid-plane density. H-mode data has not been obtained as the probe characteristics are strongly perturbed by the ELMs.

2.3.2 Neutral particle compression. The loss of hydrogenic and impurity neutrals from the divertor into the main chamber increases the neutral pressure in the main chamber and adversely affects the H-mode power threshold, deteriorates H-mode confinement, and increases the release of impurities from the main chamber walls by charge exchanged neutral sputtering. Neutral particle retention in the divertor (or closure of the divertor) is important and is generally expressed as a compression ratio between the neutral particle fluxes in the divertor and the main chamber using calibrated hot-ion cathode gauges and D_α measurements. It is found that the compression ratio is higher by a factor of 2 - 2.5 in Mk IIA than Mk I. Particle removal with the cryopump is similarly increased. This result has been confirmed by the measurement of the decay time of injected Neon which is found to be a factor 2 to 4 greater in Mk I (Fig.3).

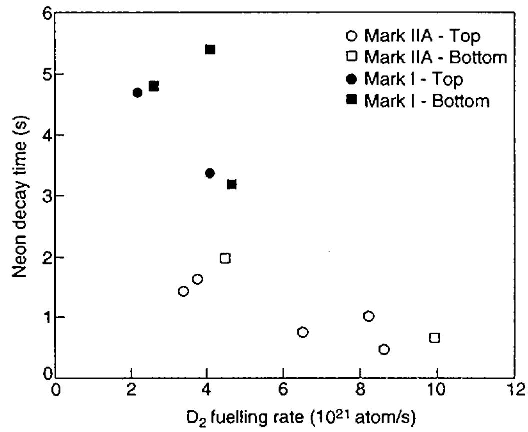

FIG. 3. Comparison of neon decay time as a function of D_2 fuelling rate in the Mk I and Mk IIA divertors in neon puff experiments. Top and bottom refer to D_2 fuelling in the main chamber and in the divertor respectively.

2.4 Modelling

The multifluid plasma code EDGE2D/U coupled to the Monte Carlo neutral particle code NIMBUS has been used at JET to simulate and compare the modelled and experimentally measured divertor performance. The codes calculate the distribution of deuterium and impurity density, temperature and flow, and other quantities corresponding to measurements such as the ion saturation current density (measured by probes at the divertor target), D_α and bremsstrahlung radiation signals, and the impurity and deuterium radiation power densities. The basic equations include classical (collisional) parallel (along the magnetic field lines) plasma transport for electrons, hydrogenic and impurity ions. Anomalous transport across the field lines is described by a simple prescription in which the transport coefficients are specified and generally taken constant across the SOL. The modelling of divertor plasmas has made good progress during the last few years, but there is still no satisfactory modelling of ELMy H-mode plasmas. The difficulty arises principally from the very large variations in density during and after an ELM and in periods between ELMs. Although between ELMs, the magnetic geometry is well defined, it can be strongly perturbed during the ELM itself. Modelling of long ELM-free H-modes as well as grassy ELMs in radiative H-mode plasmas has been successful since the variation in plasma parameters does not change appreciably on the short time scale.

Generally the modelling of tokamak plasmas treats the edge and core plasma separately, which often leads to artificial boundary conditions between the two regions. At JET, the transport codes describing the plasma core (JETTO) and the plasma edge (EDGE2D/U-NIMBUS) have been coupled using transport

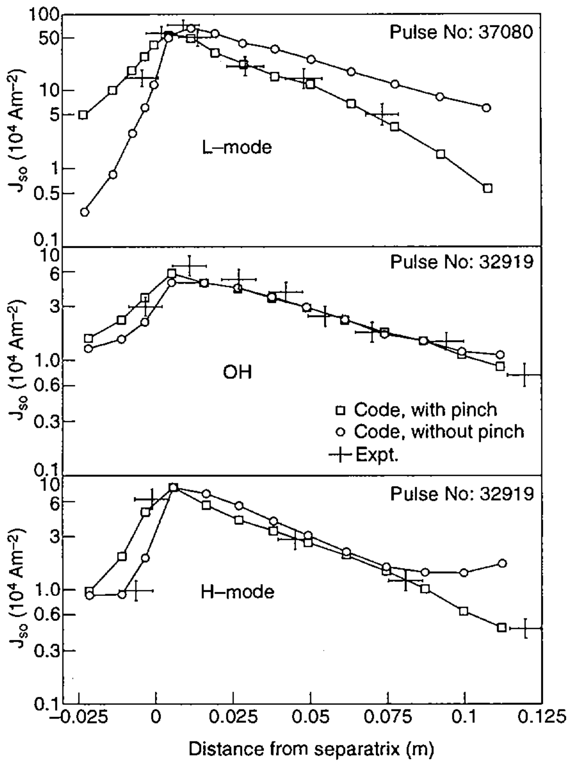

FIG. 4. Measured ion saturation current density versus distance from the separatrix in the Mk IIA divertor in L-mode, OH and H-mode discharges is compared with code calculations with and without a pinch term.

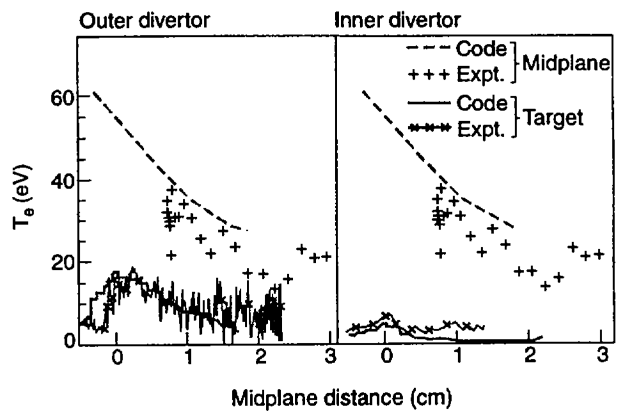

FIG. 5. Measured and code calculated electron temperature profiles in the mid-plane and the divertor target for the inner and outer legs of the divertor in an L-mode discharge as a function of distance from the separatrix at the outer mid-plane.

coefficients and fluxes which allow self-consistent modelling [12]. A pinch term is found to be required in the edge transport to simulate the observed narrow SOL. This has allowed an ELM-free hot-ion H-mode to be modelled self-consistently and the results are given in Fig.4.

An example of a JET L-mode discharge modelled with EDGE2D/U-NIMBUS is shown in Fig.5 [13]. The electron temperature and pressure drop is reproduced by the calculations which include radiation losses in the divertor and SOL.

3. CONFINEMENT ISSUES

3.1 ITER similarity experiments

The prediction of energy confinement in ITER is based on a confinement scaling (ITERH93-P) derived from a multi-machine data base of H-mode discharges. There is a need to confirm this scaling and improve its accuracy by conducting experiments in which dimensionless parameters describing the plasma are varied around ITER values. The most relevant variables are (i) normalised Larmor radius ρ^*, (ii) normalised collisionality ν^* and (iii) normalised plasma pressure β. The ITERH93-P scaling has been written in the dimensionless form as follows [14]:

$$B\,\tau_{ITERH93\text{-}P} \propto \rho^{*\,-2.7}\,\nu^{*\,-0.28}\,\beta^{-1.2} \qquad (1)$$

where the parameters ρ^*, ν^* and β are defined in terms of their average values. Recently, careful experiments have been carried out in JET in which each of the three parameters was changed while keeping the other two fixed. Moreover, the power level was significantly above the H-mode threshold and producing type I discrete ELMs. It is concluded (Fig.6) that the dependence on ρ^* (close to gyro-

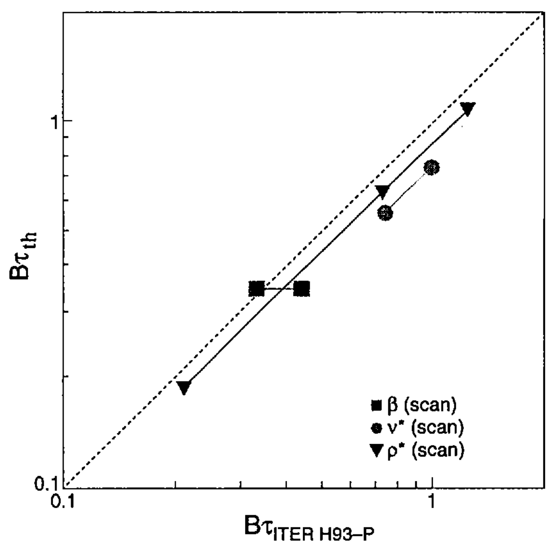

FIG. 6. Normalised confinement time $B\tau_{th}$ is plotted as a function of $B\tau_{ITERH93\text{-}P}$ scaling for ρ^*, ν^* and β-scans. B represents the cyclotron frequency.

Bohm) and ν^* is correctly described in the ITERH93-P scaling but the dependence on β is found to be very weak ie $\beta^{-0.05}$. It is suspected that the ITERH93-P scaling is based on data which includes some taken too close to the MHD β-limit. This new result on β scaling is more favourable and, if confirmed by other experiments, would increase the ITER confinement at ignition by 10 to 15 %.

3.2 H-mode threshold

Existing H-mode threshold scalings have large data dispersion leading to uncertainty in the threshold: P_{th} = 50 - 200 MW in ITER at a density of 5 x 10^{19} m^{-3}. As the power threshold decreases with density, it is considered to enter the H-mode at low density (2-3 x 10^{19} m^{-3}) and then to increase the density progressively as the α-particle heating increases. The input power has to be somewhat higher than the power threshold, otherwise the confinement is insufficient. ITER ignition scenarios also depend on a possible hysteresis between H to L and L to H transitions. Although there is evidence of hysteresis in ELM-free H-modes, more recent experiments in JET [14] in ELMy H-modes indicate that there is essentially no hysteresis. This behaviour might be different in JET because of the high temperature walls and high pumping which are very effective at controlling recycling. The data on threshold power in Mk IIA can be described by $P_{th} \sim 0.3\, n_{20}\, B\, R^{2.5}$ (x 10^{20} m^{-3} T $m^{2.5}$) but data dispersion is still large, indicating that other aspects will have to be included for an appropriate description of the scaling. The threshold power was found to be independent of the type of additional heating (NBI or ICRH).

3.3 Effect of plasma configuration

The ELM behaviour in JET depends on plasma shape (triangularity), divertor magnetic configuration (high or low flux expansion), neutral recycling in the divertor and in the main chamber, and gas fuelling at the edge. High flux expansion with high triangularity, low recycling and no edge fuelling produces long ELM-free periods during which the confinement time increases continuously to 1.2 - 1.5 times ITERH93-P scaling. Figure 7 shows that, in

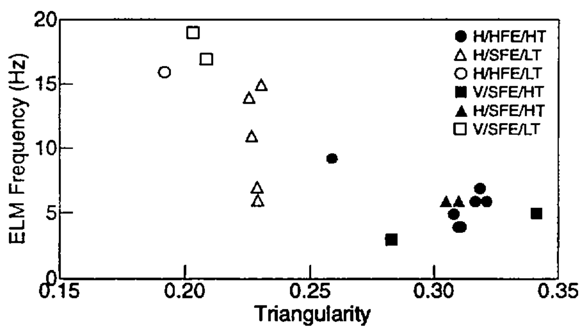

FIG. 7. ELM frequency versus plasma triangularity for 2.5 MA, 2.5 T discharges with 12 MW beam power. The notation for the plasma equilibria A/B/C indicates target orientation (H = horizontal, V = vertical), flux expansion (HFE = high, SFE = standard) and triangularity (HT = high, LT = low) respectively.

steady-state discharges with constant power and fuelling, the ELM frequency decreases with increasing triangularity; on the other hand, the energy confinement appears to be independent of triangularity [11].

3.4 Highly radiative ELMy H-modes

Highly radiative plasmas reduce the heat load to the divertor target plates avoiding excessive erosion of the target. An example of a highly radiative divertor discharge [2] which was heated at a power level of 32 MW (17 MW of NBI and 15 MW of ICRH) is shown in Fig.8. Such a discharge was obtained by nitrogen injection to enhance radiation and indeed the radiated power fraction reached 70 % of the total input power. The density reaches steady-state and the H-mode quality factor relative to ITER89-P scaling is about 1.5.

The confinement quality degrades progressively with increasing radiation and impurity concentrations in the main plasma can be high if the plasma density is too low. When the radiated power fraction is larger than 0.5, the confinement scaling is seen to become worse than gyro-Bohm scaling (Fig.9, [15]). A multi-machine size scaling for Z_{eff} in radiating divertor plasmas has been established so that a value for ITER can be predicted. The data from various divertor tokamaks world-wide is included with the proviso that discharges have a radiated power fraction larger than 50 %. The following scaling best represents the data [16]:

$$Z_{eff} = 1 + 5.6\, P_R\, Z^{0.19} / (< n_e >^{1.95}\, S^{1.03}) \qquad (2)$$

where P_R (MW) is the radiated power, S (m^2) is the plasma surface area, $< n_e >$ ($10^{20}\ m^{-3}$) is the line averaged density and Z is the atomic number of the seeded

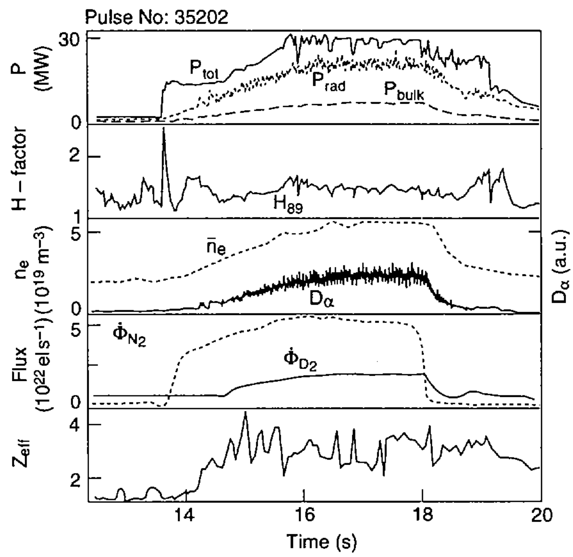

FIG. 8. Time traces of an H-mode discharge with 30 MW of combined ICRF and NB heating and more than 70% of the power exhausted by radiation from seeded nitrogen.

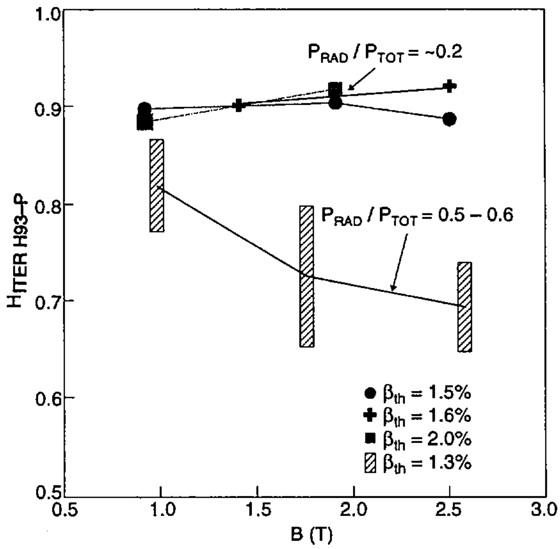

FIG. 9. Confinement (normalised to ITERH93-P) versus toroidal field B in discharges with low and high radiated power fractions. Confinement degrades with radiation and loses gyro-Bohm scaling.

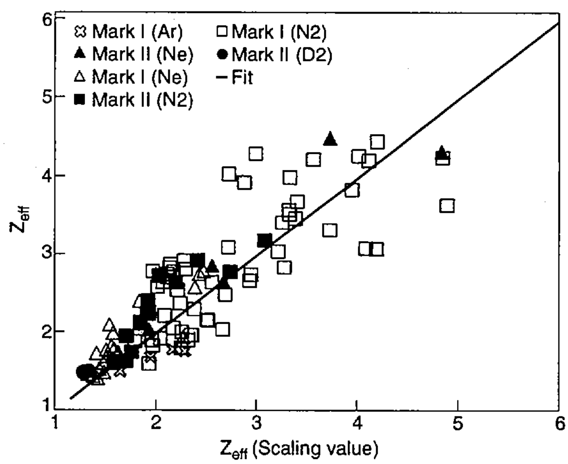

FIG. 10. Measured effective charge (Z_{eff}) versus the scaling of Eq. (2) for a number of JET discharges in Mk I and Mk IIA with seeded impurity gas as indicated. The solid line is a fit to the data.

impurity. The Z_{eff} data obtained with the Mk I and Mk IIA divertors of JET are plotted as a function of this scaling as shown in Fig.10. The value of Z_{eff} predicted for ITER in such highly radiating discharges (85 %) and $< n_e > = 1.2 \times 10^{20}$ m^{-3} would be about 1.6. According to this scaling, ITER would have a tolerable impurity level. There is a clear need to increase the data set with data obtained in other divertor configurations.

4. ENERGETIC PARTICLE EFFECTS

Alpha particles will be the dominant power source in ITER. Therefore, the confinement of the energetic α-particles and the impact on plasma performance are important issues. Moreover, any uncontrolled loss of α-particles either by collective instabilities such as Toroidal Alfvén Eigenmodes (TAE) or ripple induced losses could have serious consequences for the first wall.

4.1 TAE excitation

Global Alfvén eigenmodes can be excited by energetic particles such as fusion born α-particles, injected neutral beam ions or fast-ions accelerated by ICRH. In a reactor, the destabilisation of these modes can lead to a spatial redistribution or an enhanced loss of α-particles with the result that they may not fully heat the plasma. There are a variety of effects which can dampen the modes

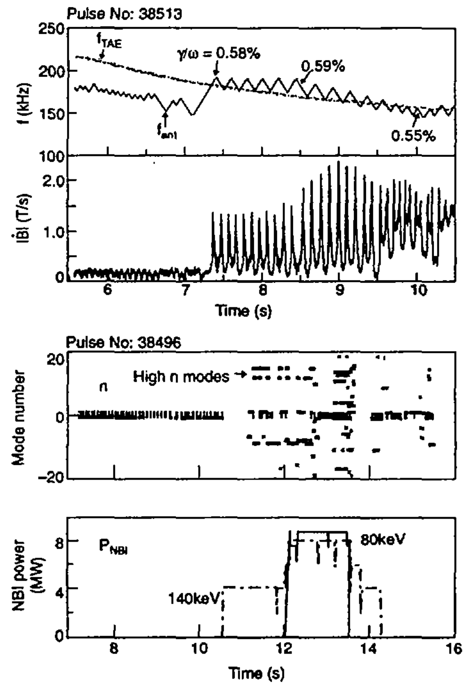

FIG. 11. Tracking during the ohmic phase of TAEs (n = 1) excited by the saddle coils and high-n modes driven unstable at $V_A/3$ by high power 140 keV NB heating.

and both the driving and damping effects must be evaluated to assess the linear stability. External excitation of the modes has been done in two ways: (i) by saddle-coils mounted inside the vacuum vessel and (ii) by beat waves generated by two ICRH antennas run master-slave at slightly different frequencies (100 - 200 kHz at 50 MHz). A coherent detection of AEs in the magnetic, electron cyclotron emission or reflectometry diagnostics provides a means of determining their damping rates. Measurements are made in the presence of a varying fast particle drive, such as 140 keV deuterium NBI, in order to resolve the differences in damping and driving rates of the mode. A feedback loop acting on the frequency of the exciter is used to track chosen eigenmodes during the discharge. Figure 11 shows such a real-time tracking of AEs [17] over a period of 2.5 s in which the frequency of the exciter oscillates around the mode frequency and provides a means of determining the damping rate as a function of time. Values of $\gamma / \omega = 0.55 - 0.59$ % are found, compared to the theoretical estimates of about 1 %. The application of high power NB heating appears first to dampen the n = 1 mode but later the phase resolved measurements by several MHD coils indicate that higher order modes up to $n = \pm 20$ start to grow at the AE frequency. These modes are routinely observed during hot ion H-modes with 140 keV NBI with $V_{\parallel} = V_A / 3$ and could be responsible for limiting the fusion performance. Kinetic TAEs have been identified. Ballooning AEs have also been observed.

4.2 Confinement of fast ions

Ion cyclotron minority heating has been used previously in JET to produce 1 - 1.5 MeV He^3 ions with an energy content up to 2 - 2.5 MJ corresponding to almost 40 - 50 % of the total plasma energy of such discharges [18]. The suprathermal ion energy could be described by classical slowing down of the fast ions. Further studies have been carried out of central ICRF heating at the third harmonic of deuterium in JET where suprathermal effects are dominant and a very energetic tail is expected to develop that does not cut off until 4 MeV when the ion orbits reach the limiters. The deuterium neutron rate in these discharges is observed to reach a high value of 9×10^{15}/s due to the energetic deuterium tail. These results were well reproduced by PION code calculations, giving confidence in the understanding of the production and confinement of energetic tails [19].

4.3 Ripple experiments

The effect of toroidal field ripple on plasma behaviour and fast particle losses was studied with the Mk I divertor. The ripple was varied in the ITER relevant range of 0.1 to 2 %. Ripple induced losses of thermal and high energy particles (125 keV neutral beam ions and 1 MeV tritons) were less than 1 % and were consistent with theoretical estimates. However, the observed losses of particles of intermediate energy (thermal to tens of keV) were higher than predicted [2]. The slowing down of rotation due to ripple was also a notable result of these experiments.

5. HIGH PERFORMANCE AND STEADY STATE REGIMES

In preparing for the D/T phase, JET is pursuing two scenarios for high fusion performance: (i) hot-ion H-mode and (ii) optimised shear mode. Good fusion performance is also achieved in steady-state at high current (5 MA) in a regime directly relevant to ITER.

5.1 Hot ion H-mode

Traditionally "hot ion H-mode" refers to operation with strong neutral beam heating of a low electron density target plasma, with high triangularity (0.25) and high flux expansion in the divertor. Central NB power deposition and central fuelling produces a moderately peaked density profile. The neutral beam predominantly heats the ions and T_i exceeds T_e considerably (> 2 - 2.5) over the inner half of the plasma radius. The high performance lasts for about 2 s and is terminated either brutally or softly ("roll over") by a complex and largely unexplained event [20] involving (i) sawteeth or other internal MHD phenomena occurring in the central region, (ii) "outer-modes" occurring in the body of the plasma and (iii) "giant" ELMs at the plasma edge. The outer modes have now been identified by detailed soft X-ray measurements as ideal kink modes [20] and giant ELMs appear when the ballooning instability criterion is satisfied. The rollover in performance could be linked to the excitation of TAEs (Section 4.1) where the TAE resonance condition $V_{||} = V_A / 3$ for the 140 keV neutral beam is satisfied. Code calculations suggest that, at the resonance condition, sufficient beam ion redistribution within the plasma could account for the degradation in performance.

LHCD has been used to eliminate the sawteeth and to soften the effect of the outer modes but the performance is still limited at a normalised $\beta_N \approx 1.8$ well below the Troyon limit ($\beta_N = 2.8$). More recently, ICRH has been applied to hot ion H-modes [21]. The effect of the ICRH is shown in Fig.12. The addition of 6 MW of ICRH improves the rate of rise of the neutron rate, increases the stored energy by about 5 MJ and T_e by about 30 %. Therefore good confinement is maintained even when the power input to the electrons is substantially increased. A stored energy of up to 14 MJ was obtained with combined heating. Power step-down experiments allow the highest Q to be reached.

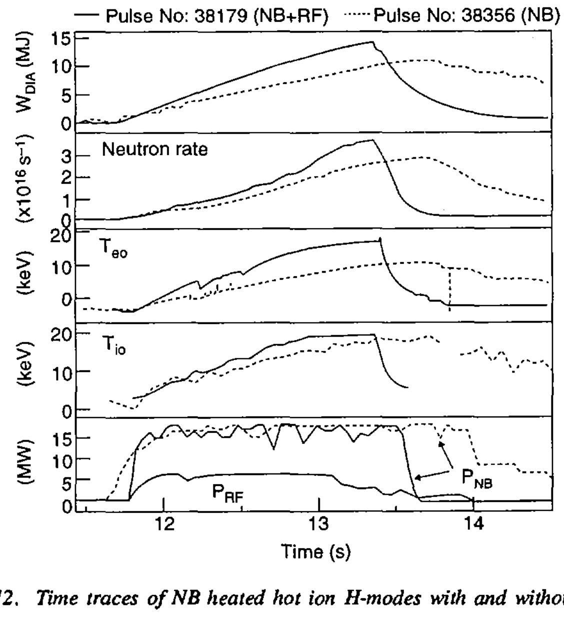

FIG. 12. Time traces of NB heated hot ion H-modes with and without ICRH.

5.2 Discharges with optimised shear

Weak or reversed magnetic shear has been associated with improved core confinement since the JET experiments with deep pellet injection (PEP mode [22]). MHD instabilities like ballooning, resistive tearing and internal MHD modes are then stabilised provided that low rational values of q are avoided. Shear of plasma rotation (plasma flows) has also been shown by theory to stabilise microinstabilities involved in anomalous transport. In such a situation, an internal transport barrier can be established and the resulting steep ion temperature gradient produces more rotation shear.

In JET, optimised shear experiments [23] are carried out immediately after the current rise phase of the discharge where advantage is taken of the natural delay in the current diffusion to the plasma centre as the current is ramped up. The current diffusion can be further delayed by electron heating by ICRH. The target plasma has $q > 1$ everywhere. Neutral beams and ICRH are injected at optimised times in the low target plasma density. An example of time traces of such a high performance discharge is shown in Fig.13 where the maximum neutron rate of 3.4×10^{16} /s is flat for ~ 0.5 s, the stored energy is 9.4 MJ and the peak T_e and T_i are 14 keV and 28 keV respectively. The q profile obtained from a combination of EFIT equilibrium code and Faraday rotation measurements shows that the magnetic shear in the core is weak and slightly positive just before and during the heating. Figures 14 and 15 compare the profiles of T_i, pressure P and rotation ω in the above two high performance modes. The internal confinement barrier corresponds to r/a ~ 0.55. The shear in plasma rotation is large at this location.

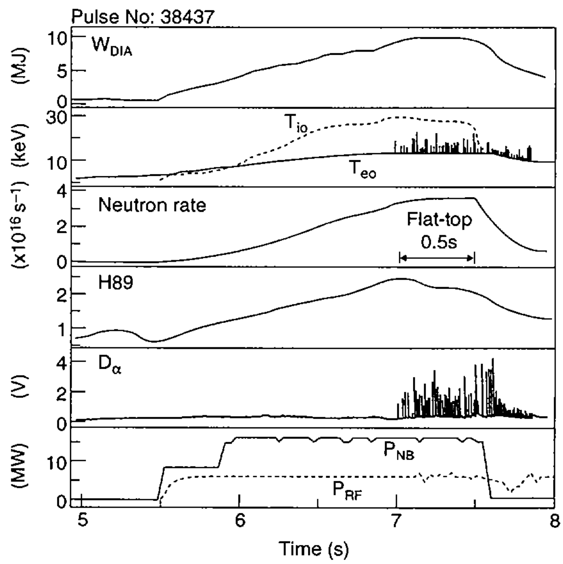

FIG. 13. Time traces of a combined (NB + ICRF) heating optimised shear discharge giving enhanced core confinement. H89 refers to an improvement of confinement over the ITER89-P (L-mode) scaling.

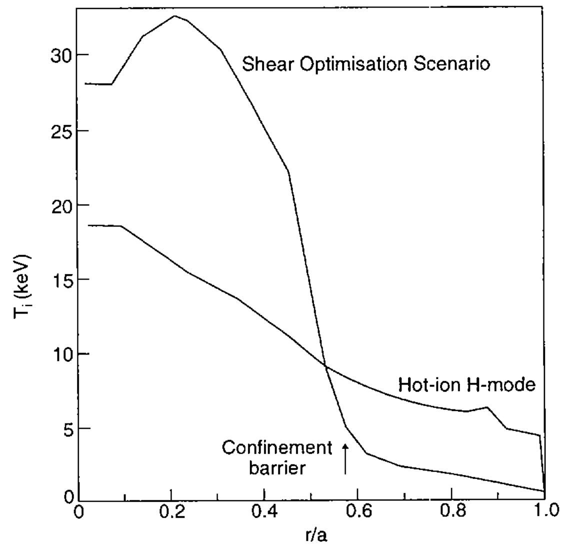

FIG. 14. Comparison of typical ion temperature profiles in a hot ion H-mode and an optimised shear discharge.

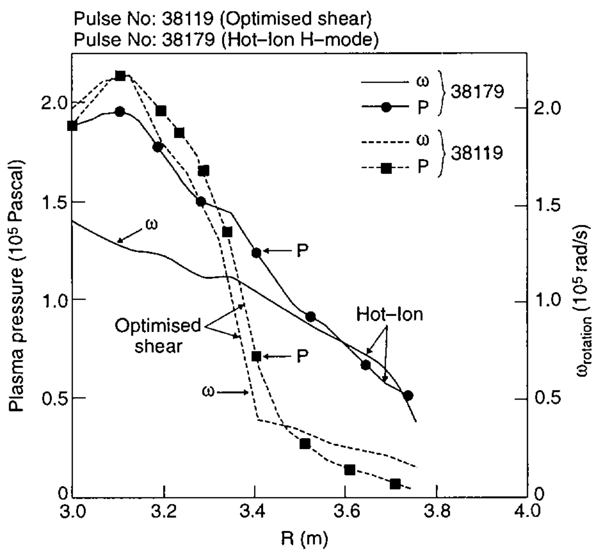

FIG. 15. Profiles of total plasma pressure and poloidal rotation frequency in a hot ion H-mode and an optimised shear discharge.

5.3 High current plasmas and approach to steady-state

The combined advantages of the high power handling of Mk IIA, the divertor cryopump and the high recycling conditions established in the divertor enable the production of long pulse steady-state H-modes. ELMy H-modes of 20s duration at 2 MA were achieved in Mk I [24]. Recently, this regime has been extended to higher plasma currents (4.7 MA) and higher input powers with combined ICRH and NB heating. An example of a discharge at 4.7 MA is given in Fig.16 where a fusion triple product of 4 x 10^{20} (m^{-3} s keV) is maintained for 1.5s. This constitutes substantial progress from the best steady-state performance presented [24] at the 1994 IAEA Conference (2.65 x 10^{20} m^{-3} s keV). At higher power (28 MW), the plasma stored energy reached a new world record of 15 MJ. However, steady-state was not achieved in this case. The reasons for this are not clear. It should be noted that in these high current discharges the plasma density increases over several seconds and it is more difficult to maintain the input power above the H-mode power threshold.

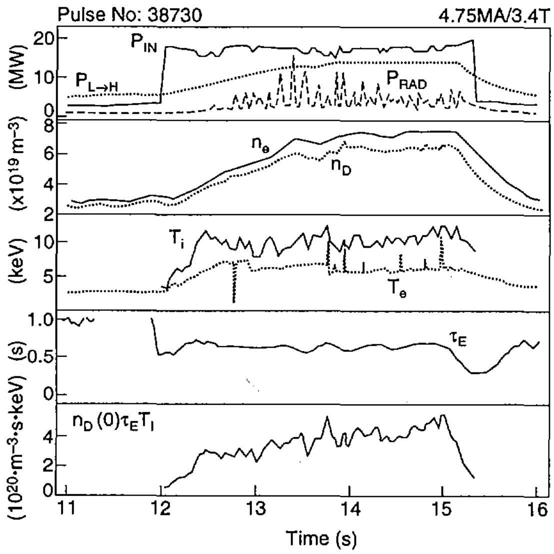

FIG. 16. Time traces of a high power 4.7 MA discharge where the fusion triple product reaches a value of 4 × 10^{20} m^{-3} s keV. P_{L-H} ∝ nBS represents an L- to H-mode threshold power scaling.

6. JET FUTURE PROGRAMME

In the present Mk IIA configuration the conductance of the "by-pass leak" between the divertor and the main torus chamber is comparable to the pumping rate of the cryopumps. These leaks reduce the neutral pressure in the divertor and increase it in the main chamber. They could contribute to the pollution of the main plasma and adversely affect the evaluation of the divertor performance such as the effect of pumping, gas fuelling at different locations within the divertor and seeding of N_2 impurity. The conductance will be reduced by a factor of 5 after a machine intervention in October 1996 to close the larger gaps.

Another divertor configuration is scheduled to be investigated in JET during 1997/98: the so-called Gas Box configuration which will simulate the presently chosen configuration for ITER. It has a large open region close to the target and a narrower entrance. The X-point is high to achieve the longest divertor leg length adjacent to the region of free recirculation of neutrals from the target while minimising the escape of neutrals to the main chamber. Operation with Mk II GB would emphasise the divertor SOL plasma being extinguished (detached) before the target plates are reached. The target configuration can be changed from vertical to horizontal targets by removing parts of the tiles. The target tiles and the tile carriers are both fabricated from CFC and will be installed in JET by remote handling just after the DTE1 experiments.

D/T operation (DTE1) is planned to start on JET in early 1997. The effect of tritium on energy confinement and H-mode threshold will be assessed for the first time in an ITER-like divertor configuration. These experiments are also aimed at demonstrating long-pulse fusion power production with expected fusion power output in the range of 10 MW for several confinement times. A second period of high performance D/T operation (DTE2) is scheduled to take place in 1999. It will take advantage of a preceding period for optimising the operating modes and the in-vessel configuration. This period of D/T operation will also provide a full scale test of the technology of processing tritium in conjunction with an operating tokamak and the experiments will address α-particle heating and associated effects.

7. DISCUSSION AND CONCLUSIONS

JET has conducted a wide range of experiments in both an open and moderately closed divertor configuration. The issues of confinement quality, plasma purity and divertor operating conditions have been addressed and are reported in ten papers at this Conference. The excellent power handling of the Mk IIA divertor has been demonstrated and has allowed new performance developments including a record plasma energy of 15 MJ and a high fusion triple product in high current steady-state discharges.

Modelling of the particle and power exhaust in the divertor has progressed and describes the observations well, with the notable exception of discharges with large ELMs which are not presently taken into account accurately.

Long pulse ITER dimensionless conditions and type I ELMs satisfy the ITER confinement requirements. The ITERH93-P confinement scaling is confirmed over a broad range of parameters but the scaling with β is found to be more favourable. If this is confirmed on other experiments, the confinement time predicted for ITER should increase by about 10 to 15 %.

Confinement degrades in highly radiating discharges and Z_{eff} can be large in impurity seeded discharges at low density. Plasma purity is better at high density and a data base quantifies the expected plasma purity in ITER.

In addition to the hot ion H-mode, a second high performance regime has been developed in JET. It is based on optimising the plasma current profile. With low central magnetic shear and $q > 1$ everywhere in the plasma, internal confinement barriers are observed above a power threshold which is presently about 17 MW. This regime appears similar to that obtained with identical geometry in DIII-D. It is significant that the confinement barrier appears in JET despite a lower fuelling and toroidal momentum input in JET than in DIII-D.

D/T experiments will start in early 1997. The experiment will address the effect of tritium on energy confinement and H-mode threshold in an ITER-like divertor configuration.

ACKNOWLEDGEMENTS

The JET team wishes to acknowledge the collaborations with the European Institutions which were essential to the progress made throughout this research. The optimised shear experiments reported here were conducted in collaboration with the DIII-D team (General Atomics, USA). The author wishes to thank Dr V Bhatnagar for the preparation and editing of this paper.

REFERENCES

[1] JET TEAM, in Plasma Physics and Controlled Nuclear Fusion Research 1990 (Proc. 13th Int. Conf. Washington, DC, 1990), Vol. 1, IAEA, Vienna (1991) 27.
[2] JET TEAM, Plasma Phys. Control. Fusion **37** (1995) A3.
[3] JET TEAM, Nucl. Fusion **32** (1992) 187.
[4] VLASES, G.C., SIMONINI, R., in Controlled Fusion and Plasma Physics (Proc. 18th Eur. Conf. Berlin, 1991), Vol. 15C, Part III, European Physical Society, Geneva (1991) 221.
[5] STOTT, P., in Proc. 19th Symp. on Fusion Technology (SOFT), Lisbon, 1996.
[6] FASOLI, A., et al., Nucl. Fusion **35** (1995) 1485.
[7] PUPPIN, S., et al., in Proc. 19th Symp. on Fusion Technology (SOFT), Lisbon, 1996.
[8] JET TEAM, IAEA-CN-64/AP1-18, this volume.
[9] REBUT, P.H., et al., Fusion Eng. Des. **22** (1993) 7.
[10] JET TEAM, Plasma Phys. Control. Fusion **37** (1995) A227.
[11] JET TEAM, IAEA-CN-64/A4-1, this volume.
[12] JET TEAM, IAEA-CN-64/D3-3, these Proceedings, Vol. 2.
[13] LOARTE, A., in Proc. 12th Int. Conf. on Plasma Surface Interactions in Controlled Fusion Devices, St. Raphael, France, 1996, J. Nucl. Mater. (in press).
[14] JET TEAM, IAEA-CN-64/AP1-2, this volume.
[15] JET TEAM, IAEA-CN-64/A1-1, ibid.
[16] MATTHEWS, G.F., et al., in Proc. 12th Int. Conf. on Plasma Surface Interactions in Controlled Fusion Devices, St. Raphael, France, 1996, J. Nucl. Mater. (in press).
[17] JET TEAM, IAEA-CN-64/A2-6, this volume.
[18] JACQUINOT, J., et al., Fusion Technol. **21** (1992) 2254.
[19] N'GUYEN, F., et al., in Controlled Fusion and Plasma Physics (Proc. 22nd Eur. Conf. Bournemouth, 1995), Vol. 19C, Part II, European Physical Society, Geneva (1995) 353.
[20] JET TEAM, IAEA-CN-64/A3-2, this volume.
[21] JET TEAM, IAEA-CN-64/A1-5, ibid.
[22] HUGON, M., et al., Nucl. Fusion **32** (1992) 33.
[23] JET TEAM, IAEA-CN-64/A5-5, this volume.
[24] JET TEAM, in Plasma Physics and Controlled Nuclear Fusion Research 1994 (Proc. 15th Int. Conf. Seville, 1994), Vol. 1, IAEA, Vienna (1995) 51.

Appendix I

THE JET TEAM

JET Joint Undertaking, Abingdon, Oxon, OX14 3EA, U.K.

J.M. Adams[1], P. Ageladarakis, S.Ali-Arshad, B. Alper, H. Altmann, P. Andrew, N. Bainbridge, P. Bak[12], B.Balet, Y. Baranov[8], P. Barker, R. Barnsley[2], M. Baronian, K. Barth, D.V. Bartlett, A.C. Bell, E. Bertolini, V. Bhatnagar, A.J. Bickley, H. Bindslev, K. Blackler, D. Bond, T. Bonicelli, D. Borba, M. Brandon, P. Breger, H. Brelen, P. Brennan, W.J. Brewerton, M.L. Browne, T. Budd, A. Burt, P. Burton, T. Businaro, M. Buzio, C. Caldwell-Nichols, D.J. Campbell, D. Campling, P. Card, G. Celentano, C.D. Challis, A.V. Chankin, A. Cherubini, D. Chiron, J. Christiansen, P. Chuilon, D. Ciric, R. Claesen, H.E. Clarke, S. Clement, J.P. Coad, U. Cocilovo[10], I. Coffey[7], G. Conway[17], S. Cooper, J.G. Cordey, G. Corrigan, G. Cottrell, M. Cox[7], P. Crawley, R. Cusack, N. Davies, S.J. Davies, J.J. Davis, M. de Benedetti, H. de Esch, J. de Haas, E. Deksnis, N, Deliyanakis, E. di Marchi, A. Dines, S.L. Dmitrenko, J. Dobbing, N. Dolgetta, S.E. Dorling, P.G. Doyle, H. Duquenoy, A.M. Edwards[7], A.W. Edwards, J. Egedal, J. Ehrenberg, A. Ekedahl[11], T. Elevant[11], J. Ellis, M. Endler[13], S.K. Erents[7], L.G. Eriksson, H. Falter, J.W. Farthing, A. Fasoli[18], B. Fechner, M. Fichmüller, B. Fischer, G. Fishpool, C. Froger, K. Fullard, M. Gadeberg, L. Galbiati, E. Gauthier[3], R. Giannella, A. Gibson, R.D. Gill, D. Godden, A. Gondhalekar, M. Goniche[3], D. Goodall[7], C. Gormezano, C. Gowers, J. Graham, K. Guenther, R. Guirlet[3], H. Guo[22], A. Haigh, B. Haist[4], C.J. Hancock, P.J. Harbour, N.C. Hawkes[7], N.P. Hawkes[1], J.L. Hemmerich, T. Hender[7], J. Hoekzema, L. Horton, J. How, A. Howman, M. Huart, T.P. Hughes, F. Hurd, G. Huysmans, A. Hwang, C. Ibbott, C. Ingesson[15], B. Ingram, M. Irving, J. Jacquinot, H. Jaeckel, P. Jaeckel, J.F. Jaeger, O.N. Jarvis, F. Jensen, M. Johnson, E.M. Jones, L.P.D.F. Jones, T.T.C. Jones, J-F. Junger, F. Junique, A. Kaye, B.E. Keen, M. Keilhacker, W. Kerner, N.G. Kidd, Q.A. King, S. Knipe, R. Konig, J.G. Krom, H. Kubo[19], P. Kupschus, P. Lamalle[14], R. Lässer, J.R. Last, L. Lauro-Taroni, K. Lawson[7], M. Lennholm, J. Lingertat, A. Loarte, P.J. Lomas, M. Loughlin, T. Lovegrove, C. Lowry, A.C. Maas[15], B. Macklin, C.F. Maggi[16], M. Mantsinen[5], V. Marchese, F. Marcus, J. Mart, D. Martin, T. Martin, G. Matthews, H. McBryan, G. McCormick[13], G. McCracken, P.A. McCullen, A. Meigs, P. Miele, F. Milani, J. Mills, R. Mohanti, R. Monk, P. Morgan, D. Muir, G. Murphy, F. Nave[21], G. Newbert, P. Nielsen, P. Noll, W. Obert, D. O'Brien, E. Oord, R. Ostrom, M. Ottaviani, S. Papastergiou, V.V. Parail, R. Parkinson, W. Parsons, B. Patel, A. Paynter, A. Peacock, N. Peacock[7], R.J.H. Pearce, C. Perry, M.A. Pick, J. Plancoulaine, O. Pogutse, L. Porte, R. Prentice, S. Puppin, G. Radford[9], T. Raimondi, R. Reichle, V. Riccardo, E. Righi, F. Rimini, A. Rolfe, A. Rookes[12], R.T. Ross, A. Rossi, L. Rossi, G. Sadler, G. Saibene, M. Salisbury[12], A. Santagiustina, F. Sartori, R. Sartori, R. Saunders, P. Schild, M. Schmid, V. Schmidt, B. Schokker[15], B. Schunke, M. Scibile, S.M. Scott, S. Sharapov, A. Sibley, R. Simonini, A.C.C. Sips, P. Smeulders, O. Smith[12], P. Smith, R. Smith, F. Söldner, J. Spence, E. Springmann, M. Stamp, P. Stangeby[20], D.F. Start, D. Stork, P.E. Stott, P. Stubberfield, D. Summers, L. Svensson, P. Svensson, A. Tabasso[12], M. Tabellini, J. Tait, A. Tanga, A. Taroni, C. Terella, P.R. Thomas, K. Thomsen, B. Tubbing, Y. Ul'Haq[12], A. Vadgama, P. van Belle, R. van der Linden, G. Vlases, M. von Hellermann, T. Wade, R. Walton, D. Ward, M.L. Watkins, N. Watkins[1], M.J. Watson, J. Wesson, M. Wheatley, D. Wilson, T. Winkel, C. Woodward, D. Young, I.D. Young, Q. Yu[6], F. Zannelli, K-D. Zastrow, W. Zhang[12], N. Zornig, W. Zwingmann.

PERMANENT ADDRESSES

1. UKAEA, Harwell, Didcot, Oxon, UK.
2. University of Leicester, Leicester, UK.
3. CEA, Cadarache, France.
4. KFA, Jülich, Germany.
5. Helsinki University of Technology, Espoo, Finland.
6. Institute of Plasma Physics, Hefei, P R of China.
7. UKAEA Culham Laboratory, Abingdon, Oxon, UK.
8. A.F. Ioffe Institute, St. Petersburg, Russia.
9. Institute of Mathematics, University of Oxford, UK.
10. ENEA, CRE Frascati, Roma, Italy.
11. Royal Institute of Technology, Stockholm, Sweden.
12. Imperial College, University of London, UK.
13. Max Planck Institut für Plasmaphysik, Garching, Germany.
14. Plasma Physics Laboratory, ERM-KMS, Brussels, Belgium.
15. FOM Instituut voor Plasmafysica, Nieuwegein, The Netherlands.
16. Dipartimento di Fisica, University of Milan, Milano, Italy.
17. University of Saskatchewan, Saskatoon, Canada.
18. EPFL, Lausanne, Switzerland.
19. JAERI, Tokyo, Japan.
20. Institute for Aerospace Studies, University of Toronto, Canada.
21. LNETI, Savacem, Portugal.
22. INRS-Energieet Materiaux, Univ. du Quebec, Canada.

At July. 1996

DISCUSSION

R.J. GOLDSTON: It is somewhat difficult to understand the meaning of your scaling of Z_{eff} as a function of P_{rad}. Does your ITER point imply that adequate radiation can be achieved in ITER at $Z_{eff} \approx 1.2$ (plus helium)?

J. JACQUINOT: The scaling is a simple relationship (dimensionally correct) linking the separatrix surface (S), the charge of the impurity (Z), the plasma density (n_e), the radiated power P_{rad} and Z_{eff}. The relation holds for machines with available data, despite large variations of the parameters. The ITER point corresponds to a reference ITER scenario with 83% radiated power.

M. PORKOLAB: In your optimized shear regime, have you done a transport analysis (similar to that done on TFTR and DIII-D)? If so, what can you say about the ion (and the electron) transport as compared will neoclassical predictions?

J. JACQUINOT: Preliminary analyses using TRANSP calculations show that the electron and ion thermal diffusivities are of the same order and are a few times the neoclassical ion thermal diffusivity.

OVERVIEW OF ASDEX UPGRADE RESULTS

M. KAUFMANN[1], J. SCHWEINZER[1], M. ALBRECHT[1],
M. ALEXANDER[1], K. ASMUSSEN[1], G. BECKER[1], K. BEHLER[1],
K. BEHRINGER[1], R. BEHRISCH[1], E. BERGER[1], A. BERGMANN[1],
M. BESSENRODT-WEBERPALS[1], K. BORRASS[1], H.-S. BOSCH[1],
B.J. BRAAMS[15], M. BRAMBILLA[1], F. BRAUN[1], H. BRINKSCHULTE[1],
C. BROSIG[1], K. BÜCHL[1], A. BUHLER[1], H. CALLAGHAN[4],
A. CARLSON[1], R. CHODURA[1], D.P. COSTER[1], L. CUPIDO[2],
H.J. DE BLANK[1], S. DE PEÑA HEMPEL[1], S. DESCHKA[1],
V. DOSE[1], C. DORN[1], G. DODEL[9], R. DRUBE[1], R. DUX[1],
A.S. EGOROV[10], W. ENGELHARDT[1], J. ENGSTLER[1],
H.U. FAHRBACH[1], U. FANTZ[9], H.U. FEIST[1], S. FIEDLER[17],
G. FIEG[3], A. FIELD[1], P. FRANZEN[1], J.C. FUCHS[1],
G. FUSSMANN[1], J. GAFERT[9], G. GANTENBEIN[9],
G. GARCIA-ROSALES[1], O. GEHRE[1], J. GERNHARDT[1],
T. GROSSMANN[2], O. GRUBER[1], S. GÜNTER[1], G. HAAS[1],
K. HALLATSCHEK[1], J. HARTMANN[1], B. HEINEMANN[1],
P. HEIMANN[1], A. HERRMANN[1], W. HERRMANN[1],
G. HERPPICH[1], F. HERTWECK[1], K. HIRSCH[9], S. HIRSCH[1],
M. HOEK[1], F. HOFMEISTER[1], F. HOENEN[7], E. HOLZHAUER[9],
H. HOHENÖCKER[1], P. IGNACZ[5], D. JACOBI[1], B. JÜTTNER[1],
W. JUNKER[1], M. KAKOULIDIS[8], A. KALLENBACH[1],
V. KAPRALOV[10], N. KARAKATSANIS[8], O. KARDAUN[1],
T. KASS[1], H. KASTELEWICZ[1], C.C. KLEPPER[13], H. KOLLOTZEK[1],
W. KÖPPENDÖRFER[1], W. KRAUS[1], K. KRIEGER[1], B. KURZAN[1],
B. KUTEEV[10], G. KYRIAKAKIS[8], K. LACKNER[1], P.T. LANG[1],
R. LANG[1], S. LASHKUL[11], M. LAUX[1], B. LEBLANC[12], L. LENGYEL[1],
A.W. LEONARD[14], F. LEUTERER[1], G. LIEDER[9], C. LOUREIRO[2],
J. MAIER[1], R. MAINGI[13], M.E. MANSO[2], M. MARASCHEK[1],
M. MARKOULAKI[8], M. MAST[1], P. McCARTHY[4], D. MEISEL[1],
H. MEISTER[1], R. MERKEL[1], V. MERTENS[1], I. MIROSHNIKOV[10],
H.W. MÜLLER[1], F. MÜNICH[1], H. MURMANN[1], B. NAPIONTEK[1],
D. NAUJOKS[1], G. NEU[1], R. NEU[1], J. NEUHAUSER[1],
J.-M. NOTERDAEME[1], M. NIETHAMMER[9], L. O'SHEA[4],
M. PACCO-DÜCHS[1], E. PASCH[1], G. PAUTASSO[1], A.G. PEETERS[1],
G. PETRAVICH[5], C.S. PITCHER[6], W. POSCHENRIEDER[1],
I. PRECHT[1], F. PURI[1], G. RAUPP[1], K. REINMÜLLER[1],
H. REIMERDES[1], R. RIEDL[1], V. ROHDE[1], H. RÖHR[1],
J. ROTH[1], F. RYTER[1], H. SALZMANN[1], W. SANDMANN[1],
J. SANTOS[2], W. SCHÄRICH[1], H.-B. SCHILLING[1],
M. SCHITTENHELM[1], D. SCHLÖGL[1], H. SCHNEIDER[1],
R. SCHNEIDER[1], U. SCHNEIDER[1], W. SCHNEIDER[1],

K. SCHÖNMANN[1], G. SCHRAMM[1], U. SCHUMACHER[9],
T. SCHÜTTE[9], S. SCHWEIZER[1], R. SCHWÖRER[1],
B. SCOTT[1], U. SEIDEL[1], S. SESNIC[1], F. SERRA[2],
A. SILVA[2], M. SOKOLL[1], P. SPATHIS[19], E. SPETH[1],
A. STÄBLER[1], K.-H. STEUER[1], J. STOBER[1], B. STREIBL[1],
W. SUTTROP[1], A. THOMA[1], C. TICHMANN[1], R. TISMA[1],
W. TREUTTERER[1], M. TROPPMANN[1], N. TSOIS[8],
M. ULRICH[1], P. VARELA[12], I. VESELOVA[16], H. VERBEEK[1],
P. VERPLANCKE[1], O. VOLLMER[1], M.R. WADE[13], H. WEDLER[1],
U. WENZEL[1], F. WESNER[1], M. WEINLICH[1], H. WERTHMANN[1],
R. WILHELM[1], R. WOLF[1], R. WUNDERLICH[1], D. WUTTE[17],
N. XANTOPOULOS[8], R. ZANINO[18], D. ZASCHE[1], H.P. ZEHRFELD[1],
T. ZEHETBAUER[1], M. ZILKER[1], H. ZOHM[1], M. ZOUHAR[1]

Abstract

OVERVIEW OF ASDEX UPGRADE RESULTS.

The experimental ASDEX Upgrade results of the Divertor I phase are reviewed with emphasis on H-mode physics, power handling, plasma edge and divertor physics, operational limits (β and density), disruption behaviour and testing of tungsten as a target plate material. All these investigations are focused on the preparation of the ITER physics database. The change to the new divertor is briefly outlined.

[1] Max-Planck-Institut für Plasmaphysik, Euratom-IPP Association, Garching and Berlin, Germany.
[2] Centro de Fusão Nuclear, Lisbon, Portugal.
[3] FZK Karlsruhe, Germany.
[4] University of Cork, Ireland.
[5] Research Institute for Particle and Nuclear Physics, Budapest, Hungary.
[6] Institute for Aerospace Studies, Toronto, Canada.
[7] KFA Jülich, Germany.
[8] NSCR Demokritos, Athens, Greece.
[9] Institut für Plasmaforschung, Universität Stuttgart, Germany.
[10] Technical University, St. Petersburg, Russian Federation.
[11] Ioffe Physico-Technical Institute, St. Petersburg, Russian Federation.
[12] Princeton Plasma Physics Laboratory, Princeton, New Jersey, USA.
[13] Oak Ridge National Laboratory, Oak Ridge, Tennessee, USA.
[14] General Atomics, San Diego, California, USA.
[15] New York University, New York, USA.
[16] LPI, St. Petersburg, Russian Federation.
[17] Institut für Allgemeine Physik, Technische Universität, Vienna, Austria.
[18] Technical University, Turin, Italy.
[19] IESL FORTH, Heraklion, Greece.

1. Introduction

ASDEX Upgrade (AUG) is a mid-size tokamak with non-circular cross section (major radius R_0 = 1.65 m, horizontal minor radius a = 0.5 m, elongation b/a = 1.6), designed as a poloidal divertor device rather similar to ITER with respect to magnetic configuration. All poloidal field coils of AUG are placed outside the toroidal ones. A saddle coil ('PSL' .. passive stabilising loop) inside the vacuum vessel damps the vertical displacement instability. The present divertor configuration (Divertor I) places the target plates relatively close to the X-point (cf. fig. 15).
In general all plasma-facing components are graphite-covered (except target plates, cf. chapt. 8), the vessel is routinely boronized and turbomolecular pumps (15 m^3/s for D_2) allow the control of hydrogen and noble gas particle content of the vessel. Usually, AUG is operated in a single-null divertor configuration (SN) and in the following regime of global parameters: $|B_T|$ = 1.5 - 3 T, I_P = 0.6 - 1.2 MA (q_{95} = 2.1 - 5.8) and ion ∇B drift towards the X-point. Discharges are usually D_2 or H_2 gas-fuelled, but fuelling by pellets is also possible (cf. chapt. 6).
For additional heating ICRH, ECRH and NBI (neutral beam injection) systems are applied. The ICRH system has a broad frequency range (30 $\leq$ f $\leq$ 120 MHz) and a power capability of each of its four generators of up to 1.5 MW. Recently an ECRH system (140 GHz, up to 400 kW) has been installed which is mainly used for modulation experiments. The NBI system (beam energy 65 keV for D_2) reaches routinely injected powers of up to 10 MW. In addition the beam can be chopped with variable duty cycle permitting fine-tuning of the injected power.
Being one of the most ITER-similar experiments, AUG has directed the efforts mainly towards the solution of the most crucial problems for the successful operation of the ITER fusion reactor as there are power handling, impurity control and helium pumping. Further objectives are H-mode physics, operational limits, discharge control, disruption dynamics and plasma-facing materials.
This paper reviews the most important results of the experimental campaigns until this current IAEA conference. In addition, the future program of AUG, especially the adaptation of the divertor (Divertor II), will be briefly described.

2. Development of Diagnostics

AUG is equipped with an extensive range of diagnostic systems, many of them being aimed at edge and divertor parameters. Three examples for recent development of diagnostic systems will be presented in the following.

2.1. Fast ECE Radiometer

Fast, local T_e measurements on AUG are performed by means of a 45-channel ECE heterodyne radiometer with horizontal line-of-sight at the midplane on the low field side. As an example of the results obtained with this system, the formation of tearing modes for ohmic density limit discharges will be described.
As tearing modes rotate toroidally with respect to the fixed line of sight of the ECE diagnostic, a two-dimensional toroidal flux surface map can be reconstructed from the $T_e(t,r)$ measurement during the time of one toroidal rotation. Fig. 1 shows a contour plot of T_e measured during the current profile contraction phase between two minor disruptions. Regions with a temperature variation of less than 20 eV around q=2 and less than 10 eV for q $\geq$ 3 are identified as islands with m=2 and m=3 mode numbers, respectively [1].
In high q discharges the MHD activity leading to the density limit seems to be initiated by radiative cooling of the m=3 island ('Rebut-mechanism'). Repetitive minor disruptions happen due to coupling of (3,1) and (2,1) islands.

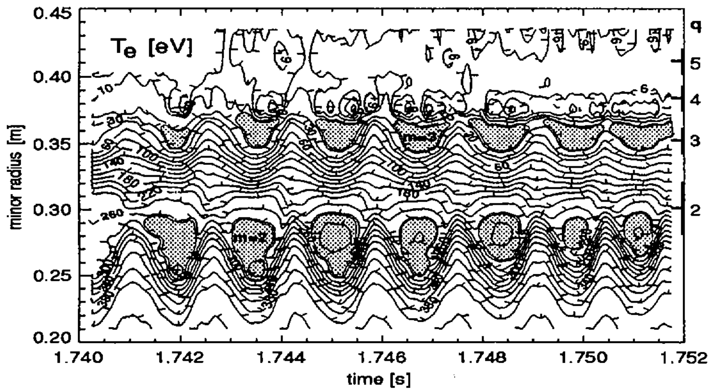

Fig. 1: Reconstruction of coupled (2,1) and (3,1) islands from ECE T_e measurement in a time interval during current profile contraction between two minor disruptions. Islands recognised by regions of flat T_e are marked by shaded areas. While the (3,1) island grows, the (2,1) island shrinks. q(r) is derived from equilibrium reconstruction at t=1.75s.

2.2. Radial Electric Field from CX Neutral Analysis

Fluxes of neutrals that result from charge-exchange processes of slowing-down ions from the neutral injection that have scattered into the ripple-trapped domain, can deliver information about radial electric fields E_r in the plasma [2]. This method provides data with improved time resolution (≈ 100 μs) compared to spectroscopic measurements.

Especially for the L-H transition the behaviour and temporal development of E_r plays a decisive role in various theories [3]. In Fig. 2 energy spectra of neutrals originating from ripple trapped particles are plotted for five different time points relative to the L-H transition (t=0 corresponds to the drop in the D_α signal, not shown). The change in the energy spectra is due to an increase of E_r which confines ripple-trapped particles with increasing energy. According to single particle calculations the spectrum for t=132.5 ms suggests that the electric field E_r has reached a final value of 19 kV/m after a slow L-H transition process.

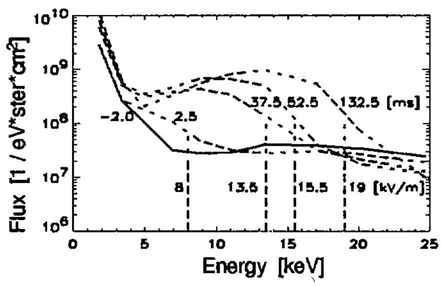

Fig. 2: Energy spectra of ripple trapped ions at five different time points relative to the L-H transition.

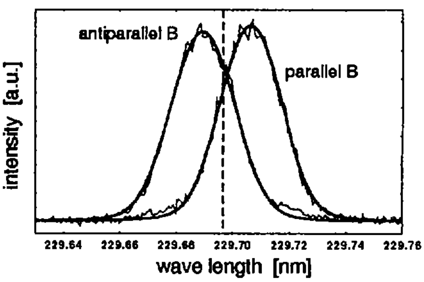

Fig. 3: CIII singlet line spectra for two toroidal chords parallel and antiparallel to the magnetic field, respectively.

2.3. Impurity Flow towards the Divertor

Drift velocities of impurity ions in the divertor region have been determined by measuring Doppler shifts of emission lines. Fig. 3 shows the CIII-line emission which was recorded from chords viewing toroidally in opposite directions in the divertor above the recycling zone. The opposite line shifts result from a net drift of C^{2+} ions towards the outer target plates and correspond to a toroidal drift velocity of about $1.1 \cdot 10^4$ m/s [4]. With an ion temperature of 6 eV as obtained from the width of the spectra, a Mach number of 0.4 - 0.5 can be derived for the CIII emission region which is in agreement with B2-EIRENE model calculations [5].

3. Transport

Confinement is an essential issue for ITER which will probably require the improved confinement of the H-mode. Therefore, in AUG, L and H-mode confinement properties were compared, in particular under conditions relevant for ITER.

3.1. Global Confinement Characteristics

For ion ∇B drift towards the X point and medium deuterium density the H-mode power threshold is low. Under such operational conditions, the H-mode exhibits higher confinement than the L mode by an enhancement factor $f_H = 1.6 - 2$ [6]. However, under conditions of high threshold (hydrogen instead of deuterium, ion ∇B drift away from X point) the L-mode confinement gradually improves with power and approaches that of the H-mode, leading to a vanishing hysteresis in the L-H, H-L transition [3].
Whereas the L-mode confinement is only weakly influenced by increasing edge density or neutral density in the divertor, the H-mode confinement is significantly deteriorated in high density discharges (cf. chapt. 6.2).
Puffing of impurities for radiative cooling (cf. chapt. 7.2] in such high density discharges leads to less degradation of confinement, because moderate peaking of the electron density profile compensates for this effect [6].

3.2. Transport Investigations by Heat Waves

We have investigated the electron heat conductivity χ_e using both sawtooth (χ_e^{ST}) and ECRH modulation (χ_e^{ECRH}) heat pulse propagation ($P_{ECRH} \leq 400$ kW) in ohmic and L-mode discharges. Results for χ_e from such perturbative experiments in comparison with values obtained from power balance (χ_e^{PB}) considerations are summarised in fig. 4 [6]. The analysis of sawteeth yields $1 < \chi_e^{ST} / \chi_e^{PB} \leq 6$ and no correlation between χ_e^{ST} and χ_e^{PB} is found. However, in the case of ECRH modulation, χ_e^{ECRH} is at most two times larger than χ_e^{PB}, which is in agreement with the assumption $\chi_e \propto (\nabla T_e)^\alpha$ ($\alpha \leq 1$) [7]. Therefore, we conclude that the results from the ECRH modulation represent the steady-state transport, whereas the sawtooth analysis in general does not, because the perturbation in the latter case is too high [6].

3.3. Scaling of 'Dimensionally Similar' Discharges

The scaling of confinement with the normalised gyroradius ρ^* has been examined with 'dimensionally similar' discharges by varying just ρ^* while leaving all other dimensionless parameters (safety factor q, collisionality ν^* and normalised pressure β_N) unchanged. Such an approach has the advantage that the transport behaviour of future devices like ITER with similar q, ν^*, β_N values can be derived from existing data, if the scaling with a single parameter ρ^* is known.
In a series of 'dimensionally similar' L-mode discharges a Bohm like scaling of the confinement has been observed [6].

The confinement variation in a similar H-mode scan with $\nu_{min}^* \approx 0.1$ which yielded gyro-Bohm like scaling confirms results from JET and DIII-D which were found for an even more collisionless regime ($\nu_{min}^* \approx 0.01$). Thus the Ansatz of a simple power law in ρ^* for the thermal diffusivity was justified in a wide range of collisionality.

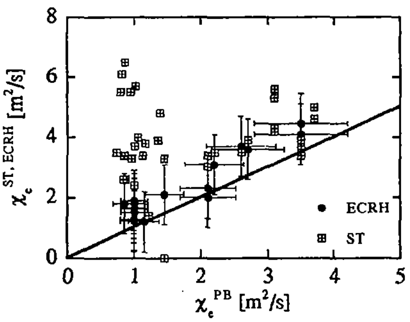

Fig. 4: Thermal conductivity derived from modulation experiments vs. corresponding ones from power balance considerations for Ohmic and L-mode discharges. All χ_e^{PB} values above 2 m^2/s are from hydrogen discharges (cf. text).

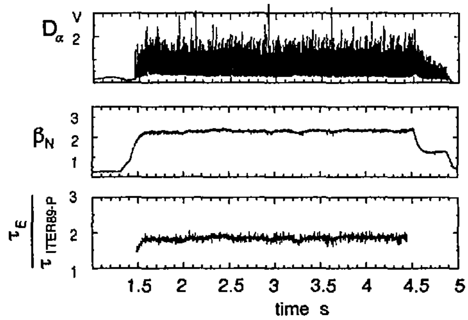

Fig. 5: Time traces of D_α, β_N and the normalised confinement time τ_E for a stationary ELMy H-mode discharge (P_{heat} = 7.5 MW, q = 3, I_P=1 MA, B_T = 2 T) near the ITER operation point (cf. chapt. 4).

4. β-Limit

The operational space of tokamak devices is limited in the safety factor q, the density n_e (cf. chapt. 6) and the plasma pressure β by the occurrence of MHD activity. Here we discuss the MHD characteristics of these limits. The need for high β operation in ITER has triggered a series of β–limit experiments on AUG in ITER-similar geometry. In the following we use β_N which is normalised according to the Troyon scaling [8] and the q value at the 95% flux surface.

The maximum achievable β_N^{max} in a discharge as a function of q was determined and a maximum of $\beta_N^{max} \approx 3$ around $q \approx 3$ was found. Ideal MHD stability theory predicts a higher limit ($\beta_N^{max} \approx 4$), but low (m,n) tearing modes develop leading to the lower value found in the experiment. Near the desired ITER operation point of β_N = 2.5 and q=3 discharges exhibited stationary behaviour over more than 30 confinement times. This is documented in fig. 5 for a 7.5 MW NBI heated ELMy H-mode discharge where time traces of Dα, β_N and the normalised confinement time τ_E are presented. However, even for such cases of reduced β_N, the occurrence of tearing modes leading to confinement deterioration cannot be ruled out completely.

There is strong evidence that the observed tearing modes are of neo-classical origin [33]. For q values lower than 3, β limit discharges terminate with a disruption due to locking of the neoclassical modes, whereas for higher q values these modes do not lock and generally no disruption occurs. In the latter case, tearing modes persist also after the β drop, but lead only to enhanced core transport.

5. H-Mode Operation Window in terms of Local Parameters

The H-mode with Edge Localised Modes (ELMs) is still regarded as the most promising stationary regime of enhanced confinement for a future reactor-size fusion device. The H-mode operation space is usually characterised by global plasma parameters [3]. However, both theory [9] and experiment suggest that H-mode behaviour is connected to edge rather than to global parameters. Therefore, we have correlated the L-H transition with local measurements of T_e (ECE radiometer, Thomson scattering) and n_e (Li-Beam, DCN interferometer). These measurements (T_e^b, n_e^b) are taken in the barrier region about 2 cm inside the separatrix where the physics of closed field lines dominates over SOL physics. We find for T_e^b at the L-H and H-L transitions a general trend towards a slight decrease at increasing n_e^b. Furthermore, only a weak variation of T_e^b at the L-H and H-L transition occurs, suggesting that the hysteresis in P_{tot} is not a collisionality effect, but mainly due to a change in confinement [10].
Fig. 6 shows forbidden (shaded) areas as well as various stable operational regimes in a T_e^b, n_e^b diagram. One can distinguish between regions of L-mode, instationary ELM-free H-mode and ELMy H-mode with two different ELM types. Type-I ELMs occur at $T_e^b \cdot n_e^b$ = const. = $p_{e,edge}$ which indicates, assuming a roughly constant radial decay length, a limit to the pressure gradient as is in accordance with the ideal ballooning limit [3]. In addition the L-H transition as well as the boundary of the Type-III ELM regime are indicated by the dashed lines. Type-III ELMs mainly occur below a certain critical temperature suggesting that resistivity plays a decisive role for their understanding. Both ELM types are observed in the same density range. Type-I and Type-III ELMs are also distinguished by the heating power dependence of their repetition frequency as well as by clear differences in the magnetic precursors [3]. The latter have been found for the first time for Type-I ELMs at very low frequencies (below 10 kHz).

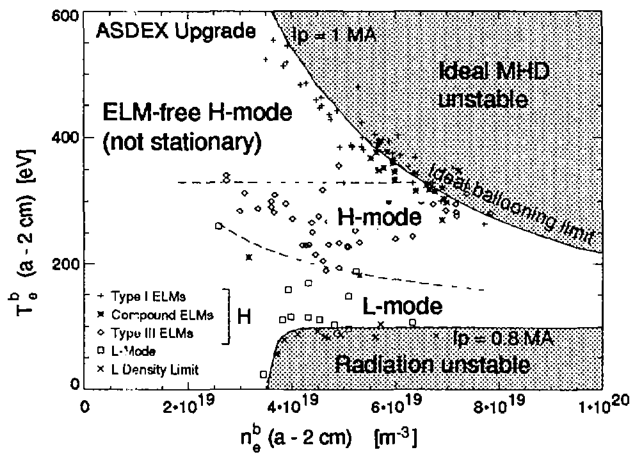

Fig. 6: Regions of stable and unstable discharge behaviour for L and H-mode confinement in a T_e^b, n_e^b - plane (cf. text).

6. Density Limit

The line-averaged density corresponding to the density limit (DL) which is normally disruptive in tokamaks is empirically described by the 'Greenwald' limit (GL) [11], which depends on elongation and plasma current density and is insensitive to heating power. Future fusion devices like ITER envisage operation at densities beyond the DL when this scaling law is assumed for extrapolation.
Raising the density in H-mode discharges leads to an H-L transition prior to the standard L-Mode DL. The validity of the present scaling law for the H-mode threshold using global parameters is not proven in the high density regime. In addition to global parameters also local ones of the plasma boundary have to be taken into consideration.
Therefore, AUG has investigated also in terms of edge parameters the ITER-relevant high power, high density regime in order to establish a more secure basis for extrapolation to ITER.

6.1. The Disruptive Density Limit in the L-Mode

In order to investigate the power dependence of the DL in L-mode, it was necessary to prevent a transition to H-mode. This can be achieved by increasing the H-mode power threshold by using hydrogen instead of deuterium or more advanced by carefully raising both density and heating power simultaneously in appropriate steps [11]. In contradiction to the GL, we found in clean (no additional impurity puffing) discharges a moderate but distinct increase of $\bar{n}_e$(DL) with rising heating power P_{heat} as one would expect assuming Marfes to be the cause for the DL. For hydrogen discharges with $\bar{n}_e(DL) \propto P_{heat}^{0.3}$ a slightly stronger dependence as for deuterium discharges with $P_{heat}^{0.23}$ [11] is found. In addition the GL has been slightly surpassed with deuterium and clearly overcome by a factor of 1.4 with hydrogen. This difference is probably due to cleaner discharges and therefore smaller Z_{eff} values in the case of hydrogen compared to deuterium. Considering edge parameters the dependence between density n_e^{sep}(DL) and the power crossing the separatrix, P_{sep}, is considerably more pronounced with $n_e^{sep}(DL) \propto P_{sep}^{0.6}$ [11].
The DL in highly radiating impurity dominated L-mode discharges ($f_{rad} = P_{rad}/P_{heat} > 90\%$, averaged $Z_{eff} \leq 4$) seems to be independent of P_{heat}, although the same detachment and Marfe sequence as in the clean hydrogen/deutrium case is observed [12]. Increasing P_{heat} in such 'dirty' discharges leads obviously only to a higher radiation level, but cannot be translated into increased density. In such highly radiating AUG discharges Z_{eff} might be artificially connected to P_{heat} by the applied feedback control of f_{rad} (cf. chapt. 7.2). Thus, higher P_{heat} causes higher Z_{eff} leading to a power insensitivity of the DL, which occurs normally at densities of 60% to 80% of the GL.

6.2. Upper Density for H-Mode Operation

The maximum achievable density in H-mode discharges is limited by an H-L transition. The line in fig. 6 corresponding to both the L-H and the H-L transition (note, no hysteresis in this picture) terminates at a maximal density value. Attempts to overcome this value by strong gas puff accompanied with high NBI heating power did not succeed. [13, 11]. A considerable degradation in H-Mode confinement with increasing edge density has to be assumed to explain this behaviour. Because of this unfavourable change in H-mode confinement properties, the achievement of the necessary edge temperatures at reasonable heating powers in the high density regime of gas fuelled discharges seems to be almost impossible. This effect is also found in global confinement where τ_E in the H-mode decreases with increasing edge density [14]. The fundamental reason for this degradation is still unclear.

6.3. Pellet Fuelled Discharges

Approaching in a gas-puff fuelled H-mode discharge the H-L transition by increasing the neutral density causes higher edge density but increases the central one only weakly. Particle refuelling by pure gas puff has touched hard limits in the operational space at least when H-mode confinement is aspired (cf. chapt. 6.2). Therefore, higher densities might only be possible by introducing an additional particle source inside the plasma.

Combining repetitive pellet injection with moderate gas puff fuelling permits the achievement of stationary phases of high density exceeding the GL. In a first attempt densities twice the GL have been reached transiently in non-stationary discharges, which suffered from excessive plasma cooling caused by the pellets. As a special tool to maintain long lasting high density phases we applied a control algorithm using a bremsstrahlung signal as a measure of the line averaged density to inhibit the injection of pellets when a pre-programmed n_e is reached. In this way stationary phases with line averaged densities of up to 1.5 GL in ELMy H-mode discharges have been achieved.

In Type-I ELMy H-mode discharges each pellet triggers an ELM which expels a part of the injected fuel [12] and thus lowers the fuelling efficiency in addition to the well-known reduced efficiency at higher T_e. All previous pellet fuelling experiments on tokamaks have operated on the low field side (LFS) suffering from outward drift effects which lead to unfavourable results at higher heating power.

In recent investigations on AUG high efficient fuelling of H-mode discharges by pellets was demonstrated. This considerable improvement in fuelling efficiency by a factor of 4 (cf. fig. 7) could be achieved by injecting pellets from the high field side (HFS) [15]. Injection from the HFS takes advantage of drifts which help to transport the deposited pellet material towards the plasma center.

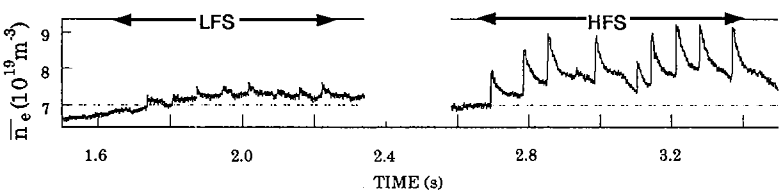

Fig. 7: Line averaged density for a discharge fuelled by identical pellets first from the low field (LFS) and subsequent from the high field (HFS) side.

7. Plasma Edge and Divertor

7.1. H-Mode and Radiating Boundary

Radiative cooling of the plasma boundary by controlled injection of impurities yields substantial reduction of the power flow to the target plates which is indispensable for future reactors. The compatibility of such radiative discharges with H-mode confinement, high heating power and divertor operation was for the first time demonstrated on AUG [16, 14, 17].

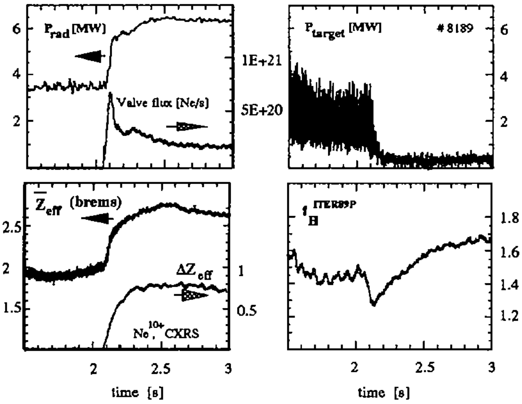

Fig. 8: Radiated power in the main chamber, feedback-controlled Ne flux, total divertor power load from thermography, central line-averaged Z_{eff} from bremsstrahlung and the Z_{eff}-contribution of Ne^{10+} from CXRS, and energy confinement normalised to the ITER89P scaling for a typical H-CDH mode transition.

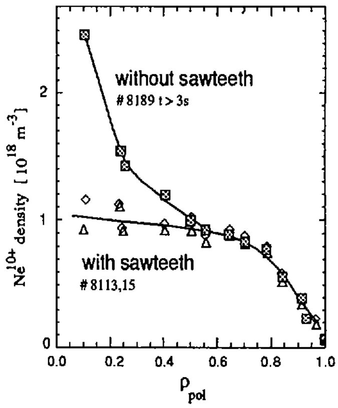

Fig. 9: Radial profiles of fully stripped Neon from CXRS for CDH-discharges with and without sawtooth activity [19].

In these experiments the radiated power fraction was adjusted [18] by a feedback loop controlling the puff rate of the seed impurity (mainly neon) to such a value that the power flow across the separatrix was just above the H-L power threshold. By these means an H-mode with frequent small amplitude Type-III ELMs accompanied by complete divertor detachment (CDH-mode) can be achieved. Thus, high heat loads of the target plates and intolerable Type-I ELMs are avoided. A significant fraction of radiation in a CDH discharge emanates from an edge region inside the separatrix, thus lowering the power flow across the separatrix which has to be kept above the H-L threshold. Fig. 8 shows time traces for the transition from H to CDH mode. Right after the onset of Ne puffing at t=2.05 s, the CDH-mode is obtained, as indicated by the reduced peak target power load of less than 1 MW. However, this reduction of the power flow to the target plates is accompanied by a considerable increase of the central Z_{eff} values. The observed improvement in energy confinement is probably due to a peaking of the electron density profile [17]. The peaking seems to be correlated to the central Z_{eff} [20]. Fig. 9 compares Ne^{10+} profiles measured by CXRS for CDH-mode discharges with and without sawtooth activity. If sawteeth are lost, central impurity peaking is always observed, while with sufficiently high sawtooth frequency, the profiles remain flat. Only a slight increase in energy content and no improvement of radiative characteristics due to sawtooth suppression was found. In particular with respect to dilution sawtooth suppression should be avoided.

In contrast to the standard H-mode no power threshold hysteresis is found in CDH-phases. When the power flow to the edge drops below the H-L transition threshold, the CDH mode converts to a radiative L-mode with still improved confinement compared to ITER-89P L-mode scaling. At high radiation level ($P_{rad}/P_{tot} \geq 0.8$) L and H-modes tend to converge with respect to confinement, although they can still be distinguished by the Type-III ELM signature [17].

The quality of a radiating diverted discharge can be characterised by two parameters $P_z = \Delta P_{rad} / \Delta Z_{eff}$ describing the achieved radiated power per central Z_{eff} increase and by the fraction f^{in} of main chamber radiation emitted from inside

the separatrix [14]. High values for P_z and low values for f^{in} are aspired. The first can be achieved by increasing the edge electron density n_e^b, since ΔP_{rad} scales with ΔZ_{eff}^b and with the square of n_e^b. [19, 21]. On the other hand, f^{in} depends mainly on the choice of the seed impurity and decreases with lower Z. With respect to dilution, however, higher Z values are favoured.
The CDH-mode certainly fulfils the requirement of an operational mode for ITER as far as the power load to the target plates is concerned. However, extrapolation to a ITER size device seems difficult because the H-mode threshold scaling (cf. chapt. 6) is still uncertain.
In addition, the increase of central Z_{eff} in CDH phases is a major concern. However, if appropriate scaling based on data from various machines is used for the extrapolation to ITER, no huge improvement over current experimental results seems necessary to meet the goal of the required low Z_{eff} for ITER [21].

7.2. Pumping of Noble Gases

Exhaust of impurities is not only a technical matter of pumping, but also depends strongly on transport in the scrape-off layer (SOL) and on the divertor retention. These quantities determine the impurity density at the pump duct. Investigations on AUG have shown for Ne [14] and for He [22] that the compression (ratio of divertor and midplane edge neutral density of the respective impurity) increases strongly with the divertor neutral gas flux density. This effect has been shown to be independent of external gas fluxes and determined exclusively by the neutral gas flux density in the divertor [23]. 2D-modelling of impurity transport in the SOL using B2-Eirene has verified this scenario and has reproduced the experimental observations, namely the increasing compression with increasing divertor neutral density. In addition it has been shown that the Ne compression is larger than the He compression (due to the larger ionisation mean free path of He with respect to Ne) [5].
Converting the compression values into enrichment factors (He-compression normalised to deuterium compression) yields values above 0.3 for the H-mode and CDH-mode regime, which is sufficient for He exhaust in ITER. A different way of looking at He exhaust is the normalised confinement time $\rho^* = \tau^*_{He} / \tau_E$ which is often used in 1D burn criteria [24]. Figure 10 shows ρ^* as a function of the neutral gas flux density in the divertor chamber (measured with an ionisation gauge).

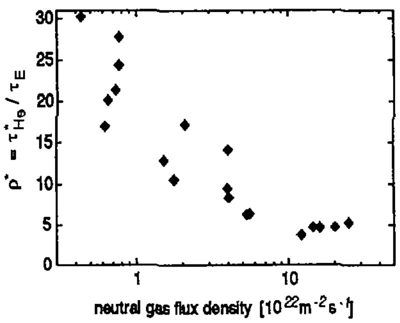

Fig. 10: Normalised confinement time ρ^* vs. neutral gas flux density in the divertor for different discharge modes.

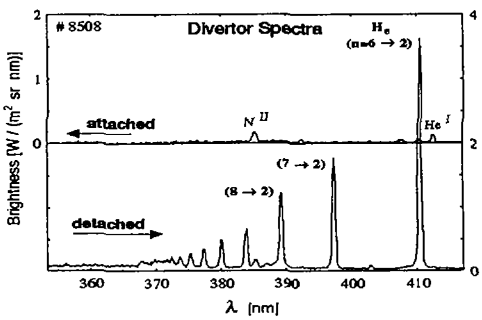

Fig. 11: Spectra of Balmer series measured in the outer divertor at an attached and detached phase (cf. chapt. 7.3).

Again one can see that for H-mode and CDH-mode plasmas (neutral gas flux density $\geq 10^{20}$ m^{-2} s^{-1}), ρ^* is below 10, i.e. it is sufficiently low to allow a continuously burning plasma.

7.3. Volume Recombination

Recently, spectroscopic measurements in the divertor region were performed using lines-of-sight parallel and close to the outer target plate. By this means, we investigated the temporal evolution of the Balmer series during NBI-heated discharges with rising densities approaching the density limit. In such discharges the intensity of continuum and line radiation due to proton-electron recombination processes increased dramatically (cf. fig. 11, where spectra for two densities are compared) at the onset of detachment, indicating that volume recombination contributes significantly to the neutralisation of incoming protons in front of the target plates. In addition a sensitive method for determining T_e in the T_e-region $\leq$ 5 eV has been developed by evaluating these spectroscopic measurements [25]. In a distance 1 - 5 cm above the target plate in the outer divertor T_e values between 0.8 - 1.4 eV were found in the highest density phases.

8. Tungsten Divertor Target Plates

So far no definitive material has been chosen for divertor plates and for the first wall in a future fusion reactor [26]. Under high density and low temperature divertor conditions, which are necessary for power handling in general, high Z-materials like tungsten have the advantage of low sputtering yields and high probability of 'prompt' redeposition of the sputtered atoms [27]. Therefore, tungsten coated tiles, manufactured by plasma spray on graphite, were mounted in the divertor of AUG [28]. Almost 90% of the plasma-facing surface in the strike zone was covered by this tungsten layer. More than 600 discharges with the tungsten divertor have been performed covering the full operational range of AUG (cf. chapt. 1).

Because of the high radiation losses expected from high-Z atoms penetrating the central plasma, the erosion and the transport behaviour of sputtered atoms from the plasma boundary to the core region is very critical and has to be investigated in

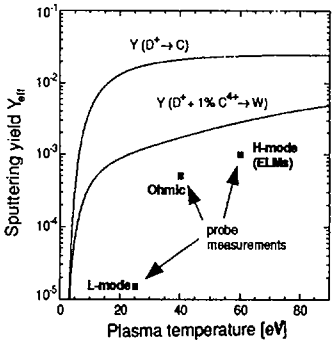

Fig. 12: Measured erosion yields of tungsten for various discharge conditions compared to results from ion-beam measurements [cf. 29].

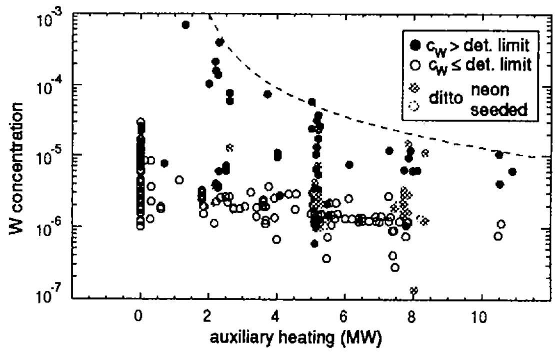

Fig. 13: Concentration of tungsten vs. auxiliary heating power in the main plasma deduced from spectral line emission at 5 nm vs. heating power.

detail in order to prove the suitability of high-Z materials for future application in a fusion device. The effect of prompt redeposition is clearly observed and leads to a reduction of the effective erosion rate in comparison to results from ion-beam measurements (cf. fig. 12). Thus the unwanted flux of sputtered atoms towards the plasma is further reduced in particular for low T_e [29].
In most cases, under normal discharge conditions the volume-averaged concentration of tungsten (relative to electron density) in the main plasma was close to, or even lower than, 10^{-5} (cf. fig. 13). Because of these low concentrations found in most discharges no influence of tungsten on the plasma parameters and the discharge performance was detected. Only in a few low power discharges did accumulation of tungsten occur, which could be explained by trapping of tungsten in a central snake-type m=1 mode [30].
Spectroscopic observation of tungsten both in the main plasma and in the divertor did not reveal a strong correlation between tungsten influx from the target plates and the tungsten content in the central region. The maximum concentration did not increase with rising heating power (cf. fig. 13) concluded from preliminary evaluation of spectroscopic data. A more detailed evaluation of various diagnostic measurements promising a comprehensive picture of erosion and transport of tungsten can be expected in the near future.

9. Disruption Physics and Mitigation

In vertically elongated AUG plasmas disruptions are closely linked with vertical displacement events (VDE) which induce large poloidal halo currents (I_H) and large forces on mechanical structures. Measurements at 6 toroidal positions showed that the maximal I_H values can reach up to 50% of the pre-disruption plasma current (I_P). The toroidal distribution of I_H indicates an n=1 structure with an averaged peaking factor of 1.6 ± 0.5 with respect to the toroidal average. No correlation of this peaking factor with the normalised halo current I_H / I_P was found [8]. For discharges with similar plasma shape and similar vertical shifts, I_H is proportional to I_P / q_{95}.

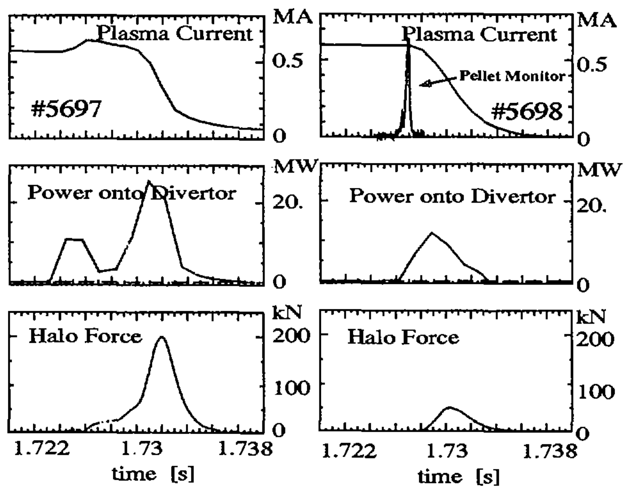

Fig. 14: Comparison of disruption properties in similar discharges with (right) and without (left) 'Ne-killerpellet' injection (cf. text].

The resulting forces on the vessel and the PSL during the disruption (cf. chapt. 1) are reduced both by the interaction of the eddies with the external poloidal field and by the inertial damping of the vessel and reach maxima which are proportional to $I_H \cdot B_t$.
Deposition of the plasma energy on the target plates during disruptions is also a major concern. In clean discharges we observe that up to 100% of the plasma thermal energy and up to 30% of the total (thermal and magnetic) energy is deposited onto the divertor plates during the thermal and current quench respectively. Strong neon puffing reduces these numbers by a factor of two [8].
The extrapolation of our observations to ITER concerning forces and heat loads leads to the conclusion that safety setups will be indispensable. A significant mitigation can be achieved in AUG by injection of neon pellets ($2 \cdot 10^{20}$ atoms, v=560 m/s) penetrating to the plasma core. Such 'killerpellets' cool the plasma in less than 1 ms and trigger a fast current quench. Fig. 14 compares ohmic density limit disruption with a pellet-induced one. After injection of the pellet the energy flux to the divertor is fully suppressed in the thermal quench and even in the following current quench the heat load is significantly reduced as well as the Halo force. In addition the maximal vertical forces on the vessel reach just 50% of the values in the comparable flat-top disruption [31].

10. Outlook

From the experimental experience gained on AUG so far, high radiation, high density, cold divertor operation in combination with high confinement conditions is always connected to only moderate radiation levels in the SOL and divertor. As long as this behaviour cannot be altered by improved divertor concepts, necessary reduced target power loads can only be achieved in such scenarios if the H-mode threshold is low. In addition better compression of impurities in the divertor is required to enhance divertor radiation levels and at the same time decrease the impurity concentration in the main plasma. The final conclusion from all this observations suggests the design of a more closed divertor exhibiting improved retention of all neutral particles.

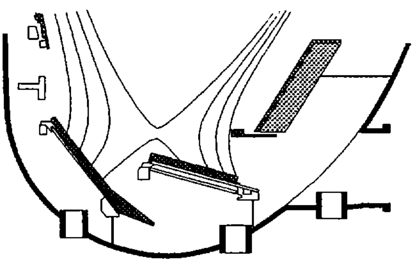

Fig. 15: Poloidal cross section of the present Divertor I.

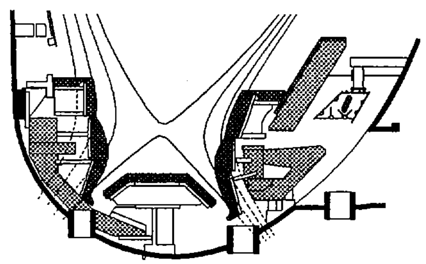

Fig. 16: Poloidal cross section of the future Divertor II LYRA.

In addition, the energy flux density on the AUG target plates has already reached values close to the handling capabilities of the present Divertor I (cf. fig. 15) and measures have to be taken because a second NBI-system (P_{heat}=10 MW) will be installed in the near future.

Therefore, because of these physics and technical reasons, a new divertor design (Divertor II) based on extensive model calculations for the AUG and ITER divertor has been developed [32]. Divertor II consists of two basic structures for the heat load carrying target plates, constructed in modular form in order to allow within a short time the change of various elements and thus the divertor geometry. The first Divertor II campaign will start with inward directed, inclined target plates ('LYRA', cf. fig. 16). A specific effect of these plates is that recycling neutrals shall be directed towards the region of highest energy flux leading to the desired increased retention.
Experiments with this 'LYRA' divertor design will start in spring 1997. Testing experiments with two different GAS BAG divertor geometries are envisaged as the following step.

Acknowledgement

The authors express their appreciation to the technical and engineering staff who contributed significantly to the execution of the presented experiments.

REFERENCES

[1] SUTTROP, W., et al., Nucl. Fusion **37** (1997) 119.
[2] HERRMANN, W., ASDEX UPGRADE TEAM, Phys. Rev. Lett. **75** (1995) 4401.
[3] ZOHM, H., et al., IAEA-CN-64/A5-1, this volume.
[4] GAFERT, J., et al., in Controlled Fusion and Plasma Physics (Proc. 23rd Eur. Conf. Kiev, 1996), Vol. 20C, European Physical Society, Geneva (1996).
[5] SCHNEIDER, R., et al., IAEA-F1-64/D3-1, these Proceedings, Vol. 2.
[6] RYTER, F., et al., IAEA-F1-64/AP-5, this volume.
[7] STROTH, U., et al., Plasma Phys. Control. Fusion **38** (1996) 611.
[8] GRUBER, O., et al., IAEA-F1-CN-64/A3-5, this volume.
[9] ITOH, K., et al., Plasma Phys. Control. Fusion **38** (1996) 1.
[10] SUTTROP, W., et al., in Controlled Fusion and Plasma Physics (Proc. 23rd Eur. Conf. Kiev, 1996), Vol. 20C, European Physical Society, Geneva (1996).
[11] MERTENS, V., submitted to Nucl. Fusion.
[12] MERTENS, V., et al., in Controlled Fusion and Plasma Physics (Proc. 23rd Eur. Conf. Kiev, 1996), Vol. 20C, European Physical Society, Geneva (1996).
[13] MERTENS, V., et al., IAEA-CN-64/A4-4, this volume.
[14] KALLENBACH, A., et al., Nucl. Fusion **35** (1995) 1231.
[15] LANG, P. (in preparation).
[16] GRUBER, O., et al., Phys. Rev. Lett. **74** (1995) 4217.
[17] NEUHAUSER, J., et al., Plasma Phys. Control. Fusion **37** (1995) A37.
[18] RAUPP, G., et al., submitted to Fusion Technol.
[19] KALLENBACH, A., in Controlled Fusion and Plasma Physics (Proc. 23rd Eur. Conf. Kiev, 1996), Vol. 20C, European Physical Society, Geneva (1996).
[20] BECKER, G., Nucl. Fusion **36** (1996) 1751.
[21] MATTHEWS, G.F., et al., to be published in J. Nucl. Mater.
[22] BOSCH, H.-S., et al., to be published in J. Nucl. Mater.
[23] BOSCH, H.-S., et al., Phys. Rev. Lett. **76** (1996) 2499.
[24] BOSCH, H.-S., et al., IAEA-CN-64/AP2-3, this volume.
[25] NAPIONTEK, B., et al. (in preparation).

[26] PARKER, G., et al., to be published in J. Nucl. Mater.
[27] NAUJOKS, D., et al., Nucl. Fusion **36** (1996) 671.
[28] NEU, R., et al., to be published in J. Nucl. Mater.
[29] KRIEGER, K., et al., IAEA-F1-64/AP2-4, this volume.
[30] ASMUSSEN, K., et al. (in preparation).
[31] PAUTASSO, G., et al., Nucl. Fusion **36** (1996) 1291.
[32] BOSCH, S.H., Rep. IPP 1/281a, Institute for Plasma Physics, Garching (1994).
[33] ZOHM, H., et al., in Controlled Fusion and Plasma Physics (Proc. 23rd Eur. Conf. Kiev, 1966), Vol. 20C, European Physical Society, Geneva (1996).

DISCUSSION

S.I. ITOH: You reported that Type I ELMs are dangerous and Type III ELMs are tolerable. Could you explain the reasons for this and give us some prospects for future machines.

M. KAUFMANN: Type I ELMs normally lead to a very high power load to the target plates, connected with a high divertor plasma temperature. In addition, they produce recycling and erosion in a wide region outside the SOL.

In addition to further work on the characterization of the different ELM types, the limitation of the loads by ELMs will be a focal point of our work.

F. ENGELMANN: Do you see runaway electron generation during disruptions with or without killer pellets in ASDEX-Upgrade?

M. KAUFMANN: In neither case do we see runaways.

O. GRUBER: May I add that not only did we have no indication of runaway electrons during disruptions, whether during 'normal' disruptions or with killer pellets, but other divertor experiments did not see runaways during the current quench phase either, where you would expect problems for ITER in view of theoretical considerations. Only during the thermal quench have divertor plasmas shown a small runaway population.

Y.-K.M. PENG: Could you comment on the heat flux (and duration) experienced by the tungsten coated divertor plate in recent ASDEX-Upgrade experiments.

M. KAUFMANN: The tungsten coating of the graphite target plates had a design limit of 7.5 MW/m^2 for 1 s. The maximum value experimentally deposited was 6 MW/m^2 for typically 2 s, and we had a temporary maximum value of 15 MW/m^2 during Type I ELMs. One should keep in mind that the technical design in ASDEX-Upgrade must be considered as the final technical solution.

DIII-D TOKAMAK CONCEPT IMPROVEMENT RESEARCH*

V.S. CHAN for the DIII-D TEAM[1]
General Atomics,
San Diego, California,
United States of America

Abstract

DIII-D TOKAMAK CONCEPT IMPROVEMENT RESEARCH.

Recent results in tokamak performance optimization and understanding through shape and plasma profile control have brought DIII-D closer to its goal of advanced tokamak (AT) demonstration ($H \equiv \tau_E/\tau_{ITER89P}$ up to 4, and $\beta_N \equiv \beta_T/(I/aB)$ up to 6, simultaneously in steady-state). A high performance regime characterized by negative central magnetic shear has resulted in a high $\beta_N H$ product of up to 18, and $Q_{dt\text{-}equivalent} = 0.32$. Strong plasma shaping coupled with the control of current and pressure profiles is responsible for the improvement in MHD stability, and stabilization of microturbulence by sheared E×B flow plays a dominant role in the reduction of transport. Density control and helium exhaust are demonstrated with divertor pumping, and reduction of heat flow to the divertor by an order of magnitude through radiative cooling suggests an effective heat exhaust scheme compatible with AT operation. Active current profile control using a combination of a neutral beam system, bootstrap current and a fast wave system has been initiated. Achievement of long-pulse AT operation is the future focus of the DIII-D Program.

1. INTRODUCTION

The objective of tokamak concept improvement research is to identify a cost effective and shorter time scale path for the development of the tokamak as a fusion power plant. For a more economical and environmentally attractive fusion power plant, the requirements are: high fusion power density (high β), high ignition margin (high τ_E), continuous operation with low recirculating power (high bootstrap fraction) and adequate heat removal and impurity and particle control. The developmental path can be significantly shortened if improvements in the four areas can be separately or simultaneously demonstrated in existing tokamak facilities, concomitant with development of good scientific understanding and predictive capability. The DIII–D tokamak (Fig. 1) with its unique flexibility to assess a wide range of configurations and operating regimes is well suited for exploring AT operation through active control of the plasma shape and plasma profiles. It also has available a 20 MW neutral beam (NB) system, a 6 MW fast wave (FW) system and a 1 MW electron cyclotron heating (ECH) system (up to 3 MW of ECH in the near future) for extending the duration of the high performance regimes to demonstrate steady-state relevance. Its divertor provides the pumping capability for particle control and heat exhaust. Additionally, a comprehensive set of spatially and temporally resolved diagnostics provides detailed measurements essential for developing the scientific understanding.

---

* Work supported by the US Department of Energy under contracts DE-AC03-89ER51114, DE-AC05-96OR22464, DE-AC04-94AL85000 and W-7405-ENG-48, and grants DE-FG03-86ER53266 and DE-FG03-95ER54294.

[1] See Appendix.

In this paper, we report progress in the past two years on the optimization and understanding of these four key areas of research in the DIII–D tokamak and the effort in integrating the progress into a self-consistent advanced tokamak scenario relevant to a fusion power plant.

2. ADVANCED TOKAMAK OPERATION IN DIII–D

Recently a high performance mode involving a negative central magnetic shear (NCS) configuration in DIII–D has demonstrated attractive stability, confinement and bootstrap alignment properties which are desirable for a compact ignition machine. The NCS regime is a modification of the internal magnetic structure which is theoretically predicted to improve performance. Both a reduction and an increase in magnetic shear from that obtained in a standard ohmically driven discharge are predicted to be favorable [1], and this leads to the development of two AT operational regimes: NCS and high internal inductance (ℓ_i). For the past two years, DIII–D has concentrated mostly on the NCS path to high performance.

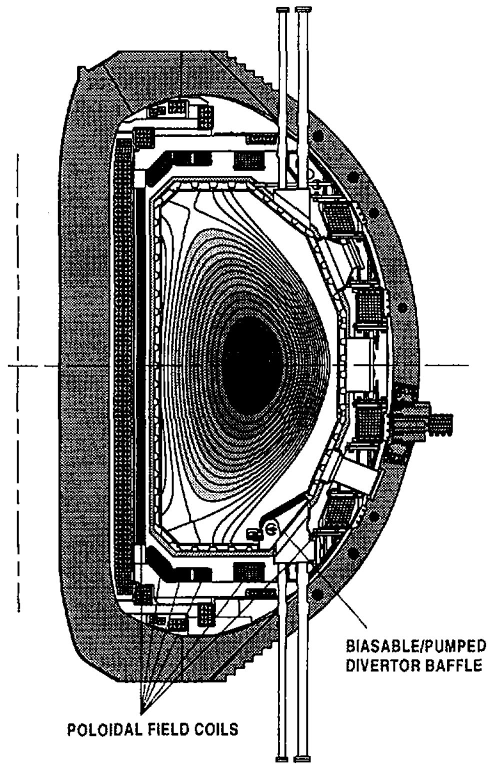

FIG. 1. Cross section of the DIII-D tokamak: 18 individually controlled poloidal field coils and the existing pumped divertor are indicated.

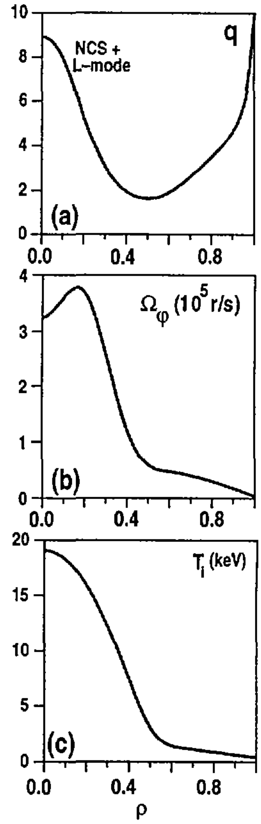

FIG. 2. Characteristic features of NCS discharges: non-monotonic q-profile (a), internal transport barriers in (b) Ω_ϕ and (c) T_i.

NCS discharges are characterized by a non-monotonic safety factor (q) profile and the existence of internal transport barriers supporting steep gradients in T_i and V_ϕ, as shown in Fig. 2. Steep gradients in T_e and n_e are also observed in some cases. L-mode and H-mode NCS discharges with inside limiter, single-null divertor (SND), and double-null divertor (DND) configurations have been produced in DIII-D. Figure 3 summarizes the highest performance NCS discharge [2] which is a high triangularity DND configuration; achieved parameters are $\beta_N = 4.0$ $\beta_T = 6.7\%$ at $B_T = 2.1$ T, H $\geq$ 4.0,W = 4.2 MJ and $\tau_E = 0.4$s. This discharge reached a new DIII-D record in fusion neutron yield of $Q_{DD} = 1.5 \times 10^{-3}$, corresponding to $Q_{DT}^{eq} = 0.32$. Compared with the previous highest Q_{DD} discharge (which is a hot ion VH-mode), the increase in neutron yield can be attributed to a larger volume of enhanced confinement.

2.1. High Beta Regimes

The NCS approach aims to access the second stable regime to ballooning mode in the plasma core using current profile control. The first NCS discharge on DIII-D was produced by rapid shape elongation with high power NB heating [3]. β_T (0) of 44%was achieved demonstrating access to a second stable core. More recent NCS discharges are produced using NB injection into a low density target plasma during the early current ramp-up phase (Fig. 4). The beam heating raises the plasma temperature rapidly which lengthens the current diffusion time. As a result, the hollow current profile even though not in steady-state remains hollow for a longer duration [4]. This allows study of stability and transport properties in the absence of a steady-state profile control tool. Early beam injection in concert with rapid current ramp-up has become the method of choice for many tokamaks including DIII-D, JET, JT60-U, Tore Supra, and TFTR [5] to produce and study negative magnetic shear configurations.

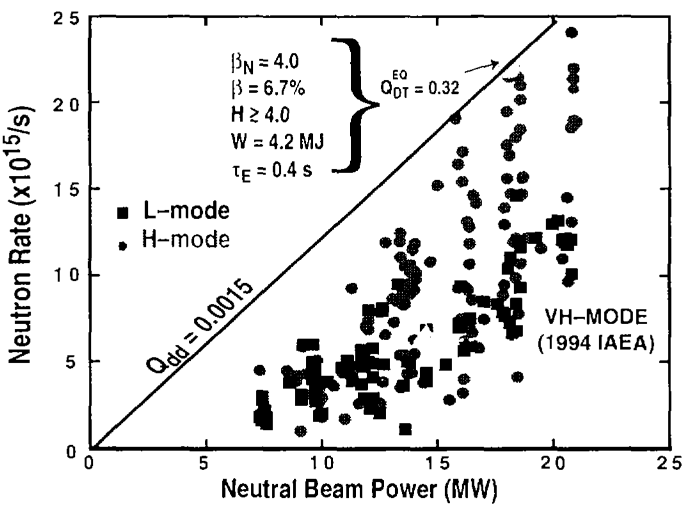

FIG. 3. Fusion performance of NCS discharges in DIII-D (VH-mode data point from DIII-D TEAM, in Plasma Physics and Controlled Nuclear Fusion Research 1994 (Proc. 15th Int. Conf. Seville, 1994), Vol. 1, IAEA, Vienna (1995) 83).

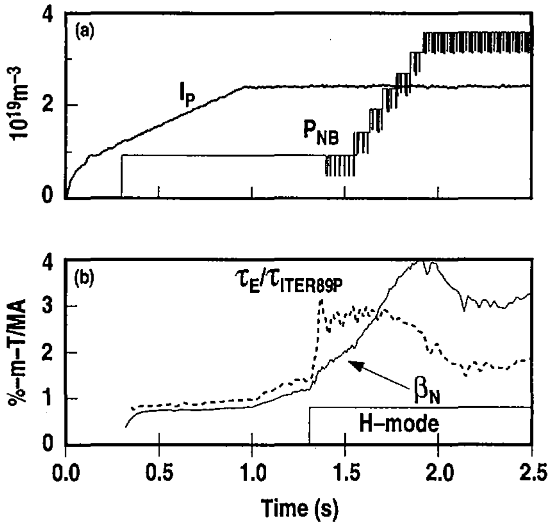

FIG. 4. Time traces showing (a) NCS formation by early NBI during I_p ramp; (b) temporal behavior of β_N and $\tau_E/\tau_{ITER89P}$.

In DIII–D, NCS plasma core can exist in combination with different edge conditions including L–, H– and VH–mode with different pressure profiles. The β limit due to kink modes critically depends on the plasma shape and pressure profile. The highest β_N achieved ($\beta_N \sim 5$) is in a high triangularity (δ) NCS H–mode with a relatively broad pressure profile [6]. The higher β_N limit with strong shaping is qualitatively consistent with ideal MHD theory. However, theoretical studies using optimized profiles predict further improvement in β_N may be possible [7]. The high β phase is sustained for only

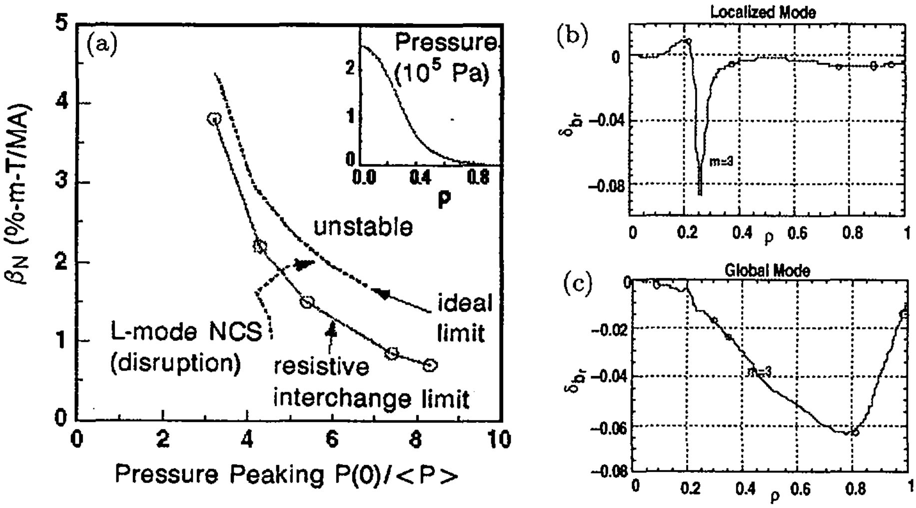

FIG. 5. (a) β-limits of NCS plasmas versus pressure profile peakedness p(0)/⟨p⟩; (b) mode structure of resistive interchange mode; (c) mode structure of double tearing mode.

a short duration and is terminated by either a soft collapse or a slow decay to lower β values (Fig. 4). The soft collapse, which results in a drop in β but does not terminate the discharge, is usually accompanied by enhanced MHD activities with toroidal mode number n = 2 to 5. The edge motional Stark effect (MSE) diagnostic supports the picture that as the plasma evolves to higher β, the edge builds up a significant bootstrap current and pressure gradient. The discharge becomes susceptible to edge kink mode instability, similar to what has been observed for VH–mode [8]. We believe the edge kink modes are responsible for the loss in stored energy during the collapse. We also found evidence that the vessel wall together with plasma rotation is effective in stabilizing the external modes until the edge current and pressure become too large at high β [9]. The slow β decay appears well correlated to the slowly decreasing q-profile in the absence of steady-state current profile control and the onset of MHD activities associated with lower order mode rational surfaces. Theory also predicts the edge kink mode to become more global in character with existence of low mode rational surfaces and can eventually cause the discharge to terminate. Stabilization of the external kink mode and sustainment of the optimum q profile and pressure profile are key factors for increasing β_N further and extending the high β phase of the NCS H–mode.

NCS plasmas with an L–mode edge exhibit very different behavior. They are characterized by highly peaked pressure profiles: $p(0)/\langle p\rangle \sim 5$. While these very peaked pressure profiles contribute to enhanced fusion power production, they often lead to discharge termination with a hard disruption when β_N reaches values of 2.0 to 2.5 [10]. The disruption is preceded by a fast growing rotating n = 1 magnetic precursor with a growth time between the resistive and ideal MHD growth time. The β value at which these discharges terminate is below that predicted by ideal n =1 mode theory. The strong core pressure gradient and large negative magnetic shear result in a condition which violates the resistive interchange stability criterion. Analysis shows that these DIII–D discharges are unstable to localized resistive interchange modes [11]. In Fig. 5, the stability limit against the n = 1 resistive interchange mode is shown in terms of β_N and $p(0)/\langle p\rangle$. Also shown is the localized structure of this mode. Later in time, a double tearing mode is also found to be unstable. While not yet proven, we suspect

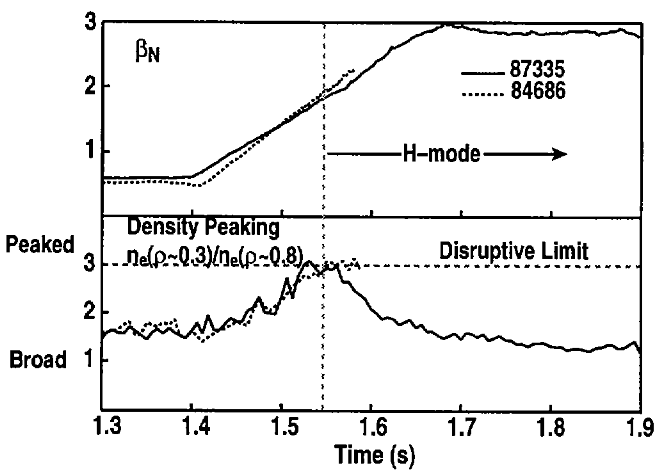

FIG. 6. Evolution of β_N and density profile with transition from L- to H-mode edge for NCS.

that the resistive interchange coupled with the double tearing instability, which has a global mode structure, is the cause for the hard disruption. The NCS L–mode appears to behave similarly to the enhanced reverse shear (ERS) mode observed in TFTR, although the termination of ERS has been attributed to internal kink modes [12].

A way of combining the favorable feature of enhanced fusion yield in an NCS L–mode with the higher β limit of NCS H–mode was successfully implemented in DIII–D. This is illustrated in Fig. 6. An NCS L–mode is produced initially and its β and core pressure are allowed to increase with further heating up to the point when the β limit is approached. Plasma shape control is then deployed to induce a transition to H–mode. The density profile flattens quickly resulting in a broadened pressure profile which in turn raises the β limit. This technique allows a steeper core pressure profile than standard H–mode and a higher β than NCS L–mode. Since the fusion production rate depends on optimizing both, this path leads to the highest neutron rate on DIII–D to date $\left(Q_{DT}^{eq}=0.32\right)$ [13].

Transition from L–mode to H–mode is effective in producing a broad pressure profile but does not control the density rise associated with ELM-free H–mode. The density rise reduces core NB heat deposition and current drive efficiency. To gain control of both the density and density profile, an upper divertor pump and baffle are being added to DIII–D for pumping high δ plasma shapes.

2.2. High Confinement Regimes

Transport improvements in plasmas with negative magnetic shear have been seen in many tokamaks: DIII–D, JET, JT60-U, TFTR, and Tore Supra. The improvements are qualitatively similar. Reduction in χ_i and D to neoclassical levels in the plasma core has been observed in DIII–D, JET, JT60-U, and TFTR [5]. Significant χ_e reduction has been seen in JT60-U with NBI, and both JT60-U and Tore Supra [14] have observed χ_e reduction using lower hybrid radiofrequency waves for direct electron heating. In DIII–D, when electron heating by FWCD is applied to NCS discharges, reduction in χ_e is also directly observed [15]. Combining NCS with improved edge confinement, DIII–D has successfully demonstrated for the first time transport reduction and turbulence suppression across the entire plasma (Fig. 7). A unifying explanation of the transport improvements in all channels and across the entire plasma is strongly hinted by data from the Charge Exchange Recombination (CER) diagnostic in DIII–D [6,16]. Figure 8 shows strong temporal and spatial correlations between the increase in ExB shear damping calculated using CER data with the transport reduction in regions where the flow shear dominates over microinstability growth rate. This is further supported by physics-based modeling of experiments which includes the effects of ExB shear and magnetic shear stabilization [17]. It is found that the ExB shear damping rate (ω_{ExB}) can become so large as to shut off transport from low-k ion temperature gradient modes (ITG) in all channels allowing only neoclassical transport over a large core plasma. A residual electron heat transport caused by high-k η_e modes may still exist. Their larger growth rates prevent η_e modes from being stabilized by the ExB shear, although the magnitude of their transport is usually quite small. Additionally, Beam Emission Spectroscopy, which measures electrostatic fluctuations in the core, shows local suppression of plasma turbulence. In discharges where the transport is reduced across the entire plasma, far infrared scattering, which measures fluctuations across the entire plasma, shows a clear suppression of turbulence across the plasma [18]. An in-out asymmetry in the turbulence is sometimes observed consistent with the ExB flow shear explanation of core transport reduction in NCS discharges.

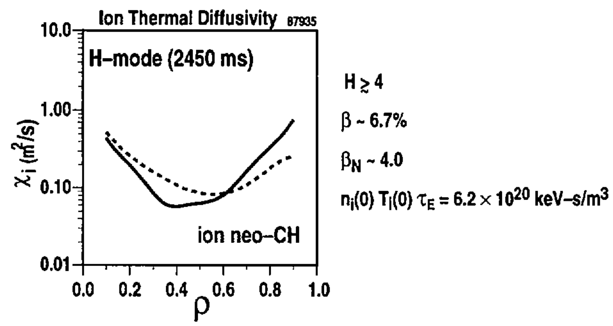

FIG. 7. χ_i as a function of ρ for high performance in NCS H-mode.

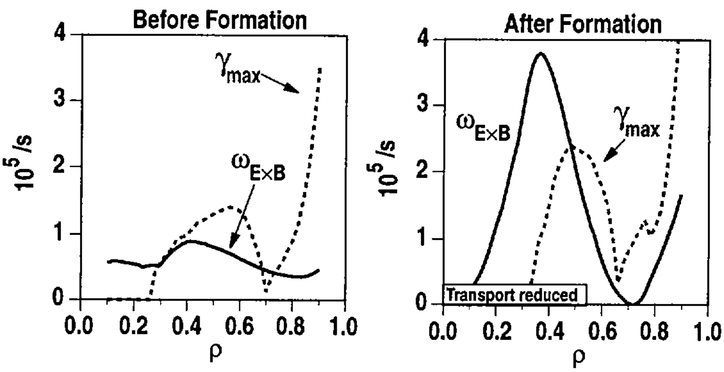

FIG. 8. Comparison of E×B shearing rate $\omega_{E\times B}$ and microinstability growth rate γ_{max} before and after transport barrier formation. γ_{max} = ITG growth rate.

What is the role of negative magnetic shear? In DIII–D, we have produced discharges with NCS but no transport improvement. Likewise, TFTR has enhanced reverse shear (ERS) and reverse shear (RS) discharges with the same q-profile but different confinement [12]. Kinetic stability analysis [17,19] of DIII–D discharges confirms that the stabilization effect on the ITG modes by negative magnetic shear alone is not sufficient to explain the core transport barrier formation *i.e.*, the region of improved confinement is broader than the region where ITG modes are stabilized by magnetic shear. There is clearly some correlation between NCS and the internal transport barrier. When it forms, the foot of the transport barrier is at or slightly outside the minimum in safety factor q_{min}. Comparing NCS with hot ion mode, the internal density transport barrier appears to form more readily. When counter-FWCD is used to enhance the NCS, the internal transport barrier was more readily established [15]. Analysis has confirmed the NCS region to be in the second stable regime to ballooning modes. This together with $q_{min} > 2$ would allow the core to be free of MHD activities and the development of a much steeper pressure gradient. The high central q value also contributes to enhancing the ExB shear suppression rate. The conclusion we can draw from all the evidence is that magnetic and ExB shear work together in enhancing confinement in NCS plasmas. Magnetic shear and Shafranov shift (local shear) act to lower the growth rate while ExB shear suppresses the residual microturbulence.

Understanding what determines the input power threshold for transport barrier formation is important for projection to future tokamaks. Theory has suggested that the threshold is given by the balance between the microinstability growth rate and the ExB shear damping rate, and the internal transport barrier should first form in the plasma core where the magnetic shear stabilization has the biggest impact [20]. This is corroborated by DIII–D measurements which show the core transport barrier first formed in the interior and expanded with increased beam power and contracted with decreased power [18]. The threshold power varies over a wide range in present experiments. DIII–D requires only a few MW to produce the transition to high confinement with internal transport barriers while other tokamaks such as TFTR and JT60-U typically require much higher power. This could perhaps be explained by two possible reasons. The first may be related to the different mechanisms which drive the ExB shear flow. The ExB shear damping rate in toroidal geometry is given by

$$\omega_{ExB} = \left(B_\theta R/B\right) d\left(E_r/RB_\theta\right)/dr \ , \qquad 1/\left(RB_\theta\right) d/dr = d/d\psi \ , \tag{1}$$

and assuming neoclassical ion poloidal velocity,

$$E_r/\left(RB_\theta\right) \cong V_\phi/R + \left(1-K_1\right)/\left(Z_i e\right) dT_i/d\psi + T_i/\left(Z_i e n_i\right) dn_i/d\psi \ , \tag{2}$$

Since $K_1 \sim 1$ in the plasma core, only toroidal flow and density gradient contribute significantly to producing the ExB flow. DIII–D with tangential NBI can induce turbulence suppression effectively with toroidal flow shear from the toroidal momentum input. This is absent for balanced beam injection in which case the flow is purely diamagnetic and the flow drive depends largely on the density gradient. High beam power may thus be required to provide a steep density gradient to drive the flow. The second speculation is that the turbulence growth rate and thus the threshold depends strongly on shape in addition to magnetic shear. This is supported by the H–mode power threshold observed in the DIII–D elongation-ramp experiment [21] and is also consistent with a recent experiment to study bean and peapod configurations on DIII–D. Preliminary results from this experiment indicate that these configurations produce transitions to higher confinement modes readily at low input power. The power threshold to enter an enhanced confinement regime is clearly a subject which needs further study if these enhanced confinement modes are to be applied to next step experiments.

3. ISSUES FACING ACCEPTANCE OF AT MODES FOR FUSION POWER PLANTS

3.1. Long Pulse and Steady-State Operation

For an economically attractive fusion power plant, steady-state operation with minimized recirculating power is desirable. This requires operation with high bootstrap current fraction. Combining this with the requirement for high power density, we are led to explore AT modes with both high β_T and β_P. The quantities β_T and β_P are related by

$$\beta_T * \beta_p = 25\left[\left(1+\kappa^2\right)/2\right]\left(\beta_N/100\right)^2 , \quad (3)$$

Simultaneous high β_T and β_P can only be achieved with high β_N and strongly shaped plasmas. DIII–D has produced a variety of discharges including high ℓ_i, high β_P and NCS modes, with both large β_N and β_P. The high performance phase of all DIII–D discharges with β_N values significantly above 3 lasted only for short durations. The termination of the high β_N phase can be either a soft β collapse (or slow decay) with the plasma settling back to a more modest β_N value, or a hard disruption. To extend the duration of the high performance phase, we have chosen a strategy to avoid the modes with hard disruptions and focus on circumventing the soft β collapses. There is strong evidence that the edge kink mode is a key factor in the β collapse for all high performance discharges with H–mode edge. We believe the steep edge current density and pressure gradient developed with the increased β, the presence of low q rational surfaces and possibly the slowing down of plasma rotation due to loss of beam ions all play a role in destabilizing the edge kink mode. Some progress has been made to develop techniques to control these quantities, although no reliable technique exists for mitigating the edge kink mode and extending the high performance phase duration.

We have explored controlling the edge plasma density of AT modes using the divertor cryopump as a means to control the edge pressure gradient. The cryopump has been shown to be effective in controlling the density and recyling rate for ELMing H–mode plasmas. However, because of its present location, it is only effective for pumping low triangularity (δ), SND plasmas. Since our highest performance NCS H–mode plasmas are high δ DND, ELM-free H–mode plasmas, the present cryopump is not ideal for this purpose. We were encouraged by recent success in producing high performance NCS discharges on DIII–D in JET-shaped plasmas (SND with δ ~ 0.3) with simultaneously achieved values of β_N ~ 4 and H ~ 4. Low amplitude, high frequency ELMs in SND NCS discharges at lower beam power and the cryopump were effectively used to control the edge density and the edge pressure gradient. Key results are depicted in Fig. 9. Approximately constant line-averaged density and values of β_N

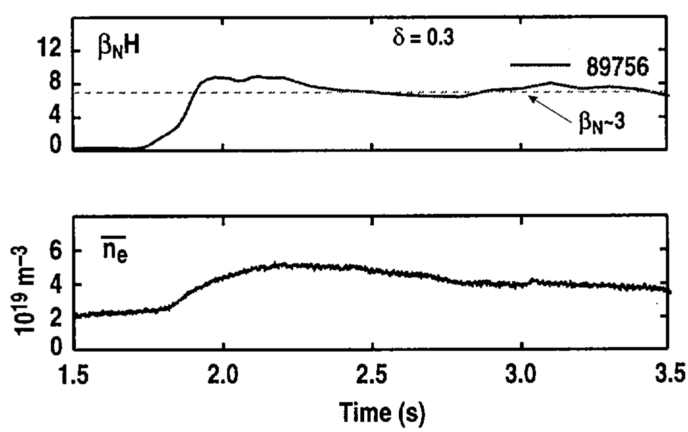

FIG. 9. Long-pulse high performance NCS with ELMing H-mode edge.

~ 3 and H ~ 2.5 were maintained simultaneously for 1.5 s. The $\beta_N H$ product is among the highest achieved for H–mode lasting over several τ_E. During this duration, no significant MHD activities were observed indicating some beneficial effect from the edge control. Higher β_N has not been attained because additional power tends to lead to large amplitude ELMs which result in further confinement degradation. The lower δ also lowers the ideal β limit significantly. Since it is easier to produce small amplitude, high frequency ELMs in high δ DND plasmas, which also have higher stability limits, an upper pump and baffle for high δ operation, presently being installed, should ease both limitations.

DIII–D has produced a large number of long pulse discharges including H–mode and high β_P mode and with various shapes including ITER-demonstration discharges. These plasmas are maintained by a combination of NB, bootstrap, and radiofrequency driven currents. Some of them have up to 80% bootstrap fraction. They typically have monotonic q-profiles and are limited to $\beta_N < 3$ and $H < 2$. Analysis confirmed that these plasmas are below the ideal β limit. However, attempts to increase β by increasing beam power have resulted in enhanced MHD activities which limit the stored energy and sometimes result in hard disruptions. There is strong indication that this limitation is due to the destabilization of resistive tearing modes by neoclassical bootstrap current [22]. The conditions favoring this are presence of seed islands (possibly introduced by sawteeth and ELMs), positive magnetic shear and low ExB flow. A scaling of the experimentally obtained critical β with collisionality appears consistent with this theory [23]. Because of this result, one might question: even if we can mitigate the edge kink mode for NCS H–mode, will the maximum β be limited by neoclassical tearing mode for long durations? With NCS, absence of sawtooth ($q > 1$) and strong ExB flow, theory would predict stability for NCS discharges. Whether this holds true experimentally can only be answered when we have the off-axis ECRF current drive tool to control the current density profile for long durations.

3.2. Particle Control and Heat Exhaust

We are working to develop methods of particle and heat exhaust compatible with AT operation in the plasma core. In the "standard model" of divertor physics (*i.e.*, classical parallel heat conduction, constant pressure along the field lines, coronal equilibrium radiation rates, and constant impurity concentration in the core, scrape-off-layer (SOL), and divertor) the amount of power that can be radiated in the divertor is directly linked to the core Z_{eff} and dilution. For example, in ITER for light impurities when the core Z_{eff} limit is reached, the standard model only allows 100 MW radiation in the divertor. The remainder of the power exhaust must be made up by core plasma radiation. While results from TEXTOR are promising on maintaining good core performance with a nearly 100% radiative mantle [24], we are concentrating on ways to increase divertor radiation while maintaining low core impurity levels and gas fueling burdens using physics approaches outside the standard model: plasma detachment, 2-D cross-field heat flow effects, non-coronal radiation enhancements, non-thermal distribution effects, and divertor impurity enrichment [25].

We have employed a new divertor Thomson scattering system in conjunction with radial X-point sweeping to make detailed 2-D documentation of divertor plasma detachment, which lowers the divertor plasma temperature and the heat flux to the divertor plates [26] (Fig. 10). In attached plasmas, irrespective of confinement mode or heating mode, we find the total plasma pressure along the field lines in the SOL is conserved to within a factor of two. With detachment produced by deuterium puffing, the

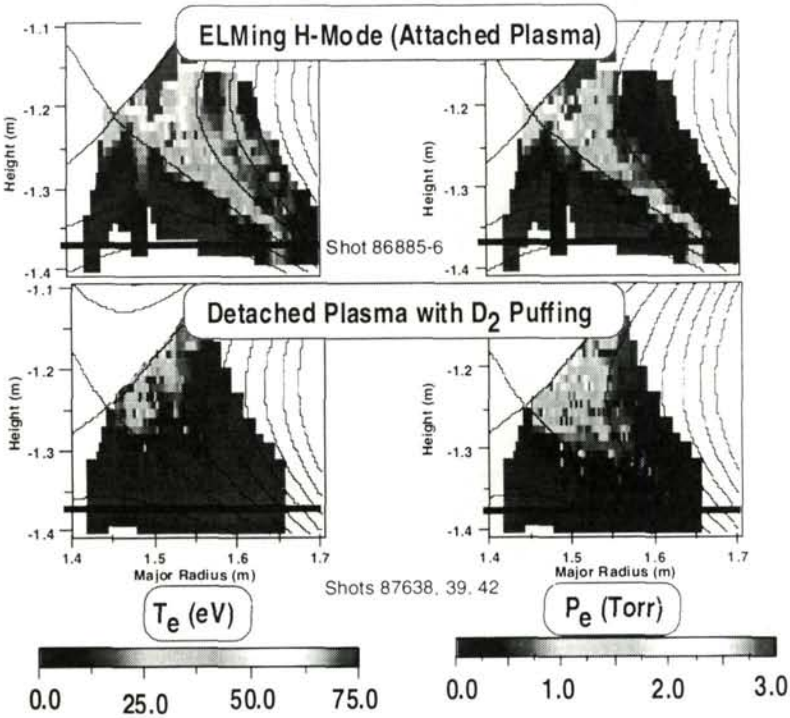

FIG. 10. Divertor Thomson data showing T_e and P_e drop and plasma detachment with D_2 pumping.

pressure drops more than ten times along the separatrix to the divertor strike point while remaining high further out in the SOL; we refer to this condition as a partially detached divertor. We have also found that the electron temperature in the divertor plasma is reduced into the range 1–3 eV, a range where volume recombination of the plasma should be strong. Modeling with the UEDGE code has successfully matched most key features of our divertor data in a detached plasma and shows that volume recombination is a dominant process [27]. Volume recombination increases the radiation from the divertor by producing the recombination power in the plasma rather than in the divertor plate. We have been able to use partially detached plasmas to produce a long (50 cm), radiating divertor leg with only a 2:1 variation of the emission along the leg, exceeding the ITER requirement [26] (Fig. 11). The aim of the ITER divertor solution is to reduce the peak heat flux at the divertor plate by spreading the heat flux along the divertor channel, but ITER only requires a 6:1 uniform spreading. Preliminary analysis indicates that the length of the radiating zone in Fig. 11 exceeds substantially the predictions of the standard model, requiring investigation of the role of non-coronal and convective effects. The core plasma confinement in the case of Fig. 11 was progressively reduced to the L-mode level by the high neutral pressures (reaching 1 mTorr) near the core plasma that resulted from the strong gas flow through to the divertor pump and the inadequate divertor baffling in DIII–D. The full installation of the double null, triangular plasma, Radiative Divertor in DIII–D will provide the

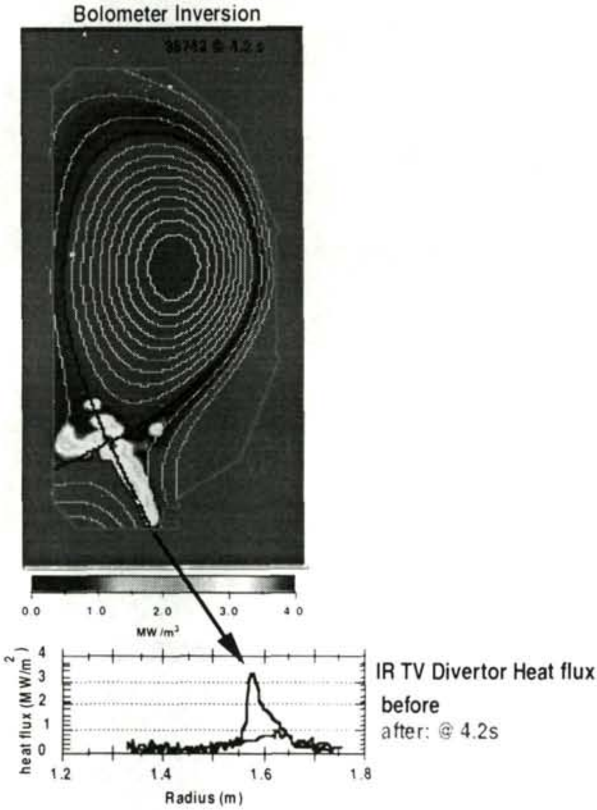

FIG. 11. Long radiating divertor leg demonstrating effective radiation exceeding ITER requirements.

baffling needed to allow simultaneous high performance core plasmas with low impurity and neutral pressures with high plasma and neutral densities in the detached divertor.

A divertor impurity enrichment (defined as the ratio of impurity concentration in the divertor to the impurity concentration in the core plasma) greater than one can enhance divertor radiation while maintaining limits on core Z_{eff} and radiation. An enrichment of three in ITER would enable essentially all the exhaust power to be radiated in the divertor. Increased enrichment is expected from strong fuel ion flows that drive impurity ions down the field lines overcoming the thermal gradient force that pushes impurity ions up the field lines. In our so-called "puff and pump" experiments in which fuel gas flows up to 150 $T\ell/s$ are admitted at the top of the machine and exhausted through the divertor pump, we have documented carefully a modest enrichment (1.4–2) [26,28] in the divertor pump plenum using neon impurity gas and obtained preliminary indications of a much larger enrichment using argon impurity gas.

In most divertor tokamaks, attempts to raise the core plasma density above the Greenwald limit have been frustrated by detachment of the divertor leading (under high gas puffing) to a divertor MARFE which migrates into the core plasma. By lightly pumping the divertor and using pellet fueling instead of gas fueling, we have been able to prevent the collapse of the divertor and so gain a view of the physical processes in the plasma core that limit the density. We have obtained densities 1.5 times the Greenwald density limit while maintaining energy confinement at 1.8 times ITER–89P scaling [25]. Particle transport after pellets is largely independent of density relative to the Greenwald limit. Core radiative collapses and tearing mode effects are seen.

Our divertor results have provided some strong support of key features of the ITER divertor concept: detached plasmas, radiation distributed uniformly along the divertor leg, and densities above the Greenwald limit. Promising lines of investigation to increase divertor radiation while maintaining clean, high performance core plasmas are being pursued.

3.3. Core Impurity Control in Enhanced Confinement Regimes

Associated with transport reduction is the potential build-up of impurities in the plasma core which will have a deleterious effect on the tokamak performance. For AT operation to be acceptable for fusion power plants, adequate control of impurity contaminants and helium "ash" has to be demonstrated. Experiments have been conducted on DIII–D to characterize both global and local impurity transport characteristics under a variety of conditions. Progress has been made in identifying AT operations in which impurity contamination is simultaneously being minimized.

To address the issue of helium ash exhaust, previous experiments on DIII–D with helium introduced via gas puffing at the plasma edge have shown that sufficient helium exhaust can be achieved $\left(\tau^*_{He}/\tau_E \sim 8\right)$ simultaneously with good energy confinement in an ELMing H–mode plasma [29]. These results have been extended in more recent experiments utilizing helium neutral beam injection as a central source of helium. This central helium source coupled with simultaneous divertor exhaust using a divertor cryopump provide a better simulation of the central source of fusion produced alpha products. In these experiments, substantial helium exhaust is observed with $\tau^*_{He}/\tau_E \sim 8.5$. The measured helium density profile is observed to remain essentially the same during the He beam injection phase after a brief transient. This observation suggests that the exhaust of helium in this case is limited by the effective exhaust efficiency of the pumping configuration and not by helium transport within the plasma core.

In DIII–D, the carbon behavior in NCS discharges appears to be dependent on whether the edge plasma exhibits an L–mode or H–mode character [30]. As illustrated in Fig. 12, for NCS L–mode, both electron and carbon density are observed to increase in the core while the edge carbon density remains nearly constant. Consequently, the carbon concentration and Z_{eff} change little. In the ELM-free NCS H–mode case, the carbon inventory increases linearly in time during the high confinement phase, accumulating primarily in the plasma edge while the core remains relatively clean. Finally, discharges in which NCS has been maintained simultaneously with ELMs exhibit a clamping and subsequent decrease in carbon concentration once ELMs begin, similar to what is observed in standard ELMing H–mode plasmas.

The DIII–D studies have identified the AT operating conditions most compatible with effective impurity and helium "ash" exhaust as an ELMing H–mode edge with divertor pumping. ELMs are also desirable for self-regulating the edge pressure gradient which is useful for mitigating the edge kink mode instability. At present, the highest performance AT modes are ELM-free discharges. A key focus for the DIII–D AT Program in the future will be to produce enhanced performance NCS H–modes with ELMing edge.

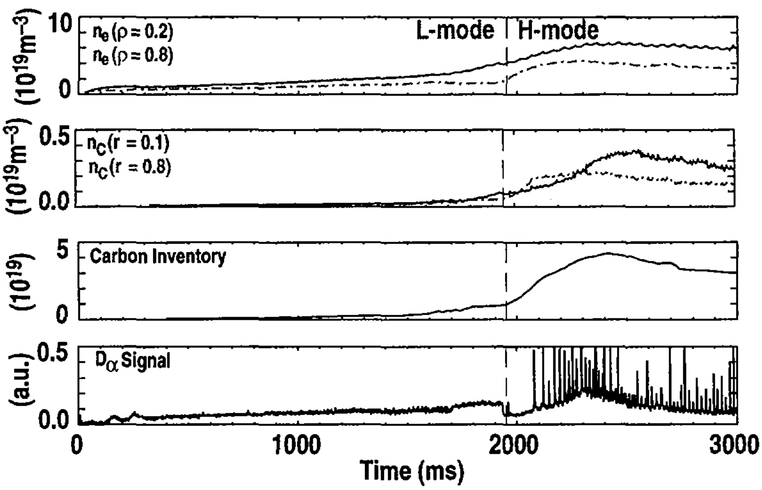

FIG. 12. ELMing NCS H-mode showing a clamping and subsequent decrease in carbon impurities.

4. SUMMARY AND FUTURE DIRECTIONS

A significant achievement in tokamak concept improvement research on DIII–D for the past two years is the development of a reproducible enhanced performance mode which possesses simultaneously attractive stability, transport and bootstrap alignment properties for a compact fusion power plant. This mode is achieved by producing a NCS configuration under several shapes (δ = 0.8 DND and 0.3 SND), and plasma edge conditions (L–, ELM-free H– and ELMing H–mode). The highest performance in terms of fusion gain is achieved for a DND NCS H–mode plasma, achieving a Q_{DD} value of 0.0015. These experiments achieved record stored energy for DIII–D, in excess of 4 MJ, increased the triple product to $n_D(0)T_i(0)\tau_E = 6.2 \times 10^{20}$ keV s m^{-3} , and neutron rates up to 2.2×10^{16} s^{-1}. The highest $\beta_N H$ product = 20 with β_N value of 5 and H of 4, is achieved in a weakly negative magnetic shear H–mode plasma. Numerical simulations using optimized pressure profiles indicate further increase in β_N should be achievable. The transport reduction to the neoclassical level and the formation of transport barriers from measurements of core fluctuation and electric field are consistent with theoretical predictions of ExB shear flow suppression of microturbulence.

The high performance phase has only been maintained for relatively short durations (<0.5 s), and is terminated either by a soft β collapse or hard disruption depending on the pressure profile peakedness. MHD instabilities responsible for the termination have been qualitatively identified as edge kink modes and resistive interchange/double tearing modes, respectively. To demonstrate the viability of AT modes for fusion power plants, the existence of steady-state relevant operation has to be proven. To this end, we need to ameliorate the soft β collapse by maintaining the optimized current and pressure profile for enhanced stability and transport. We plan to achieve this by exploring (a) a combination of radiofrequency current drive and well-aligned bootstrap current for current profile control; (b) particle pumping in strongly shaped plasmas for core and edge density control; and (c) the operation of NCS with ELMing H–mode edge.

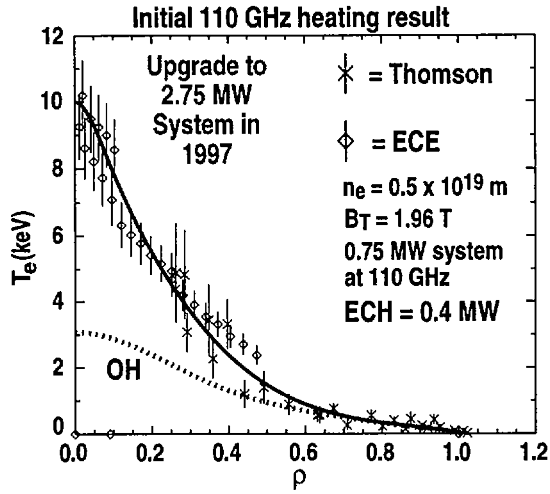

FIG. 13. T_e increases with 0.4 MW of electron cyclotron heating at 110 GHz.

Electron cyclotron current drive is the key for off-axis current profile control. With a 3 MW ECH system operational in 1997, we plan to extend the pulse length of NCS discharges significantly. Upgrading the system to 6 MW will allow full demonstration of steady-state operation. We are encouraged by preliminary heating results with the new 110 GHz 1 MW system as shown in Fig. 13. With 0.4 MW out of 1 MW coupled to a low density plasma, T_e of 10 keV has been achieved at $n_e = 5{\times}10^{18}\ m^{-3}$. The DIII–D tokamak is presently being vented to install a new divertor cryopump compatible with high δ AT operation This capability is essential to demonstrate a fully integrated AT scenario. It will be used to explore edge pressure control in DND plasmas including both density and ELM control, divertor detachment and heat exhaust in strongly shaped configuration, and impurity contaminant control in enhanced confinement regimes.

Studies in DIII–D have shown that plasma detachment is effective in reducing the heat flow to the divertor plate. A pressure drop of >10 times with T_e at the plate reduced to 1–3 eV has been achieved. Comparison with numerical modeling has provided insight of dominant atomic physics in low T_e divertor plasma. We will continue to explore the effectiveness of impurity enrichment for radiative divertors. The proposed radiative divertor modification [31] which is now being scheduled for 1998 will allow continuous evolution of the concept and undoubtedly will add to the performance of the divertor.

In conclusion, the DIII–D tokamak concept improvement research has made significant strides in developing the scientific understanding and predictive capability of AT operating regimes. This underlying understanding accomplished by detailed diagnostic measurements will remain an important element of our research. Looking ahead, the availability of off-axis ECCD and upper divertor pumping will allow the program to proceed with the integrated demonstration of high performance, long-pulse operation compatible with efficient heat exhaust and particle control.

REFERENCES

[1] TURNBULL, A.D., et al., Phys. Rev. Lett. **74** (1995) 718;
KESSEL, C., et al., Phys. Rev. Lett. **74** (1995) 1212.

[2] LAZARUS, E.A., et al., Phys. Rev. Lett. **77** (1996) 2714;
LAZARUS, E.A., et al., Nucl. Fusion **37** (1997) 7.

[3] LAZARUS, E.A., et al., Phys. Fluids B **4** (1992) 3644.

[4] RICE, B.W., et al., Plasma Phys. Control. Fusion **38** (1996) 869.

[5] NAVRATIL, G.A., et al., "Review of tokamak regimes with negative magnetic shear", Controlled Fusion and Plasma Physics (Proc. 23rd Eur. Conf. Kiev, 1996), Vol. 20C, European Physical Society, Geneva (1996).

[6] LAO, L.L., et al., Phys. Plasmas **3** (1995) 1951.

[7] TURNBULL, A.D., et al., IAEA-CN-64/DP-1, these Proceedings, Vol. 2.

[8] STRAIT, E.J., et al., in Controlled Fusion and Plasma Physics (Proc. 20th Eur. Conf. Lisbon, 1993), Vol. 17C, Part I, European Physical Society, Geneva (1993) 211.

[9] STRAIT, E.J., et al., Phys. Rev. Lett. **74** (1995) 2483.

[10] STRAIT, E.J., et al., Phys. Rev. Lett. **75** (1995) 4421;
RICE, B.W., et al., Phys. Plasmas **3** (1995) 1983.

[11] CHU, M.S., Phys. Rev. Lett. **77** (1996) 2710.

[12] LEVINTON, F.M., et al., Phys. Rev. Lett. **75** (1995) 4417.

[13] LAZARUS, E.A., et al., IAEA-CN-64/A1-2, this volume.

[14] USHIGUSA, K., et al., IAEA-CN-64/O1-3, ibid.;
SAOUTIC, B., et al., IAEA-CN-64/O2-2, ibid.

[15] FOREST, C.R., et al., Phys. Rev. Lett. **77** (1996) 3141;
PRATER, R., et al., IAEA-CN-64/E-1, these Proceedings, Vol. 3.

[16] BURRELL, K.H., paper presented at Transport Task Force Workshop, Varenna, 1996;
SCHISSEL, D.P., et al., IAEA-CN-64/A5-3, this volume.

[17] WALTZ, R.E., et al., IAEA-CN-64/D1-6, these Proceedings, Vol. 2.

[18] DOYLE, E.J., et al., IAEA-CN-64/A6-4, this volume.

[19] REWOLDT, G., et al., Phys. Plasmas **3** (1996);
WALTZ, R.E., Phys. Plasmas **2** (1995) 2408.

[20] STAEBLER, G.M., et al., Phys. Plasmas **1** (1994) 909;
DIAMOND, P.H., et al., Phys. Plasmas **2** (1995) 3685.

[21] LAO, L.L., et al., Phys. Rev. Lett. **70** (1993) 3435.

[22] HEGNA, C.C., CALLEN, J.D., Phys. Plasmas **1** (1994) 2308.

[23] LA HAYE, R.J., et al., IAEA-CN-64/AP1-21, this volume.

[24] WOLF, G.H., et al., IAEA-CN-64/O2-5, ibid.

[25] MAHDAVI, M.A., et al., IAEA-CN-64/A4-3, ibid.

[26] FENSTERMACHER, M.E., "Comprehensive 2-D measurements of radiative divertor plasmas in DIII-D", Proc. 12th Int. Conf. on Plasma Surface Interactions in Controlled Fusion Devices, St. Raphael, France, 1996, J. Nucl. Mater. (in press).

[27] PORTER, G.D., Phys. Plasmas **3** (1995) 1967.

[28] SCHAFFER, M.J., "Direct measurement of divertor exhaust neon enrichment in DIII-D", Proc. 12th Int. Conf. on Plasma Surface Interactions in Controlled Fusion Devices, St. Raphael, France, 1996, J. Nucl. Mater. (in press).

[29] WADE, M.R., et al., Phys. Rev. Lett. **74** (1995) 2702;
WADE, M.R., et al., Phys. Plasmas **2** (1995) 2357.

[30] WADE, M.R., et al., "Characterization of core impurity transport and accumulation in various operating regimes in DIII-D", Controlled Fusion and Plasma Physics (Proc. 23rd Eur. Conf. Kiev, 1996), Vol. 20C, European Physical Society, Geneva (1996).

[31] ALLEN, S.L., et al., Plasma Phys. Control. Fusion **37** (1995) A191.

Appendix

DIII-D TEAM

S.L. Allen,[a] P.M. Anderson, M.E. Austin,[b] D. Baggest, F.W. Baity,[c] D.R. Baker, D.E. Baldwin, G. Barber,[c] C.B. Baxi, J.D. Broesch, N.H. Brooks, D. Buchenauer,[d] K.H. Burrell, R.W. Callis, G.L. Campbell, T.N. Carlstrom, E. Carolipio,[e] W.P. Cary, V.S. Chan, M. Chance,[f] E. Chin, H. Chiu, S.C. Chiu, M.S. Chu, S. Coda,[g] J. Cuthbertson,[h] J.C. DeBoo, J.S. deGrassie, G. Diao,[i] J.L. Doane, E.J. Doyle,[j] T.E. Evans, M.E. Fenstermacher,[a] J.R. Ferron, D.K. Finkenthal,[k] R.K. Fisher, R Fitzpatrick,[l] C.B. Forest, J. Freeman, R.L. Freeman, T. Gianakon,[m] P. Gohil, A.M. Gootgeld, J. Greene, K.L. Greene, C.M. Greenfield, R.J. Groebner, H.J. Grunloh, T.E. Harris, R.W. Harvey, W.W. Heidbrink,[e] P.A. Henline, D.N. Hill,[a] D.L. Hillis,[c] F.L. Hinton, T.R. Hodapp, D.J. Hoffman,[c] J. Hogan,[c] K.L. Holtrop, M.A. Hollerbach, R-M. Hong, W. Houlberg,[c] C.L. Hsieh, D.A. Humphreys, A.W. Hyatt, H. Ikezi, G.L. Jackson, F. Jaeger,[c] G. Jahns,[n] T. Jarboe,[o] T.H. Jensen, T. Jernigan,[c] E. Joffrin,[p] R. Jong,[a] R. Junge, Y. Kawano,[q] K.M. Keith, A.G. Kellman, D.H. Kellman, R. Khayrutdinov,[r] K.W. Kim,[j] Y. Kim, C.C. Klepper,[c] J.A. Konings,[s] R.J. La Haye, L.L. Lao, C.J. Lasnier,[a] G.J. Laughon, E.A. Lazarus,[c] B. Lee,[j] J.-H. Lee,[j] R. Lee, R. Lehmer,[h] A.W. Leonard, J.A. Leuer, Y-R. Lin-Liu, J.M. Lohr, G. Lu, T.C. Luce, S. Luckhardt,[h] V. Lukash,[r] J.L. Luxon, M.A. Mahdavi, R. Maingi,[t] M.E. Mauel,[u] W.B. McHarg, G. McKee,[c] R.L. Miller, P.K. Mioduszewski,[c] C.P. Moeller, G. Monier,[p] R.A. Moyer,[h] M. Murakami,[c] G.A. Navratil,[u] A. Nerem, D. Nilson,[a] R.C. O'Neill, T.H. Osborne, L. Owen,[c] R. Patterson, W.A. Peebles,[j] B. Penaflor, Q. Peng, P.I. Petersen, T.W. Petrie, C.C. Petty, D.A. Phelps, W. Phelps, J. Phillips, R.I. Pinsker, P.A. Politzer, D. Ponce, M. Porkolab,[g] G.D. Porter,[a] R. Prater, A. Reiman,[f] E.E. Reis, D. Remsen, C. Ren,[m] M.E. Rensink,[a] C.L. Rettig,[j] G. Rewoldt,[f] T.L. Rhodes,[j] B.W. Rice,[a] J. Robinson, J. Rogers,[f] M. Rosenbluth,[h] D.A. Rothwell, E. Ruskov,[e] S. Sabbagh,[u] O. Sauter,[v] M.J. Schaffer, D.P. Schissel, J.T. Scoville, D.L. Sevier, T.C. Simonen, A. Sips,[w] J.P. Smith, R.T. Snider, F. Söldner,[w] G.M. Staebler, B.W. Stallard,[a] R.D. Stambaugh, H. St. John, R.E. Stockdale, E.J. Strait, D.W. Swain,[c] P.L. Taylor, T.S. Taylor, T. Terpstra,[f] D.M. Thomas, J.F. Tooker, A.D. Turnbull, F. Waelbroeck,[l] M.L. Walker, M.R. Wade,[c] R.E. Waltz, J.G. Watkins,[d] W.P. West, D.G. Whyte,[x] D. Wròblewski,[n] C.P.C. Wong, R.D. Wood,[a] X. Wu,[y] D. Zhang,[y] and J. Zhang[h]

PERMANENT ADDRESS

(*a*) Lawrence Livermore Natl Lab., USA
(*b*) U. of Maryland, USA
(*c*) Oak Ridge Natl Lab., USA
(*d*) Sandia Natl Labs, USA
(*e*) U. of California at Irvine, USA
(*f*) Princeton Plasma Phys. Lab., USA
(*g*) Massachusetts Institute of Technology, USA
(*h*) U. of California at San Diego, USA
(*i*) Southwestern Institute of Phys., China
(*j*) U. of California at Los Angeles, USA
(*k*) U. of California at Berkeley, USA
(*l*) U. of Texas at Austin, USA
(*m*) U. of Wisconsin, USA
(*n*) ORINCON Corp., USA
(*o*) U. of Washington, USA
(*p*) Commissariat a'l'energie Atomique, France
(*q*) Japan Atomic Energy Research Institute, Japan
(*r*) TRINITI, Russia
(*s*) FOM Inst., The Netherlands
(*t*) Oak Ridge National Universities, USA
(*u*) Columbia U., USA
(*v*) EPFL, Switzerland
(*w*) JET, United Kingdom
(*x*) INRS — Energie et Materiaux, Canada
(*y*) ASIPP, China

DISCUSSION

B. COPPI: You refer to the excitation of the resistive interchange mode, but this is very weak, especially at high temperatures.[1] Have you verified the relevant stability conditions and found them to be violated?

V.S. CHAN: Yes, we have done a detailed stability analysis for equilibria similar to the experimental conditions. We found the resistive interchange mode to be unstable, driven by the peaked pressure profile and strong negative magnetic shear. This result has been verified by several independent calculations.

F. WAGNER: You addressed the issue of impurity accumulation. Could you describe in more detail the impurity transport characteristics (in terms of D and v_{in}) for the plasma core region where $\chi_i << \chi_i^{Chang-Hinton}$.

V.S. CHAN: We have not analysed the data from our impurity study in long pulse NCS discharges. We do have results from an experiment in which helium is injected into the core of an ELMing H mode using neutral beam injection. With divertor pumping, we did not see a significant change in the impurity profile after an initial transient phase. The preliminary conclusion we draw is that the core impurity transport is limited by the pumping efficiency rather than the core confinement.

[1] COPPI, B., ROSENBLUTH, M.N., in Plasma Physics and Controlled Nuclear Fusion Research 1965 (Proc. Int. Conf. Culham, 1965), Vol. 1, IAEA, Vienna (1966) 617.

OVERVIEW OF HELICAL SYSTEMS

A. IIYOSHI
National Institute for Fusion Science,
Nagoya, Japan

Abstract

OVERVIEW OF HELICAL SYSTEMS.

Recent experimental results, mainly from heliotron/torsatron devices and an advanced stellarator, are reviewed. An international helical system database on the energy confinement time has been compiled; the confinement time scaling is similar to the tokamak L mode. Improved confinement regimes, i.e. high T_i mode, pellet mode, H mode and reheat mode, have also been investigated. In L mode and improved confinement regimes the energy confinement scaling has a favourable density dependence, and the operating density limit by radiation collapse in helical devices has a much steeper magnetic field dependence than in tokamaks. The maximum attainable β of about 2% is not limited by MHD instabilities but by the absorbed heating power. Investigations of divertor configurations, including local island divertors and natural island divertors, showed that next generation devices are very promising for steady state operations. On the basis of these results, next generation devices (LHD and WVII-X) with a major radius in the range of 4 to 5.5 m, have been under construction or have been approved for construction. A small Heliac has started its operation, and another has been under construction. A small modular stellarator with quasi-helical symmetry has also been under construction.

1. INTRODUCTION

Experimental investigations have been carried out in a variety of helical devices. The maximum machine parameters of heliotron/torsatron type devices and an advanced stellarator [1–4] fall into the following ranges: machine major radius: R_0 = 2–2.2 m; plasma minor radius: a_p = 0.2–0.3 m; magnetic field: B_0 = 2.5 T; and absorbed heating power: P_{abs} = 3–4 MW. The maximum plasma parameters obtained to date are as follows: central electron temperature: $T_e(0)$ = 3 keV; central ion temperature: $T_i(0)$ = 1.6 keV; line averaged density: n_e = (2–3) $\times 10^{20}$ m^{-3}; volume averaged β: $\langle\beta\rangle$ = 2.1%; and energy confinement time: τ_E = 40 ms (these parameters have not been obtained simultaneously). One main thrust of these experimental investigations has been to exploit to advantage the magnetic configurations characteristic of helical devices in improving transport, raising β, utilizing various heating methods (especially wave heating), and verifying the divertor function.

A next generation device, LHD [5, 6], is approaching the final stage of its construction, and another, WVII-X [7], has been approved for construction. Small machines of a fully three dimensional axis type are expected to extend our experimental knowledge into hitherto unexplored regimes.

Helical devices in operation and under construction are summarized in Table I.

TABLE I. MACHINE PARAMETERS OF HELICAL DEVICES IN OPERATION AND UNDER CONSTRUCTION

	R_0 (m)	a_p (m)	V_p (m^3)	B_0 (T)	P_{heat} (MW)	Remarks on configuration[a]
H-E (Kyoto)	2.2	0.2	1.74	2.0	7	ℓ = 2, m = 19, high ι, high shear
CHS (Nagoya)	1.0	0.2	0.79	2.0	3	ℓ = 2, m = 8, medium ι, magnetic well
L2-M (Moscow)	1.0	0.11	0.24	1.5	0.9	ℓ = 2, m = 14, medium ι, medium shear
U-3M (Kharkov)	1.0	0.13	0.33	2.0	0.2	ℓ = 3, m = 9, open helical divertor
CAT (Auburn)	0.53	0.1	0.10	0.1		ℓ = 1 + 2, m = 5
U-2M (Kharkov)	1.7	0.22	1.62	2.4	2.0	ℓ = 2, m = 4, low helical ripple
LHD (Toki)	3.9	0.6	28	3.0	28	ℓ = 2, m = 10, SC, closed helical divertor
WVII-AS (Garching)	2.0	0.2	1.58	2.5	5	m = 5, low shear, low P-S current
WVII-X (Greifswald)	5.5	0.5	27	2.5		m = 5, SC, optimization
HSX (Madison)	1.2	0.15	0.53	1.25	0.2	m = 4, quasi-helical symmetry
H-1 (Canberra)	1.0	0.2	0.79	1.0	0.2	m = 3, heliac
TJ-IU (Madrid)	0.6	0.1	0.12	0.7	0.6	ℓ = 1, m = 6
TU-Heliac (Sendai)	0.48	0.07	0.05	0.35		m = 4, heliac
TJ-II (Madrid)	1.5	0.2	1.18	1.0		m = 4, flexible heliac

[a] ℓ stands for multipolarity and m for toroidal period number.

2. TRANSPORT STUDIES

2.1. Global confinement

A major progress in the area of transport studies is the establishment of an empirical scaling law for the global confinement time in helical systems. A database of 859 L mode discharges from ATF, CHS, Heliotron-E (H-E), WVII-AS and WVII-A has been compiled, and a regression analysis has been performed [8]. The confinement time data are shown in Fig. 1. The proposed scaling law is given by

$$\tau_E = 0.079\, a_p^{2.21} R_0^{0.65} P_{abs}^{-0.59} n_e^{0.51} B_0^{0.83} \iota^{0.40} \tag{1}$$

In performing the regression, the ansatz was made that the rotational transform evaluated at r = 2a/3 is relevant. Let us make a few remarks on the scaling law. The exponents of the independent variables R_0, a_p, P_{abs}, n_e and B_0 are similar to those of the LHD scaling [9]. The density exponent here is somewhat smaller. The predicted τ_E is in a range similar to that for the L mode in tokamaks. This similarity may reflect the fact that neoclassical ripple transport is not a major loss mechanism in the discharges included in the database. (A reduction of ripple transport has been attempted, either by using the radial electric field in heliotron/torsatron devices or

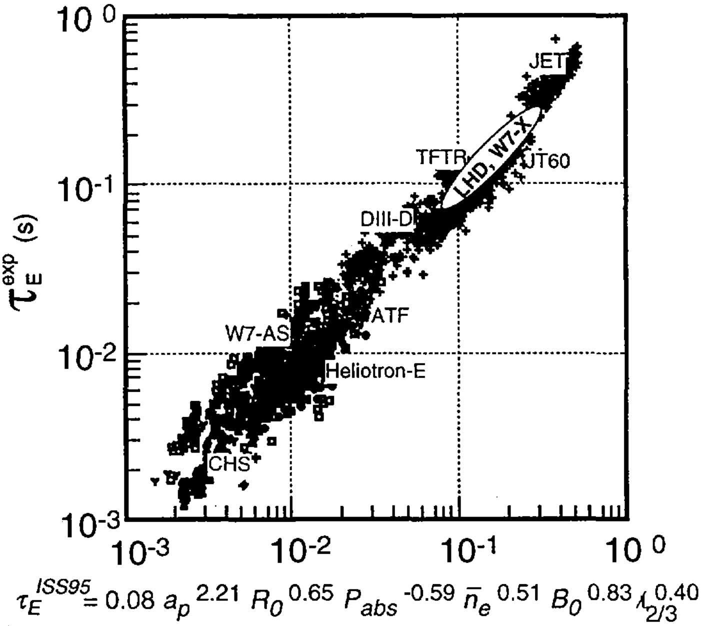

FIG. 1. Global energy confinement time scaling based on the international helical system database. SI units are used: $\tau_E(s)$, $a_p(m)$, $R_0(m)$, $P_{abs}(MW)$, $n_e(10^{19}\ m^{-3})$ and $B_0(T)$ (based on Ref. [8]).

by optimizing the ripples in an advanced stellarator.) The confinement in WVII-AS in terms of scaling is better than in ATF, H-E or CHS. An explicit demonstration of the relative advantages of each device, however, must wait for future experiments in higher temperature and less collisional plasmas. The density dependence of the energy confinement time is favourable. However, τ_E has been observed to saturate at high densities. This saturation could be removed by using the reheat mode (see next section).

Operating at high densities is important for helical devices because it reduces ripple transport. For this reason, the density limit has been studied intensively. Some results are shown in Fig. 2. The density limit in present devices is set by a radiation collapse at the plasma edge; it is given by the following scaling law:

$$n_e \propto B_0^a P_{abs}^b \tag{2}$$

where the exponents, a and b, are reported as 0.5 and 0.5 in the high heating limit in H-E [9] and as nearly 1.0 and 0.4 in WVII-AS [10]. The density limit is much higher in a helical device than in a tokamak of similar size. A possible reason for this is that helical devices do not show current disruptions, which are a serious problem at the density limit in tokamaks. The size dependence of the density limit is now being studied by comparing WVII-AS and CHS.

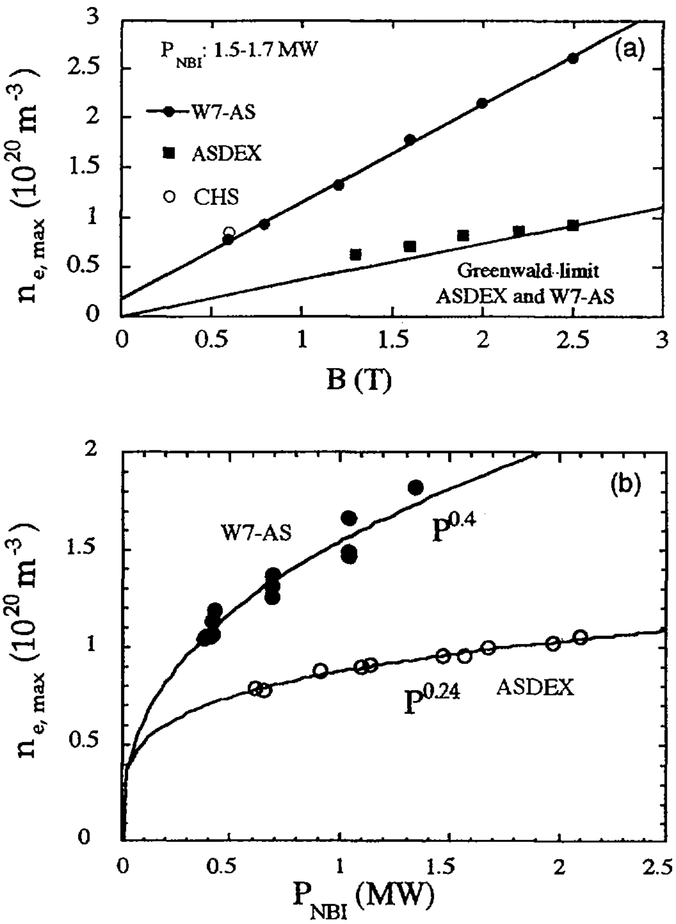

FIG. 2. (a) Density limit as a function of magnetic field strength; (b) density limit as a function of NBI power. In comparing to the Greenwald limit, the plasma current is replaced by the rotational transform in W7-AS (based on Ref. [10]).

The configuration dependence of τ_E has been studied. An inward shift of the magnetic surfaces has been found favourable in heliotron/torsatron devices [11] as well as in stellarators [12]. Improved heating efficiency [11] and reduction of ion neoclassical loss [12] are considered candidates for explaining the improved confinement. Increased shear has also been pointed out as being effective in reducing the anomalous transport when the magnetic axis is shifted in heliotron/torsatron devices [13]. The role of magnetic shear has also been tested on an advanced stellarator. The magnetic shear was reduced or enhanced in WVII-AS by using RF driven currents, but the effect of the change on confinement was found to be small [14]. An explanation for this discrepancy may be that the region of shear modification was small and that the negative sher simultaneously enhanced the neoclassical loss, because of a substantial reduction iota. Changes in the magnetic structure have been found to reduce the threshold power for L–H transitions in CHS [15].

Further efforts to improve confinement are necessary for arriving at an attractive reactor design based upon a helical system.

2.2. Improved confinement modes

Improved confinement modes have been studied in helical systems; those observed in CHS, H-E and WVII-AS are summarized in Table II.

High T_i mode

The high ion temperature mode has been observed in neutral beam heated plasmas in H-E ($T_i(0)$ = 1.1 keV) [16, 17] and WVII-AS ($T_i(0)$ = 1.6 keV) [12] at

TABLE II. IMPROVED CONFINEMENT MODES OBSERVED IN CHS, H-E and WVII-AS

Operating electron density	Mode	CHS	H-E	WVII-AS
Low	High T_i		$T_i^{CXS}(0) = 0.85$ keV $\Delta\tau_E \le 40\%$ $\Delta T_i(0) \le 80\%$ $\chi_i(0.1) = 0.5\ m^2/s$ $n_e = 2.5 \times 10^{19}\ m^{-3}$ [16] $T_i^{NPA}(0) = 1.1$ keV [17]	$T_i^{NPA,CXS}(0)$ $= 1.6$ keV [12]
Medium	Pellet		$T_i^{CXS}(0) = 0.7$ keV $\Delta T_i(0) \le 60\%$ $\chi_i(0.1) = 0.7\ m^2/s$ $n_e = 4 \times 10^{19}\ m^{-3}$ [19]	
Medium	H	$\Delta\tau_E = 15\%$ $n_e = 3 \times 10^{19}\ m^{-3}$ [15, 22]		$\Delta\tau_E \le 30\%$ $M_{pol} = 0.5\text{–}1$ $n_e = 5 \times 10^{19}\ m^{-3}$ [20, 21]
High	Reheat	$\Delta\tau_E \le 20\%$ $n_e = 6 \times 10^{19}\ m^{-3}$ [23]		

relatively low densities. The energy confinement time in the high T_i mode in these devices is 40% longer than in the L mode in H-E. High T_i mode plasmas are characterized by peakedness of both ion temperature and electron density profiles. Peaked density profiles in the high T_i mode are produced by neutral beam fuelling with low wall recycling in H-E, and off-axis electron cyclotron heating (ECH) in WVII-AS [18]. From measurements of the profile of the radial electric field, its shear is believed to be responsible for the observed reduction in χ_i (= 0.5 m^2/s) near the plasma centre in H-E.

Pellet mode

Injection of a frozen pellet of working gas was found to be effective in achieving a high central ion temperature in helical devices, just as pellet injection was found to be effective in achieving a high density in tokamaks. This was demonstrated in the pellet injection mode in H-E ($T_i(0)$ = 0.7 keV, $n_e(0) = 7.3 \times 10^{19}$ m^{-3}) [19]: the ion temperature profile became peaked, and $T_i(0)$ increased after pellet injection.

H mode

Transition into the H mode was clearly observed in WVII-AS [20, 21] and CHS [15, 22]: the intensity of H_α light dropped, and the edge density rose rapidly. However, an increase in the energy confinement time of up to 30% was less than that usually observed in divertor tokamaks. At L to H transitions, a jump in the poloidal rotation velocity in the electron diamagnetic direction (more negative electric field) was also observed in helical systems. The critical poloidal Mach number, $M_{pol} = v_\theta/v_{thermal}(B/B_\theta)$, at L to H or H to L transitions was 0.5–1.

Reheat mode

An increase in the stored energy was observed, together with density peaking when gas puffing was turned off in a high density regime. This was called reheating in CHS [23]. The reheat mode is characterized by a peaked density profile triggered by the decrease in the neutral density at the plasma edge.

Similarities exist in plasma characteristics between improved confinement modes in helical devices and tokamaks. The density and ion temperature profiles in the high T_i mode are similar to those observed in the core enhanced confinement modes in tokamaks (supershot [24], PEP mode [25], VH mode [26], high β_p mode [27]). The existence of a critical M_{pol} suggests that a similar mechanism for the H mode prevails both in helical systems and in tokamaks (see Ref. [28] for review). The plasma behaves very similarly in the reheat mode in helical devices and in IOC mode in tokamaks [29]. Quantitative performance comparisons of improved modes in helical devices and tokamaks must wait for studies in LHD plasmas with improved particle confinement at larger size and reduced edge neutral densities made possible by a helical divertor.

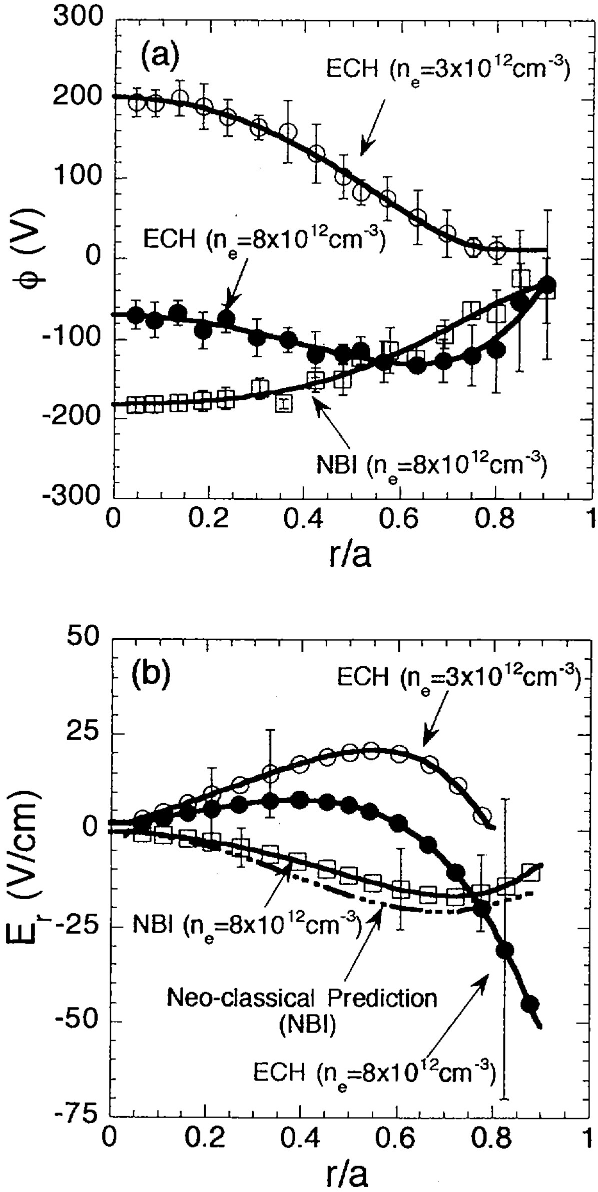

FIG. 3. (a) Potential and (b) electric field profiles of ECH and NBI plasmas for R_{ax} = 0.921 m and B_0 = 0.9 T in CHS. The electric field profile of a medium density plasma shows strong shear (solid line). The expected electric field from neoclassical theory is shown by the dashed-dotted line (quoted from Ref. [35]).

2.3. Local transport

The measured electron thermal diffusivity, χ_e, is of the order of 1–10 m^2/s in helical devices. The radial diffusivity profile is relatively flat, or even increases towards the plasma centre [30, 31]. This is in contrast to tokamaks, in which the diffusivity decreases sharply towards the plasma centre. In the L mode the ion thermal diffusivity, χ_i, is similar to χ_e in its magnitude and profile. In improved modes, however, χ_i decreases towards the plasma centre, and the central values are 0.5–1 m^2/s. These values are close to those observed in improved modes in tokamaks [24]. In general, the measured thermal diffusivities are much larger than the neoclassical values, except near the plasma centre at low collisionality, where the neoclassical values are large. Theoretical efforts have been made to model the anomalous transport. A non-linear theory has been developed for a current diffusive ballooning/interchange mode [32], which gives a qualitative explanation for the transport anomaly.

2.4. Radial electric field

The radial electric field and the associated space potential profile have been investigated intensively as a possible means of reducing the ripple loss and preventing confinement degradation in helical systems [33, 34]. These investigations were motivated by the expectation that the ripple loss and other neoclassical transport losses become more important in higher temperature, lower collisionality plasmas in future devices. The radial electric field depends on both heating scheme and plasma density. Recently, a 200 kV HIBP measurement started to obtain a radial profile of electric potentials in CHS [35]. A positive field was observed in ECH plasmas, while a negative field was seen in NBI plasmas [33, 35, 36], as shown in Fig. 3. In NBI plasmas, the field became more negative as the electron density increased, but the field became less negative as the density decreased. A bifurcation of the radial electric field was seen in transitions from the ion root to the electron root [37], or in L to H transitions [38]. Measurements in low density plasmas in CHS heated by high power ECH suggested the appearance of a potential structure that acts as an internal transport barrier [36]. Some aspects of the radial electric field behave in accordance with neoclassical theories, but the magnitude and the radial profile of the field do not always agree with predictions of neoclassical theories [28, 39].

3. HIGH β PLASMA

Design values of the volume averaged β limit are typically 5% for the next generation helical systems [5–7]. In present experiments, β values of up to 2% have been achieved with neutral beam injection [40–43]. This observed experimental limit is close to the theoretical stability limit in H-E, but is far below the theoretical limit in other devices. In CHS experiments, the global energy confinement was not degraded further than that given by Eq. (1); the density was increased along with the input power, and the measured magnetic fluctuations did not increase as β increased. The maximum β values in the present CHS experiments are determined by a density limit set by radiation loss and degradation of beam heating efficiency in low magnetic field operations [44].

Thanks to recent advances in supercomputer technology, the development of three dimensional MHD codes enabled greatly improved comparisons of experimental and theoretical equilibria of high β plasmas. A measured dependence of the Shafranov shift on the plasma pressure could be clearly described by model MHD calculations [3, 45]. The Shafranov shift was observed to be reduced in WVII-AS as was expected from the reduction in Pfirsch–Schlüter current. This experimental confirmation of a theoretical expectation was one of the most important objectives of configuration optimization in WVII-AS.

Various saturated MHD modes have been studied in helical devices. A burst type mode in NBI plasmas in CHS was examined with local potential measurements using HIBP [35]. The dynamic structure of pressure driven instabilities was studied in H-E by using a 2-D tomographic analysis of soft X ray signals [46]. A similar technique was used for the analysis of a type of Alfvén eigenmode (GAE) in NBI plasmas in WVII-AS [47]; no significant fast ion loss has been observed, so far.

A ballooning instability was recently investigated theoretically for plasmas in helical devices. The instability had been considered less serious in the past because of a favourable magnetic shear structure of helical systems [48].

4. DIVERTOR STUDIES

In a heliotron/torsatron type configuration a built-in separatrix configuration in the free space between the helical coils leads to a helical divertor structure. In designing LHD, careful consideration was given to realizing a helical divertor also in a relatively low aspect ratio device. The basic function of helical divertors was studied in H-E, which has a clearly defined divertor structure due to its high aspect ratio. Particle and heat flux profiles were measured at the plasma boundary, which demonstrated the existence of localized structures at the divertor traces [49].

The boundary field of a modular stellarator does not possess a simple divertor, because of the overlapping of various mode structures. The island divertor concept has been developed, instead, to realize an effective divertor function at the boundary. The island divertor was studied in WVII-AS [50] by taking advantage of natural islands in the vicinity of the outermost magnetic surface. Figure 4 shows density profiles within an island near the surface, which demonstrate the presence of a high density plasma within the island when the main plasma density is high enough. This spontaneous increase in the density within the island provides a basis for establishing a cold dense plasma in island divertors. Three dimensional modelling of divertor plasmas is also in progress [51]. The island divertor is considered to be a main candidate for modular systems such as WVII-X.

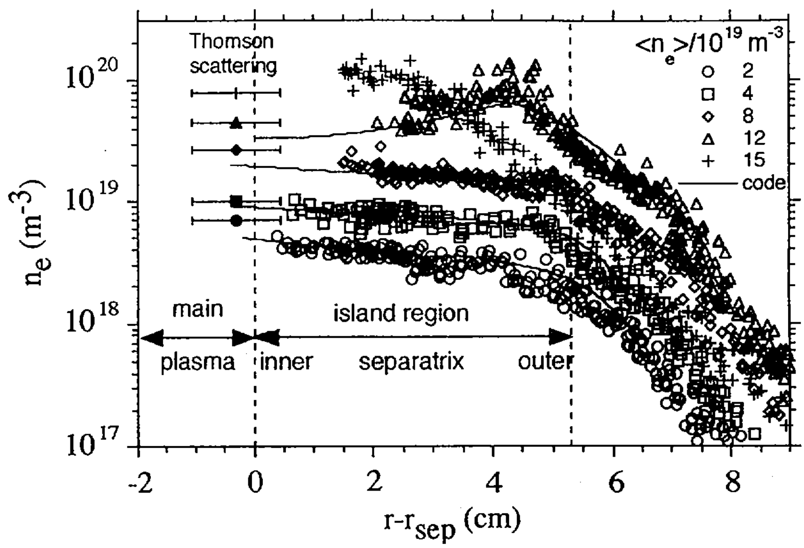

FIG. 4. Electron density profiles inside natural islands for various electron densities of the main plasma in WVII-AS. When the main plasma density is high the density inside the island becomes peaked (quoted from Ref. [50]).

A similar island divertor called LID (local island divertor) [52] can be constructed in LHD by introducing a perturbation field to create artificial islands at the plasma boundary. The island structure is designed to enhance the efficiency of a standard pumped divertor. LID is designed to be an alternative to a standard helical divertor for LHD. Preliminary experiments to demonstrate the LID concept were performed in CHS [53]. The main plasma density was observed to decrease, and the plasma flow into, and the gas pressure within, the pumped divertor both increased when an artificial island structure was created.

5. DEVELOPMENT IN HEATING

ECH is a main heating resource in almost all helical devices. For example, an ECH power density of a few MW/m^3 is expected in L-2M [54]. Long pulse (4667 s) operation of ECH plasma was achieved in ATF by using a 28 GHz gyrotron with the injected power of 70 kW [55]. The required gyrotron frequency continues to rise as the confining field in present and future devices increases. Recently, overdense plasmas without electron cyclotron resonance could be heated with ECH in WVII-AS [56]. Here, an O-X-B mode conversion took place with the following parameters: $B_0 = 2.0$ T, 140 GHz, $n_e = 1.6 \times 10^{20}\ m^{-3}$, while the second harmonic mode cut-off of 140 GHz occurs at $B_0 = 2.5$ T and $n_e = 1.2 \times 10^{20}\ m^{-3}$.

ICRF alone could sustain plasmas for a maximum RF pulse length of 70 ms in CHS. In these experiments, electrons were primarily heated via a mode conversion of an ion cyclotron wave to an ion Bernstein wave in deuterium (H minority of 30%) plasmas [57]. ICRF alone could also sustain deuterium plasmas (H minority of 10%) in WVII-AS, and the ion tail distribution was observed [58].

6. FUTURE PLANS

LHD is in the final stage of its construction; superconducting helical windings have been completed [59–61]. The first plasma is scheduled in April 1998 with 1 MW ECH and diagnostics for the basic plasma parameters. WVII-X, which is fully optimized for a Helias type reactor, is scheduled to be operational in 2004. The large plasma volume and heating power, and the superconducting magnets in these facilities, will open a new era in studies of plasma confinement and steady state operations of helical devices. Reactor relevant plasmas will be realized in these devices. The U-2M torsatron with a low helical ripple is waiting for resumption of operation [62]. A small Heliac has started its operation (H-1 [63]), and another is in the final stage of construction (TJ-II [64]). In these Heliac devices, plasma confinement in configurations with a fully three dimensional magnetic axis will be studied; the $\ell = 1$ component is a key element for stellarator optimization. A small modular stellarator, HSX [65], based on the principle of quasi-helical symmetry [66], is under construction in the United States of America. This principle results in the absolute confinement of particle orbits.

7. SUMMARY

Helical systems have a variety of magnetic configurations. Although the systems have well-known inherent advantages, i.e. no major disruptions and steady state operations, there remain key issues to be addressed: improving confinement by a significant factor, achieving high β ($>5\%$) and demonstrating steady state operations with appropriate exhaust. These issues are expected to be solved in the next generation devices, LHD and WVII-X, which are optimized on the basis of results from presently operating heliotron/torsatron devices and an advanced stellarator, respectively. A new trend based on stellarator optimization is also emerging. Intensive investigations of helical systems are currently in progress from both physics and engineering standpoints.

ACKNOWLEDGEMENTS

The author would like to thank members of the fusion research community working on helical systems who have kindly provided valuable information for this review, as well as Professor F. Wagner for valuable comments.

REFERENCES

[1] UO, K., et al., in Plasma Physics and Controlled Nuclear Fusion Research 1982 (Proc. 9th Int. Conf. Baltimore, 1982), Vol. 2, IAEA, Vienna (1983) 209.
[2] MATSUOKA, K., et al., in Plasma Physics and Controlled Nuclear Fusion Research 1988 (Proc. 12th Int. Conf. Nice, 1988), Vol. 2, IAEA, Vienna (1989) 411.
[3] RENNER, H., et al., in Plasma Physics and Controlled Nuclear Fusion Research 1990 (Proc. 13th Int. Conf. Washington, 1990), Vol. 2, IAEA, Vienna (1991) 439.
[4] FUJIWARA, M., in Plasma Physics and Controlled Nuclear Fusion Research 1992 (Proc. 14th Int. Conf. Würzburg), Vol. 4, IAEA, Vienna (1993) 23.
[5] IIYOSHI, A., et al., Fusion Technol. **17** (1990) 169.
[6] MOTOJIMA, O., et al., in Plasma Physics and Controlled Nuclear Fusion Research 1990 (Proc. 13th Int. Conf. Washington, 1990), Vol. 3, IAEA, Vienna (1991) 513.
[7] GRIEGER, G., et al., in Plasma Physics and Controlled Nuclear Fusion Research 1988 (Proc. 12th Int. Conf. Nice, 1988), Vol. 2, IAEA, Vienna (1989) 369.
[8] STROTH, U., et al., Nucl. Fusion **36** (1996) 1063.
[9] SUDO, S., et al., Nucl. Fusion **30** (1990) 11.
[10] HOFMANN, J., et al., invited paper presented at 23rd Eur. Conf. Controlled Fusion and Plasma Physics, Kiev, 1996; to be published in Plasma Phys. Control. Fusion.
[11] KANEKO, O., et al., in Plasma Physics and Controlled Nuclear Fusion Research 1990 (Proc. 13th Int. Conf. Washington, 1990), Vol. 2, IAEA, Vienna (1991) 473.
[12] WELLER, A., et al., in Plasma Physics and Controlled Nuclear Fusion (Proc. 7th Int. Conf. Toki, 1995); to be published in Fusion Eng. Des.
[13] ITOH, K., et al., in Plasma Physics and Controlled Nuclear Fusion Research 1994 (Proc. 15th Int. Conf. Seville, 1994), Vol. 3, IAEA, Vienna (1995) 391.
[14] ERCKMANN, V., et al., in Controlled Fusion and Plasma Physics (Proc. 22nd Eur. Conf. Bournemouth, 1995), Vol. 19C, Part I, European Physical Society, Geneva (1995) 389.
[15] TOI, K., et al., in Plasma Physics and Controlled Nuclear Fusion Research 1992 (Proc. 14th Int. Conf. Würzburg, 1992), Vol. 2, IAEA, Vienna (1993) 461.
[16] IDA, K., et al., Phys. Rev. Lett. **76** (1996) 1268.
[17] OBIKI, T., et al., in Plasma Physics and Controlled Nuclear Fusion Research 1994 (Proc. 15th Int. Conf. Seville, 1994), Vol. 1, IAEA, Vienna (1995) 757.
[18] KUEHNER, G., et al., ibid., p. 145.
[19] IDA, K., et al., IAEA-CN-64/CP-5, these Proceedings, Vol. 2.
[20] ERCKMANN, V., et al., Phys. Rev. Lett. **70** (1993) 2086.
[21] WAGNER, F., et al., Plasma Phys. Control. Fusion **36** (1994) A61.
[22] TOI, K., et al., Plasma Phys. Control. Fusion **36** (1994) A117.
[23] MORITA, S., et al., in Plasma Physics and Controlled Nuclear Fusion Research 1992 (Proc. 14th Int. Conf. Würzburg), Vol. 2, IAEA, Vienna (1993) 515.
[24] HAWRYLUK, R.J., et al., Plasma Phys. Control. Fusion **33** (1991) 1509.
[25] KEILHACKER, M., et al., Plasma Phys. Control. Fusion **33** (1991) 1453.
[26] OSBORNE, T.H., et al., Plasma Phys. Control. Fusion **36** (1994) A237.
[27] KOIDE, Y., et al., in Plasma Physics and Controlled Nuclear Fusion Research 1994 (Proc. 15th Int. Conf. Seville), Vol. 1, IAEA, Vienna (1995) 199.
[28] For a review of electric field and improved confinement see: ITOH, K., et al., Plasma Phys. Control. Fusion **38** (1996) 1; ITOH, S.-I., et al., J. Nucl. Mater. **220–222** (1995) 117.
[29] SÖLDNER, F.X., et al., Phys. Rev. Lett. **61** (1988) 1105.
[30] RINGLER, H., et al., Plasma Phys. Control. Fusion **32** (1990) 933.
[31] IGUCHI, H., et al., in Controlled Fusion and Plasma Physics (Proc. 17th Eur. Conf. Amsterdam, 1990), Vol. 14B, Part II, European Physical Society, Geneva (1990) 451.

[32] ITOH, K., et al., Phys. Rev. Lett. 69 (1992) 1050;
ITOH, K., et al., Plasma Phys. Control. Fusion 36 (1994) 1501.
[33] KONDO, K., et al., Rev. Sci. Instrum. 59 (1988) 1533.
[34] WOBIG, H., et al., in Plasma Physics and Controlled Nuclear Fusion Research 1986 (Proc. 11th Int. Conf. Kyoto, 1986), Vol. 2, IAEA, Vienna (1987) 369.
[35] FUJISAWA, A., et al., IAEA-CN-64/C1-5, these Proceedings, Vol. 2.
[36] IDA, K., et al., Phys. Fluids B 3 (1991) 515; Phys. Fluids B 4 (1992) 1360.
[37] IDEI, H., et al., Phys. Rev. Lett. 71 (1993) 2220.
[38] HOFMANN, J.V., et al., in Controlled Fusion and Plasma Physics (Proc. 21st Eur. Conf. Montpellier, 1994), Vol. 18B, Part I, European Physical Society, Geneva (1994) 392.
[39] SANUKI, H., et al., Phys. Scr. 52 (1995) 461.
[40] MOTOJIMA, O., et al., Nucl. Fusion 25 (1985) 1783.
[41] MURAKAMI, M., et al., Phys. Fluids B 3 (1991) 2261.
[42] OKAMURA, S., et al., Nucl. Fusion 35 (1995) 283.
[43] KICK, M., et al., IAEA-CN-64/C1-4, these Proceedings, Vol. 2.
[44] MURAKAMI, S., et al., IAEA-CN-64/CP-6, ibid.
[45] YAMADA, H., et al., Nucl. Fusion 32 (1992) 25.
[46] ZUSHI, H., et al., IAEA-CN-64/CP-4, these Proceedings, Vol. 2.
[47] WELLER, A., et al., Phys. Rev. Lett. 72 (1994) 1220.
[48] NAKAJIMA, N., et al., IAEA-CN-64/D3-6, these Proceedings, Vol. 2.
[49] MATSUURA, H., Nucl. Fusion 32 (1992) 405.
[50] GRIGULL, P., et al., IAEA-CN-64/CP-25, these Proceedings, Vol. 2;
GRIGULL, P., et al., paper presented at Plasma-Surface Interactions Conference, St. Raphael, 1996; to be published in J. Nucl. Mater.
[51] FENG, Y., et al., ibid.
[52] KOMORI, A., et al., in Plasma Physics and Controlled Nuclear Fusion Research 1994 (Proc. 15th Int. Conf. Seville, 1994), Vol. 2, IAEA, Vienna (1995) 773.
[53] KOMORI, A., et al., IAEA-CN-64/C1-2, these Proceedings, Vol. 2.
[54] BIGELOW, T.S., et al., Bull. Am. Phys. Soc. 39 (1994) 1603.
[55] ERCKMANN, V., et al., IAEA-CN-64/CP-1, these Proceedings, Vol. 2.
[56] NISHIMURA, K., et al., in Plasma Physics and Controlled Nuclear Fusion Research 1994 (Proc. 15th Int. Conf. Seville, 1994), Vol. 1, IAEA, Vienna (1995) 783.
[57] HARTMANN, D., et al., Stellarator News 44 (1996) 5.
[58] IIYOSHI, A., et al., Phys. Plasmas 2 (1995) 2349.
[59] FUJIWARA, M., et al., Trans. Fusion Technol. 27 (1995) 58.
[60] MOTOJIMA, O., et al., IAEA-CN-64/G2-4, these Proceedings, Vol. 3.
[61] PAVLICHENKO, O.S., et al., Plasma Phys. Control. Fusion 35 (1993) B223.
[62] BLACKWELL, B.D., et al., in Plasma Physics and Controlled Nuclear Fusion Research 1994 (Proc. 15th Int. Conf. Seville, 1994), Vol. 2, IAEA, Vienna (1995) 337.
[63] ASCASIBAR, E., et al., ibid., Vol. 1, p. 749.
[64] MATTHEWS, P.G., et al., in Stellarators (Proc. 10th Workshop, 1995) 167.
[65] NUEHRENBERG, J., et al., Phys. Lett. A 129 (1988) 113.

DISCUSSION

D.D. RYUTOV: In the pellet mode you mentioned, the diffusion coefficient was ~0.6 m^2/s. How does this compare with neoclassical transport?

A. IIYOSHI: The ion thermal diffusivity measured ($\chi_i \approx 0.6$ m^2/s) is comparable to that expected from neoclassical transport near the plasma centre, although the measured edge χ_i is much larger than the neoclassical values.

OVERVIEWS 2

(Session O2)

Chairperson

R. PARKER
ITER

DIVERTOR DETACHMENT, He EXHAUST AND COMPACT TOROID INJECTION ON TdeV*

R. DÉCOSTE[1], B.L. STANSFIELD[2], R. RAMAN[3], G. ABEL[2], C. BOUCHER[2], P. BROOKER[4], A. CÔTÉ[1], C. CÔTÉ[5], Y. DEMERS[4], J.-L. GAUVREAU[1], B.C. GREGORY[2], J.P. GUNN[2], E. HADDAD[4], J. KALNAVARNS[4], J.-L. LACHAMBRE[1], G. LE CLAIR[4], H.H. MAI[2], J. MAILLOUX[2], R. MARCHAND[2], F. MARTIN[2], F. MÉO[2], D. MICHAUD[4], G.W. PACHER[1], D. PINSONNEAULT[2], B. QUIRION[5], N. RICHARD[4], A. SARKISSIAN[2], M.M. SHOUCRI[1], M. St.-ONGE[4], B. TERREAULT[2], W. ZUZAK[2]
Centre canadien de fusion magnétique,
Varennes, Quebec, Canada

Abstract

DIVERTOR DETACHMENT, He EXHAUST AND COMPACT TOROID INJECTION ON TdeV.

Progressive detachment with increasing density is shown to proceed with a marked reduction of the ion flux to the divertor plates, a pressure gradient between an ionization front and the plate, and strong cross-field transport in the divertor. The divertor He exhaust is not affected by detachment although the He enrichment remains low but constant. A moderate density of $\bar{n}_e \sim 5 \times 10^{19}$ m^{-3} seems to be sufficient both for efficient peak power load reduction at the plate and good He exhaust through the divertor. Simulations indicate possible divertor geometry improvements which will soon be verified experimentally in the new TdeV-96 divertor upgrade. Finally, central fuelling with compact toroid injection is reported with no detrimental effects on the plasma.

1. INTRODUCTION

Edge plasma and divertor studies have been performed on TdeV for the last few years [1,2], providing unique and interesting results on divertor detachment [3], exhaust [4] and biasing [5] simultaneously. This paper describes the physics of divertor detachment [6] and demonstrates how moderate detachment reduces efficiently the peak power load on the divertor components without impeding the He retention and exhaust capability of the divertor. Simulations are also used to show how He exhaust can be affected by varying the

* The Centre canadien de fusion magnétique is funded by the Government of Canada, Hydro-Québec and the Institut national de la recherche scientifique. The compact torus injector is funded by the Canadian Fusion Fuels Technology Project.

[1] Hydro-Québec, Varennes, Quebec, Canada.
[2] INRS-Energie et Matériaux, Varennes, Quebec, Canada.
[3] Canadian Fusion Fuels Technology Project, Mississauga, Ontario, Canada.
[4] MPB Technologies Inc., Dorval, Quebec, Canada.
[5] Décatron Inc., St.-Bruno, Quebec, Canada.

divertor geometry in the upcoming TdeV-96 upgrade. Finally, much improved results are presented on compact toroid injection, a novel core fuelling technique scalable to large tokamaks.

TdeV is a divertor tokamak (R= 0.86 m, a= 0.27 m, I_p= 0.25 MA) with a full complement of diagnostics mostly for the edge plasma and the divertors. The divertors use a triplet coil geometry, with closed outer divertors, open inner divertors and electrically insulated plates for biasing. The outer upper divertor chamber is equipped with steady-state cryosorption pumps that can exhaust He as well as D_2. A flexible 1.3 MW lower hybrid (LH) system is used for both heating and current drive [7]. The results presented in this paper are obtained in the single null (top) configuration with or without LH heating.

2. DIVERTOR DETACHMENT

Detachment involves the creation of a pressure gradient along the field lines inside the divertor from increased radiation and lateral transport losses. Figure 1 (a) shows D_α images of the divertor that demonstrate the transition from a high recycling regime at low density to a detached configuration at high density. Although the radiation zone has moved near the X-point at high density, the region of maximum density remains within the divertor. Radiation losses appear to be important to establish detachment since the radiation zone is upstream from the region of decreasing density toward the plate. HeI line

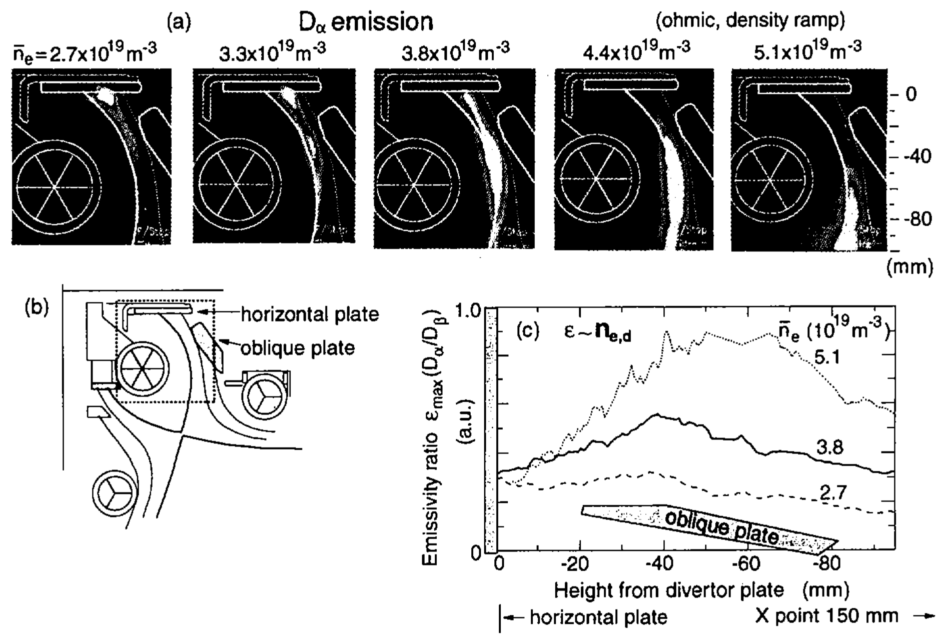

FIG. 1. (a) D_α emission images showing progressive detachment as the central electron density is increased. (b) Images obtained from a tangential view of the divertor. (c) Ratio of the peak emissivity D_α/D_β proportional to the electron density along the field lines [8].

ratio measurements [9] indicate that the electron temperature just below the horizontal plate has dropped to less than 5 eV for $\bar{n}_e$~5×10^{19} m^{-3}. Mach probe measurements in the divertor also show an upstream temperature which is higher than the downstream temperature, a further evidence that the temperature is decreasing toward the plate and that a significant pressure gradient exists along the field lines inside the divertor.

Figure 2 shows that the ion flux to the horizontal plate is decreasing simultaneously. Detachment does not however impede the neutral throughput of the divertor, as shown later in Fig. 6 with the divertor pressure rising with the central density. The D_α profile just below the horizontal plate is relatively narrow at low densities [Fig. 2 (b)]. At higher densities however, the profiles of both the emission layer [Fig. 2 (b), (c) and (e)] and the particle flux to the horizontal divertor plate [Fig. 2 (a)] show that the plasma fan is significantly broader. On the other hand, density profiles outside the divertor throat show that the SOL profile is not significantly broader under detached conditions. There must then be significant cross-field transport within the divertor, carrying the incoming ions both inward into the private flux region and outward onto the inclined plates. Several mechanisms involving ions and/or neutrals could explain this enhanced lateral transport, including recombination to reduce the total ion flux to the horizontal plate.

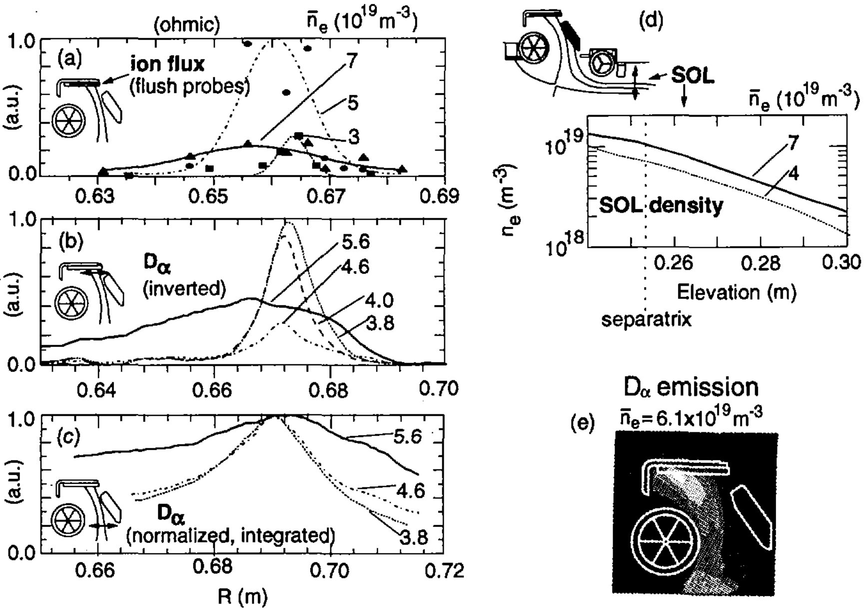

FIG. 2. Radial profiles for various line average densities for (a) the ion flux on the horizontal plate, (b) D_α emission just in front of the plate (Abel inverted), (c) D_α emission further upstream and (d) SOL electron density at the divertor entrance. (e) Enhanced D_α emission under complete detachment from molecular processes near the plate.

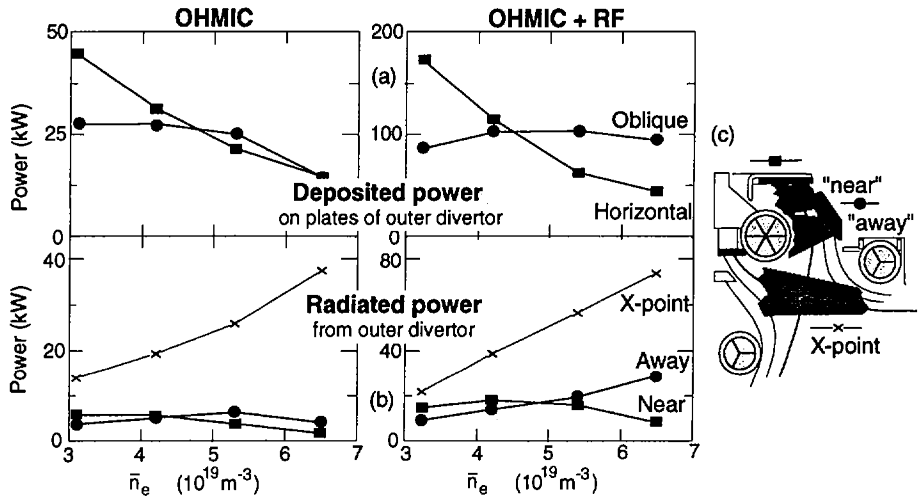

FIG. 3. Power deposited on (a) and radiated from (b) the outer divertor versus central line average density. The deposited power is from thermocouples cross-referenced with an infrared camera. The radiated power is from bolometers looking at the shaded areas shown in (c). The X-point radiation is deconvoluted from several bolometers.

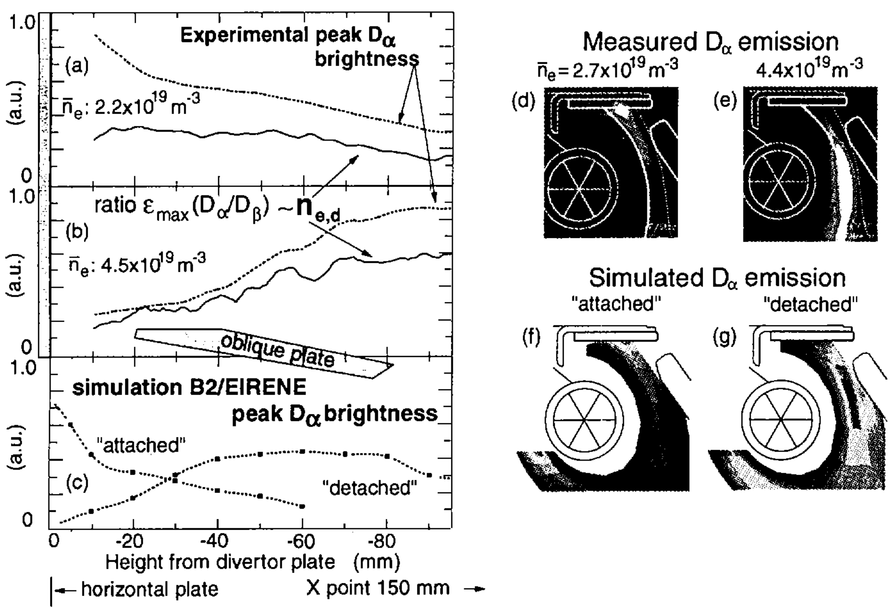

FIG. 4. Measured peak D_α brightness (dashed) and D_α/D_β ratio (solid) along the field lines in the divertor for (a) an attached and (b) a detached plasma. (c) Calculated D_α brightness from simulations for the attached and detached plasmas. (d)-(g) Comparison of measured and reconstructed D_α images.

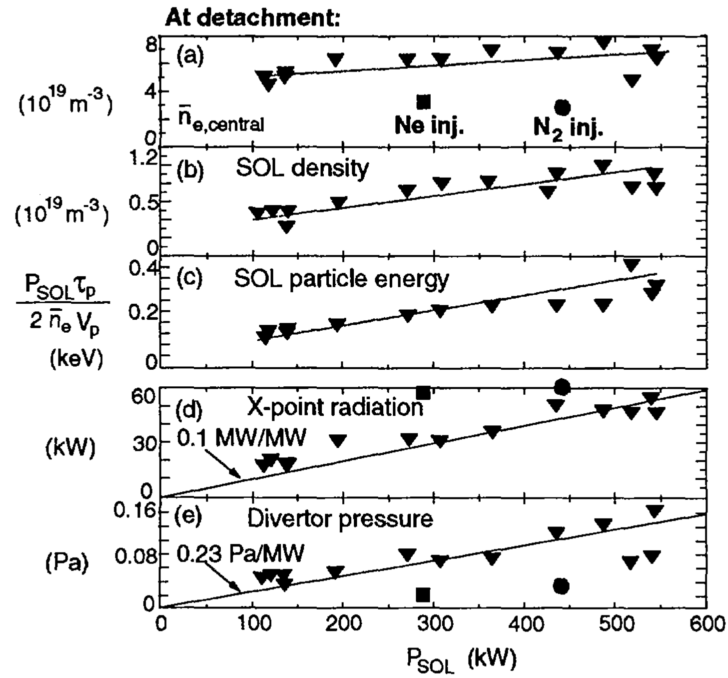

FIG. 5. At detachment, as a function of the SOL power: (a) line average density of the central plasma, (b) line average density in the SOL, (c) energy per particle in the SOL going to the divertors, (d) radiated power in the outer divertor and (e) pressure in the outer divertor. Detachment is defined here as a fixed ratio between the radiated power 'near' and 'away' from the horizontal plate (see Fig. 3(c)).

This large radial transport in the divertor under detachment is consistent with an increasing fraction of the divertor power flowing to the oblique plates [Fig. 3 (a)]. Simultaneously, the power to the horizontal plate is reduced by a factor of 4 as the central density is raised from 3 to 6×10^{19} m^{-3}. About half the missing power to the plates can be accounted for by the increased radiation from the X-point or the region just above it. This enhanced radiated power under detachment is however insufficient to account for the power redistribution to the oblique plates which must involve ions and/or neutral transport.

The proximity of the emission region to the horizontal plate in Fig. 2 (e) and its correlation with the reduction of the ion flux to the plate suggest that molecular processes could play an important role at least for the low temperature near the plates during detachment. Recombination involving dissociative attachment [10] or ion conversion [11], which invoke excited molecules coming from the surface, could explain the enhanced D_α near the plate and could play an important role in the power redistribution near the plates.

The B2/EIRENE codes have been used to model the experiments under both attached and detached conditions. Figure 4 shows a comparison between experimental and calculated D_α emission characteristic of an attached ($\sim2\times10^{19}$ m^{-3}) and a moderately detached (~4.5-5.0×10^{19} m^{-3}) plasma. The agreement is good, specially for the attached case. For the detached case, the simulation is able to reproduce the appearance of the pressure gradient and the displacement upstream of the D_α emission zone [Fig. 4 (g)]. However, the exact shape of the poloidal distribution is quite sensitive to the boundary conditions assumed to reproduce the pumping slot and the oblique plate in the simulation, indicating once again the sensitivity of poloidal distributions to the divertor geometry.

The effect of auxiliary heating on detachment is summarized in Fig. 5. The central density at which the plasma detaches from the horizontal plate increases slightly with the power flow across the separatrix P_{SOL} (total input power minus radiated power) [Fig. 5 (a)]. Due to a degradation of the particle confinement, auxiliary heating increases the SOL density [Fig. 5 (b)] and the energy per particle in the SOL [Fig. 5 (c)] with the net effect that the particle flux toward the divertor is increased. Detachment requires first to cool down the plasma near the divertor entrance through radiation near or just above the X-point and then to remove energy and momentum using neutrals from the divertor. Figures 5 (d) and (e) show that the radiated power at the X-point and the neutral pressure increase both at about the same rate and almost linearly with the SOL power in order to maintain detachment at the plate. Figure 5 also shows that detachment can be obtained at significantly lower central densities by increasing the X-point radiated power with controlled impurity injection. Lower SOL temperatures inside the divertor allow more efficient exchange with the neutrals.

3. He EXHAUST

Figure 6 (a) gives a simple example of $\tau^*_{p,He}$ measurements, the He exhaust time constant, using spectroscopic observation of HeII in the edge plasma. The divertor compression ratio is defined as $C=n_d/n_p=(N_dV_p)/(N_pV_d)$, where the "p" and "d" subscripts refer to the central plasma and the divertor respectively. Helium compression can be inferred from $\tau^*_{p,He}$ using a simple two-reservoir model [2, 12], whereas the deuterium compression can be obtained from the divertor pressure and interferometry measurements.

In the low density case of Fig. 6 (a), substantial tile pumping was used to demonstrate that $\tau^*_{p,He}/\tau_E\sim 10$ can be achieved (case with bias and LH) as required by a reactor [13] if sufficient pumping speed is available. Auxiliary heating with the LH system achieves a lower $\tau^*_{p,He}$ than ohmic but a similar $\tau^*_{p,He}/\tau_E$ due to a simultaneous degradation of both the particle and energy confinement. Biasing [5, 14] does better by setting up a strong E×B flow toward the divertor while the energy confinement time remains unaffected.

Figure 6 (b) characterises the divertor exhaust as the central density is raised through detachment with pumping from the steady-state divertor cryosorption pumps only. Tile pumping was subtracted out by repeating similar discharges with and without cryopumping and assuming that $1/\tau^*_p=(1/\tau^*_p)_{cryopumps}+(1/\tau^*_p)_{tiles}$. Tile pumping dominates the divertor cryopumps by about a factor of 5 at low densities ($\bar{n}_e\sim 3\times 10^{19}$ m^{-3}) without any significant saturation. Alternatively, the divertor cryopumping completely dominates at higher densities ($\bar{n}_e>5\times 10^{19}$ m^{-3}) where tile pumping saturates quickly. Figure 6 (b) indicates that detachment, occurring around $\bar{n}_e\sim 5\times 10^{19}$ m^{-3}, does not impede the divertor exhaust of either deuterium or He. Helium enrichment remains low and almost constant at ~0.2 and is independent of whether divertor pumping, LH heating or biasing are used or not.

TdeV's results generally support ITER's assumptions, especially for critical parameters such as the compression ratio and He enrichment. TdeV's difficulty in achieving $\tau^*_{p,He}/\tau_E\sim 10$ with steady-state pumping is not critical since the limitation is from

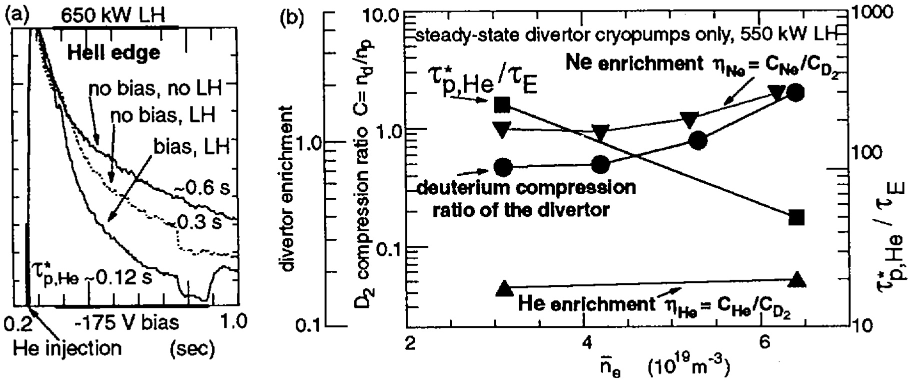

FIG. 6. (a) Example of He exhaust measurements. He, injected in a short puff at the equatorial plane, represents about 10% of the plasma density initially. A large pumping speed is provided by the carbon tiles, which have been preconditioned with low density discharges in this case. (b) He and Ne enrichment, D_2 compression ratio and normalized He exhaust time versus line average density of the central plasma. The effect of tile pumping at low density has been subtracted here. The pumping speed for the divertor is 6 m^3/s for both D_2 and He, provided by six commercial cryosorption pumps.

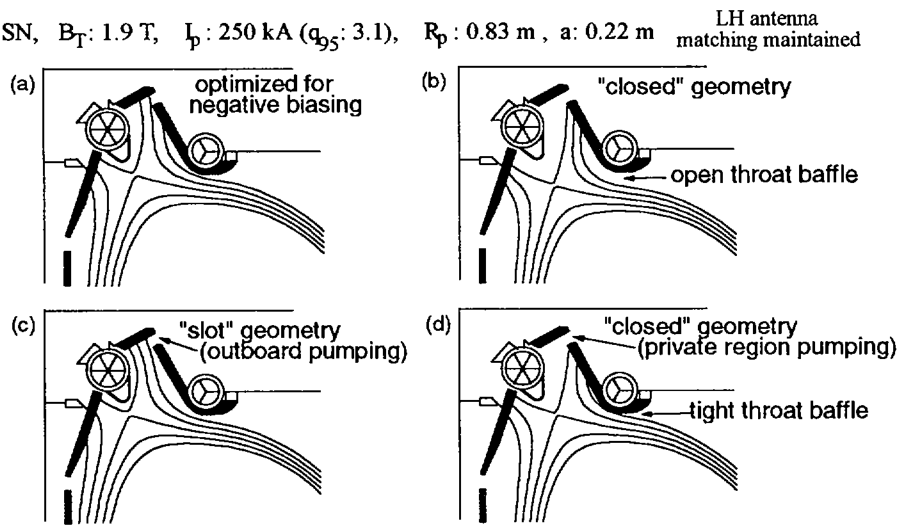

FIG. 7. Flexible divertor geometries possible with the TdeV-96 upgrade. The horizontal slot between the two plates in the outer divertor gives access to a closed plenum pumped by the steady-state cryosorption pumps (6 m^3/s for D_2 and He in the upper divertor and 4 m^3/s in the lower divertor). The divertor throat baffling can be varied during the discharge by adjusting the internal coil currents.

the low divertor pumping speed S_{ex} and not the plasma exhaust. The figure of merit $S_{ex}/(V_p/\tau_E)$, used to compare the pumping capability between devices, is ten times higher for ITER mostly because of the much larger divertor pumping speed on ITER compared to TdeV or for that matter any existing tokamak. The lack of space around small tokamaks is the main limitation and small devices like TdeV will therefore require a higher divertor compression ratio to achieve $\tau^*_{p,He}/\tau_E \sim 10$ with steady state pumping.

4. DIVERTOR GEOMETRY EFFECTS

Figure 7 shows some examples of various divertor geometries that will soon be available on the TdeV-96 upgrade, which includes completely new divertors and a precise control of the plasma shape in either single or double null configuration. The open inner divertors allow a wide range of plasma pressures ($\beta_p+\ell_i/2$) and a high triangularity. The divertor tiles are made of carbon fibre composites (CFC) except for the outer lower divertor tiles which are tungsten deposited on molybdenum, allowing an in-situ comparison of carbon and metallic tiles in the same device. A new electron cyclotron resonant heating (ECRH) system (1.5 MW, 110 GHz) is also planned for 1997, increasing the total heating/current drive capability to about 2.5 MW. Accordingly, divertor tile area and shaping have been maximised to reduce the power flux intensity and increase the heat load

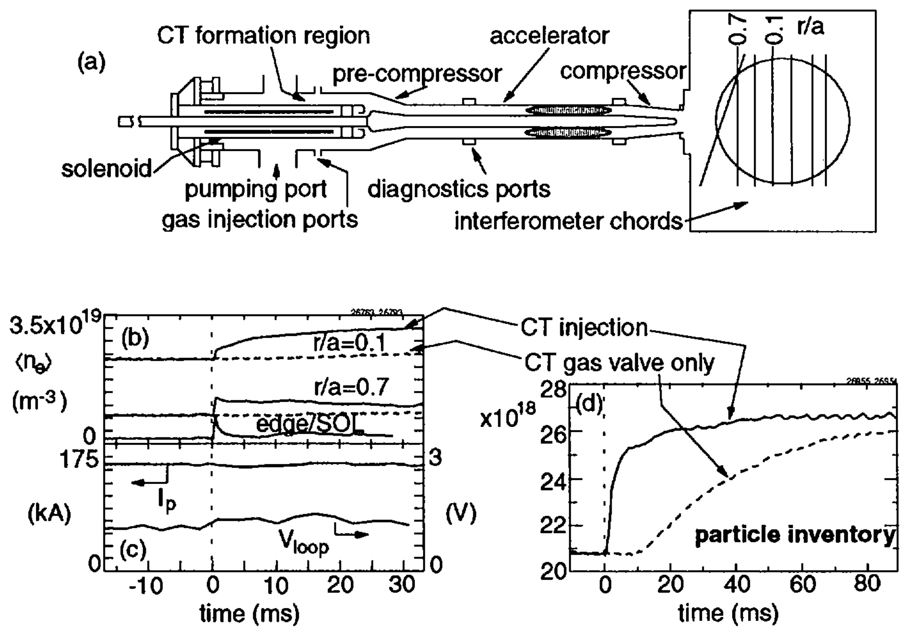

FIG. 8. CT injection on TdeV. (a) Schematic of the injector. (b, c) Penetration to the centre of the tokamak plasma at 1.4 T. The parasitic post-CT edge fuelling contribution from trailing gas after the CT is indicated by dashed lines and is clearly seen on the edge/SOL chord after 10 ms. (d) Particle inventory versus time comparing a CT injection to a single pulse fuelling from the CT gas valves only.

capability to 20 MJ each for the top and bottom divertors in anticipation of longer pulse experiments. The divertors are fully biasable with the plates electrically insulated and connected externally.

Figure 7 (a) shows a divertor geometry optimized for negative biasing [5], while Figs. 7 (b) and (d) compare geometries with an open and tight throat baffling respectively. Finally, Figs. 7 (c) and (d) compare geometries with pumping from the private region and the outboard location respectively. This latter comparison was simulated with B2/EIRENE to see the sensitivity of detachment and exhaust to the geometry. Detachment in the high power flow region is found to be similar for these two cases but the exhaust characteristics are different. The simulations indicate that the He flux incident on the horizontal pumping slot in the outer divertor is similar for both cases but that the deuterium flux is reduced by almost a factor of two for Fig. 7 (d). The He enrichment factor would then be higher by almost a factor of two for the private region pumping geometry. Detachment appears to favour He neutral transit toward the private region as it streams toward the divertor plate close to the separatrix. This effect will be examined in future experiments.

5. COMPACT TOROID INJECTION

Core fuelling would improve the burn efficiency and should lower the edge density [15] on a reactor compared to edge fuelling. Figure 8 demonstrates the viability of core fuelling with a single pulse compact toroid (CT) injector, a device that could centre fuel a reactor when using high repetition rate technologies. Impurity contamination, a problem that plagued earlier experiments [16], has now been reduced to a very low acceptable level through electrode conditioning.

Figure 8 (b) shows a fast increase of the central interferometer chord (r/a=0.1), indicating central penetration of the CT and gradual peaking of the density profile as time evolves. The penetration distance is determined by the balance between kinetic energy density of the CT and local magnetic energy density. The particle inventory is increased by 27% and the energy confinement by 38% after 30 ms. The fuelling efficiency (plasma mass increase divided by the CT mass) is 42% for this case compared to only 6% for CT gas valve fuelling providing the same particle inventory increase [Fig. 8 (d)]. The CT fuelling efficiency could be significantly increased by decreasing the ratio of the CT length to the tokamak minor radius, which is close to one in the present case. Parasitic post-CT edge fuelling from trailing gas will also have to be reduced for good density profile control with high repetition rate CT injection.

Simulations of CT injections for ITER parameters with the RLW transport model demonstrate the potential of reducing the edge density at constant fusion power by almost a factor of 2 compared with edge-fuelled cases provided that the CT penetrates to approximately mid-radius and that the parasitic gas load is of the order of or smaller than the CT inventory. Central fuelling with CT could therefore allow ITER to exceed the Greenwald density limit.

6. CONCLUSIONS

Detachment is characterized by a reduction of both the temperature and density in front of the divertor plate and a reduction of the ion flux at the plate as the density is increased. Radiation first cools the plasma at or just beyond the X-point and neutrals and/or ions transport laterally energy and momentum over a larger area inside the divertor. Partial detachment at moderate density ($\sim 5 \times 10^{19}$ m^{-3}) is sufficient for significant (4×) peak power reduction on the plates. Enhanced radiation near the X-point with impurity injection facilitates detachment at lower densities. Divertor exhaust is not impeded by detachment but the divertor He enrichment with respect to D_2 remains low at ~0.2, almost independent of the density and auxiliary heating level. Simulations indicate however that the enrichment is sensitive to the divertor geometry, a point that will soon be tested on the TdeV-96 upgrade. Finally, core fuelling with CT injection has been demonstrated without any adverse effect on the plasma, opening the possibility of better density profile control with lower edge densities and much improved fuelling efficiencies.

ACKNOWLEDGMENTS

The authors thank IPP-Garching, KfK Jülich, and B. Braams for the B2/EIRENE codes and D. Coster, A. Kukushkin, D. Reiter and R. Schneider for their help in its use.

REFERENCES

[1] DÉCOSTE, R., et al., in Plasma Physics and Controlled Nuclear Fusion Research 1994 (Proc. 15th Int. Conf. Seville, 1994), Vol. 1, IAEA, Vienna (1995) 593.
[2] DÉCOSTE, R., et al., in Controlled Fusion and Plasma Physics (Proc. 23rd Eur. Conf. Kiev, 1996), Vol. 20C, European Physical Society, Geneva (1996).
[3] STANSFIELD, B.L., et al., in Proc. 12th Int. Conf. on Plasma Surface Interactions in Controlled Fusion Devices, St. Raphael, France, 1996.
[4] GAUVREAU, J.-L., et al., paper presented at 3rd Int. Workshop on Helium Transport and Exhaust, Charleston, SC, 1995.
[5] DÉCOSTE, R., et al., Phys. Plasmas **1** (1994) 1497.
[6] BORRASS, K., JANESCHITZ, G., Nucl. Fusion **34** (1994) 1203.
[7] CÔTÉ, A., IAEA-CN-64/EP-5, these Proceedings, Vol. 3.
[8] FUJIMOTO, T., MIYACHI, S., SAWADA, K., Nucl. Fusion **28** (1988) 1255.
[9] SCHWEER, B., et al., J. Nucl. Mater. **196–198** (1992) 174.
[10] POST, D., HULSE, R., STOTLER, D., Contrib. Plasma Phys. **34** (1994) 300.
[11] KRASHENINNIKOV, S.I., et al., Rep. PFC/JA-95-37, Plasma Fusion Center, Massachusetts Inst. of Technology, Cambridge (1995).
[12] KALLENBACH, A., et al., Nucl. Fusion **35** (1995) 1231.
[13] REITER, D., WOLF, G.H., KEVER, H., Nucl. Fusion **30** (1990) 2141.
[14] STAEBLER, G.M., J. Nucl. Mater. **220–222** (1995) 158.
[15] POST, D., Report of the Fourth ITER Divertor Physics and Divertor Modelling and Database Expert Group Workshop, San Diego, CA, 1996.
[16] RAMAN, R., et al., Phys. Rev. Lett. **73** (1994) 3101.

DISCUSSION

Y. SHIMOMURA: Do you have any data on the impurity level of the CT?

R. DÉCOSTE: Tungsten impurities that could have been produced from erosion of the central electrode of the CT could not be detected in the plasma and are therefore at a very low level. Low Z impurities are the main contaminant and they should be reduced in the new gun with better electrode conditioning.

R.D. STAMBAUGH: You apparently had neon enrichment as high as 3. Could you discuss how this was measured (defined) and obtained.

R. DÉCOSTE: Neon enrichment, as with helium, is the neon divertor concentration normalized to the deuterium concentration. Dynamic (τ_p^*) and static (partial pressure) measurements give similar neon enrichments, which are typically above 1. Nitrogen enrichment is even higher.

PROGRESS TOWARDS ENHANCED CONFINEMENT, LONG DURATION DISCHARGES ON TORE SUPRA

EQUIPE TORE SUPRA*
(Presented by B. Saoutic)
Association Euratom-CEA,
Saint-Paul-lez-Durance,
France

Abstract

PROGRESS TOWARDS ENHANCED CONFINEMENT, LONG DURATION DISCHARGES ON TORE SUPRA.

Recent Tore Supra results supporting the feasibility of high-confinement, long duration discharges are reported. Two-minute discharges with improved confinement have been obtained. This progress is largely due to improvements in the operating control system of Tore Supra, which now allows real-time feedback control of global plasma parameters. A clear correlation between improved confinement and current profile shape has been established. Transport barriers for electron heat diffusion are observed in experiments where the magnetic shear is weak or negative in the central part of the plasma. These observations strongly support development of new current drive schemes for current profile control. Considerable progress concerning particle and heat exhaust has also been achieved. A new technique allowing conditioning in the presence of a toroidal magnetic field has been implemented. A vented limiter has been tested as a means of particle exhaust through collection of neutrals, and its performance is compared with that of a "classical", ion collecting throat limiter. The knowledge gained from extensive long pulse experimentation has been used to develop a new generation of plasma facing components, which will permit further development of the long discharge capablity of Tore Supra.

1. Introduction

Producing high confinement, long-duration discharges remains one of the most challenging issues for magnetic fusion research. This is illustrated by Fig. 1 which shows plasma performance (through the usual criterion $n\,\tau\,T_i$) versus pulse duration, and where the present results stand with respect to ITER objectives. Fulfilling this goal requires developing heating and current drive scenarios as well as solving particle and heat flux problems in steady state. Such investigations are particularly appropriate for thc superconducting tokamak Tore Supra (major radius R= 2.2–2.4 m, minor radius a < 0.8 m, toroidal field on axis $B_t < 4.2$ T, plasma current $I_p < 2$ MA) research program which is aimed at the study of long, high-performance pulses.

This paper summarises recent results, obtained on Tore Supra (TS), which pave the way towards the realisation of enhanced confinement, long duration discharges. The next section reports on new long-duration discharges obtained during the 1995-96 experimental campaign. Enhanced confinement and transport issues are then discussed in section 3. Section 4 deals with the non inductive current drive scenarios, with particular emphasis on current-profile control. New tools, which have been developed to control the particle inventory of the wall and

* See Appendix.

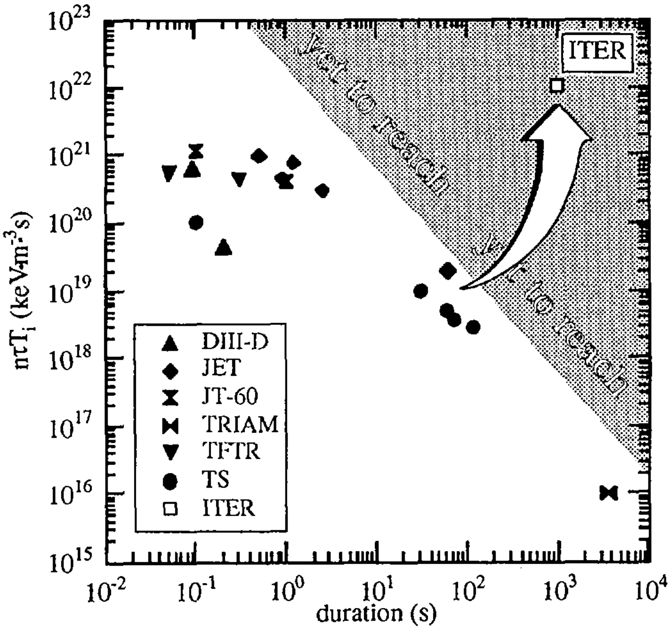

FIG. 1. Plasma performance versus pulse duration.

of the plasma, are presented in section 5. Finally, section 6 describes the heat exhaust capability of the various actively plasma facing components which have been tested on TS and which are presently being further developed in view of expanding the TS tokamak performances.

2. Progress in long-pulse operation

The 1995-96 experimental campaign greatly increased the long-discharge data base of TS [1]. This is illustrated (solid symbols) by Fig. 2, which displays the total radio frequency (RF) energy injected in the tokamak versus the RF power. Most of these discharges have been obtained using lower hybrid current drive (LHCD), at power level up to 3.5 MW, and with the plasma limited on the actively cooled inner wall. Among these new discharges, three classes deserve a particular attention:

- discharges at nominal current (I_p = 1.7 MA, surface loop voltage V_{loop} = 0.25 V) which lasted up to 32 seconds,
- fully non-inductive discharges (V_{loop} = 0 V) at a current of 0.62 MA, with improved confinement, which lasted up to 75 seconds,
- discharges at a current of 0.8 MA (V_{loop} = 0.1 V) with improved confinement, which lasted up to 2 minutes.

2.1 Plasma feedback control

The progress in maintaining long-duration discharges is largely due to the improvement of the plasma control capability of TS. This has been achieved by an upgrade of the operating control system which now allows real-time feedback control of global plasma parameters (plasma current, edge safety factor, plasma surface flux...) through the poloidal and LH heating systems. This system has already made possible scenarios where the edge safety factor is kept constant during the whole shot, thus allowing higher current ramp-up rates[2]. A striking example of its use, for long pulse operation, is given in the 75-second duration, fully non-inductive discharge (see Fig. 3): in the initial ohmic phase, the plasma current is ramped up to a plateau of 1 MA; at 5 s, the feedback control on the plasma surface flux is switched on, leading to constant flux operation; subsequently the loop voltage drops to zero and the plasma current decreases. Later on, at 5.7 s, feedback is applied to the plasma current, using LHCD power instead of the usual ohmic power; the plasma current then quickly stabilises and is maintained close to the reference value (0.65 MA) for 70 seconds.

This control capability not only results in substantial progress toward steady-state operation, but also provides a reliable practical means for studying many other aspects of continuous tokamak operation. For example, preliminary experiments have shown that it was possible to control the internal inductance of the plasma, using LHCD launcher phase as feedback [3], thus preparing the way to real-time control of the current profile.

2.2 Two-minute long shot

Figure 4 displays a two minute long shot during which a total energy of 280 MJ has been injected to the plasma, thus establishing a new world record. During the first minute of the discharge, the electron density remains constant, but then begins to increase slowly. Moreover, the effective charge (Z_{eff}) increases from

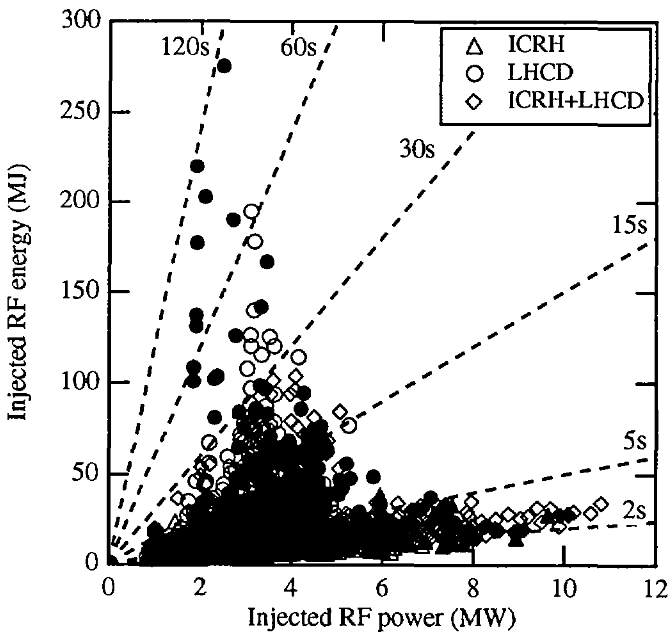

FIG. 2. Injected RF energy versus RF power for ion cyclotron resonant heating (ICRH) alone (△), lower hybrid current drive alone (○) and combined operations (◇). The ICRH points comprise data from both minority and fast-wave electron heating experiments. Open and solid symbols correspond, respectively, to data before and during the 1995–96 campaign.

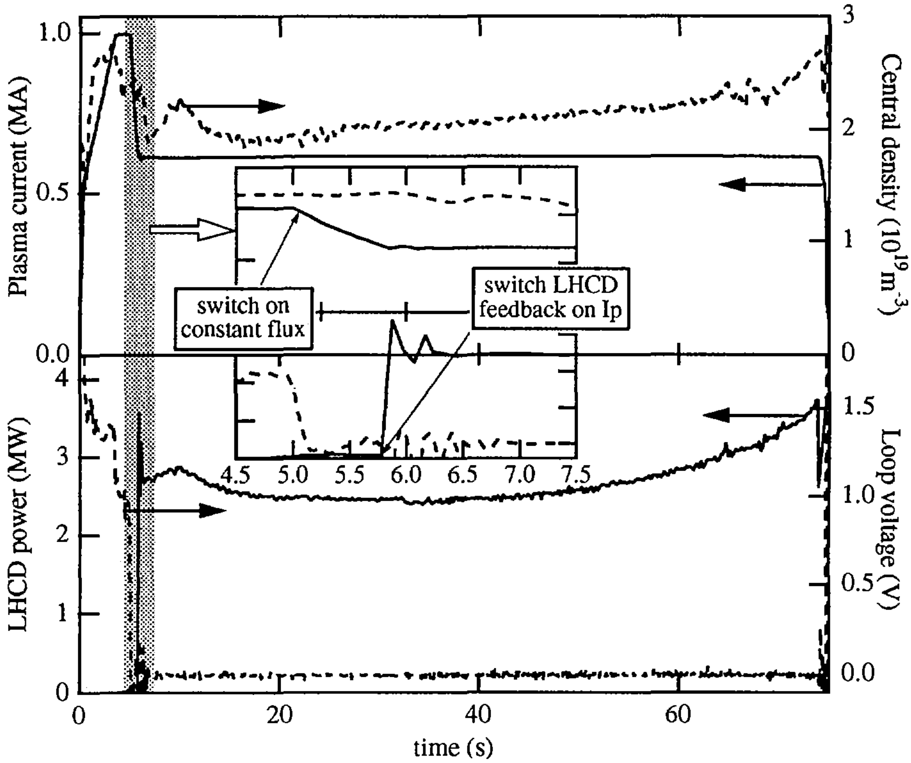

FIG. 3. Plasma current, central electron density, LHCD power and loop voltage versus time during the 75 s duration, fully non-inductive discharge.

a value of 2 during the first minute to a value of 2.2 at the end of the discharge. This Z_{eff} increase is due to increased oxygen and silver contents. Their densities increase continuously during the second part of the discharge (from 0.4 10^{17} to 1.2 10^{17}m^{-3} for O, from 0.1 10^{15} to 2.0 10^{15} m^{-3} for Ag). During the same period, the density of carbon remains constant around 3 10^{17}m^{-3}, and the global density of heavy impurities (Ti, Cr, Fe, Ni and Cu) does not exceed 0.4 10^{15}m^{-3}. Thus, the electron density increase due to impurities is less than 15% of the total electron density rise, which is thus dominated by helium and hydrogenic species. The most probable explanation for the density rise is the presence of some internal components which are not yet actively cooled (outboard pump limiter, some parts of the vacuum chamber....): their temperature continuously rises throughout the discharge, and, eventually, parts which cannot be conditioned (except by long pulse operation) begin to outgas. This underlines the importance of active cooling for all plasma facing components and an effective steady-state particle exhaust scheme.

This two minute discharge exhibits another remarkable feature: during its entire duration, the plasma displays the characteristics of the lower hybrid enhanced performance (LP) regime [4,5]. The safety factor profile flattens at the centre, and the magnetic shear increases in the outer part of the plasma. At 55 seconds, the usual transition to a hot core LHEP is observed (the central temperature rises from 6 to 8 keV). The electron total thermal content exceeds the

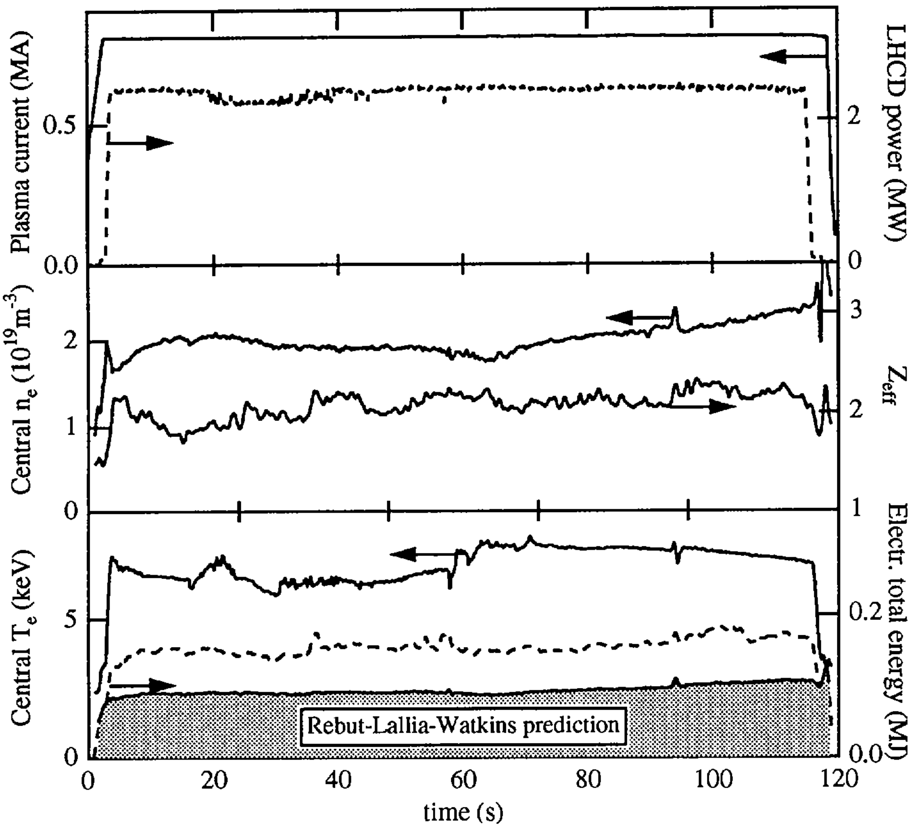

FIG. 4. Plasma current, LHCD power, central electron density, effective charge, central electron temperature and electron total energy versus time during the 120 s long discharge.

Rebut-Lallia-Watkins (RLW) scaling predictions by a factor of 1.6 throughout the entire discharge. Such a discharge clearly demonstrates that improved confinements due to current profile shaping can be extrapolated to continuous tokamak operation.

3. Enhanced confinement and transport issues

In order to assess the enhanced confinement regimes observed on TS, a new scaling law for the total thermal energy confinement time has been derived from TS L-mode data base:

$$\tau_{Eth} = 0.0199\ R^{2.0}\ I_p^{0.98}\ B_t^{0.2}\ n_{bar}^{0.43}\ P_{tot}^{-0.75}$$

where τ_{Eth}, R, I_p, B_t, n_{bar} (line averaged density), P_{tot} (total injected power) are respectively expressed in units of s, m, MA, T, $10^{19}m^{-3}$, MW. This scaling exhibits no (or very weak) mass dependence, a strong density dependence and a P_{tot} dependence less favourable than the inverse square root. A similar scaling for the total thermal energy confinement time has been seen on JT60-U[6]. This law has

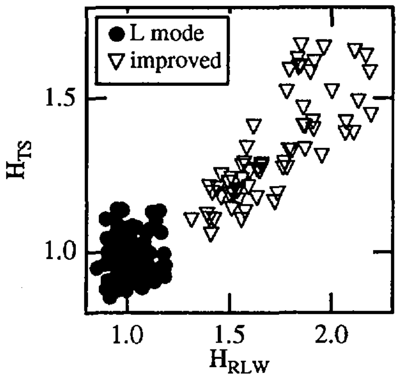

FIG. 5. H_{TS} versus H_{RLW} for L-mode (●) and improved confinement (∇) regimes.

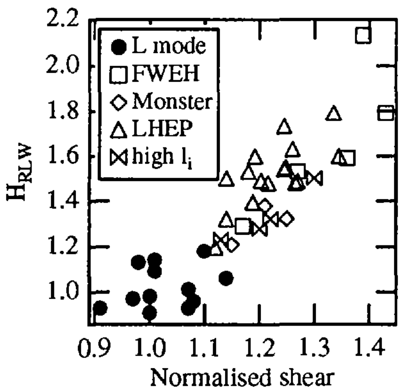

FIG. 6. H_{RLW} versus normalised shear at mid radius for several regimes: L-mode (●), FWEH (□), monster sawtooth (◇), LP (△) and high-l_i (⋈).

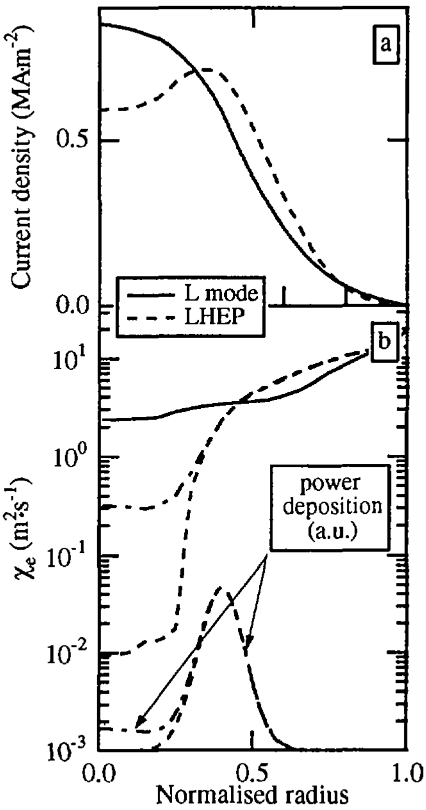

FIG. 7. Current density (a) and χ_e (b) profiles for L-mode (plain line) and LP (dashed lines) regimes. The dashed and dot-dashed lines correspond to two different LHCD power deposition profiles.

the characteristics of a gyro-Bohm scaling, probably because the heating schemes used on TS heat mainly the electrons. In the enhanced confinement regime, the total energy content can exceed the prediction of this scaling up to a factor H_{TS} of 1.7. In correlation with the increase of H_{TS}, the electron energy content also exceeds the RLW scaling, by up to a factor H_{RLW} of 2.2 (see Fig. 5).

A clear correlation between enhanced confinement and increased magnetic shear at mid-radius has been established. This is illustrated in Fig. 6, where the enhancement factor is plotted versus the normalised shear (ratio of the value of the magnetic shear during the heating phase to its value during the ohmic phase), for L-mode and four improved confinement regimes: fast wave direct electron heating (FWEH), monster sawtooth, LHEP and high-l_i regimes. This correlation is confirmed by fluctuation measurements. For the L-mode regime, the density and magnetic fluctuation level strongly increase with the electron temperature gradient, with evidence of a critical gradient threshold. For high magnetic shear regimes, there is almost no dependence of the density fluctuation level on the temperature gradient [7].

During LHEP regime operation, transport barriers have also been observed. These imply electron thermal conductivity coefficients of the order of neo-classical values in the plasma core, where the magnetic shear is weak or even negative. Figure 7 shows the electron heat diffusion coefficient χ_e for two LHCD power deposition profiles. The most realistic deposition profile (dashed lines) corresponds to a ray-tracing/Fokker-Planck calculation using a hot electron diffusion coefficient determined by simulating the hard X-ray diagnostic measurement. The second deposition profile corresponds to the maximum central power deposition still compatible with the hard X-ray measurements within the error bars.

4. Non inductive current drive scenarios

As shown in §2, discharges in the LHEP regime can last as long as two minutes. However, in some discharges, a transition occurs during the early phase of the LHEP regime, when the current profile is still evolving. Following this, the plasma returns to an L-mode regime characterised by a strong, sawtooth-like n=1, m=2 MHD activity [8]. This clearly indicates the importance of current profile

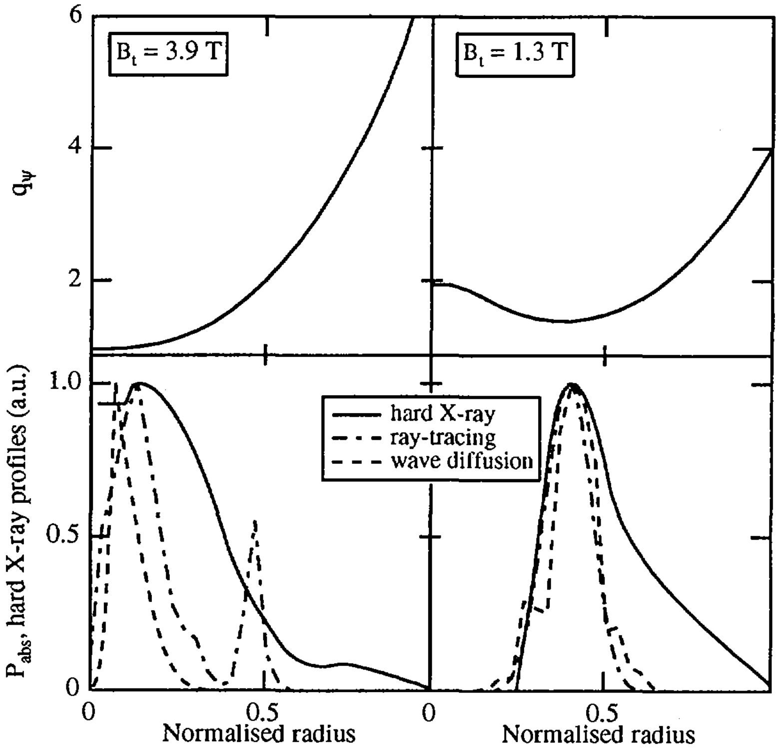

FIG. 8. Safety factor (top row), hard X-ray and LHCD power deposition (bottom row) profiles versus normalised radius for high (left column) and low (right column) B_t.

tailoring and control for obtaining stable, steady-state discharges with enhanced confinement. Thus, new current drive schemes allowing on and off-axis current control must be developed.

A new scenario has been developed to ensure efficient mode conversion (MC) heating with low field side antennas [9]. Rather than maximising the first pass damping, this scheme avoids competitive damping, as is done for FWEH. Consequently, it is much less sensitive to the plasma ion species mix than other MC scenarios. Experiments at the 2.5 MW power level demonstrate that this scheme can be as efficient as minority ion cyclotron heating. It makes it possible to test, in the future, MC current drive and ion Bernstein wave / LHCD synergism, two scenarios which offer the possibility to localise the current drive where desired.

The use of fast wave current drive to control the plasma current at the centre of the plasma has already been demonstrated [10]. The operation range of fast wave direct electron heating has been extended, on TS, up to 9.5 MW of coupled power and up to a magnetic field of 4 T. Discharges have been obtained with bootstrap current fractions as high as 70% during transient and 40% in steady-state conditions (5 second duration). Various bootstrap calculation models have been tested on these shots. The best agreement with the experimental data is obtained for models solving the flux-surface averaged parallel momentum and heat-flow balance for each plasma species [11]. It is important to note that approximate formulas are not valid over the whole range of FWEH operation.

In order to achieve off-axis LHCD, experiments have been conducted at lower toroidal field, where the wave does not access the plasma centre. These shots are dimensionally similar to higher field and density shots but allow the attainment of zero loop voltage at lower LHCD power. Clear evidence of off-axis current drive has been observed on the hard X-ray diagnostic (hot electron localisation) as well as on the current profile (from polarimetry measurements). This result is reproduced well by numerical simulations using both ray-tracing and wave diffusion/Fokker-Planck codes (see Fig. 8).

5. Particle control

5.1 Control of wall particle inventory

The density rise at the end of the two-minute shot demonstrates that particle exhaust capability is a vital requirement for long pulse operation. The inner wall which is presently the main heat exhaust device of TS does not have particle exhaust capability beyond that of wall pumping. For this reason, long-pulse operation on TS relies on intensive boronization and helium glow discharge cleaning. However, because of the super-conducting coils of TS, the toroidal magnetic field is continuously present during operation, making glow discharge cleaning impossible between discharges: the wall pumping capacity then decreases continuously from shot to shot, eventually leading to a completely saturated wall and to systematic disruptions.

The evolving deuterium content of the wall is monitored using an original technique relying on the pre-magnetization plasma parameters [12]. At the start of the pre-magnetization phase, which occurs 1.8 s prior to the main plasma breakdown, a small deuterium gas puff causes breakdown of a plasma. This pre-magnetization plasma can be stable if the plasma poloidal field compensates the destabilising vertical field. However, the rise time of this poloidal field (τ_B) is of the order of 60 ms. For unsaturated conditions, the effective particle life time ($\tau_p{}^*$) is much shorter than τ_B, because of the high pumping rate of the wall, and the plasma rapidly collapses. In contrast, for saturated conditions, $\tau_p{}^*$ is longer than τ_B, and the plasma lifetime is four to five times longer than in the unsaturated case. The duration of the pre-magnetization plasma gives then a direct measurement of the degree of wall saturation, before the main discharge begins. This will be used, in real time, to adjust the plasma prefill pressure and/or the plasma break-down voltage, in order to insure a successful start-up of the discharge, regardless of wall saturation. This will also indicate when conditioning becomes necessary.

The continuous evolution of the wall saturation has a major drawback: it makes it difficult to obtain reproducible and optimised operation conditions. To cope with this problem (that ITER will also encounter), a new conditioning technique has been developed [13]. It uses the ion cyclotron resonant heating (ICRH) system to produce low density plasma (ICRH power 30-350 kW, averaged line density 1-6 $10^{18}m^{-3}$, electron temperature 1.5-10 eV, helium fill gas). The B_t value is set at 3.8 T so that the fundamental cyclotron layer of hydrogen and the second harmonic layer of deuterium lie inside the vacuum chamber. This technique results in a hydrogen removal rate of about 50 $Pa.m^3h^{-1}$ on average, with a maximum value of 260 $Pa.m^3h^{-1}$ at the start of conditioning. These rates are one order of magnitude higher than those obtained in the usual helium glow discharges, and would allow the recovery, within ten minutes of ICRH conditioning, of the total quantity of gas injected during a discharge (typically 10 $Pa.m^3$ in TS). This higher cleaning efficiency is attributed to the presence of energetic particles created by ICRH (up to 50 keV observed on the neutral particle analysers): these particles can penetrate deeper in the carbon layers of the wall. Such a technique is very promising for conditioning of deep saturated layers and for tritium removal by isotope substitution; these two subjects are of great interest for ITER.

5.2 Plasma particle exhaust

Particle control is mandatory for long pulse operation, and an extensive program of design and testing of particle exhaust structures is being pursued on Tore Supra. Two methods exist to pump particles in a tokamak plasma (either limited or diverted): throat structures which pump the parallel ion flux, and vented structures which pump the neutral recycled flux.

In throat structures, high exhaust efficiency entails high ion flux in the throat and, consequently, high thermal loads on the leading edge. In contrast, in vented structures, the cascade of reactions experienced by the recycled particles (dissociation, ionisation, charge exchange...) yields a nearly isotropic neutral distribution, and half of the recycled flux returns to the wall. In a structure which is semi-transparent to neutrals, a significant fraction of the back-flowing flux enters the limiter plenum and can be pumped. The vented system thus pumps without requiring high heat fluxes on the leading edge of the limiter itself. Vented structures are also well adapted to either axisymmetric or ergodic divertor configurations. Even for highly radiating, detached plasmas, vented structures retain some exhaust capability because there is always a neutral flux flowing to the wall [14].

Experiments on TS have compared the performance of a "classical" throat pump limiter (TPL, Fig. 9.a) and a prototype vented pump limiter (VPL, Fig. 9b) for deuterium and helium discharges. As expected, the surface temperature distribution is nearly uniform in the case of the VPL, while the TPL exhibits the usual overheating of the leading edge. This is illustrated in Fig. 10, which shows, for both TPL and VPL, the ratio of the maximum temperature to the surface averaged temperature during two similar shots. In both cases, the neutral pressure in the limiter plenum increases as the square of the plasma density and approximately as the cube root of the total power injected into the plasma (see Fig. 11). Nevertheless, this pressure is lower for the VPL, leading, for deuterium plasmas, to a particle exhaust efficiency (ratio of the extracted flux to the net outflux of the plasma) 3.5 time lower for the VPL (6-10%) than for the TPL (20-

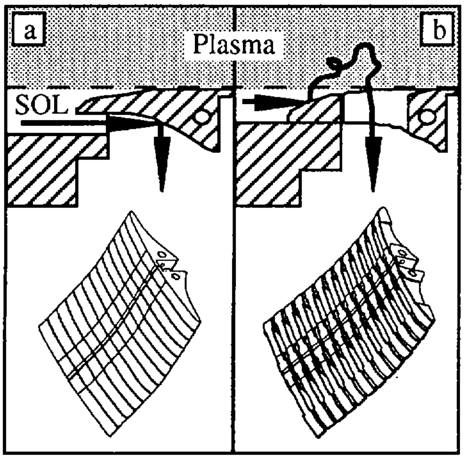

FIG. 9. Schematics of throat (a) and vented (b) pump limiters.

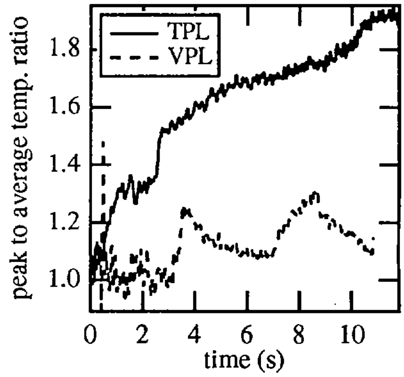

FIG. 10. Ratio of maximum limiter temperature to surface-averaged temperature during two similar shots. Solid and dashed lines correspond to throat and vented pump limiter, respectively.

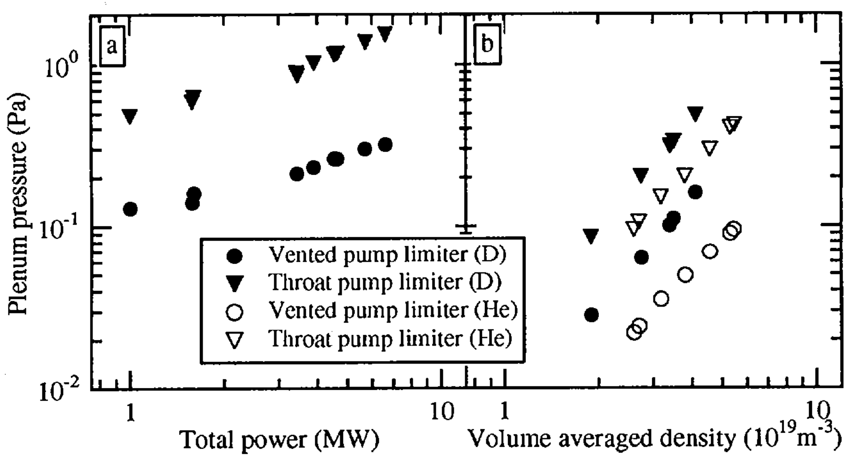

FIG. 11. Pressure in the pump limiter plenum versus total power injected to the plasma (a), and versus volume averaged density (b) for throat (▽) and vented (○) pump limiters. Solid and open symbols correspond to deuterium and helium plasmas, respectively.

35%) [15]. Even so, the VPL exhaust efficiency is already high enough to allow plasma density control, and it can be increased by a factor of 2 by optimising the shape of the VPL slots.

6. Actively cooled plasma facing components

The most stringent limitation on the long-pulse performance of Tore Supra remains the heat exhaust capacity of the plasma facing components. This is illustrated in Fig. 2, which shows that the limit in injected energy decreases with increasing injected power, and hence with increasing heat flux. The development, manufacture, and test of full-size, actively-cooled components, are thus major physical and technological challenges for the TS program.

The actively cooled inner wall of TS, which was designed in 1985, is composed of modular elements made of 10 mm thick polycrystalline graphite tiles, brazed on stainless steel. It can withstand a peaked heat flux of 0.3-0.4 $MW m^{-2}$. for one minute. In these experiments, the active cooling keeps the average temperature of the wall low (≅ 300 °C), thus avoiding deleterious phenomena such as carbon blooms. However, localized overheating in regions of braze flaws and tile cracks does occur. Infrared camera measurements show that these defects can expand and degrade the heat exhaust capacity of the damaged tiles; this can lead to detachment of tile fragments and plasma disruption. Such phenomena are the most probable explanation for the observed power exhaust limitations: higher injected power corresponds to higher thermal flux which induces higher temperature gradients and stresses around defects in the tiles.

These observations suggest that, to improve heat exhaust capability, the number of flaws must be reduced and their effects minimised. These goals have guided the design of new inner wall elements. for Tore Supra. To reduce the effects of the flaws, polycrystalline graphite has been replaced by CFC, which exhibits better crack arrest properties and higher thermal conduction. Prior to the brazing to the stainless steel tubes, the CFC tiles are laser treated[1], a process which enhances the adherence of the braze joint. To minimise the number of flaws, rigorous quality control of the components has been implemented, from the beginning of their fabrication until their installation in TS [16]. Fracture shear stress and destructive metallographic tests on reference pieces are systematically done for each braze cycle. Each tile attachment is checked by X-ray radiography and thermography. Before the 1995-96 experimental campaign, two modules of this new inner wall (40° toroidal sector) were installed in TS. They have successfully withstood the long-duration discharge experiments without displaying any hot spots. However, they have been only tested up to the power handling limits of the original inner wall modules, which are still in place. To test further these new modules during the next experimental campaign, they will be advanced 2 mm in front of the other modules in major radial position.

In addition to development of plasma-facing components designed to withstand moderate heat fluxes (≤ 1 MWm^{-2}), a substantial effort is also devoted to the realisation of higher performance components, with heat removal capability in the multi-MWm^{-2} range. The first generation of high heat flux components was composed of modular bottom pump limiters made of 3 mm thick polycrystalline graphite tiles brazed on CuCrZr tubes. Powers up to 0.7 MW have been exhausted, in thermal equilibrium situations a single limiter. This corresponds to an average heat flux of 4 $MW{\cdot}m^{-2}$, with the leading edge withstanding a peak flux of 8 $MW{\cdot}m^{-2}$. Using three of these limiters together, it has been possible to obtain a 45-second discharge sustained by 2.5 MW of injected power.

A new generation of high heat flux components is presently being designed. They take full advantage of the considerable technological progress which has been made. A full scale prototype "finger" element has been constructed. It is trapezoidal in shape and 0.5 m long. It is based on CFC tiles bonded to CuCrZr tube by active metal casting[1]. Tested in the electron beam facility, it has successfully exhausted a uniform heat flux of 14.7 $MW{\cdot}m^{-2}$ for 1000 thermal cycles without any damage. Such components could satisfy the thermal constraints for the ITER divertor baffles. They will be used in the near future to build a toroidal pump limiter for Tore Supra. This limiter will be composed of 576 fingers

[1] Process developed by Metallwerk-Plansee, Reutte, Austria.

assembled on a rigid structure. It is designed to remove 15 MW of convective power and will permit further extension of the performance of Tore Supra.

7. Conclusion

The Tore Supra discharges which maintain enhanced confinement for up to two minutes demonstrate that these regimes can be extrapolated to continuous tokamak operation. A clear correlation between improved confinement and current profile shaping is seen. Further progress will require active tailoring of the current profile and effective continuous exhaust of particles and heat. The first steps have already been taken by developing new plasma control systems, effective heating and current drive schemes (mode conversion, fast wave current drive, off-axis LHCD, high bootstrap fraction), new particle pumping concepts (vented structures) and second-generation, actively-cooled plasma facing components (new inner wall elements, prototype finger element for the toroidal pump limiter).

In parallel, a vigorous effort is underway to explore alternative heat removal concepts. In particular, an upgraded ergodic divertor and associated diagnostic set are now being installed in Tore Supra. These will be used to test the viability of the radiative layer concept for long pulse operation over the next two years.

Because of its super-conducting toroidal field system, Tore Supra offers a unique opportunity to integrate many of the constraints relevant to a steady-state fusion device and to explore the associated physics. Its recent results provide a firm basis for this extensive and challenging programme.

REFERENCES

[1] VAN HOUTTE, D., EQUIPE TORE SUPRA, Nucl. Fusion **33** (1993) 137.

[2] EQUIPE TORE SUPRA, paper presented at Symp. Fusion Engineering, Champaign, 1995.

[3] WIJNANDS, T., MARTIN, G., to be published in Nucl. Fusion.

[4] MOREAU, D., et al., in Plasma Physics and Controlled Nuclear Fusion Research 1992 (Proc. 14th Int. Conf. Würzburg, 1992), Vol. 1, IAEA, Vienna (1993) 649.

[5] HOANG, G.T., et al., Nucl. Fusion **34** (1994) 75.

[6] SHIRAI, H., et al., in Plasma Physics and Controlled Nuclear Fusion Research 1994 (Proc. 15th Int. Conf. Seville, 1994), Vol. 1, IAEA, Vienna (1995) 355.

[7] LAVIRON, C., et al., IAEA-CN-64/A6-3 this volume.

[8] EQUIPE TORE SUPRA, in Controlled Fusion and Plasma Physics (Proc. 23rd Eur. Conf. Kiev, 1996), European Physical Society, Geneva (1996); invited paper to be published in Plasma Phys. Control. Fusion.

[9] SAOUTIC, B., et al., Phys. Rev. Lett. **76** (1996) 1647.

[10] FOREST, C.B., et al., Phys. Plasmas **3** (1996) 2846.

[11] KESSEL, C.E., Nucl. Fusion **34** (1994) 1221.

[12] GRISOLIA, C., et al., in Plasma-Surface Interactions (Proc. 12th Conf. Saint-Raphael, 1996), J. Nucl. Mater. (in press).

[13] GAUTHIER, E., et al., ibid.

[14] LOARER, T., et al., Plasma Phys. Control. Fusion **37** (1995) A203.

[15] PEGOURIE, B., et al., in Plasma-Surface Interactions (Proc. 12th Conf. Saint-Raphael, 1996), J. Nucl. Mater. (in press).

[16] EQUIPE TORE SUPRA, ibid.

APPENDIX

G. Agarici, J.P. Allibert, J.M. Ané, R. Arslanbekov, J.F. Artaud, S. Balme, V. Basiuk, P. Bayetti, L. Baylor[1], B. Beaumont, A. Bécoulet, M. Benkadda[2], G. Berger-By, S. Bério, P. Bibet, J.P. Bizarro[3], S. Boeddeker, G. Bon-Mardion, J.M. Bottereau, F. Bottiglioni, S. Brémond, R. Brugnetti, R.V. Budny[4], Y. Buravand, H. Capes, J.J. Capitain, J.L. Carbonnier, J. Carrasco, P. Chappuis, E. Chatelier, M. Chatelier, J.H. Chatenet[5], F. Cherigier, D. Ciazynski, F. Clairet, L. Colas, J.J. Cordier, A. Côté[6], B. Couturier, J.P. Crenn, P. Cristofani, C. Deck, P. Decool, B. DeGentile, E. De la Cal, H. Demarthe, C. De Michelis, P. Deschamps, C. Desgranges, P. Devynck, L. Doceul, C. Doloc, M. Dougnac, M. Druetta[7], M. Dubois, J.L. Duchâteau, L. Dupas, D. Edery, D. Elbèze, D. Escande, J.L. Farjon, J.R. Ferron[8], M. Fois, C. Forrest[8], D. Fraboulet, V. Fuchs[6], M. Fumelli, B. Gagey, L. Garampon, X. Garbet, E. Gauthier, A. Géraud, F. Gervais[10], P. Ghendrih, C. Gil, G. Giruzzi, M. Goniche, R. Gravier, B. Gravil, M. Grégoire, D. Grésillon[10], C. Grisolia, A. Grosman, D. Guilhem, B. Guillerminet, R. Guirlet, L. Guiziou, J. Harris[1], P. Hennequin[10], F. Hennion, P. Hertout, W.R. Hess, M. Hesse, G.T. Hoang, J. Hogan[1], W.A. Houlberg[1], T. Hutter, C. Jacquot, B. Jager, E. Joffrin, J. Johner, J.Y. Journeaux, P. Joyer, C. Klepper[1], F. Kazarian, H. Kuus, L. Ladurelle, D. Lafon, P. Laporte, J. Lasalle, L. Laurent, C. Laviron, G. Leclert[11], A. Ledyankine, P. Libeyre, M. Lipa, X. Litaudon, T. Loarer, P. Lotte, J.F. Luciani[5], T. Lutz[13], P. Magaud, W. Mandl, G. Martin, A. Martinez, E.K. Maschke, R. Masset, M. Mattioli, G. Mayaux, B. Meslin, Y. Michelot, P. Mioduszewski[1], J. Misguich, R. Mitteau, P. Mollard, P. Monier-Garbet, D. Moreau, F. Moreau, P. Moreau, J.P. Morera, B. Moulin, D. Moulin, M. Moustier, R. Nakach, F. Nguyen, R. Nygren[13], P. Ouvrier-Buffet, L. Owen[1], M. Pain, J. Pamela, F. Parlange, G. Pastor, R. Patris, M. Paume, A.L. Pecquet, B. Pégourié, Y. Peysson, D. Piat, P. Platz, C. Portafaix, M. Prou, A. Quéméneur[10], G. Rey, B. Rothan, R. Ruggieri, S.A. Sabbagh[16], R. Sabot, F. Samaille, B. Saoutic, Y. Sarazin, E. Sebelin, J. Schlosser, J.L. Segui, K. Soler, P.G. Sonato[17], M. Spuig, Y. Stephan[18], J.M. Theis, M. Tokar[19], G. Tonon, A. Torossian, A. Truc[10], E. Tsitrone, B. Turck, S. Turlur, J.C. Vallet, D. Van Houtte, A. Verga[2], H. Viallet, I. Voitsekovitch, J. Weisse, R. White[4], T. Wijnands, M. Zabiego, X.L. Zou.

[1] Oak Ridge National Laboratory, Oak Ridge, Tennessee, USA.
[2] Equipe Turbulence Plasma, Institut Méditerranéen de Technologie, Marseille, France.
[3] Instituto superior técnico, Association EUR-IST, Lisbon, Portugal.
[4] Plasma Physics Laboratory, Princeton University, Princeton, New Jersey, USA.
[5] Centre de physique théorique, Ecole polytechnique, Palaiseau, France.
[6] Centre Canadien de fusion magnétique, Varennes, Quebec, Canada.
[7] Laboratoire de traitement du signal et d'instrumentation, CNRS, St Etienne, France.
[8] General Atomics, San Diego, California, USA.
[9] C.R.E. Association Euratom-ENEA, Frascati, Italy.
[10] Physique des milieux ionisés, Ecole polytechnique, Palaiseau, France.
[11] L.P.M.I., Université de Nancy I, Vandœuvre les Nancy, France.
[12] Institute of Plasma Physics, Hefei, China.
[13] Sandia National Laboratories, Albuquerque, New Mexico, USA.
[14] Université Paris XI, Orsay, France.
[15] Max-Planck-Institut für Plasmaphysik, Association Euratom-IPP, Garching, Germany.
[16] Department of Applied Physics, Columbia University, New York, N.Y., USA.
[17] C.S. Gas Ionizzati, Association Euratom-ENE-CNR, Padova, Italy.
[18] CISI Ingénierie, Centre d'études de Cadarache, Saint-Paul-lez-Durance, France.
[19] Association Euratom-KFA Jülich, Germany.

DISCUSSION

Y. KAMADA: What is the β_N value in your 2 min discharge?

B. SAOUTIC: The β_N value for the 2 min discharge is 0.25. This low value is due to the fact that the main limitation for long discharge operation is heat exhaust. Consequently the LHCD power is at present limited to less than 3 MW for such discharges. For short pulses, a β_N value of 1.7 has been attained. It is intended to overcome this limitation by using a toroidal pump limiter, with the capacity to extract 15 MW of convected power.

Y. KAMADA: Have you observed a decrease in lifetime with increasing β?

B. SAOUTIC: No. In fact, the H factor increases linearly with β.

K. IDA: The q profile in the discharge with LHCD shows negative magnetic shear. Did you observe an improvement in energy confinement and $\mathbf{E} \times \mathbf{B}$ velocity shear associated with negative magnetic shear in Tore Supra?

B. SAOUTIC: We do observe a transport barrier in the area where the magnetic shear flattens or becomes negative. In such a regime we do not observe a change in toroidal rotation, but we have not yet diagnosed the plasma to draw any conclusion on $\mathbf{E} \times \mathbf{B}$ velocity shear.

B. COPPI: What is the range of density variation that you can obtain?

B. SAOUTIC: The range of density variation that we can obtain during long pulse operation is 2×10^{19} m^{-3} < n_{e0} < 3×10^{19} m^{-3}.

B. COPPI: How does the nature of the plasma–wall interaction change with density?

B. SAOUTIC: Producing a long pulse at a higher density would require injecting LHCD at a power level in excess of the heat exhaust capability. Hence we have not been able to study the change in plasma–wall interaction with density variation.

HIGH-FIELD COMPACT DIVERTOR TOKAMAK RESEARCH ON ALCATOR C-MOD*

I.H. HUTCHINSON, R.L. BOIVIN, F. BOMBARDA[1], P.T. BONOLI,
C. CHRISTENSEN, C.L. FIORE, D.T. GARNIER, J.A. GOETZ,
S.N. GOLOVATO[2], R.S. GRANETZ, M.J. GREENWALD, S.F. HORNE[3],
A.E. HUBBARD, J.H. IRBY, D. JABLONSKI[4], B. LaBOMBARD,
B. LIPSCHULTZ, E.S. MARMAR, M. MAY[5], A. MAZURENKO,
G.M. McCRACKEN[6], R. NACHTRIEB, A. NIEMCZEWSKI[7], H. OHKAWA,
P.J. O'SHEA, D. PAPPAS, M. PORKOLAB, J. REARDON, J.E. RICE,
J.C. ROST, J.M. SCHACHTER, J.A. SNIPES, P.C. STEK, Y. TAKASE,
J.L. TERRY, Y. WANG, R.L. WATTERSON[8], B. WELCH[9], S.M. WOLFE
Plasma Fusion Center,
Massachusetts Institute of Technology,
Cambridge, Massachusetts,
United States of America

Abstract

HIGH-FIELD COMPACT DIVERTOR TOKAMAK RESEARCH ON ALCATOR C-MOD.

Alcator C-Mod has demonstrated H-mode confinement that exceeds recent empirical H-mode scalings by a factor of 1.5. A new type of ELM behavior has been observed that avoids high instantaneous heat outflux. The compact, high-field plasmas obtained have enabled divertor studies to be performed at parallel power fluxes close to those predicted for ITER. Detached-divertor H-modes have been obtained by nitrogen puffing. Very high divertor neutral pressures are observed, which persist into the detached state. Highlights of these and other recent experimental results are presented.

---

* Supported by US Department of Energy contract DE-AC02-78ET51013.

[1] Associazione Euratom–ENEA sulla Fusione, Frascati, Italy.

[2] Presently at Tokyo Electron America, Beverly, Massachusetts, USA.

[3] Presently at ASTeX, Woburn, Massachusetts, USA.

[4] Presently at the US Air Force, Washington, D.C., USA.

[5] Johns Hopkins University, Baltimore, Maryland, USA.

[6] Presently at JET Joint Undertaking, Abingdon, Oxfordshire, UK.

[7] Presently at McKinsey & Co., Inc., London, UK.

[8] Presently at CPClare Corporation, Lexington, Massachusetts, USA.

[9] University of Maryland, College Park, Maryland, USA.

1. INTRODUCTION

The Alcator C-Mod tokamak [1] ($R = 0.67$ m, $a = 0.21$ m, $\kappa \lesssim 1.85$) produces high-field, compact, high performance plasmas. The research program is focussed on using this capability to explore plasmas with unique dimensional parameters but at dimensionless parameters comparable to those of much larger fusion experiments. Through comparisons with these other experiments, Alcator thereby provides critical scientific tests of physics scaling and theoretical understanding. In addition, the high power-densities achievable allow us to explore questions of critical importance to ITER and future reactors. In particular, C-Mod has a closed, shaped, vertical plate divertor, which experiences scrape-off-layer (SOL) parallel heat fluxes close to those expected in ITER, and which, despite the high heat flux, can be operated in a collisional conduction-limited, or even detached, state because of the high particle densities in C-Mod. The consequent reduction in power to the divertor plates is critical for future designs. Understanding of the physics of the divertor, essential for extrapolation, is rapidly growing.

Molybdenum is used throughout for the plasma facing components. We have therefore been studying and demonstrating the use of high-Z metals for such internal components. In many cases, the experience has been very satisfactory, but in some plasma regimes, detailed below, the core confinement of such impurities gives cause for concern about their use in future experiments. Boronization reduces the molybdenum levels by up to a factor of ten.

Experiments over the last two years have seen operation predominantly in the range $2.5 \leq B_t \leq 8$ T, and $0.4 \leq I_p \leq 1.2$ MA. We have not operated above a maximum current of 1.5 MA so far, because of concerns about the structural consequences of non-axisymmetric halo currents and other disruption effects, which will not be discussed further here [2]. Auxiliary heating is 4 MW (source) of ICRF at 80 MHz, which is resonant with hydrogen minority at 5.3 T and He^3 at 7.9T. (An additional 4 MW of tunable frequency power is in preparation). Up to 3.5 MW has been launched into the plasma with excellent heating efficiencies. Electron temperatures up to almost 6 keV (peak) and ion temperatures up to 4 keV (sawtooth averaged) have been obtained using these minority schemes [3]. In addition, mode-conversion direct electron heating has been demonstrated both on- and off-axis. The mode-conversion scheme gives highly localized power deposition and shows promise for current profile control with the asymmetric spectrum that can be launched from a current drive antenna currently under design.

2. DIVERTOR RESEARCH

The C-Mod divertor configuration is designed to spread the heat outflux over as much area as possible of the outer vertical plate, and maximize the effects of recycling at the plates. It has been found also to give a divertor chamber that is very well isolated from the main chamber in respect of neutral gas pressure. Detailed analysis of the neutral dynamics indicated that in the configuration used till Nov 1995, a major influence on the divertor to main-chamber neutral pressure "compression ratio" was leakage through small slots in the outer divertor structure. This leakage was then substantially reduced by blocking the slots. Compression ratios of typically 100–200, and up to 500 on occasions, have since been obtained, with divertor pressures rising as high as 0.1 mbar and remaining high even when the divertor is detached. The persistence of high divertor pressure even after the ion recycling flux to the divertor plate has dropped by a large factor at detachment indicates that the plasma plugging of the divertor throat is highly efficient, and it has been estimated that the albedo of the plasma for reflection of neutrals is as high as 0.95 at highest densities [4].

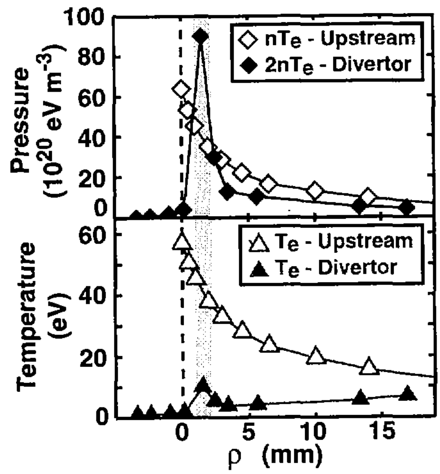

FIG. 1. Example of the local DR that often occurs near the detachment threshold. Coordinate ρ is the flux surface distance from the separatrix at the outer mid-plane. Divertor plate measurements are compared with reciprocating probe measurements made upstream.

Another indication of the importance and complexity of the neutral dynamics in the divertor is the observation of a very local "Densified Region", (also known as "Death Ray", DR)[5]. This expression refers to the observation of a region on the divertor plate where the plasma pressure (product of n_e and T_e) rises *above* the value on the same flux surface upstream. The DR also has much larger pressure than on adjacent flux surfaces, that is, it is highly localized in radius, as shown in Fig 1. This is a quite common phenomenon in our experiments, and occurs just at the threshold of divertor detachment, when neutral momentum is presumably becoming important. We attribute the pressure rise to the cross-field transport of momentum from adjacent flux-surfaces by charge-exchange neutrals which then deposit their momentum in this hotter region by subsequent exchange or ionization. This interpretation appears to be supported by observations in numerical simulations of C-Mod divertor cases of similar phenomena. As full detachment proceeds, the DR disappears.

Even before the reduction of divertor leakage, detachment of the plasma pressure from the vertical divertor surfaces was achieved in L-mode, without added impurities, at core electron density as low as 0.25 times the Greenwald limit [6]. Closure of the divertor leakage did not greatly affect this detachment density. The addition of neon, in concentrations that increased the Z_{eff} by up to 0.8, was found to lower the detachment threshold density by up to a factor of 2.

For H-mode plasmas it is much more difficult to detach the divertor, presumably because of the substantially increased parallel heat flux-density ($q_{||}$), that results from a narrower SOL and higher heating power. The SOL e-folding width for $q_{||}$, λ_q, decreases from 3–5 mm at the outer midplane in L-mode to 1–2 mm in H-mode, raising the value of $q_{||}$ to typically 0.5 GW/m^2. This reduction in λ_q is indicative of a decrease of the thermal diffusivity in the first few millimeters of the SOL by a factor of $\sim$ 3 under H-mode conditions. Further out in the SOL the diffusivity apparently remains at the L-mode level [7]. Detachment of H-mode plasmas has been explored by addition of radiating impurities [6]. As illustrated in Fig 2, starting at a main-chamber radiation fraction < 0.4 of the input power, prior to impurity puffing, and a confinement enhancement factor relative to ITER89-P of about 1.8, the addition of impurities simultaneously increases the radiation, and decreases the H-factor. With argon and neon, detachment of the divertor was not obtained in H-mode even with radiation fractions up to 0.8, at which stage the H-factor had dropped to about 1.2. Nitrogen puffing, unlike argon and neon, is observed to increase the radiation in the divertor. It produces divertor detachment with H-factor above 1.6.

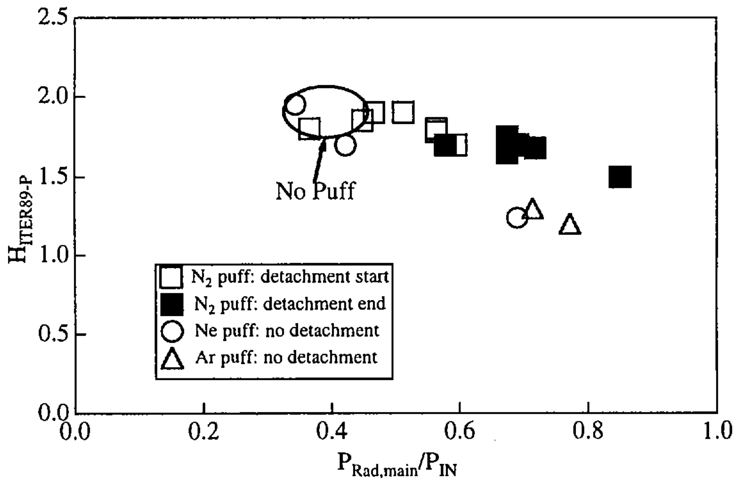

FIG. 2. H-factor relative to ITER89-P obtained in divertor detachment with impurity puffing. The nitrogen-puffed cases have progressively deeper detachment and greater impurity content. The argon and neon cases never detached.

These differences with different gases indicate that it is important to put significant radiation outside the separatrix, by appropriate choice of radiating species, in order to obtain divertor detachment and good H-mode confinement at the same time.

Tomographic reconstructions of the power-loss profiles in the divertor region from bolometers [8], illustrated in Fig 3, show that in the case of L-mode divertor detachment, the radiative region rises to the x-point and there is significant localized radiation *inside* the separatrix. In contrast, for H-modes, the radiation does not appear to occur significantly above the x-point. We attribute this difference to the observed higher separatrix (and x-point) temperature associated with H-mode. In either case, extremely high volumetric power loss densities are obtained: up to 60 MW/m^3.

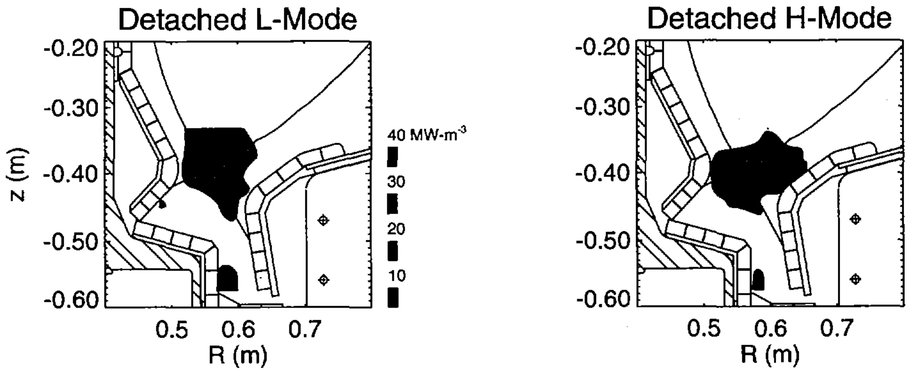

FIG. 3. Tomographic reconstructions of radiative power loss in the divertor for L- and H-mode divertor detachment, from 20 divertor bolometer chords.

Studies of the asymmetries between the inboard and outboard legs of the single-null divertor [9] have shown marked dependence on the direction of the magnetic field, and hence particle drifts. We find that the ratio (outboard to inboard) of the electron temperature reaches a factor of ten at the lowest densities studied, for the normal field direction (negative B_ϕ). This asymmetry reverses almost completely when the field direction is reversed, and the inboard is then hotter than the outboard. The SOL appears to be in a state where there is always one cold ($\sim$ 5 eV) end, normally at the inboard. Divertor detachment occurs when the temperature at the hotter end is also reduced to this value by radiative losses. These observations reemphasize the importance of particle drift effects in the physics of the SOL and divertor.

The performance of the divertor in screening the core plasma from incoming impurities has been studied using impurity puffing[10]. For a recycling impurity, such as argon, the penetration factor is expressed simply as the ratio of the total number of impurity ions observed spectroscopically in the core plasma to the number of atoms puffed. Fig 4 summarizes the results from various L-mode plasmas for $I_p = 0.8$ MA, $B_t = 5.3$ T.

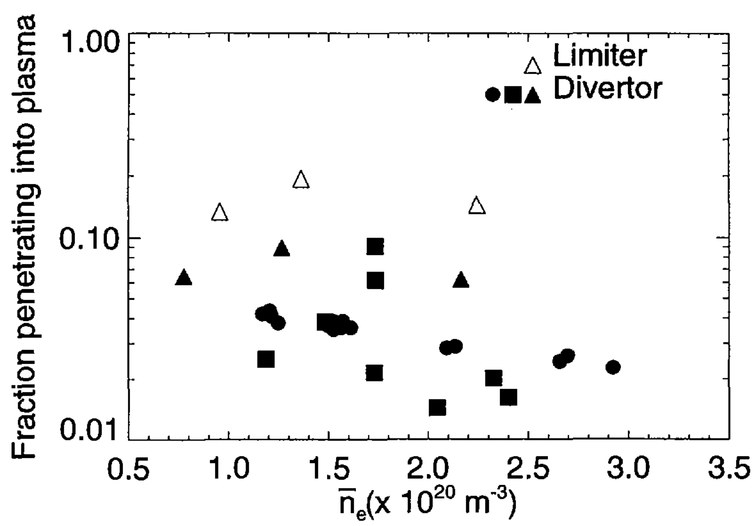

FIG. 4. Fraction of injected argon particles that enters the main plasma under L-mode conditions. Circles are from a density scan at constant shape. Triangles are from a divertor/limiter comparison. Squares have the divertor leakage blocked.

For a systematic density scan at constant configuration, penetration decreases with increasing density, but variations in the plasma configuration (and possibly wall conditioning) also cause large variations. Penetration factors down to below 1% have been observed. In other C-Mod experiments [11], penetration factors up to 30% for limiter plasmas have been observed and up to 60% if the impurity is puffed at the contact-point of the plasma with the wall.

Experiments with nitrogen puffing, which acts as a *non-recycling* impurity, show similar trends. For puffs away from the inboard, penetration is 5–20 times greater for limiter plasmas than for attached divertor plasmas. Detached divertor plasmas, however, have penetration only 1–3 times less than limiter plasmas.

3. CORE PLASMA TRANSPORT

Alcator C-Mod plasmas enter the H-mode regime of confinement relatively easily, under ohmic as well as ICRF-heated conditions [12,13]. In terms of the widely observed scaling of the power threshold for the L-H transition, $P = C\bar{n}_e B_t S$, where S is the plasma surface area, the C-Mod threshold can be reasonably described by a constant of proportionality, $C = 0.02 - 0.04 \times 10^{20}$ MW m T. This is as much as a factor of 2 lower than the coefficient derived by ASDEX-U [14], which itself is one of the lowest coefficients observed on tokamaks world-wide. This observation raises questions about the scaling's accuracy for extrapolations to ITER. The discrepancy cannot be accounted for purely in terms of the size scaling, since there are other tokamaks such as Compass [15]

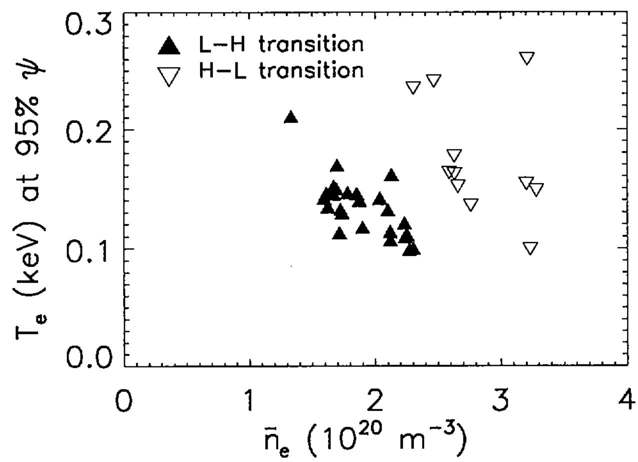

FIG. 5. Edge T_e for plasmas with I_p = 1.0–1.2 MA and B_t = 5.3 T, at the time of transition.

that are compact, like C-Mod, yet see a higher coefficient, C. Moreover, in comparison with larger machines, our observations would require a faster than linear scaling with S, in contradiction to the JET/DIIID comparison [16] which indicated weaker (approximately $S^{0.5}$) size dependence. C-Mod's uniqueness lies in high values of $\bar{n}_e$ and B_t. Therefore, a weaker dependence on these parameters is indicated by our experiments. Evidence from elsewhere (e.g. [17]) has suggested a weaker *density* dependence. The observed scatter in the threshold, due presumably to other variables such as wall conditions, neutral pressure, or other unknown factors, prevents a clear distinction between density and field dependencies from our data at this time. Boronization on Alcator C-Mod has not substantially decreased the lowest power thresholds.

Beyond the studies of global threshold scalings, Alcator C-Mod has demonstrated striking evidence for the dependence of the H-mode transition on *local* edge parameters, especially T_e. We find that the electron temperature measured at the 95% poloidal flux surface (as a convenient edge reference) at the L-H transition is substantially independent of density over the range $0.9 \lesssim \bar{n}_e \lesssim 2.5\times10^{20}$ m^{-3}, having a value 0.12 keV ±15%, regardless of heating power, in a controlled scan at fixed current (0.8 MA) and toroidal field (5.3T) [18]. The temperature at the L-H transition remains relatively close to this value up to currents of 1.2 MA as shown in Fig 5.

Moreover, as Fig 5 shows, the H-L back-transition occurs also at nearly the same edge temperature. Thus, there is no hysteresis in the dependence of the transition on edge temperature. These observations suggest that the driving mechanism of the H-mode bifurcation is the heating that results from reduced fluctuation transport, with temperature the controlling parameter. (Reflectometer measurements on C-Mod show the striking drop in density fluctuation level at the L-H transition that has been observed elsewhere [19]. We cannot at this stage distinguish between T_e and T_i which are well coupled.)

Experiments on C-Mod with reversed toroidal field, so that the cross-field drifts are in the unfavorable direction for obtaining H-mode, find that H-mode is not attained until the edge temperature is a factor of 2 or more higher than with the normal field direction. Also, clear dependence of the threshold temperature on B_t is observed, slightly stronger than linear. These facts support the idea that cross-field drift effects, determined by the gyroradius, are critical to the H-mode threshold. We observe both β and collisionality to have wide variation at threshold.

In experiments since boronization, sustained high-performance H-modes have been obtained with ICRF heating up to 3.5 MW. Confinement times up to 2.5 times the ITER89-P L-mode scaling, $\tau_E = 0.048 I_p^{0.85} B_t^{0.2} R^{1.5} n_e^{0.1} \epsilon^{0.3} \kappa^{0.5} m^{0.5} P^{-0.5}$, have been observed in ELM-free cases. These plasmas do not show the characteristics of VH-modes [20], in particular, they have sawteeth, and the transport barrier appears to remain predominantly at the edge.

The duration of ELM-free H-modes is ultimately limited by impurity accumulation. This problem has been investigated by injection of trace amounts of scandium by laser ablation to measure impurity confinement. Figure 6 shows an example. During the ELM-free phase, from 0.6 to 0.86 s, no measurable decay of the total scandium content is observed (profile peaking accounts for the slightly rising emission intensity), indicating impurity confinement times at least ten times the energy confinement time, which itself is roughly 70 ms. During

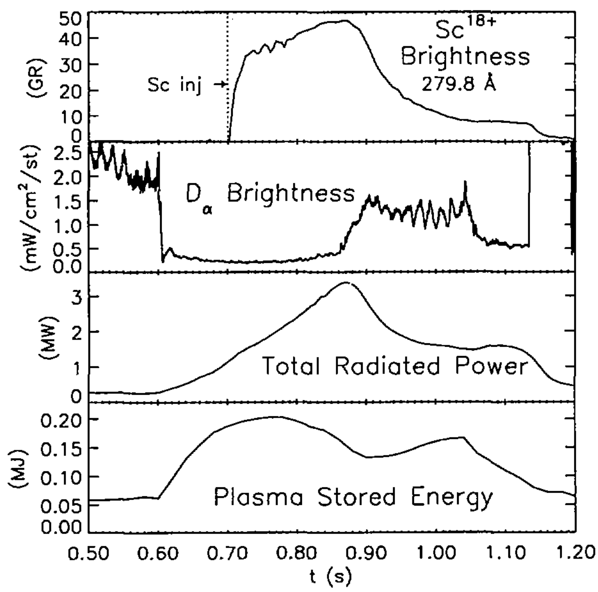

FIG. 6. Traces illustrating the near perfect confinement of injected impurities during ELM-free H-mode, but much reduced impurity confinement during "Enhanced D_α" H-modes. ICRF heating power of 2.5 MW was applied during the time 0.6 to 1.05 s. (I_p = 1 MA; $\bar{n}_e$ reaches 3.3×10^{20} m^{-3} at 0.85 s.)

this period, the total radiation power loss, which is dominated by molybdenum, rises with almost constant slope, consistent with a constant influx and no loss. Simulations show this behavior to imply a very strong inward pinch velocity and low diffusivity at the plasma edge, as was also indicated by JET experiments [21]. Our edge values are approximately consistent with neoclassical theory.

At 0.86 s the ELM-free behavior ends, as evidenced by the D_α rise, although the plasma is still definitely in H-mode, based on enhanced thermal and bulk particle confinement. The scandium immediately starts to pump out, and so does the molybdenum, with characteristic time approximately 90 ms. Following a lower D_α phase, brought about by switching off the ICRF at 1.05 s, the H-mode terminates at 1.13 s, and the scandium pumps out even faster, with a characteristic time of about 20 ms.

The period of enhanced D_α emission, 0.86 to 1.05 s, which we loosely refer to as "ELMy", illustrates a new and promising behavior which often occurs on C-Mod [13]. Unlike the type 1 ELMs observed at high power in other machines, there are few clearly distinct peaks in the edge power flow. Instead, there is a much more benign continuous degradation of the edge transport barrier, which gives much lower instantaneous heat flux than ELMs. This phenomenon does not appear to be related to type 3 ELMs because the enhanced D_α behavior increases with increasing heating power.

The occurrence and relative peak performance of the enhanced D_α modes are illustrated by the scans downward (at 0.8 MA) and upward (at 1 MA) of plasma target density, plotted in Fig 7. There is only weak dependence on previous wall history. The highest confinement occurs for ELM-free cases, close to the low-density limit of H-mode accessibility. At higher divertor pressures, corresponding to higher pre-RF target density, the enhanced D_α modes have confinement that is degraded by perhaps 20 to 30% from the ELM-free.

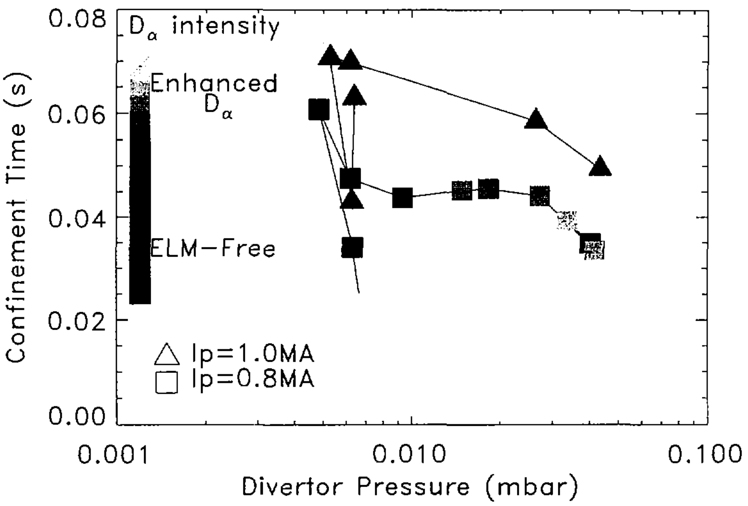

FIG. 7. Energy confinement time versus divertor neutral pressure for controlled scans during a single day. Each point is shaded according to the relative intensity of main-chamber D_α.

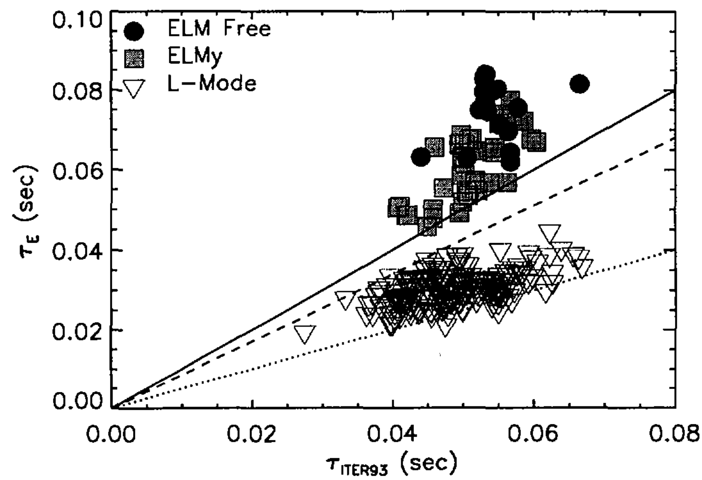

FIG. 8. Experimental energy confinement time (τ_E) versus the ITER93 ELM-free scaling (τ_{ITER93}). The dashed and dotted lines indicate 0.85 and 0.5 times the scaling, respectively. All Alcator H-mode data are substantially higher than would be predicted from this scaling.

Comparison with H-mode scalings is particularly significant [22] because versions developed prior to the availability of C-Mod results tend to have a stronger size dependence than L-mode and consequently to predict H-mode performance for C-Mod parameters that is little better than L-mode.

Fig 8 shows C-Mod experimental results plotted versus the ITER93 ELM-free scaling, $\tau_{\rm ITER93} = 0.048 I_p^{0.87} B_t^{0.45} R^{1.84} n_e^{0.03} \epsilon^{-0.02} \kappa^{0.53} m^{0.43} P^{-0.55}$. Even our "ELMy" (mostly enhanced D_α) plasmas lie above this line and the ELM-free cases well above. Our L-mode data spans the range between $0.5\tau_{\rm ITER93}$ and $0.85\tau_{\rm ITER93}$, the latter being often taken as an approximation of ELMy conditions. Clearly, therefore, these scalings must be reconsidered. An optimistic interpretation is that we have demonstrated better confinement than the scaling. However, more likely, one should conclude that the scaling is inaccurate and that the actual variation with size is not as strong as the scaling suggests. This interpretation is less favorable for projections to ITER.

ACKNOWLEDGEMENTS

We are grateful for the outstanding efforts of the Alcator engineering team.

REFERENCES

[1] HUTCHINSON, I.H., et al., Phys. Plasmas **1** (1994) 1511.

[2] GRANETZ, R.S., et al., Nucl. Fusion **36** (1996) 545.

[3] BONOLI, P.T., et al., IAEA-CN-64/EP-1, these Proceedings, Vol. 3.

[4] NIEMCZEWSKI, A., HUTCHINSON, I.H., LaBOMBARD, B., LIPSCHULTZ, B., McCRACKEN, G.M., Nucl. Fusion **37** (1997) 151.

[5] LaBOMBARD, B., "Experimental investigation of transport phenomena in the scrape-off layer and divertor", Plasma Surface Interactions in Controlled Fusion Devices (Proc. 12th Int. Conf. St. Raphael, France, 1996), J. Nucl. Mater. (in press).

[6] LIPSCHULTZ, B., et al., "Modification of the divertor detachment onset density", ibid.

[7] LaBOMBARD, B., et al., IAEA-CN-64/AP2-5, this volume.

[8] GOETZ, J.A., J. Nucl. Mater. **220–222** (1995) 971.

[9] HUTCHINSON, I.H., et al., Plasma Phys. Control. Fusion **37** (1995) 1389.

[10] McCRACKEN, G.M., et al., IAEA-CN-64/AP2-6, this volume.

[11] GRANETZ, R.S., et al., "A comparison of impurity screening between limiter and divertor plasmas in the Alcator C-Mod tokamak", Plasma Surface Interactions in Controlled Fusion Devices (Proc. 12th Int. Conf. St. Raphael, France, 1996), J. Nucl. Mater. (in press).

[12] SNIPES, J.A., et al., Plasma Phys. Control. Fusion **38** (1996) 1127.

[13] TAKASE, Y., et al., IAEA-CN-64/A5-4, this volume.

[14] RYTER, F., et al., Plasma Phys. Control. Fusion **36** Suppl. (7)A (1994) A99.

[15] FIELDING, S.J., et al., Plasma Phys. Control. Fusion **38** (1996) 1091.

[16] CARLSTROM, T.N., et al., Plasma Phys. Control. Fusion **38** (1996) 1231.

[17] SATO, M., et al., Plasma Phys. Control. Fusion **38** (1996) 1283.

[18] HUBBARD, A.E., et al., IAEA-CN-64/AP2-11, this volume.

[19] DOYLE, E.J., et al., Rev. Sci. Instrum. **61** (1990) 3061.

[20] JACKSON, G.L., et al., Nucl. Fusion **30** (1990) 2305.

[21] PASINI, D., et al., Plasma Phys. Control. Fusion **34** (1992) 677.

[22] GREENWALD, M., et al., H-mode Confinement in Alcator C-Mod (in preparation).

DISCUSSION

R.J. TAYLOR: What is your expected (projected) Q for the Alcator programme based on the best scaling obtained so far?

I.H. HUTCHINSON: If a confinement enhancement factor of 2 relative to the ITER89P scaling can be maintained up to a plasma current of 2.5 MA, which is within the original design capability of the tokamak, then DT equivalent Q exceeding 0.3 is projected.

H.L. BERK: The SOL properties and H mode transitions you describe are quite dramatic. Is there any indication that the magnitude of B could be a scaling parameter that needs to be looked at? Your machine has much higher B than other tokamaks.

I.H. HUTCHINSON: Clearly, how the SOL transport scales is a very important question, and I refer you to the paper by LaBombard et al. (IAEA-CN-64/AP2-5) for the Alcator results. I think international fusion research is in the early days of developing an understanding of how those transport scalings work. The magnetic field is an important parameter. Perhaps the more predominant one is actually electron temperature.

DIVERTOR BIASING EFFECTS TO REDUCE THE L-H POWER THRESHOLD IN THE JFT-2M TOKAMAK

Y. MIURA, Y. ASAHI, K. HANADA[1], K. HOSHINO, K. IDA[2], Y. ISHIGE, S. KASAI, T. KAWAKAMI, H. KAWASHIMA, M. MAEDA[3], M. MAENO, K. NAGASHIMA, K. OASA, H. OGAWA, T. OGAWA, M. SASAKI, M. SATO, S. SENGOKU, T. SHIINA, K. SHINOHARA[1], S. SHIRAIWA[1], T. SHOJI, N. SUZUKI, K. UEHARA, T. YAMAUCHI, K. HASEGAWA, K. ITOH, Y. KASHIWA, K. KIKUCHI, T. KOIKE, M. KOMATA, Y. OHUCHI, F. OKANO, M. SAITO, M. SAWAHATA, N. SEKI, T. SHIBATA, S. SUZUKI, H. TAKEUCHI, T. TANI, Y. TOMIYAMA, K. UMINO

Naka Fusion Research Establishment,
Japan Atomic Energy Research Institute,
Naka-machi, Naka-gun, Ibaraki-ken, Japan

Abstract

DIVERTOR BIASING EFFECTS TO REDUCE THE L-H POWER THRESHOLD IN THE JFT-2M TOKAMAK.

Divertor biasing effects to reduce the L–H power threshold are discussed. The L–H power threshold is reduced by the biasing only when a negative radial electric field is formed in the scrape-off layer (SOL) and the compression of neutrals in the divertor region is observed. If the ion ∇B drift direction is reversed to be away from the X point, which means a change of the $E \times B$ flow direction in the SOL, the reduction of the power threshold is not observed. In this case, the compression of neutrals in the divertor region is not observed either. The effects of the compressed neutrals are investigated in an intense gas puffing experiment. After short, intense gas puffing, there is some delay before the local gas puffing effects disappear and the neutrals are compressed in the divertor region. At that time, the L–H transition occurs at lower heating power than in the case without the gas puffing. The compression of neutrals in the divertor region is favourable for reducing the L–H power threshold. These observations may be explained by an H mode theory based on ion loss. Since the ion poloidal gyroradius is enlarged near the X point where the neutral density is high, banana ions may be taken away by the charge exchange reaction without having unfavourable effects on the plasma inside the separatrix.

---

[1] University of Tokyo, Tokyo, Japan.
[2] National Institute for Fusion Science, Nagoya, Japan.
[3] Saitama University, Urawa, Japan.

1. INTRODUCTION

It is well known that divertor biasing reduces the L–H transition power [1–3]. However, the mechanism is not clearly understood yet. Since H mode is required to demonstrate ignition in a next generation tokamak, such as ITER, it is one of the most important physics issues to understand the mechanism of the L–H power threshold and to find a tool to reduce the threshold. The scaling study [4] shows that the transition power increases with increasing main plasma density. On the other hand, the condition of a low heat load to the divertor target is realized only at high density at present. Thus it is very important to find a low L–H power threshold at high density for compatibility between high confinement and reduced heat load to the divertor target. In this paper, the effects of biasing for reducing the L–H power threshold are discussed from the viewpoint of the neutrals. It is found that the compression of the neutrals in the divertor region is produced by biasing and has a good correlation with the reduction of the L–H power threshold. This effect of the neutral compression is reconfirmed by an intense gas puffing experiment [5]. It is concluded that the neutral compression in the X point region is favourable for reducing the L–H power threshold. Control of the neutrals also has the potential to reduce the power threshold at high density.

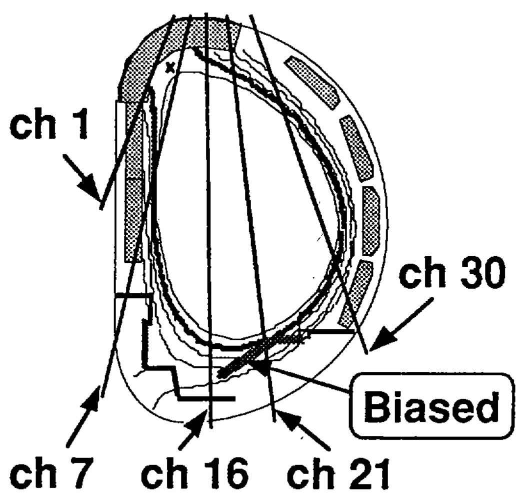

FIG. 1. Upper single null divertor plasma configuration and typical sight-lines of a fan array for H_α measurement (through the gap of the discrete divertor plates). Only the outside baffle plate is biased with respect to the vacuum vessel.

2. EXPERIMENTAL SET-UP

The JFT-2M is a medium size tokamak (major radius R = 1.31 m, minor radius $a \leq 0.35$ m, elongation $\kappa \leq 1.7$, toroidal magnetic field $B_t \leq 2.2$ T). The following experimental study of the biasing and the intense gas puffing experiments were performed with a deuterium plasma heated by a hydrogen neutral beam (NB). The primary energy of the hydrogen NB is 32 keV. The injection angle is about 38° to the magnetic axis and the injection is parallel to the plasma current (co-injection). Figure 1 shows the plasma configuration of upper single null divertor (R = 1.30 m, a = 0.25 m, $\kappa = 1.33$) with plasma current I_p of 195 kA, toroidal field B_t of 1.27 T and q_{surf} of about 3. The direction of the plasma current and of the toroidal field viewed from the top of the torus is clockwise (CW) and counter-clockwise (CCW), respectively. The ion ∇B drift direction is towards the X point in this case. Only the outside baffle plate (for a closed lower single null configuration) is biased, as shown in Fig. 1.

3. BIASING EXPERIMENT

The time evolution of a typical H mode with biasing is shown in Fig. 2. Positive biasing of about 200 V is applied from 650 ms. The H_α intensities of channels 7 and 16, whose sight-lines include the outside divertor region (see Fig. 1), are increased by the biasing. However, the H_α intensity around the main plasma (channel numbers greater than 21) is reduced. The L–H transition triggered by a sawtooth crash occurs at 780 ms. The threshold power is reduced by about 30% compared with the case without biasing. Figure 3 shows the changes of H_α profile resulting from the biasing. The ratio of the increased H_α intensity to the intensity before the bias is applied is shown. In the case of the positive biasing (negative radial electric field induced in the SOL by the biasing) with B_t of CCW direction, the H_α intensities whose sight-lines include the outside divertor region are increased by the biasing, and the H_α intensity around the main plasma is reduced. This means that a compression of neutrals in the divertor region occurs. However, in the cases of the negative biasing or the positive biasing with B_t of CW direction, the compression of the neutrals is not seen and the reduction of the power threshold is not observed. The compression of neutrals has a good correlation with the reduction of the power threshold. Since the plasma potential connected to the positive electrode follows the positive potential, the SOL plasma connected to the positive plate through the flux tube has more positive potential. Figure 4 shows the floating potential [6] measured by the movable probe with and without biasing. The position zero on the horizontal axis corresponds to the position where the flux tube touches the biasing electrode; it is shown by the thick flux tube in Fig. 1. Therefore, a negative radial electric field is formed just outside the separatrix. The negative electric field does not change for ohmic, L and H mode. The compression of the neutrals is only observed in the case

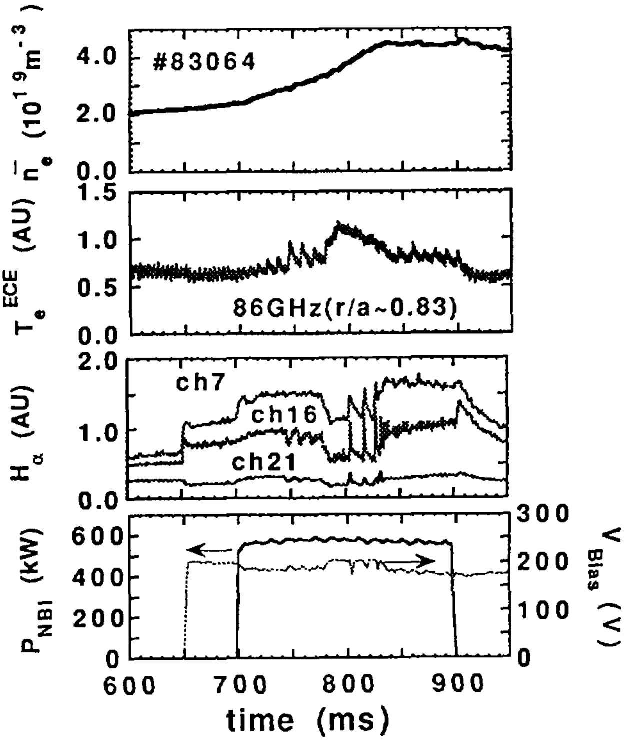

FIG. 2. Time evolution of line averaged density, electron temperature at the edge (r/a = 0.83), H_α intensities, NB injection power and applied bias voltage.

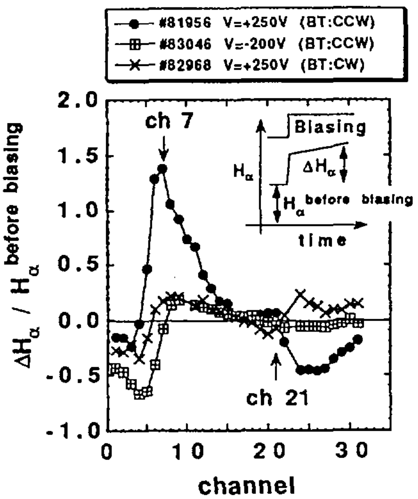

FIG. 3. Change in the H_α profile resulting from the biasing. The H_α intensity around the X point region is increased and that around the main plasma is reduced in the case of positive biasing.

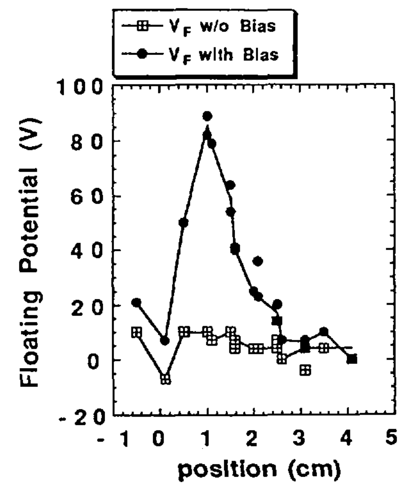

FIG. 4. Floating potential measured by the movable probe (from outside at z = −10 cm) in the cases of positive biasing and no biasing. The location of the separatrix is about −2 cm in this graph.

of the favourable ion ∇B drift direction together with the negative radial electric field in the SOL. This compression of neutrals may be coming from the decrease of the perpendicular diffusion in the SOL by the $\mathbf{E} \times \mathbf{B}$ flow and the SOL current [7–10].

4. INTENSE GAS PUFFING EXPERIMENT

We performed an intense gas puffing experiment to study the effects of the neutrals on the L–H transition power. Since a divertor configuration is favourable for obtaining H mode and the scaling study shows a higher power threshold at high density, it is believed that neutrals are unfavourable to the L–H transition. We found, however, that the H mode is caused by the intense gas puffing. The time history of the L–H transition produced by the intense gas puffing is shown in Fig. 5. Deuterium gas puffing of about 3.5 $Pa \cdot m^3 \cdot s^{-1}$ is applied from the bottom of the torus during the NB heated L mode phase. The density increases from $\sim 3 \times 10^{19}$ m^{-3} to $\sim 4 \times 10^{19}$ m^{-3} and a clear L–H transition occurs 60 ms after switching off the gas puffing. The ELM free H mode continues even after switching off the NB heating.

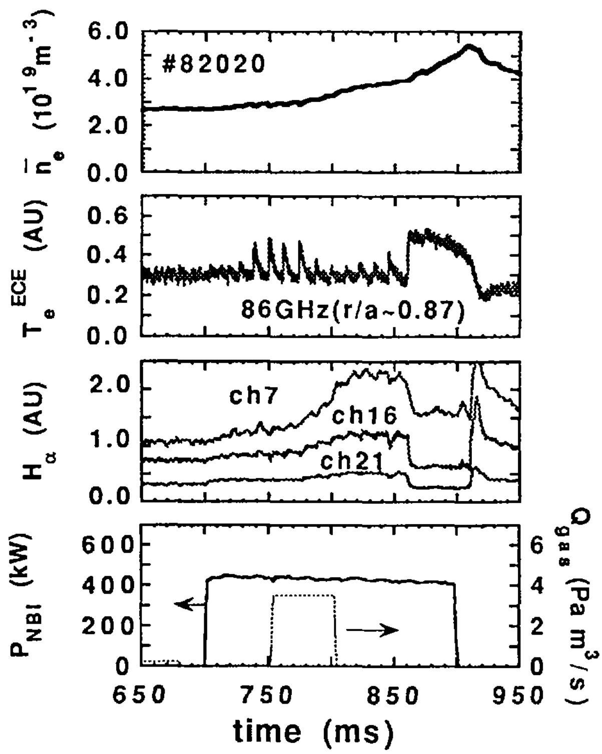

FIG. 5. Time evolution of the line averaged density, electron temperature at the edge (r/a = 0.87), H_α intensities, NB injection power and gas puffing rate from the bottom of the torus.

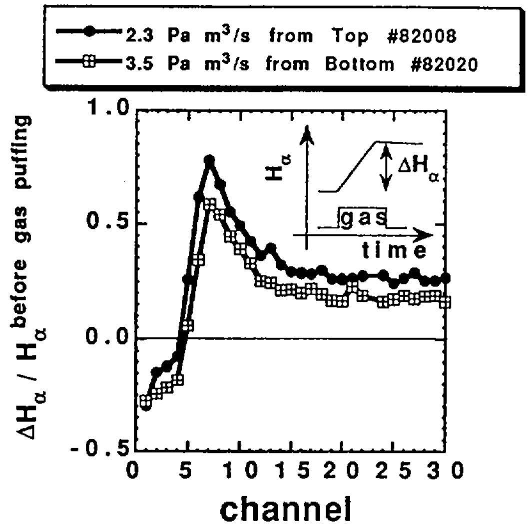

FIG. 6. Change in the H_α profile resulting from the intense gas puffing. The H_α intensity around the X point region is increased compared with that around the main plasma.

The H_α intensities of channels 7, 16 and 21 show an increase from the gas puffing. The L–H transition occurs during the very slow decay phase of the H_α intensity. The small dip in the H_α signal after the gas puffing is switched off ($\sim$845 ms) indicates a short H phase triggered by a sawtooth crash. The H phase becomes longer after the gas puffing is switched off and finally the plasma goes into an ELM free H mode. A drop of the time averaged electron temperature caused by the gas puffing is not clearly observed, but the peak electron temperature in the case of a sawtooth crash decreases. Even with a low peak electron temperature, we can see the short L–H transition (see the sawteeth at 775 ms and 845 ms). This suggests that the electron temperature may not be playing a major role for the L–H transition. The power threshold for the H mode is reduced by about 200 kW ($\sim$30%) compared with a plasma without gas puffing.

Figure 6 shows the change of H_α profile caused by the gas puffing. The ratio of the increased H_α intensity to the intensity before the gas puffing is shown. Since the toroidal location of the H_α measurement is far away from both the top and the bottom gas puffing positions (112.5° and 157.5° away, respectively), a difference in the H_α profile caused by the top or the bottom gas puffing is not clearly observed. The neutrals from the gas puffing are toroidally localized. The localization of neutrals by the gas puffing is confirmed by the large difference in the neutral out-flux measured by the time-of-flight (TOF) diagnostic system [11, 12]. The toroidal location of the top gas puffing and the TOF diagnostic is the same, and the poloidal distance between them is only about 14 cm. The top gas puffing of 2.3 $\mathrm{Pa \cdot m^3 \cdot s^{-1}}$

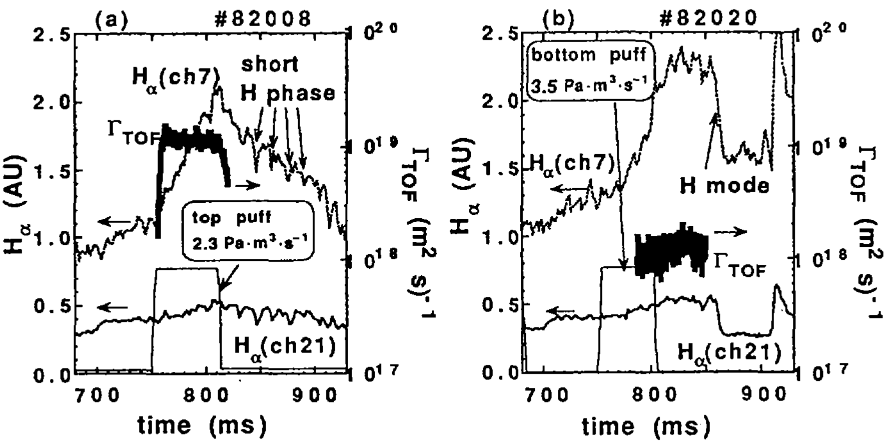

FIG. 7. Difference in the time evolution of H_α intensities, neutral out-flux measured by the TOF diagnostic and gas puffing rate with (a) top or (b) bottom gas puffing. The TOF neutral out-flux is affected dramatically by the top gas puffing, which is at the same toroidal position as the TOF diagnostic.

increases the TOF neutral out-flux by more than an order of magnitude, as shown in Fig. 7(a). However, the bottom gas puffing of 3.5 $Pa \cdot m^3 \cdot s^{-1}$, which is located 45° away toroidally from the TOF diagnostic, does not change the out-flux (see Fig. 7(b)). In Fig. 7(a), the large difference in the decay time of the H_α intensity and the TOF neutral out-flux can be seen. The time of 1/e in the H_α intensity (channel 7) is about 250 ms and that in the TOF neutral out-flux is about 10 ms. It is understood that the puffed neutrals are pumped out rapidly by the ionization, but the recycled neutrals around the divertor region decay slowly with a time constant of the effective particle confinement. The short H mode phase triggered by a sawtooth can be seen at the time when the local effect of the gas puffing disappears in Fig. 7(a), and a clear ELM free H mode is observed 60 ms after switching off the gas puffing in Fig. 7(b). In both cases shown in Figs 7(a) and (b), there is a local effect of the gas puffing that is not favourable for obtaining H mode. Therefore, the H mode is observed several tens of milliseconds after the gas puffing is switched off. At that time the compression of the neutrals in the divertor region is maintained and the local effect of the gas puffing disappears. These are good conditions for the L–H transition.

5. DISCUSSION

The increased charge exchange reaction by the compressed neutrals around the X point might have a favourable effect for obtaining H mode [13] without having unfavourable effects on the main plasma. This does not contradict some theories [14, 15] of the L–H transition that predict an important role for ions in the formation of a radial electric field inside the separatrix. The poloidal field is very weak around

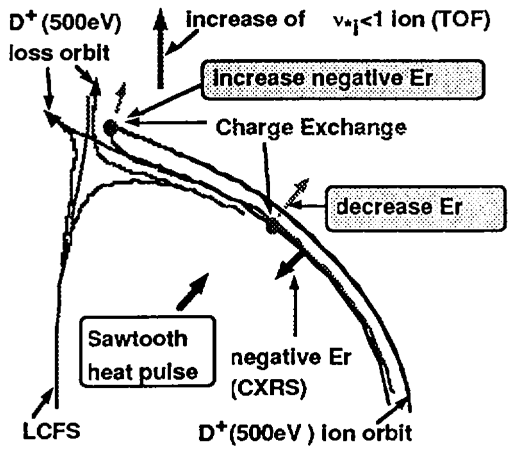

FIG. 8. Calculated 500 eV D^+ ion orbit at the edge. The process of formation of the radial electric field (E_r) is schematically shown (see text). The increase of collisionless ion flux and negative E_r is observed by TOF [12] and CXRS [16] measurement. LCFS: last closed flux surface.

the X point, so the banana width is enlarged in that region, as shown in Fig. 8. Therefore, if a charge exchange reaction occurs between the compressed neutrals around the X point and a banana ion, whose orbit is from inside to outside the separatrix, then the banana ion counts as an ion loss for the plasma inside the separatrix. The electricity is conserved by the charge exchange reaction, but the energy of the ion is lost. This means that the collisionality changes from less than one to larger than one as a result of the charge exchange reaction and the ion is lost to the divertor. Therefore, the neutrals help to form the negative electric field. However, the neutrals inside the separatrix (around the main plasma) dump the torque of the electric field by momentum loss (through the charge exchange reaction), which is unfavourable for obtaining H mode. This effect might correspond to the local effect of the gas puffing.

6. SUMMARY

We have observed the reduction of the L–H transition power by biasing or by intense gas puffing. In both cases, the compression of neutrals in the divertor region is observed from the H_α measurement. The compression of neutrals in the divertor region is favourable for obtaining H mode. These phenomena may be explained by an ion loss theory for obtaining H mode.

ACKNOWLEDGEMENTS

The authors acknowledge fruitful discussions with S.I. Itoh (Kyushu University), K. Itoh (National Institute for Fusion Science), and T. Takizuka, M. Mori, R. Yoshino and S. Konoshima (Japan Atomic Energy Research Institute). They also express their gratitude to H. Kishimoto, A. Funahashi, M. Azumi and M. Shimizu for their continuous encouragement.

REFERENCES

[1] SHOJI, T., et al., in Plasma Physics and Controlled Nuclear Fusion Research 1992 (Proc. 14th Int. Conf. Würzburg, 1992), Vol. 1, IAEA, Vienna (1993) 323.
[2] SCHAFFER, M.J., et al., in Controlled Fusion and Plasma Physics (Proc. 18th Eur. Conf. Berlin, 1991), Vol. 15C, Part III, European Physical Society, Geneva (1991) 241.
[3] KAYE, S.M., et al., Plasma Phys. Control. Fusion **36** (1994) A135.
[4] RYTER, F., et al., Nucl. Fusion **36** (1996) 1217.
[5] MIURA, Y., et al., Effects of intense gas puffing on L/H power threshold in the JFT-2M tokamak (in preparation).
[6] HANADA, K., et al., IAEA-CN-64/AP2-12, this volume.
[7] TOYAMA, H., et al., in Plasma Physics and Controlled Nuclear Fusion Research 1994 (Proc. 15th Int. Conf. Seville, 1994), Vol. 1, IAEA, Vienna (1995) 575.
[8] TAMAI, H., et al., ibid., p. 137.
[9] TERREAULT, B., et al., Nucl. Fusion **32** (1992) 1181.
[10] LACHAMBRE, J.-L., et al., Nucl. Fusion **34** (1994) 1431.
[11] MIURA, Y., et al., Rev. Sci. Instrum. **61** (1990) 3581.
[12] MIURA, Y., et al., Phys. Rev. Lett. **69** (1992) 2216.
[13] TODA, S., et al., "A theoretical model of H-mode transition triggered by condensed neutrals near X-point", Proc. Int. Conf. on Plasma Physics, Nagoya, 1996, 9E09.
[14] SHAING, K., CRUME, E.C., Jr., Phys. Rev. Lett. **63** (1989) 2369.
[15] ITOH, S.I., ITOH, K., J. Phys. Soc. Jpn. **59** (1990) 1364.
[16] IDA, K., et al., Phys. Rev. Lett. **65** (1990) 1364.

DISCUSSION

M. KAUFMANN: Are you sure that the neutral gas flux is the primary reason for the change in the L–H threshold, because you modify the plasma edge parameters by gas puffing?

Y. MIURA: Yes, I think that the gas puffing changes the L–H transition. A modification of the edge plasma parameters is observed. The drop in the peak electron temperature caused by a sawtooth heat pulse is clearly observed. However, the ion temperature is not reduced much. I think (n_iT_i) at the edge may play an important role at the L–H transition.

QUASI-STATIONARY ELM FREE HIGH CONFINEMENT WITH EDGE RADIATIVE COOLING IN TEXTOR-94

G.H. WOLF[1], J. ONGENA[2*], A.M. MESSIAEN[2*], J.A. BOEDO[4], R. JASPERS[3], L. KÖNEN[1], H.R. KOSLOWSKI[1], G. MANK[1], U. SAMM[1], B. UNTERBERG[1], P.E. VANDENPLAS[2], G. VAN OOST[2], G. VAN WASSENHOVE[2], G. WAIDMANN[1], J. WINTER[1], G. BERTSCHINGER[1], G. BONHEURE[2], M. BRIX[1], P. DUMORTIER[2], F. DURODIÉ[2], K.H. FINKEN[1], G. FUCHS[1], B. GIESEN[1], D.L. HILLIS[5], P. HÜTTEMANN[1], R. KOCH[2], C. KÖNIGS[2], A. KRÄMER-FLECKEN[1], A.I. LYSSOIVAN[2], P. MERTENS[1], A. POSPIESZCZYK[1], A. POST-ZWICKER[5], J. RAPP[1], M. SAUER[1], B. SCHWEER[1], J. SCHWELBERGER[4], G. TELESCA[1], M.Z. TOKAR'[1], R. UHLEMANN[1], M. VERVIER[2], R.R. WEYNANTS[2]

[1]Institut für Plasmaphysik, Forschungszentrum Jülich,
Association Euratom-KFA, Jülich, Germany

[2]Laboratoire de physique des plasmas — Laboratorium voor Plasmafysica,
Association Euratom-Belgian State,
Ecole royale militaire — Koninklijke Militaire School,
Brussels, Belgium

[3]FOM Instituut voor Plasmafysica Rijnhuizen,
Associatie FOM-Euratom, Nieuwegein, Netherlands

[4]Fusion Energy Research Program, Mechanical Engineering Division,
University of California at San Diego, La Jolla, California, USA

[5]Oak Ridge National Laboratory, Oak Ridge, Tennessee,
United States of America

Abstract

QUASI-STATIONARY ELM FREE HIGH CONFINEMENT WITH EDGE RADIATIVE COOLING IN TEXTOR-94.

On TEXTOR-94 a new regime of high confinement at high density has been established with virtually ELM free H-mode confinement. It is obtained in quasi-stationary discharges with strong additional heating in the presence of neutral beam co-injection and edge radiation cooling using feedback control of the energy content and of neon edge impurity seeding. This new regime combines high confinement, low q-edge values and high density close to the Greenwald limit with dominant radiative heat exhaust (edge radiation cooling); it is called Radiative I-mode (RI-mode). It is obtained in a pump limiter configuration, and if these results can be extrapolated the RI-mode may become an attractive operational scenario for a future fusion power reactor.

---

* Researcher at NFSR, Belgium.

1. INTRODUCTION

Previous work on TEXTOR - a pump limiter tokamak with circular plasma cross section - has shown that on the one hand non-detached plasmas with significant edge radiation cooling are possible [1-3] and on the other hand a regime of improved confinement with respect to the L-mode - called the I-mode - can be found in which, however, the enhancement factor f_H decreases with density [4]. More recently, work on improved confinement has been extended in the presence of edge radiation cooling [2,3] and a new regime with further improved confinement and a much more favourable density scaling has been identified [5]; it is called "Radiative I-mode" or RI-mode. Enhancement factors for the energy confinement of up to (and even above) 1 with respect to the ITERH93-P ELM-free scaling law have been obtained. The energy confinement scales linearly with density but shows only a weak current dependence [6], in contrast to the usual L- and H-mode scaling and also to the previously observed I-mode without radiation cooling [4]. No additional operational difficulties have been encountered when going to rather low cylindrical q_a (i.e. $q_a < 3$); this results in a natural way in high values for the figure of merit for ignition margin [7] under high density conditions. The neon seeding required for and characteristic of the RI-mode does not affect the total neutron fusion yield indicating a low non-accumulating central impurity concentration, even at the high radiation fractions needed to solve the heat exhaust problem. There is no power threshold to obtain this regime and no ELMs have been observed. Although the underlying mechanism that leads to the transition into the favourable conditions of the RI-mode is not yet understood, it appears that it is accompanied by an increase of the central current density and a reduction of the edge electron temperature.

2. EXPERIMENTAL SET-UP

TEXTOR-94 is a long-pulse medium size circular limiter tokamak (major radius R=1.75m, minor radius a=0.46m, pulse lengths of about 10 s) equipped with the pumped toroidal belt limiter ALT-II [8]. The experiments described below are conducted at plasma currents I_p between 280 and 480 kA and at a toroidal magnetic field B_t=2.25 T. Additional heating consists of co-injection ($D^+ \rightarrow D^0$ injection at about 50 keV) combined with ICRF heating (at $\omega = 2\omega_{CD}$ - i.e. at a frequency of 32 MHz - with π-phasing of the two antenna pairs, one with and one without Faraday screen). A necessary ingredient to obtain the transition to the RI-mode regime is the presence of a minimum level of about 20% of NBI-co in the total applied power P_{tot}. The energy content of the plasma during the stationary phase has been feedback controlled by acting on the level of ICRH heating. In this way, the transition to improved confinement and its changes on β are compensated in real time by changing the amount of the ICRH power. The feedback control of the edge radiation, which keeps a prescribed emission level of Ne VIII, acts on the Ne inlet valve [1] while the action of the pump limiter is required as a sink for Ne in the feedback loop. In this way, quasi-stationary plasmas can be routinely obtained with a radiated power fraction $\gamma = P_{rad}/P_{tot}$ (where P_{rad} is the total radiated power) of up to 0.9.

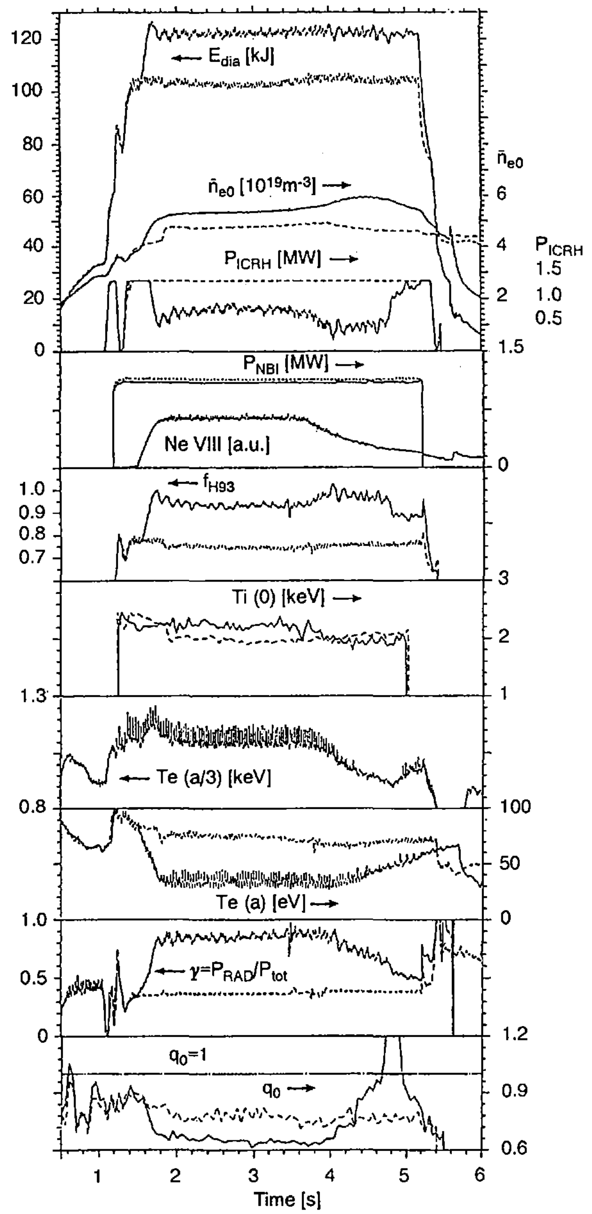

FIG. 1. Comparison of different plasma parameters for two discharges obtained on TEXTOR-94 with (#67130, plain curves) and without (#67133, dashed curves) edge neon seeding. Shown are, as a function of time, the signal of the diamagnetic energy, E_{dia}; the central line averaged density, $\bar{n}_{e0}$; the applied additional heating powers, P_{NI} and P_{ICRH}; the intensity of the NE VIII line; the enhancement factor f_{H93} with respect to ITERH93-P; the central ion temperature T_{i0} from CXES of a C VI line; the electron temperature at $r = a/3$ (from ECE diagnostics); the edge electron temperature (from the He beam diagnostic); the radiated power fraction, $\gamma = P_{rad}/P_{tot}$; and the value of the safety factor at the magnetic axis (with an error of about 30%) from polarimetry.

3. DISCHARGE CHARACTERISTICS

Fig. 1 compares the temporal evolution of the main plasma parameters of two discharges at I_p = 400 kA (i.e. q_a=3.4) heated by the combination of ICRH and NBI-co, one with (#67130) and one without (#67133) neon seeding. During the interval between 1.5 to 3.7s, the NeVIII radiation, (which is nearly proportional to the radiated power) is feedback controlled [1] resulting in quasi-stationary plasma conditions with a radiated power fraction $\gamma \cong 90\%$. From t=3.7s on, the neon inlet valve is closed and the neon radiation decreases due to the pumping action of ALT-II.

Remarkable in this figure is the evolution of : (i) the diamagnetic plasma energy E_{dia}, (ii) the enhancement factor for the energy confinement time versus the ELM-free H-mode scaling ITERH93-P, f_{H93}, and (iii) the feedback controlled ICRH power, P_{ICRH}. A distinct transition of the energy confinement is triggered by the seeding of Ne (starting at t = 1.5s) as soon as $\gamma \cong 50\%$. There these signals show a sharp change and the energy feedback system starts to reduce P_{ICRH} in order to maintain the preset value (E_{dia} = 120 kJ) for the plasma energy. If E_{dia} does not reach the preset value, P_{ICRH} is limited to 1.35 MW in the present case. Note the long duration of the high confinement phase which is about 50 confinement times ($\tau_E \cong$ 60ms). Maximum stationary phases obtained up to now are limited by technical constraints of the machine and last over 5s corresponding to about 100 confinement times.

Together with the increase in energy confinement, the plasma density is rising, reaching values close to the Greenwald density limit (defined as ($\bar{n}_{eo,Greenwald} = I_p/(\pi a^2)$ with as units $10^{20}m^{-3}$, MA, m [9] and equal to 6.0 $10^{19}m^{-3}$ for this discharge). TRANSP code analyses show that at these high densities the improved confinement is not caused by a dominating fast particle contribution. The rise in the plasma energy content occurring in the Ne cooled discharge, notwithstanding the lower level of additional heating, is reflected by the increase of both the line averaged central density $\bar{n}_{eo}$ and the central ion temperature T_{io}.

The further slight improvement of f_{H93} occurring near the end of the heating pulse is linked to the slight density rise there (as will be discussed below) and is reflected in the signal for the applied ICRH power, which is decreasing as a consequence of the feedback system. The relative decrease of P_{ICRH} there is larger than the increase of f_{H93} according to the relation $P_{tot}(f_{H93})^3 \cong$ constant (where $P_{tot} = P_{ICRH} + P_{NBI} + P_{OH}$ is the sum of the ICRH, NBI and OH power applied) as can be seen from the ITERH93-P scaling.

Also shown in the figure is the large difference in the radiation fraction γ. The necessity of a certain threshold level of edge radiation to initiate the transition to improved confinement and in addition to maintain it, is illustrated by the switch off of the neon puffing in the later phase of the discharge, i.e. at t=3.7s. It causes a gradual decay of the radiation fraction, initially with still high confinement, until a minimum critical level for γ is reached, leading to a confinement degradation at t = 4.7s, as can be clearly seen in the traces of P_{ICRH}, f_{H93} and E_{dia}.

After the end of the stationary part of the RI-mode phase (1.8s < t < 4.0s), a remarkable change in the inner MHD activity has been found. With the increase in density there, the sawteeth oscillations are first reduced in amplitude (with a collapse time increasing to 2-4 ms), then become irregular and finally cease completely. This can be seen on the trace of the ECE temperature outside the q=1 surface, $T_e(r \cong a/3)$, where until t=4.0s regular heat pulses are clearly seen corresponding to the sawteeth crashes. When the sawtooth activity ceases, irregular

MHD oscillations in the centre remain, as also observed in the Z-mode of ISX-B [10]. At the edge, also under these conditions, no signs of ELMs are observed.

Fig.1 shows also that q_0, the safety factor at the magnetic axis, drops during the stationary RI-mode phase to a value as low as 0.65 compared to 0.8 for the discharge without neon seeding. This feature has been seen for several pairs of discharges at different plasma currents. This corresponds to a peaking of the current profile with an increase of 15-20% of the current density on axis. After the switch-off of the Ne seeding, an increase of q_0 above 1 is correlated with the disappearance of the sawtooth activity, but note that still high confinement is observed.

Remarkable in this figure is also the decrease of the edge electron temperature $T_e(r=a)$, due to the neon seeding as measured by the He-beam diagnostic [11] and a scanning probe array [12]. This last diagnostic shows in addition that the edge electron temperature profile (r=45.5-50cm) generally changes from a profile with a decay length of about 1.2 to 1.5 cm to a nearly flat profile in the presence of Ne seeding.

4. CONFINEMENT AND PERFORMANCES

On Fig. 2 the enhancement factor f_{H93} of RI-mode discharges is plotted as a function of $\bar{n}_{eo}$ for different values of I_p and for a large range of γ, P_{tot} and P_{NBI}/P_{tot} ($1.5 < P_{tot} < 4.5$ MW, $0.45 < \gamma < 0.95$, $0.25 < P_{NBI}/P_{tot} < 0.9$). Several important features are visible in this figure : (i) the enhancement factor f_{H93} increases rapidly with density which is reminiscent of the Z-mode of ISX-B [10]; (ii) $f_{H93} = 1$ (i.e. equivalent to ELM-free H-mode confinement) is obtained for each current but at densities which increase with the plasma current; (iii) the Greenwald upper density limit is reached for each current without losing the characteristics of the RI-mode. No attempt has yet been made to investigate the density limit of the RI-mode.

In Fig. 3 the figure of merit for ignition margin f_{H89}/q_a (with f_{H89} the enhancement factor with respect to ITERL89-P and q_a the safety factor at the edge) is plotted versus density for the same set of data as in Fig. 2. The triple fusion product is proportional to the square of this parameter. It is clear that the data corresponding to the different currents overlap, signifying that the RI-mode has a confinement independent of the plasma current, but depends strongly on the density in contrast to the L- and H-mode scaling laws ($\tau_{ITERL89\text{-}P} \propto \bar{n}_{eo}^{0.10} P_{tot}^{-0.50} I_p^{0.85}$ and $\tau_{ITERH93\text{-}P} \propto \bar{n}_{eo}^{0.17} P_{tot}^{-0.67} I_p^{1.06}$). A careful analysis shows that the RI-mode scaling equals roughly the Neo-Alcator scaling, degraded by $(P_{OH}/P_{tot})^{0.50}$ [6]. Fig. 3 shows also that the value required for ITER, i.e. $f_{H89}/q_a \cong 0.60$, is found for the highest densities and currents. Finally, in Fig. 4 we plot for the same set of data as Fig.2, the normalised beta ($\beta_n = \beta_t a B_t/I_p$) versus the ratio $\bar{n}_{eo}/\bar{n}_{eo,Gr}$. This shows clearly that not only the β_n limit of the previous experimental campaigns ($\beta_n = 2$) [4] is obtained in the RI-mode but also that this could be obtained at densities around the Greenwald limit with a confinement as good as ELM-free H-mode.

During the RI-mode, together with the energy confinement time τ_E, $\tau_{p,D}$, the particle confinement time of deuterium also rises as a consequence of the decrease of the edge electron temperature. This in turn leads to an increase of the penetration depth of the neutrals and a decrease of particle diffusion coefficient of the edge which is assumed to be Bohm-like [13]. Furthermore, we observe a steepening of the density profile. All together these effects lead to an increase of $\tau_{p,D}$ by a factor 2 to 3 for the discharges shown in Fig.1.

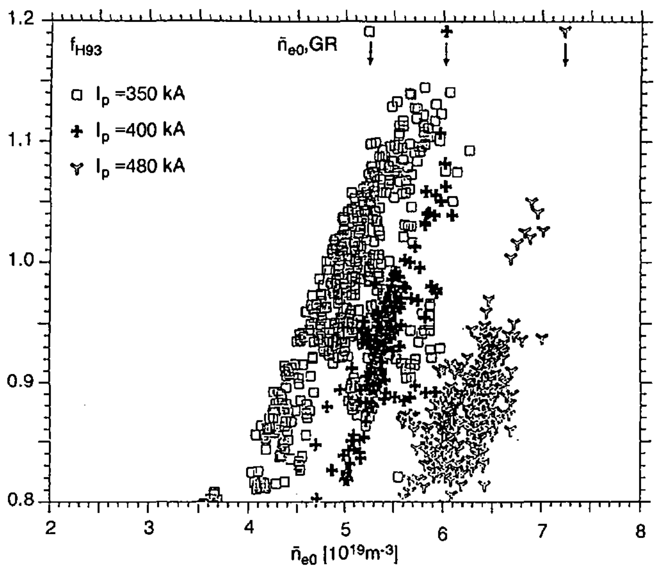

FIG. 2. Values of the enhancement factor f_{H93} versus $\bar{n}_{e0}$ obtained in RI-mode discharges for three different plasma currents and for a wide range of different plasma parameters. The location of the Greenwald limit density for the three currents is indicated by the arrows on top of the figure.

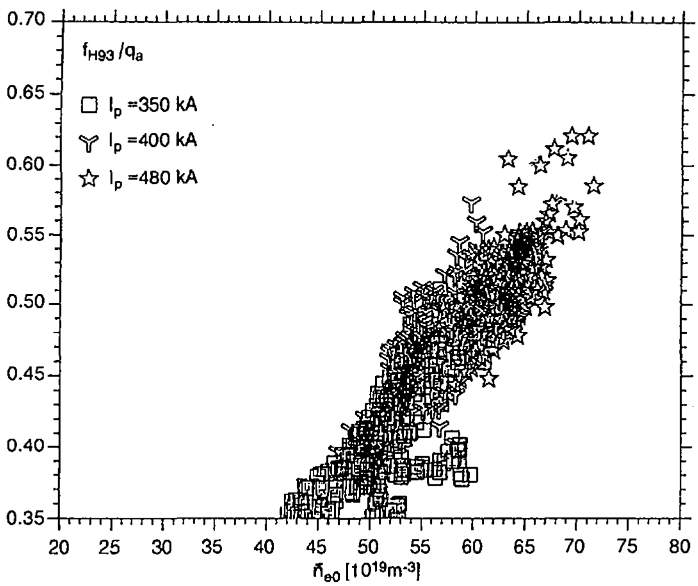

FIG. 3. Values for the figure of merit for ignition margin, f_{H89}/q_a, versus $\bar{n}_{e0}$ for I_p = 350, 400 and 480 kA.

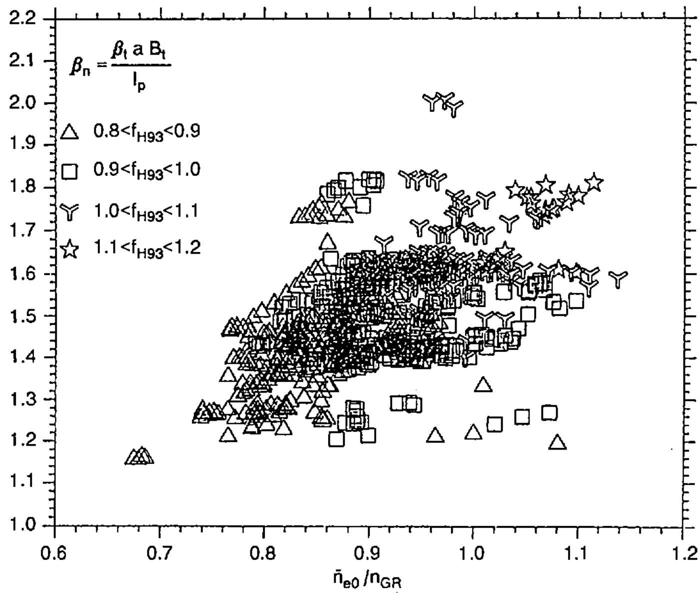

FIG. 4. Normalized beta values obtained in RI-mode discharges on TEXTOR-94 plotted as a function of the ratio $\bar{n}_{e0}/\bar{n}_{e0,Gr}$. The symbols indicate the values achieved for the enhancement factor f_{H93}.

The measured effective particle confinement time for He $\tau_{p,He}^*$ rises for similar RI-mode discharges by a factor of about 2 (2.3 as measured by CXES and 1.8 as found from direct pressure measurements in the ALT pumping duct). At the same time the energy confinement τ_E increases by a factor 1.6, such that the ratio $\tau_{p,He}^*/\tau_E$ shows only a moderate increment. Note also that this implies that the ratio $\tau_{p,He}^*/\tau_{p,D}$ remains the same with or without neon seeding, which can be understood as if $\tau_{p,He} \propto \tau_{p,D}$ with the same removal efficiency independent of the neon seeding.

5. POWER EXHAUST AND FUSION REACTIVITY

An approximately poloidally uniform power exhaust, needed to decrease the heat load on critical wall elements in a future reactor, is obtained at sufficiently high radiation levels due to the dominance as a radiator of the seeded impurity neon over the intrinsic impurities C and O, which radiate more in the vicinity of the toroidal belt limiter ALT-II. The Li- and Be-like states of Ne, having a larger ionisation time than the intrinsic impurities and thus being more uniformly distributed, account for most of the radiation. There is only a small contribution to the total radiated power from the central plasma, where the hydrogen like, helium like and fully ionised neon ions are located.

For the whole duration of the feedback controlled Ne seeding, there is no central impurity accumulation as can be verified from the constant ratio of the brilliance of various charge states of different impurities (C,O and Ne), from the neutron reactivity and also from the unchanged current profile peaking.

The neutron reactivity does not show any deleterious effect of the seeded impurity as follows from a detailed analysis of the neutron yield at different levels of neon seeding [5,14]. This can be partially understood by a replacement of the intrinsic impurities C and O by Ne, such that the dilution remains unchanged. This results from a reduced sputtering of wall material due to a lower edge temperature in the presence of neon seeding as shown in Fig.1, Indeed, the carbon concentration decreases by a factor of 1.8 in the discharge with radiation cooling of Fig.1, as evaluated from the CV brilliance, taking into account electron temperature and density changes. Note that although the dilution is the same, Z_{eff} will increase when the atomic number of the seeded impurity is larger than that of the intrinsic impurities

As discussed in [5], an estimate of the average neon concentration in the plasma volume can be found from a detailed particle balance for the seeded neon and the Z_{eff} measurement. This leads to an estimated upper limit for the average concentration of about 1.5% Ne.

6. CONCLUSIONS

Recently, a new and favourable confinement regime, the so-called Radiative I-mode, has been discovered on TEXTOR. It can be maintained under quasi-stationary conditions for intervals of up to $100 \times \tau_E$, comparable to the skin resistive time using as indispensable tools the feedback control of the impurity seeding and the plasma energy content.

The most striking features of the RI-mode can be summarized as follows : (i) it permits high densities close to or above the Greenwald limit, (ii) it exhibits high confinement, scaling linearly with the plasma density, and at the highest densities reached, as good as ELM-free H-mode confinement is obtained together with sufficiently large normalised beta values, (iii) going to low edge q values poses no operational difficulties, (iv) it leads in a natural way to high values for the figure of merit for ignition margin f_{H89}/q_a, (v) it can be obtained with high edge radiation fractions, offering a possible solution for the heat exhaust of a fusion reactor, (vi) it does not show a power threshold nor ELMs and (vii) no detrimental effects of the seeded impurity on the fusion reactivity are observed.

In order to extrapolate to reactor ignition, scaling with plasma size and shape and with B_T has to be assessed.

REFERENCES

[1] SAMM, U., et al., Plasma Phys. Control. Fusion **35** (1993) B167.
[2] ONGENA, J., et al., in Controlled Fusion and Plasma Physics (Proc. 20th Eur. Conf. Lisbon, 1993), Vol. 17C, Part I, European Physical Society, Geneva (1993) 127.
[3] MESSIAEN, A.M., et al., Nucl. Fusion **34** (1994) 825.
[4] ONGENA, J., et al., Nucl. Fusion **33** (1993) 283.
[5] MESSIAEN, A.M., et al., Phys. Rev. Lett. **77** (1996) 2487.
[6] MESSIAEN, A.M., et al. (in preparation).
[7] PERKINS, F., et al., in Plasma Physics and Controlled Nuclear Fusion Research 1994 (Proc. 15th Int. Conf. Seville, 1994), Vol. 2, IAEA, Vienna (1995) 477.
[8] DIPPEL, K.H., et al., J. Nucl. Mater. **145-147** (1989) 3.
[9] GREENWALD, M., et al., Nucl. Fusion **28** (1988) 2199.
[10] LAZARUS, E.A., et al., Nucl. Fusion **25** (1985) 135.

[11] HINTZ, E., SCHWEER, B., Plasma Phys. Control. Fusion **37** (1995) A87.
[12] BOEDO, J., et al., in Controlled Fusion and Plasma Physics (Proc. 22nd Eur. Conf. Bournemouth, 1995), Vol. 19C, Part I, European Physical Society, Geneva (1995) 293.
[13] TOKAR', M.Z., Phys. Scr. **51** (1995) 665.
[14] MESSIAEN, A.M., et al., in Plasma Physics and Controlled Nuclear Fusion Research 1994 (Proc. 15th Int. Conf. Seville, 1994), Vol. 1, IAEA, Vienna (1995) 333; Nucl. Fusion **36** (1996) 39.

DISCUSSION

F.X. SÖLDNER: You mentioned a peaking of the density profile in radiative discharges. Could this provide an explanation for the high line average densities exceeding the Greenwald limit, with the edge density being kept low? This would be consistent with previous results in regimes of peaked density profiles, e.g. with pellet injection, where the edge density was identified as the ruling parameter for the density limit.

G.H. WOLF: In a global sense this may be so. Unlike the case with pellet fuelling, however, particle transport through the radiative boundary layer is also the only channel for the inward flux. Therefore this may not explain the underlying driving mechanism.

R.J. TAYLOR: In your experiment, the neon puffing changes the edge symmetry. How important can this be for reaching the improved performance?

G.H. WOLF: Intuitively, I share the assumption that the improved poloidal symmetry of edge radiation is an important ingredient. However, without the other tools for obtaining the RI mode (such as NBI co-injection), this symmetry is not sufficient. For details on the radiating layer I refer to the TEXTOR article, G. TELESCA et al., Nucl. Fusion **36** (1996) 347.

CONCEPT OPTIMIZATION 1

(Session A1)

Chairperson

H. KISHIMOTO
Japan

OPTIMISATION OF JET STEADY-STATE ELMy DISCHARGES WITH ITER-RELEVANT DIVERTOR CONDITIONS

JET TEAM[1]
(Presented by D. Stork)

JET Joint Undertaking,
Abingdon, Oxfordshire,
United Kingdom

Abstract

OPTIMISATION OF JET STEADY-STATE ELMy DISCHARGES WITH ITER-RELEVANT DIVERTOR CONDITIONS.

Experiments with the JET Mark IIA divertor involving optimisation of performance with gas fuelling are discussed. The development of plasmas in the Mark IIA configuration at high current ($\geq$4.5 MA) and low q ($q_{95} \leq 2.6$) is presented. The results of a preliminary experiment to study the dimensionless (ρ^* and ν^*) scaling of energy confinement in impurity-seeded plasmas with high radiated power are discussed. It is found that the energy confinement is not consistent with gyro-Bohm scaling and does not follow the ITERH93-P scaling law for ELM-free plasmas.

1. INTRODUCTION

JET is now in the middle of a programme designed to investigate the effect of divertor geometry on plasma performance. The configurations studied so far are the Mark I (Fig.1(a)) and the Mark IIA (Fig.1(b)). This series will conclude with an ITER-specific "Gas Box" (Mark IIGB) in 1997/98. The programme follows a progressively more closed series of configurations. Each of the divertors uses a cryopump with a nominal pumping speed (deuterium) of $240\mathrm{m}^3\cdot\mathrm{s}^{-1}$.

Optimisation of plasma performance in steady-state ELMy H-mode discharges in the Mark IIA divertor has concentrated on the effect of changes in plasma configuration and fuelling. Changes in bulk plasma parameters (such as plasma triangularity) and in divertor closure-related parameters (such as magnetic flux expansion at the target) are covered in a related paper [1] which also addresses the behaviour of type I ELMs in the Mark IIA. The changes in plasma performance due to main species (D_2) fuelling are discussed in Section 2 below.

The steady-state ELMy H-mode is a candidate for production of high performance (in terms of stored energy and fusion yield) plasmas in the forthcoming deuterium-tritium experiments in JET (DTE1) scheduled for early 1997. The optimisation of this regime at high current ($\geq$ 4.5MA) and full field ($3.4 \geq B_T \geq 3.1$T) in JET involves plasma operation at low values of q ($q_{95} < 2.6$) where experimental input would provide useful information for ITER operation. The status of this work is described in Section 3.

[1] See Appendix to paper IAEA-CN-64/O1-4, this volume.

The highly-radiating impurity-seeded divertor plasmas which were first studied in JET in the Mark I campaign [2] have been the subject of further study in Mark IIA [1]. An important issue is whether the confinement quality of these discharges, which is barely acceptable for ITER [1,2], is maintained as the dimensionless variables (ρ^* and ν^*) are increased towards the ITER range. Investigations into this topic in Mark IIA are described in Section 4.

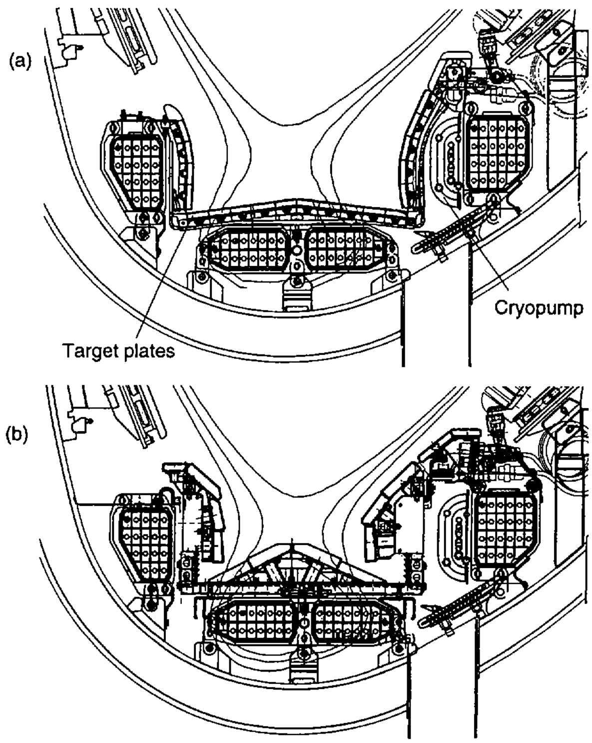

Fig.1 JET divertor geometries: (a) Mark I divertor (1994/95) (b) Mark IIA divertor(1996).

2. DIVERTOR PLASMA BEHAVIOUR WITH FUELLING VARIATIONS

2.1 Discharges with fuelling only from neutral beams

As with the Mark I divertor [3], steady-state discharges with Type I ELMs are routinely achieved in the Mark IIA divertor. The "natural" behaviour of discharges which are not fuelled by added gas, but only sustained by neutral beams and the input from edge recycling, has been extensively studied [1]. This natural behaviour can be summarised as follows:

- the type I ELMy H-modes have a similar confinement to Mark I plasmas with confinement enhancement (H_{93}) relative to the ITERH93-P ELM-free H-mode scaling of $0.9 \leq H_{93} \leq 1.1$ at plasma currents from 2.5-3.5MA;
- the discharges reach a steady-state density which for a fixed plasma configuration scales as

$$\langle n_e \rangle \propto \left(I_p \cdot P_{nbi}\right)^{0.5} / \pi a^2$$

similar to the behaviour in Mark I but with a 15% lower density for similar configurations [4];

- the discharges have similar low fraction of radiated power (around 20% of input power) and moderate Z_{eff} (1.5-2.5). Z_{eff} is highest in discharges with higher triangularity, principally because of the reduced ELM frequency in such discharges [1]. Carbon is the predominant impurity.

2.2 Discharges with external deuterium gas fuelling

Heavy D_2 gas puffing (up to ~ 5 10^{22} atoms s^{-1}) has been applied to all the Mark IIA plasma configurations. The fuelling efficiency is lower than in Mark I. This is partly due to the fact that the rate of pumping in Mark IIA is higher than in Mark I [1], the Mark IIA geometry behaving as a moderate slot divertor by trapping the returning neutrals near the pumping ports.

The fuelling efficiency is found to be independent of the location of the gas feed. Fuelling in the upper vessel; in the private region; in the outboard midplane and at the inner and outer strike zones, all achieve the same asymptotic density for a given fuelling rate, plasma current and configuration.

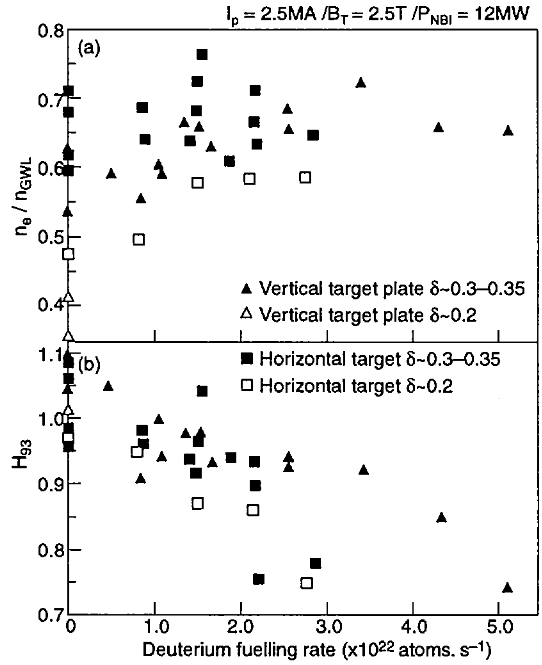

Fig.2 (a) Plasma density achieved (as a fraction of the Greenwald limit) against deuterium gas fuelling in the various Mark IIA configurations. (b) Confinement enhancement relative to the ITERH93-P scaling law (H_{93}) as a function of deuterium gas fuelling for the discharges in (a).

As the fuelling is increased, the ELM frequency rises and the confinement begins to degrade [1]. The confinement degradation is correlated with an increase in the outer midplane pressure or outer midplane recycling, which rise due to the imperfect closure of the Mark IIA configuration. The same global behaviour was observed in Mark I [3,5]. The plasma density increases at first as fuelling is increased (Fig.2(a)) but eventually a maximum density is reached beyond which a further density rise is impeded because the ELMing rate continues to increase with increased fuelling and density is expelled. The maximum density is not accompanied by any dramatic fall in confinement (Fig.2(b)) which continues to decline slowly. The density limit appears to be related to poor fuelling efficiency as ionised neutrals are unable to convect into the plasma against the increasing ELM frequency. The limit is not associated with a disruptive or radiative collapse.

For all configurations, the plasmas with Vertical Target (VT) strike zone positions are most tolerant to high fuelling rates. They are able to maintain their confinement at higher values of fuelling, and reach their maximum density at higher fuelling rates (Fig.2). Thus they sustain a higher radiated power fraction with a less strongly deteriorated confinement. The radiated power fractions in a fuelling scan on VT plasmas at 2.5MA/2.5T with fixed beam power are shown in Fig.3(a). The radiated power reaches ~ 45% of the input power and the increase in radiation with fuelling comes entirely from the divertor region. In a reactor plasma this would be beneficial for target loading and erosion. The plasma purity also increases steadily in this scan (Fig.3(b)) partly offsetting the decline in H_{93}.

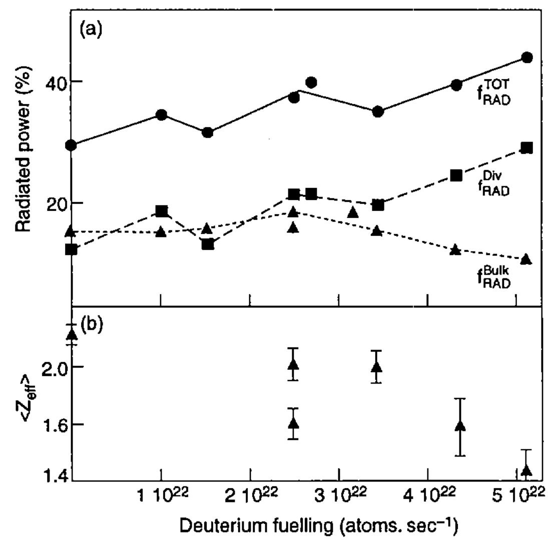

Fig.3 (a) Radiated power as a function of deuterium gas fuelling for the Vertical Target, higher triangularity discharges from the dataset in Fig.2. (I_p=2.5MA; B_T=2.5T; P_{nbi}=12MW). (b) Z_{eff} as a function of deuterium fuelling for the dataset of Fig.3(a).

The density limit in the Mark IIA configuration lies close to the Greenwald limit (Fig.4(a)). In contrast, with Mark I it was possible to exceed the Greenwald limit at low current (Fig.4(b)). There appears to be a trend towards a lower density limit as the divertor geometry becomes more closed. In the pre-1992 JET configuration with its open divertor, the Greenwald limit could be exceeded over a much larger range of I_p.

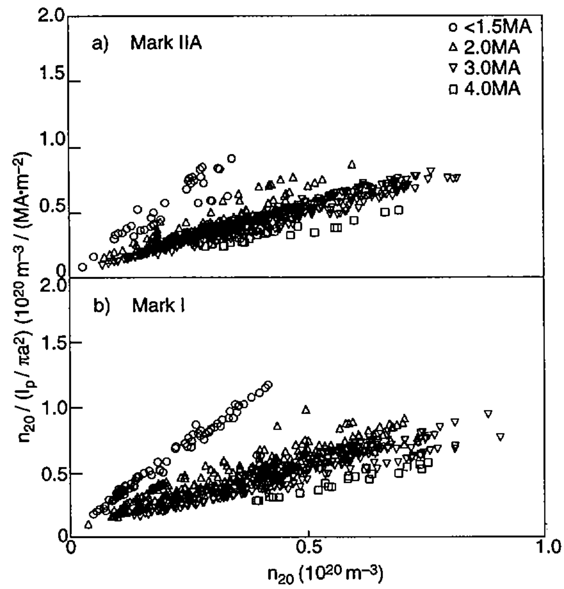

Fig.4 Plasma density (n_{20}) scaled to the Greenwald limit expression ($I_p/\pi a^2$) as a function of density and current for (a) Mark IIA plasmas; (b) Mark I plasmas.

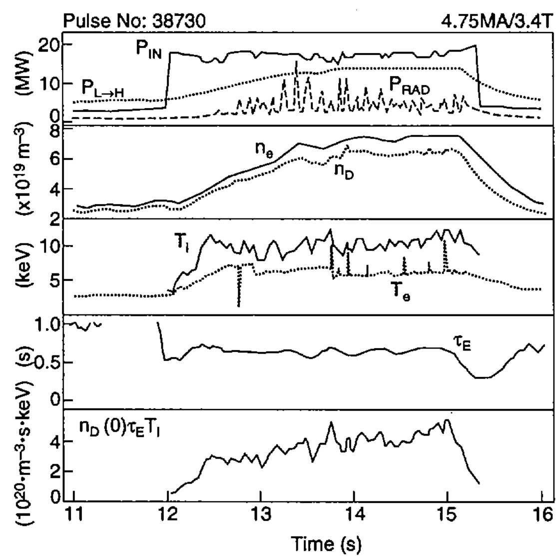

Fig.5 Time evolution of a steady-state type I ELMy H-mode at high current and low q (q_{95}~2.5).

3. CONFINEMENT IN STEADY-STATE ELMY H-MODES AT HIGH CURRENT AND LOW q

ELMy H-modes lasting up to 10 energy confinement times have been obtained in diverted plasmas at plasma currents ≥ 4.5MA. An example of such a discharge is shown in Fig.5. Operation above 4.5MA in JET requires low q_{95} (≤ 2.5) as the toroidal field is presently limited to 3.4T. Thus optimisation of these plasmas is addressing a regime of particular interest to ITER.

It is found that energy confinement enhancement (H_{93}) does not degrade at low q in JET relative to the ITERH93-P law, but H_{93} in discharges with combined high current and low q (q_{95} ~ 2.4-2.5) is about 10% down on the mean values achieved at lower I_p. The energy confinement of ELMy H-modes with steady ELMy conditions lasting > $3 \cdot \tau_E$ is shown in Fig.6 where H_{93} is plotted against q_{95}. The discharges above 4.5MA have a restricted triangularity range ($0.2 < \delta < 0.23$).

Although good confinement can be achieved at low q, a significant number (~ 50%) of the ELMy H-modes produced at low q show a deterioration in confinement from one of two mechanisms:

i) Discharges with q_{95} ~ 2.4 are prone to the appearance of large n=2 MHD activity which, whilst the ELMy H-mode steady-state is maintained, leads to a loss of confinement by 10-15%. Examples of the steady-state confinement deterioration obtained are marked in Fig.6. It can be seen that this is a low q rather than a high current phenomenon. These modes were present only rarely in Mark I. The nature of their appearance in Mark IIA is not yet understood, but the causal link with lack of confinement is clear.

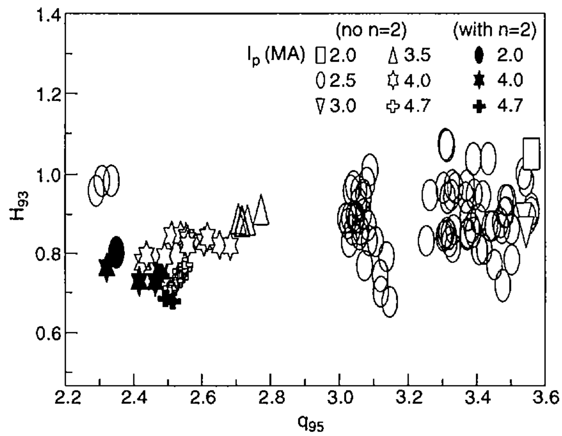

Fig.6 H_{93} as a function of q_{95} for steady-state ($\tau_H > 3 \cdot \tau_E$) ELMy H-modes. The solid symbols indicate discharges accompanied by strong n=2 MHD activity.

ii) Many discharges at $q_{95} < 2.6$ and $I_p > 4.0$MA suffer H-L transitions which occur randomly, frequently after many energy confinement times. A few of these discharges have input powers which are close to the L-H power threshold when bulk radiated power is subtracted. For the rest, the reverse transition occurs spontaneously and is accompanied by impurity influx and often by a slowly rotating or locked n=1 mode. These are generally thought to be effects of the loss of confinement rather than the causes. It is

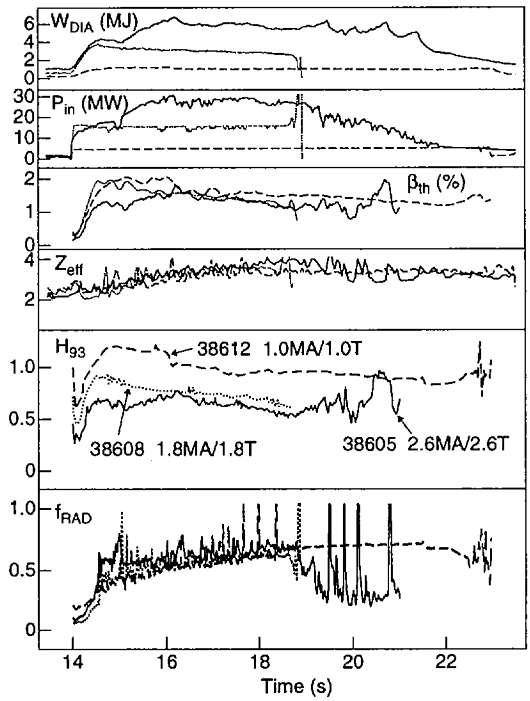

Fig.7 Comparative time evolution of stored energy; input power, thermal β; Z_{eff}; H_{93} and radiated power fraction for three discharges in the (ρ,ν*) scan of radiative divertor plasmas.*

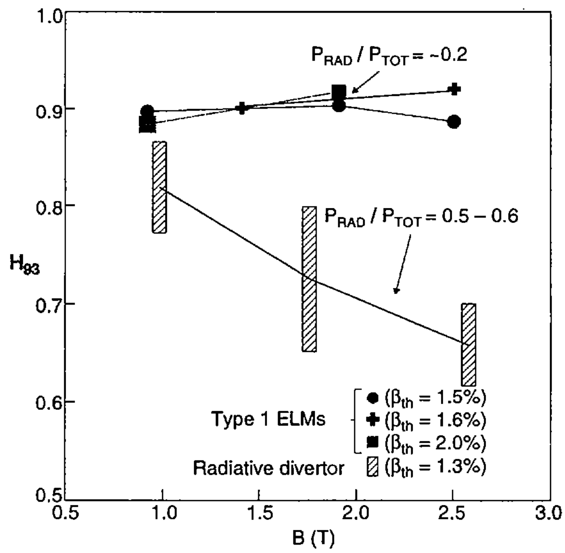

Fig.8 H_{93} as a function of toroidal field for the JET radiative divertor plasmas at similar (β, q, δ, κ, a, Z_{eff}, f_{RAD}). Also plotted are the type I ELMy H-modes from the ρ scan in JET (see [6]).*

possible, at this early stage in the high current development, that the vessel has not been conditioned sufficiently for reproducible behaviour at high current and power.

Up to 25MW of combined heating power (17MW NBI and 8MW ICRF) has been coupled into JET plasmas at 4.7MA and 3.4T. The fusion triple product $n_D(o) \cdot \tau_E \cdot T_i(o)$ has reached ~ $4 \cdot 10^{20} m^{-3} \cdot s \cdot keV$ for three energy confinement times. Such plasmas would give a fusion amplification factor in D-T plasmas (Q_{D-T}) of around 0.25.

4. CONFINEMENT SCALING WITH DIMENSIONLESS PARAMETERS IN RADIATIVE DIVERTOR DISCHARGES

The scaling of energy confinement in discharges with a high fraction (> 50%) of radiated power, seeded by N_2 gas, has been studied in a series of plasmas which are dimensionally similar, except for the variation in normalised ion Larmor radius (ρ^*) and collisionality (ν^*). The aim of these experiments was to ascertain whether these ITER-relevant discharges are consistent with a gyro-Bohm scaling [6] such as ITERH93-P.

The time development of these H-mode discharges at 1MA/1T, 1.8MA/1.8T and 2.6MA/2.6T is shown in Fig.7. The discharges had the same q_{95} (=3.1), triangularity (δ ~ 0.3), minor radius, elongation and were all seeded by a mixture of N_2 and D_2 gas such that they reached a radiated power fraction ~ 60%. It can also be seen that they attained the same Z_{eff} of about 3.5. The input powers were adjusted such that the same thermal β_T was obtained (~ 1.3%). This involved scaling the input powers approximately as B^2. Due to the difficulty in adjusting the plasma density, ν^* was not kept constant from shot to shot, but varied by a factor ~ 1.7. Since the collisionality scaling of ITERH93-P (gyro-Bohm like) and Bohm like scalings such as ITER89P are similar (~ $\nu^{*-0.3}$) the dataset should be capable of distinguishing the ρ^* scaling. The variation in ρ^* across the dataset is close to a factor 2.

It can be seen from the plot of H_{93} as a function of toroidal field in Fig.8 that confinement progressively decays relative to ITERH93-P as B increases. This is in contrast to the type I ELMy H-mode discharges in JET, which satisfy gyro-Bohm ρ^* scaling [6].

This data suggests that the radiative discharges are not consistent with a gyro-Bohm scaling law. Note also the tendency (Fig.8) for the confinement to approach the type I ELMy discharges at low toroidal field (higher ρ^*).

5. CONCLUSIONS

The scaling of density with power and current in ELMy H-modes in the Mark IIA divertor without added gas fuelling is similar to that seen in Mark I.

With gas fuelling, confinement progressively degrades from equality with the ITERH93-P scaling law. This degradation may be due to interaction caused by increased midplane pressure and recycling which occurs at high gas fuelling due to bypass leaks from the divertor region.

The vertical target plasmas are most tolerant of gas fuelling, maintaining their confinement to higher fuelling rates and producing radiative power fractions of 40-50% with good plasma purity.

There is a maximum density for gas fuelling in any particular plasma configuration. As fuelling rates are increased further the plasma density declines. It has not yet been possible to exceed the Greenwald limit in Mark IIA although operation close to this limit has been possible. The density limit appears to be an inability to maintain fuelling efficiency because of increased ELM activity. JET data supports the conclusion that the density limit becomes lower as divertor closure improves.

Confinement does not degrade relative to the ITERH93-P scaling law at low q in steady-state ELMy discharges. There is a slight degradation at high current but this may be due to insufficient conditioning at high current and power. Low q discharges are more susceptible to n=2 MHD activity in Mark IIA than in Mark I. There is also a significant increase in the number of low q, high current discharges with unexplained reverse H→L transitions.

The confinement scaling in JET radiative divertor ELMy H-modes at constant shape, q and β is not consistent with a gyro-Bohm scaling such as ITERH93-P. Further work is needed on truly dimensionless discharges in this regime to determine the precise dependence on ρ^*.

REFERENCES

[1] JET TEAM (presented by G. Vlases), IAEA-CN-64/A4-1, this volume.

[2] JET TEAM, Plasma Phys. Control. Fusion 37 (1995) 227.

[3] STORK, D., et al., in Controlled Fusion and Plasma Physics (Proc. 22nd Eur. Conf. Bournemouth, 1995), Vol. 19C, Part II, European Physical Society, Geneva (1995) 125.

[4] JET TEAM (presented by L.D. Horton), paper presented at 23rd Eur. Conf. Controlled Fusion and Plasma Physics, Kiev, 1996, to be published in Plasma Phys. Control. Fusion.

[5] SAIBENE, G., et al., in Plasma-Surface Interactions (Proc. 12th Int. Conf. St. Raphael, 1996), to be published in J. Nucl. Mater.

[6] JET TEAM (presented by J.G. Cordey), IAEA-CN-64/AP1-2, this volume.

DISCUSSION

R.J. HAWRYLUK: You presented very encouraging data about maintaining high values of H at $q_\Psi < 3$. Has this enabled you to optimize the fusion power at $q_\Psi < 3$ as well?

D. STORK: In the case of JET, the optimization of fusion power (as represented by the Q_{DT} figure of merit) is performed in ELM free discharges, such as the hot ion H mode, rather than the ELMy H modes which were the subject of my talk. For these ELM free H modes, as is shown in the talk presented by my colleague P.J. Lomas (IAEA-CN-64/A1-5), the optimum value of q remains above 3. In the case of the JET hot ion H mode, the optimum is in the region of $3.1 < q \leq 3.8$.

S. ISHIDA: You showed a high performance ELMy H mode discharge at low q. What is the value of normalized beta for this discharge?

D. STORK: The high current ELMy H modes have relatively low normalized beta values. The 4.7 MA discharges have typical normalized beta values of around 1.1–1.2. So far, this value is limited by the power which we have been able to couple into the discharges.

STABILITY IN HIGH GAIN PLASMAS IN DIII-D*

E.A. LAZARUS[1], G.A. NAVRATIL[2], E.J. STRAIT, B.W. RICE[3], J.R. FERRON, C.M. GREENFIELD, M.E. AUSTIN[4], D.R. BAKER, K.H. BURRELL, T.A. CASPER[3], V.S. CHAN, J.C. DeBOO, E.J. DOYLE[5], R.D. DURST[6], C.B. FOREST, P. GOHIL, R.J. GROEBNER, W.W. HEIDBRINK[7], R.-M. HONG, W.A. HOULBERG[1], A.W. HOWALD, C.-L. HSIEH, A.W. HYATT, G.L. JACKSON, J. KIM, R.J. LA HAYE, L.L. LAO, C.J. LASNIER[3], A.W. LEONARD, J. LOHR, R. MAINGI[8], R.L. MILLER, M. MURAKAMI[1], T.H. OSBORNE, L.J. PERKINS[3], C.C. PETTY, C.L. RETTIG[5], T.L. RHODES[5], S.A. SABBAGH[2], D.P. SCHISSEL, J.T. SCOVILLE, A.C.C. SIPS[9], R.T. SNIDER, F.X. SÖLDNER[9], H.E. St. JOHN, G.M. STAEBLER, B.W. STALLARD[3], R.D. STAMBAUGH, R.E. STOCKDALE, P.L. TAYLOR, T.S. TAYLOR, D.M. THOMAS, A.D. TURNBULL, M.R. WADE[1], D.G. WHYTE[10], R.D. WOOD[3]
General Atomics,
San Diego, California,
United States of America

Abstract

STABILITY IN HIGH GAIN PLASMAS IN DIII-D.

Fusion power gain has been increased by a factor of 3 in DIII-D through the use of strong discharge shaping and tailoring of the pressure and current density profiles. H-mode plasmas with weak or negative central magnetic shear are found to have neoclassical ion confinement throughout most of the plasma volume. Improved MHD stability is achieved by controlling the plasma pressure profile width. The highest fusion power gain Q (ratio of fusion power to input power) in deuterium plasmas was 0.0015, which extrapolates to an equivalent Q of 0.32 in a deuterium–tritium plasma and is similar to values achieved in tokamaks of larger size and magnetic fields.

---

* Work supported by US Department of Energy contracts DE-AC03-89ER51114, DE-AC05-96OR22464 and W-7405-ENG-48, and grants DE-FG03-86ER53266 and NDE-FG05-86ER5.

[1] Oak Ridge National Laboratory, Oak Ridge, Tennessee, USA.
[2] Columbia University, New York, N.Y., USA.
[3] Lawrence Livermore National Laboratory, Livermore, California, USA.
[4] University of Maryland, College Park, Maryland, USA.
[5] University of California, Los Angeles, California, USA.
[6] University of Wisconsin, Madison, Wisconsin, USA.
[7] University of California, Irvine, California, USA.
[8] Oak Ridge Associated Universities, Oak Ridge, Tennessee, USA.
[9] JET Joint Undertaking, Abingdon, Oxfordshire, United Kingdom.
[10] INRS-Energie et Materiaux, Varennes, Quebec, Canada.

1. INTRODUCTION

A compact, economical tokamak fusion power plant requires both good energy confinement and magnetohydrodynamic (MHD) stability at high beta. Recent experiments [1–3] have demonstrated greatly improved core confinement in tokamak plasmas with negative central magnetic shear (NCS), while ideal MHD calculations [4–6] predict that a central region with negative shear in the safety factor will enhance plasma stability. (Here $\beta = 2\mu_0 \langle p \rangle / B^2$ is the ratio of plasma pressure to magnetic field pressure, while the magnetic shear is defined as $(2V/q)dq/dV$ where q is the tokamak safety factor and V is the volume enclosed by a flux surface.) Earlier studies [7] have also shown the importance of strong discharge shaping in improving plasma stability.

High performance plasmas with negative central shear are an important part of the DIII–D research program toward tokamak concept improvement [8]. Control of the initial current density profile leads to reduction of the ion thermal conduction to neoclassical transport levels, [9,10] correlated with suppression of microturbulence by **E**×**B** flow shear [11]. Strong discharge shaping and tailoring of the pressure profile improve the MHD stability of NCS plasmas at high beta, [12] leading to record values of fusion reactivity in DIII–D [13]. These results offer the prospect of reduction in the size and field required for achieving higher gain approaching fusion ignition conditions in a plasma and support the viability of the concept [14] of a smaller, economically attractive tokamak power plant [15] through tailoring of the equilibrium profiles.

2. STABILITY OF NCS PLASMAS

Modification of the current density profile in DIII–D leads to plasmas with enhanced core confinement and strongly peaked pressure profiles. Low power neutral beam injection (NBI) during the initial plasma current ramp produces a target plasma with negative central magnetic shear, [16] which develops a core transport barrier as the heating power is increased. H–mode plasmas have an additional transport barrier near the edge, leading to a broader pressure profile. However, NCS plasmas with an L–mode edge exhibit strongly peaked pressure profiles but invariably disrupt at values of normalized beta $\beta_N = \beta aB/I \sim 2$, about a factor of two less than the values achieved in H–mode [17,18].

This lower L–mode beta limit is consistent with ideal and resistive MHD stability limits. [12] Ideal n=1 kink mode calculations for strongly shaped plasma cross sections predict significant increases in the stability limits for both β and β^* as the pressure profile becomes broader, accompanied by a large increase in plasma reactivity, as shown in Fig. 1. (The rms-average beta, $\beta^* = 2\,\mu_0\,\langle p^2 \rangle^{1/2}/B^2$, is more representative of fusion reactivity.) In contrast, the β^* limit has little improvement with the width of the pressure profile in circular cross-section discharges. The disruption itself is consistent with a related resistive instability lying just below the ideal stability limit. [17,19]

Modification of the pressure profile improves the stability, avoiding disruptions and allowing the discharge to reach significantly higher beta and higher fusion performance. The experimental tool used is the timing of the L-H transition, with the transition to H–mode serving to broaden the pressure profile. The evolution of an L–mode and an H–mode plasma are compared in Fig. 2. Small, controlled changes in plasma shape induce an H–mode transition in one case at 2.1 s, indicated by the edge pressure rise [Fig. 2(c)]. The L–mode case disrupts at about 2.25 s [Fig. 2(a)]. The H–mode plasma continues to increase its stored energy [Fig. 2(d)] and fusion reaction

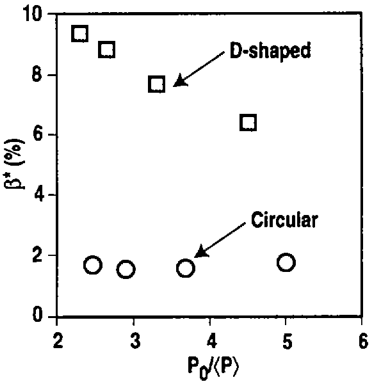

FIG. 1. Maximum β^* (fusion weighted β) stable to the ideal $n = 1$ kink mode versus pressure peaking factor $p_0/\langle p\rangle$, for profiles of the form $p = p_0(1 - \rho^2)^\alpha$. Results are shown for a circular cross section and a D-shaped cross section with elongation 1.7 and triangularity 0.7.

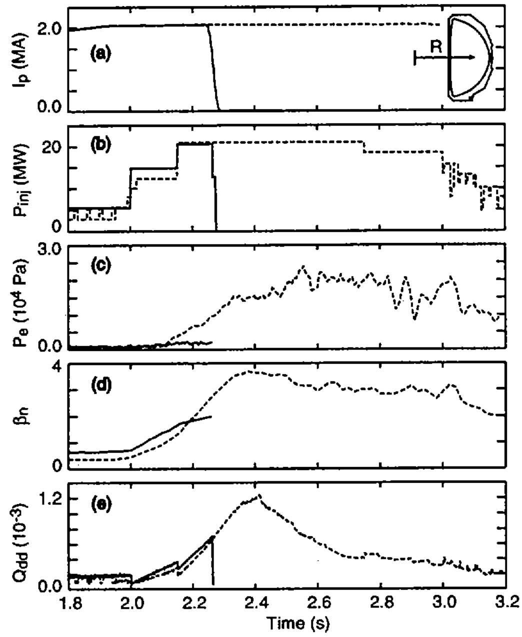

FIG. 2. Time evolution of two similar discharges: 87887 (solid line), which remains in L-mode and disrupts, and 87937 (broken line), which makes a transition to H-mode at 2.1 s. (a) Plasma current; (b) injected neutral beam power; (c) edge electron pressure; (d) β_N (= $\beta aB_t/I_p$) in units %, m, T/MA; (e) Q_{dd} = P_{fusion}/P_{NB}.

rate [Fig. 2(e)] until a stability limit is reached at $\beta_N = 3.7$. The broadening of the pressure profile after the L–H transition is shown in Fig. 3, where profiles are shown just prior to the disruption of the L–mode plasma and 0.125 s after the L–H transition for the H–mode case.

The improved stability with a controlled L-H transition has led to record reactivity for DIII–D plasmas, as shown in Fig. 4 where the D-D fusion neutron rate S_n in discharges with an NCS target phase is plotted against heating power. The L–mode plasmas (solid squares), which typically have pressure peaking ratios $p_0/\langle p\rangle$ in the range 4–5, consistently produce a lower S_n and terminate in a disruption, while H–mode plasmas with $p_0/\langle p\rangle \sim 2$–3 reach much higher S_n. A large shaded circle indicates the discharge with the highest fusion power gain Q (ratio of fusion power to input power), to be discussed below.

The discharges with a broad pressure profile do not typically disrupt, and reach values of β significantly higher than discharges with strong pressure peaking. Eventually they reach stability limits which depend, at least in part, on the form of the q-profile. Figure 5 compares the evolution of the neutron emission, a sensitive indicator of the quality of core confinement, in three discharges with different initial q-profiles.

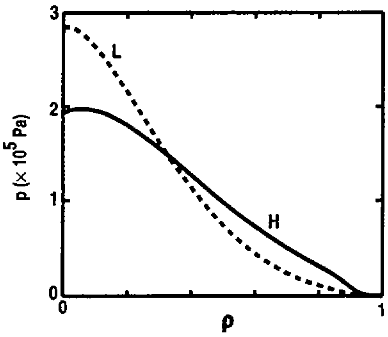

FIG. 3. *Pressure profiles for discharges 87887 (L) and 87937 (H) at 2245 ms, showing the broadening of the H-mode versus ρ, the square root of toroidal normalized flux. The time evolution of these discharges is shown in Fig. 2.*

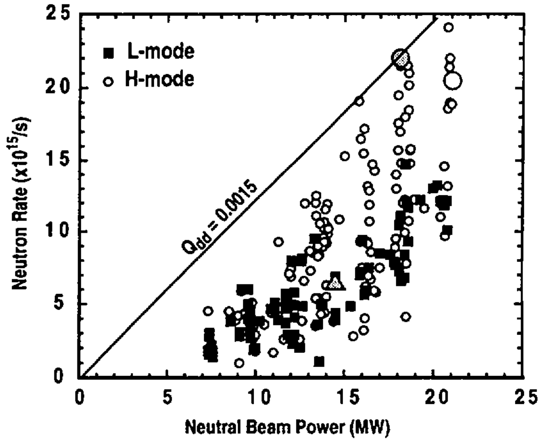

FIG. 4. *Results from this experiment displayed as peak neutron rate, S_n, versus neutral beam power. The solid squares are L-mode plasmas and the open circles are H-mode. The large shaded circle is discharge 87977, discussed in Figs 5 and 6 and Table I. The large open circle is discharge 87937, shown in Figs 2 and 3.*

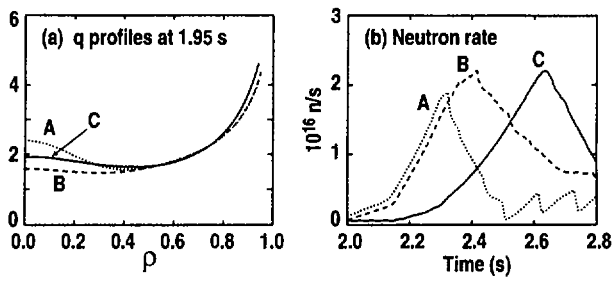

FIG. 5. *Comparison of (a) "target" q-profiles before high-power heating and (b) time evolution of the neutron rate, in discharges 87977 (solid lines), 87937 (dashed lines), and 87953 (dotted lines).*

The initial rate of rise of neutron emission in Cases A and B is comparable, indicating similar behavior in the core, while reduced heating power leads to a somewhat slower initial rise in Case C.

Case A (discharge 87953, with strongly negative central shear) suffers a collapse of the central pressure at t = 2.32 s. Earlier, at about t = 2.28 s, this discharge develops a non-rotating n=1 mode near the edge, in the positive shear region. We speculate that this is a consequence of the large current density gradient near the edge, combined with insufficient rotation to maintain wall stabilization. Resistive stability analysis is in progress. The non-rotating mode initially has very little effect on the core plasma and neutron rate. However, the large stationary island reduces the pressure in the outer part of the plasma leading to a steep pressure gradient in the region of the internal transport barrier. The central collapse is caused by a rapidly growing internal mode, presumably a global resistive mode lying near the ideal stability boundary. The observed internal instability is located in the high pressure gradient region and has a large n=2 component. This is consistent with ideal stability calculations showing that the discharge is stable to n=1, but is marginally unstable to an n=2 kink mode, within the uncertainty of the experimentally measured pressure gradient.

Case B (discharge 87937, also shown as the H–mode case in Fig. 3) has weaker, but still negative, central shear. In this discharge there is no locked mode, but the onset of ELMs at t = 2.32 s leads to mild saturation of the neutron rate and reduction of the edge pressure. The central collapse occurs about 100 ms later than in Case A, after the discharge has reached a higher beta and neutron emission. The collapse is caused by combined internal n=3 and n=2 modes, similar to that of Case A and again near the calculated n=2 ideal stability limit.

Case C (discharge 87977, with highest fusion power gain as discussed below) also has weakly negative central shear with slightly higher central q. It does not have a central collapse but shows a gentle saturation and decline in neutron emission after the onset of ELMs at t = 2.62 s. The ELMs are correlated with MHD instabilities having toroidal mode number n~4, located near the plasma edge. This is in qualitative agreement with ideal high-n ballooning stability calculations which show that the discharge has a broad central region of access to the second stable regime extending over at least half the minor radius, but has reached the first regime stability limit near the edge in the region of the H–mode transport barrier.

The density rise which occurs during H–mode is probably also an important factor in the evolution of these discharges, broadening the neutral beam deposition profile and reducing the central source of energy and momentum needed to sustain the internal transport barrier. Although there is initially no direct effect on discharge performance, this may be the reason that Cases A and B cannot recover from their relatively mild central instabilities. Broadening of the beam deposition may also be the reason for the slow decline of performance in Case C even in the absence of a central instability. The high-triangularity pumped divertor now being installed in DIII–D should make it possible to control the density and maintain central beam deposition in high-performance NCS discharges.

3. TRANSPORT IN NCS PLASMAS

In the discharge with maximum fusion power gain, transport is reduced to neoclassical levels nearly everywhere in the plasma. [9,10] Analysis of discharge 87977 with the TRANSP [20] code shows that the dominant power flow is from the neutral beams to the ions, with the dominant loss terms being convection and collisional transfer to the electron channel. Here we use an effective ion thermal diffusivity $\chi_i^{tot} = Q_i^{tot}/(n_i \nabla T_i)$, avoiding the difficulty of separating the ion heat loss into convective and conductive parts, and in Fig. 6 we compare the experimental χ_i^{tot} to the Chang-Hinton formula [21] for neoclassical diffusivity. This formula is derived in the limit of circular flux surfaces at finite aspect ratio with a correction accounting for an impurity concentration. At a representative time during the L–mode high-power phase (Fig. 6(a)) χ_i^{tot} approaches the neoclassical value in the center of the plasma. A dramatic reduction in ion transport occurs during the H–mode phase [Fig. 6(b)]. At a time near the peak

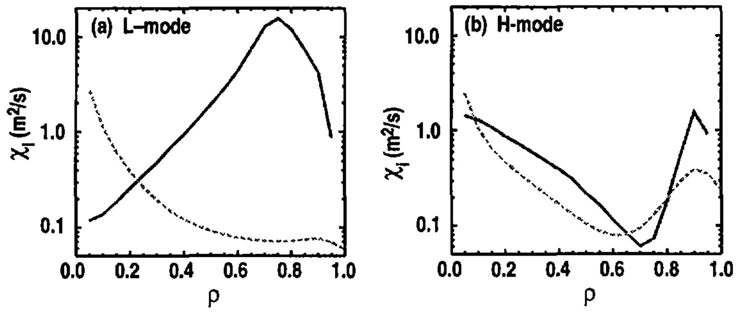

FIG. 6. Ion thermal diffusivity versus ρ, square root of the normalized toroidal flux. The solid lines are the experiment and the dashed lines are the calculated neoclassical values. Representative time during (a) the high power L-mode phase and (b) the H-mode phase in discharge 87977.

neutron rate and with β in excess of 6%, χ_i^{tot} over the entire plasma is comparable to the neoclassical level. In a more complete treatment using the formulation of Hirshman and Sigmar [22] with the actual equilibrium geometry, the experimentally measured ion heat flux again is consistent with neoclassical predictions [9].

Density fluctuations, measured with far-infrared scattering and beam emission spectroscopy diagnostics, show reductions which correlate well with the observed reduction of the ion transport, suggesting micro turbulence as responsible for the transport. [11] The measured E×B flow shear is sufficient to stabilize ion temperature gradient modes [17], and the large extent of the region of neoclassical level ion transport is consistent with theoretical modeling of suppression of turbulence at high power which can allow a transport bifurcation to develop.[23] In these experiments in DIII–D the E×B flow shear is predominantly driven by toroidal rotation and not the ion pressure gradient.

4. HIGH FUSION GAIN PLASMAS

As shown in Fig. 4, several discharges in these experiments have reached fusion power gains Q_{dd} of about 0.0015. A fusion gain of $Q_{dt} = 0.32$ is projected for a deuterium-tritium plasma under the same conditions as discharge 87977. This estimate of Q_{dt} is obtained from the ratio $Q_{dt}/Q_{dd} = 222$ predicted by simulations using the TRANSP analysis code. No isotopic transport improvements were assumed in the simulations. The measured profiles of 87977 (temperatures, densities, toroidal rotation) were maintained in the simulation and the deuterium was replaced with a nominal 50:50 mixture of deuterium and tritium. The Q_{dt} value is found to be insensitive to uncertainties in the plasma equilibrium, and the dominant uncertainty in Q_{dd} is the 15% statistical uncertainty in the measurement of the neutron emission rate S_n. The peak value $S_n = 2.2 \times 10^{16}$ s^{-1} was measured with a calibrated scintillation counter. Values of $S_n = 2.3 \times 10^{16}$ s^{-1} measured with a fission product counter and $S_n = 2.5 \times 10^{16}$ s^{-1} from a TRANSP calculation using the measured temperature, density and rotation profiles provide confidence in these results.

For purposes of comparison between tokamaks and extrapolation to future devices, we wish to express Q_{dd} in a way that clearly separates the effects of machine size and field strength from the intrinsic plasma properties of confinement and stability. The fusion gain, Q, is given by

$$Q_{dd} = \frac{1}{2}\frac{\int n_i^2 \overline{\sigma v}\xi_r dV}{P_{input}} \cong \frac{\overline{\sigma v}\xi_r}{2T_i^2}\frac{\langle p^2\rangle}{\langle p\rangle^2}\frac{(2\pi R)\pi a^2 \kappa \langle p\rangle^2}{P_{input}(1+T_e/T_i)^2} \tag{1}$$

For ion temperatures T_i in the range of interest, the fusion reaction rate scales approximately as T_i^2, so $C_f \equiv \overline{\sigma v}\xi_r/2T_i^2$ is approximately constant and the fusion power scales as the square of the plasma pressure. Here the volume is approximated as that of an ellipsoid of revolution. Equation (1) is correct but contains no insight on the relation of Q to tokamak physics. We now describe the plasma geometry by defining an effective inverse aspect ratio E [7,24] in analogy to the usual inverse aspect ratio ε. For diverted plasmas q_{95} is substituted for q in the expression for E.

$$\varepsilon = a/R = q_{cyl}\left(\frac{\mu_0 I_p}{2\pi a B}\right) \Rightarrow E \equiv q_\psi\left(\frac{\mu_0 I_p}{2\pi a B}\right) \tag{2}$$

The energy confinement time is expressed as

$$\tau_E = \frac{W}{P_{input} - dW/dt} = \frac{3}{2}\frac{(2\pi R)\pi a^2\kappa}{P_{input} - dW/dt}\frac{\beta B^2}{2\mu_0} \tag{3}$$

A simple scaling for global confinement time in ELM-free H–mode plasmas [25], DIII–D/JET scaling can be approximated as

$$\tau_E = \frac{W}{P_{input} - dW/dt} = 1.1 \times 10^{-4} \cdot H_{JD}\frac{I_p R^{3/2}}{\sqrt{P_{input} - dW/dt}} \tag{4}$$

(in SI units) where H_{JD} is an enhancement factor over the original scaling. Combining the above relations we find

$$Q_{dd} = 1.2 \times 10^{-8}\left[\frac{8C_f}{9\mu_0^2(1+T_e/T_i)^2}\right] B^2R^2 \left[\frac{\beta^*}{\beta}\right]^2 \left[\frac{E}{\sqrt{\kappa}q}\right]^2 H_{JD}^2. \tag{5}$$

The quantity B^2R^2, proportional to the square of the center post current, represents the stress limit in tokamak construction. The shaping factor E is related to n=0 stability, [24] while q and the pressure profile peaking factor, (β^*/β), are related to n=1 stability. In DIII-D, the quantity $(\beta^*/\beta) \cdot (E/q\sqrt{\kappa})$ appears to reach values quite close to the ideal MHD stability limitation. The confinement scaling and the enhancement factor, H_{JD}, are strictly empirical.

To demonstrate more clearly how these results extrapolate to requirements for achieving higher gain approaching fusion ignition conditions in a plasma, we separate

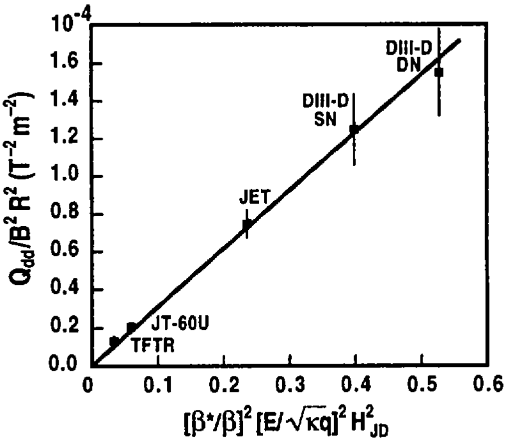

FIG. 7. Q^*_{dd} versus scaling relation discussed in the text for the highest DIII-D Q_{dd} and the highest values reported by TFTR, JET, and JT-60.

TABLE I. COMPARISON OF D–D FUSION REACTIVITY FOR SEVERAL TOKAMAKS

	DIII-D (double-null)	DIII-D (single-null)	TFTR [28]	JT-60U [27]	JET [26]
Discharge	87977	88964	68522	17110	26087
B (T)	2.15	2.15	5.00	4.40	2.80
R (m)	1.67	1.69	2.50	3.05	2.95
$E/\kappa^{1/2}$	0.98	0.76	0.35	0.39	0.60
H_{JD}	2.4	2.6	1.2	1.8	2.3
q	4.2	3.7	3.8	4.0	3.8
τ_E (s)	0.40	0.43	0.19	0.54	1.30
β (%)	6.7	5.8	1.0	1.5	2.2
$\langle p^2\rangle/\langle p\rangle^2$ [a]	1.6	1.3	3.0	2.0	1.8
Q^*_{dd}	0.0020	0.0016	0.0021	0.0037	0.0051

[a] Estimated from the ratio of peak to average pressure. A radial profile of the form $p(\rho) \propto (1 - \rho^2)^\alpha$ is assumed, yielding $\alpha = p_0/\langle p\rangle - 1$ and $f_p = \langle p^2\rangle/\langle p\rangle^2 = (\alpha + 1)^2/(2\alpha + 1)$.

the parametric dependence of Q_{dd} on primarily economic and technological factors, B^2R^2, from the dependence on dimensionless plasma parameters, $[(\beta^*/\beta)\cdot(E/q\sqrt{\kappa})H_{JD}]^2$. Calculations similar to those in Ref. [15], with the reactor design systems code (SuperCode) show that the capital cost of the tokamak reactor core increases approximately linearly with B^2R^2. As shown in Fig. 7, the simple expression for $Q_{dd}/(BR)^2$ given by Eq. (5) is adequate to describe the highest performance plasmas in several other tokamaks. [26,27,28] For purposes of comparison with other published values we have plotted $Q^*_{dd} \equiv P_t/(P_{NBI} - \dot{W}) + (P_{bt} + P_{bb})/P_{NBI}$, where P_t, P_{bt}, and P_{bb} are the fusion powers from thermal-thermal, beam-thermal, and beam-beam reactions respectively. Here both the thermonuclear fusion reaction rate and the energy confinement time are referenced to the input power which would be required to sustain the plasma's thermal energy in steady state. Details such as impurity concentration, individual form factors for temperature and density profiles, T_i/T_e, the thermal fraction of fusion power, and neutral beam deposition profile are sufficiently similar to be ignored. Additionally, all are free of sawteeth because of the current profile. The confinement factor, H_{JD}, is determined from the experimental data and no predictive capability is implied. The relative importance of the individual terms in the abscissa is shown in Table I.

Normalized to B^2R^2 the fusion gain results reported here are between 2 and 9 times larger than those achieved in other tokamaks, primarily as a consequence of strong shaping and enhanced confinement. As shown in Table I, DIII–D has smaller *B* and *R* than the other tokamaks listed, but this is counterbalanced by the strong shaping and associated enhanced confinement which allow it to operate at higher beta with modest input power.

Low-triangularity single-null DIII–D discharges with negative central shear [29] are also consistent with the scaling for Q_{dd}. The discharge shape and profiles are shown in Fig. 8. These discharges extend the regime of neoclassical core confinement associated with negative or weak central magnetic shear to plasmas with the low safety factor ($q_{95} \sim 3.3$) and triangularity ($\delta \sim 0.3$) anticipated in future tokamaks such as ITER. Energy confinement times exceed the ITER–89P L–mode scaling law by up to a factor of 4, and are almost twice as large as in previous single-null cases with $3 \le q_{95} \le$

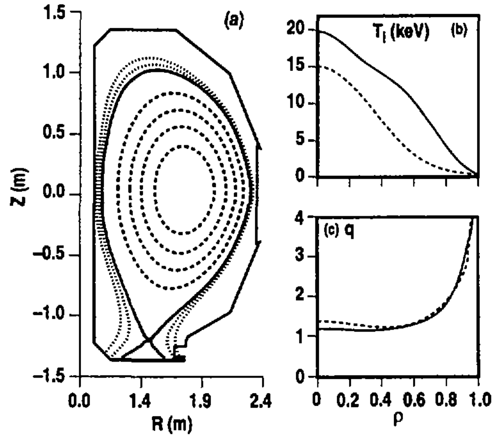

FIG. 8. High performance single-null plasma with negative central shear (88964), showing (a) the plasma shape with (b) T_i and (c) q profiles at times with an L-mode edge (broken lines, t = 2.1 s) and an H-mode edge (solid lines, t = 2.4 s).

4. The normalized beta [β (aB/I)] reaches values as high as 4, comparable to the best previous single-null discharges, with no confinement deterioration. The peak fusion power gains of $Q_{dd} = 1.0 \times 10^{-3}$ and D-D neutron rates of 1.4×10^{16} s^{-1} are more than double the previous maximum values for single-null discharges. Although high triangularity allows a larger plasma current and theoretically a higher β-limit, the fusion gain in these low triangularity plasmas is similar to that of high triangularity double-null plasmas at the same plasma current. These results are favorable for advanced performance operation in ITER, JT-60U and for D-T experiments in JET; high performance experiments in deuterium NCS plasmas have recently begun in JET with encouraging results [30].

5. CONCLUSIONS

In conclusion, control of the pressure profile has been accomplished by selective timing of the L-H transition. The resulting increase in β^* is consistent with expectations based on ideal MHD stability calculations. The plasmas exhibit a neoclassical level of ion transport in the core during the L–mode phase and this level extends over the entire plasma cross-section after the L-H transition. Negative magnetic shear early in the discharge appears to be a necessary condition in achieving good core confinement. However, later in the discharge other mechanisms are responsible for transport reduction, and the details of the shear profile become less important to the ion transport. The highest-performance plasmas evolve to a weakly negative or weakly positive shear in the central region. Plasmas with increased shear reversal show similar ion transport but reduced stability in that they collapse at lower β^*. The improved stability and confinement has allowed DIII–D to achieve a fusion gain in deuterium plasmas of $Q_{dd} = 0.0015$, which extrapolates to $Q_{dt}^{equiv} = 0.32$ in a deuterium-tritium mixture. The Q_{dd} is comparable to that achieved in larger tokamaks with higher magnetic fields.

REFERENCES

[1] HUGON, M., et al., Nucl. Fusion **32** (1992) 33.
[2] STRAIT, E.J., et al., Phys. Rev. Lett. **75** (1995) 4421.
[3] LEVINTON, F.M., et al., Phys. Rev. Lett. **75** (1995) 4417.
[4] SYKES, A., TURNER, M.F., in Controlled Fusion and Plasma Physics (Proc. 9th Eur. Conf. Oxford, 1979), European Physical Society, Geneva (1979).
[5] TURNBULL, A.D., et al., Phys. Rev. Lett. **74** (1995) 718.
[6] KESSEL, C., et al., Phys. Rev. Lett. **72** (1995) 1212.
[7] LAZARUS, E.A., et al., Phys. Fluids B **3** (1991) 2220.
[8] CHAN, V.S., et al., IAEA-CN-64/O1-6, this volume.
[9] LAZARUS, E.A., et al., Phys. Rev. Lett. **77** (1996) 2714.
[10] SCHISSEL, D., et al., IAEA-CN-64/A5-3, this volume.
[11] DOYLE, E.J., et al., IAEA-CN-64/A6-4, ibid.
[12] TURNBULL, A.D., et al., IAEA-CN-64/DP-1, these Proceedings, Vol. 2.
[13] LAZARUS, E.A., et al., Nucl. Fusion **37** (1997) 7.
[14] TAYLOR, T.S., et al., Plasma Phys. Control. Fusion **36** (1994) B229.
[15] GALAMBOS, J.D., et al., Nucl. Fusion **35** (1995) 551.
[16] RICE, B.W., et al., Plasma Phys. Control. Fusion **38** (1996) 869.
[17] LAO, L.L., et al., Phys. Plasmas **3** (1996) 1951.

[18] RICE, B.W., et al., Phys. Plasmas 3 (1996) 1983.
[19] CHU, M.S., et al., Phys. Rev. Lett. 77 (1996) 2710.
[20] GOLDSTON, R.J., et al., J. Comput. Phys. 43 (1981) 61.
[21] CHANG, C.S., HINTON, F.L., Phys. Fluids 29 (1986) 3314.
[22] HIRSHMAN, S.P., SIGMAR, D.J., Nucl. Fusion 21 (1981) 1079.
[23] STAEBLER, G.M., et al., Phys. Plasmas 1 (1994) 99.
[24] LAZARUS, E.A., et al., Phys. Fluids B 4 (1992) 3644.
[25] SCHISSEL, D.P., et al., Nucl. Fusion 31 (1991) 73.
[26] JET TEAM, Nucl. Fusion 32 (1992) 187.
[27] NISHITANI, T., et al., Nucl. Fusion 34 (1994) 1069.
[28] HAWRYLUK, R.J., et al., in Plasma Physics and Controlled Nuclear Fusion Research 1994 (Proc. 15th Int. Conf. Seville, 1994), Vol. 1, IAEA, Vienna (1995) 11.
[29] STRAIT, E.J., et al., in Controlled Fusion and Plasma Physics (Proc. 23rd Eur. Conf. Kiev, 1996), Vol. 20C, European Physical Society, Geneva (1996).
[30] JET TEAM, IAEA-CN-64/A5-5, this volume.

DISCUSSION

K. LACKNER: As Q_{DT}^{eff} increases there should be a shift of the major contribution from beam–target to thermal reactions. How can you obtain a uniform scaling across a large range of Q_{DT}?

G.A. NAVRATIL: The relation presented is for Q_{DD} and includes only the contributions from thermal fusion reactions. Since for three of the comparison experiments the thermal contribution to Q_{DD} is between 50% and 60% and only the result from TFTR is somewhat lower than 50%, the linear relationship we obtain is expected.

Y.-K.M. PENG: Are there MHD β limit calculations for the cases with $\beta_N \geq 4$? If so, is a nearby conducting shell needed to provide stability for such plasmas?

G.A. NAVRATIL: Yes, the low n stability of these high gain plasmas was modelled including the effects of a nearby conducting wall, and they were found to be stable. However, a systematic study of the effect of varying the wall position to assess quantitatively the contribution of the wall to increasing the β limit has not yet been completed.

F.X. SÖLDNER: The peaked pressure profiles suggest that the bootstrap current profile is not aligned with the total current profile but is also peaked. Does this mean that additional non-inductive off-axis current drive is still required?

G.A. NAVRATIL: In these plasmas the bootstrap current contributes only 30–40% of the total toroidal plasma current. To prevent the q profile from continuing to evolve will require additional non-inductive current drive.

M.G. BELL: I was interested that you chose to identify the regime of higher Q_{DD} with negative central shear, since you indicated that q was actually monotonic during the highest performance phase. Would you comment on whether NCS is responsible for the improvement or merely the fact that $q_0 > 1$ (and sawteeth are thereby suppressed).

G.A. NAVRATIL: The use of NCS plasma targets prior to the application of the high power beam heating phase does appear to be necessary for establishing a high performance core plasma with improved confinement. However, once the high pressure plasma core with $T_i > 2T_e$ is established, the relaxation of the q profile to neutral or even weakly positive shear does not lead to loss of the confinement improvement.

TRANSPORT PHYSICS IN REVERSED SHEAR PLASMAS

F.M. LEVINTON[1], S.H. BATHA[1], M.A. BEER[2], M.G. BELL[2], R.E. BELL[2], R.V. BUDNY[2], C.E. BUSH[3], P.C. EFTHIMION[2], E. MAZZUCATO[2], R. NAZIKIAN[2], H.K. PARK[2], A.T. RAMSEY[2], G.L. SCHMIDT[2], S.D. SCOTT[2], E.J. SYNAKOWSKI[2], G. TAYLOR[2], S. VON GOELER[2], M.C. ZARNSTORFF[2]

[1]Fusion Physics and Technology, Inc.,
Torrance, California

[2]Plasma Physics Laboratory,
Princeton University,
Princeton, New Jersey

[3]Oak Ridge National Laboratory,
Oak Ridge, Tennessee

United States of America

Abstract

TRANSPORT PHYSICS IN REVERSED SHEAR PLASMAS.

Reversed magnetic shear is considered a good candidate for improving the tokamak concept because it has the potential to stabilize MHD instabilities and reduce particle and energy transport. With reduced transport, the high pressure gradient would generate a strong off-axis bootstrap current and could sustain a hollow current density profile. Such a combination of favorable conditions could lead to an attractive steady-state tokamak configuration. Indeed, a new tokamak confinement regime with reversed magnetic shear has been observed on the Tokamak Fusion Test Reactor (TFTR) where the particle, momentum, and ion thermal diffusivities drop precipitously, by over an order of magnitude. The particle diffusivity drops to the neoclassical level and the ion thermal diffusivity drops to much less than the neoclassical value in the region with reversed shear. This enhanced reversed shear (ERS) confinement mode is characterized by an abrupt transition with a large rate of rise of the density in the reversed shear region during neutral beam injection, resulting in nearly a factor of three increase in the central density to $\sim 1.2 \times 10^{20}$ m^{-3}. At the same time the density fluctuation level in the reversed shear region dramatically decreases. The ion and electron temperatures, which are about 20 keV and 7 keV respectively, change little during the ERS mode. The transport and transition into and out of the ERS mode have been studied on TFTR with plasma currents in the range 0.9–2.2 MA, with a toroidal magnetic field of 2.7–4.6 T, and the radius of the $q(r)$ minimum, q_{min}, has been varied from r/a = 0.35 to 0.55. Toroidal field and co/counter neutral beam injection toroidal rotation variations have been used to elucidate the underlying physics of the transition mechanism and power threshold of the ERS mode.

1. Introduction

The economic attractiveness of the tokamak as a candidate for a fusion reactor depends on development of a magnetic configuration that has good confinement, stability, and low recirculating power for steady state current drive. This requires a high fraction of self-sustaining bootstrap current that is well aligned with an optimized current density profile for confinement and stability. Recent studies[1] of the optimization of the current density profile suggest that reversed magnetic shear (i.e., a hollow current density profile), is desirable for confinement, stability, and bootstrap alignment. Shear is defined as $s \equiv (2V/q)(dq/d\psi)(d\psi/dV) \approx (r/q)(dq/dr)$, where ψ is the enclosed poloidal flux, V is the enclosed volume, q is the safety factor and r is the minor radius. Reversed shear, $s < 0$, is thought to be important because it can stabilize some classes of microinstabilities such as trapped electron modes[2,3], a candidate which may explain the observed anomalous electron transport in tokamaks. Reversed magnetic shear can also stabilize some magnetohydrodynamic (MHD) instabilities such as ballooning modes[4] and resistive tearing modes. If improved core confinement can be attained, the high pressure gradient would generate a strong off-axis bootstrap current which may sustain the hollow current density profile. This scenario may lead to an attractive concept for a steady state tokamak reactor[5]. Most tokamaks operate with inductive current drive which normally produces a peaked current density profile at the magnetic axis due to the strong dependence of the plasma conductivity on the electron temperature. Only by non-inductive current drive or transient techniques can a hollow current density profile be generated. This has been done in several experiments reporting improved confinement[6–8] and stability[9]. In addition, several other experiments have reported the stabilization of MHD modes in the high β_p regime[10–12].

Recent experiments on the Tokamak Fusion Test Reactor (TFTR)[13] have demonstrated a reversed shear configuration with greatly improved particle and ion thermal transport[5,14] in the reversed shear region that is more than an order of magnitude lower than reported in previous experiments, including reversed shear experiments. The $q(R,t)$ profile is obtained from the motional Stark effect (MSE) polarimeter[15,16] measurement of the local magnetic field pitch, in contrast to the indirect methods used in many previous experiments. The diagnostic provides good temporal and spatial resolution and shows the correlation of the magnetic shear with changes in transport. This regime of operation holds promise for significantly improving the tokamak reactor concept and can lead to a dramatic increase in the performance of present tokamaks.

2. Reversed Shear Formation

With the use of early neutral beam injection (NBI) to heat the plasma and drive current a reversed shear q—profile can be obtained. The early NBI heat-

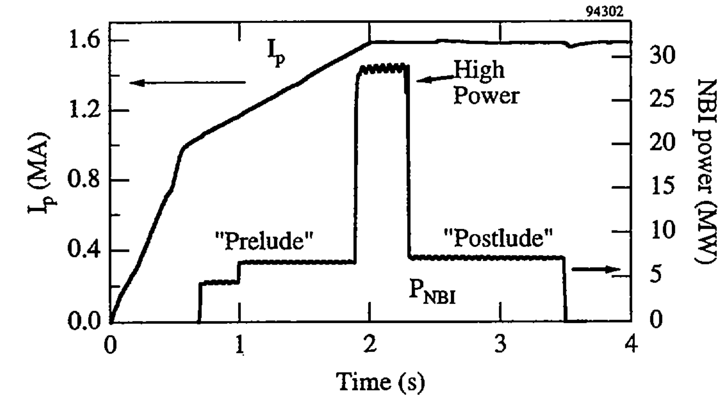

FIG. 1. Plasma current and neutral beam power for a 1.6 MA reversed shear discharge.

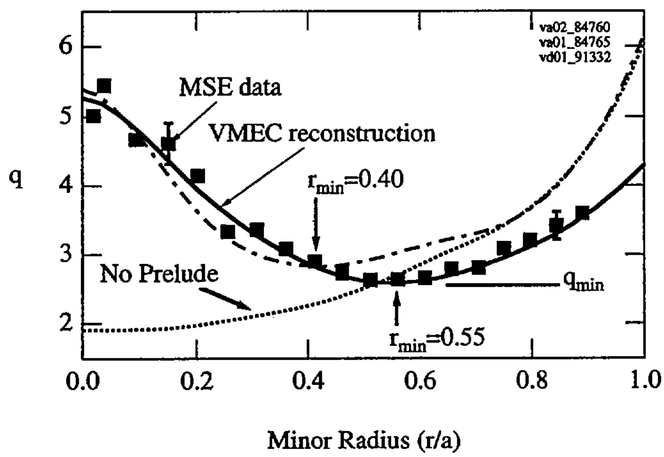

FIG. 2. q-profiles at the beginning of the current flattop at t = 2 s for a 1.6 MA startup (dashed-dotted line), a fast ramp 2.2 MA startup (solid line) with MSE data and a case with no early NBI heating phase (dotted line).

ing during the plasma current ramp phase increases the electron temperature to several kilo-electronvolts and the current penetration time increases to $\sim$ 10 seconds, resulting in a hollow current density profile and a reversed shear q—profile that can be maintained for several seconds. The plasma current is initially increased at a ramp rate of 1.8 MA/s to about 1.0 MA and then at a reduced rate until the final plasma current is reached, as shown in Fig. 1. With variations of the rate of rise of the plasma current and timing of the neutral beam injection a wide range of q—profile minima, q_{min}, and q_{min} radii, r_{min}, can be generated for transport and stability studies. In the plasmas discussed here the major radius is 2.60 m, the minor radius is 0.94 m, and the toroidal field is 4.6 T with an edge safety factor of $\sim 6.2 - 4.3$ corresponding to plasma currents of 1.6-2.2 MA. Plasmas at lower toroidal field with $q(a) \sim 6.2$ have also been investigated. Typical q-profiles resulting from different current ramp rates and NBI timing are shown in Fig. 2. The profiles have been reconstructed with the VMEC free-boundary equilibrium code[17] from MSE data, kinetic pressure data, calculated fast ion pressure from the TRANSP code[18], and external magnetic data. The uncertainties in $q(R)$ are 10% or less across the profile[19]. The MSE analysis for these $q(R)$ profiles includes corrections due to the plasma radial electric field E_r [20]. The quantities $q(0)$, q_{min}, and r_{min} slowly decrease on a time scale of several seconds and reach $q(0) \sim 3 - 4$, $q_{min} \sim 2$, and $r_{min}/a \sim 0.3 - 0.5$ after three seconds of beam heating, consistent with the neoclassical current diffusion rate and the calculated driven currents.

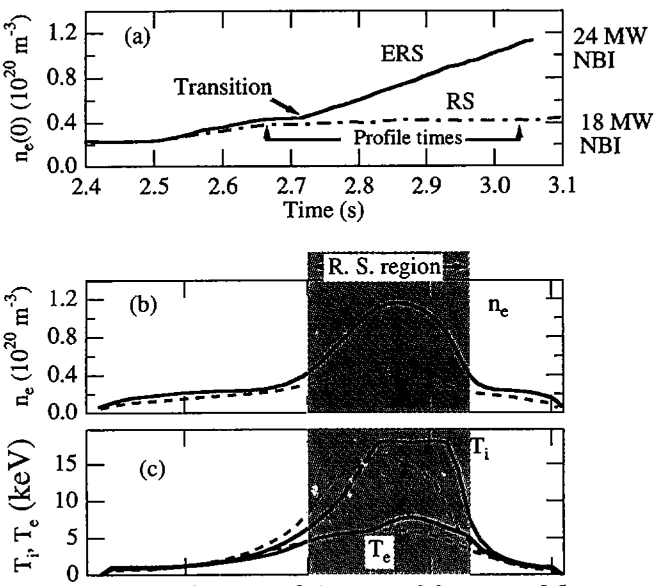

FIG. 3. (a) Evolution of the central density for a discharge that makes a transition into the ERS-mode at 2.715 s (solid line) and a similar reversed shear discharge at lower NBI power which does not (dashed-dotted line). (b) Density and (c) temperature profiles before a transition into the ERS-mode (dashed line) and at the time of peak density (solid line).

3. ERS-Mode Characterization

Below NBI powers of 18 MW, the plasmas formed in the reversed shear configuration appear to be similar to supershots[21], with a central ion temperature of $\sim$ 24 keV, electron temperature of $\sim 6-8$ keV and a central electron density of $\sim 4\times10^{19}\,\mathrm{m}^{-3}$. However, above an empirical threshold in neutral beam power, in the range of $\sim$ 18-30 MW, the particle and thermal transport dramatically improve in the plasma core where the shear is reversed. The transition to the highly peaked, enhanced reversed shear (ERS) mode occurs abruptly during the discharge, within 0.1-0.9 seconds after the start of the high power heating phase. Shown in Fig. 3(a) is the evolution of the central density, with a transition into the ERS-mode at $t = 2.715$ s. Also shown in Fig. 3(a) is a discharge without an ERS-mode transition, which has slightly lower NBI power and similar reversed shear q-profile. The electron density profile is shown in Fig. 3(b) at two times, just before the transition into the ERS-mode and near the time of peak density. The corresponding electron and ion temperature profiles are shown in Fig. 3(c).

When the radius of q_{min} is increased, the density and temperature profiles are broadened. In Fig. 4(a) is the q-profile for a typical ERS discharge at the time of peak beta compared to an ERS discharge formed with a faster plasma

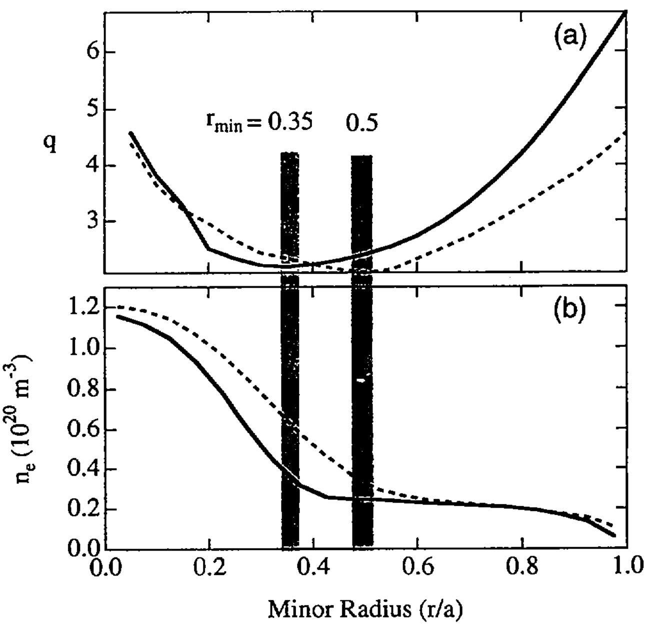

FIG. 4. (a) q-profiles with r_{min} at r/a = 0.35 (solid line) and r/a = 0.5 (dashed line) along with the corresponding (b) density profiles.

current ramp-up which results in a larger r_{min}. The corresponding electron density profiles are shown in Fig. 4(b). Similarly the temperature profiles are broader and the particle and ion thermal diffusivity profiles have a wider region of reduced transport, demonstrating the correlation of reversed shear with the reduction of particle and thermal transport.

4. Particle Transport

The effects on local transport by the ERS-mode are assessed with the $1\frac{1}{2}$-D time-dependent code, TRANSP, using experimentally measured temperature, density, and q−profiles. The $T_e(R,t)$ profile is measured by electron cyclotron emission (ECE), $T_i(R,t)$ and toroidal rotation by charge-exchange emission spectroscopy, $n_e(R,t)$ by a ten-channel far-infrared interferometer array, $q(R,t)$ is measured by MSE, and Z_{eff} is calculated using a tangential visible bremsstrahlung array. After the transition into the ERS-mode, the inferred particle and ion thermal diffusivity drop precipitously throughout the region of reversed shear, which extends out to $r/a \sim 0.35$. The improved confinement extends beyond the reversed shear radius, into the region of reduced shear as well. The inferred particle diffusivity, D_e, assuming no pinch terms, drops by a factor of ~ 40 in the reversed shear region to roughly the neoclassical level or perhaps lower, as shown in Fig. 5. The low value of the electron particle diffusivity has been found to persist for several hundred milliseconds after the neutral beam power is reduced substantially to 5 MW in a low power "postlude" phase. This reduces the uncertainty of the inferred particle diffusivity, since the the terms that determine the flux in the particle balance equation, the neutral beam source of particles and density rate of rise, are much smaller, and hence the uncertainty arising from their difference is much lower.

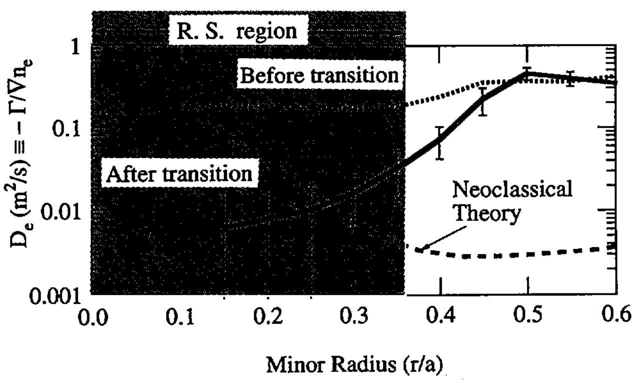

FIG. 5. Electron particle diffusivity profile before a transition (dotted line) at 2.6 s and after a transition (solid line) at 3.0 s with the estimated neoclassical particle diffusivity (dashed line). The reversed shear region extends to r/a ~ 0.35.

Along with the reduction of particle transport, a reduced level of density fluctuations is measured by a microwave reflectometer. Both the temporal evolution and spatial location of the reduced fluctuation level coincide with the reduction in particle transport[22].

TFTR is uniquely equipped to study hydrogenic ion transport using non-perturbing tritium puffs at the plasma edge, and observing the D-T neutrons with a 12 channel neutron collimator. The tritium density is inferred from the neutrons. A perturbation analysis is used to determine the diffusivity and convective velocity profiles. Due to the much larger cross section for D-T compared to D-D fusion and higher detector sensitivity to D-T neutrons, the tritium puff can be quite small and perturbs the density by about 1%. This technique had previously been developed on TFTR for studying hydrogenic transport in supershots[23]. A similar analysis in the ERS-mode finds the tritium diffusivity in the reversed shear region to be much lower than outside r_{min} and is comparable to that predicted by neoclassical theory. The helium profile evolution, measured with charge exchange recombination spectroscopy, from a small gas puff is similar to the tritium puff results and also indicates that the diffusive transport is markedly reduced inside r_{min} as compared to outside.

5. Thermal Transport

In ERS plasmas the ion power balance has little convective loss since the particle diffusivity is so small. This is in contrast to typical supershot discharges on TFTR which are dominated by convective loss in the plasma core[24]. However,

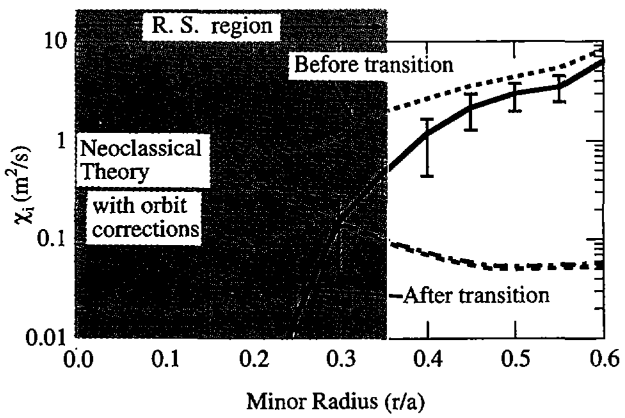

FIG. 6. Ion thermal diffusivity profile before a transition (dotted line) at 2.6 s and after a transition (solid line) at 3.0 s, and the neoclassical ion thermal diffusivity (dashed line) including orbit corrections (dashed-dotted line). The reversed shear region extends to r/a ~ 0.35.

in ERS plasmas the ion power balance does have a large loss from electron-ion energy exchange, $q_{ie} = 3n_i\nu_e\frac{m_e}{m_i}(T_i - T_e)$, where n_i is the ion density, ν_e is the electron collision frequency, $m_{e(i)}$ is the electron (ion) mass and $T_{e(i)}$ is the electron (ion) temperature. This is due to the large difference between the ion and electron temperatures and the large central density. Assuming classical electron-ion energy exchange and no pinch term it is found that the ion thermal diffusivity, χ_i, drops substantially to a level that is much less than the estimated neoclassical[25] value, χ_i^{nc}, which is widely believed to be the irreducible minimum transport possible. Profiles of the inferred ion thermal diffusivity, before and after a transition into the ERS-mode compared to estimated neoclassical ion thermal diffusivity, are shown in Fig. 6. It is quite remarkable that the ion thermal diffusivity is less than predicted by conventional neoclassical theory. One possible explanation for the observed sub-neoclassical ion thermal diffusivity is that the measured ion pressure gradient scale length is comparable to or less than the ion poloidal gyroradius, violating the assumptions of standard neoclassical theory. The strong pressure gradient is predicted to produce a large radial electric field gradient which squeezes the ion banana orbit, reducing neoclassical transport[26]. Other potential explanations include the existence of a thermal pinch or an anomalous ion-electron thermal equilibration. Recent analysis of neoclassical theory[27] with the poloidal ion gyroradius comparable to the pressure gradient scale length has found the trapped particle fraction and banana width are modified. The resulting effect is to reduce significantly the neoclassical ion thermal diffusivity, by as much as two orders of magnitude in the plasma core, which is also shown in Fig. 6.

The systematic and statistical uncertainties of the transport coefficients have been estimated. Their statistical variation over a period of 200 ms is used to determine the statistical standard deviation of the transport coefficients, which are computed every 10 ms. The systematic uncertainty is determined from the propagation of the systematic uncertainties of the input data in the transport equations. The uncertainties shown in Figs. 5 and 6 reflect the combined statistical and systematic uncertainties.

Neoclassical momentum diffusivity is predicted[28] to be much lower than neoclassical ion thermal diffusivity. However measurements from TFTR[29,30] supershot and L-mode plasmas find the momentum diffusivity profile is approximately equal to the ion thermal diffusivity and hence much larger than the predicted neoclassical momentum diffusivity. Theories based on electrostatic turbulence[31] or non-Maxwellian ion distribution[32] have been proposed to explain the observations of enhanced momentum diffusivity. Measurement of the momentum diffusivity in an ERS plasma provides independent confirmation of the reduced ion thermal diffusivity in ERS plasmas, which does not depend on thermal pinches or ion-electron energy exchange, as well as provide insight into the mechanism driving the enhanced ion and momentum diffusivity. Experiments have been done on TFTR with beam co-injection and counter to the plasma current in the low power (5-15 MW) postlude phase. With unbalanced

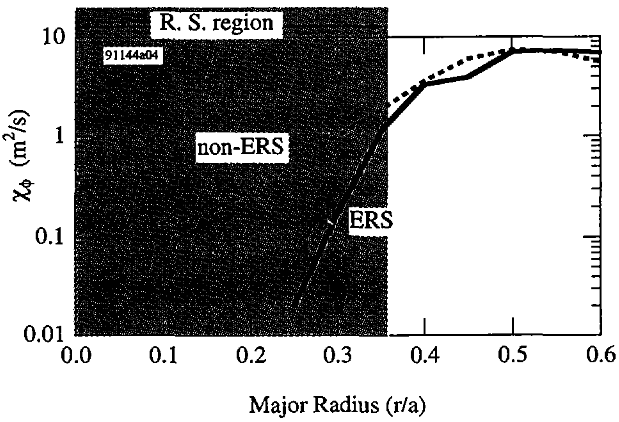

FIG. 7. Momentum diffusivity profile during the ERS-mode (solid line) and after a transition out of the ERS-mode (dashed line).

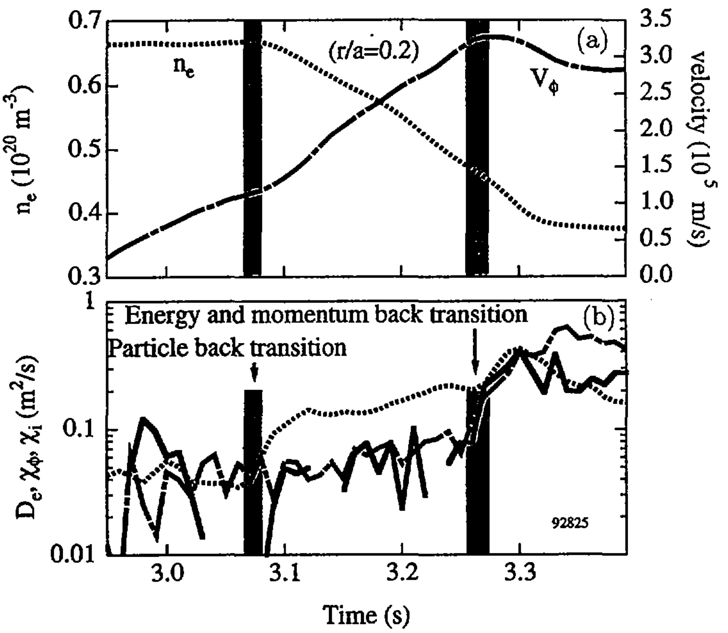

FIG. 8. (a) Time evolution of the electron density (dotted line) and rotation velocity (dashed-dotted line) at r/a = 0.2. (b) Temporal evolution of the particle (dotted line), ion thermal (solid line), and momentum diffusivity (dashed-dotted line) at r/a = 0.2 during the low power (7 MW) phase.

beam injection the toroidal velocity of the plasma increases rapidly during the ERS-mode, resulting in a calculated χ_ϕ that is reduced, consistent with the reduction in χ_i. After the transitions out of the ERS-mode, χ_ϕ increases to a much larger level. The χ_ϕ profiles during the ERS mode and after a transition out of the ERS mode are shown in Fig. 7. The time of the back transition of χ_ϕ and χ_i, out of the ERS-mode is also in good agreement. However, the particle diffusivity makes a transition out of the ERS-mode 50-200 ms before χ_ϕ and χ_i. The time evolution of the electron density and rotation velocity at $r/a = 0.2$ is shown in Fig. 8(a). The density has a clear back transition at 3.08 seconds when it begins to decrease. The corresponding electron particle diffusivity also shows a sharp increase at that time (Fig. 8(b)). The toroidal rotation velocity continues to accelerate during this time until 3.26 seconds when it abruptly stops accelerating and begins to slow down. The corresponding momentum diffusivity rises indicating the momentum diffusivity back transition is almost 0.2 seconds after the particle diffusivity back transition. The ion thermal diffusivity rises at the same time the momentum diffusivity increases, shown in Fig. 8(b). The start of reduced χ_i into the ERS-mode appears to occur at about the same time as the reduction of the particle diffusivity. However, the particle diffusivity appears to decrease more rapidly. This suggests the physical mechanism responsible for driving the particle transport is not the same as that causing the ion thermal and momentum transport.

The electron temperature increases and the profile is broader in ERS plasmas. This can be accounted for by the increased electron heating from ion-electron energy exchange due to the higher density. This results in little if any change in the inferred electron thermal diffusivity, χ_e.

6. Transition Physics

The underlying physics of the ERS transition has been a subject of study on TFTR. Analysis with a comprehensive gyrofluid simulation[33] has found that the dominant instability is the trapped electron mode (TEM). Stabilization can occur due to the reversed magnetic shear and Shafranov shift effects, which reverse the direction of the toroidal drift precession of barely trapped electrons so that the resonances that drive the TEM are eliminated. Another possible mechanism that can lead to reduced turbulence is flow shear[34], driven by gradients in the radial electric field that are generated by pressure and velocity gradients. A positive feedback mechanism involving pressure gradient driven flow shear stabilization has also recently been proposed[35]. Comparison of the $\gamma_{E\times B}$ flow shear stabilization and the maximum linear growth rate indicates qualitative agreement when $\gamma_{E\times B} > \gamma^{max}$[36,37]. The flow shear is defined as $\gamma_{E\times B} = \frac{RB_\theta}{B}\frac{d}{dR}\frac{E_r}{RB_\theta}$[38], where E_r is evaluated by solving the radial component of the force balance equation for carbon ions, $E_r = \frac{1}{n_i e Z}\nabla p_i + V_\phi B_\theta - V_\theta B_\phi$, where p_i is the carbon pressure and V_ϕ the toroidal velocity measured with charge exchange spectroscopy, B_ϕ is the toroidal field, and B_θ is the poloidal field measured with MSE. The poloidal velocity, V_θ, is evaluated using a comprehensive numerical calculation[39].

The flow shear model has been tested on TFTR using co/counter-injected neutral beams to control the toroidal velocity profile and hence the radial electric field profile. This will affect the velocity driven contribution to the radial electric field but not the pressure driven part. By varying the amount and direction of rotation, the velocity contribution to the radial electric field can either increase the total electric field (counter-injection) or decrease the electric field (co-injection). Shown in Fig. 9(a) is the time evolution of the central density for three discharges that have different fractions of co-injected power at constant total power, 15 MW. The time of the transition out of the ERS mode occurs later as the counter-injected fraction is increased. This is consistent with $E_r \times B$ flow shear which, as shown in Fig. 9(b), decreases earlier with co-injection fraction as a result of the reduced electric field shear. Direct comparison of the shearing rates to the maximum linear growth rate indicates that the back transitions occur when $\gamma_{E_r \times B} \sim (0.5-1)\gamma^{max}$, consistent with the shear suppression criterion of Ref.[36]. However, the start of the ERS-mode is not consistent with this model. The transition threshold favors near balanced injection. In conditions

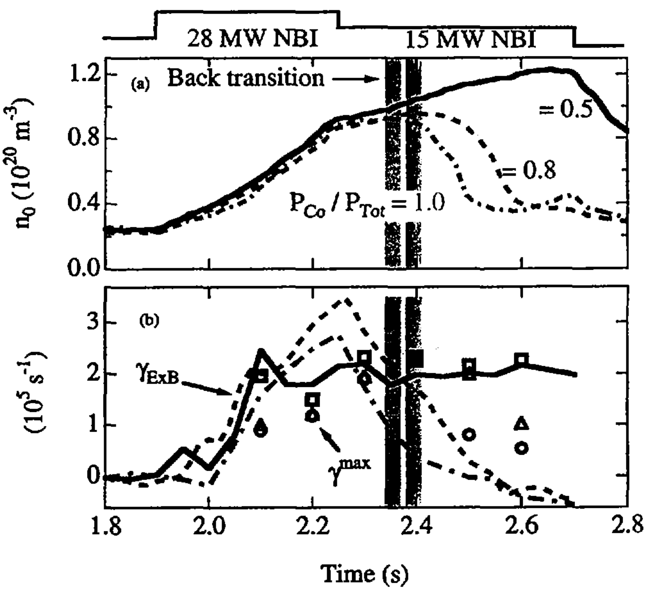

FIG. 9. (a) Time evolution of the central density with co-injected fractions of 1.0 (dashed-dotted line), 0.8 (dashed line) and 0.5 (solid line). (b) Corresponding evolution of flow shear and growth rate for co-injected fractions of 1.0 (circles), 0.8 (triangles) and 0.5 (squares).

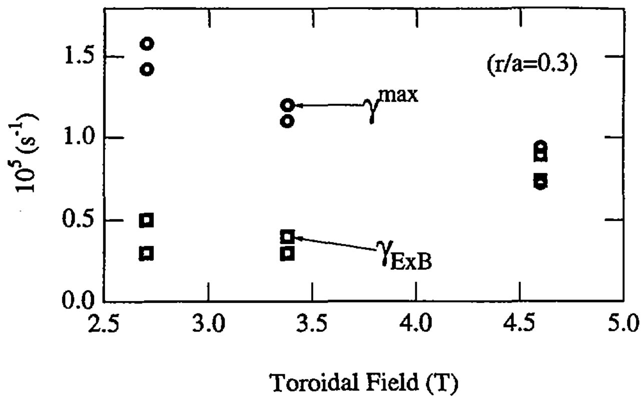

FIG. 10. Linear growth rates (circles) and flow shear rates (squares) for various toroidal magnetic fields at the time of the ERS-mode transition.

where the flow shear exceeds the growth rate, transitions do not occur if the beams are strongly co- or counter dominated. Conversely, in a toroidal magnetic field scan, which shows that the threshold is a strong function of B_ϕ, the power threshold is found to be lower than predicted by the flow shear model at magnetic fields lower than 4.6 T. Shown in Fig. 10 are the shearing and growth rates just before an ERS transition as the toroidal magnetic field is varied. At high toroidal magnetic field the two terms are about equal just before the transition occurs, but at lower toroidal magnetic field the shearing rate is much less than the growth rate.

7. Conclusion

In conclusion, highly peaked density and pressure profiles in a new reversed shear operating regime have been observed on TFTR. The particle transport is reduced to roughly the neoclassical level, and the ion thermal diffusivity is well below predictions from conventional neoclassical theory. As in supershots, the momentum diffusivity is observed to remain approximately equal to the ion thermal diffusivity. Little or no change is seen in the electron thermal diffusivity. A possible explanation for the inferred sub-neoclassical ion thermal diffusivity is the violation of the assumptions of standard neoclassical theory. A modified neoclassical analysis reduces the standard neoclassical ion thermal diffusivity significantly. The improved transport is observed throughout the region of reversed shear and is found to broaden as r_{min} is increased. The mechanism of transport suppression is a question of fundamental importance in understanding tokamak transport and developing the tokamak, or some other magnetic confinement concept, into an attractive reactor. Experimental and theoretical studies to date point to stabilization of the trapped electron mode by a combination of reversed shear, Shafranov shift, and radial electric field shear.

The model agrees well with the back transition data, but the simple shear flow model is not consistent with the power threshold results dependence on toroidal magnetic field. Further improvements of the models including nonlinear simulations incorporating $E_r \times B$ are needed, but comparison of data to models would greatly benefit with a direct measurement of the E_r profile. Neoclassical transport is usually thought to be the minimum transport possible, and these results represent a dramatic improvement in confinement and performance. With the low transport coefficients found in the ERS-mode, dramatic improvements in the performance of present and future tokamak reactors may be possible if the improved confinement can be achieved in an MHD stable regime with a large bootstrap current consistent with the desired current profile.

We would like to thank the TFTR staff for their support and operation of TFTR and W. Houlberg for the use of his code for calculating the neoclassical transport. This work was supported by United States Department of Energy Contract No. DE-AC02-76-CHO-3073.

REFERENCES

[1] KESSEL, C., MANICKAM, J., REWOLDT, G., TANG, W.M., Phys. Rev. Lett. **72** (1994) 1212.
[2] KADOMTSEV, B.B., POGUTSE, O.P., Sov. Phys. JETP **24** (1967) 1172.
[3] ROSENBLUTH, M., SLOAN, M.L., Phys. Fluids **14** (1971) 1725.
[4] SYKES, A., WESSON, J.A., COX, S.J., Phys. Rev. Lett. **39** (1977) 757.
[5] GOLDSTON, R.J., et al., Plasma Phys. Control. Fusion **36** (1994) B213.
[6] JET TEAM, in Plasma Physics and Controlled Nuclear Fusion Research 1988 (Proc. 12th Int. Conf. Nice, 1988), Vol. 1, IAEA, Vienna (1989) 215.
[7] MOREAU, D., et al., in Plasma Physics and Controlled Nuclear Fusion Research 1992 (Proc. 14th Int. Conf. Würzburg, 1992), Vol. 1, IAEA, Vienna (1993) 649.
[8] STRAIT, E.J., et al., Phys. Rev. Lett. **75** (1995) 4421.
[9] LAZARUS, E.A., et al., Phys. Fluids B **3** (1991) 2221.
[10] ISHIDA, S., et al., Phys. Rev. Lett. **68** (1992) 1531.
[11] KESNER, J., et al., Phys. Fluids B **5** (1993) 2525.
[12] POLITZER, P.A., et al., Phys. Plasmas **1** (1994) 1545.
[13] MEADE, D.M., et al., in Plasma Physics and Controlled Nuclear Fusion Research 1990 (Proc. 13th Int. Conf. Washington, DC, 1990), Vol. 1, IAEA, Vienna (1991) 9.
[14] LEVINTON, F.M., et al., Phys. Rev. Lett. **75** (1995) 4417.
[15] LEVINTON, F.M., et al., Phys. Rev. Lett. **63** (1989) 2060.
[16] LEVINTON, F.M., Rev. Sci. Instrum. **63** (1992) 5157.
[17] HIRSHMAN, S.P., et al., Phys. Plasmas **1** (1994) 2277.
[18] HAWRYLUK, R.J., in Proc. Course on Physics of Plasmas Close to Thermonuclear Conditions, Varenna, 1979, Vol. 1, European Commission, Brussels (1980) 19.
[19] BATHA, S.H., LEVINTON, F.M., HIRSHMAN, S.P., BELL, M.G., WIELAND, R.M., Nucl. Fusion **36** (1996) 1133.
[20] ZARNSTORFF, M.C., LEVINTON, F.M., BATHA, S.H., SYNAKOWSKI, E.J., The effect of E_r on MSE measurements of q, a new technique for measuring E_r, and a test of the neoclassical electric field, Phys. Plasmas (in press).

[21] STRACHAN, J.D., et al., Phys. Rev. Lett. 58 (1987) 1004.
[22] MAZZUCATO, E., et al., Phys. Rev. Lett. 77 (1996) 3145.
[23] EFTHIMION, P.C., et al., Phys. Rev. Lett. 75 (1995) 85.
[24] ZARNSTORFF, M.C., et al., in Plasma Physics and Controlled Nuclear Fusion Research 1988 (Proc. 12th Int. Conf. Nice, 1988), Vol. 1, IAEA, Vienna (1989) 183.
[25] CHANG, C.S., HINTON, F.L., Phys. Fluids 29 (1986) 3314.
[26] SHAING, K.C., HSU, C.T., HAZELTINE, R.D., Phys. Plasmas 1 (1994) 3365.
[27] LIN, Z., TANG, W.M., LEE, W.W., Phys. Rev. Lett. 78 (1997) 456.
[28] ROSENBLUTH, M.N., RUTHERFORD, P.H., TAYLOR, J.B., FRIEMAN, E.A., KOVRIZHNYKH, L.M., in Plasma Physics and Controlled Nuclear Fusion Research 1971 (Proc. 4th Int. Conf. Madison, 1971), Vol. 1, IAEA, Vienna (1971) 495.
[29] SCOTT, S.D., et al., in Plasma Physics and Controlled Nuclear Fusion Research 1988 (Proc. 12th Int. Conf. Nice, 1988), Vol. 1, IAEA, Vienna (1989) 655.
[30] SCOTT, S.D., et al., Phys. Rev. Lett. 64 (1990) 531.
[31] MATTOR, N., DIAMOND, P.H., Phys. Fluids 31 (1988) 1180.
[32] WARE, A.A., Phys. Rev. Lett. 64 (1990) 2655.
[33] BEER, M.A., PhD Thesis, Princeton Univ., NJ (1995).
[34] BIGLARI, H., DIAMOND, P.H., TERRY, P.W., Phys. Fluids B 2 (1990) 1.
[35] DIAMOND, P.H., et al., On the transition to enhanced confinement in reversed magnetic shear discharges (in preparation).
[36] WALTZ, R.E., KERBEL, G.D., MILOVICH, J., Phys. Plasmas 1 (1994) 2229.
[37] WALTZ, R.E., KERBEL, G.D., MILOVICH, J., HAMMETT, G.W., Phys. Plasmas 2 (1995) 2408.
[38] HAHM, T.S., BURRELL, K.H., Phys. Plasmas 2 (1995) 1648.
[39] HOULBERG, W., SHAING, K.C., HIRSHMAN, S.P., ZARNSTORFF, M.C., Bootstrap current and neoclassical transport in tokamaks of arbitrary collisionality and aspect ratio (in preparation).

DISCUSSION

K. LACKNER: Do any of the theoretical ideas you mentioned offer an explanation for the observation of distinct back-transitions for particle and energy/momentum diffusivities?

F.M. LEVINTON: No, but we have recently begun looking into possible explanations.

V. PARAIL: The fact that you see different transitions for density and ion momentum flow probably indicates that particle transport is controlled by the electrons. In this case you should see a sudden change in the radial electric field. Did you find this kind of electric field modification?

F.M. LEVINTON: We have not yet looked into this possibility.

K. IDA: If the $\mathbf{E} \times \mathbf{B}$ velocity shear driven by the pressure gradient plays an important role in an ERS discharge, the improvement of transport (reduction of χ_i) should be slow. Do you see a gradual change of χ_i after the transition from L mode to ERS mode? The back-transition from ERS to L mode depends on beam configuration (co- or balanced injection). The transition from L mode to ERS should be affected by the beam configuration, and a faster increase in $\gamma_{E\times B}$ should be predicted for balanced injection than for co-injection. Are there differences in delay time for the transition from L mode to ERS after the high power NBI is turned on, between co- and balanced injection?

F.M. LEVINTON: Yes, we see a gradual decrease in the ion thermal transport. We find the transition occurs with balanced beams at lower power. However, the time of the transitions is about the same for both cases.

ENHANCED CORE CONFINEMENT IN JT-60U REVERSED SHEAR DISCHARGES

T. FUJITA, S. IDE, H. KIMURA, Y. KOIDE, T. OIKAWA, S. TAKEJI,
H. SHIRAI, T. OZEKI, Y. KAMADA, S. ISHIDA, JT-60 TEAM
Naka Fusion Research Establishment,
Japan Atomic Energy Research Institute,
Naka-machi, Naka-gun, Ibaraki-ken,
Japan

Abstract

ENHANCED CORE CONFINEMENT IN JT-60U REVERSED SHEAR DISCHARGES.

Enhanced core confinement with an internal transport barrier (ITB) has been obtained in JT-60U reversed shear discharges. Clear internal pedestals for n_e, T_e and T_i profiles were observed in the negative magnetic shear region. The highest energy confinement time (τ_E = 1.08 s) and the highest stored energy (W_{dia} = 9.56 MJ) in JT-60U were obtained. The record of DT equivalent energy gain, Q_{DT}, in JT-60U has also been broken and a new value of Q_{DT} = 0.83 (fusion triple product $n_D(0)T_i(0)\tau_E$ = 6.8×10^{20} keV·s·m^{-3}) was achieved. In these high performance plasmas, over 80% of DD neutrons were produced by thermal–thermal reactions; $T_i(0)/T_e(0)$ was about two. The position of the outer edge of the ITB corresponds to the position of minimum q and extends beyond 70% of the plasma minor radius. The H factor increased with the minor radius of ITB and reached 3.4 with an L mode edge condition. A high confinement time was obtained with high densities, and the central electron density reached 1×10^{20} m^{-3}, with an H factor of 3.35. The values of Z_{eff}, however, were relatively high (3.5–4), and the maximum deuterium density was 4.5×10^{19} m^{-3}. At present, high performance discharges always terminate in a disruption due to a beta collapse with $\beta_N < 2$.

1. INTRODUCTION

A reversed shear configuration with negative magnetic shear in the inner and positive one in the outer region has been proposed for advanced tokamak operation [1–3]. The reversed shear configuration is a candidate for operation in an economical steady state tokamak reactor with high β, good confinement and a large bootstrap current fraction. Here, β is the ratio of plasma to magnetic field pressure. Recent progress in q profile measurements by motional Stark effect (MSE) diagnostics [4–7] motivates experimental studies on reversed shear discharges. In TFTR and DIII-D, enhanced core confinement or formation of an internal transport barrier was observed in a reversed shear configuration which was created during the initial current ramp with neutral beam (NB) heating. High electron temperature (T_e) with NB retards current penetration and helps to form a hollow current profile as is necessary for the reversed shear configuration. In TFTR, peaked profiles of ion temperature (T_i) and electron density (n_e) were observed; the particle diffusivity and the ion thermal diffusivity were remarkably reduced [8]. In DIII-D, peaked T_i profiles and high values of normalized beta, β_N of up to 4% mT/MA and an H factor of up to 3 were obtained [9]. Here, β_N is defined as $\beta_N = \beta a B_T/I_p$, where a is the (horizontal) plasma minor radius, B_T the toroidal field at the plasma centre and I_p the plasma current; the H factor is defined as confinement enhancement over the ITER89 power law scaling [10]. Furthermore, internal transport barriers were observed for the ion temperature in JT-60U high β_p plasmas [11] (β_p is the ratio of plasma to poloidal magnetic field pressure). This paper describes the observation of a new type of internal transport barrier in the negative magnetic shear region with clear internal T_i, T_e and n_e pedestals and the results of high performance reversed shear experiments.

2. OBSERVATION OF INTERNAL TRANSPORT BARRIER

Reversed shear experiments in JT-60U were started in the low current (1.2 MA), high q (q_{95} = 5.4) regime. A plasma configuration with large R_p (R_p = 3.4 m) was used for the MSE [12] as well as Thomson measurements, in spite of the large ripple loss. The injection of NB and the ramp of the plasma current were started at the same time after the divertor configuration had been established at low plasma current (0.3 MA). Clear internal pedestals for n_e and T_e were observed after high power (>20 MW) heating at the current flat-top. The outer edge of the internal transport barrier (ITB) was at 0.63 a, which corresponded to the position of q_{min}.

The electron and ion thermal diffusivities, χ_e^{eff} and χ_i^{eff}, were obtained by transport analysis [13]. Here, the convective loss is included in χ_e^{eff} and χ_i^{eff}. The value of χ_e^{eff} drops sharply by a factor of 20 at the outer edge of the ITB. The value of χ_i^{eff} was lower than the prediction of conventional neoclassical theory [14] inside the ITB.

The internal T_e pedestal and the clear reduction of χ_e^{eff} are distinctive features that were not observed in TFTR or DIII-D reversed shear discharges [8, 9] or in the JT-60U high β_p mode [11]. Relatively low $T_i(0)/T_e(0)$ (less than 1.5) was realized because of this electron transport reduction, in spite of dominant ion heating by NB. In TFTR and DIII-D reversed shear discharges and in the JT-60U high β_p mode, mainly the ion transport was reduced, and a hot ion regime ($T_i(0)/T_e(0) > 3$) was obtained. Reduction of χ_e in the central region was observed in the JET pellet enhanced performance mode [15] and in Tore Supra lower hybrid wave current drive experiments [16]. In both cases, however, no sharp change was observed in the radial profile of the thermal diffusivity. Thus, this is the first observation of a sharp T_e pedestal and a sharp spatial change in χ_e^{eff}, induced in the reversed shear configuration.

3. DISCHARGE CHARACTERISTICS OF HIGH PERFORMANCE SHOTS

High performance reversed shear experiments were carried out in the high current regime with B_T = 4.3 T. An inner shifted plasma configuration with

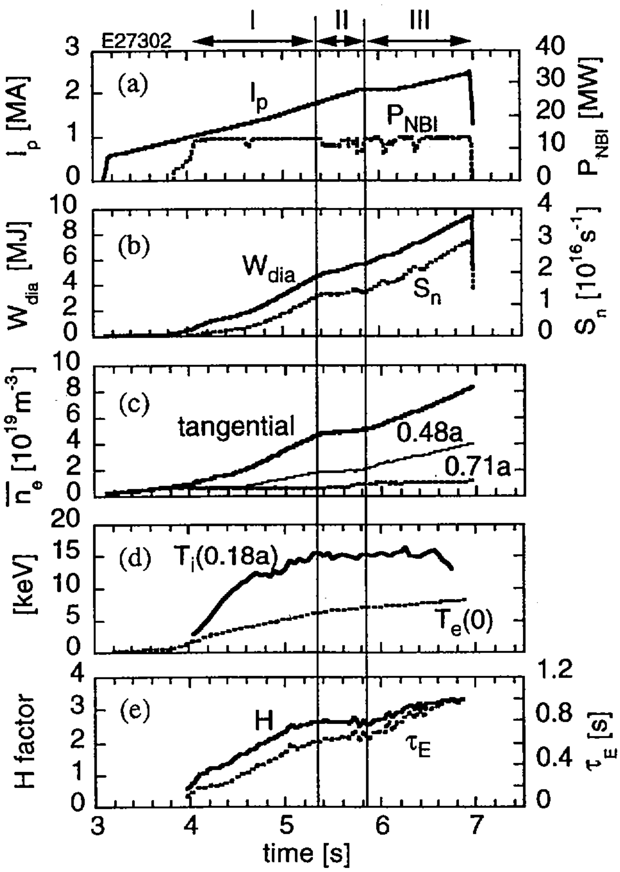

FIG. 1. Waveforms for typical high performance discharge: (a) plasma current I_p and NBI power P_{NBI}; (b) diamagnetic stored energy W_{dia} and neutron production rate S_n; (c) line averaged densities along tangential chord and vertical chords (r/a = 0.48 and 0.71);, (d) ion temperature at r = 0.18a, T_i(0.18a), and electron temperature at the centre, $T_e(0)$; (e) H factor and energy confinement time, τ_E.

R_p = 3.1–3.15 m in the high elongation connection was adopted to reduce the ripple loss and to increase the central NB heating power. With this configuration, the ripple induced fast ion loss is estimated to be 10–15% by the OFMC (orbit following Monte Carlo) code. In this paper, the ripple loss power is not subtracted from the absorption power for calculating τ_E, H factor or equivalent Q_{DT}.

The evolution of one of the best reversed shear discharges is shown in Fig. 1. The n_e, T_i, T_e and q profiles at t = 6.6 s are shown in Fig. 2. Steep gradients are seen in the n_e,T_i and T_e profiles. The outer edge of the ITB extended to 70% of the plasma minor radius.

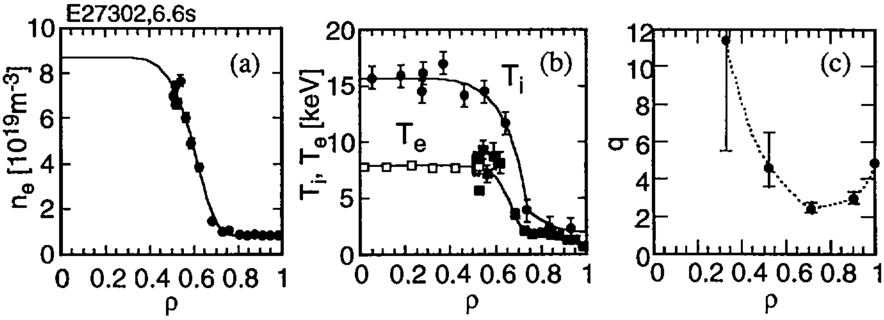

FIG. 2. Profiles of discharge shown in Fig. 1 at t = 6.6 s: (a) electron density, n_e, measured by Thomson scattering; the solid curve is obtained so as to fit the interferometer data (one tangential one and two vertical ones); (b) T_i by CXRS and T_e; in the T_e profile, closed points are measured by Thomson scattering and open points by ECE; (c) q profiles found by MSE.

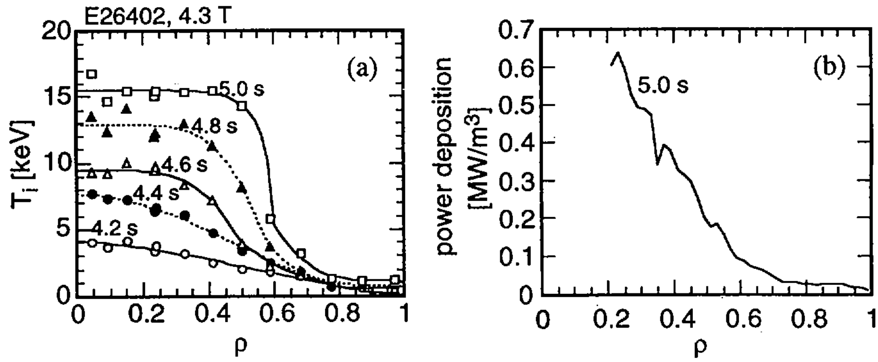

FIG. 3. (a) T_i profiles at the beginning of NB heating; (b) power deposition profile at t = 5 s, calculated by an OFMC.

The initial plasma current was 0.6 MA, and the plasma current was ramped up with 0.5 MA/s in the limiter configuration until 0.9 MA. A hollow current profile was formed even without NB heating during this phase. At t = 3.8 s, when the plasma current reached 0.9 MA, the divertor configuration was formed, and NB injection was started. Some amount of gas puffing was applied at the start of NB to raise the density to about 0.7×10^{19} m^{-3}. The period of NB injection can be divided into three phases (I, II and III) as is shown in the figure.

In phase I, the ion and electron temperatures near the axis and the central (tangential) line averaged electron density increased while the edge (vertical) line averaged electron density was kept almost constant. This indicates peaking of the pressure profile or formation of an internal transport barrier. The formation of the internal transport barrier at the initial stage of NB injection was effective in suppressing MHD instabilities during the I_p ramp. When the ITB was not formed because of lower NB power or unsuitable (too low or too high) target density, the discharge suffered from MHD instabilities, which resulted in a narrower ITB region and in poorer performance. In Fig. 3, T_i profiles during the formation of ITB were shown. The medium NB heating (12 MW) was started at 4.0 s. At t = 4.6 s, spatial change of the T_i slope appeared at $\rho = 0.5$ and the central T_i profile became flat. After that, the position of the steep gradient moved outwards and the extent of the central flat position became large. The flat density and temperature profiles near the axis are among the distinctive features of JT-60U reversed shear discharges. Figure 3 shows that this flat profile is formed at the early stage of ITB formation. The beam power deposition profile is shown in Fig. 3(b) at t = 5.0 s. Since the electron density inside the ITB was not so high (3.6×10^{19} m^{-3}) at this time, the attenuation of the neutral beam was small, and centrally peaked power deposition was realized. Hence, the flatness of the profiles near the axis is not due to the hollow power deposition but to the degradation of transport near the axis.

In phase II (t = 5.35–5.85 s), the H factor saturates. This phase is usually observed in this series of discharges. In Fig. 4, the time evolutions of T_i and q at several points are shown. The saturation phase corresponds to the period when q_{min} passes across 3. During this period, MHD fluctuations with low toroidal mode numbers were observed, and the ion temperature in the ITB (T_i at 0.64a in the figure) decreased. This indicates inward movement or shrinkage of the ITB as is shown in Fig. 4(c).

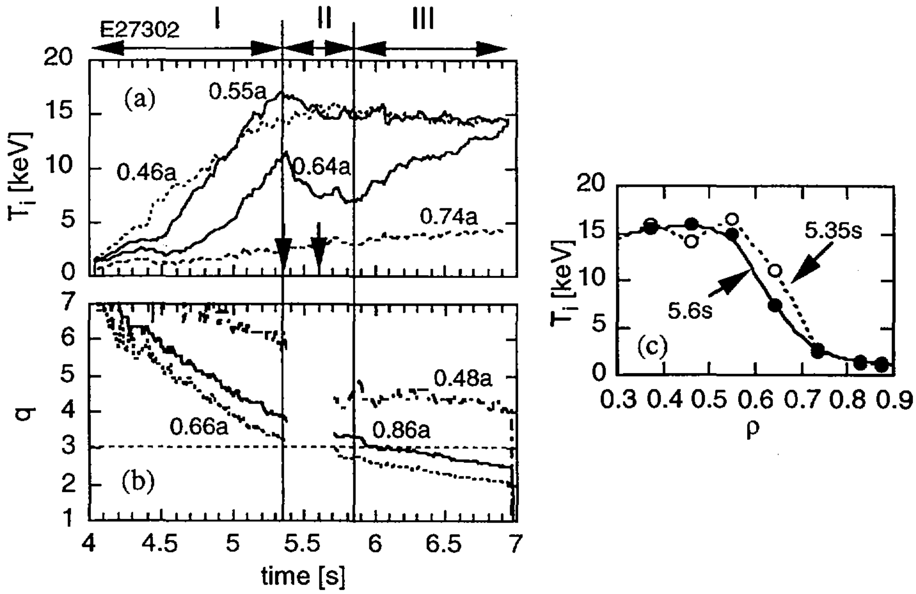

FIG. 4. Evolution of (a) T_i and (b) q in the discharge of Fig. 1; (c) T_i profiles at t = 5.35 s and 5.6 s.

In phase III (after t = 5.85 s), the position of ITB moved outward again, and the H factor started to increase again. A wide ITB as shown in Fig. 2 was formed. The major difference of the profiles from those in the low current regime is the density inside the ITB. It was about 4×10^{19} m^{-3} in the low current cases, but high densities of about 8×10^{19} m^{-3} were obtained in high current plasmas. The ion and electron temperatures were the same as those in the low current discharges. The edge density did not increase with the plasma current. This is partly because no H mode transition occurred in high field (4.3 T) reversed shear discharges with low edge density ($<1 \times 10^{19}$ m^{-3}) and with medium heating power (<15 MW). The stored energy, the neutron production rate and the central electron density continued to increase, and the discharge terminated into a β collapse at t = 6.9 s. Just before the collapse, W_{dia} was 9.4 MJ, τ_E was 1.01 s and the H factor was 3.35. The q_{min} shown in Fig. 4 was about 2.0 at the collapse. Up to now, we have had no discharges with $q_{min} < 2$.

4. CONFINEMENT AND STABILITY

In Fig. 5, τ_E and W_{dia} are shown as functions of the plasma current. Both increased with the plasma current and, in particular, the improvement in τ_E was large. At 2.4 MA, the highest values of τ_E (1.08 s) and W_{dia} (9.56 MJ) were obtained in separate shots. Both of these are record values of JT-60U. Figure 6 shows the relation of τ_E and the line averaged density. High confinement was obtained with high density. We find from this figure that discharges with different current and the same density have nearly equal τ_E. This means that the confinement is mainly determined by the density and that the dependence of I_p on τ_E is small for fixed density.

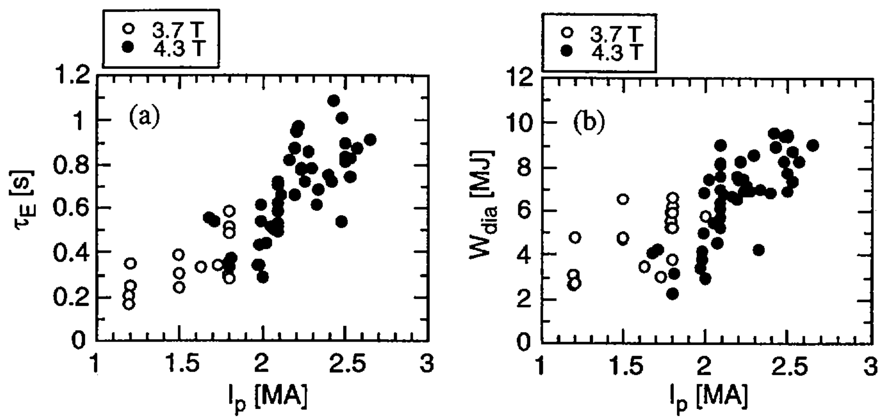

FIG. 5. (a) τ_E and (b) W_{dia} as functions of I_p. Open symbols: 3.7 T; closed symbols: 4.3 T discharges.

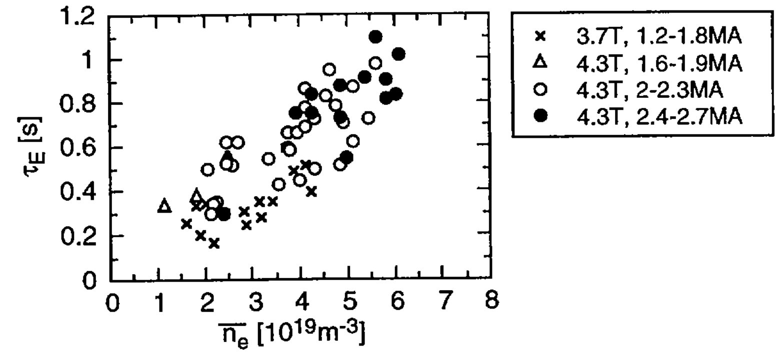

FIG. 6. τ_E versus line averaged density.

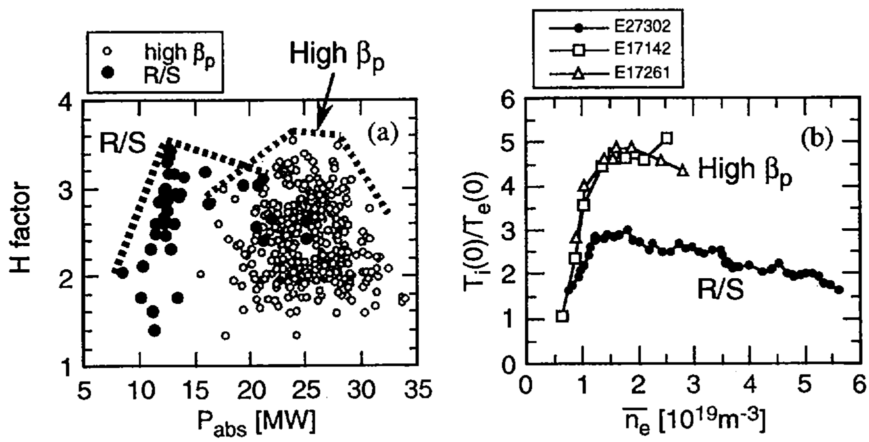

FIG. 7. Comparison of reversed shear and high β_p H mode discharges: (a) H factor as a function of absorption power; (b) $T_i(0)/T_e(0)$ versus line averaged density.

Though the values of W_{dia} in high β_p H mode plasmas are close to this record [19], the injected beam power was quite different. The H factors are plotted against the absorption power for reversed shear and high β_p H mode plasmas in Fig. 7(a). In high β_p H mode, the best confinement was obtained around P_{abs} = 25 MW. In reversed shear plasmas, the H factor increases quickly at low power and becomes larger than 3 at 12 MW. The fact that the same H factor was obtained at different absorption power means that the fraction of dW/dt in the absorption power was different. In reversed shear discharges, it was typically less than 30%, while it was about 40–60% in high β_p H mode plasmas. Another difference between reversed shear discharges and high β_p (H mode) discharges is the value of $T_i(0)/T_e(0)$ as mentioned before. Figure 7(b) shows $T_i(0)/T_e(0)$ as a function of the line averaged density. In reversed shear

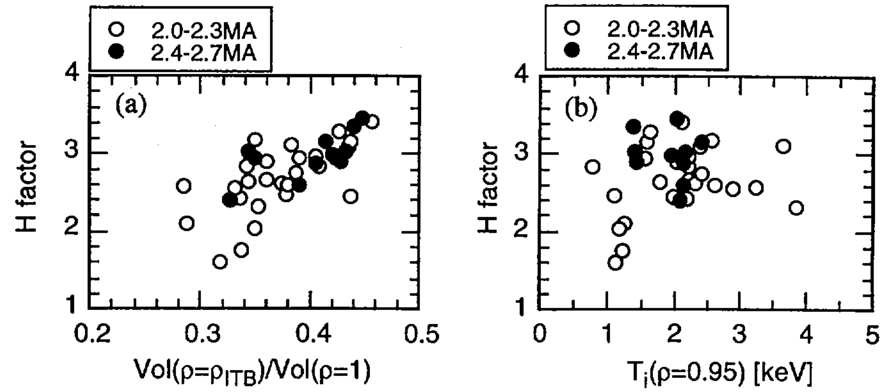

FIG. 8. (a) H factor as a function of normalized volume inside ITB; (b) H factor as a function of edge ion temperature.

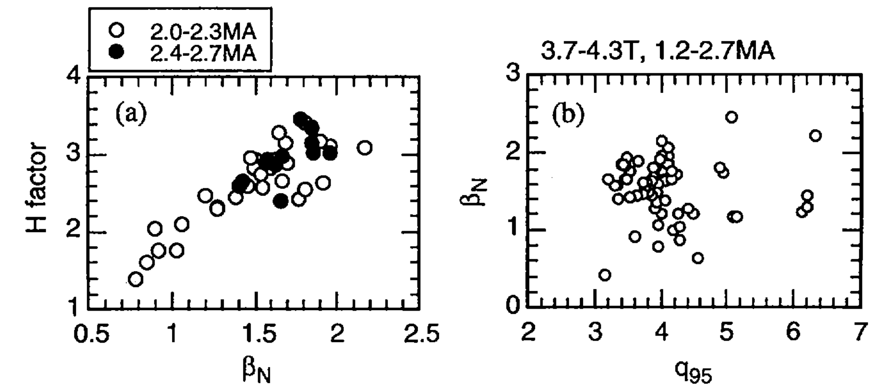

FIG. 9. (a) H factor versus β_N for 4.3 T high I_p discharges; (b) β_N versus q_{95}.

discharges, $T_i(0)/T_e(0)$ goes up to three after NB injection, but starts to decrease when the density becomes higher than 1.5×10^{19} m^{-3}. On the other hand, in the high β_p mode, $T_i(0)/T_e(0)$ goes up to four to five and maintains this value during heating.

In Fig. 8(a), the H factor is plotted against the normalized volume inside the ITB. Here, the radial position of the ITB, ρ_{ITB}, is defined as the position (normalized with the plasma minor radius) where $T_i(\rho_{ITB}) = 0.5*(T_i^{max} + T_i^{edge})$. The H factor increases with ρ_{ITB}, which indicates that the improvement of confinement is mainly due to the energy stored inside the ITB. The highest ρ_{ITB} was 0.68, where an H factor of 3.4 was obtained. The H factor is plotted against the edge ion temperature in Fig. 8(b). No clear dependence is seen. Thus, in these reversed shear discharges, the confinement improvement due to the effect of the edge is small whereas core improvement is dominant.

In Fig. 9(a), the relation between H factor and β_N is shown. The H factor increases with β_N. This means that it is important to maintain stability at high beta in order to obtain high confinement. The stability limit is shown in Fig. 9(b). The maximum normalized beta, β_N, was 2.4 at $q_{95} = 5$, which was similar to that of the high β_p mode. In the lower q_{95} regime below 4, β_N is restricted to values below 2.2. β_N decreased with decreasing q_{95} below $q_{95} = 4$. This regime corresponds to the high current region, where excellent performance is obtained. Thus, the performance of reversed shear discharges is determined by the stability limit for the collapse.

In the high β_p mode, the H mode transition (high β_p H mode) served to avoid collapses, and a quasi-steady state was realized with the ELMy H mode edge. In contrast, in high performance reversed shear discharges we have few shots with clear H mode transitions, which makes it difficult to avoid collapses.

5. FUSION PERFORMANCE

Very high fusion performance has been achieved by reversed shear discharges. In Fig. 10, Q_{DT} was plotted against the plasma current. Here, the fusion performance was analysed by the 1.5 D tokamak transport code system TOPICS, on the assumption that a deuterium beam is injected into a 50:50 deuterium–tritium target plasma. For comparison, the highest Q_{DT} in the high β_p H mode [17] is also plotted. Here, Q_{DT} is defined as $Q_{DT} = P_{DT}^{(th\text{-}th)}/(P_{abs} - dW/dt - P_\alpha) + P_{DT}^{(b\text{-}th)}/P_{abs}^{NB}$ [18], where $P_{DT}^{(th\text{-}th)}$ is the calculated value of the DT fusion power from thermal–thermal reactions, P_α is the calculated value of the alpha heating power from thermal–thermal reactions ($P_\alpha = 0.2{*}P_{DT}^{(th\text{-}th)}$) and $P_{DT}^{(b\text{-}th)}$ is the calculated value of the DT fusion power from beam–thermal reactions. As is shown in the figure, we could succeed in renewing the

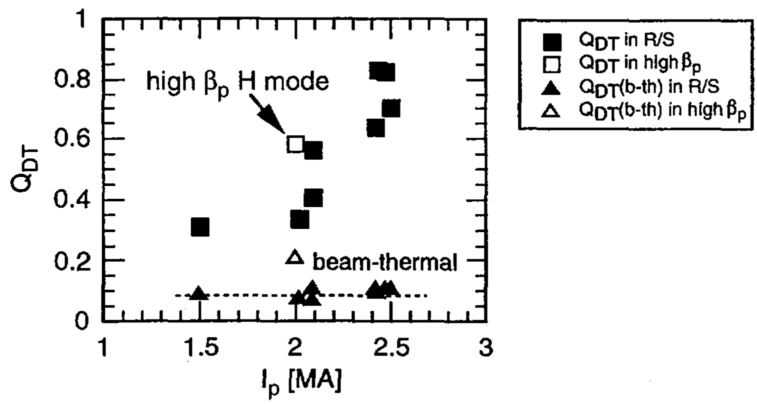

FIG. 10. Equivalent Q_{DT} values of reversed shear discharges (solid squares) and high β_p H mode discharge with highest Q_{DT} (open square). Q_{DT} values due to beam–thermal reactions are shown by triangles.

TABLE I. SIMULTANEOUSLY ACHIEVED PARAMETERS AND ANALYSED RESULTS FOR THE BEST REVERSED SHEAR DISCHARGE E 27 302

I_p	2.47 MA	S_n	2.97×10^{16} n/s
B_T	4.28 T	W_{dia}	9.42 MJ
q_{95}	3.46	τ_E	1.01 s
$P_{NB(inj)}$	12.2 MW	$\tau_E/\tau_E^{ITER89\text{-}P}$	3 35
$n_e(0)$	1.01×10^{20} m^{-3}	β_N	1.84
Z_{eff}	3.77	$n_D(0)\tau_E T_i(0)$	6.8×10^{20} m^{-3}·s·keV
$n_D(0)$	4.5×10^{19} m^{-3}	Q_{DD}	3.73×10^{-3}
$T_i(0)$	15 keV	Q_{DT} (without P_α corr.)	0.73
$T_e(0)$	8.1 keV	Q_{DT} (with P_α corr.)	0.82

Q_{DT} values substantially. The plasma parameters for one of the best shots are summarized in Table I. The value of Q_{DT} was 0.82. In the table, the value of Q_{DT} without subtraction of P_α is also shown. For the highest τ_E shot (τ_E = 1.08 s), Q_{DT} was 0.83. The thermal–thermal reactions account for 82% of the total neutron emission of 3.0×10^{16} n/s. The high fraction of the thermal fusion reaction is a feature of JT-60U reversed shear plasmas. In Fig. 10, the beam–thermal component of Q_{DT}, $Q_{DT}^{(b\text{-}th)} = P_{DT}^{(b\text{-}th)}/P_{abs}^{NB}$, is also shown. This component did not increase with I_p but stayed almost constant (0.1). This reflects the fact that the electron temperatures do not increase with I_p. As I_p increases, the thermal component of Q_{DT}, $Q_{DT}^{(th\text{-}th)}$ increases and accounts for 90% of the total Q_{DT} at 2.5 MA. Since the fraction of dW/dt in P_{abs} is small (26% for the case of Table I), the value of Q_{DT}^* defined as $Q_{DT}^* = P_{DT}^{(tot)}/P_{abs}$ is also high (Q_{DT}^* = 0.56).

We noted that the value of Z_{eff} is high and the ratio of deuterium to electron density is small in Table I. One reason for the high Z_{eff} value in reversed shear plasmas is the low beam power which results in a low beam fuelling rate. With higher beam power around 22 MW, however, Z_{eff} was still about 3.5. The impurity behaviour in reversed shear plasmas has to be investigated.

6. CONCLUSIONS

A new type of ITB was observed in the negative magnetic shear region in JT-60U. It accompanies the reduction of electron and ion energy transport; χ_e^{eff} drops sharply by a factor of 20 within 5 cm, while χ_i^{eff} is lower than the neoclassical value. Excellent confinement and performance of reversed shear plasmas have been demonstrated in JT-60U experiments. JT-60U record values of energy confinement time, stored energy and equivalent DT fusion power gain were obtained under the condition that the thermal–thermal fusion reactions were dominant. These results prove that the reversed shear configuration is a very promising candidate for operation in a tokamak with improved performance.

ACKNOWLEDGEMENTS

The authors would like to thank the members of the Japan Atomic Energy Research Institute who contributed to the JT-60U project. They also express their gratitude to the DIII-D (General Atomics) and TFTR groups for fruitful discussions on the physics of reversed shear discharges.

REFERENCES

[1] OZEKI, T., et al., in Plasma Physics and Controlled Nuclear Fusion Research 1992 (Proc. 14th Int. Conf. Würzburg, 1992), Vol. 2, IAEA, Vienna (1993) 187.
[2] KESSEL, C., et al., Phys. Rev. Lett. **72** (1994) 1212.
[3] TURNBULL, A.D., et al., Phys. Rev. Lett. **74** (1995) 718.
[4] LEVINTON, F.M., Rev. Sci. Instrum. **63** (1992) 5157.
[5] LEVINTON, F.M., et al., Phys. Fluids B **5** (1993) 2554.
[6] WROBLEWSKI, D., LAO, L.L., Rev. Sci. Instrum. **63** (1992) 5140.
[7] RICE, B.W., et al., Rev. Sci. Instrum. **66** (1995) 373.
[8] LEVINTON, F.M., et al., Phys. Rev. Lett. **75** (1995) 4417.
[9] STRAIT, E.J., et al., Phys. Rev. Lett. **75** (1995) 4421.
[10] YUSHMANOV, P.N., et al., Nucl. Fusion **30** (1990) 1999.
[11] KOIDE, Y., et al., Phys. Rev. Lett. **72** (1994) 3662.
[12] FUJITA, T., et al., Fusion Eng. Des. (in press).
[13] FUJITA, T., et al., submitted to Phys. Rev. Lett.
[14] CHANG, C.S., HINTON, F.L., Phys. Fluids **25** (1986) 3316.
[15] SMEULDERS, P., et al., Nucl. Fusion **35** (1995) 225.
[16] HOANG, G.T., et al., Nucl. Fusion **34** (1994) 75.
[17] KOIDE, Y., et al., in Plasma Physics and Controlled Nuclear Fusion Research 1994 (Proc. 15th Int. Conf. Seville, 1994), Vol. 1, IAEA, Vienna (1995) 199.
[18] JET TEAM, Nucl. Fusion **32** (1992) 187.
[19] ISHIDA, S., et al., IAEA-CN-64/A3-1, this volume.

DISCUSSION

R.R. WEYNANTS: In this mode you have high density and high Z_{eff}. How much is the radiated power compared with the input power?

T. FUJITA: Typically, the radiated power is about 30% of the input power.

G. BATEMAN: In the JT-60U discharge with $Z_{eff} = 3.8$, what is the impurity (carbon or high Z) and what is the time history of Z_{eff}?

T. FUJITA: The dominant impurity is carbon. The value of Z_{eff} is almost constant during beam injection.

J. JACQUINOT: Could you comment on the power threshold for the formation of the internal confinement barrier and its scaling with machine parameters.

T. FUJITA: There seems to be a density window where the threshold power becomes low, but a systematic study on threshold power has not been completed.

HIGH FUSION PERFORMANCE ELM FREE H-MODES AND THE APPROACH TO STEADY OPERATION

JET TEAM[1]
(Presented by P.J. Lomas)

JET Joint Undertaking,
Abingdon, Oxfordshire,
United Kingdom

Abstract

HIGH FUSION PERFORMANCE ELM FREE H-MODES AND THE APPROACH TO STEADY OPERATION.

The highest fusion yield in JET has been obtained in the hot ion H-mode regime. The paper reports progress in fusion performance in this regime. Since the last IAEA Conference in Seville (1994) the fusion performance on the MKI pumped divertor has been doubled, with D-D neutron rates up to 4.65×10^{16} n/s demonstrated, equivalent to $Q_{DT} \sim 1$, similar to the PTE-1 series. More recently, a more closed divertor MKII has been installed, and the new results are described.

1. BASIC FEATURES OF THE REGIME

Figure 1 shows a typical hot ion H-mode plasma obtained with the new MKII divertor. After formation of the X-point the density is allowed to pump out to $\sim 1 \times 10^{19} m^{-3}$ before the application of high power neutral beam (NB) heating. After a period of threshold ELMs the plasma becomes ELM free, during which time both stored energy and D-D neutron rate increase steadily. The ion temperature, on the other hand, reaches a maximum and then declines somewhat as the density continues to increase. The loss power, P_{NB}-dW/dt-P_{SH} (where P_{SH} corresponds to the calculated shine through power), increases with time as does the stored energy, indicating approximately constant confinement time. The high performance phase is limited in this case by beam switch off followed 50ms later by a giant ELM and sawtooth (coincident to within 100μs). These and other limitations to performance are discussed in [1].

The duration of the ELM free phase is similar on both MKI and MKII for similar core plasma shapes, edge shear, $S_{95} \gtrsim 3.5$, triangularity, $\delta \gtrsim 0.3$. Higher triangularity configurations have been tested up to $\delta \sim 0.6$, $S_{95} \sim 4.0$ at 2.5MA but have not demonstrated any significant improvement in confinement quality. Configurations with low edge shear $S_{95} \lesssim 3$ and low triangularity $\delta \lesssim 0.2$ show repetitive giant ELM's with frequencies $\gtrsim 5Hz$.

Given the similarities in plasma behaviour in MKI and MKII it is not surprising that the fusion performance of the NB only data is also similar at the same beam power and shows the same strong scaling with NB power as illustrated in Fig.2. Thus far, for technical reasons, the NB power on MKII has been limited to <17MW, but this deficiency is being corrected, and this is expected to restore the MKI performance later this year. Note also that steady neutron yields can be maintained for about 1s by step-down of the beam power to the level of the loss power in the preceding transient phase.

[1] See Appendix to paper IAEA-CN-64/O1-4, this volume.

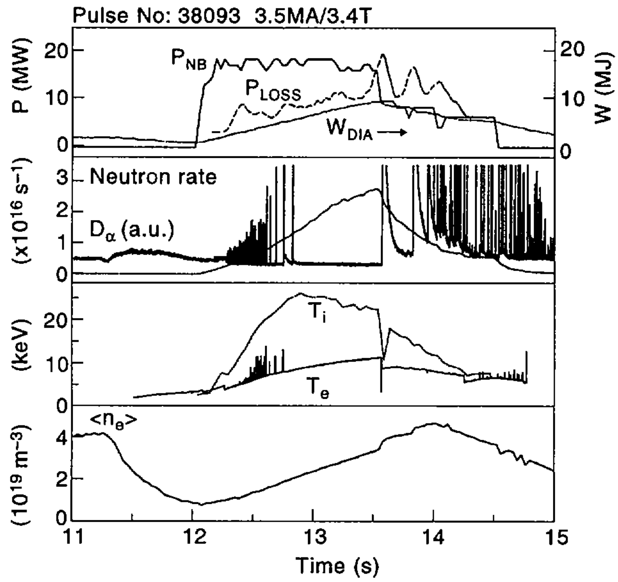

Fig.1 Typical time traces for an hot ion plasma showing neutral beam power P_{NB}, loss power P_{Loss} (see text), diamagnetic stored energy W_{DIA}, D-D neutron rate, D_α, ion and electron temperatures T_i and T_e and volume averaged density $<n_e>$.

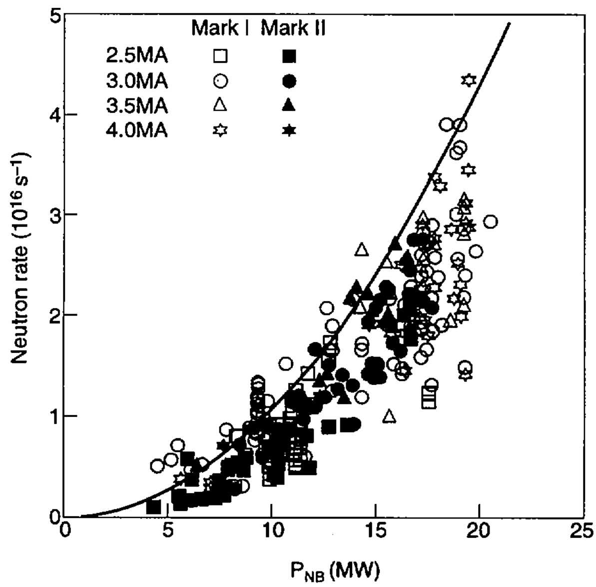

Fig.2 Neutron rate plotted against total neutral beam power. Open symbols refer to MKI and closed symbols refer to MKII. The shape of the symbols shows plasma current: squares 2.5MA, circles 3MA, triangles 3.5MA and stars 4MA.

2. THE TRANSPORT BARRIER

A model has been developed [2] which accounts for many of the features observed in JET ELM free H-modes. The model assumes: (1) transport inside the barrier region is given by ion neo-classical together with anomalous terms including both Bohm (global) and gyro-Bohm terms, (2) transport coefficients within the transport barrier $D \sim \chi_i \sim \chi_e \sim \chi_i^{neocl}$ are given by the ion neo-classical diffusivity and (3) the width of the transport barrier is given by the ion poloidal banana width $\Delta \sim \sqrt{\varepsilon}\rho_{\theta i}$. Note that the Bohm terms dominate the transport in the outer regions of the plasma up to the transport barrier and the gyro-Bohm terms dominate the central confinement.

With these assumptions it is possible to construct a complete set of transport equations for n_e, T_e, T_i and J which can be solved self consistently. A single free parameter remains which can be the edge density (or alternatively the net recycling coefficient) which is adjusted to match the observed density evolution. When applied to hot ion plasmas the time evolution of plasma parameters and profiles is well reproduced. In particular, the initial linear rise in stored energy is well described, and is followed by a progressive saturation which the model suggests is due to the density rise. The model describes accurately the evolution of power step-down pulses and the effect of strong gas puffing, and can account qualitatively for the temporary degradation of confinement following a sawtooth crash. The code predicts the time when ballooning modes become unstable which is consistent with the experimentally observed appearance of giant ELM's as shown in Fig.3. Indeed, this confirms, in a very satisfying manner, that the transport is close to ion neo-classical in the barrier region because an increase in transport would lead to ballooning modes always being stable.

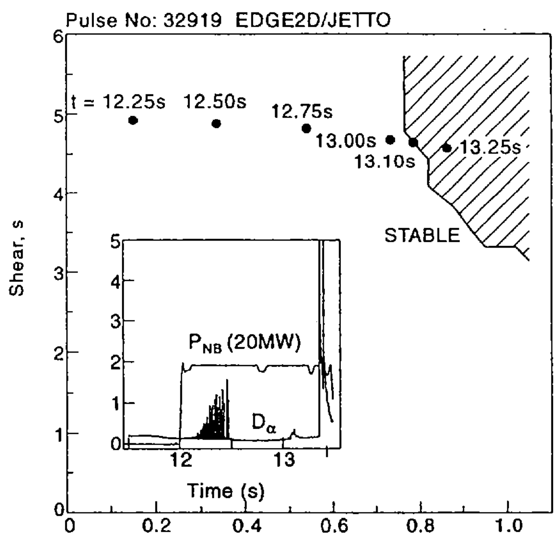

Fig.3 Trajectory of the model simulation of pulse 32919 in the S-α (shear versus normalised pressure gradient) diagram. The ballooning unstable region is shown shaded. Ballooning instability is predicted at 13.1 s which should be compared with the ELM time of 13.4 s shown in the inset.

Measurements of both ion and electron temperature profiles across the transport barrier are shown in Fig.4(a). The transport barrier is most clearly defined in the electron temperature data and this width is plotted against the best fit in Fig.4(b). Note that this result does not conform to the expected scaling $T_i^{1/2}/I_p$. Further analysis is in progress which may resolve these discrepancies, but it may be necessary to include more physics elements such as the penetration depth of cold neutrals. The first attempt to self consistently compute the scrape-off layer (SOL) and core transport together with neutral penetration is described in [3].

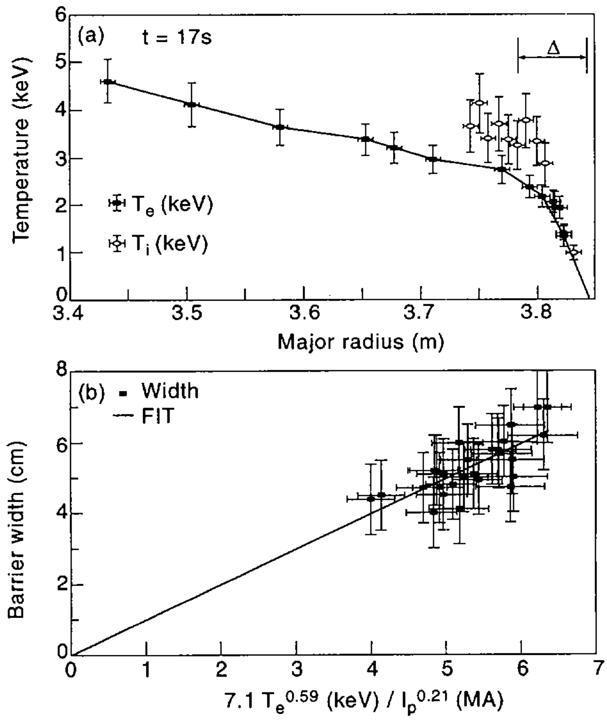

Fig.4 (a) Ion and electron temperature profiles for pulse 37444 (2.6MA/2.54T) from which the transport barrier width Δ is determined. (b) barrier width against fitted dependence on temperature and plasma current. Note the weak dependence on I_p.

3. THE ROLE OF RECYCLING

It was already described at the last IAEA conference [4] how the main chamber recycling plays an important role influencing both ELM free period and performance. Simulations with the model described above confirm this sensitivity. The distribution of the D_α light clearly shows the brightest signals from the divertor strike zones but reveals some contribution from the inboard (small major radius) plasma edge.

Measurements of Zeeman split D_α on a horizontal chord indicates approximately 4 times the light from the small major radius side of the plasma compared to the large major radius side.

In order to quantify the relative contribution of recycling in the main chamber compared to the divertor a selective hydrogen loading experiment was performed. The measured H/H+D fraction determined from vertical chord H_α and D_α is shown in Fig.5 as a function of pulse number for 4 sequences of pulses repeated on two successive days.

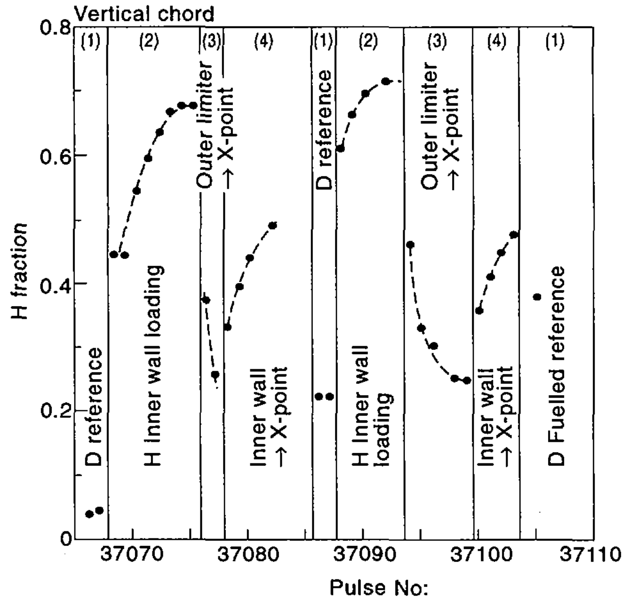

Fig.5 Ratio of H/H+D from H_α, D_α light measured on a vertical chord for a series of pulses from the selective hydrogen loading experiment (see text). Where the plasma pulse includes both limiter and X-point phases the measurement is taken during the deuterium beam fuelled H-mode in the X-point phase. The figure shows two cycles of experiments 37066-37084 and 37086 - 37105 repeated on successive days.

The sequence of pulses are as follows (as labelled on Fig.5): (1) reference pulse with deuterium gas fuelled inner limiter phase followed by deuterium beam fuelled H-mode, (2) inner wall limited pulses with hydrogen gas fuelling (3) pulses with deuterium gas fuelled outboard limiter phase followed by deuterium beam fuelled H-mode (4) pulses with hydrogen gas fuelled inner wall limiter phase followed by deuterium fuelled H-mode. For clarity the data points in Fig.5 represent the X-point phase when there is more than one phase. Generally the hydrogen concentration is low during the outboard limiter phases of sequences (1) and (3). The H/H+D ratio during the inner wall hydrogen loading pulses (2) behaves in a similar manner to previous isotope exchange experiments [5]. Note that sequence (3) has no direct contact with the inner wall and its inventory of hydrogen, and yet the X-point phase starts with a high concentration of hydrogen which decreases pulse by pulse. In sequence (4), where the hydrogen concentration is topped up during the inner wall phase, the concentration during the X-point phase increases pulse by pulse. These results demonstrate that there is significant exchange, during the H-mode phase only, of hydrogen from the inner wall to the divertor target and of deuterium from the divertor target to the inner wall. Thus a significant fraction (0.25 - 0.5) of the recycled particles originate from the inner wall, demonstrating the importance of the main chamber recycling during diverted H-modes.

The more closed MKII divertor was predicted to increase the pressure of neutrals in the diverted region and hence increase pumping. The data in Fig.6 clearly shows the increase in pumping during ELM free H-modes in MKII compared with MKI. Indeed in MKII the density rise during the ELM-free H-modes is reduced by ~ 30% such that it is necessary to add gas to optimise the fusion yield (minimise NB shine through losses and Z_{eff}). At low gas puff there is a clear net source of particles from either walls or target whereas at sufficiently high gas flow these surfaces provide a net pump. Alternatively these results can be thought of as a decrease in gas fuelling efficiency (from ~ 50% to $\lesssim$ 10%). This strong divertor pumping has reduced the need for extensive conditioning for access to the hot ion regime and increased the reproducibility of the performance achieved but has not, as yet, significantly improved the performance or confinement quality.

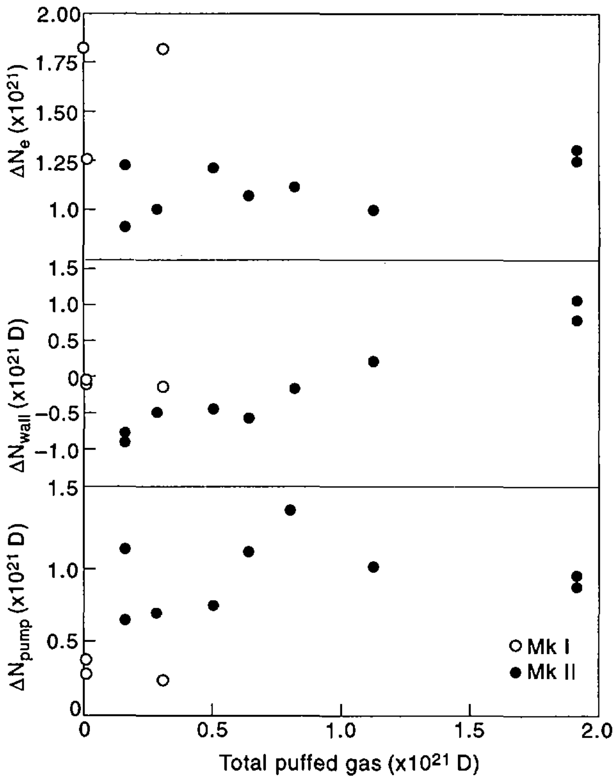

Fig.6 Particle balance over the first second of neutral beam heating for a series of ELM free H-modes. The change in plasma particle inventory, wall inventory and pump inventory are shown as a function of total gas puffed in the same interval. Open symbols refer to MKI and closed symbols refer to MKII. The neutral beams inject 17MW and 1.4 10^{21} particles per second.

4. COMBINED HEATING

Ion cyclotron resonance heating (ICRH) has been coupled in conjunction with NB heating to produce ELM free H-modes with combined heating (NBRF). The coupling resistance falls during the ELM free H-mode from about 2Ω to 1.5Ω. Nevertheless, it has been possible to couple up to 9.5MW. Together with NB a total power up to 25MW has been applied for plasma currents up to 3.8MA generating stored energies up to 14MJ. The diamagnetic energy confinement time $\tau = W_{dia}/(P_{NB} + P_{RF} - dW/dt)$ is about 1 s in these cases, similar to the NB only cases, suggesting no strong effect according to different proportions of electron and ion heating.

Figure 7 compares high D-D yield pulses at similar NB power with and without 6.5MW of ICRH resonant on axis with hydrogen and second harmonic deuterium. The increase in stored energy, D-D neutron yield, ion and electron temperatures is clear, and the shorter ELM free phase is as expected. The high energy neutral particle analyser clearly shows the generation of a deuteron tail with energies up to 1MeV, as expected from PION code calculations. Neutron accounting using kinetic data suggest increased neutron production from both thermonuclear and non-thermal reactions. With added hydrogen or mixed

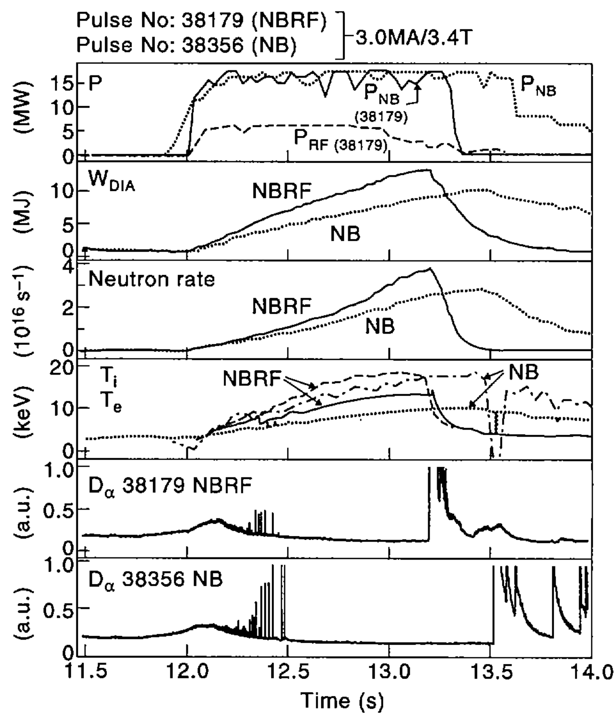

Fig.7 Typical time traces comparing NB only (38356) and combined heating NBRF (38179). The traces shown are input powers, P_{NB}, and P_{RF}, diagmagnetic stored energy W_{DIA}, neutron rates, ion and electron temperatures and D_α.

frequency (multiple resonance position) ICRH the observed tail can be smaller by an order of magnitude and yet still the D-D neutron rate is increased over and above the NB only cases. These results suggest a useful increase in fusion yield when ICRH is applied to DT plasmas, but it is too early to make quantitative predictions.

5. DT EXPECTATIONS

The best NB only plasma in MKI has demonstrated $n_D(0)\tau_E T_i(0) \sim 8.8\times10^{20}$ and TRANSP analysis indicates $Q_{DT}^{equiv} \sim 1$ (with the definition in [6]). High performance can be sustained for about 1 s by stepping down the NB power to about the loss power and in such cases $Q_{DT}^{equiv} > 0.8$ for 1s. Similar results are expected with MkII when the full beam power is restored later in 1996.

These extrapolations assume that 50:50 D:T mix can be achieved. By operation of the tritium beams at full power and the deuterium beams at reduced power 20 MW can be delivered with comparable deuterium and tritium fluxes. Provided that the core is dominated by beam fuelling a 60:40 mix should be readily achievable. Contributions to the core D-T mix from recycling could be offset by tritium beam prefuelling or gas puffing. Operation of the deuterium beams at full power would deliver $\simeq$ 23MW and would be expected to increase the D-T neutron yield by up to 30% provided that the shortfall in tritium fuelling can be made up (by gas puffing or prefuelling).

6. CONCLUSIONS

The behaviour of the hot ion ELM free H-mode regime is reassuringly similar in the MKI and MKII divertor. Improved pumping has reduced the characteristic density rise and increased operational flexibility, but has not as yet led to any significant improvement in performance. Similar high fusion performance, as already demonstrated on MKI, is expected on MKII when the neutral beam power is restored. Improved performance has been demonstrated with the addition of ICRH power to the hot ion ELM-free regime. The transport model continues to describe the main features of this regime and recently detailed edge temperature measurements have been made which should enable a refinement of the physics of the transport barrier.

Last, but not least, the rapid progress so far achieved with the MKII divertor shows great promise for the forthcoming DT experiments.

REFERENCES

[1] JET TEAM (presented by P.R. THOMAS), IAEA-CN-64/A3-2, this volume.

[2] BAK, P., et al., Nucl. Fusion **36** (1996) 321.

[3] JET TEAM (presented by A. TARONI), IAEA-CN-64/D3-3, these Proceedings, Vol. 2.

[4] JET TEAM (presented by P.J. LOMAS) in Plasma Physics and Controlled Nuclear Fusion Research 1994 (Proc. 15th Int. Conf. Seville, 1994), Vol. 1, IAEA, Vienna (1996) 211.

[5] HORTON, L.D., et al., J. Nucl. Mater. **196-198** (1992) 139.

[6] BALET, B., et al., Nucl. Fusion **33** (1993) 1345.

HIGH TRIANGULARITY DISCHARGES WITH IMPROVED STABILITY AND CONFINEMENT IN JT-60U

Y. KAMADA, R. YOSHINO, K. USHIGUSA, Y. NEYATANI,
T. OIKAWA, O. NAITO, S. TOKUDA, H. SHIRAI,
T. TAKIZUKA, T. OZEKI, M. AZUMI, T. HATAE,
T. FUJITA, S. TAKEJI, M. MATSUKAWA, Y. KOIDE,
T. FUKUDA, S. ISHIDA, JT-60 TEAM
Naka Fusion Research Establishment,
Japan Atomic Energy Research Institute,
Naka-machi, Naka-gun, Ibaraki-ken,
Japan

Abstract

HIGH TRIANGULARITY DISCHARGES WITH IMPROVED STABILITY AND CONFINEMENT IN JT-60U.

In JT-60U, energy confinement and stability were improved by a new high triangularity (δ) operation where δ was increased from the original value of ~0.1 to ~0.48. The advantages of high δ operation were demonstrated for the enhanced integrated performance required for steady state tokamak operation: (1) The edge pressure limit at the onset of giant ELMs was improved by a factor of 2. The attainable normalized edge density in ELMy H mode with H factor > 2 was increased by a factor of 2. Grassy ELMs at $\delta > 0.3$ with $\beta_p > 2$ were also observed. (2) The H factor ($= \tau_E/\tau_E^{ITER89P}$) increased with δ at a given heating profile. (3) Achievable β_N values increased with δ by ~50% and a high value of $\beta_N = 3.1$ was obtained at a high field of $B_t = 3.6$ T without I_p ramp-down ($q_{95} = 4.0$, $\delta = 0.34$). At a fixed q_{95} (= 2.8–4.2), the value of β_N/ℓ_i was almost constant over a wide range of B_t (1.5–4.5 T), and $\beta_N/\ell_i \approx 2.5$ at $\delta < 0.1$ and 3.5 at $\delta > 0.3$–0.4. (4) At fixed values of q_{95} and ℓ_i, the maximum β_N was obtained at a medium peakedness of the pressure profile determined by the edge stability (giant ELMs) and the fast central collapse. The optimum peakedness at high δ was smaller than that at low δ mainly because of improved edge stability. (5) The integrated performance with H factor = 2–2.5 and $\beta_N = 2.6$–3.1 was sustained for ~2 s (~$10\tau_E$) at $I_p = 1$ MA/$B_t = 3$ T under full non-inductive current drive (NB driven ≈ 40% and bootstrap ≈ 60%). At $I_p = 1.5$ MA, a high fraction (70–80%) of non-inductive current was sustained for 2.5 s with $\beta_N \approx 2.5$ and H factor ≈ 2.5. At $I_p = 1.8$ MA and $B_t = 3.6$ T a quasi-steady ITER-like ELMy discharge was sustained for 0.7 s (~$2\tau_E$) with $\beta_N = 2.7$–2.9, H factor ≈ 2.5, H/q_{95} = 0.74 with dW/dt = 0 and $Q_{DT} = 0.25$–0.3 ($q_{95} = 3.4$, $\delta = 0.3$, $\kappa = 1.5$).

1. INTRODUCTION

The major goal of JT-60U is the simultaneous achievement of (i) high confinement, (ii) high β, (iii) full non-inductive current drive with a high bootstrap fraction and (iv) high efficiency of heat and particle exhaust in the steady state. The JT-60U experiments have been devoted to satisfying the integrated performance [1] required in the Steady State Tokamak Reactor (SSTR) [2]. We demonstrated the feasibility of the SSTR concept in an ELMy H mode at I_p = 1 MA and B_t = 3 T where high values of H factor ≈ 2.5 and β_N ≈ 2.9 were sustained for ~0.7 s with full non-inductive current drive (bootstrap = 74%, NBCD = 37%) [1]. We also sustained a high fusion product of (4–4.5) × 10^{20} m^{-3} s·keV in the quasi-steady ELMy phase lasting for 1.5 s ($5\tau_E$) at the ITER-relevant value of q_{95} = 3.1 [1]. However, these results demonstrated only an integrated core plasma performance on a time-scale shorter than the current diffusion time. Issues awaiting solution are achievement of high confinement at a high density required for the cold and dense divertor, and sustainment of high β values in a steady state longer than the current diffusion time [3]. Concerning the former problem, the issue is that energy confinement time is decreasing with increasing density accompanied by increasing ELM frequency. Concerning the latter problem, the issue is that the β limit in a quasi-steady state is lower (~70%) than that obtained transiently [1]. The main purpose of our high δ experiment is to overcome these issues. A modified connection of the poloidal coil system enabled us to control δ from −0.06 to +0.6 at I_p = 1 MA and up to 0.3 at I_p = 2 MA (so far $\delta < 0.48$ for NB heating). Triangularity in this paper is defined as the average of upper and lower triangularities at the outermost flux surface and $\delta_{95} \approx 0.85\delta$.

2. IMPROVED EDGE PRESSURE LIMIT FOR GIANT ELMs

Concerning the onset conditions of giant ELMs which limit energy confinement in H mode, the effects of plasma shape on the onset condition have been studied by changing δ and elongation κ independently [4]. Figure 1(a) shows electron density (central and peripheral chords), edge T_e (r/a = 95%) and edge T_i (r/a = 95%) at the onset of the first giant ELM after an ELM free phase. These values increase with increasing δ. At δ = 0.3–0.4, the improvement is 30–50% for density and ~50% for temperature compared with the original δ of ~0.1. The onset condition of giant ELMs can be described with the α parameter (normalized pressure gradient) defined by $-\nabla p^{th}_{edge}/(B_t^2/2\mu_0 R q_{95}^2)$, where p^{th}_{edge} is the thermal pressure given by $\bar{n}_e(\sim 0.7a)$ × [fT_i(r/a = 95%) + T_e(r/a = 95%)] and f is a function of Z_{eff}. In this paper, we assumed Z_{eff}(95%) = 3.5 and carbon impurity. The pressure gradient ∇p^{th}_{edge} is given by p^{th}_{edge}/Δ, where Δ is the width of the edge pressure pedestal. We assumed that $\Delta = 4\epsilon^{0.5}\rho_i$ on the basis of Ref. [5], where ϵ is the inverse aspect ratio and ρ_i is the poloidal gyroradius of thermal ions: $\rho_i \approx T_i(95\%)^{0.5}/B_p(a)$. For the low δ (~0.1) discharges, we found that the α parameter is almost constant (1.5–3) over a wide range of I_p (0.4–4.5 MA), while the absolute values of edge pressure gradient change by a factor of 50 (from −0.2 × 10^5 Pa/m to −11 × 10^5 Pa/m), and the α parameter increases with κ and ℓ_i [4]. Therefore, giant ELMs are concluded to be the high n ballooning mode or a phenomenon determined on the s(shear)–α diagram. We found the α value clearly increased with increasing δ (Fig. 1(b)) when κ was fixed (= 1.38–1.54). The values of β_N at the onset of giant ELMs also increased by a factor of 2 at a fixed pressure profile p(r) (Fig. 5).

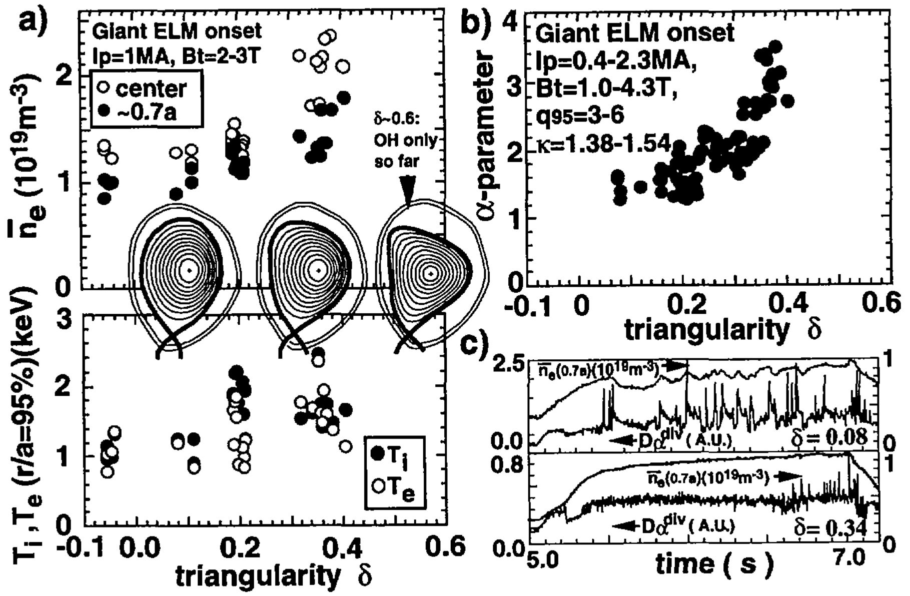

FIG. 1. (a, b) Increasing $\bar{n}_e$(central chord), $\bar{n}_e(0.7a)$, $T_e(r/a = 95\%)$, $T_i(r/a = 95\%)$ and edge α parameter with increasing triangularity at onset of giant ELMs. (c) Time traces of D_α^{div} and $\bar{n}_e(0.7a)$ for giant ELMs ($\delta = 0.08$) and grassy ELMs ($\delta = 0.34$, $\beta_p = 2.4$) with $P_{NB} = 20$ MW and $I_p = 0.6$ MA.

At $\delta \gtrsim 0.3$ with $\beta_p \gtrsim 2$, minute grassy ELMs appeared [4] (Fig. 1(c)). These ELMs can be distinguished from giant ELMs by their small amplitude and high frequency almost independent of heating power. (The frequency of giant ELMs increases linearly with heating power [6].) The peak heat load on the divertor plates per grassy ELM was small compared with giant ELMs. This result may be beneficial for reduction of erosion of divertor tiles. In this parameter region, numerical analyses suggest the possibility of access to the second stability regime.

3. IMPROVED ENERGY CONFINEMENT

In JT-60U, attainable values of the H factor are affected by plasma position (major radius R_p) because NB heating profiles and loss of fast ions by toroidal field ripple are functions of R_p. In this paper, the ripple loss (~15% for typical high δ discharges) is not subtracted in estimating the H factor. The typical high δ configuration in JT-60U has a relatively off-axis heating profile compared with the low δ configurations because of a horizontally outward shift of the magnetic axis. Figure 2(a) shows that the H factors of both ELM free and ELMy H modes are increasing with δ at a fixed R_p. At this R_p, the NB heating profile is off-axis

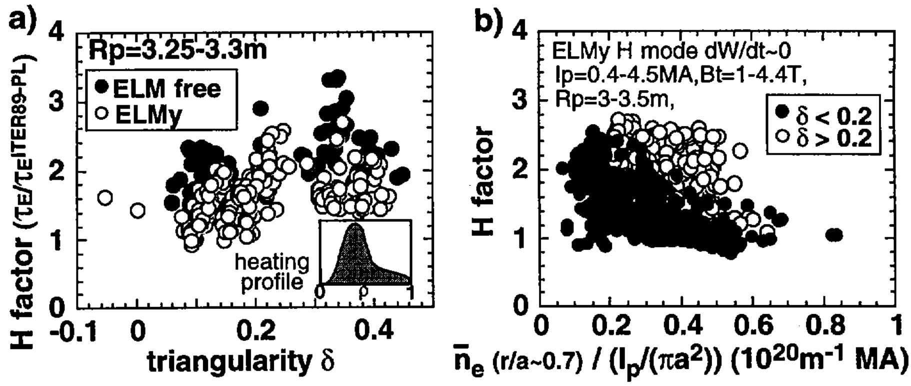

FIG. 2. (a) Increasing H factor with δ in ELM free and ELMy H modes at a fixed major radius R_p (off-axis heating). (b) H factor and normalized line averaged edge $\bar{n}_e(0.7a)$. With increasing δ, high H factor can be obtained at high normalized edge density (ELMy H mode, $dW/dt \approx 0$).

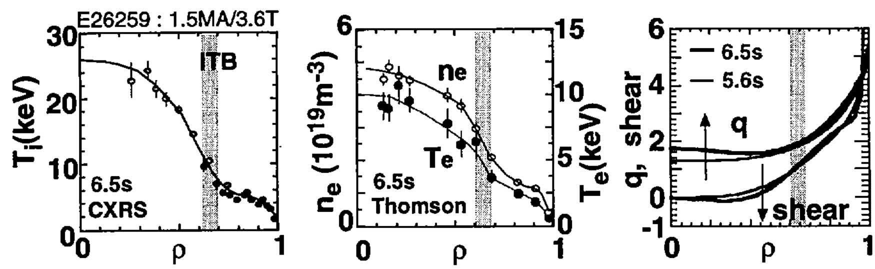

FIG. 3. Typical profiles of $T_i(r)$, $n_e(r)$ and $T_e(r)$ at $t = 6.5$ s (just before the fast β collapse) with the ITB. Profiles of q and shear at 5.6 s (just at NB turn-on) and at 6.5 s (discharge A in Fig. 5, $\delta = 0.34$, $q_{95} = 4.1$).

(Fig. 2(a)) and it is difficult to produce a clear internal transport barrier (ITB) characterizing the high β_p mode [7] for low δ discharges, whereas for high δ discharges, formation of the ITB was observed (Fig. 3). In addition, a peaked T_e profile was formed inside the barrier, which is different from the standard high β_p mode. In Fig. 3, the safety factor profile q(r) measured by the motional Stark effect system shows a gradual flattening of central shear caused by a high fraction ($\sim 60\%$) of bootstrap current. Although the central shear is reversed at 6.5 s in Fig. 3, the ITB is located in the weak positive shear ($\lesssim 1$) region, which is similar to the standard high β_p H mode in JT-60U. On the other hand, regarding the edge confinement, a clear inward penetration of the edge transport barrier, as in the case of the VH mode [8], has not been observed.

Concerning the simultaneous achievement of high confinement and remote radiative cooling from the divertor area, achievement of a high edge density is the important issue. However, the H factor tends to decrease with increasing edge n_e in ELMy H mode. Figure 2(b) shows H factor (dW/dt $\approx$ 0) and line averaged edge density $\bar{n}_e(0.7a)$ normalized by $(I_p/\pi a^2)$ following the Greenwald normalization [9] for ELMy H mode discharges. By increasing δ, the attainable normalized edge density with H factor > 2 was increased by a factor of 2 mainly because of the increased edge density limit for giant ELMs.

4. IMPROVED β_N LIMIT

It is known that the β_N limit increases almost linearly with ℓ_i [10–12], decreases with decreasing safety factor at the edge [1] and becomes maximum at a medium peakedness of p(r) [1]. In addition to these dependencies, this section describes the effects of δ on the β limit. In JT-60U, the maximum β_N at a given q_{95} and ℓ_i is limited mainly by low n pressure driven modes [13]. Figure 4(a) shows the relation between β_N and q_{95} for $\delta < 0.2$ and $\delta > 0.2$ cases. The upper boundaries of β_N for both $\delta > 0.2$ and $\delta < 0.2$ at $q_{95} > 2.8$ are mostly limited by the low n

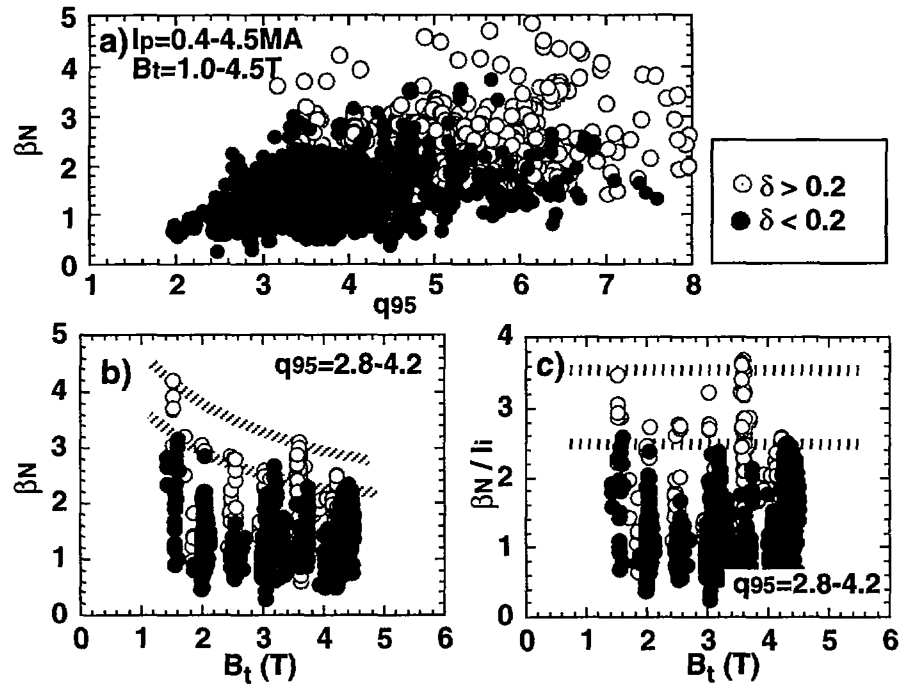

FIG. 4. (a) β_N values for low δ and high δ discharges as a function of q_{95}. (b, c) At relatively low q_{95} (2.8–4.2), although the achievable β_N value decreases with increasing B_t, the value of β_N/ℓ_i is almost constant (without I_p ramp-down).

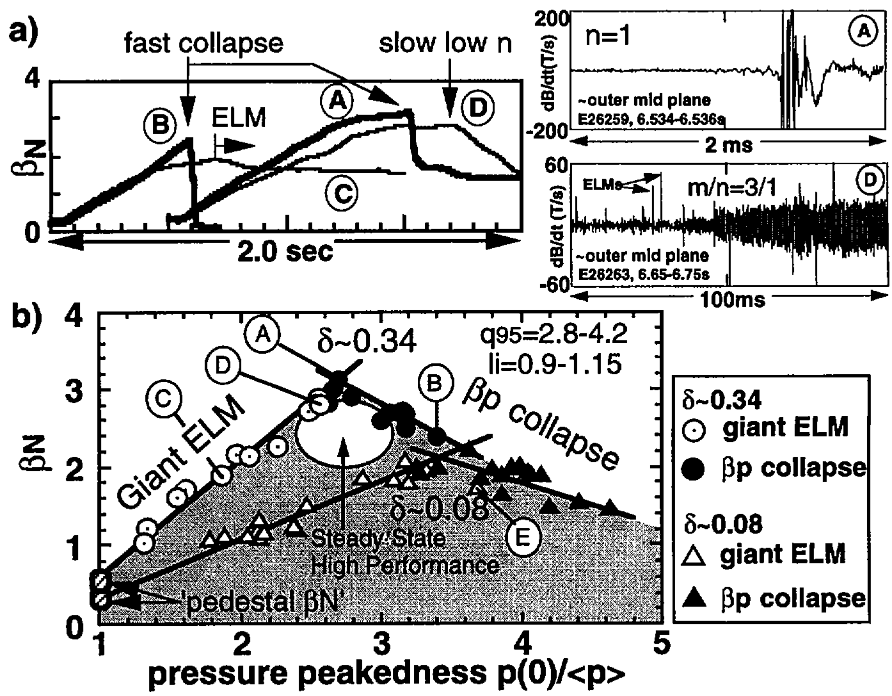

FIG. 5. (a) Four cases of β_N limits and dB/dt signals for the fast collapse and the slowly growing mode. (b) Achievable β_N values as a function of peakedness of total pressure for q_{95} = 2.8–4.2 and ℓ_i = 0.9–1.15 (open symbols: limited by giant ELMs; full symbols: limited by β_p collapse; circles: $\delta \approx 0.34$ with I_p = 1.5–1.8 MA/B_t = 3.1–3.6 T; triangles: $\delta \approx 0.08$ with I_p = 2–2.7 MA/B_t = 4.2–4.4 T). Pedestal β_N is given by edge thermal pressure (r/a = 95%) × plasma volume. A–D: Discharges with different p(r) and different instabilities. E: A high $n_D(0)\tau_E T_i(0)$ ELMy discharge sustained for 1.5 s [1].

modes. At $q_{95} < 2.8$, β_N is limited by giant ELMs. The β_N limit for high δ discharges is systematically higher than that for low δ. Figures 4(b) and (c) show values of β_N and β_N/ℓ_i without I_p ramp-down as functions of B_t at the low q_{95} (= 2.8–4.2), close to the value in ITER. Although the achievable β_N decreases with increasing B_t, β_N/ℓ_i is almost constant. This is because the ℓ_i value tends to be higher at lower B_t (or lower I_p at fixed q_{95}), where the current penetration is faster. The values of β_N/ℓ_i are ~2.5 at $\delta < 0.2$ and ~3.5 at $\delta > 0.2$. In Fig. 3(b), a high value of $\beta_N = 3.1$ was obtained at $B_t = 3.6$ T ($I_p = 1.5$ MA, $q_{95} = 4.0$, $\delta = 0.34$). At $B_t = 1.5$ T, the highest value of β_t (= 2.7%) in JT-60U was obtained at $\beta_N = 4.2$, $\delta = 0.38$, $I_p = 0.9$ MA and $q_{95} = 3.9$. In these two cases, β_N values were limited by n = 1 modes with a fast growth time of 10–100 μs without observable precursors.

For the achievement of high β_N values, there is an optimum peakedness for p(r) [1], and the critical instability limiting β_N is changing with p(r).Figure 5(a) gives four cases (A–D) of the β_N limit with different p(r) and different instabilities, and signals of dB/dt for the fast collapse (A) (growth time $< 50\ \mu s$; $1/v_{Alfvén\text{-}pol} \approx 1\ \mu s/m$) and for the slowly growing (order of ~ 10 ms) low n mode (D). Figure 5(b) shows achievable β_N values as a function of peakedness of total pressure $p(0)/\langle p \rangle$ at fixed values of $q_{95} = 2.8$–4.2 and $\ell_i = 0.9$–1.15. In both high δ and low δ discharges, the maximum β_N is obtained at a medium $p(0)/\langle p \rangle$ because the medium peakedness is the optimum if both fast collapses (consistent with the calculated ideal low n kink–ballooning limit [14]) and giant ELMs are taken into account. In Fig. 5(b), β_N values at higher $p(0)/\langle p \rangle$ are limited by the fast collapses (closed symbols) and those at smaller $p(0)/\langle p \rangle$ are limited by ELMs (open symbols). The pedestal β_N at $p(0)/\langle p \rangle = 1$ is calculated from $p^{th}_{edge}(r/a = 95\%) \times$ plasma volume at the onset of giant ELMs (see Section 2) to estimate the contribution of the edge transport barrier. The optimum peakedness at high δ was smaller than that at low δ mainly because of the improved edge stability against giant ELMs. Discharge A corresponds to the highest β_N at $B_t = 3.6$ T shown in Fig. 4(b) (profiles were given in Fig. 3). There seems to be an advantage of high δ against β_p collapses at $p(0)/\langle p \rangle \approx 3$. However, at the high value of $p(0)/\langle p \rangle > 3.5$, the slope of the closed circles suggests that the improvement in β_N by increasing δ is small, which is consistent with the ideal low n kink mode analyses using ERATO. The reason is that the high δ shaping does not penetrate to the inner flux surfaces on which the main driving force of the collapse is produced. On the other hand, at relatively low values of $p(0)/\langle p \rangle$, high δ values may contribute to the enhanced low n stability because the eigenfunction of the dominant mode becomes more global at broader p(r) [14]. The favourable quasi-steady high performances at high δ (Figs 8, 9) and at low δ (E) were obtained around the optimum p(r) with $\beta_N \approx (0.8$–$0.9)\beta_N^{max}$. The low δ discharge E is the high $n_D(0)\tau_E T_i(0)$ ($= (4$–$4.5) \times 10^{20}$ m$^{-3}\cdot$s$\cdot$keV) ELMy discharge sustained for 1.5 s at $q_{95} = 3.1$ [1]. From Fig. 5, the importance of pressure profile control is clearly understood.

5. ENHANCED INTEGRATED PERFORMANCE AND CURRENT DRIVE

This section describes the advantages of high δ operation for the simultaneous achievement and sustainment of high H factor, high β_N and high bootstrap fraction. Figure 6(a) compares β_N and H factor (including dW/dt) for the low δ and the high δ discharges. In the case of the high δ discharges, high values of β_N and H factor were obtained simultaneously and the maximum value of the product β_NH reached 13.5 (1.5 T, 0.9 MA, $q_{95} = 3.9$, $\delta = 0.38$). Figure 6(b) shows β_NH for the ELMy H mode with dW/dt = 0. At high δ, the value of β_NH (~ 7) required in SSTR has been obtained at I_p up to 1.8 MA ($B_t = 3.6$ T, $\delta \approx 0.3$).

Figure 7(a) shows that the limit of β_N/ℓ_i increases with δ for discharges with $\beta_p > 1.6$ and H factor > 2 (dW/dt = 0), which demonstrates the advantage of high δ operation for achieving high integrated performance. In this figure, the upper boundary is limited by the fast collapses. Data A, B and C correspond to quasi-steady

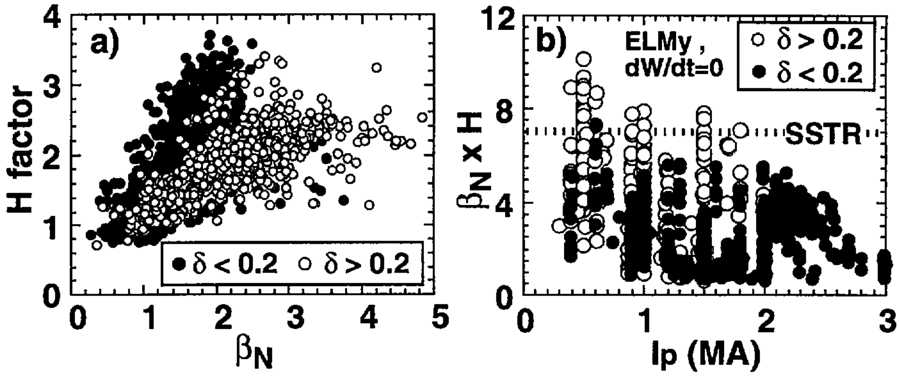

FIG. 6. (a) β_N and H factor (including dW/dt) for low δ and high δ discharges. (b) $\beta_N H$ versus I_p for ELMy discharges with dW/dt = 0.

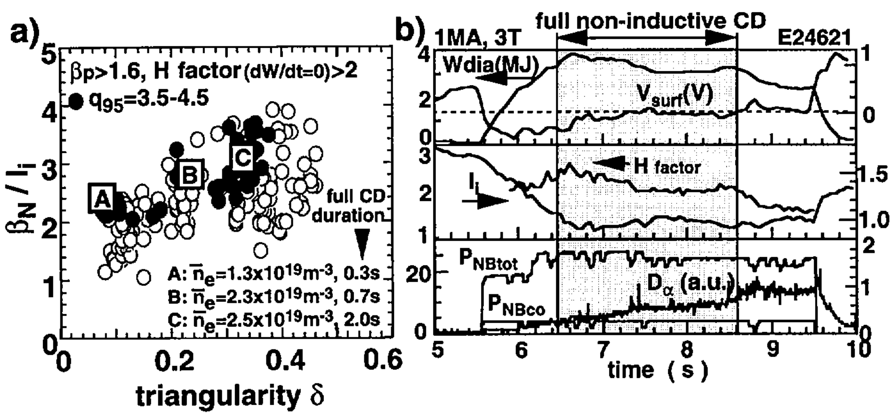

FIG. 7. (a) Limit of β_N/ℓ_i increasing with δ for discharges with H factor > 2 (dW/dt = 0) and β_p > 1.6 (open circles: q_{95} = 4.5–6; full circles: q_{95} = 3.5–4.5). A–C: Quasi-steady full non-inductive current drive cases at I_p = 1 MA (NB driven = 30–40% and bootstrap = 60–70%). Sustainable duration of the full current drive state becomes longer with increasing δ. (b) Evolution of discharge C: full current drive (NB driven ≈ 40%, bootstrap ≈ 60%) with H factor = 2–2.5 and β_N = 2.6–3.1 sustained for 2 s (~$10\tau_E$).

full non-inductive current drive discharges at I_p = 1 MA (NB driven = 30–40% and bootstrap = 60–70%). The sustainable duration of the integrated performance with the high values of β_p, β_N and H factor was extended with increasing δ: A, 0.3 s; B, 0.7 s; and C, 2.0 s. The parameter β_N/ℓ_i is useful for understanding the stability margin. At a high bootstrap fraction, ℓ_i is decreasing in time (see Fig. 7(b)). Therefore, if the limit of β_N/ℓ_i is low, the discharge cannot survive for a long time by keeping a high value of β_N. We need a sufficiently high limit of β_N/ℓ_i

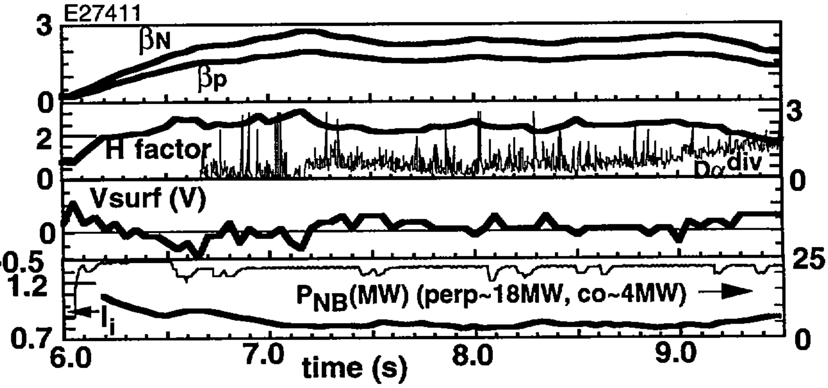

FIG. 8. Time traces of a high confinement discharge with a high fraction (70–80%) of non-inductive driven current sustained for ~2.6 s (~$8\tau_E$) with $\beta_N \approx 2.5$ and H factor ≈ 2.5. At t = 7.1 s, $Q_{DT} = 0.27$, bootstrap current = 0.85 MA, beam driven current = 0.39 MA (82% non-inductive) and H factor = 3.

tolerable in the final equilibrium with a low ℓ_i. From this point of view, high δ operation is favourable to expand the stability margin. The time evolution of discharge C is given in Fig. 7(b). The full non-inductive current drive condition (NB driven $\approx$ 40% and bootstrap $\approx$ 60%) was sustained for 2 s (~ $10\tau_E$) with $\beta_N = 2.6$–3.1, H factor = 2–2.5 and $\beta_p = 2.4$–2.8. However, although the value of β_N/ℓ_i in discharge C was lower than the limit for the fast collapses (Fig. 7(a)), the discharge was degraded from t = 8.6 s. This degradation was again correlated with a slowly growing n = 1 mode. The sustainable duration of such discharges is mainly limited by the gradual growth of the low n modes or the increase of carbon influx from divertor tiles exposed to a large heat flux. In addition to the enhanced stability margin, the extended lifetime at high δ is also caused by the increased density (n_e is increasing from A to C, as shown in Fig. 7(a)), which reduces the heat load onto the divertor tiles.

To extend the operation region with high integrated performance, we increased I_p by keeping p(r) around the optimum value given in Fig. 5(b). Figure 8 shows time traces of a discharge at I_p = 1.5 MA, B_t = 3.6 T and q_{95} = 4.0 with a high fraction (70–80%) of non-inductive driven current sustained for ~2.6 s (~ $8\tau_E$) with $d\ell_i/dt \approx 0$, where high values of $\beta_N \approx 2.5$ and H factor $\approx$ 2.5 were sustained even at a small value of $\ell_i \approx 0.8$. At t = 7.1 s, Q_{DT} = 0.27, H factor = 3, bootstrap current = 0.85 MA and beam driven current = 0.39 MA (82% non-inductive). The β_N value in Fig. 8 is ~80% of the transiently achievable β_N limit in this range of q_{95}. The sustainable duration of such integrated performance becomes shorter at higher β_N.

Figure 9 shows time traces of a high confinement ITER-like discharge at I_p = 1.8 MA, B_t = 3.6 T, q_{95} = 3.4, δ = 0.3 and κ = 1.5, where high values of $\beta_N \approx 2.7$–2.9, H factor $\approx$ 2.5 and H/q_{95} = 0.74 with dW/dt = 0 were sustained

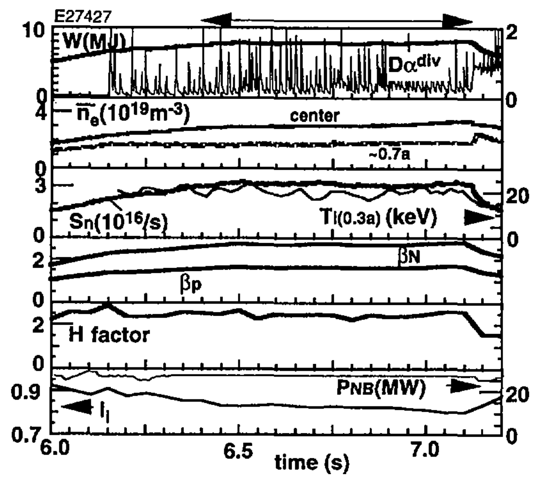

FIG. 9. Time traces of a high confinement ITER-like discharge sustained for ~0.7 s (~$2\tau_E$) with $\beta_N \approx 2.7$–2.9, H factor ≈ 2.5, $H/q_{95} = 0.74$ with $dW/dt = 0$ and $Q_{DT} = 0.25$–0.3 (1.8 MA, 3.6 T, $q_{95} = 3.4$, $\delta = 0.3$, $\kappa = 1.5$).

for ~0.7 s (~$2\tau_E$). These values of β_N and H factor (or H/q_{95}) satisfy the ITER requirements. Here, $Q_{DT} = 0.25$–0.3 with $T_i(0) \approx 24$ keV, $T_e(0) \approx 9$ keV, $n_e(0) \approx 5.8 \times 10^{19}$ m^{-3}, $n_D(0) \approx 4.0 \times 10^{19}$ m^{-3}, $\tau_E = 0.3$–0.35 s. In this discharge, even at a medium I_p of 1.8 MA, the value of Q_{DT} is the same as that obtained in high current (2.5 MA), high β_p ELMy H mode with $\delta \approx 0.8$.

6. SUMMARY AND DISCUSSION

Energy confinement and stability were improved with a new high triangularity operation in JT-60U and the advantages of the high triangularity shape were demonstrated with respect to the enhanced integrated performance in steady state reactors. For this purpose, the most important issue is that the stability limit in the steady state is different from that obtained transiently. In JT-60U, the maximum β_N sustainable in the quasi-steady state with a high bootstrap fraction ($\gtrsim$ 50%) is 2.5–3, which is much smaller than that obtained transiently (up to 4.8) [1]. Regarding the fast collapse, the collapse at t = 7.1 s in Fig. 9 seems to be destabilized both by broadening of the current profile (decreasing ℓ_i) due to bootstrap current and by peaking of the pressure profile (the central density is increased whereas the edge density is kept constant by ELMs). Another important point is that the β_N values tend to be limited by resistive instabilities in the quasi-steady state even at a sufficiently small β_N compared with the ideal limit [15]. For example, Ref. [12] showed a quasi-steady high β_p discharge with naturally produced reversed shear in which confinement was degraded by a resistive pressure driven n = 2/m = 5 mode destabilized when the q profile had a pitch minimum at q ≈ 2.5 (calculation). In discharge D in Fig. 5, β_N was limited by the appearance of a slowly growing m/n = 3/1 mode in an ELMy phase where the collisionality ν^* around the resonant surface was 0.03–0.05. Optimization of both confinement and stability should be demonstrated with the final equilibrium in the steady state where pressure and current profiles have been fully diffused, for which both ideal and resistive modes should be safely stabilized.

The above improvements are suitable for the further improvement of the steady state performance using negative ion based NB injection with a high energy of 300–500 keV [16], which requires a high density to reduce shine-through and a high β limit to tolerate large fast ion pressure.

ACKNOWLEDGEMENTS

The authors would like to thank the members of the Japan Atomic Energy Research Institute who have contributed to the JT-60U project.

REFERENCES

[1] KAMADA, Y., et al., in Plasma Physics and Controlled Nuclear Fusion Research 1994 (Proc. 15th Int. Conf. Seville, 1994), Vol. 1, IAEA, Vienna (1995) 651.
[2] SEKI, Y., et al., in Plasma Physics and Controlled Nuclear Fusion Research 1990 (Proc. 13th Int. Conf. Washington, DC, 1990), Vol. 3, IAEA, Vienna (1991) 473.
[3] KAMADA, Y., Plasma Phys. Control. Fusion **38** (1996) 1173.
[4] KAMADA, Y., et al., Plasma Phys. Control. Fusion **38** (1996) 1387.
[5] HATAE, T., et al., in Proc. 37th Annu. Mtg, American Physical Society, Plasma Physics Division, Louisville, KY, 1995, 5R.13.
[6] KAMADA, Y., Plasma Phys. Control. Fusion **36** (1994) A123.
[7] KOIDE, Y., et al., in Plasma Physics and Controlled Nuclear Fusion Research 1994 (Proc. 15th Int. Conf. Seville, 1994), Vol. 1, IAEA, Vienna (1995) 199.
[8] TAYLOR, T.S., et al., in Plasma Physics and Controlled Nuclear Fusion Research 1992 (Proc. 14th Int. Conf. Würzburg, 1992), Vol. 1, IAEA, Vienna (1993) 167.
[9] GREENWALD, M., et al., Nucl. Fusion **28** (1988) 2199.
[10] TAYLOR, T.S., et al., in Plasma Physics and Controlled Nuclear Fusion Research 1990 (Proc. 13th Int. Conf. Washington, DC, 1990), Vol. 1, IAEA, Vienna (1991) 177.
[11] SABBAGH, S.A., et al., Phys. Fluids B **3** (1991) 2277.
[12] KAMADA, Y., et al., Nucl. Fusion **34** (1994) 1605.
[13] NEYATANI, Y., et al., Plasma Phys. Control. Fusion **37** (1995) 741.
[14] OZEKI, T., et al., Nucl. Fusion **35** (1995) 861.
[15] PERKINS, F.W., et al., IAEA-CN-64/FP-24, these Proceedings, Vol. 2.
[16] USHIGUSA, K., et al., IAEA-CN-64/O1-3, this volume.

DISCUSSION

K. LACKNER: You stressed the necessity of controlling the resistive modes to extend the high bootstrap fraction discharges. Do you have plans as to how to achieve this on JT-60U?

Y. KAMADA: We plan to study the stability of the resistive mode by active current profile control using NBCD. We shall also try to control the bootstrap current profile by changing the pressure and density profiles.

S.A. SABBAGH: It is exciting to see an increase of β_N/ℓ_i with increasing δ. In the future run of JT-60U, will you be able to produce higher I_p plasmas with high δ and high ℓ_i to investigate the scaling of β_N/ℓ_i to δ at high $I_p > 1.5$?

Y. KAMADA: Yes. We have a plan to reinforce the shaping coil next year, and then we will be able to increase I_p up to 2.5 MA with a triangularity of ~0.3.

CONFINEMENT AND α PARTICLES

(Session A2)

Chairperson

D.M. MEADE
United States of America

SAWTOOTH MIXING OF ALPHA PARTICLES IN TFTR D–T PLASMAS*

M.P. PETROV[1], N.N. GORELENKOV[2], R.V. BUDNY[3], Z. CHANG[3], D.S. DARROW[3], H.H. DUONG[4], R.K. FISHER[4], R.J. FONCK[5], H.W. HERRMANN[3], G.R. McKEE[5], S.S. MEDLEY[3], A. ODBLOM[6], A.L. ROQUEMORE[3], B.C. STRATTON[3], F. WISING[7], R.B. WHITE[3], Y. ZHAO[3], S.J. ZWEBEN[3]
A.F. Ioffe Physico-Technical Institute,
St. Petersburg,
Russian Federation

Abstract

SAWTOOTH MIXING OF ALPHA PARTICLES IN TFTR D–T PLASMAS.

Radially resolved confined alpha particle energy and density distributions are routinely measured on TFTR using two diagnostics: PCX and α-CHERS. The Pellet Charge-eXchange (PCX) diagnostic uses the ablation cloud formed by an impurity pellet (Li or B) for neutralization of the alphas followed by analysis of the escaping helium neutrals. PCX detects deeply trapped alpha particles in the energy range of 0.5–3.8 MeV. The α-CHERS technique, where the alpha signal is excited by charge exchange between alphas and the deuterium atoms of one of the heating beams and appears as a wing on the He^+ 468.6 nm line, detects mainly passing alphas in the range of 0.15–0.7 MeV. Studies of alpha losses during D–T experiments on TFTR have also been conducted by using lost alpha detectors located on the walls of the plasma chamber. All these diagnostics were used for investigating the influence of sawtooth crashes on alphas in high power D–T discharges in TFTR. Both PCX and α-CHERS measurements show a strong depletion of the alpha core density and transport of trapped alphas radially outwards well beyond the $q = 1$ surface after a sawtooth crash. Lost alpha detectors measure bursts of alpha loss coincident with sawtooth crashes which represent a very small fractional loss of the previously confined alphas (<1%). Thus, a sawtooth crash mainly leads to radial redistribution of the alphas rather than losses. For modeling of alpha sawtooth mixing, a code is used which is based on the conventional model of magnetic reconnection and the conservation of particles, energy and magnetic flux. The effect of the particle orbit averaged toroidal drift in a perturbed helical electric field generated by the crash has also been included in the code. It is shown that mixing of the passing alphas is dominated by the magnetic reconnection whereas trapped alphas are affected mainly by the $E \times B$ drift.

---

* Work supported by the US Department of Energy under Contract No. DE-AC02-76CH0-3073 and Grant No. DE-FG03-92ER54150.

[1] A.F. Ioffe Physico-Technical Institute, St. Petersburg, Russian Federation. Present affiliation: Princeton Plasma Physics Laboratory, Princeton, New Jersey, USA.

[2] TRINITI, Troitsk, Russian Federation. Present affiliation: Princeton Plasma Physics Laboratory, Princeton, New Jersey, USA.

[3] Princeton Plasma Physics Laboratory, Princeton, New Jersey, USA.

[4] General Atomics, San Diego, California, USA.

[5] University of Wisconsin-Madison, Madison, Wisconsin, USA.

[6] Chalmers University of Technology, Gothenburg, Sweden.

[7] Massachusetts Institute of Technology, Cambridge, Massachusetts, USA.

1. Introduction

Effective operation of a D-T fusion reactor requires that the alpha particles deposit most of their energy in the plasma before they are lost. MHD activity (e.g. sawtooth oscillations) can transport alphas from the plasma core which might affect ignition and/or damage of the first-wall components of the vessel by feeding the alphas into the stochastic ripple loss region. The purpose of this paper is to report both the experimental observations of alpha mixing and the efforts to model the effect of sawteeth on fusion alpha transport.

In D-T experiments on TFTR, the behavior of fast confined alphas was investigated in both quiescent plasma regimes and also in the presence of MHD activity. The radially resolved confined alpha particle energy and density distributions are measured using two diagnostics: PCX [1] and α–CHERS [2]. In MHD-quiescent plasmas, both diagnostics observed classical slowing down and neoclassical confinement [2, 3]. Both diagnostics have observed evidence for sawtooth mixing of confined alphas by sawtooth crashes [4, 5]. The influence of sawtooth effects on injected neutral beam ions, RF driven minority ions and fusion products in DD plasmas has been discussed elsewhere [6 - 8]. Below we present experimental data on alpha sawtooth mixing taken by PCX and α-CHERS diagnostics in TFTR D-T discharges and describe the approaches for modeling of these phenomena. Also, we present the results of measurements of lost alphas [9] during sawtooth crashes in TFTR D-T discharges.

2. PCX Experimental Data

The Pellet Charge-eXchange (PCX) diagnostic on TFTR uses the ablation cloud formed by an impurity pellet (Li or B) injected along a midplane major radius with velocities in the range of 500-700 m/s to neutralize alphas by double or sequential single electron capture. The escaping helium neutrals are mass and energy analyzed using a high energy Neutral Particle Analyzer (NPA) having eight energy channels. The NPA views the pellet from behind with a sight line at a toroidal angle of 2.75° to the pellet trajectory. Consequently, only near perpendicular alphas with velocities close to $v_{||}/v$ = - 0.048 are detected in these experiments.

The radial position of the pellet as a function of time is measured using a linear photodiode array located on the top of the vacuum vessel. By combining this measurement with the time dependence of the observed NPA signals, radially resolved alpha energy spectra and radial density profiles can be derived in the energy range of 0.5 - 2.0 MeV for Li pellets and 0.5 - 3.8 MeV for B pellets with a radial resolution of ~ 5 cm. The PCX diagnostic is not absolutely calibrated because of the difficulties in determining the densities of the ion charge states in the cloud [1].

Pellets are injected 0.2 - 0.5 s after termination of neutral beam heating. This timing delay leads to deeper penetration of the pellet as a result of decay of the electron temperature as well as to enhanced signal-to-noise ratio because the neutron background decays significantly faster than the confined alpha population.

The experiments were performed in standard TFTR D-T supershots [10] with a plasma current of 2.0 MA, a toroidal magnetic field of 5T, major and minor radii of R = 2.52 m and a = 0.87 m and 20 MW of DT neutral beam power injection. Sawteeth do not normally occur during beam injection in these supershots. Large sawtooth crashes begin to develop 0.2 - 0.3 s after the

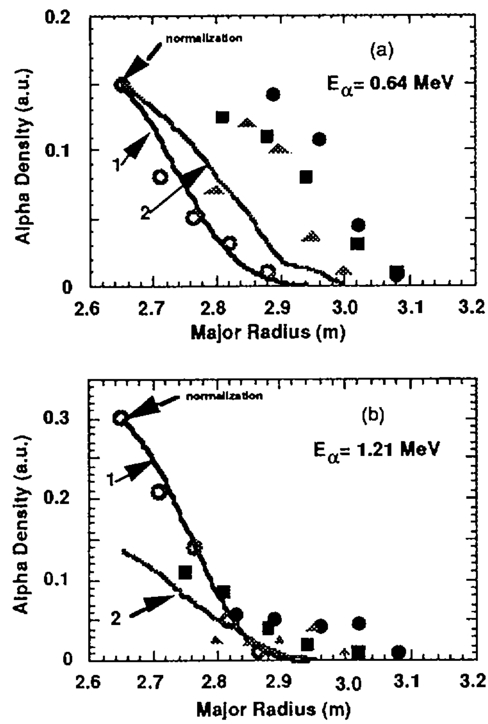

FIG. 1. Precrash (open circles) and postcrash (solid symbols) PCX alpha particle density radial profiles for (a) E_α = 0.64 MeV and (b) E_α = 1.21 MeV. Curves 1 refer to precrash conditions using the FPPT model normalized to PCX data. Curves 2 correspond to postcrash conditions using the model based on the freezing of trapped alphas into the magnetic field and on conservation of energy.

termination of beam injection when the plasma β drops below the level required to suppress sawteeth. To get PCX data , a Li pellet was injected before and after the sawtooth crashes in sequential similar discharges. Measured alpha radial density profiles for alpha energies of 0.64 MeV and 1.21 MeV for precrash (open circles) and postcrash moments (solid symbols) are shown in Fig. 1 (a and b). Postcrash experimental data for three discharges are shown. There is some variation in the postcrash data due to minor differences in the timing and amplitude of the sawteeth. Solid lines are the results of modeling which will be described below. The PCX data indicate that a significant broadening of the trapped alpha density profile occurs for postcrash conditions. It is also seen that this broadening decreases with increasing alpha energy.

3. α-CHERS Experimental Data

In the α–CHERS technique [2], the alpha signal is excited by charge exchange between alphas and heating beam deuterium atoms and appears as a wing on the long-wavelength side of the He^+ 468.6 nm line. Five spatial channels are available, with sightlines intersecting three of the heating neutral beams in the

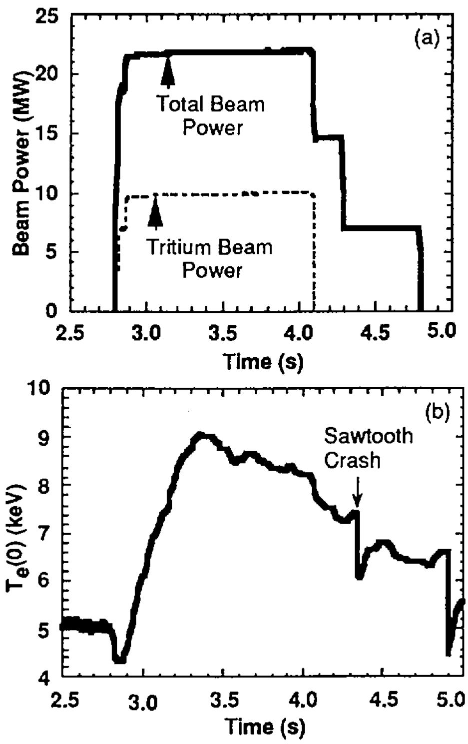

FIG. 2. Time evolution of (a) the injected neutral beam power and (b) core electron temperature in the α-CHERS experiment.

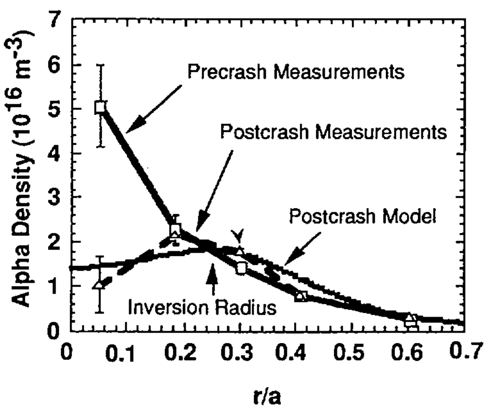

FIG. 3. Experimental data and modeling results for α-CHERS measurements during precrash and post-crash sawtooth conditions.

toroidal midplane at radii spanning the region r/a = 0.05 - 0.6. Three spatial channels may be observed in a single discharge, making it necessary to combine data from two similar discharges to get a complete five-point radial profile. The data were averaged over 0.2 s intervals to improve the signal-to-noise ratio. The α-CHERS system is absolutely calibrated, allowing absolute measurements of the alpha density to be made.

The experiment was performed in standard TFTR supershots similar to those which were used for the PCX measurements. The time evolution of the injected neutral beam power and core electron temperature is shown in Fig. 2 (a and b). The sawtooth crash was induced in this experiment by dropping the beam power 0.2 s after termination of the D-T beam phase, as shown in Fig. 2a. By inducing the sawtooth in this way, the alpha density profile could be measured before and after the sawtooth crash. The alpha density profiles were obtained by combining data from two similar discharges. The results of these measurements are presented in Fig. 3. Alpha energies here are averaged over the range 0.15 - 0.6 MeV. The α–CHERS measurements show a sharp drop in the core alpha density (by a factor of ~5) after the crash and broadening of the passing alpha radial density profile. However, the relative broadening of the passing alphas is significantly smaller than that observed by the PCX diagnostic for the trapped alphas. The total number of alphas in the observed energy and radial profile ranges is consistent with particle conservation. The lost alpha detectors measure no alpha loss in these shots.

4. Lost Alpha Detector Data

Extensive studies of alpha losses during DT experiments on TFTR are routinely conducted using lost alpha detectors located on the walls of the vacuum vessel [11]. Here we present the data for the detector located 20 degrees below the outer midplane . The detector integrates the data over a pitch angle range of 45 - 85 degrees with respect to the co-toroidal direction and over an alpha energy range of 0.5 - 4 MeV.

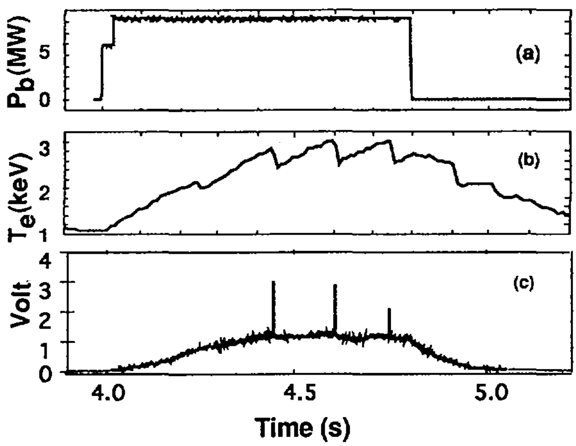

FIG. 4. Time evolution of (a) neutral beam power, (b) core electron temperature, and (c) the lost alpha detector signal.

Figure 4 shows the neutral beam time evolution, core electron temperature and lost alpha signal in a TFTR discharge with a plasma current of 1.4 MA, a toroidal magnetic field of 3.2 T, 7.5 MW of neutral beam power and major and minor radii R = 2.52 m and a = 0.87 m, respectively. There were three strong sawtooth crashes during the neutral beam heating period due to low NBI power and low q(a) and the lost alpha detector measured 0.1 - 1 ms bursts of alpha loss coincident with the crashes. The integrated loss in the bursts represent a very small fractional loss of the previously confined alphas (<1%). The lost alpha measurements on plasmas similar to those where the PCX and α–CHERS data were taken indicate that the alphas are not ejected.

5. Modeling of Alpha-Particle Distributions in TFTR

The slowing down alpha particle energy spectra in a quiescent plasma (without any MHD activity), was modeled with the TRANSP [12] Monte-Carlo code which follows the orbits of alphas as they slow down and pitch-angle scatter by Coulomb collisions with the background plasma. TRANSP assumes that alphas are well confined during slowing down and takes into account the spatial and temporal distributions of plasma parameters in each discharge. TRANSP was recently modified to include stochastic ripple diffusion of alphas [13]. Since the Monte-Carlo methods used in TRANSP are computationally intensive, we developed a Fokker-Planck post-TRANSP (FPPT) processor code [14]. The FPPT code solves the drift-averaged Fokker-Planck equation using the pitch angle integrated alpha source distribution provided by TRANSP as input and includes modeling of the ripple effect. The FPPT code is very effective for rapid modeling of the PCX data which is acquired in a narrow pitch angle window during a very short time interval (~1 ms),

The curves 1 in Fig. 1(a and b) present FPPT modeling results for the alpha radial density profiles normalized to the precrash PCX experimental data. These modeling examples for the PCX data show that for sawtooth free conditions, the alpha distribution functions have the classical character.

Models of the effect of the sawtooth on confined fast ions [15] were developed for neutral beam injected passing particles having small radial deviations from the magnetic surface. Conservation of particle energy during mixing was assumed. In such an approach, the fast particles follow the magnetic surface during the crash and the models tended to describe the sawtooth effect on the measured neutron fluxes due to beam-plasma fusion reactions [6]. This model was used for the α-CHERS data for fast particle mixing (postcrash model curve in Fig. 3). A small radial diffusion coefficient $D_\alpha = 0.03\ m^2/s$ (consistent with neoclassical diffusion and α-CHERS measurements of alpha radial profiles in MHD-quiescent discharges [16]) was implemented into the model to allow comparison with the experimental data averaged over 0.2 s. The agreement of the model with the experiment data indicates that energetic passing alphas redistribute with the magnetic flux [5].

Application of a similar model to the PCX data (curves 2 in Fig. 1 a and b), however, does not yield satisfactory agreement: the measured local density of trapped alpha particles on the outside of the torus is significantly higher after the sawtooth crash than indicated by the model, as might be caused by radial expulsion of trapped alphas from the center accompanied by a change in their energy. Recent theoretical research [14, 17] treats this phenomenon by inclusion of an electric field produced by the crash. The toroidal drift in the perturbed helical electric field determines the energy change of alpha particles during the sawtooth crash. In [14], a simple approach to alpha particle energy redistribution

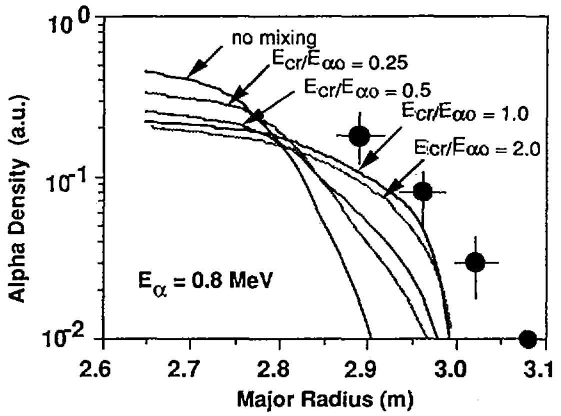

FIG. 5. Application of the E × B model in the FPPT code to the experimental PCX data.

was proposed which is shown to obey a diffusion type of equation. An analytical transformation formula for alpha particle redistribution was obtained and included in the FPPT code. A helical electric field is assumed to be generated during the so-called "collapse" period of the sawtooth oscillation on a very short time scale $\tau_{cr} \sim 10^{-5}$ - 10^{-4} s where τ_{cr} is the crash time. In this approach, particles can undergo significant displacement within the alpha mixing radius during the crash. The interaction of the fast particles with the perturbed electric field can be considered as resonant, even though the mode itself has very low frequency and was assumed not to be rotating during the short crash. Therefore, particles with energy higher than some critical value E_{cr} perform toroidal precession during the crash and do not interact with perturbed electric field (see also [17]). We define $E_{cr} = 2\omega_c m_\alpha rR/\tau_{cr}$ from comparison of the particle toroidal rotation time and the sawtooth crash time τ_{cr}, where ω_c is the cyclotron frequency, m_α is the alpha particle mass, and r, R are the minor and major radii, respectively. E_{cr} plays the role of an adjustable parameter in simulations of the experimental data as discussed below. Introducing E_{cr} as an adjustable parameter avoids the need for precise knowledge of the crash time τ_{cr} $\{E_{cr}(\mathrm{MeV}) = 35/\tau_{cr}(10^{-5}\ \mathrm{s})\}$. A more consistent model of fast particle redistribution has been presented in [18], where the fast particle drift kinetic equation, including sawtooth-generated electric and magnetic fields, was solved numerically. The analysis is based on results of [17] and shows qualitatively the same dependence of the trapped fast particles on energy as in [14].

A different approach for fast particle-sawtooth interaction was used by Y. Zhao and R. White, where direct Monte-Carlo simulation of fast particle orbits in the presence of two or more nonlinearly interacting modes was performed. Results show rather flat fast particle profiles versus minor radius after the crash and agree with the α-CHERS measurements which relate to mainly passing particles. The results of this analysis for trapped particles give more peaked profiles than measured by PCX. This probably indicates that the time scale length of the perturbations was chosen to be too long and all trapped fast particles have performed more than one toroidal precession around the torus or $E > E_{cr}$ in the terminology of Refs. [14, 17].

Figure 5 illustrates the procedure used to determine the adjustable parameter, E_{cr} , used in application of the Gorelenkov model including ExB drift

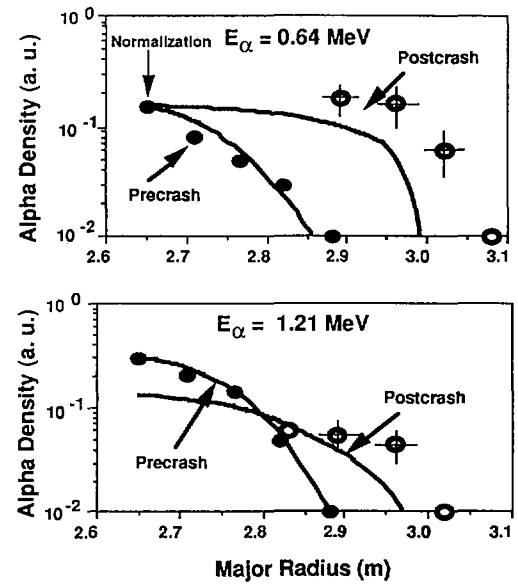

FIG. 6. Comparison of PCX experimental data with the FPPT model for alpha energies $E_\alpha = 0.64$ MeV and $E_\alpha = 1.21$ MeV with $E_{cr}/E_{\alpha 0} = 1$ and $r_{mix} = 1.5\ r_s$.

of the alphas [14] to the experimental PCX data for sawtooth mixing of trapped alphas. The PCX experimental points are shown as solid circles. The precrash curve is normalized to the PCX data for a similar shot without sawteeth. One can see from profile comparisons that $E_{cr}/E_{\alpha o} = 1$ gives the best fit to the data. In all the calculations, a mixing radius of $r_m = 1.5r_s$ ($q(r_s) = 1$) was used. This mixing radius is a second adjustable parameter used in the model. The value of $r_m = 1.5r_s$ is about the sawtooth mixing radius for the bulk plasma and yields the best fit to the PCX data. Figure 6 (a and b) shows the comparison of the PCX data with the ExB sawtooth mixing model for two alpha energies. The model describes well both the broadening of alpha radial profiles and the dependence of this broadening on the alpha energy (higher energy corresponds to smaller broadening) that is observed experimentally.

An additional limitation on the parameter r_m is the stochastic ripple diffusion boundary. Models which incorporate stochastic ripple diffusion indicate that beyond the stochastic ripple boundary, the energetic trapped alphas diffuse out of the plasma in a few milliseconds. Figure 7 shows ExB modeling of the postcrash PCX data with and without toroidal field ripple. The stochastic ripple diffusion boundary according to the Goldston-White-Boozer theory [19] is also indicated. The alphas are redistributed by the sawtooth crash very close to, but not beyond, the stochastic ripple boundary. This is consistent with the fact that lost alpha detectors do not detect significant losses of the alphas, as it was shown in Sec. 3. If we use $r_m > 1.5r_s$ in the modeling of the post crash alpha profile, large ripple and prompt alpha losses are predicted.

Within the accuracy of the PCX measurements and the model, good agreement is seen in comparisons of the experimental alpha density profiles and spectra with the ExB model. The application of this model to the passing

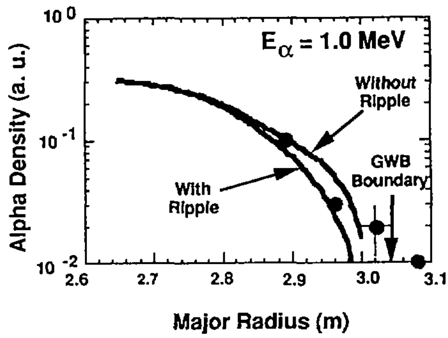

FIG. 7. PCX experimental postcrash sawtooth data and FPPT modeling with and without toroidal field ripple.

particles does not produce alpha redistribution because of the very fast toroidal rotation of those particles. A unified version of the FPPT sawtooth mixing code is being developed which includes both the freezing of the particles to the magnetic surfaces and the ExB drift model, which is expected to describe sawtooth mixing for both passing and trapped alpha particles.

6. Conclusion

PCX and α-CHERS diagnostic measurements show significant radial redistribution of trapped and passing alphas after sawtooth crashes in TFTR DT plasmas. Modeling of the experimental data has shown that two different mechanisms dominate the sawtooth mixing of the passing and trapped alphas: 1) the freezing of the passing alphas in the magnetic field and, 2) the drift of the trapped alphas in the electric field produced by the sawtooth crash. Comparison of the PCX and α-CHERS data with lost alpha measurements shows that in the sawtooth crashes, radial redistribution of the alphas occurs without significant ripple losses of particles. The sawtooth oscillations effectively transport the alphas outward along the major radius close to the stochastic ripple domain. Under conditions of larger mixing radius than occurs in TFTR, this transport might lead to enhanced ripple loss of fusion alpha particles in tokamaks. Theoretical understanding of the effect of sawteeth on nonthermal alphas has progressed sufficiently so that the effects of sawteeth on alpha behavior in ITER can be predicted.

Acknowledgments

The authors wish to acknowledge the dedicated efforts of the entire TFTR Group who provided excellent support for these experiments. H. H. Duong is a General Atomics ORAU Fellow at PPPL.

REFERENCES

[1] FISCHER, R.K., et al., Phys. Rev. Lett **75** (1995) 846.
[2] McKEE, G.R., et al., Phys. Rev. Lett **75** (1995) 649.
[3] MEDLEY, S.S., et al., Plasma Phys. Control. Fusion **38** (1996) 1.
[4] PETROV, M.P., et al., Nucl. Fusion **35** (1995) 1437.
[5] STRATTON, B., et al., Nucl. Fusion **36** (1996) 1586.
[6] ANDERSON, D., et al., Nucl. Fusion **34** (1994) 217.
[7] MARCUS, F.B., et al., Nucl. Fusion **34** (1994) 687.
[8] DUONG, H.H., HEIDBRINK, W.W., Nucl. Fusion **33** (1993) 211.
[9] ZWEBEN, S.J., et al., Nucl. Fusion **35** (1995) 1445.
[10] STRACHAN, J.D., et al., Phys. Rev. Lett. **72** (1994) 3526.
[11] DARROW, D.S., et al., Rev. Sci. Instrum. **66** (1995) 476.
[12] BUDNY, R.V., et al., Nucl. Fusion **35** (1995) 1497.
[13] REDI, M.H., et al., Nucl. Fusion **35** (1995) 1509.
[14] GORELENKOV, N.N., et al., Modeling of α–Particle Redistribution by Sawteeth in TFTR Using FPPT Code, Rep. PPPL 3184, Princeton Plasma Phys. Lab. (1996), submitted to Nucl. Fusion.
[15] KOLESNICHENKO, Ya.I., et al., Nucl. Fusion **32** (1992) 449.
[16] McKEE, G.R., et al., submitted to Nucl. Fusion.
[17] KOLESNICHENKO, Ya.I., et al., Nucl. Fusion **36** (1996) 159.
[18] KOLESNICHENKO, Ya.I., et al., in Controlled Fusion and Plasma Physics (Proc. 23rd Eur. Conf. Kiev, 1996), Vol. 20C, European Physical Society, Geneva (1996).
[19] GOLDSTON, R.J., et al., Phys. Rev. Lett. **47** (1981) 647.

DISCUSSION

Ya.I. KOLESNICHENKO: The reported work gives experimental evidence, based on the use of two independent diagnostics, that sawteeth affect fusion produced α particles. However, the available data are relevant only to deeply trapped and well circulating particles. Therefore, further experiments are required to obtain a complete picture of the behaviour of α particles in the presence of sawtooth oscillations.

Concerning the theory, I should note that the main ideas and first results of the so called $\mathbf{E} \times \mathbf{B}$ drift model were contained in the work by Kolesnichenko and Yakovlenko reported at the IAEA's Technical Committee meeting on α Particle Physics (Princeton, April 1995). At that meeting, R. White commented that resonances between the toroidal and poloidal motion may contribute to particle transport. I agree with him and think that the first results in this direction will be ready soon, probably in our collaboration with Princeton. At present, however, when resonances are neglected, the only mechanism driving particle redistribution is the $\mathbf{E} \times \mathbf{B}$ drift, and I want to emphasize that this is true for both trapped and circulating particles.

I should also like to comment on the name given to our earlier model — the 'reconnection model'. This name can lead to misunderstanding because reconnection of the magnetic field lines is an important element of all proposed models, not only of the earlier model. I would therefore suggest a different name: 'approximation of flux surface attached particles'.

PROSPECTS FOR ALPHA CHANNELING: INITIAL RESULTS FROM TFTR

N.J. FISCH, M.C. HERRMANN, D.S. DARROW, H.P. FURTH, R.F. HEETER, H.W. HERRMANN, J.C. HOSEA, R. MAJESKI, C.K. PHILLIPS, J.H. ROGERS, G. SCHILLING, S.J. ZWEBEN
Plasma Physics Laboratory,
Princeton University,
Princeton, New Jersey,
United States of America

Abstract

PROSPECTS FOR ALPHA CHANNELING: INITIAL RESULTS FROM TFTR.

Numerical simulations show that for a reactor-sized tokamak, a combination of excited toroidal Alfvén eigenmodes (TAE) and mode-converted ion Bernstein waves (IBW) might extract more than half the energy from a birth distribution of α particles in a tokamak DT reactor. Preliminary results on TFTR are analyzed with a view towards addressing the underlying assumptions in these simulations. The data support several of the necessary conditions for realizing the alpha channeling effect.

1. Introduction

Tokamak reactors would be much improved by the alpha-channeling effect [1, 2], where α particles amplify waves that then damp on ions, thereby enabling hot-ion mode operation [3]. This effect, however, is likely to be realized only through a combination of waves [4]. Numerical simulations show that, for a reactor-sized tokamak, a combination of excited TAE and mode-converted IBW might extract more than half the energy from a birth distribution of α particles in a tokamak DT reactor [5]. An idealized model for both TAE and IBW spectra shows that 60% of the alpha power goes into the waves, with 20% going into high-n TAE (likely to damp on fuel ions), and with 40% going into a low-field-side IBW (which might damp on tritium fuel ions [6]).

This paper explores the experimental support for such speculations, obtained in a series of experiments on TFTR in 1995 [7] and 1996, emphasizing evidence relating to the use of the mode-converted ion-Bernstein wave. The experiments were carried out in D^3He plasmas, with fast magnetosonic waves at 43 MHz launched from the low-field periphery. These waves mode-convert to IBW waves at the D^3He ion-ion resonance, which was controlled by varying the minority ^3He fraction between 10 and 25% of the electron density. The plasma current was typically 1.4 MA, with the toroidal magnetic field ranging from 4.4 to 5.3 T, placing the mode-conversion layer within 25 cm of the magnetic axis.

In the presence of a mode-converted IBW wave, enhanced losses of energetic ions were observed. The lost ions impinge on a poloidal array of detectors [8, 9, 10]. These detectors are located at 90°, 60°, 45°, and 20° below the outer midplane and are each capable of resolving both the pitch-angle and gyroradius of lost energetic ions. Thus, 1.75 MeV deuterons, 1.16 MeV tritons, and 3.5 MeV α particles all have the same gyroradius signature, but the species might be inferred by other means. The resulting signature, in poloidal angle, pitch angle, and energy, is so detailed that only accurate assumptions about the wave physics allow the full data to be simulated numerically, thus revealing important details of both the wave propagation and the wave-particle interaction physics.

Note that the experiments reported on here exhibit heating of energetic ions, rather than cooling. However, we would have confidence that cooling can also be obtained, if our theoretical understanding of this heating were confirmed by these experiments. Of course, cooling requires the suitable employment of several waves [5], rather than the sole use of the IBW wave.

2. Fast Ion Interactions with the Mode-Converted IBW

Interactions of the mode-converted IBW wave with beam deuterons have been demonstrated. Among the experimental variables affecting these interactions is the placement of the mode conversion layer. In D^3He plasmas on TFTR, this placement has been accomplished routinely by varying the ^3He fraction, verified by observing the radius of the electron heating [11]. Controlling the location of the mode conversion layer is of major importance for channeling α power in a reactor.

The IBW wave interaction with beam deuterons has been deduced as follows: Enhanced losses were observed with deuterium beam heating only [12], with the mode conversion layer near the magnetic axis. In principle, the lost ions could be α particles, fusion tritons, or very much heated beam deuterons. The fusion tritons result from the interaction $D + D \rightarrow T\,(1\,\mathrm{MeV}) + p\,(3\,\mathrm{MeV})$. In view of the other equally likely branch for DD, there is a neutron produced for every triton. The α particles result from the interaction $D + {}^3He \rightarrow {}^4He\,(3.6\,\mathrm{MeV}) + p\,(14.7\,\mathrm{MeV})$. If the loss were accelerated deuterons, up to 2.1 MeV deuterons would be indicated, with about 2 MeV absorbed from the waves. If tritons or α particles, energies of 1.5 the birth energy would be indicated.

The ambiguity concerning the lost species is resolved by the data in Fig. 1, which shows very different loss signatures under co and counter deuterium beams, and π phased rf (both signs of n_ϕ present). Neither fusion product distribution would be affected significantly by the direction of the beams, thus identifying heated beam deuterons as the dominant lost species.

Evidence suggestive of an interaction between the IBW and α particles during T gas puffing was described in Ref. 13. However, the number of α particles in the discharge is too small to explain the losses observed, even if all of the α particles are lost. α particles might be interacting with the IBW in these discharges but their loss would be difficult to observe against the background of a much larger loss of heated beam ions. When T beams are injected into D^3He plasmas, in the presence of the IBW, there is no anomalous loss observed. Thus a demonstration of an interaction between the IBW wave and α particles is not yet in hand.

3. Modeling the Interaction with the IBW

Although successful identification of the lost species is made, certain quizzical features of the data still remain. For example, why are lost beam tritons not observed, whereas beam deuterons are? Why are lost fusion α particles produced by tritium beams not observed, even while anomalous losses are observed in similar discharges driven by deuterium beams?

These questions have been addressed through numerical calculations of the wave-particle interactions. The detailed agreement with the experimental observations lends important support to the use of the same model in cases relevant to a reactor, for example when two waves are employed, and where the α cooling effect is predicted.

Particles interacting with the IBW wave are modeled as diffusing in the constants-of-motion space E-μ-P_ϕ along the trajectory

$$dP_\phi/dE = n_\phi/\omega \tag{1a}$$

$$d\mu/dE = en/(m\omega), \tag{1b}$$

where E is the energy, μ is the magnetic moment, P_ϕ is the canonical angular momentum, and n_ϕ is the toroidal mode number, ω is the IBW wave frequency, and n is the resonance order (for deuterons in a D^3He plasma, $n = 1$; for tritons, $n = 2$). With

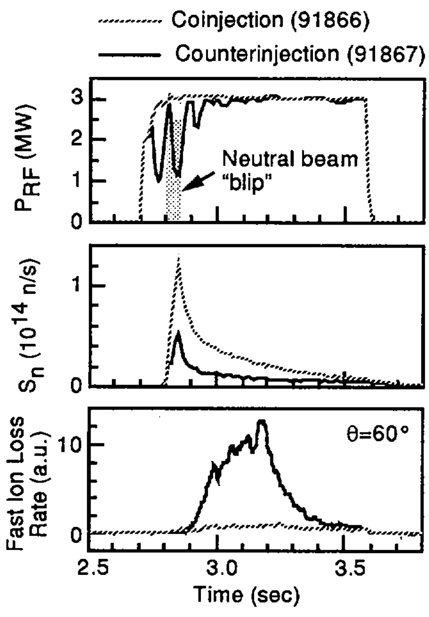

FIG. 1. Losses of co and counter deuterium beam ions in the presence of π phased rf. Discharge at 4.8 T, 1.4 MA with mode conversion layer on axis.

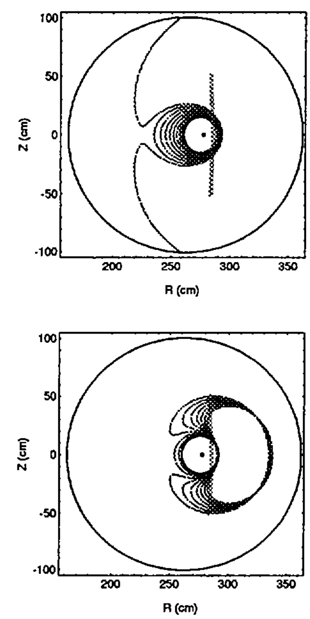

FIG. 2. A deuteron (top) and a triton (bottom) interacting with an IBW (shaded strip). The 100 keV particles are initially passing near the center, later becoming trapped.

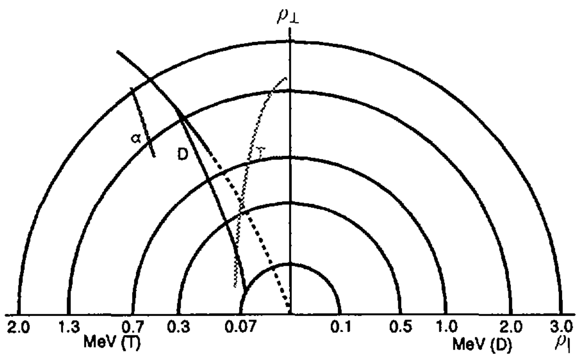

FIG. 3. Passing/trapped boundary and trajectories of 100 keV D, 100 keV T and 3.5 MeV α particles diffused by IBW versus $\rho_\|$ and $\rho_\perp$.

each traversal of the mode conversion region, resonant ions randomly jump to a nearby E-μ-P_ϕ coordinate along the trajectory described by Eqs. (1). Resonant ions satisfy

$$\omega - k_{||}v_{||} = n\Omega_i, \tag{2}$$

where Ω_i is the cyclotron frequency of the resonant ion.

Fig. 2a shows a counterpassing 100 keV deuteron heated to 2 MeV. By counterpassing, we mean ions traveling opposite to the plasma current. The innermost orbit shown is its initial orbit; each time it interacts with the IBW wave, it jumps to a wider orbit if it gains energy. If it loses energy, it jumps to an interior orbit (the orbits less than the initial energy are not shown). The widest orbit shown indicates that after it has gained 2 MeV, it becomes trapped, with an orbit intercepting the 90° detector. Fig. 2b shows a counterpassing 100 keV triton heated to 1 MeV. The innermost orbit shown is its initial orbit; the wider orbits shown are trapped orbits, but none intercept the tokamak periphery. Thus, whereas the 100 keV deuteron eventually is detected at the 90° detector, the 100 keV triton remains trapped in the plasma.

This very different behavior displayed by deuterium and tritium can be seen by considering trajectories in $v_{||}$–$v_\perp$ (or, equivalently, $\rho_{||}$–$\rho_\perp$, where ρ is the gyroradius) space, assuming that particles remain roughly on a flux surface during the interaction. In Fig. 3, the right side coordinates are for deuterium energies (in MeV), while the left side coordinates indicate tritium energies. The dotted line shows the passing–trapped boundary; this line is continued as a solid line for those trajectories that intersect the tokamak boundary. Thus, it can be seen that the deuterium ions (line D) are heated to about 2 MeV before being lost, whereas the tritium beam ions (line T) cannot reach the detector. However, it can also be seen that 1 MeV tritium, born of the DD reaction, can reach the loss region at around 1.5 MeV. Thus, the model of the IBW interaction supports both deuterium beam ions and energetic tritons as candidates for the 90° detector signal, while explaining the absence of a similar signal with tritium beams. The 1.5 MeV tritons, however, are evidently (from Fig. 1) not the dominant species.

To explain the absence of α-particle loss with tritium beams, note that in the case of tritium beams, the mode conversion layer is far from the α cyclotron resonance. From Eqs. (1b) and (2), we have $\Delta v_{\|}/\Delta v_{\perp} = (v_{\perp}/v_{\|})(\omega - \Omega_{\alpha})/\omega$. Hence, from Fig. 3 it can also be seen that α particles, far from the α resonance, move along too gentle a slope to intercept the trapped-passing boundary, except at very high energy, perhaps 8 MeV, which would be outside the gyroradius range of the lost-α detectors.

4. Deducing the $k_{\|}$-flip

The numerical solutions that produce significant alpha channeling rely on the so-called "$k_{\|}$-flip," which has been predicted theoretically [6], but never observed experimentally.

The $k_{\|}$-flip occurs as follows: As the IBW wave emerges from the mode-conversion layer, there is a rapid increase, as a function of horizontal position, in k_x, the perpendicular wavenumber in the direction of the magnetic field gradient (here, the horizontal or $\hat{x}$-direction). Since the poloidal magnetic field has a component in the $\hat{x}$-direction, the parallel wavenumber can be written as

$$k_{\|} = n_{\phi}/R + k_x \hat{x} \cdot \hat{B}, \tag{3}$$

where n_{ϕ}/R is the launched $k_{\|}$, and where $\hat{B}$ is the direction of the magnetic field. For parameters of interest, $n_{\phi}/R \simeq .08\ \mathrm{cm}^{-1}$. At about 15 cm off the horizontal midplane, $\hat{x} \cdot \hat{B} \simeq .05$. In addition, from numerical calculations [6], one can expect $k_x \rho_t \simeq 1$, where ρ_t is the ion thermal gyroradius. Thus, either above or below the midplane, $k_{\|}$ may change sign from the launched $k_{\|}$.

This is a crucial feature of the mode-converted IBW in producing the α-channeling effect [5]. To see this, note that a particle moving from the center to the periphery of the plasma moves to lower P_{ϕ} (assuming its drift from its flux surface is small compared to the tokamak minor radius). Then, from Eq. (1a), α particles will cool as they leave the plasma only for $n_{\phi} > 0$. Repeated interactions of trapped α particles with the IBW, when the wave extracts energy from the α-particle, require the wave-particle interaction to be on the outer leg (low-field side) of the trapped orbit, where the α-particle is comoving. From the resonance condition, we have $v_{\|} = (\omega - \Omega_{\alpha})/k_{\|} > 0$. Mode conversion in DT plasmas occurs to the high field side of the deuterium gyroresonance layer, so that $\omega < \Omega_{\alpha}$. Thus, where the wave particle interaction occurs, $k_{\|}$ must be negative, which is necessarily opposite in sign to the launched $k_{\|}$.

Fig. 4 shows large anomalous loss at the 45° detector for rf launched opposite to the direction of the current ($n_{\phi} < 0$, which is by convention called "90° phasing"), in the presence of deuterium beams costreaming in the direction of the toroidal current. When $-90°$ rf is launched ($n_{\phi} > 0$) with costreaming beams, there is no rf-induced fast ion loss. Hence, the wave can be deduced to be well-directed and that this directivity is critical to the particle loss. In a D^3He plasma, the deuterium resonance is on the high field side of the mode conversion layer, so $\omega > \Omega_D$. Thus, to affect cogoing particles, $k_{\|} > 0$, which is opposite in direction to n_{ϕ}, hence "flipped."

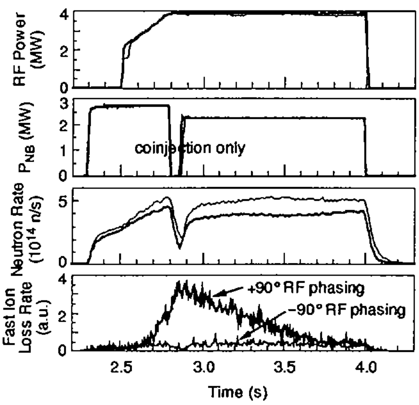

FIG. 4. Losses of co deuterium beams in the presence of phased rf; +90° phasing (counter to the current) results in significantly enhanced losses, whereas −90° phasing (co to the current) shows first orbit losses of fusion products only.

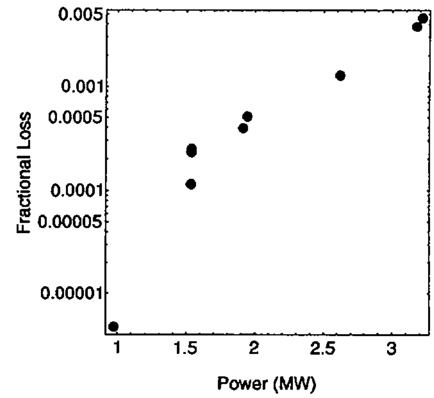

FIG. 5. Approximate losses of deuterium ions (fraction of beam ions) versus rf power. The measured loss is assumed to be constant over a portion of the outer midplane.

5. Diffusion Coefficient

The α channeling effect relies upon the extraction of the α-particle energy by waves in a time short compared to their slowing down time. Observations of the so-called "beam blip" losses on TFTR suggest that this collisionless limit has been very nearly reached experimentally with very modest rf power. Deuterium beams with duration of only 50 ms are fired into discharges with varying amounts of IBW power. The data is then quite quite rich in detail; in addition to the poloidal angle, energy, and pitch angle data, there is now the time-history of this data as a function of rf power.

A simple one-dimensional model of these losses suggests the following: in the limit of infinite rf power, the main losses should be observed at about time $\tau_D \equiv (\Delta v)^2/D_{\mathrm{QL}}$ after the beam blip, where Δv is the deuteron exit speed and D_{QL} is the rf diffusion coefficient. In the opposite limit, namely the collisional limit, $\nu\tau_D \gg 1$, the delay to the main loss should be about ν^{-1}, where ν is the collisional slowing down rate. The fraction of ions lost approaches one in the collisionless limit and zero in the collisional limit, since ions are presumed to interact with the wave only above a threshold velocity. This model suggests further that the dependence of the number of particles lost is extremely sensitive to the parameter $\nu\tau_D$ in the range $\nu\tau_D \simeq 1$.

Fig. 5 shows an estimate of the fraction of beam particles lost as a function of IBW power. The clearly very sensitive dependence on rf power suggests that the limit $\nu\tau_D \simeq 1$ has been attained; moreover, the large number of particles lost at 3 MW (about 0.5%) suggests that by increasing the rf power only by a factor of a few should access the fully collisionless limit. The data is sufficiently rich in detail that through comparisons with a more accurate simulation more quantitative predictions should be possible.

6. Mode Conversion in DT Plasmas

Recent modifications of the TFTR ICRF system now permit n_ϕ in the range 10–30, at 30 MHz, and with directed phasing. Thus, the IBW wave could be excited on axis or to the low-field side of the axis in DT plasmas, rather than in D^3He plasmas. However, experiments to date have not succeeded in efficient mode conversion in DT, apparently because of the presence of vigorous ^7Li minority heating [14]. It is thought that the presence of ^7Li can be avoided by conditioning exclusively with ^6Li, which has the same gyrofrequency as the deuterium.

If the mode conversion can indeed be made efficient, then several interesting directions of research are indicated. First, the observations in D^3He ought to be checked in DT. Second, according to numerical simulations, an IBW wave excited on axis in a reverse-shear DT plasma should exhibit cooling of certain α particles, even as other α particles are heated. Fig. 6 shows the predicted very distinctive lost-α signature, which shows the cooling effect observed on the 20° detector, well separated from the heated α particles, which are ejected only in the vicinity of the 90° detector.

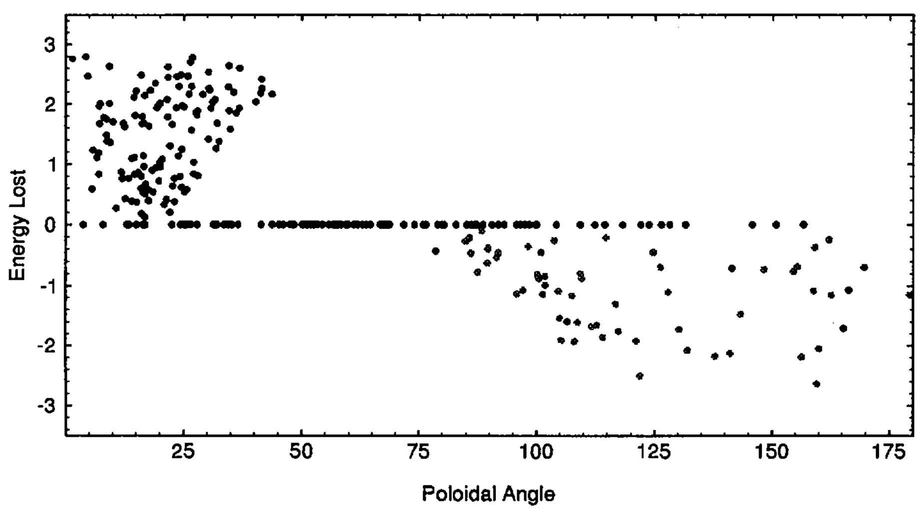

FIG. 6. Energy lost to the wave (MeV) and poloidal exit angle of α particles in simulated reverse shear TFTR discharge with $B = 5.3$ T, $I = 1.85$ MA (scaled shot #84011); 1000 particles are simulated. Particles exiting with zero energy lost correspond to first orbit losses (11%); 13.7% of the α particles are cooled, exiting near the outer midplane; and 3.8% are heated, exiting between the inner midplane and the bottom.

7. Summary and Conclusions

Several key requirements for α channeling are supported by experiments with the mode-converted IBW wave on TFTR. In particular, we find that the IBW wave can be situated at will, that it can interact with beam deuterons, accelerating them from 100 keV to 2 MeV, and that the wave-particle diffusion coefficient is near the collisionless limit.

Of major significance is the experimental verification of theoretical predictions that these interactions can take place with $k_{\|}$ opposite in sign to n_{ϕ}. The agreement obtained between the very detailed experimental observations and computer modeling lends important support to the far-reaching predictions of α channeling in a reactor, based on the same numerical code. The results obtained suggest an important direction for further research, wherein the cooling of a significant population of fusion α particles could be observed in a reverse shear discharge on TFTR, if the mode conversion can be made efficient in a DT plasma.

The high magnetic fields and copious α-particle population place TFTR as the only experiment capable of establishing the low-field-side IBW-α interaction physics. Studies of the TAE mode, which has been driven directly in JET using beat waves or a saddle coil antenna [15, 16], help to complete the physics basis for the full α-channeling effect. Establishing, even separately, the effects of the central TAE and low-field-side IBW lends confidence to the very promising numerical simulation of their combined effect.

Acknowledgment

The efforts of the full TFTR team are very much appreciated. This work was supported by the US DOE under contract number DE–AC02–76–CHO3073. MCH and RFH acknowledge the support of the Fannie and John Hertz Foundation.

REFERENCES

[1] FISCH, N.J., RAX, J.M., Phys. Rev. Lett. 69 (1992) 612.
[2] FISCH, N.J., HERRMANN, M.C., Nucl. Fusion 34 (1994) 1541.
[3] CLARKE, J.F., Nucl. Fusion 20 (1980) 563.
[4] FISCH, N.J., HERRMANN, M.C., Nucl. Fusion 35 (1995) 1753.
[5] HERRMANN, M.C., FISCH, N.J., Phys. Rev. Lett. (in press).
[6] VALEO, E.J., FISCH, N.J., Phys. Rev. Lett. 73 (1994) 3536.
[7] MAJESKI, R., et al., Phys. Plasmas 3 (1996) 2006.
[8] ZWEBEN, S.J., et al., Nucl. Fusion 30 (1990) 1551.
[9] DARROW, D.S., et al., Rev. Sci. Instrum. 66 (1995) 476.
[10] BOIVIN, R.L., et al., Rev. Sci. Instrum. 61 (1990) 3163.
[11] MAJESKI, R., et al., Phys. Rev. Lett. 76 (1996) 764.
[12] DARROW, D.S., et al., Phys. Plasmas 3 (1996) 1875.
[13] DARROW, D.S., et al., Nucl. Fusion 36 (1996) 509.
[14] ROGERS, J.H., et al., IAEA-CN-64/EP-2, these Proceedings, Vol. 3.
[15] FASOLI, A., et al., Nucl. Fusion 35 (1995) 1485.
[16] JET TEAM, IAEA-CN-64/A2-6, this volume.

DISCUSSION

K. LACKNER: Under what conditions would you observe spontaneous excitation of these IBWs through this amplification effect? I had the impression that a given fast wave (in $\mathbf{k}$, ω) ϕ can access only a limited fraction of the spatial and energetic

α particle distribution, so unless you have spontaneous amplification from existing noise you should need broadband excitation.

N.J. FISCH: There are two questions here. One is how a single wave interacts with a large fraction of the α distribution. The answer is that $k_{\parallel}$ is rapidly varying as a function of space as the wave leaves the mode conversion layer. So a single wave resonates at nearby spatial points with different α particles. The second question concerns conditions for spontaneous emission. The waves we are using here are all convectively unstable and therefore amplified; then they damp on tritium ions near the tritium resonance. Spontaneous excitation would occur only for a standing wave that is made absolutely unstable.

OBSERVATION OF ALPHA PARTICLE DRIVEN TOROIDAL ALFVÉN EIGENMODES IN TFTR DT PLASMAS

R. NAZIKIAN, S.H. BATHA[1], M.G. BELL, R.E. BELL,
R.V. BUDNY, C.E. BUSH, Z. CHANG, Y. CHEN, C.Z. CHENG,
D.S. DARROW, H.H. DUONG[2], P.C. EFTHIMION,
E.D. FREDRICKSON, G.Y. FU, N.N. GORELENKOV[3],
B. LeBLANC, F.M. LEVINTON[1], R. MAJESKI, E. MAZZUCATO,
S.S. MEDLEY, H.K. PARK, M.P. PETROV[4], D.A. SPONG[5],
E.J. SYNAKOWSKI, G. TAYLOR, S. VON GOELER,
R.B. WHITE, K.L. WONG, S.J. ZWEBEN
Plasma Physics Laboratory,
Princeton University,
Princeton, New Jersey,
United States of America

Abstract

OBSERVATION OF ALPHA PARTICLE DRIVEN TOROIDAL ALFVÉN EIGENMODES IN TFTR DT PLASMAS.

Toroidal Alfvén Eigenmodes (TAEs) driven by energetic alpha particles have been observed for the first time in TFTR DT plasmas. These modes occur 100–300 ms after the termination of DT neutral beam injection in plasmas with elevated central safety factor ($q(0) > 1$) and reduced central magnetic shear. TAEs are observed with very low central alpha particle pressure ($\beta_\alpha(0) \geq 0.01\%$, β_α = alpha particle pressure/magnetic pressure) in $q(0) > 2$ discharges, consistent with linear stability calculations for plasmas with elevated $q(0)$ and low beam ion damping following the end of neutral beam injection. Modes appear in the TAE range of frequencies, 150–250 kHz, with toroidal mode numbers n = 2, 3, 4. From core reflectometer measurements the dominant n = 3 mode is localized near r/a ≈ 0.3–0.4, which coincides with the region of large $\nabla\beta_\alpha$. No enhanced alpha loss or significant alpha redistribution is measured during the TAE activity, consistent with nonlinear simulations for a single core localized mode with weak linear growth rate ($\gamma/\omega < 0.5\%$) and low saturated amplitude $\tilde{B}_\theta/B \sim 10^{-5}$.

---

[1] Fusion Physics and Technology, Torrance, California, USA.
[2] General Atomics ORAU Fellow.
[3] Troitsk Institute for Innovation and Thermonuclear Research (TRINITI), Moscow, Russian Federation.
[4] A.F. Ioffe Physico-Technical Institute, St. Petersburg, Russian Federation.
[5] Oak Ridge National Laboratory, Oak Ridge, Tennessee, United States of America.

1. INTRODUCTION

Continued investigation of Toroidal Alfvén Eigenmodes (TAEs) [1] driven by energetic particles in tokamaks is motivated by the potential for such instabilities to eject energetic alphas from the core of a fusion reactor, possibly leading to first wall damage and/or significant reduction of central alpha heating efficiency. Theoretical predictions of unstable TAEs in the International Thermonuclear Experimental Reactor (ITER) [2,3] underscore the need for adequate benchmarking of linear stability, nonlinear saturation and alpha loss calculations. Thus far the characteristics of TAEs and associated fast ion losses have been studied in experiments utilizing neutral beam injection in low toroidal magnetic field plasmas [4-6] and Ion Cyclotron Resonance Frequency (ICRF) heated minority ions in DD and DT discharges [7-10]. In these experiments, significant losses of beam ions (up to 50%) and minority ions (up to 10%) have been observed, [11] indicating the potential for TAEs to redistribute resonant particles in a fusion reactor.

Deuterium-Tritium experiments on TFTR produced discharges with up to 10 MW of fusion power and central $\beta_\alpha(0) \approx 0.33\%$ (shot # 80539), but with no observable TAE activity in external magnetic or internal reflectometer measurements [12]. However, recent theoretical studies have indicated that a new class of core-localized TAEs can be unstable in TFTR under conditions of low beam ion damping, low plasma pressure and weak central magnetic shear [13]. Such core localized TAEs have been observed in high-current ICRF heated plasmas on TFTR [13,14]. Theory also suggested that elevated central safety factor, $q(0) > 1$, can significantly affect mode stability, as could the rapid cooling of the discharge by use of pellets and large He gas puffs [15].

Previous studies have indicated that the most likely period for observing alpha-driven TAEs is following neutral beam injection, after the slowing down of beam ions ($\tau_b \approx 80 - 100$ ms) but before the alpha particle slowing down time ($\tau_\alpha \approx 300 - 500$ ms) [16,17]. The combination of all these methods aims to affect mode stability by reducing beam and thermal ion Landau damping, and by enhancing alpha particle drive through the reduction of central magnetic shear and alignment of low-n gaps [located near $q \approx (m + 1/2)/n$ where m is the poloidal mode number] to the peak in the alpha pressure gradient [18-20]. A further advantage of raising $q(0)$ is to maintain a more open gap structure for global TAEs by keeping the Alfvén frequency constant across the plasma radius. Early attempts at modifying the q-profile by use of a partial plasma growth scenario [21] or by perturbatively cooling the plasma using Li pellets and He gas puffs yielded no observable TAE activity in TFTR [22].

In this paper we report the first observation of alpha-driven TAEs in TFTR D-T plasmas. These modes are observed after the termination of neutral beam injection in plasmas with $q(0) > 1$ and reduced central magnetic shear. Section 2 describes the plasma parameters. Experimental results are presented in

Section 3. Section 4 compares experimental results with linear stability calculations [23] and the measured mode amplitude is compared with nonlinear calculations.

2. PLASMA CONDITIONS

The main objective of this experiment was to test a fundamental prediction of theory, namely that TAEs could be destabilized with modest fusion power levels in TFTR through the reduction of central magnetic shear and the elevation of $q(0)$. A number of techniques have been developed for producing plasmas with $q(0) > 1$ on TFTR [24]. In order to achieve a modest increase in $q(0)$ while avoiding strong magnetic shear reversal, the plasma discharge was initiated at large major radius but without early neutral beam injection characteristic of Enhanced Reverse Shear (ERS) plasmas.

Figure 1 shows the evolution of plasma parameters in a D-T discharge (#95796) with strong alpha-driven TAE activity. The discharge parameters are: $q(0) \approx 1.1$ (obtained from Motional Stark Effect (MSE) measurements [25]

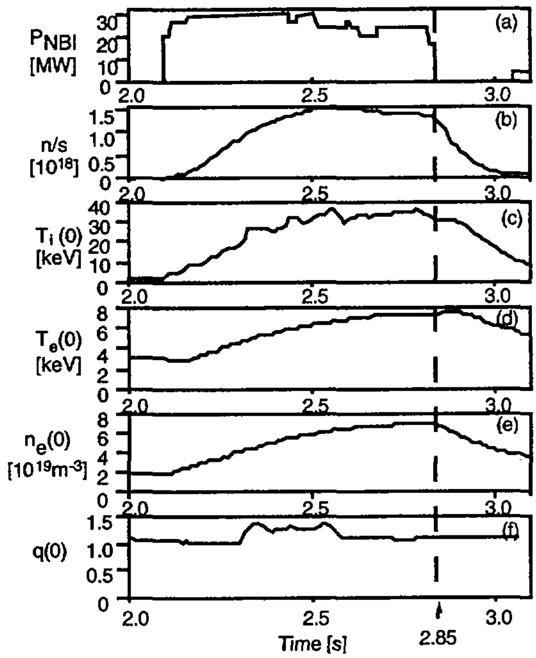

FIG. 1. Evolution of (a) neutral beam power, (b) DT neutron source rate, (c) central ion temperature, (d) central electron temperature, (e) central electron density and (f) central safety factor q(0), obtained from a combination of MSE measurements during neutral beam injection and TRANSP simulation. Dashed line denotes time of neutral beam turn off.

combined with TRANSP simulation [20] of the current evolution following termination of neutral beams). The plasma parameters during mode activity are: B_T=5.0T, I_p=2.0 MA, R=2.52 m, P_{NBI}=29 MW and P_{fus}=4.0, $n_e(0) \approx 4.3 \times 10^{19} m^{-3}$, $T_e(0) \approx 6$ keV and $T_i(0) \approx 15$ keV. A second plasma condition (not shown) with higher q(0) and lower central ion temperature also produced observable alpha-driven TAE activity following the end of neutral beam injection with the following plasma parameters: q(0)≈1.9-2.4, B_T=5.3T, I_p=1.6 MA, R=2.60 m, P_{NBI}=26 MW and P_{fus}=2.5 MW, $n_e(0) \approx 3.5 \times 10^{19} m^{-3}$, $T_e(0) \approx 5.3$ keV and $T_i(0) \approx 10$ keV. The Alfvén velocities for the two discharges are $\sim 1.1 - 1.3 \times 10^7$ m.s^{-1}, comparable to the alpha birth velocity $V_{\alpha 0} \approx 1.3 \times 10^7$ m.s^{-1}. These discharges are relatively free of large amplitude low frequency MHD activity, and sawteeth are delayed by more than one second following termination of neutral beams, consistent with MSE measurements of $q(0) > 1$.

Figure 2 shows the evolution of beam ion and alpha particle slowing down velocities for the discharge of Fig. 1. The analysis assumes classically slowing down neutral beam and alpha particles following the end of neutral beam injection. The particle velocities are based on TRANSP calculations of the slowing down times, while the Alfvén velocity is calculated from the TRANSP equilibrium analysis including mass density corrections for the relative concentration of deuterium, tritium, hydrogen and helium in the plasma core. Beam ions are predicted theoretically to damp TAEs through the sideband resonance $V_b \approx V_A / 3$. However the rapid decay of the central plasma density indicates that beam damping on the sideband resonance should not be significant much longer than 20-30 ms following the end of neutral beam injection. For energetic alpha particles to destabilize TAEs, the fundamental resonance condition $V_\alpha \approx V_A$, or the weaker sideband resonance $V_\alpha \approx V_A / 3$ should be satisfied for passing particles while the precessional frequency resonance condition should be satisfied for deeply trapped particles [more likely at high $q(0)$]. From Fig. 2, $V_\alpha / V_A \approx 1.5$ at the end of neutral beam injection, and the sideband resonance condition is

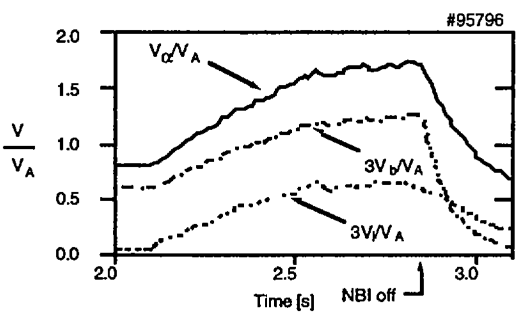

FIG. 2. Evolution of the ratio of particle velocity to Alfvén velocity in the center of the discharge for alpha particles (V_α), D and T beam ions (V_b) and thermal ions (V_i).

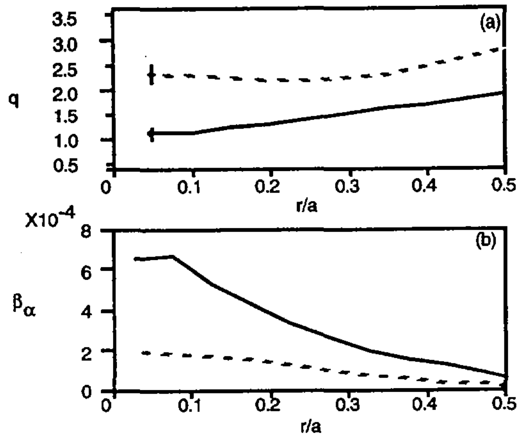

FIG. 3. Profiles of safety factor (a) and alpha beta (b) at $t = 3.0$ s (~50 ms following end of beam injection) for the case of high q(0) (dashed line) and low q(0) (solid line).

satisfied for partially thermalized alpha particles well after neutral beam ions thermalize. In practice, significant alpha particle production continues after termination of D-T beam injection (Fig. 1) so that these estimates of peak alpha particle velocity are conservative.

Figure 3 shows q and β_α profiles 150 ms after beam injection for the two cases of interest. The evolution of β_α is based on TRANSP calculations of the classically slowing down alpha particles, and is consistent with Pellet Charge Exchange (PCX) measurements of the alpha particle distribution in discharges with monotonic q-profiles [18]. Note that the case of $q(0) > 2$ has lower β_α, however the net alpha drive is predicted theoretically to increase strongly with increasing $q(0)$ and decreasing central magnetic shear [13].

3. EXPERIMENTAL RESULTS

Figure 4 shows the magnetic fluctuation level detected on the external Mirnov coils for the case of $q(0) \approx 1.1$ discharge of Fig. 1. Multiple modes are observed between 100-200 ms following the end of neutral beam injection with dominant toroidal mode number n=3, with n=4 and n=2 modes at weaker levels. The n=3 mode is also dominant in the $q(0) > 2$ discharges. All the modes appear in the frequency range 220-250 kHz and propagate toroidally in the diamagnetic drift direction as expected for TAEs. The peak fluctuation level of 0.5 mGauss corresponds to $\tilde{B}/B \approx 10^{-8}$ at the plasma edge, which is comparable to the TAE fluctuation level observed with 3-4 MW H-minority ICRF heating on TFTR. These modes have only been observed in D-T plasmas above a threshold fusion power which differs for the two plasma conditions. From the TRANSP calculations,

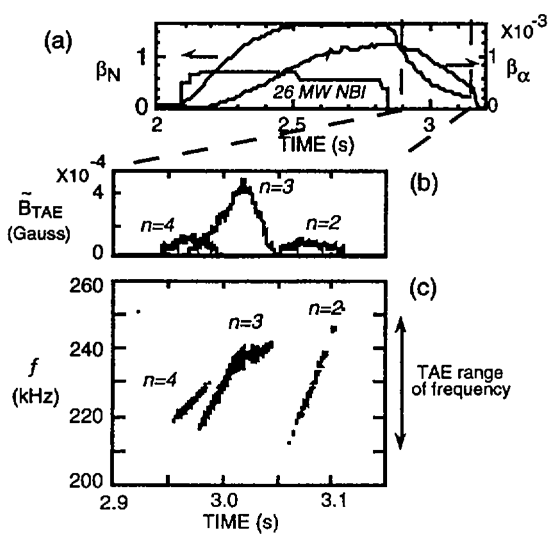

FIG. 4. Alpha driven TAEs with q(0) ~ 1.1. Evolution of normalized plasma beta and alpha particle beta (a), TAE mode amplitude on Mirnov coils following termination of NBI (b), and frequency evolution of the same modes (c). The dominant mode number is n = 3, and the frequency increase in (c) is correlated with the central density decrease after NBI, expected for Alfvén waves.

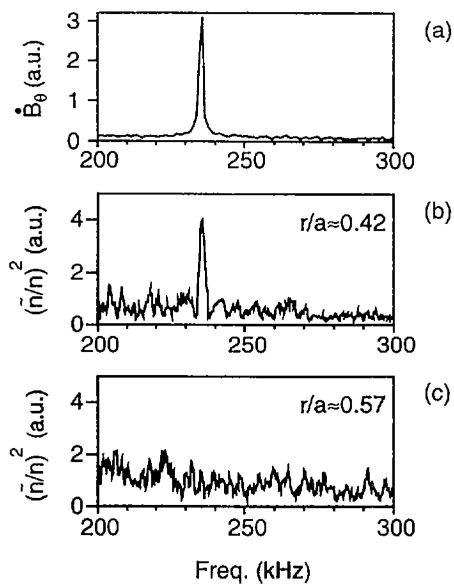

FIG. 5. Spectrum of Mirnov signal (a), reflectometer signal at r/a = 0.42 (b) and reflectometer signal at r/a = 0.57 (c), taken over a 5 ms time window centered at t = 3.009 s for the dominant n = 3 mode in Fig. 4.

$\beta_\alpha(0)$ decays by $\approx$30% from the end of neutral beam injection to the time of peak mode amplitude, whereas the normalized plasma beta β_N decays by up to 80% over the same period.

Figure 5a shows the spectrum of edge magnetic fluctuations evaluated over a 5 ms interval for the data of Fig.4. The Mirnov spectrum in Fig. 5a shows a strong peak at 234 kHz corresponding to the dominant n=3 mode. Figures 5b and 5c show reflectometer spectra of density fluctuations at r/a$\approx$0.42 and 0.57, respectively. These radial locations correspond to the right hand cutoff layers for 135 GHz and 128 GHz microwaves launched into the plasma from waveguides mounted on the outboard midplane of TFTR [26,27]. No coherent mode activity is observed at r/a$\approx$0.57 or at larger radii, however the dominant n=3 mode is clearly observed on the reflectometer channel at r/a$\approx$0.42. From the reflectometer phase fluctuation level and assuming the validity of geometric optics for scattering from very long wavelength modes, an estimate of the density fluctuation level $\tilde{n}/n \approx 1\times10^{-4}$ is obtained. Time series analysis of the core reflectometer and edge magnetic measurements reveal a high correlation coefficient ($\gamma \approx 0.5$), indicating that the two diagnostics observe the same mode with frequency close to TAE frequency $V_A/4\pi qR \approx 250$ kHz, evaluated at r/a$\approx$0.3-0.4. The upward sweep of the mode frequency in Figure 4 is consistent with the increase in the Alfvén velocity in the plasma core after termination of neutral beam injection. At the time of mode activity, the correction due to plasma toroidal rotation is $\approx$ 5 kHz for the n=3 mode at r/a$\approx$0.3.

From the reflectometer measurement of the density fluctuations in the plasma core, we can obtain an estimate of the corresponding level of internal magnetic fluctuations. Using $\tilde{B} \approx B\cdot\nabla\xi_r$, where $\xi_r \approx L_n\tilde{n}/n$, and $k_\parallel \approx 1/2qR$ for TAEs, we obtain the core fluctuation level estimate $\tilde{B}/B \approx 10^{-5}$. This represents a 10^3 variation in $\tilde{B}/B$ from the plasma core to the plasma edge, indicative of core

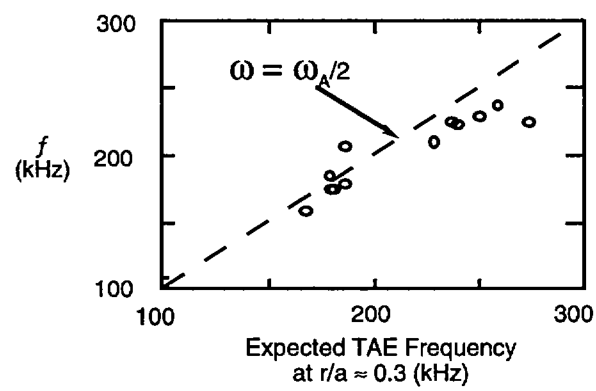

FIG. 6. Observed mode frequency scales as $\omega_A/2$ evaluated at r/a $\approx$ 0.3.

localized modes. From the broadband noise on the reflectometer channels, an upper bound on the density fluctuation level of $\tilde{n}/n < 3\times10^{-5}$ for $r/a \geq 0.55$ is determined.

In the $q(0) > 2$ plasmas, mode activity was observed around 170 kHz on external Mirnov coils with dominant toroidal mode number n=3, although in several discharges an n=2 mode was also observed. The mode amplitude at higher $q(0)$ is comparable to the observed amplitude at low $q(0)$, but mode activity appears at lower fusion power (≈1.5 MW) and $\beta_\alpha(0) > 0.01\%$.

No TAE activity was measured on the reflectometer channels in the high $q(0)$ plasmas. One possible reason is that the reflectometer channels did not penetrate far enough into the plasma to observe the modes. However, assuming these modes are localized to the core region of the discharge around r/a≈0.3, then we obtain a TAE frequency estimate of ≈180 kHz which matches closely the measured mode frequencies. Figure 6 shows the measured frequencies for all the data at high and low $q(0)$ at the time of peak mode amplitude, plotted against the approximate value of the TAE frequency $V_A/4\pi qR$ evaluated at r/a≈0.3. The estimated TAE frequency at r/a≈0.3 includes the q-profile from MSE measurements and the mass density profile from the TRANSP code kinetic analysis.

Figure 7 shows the variation of the mode amplitude with fusion power for the case of low $q(0)$ discharges. A rapid increase in mode amplitude is observed with increasing fusion power for these plasmas, expected for modes near marginal stability. However a similar scaling is not obtained for the high $q(0)$ plasmas, partly because of the limited range of fusion power (due to poor confinement) and to the higher variability of the central q and discharge conditions ($1.9<q(0)<2.4$). The alpha particle drive is calculated theoretically to be highly sensitive to the Alfvén continuum gap structure, which is strongly controlled by

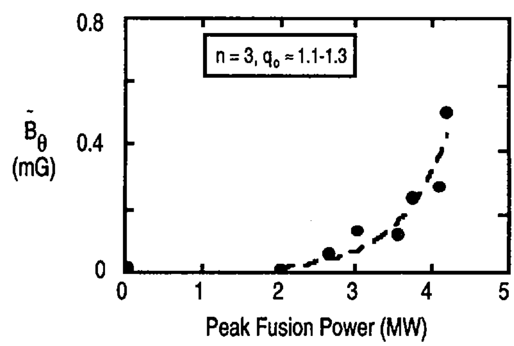

FIG. 7. Strong amplitude increase observed on edge Mirnov signals with increasing fusion power, as expected for alpha driven TAEs near the threshold condition for instability. Modes are observed with $\beta_\alpha(0) > 0.03\%$ for $q(0) \sim 1.1$–1.3.

the q-profile. Indeed, theory indicates that the linear stability of TAEs is highly sensitive to small variation in $q(0)$ for plasmas with low central magnetic shear [28].

No enhancement in alpha loss is observed on the lost alpha detectors during TAE activity. These detectors are located poloidally 45, 60 and 90 degrees below the outer midplane and are capable of observing energetic particle losses induced by MHD activity in the plasma core. However, the absence of enhanced loss is not surprising given the very low loss of minority ions for similar amplitude TAEs ($\tilde{B}/B \sim 10^{-8}$) in 3-4 MW H-minority ICRF heating experiments on TFTR. There is also no indication of significant redistribution of deeply trapped alpha particles resulting from the TAE activity, as measured by the Pellet Charge Exchange (PCX) diagnostic [18].

4. LINEAR STABILITY AND NONLINEAR SATURATION

Figure 8 shows the n=3 toroidicity induced gap in the Alfvén continuum for the two cases of interest with $q(0)\approx 2.4$ and $q(0)\approx 1.1$, together with the measured mode frequency in each of these discharges and the location of the reflectometer channel which observed the n=3 mode. The gap structure is calculated using NOVA-K [28] with equilibrium profiles computed by TRANSP.

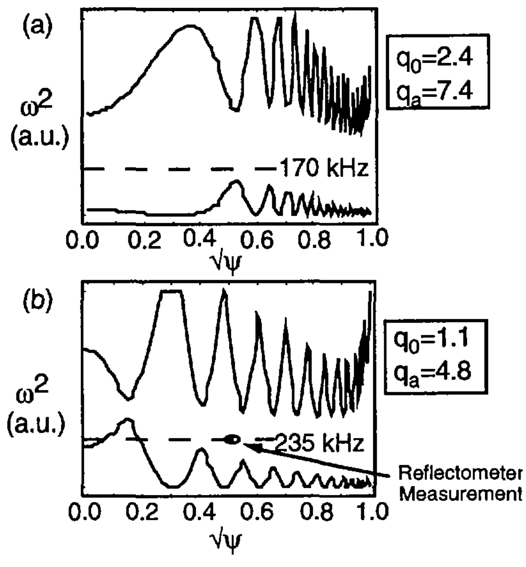

FIG. 8. Mode frequency lies inside calculated gap in n = 3 Alfvén continuum for r/a > 0.2 in both high q(0) (a) and low q(0) (b) discharges.

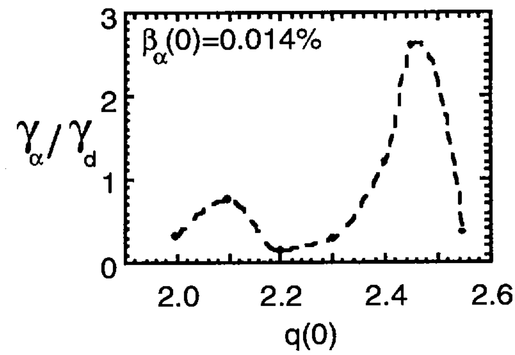

FIG. 9. Ratio of drive to damping versus q(0) for the n = 3 core mode.

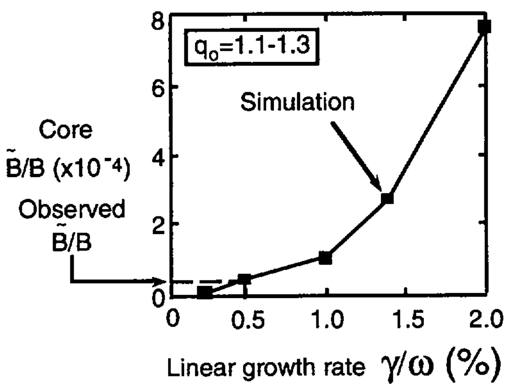

FIG. 10. Nonlinear (ORBIT) simulation of n = 3 core TAE predicts saturation at a very low level for weak linear growth rate. The observed mode amplitude is consistent with simulation for $\gamma/\omega < 1\%$ calculated by NOVA-K.

In the high $q(0)$ case (Fig. 8a) the n=3 gap structure is very well aligned from the plasma core to the edge and the observed frequency lies well within the gap. In particular the KTAE frequency at the top of the gap is ≈250 kHz, well above the observed mode frequency.

For $q(0)\approx1.1$ in Fig. 8(b) the gap is closed for the measured frequency, but only in a narrow region in the core of the plasma. Theoretical analysis indicates that the mode is unstable for a modest increase in $q(0)$ from 1.1 to 1.35. Also, the KTAE frequency is ≈320 kHz, and NOVA-K analysis indicates that the KTAE - as well as the odd TAE mode in the upper limit of the n=3 gap - are stable in these plasmas.

The sensitivity of the linear growth rate to small variations in $q(0)$ for a core localized n=3 mode is shown in Fig. 9 for the case of $q(0)\approx2.0$-2.5 and

$\beta_\alpha(0) \approx 0.014\%$. At $q(0) \approx 2.4$ NOVA-K calculations indicate that the n=3 core mode is unstable. Furthermore, the dominant mode number from NOVA-K in both these discharge conditions is n=3, again consistent with experiment. These results suggest that a detailed $q(0)$ scan is required in order to test theoretical predictions of core mode stability as well as to maximize the amplitude of alpha-driven TAEs in TFTR for alpha loss measurements.

Nonlinear ORBIT [29-31] code simulations of mode saturation and alpha particle loss have been carried out for the n=3 core mode with $q(0) \approx 1.1$. Figure 10 shows a rapid increase in saturated mode amplitude as a function of input linear growth rate. For $\gamma / \omega < 0.5\%$, corresponding to a reasonable upper bound from the NOVA-K (ignoring all damping terms), the estimate of the saturated mode amplitude from ORBIT analysis is very weak ($\tilde{B}/B \sim 10^{-4}$). This result is consistent with the weak mode amplitude estimated from core density fluctuations ($\tilde{B}/B \sim 10^{-5}$). However, the saturated mode amplitude and corresponding alpha loss are expected to increase dramatically for higher linear growth rates for single modes, and particularly for multiple overlapping modes [32] predicted in ITER.

5. CONCLUSION

Recent DT experiments on TFTR have identified alpha particle driven TAEs under conditions of elevated central safety factor, reduced central magnetic shear and low plasma pressure. These modes have only been observed in D-T plasmas with elevated central safety factor. Some characteristics of the modes are : (i) the mode frequency scales with the TAE frequency, (ii) the modes appear in the core of the plasma near the region of large alpha particle drive, (iii) the modes appear after neutral beam ions thermalize but before the slowing down time of fusion alpha particles, (iv) the dominant observed mode number is n=3, consistent with linear stability calculations at low and high $q(0)$, (v) the observed saturated mode amplitude is consistent with calculated weak linear growth rate of the mode. Theory indicates that TAE stability is highly sensitive to $q(0)$, indicating the need for a fine $q(0)$ scan in future experiments. Such a scan is necessary to test theoretical predictions and maximize mode amplitude for alpha loss studies. These studies will allow better theoretical calculations of TAE stability and alpha particle confinment in ITER.

ACKNOWLEDGMENTS

We are indebted to R.J. Hawryluk and K. McGuire for their strong support of these experiments. Thanks also to J. VanDam for many helpful discussions and M. McCarthy for the maintenance of the reflectometer. This work was performed under DoE contract # DE-AC02-CHO-3073.

REFERENCES

[1] CHENG, C.Z., et al., Ann. Phys. (N.Y.) 161 (1984) 21.
[2] CHENG, C.Z., et al., in Plasma Physics and Controlled Nuclear Fusion Research 1994 (Proc. 15th Int. Conf. Seville, 1994), Vol. 3, IAEA, Vienna (1996) 373.
[3] CHENG, C.Z., et al., IAEA-CN-64/FP-23, these Proceedings, Vol. 2.
[4] WONG, K.L., et al., Phys. Rev. Lett. 66 (1991) 1874.
[5] HEIDBRINK, W.W., et al., Nucl. Fusion 31 (1991) 1635.
[6] STRAIT, E.J., et al., Nucl. Fusion 33 (1993) 1849.
[7] WILSON, J.R., et al., in Plasma Physics and Controlled Nuclear Fusion Research 1992 (Proc. 14th Int. Conf. Würzburg, 1992), Vol. 1, IAEA, Vienna (1993) 661.
[8] TAYLOR, G., et al., Phys. Fluids B 5 (1993) 2437.
[9] SAIGUSA, M., et al., Plasma Phys. Control. Fusion 37 (1995) 295.
[10] WONG, K.L., et al., Phys. Rev. Lett. 76 (1996) 2286.
[11] DARROW, D.S., et al., Nucl. Fusion 37 (1997) (in press).
[12] STRACHAN, J.D., et al., Phys. Rev. Lett. 72 (1994) 3526.
[13] FU, G.Y., et al., Phys. Rev. Lett. 75 (1995) 2336.
[14] FREDRICKSON, E.D., et al., Nucl. Fusion 35 (1995) 1457.
[15] SPONG, D., HEDRICK C.L., CARRERAS, B.A., Nucl. Fusion 35 (1995) 1687.
[16] CHENG, C.Z., et al., in Plasma Physics and Controlled Nuclear Fusion Research 1992 (Proc. 14th Int. Conf. Würzburg, 1992), Vol. 2, IAEA, Vienna (1993) 51.
[17] BUDNY, R.V., et al., Nucl. Fusion 32 (1992) 429.
[18] PETROV, M.P., et al., Nucl. Fusion 35 (1995) 1437.
[19] McKEE, G., et al., Phys. Rev. Lett. 75 (1995) 649.
[20] BUDNY, R.V., et al., Nucl. Fusion 35 (1995) 1497.
[21] BATHA, S.H., et al., Nucl. Fusion 35 (1995) 1463.
[22] ZWEBEN, S.J., et al., Nucl. Fusion 36 (1996) 987.
[23] CHENG, C.Z., Phys. Rep. 211 (1992) 1.
[24] LEVINTON, F.M., Phys. Fluids B 5 (1993) 2554.
[25] BATHA, S.H., et al., Nucl. Fusion 36 (1996) 1133.
[26] NAZIKIAN, R., MAZZUCATO, E., Rev. Sci. Instrum. 66 (1995) 392.
[27] MAZZUCATO, E., NAZIKIAN, R., Phys. Rev. Lett. 71 (1993) 1840.
[28] FU, G.Y., et al., IAEA-CN-64/D2-6, these Proceedings, Vol. 2.
[29] WHITE, R.B., et al., Nucl. Fusion 35 (1995) 1707.
[30] WHITE, R.B., CHANCE, M.S., Phys. Fluids 27 (1984) 2455.
[31] CHEN, Y., WHITE, R.B., Rep. 3138, Plasma Physics Lab., Princeton Univ., NJ (in press).
[32] BERK, H.L., et al., IAEA-CN-64/D2-5, these Proceedings, Vol. 2.

DISCUSSION

C. GORMEZANO: Since these modes are so sensitive to the value of q(0) at the centre, have you observed similar DT induced TAEs in shear reversed discharges?

R. NAZIKIAN: The objective of these experiments was to raise q(0) sufficiently to reduce the central magnetic shear so as to minimize radiative damping and maintain the open gap structure in the Alfvén spectrum for low n modes. In strongly reversed shear discharges, the gap structure is usually closed for low n modes, and no modes have been observed in such plasmas on TFTR. However, high n TAEs localized in the weak shear region at $q = q_{min}$ have been observed in JT-60 reversed shear discharges.

H.L. BERK: I wish to point out that the steady saturation levels can be explained using α particle collisionality (see IAEA-CN-64/D2-5).

STUDY OF TFTR DT NEUTRON SPECTRA USING NATURAL DIAMOND DETECTORS

A.V. KRASILNIKOV[1], A.L. ROQUEMORE[2],
N.N. GORELENKOV[1], R.V. BUDNY[2]

[1]Troitsk Institute of Innovation and
Thermonuclear Research (TRINITI),
Troitsk, Moscow,
Russian Federation

[2]Plasma Physics Laboratory,
Princeton University,
Princeton, New Jersey,
United States of America

Abstract

STUDY OF TFTR DT NEUTRON SPECTRA USING NATURAL DIAMOND DETECTORS.

Three natural diamond detector (NDD) based spectrometers have been used for neutron spectrum measurements during DT experiments using high power neutral beam injection and ion cyclotron resonance heating on TFTR in 1996. A 2-3% energy resolution and the high radiation resistance of NDDs (5×10^{14} n/cm^2) make them ideal for measuring the DT neutron spectra in the high radiation environment of TFTR tritium experiments. The compact size of the NDDs made it possible to insert one of them into one of the centre channels of the TFTR multichannel neutron collimator to provide a vertical view perpendicular to the vessel midplane. Two other detectors were placed inside shields in the TFTR test cell and provided measurements of the neutrons having angles of emission of 110-180° and of 60-120° with respect to the direction of the plasma current. By using a 0.25 μs shaping time of the Ortec 673 spectroscopy amplifier, it was possible to accumulate useful spectrometry data at count rates of up to 1.5×10^3 counts/s. To model the DT neutron spectra measured by each of the three NDDs, the Neutron Source post-TRANSP (NST) code and a semianalytical model were developed. A set of DT and DD plasmas is analysed for the dynamics of DT neutron spectral broadening for each of the three NDD cones of view. The application of the three NDD based DT neutron spectrometer arrays demonstrated the anisotropy of the ion distribution function, provided a measure of the dynamics of the effective ion temperatures for each detector view and determined the tangential velocity of resonant tritons during ion cyclotron resonance heating.

1. INTRODUCTION

During the last three years, DT experiments using high power neutral beam injection (NBI) and ion cyclotron resonance heating (ICRH) have been carried out on TFTR. During this experimental phase, up to six NBI sources were aimed in the counter-direction and six in the co-direction, with a total power of 36 MW of 105 keV DT injection. Up to 3 MW of RF power at 30 MHz was injected with wave phasings of 60° (counter), 180° (π) and 300° (co) with respect to the plasma current during ICRH at the fundamental triton cyclotron frequency. The high flux of 14 MeV neutrons during high power deuterium and tritium NBI and ICRH experiments on TFTR has made it possible to use neutron spectrometry to study the ion distribution under reactor-like conditions. The TFTR ion distribution function during NBI, as calculated by the two dimensional transport code TRANSP [1], is non-Maxwellian and anisotropic. This anisotropy is directly reflected in the DT neutron energy and angular emission distributions, so that a measure of its dynamics provides information about the ion energy distribution, transport, confinement and the slowing down time of high energy particles, and about the α particle birth energy distribution. In the case of ICRH it shows the efficiency of heating by the resonant particles.

2. DIAGNOSTIC ARRANGEMENT

Three neutron spectrometers based on natural diamond detectors (NDDs) were developed in the Russian Federation [2–4] and have been used for DT neutron spectrum measurements during NBI and ICRH on TFTR in a variety of locations [5]. The 14 MeV peak of the NDD pulse height spectra arising from the $^{12}C(n,\alpha_0)^9Be$ reaction has an energy resolution of 2–3%. Such a high resolution and the high radiation resistance of diamonds (5×10^{14} n/cm^2) make the NDD ideal for measuring the DT neutron spectra in the high radiation environment of TFTR tritium experiments. The sensitivities of the detectors and the speed of the signal processing electronics drive the location and shielding required for each detector [5]. The compact size of the NDD housing (~ 1 cm^3) allowed the detectors to be inserted into the TFTR multichannel neutron collimator and fusion shield without interfering with other detectors operating there. The first detector (NDD1) was placed inside a central channel of the TFTR vertical neutron collimator to provide a view perpendicular to the plasma current axis [5]. During the 1996 experiments, a second detector (NDD2) was placed inside the TFTR fusion γ shield and it measured neutrons with emission angles in the range 110–180° with respect to the plasma current [5]. The third detector (NDD3) was placed inside a small specially designed shield in the TFTR test cell 11 m from the plasma axis. It provided measurements of the spectral broadening of 14 MeV neutrons having angles of emission of 60–120° with respect to the plasma current [5].

The signal from each of the NDDs is fed into a standard Ortec spectroscopy electronics. By using a 0.25 μs shaping time and employing the pile-up rejection feature of the Ortec 673 spectroscopy amplifier we were able to accumulate useful spectrometry data in the $^{12}C(n,\alpha_0)^9Be$ peak at count rates of up to 1.5×10^3 counts/s.

The full width at half-maximum (FWHM) of the $^{12}C(n,\alpha)^9Be$ line of the NDD pulse height spectrum is a measure of the broadening of the energy distribution of the DT neutrons [4] that leave the plasma along the detector viewing cone and contains information about the corresponding mean effective ion temperature T_{eff}.

3. RESULTS AND ANALYSIS

For a Maxwellian DT plasma with ion temperature T, the analytical calculations [6] yield a DT neutron spectrum with a Gaussian shape:

$$f(E_n) = \frac{1}{\sqrt{2\pi}\,\sigma_E} \exp[-(E_n - \langle E_n \rangle)^2/2\sigma_E^2] \tag{1}$$

where σ_E is the standard deviation. The FWHM is given by $\Delta E_n = \sqrt{8 \ln 2}\,\sigma_E$. For plasmas with ion temperatures in the range 30–50 keV,

$$\Delta E_n = 180\sqrt{T_{eff}} \tag{2}$$

where ΔE_n and T_{eff} are in kiloelectronvolts [7].

The ion component in TFTR contains both thermal and hot beam ions. The sources of thermal ions are gas puffing, emission from the walls and limiter, including a few per cent of tritium in the hydrogen influx, and thermalization of beam ions. The emitted neutrons result from three channels: beam–plasma interactions (55–75%), beam–beam interactions (0–20%) and thermal neutrons (10–30%). To model the DT neutron spectra measured by each of the three NDDs, the Neutron Source post-TRANSP (NST) code was developed. This code utilizes TRANSP [1] to calculate the deuterium and tritium plasma densities and temperatures, as well as the deuterium and tritium beam distribution functions, and applies fusion cross-sections to derive the neutron emission spectra using a well known formulation [8]. Spectral broadening of DT neutrons escaping from the TFTR plasma with emission angles of 90°, 110–180° and 60–120° was observed by NDD1, NDD2 and NDD3, respectively. These measurements were made with an NBI power of 17–36 MW and ICRH power of up to 3 MW, and demonstrated the anisotropy of the ion distribution function in TFTR. The dynamics of the $T_{eff,\perp}$ measured by NDD1 during 22 MW NBI and modelled by the NST code are in good agreement and are shown in Fig. 5 of Ref. [7].

In addition to the NST code, we developed a relatively simple semianalytical model [7] for calculations of DT neutron spectra for plasmas with anisotropic deuteron and triton distribution functions. We consider each deuterium and tritium (beam or plasma) component to be a displaced Maxwellian with effective perpendicular and parallel temperatures and having a certain directed parallel velocity, which can be found from the actual distribution by averaging over velocity space. According to this model, we approximated the DT neutron distribution function at different angles ($\cos^{-1}\chi$) between the directions of the neutron emission and the plasma current by a Gaussian (Eq. (1)) with the standard deviation

$$\sigma_E^2 = \frac{4m_n\langle E_n \rangle}{m_n + m_\alpha} \frac{T_\parallel T_\perp}{[\sqrt{T_\parallel} + \chi^2(\sqrt{T_\perp} - \sqrt{T_\parallel})]^2} \tag{3}$$

where

$$T_{\parallel} = T_{\parallel ij} = \frac{m_D T_{\parallel Di} + m_T T_{\parallel Tj}}{m_D + m_T} \tag{4a}$$

and

$$T_{\perp} = T_{\perp ij} = \frac{m_D T_{\perp Di} + m_T T_{\perp Tj}}{m_D + m_T} \tag{4b}$$

$$T_{\parallel Di} = \langle E_{\parallel Di} \rangle,\ T_{\perp Di} = \langle E_{\perp Di} \rangle/2,\ T_{\parallel Ti} = \langle E_{\parallel Ti} \rangle,\ T_{\perp Ti} = \langle E_{\perp Ti} \rangle/2 \tag{5}$$

The DT neutron average energy for such an anisotropic plasma also depends on χ:

$$\langle E_n \rangle = \frac{m_\alpha}{m_n + m_\alpha} Q + \frac{3}{2}\left(\frac{m_n}{m_n + m_\alpha} T + \frac{m_\alpha}{m_n + m_\alpha}\,\frac{m_D T_T + m_T T_D}{m_n + m_\alpha}\right)$$
$$+ \frac{m_\alpha}{m_n + m_\alpha} \Delta E_{\parallel} + \sqrt{2}\,\frac{m_D \langle v_{\parallel Di} \rangle + m_T \langle v_{\parallel T_j} \rangle}{m_n + m_\alpha}$$
$$\times \sqrt{\frac{m_n m_\alpha Q}{m_n + m_\alpha}}\,\chi \tag{6}$$

where

$$T_{D,T} = T_{\parallel D,T} + T_{\perp D,T},\ \Delta E_{\parallel ij} = \frac{(\langle v_{\parallel Di} \rangle - \langle v_{\parallel Tj} \rangle)^2 m_D m_T}{m_D + m_T}$$

Q is the nuclear energy release of the reaction; $\langle v_{\parallel Di} \rangle$ and $\langle v_{\parallel Tj} \rangle$ are averaged over the distribution function velocities of deuterons and tritons; m_n, m_D, m_T and m_α are the masses of the corresponding particles; and i and j refer to beam and plasma.

An example of the measurements versus modelling is shown in Fig. 1. In this case, 18 MW of balanced tritium NBI was injected into a deuterium plasma. The tangential detector showed large broadening of the neutron spectra due to the momentum of beam tritons in the tangential direction. The NST code calculates the total contributions from beam–plasma and plasma–plasma interactions and fits the resulting data with a Gaussian. The semianalytical model based on Eqs (3–6) was also applied to the neutron spectrum calculations, and the derived spectrum is shown in Fig. 1 by the dashed curve. The values of $T_{\parallel Di}$, $T_{\perp Di}$, $T_{\parallel Ti}$, $T_{\perp Ti}$, $\langle v_{\parallel Di} \rangle$ and $\langle v_{\parallel Tj} \rangle$ were determined by averaging over deuteron and triton distribution functions calculated by TRANSP. Fusion reactivity $\langle \sigma v \rangle$ was calculated in accordance with Ref. [8]. The neutron source in the case of an anisotropic plasma is

$$S_{nij} = f_n(E)\langle \sigma v \rangle\left(\frac{m_D T_T + m_T T_D}{m_n + m_\alpha} + \frac{2}{3}\Delta E_{\parallel ij}\right) n_{Di} n_{Tj} \tag{7}$$

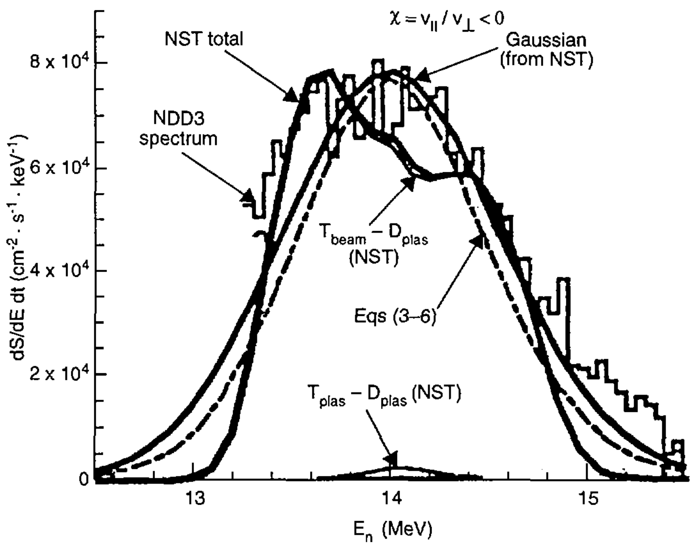

FIG. 1. Comparison of the measured tangential spectra with models using the NST and the semianalytical codes for 18 MW tritium beam injection.

Good agreement is seen between measurements, NST and the semianalytical model.

The system of three NDD based DT neutron spectrometers was used to study the dynamics of DT neutron distribution functions and fluxes during the TFTR fundamental tritium ICRH experiment. During these experiments, plasmas with major radius 277 cm (with Shafranov shift) and minor radius 96 cm were heated for 1 s (from 2.1 to 3.1 s) by 17 MW NBI and for 0.8 s (from 2.3 to 3.1 s) with up to 3 MW ICRH at a frequency of 30 MHz with wave phasings of 60° (counter), 180° (π) or 300° (co) with respect to the plasma current. The resonance layer for the first harmonic of tritons was at major radius 235 cm for a wave phasing of 180° and moved in the range 221–249 cm in accordance with the well known condition for single particle resonance, $\omega - k_{\parallel} v_{\parallel} = \omega_c$, where ω is the wave frequency, $k_{\parallel}$ the tangential component of wavenumber, $v_{\parallel}$ the tangential component of triton velocity and ω_c the triton cyclotron resonance frequency. Figure 2 shows the dynamics of T_{eff} as measured by the three NDD based neutron spectrometers during experiments with an NBI power of 17 MW and an ICRH power of 2 MW. The FWHM of the neutron energy distributions for perpendicular and tangential emission (with respect to the plasma current axis) are different owing to the anisotropy of the hot beam ions, since the majority of the neutrons from TFTR are from beam–plasma and beam–beam interactions [1]. The FWHM is a function not only of the plasma ion temperature but also of the average energy of the beam ions along the detector viewing cone, which in turn is a function of the electron density. The decrease in the effective tangential temperature (Fig. 2, curve 1) and the increase in the effective perpendicular temperature (Fig. 2, curves 2 and 3) during the first half of the beam phase are functions of the

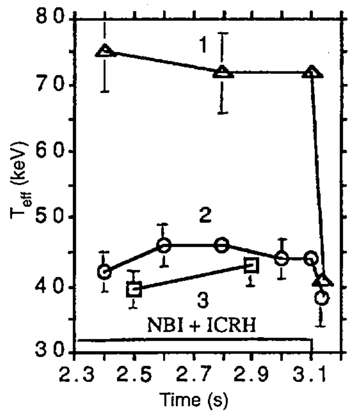

FIG. 2. Tangential (curve 1) and perpendicular (curves 2 and 3) triton effective temperature during tritium ICRH experiments: NBI power 17 MW, ICRH power 2 MW (curves 1 and 2); without ICRH (curve 3).

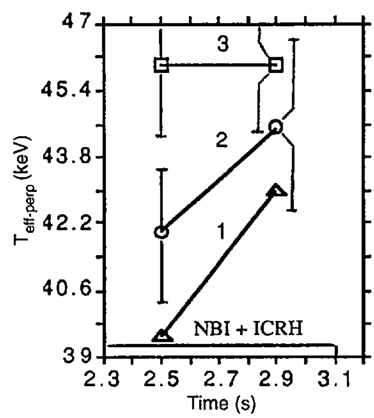

FIG. 3. Perpendicular triton effective temperature during triton ICRH experiments without ICRH (curve 1), with 2.1 MW ICRH and high (~25%) triton concentration (curve 2), and with 2.4 MW ICRH and low (~10%) triton concentration (curve 3).

change of beam penetration due to the increase of plasma density. The difference between curves 2 and 3 illustrates the increase in perpendicular energy of the tritons due to ICRH. The triton slowing down time was estimated from the decrease of the tangential effective temperature (Fig. 2, curve 1) after the deuterium and tritium beams were turned off. The derived value of about 100 ms is in reasonable agreement with calculations.

Figure 3 shows the difference in dynamics of the perpendicular effective temperature measured in experiments with the same NBI power but without ICRH (curve 1), with 2.1 MW ICRH and high (~25%) triton concentration (curve 2) and with 2.4 MW ICRH and low (~ 10%) triton concentration (curve 3). These measurements demonstrated that the highest heating of tritons occurred in experiments with lower triton concentration.

ICRH is usually considered to cause dispersion only in $v_\perp$. However, as shown by Stix [9], during ICRH quasi-linear diffusion in velocity space directed along the circles $v_\perp^2 + (v_\parallel - \omega/k_\parallel)^2 = \text{const}$, and in the case of co or counter wave phasing, resonant particles should receive some velocity in the tangential direction also. In the case of the TFTR tritium ICRH experiments in accordance with (6)

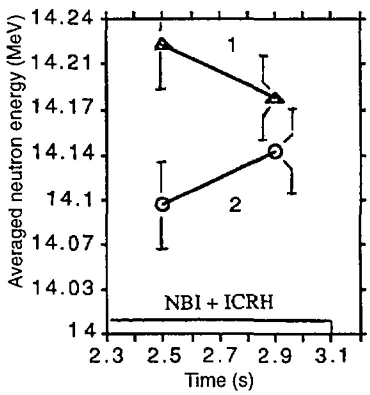

FIG. 4. Peak energy of tangential neutron energy distribution during triton ICRH experiments with counter (curve 1) and co (curve 2) wave phasing.

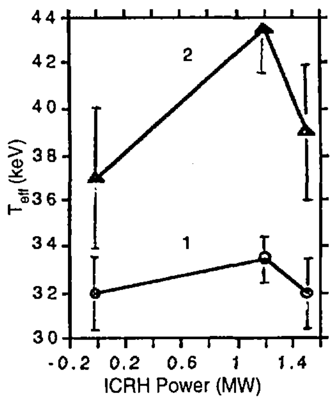

FIG. 5. Perpendicular (curve 1) and tangential (curve 2) effective ion temperature of plasma with a few per cent of tritium due to gas puffing during 16.8 MW deuterium NBI and ICRH with π phasing (1.2 MW) and with counter-phasing (1.5 MW).

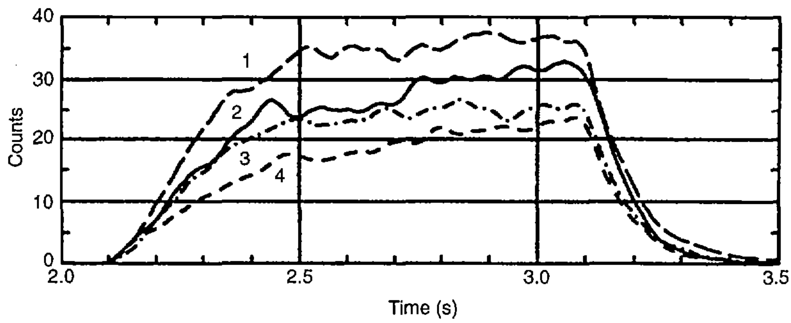

FIG. 6. Dynamics of DT neutron fluxes measured by NDD2 during shots with almost balanced 17 MW NBI with six deuterium sources and one tritium source. The tritium source was directed in the co direction (curves 1 and 2) and in the counter direction (curves 3 and 4). In addition, 2 MW of ICRH was injected with co (curves 1 and 3) and with counter (curves 2 and 4) wave phasing.

this should cause a shift in average energy of the DT neutrons emitted from the plasma in the tangential direction. These shifts for co and counter-phasing of ICRH waves were measured by NDD2 and are shown in Fig. 4. During the first half of the heating time, the measured shift corresponded to average triton tangential velocities of $\pm 10^7$ cm/s and during the second half of $\pm 7 \times 10^6$ cm/s. The decrease in the average triton tangential velocities can be explained by the increase of plasma density during NBI.

Energetic banana particles in a tokamak can hit the wall or the limiter and are thus in the 'loss region' of kinetic space. During TFTR tritium ICRH experiments the resonance layer crosses the plasma at major radius 235 cm, so we calculate the loss region boundaries for the magnetic surface with a minor radius of 0.4a. These calculations were produced in accordance with the model suggested by Rome et al. [10] and gave for the co-ordinates of the loss region peak values $E_{min} = 150$ keV and $\cos^{-1}\chi_{min} = -56°$. This means that some resonant counter-moving tritons with energies higher than 150 keV can be lost during TFTR off-axis triton ICRH. The influence of the triton first orbit losses on the ICRH efficiency is shown in Fig. 5. The NBI in these experiments was of pure deuterium. Tritium was injected into the plasma by gas puffing. Both the tangential and the perpendicular ion temperatures measured by the NDD2 and NDD1 spectrometers are higher for the case of ICRH with π phasing and a power of 1.2 MW than for ICRH with counter-phasing and a power of 1.5 MW.

The DT neutron flux dynamics measured (in parallel with spectrometry) by NDD2 during four shots are shown in Fig. 6. These shots were with almost balanced 17 MW NBI from six deuterium sources and one tritium source directed in the co direction (shots 93 332 and 93 335) and in the counter direction (shots 93 336 and 93 337), and with 2 MW ICRH with co (shots 93 335 and 93 336) and with counter (shots 93 332 and 93 337) wave phasing. The DT neutron flux decreased in the case of counter wave phasing or tritium counter-injection, when more tritons can reach the loss region during ICRH.

4. CONCLUSION AND DISCUSSION

Spectrometers based on NDDs have successfully measured the dynamics of both perpendicular and tangential DT neutron spectra during TFTR experiments with high power NBI and ICRH. The results of these measurements and simulations using the NST code and a semianalytical model yield information about the effective ion temperature, averaged perpendicular and tangential beam ion energies, triton slowing down time, and averaged tangential velocity of resonant tritons during ICRH with co and counter wave phasing. Spectrometry and flux measurements made using NDDs show the decreases of effective temperatures and DT neutron fluxes during ICRH with triton neutral beam counter-injection or counter wave phasing. This can be explained by the increase of the RF driven velocity space diffusion of tritons onto loss orbits. The excellent energy resolution, high radiation resistance (5×10^{14} n/cm^2) and very small size (detector housing of ~ 1 cm^3) of NDDs make them one of the best choices for neutron spectrometry in future burning plasma experiments such as ITER.

ACKNOWLEDGEMENTS

We are grateful to E.A. Azizov, V.S. Khrunov, K.M. Young, D.W. Johnson, S. Von Goeler, S.J. Zweben, R. Majeski and D.S. Darrow for useful discussions, and for the support for this work, which was done as a part of the Princeton Plasma Physics Laboratory–TRINITI collaboration under US Department of Energy contract DE-AC02-76-CHO-3073.

REFERENCES

[1] BUDNY, R.V., et al., Nucl. Fusion **35** (1995) 1497.
[2] KONOROVA, E.A., et al., Sov. Phys. — Semicond. **4** (1971) 1600.
[3] LUCHANSKII, A.E., et al., Sov. At. Energy **63** (1987) 639.
[4] KRASILNIKOV, A.V., in Diagnostics for Experimental Thermonuclear Fusion Reactor (STOTT, P.E., et al., Eds), Plenum Press, New York and London (1995) 435.
[5] KRASILNIKOV, A.V., et al., Rev. Sci. Instrum. (in press).
[6] BRYSK, H., Plasma Phys. **15** (1973) 611.
[7] KRASILNIKOV, A.V., et al., in Controlled Fusion and Plasma Physics (Proc. 23rd Eur. Conf. Kiev, 1996), Vol. 20C, European Physical Society, Geneva (1996).
[8] PUTVINSKIJ, S.V., Rev. Plasma Phys. **18** (1990) 221.
[9] STIX, T.H., Nucl. Fusion **15** (1975) 737.
[10] ROME, J.A., et al., Nucl. Fusion **16** (1976) 55.

ALFVÉN EIGENMODES AND FAST PARTICLE PHYSICS IN JET REACTOR RELEVANT PLASMAS

JET TEAM[1]
(Presented by D.F.H. Start)

JET Joint Undertaking,
Abingdon, Oxfordshire,
United Kingdom

Abstract

ALFVÉN EIGENMODES AND FAST PARTICLE PHYSICS IN JET REACTOR RELEVANT PLASMAS.

Alfvén eigenmodes have been directly excited by using the JET saddle coils with a system which locks the drive frequency to the mode frequency. The technique has shown that neutral beams do not excite low n modes whereas high n modes are destabilised. Such modes are often generated by NBI alone in hot ion H-mode plasmas when the Alfvén speed is about three times the parallel velocity of the beam ions. Kinetic TAE modes have been identified and theoretical calculations predict that these should be destabilised at the fast ion densities present. A new technique for generating TAE modes with ICRH beat waves has been demonstrated. Simulated α-particle heating by ICRH accelerated fast ions has produced electron temperatures of 15 keV in hot ion H-modes and in shear reversed plasmas. Third harmonic ICRH has achieved a D-D neutron rate of 9×10^{15} s^{-1}, which is well simulated by PION code calculations.

1. INTRODUCTION

In a tokamak reactor the slowing down of α-particles will provide the main source of plasma heating. From present day experiments there is evidence that the slowing down is classical. Two important consequences are discussed in this paper. Firstly, the α-particle population is characterised by energies greater than the equipartition energy so that the energy is transferred to the electrons in the core region. A burning plasma will have T_e close to, but higher than T_i. Such plasmas with T_e = 15keV and T_i = 14keV have been achieved in JET with fast particle heating. These values approach the expected temperatures at ignition on ITER (≈20keV), although at lower density. Thus the JET discharges allow electron and ion heat transport to be studied at temperatures relevant to the ignition path and the burn phase in a reactor. Transport analysis results are given for these plasmas and for reversed shear discharges in which T_e and T_i reached 15keV and 32keV, respectively. Secondly, the α-particles generate pressure gradients that can drive collective instabilities such as Alfven eigenmodes. Extensive studies of these modes have been made on JET by both direct and indirect excitation methods.

[1] See Appendix to IAEA-CN-64/O1-4, this volume; together with R. HEETER, Princeton Plasma Physics Laboratory, Princeton, USA; P. LAVANCHI, J. LISTER and Y. MARTIN, CRPP, Lausanne, Switzerland; L.C. APPEL and S. PINCHES, UKAEA, Culham Laboratory, Abingdon, UK; F. NGUYEN, CEA, Cadarache, France; and J. CANDY, Institute for Fusion Studies, University of Texas at Austin, Texas, USA.

2. FAST PARTICLE PHYSICS

ICRF heating at the deuterium third harmonic resonance has provided the most stringent test of both fast particle confinement in JET and the accuracy of simulation codes such as the PION code [1]. The results of these experiments are given in section 2.1. Minority ICRH provides a good simulation of α-particle heating in ITER since the minority ions might reach MeV energies and fast ion beta can exceed that of the α-particle population in a reactor. Collisional transfer of the fast ion energy takes place to the electrons and this feature is exploited to investigate electron heat transport in a variety of plasma regimes. Such measurements complement ion transport studies with neutral beams which typically transfer 80% of their energy to the majority ions. The results of electron heating experiments, which achieved central temperatures up to 15keV, are described in section 2.2.

2.1 Third harmonic ICRH

These experiments were carried out with the third harmonic deuterium resonance in the centre of a 2MA plasma with a toroidal field of 2.2T. Transit time magnetic pumping (TTMP) was the main competing damping mechanism to the cyclotron damping. The time evolution of the neutron rate (Fig.1) increases strongly during the high power RF phase and reaches $9\times10^{15}s^{-1}$ which is a record for ICRH in JET. The neutron rate is the same as that achieved with NBI at the same power level in a similar discharge and is produced by the energetic deuterium tail. A simulation of the time evolution of the D-D neutron rate (Y_{DD}) has been made with the PION code which produces a self-consistent calculation of the power absorption and the deuterium tail. It includes TTMP absorption and effects due to the finite orbit of the fast tail. The result is shown in Fig.1. To achieve the good agreement with experiment it was necessary to include a

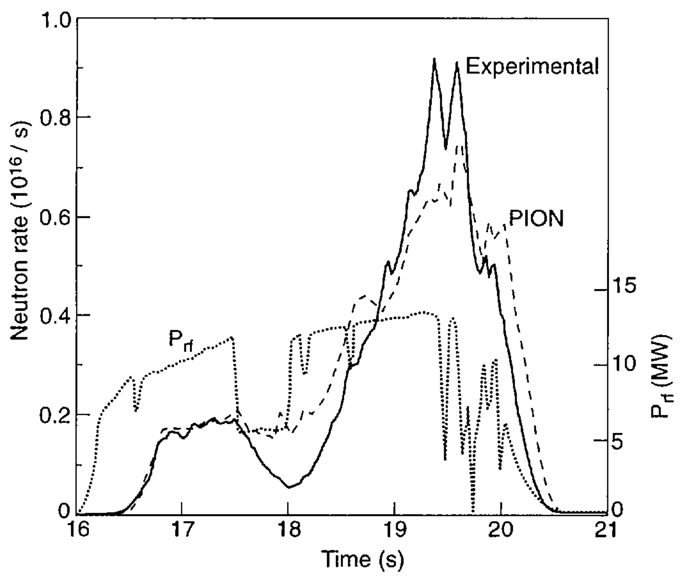

Fig.1 Experimental and PION code neutron rate for $3\omega_{CD}$ ICRH

"parasitic damping" of the order of 4% per pass and a particle loss term that removed particles with energy in excess of 4MeV which were not confined in the plasma. The parasitic damping only played a role at the beginning of the RF pulse when the tail energy was low, and was essential to obtain the time delay between the start of the RF pulse and the rise of Y_{DD}. A similar level of parasitic damping is found in TTMP current drive experiments in DIII-D and could be due to wall loss, RF sheath formation or hydrogen minority damping at the plasma edge. The strong increase in Y_{DD} at the end of the pulse is due to the density increase which reduces the tail energy and also the number of lost ions so that the fast particle density remains almost constant. Thus the D-D neutron rate due to the interaction between the fast tail and thermal ions increases in proportion to the deuterium density.

2.2 Electron heating and transport

These experiments have been carried out in hot ion H-modes, central reversed shear discharges and RF-only H-modes. The plasma currents ranged from 2.5MA to 3.5MA and the toroidal fields from 2.6T to 3.4T. The RF frequency was chosen to locate the hydrogen minority resonance layer in the plasma centre. The highest central value of $T_e = 15$keV was produced in a 3MA/3.1T reversed shear plasma with 14MW of NBI and 5MW of ICRH, but similar temperatures were also achieved in the hot ion H-modes and RF-only H-modes in high triangularity plasmas.

Transport analyses of several of the discharges have been made with the TRANSP code. The results are characterised by the values of χ_e at a minor radius r/a = 0.3. The highest performance discharges have very similar values of χ_e (r/a = 0.3) close to 0.5m^2/s. The 3MA RF-only H-modes have χ_e (r/a = 0.3) $\approx$1m^2/s. For the hot ion H-modes the value of χ_i is about 50% greater than χ_e whereas χ_i is generally less than χ_e inside the confinement barrier of reversed shear plasmas.

3. ALFVEN EIGENMODES

Over the α-particle slowing down time, the fast ion cross field transport, associated with both neo-classical and anomalous effects due to electrostatic or electromagnetic turbulence, is in general negligible. Significant transport and losses of suprathermal particles may take place only in the presence of waves which resonate with them. Of particular importance are weakly damped modes with phase velocities of the order of the α-particle speeds before thermalisation, such as Alfven eigenmodes (AE) which exist within the gaps of the shear Alfven spectrum in magnetically confined toroidal plasmas. It is estimated that if the α-particle losses in ITER are greater than 2% they might damage the first wall and if greater than 20% the fusion reaction will be quenched. Furthermore, Alfven eigenmodes will resonate with the 1MeV neutral beams planned for ITER and might reduce current drive capability. The following sections present studies of the stability of Alfven eigenmodes, excitation by fast particles and ICRF beat waves and the effect on fast ions.

3.1 Stability studies with direct excitation

The saddle coils in JET are used to excite low n Alfven eigenmodes in the 30kHz to 500kHz range and the modes are detected with a set of toroidal and poloidal synchronous detector coils plus ECE and reflectometer diagnostics. The Alfven character of the modes has been verified by the scaling of the resonant frequency with density and magnetic field [2]. Recently, a system has been installed to lock the drive frequency to that of a single mode and to track this

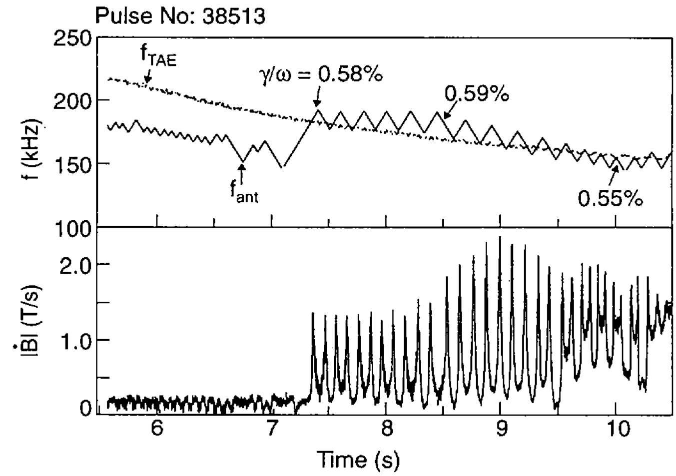

Fig.2 TAE excitation with mode-locked saddle coil drive frequency

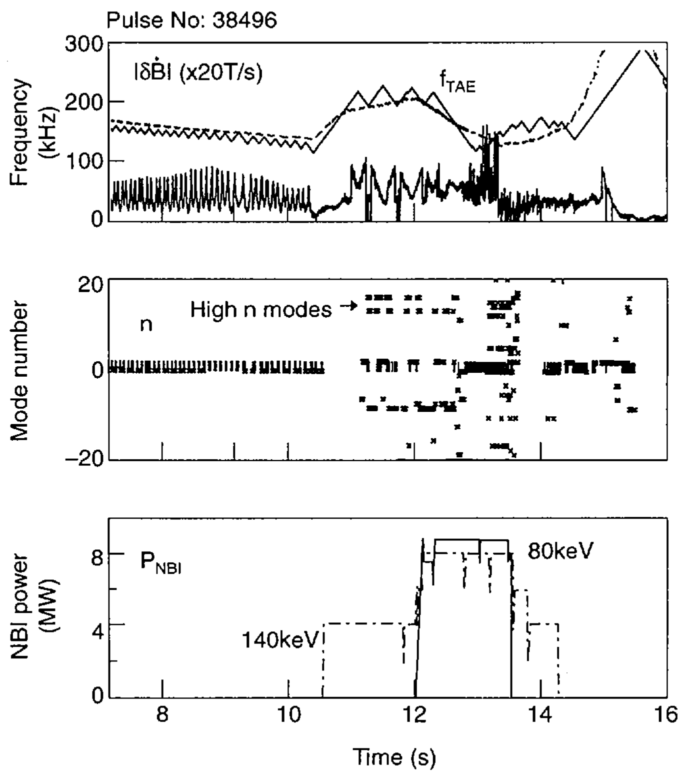

Fig.3 High n TAE modes driven unstable by 140keV NBI

mode in real time. An example is shown in Fig.2 where a mode is detected at 7.3s close to the expected TAE frequency and is tracked until 10.5s. A small sweep is imposed on the resonance frequency to enable the damping to be measured as a function of time. In this case the damping rate (γ) is consistent with radiative damping. The locking gives a powerful technique for studying fast particle effects on mode stability. In a discharge heated by 3MW of 140keV NBI the width of the resonance ($\gamma/\omega \cong 1\%$) of a driven n = 1 mode increased by a factor of two compared with the value in the ohmic phase. Since $\gamma = \gamma_{damping} - \gamma_{drive}$, it appears that the fast ions produce extra damping and do not drive low n modes. This conclusion is supported by the observations shown in Fig.3. During the ohmic limiter phase the system locks to an n = 1 mode driven by the saddle coils. Then a divertor plasma is formed and the NBI is applied at 10.5s. At this point the driving term is dominated by the fast ions, the mode locking ceases but the system still applies the calculated TAE frequency as reference for the detection coils. During the NBI phase high n modes are seen and these have similar amplitudes at the edge to the n = 1 mode in the limiter phase ($\delta B/B \cong 10^{-6}$). In the core region the amplitude of the high n modes can be several hundred times greater (for kinetic TAE modes) than the amplitude at the edge; for the n = 1 modes the maximum amplitude is similar to the edge magnetic field. Thus

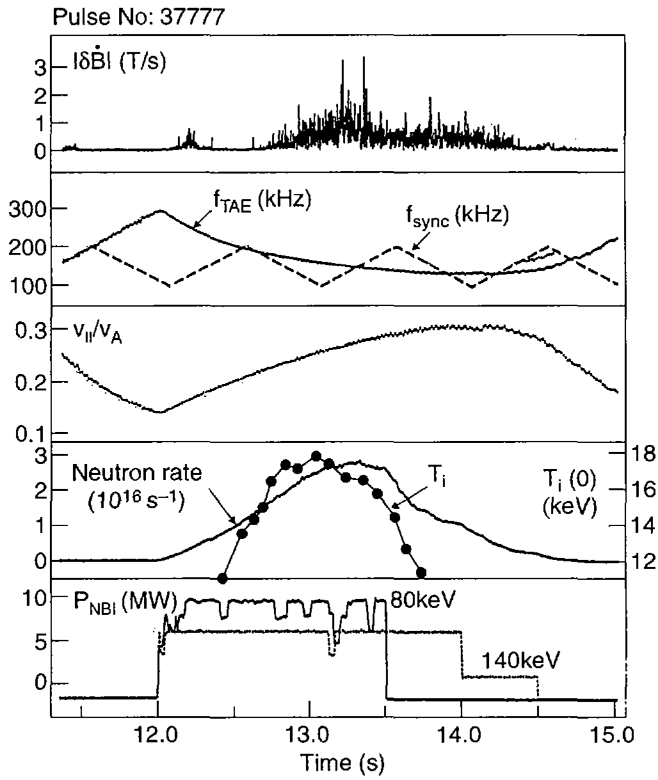

Fig.4 TAE modes excited by NBI at $v_{//} \cong v_A/3$ in a hot ion H-mode.

δB/B could be higher than 10^{-4} which is approaching the threshold (10^{-3}) for stochasticity and reduced fast ion confinement. The excitation of high n modes by 140keV beams with $v_{//} = v_A/3$, where v_A is the Alfven speed, agrees with calculations using the CASTOR code [3] which predict, for example, an n =14 kinetic TAE (KTAE) to be excited at $\beta_{fast} \geq 1\%$: in Fig.3 the value of β_{fast} was 1.3%.

3.2 Excitation by fast particles

In JET hot ion H-modes there is invariably Alfven eigenmode excitation when $v_{//}$ of the 140keV beams is close to $v_A/3$. An example is shown in Fig.4. The

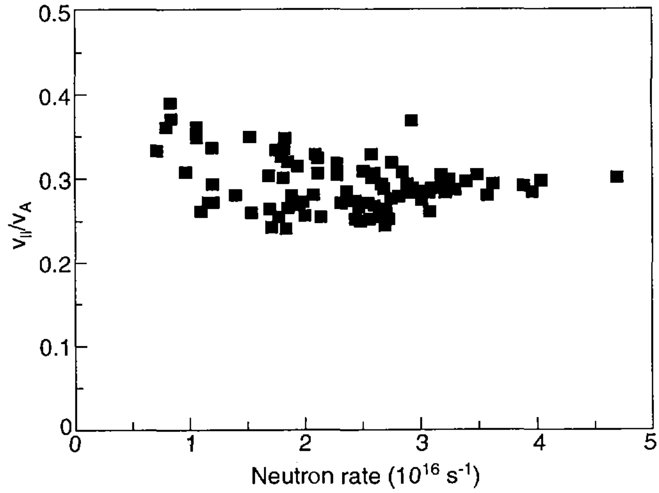

Fig.5 Ratio of $v_{//}/v_A$ for TAE destabilisation in hot ion H-modes

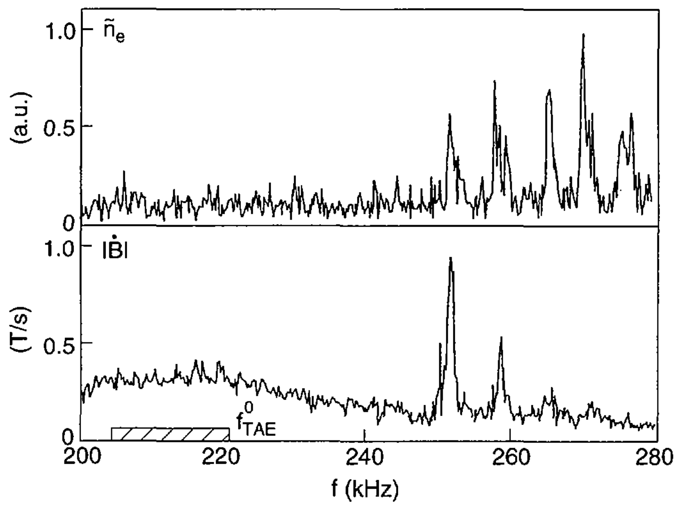

Fig.6 Observation of KTAE modes in an ICRH + LHCD heated plasma

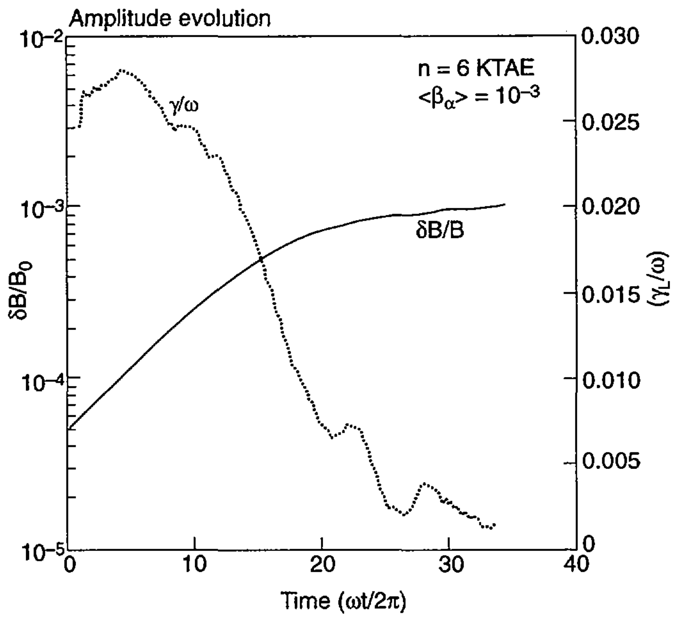

Fig.7 HAGIS prediction of KTAE amplitude and growth rate for 0.1% β_{fast}.

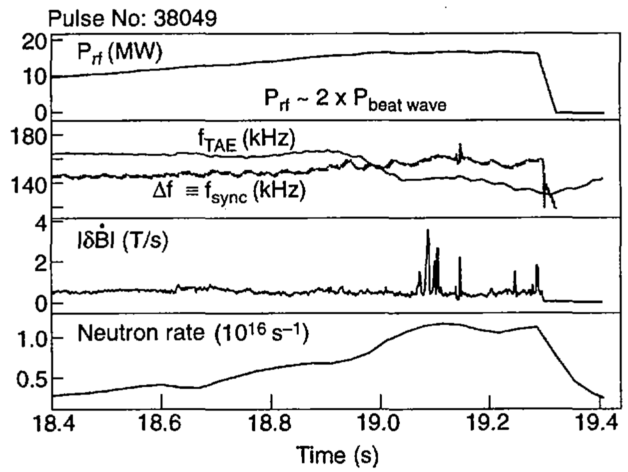

Fig.8 ICRH beat wave drive of TAE modes.

TAE system was in detection mode (no saddle coil excitation) in which the reference frequency is derived from the calculated Alfven frequency plus a small modulation. The Alfven frequency decreases during beam heating since the density is increased due to both the NBI fuelling and the formation of an ELM-free H-mode at 12.1s. As $v_{//}$ approaches $v_A/3$ there is a strong increase in the Alfven mode activity. There is also a tendency for the neutron rate to saturate and even decrease (roll-over). Such a degradation is often associated with either a sawtooth crash or a giant ELM but this is not the case for the discharge shown in

Fig.4. Some statistics of the resonance condition at the soft roll-over for the 140keV beams are shown in Fig.5. These data were taken for plasma currents ranging from 1.7MA to 5.1MA and for toroidal fields between 2.1T and 3.4T. Almost all the points lie in the range $v_{//}/v_A = 0.3 \pm 0.05$.

Since the signals are of the order of 10^{-6}T the eigenmodes need to be kinetic TAE to possibly affect fast ion confinement. Such KTAE modes [3] have been driven by the saddle coils. An example is shown in Fig.6 for a 3MA, 3.1T plasma heated by 6MW of ICRH and 2.5MW of lower hybrid heating. Figure 6 shows the magnetic field and density oscillation amplitudes. The constant frequency difference between modes for the same mode number and the fact that the frequencies are greater than the TAE frequency are characteristic of KTAE modes.

Theoretical calculations of the effect of KTAE modes on the fast ion distribution have been made using the HAGIS code [4] which gives a self-consistent treatment of the wave field and the fast ion distribution. HAGIS is an efficient Monte Carlo code which treats just the perturbation of the fast ions thereby saving a factor of 10^2 in the number of particles required. An example is shown in Fig.7 for α-particles with $<\beta>\sim 10^{-3}$, which is similar to values expected for 10MW of D-T fusion power in JET. The n=6 mode rises with a γ/ω = 3% to a saturated level $\delta B/B=10^{-3}$. Such a value is close to the threshold for stochasticity.

3.3 Excitation by ICRF beat waves

Figure 8 shows the excitation of n = 3 TAE modes using ICRH beat waves [5]. In this discharge the difference in frequency between two ICRH antennas is around 160kHz and when the TAE frequency is close to this value (140kHz), TAE modes occur with large amplitude. Optimisation experiments have shown that the largest amplitude TAE modes are produced when the antenna phasing is 0π0π and adjacent rather than opposite antennas are used, probably due to the greater overlap of the RF fields.

4. SUMMARY

The JET saddle coils have been used to excite low-n TAE modes with a system which locks to the resonance frequency. The technique has demonstrated that fast neutral beam ions do not excite low n modes but can drive high n-modes unstable in accordance with theoretical expectations. The system will also be used in JET D-T experiments to measure the intrinsic excitation by α-particles. Neutral beam ions produce TAE modes when $v_{//}=v_A/3$ and there is possible evidence of performance limitation by such activity. Kinetic TAE modes have been observed and theoretical calculations suggest that these can be driven unstable at a fast ion beta value of only a few percent. A new method of directly exciting TAE modes using beat waves generated by fast waves has been established. Simulated α-particle heating using MeV fast ions generated by ICRH has produced electron temperatures up to 15keV. Transport analysis of such discharges has shown a factor of two improvement in χ_e in the core of hot-ion H-modes and reversed shear plasmas compared to RF-only ELMy plasmas. A neutron rate of $9\times10^{15}s^{-1}$ has been attained by third harmonic deuterium ICRH. This has been successfully reproduced by the PION code which is used extensively to predict D-T performance in JET and ITER.

ACKNOWLEDGEMENT

This work was performed under Task Agreements with CRPP, Lausanne, Switzerland, UKAEA Culham Laboratory, Abingdon, UK and CEA, Cadarache, France, and in collaboration with Princeton Plasma Physics Laboratory, Princeton, USA and Institute for Fusion Studies, University of Texas, Texas, USA.

REFERENCES

[1] ERIKSSON, L.G., et al., Nucl. Fusion **33** (1993) 1037.
[2] FASOLI, A., et al., Nucl. Fusion **35** (1995) 1485.
[3] HUYSMANS, G.T.A., et al., Phys. Fluids **B 5** (1993) 1545.
[4] APPEL, L.C., et al., Nucl. Fusion **35** (1995) 697.
[5] FASOLI, A., et al., Nucl. Fusion **36** (1996) 258.

DISCUSSION

R.J. GOLDSTON: Have you used the saddle coils to investigate damping rates, etc., of TAEs during hot ion H modes? Also, have you used the coils as a way to examine the approach to MHD instability, e.g. to kinks? It seems to me that they might be useful for steering an advanced tokamak through dangerous terrain.

D.F.H. START: So far the saddle coils have not been used in either of these ways but such applications could be made, at least for low n modes.

OPERATIONAL LIMITS AND DISRUPTIONS

(Session A3)

Chairperson

D. ROBINSON
United Kingdom

HIGH PERFORMANCE EXPERIMENTS IN JT-60U HIGH CURRENT DIVERTOR DISCHARGES

S. ISHIDA, Y. NEYATANI, Y. KAMADA, A. ISAYAMA, T. FUJITA, T. OIKAWA, Y. KOIDE, Y. KAWANO, H. SHIRAI, T. OZEKI, T. NISHITANI, S. TAKEJI, H. KIMURA, T. HATAE, T. FUKUDA, N. ISEI, JT-60 TEAM
Naka Fusion Research Establishment,
Japan Atomic Energy Research Institute,
Naka-machi, Naka-gun, Ibaraki-ken,
Japan

Abstract

HIGH PERFORMANCE EXPERIMENTS IN JT-60U HIGH CURRENT DIVERTOR DISCHARGES.

Hot ion H mode and high β_p H mode regimes in JT-60U have been extended up to 4.5 MA with $q_{95} = 2.0$ and to 2.7 MA with $q_{95} = 2.5$, respectively, with intense NBI power of up to 41 MW. The optimal safety factor was sought for improving the plasma performance in such high current low q regimes; the maximum performance was found to be commonly attained at around $q_{95} \approx 3$, which is in support of ITER. In the high β_p H mode regime, performance parameters of H/q_{95} and β_N/q_{95} reached ~1.2 and ~0.75, respectively, in the low q region where the highest fusion triple product of $n_D(0)\tau_E T_i(0) \approx 1.5 \times 10^{21}$ $m^{-3}\cdot s\cdot keV$ was achieved with a very high ion temperature $T_i(0) = 45$ keV. The limitation for the hot ion H mode performance was due to a non-disruptive ELM event at a low Troyon factor during persistent m = 1 modes with significant toroidal mode couplings. The high β_p H mode discharges have encountered disruptive β limits at around $q_{95} \approx 3$ in which the simultaneous growth of low m internal modes was observed just prior to the disruption near the stability limit for ideal kink-ballooning modes. Successive ELM activity near the β limit induced an m = 3/n = 1 mode and turned into non-local collapses followed by disruptions, which limited the sustainment of ELMy high β_p H mode discharges. The limitation features observed in the two high performance regimes are characterized by the difference in pressure profiles and the attainable stability.

1. INTRODUCTION

A high current low q regime in a large tokamak is of increasing importance to the question of whether the self-ignition operation scenario for ITER is workable at $q_{95} \approx 3$. In JT-60U, high performance experiments for hot ion H mode and high β_p H mode discharges have been conducted to demonstrate high reactivity plasmas and show reactor potential in such a low q regime by progressive extension of the plasma current with improving plasma performance. Consequently, the experiments have been advanced to the low q regime below $q_{95} = 3$ to address the subject of the optimal safety factor for maximizing the fusion energy production at the maximum toroidal field strength of the tokamak.

In 1995, the plasma current for the hot ion H mode discharges was increased with enhanced confinement up to 4.5 MA with $q_{95} = 2.0$. The modification of the NBI system was implemented for increasing the beam fuelling rate into the centre of the plasma as well as the injection power by means of narrowing the distance between extraction electrodes by 20% to a nominal value in the ion sources. In 1996, high β_p H mode confinement has been successfully achieved at up to 2.7 MA with $q_{95} = 2.5$ by utilizing intense NBI power of up to 41 MW. This paper presents the achievements and limitations of the high performance discharges produced with deuterium beam injection into deuterium plasmas in non-circular divertor configurations in JT-60U.

2. DISCHARGE CHARACTERISTICS

2.1. Hot ion H mode discharges

The hot ion H mode experiment in 1995 addressed confinement optimization at plasma currents in the range $I_p = 3.0$–4.5 MA, higher than those of up to $I_p = 3.5$ MA in the previous experiments in 1991–1992 [1] and in 1993–1994 [2]. The hot ion H mode discharges with a high aspect ratio $A \approx 3.8$ and a low triangularity $\delta \approx 0.06$ were produced with beam injection power of up to $P_{NBI} = 30$ MW at a fixed toroidal field strength $B_t \approx 4.2$ T. The plasma was configured with a large volume (typically 70 m^3), which makes the beam deposition profile broader and the ripple induced fast ion losses substantial — as much as ~10–35% of the beam injection power. This ripple loss power composed of ripple trapped and banana drift losses calculated using the OFMC (orbit following Monte Carlo) code is extracted from the beam injection power in order to evaluate the actual energy confinement time only for the hot ion H mode discharges in this paper.

Sawtoothing target plasmas were created with a high internal inductance $\ell_i \approx 1.0$–1.2, so that the prolongation of the sawtooth period was important for improvement in performance. Shown in Fig. 1 are waveforms for the highest performance hot ion H mode discharge at $q_{95} = 2.5$, where the diamagnetic stored energy reaches $W_{dia} = 8.0$ MJ and the neutron rate reaches $S_n = 2.3 \times 10^{16}$/s with an H factor of 2.0 against the ITER89P scaling just before an ELM event. As shown in Fig. 1(b), a peaked ion temperature profile from charge exchange recombination spectroscopy measurement utilizing the C VI line emission and a broad electron temperature profile from ECE measurement are observed in the hot ion H mode phase, while the electron density profile obtained from Thomson scattering measurement and interferometers is quite broad even after the ELM event. The H mode transition is clearly indicated by the increase in the edge ion temperature and the decrease in the edge toroidal velocity. While the sawtooth activity is suppressed during the ELM free phase except for a compound sawtooth, the H mode characteristic is lost owing to the ELM event at a low Troyon factor $\beta_N = 1.1$, and the dis-

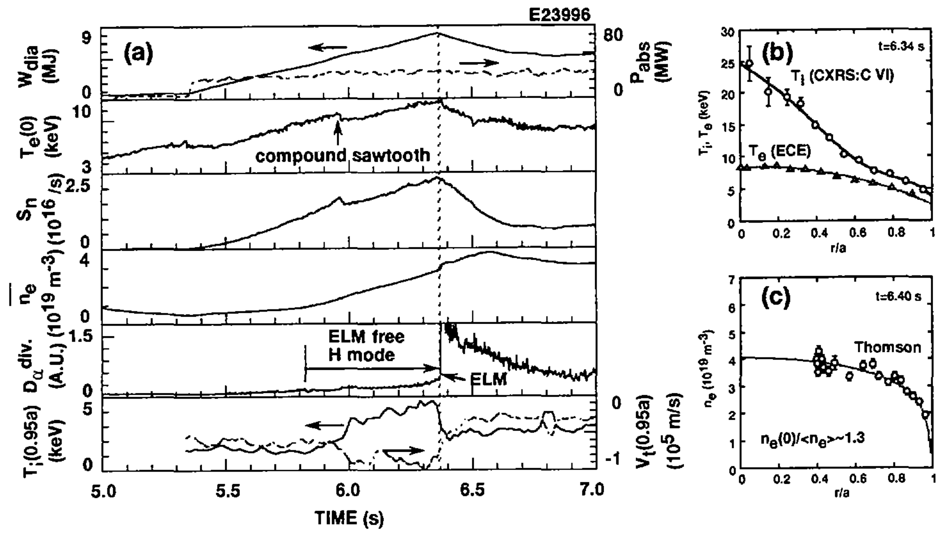

FIG. 1. (a) Waveforms for the highest performance hot ion H mode discharge at 3.5 MA with major radius R_p = 3.15 m, minor radius a = 0.82 m, ellipticity κ = 1.7 and B_t = 4.25 T; (b) ion and electron temperature profiles just before the ELM; (c) electron density profile just after the ELM.

charge reverted to an L mode edge condition (see Section 4.1). Note that the onset is not due to the H to L back-transition since the usual ELM onset conditions such as the edge pressure gradient and density limit observed in JT-60U are satisfied here.

2.2. High β_p H mode discharges

The following new technical advances have contributed to high β_p H mode experiments in 1996: (1) fast current ramp-up operation allowing the main beams to be injected in the current flat-top phase at high current of up to 2.7 MA; (2) intense beam power of up to 41 MW at 90–95 keV. Consequently, high β_p H mode confinement has been achieved at up to I_p = 2.7 MA, with W_{dia} reaching 9.4 MJ at 2.6 MA. The high β_p H mode discharges were configured to achieve a peaked beam deposition profile with a large A of ~4.3 and a low δ of ~0.05 [3, 4]. Since the ripple induced fast ion losses were less than ~5% of the injection power for the high β_p discharges, the ripple loss power is not taken into account for evaluating the energy confinement time. It is essential for achieving high β_p H mode confinement to create a sawtooth free target plasma with a central q slightly above unity by injecting the main beams before the sawtooth onset.

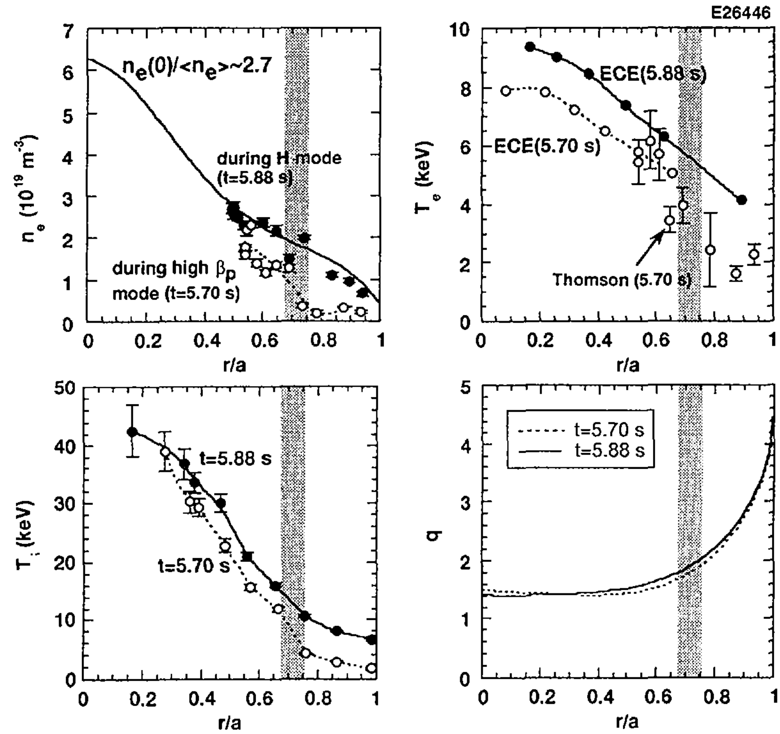

FIG. 2. Profiles of n_e, T_i, T_e and q during high β_p mode and high β_p H mode for a high performance high β_p H mode discharge at 2.2 MA and B_t = 4.4 T, showing the location of an internal transport barrier.

The high β_p H mode is characterized by the combination of high β_p mode characteristics with an internal transport barrier and H mode characteristics with an edge transport barrier. The characteristic profiles are shown in Fig. 2 for a high performance high β_p H mode discharge at 2.2 MA with q_{95} = 3.3, where H = 3.3, $S_n = 5.4 \times 10^{16}$/s, W_{dia} = 9.0 MJ and $n_D(0)\tau_E T_i(0) \approx 1.3 \times 10^{21}\cdot m^{-3}\cdot s\cdot keV$ were achieved. Assuming the injection of deuterium beams into 50:50 DT plasmas, the fusion amplification factor Q_{DT} would be $\sim$0.55 extracting α heating power P_α; Q_{DT} is calculated using the same definition as in Ref. [5]. In the high β_p mode phase just before the H mode transition, the presence of the internal transport barrier is clearly indicated in the electron density and ion temperature profiles at r/a $\approx$ 0.7 in Fig. 2. The q profiles measured from motional Stark effect (MSE) spectroscopy reveal a central q value of $\sim$1.4, slightly above unity with a weak central magnetic shear configuration. The main parameters for typical high performance high β_p H mode discharges are listed in Table I.

TABLE I. PLASMA PARAMETERS FOR TYPICAL HIGH β_p H MODE DISCHARGES

	E26446	E26939	E26949
ELM activity	ELM free	ELM free	ELMy
Time (s)	5.884	5.830	6.347
I_p (MA)	2.2	2.4	2.5
B_t (T)	4.4	4.3	4.3
P_{NBI} (MW)	26.6	32.7	35.0
R_p (m)	3.09	3.11	3.12
a (m)	0.73	0.72	0.74
κ	1.7	1.7	1.7
q_{95}	3.3	2.9	3.0
W_{dia} (MJ)	8.6	8.4	9.3
S_n (10^{16}/s)	5.4	5.2	4.8
$n_e(0)$ (10^{19} m^{-3})	6.5	6.0	5.9
$n_D(0)$ (10^{19} m^{-3})	4.6	4.6	4.3
$T_i(0)$ (keV)	42.5	45.0	35.5
$T_e(0)$ (keV)	9.3	10.6	11.0
τ_E (s)	0.66	0.75	0.33
$\tau_E/\tau_E^{ITER89P}$	3.3	3.3	2.1
β_N	2.2	2.0	2.0
$n_D(0)\tau_E T_i(0)$ (10^{21} m$^{-3}\cdot$s$\cdot$keV)	1.3	1.5	0.51
Q_{DD} (10^{-3})	4.0	3.5	1.8
Q_{DT} (not extracting P_α)	0.52	0.41	0.28
Q_{DT} (extracting P_α)	0.55	0.43	0.30
P_{DT} (MW)	8.2	7.0	8.3

3. ACHIEVED PERFORMANCE AND OPTIMAL q

3.1. Achieved performance

The ratio of the H factor to the safety factor, H/q, is a useful figure of merit for ignition margin since $(H/q)^2$ is proportional to the fusion product; $H/q_{95} \geq 0.6$ is required for sustained ignition in ITER [6]. The H/q_{95} values are shown in Fig. 3 for high β_p discharges at I_p = 0.7–2.7 MA and hot ion H mode discharges at I_p = 2.5–4.5 MA. H/q_{95} reaches 0.78 at q_{95} = 2.5 in the hot ion H mode regime and 1.16 at q_{95} = 3.0 in the high β_p H mode regime. In terms of DD reactivity, the ratio of DD fusion power to the beam absorption power (P_{DD}/P_{abs}) is maximized to 1.5×10^{-3} at q_{95} = 3.0 for hot ion H mode discharges and to 2.8×10^{-3} at

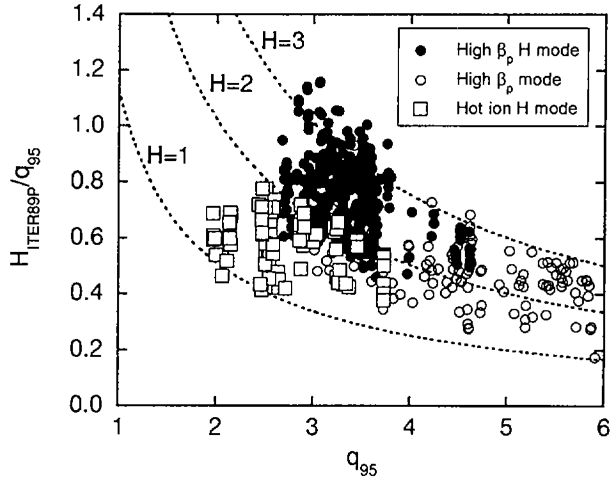

FIG. 3. H/q_{95} as a function of q_{95} for high β_p and hot ion H mode discharges, with contour lines showing H, the H factor against the ITER89P scaling.

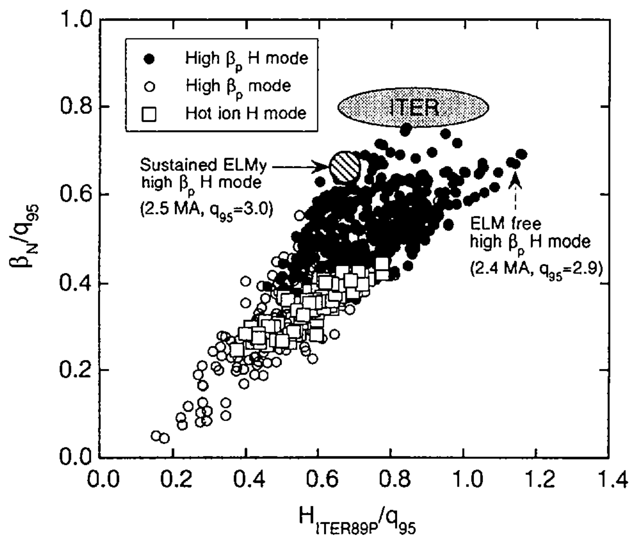

FIG. 4. β_N/q_{95} as a function of H/q_{95} for high β_p mode, high β_p H mode and hot ion H mode discharges. The operating domain for ITER is also shown.

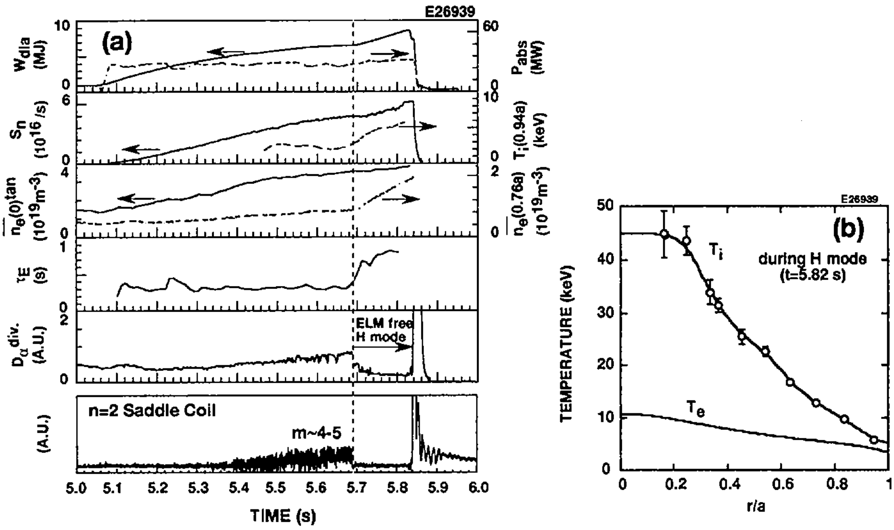

FIG. 5. (a) Waveforms for the high β_p H mode discharge at 2.4 MA achieving the highest fusion product, along with the n = 2 saddle coil signal; (b) ion and electron temperature profiles at the peak performance.

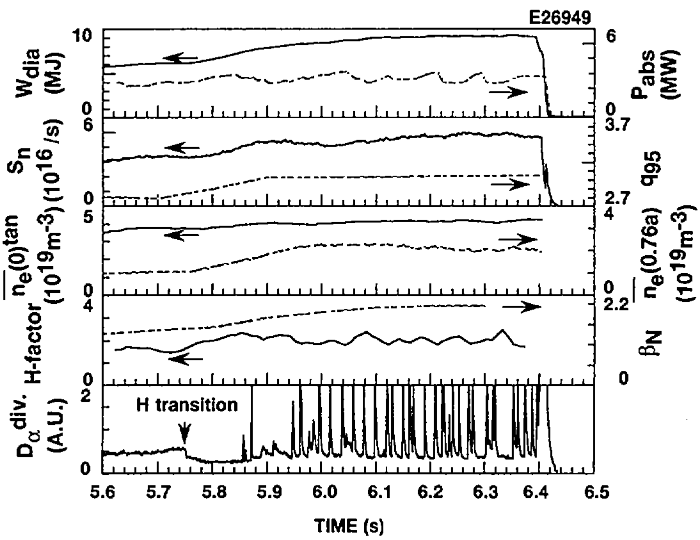

FIG. 6. Waveforms for a sustained ELMy high β_p H mode discharge with high stationary performance at 2.5 MA with q_{95} = 3.0.

$q_{95} = 3.2$ for high β_p H mode discharges. In addition, these performance parameters are peaked at around $q_{95} \approx 3$, independent of transient or stationary states ($dW/dt \approx 0$) or the two enhanced confinement modes. Thus, the fusion performance is found to be commonly maximized at around $q_{95} \approx 3$, which is in support of the self-ignition operation scenario for ITER.

The relation of the fusion performance (H/q_{95}) and the stability performance (β_N/q_{95}) is shown for the two regimes in Fig. 4; β_N/q_{95} is proportional to the toroidal β normalized to the inverse aspect ratio. In the hot ion H mode regime, the stability performance is apparently limited to low β_N/q_{95} of at most 0.45 at $q_{95} = 2.5$, while the fusion performance is transiently improved to some extent. The high β_p H mode discharges are shown to almost reach the ITER domain transiently for both fusion and stability performance, where β_N/q_{95} reaches 0.75 at $q_{95} = 2.7$, and to be closely approaching it in the case of sustained ELMy high β_p H modes.

3.2. High performance discharges at around $q_{95} \approx 3$

The highest fusion triple product was achieved with high power injection of 37 MW at peak and $Z_{eff} \approx 2.2$ at $q_{95} = 2.9$ during an ELM free high β_p H mode, as shown in Fig. 5, where $n_D(0)\tau_E T_i(0) = 1.5 \times 10^{21}$ $m^{-3}\cdot s\cdot keV$, with $T_i = 45 \pm 5$ keV, $W_{dia} = 8.6$ MJ, and $S_n = 5.2 \times 10^{16}/s$ at peak. The ELM free H mode appears together with a significant increase in electron density and ion temperature at the edge just as continuous $n = 2$ modes with $m \approx 4$–5 (~ 18 kHz) disappear. A fast disruption follows the growth of $n = 1$ modes for ~ 10 ms during the ELM free H mode period as the discharge encounters a disruptive β limit at $\beta_N = 2.0$. Such continuous low n modes ($n = 1$, 2 or 3) were often observed at $q_{95} \approx 3$ with some mode mixture before the H mode transition for high performance discharges. These low n modes would deteriorate the high β_p mode confinement as the internal transport barrier became unclear.

A high performance high β_p H mode plasma was sustained at $q_{95} = 3.0$ with successive ELMs, as shown in Fig. 6, utilizing a flux expansion technique to increase the plasma volume by 10% at a fixed major radius within a short period of 200 ms from $t = 5.7$ s to $t = 5.9$ s. During the ELMy high β_p H mode, high stored energy $W_{dia} \approx 8$–9 MJ and neutron rate $S_n \approx (4$–$5) \times 10^{16}/s$ are shown to be sustained with $H/q_{95} \approx \beta_N/q_{95} \approx 0.67$ for ~ 1.5 times the energy confinement time. At peak, W_{dia} and S_n reach 9.3 MJ and $4.9 \times 10^{16}/s$, where $n_D(0)\tau_E T_i(0) = 5.1 \times 10^{20}$ $m^{-3}\cdot s\cdot keV$ was achieved. In this discharge, high fusion power $P_{DT} \approx 8.3$ MW would be sustained with equivalent $Q_{DT} \approx 0.30$. The duration of the high performance phase was limited by a β limit disruption with $m = 3/n = 1$ modes induced by ELMs, as discussed later in connection with Fig. 10.

4. LIMITATIONS FOR PERFORMANCE

4.1. Non-disruptive ELM limit for hot ion H mode discharges

The observed low Troyon factors for the hot ion H mode discharges arise from the fact that the edge pressure gradient during an ELM free phase reaches a critical value for edge stability before the core pressure develops sufficiently. While the performance of hot ion H mode discharges is generally limited by the ELMs, other MHD activities related to a significant extension of the q = 1 surface become influential on confinement at low q. Typical internal MHD activities associated with the ELM onset are shown in Fig. 7 with the T_e profile evolution from ECE grating polychromator measurements [7] for the high performance hot ion H mode discharge of Fig. 1. Here the H mode characteristic is lost through an ELM event during persistent m = 1 activity with significant toroidal couplings. An interaction between the

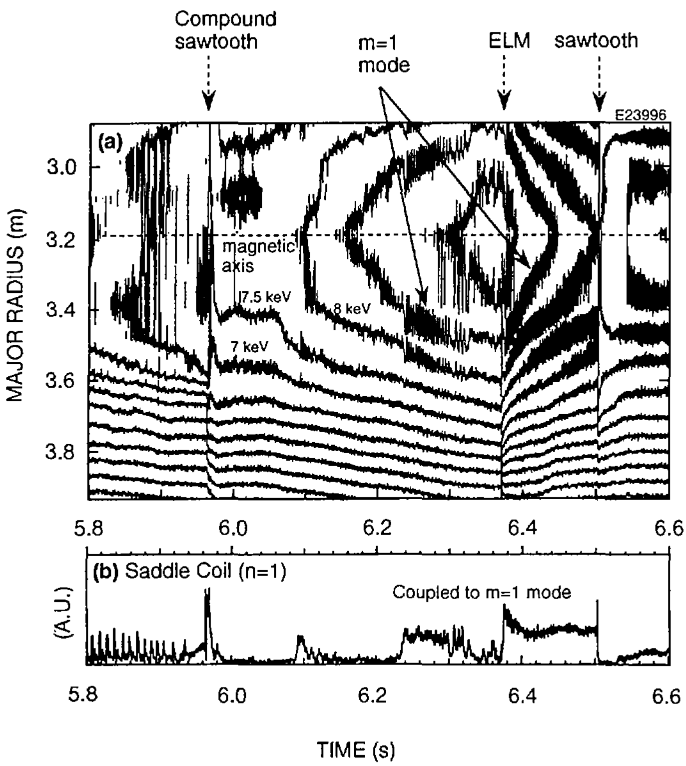

FIG. 7. Time evolution of the electron temperature profile for the high performance hot ion H mode discharge of Fig. 1 showing the internal MHD activities along with the n = 1 saddle coil signal. The contour step size is 500 eV.

m = 1 mode and the ELM onset is seen in a change of the m = 1 mode frequency in this figure. It is suggested that global mode couplings due to the ELM in combination with the m = 1/n = 1 mode would enhance a loss of H mode confinement for such a low q discharge.

4.2. Disruptive β limits for high β_p H mode discharges

As shown in Fig. 5, the high performance high β_p H mode discharge at around $q_{95} \approx 3$ was often terminated by high β disruptions. The precursor oscillations

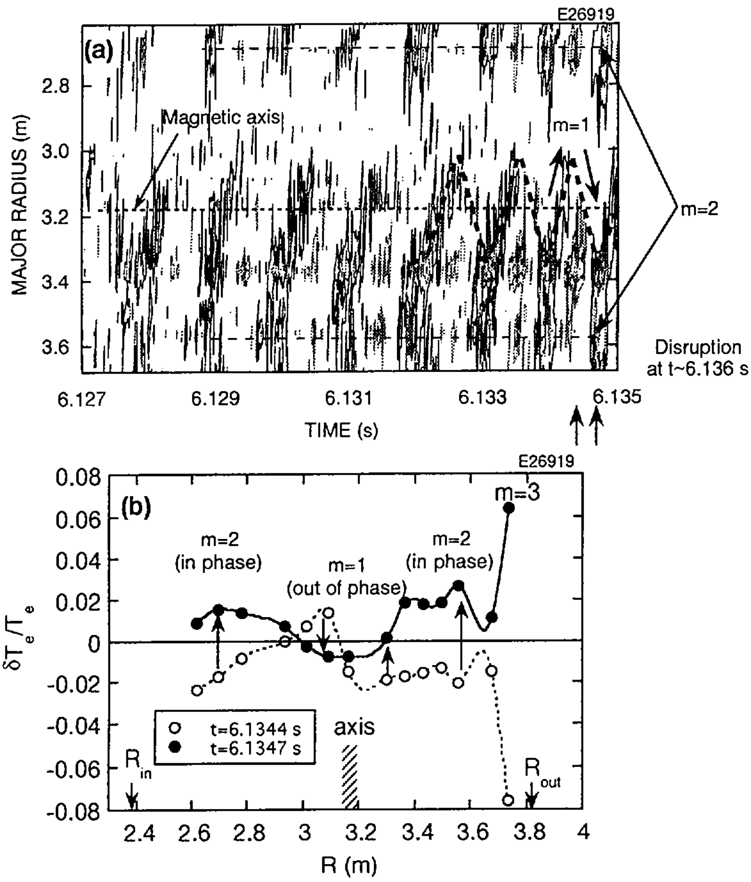

FIG. 8. (a) Time evolution of the perturbation in the electron temperature profiles showing m = 1 and m = 2 modes with the same frequency at different locations. The contour step size is 50 eV. The discharge is disrupted at t ≈ 6.136 s. (b) Electron temperature fluctuation level as a function of the major radius observed just before the disruption for a high performance high β_p H mode at 2.5 MA with q_{95} = 2.8.

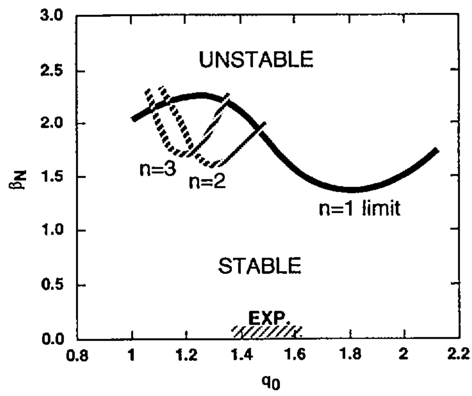

FIG. 9. β_N limits for ideal low n kink-ballooning modes (n = 1, 2 or 3) as a function of central q for a plasma with a peaked pressure profile ($p(0)/\langle p\rangle \approx 5$) and a weak central magnetic shear profile calculated with the ERATO-J code. The typical range of the central q experimentally observed is indicated by hatching.

were observed most often with n = 1 mode growth on Mirnov coils, with a variety of growth times of the order of 10 μs to 1 ms, in which the m = 3 mode is observed to be dominant for both ELM free and ELMy high β_p discharges at around $q_{95} \approx 3$.

Experimental evidence of kink-ballooning modes was observed prior to the disruption, with a clear separation of each low m mode from the ECE grating polychromator measurements, as shown in Fig. 8, where the discharge at 2.5 MA with $q_{95} = 2.8$ was disrupted at $\beta_N = 1.9$ during the ELM free high β_p H mode. This figure reveals the simultaneous observation of m/n = 1/1 and 2/1 modes within the plasma with the same frequency but different phase relation; the identification of the mode numbers is consistent with the q profile from MSE measurement. The m = 3/n = 1 mode on the ECE signals indicated in Fig. 8(b) is also detected on Mirnov coils with the same frequency. The observed distributions of the internal modes are similar to the distributions of the displacement eigenfunction for ideal n = 1 kink-ballooning modes calculated with the ERATO-J code, while the growth time of ~2 ms in this case is relatively long.

The β_p collapse observed at high q in JT-60 [8] and JT-60U [3] is a non-disruptive fast β collapse at a low Troyon factor for which the precursor perturbations on the ECE signals are relatively localized in a region of high pressure gradient within the plasma. As q is decreased with increasing plasma current, the toroidally coupled mode structure becomes more global, extending to the plasma boundary. This global mode coupling from the core to the edge observed near the β limit at low q would result in the disruption.

The q profile for high β_p H mode discharges was measured to represent a weak central magnetic shear with a central q value (q_0) around ~1.4–1.6, as shown in Fig. 2. The ERATO-J code calculations based on the measured q profile show that the stability for n = 1 kink–ballooning modes is strongly dependent on the central q value, as shown in Fig. 9, where the plasma internal inductance and pressure peaking factor are almost fixed at around $\ell_i \approx 1.0$ and $p(0)/\langle p \rangle \approx 5$. The observed β limits are roughly in accordance with the stability limit for ideal low n kink-ballooning modes in this figure. The $n \geq 2$ mode stability more sensitively depends on the details of pressure and current profiles; if the pressure profile becomes broader, the $n \geq 2$ mode limits tend to be increased above the n = 1 limit.

4.3. ELM effect on stability near the β limit

Although successive ELMs are generally considered necessary to sustain the high performance discharges as adopted for operation in ITER, the effect of ELM activity on the β limit is not yet understood satisfactorily. While the high β_p H mode discharge can be sustained for a while near the β limit, as shown in Fig. 6, the abrupt termination of the discharge by a disruption occurs during the ELMy phase. Figure 10 shows the change of ELMs to non-local collapses resulting in the disruption at $\beta_N = 2.0$ for the ELMy high β_p H mode discharge shown in Fig. 6. First,

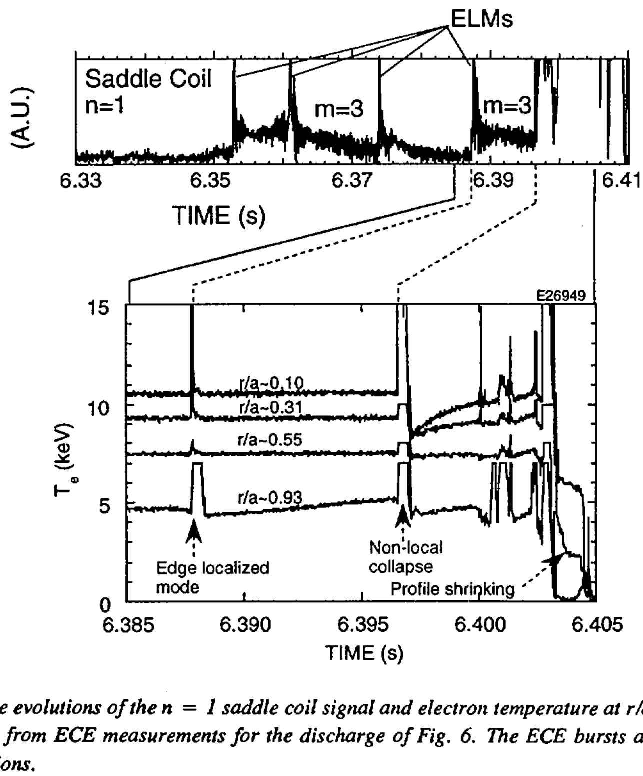

FIG. 10. Time evolutions of the n = 1 saddle coil signal and electron temperature at r/a ≈ 0.1, 0.31, 0.55 and 0.93 from ECE measurements for the discharge of Fig. 6. The ECE bursts are due to non-thermal emissions.

the successive ELMs induce an m = 3/n = 1 mode but do not affect the core plasma. The ELM event with non-thermal emissions at t ≈ 6.396 s is accompanied by the core collapse near the centre. With this event, the ELM appears to be no longer localized near the edge and it turns into global collapses. While the causality of the non-local collapse with the ELM is not clear owing to the strong non-thermal emissions, it is suggested as a possibility that, near the β limit at low q, the internal modes can be destabilized with the ELM activity inducing the peripheral m = 3 mode, resulting in a non-local collapse which would enhance the plasma-wall interaction, followed by a disruption.

5. ACHIEVED STABILITY AND PROFILE EFFECTS

The limitations for performance are summarized as: (1) a non-disruptive ELM limit for hot ion H mode discharges; (2) a non-disruptive β_p collapse limit for high β_p mode discharges; (3) a non-disruptive ELM limit for high β_p H mode discharges; (4) a disruptive β limit during high β_p mode, ELM free high β_p H mode and ELMy high β_p H mode for high β_p discharges. The achieved stability for the high performance experiments is shown in Fig. 11, which indicates the limitations for hot ion H mode, high β_p mode and high β_p H mode discharges. It is found that the β_N/ℓ_i

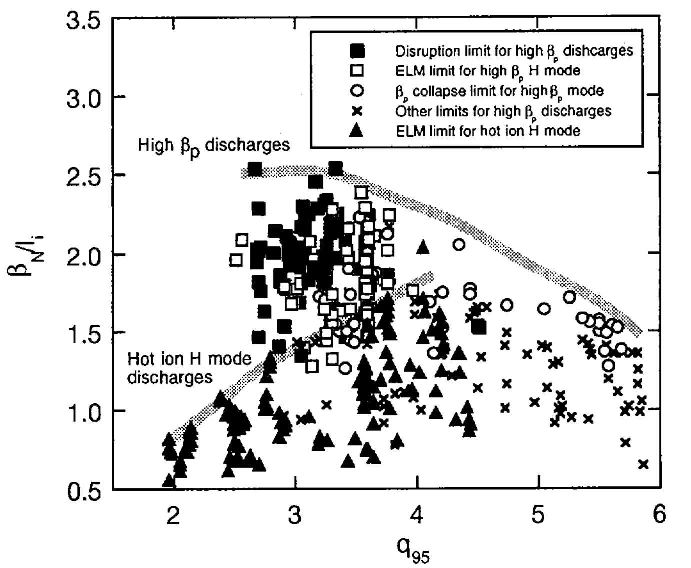

FIG. 11. Attainable β_N/ℓ_i as a function of q_{95} with various limitations for high β_p mode, high β_p H mode and hot ion H mode discharges. The upper envelopes of the β_N/ℓ_i limits are shown for the hot ion H mode regime and the high β_p regime.

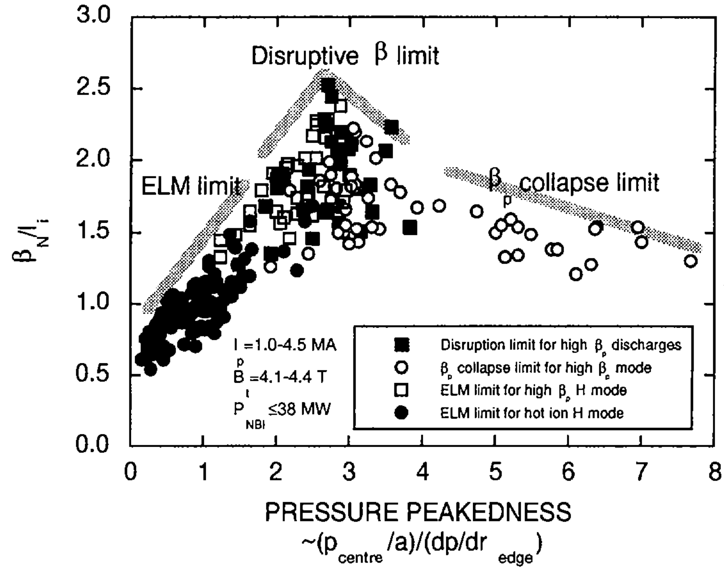

FIG. 12. β_N/ℓ_i as a function of relative pressure profile peakedness. Also shown are various limitations for high β_p mode, high β_p H mode and hot ion H mode discharges.

attainable for the high β_p H mode discharges is increased with decreasing q_{95} as the limitations change from β_p collapse limit to ELM limit and disruptive β limit. The stability of high β_p H mode plasmas almost reaches the requirement for ITER of $\beta_N = 2.2$–2.4 at $q_{95} \approx 3.0$ without a particular triangular plasma shape but with effective pressure profile alignment by beam deposition control in combination with the high β_p H mode characteristics. In contrast, the stability of the hot ion H mode discharges limited by ELMs is degraded with decreasing q_{95}, since the pressure profile is broadened with decreasing q_{95}.

To clarify the impact of pressure profile on the limitations for performance, β_N/ℓ_i is plotted in Fig. 12 as a function of the indication of relative pressure profile peakedness defined as the core pressure gradient normalized to the edge pressure gradient; the core pressure gradient is deduced from $(G\langle p\rangle)/a$, where $G = S_n V_p / W_{dia}^2$ is the profile peaking factor [9] and the edge pressure gradient is taken from the ELM onset condition to be proportional to $B_t^2/2\mu_0 R_p q_{95}^2$ [10]. As shown here, an excess of the profile peaking and broadening brings about a non-disruptive β_p collapse limit and an ELM limit, respectively. A moderate pressure profile produced with the high β_p H modes makes the stability maximized at $q_{95} \approx 2.6$–3.5. In consequence of the attained high plasma pressure, the discharge encounters the disruptive β limit, which obstructs further improvement in performance.

6. CONCLUSIONS

Enhanced confinement regimes with hot ion H mode and high β_p H mode have been progressively extended substantially below $q_{95} = 3$ in JT-60U. In consequence of these high performance experiments, the optimal q for maximizing the fusion energy production was found to exist at around $q_{95} \approx 3$. The highest fusion triple products and peak performance parameters of H/q_{95} and β_N/q_{95} were achieved at $q_{95} \approx 3$ for high β_p H mode discharges, so that the transient performance almost reached, and the stationary performance closely approached, the conditions required for ITER. The demonstrated results offer favourable prospects for the ITER operation scenario.

The important limitations for the plasma performance in the low q region are manifested as a non-disruptive ELM limit for hot ion H mode discharges and a disruptive β limit for high β_p H mode discharges. Global mode coupling due to toroidal effects for high performance plasmas at low q is emphasized by the experimental evidence of a loss of H mode confinement due to ELM activity coupled to persistent m = 1 modes, the disruptive β limit due to low n kink–ballooning modes and the successive ELM effect on stability near the β limit. These limitations for the performance in the two regimes are found to arise from the significant difference in the pressure profile and the related stability limit. These results suggest the importance of stability margins, with emphasis on profile control utilizing improved confinement characteristics as well as external heating sources for sustained ignition in future tokamaks such as ITER.

ACKNOWLEDGEMENTS

The authors would like to express thanks to the engineering and technical staff for their continuous contributions to this research.

REFERENCES

[1] KIKUCHI, M., et al., in Plasma Physics and Controlled Nuclear Fusion Research 1992 (Proc. 14th Int. Conf. Würzburg, 1992), Vol. 1, IAEA, Vienna (1993) 189.

[2] SATO, M., et al., in Plasma Physics and Controlled Nuclear Fusion Research 1994 (Proc. 15th Int. Conf. Seville, 1994), Vol. 1, IAEA, Vienna (1995) 265.

[3] ISHIDA, S., et al., in Plasma Physics and Controlled Nuclear Fusion Research 1992 (Proc. 14th Int. Conf. Würzburg, 1992), Vol. 1, IAEA, Vienna (1993) 219.

[4] KOIDE, Y., et al., in Plasma Physics and Controlled Nuclear Fusion Research 1994 (Proc. 15th Int. Conf. Seville, 1994), Vol. 1, IAEA, Vienna (1995) 199.

[5] FUJITA, T., et al., IAEA-CN-64/A1-4, this volume.

[6] PERKINS, F., et al., in Plasma Physics and Controlled Nuclear Fusion Research 1994 (Proc. 15th Int. Conf. Seville, 1994), Vol. 2, IAEA, Vienna (1995) 477.

[7] ISHIDA, S., et al., Rev. Sci. Instrum. 61 (1990) 2834.

[8] ISHIDA, S., et al., Phys. Rev. Lett. 68 (1992) 1531.
[9] PARK, H.K., et al., in Plasma Physics and Controlled Nuclear Fusion Research 1994 (Proc. 15th Int. Conf. Seville, 1994), Vol. 2, IAEA, Vienna (1995) 3.
[10] KAMADA, Y., et al., ibid., Vol. 1, p. 651.

DISCUSSION

C. GORMEZANO: When comparing the respective performances of hot ion H modes and high β_p plasmas, what is the importance of lack of sawteeth as compared with high β_p and how could the hot ion H mode be improved?

S. ISHIDA: The lack of sawteeth is important for producing the enhanced core confinement associated with the internal transport barrier. The performance of the hot ion H mode could be improved by using intense central heating such as negative ion NBI instead of the present off-axis heating.

K. LACKNER: Other experiments ascribe the limitation of β to neoclassical tearing modes. Do you have any evidence (e.g. topology of perturbation, dependence on collisionality) in this direction?

S. ISHIDA: No, we do not observe any evidence of neoclassical tearing modes associated with the β limit. Since the time-scale of precursor oscillations and collapse is so fast, it is not the tearing modes that cause the β limit for the high performance discharges discussed here.

PERFORMANCE LIMITATIONS IN JET HOT ION H-MODES

JET TEAM[1]
(Presented by P.R. Thomas)

JET Joint Undertaking,
Abingdon, Oxfordshire,
United Kingdom

Abstract

PERFORMANCE LIMITATIONS IN JET HOT ION H-MODES.

Hot ion H-modes have produced the highest fusion yields in JET and will play an important role in future DT experiments. The high yield phase of these plasmas is transient and is terminated, usually irreversibly, by a deterioration of confinement associated with a variety of mhd activity. In this paper, the limiting phenomena are described, and the identification of the mhd modes is made. The connection between mhd and confinement deterioration is not entirely clear; several hypotheses are outlined but none has been confirmed unequivocally. The irreversibility is due to a combination of confinement degradation and density increase, which reduces central power deposition by neutral beams and couples the ion and electron temperatures. The prospects for reducing or removing the performance limitations are discussed.

1. INTRODUCTION

Hot ion H-modes, heated by high power neutral beams and supplemented in some cases by ICRF, have produced the highest fusion yields in JET [1] and will form a cornerstone of the forthcoming DT experiment, DTE1. However, the phase during which high fusion yield is obtained is short-lived and decays, usually irreversibly, to a lower level of performance after 1-2s. This performance deterioration is due to a fall in energy confinement which is associated with a variety of mhd activity. Developing an understanding of the processes which influence the observed behaviour is an essential element of the JET programme as they limit the peak fusion output and its duration. Also, these phenomena introduce variability in the fusion performance which is a concern for DTE1.

This paper will restrict itself to the hot ion H-mode because the reverse shear regime [2] is a relatively new development in JET and the study of the performance limitation mechanisms has only just commenced. Furthermore, disruptions and vertical displacement events either limit performance directly or constrain the operating space to the same effect but these are described elsewhere [3].

2. A DESCRIPTION OF THE PERFORMANCE LIMITATION

High power neutral beam heating is applied to a low recycling, low density divertor plasma. After a period of threshold ELMs, an ELM-free H-mode starts in which the energy, density and fusion power rise continuously until a terminating

[1] See Appendix to IAEA-CN-64/O1-4, this volume.

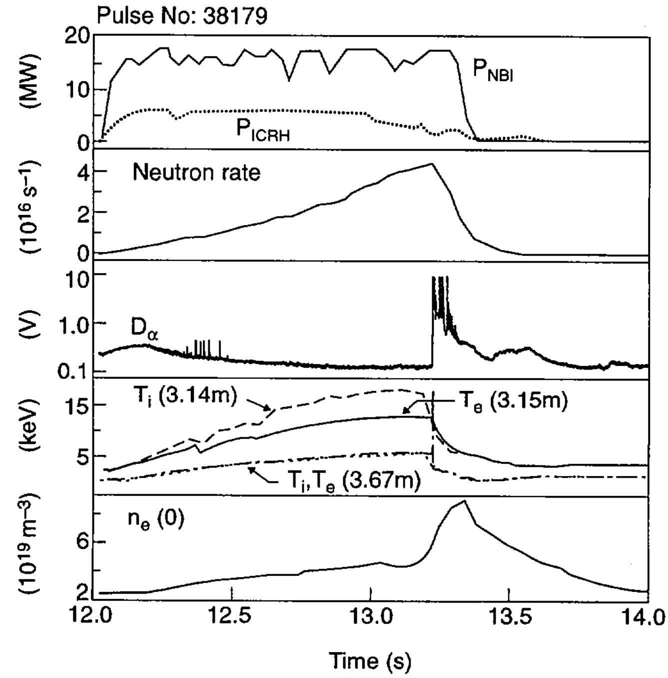

Fig.1 The time history of an hot ion H-mode, heated with NBI and ICRH, which terminates with an ELM. Shown are the heating powers, the neutron rate, the D_α rate, temperatures near the axis and half minor radius and, last, the central electron density.

event occurs, after which the confinement is degraded. Shortly before the terminating event, the plasmas are characterised by energy confinement up to 1.4 times ITERH93-P and central ion temperatures up to 30keV. During the ELM-free phase, the confinement barrier forms a very pronounced edge pedestal, particularly in the ion temperature, and a significant bootstrap current flows at or near to the separatrix. Pressure gradients approaching $1MPa.m^{-1}$ are found in the barrier region and have a profound effect on plasma stability.

The termination of the high performance phase is often triggered by a global MHD event such as an ELM or a sawtooth collapse plus ELM. Here and in the following, ELM is used unambiguously to mean type I [4] or giant ELMs. Many terminations do not show such global mhd but instead have low m/n activity close to the edge, dubbed "outer modes" [5]. The outer modes are associated with a reduction in confinement and a rapid fall in fusion rate.

The distribution between the various kinds of mhd is rather uniform. More than half the terminations involve two or more kinds of mhd instability together. The mhd do not always cause a termination but their ability to do so increases throughout the ELM-free phase. In view of this and the small amplitude of outer modes, compared with the resulting transport, it is supposed that the mhd is coupling to the underlying transport mechanism to trigger a change of state.

A termination which is triggered by an ELM is seen in Fig.1. The D_α spike at the ELM lasts tens to hundreds of ms and corresponds to ionisation of order of the plasma ion inventory: up to 10^{22} ionisations. This is reflected in an increase in plasma density, which can double in a few hundred ms. The outer half of the pressure profile is eaten away by the ELM, as illustrated in Fig.2, after which a cold wave propagates to the core and the central pressure starts to decline. The fusion rate falls because of the propagation of the cold wave to the core and the cooling due to the density increase.

A sawtooth, or other core mhd, becomes an effective cause of confinement limitation above β_N~1.5, or so, because a large proportion of the plasma cross-section is affected and strong coupling to ELMs and outer modes occurs. The core pressure collapses and the energy is distributed in the outer regions of the plasma column. When the core mhd triggers an ELM or outer mode, the decrement of the core energy is able to propagate through the outer regions of the plasma, with little or no change to the pressure or temperature profiles there. This implies that a plasma, in these conditions, must be able to support different levels of transport.

Outer modes are observed in the outer regions of the plasma; typically near the q=3 surface, as shown in Fig.2. Toroidal mode numbers 1-4 and poloidal mode numbers 3-12 are observed. Modes with n=1 typically have a frequency of around 10kHz. A noticable signature of the outer mode is a small, slow increase in the D_α emission which indicates a loss of confinement. As well as an immediate deterioration of core confinement, a cold pulse propagates into the plasma core over tens of ms and together cause the degradation of fusion performance. Evidently, the irreversible performance limitation due to an outer mode alone arises from the particle influxes which are rapidly transported inwards through the region affected by mhd. Note, however, that the plasma can recover from the effects of outer modes which occur early in the ELM-free period.

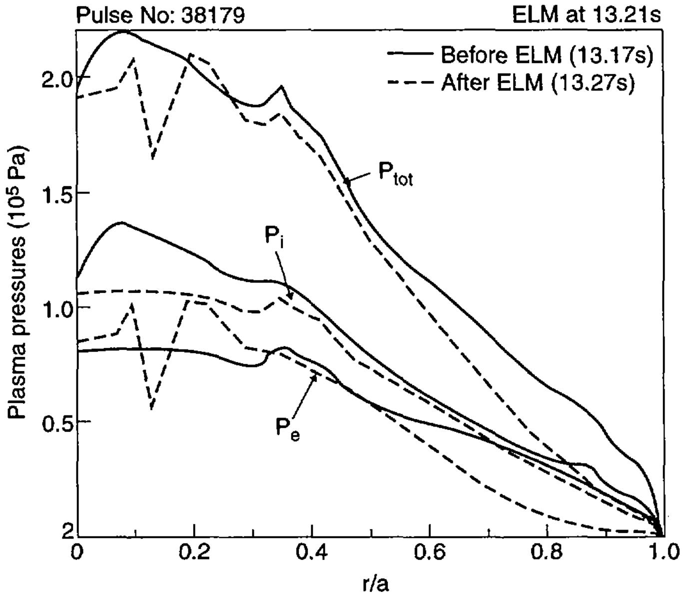

Fig.2: The pressure profiles before and after a terminating giant ELM. P_{tot}, P_i and P_e are the total, ion and electron pressures respectively. Note that the ELM has eaten away the outer half of the electron profile,in particular.

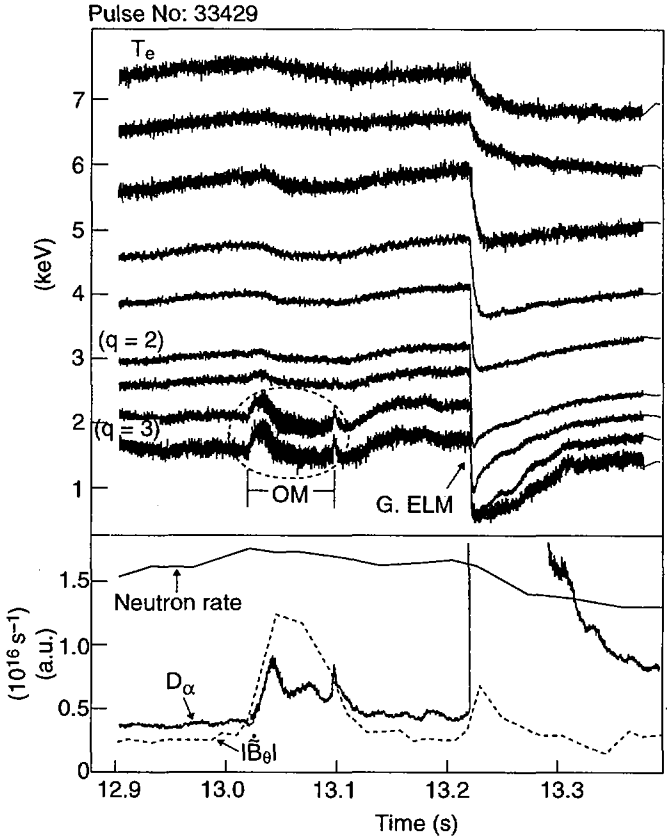

Fig.3 A plasma limited by an outer mode (OM) and a giant ELM (G.ELM). A range of electron temperature traces are shown from the axis to the plasma periphery, together with the neutron rate, D_α and magnetic pick-up coil signals.

Prior to the installation of the pumped divertor [6,7], the loss in confinement generated a heat pulse which caused a rise in target tile temperature and generated a carbon bloom. The resultant influx of impurities, coupled with the rise in core transport, prevented any recovery in performance and confused the analysis of the core behaviour. The improved design of the pumped divertor target has eliminated the carbon bloom. However, the link between the mhd instabilities and the loss of core confinement remains unclear and the resulting change in performance continues to be irreversible, for the reasons described above. Even without the carbon bloom, impurity influxes increase during the terminating mhd activity, as does the main plasma Z_{eff}. It seems that although impurities might contribute to the performance deterioration they are not fundamental to the observed behaviour.

Magnetic fluctuations, identified as TAE modes [8], are often observed during performance limitations ascribed to outer modes. It is found that their onset is coincident with the plasma density rising to the point where some of the slowing-down NB particles are resonant with $v_A/3$. Some improvement in the comparison between the measured neutron yield and that estimated from the profiles can be obtained if it is assumed that this resonance causes ejection of the fast ions. However, plasmas have been obtained where TAE modes should have been excited but which have good agreement between experimental and simulated neutron yields. Thus, definitive experiments and measurements will have to be devised before the role of TAEs in these plasmas can be clarified and the fast ion losses demonstrated.

3. MHD STABILITY ANALYSIS

The ideal mhd stability of the hot ion H-modes has been studied; both against low m,n kinks and ballooning modes. It is found that the edge pedestals are very important for determining mhd stability. The pressure gradient is such that, before the terminating events, it is close to or at the ballooning limit. The pressure gradient also drives a bootstrap current which is close enough to the separatrix surface to drive kink instability. This is illustrated in Fig.4 by plotting the trajectory of plasmas in the edge pressure gradient versus normalised edge current density space. The stable region is bound from above by the ballooning limit and on the right by kink instability. Different hot ion H-modes appear to limit at both boundaries and suffer ELMs where the boundaries meet. An important determinant of the trajectory is the recycling level or edge density; when these are high the ballooning boundary is encountered first.

Analysis, using the CASTOR code [9], shows that ideal external kinks with n=1-4 are linearly unstable when outer modes are present. The vessel wall in JET is too far from the plasma to have any significant stabilising effect. That outer modes are observed when instability is predicted and with n values from 1 to at least 4, encourages the identification of outer modes with saturated kinks.

The structure of outer modes, measured with the internal soft X-ray cameras, has been compared with the computed kink eigenmodes. This has been

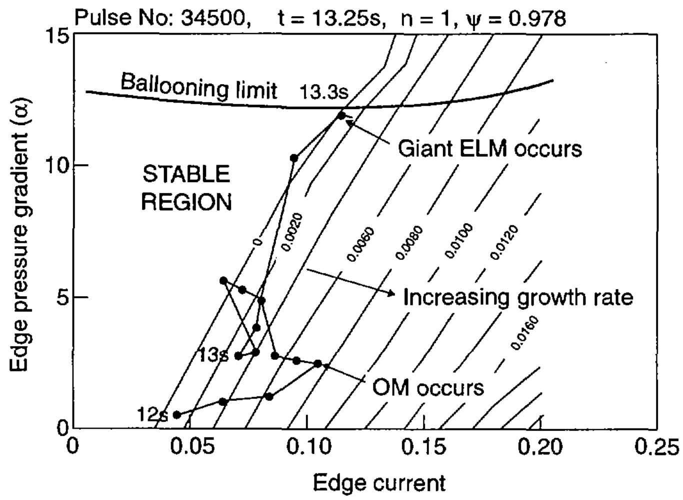

Fig.4 Edge stability diagram of normalised pressure gradient($=2\mu_0 Rq^2p'/B_T^2$) versus normalised edge current($=J_{edge}/J_0$). The lines to the right of the stable region are contours of the ideal kink growth rate. The trajectory of pulse 34500 (see Fig.7), which showed outer modes and ELMs can be seen.

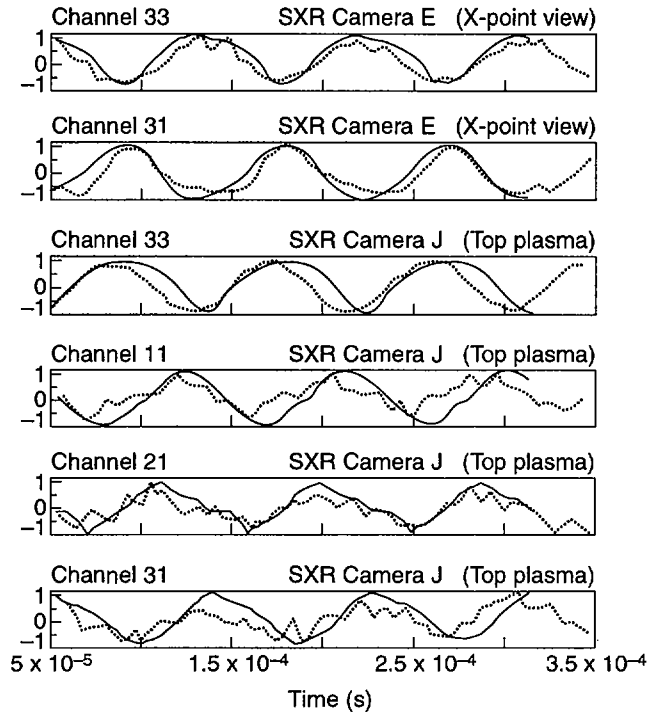

Fig.5 The comparison of the phases of a number of soft X-ray camera signals(·······) with the simulation described in the text(———). The top two panels are particularly significant for showing the 180° phase shift between adjacent channels, looking towards the X-point.

done by distorting the equilibrium soft X-ray emission profile by the kink displacements and recomputing the signal which should be seen in the individual detectors. The approach is suited to identifying kink modes because the concentration of lobes around the X-point and the top of the plasma leads to phase inversions in the fluctuations between adjacent detectors. This is in fact what is observed and the observed phases show excellent agreement with the kink mode simulations, as seen in Fig.5. The fluctuating amplitudes are in reasonable agreement. The predicted displacement amplification, of ~1.2cm in the midplane to ~15cm at the X-point, due to the poloidal flux expansion, is confirmed by the data.

Tearing modes have also been simulated and compared with the outer mode soft X-ray signals, using the same method. Extra structure appears in the simulated signals because of the phase inversion within the resonant surface. The data show no signs of this structure, so securing the identification of the outer mode with ideal kinks.

The β_N at which outer modes appear decreases with increasing plasma current and magnetic field, or equivalently decreasing collisionality. It has been suggested that this is indicative of the importance of neoclassical mhd. There is no evidence to support this conjecture; particularly in respect of the lack of β dependence in the strength of the observed modes and the lack of any signs of tearing. In fact, there is evidence that the fall-off in β_N is an effect of the transport processes operating in this plasma regime, as discussed later.

In discharges limited by an ELM, the edge pressure gradient, evaluated at the 95% flux surface, is at or close to the ideal ballooning limit. A range of different plasma conditions confirm this and the experimental dependence on shear and poloidal field strength correspond to theoretical expectations.

However, there is no direct experimental evidence for ballooning modes at or near the termination of hot ion H-modes in JET. The difficulty of detecting them is probably the determining factor here; not only is the current bandwidth of the data aquisition system smaller than is desirable for this purpose but the predicted unstable region is also in the low emissivity part of the plasma. However, the pressure profile has been observed to saturate at the ballooning limit for hundreds of ms before the terminating ELM, as seen in Fig.6. Whilst not definitive, this does indicate that ballooning modes are playing a role in ELM terminations.

Plasmas limited by ELMs are also predicted to be unstable to kinks. Soft X-ray cameras show precursors to many giant ELMs with the same characteristics as outer modes and lasting tens of ms. In these cases, the degradation of fusion power starts with the outer mode and is not greatly perturbed by the ELM. Given the identification described above, it is likely therefore that kinks are also observed in conjunction with ELMs.

It seems possible that the combination of ballooning and kink instability is needed for ELMs to occur; although it should be stressed that there is no evidence to support this and that there are ELMs with no detectable precursor activity. Nonetheless, the conjunction between predicted instability of both modes and their observation in conjunction with ELMs does seem compelling.

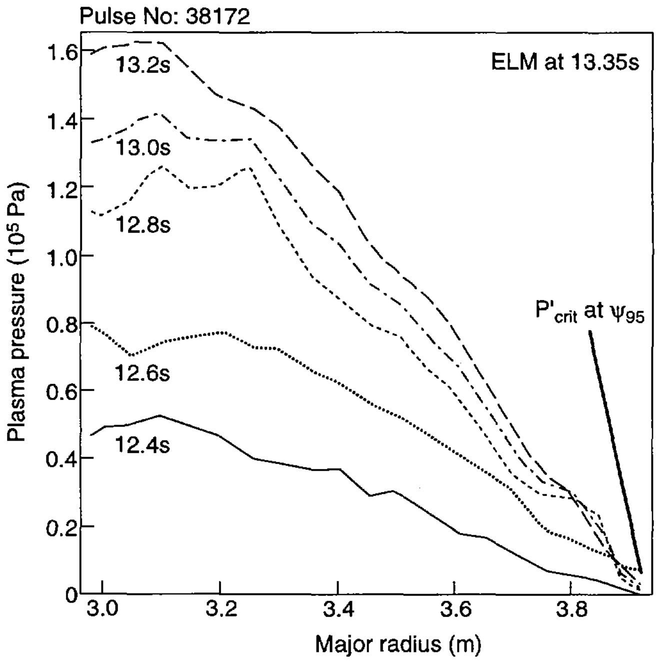

Fig.6 A sequence of pressure profiles, obtained from Thomson scattering and charge exchange recombination spectroscopy, for a pulse which had an ELM at 13.35s. Also shown is the critical pressure gradient for ideal ballooning at the 95% flux surface.

4. TRANSPORT EFFECTS DURING TERMINATION

The relationship between the observed mhd activity and the substantial drop in confinement which occurs is a persistent conundrum. The mhd activity is short lived, with timescales 100μs-100ms. However, the global energy confinement, which usually increases throughout the high performance phase, falls at the termination, by as much as a factor of three, and the neutron yield declines thereafter, usually irreversibly. The irreversibility is likely to be due both to the deteriorated confinement and the density increase, which results from ELMs particularly, preventing a rebuilding of central pressure and a separation of the ion and electron temperatures.

In cases with a core temperature collapse, the outer temperature and pressure profiles can recover to their pre-termination values. The core losses, which can amount to tens of MW, are transported through the outer region which had been transporting approximately 10MW. This increased heat transport where plasma conditions are unchanged is perhaps indicative of proximity to a turbulent threshold or of super-critical conditions, where a perturbation can trigger a return to degraded transport. Such behaviour is observed during the L-H transition and is the reason why simulations rely on core transport models which depend on edge conditions in order to reproduce the data.

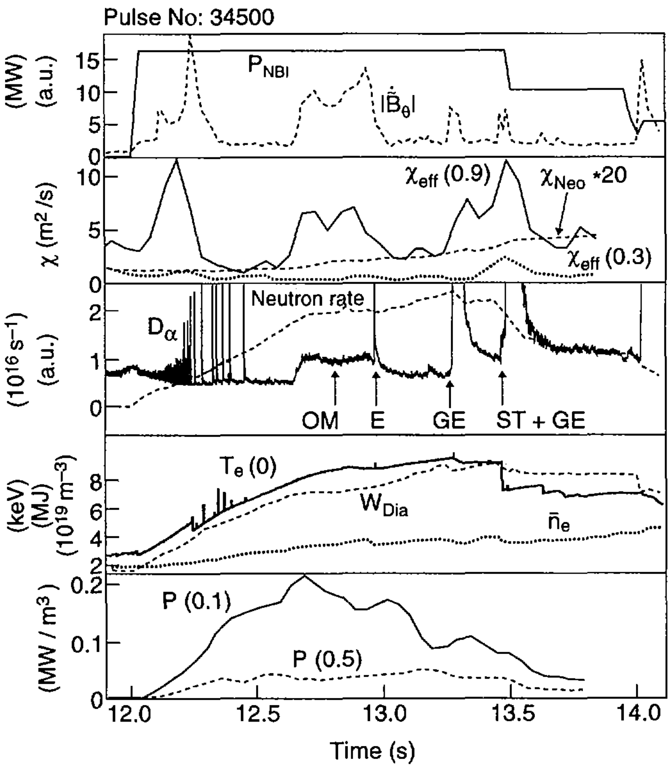

Fig.7 Time history for a pulse which has a range of limiting activity; an outer mode (OM), ELMs (E and GE) and sawtooth plus ELM (ST+GE). The effect on the effective plasma conductivity is shown in the second box.

It is clear that outer modes cannot directly cause the associated transport deterioration; there is no sign of tearing and their amplitude is, in any case, too small. Analysis of pulse 34500, shown in Fig.7, indicates that an outer mode increased the effective conductivity from 1.5 to $6m^2s^{-1}$ at the plasma edge. The analysis also shows the outer 25% of the plasma to be exhibiting transport enhanced to the level characteristic of ELMy H-modes. A typical amplitude of $|\delta B/B_\theta| \approx 2.10^{-4}$ would correspond to an island width of 0.025m, if tearing were occurring. In contrast, the island width needed to match the observed change in ion transport is estimated to be 0.2m, assuming ion-ion collisions and a step size equal to the island width. Thus, even were tearing detected, the resulting transport would be smaller than that observed by at least an order of magnitude.

ELMs have a similar effect on the effective conductivity to outer modes and act over the same outer part of the plasma cross-section. This might not be too surprising if an important component of the ELM is an outer mode.

A number of potential mechanisms for the link between mhd and transport have been investigated:

(i) That mhd induced changes in density profiles lead to poorer NB deposition has been shown to be insufficient of itself. Not only is the deposition profile being both calculated to be continuous across the mhd events but Beam Emission Spectroscopy, monitoring the profile of beam D_α, shows this as well. Thus, whilst there is a degradation of beam deposition from the start of heating to the time of peak performance, the sudden change in energy confinement at termination cannot be ascribed to a corresponding change of power deposition.

(ii) Loss of the confinement barrier alone is not sufficient to reproduce the observed behaviour. The sudden change in confinement at termination, or during an outer mode, clearly encompasses one quarter to one half of the outside of the plasma cross-section and is felt in the core as well.

(iii) ELMs generate as much ionisation in a few tens of ms as the plasma ion content. A hypothesis that the neutral cloud could penetrate to the core and so cause enhanced charge exchange losses there, is not borne out either by modelling or by experiments involving large gas puffs. In these experiments, a gas puff, of 100ms duration and magnitude to match the D_α spikes of terminations in similar pulses, was injected late in the ELM free phase of high performance plasmas. It was found that the edge cooled somewhat and that the cold pulse propagated to the plasma core on a timescale consistent with transport which was not degraded.

(iv) Transport models which connect edge conditions to core transport [10] give a satisfactory account of most termination events. Further evidence for these models is found in their ability to reproduce the gas puff experiments, described in the previous paragraph, and ability of laser ablation injection of impurities to cause changes in transport which propagate rapidly to the core. Also, the propagation of the L-H transition is reproduced. These observations encourage the belief that the transport mechanism is in some way extensive and that edge conditions are able to affect core transport.

(v) As described at the end of Section 2, magnetic activity, identified as TAE modes, is seen during fusion rate roll-over associated with outer modes. Unlike the other mechanisms, (i)-(iv), TAE modes would cause confinement degradation by reducing the input power density, rather than acting on the plasma losses. The TAE modes could be triggered by the outer mode induced density rise dropping the Alfvén velocity to match the resonance condition with the beam ions. Instability requires sufficient fast ion pressure gradient. It might be that this lies behind the variablity in the observation of shortfalls in fusion yield which could be ascribed to TAE modes and underwrites the need to verify that TAEs cause fast ion losses at all.

The data might be interpreted as showing that mhd can directly modulate the turbulence causing transport. Except for TAE modes, as described in (v) above, there do not seem to be any candidates for interactions of this kind. Since there is other evidence which indicates that the edge temperature can affect the core plasma transport, this seems the most natural mechanism for connecting mhd with the loss of confinement in the terminating events. Success in simulations encourages this view. However, unambiguous corroboration of this model is likely to be very difficult to obtain and will have to await further progress in understanding transport in general.

5. PERFORMANCE IMPROVEMENT

In principle, substantial improvements in fusion performance can be obtained by increasing the magnetic field at constant q. If it is assumed that the β limit is independent of field strength, the fusion yield should improve roughly as the fourth power of the field. For example, hot-ion H-modes at 1.7MA/1.5T are able to reach the Troyon limit and profile analysis shows that they approach 60% of the ballooning limit across the entire plasma, as seen in Fig.8(a). In contrast,

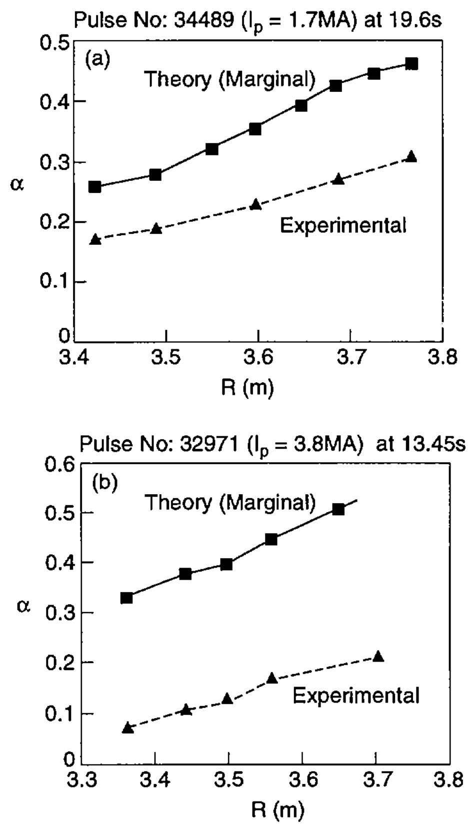

Fig.8 A comparison of the experimental profile of plasma pressure gradient compared with the ballooning threshold for (a) 1.7MA/1.5T and (b) 3.8MA/3.4T.

their 3.8MA/3.4T counterparts Fig.8(b) achieve only β_N~1.7 or so and are far from the ballooning limit, except in the outer region of the plasma. This seems to be a transport effect and modelling has been able to reproduce the difference.

The mixed Bohm/gyro-Bohm transport model, coupled to the neoclassical barrier model, has successfully simulated the 1.7MA and 3.8MA pulses. The termination of the high performance phase was represented by ideal ballooning and a limit on the edge bootstrap current, as a proportion of the plasma current, to reproduce the kink instability. It is a feature of the two components of the confinement model that the barrier improves more rapidly with magnetic field than the core confinement. Thus, in the 3.8MA pulses the ratio of the edge pressure gradient to that in the core is such that the mhd limits are encountered in the edge region long before the core. In contrast, the 1.7MA pulses limit more or less uniformly across the plasma cross-section. The density scale length in the barrier region has so far proven to be smaller than JET's diagnostics have been able to resolve. Thus it has not been possible to confirm the modelling results directly. However, the model edge pressure profiles are consistent with experiment, particularly in respect of the magnitude of the pedestal, so it is feasible that the relatively poor performance at high current is due to a transport effect. The only clear way forward is to increase the central power density at the start of the high power heating, in order that more energy is placed in the core before the heat wave arrives at the boundary and triggers the observed mhd instabilities.

Since the trigger appears to be mhd instability, it must be possible to ameliorate the behaviour, and so improve JET's fusion performance, by modification of pressure and current density profiles. A modest success in profile control has been achieved by ramping down the plasma current during the ELM-free phase. This has the effect of reducing the edge current density and so stabilising outer modes. Unfortunately, the other forms of mhd limitation replace the outer modes sooner or later and this technique does not offer any prospects for steady state!

6. CONCLUSIONS

The high performance phase of hot ion H-modes is terminated by a loss of confinement which appears to be triggered by mhd instabilities.

The mhd instabilities concerned are giant ELMs, sawteeth and outer modes, either individually or in combination. Theory and experiment are in quite good accord as to the identity and occurrence of the offending modes. The so-called outer modes have been identified as saturated low n/m external kink modes. Giant ELMs occur when the plasma is calculated to be unstable against kinks and ballooning modes simultaneously. Outer modes are observed as precursors to many ELMs. Ballooning modes have not been detected for these conditions but this is thought to be due to the diagnostic difficulty. However, the edge pressure gradient is observed to saturate at the ballooning limit for many hundreds of ms before some ELMs thus lending credence to their importance.

The most likely mechanism to connect the mhd instability with the loss of confinement is that which connects core transport with edge plasma conditions. Heuristic models based on this idea account for a range of phenomena observed in tokamaks, including the L-H transition, the propogation of cold waves following gas puffs or laser ablation impurity injection and, in combination with a neoclassical model for the barrier losses, the time delay to terminating ELMs. The detection of TAE modes during fusion rate roll-overs has led to the conjecture that the TAEs are ejecting slowing-down NB ions but this has not been proven.

If it is assumed that the mhd instability triggers the termination of the high performance phase, it should be possible to improve the fusion yield of these plasmas. However, the most destabilising features, the pressure pedestal and the resulting bootstrap current, are fundamental to the regime and amelioration might not be possible. Thus, the profile modifications which are most likely to succeed are those which peak up the core pressure relative to the pedestal: increased neutral beam power, to boost the core energy content before the heat pulse arrives at the confinement barrier; shear reversal to establish an internal confinement barrier and sawtooth suppression. All of these will be tried at JET in the near future.

REFERENCES

[1] JET TEAM (presented by P. Lomas), IAEA-CN-64/A1-1, this volume.
[2] JET TEAM (presented by C. Gormezano), IAEA-CN-64/A5-5, this volume.
[3] JET TEAM (presented by A. Tanga), IAEA-CN-64/AP1-18, this volume.
[4] ZOHM, H., et al., in Controlled Fusion and Plasma Physics (Proc. 19th Eur. Conf. Innsbruck, 1992), Vol. 16C, Part I, European Physical Society, Geneva (1992) 243.
[5] NAVE, F., et al., JET Rep. JET-P(96)14, submitted to Nucl. Fusion.
[6] JET TEAM (presented by G. Vlases), IAEA-CN-64/A4-1, this volume.
[7] JET TEAM (presented by J. Jacquinot), IAEA-CN-64/O1-4, this volume.
[8] JET TEAM (presented by D. Start), IAEA-CN-64/A2-6, this volume.
[9] HUYSMANS, G., GOEDBLOED, J., KERNER, W., Phys. Fluids B 5 (1993) 1545.
[10] JET TEAM (presented by A. Taroni), IAEA-CN-64/D3-3, these Proceedings, Vol. 2.

DISCUSSION

K.M. McGUIRE: The effects of the MHD events could be to increase the global hydrogen recycling for a short time, which could affect the global confinement. Have you looked at changes in recycling, especially from the inner wall? Your H_α arrays or H_α or C II cameras could provide some of these data.

P.R. THOMAS: Previous experiments showed a sensitivity to recycling. However, once the machine has been conditioned and the recycling has fallen to a low level, it is no longer particularly important. There is a very slight optimum level, though. We performed specific experiments to examine the effect of recycling on hot ion H modes by puffing gas into the ELM free phase. Interestingly, while the edge cooled and a cold wave propagated to the centre of the plasma, there was little discernible effect on confinement.

I.H. HUTCHINSON: You say that 'outer modes' are often precursors to giant ELMs. Can you say what determines whether an outer mode leads to an ELM or to a more gradual confinement degradation?

P.R. THOMAS: The short answer is no. The approach to the ballooning limit also seems to be a prerequisite for a giant ELM. Thus, we have formed a picture where ballooning modes saturate confinement and the fast growing outer mode is what trips the giant ELM. However, this is just speculation and so the short answer should stand.

M. KOTSCHENREUTHER: In your consideration of possible mechanisms to explain the degradation in core confinement due to ELMs, have you examined ITG modes? Marginality to ITG modes couples core temperatures strongly to the edge.

P.R. THOMAS: Yes, I agree. Any model coupling the edge conditions to the core confinement is a candidate for simulating the observations connected with the MHD events. If, for example, it does a good job on the propagation of the L–H transition, the ITG turbulence model should also be suitable.

FAST CURRENT SHUTDOWN SCENARIO FOR MAJOR DISRUPTION SOFTENING IN JT-60U

Y. KAWANO, R. YOSHINO, Y. NEYATANI, T. KONDOH,
N. ISEI, S. ISHIDA, K. TOBITA, T. HATAE, K. ITAMI,
A. SAKASAI, JT-60 TEAM
Naka Fusion Research Establishment,
Japan Atomic Energy Research Institute,
Naka-machi, Naka-gun, Ibaraki-ken,
Japan

Abstract

FAST CURRENT SHUTDOWN SCENARIO FOR MAJOR DISRUPTION SOFTENING IN JT-60U.

A fast current shutdown scenario using 'killer pellet' injection without generation of harmful runaway electrons is demonstrated. Enhanced 'burst'-like magnetic fluctuations induced by external helical magnetic fields can eliminate superthermal electrons created just after the killer pellet injection, which suppresses quick generation of runaway electrons with the current tail.

1. INTRODUCTION

The fast major disruption which terminates the plasma discharge is a serious issue in tokamak fusion reactors [1]. The release of plasma kinetic energy (thermal quench) causes severe damage of first wall materials, especially for divertor target plates. In addition, first wall materials can be irradiated by energetic runaway electrons (REs) generated and accelerated by the large one turn voltage spike during the current quench phase [2, 3]. To resolve these problems, softening [4] and avoiding [1] disruptions has been investigated in JT-60U, where vertical displacement events (VDEs) [5–8] were avoided by choosing the initial plasma central position as the neutral point [9, 10] and by controlling the height of the plasma centre during a current quench [9, 11].

To terminate discharges in order to avoid damage due to a disruption and for machine emergency cases, fast plasma shutdown has for the first time and satisfactorily been demonstrated by a disruptive termination through neon ice pellet injection ('killer pellet' injection (KPI)) in JT-60U [4]. The plasma discharge is terminated with a characteristic current decay time of about 10–30 ms; such a fast current decay does not cause any VDEs. The heat flux onto the divertor plates during the thermal quench phase is significantly reduced by enhanced radiation [12]. Energetic REs are, however, often generated during the discharge termination by the KPI, which must be avoided to establish the fast current shutdown scenario in ITER [13]. Recently, the magnetic fluctuation $n = 1$ mode has been found to play an essential role in suppressing the REs [12, 14].

In this paper, we present the suppression of REs by enhanced magnetic fluctuations induced by an external helical field.

2. EXPERIMENTAL SET-UP

The experiment is performed in the ohmically heated plasmas of the JT-60U tokamak, with a major radius of $R_p = 3.45$ m, a minor radius of $a_p = 1.05$ m, and an ellipticity of $\kappa = 1.38$. The parameters of the target plasma are: plasma current, $I_p = 1.7$ MA; toroidal magnetic field at the centre of the vacuum vessel, $B_t = 2.5$–3 T; safety factor at 95% of total flux, $q_{95} = 3.35$–4; line averaged electron density, $\bar{n}_e = (0.6$–$0.8) \times 10^{19}$ m^{-2}, and central electron temperature, $T_e(0) \approx 2$ keV. These relatively low density and high temperature values are preferred to shallow pellet deposition. A neon ice pellet (nominal size: diameter 4 mm × length 4 mm, actual size: 20–70% of the nominal size) is injected into the plasma as a 'killer pellet' with a velocity of 600–950 m/s, which results in a disruptive discharge termination with fast current quench. Figure 1 shows the dependence of the characteristic current decay time, $\tau_{I_p\text{-decay}}$, on the ratio between electron density increment and electron density, $\Delta n_eL/n_eL(0)$, for the cases of KPI and 'normal' disruptions. The increment in the electron density originates from the impurity influx into the plasma, neon influx for KPI and carbon influx for normal disruptions, where

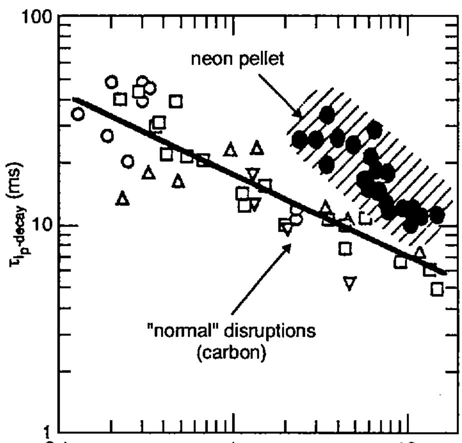

FIG. 1. Dependence of $\tau_{I_p\text{-decay}}$ on $\Delta n_eL/n_eL(0)$ for cases of the neon ice pellet (killer pellet injection (KPI)) injection and 'normal' disruptions, where $n_eL(0)$ is the electron line density just before the thermal quench, Δn_eL is the density increment up to the beginning of the current quench, $I_p(0)$ is the plasma current just before the thermal quench, and dI_p/dt (peak) is the maximum speed of the current quench. Data for 'normal' disruptions include various types of disruption caused by phenomena such as density limit, mode locking, peaked current profile (high l_i) and β_p collapse.

the carbon impurity is generated at the divertor carbon tiles by the large heat flux onto the divertor tiles during the thermal quench [15, 16]. Since these impurity influxes cool the plasma down by radiation, the plasma resistivity is increased by $T_e^{-3/2}$, which makes $\tau_{I_p\text{-decay}}$ small. Hence, smaller $\tau_{I_p\text{-decay}}$ (faster current quench) is observed at larger $\Delta n_eL/n_eL(0)$. The reason why $\tau_{I_p\text{-decay}}$ for KPI is larger than that for normal disruptions at the same $\Delta n_eL/n_eL(0)$, which indicates higher T_e for KPI, might be attributed to differences in impurity penetration into the plasma and radiation efficiency of the impurities.

The external helical field is provided by four sets of sector coils named DCWs (disruption control windings) [17]. DCW coils are installed both at the inboard and outboard sides of the vacuum vessel. When DCW coils are energized with a coil current of I_{DCW} = 15 kA, an additional radial field, B_{r_DCW}, of $\sim 4 \times 10^{-3}$ T at the plasma centre and of $\sim 2 \times 10^{-2}$ T at the plasma edge on the inboard side is produced. On the basis of the dominant toroidal coil number of 4, energized to produce B_r of opposite direction every 90°, DCW coils can produce an m/n = 3/2 magnetic field [18] with a radial magnetic field component of $\sim 7 \times 10^{-4}$ T at the plasma centre. Small magnetic fields of m/n = 4/3, 4/2 can also be produced.

For diagnostics, three interferometer chords (vertical × 2 and tangential × 1) are used for measuring the electron line density, n_eL [19, 20], and the ECE polychrometer is used for the electron temperature, T_e [21].

3. EXPERIMENTAL RESULTS

3.1. Disruptive discharge termination by neon ice pellet injection

Figure 2 shows the typical waveform of a disruptive termination generated by KPI. A neon ice pellet is injected at $t \approx 13.517$ s, which is identified by the increase in the n_eL signal. A delayed decrease of T_e at the minor radius of $r \approx 0.6a_p$ at $t \approx 13.519$ s and a further delayed drop of T_e at $r \approx 0.1a_p$ at $t \sim 13.523$ s are observed. After this first drop, T_e at $r \approx 0.1a_p$ is about 500 eV; such a high value of T_e indicates that the fraction of pellets deposited in the central plasma region is small. Thus, the pellets are deposited in the shallow plasma region. Afterwards, a thermal quench is observed at $t \approx 13.518$ s. The maximum heat flux onto the divertor plates at the thermal quench of $\sim$260 MW is significantly lower than that of $\sim$1 GW for normal density limit disruption. After the thermal quench, a positive current spike is observed; then, the current quench starts.

3.2. Generation of REs tail

Figure 3 shows a typical current quench followed by a current tail due to REs for an I_p/B_t = 1.7 MA/2.5 T discharge. The intensity of the hard X rays in the low energy range of E = 0–1 MeV indicates the presence of superthermal electrons [14].

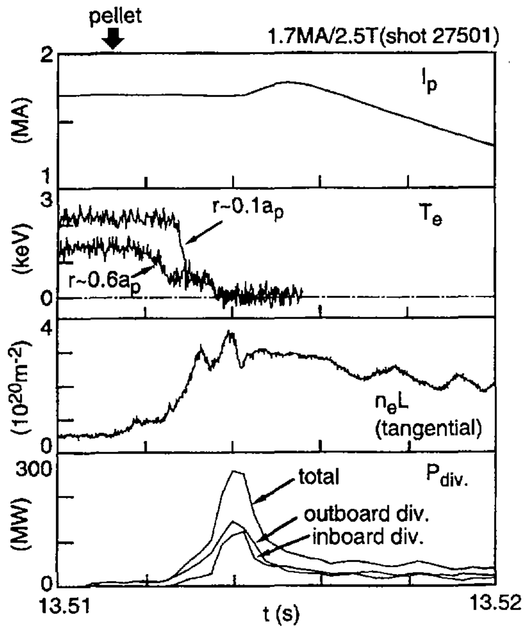

FIG. 2. Shallow pellet deposition for I_p/B_t = 1.7 MA/2.5 T, ohmically heated discharge.

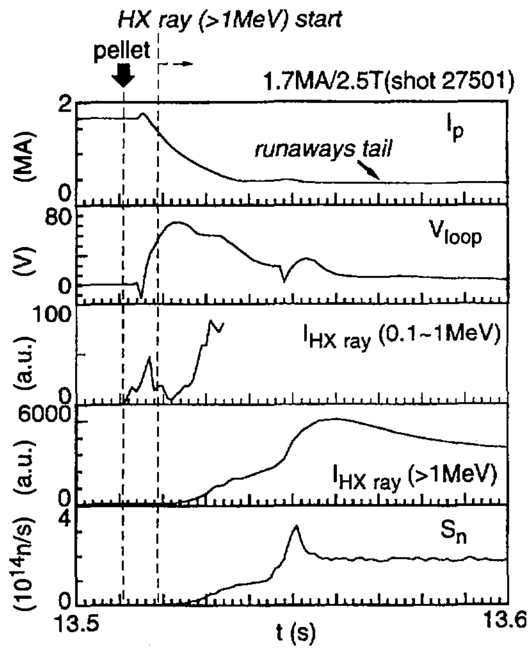

FIG. 3. Typical current tail due to runaway electrons (REs). The current tail (REs tail) is produced after the fast current quench (maximum $dI_p/dt \sim -87$ MA/s).

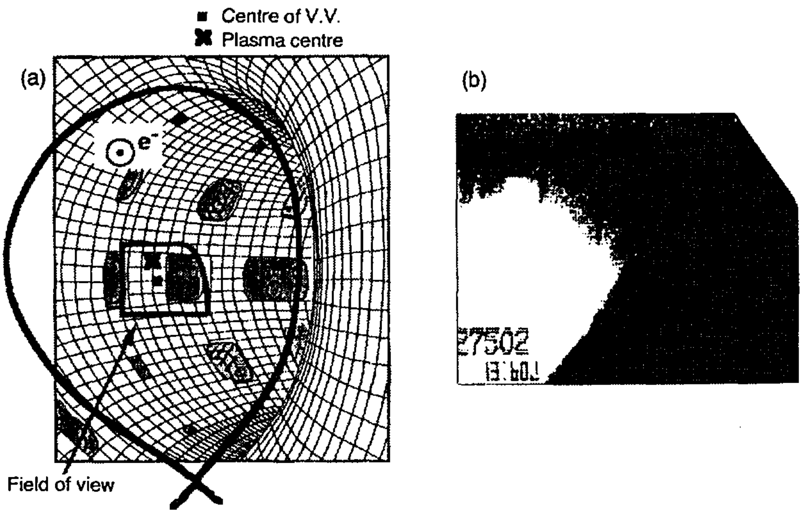

FIG. 4. Observation of infrared (IR) radiation (λ = 8–12 μm) when REs are generated: (a) field of view of a tangential viewing IR-TV camera, (b) IR image (white region) observed at the time of REs generation.

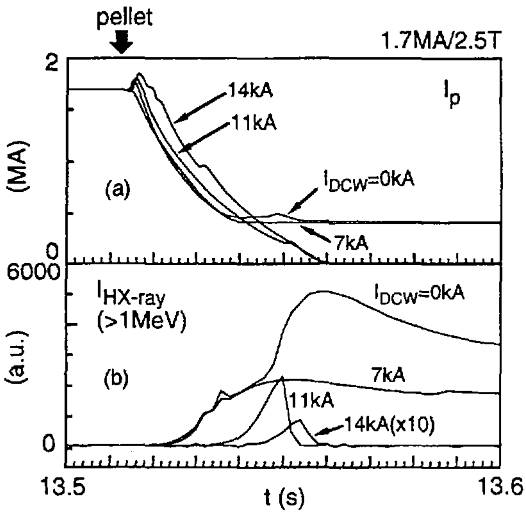

FIG. 5. Effect of energizing DCW coils on the eneration of REs: (a) REs tail suppressed for I_{DCW} = 11 kA and 14 kA; (b) generation of REs delayed by raising I_{DCW}.

Superthermal electrons are generated just after the KPI. Subsequently, they are accelerated to high energy REs, which can induce a harmful current tail (REs tail). The presence of high energy REs is identified by the hard X ray intensity at $E > 1$ MeV. The neutron emission signal due to the (γ–n) reaction at the carbon tiles indicates the production of REs with an energy of E > 26 MeV [22]. In this paper, the generation time of the REs is defined by the time when the hard X ray intensity at $E > 1$ MeV starts to increase. For measuring REs, a tangentially viewing IR-TV camera is also used to measure the infrared (IR) image in a wavelength range of 8 to 12 μm [23]. Figure 4 shows a typical IR image at the time of REs generation. The IR radiation is considered to originate from synchrotron radiation from REs as observed in TEXTOR [24].

3.3. Suppression of REs by DCW coils

By energizing the DCW coils, REs inducing the REs tail are successfully suppressed for discharges with I_p/B_t = 1.7 MA/2.5 T as is shown in Fig. 5. The DCW coils are energized ~500 ms before pellet injection. In the cases of I_{DCW} = 0 kA and 7 kA, a clear REs tail is produced. In contrast to the above mentioned results, no REs tail is observed for I_{DCW} = 11 kA and 14 kA. With the increase in I_{DCW}, the number of REs (hard X ray intensity) is strongly reduced. The generation time of REs is also significantly delayed, which results in a suppression of the REs tail. The maximum speed of the current quench is as fast as dI_p/dt = −90 MA/s to −130 MA/s, which is usually fast enough to produce an REs tail. Thus, we conclude that the DCW coils have successfully suppressed the generation of REs.

4. SUPPRESSION OF REs BY ENHANCED MAGNETIC FLUCTUATIONS

4.1. Waveforms with and without energizing DCW coils

The mechanism of suppressing REs is attributed to the enhancement of magnetic fluctuations obtained when energizing the DCW coils. Figure 6 shows typical waveforms with and without energizing the DCW coils. In the case without DCW (I_{DCW} = 0 kA), fast generation of REs is observed just after the current quench has started. In Fig. 6, the fluctuation of the poloidal magnetic field measured by a pick-up probe (dB_ω/dt at the divertor; 270°) and the absolute amplitude of the radial field fluctuation of the n = 1 component (dB_r/dt (n = 1)) measured by saddle loop coils are shown. Enhanced magnetic fluctuations are observed for I_{DCW} = 14 kA as is shown in Fig. 6(b). We found 'burst'-like fluctuations in the dB_ω/dt signal. The period where bursts prevail is termed 'burst phase'. The superthermal electrons generated just after KPI disappear during the burst phase. This means that the burst

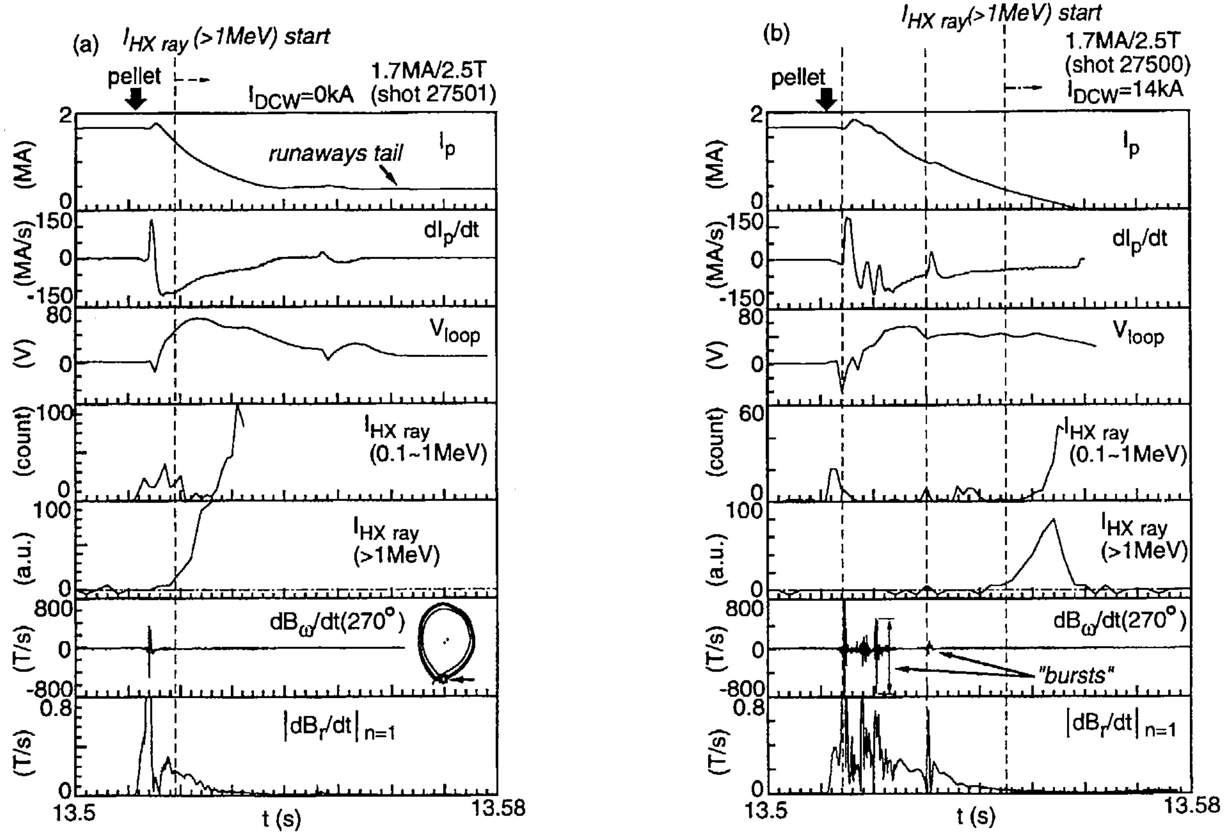

FIG. 6. Comparison between current quenches with and without REs tail: (a) Current quench with REs tail. Maximum $dI_p/dt \approx -123$ MA/s. (b) Current quench without REs tail. Maximum dI_p/dt is ≈ -160 MA/s. Enhanced magnetic fluctuations are observed in the poloidal field pick-up coils (dB_ω/dt) and saddle loop coils ($dB_r/dt(n = 1)$).

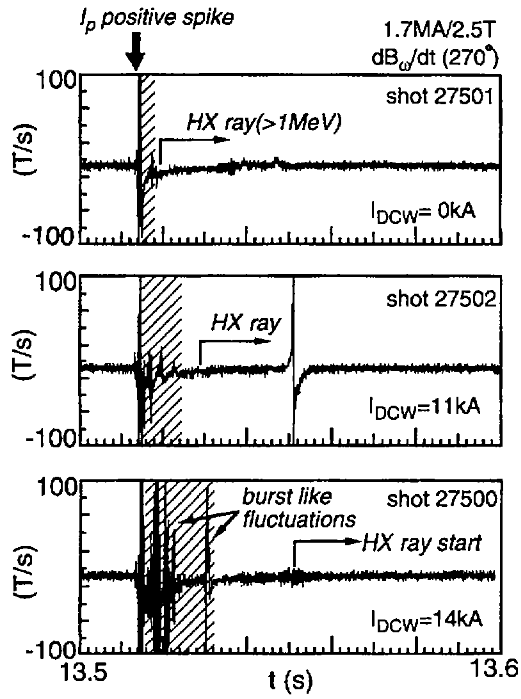

FIG. 7. 'Burst'-like magnetic fluctuations observed in pick-up coils. The duration of the burst phase becomes longer with rising I_{DCW}.

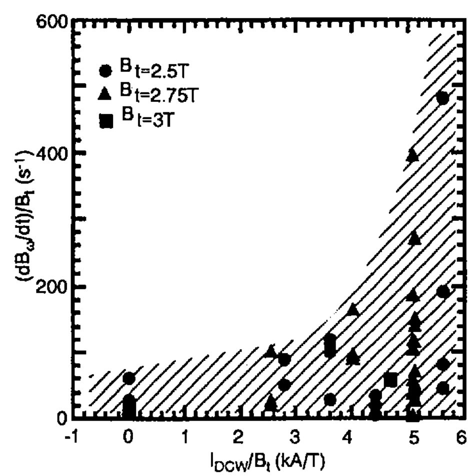

FIG. 8. Relationship between the amplitude of each burst and I_{DCW}. Both are normalized by B_t. The amplitude of the burst increases with increasing I_{DCW}.

can eliminate superthermal electrons. During the burst phase, the dB_t/dt (n = 1) signal is also enhanced, with a disturbed shape. After the end of the burst phase, dB_r/dt (n = 1) becomes quiescent and begins to decay gradually. Afterwards, REs generation is observed. We call this quiescent phase the 'burst free phase'.

4.2. Burst phase

The dominant mode at the burst is n = 0. Since a large burst is often accompanied by a positive current spike, a burst is a minor disruption. This burst is induced by energizing DCW coils as shown in Fig. 7 for discharges with I_p/B_t = 1.7 MA/2.5 T. In the case of I_{DCW} = 0 kA, few bursts are observed with fast generation of REs. On the other hand, many bursts are observed in the case of I_{DCW} = 11 kA. If I_{DCW} rises from 0 to 14 kA, the burst becomes more frequent, and the duration of the burst phase becomes longer. The amplitude of the individual burst is also enhanced with the increase in I_{DCW} as is shown in Fig. 8. Thus, it can be concluded that the burst is induced by energizing the DCW coils.

4.3. Burst-free phase

The presence of a magnetic mode structure during the current quench phase is supported by the 'snake' activity seen in line density signals where a periodic density fluctuation is observed in both line density signals viewing vertically at different minor radii. These fluctuations are out of phase with each other, which is characteristic for the 'snake'. Figure 9 shows a comparison of n = 1 mode and snake activities with and without energizing the DCW coils. In the case of I_{DCW} = 0 kA, few bursts are observed, and a snake is observed. The magnetic fluctuation intensity of the n = 1 mode is high but cannot suppress the fast generation of REs because of the high current quench rate. On the other hand, in the case of I_{DCW} = 14 kA, the snake is observed (the n = 1 mode is established) after the burst phase. The generation of REs is suppressed while the n = 1 mode amplitude is kept at a certain level. REs are observed during the later phase of the current quench after the n = 1 mode amplitude has decayed.

4.4. Regime of REs suppression and generation

According to former subsections, burst-like fluctuations and n = 1 mode activity can suppress REs generation. The regime of REs generation is shown in Fig. 10, with respect to the fluctuation amplitude normalized by B_t and the current quench speed. From Fig. 10(a), the fast generation of REs which can induce a current tail is plotted in the regime of a small burst with $(dB_\omega/dt)/B_t < 25\ s^{-1}$ and fast current quench with $dI_p/dt > -70$ MA/s. Although a delayed generation of REs is observed at low current quench speed in the late phase of current quench, the REs are not sufficient to produce the REs tail. In the burst free phase REs generation depends on the amplitude of the n = 1 mode as is shown in Fig. 10(b). Hence, it

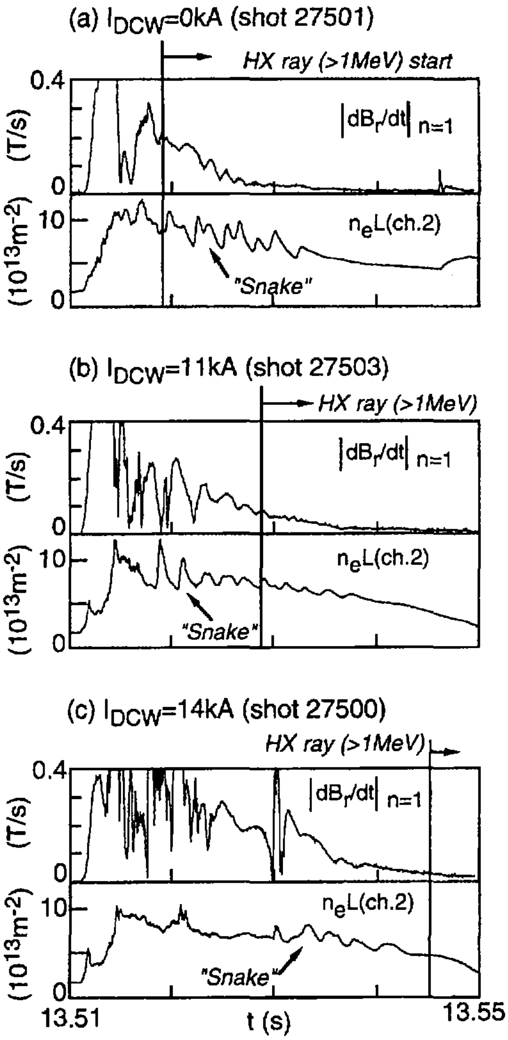

FIG. 9. n = 1 mode activity during current quench phase. The REs generation is identified where the saddle coil signal is quiescent and the fluctuation amplitude of the n = 1 mode becomes small.

can be concluded that (1) sufficient amplitude and duration of the burst phase during early current quench can suppress fast generation of REs, and (2) large magnetic fluctuation of the n = 1 mode can also suppress REs generation.

4.5. Role of magnetic fluctuation in REs generation

In these experiments, no effect of the DCW coils on REs suppression can be observed for B_t >2.75 T. For B_t = 2.5–2.75 T, REs generation is suppressed where B_{r_DCW}/B_t > 0.12–0.14% (at the plasma centre). In addition, REs generation cannot be observed without DCW coils for B_t < 2.27 T, where spontaneously enhanced magnetic fluctuations can suppress REs generation. These experimental results suggest that magnetic fluctuations at disruptive termination play an essential role in suppressing REs generation.

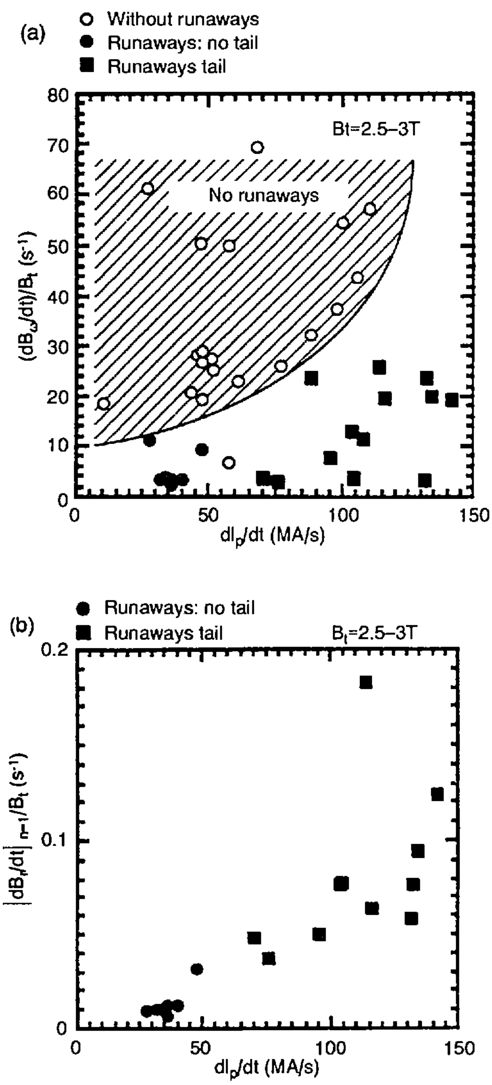

FIG. 10. Regimes of REs generation and suppression of the amplitudes of magnetic fluctuations and current quench speed. (a) Large amplitude of dB_ω/dt can suppress the generation of REs where dI_p/dt is fast enough (> ~ −70 MA/s) to produce an REs tail in ordinary low dB_ω/dt cases. (b) The onset of REs depends on the n = 1 mode amplitude in the burst-free phase.

5. SUMMARY

Suppression of harmful REs has been demonstrated at fast current shutdown enhancing magnetic fluctuations:

(1) The current quench speed is raised by the increase in the increment ratio of the electron density by neon ice pellet injection.
(2) The 'burst'-like magnetic fluctuation (n = 0) in B_ω/dt signals is enhanced by using the external helical field produced by four sets of sector coils (DCW coils).
(3) Superthermal electrons generated just after KPI can be eliminated by the burst, avoiding an REs tail.
(4) A large fluctuation amplitude of the n = 1 mode can also suppress REs generation.
(5) REs generation cannot be observed for $B_t < 2.5$ T, even without energizing the DCW coils, and REs suppression by DCW coils cannot be achieved for $B_t > 2.75$ T, which shows clearly that magnetic fluctuations by burst (minor disruption) and n = 1 mode play an essential role in suppressing REs generation.

Spontaneously enhanced magnetic fluctuations are always observed at disruptive termination, a fact that should be taken into account in assessing REs generation.

ACKNOWLEDGEMENTS

The authors wish to acknowledge the members of JAERI, who have contributed to the progress of the JT-60 projects, as well as to thank Drs S. Ide, T. Fujita, T. Fukuda, Y. Kamada, A. Morioka, Y. Kusama, N. Asakura and M. Seiki for useful discussions.

REFERENCES

[1] YOSHINO, R., et al., J. Plasma Fusion Res. **70** (1994) 1081.
[2] RUSSO, A.J., et al., Nucl. Fusion **33** (1993) 1305.
[3] JASPERS, R., et al., Nucl. Fusion **36** (1996) 367.
[4] YOSHINO, R., et al., in Plasma Physics and Controlled Nuclear Fusion Research 1994 (Proc. 15th Int. Conf. Seville, 1994), Vol. 1, IAEA, Vienna (1995) 685.
[5] GRUBER, O., et al., Plasma Phys. Control. Fusion **35** (1993) B191.
[6] NEYATANI, Y., et al., Fusion Technol. **28** (1995) 1634.
[7] NAKAMURA, Y., et al., Plasma Phys. Control. Fusion (in press).
[8] NAKAMURA, Y., et al., submitted to J. Plasma Fusion Res.
[9] YOSHINO, R., et al., Nucl. Fusion **36** (1996) 295.
[10] NAKAMURA, Y., et al., Nucl. Fusion **36** (1996) 643.
[11] YOSHINO, R., et al., Fusion Technol. (in press).
[12] YOSHINO, R., et al., submitted to Plasma Phys. Control. Fusion.
[13] ROSENBLUTH, M.N., IAEA-CN-64/FP-26, these Proceedings.
[14] KONDOH, T., et al., submitted to J. Plasma Fusion Res.

[15] WARD, D.J., et al., Nucl. Fusion **32** (1992) 1117.
[16] YOSHINO, R., J. Nucl. Mater. **220-222** (1995) 132.
[17] NINOMIYA, H., et al., Plasma Devices Oper. **1** (1990) 43.
[18] MIURA, S., Rep. JAERI-M-93-057, Japan Atomic Energy Research Inst., Tokyo (1993) 287.
[19] FUKUDA, T., Rev. Sci. Instrum. **60** (1989) 1080.
[20] KAWANO, Y., et al., Rev. Sci. Instrum. **67** (1996) 1520.
[21] ISHIDA, S., et al., Rev. Sci. Instrum. **61** (1990) 2834.
[22] JARVIS, O.N., et al., Nucl. Fusion **28** (1988) 1981.
[23] TOBITA, K., Rev. Sci. Instrum. **66** (1995) 594.
[24] FINKEN, K.H., et al., Nucl. Fusion **30** (1990) 859.

DISCUSSION

K. LACKNER: How would you expect to suppress runaways by a ramped-up magnetic field in ITER? Could you realize a passive helical current path in which the rapidly decaying plasma current itself would induce the required helical current?

Y. KAWANO: If magnetic fluctuations of sufficient amplitude are applied in the higher field of ITER, runaway generation is expected to be suppressed. There may be two ways to achieve this condition. The first one is to apply an external helical field. The error field correction coils in ITER could be used for this purpose. The second way is to utilize spontaneous magnetic fluctuations. The current profile just before pellet injection can be optimized to have large fluctuations for this purpose.

I.H. HUTCHINSON: Do the 'bursts' you see show evidence of being subsidiary disruptions, such as current profile relaxation and thermal quench?

Y. KAWANO: We consider that the bursts are strongly related to the 'minor disruptions' with current profile relaxation because they are often accompanied by a positive I_p spike but with no heat flux to the divertor.

I.H. HUTCHINSON: And what is the level of these effects necessary for runaway suppression?

Y. KAWANO: Runaway generation is suppressed at $(dB_\omega/dt)/B_t > 30\ s^{-1}$ for a current quench speed of $dI_p/dt \approx -100$ MA/s.

G.H. WOLF: You have used extremely low densities which per se show a tendency towards the development of runaways. Do you have results which show how the described phenomena vary with density, in particular with the densities to be expected in ITER?

Y. KAWANO: We have not performed the error field experiment in a higher density regime. However, according to the Dreicer process for runaway generation, it can be speculated that higher density is preferable for suppressing runaway generation at the same temperature.

MHD STABILITY AND DISRUPTION STUDIES IN ASDEX UPGRADE

O. GRUBER, M. MARASCHEK, G. PAUTASSO, H. ZOHM,
M. ALEXANDER, R.J. BUTTERY[1], J.C. FUCHS, S. GÜNTER,
T.C. HENDER[1], A. HERRMANN, T. KASS, K. LACKNER, P.T. LANG,
V. MERTENS, U. SEIDEL, S. SESNIC, M. SOKOLL, W. SUTTROP,
M. ULRICH, H.R. WILSON[1], Q. YU, ASDEX UPGRADE TEAM and
ASDEX ECRH, ICRH and NBI TEAMS
Max-Planck-Institut für Plasmaphysik,
Euratom-IPP Association,
Garching and Berlin, Germany

Abstract

MHD STABILITY AND DISRUPTION STUDIES IN ASDEX UPGRADE.

IN ASDEX Upgrade β is limited by coupled low (m,n) neoclassical tearing modes and β exhibits a maximum around $q_{95} \approx 3$ depending on current profile and shape. Stationary discharges in ELMy H-mode at the ITER target ($\beta_N \approx 2.5$, $q_{95} \approx 3$, $f_H \approx 1.85$) could be run. Density limit disruptions start with energy losses towards the boundary via coupled low (m,n) islands and lead to the final energy quench when the involved modes lock. During the final disruption toroidally asymmetric (peaking factor $\approx 1.6 \pm 0.5$) halo currents of up to 50% of the initial plasma current develop. Killer pellets help to reduce both the heat load on target plates during thermal and current quench phases (factor of 3) and the halo current and associated forces (factor of $\geq$2). Toroidal Alfvén waves are observed in ohmically heated plasmas without fast ions.

1) Introduction

The operational window of tokamak plasmas is limited in the safety factor q, density n_e and plasma pressure (ß) by the occurrence of MHD activity, which may lead to a disruptive limit. In this paper, we discuss the MHD limits, mainly the ß-limit, and the phenomena occurring prior to and during disruptions. The resulting heat and force loads during disruptions, including their asymmetries, and measures for disruption avoidance and mitigation will be described. Finally, the interaction of MHD modes and fast particles and the found characteristics of fishbones and toroidal Alfvén waves are described.

2) ß-limit studies

The need for high ß operation in ITER has prompted a series of ß-limit experiments in ASDEX Upgrade in ITER-like geometry (SN divertor configuration, $\kappa \approx 1.7 - 1.8$, $\langle\delta\rangle \approx 0.15$ at the separatrix, $I_p = 0.8 - 1$ MA, $B_t = 1.5 - 2$ T) to determine maximum

[1] UKAEA Government Division, Fusion, Culham, Abingdon, Oxfordshire OX14 3DB, UK.

ß-values as a function of q, to study the involved MHD modes and to explore the steady state operation at high ß [1]. In the following, ß is normalized to the Troyon-scaling, i.e. $\beta_N = \beta\,[\%] / (I\,[MA] / (a\,[m]\,B_t\,[T]))$.

A first series of experiments aimed at the determination of the maximum achievable $\beta_{N,max}$ as a function of q_{95}, the safety factor at the 95 % flux surface. In these discharges, the NBI power was ramped up until ß saturates or decays. All discharges exhibited type I ELMy H-mode confinement with $f_H = \tau_E / \tau_{ITER89P} \approx 1.85$ up to close to the ß-limit. The results of the q-scan are summarized in Fig. 1. As can be seen, $\beta_{N,max}$ exhibits a maximum of $\beta_N \approx 3$ at $q_{95} \approx 3$. Optimizing the shape by a slight increase of the triangularity up to $<\delta_{95}> \approx 0.22$ allowed even higher β_N limits. The significant decrease in $\beta_{N,max}$ at lower q_{95}-values is consistent with the interpretation in terms of the ideal ballooning limit, where, for fixed q(0), q_{95} limits the available shear. However, in the experiment, at the ß-limit also low (m,n) tearing modes such as (4,3) and (3,2) develop, leading to the actual ß-drop. These modes usually drive harmonics on the (1,1) surface, i.e. (3,3) and (2,2) modes respectively, that further deteriorate confinement once the ß-limit is reached. Fig. 2 shows an example of a coupled (3,2) and (2,2) structure as obtained from SXR tomography.

Ideal MHD stability calculations done with the ERATO code [2] predict stability up to $\beta_N \leq 4.1$ including wall stabilization and $\beta_N \leq 3.7$ if the wall is not taken into account. Thus, the resistive limit due to tearing modes is more stringent, as is expected from theoretical considerations. However, with more peaked current profiles, as are produced in current ramp-down experiments, we transiently achieve values of $\beta_N \approx 4.5$, limited by the same type of MHD activity. These experiments can be described by $\beta_{N,max} \approx 3.6\, l_i\, I_p / (a\, B_t)$. This is similar to results obtained in DIII-D [3].

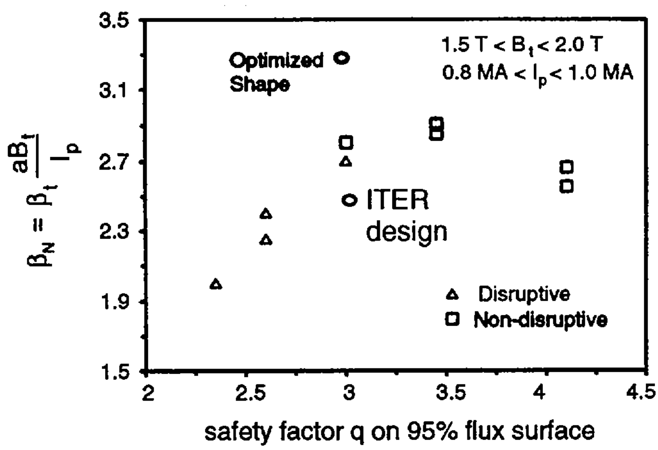

FIG. 1. Normalized ß as a function of q in ITER-like type I ELMy H-mode discharges.

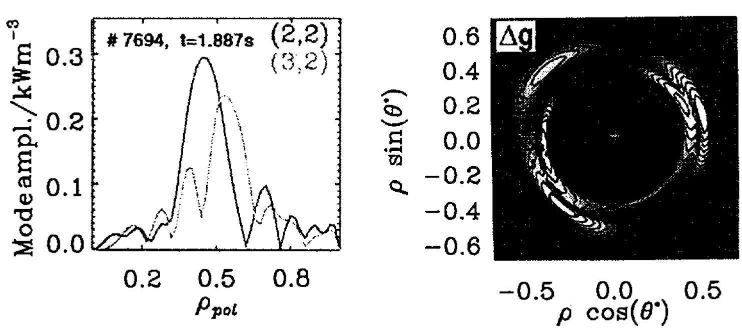

FIG. 2. Coupled (3,2) and (2,2) mode structure observed at the β-limit from SXR tomography: radial emissivity profiles of the two helicities (left, light line: (3,2); dark line: (2,2)) and emissivity (background subtracted) in straight field line coordinates (ρ is the poloidal flux surface coordinate).

There is strong evidence that the tearing modes observed in the experiment are of neoclassical origin, i.e. they grow nonlinearly due to the loss of bootstrap current in the islands: 1) δB increases linearly in time, whereas a Δ' driven mode should increase quadratically; 2) the estimated loss of bootstrap current due to the saturated (3/2) island of roughly 5 cm island width is just able to produce a magnetic island of that magnitude [4]; 3) more centrally located tearings such as the (4,3) mode usually are Δ' stable for the measured pressure and estimated current profiles; 4) the tearings are often triggered by ELMs and sawteeth, which would be consistent with the need of a "seed island"; 5) finally, our experimental data are in good agreement with the theory of diamagnetic stabilization of neoclassical tearing modes [5], explaining experiments with varying collisionality by taking into account the necessary seed island width.

For $q_{95} \leq 3$, the β-limit evolves into a disruption due to the persistence of the MHD modes even after the β-drop. It is found that at low q_{95}, the modes lock to the vessel wall and then, the disruptive sequence occurs on a slow timescale of several hundred milliseconds (loss of confinement → H-L transition → MARFE → current profile peaking and associated MHD activity → internal reconnections → disruption with thermal and current quench). No "hard" β-limit disruption, where β drops and the plasma disrupts within 10 ms, has been seen, contrary to TFTR [6].

For $q_{95} \geq 3$, the β-limit is generally not disruptive. In these cases, the tearing modes also persist after the β-drop, but they only lead to enhanced transport in the core and thus to a reduced confinement ("soft" β-limit). The difference to the low q cases is probably due to the different location of the resonant surfaces: although the modes lead to a substantial drop of toroidal rotation and therefore mode frequency, there is no mode locking at $q_{95} \geq 3$. In some cases, the β-limit is set by pure q=1 activity, namely a (1,1) mode and fishbones (see below), but increasing the heating power in these cases also leads to the occurrence of neoclassical tearing modes.

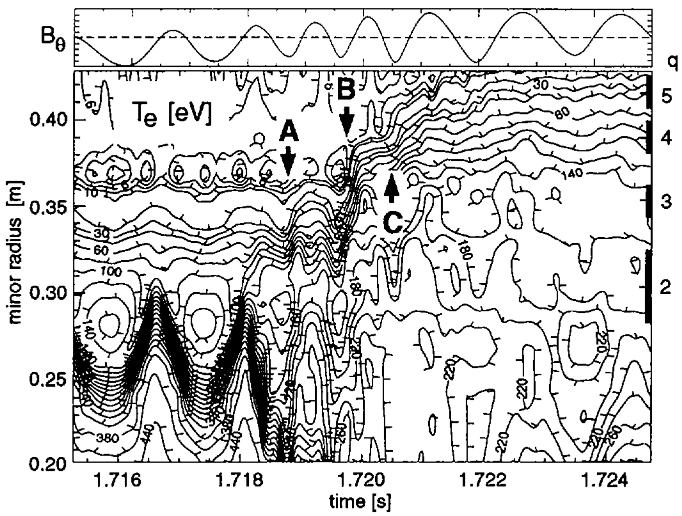

FIG. 3. Temporal evolution of magnetic islands during a minor disruption at high q_{95} = 6.5 (represented by isothermal lines measured by ECE radiometer).

As a second point of interest, steady state discharges at the ITER operation point of $\beta_N = 2.5$ and $q_{95} = 3$ were performed. Stationarity could be achieved for more than 3 s corresponding to 30 confinement times. However, sometimes even at these lower β_N values, MHD activity similar to the above described tearing modes may occur and lead to deteriorated confinement. These cases might need active control of the MHD behaviour, either via current profile control or by injecting ECCD/ECRH into the islands to suppress the nonlinear growth.

During the investigations of the ß-limit with necessary heating powers between 7.5 and 10 MW NBI deliberated $q \approx 3$ discharges with 2.5 MW NBI after the ß-limit phase exhibited a high confinement phase with $f_H \leq 2.5$ causing a strong density and ß increase. Estimations of the q = 1 radius from sawteeth inversion radius and (1,1) mode activity using soft XR diagnostics point towards a broad $q \approx 1$ region, which is already present during the ß-limit phase with its high MHD activity. A flat shear region could be a decisive ingredient of this high confinement plasma, therefore.

3) Mode behaviour near density limit

The maximum achievable density is limited by a typical sequence involving H-L transition, MARFE formation and subsequent MHD activity ending in the thermal and current quench (as decribed above). In high q discharges, the MHD activity may be initiated by radiative cooling of the m=3 island ('Rebut-mechanism'). Repetitive minor disruptions happen due to the coupling of (3,1) and (2,1) islands, which are identified by flat spots in the temperature profile located in the island O-points. Fast

ECE measurements ($\Delta r \approx 1$ cm, $\Delta t \approx 20$ µs) allow the following sequence of events to be documented (Fig. 3) [1]: At every minor disruption the thermal insulation between the islands breaks down (possibly by onset of stochastization) starting at the q=2 surface (time A) and continuing to the outer higher q surfaces (time B). Finally the outer plasma region is heated up and energy is lost across the separatrix (time C).

After this, the MARFE cools down the plasma edge again and the sequence restarts. Then the modes lock and the final energy quench takes place in two steps. The first one is connected with magnetic reconnection in the plasma interior, but with still insulating plasma edge, and the second one leads to very low temperatures initiating the current quench [1,7].

4) Heat and force loads during disruptions; toroidal asymmetries

In the vertically elongated ITER-like ASDEX-Upgrade plasmas disruptions are intimately linked with a vertical displacement event (VDE) which induces large poloidal halo currents and creates strong forces on structures [7, 8]. On the other hand, VDE's lead to a major disruption when shrinking of the plasma cross-section results in $q_{\psi 95} < 2.5$. The magnitudes of the associated halo currents and forces are generally higher in this scenario. All experimental results covering a wide range of operational scenarios are stored in a disruption data bank.

After installing further halo current measurements (shunts or Rogowski loops) at 6 toroidal sectors, which are properly distributed across all 16 sectors, the analysis showed that the maximal total halo currents $I_{h,max}$ (extrapolated from 6 sectors to the full torus) can reach up to 50% of the pre-disruption plasma current I_{po} (see Fig. 4).

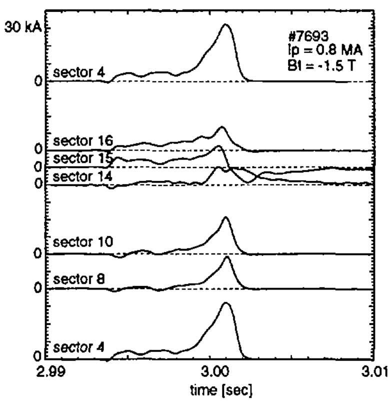

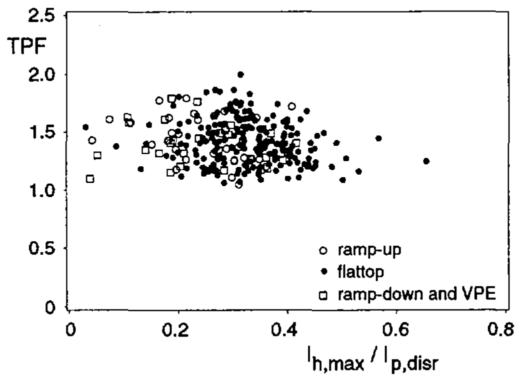

FIG. 4. Halo currents measured at six toroidal positions (left) and toroidal asymmetry versus normalized maximum halo current (right) of disruptions in the 1996 experimental campaign.

Poloidally resolved halo measurements reveal a rather broad halo current sheath (> 20 cm). The toroidal distribution of the halo currents indicates an n = 1 structure with a peaking factor TPF = $I_{h,sector}$ / $\langle I_{h,sector}\rangle$ of 1.6 ± 0.5, where $\langle I_{h,sector}\rangle$ is the toroidal average over the measurements in 6 sectors. Note that the currents in sectors 15 and 16 are only exact when summed up due to a partial short circuit. No correlation with the normalized halo current $I_{h,max}$ / I_{po} was found in agreement with results from other experiments except those from Alcator C-MOD [9]. Here, I_{po} is the pre-disruption plasma current, while I_p is used in this section for the actual current at the maximum halo current The toroidal asymmetry is fixed in position during one disruption, while the sector with the maximum halo current changes in different disruptions. At most 20% of the halo current is toroidally rotating in an n = 1 mode with a frequency of 1-2 kHz. Whether the origin of the observed toroidally asymmetric halo current is due to an m =1, n = 1 like tilting of the disrupting and vertically moving plasma remains an open question. For the experiments in the past, we are trying to determine the plasma current center at two opposite toroidal positions and to correlate it with the halo currents measured in 6 sectors.

The resulting forces on the vessel and passive stabilizing loop system (PSL) during the disruption are reduced both by the interaction of the eddies with the external poloidal field and by the inertial damping of the vessel and of its suspension rods. The second effect will be absent in ITER since the duration of the vertical movement and current decay should be comparable with the inertial time scale. In addition, this effect is presumably responsible for the strongly reduced toroidal asymmetry of the tension force on the 8 suspension rods of ≈ 1.15 as measured by strain gauges. The maxima of the halo current force ~ I_h B_t and the tension of the suspension rods are well correlated and scale with I_p I_{po} Δz, which is proportional to the destabilizing vertical force from the quadrupole moment of the poloidal magnetic field [7,8]. I_{po} stands for the not changing external poloidal field. This yields for the halo currents a scaling $I_h \sim I_{po} / q_{\psi 95}$ if similar plasma shapes and vertical shifts Δz are assumed.

Dumping of the plasma energy on the target plates is a further concern in disruptions. In disruptions without impurity injection we observe that up to 100% of the plasma thermal energy is deposited onto the divertor plates in a broad sheath of ≈ 25 cm within 1-2 ms (see Fig. 5). During the current quench still 30 % of the poloidal magnetic energy associated with the plasma current is conducted to the plates, while the major part is radiated as measured by a fast bolometer [7]. Over the whole diruption this load can amount to 30% of the total (thermal and magnetic) pre-disruption plasma energy. Strong neon puffing can reduce these numbers to 50% (of the energy during the thermal quench) and 10 % (of the thermal and magnetic energy over the whole disruption), respectively.

5) Disruption avoidance and mitigation

The extrapolation of our observations to ITER results in high heat loads and connected erosion problems during the thermal quench, and in severe forces during

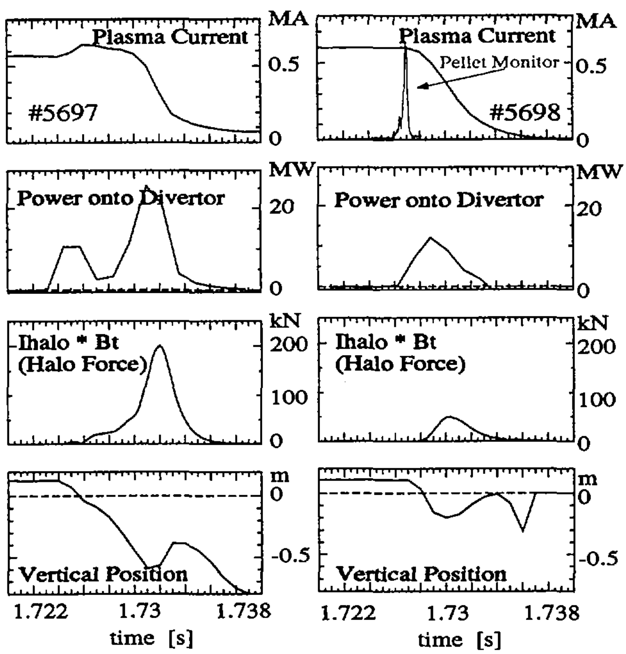

FIG. 5. Time history of current, target plate heat load, halo current force and vertical position for a density limit (left) and neon pellet induced disruption (right).

the current quench. Therefore, safety setups and disruption mitigation procedures are indispensable. A forced pulse termination acting near operational or technical machine limits by simultaneously decreasing the plasma current and its elongation is successfully used in ASDEX-Upgrade and reduces both halo currents and forces.

A strong mitigation was achieved by injection of neon pellets ($2 \cdot 10^{20}$ atoms, $v \approx 560$ m/s) penetrating up to the plasma core [10]; they immediatelly cooled down the plasma within < 1 ms and triggered the current quench. Fig. 5 compares a density limit disruption with a pellet-induced one in OH plasmas. After injection of the Ne pellet the energy flux to the divertor is fully suppressed during the thermal quench. Also during the following current quench the heat load is significantly reduced. Injection of a Ne pellet in a NBI heated plasma ($W_{th} \approx 500$ kJ) also led to a significant reduction of the heat load so that less than 12% of the total plasma energy were deposited on the target plates.

The maximal vertical forces on the vessel are considerably less (< 50% on the average) than during the flat-top disruption. This has to be attributed to the prompt decay of I_p (high resistivity caused by increased Z_{eff} and low T_e due to radiation cooling) and the associated smaller vertical plasma shift leading to a strong reduction of the induced eddies in the passive conductors and of the involved halo currents. Moreover, the TPF of the halo currents is diminished to values below 1.3.

In the pellet induced disruption shown in Fig. 5 no negative voltage spike and no accompanying positive current hump are observed indicating the absence of flattening of the current profile due to reconnecting tearing modes, which is otherwise observed. This is confirmed by Mirnov probe measurements showing no low (m,n) modes. The central deposition of impurities by the Ne pellet with the involved ionization losses may have caused a self-similar decay of plasma energy and current density profile without development of instabilities.

6) MHD modes and fast particles

Another area of growing interest is the interaction of MHD modes and a population of fast particles generated by additional heating such as NBI or ICRH. On ASDEX Upgrade, the fishbone instability and TAE modes (toroidicity induced Alfvén eigenmodes) have been studied in detail.

Fishbones are due to the interaction of trapped fast particles with the (1,1) internal mode. The destabilization of the (1,1) internal mode by the fast particles leads to a loss of the resonant particles through the mode itself, thus removing the driving term for the instability and resulting in a burst-like structure on the Mirnov signals ("fishbones"). The fast particle losses are manifested also by an enhanced flux of charge exchange neutrals and a decreasing neutron rate indicating a central loss. The fishbone mode has a toroidal frequency of 10 - 15 kHz (corresponding to the precession frequency of the trapped fast ions) and exhibits a strong $m = 1$, $n = 1$ mode structure with additional higher poloidal mode components. The mode is enhanced at the low field side near the midplane as the fast particles stay in this bad curvature region. In high-ß discharges fishbones have been identified as an ELM trigger [11].

An operational diagram characterizing the occurrence of fishbones in NBI heated ASDEX Upgrade discharges has been established, showing the occurrence of fishbones above a threshold for the driving term, the fast particle pressure, $\beta_{fast,th} \approx 0.009$ [11]. For given I_p and B_t, $\beta_{fast} \sim \beta_t / (1+\tau_E / \tau_{sd})$ is nearly independent of n_e and thus only a function of the temperature (τ_{sd} denotes the slowing down time of the fast ions). This was demonstrated in discharges with constant heating power but varying density: with higher density and lower temperature, fishbones were suppressed as β_{fast} became ≤ 0.009. Tis is in agreement with the fact that neutral beams with a more perpendicular injection preferentially lead to the occurrence of fishbones. At comparable heating power, these beams produce a higher population of trapped particles than the more tangentially injected beams.

Alfvén eigenmodes, namely TAE-modes, have been identified by their typical multi-mode spectra around 100 kHz as bursts on the magnetic fluctuation signals. The observed frequencies agree well with the resonance condition of the fast passing particle velocity with $v_A/3$, resulting in TAE mode frequencies $f_{TAE} = v_A / (4 \pi q R)$ with the local Alfvén velocity $v_A = B_t / (\mu_0 m_i n_e)^{0.5}$ on the resonant $q \approx 2.5 - 3.5$ surface. The dependence on plasma density n_e (as shown in Fig.6), magnetic field and the ion

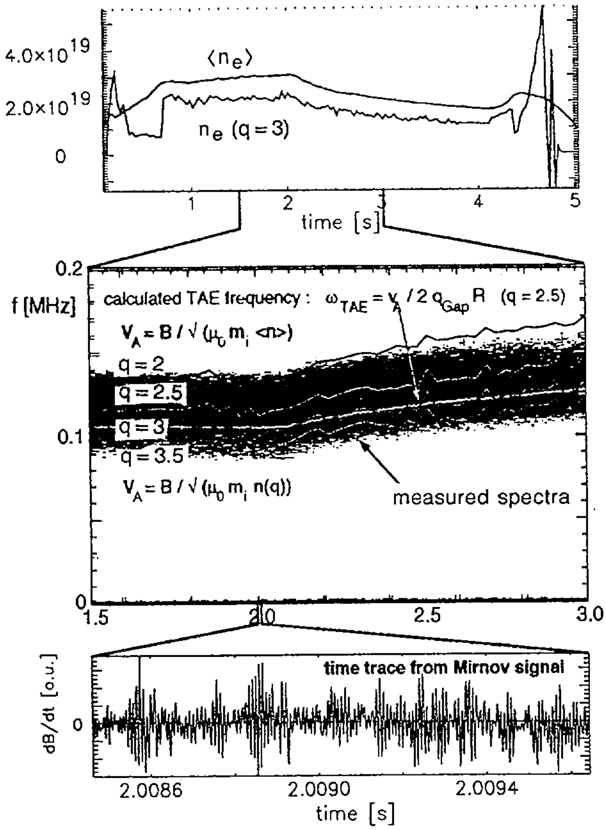

FIG. 6. TAEs in OH plasma: Mirnov signal (bottom) and variation of frequency spectrum (middle) with varying density (top). The mode frequency agrees with TAE frequency and local Alfvén velocity between $q \approx 2.5$ and 3.5.

species has been experimentally verified. The observed localization at the high field side of the plasma was confirmed by analysis of the soft-X-ray emission.

Surprisingly these modes could also be observed in a less "bursty" structure near the plasma edge, in purely ohmically heated discharges, where no fast ions are present. But there are strong indications that plasma edge turbulence has a strong electromagnetic contribution and drives drift Alvén waves at mode numbers $m \geq 30$ [12]. Those might be another driving force of TAE modes. The full mode structure of the observed TAE modes is still unresolved, but strong low mode numbers are present. The bridge between the different m numbers of edge turbulence and TAE modes, respectively, could be closed by inverse cascading in k-space.

REFERENCES

[1] ZOHM, H., et al., Plasma Phys. Control. Fusion **37** (1995) A313.
[2] LÜTJENS, H., et al., Comput. Phys. Commun. **69** (1992) 287.
[3] LAO, L.L., et al., in Plasma Physics and Controlled Nuclear Fusion Research 1992 (Proc. 14th Int. Conf. Würzburg, 1992), Vol. 1, IAEA, Vienna (1993) 565.
[4] ZOHM, H., et al., in Controlled Fusion and Plasma Physics (Proc. 23rd Eur. Conf. Kiev, 1996), Vol. 20C, European Physical Society, Geneva (1996).
[5] WILSON, H., et al., Plasma Phys. Control. Fusion **38** (1996) A149.
[6] FREDRICKSON, E., et al., Phys. Plasmas **2** (1995) 4216.
[7] GRUBER, O., et al., in Plasma Physics and Controlled Nuclear Fusion Research 1994 (Proc. 15th Int. Conf. Seville, 1994), Vol. 1, IAEA Vienna (1995) 675.
[8] GRUBER, O., et al., Plasma Phys. Control. Fusion **35** (1993) 191.
[9] WESLEY, J., et al., IAEA-CN-64/FP-25, these Proceedings, Vol. 2.
[10] PAUTASSO, G., et al., Nucl. Fusion **36** (1996) 1291.
[11] KASS, T., et al., in Controlled Fusion and Plasma Physics (Proc. 23rd Eur. Conf. Kiev, 1996), Vol. 20C, European Physical Society, Geneva (1996).
[12] SCOTT, B., et al., IAEA-CN-64/DP-18, these Proceedings, Vol. 2.

DISCUSSION

R.J. GOLDSTON: I think it is dangerous to estimate I_{halo} by balancing $I_{halo}B_T \propto nI_p^2\Delta z$. In fact, $I_{halo}B_T$ can largely balance the force due to the eddy current driven by dI_p/dt, which is frequently seen in the literature. One can either be overly assured in cases with low n, or overly frightened of high n.

DIVERTOR EXPERIMENTS

(Session A4)

Chairperson

M. SHIMADA
Japan

EFFECT OF DIVERTOR CONFIGURATION ON PLASMA PERFORMANCE IN JET

JET TEAM[1]
(Presented by G.C. Vlases)

JET Joint Undertaking,
Abingdon, Oxfordshire,
United Kingdom

Abstract

EFFECT OF DIVERTOR CONFIGURATION ON PLASMA PERFORMANCE IN JET.

JET has been operating with a new divertor, Mk IIA, since April 1996. Mk IIA is geometrically more closed than Mk I and has better power handling capacity. Pumping performance is improved, and access to high recycling and detached regimes is facilitated. Quasi-steady ELMy H-modes with $H_{89} \sim 2.0$ are produced with moderate gas puffing. The Type I ELM frequency depends primarily on triangularity and the gas puff rate at fixed power, and not strongly on target orientation or divertor magnetic flux expansion. The stored energy loss per ELM decreases with increasing frequency, but can only be reduced below 4% by strong gas puffing, with loss of confinement quality. Highly radiating, detached divertor plasmas can be produced by impurity seeding, but at the expense of confinement degradation and increased Z_{eff} (similar to Mk I results).

1. INTRODUCTION

The JET divertor programme is designed to investigate the effect of divertor geometry on plasma performance in a series of progressively more closed configurations. The programme began with Mark I (1994 - 1995, Fig.1a), presently uses a somewhat more closed divertor (Mark IIA, 1996-1997, Fig.1b), and will conclude with an ITER-specific "Gas Box" configuration (Mark II GB, 1997-1998). In addition to examining the effects of the geometrical positioning of various divertor components, the programme explores the effect of target orientation, X-point height, and flux expansion. Each of the divertors uses a cryopump with a nominal pumping speed of 240 m^3s^{-1}.

The term "closure" in this context refers to the degree to which neutrals recyling from the target plates escape from the divertor region. Closure depends on the divertor plasma temperature, density, and equilibrium geometry as well as on the geometry of the divertor components. In general, a "geometrically closed" divertor will have a larger effect on closure in the low recycling and detached plasma limits, where the ionisation mean free path becomes larger, than in the intermediate high recycling regime. The reasons for increasing closure are (a) to provide easier access to the regime of high volumetric losses in the divertor, thus reducing the target heat loading, (b) to reduce the neutral density in the main chamber, which improves main plasma confinement quality and reduces sputtering of impurities, and (c) to increase neutral pressure in the divertor chamber, thus facilitating pumping. At the same time, improved closure generally leads to reduced flow in the scrape-off-layer (SOL), which results in poorer flushing out of impurities and ash from the main chamber; this can be partly offset by increased pumping. The problem of choosing the correct geometrical closure for a divertor which must operate with Type I ELMs is particularly

[1] See Appendix to IAEA-CN-64/O1-4, this volume.

difficult because of the great disparity in effective SOL width between and during ELMs. Finally, closure does not prevent the escape of ionized impurities from the divertor region, as they are driven up the field lines by the parallel ion temperature gradient, and are only retained in regions of high SOL flow. Thus, improved closure, per se, will not generally improve impurity retention for seeded divertors.

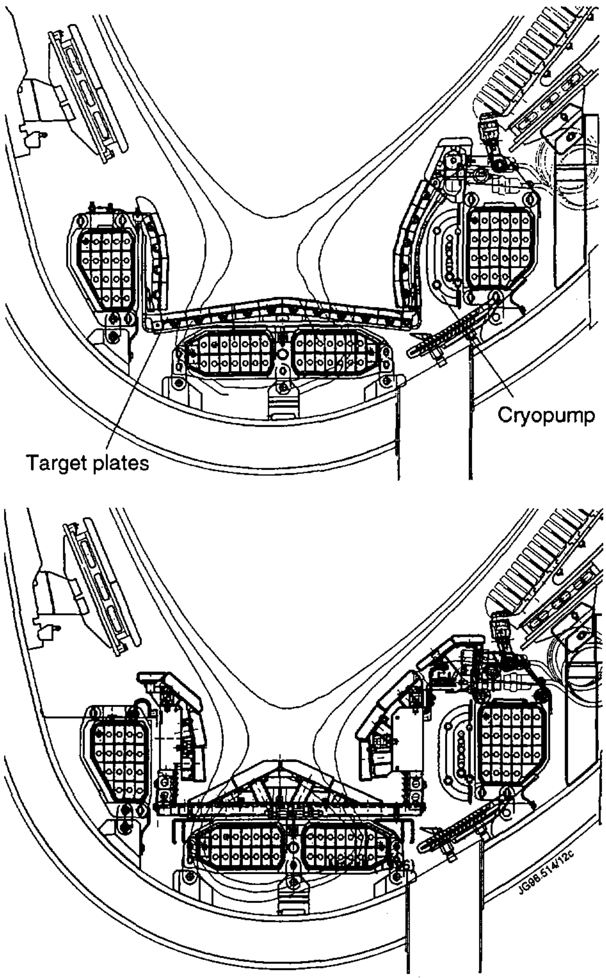

Fig.1 Poloidal cross sectional view of Mark I (top) and Mark II A (bottom).

Much attention was given in the JET Mk I campaign to the study of highly detached, highly radiating seeded divertor plasmas, where it was found possible to reduce the heat flow to the targets to very low levels. However, the confinement quality (H_{89}) was low and Z_{eff} was relatively high at high radiated power fractions with fully detached divertor plasmas [1]. Similar results have been found in other tokamaks [2-4]. Thus the use of this operating scenario for ITER is perceived to be difficult. On the other hand, it has been suggested that time-averaged power loading in ITER operating with divertor plasmas detached only near the separatrix strike points (semi-detached) and Type I ELMy H-modes, which improves confinement and Z_{eff}, may prove to be satisfactory [5]. In this scenario, the interaction of the Type I ELMs with the target becomes the main concern for the divertor design. In the Mk IIA campaign the study of seeded, radiating divertors has continued, but heavy emphasis has also been placed on the investigation of Type I ELMy H-mode discharges, and the effect of divertor configuration on them.

2. GLOBAL COMPARISON OF MK I AND MK II A

In this section the relative performance of Mk I and Mk IIA is discussed with respect to the principal divertor performance criteria: power handling capacity, approach to detachment, pumping effectiveness, and control of impurities. Mk IIA has a much larger wetted area than Mk I due to the use of large tiles and inclined target plates, and was predicted to have power handling capacity in the non-swept mode 2 - 5 times greater than that of (unswept) Mk I, depending on equilibria used. Infrared measurements of tile temperature show that Mk IIA has exceeded its design goals, and that the overheating of the tiles is not encountered in any normal JET operating scenario.

Increasing divertor geometrical closure should result in access to the high recycling-detachment regime at lower main plasma densities for a fixed power input. Figure 2 shows Langmuir probe measurements of the degree of detachment, defined as midplane SOL electron pressure divided by twice the measured divertor electron pressure [6], for equivalent L-mode density ramp discharges in the two divertors. It is seen that detachment begins at a lower density in Mk IIA than in Mk I, as expected. The "Super Fat" Mk IIA configuration has reduced divertor flux expansion and thus greater leakage than the "Standard Fat", while the HFE of Mk I is even more open. Each of these pulses ended in a density limit disruption, and the density attained decreased as the degree of closure increased. It appears that in general the "detachment window" between onset of

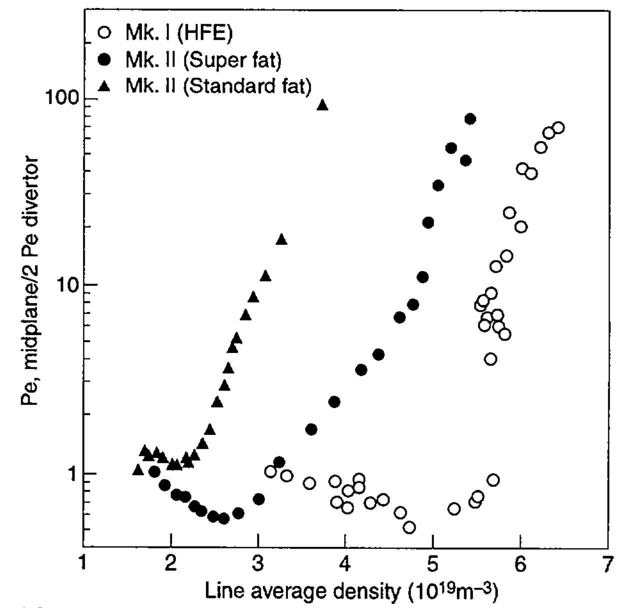

Fig.2 Degree of detachment vs. line averaged density for 3 MW L-mode discharges in Mk I and Mk IIA, showing the effect of increasing closure on the onset of detachment and the density limit.

I_{sat} rollover and disruption is smaller in Mk IIA than in Mk I for ohmic and low power L-mode pulses. (The density limit in H-mode operation is not disruptive and lies near the Greenwald limit in both divertors [7]).

The rate of pumping in Mk IIA is generally higher than in Mk I for equivalent Ohmic [8], L-mode, and ELM-free H-mode discharges, and is less sensitive to strike point position. EDGE2D/NIMBUS simulations indicate that Mk IIA is functioning as a moderate slot divertor and trapping the neutrals near the pumping ports in the lower corners.

Figure 3 shows measured Z_{eff} for Mk I and Mk IIA ELMy H-mode pulses as a function of volume averaged density, and indicates that they are quite comparable. The same statement can be made about the radiated power fraction and main plasma carbon densities. Carbon is the predominant impurity, with beryllium the next largest contributor. Improved closure in Mk IIA should lead to reduced intrinsic impurity content, if most of the sputtering is caused by neutrals originating at the target plates, rather than by direct interaction of plasma with the main chamber walls. The lack of improvement is believed to be due, at least in part, to bypass leakage of neutrals out of the divertor region, which has been increased by the higher divertor neutral pressure. The bypass leaks will be reduced by about 80% during a shutdown in October 1996.

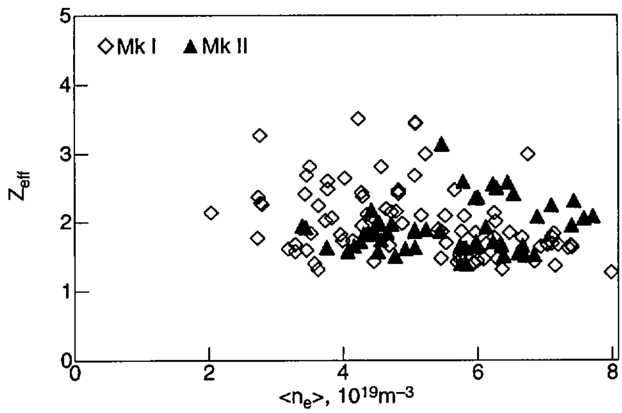

Fig.3 Measured values of Z_{eff} in Mk I and Mk IIA vs $<n_e>$ for Type I ELMy H-mode pulses with total power input ≥ 12 MW.

3. CONFIGURATIONAL EFFECTS ON STEADY STATE ELMY H-MODE DISCHARGES IN MK IIA

3.1 Discharges with beam fuelling only

In order to isolate the effects arising from configurational changes, a series of discharges was carried out with fixed plasma current, magnetic field, and neutral beam power (2.5 MA, 2.5 T, and 12 MW, respectively), in which the target orientation, flux expansion (horizontal target only), and main plasma triangularity were varied. Equilibrium reconstructions (EFIT) of the poloidal flux surfaces in the divertor region are illustrated in Fig.4 for the low triangularity cases. The high triangularity equilibria are nearly identical in the divertor, but differ in the main plasma. It was found that these discharges reached nearly steady state conditions within about 3 seconds of applying the beam power, and that this state was characterized by regularly spaced Type I ELMs. The ELM frequency depends most strongly on triangularity, without reproducible

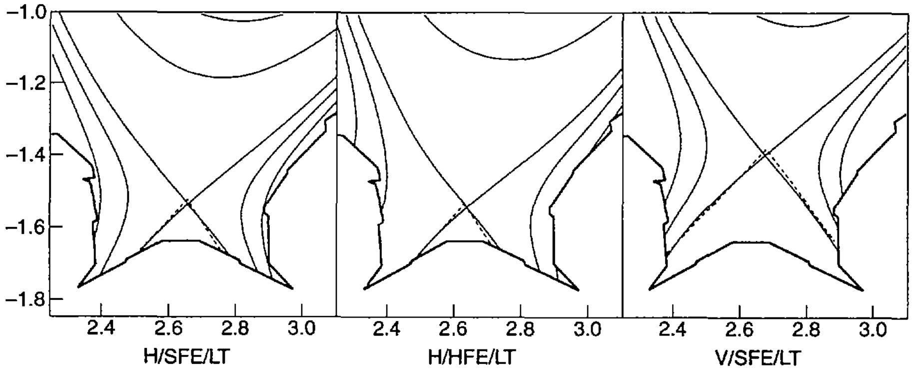

Fig.4 EFIT reconstructions of horizontal standard flux expansion, horizontal high flux expansion, and vertical standard flux expansion equilibria used in the configuration experiments. Flux surfaces shown are 1 and 2 cm distant from the separatrix at the outer midplane.

dependencies on target orientation or flux expansion, as shown in Fig.5. Although the ELM frequency f_E varies by a factor of about 6 for these pulses, the confinement quality, as measured by H_{89}, was independent of both f_E and configuration, as shown in Fig.6. However, the "natural density" at which these beam-fuelled discharges run decreases with increasing f_E. Z_{eff} also drops as f_E

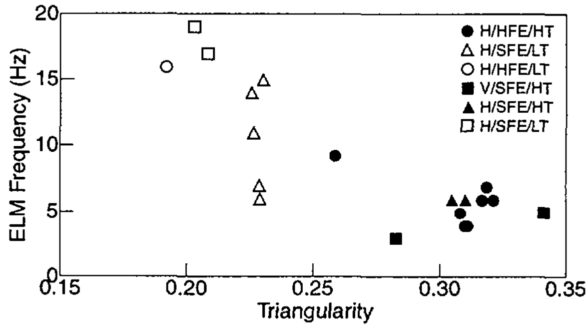

Fig.5 ELM frequency vs. triangularity for pulses with beam fuelling only. The designation of the equilibria A/BBB/CC indicates target orientation, flux expansion (high or standard), and triangularity (high or low), respectively. All of the pulses were run at 2.5 MA, 2.5 T, and 12 MW NB power.

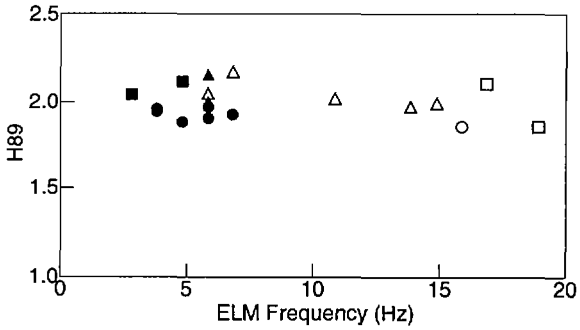

Fig.6 Variation of confinement quality, H_{89}, with ELM frequency, beam-fuelled pulses. The ITERH93-P ELM-free confinement scaling factor, H_{93}, is approximately $0.46xH_{89}$ for the pulses described in this paper.

increases, illustrating the importance of ELMs in purging the edge plasma of impurities. The radiated power fraction in these discharges was quite low for the high ELM frequency configurations, around 25%, increasing at lower ELM frequencies to about 40%.

A set of simulations has been carried out to model the quiescent periods between ELMs of the standard flux expansion horizontal and vertical 12 MW ELMy H-mode pulses described above, using the EDGE2D/NIMBUS code system and a variety of models for the perpendicular SOL transport. It was found that a pinch term gave satisfactory agreement with measured divertor profiles, whereas the customary constant diffusion coefficient model did not. The values used were $\chi_E = 0.2\ m^2s^{-1}$, $D = 0.1\ m^2s^{-1}$, and $V_{pinch} = 4.5\ ms^{-1}$. The present version of the code models the neutral particle behaviour, including the effects of the bypass leaks, more accurately than earlier versions. With this transport model and the bypass leaks included, differences between results for the horizontal and vertical targets are greatly reduced. The target ion saturation current profiles are nearly identical, while the electron temperature profile on the vertical target is flatter than on the horizontal, but not inverted, as shown in Fig.7. The midplane profiles are essentially identical for horizontal and vertical targets, and are quite narrow, with $\lambda_n = 9$ mm, $\lambda_{Te} = 7$ mm, and $\lambda_{Ti} = 12$ mm. These code results are in qualitative agreement with Langmuir probe measurements.

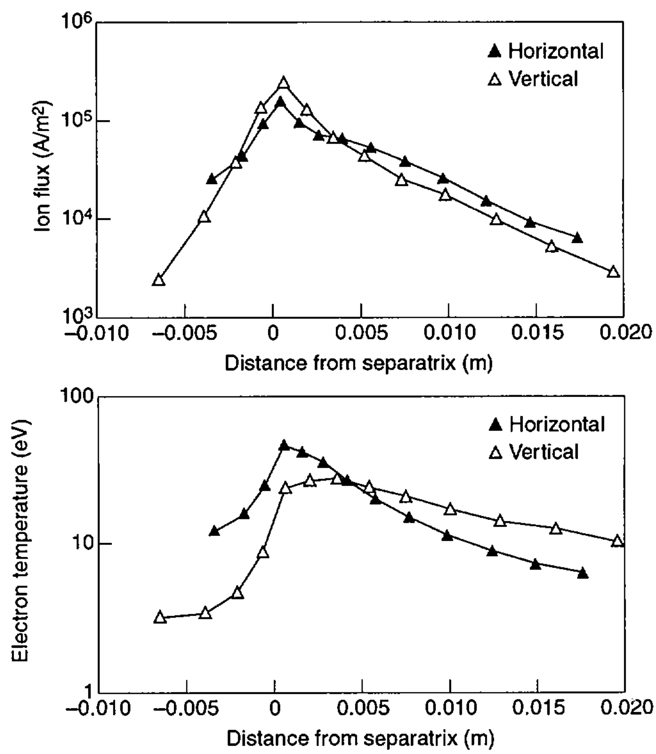

Fig.7 EDGE2D/NIMBUS simulations of target profiles of ion flux (above) and electron temperature (below) for horizontal and vertical pulses corresponding to the experiments. The distance from the separatrix has been mapped to the midplane.

3.2 Discharges with beam fuelling plus D_2 gas puffing

The above series of discharges was systematically repeated with D_2 puffing, which was varied in strength and location. It was found that the ELM frequency was increased by adding heavy fuelling (> 2 x 10^{22} s^{-1}). As puffing is added, the radiated power fraction initially stays the same or decreases slightly. As puffing increases further, the radiated power fraction also increases to a maximum of about 50%, with most of the increased radiation appearing in the divertor/X-point region. The mid-plane neutral pressure rises and the confinement quality declines, with these two variables being clearly correlated, as shown in Fig.8. In this figure the high triangularity standard flux expansion horizontal and vertical configurations appear to be the best, but there may be too few points to be statistically significant. However, as for the beam fuelled cases, the high triangularity discharges have lower ELM frequencies and higher Z_{eff} (Fig.9). The response of the main plasma density to the puffing is described in reference [7].

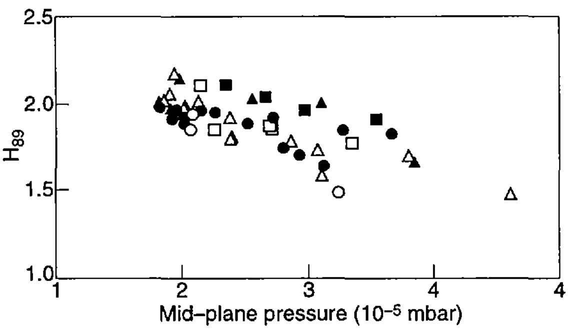

Fig.8 Variation of confinement quality, H_{89} with mid-plane neutral pressure for beam fuelled and D_2-puffed discharges.

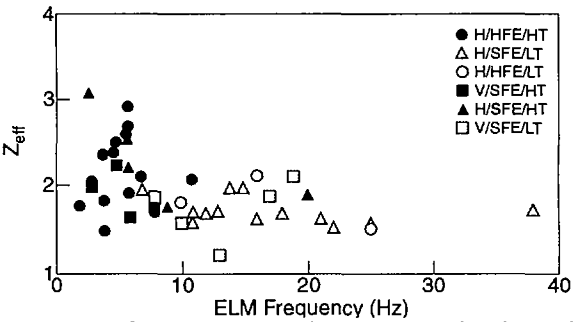

Fig.9 Variation of Z_{eff} with ELM frequency for beam fuelled and puffed discharges.

3.3 Discharges with beam fuelling plus D_2 and N_2 puffing

In order to increase the radiated power fraction beyond the 0.5 available with D_2 puffing, a series of discharges with N_2 seeding was carried out, again with varied configurations. These discharges attained total radiated power fractions up to about 0.75, and were broadly similar to those carried out with Mk I [1]. As the N_2 puff rate is increased, the character of the ELMs changes and the confinement decreases steadily and makes a gradual transition back to enhanced L-mode levels of H_{89} ~ 1.4, as shown in Fig.10. For these discharges, it appears that the decline of H_{89} with f_{rad} is less severe for the horizontal targets than for the vertical. It was shown by Matthews et. al. [9] that the Z_{eff} values for highly radiating divertor operation from several tokamaks can be described by a scaling law which can be written approximately as:

$$P_{rad} \sim (Z_{eff} - 1)\langle n_e\rangle^2 S,$$

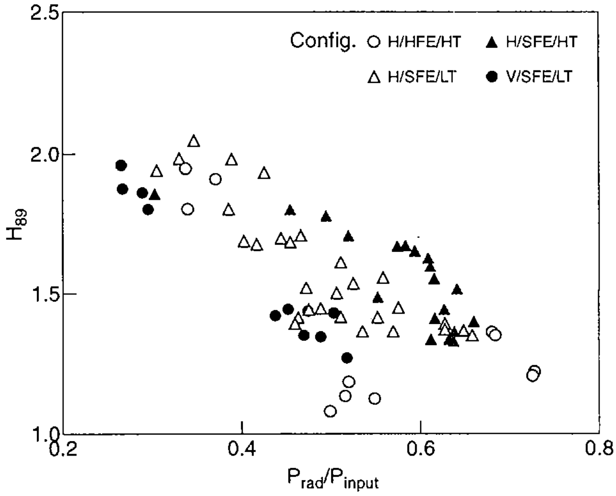

Fig.10 Confinement quality H_{89} vs. radiated power fraction in Mk IIA, for four configurations, with D_2 puffing only ($f_{rad} \leq 0.45$) and D_2 + N_2 puffing.

This scaling is not consistent with the scaling which would be observed if the bulk of the impurities were retained in the divertor. The Mk IIA data for highly radiating pulses fits the same scaling as was found for Mk I, as shown in Fig.11, indicating no improvement of seeded impurity retention, probably for the reason stated in Section 1 of this paper. Neon seeded discharges behave similarly with respect to Z_{eff} scaling, although they display a tendency to radiate more in the main plasma edge than in the X-point region, which reflects the tendency of neon to radiate less than N_2 at low T_e.

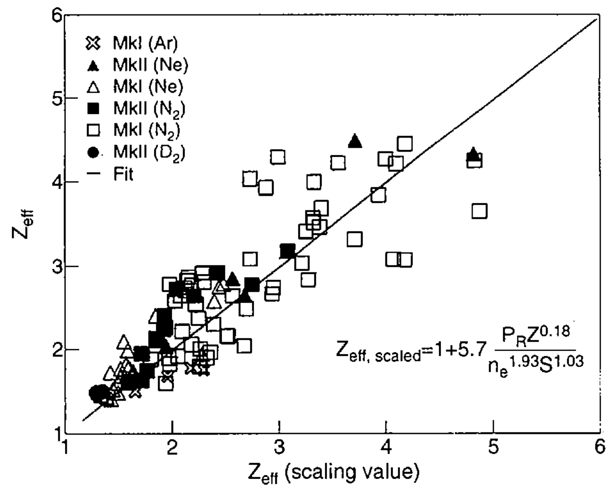

Fig.11 Measured Z_{eff} vs. $Z_{eff,scaled}$ for JET radiative discharges in Mk I and Mk IIA for a variety of seed gases.

4. DETAILED STUDIES OF TYPE I ELMS

It was shown in Section 3 that Type I ELMs are inherent to non-seeded discharges well above threshold, where good confinement and low Z_{eff} are obtained. It is thus important to understand the energy and particle loss per ELM, and the timescales associated with them, in order to assess their impact on divertor components. Figure 12 shows the total particle inventory and stored energy on a fast time scale for a typical isolated ELM. The stored energy drops extremely rapidly, on a time scale of 100-200 μsec, characteristic of parallel heat conduction. The particle inventory drop occurs more slowly, on the scale of a few milliseconds, characteristic of particle flow times in the SOL. It appears thus that the energy is conducted very quickly along the field lines to the target, with the particle efflux following the primary conduction-dominated energy dump. Figure 13 shows the percentage drop in density and energy, respectively, for 10 pulses from the database described in Section 3.2. Five of the pulses, representing five of the configurations studied, had no puffing, with a corresponding set for pulses with a moderate puff rate of 1×10^{22} s^{-1}, which is sufficiently low to have only a small effect on the ELM frequency. It can be seen that there is a general trend for the percentage energy and density drops to decrease with increasing frequency, although the time averaged energy and particle loss from ELMs, obtained by multiplying the frequency times the drops, increases with ELM frequency. Thus the low frequency, higher triangularity discharges lose less energy through ELMs in a time-averaged sense, but the individual ELMs are larger and thus potentially more damaging to the divertor plates. By increasing the puffing rate, the ELM frequency can be made larger, and the fractional energy loss per ELM can be reduced further, to about 2% in our discharges. This comes, however, at the expense of confinement, as illustrated in Fig.14. Even higher puffing causes a transition from Type I to grassy ELMs, with a further decrease in confinement to enhanced L-mode values.

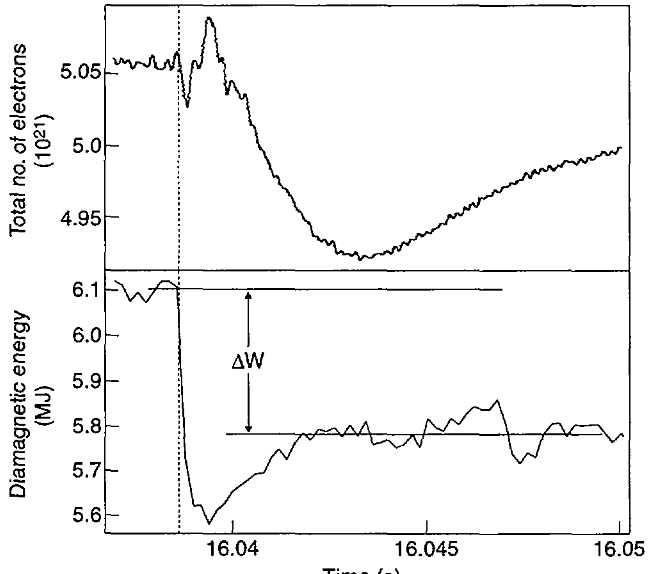

Fig.12 Traces of total particle inventory and stored energy vs. time for a typical ELM from the configuration study described in Section 3. The overshoot in ΔW is due to vessel shielding effects.

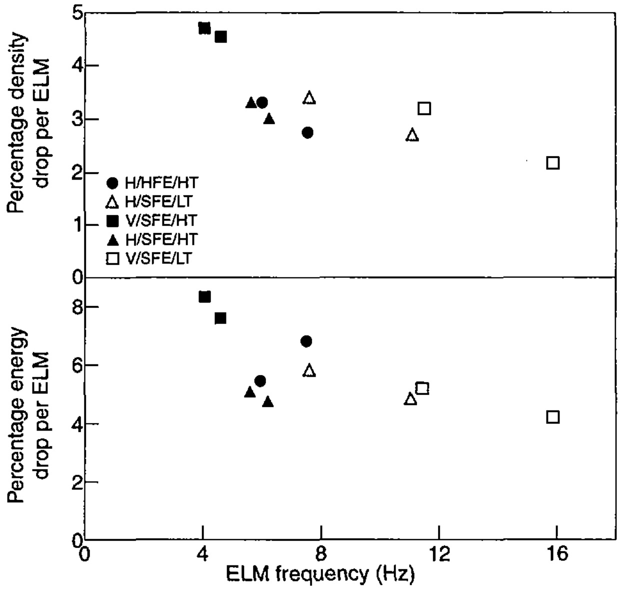

Fig.13 Percentage density drop (top) and energy drop (bottom) per ELM vs. ELM frequency for pulses from the configuration study of Section 3.

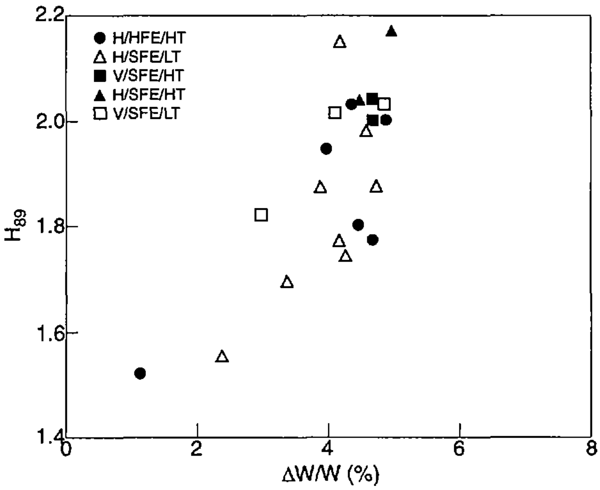

Fig.14 The confinement quality H_{89} vs. percentage energy drop per ELM, $\Delta W/W$, for the beam fuelled and D_2 puffed pulses of the configuration study.

Energy deposition on the ITER target plates of greater than about 1% of the stored energy is expected to cause severe erosion [10]. Fast Langmuir probe studies in JET show a very fast, short lived deposition of particles displaced by up to 20 cm from the pre-ELM strike point position, followed by a high-recycling deposition of particles at the original strike zones which lasts a few milliseconds, as shown in Fig.15 for an ELM on the vertical plates. Full cross section CCD views indicate that the ELM also produces a great deal of D_α radiation at the main chamber limiters and upper dump plates. Because of the relatively slow time resolution of the JET infrared cameras and bolometers, however, it is not possible to determine precisely the fraction of the energy leaving the main plasma which reaches the plates. It is known, however, that the ELM energy which does reach the plates is shifted and distributed over a larger area than that arriving between ELMs. More detailed quantification of the deposition of the ELM energy in JET must thus await more refined measurements and further analysis.

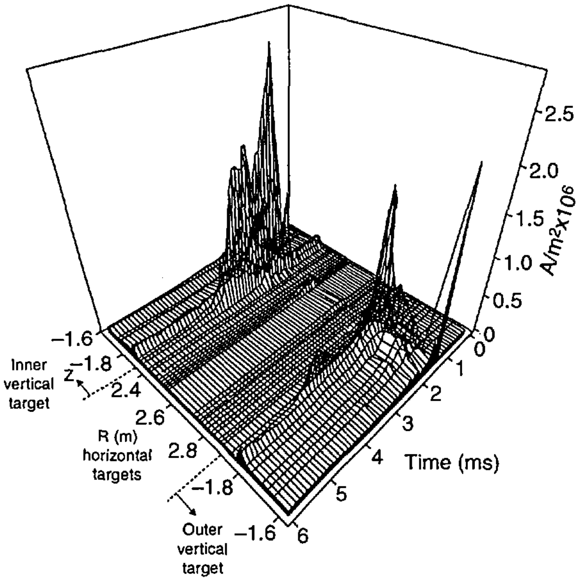

Fig.15 Unfolded 3-D plot of fast Langmuir probe ion saturation current measurement during an ELM on the vertical target.

5. CONCLUSIONS AND IMPLICATIONS FOR ITER

Compared with Mk I, the geometrically more closed Mark IIA configuration produces higher neutral pressures with correspondingly higher pumping rates, and facilitates access to the high recycling and detached plasma regimes. Although the density limit in Mk IIA is lower in ohmic and low power L-mode plasmas, it remains, as in Mk I, at roughly the Greenwald limit for H-mode pulses. The expected reduction in intrinsic impurity level in Mark IIA has not been observed, and this is believed to be due, at least in part, to bypass leakages.

For fixed power, field, and current, the ELM frequency in Type I ELMy H-mode discharges can be increased by a factor of several by decreasing the triangularity from 0.32 to 0.19, with no loss in confinement quality. The energy loss per ELM varies from about 8% to 4% as the triangularity is reduced. Further increase of the ELM frequency and decrease of amplitude, down to about 1%, was obtained by heavy D_2 puffing, but at the expense of confinement. However, ELMs somewhat larger than 1% may be acceptable to ITER, as the fraction of the ELM-expelled energy which reaches the plates is not yet well known in JET.

Differences which arise from target orientation (vertical vs. horizontal) at fixed flux expansion and triangularity appear to be quite small; both offer good confinement and plasma purity in the Type I ELMy H-mode operating regime. On the horizontal plate, large flux expansion resulted in slightly higher achievable main plasma densities, but poorer confinement and higher contamination by the intrinsic impurities. This may be due to the ELMs extending beyond the edge of the divertor.

Mark IIA operation with radiative power fractions greater than 0.5, achieved by seeding with N_2 or Neon, produced confinement degraded to a level probably not acceptable for ITER, with high Z_{eff}, as had been found in Mk I. In this series of pulses, the vertical targets showed poorer confinement at a given f_{rad}, and were not capable of going to as high values of f_{rad}.

In summary, if the L→H power threshold in ITER is such that the Type I ELMy H-mode regime can be achieved, it appears to offer high confinement and low Z_{eff}, relative to the high radiated power fraction regime. The energy deposited on the plates between ELMs for the oberved radiated power fractions would be acceptable for ITER, but the deposition pattern of the ELM energy needs further study.

REFERENCES

[1] JET TEAM, Plasma Phys. Control. Fusion **37** (1995) A227.

[2] NEUHAUSER, J., et al., Plasma Phys. Control. Fusion **37** (1995) A37.

[3] ITAMI, K., JT-60 TEAM, Plasma Phys. Control. Fusion **37** (1995) A255.

[4] ALLEN, S.L., et al., Plasma Phys. Control. Fusion **37** (1995) A191.

[5] VLASES, G.C., in Plasma-Surface Interactions (Proc. 12th Int. Conf. Saint Raphael, 1996), to be published in J. Nucl. Mater.

[6] LOARTE, A., MONK, R., to be published.

[7] JET TEAM, IAEA-CN-64/A1-1, this volume.

[8] JET TEAM, in Controlled Fusion and Plasma Physics (Proc. 23rd Eur. Conf. Kiev, 1996), Vol. 20C, European Physical Society, Geneva (1996) A269.

[9] MATTHEWS, G., et al., in Plasma-Surface Interactions (Proc. 12th Int. Conf. Saint Raphael, 1996), to be published in J. Nucl. Mater.

[10] ITER-JCT and HOME TEAMS, Plasma Phys. Control. Fusion **37** (1995) A19.

DISCUSSION

F. WAGNER: Do the differences in density limit between L and H modes, Mk I and II, remain when $\bar{n}_e$ is replaced by local $n_e(a)$?

G.C. VLASES: We do not yet have systematic measurements of $n_e(a)$ in Mk IIA, so the question whether the density limit is more related to the edge than the line averaged density cannot be answered definitively. However, the limited database which exists suggests that the ratio of line averaged to edge density for a given type of pulse (i.e. L mode, gas fuelled) is the same in Mk IIA as it was in Mk I.

F. WAGNER: Does the difference in the L phase indicate different MARFE developments?

G.C. VLASES: The different density limit behaviour in Mk I and Mk IIA for low power L mode pulses does reflect a difference in divertor MARFE formation, which occurs at lower upstream densities in Mk IIA than in Mk I for a given heating power.

F. WAGNER: Does the difference in L mode and the lack of difference in H mode point to a role of (j)r and therefore to a role of MHD?

G.C. VLASES: The density limit in H modes, which is non-disruptive, is caused by sharply increasing edge particle transport as the Greenwald limit is approached. We have not been able to establish any direct link with associated MHD activity.

R. STAMBAUGH: I have a question about H_{93} versus f_{ELM}. You showed H_{93} independent of f_{ELM} but also showed H_{93} depending on $\Delta W/W$ for the ELMs, which in turn depended on f_{ELM}. How are these observations consistent?

G.C. VLASES: H_{93} (and H_{89}) are independent of the ELM frequency, f_{ELM}, for steady H mode discharges fuelled solely by neutral injection (see Fig. 6). When gas puffing is added, the confinement quality is unaffected for puffing rates below approximately $1.5 \times 10^{22}\ s^{-1}$ (depending on configuration), but then degrades for higher rates of puffing, as indicated in Fig. 8, where the increase in midplane pressure is directly related to the puff rate.

RADIATIVE DIVERTOR WITH IMPROVED CORE PLASMA CONFINEMENT IN JT-60U

K. ITAMI, N. HOSOGANE, N. ASAKURA, A. SAKASAI,
S. KONOSHIMA, T. FUJITA, T. OIKAWA, M. SHIMADA,
R. YOSHINO, JT-60 TEAM
Naka Fusion Research Establishment,
Japan Atomic Energy Research Institute,
Naka-machi, Naka-gun, Ibaraki-ken,
Japan

Abstract

RADIATIVE DIVERTOR WITH IMPROVED CORE PLASMA CONFINEMENT IN JT-60U.

In JT-60U, a radiative divertor experiment with neon and hydrogen/deuterium gas puffing was carried out in reversed shear and ELMy H mode plasmas. The compatibility of the internal transport barrier in the reversed shear plasma with the radiative divertor was demonstrated by sustaining the reversed magnetic shear and the peaked density and temperature for 1.8 s during the divertor MARFE. Quasi-steady sustainment of divertor detachment was obtained up to P_{NBI} = 20 MW in ELMy H mode plasmas.

1. INTRODUCTION

In order to obtain core plasmas with high ion temperature, it is important to reduce particle recycling to a low level around the main plasma. It is difficult to produce cold, dense and radiative divertor plasmas with improved core plasma confinement, because of the high temperature in the scrape-off layer plasma and the high heat flux density to the divertor target in large tokamak devices. Recently, most effort in divertor studies of recent tokamak devices has been devoted to radiative divertor experiments with impurity gas puff [1]. In the ASDEX Upgrade tokamak, complete detachment at the divertor plasma was obtained during the ELMy H mode without degradation of core plasma confinement [2]. This significant reduction of the heat flux to the divertor is attributed to the enhanced radiation loss from the impurity ions in the boundary plasma. The concept of radiative divertor by impurity puffing is recognized as an alternative to the gas target divertor concept of ITER.

In discharges with hollow current profiles, the magnetic shear is reversed from negative to positive within a certain radius of the plasma column. Improved plasma confinement was found in the region of negative shear [3–5]. Reversal of the magnetic shear in the plasma centre is achieved by auxiliary heating of the plasma during the ramp-up phase of the plasma current. The internal transport barrier characterizes the improvement of core plasma confinement and the steep gradient of plasma temperature and density, which, typically, appears at r/a = 0.4–0.65 in JT-60U [3].

While high plasma performance inside the internal transport barrier in a reversed shear discharge is attractive for fusion reactors, there are no experimental results available about the behaviour of internal transport barriers in the case of high recycling and radiative edge and boundary plasmas reducing the heat flux to the divertor targets. Thus, if it is possible to sustain the internal transport barrier with high recycling and radiative edge and boundary plasmas, the reversed shear plasma becomes a promising candidate for a fusion reactor core.

The recent radiative divertor experiment in JT-60U has investigated the compatibility of improved core plasma confinement of the ELMy H mode [6] and reversed magnetic shear plasmas with a radiative boundary produced by neon gas injection. It was demonstrated in the experiment that the improved core plasma confinement in these plasmas was compatible with high recycling and radiative boundary plasma.

2. RADIATIVE DIVERTOR IN REVERSED SHEAR PLASMAS WITH HIGH ION TEMPERATURE

Most of the recent radiative divertor experiments have been carried out in a plasma with the central electron density higher than 4×10^{19} m^{-3}. This condition comes from the requirement for the edge and the scrape-off layer (SOL) plasma density to be high enough to allow sufficient particle flux to the divertor in order to obtain dense and cold divertor plasmas. In these plasmas, the ion temperature is limited to several keV in the centre, even in the recent large tokamaks, since $T_i \sim T_e$ in plasmas with high edge density. In order to demonstrate the compatibility of the radiative divertor with a high fusion reaction rate, we have carried out the radiative divertor experiment with reversed shear plasmas, with T_i lying in the range of 10 to 15 keV.

In order to obtain reversed shear plasmas with high T_i, it is necessary to reduce the particle recycling levels and to apply beam heating with P_{NB} = 15 MW to the target plasmas with an edge plasma density of $n_e \lesssim 5 \times 10^{18}$ m^{-3} during the ramp-up phase of the plasma current. The discharges took place in deuterium plasmas with I_p = 1.8 MA, B_T = 4 T and a plasma volume of V_p = 60 m^3. The neutral beam power was stepped down to P_{NB} = 10 MW before the flat-top of the plasma current. Typical wave forms of the discharges are shown in Fig. 1. The internal transport barrier (ITB) started to grow at t = 4.8 s. Two traces of the plasma density show the line averaged densities, with the chord inside and outside the barrier. Since the plasma configuration was not changed during the period shown in the figure, the separation of the two traces indicates the density increase inside the transport barrier. Neon and deuterium gas injection was applied at t = 5.3 s, 500 ms after the transport barrier had started to grow. The radiation loss from the divertor increased by 20% of the input power after the neon and deuterium gas puff.

Infrared camera measurements have shown that heat flux to the inner divertor had vanished and the heat flux to the outer divertor had decreased by 30%. The

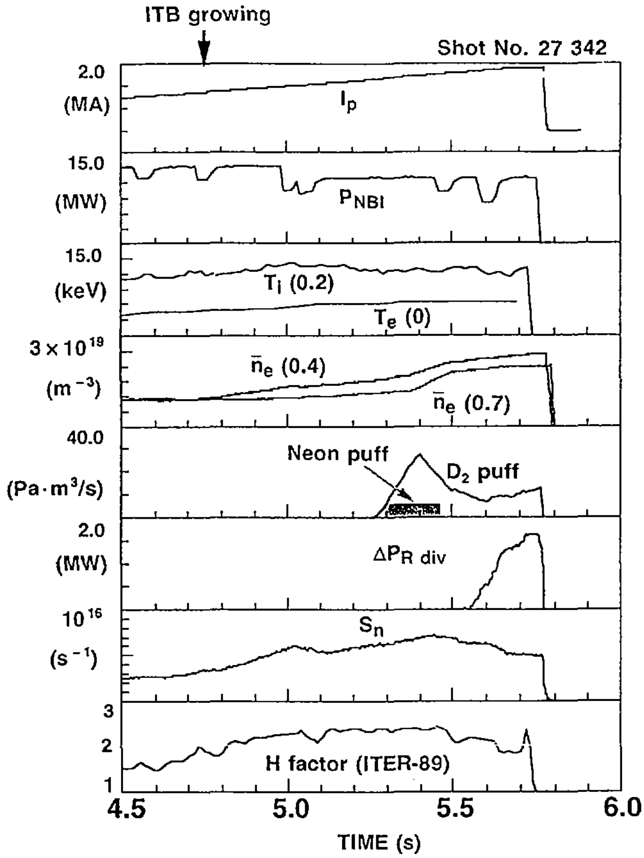

FIG. 1. Time traces of reversed shear discharges with high T_i. Neon and deuterium gas puffs were applied to increase the radiation loss from the divertor.

detachment at the inner divertor is also observed from a significant reduction of the ion saturation current and the electron temperature at a Langmuir probe located at the inner strike point of the separatrix (Fig. 2). While the electron temperature was decreased from 80 eV to ~50 eV at the outer divertor, the decrease was not sufficient for dense and cold plasmas.

Figures 3(a) and (b) show profiles of electron temperature and density measured by Thomson scattering before (t = 5.4 s) and after (t = 5.75 s) the neon and deuterium gas puff. As is seen in the figures, the transport barriers were sustained while the divertor radiation was enhanced. The reversal of the safety factor q profile at t = 5.7 s was also confirmed by MSE diagnostics [7], as is shown in Fig. 3(c).

This increase of the radiation loss in the divertor is attributed to the combined effects of neon and deuterium gas puffs. A neon gas puff without a deuterium gas

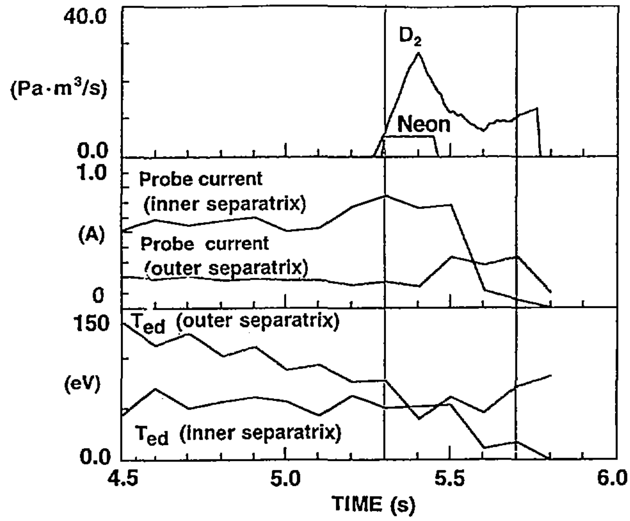

FIG. 2. Divertor plasma detachment at the inner divertor observed in Langmuir probes located at the divertor in shot No. 27 342.

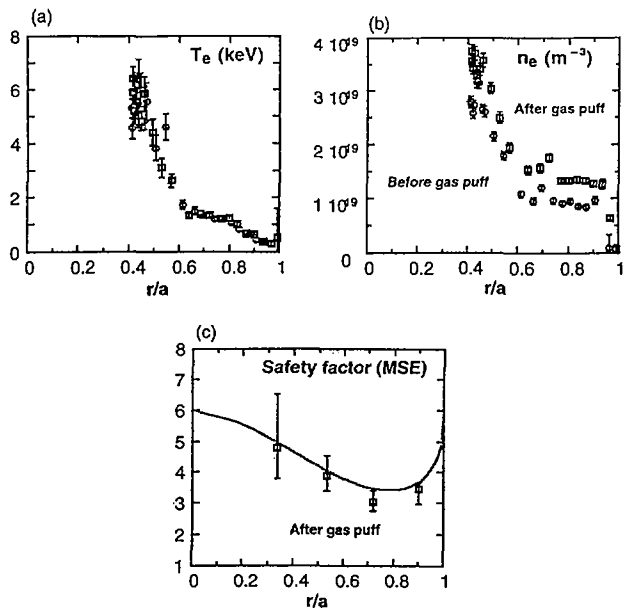

FIG. 3. Profiles in shot No. 27 342: (a) electron temperature at t = 5.4 s and t = 5.7 s; (b) electron density at t = 5.4 s and t = 5.7 s; (c) safety factor at t = 5.7 s.

puff destroyed the transport barrier. A deuterium puff as large as 60 $Pa \cdot m^3 \cdot s^{-1}$ without neon gas puff increased the heat flux to the inner divertor rather than decreasing it. This is explained as follows: The edge density increased to $2 \times 10^{19}\ m^{-3}$ by the deuterium gas puff, and the deposition of the neutral beam outside the ITB increased, reducing the radiation loss from the main plasma. While the particle flux to the divertor was increased by a factor of five as a result of such an intense gas puff, the increase in the heat flow from the main plasma compensated for the increase in the particle flux to the divertor, and divertor plasma was not cooled down. Therefore, no increase in the divertor radiation was observed. The central value of $T_i = 10$ keV was sustained during the gas puff. While the neutron rate decreased by 30%, an H factor of 1.8 was sustained up to the collapse of the reversed shear discharge.

3. SUSTAINMENT OF TRANSPORT BARRIER WITH DIVERTOR MARFE

Full detachment in the divertor was only obtained in the reversed shear plasma with high edge density. The plasma conditions were $I_p = 1.2$ MA, $B_T = 3$ T. It was also found that the internal transport barrier in the reversed shear plasma is compatible with the divertor MARFE. Figure 4 shows time traces of the discharge in

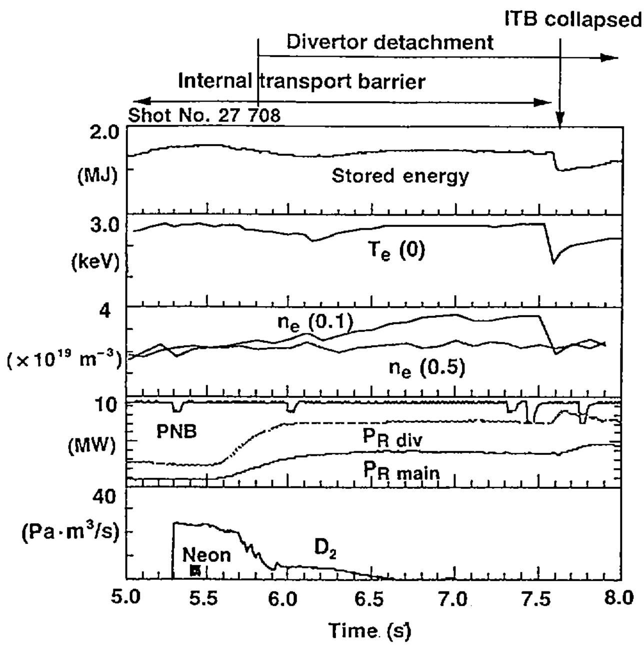

FIG. 4. Time traces of shot No. 27 708, the reversed shear discharge with high density. ITB was sustained for 1.8 s during the MARFE phase. The ITB terminated because of a beta collapse.

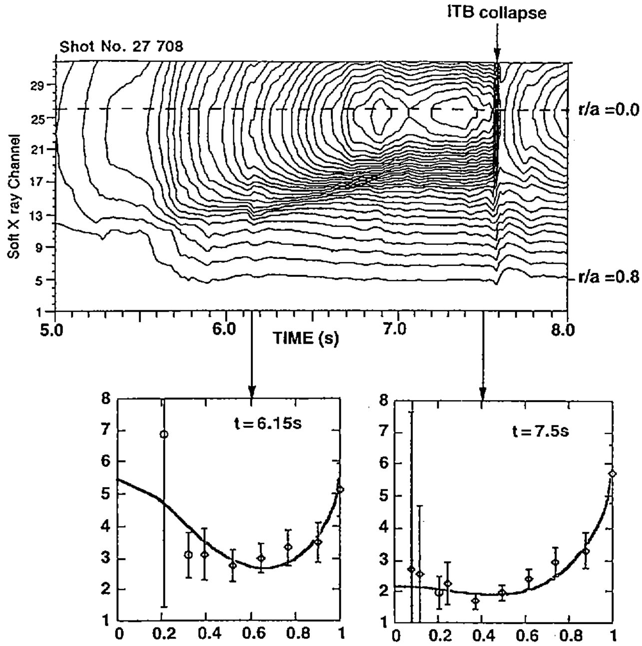

FIG. 5. Soft X ray contour plot of shot No. 27 708 with q profiles at t = 6.15 s and t = 7.5 s. While the radius of the internal transport barrier has decreased, ITB was sustained during the radiative divertor phase for 1.8 s. Negative central shear was sustained up to the collapse of the ITB.

which the internal transport barrier was sustained during the divertor MARFE phase for 1.8 s. In the discharge the internal transport barrier started to grow at t = 5.0 s. The radiative divertor plasma was formed by a neon and deuterium gas puff at t = 5.8 s and was sustained up to the end of the neutral beams. The total radiation loss from the divertor and the main plasma increased from 3 MW to 8 MW, reaching 80% of the input power. The improved confinement inside the ITB terminated by a beta collapse at t = 7.5 s. Significant drops of stored energy, plasma density and electron temperature at the beta collapse are observed in Fig. 4. A careful adjustment of the gas puff sequence and the amount of deuterium puff was required to produce the radiative divertor without beta collapse and to maintain the improved plasma confinement inside the internal transport barrier.

The behaviour of the internal transport barrier can be observed in the soft X ray contour plot. Figure 5 is a contour plot of the soft X ray intensity of discharge No. 27 708, which is constructed from the signals coming from an array of soft X ray detectors viewing the main plasma vertically. An internal transport barrier is located at the radial extent where the contour lines are concentrated. As is seen from this figure, the radiative divertor plasma was formed without destroying the transport barrier located inside the position r/a = 0.55. The position of the transport barrier moves inward from r/a = 0.55 at t = 5.6 s to r/a = 0.45 at t = 7.0 s. After t = 7.0 s, the position of the barrier is not obvious from the figure. In the almost identical discharge in which T_e and n_e profiles by Thomson scattering measurement were taken at t = 7.0 s, no clear barrier was observed in the n_e profile, but a barrier in T_e was observed inside r/a = 0.45. Profiles of the safety factor at t = 6.15 s and t = 7.5 s show that negative shear was sustained during the radiative divertor phase while shear reversal became shallow.

Figures 6(a), (b) and (c) show profiles of the heat flux density measured by an infrared camera system, the Ne I line intensity and the C II line intensity on the divertor plasma, respectively. The profiles were taken at t = 5.3 s (before the gas puff), t = 5.4 s (after the start of the deuterium gas puff), t = 5.55 s (after the pulse neon puff) and t = 5.75 s (after the formation of a MARFE). The heat flux to the inner

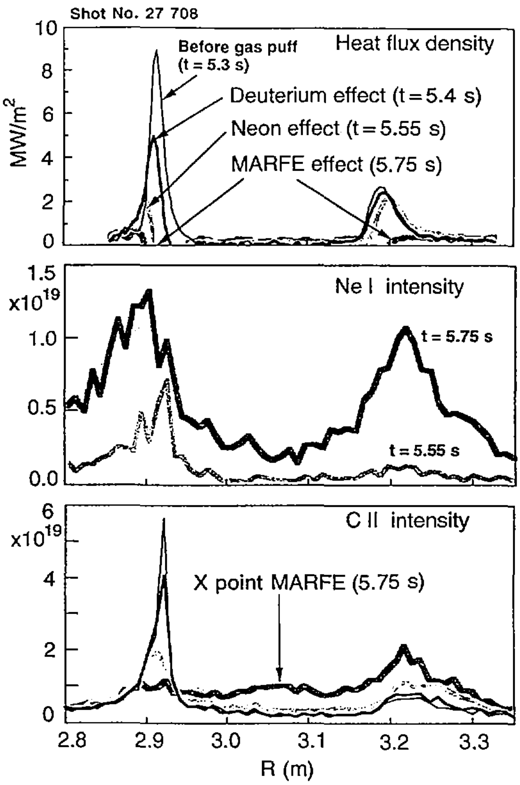

FIG. 6. Profiles of (a) heat flux density measured by an infrared camera; (b) Ne I line intensity; (c) C II line intensity on the divertor plasma during the formation of a divertor MARFE in shot No. 27 708.

divertor was significantly reduced as the Ne I intensity increased while the reduction of the heat flux to the inner divertor was less than 10%. The heat flux to the outer divertor decreased when the divertor MARFE was formed. A divertor MARFE is observed as the radiating zone shifts from the inner divertor to the X point (null point of the separatrix). The C II line intensity of the chord viewing the X point starts to increase. In this discharge, the MARFE started to grow at t = 5.6 s and finished its formation before t = 5.75 s. As is shown in the figure, both the inner and the outer divertors vanished, and the plasma was detached at the divertor. The MARFE was sustained up to the end of the neutral beams.

4. RADIATIVE DIVERTOR PLASMA IN ELMy H MODE PLASMAS WITH HIGH BEAM POWER

It was required that for a target plasma with $n_e < 1 \times 10^{19}$ m^{-3} and a low particle recycling level ($\Phi_{div} < 2 \times 10^{22}$) before neutral beam injection and with $P_{NB} > 20$ MW a high ion temperature should be achieved (~10 keV) in the ELMy H mode plasmas of JT-60U. In such an operation, the heat flux density to the divertor target q_d exceeded 5 MW/m^2, and the electron temperature in the divertor plasma, T_{ed}, reached ~80 eV; it was difficult to produce dense and cold plasmas by deuterium puffing only. With neon and deuterium gas puffing, a radiative divertor plasma was obtained in the ELMy H mode plasma with P_{NB} = 23 MW, while the H factor was maintained at a value of 1.5. The discharge was produced with low particle recycling ($\Phi_{main} = 2 \times 10^{22}$/s), the divertor radiation loss was increased by a factor of two, with particle recycling having increased by a factor of five. The increase in Z_{eff} due to neon was about 1 and total dilution of deuterium due to impurity ions was estimated to be 50%. This discharge was compared with a reference ELMy H mode plasma which was produced with high particle recycling, as is shown in Case 2 of Table I. Since in Case 1 the high T_{i0} produced in the low recycling phase was maintained up to the radiative divertor phase, the neutron rate was even larger than in Case 2, in spite of the dilution of deuterium due to neon in Case 1.

By further increasing the radiation loss at the divertor, a radiative divertor plasma dissipating 80% of incoming heat flux was produced in ELMy H mode

TABLE I. COMPARISON OF TWO DISCHARGES

	Conditions	Φ_{main} (s^{-1})	$\bar{n}_e$ (m^{-3})	P_{rad}/P_{NB}	T_{i0} (keV)	D-D neutrons (s^{-1})
Case 1	Low recycling + Ne and D_2 puff	5×10^{22}	3.2×10^{19}	50%	7	3.8×10^{15}
Case 2	High recycling + no gas puff	2×10^{22}	2.8×10^{19}	30%	5	3.1×10^{15}

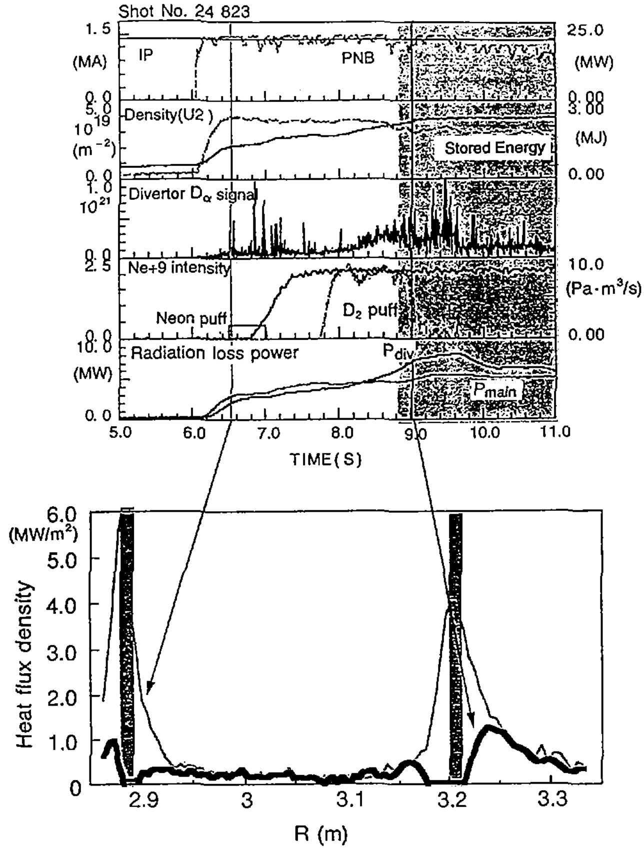

FIG. 7. *(a) Waveforms of ELMy H mode discharge with radiative divertor; (b) heat flux density profiles (before and after radiative divertor).*

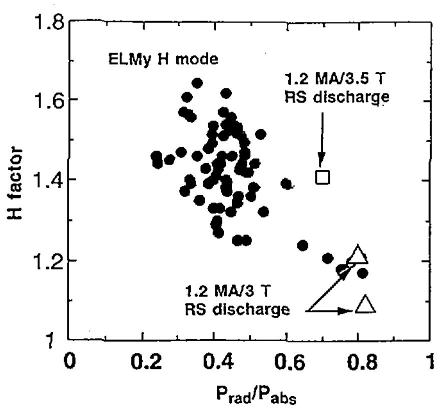

FIG. 8. *H factor versus radiation power ratio in ELMy H mode plasmas. Detached reversed shear discharges are also included.*

plasmas, with P_{NB} up to 20 MW (see Fig. 7(a)). In such a discharge, the total radiation loss from the plasma increased from 6 to 14 MW. The profiles of the heat flux density to the divertor in the initial and the radiative divertor phases are shown in Fig. 7(b). Detachment at the strike point of the separatrix occurred when the heat flux density vanished at t = 9.0 s. The divertor detachment was maintained for two seconds up to the end of NB heating.

By using a database of ELMy H mode discharges with neon and deuterium gas puff, the H factor is plotted against P_{RAD}/P_{ABS} (total radiation loss ratio divided by absorbed beam power) in Fig. 8. The plasma parameters are in the range of I_p = 1.2 MA, B_T = 2 T and $P_{NBI} < 23$ MW for ELMy H mode plasmas. Data from detached reversed shear plasmas are also plotted.

5. CONCLUSIONS

Neon and deuterium gas puffs were applied to reversed shear plasmas and ELMy H mode plasmas. A radiative divertor with 50% reduction of the divertor heat flux and partial detachment at the inner divertor was obtained with a main plasma of T_i = 10 keV and an H factor of 1.8. Reversed magnetic shear and improved plasma confinement inside ITB were sustained for 1.8 s during the divertor MARFE phase. In the ELMy H mode plasma, quasi-stationary divertor detachment was achieved with P_{NBI} = 20 MW.

REFERENCES

[1] SAMM, U., et al., Plasma Phys. Control. Fusion **35** (1993) B167.
[2] GRUBER, O., et al., Phys. Rev. Lett. **74** (1995) 4217.
[3] FUJITA, T., et al., IAEA-CN-64/A1-4, this volume.
[4] LEVINTON, F.M., et al., Phys. Rev. Lett. **75** (1995) 4417.
[5] STRAIT, E.J., et al., Phys. Rev. Lett. **75** (1995) 4421.
[6] ITAMI, K., et al., Plasma Phys. Control. Fusion **37** (1995) A235.
[7] FUJITA, T., et al., to be published in Fusion Eng. Des.

DISCUSSION

R.J. GOLDSTON: Could you comment on the concentration of neon in your detached reversed shear plasmas, compared with similarly detached normal shear cases.

K. ITAMI: The neon profile is almost the same as the electron density profile. The central neon concentration is thus determined by the neon density at the plasma edge.

M. KEILHACKER: I am not sure whether you have really shown that a highly radiative divertor plasma *and* good core confinement (H factor of 1.8) can coexist under quasi-stationary conditions in JT-60, as you seem to imply in your conclusions. In the reversed shear discharge of Fig. 1, the H factor decreases steadily after the injection of neon and the plasma disrupts after 0.4 s, and in the discharge where the internal transport barrier is sustained for 1.8 s (Fig. 4), you do not give a confinement factor. Could you please elaborate on this very important issue.

K. ITAMI: The discharge shown in Fig. 1 was terminated by β collapse, not by confinement degradation. While the H factor of the discharge shown in Fig. 4 was 1.1–1.2, the value was restricted by β collapse. The restriction should be resolved by the current and profile control.

S.I. ITOH: Regarding the compatibility of the reversed shear confinement operation and divertor functioning: did you do any quantitative assessment of the effect of the collapse of the internal transport barrier on the divertor plasma as well as on the divertor (transient heat flux, widths of the heat channel, etc.)? At present, we have to expect a finite probability of occurrence of the internal transport barrier collapse and the associated transient heat outflux from the plasma.

K. ITAMI: We believe that the edge plasma is independent of the improvement in core plasma confinement during internal transport barrier sustainment, but we have not yet analysed the transient phenomena at the collapse.

DIVERTOR PLASMA PHYSICS EXPERIMENTS ON THE DIII-D TOKAMAK*

M.A. MAHDAVI, S.L. ALLEN[1], N.H. BROOKS, R. BASTASZ[2], L.R. BAYLOR[3], J.N. BROOKS[4], D. BUCHENAUER[2], J.W. CUTHBERTSON[5], T.E. EVANS, M.E. FENSTERMACHER[1], D.N. HILL[1], D.L. HILLIS[3], J. HOGAN[3], A.W. HYATT, R.C. ISLER[3], G.L. JACKSON, T. JERNIGAN[3], R. JONG[1], C.C. KLEPPER[3], R.J. LA HAYE, C.J. LASNIER[1], A.W. LEONARD, R. MAINGI[6], P. K. MIODUSZEWSKI[3], R.A. MOYER[5], M. MURAKAMI[3], L .W . OWEN, T.W. PETRIE, G.D. PORTER[1], M.E. RENSINK[1], T.D. ROGNLIEN[1], M.J. SCHAFFER, G.M. STAEBLER, R.D. STAMBAUGH, D.M. THOMAS, M.R. WADE[5], W.R. WAMPLER[2], J.G. WATKINS[2], W.P. WEST, D.G. WHYTE[7], C.P.C. WONG, R.D. WOOD[1], DIII-D PHYSICS AND OPERATIONS TEAMS
General Atomics,
San Diego, California,
United States of America

Abstract

DIVERTOR PLASMA PHYSICS EXPERIMENTS ON THE DIII-D TOKAMAK.

An overview is presented of the results and conclusions of the authors' most recent divertor physics and development work. Using an array of new divertor diagnostics, the plasma parameters were measured over the entire divertor volume and new insights into several divertor physics issues were gained. Direct experimental evidence for momentum loss along the field lines, large heat convection, and copious volume recombination during detachment is presented. These observations are supported by improved UEDGE modeling incorporating impurity radiation. Divertor exhaust enrichment of neon and argon by action of a forced scrape-off layer (SOL) flow and divertor pumping as a substitute for conventional wall conditioning were demonstrated. A divertor radiation zone with a parallel extent that is an order of magnitude larger than that estimated from a 1-D conduction limited model of plasma at coronal equilibrium was observed. Using density profile control by divertor pumping and pellet injection, H-mode confinement at densities above the Greenwald limit was attained. Erosion rates of several candidate ITER plasma facing materials are measured and compared with predictions of a numerical model.

---

* Work supported by the US Department of Energy under Contract Nos DE-AC03-89ER51114, W-7405-ENG-48, DE-AC05-96OR22464, DE-AC04-94AL85000, and Grant No. DE-FG03-9SERS4294.

[1] Lawrence Livermore National Laboratory, Livermore, California, USA.

[2] Sandia National Laboratories, Albuquerque, New Mexico, USA.

[3] Oak Ridge National Laboratory, Oak Ridge, Tennessee, USA.

[4] Argonne National Laboratory, Argonne, Illinois, USA.

[5] University of California, San Diego, California, USA.

[6] Oak Ridge Associated Universities, Oak Ridge, Tennessee, USA.

[7] Institut national de la recherche scientifique, Energie et matériaux, Varennes, Quebec, Canada.

1. INTRODUCTION

Until recently, the DIII–D divertor data base was limited to upstream SOL parameters and plasma parameters at the target plate. Using the new and existing diagnostic systems of the DIII–D, in a recent experimental campaign we have extended the divertor data base to the bulk of the divertor plasma. We have made 2-D maps of the parameters of the divertor plasma from the inner strike point to the outer strike point and from the target plates to above the X–point [1–5]. The new dedicated divertor diagnostic systems [6–12] include: a divertor Thomson scattering system (TS), a fast scanning Langmuir probe (FSLP), and EUV and visible spectrometers, and a Penning gauge (Fig. 1). For the first time we have the capability for local transport studies in the divertor plasmas and can readily obtain a measure of the local values of parallel conducted heat flux $q_{||} = \kappa_{||} T^{5/2}\, \partial T/\partial x_{||}$. A radially averaged measure of the local radiated power density is obtained from inversion of a 48 channel bolometer array data which combined with spectroscopic results has identified the dominant radiative impurities and additional channels of heat transport. The data from these diagnostics can severely test the validity of divertor plasma models.

The Thomson scattering and the scanning Langmuir probe systems measure T_e and n_e along a vertical path at the major radius of 1.48 m above the vessel floor. The time resolutions of the measurements are 2 and 0.5 ms, respectively. By sweeping the divertor plasma across the measurement location of these two diagnostics two dimensional distributions of the plasma parameters have been obtained.

Broad spectral coverage of the DIII–D divertor is provided by an XUV SPRED and a visible survey spectrometer. In addition, two multichordal visible spectrometers with high spectral resolution give information on the radial distribution and the Doppler broadening of impurity ions.

These diagnostics are complemented with the existing DIII–D diagnostics. These systems provide: n_e and T_e in the SOL from the outer channels of the core Thomson system, and from target plate Langmuir probes; SOL T_i from Charge Exchange Recombination spectroscopy, radiated power from a 48 channel bolometer array, target plate heat and particle flux from an infrared TV, spectrally filtered 2-D images of the divertor plasma from tangentially and vertically viewing visible cameras, D_α light from arrays of fast photo diodes, and neutral pressure measured by ASDEX gauges.

Intermediate to high recycling radiative divertor conditions were measured in Ohmic, L–, and ELMing H–mode plasmas. The radiative modes studied are partially detached divertor, induced by D_2 puffing, and enhanced radiation with impurities, induced by neon or nitrogen injection. This data provides direct evidence for electron pressure drop along the field lines and evidence of copious volume recombination in detached plasmas (Section 3).

The UEDGE [13] code contains a 2-fluid model of the plasma with multi-species ions, classical parallel heat flux, anomalous perpendicular transport, and a Navier-Stokes fluid model of neutrals which permits momentum loss by charge exchange. The extensive data obtained recently is being used to examine the validity of physics models in UEDGE[14,15], and a Monte Carlo impurity (MCI) code [16]. In Section 3 we compare results of a UEDGE code simulation and experimental data from a detached plasma.

A powerful tool for enhanced divertor performance in ITER and other next generation devices is divertor pumping. We have used divertor pumping for divertor impurity enrichment, developing an extended divertor radiative zone, as a wall conditioning substitute for the conventional helium glow discharge cleaning, and to access densities above the Greenwald limit in H–mode (Section 4).

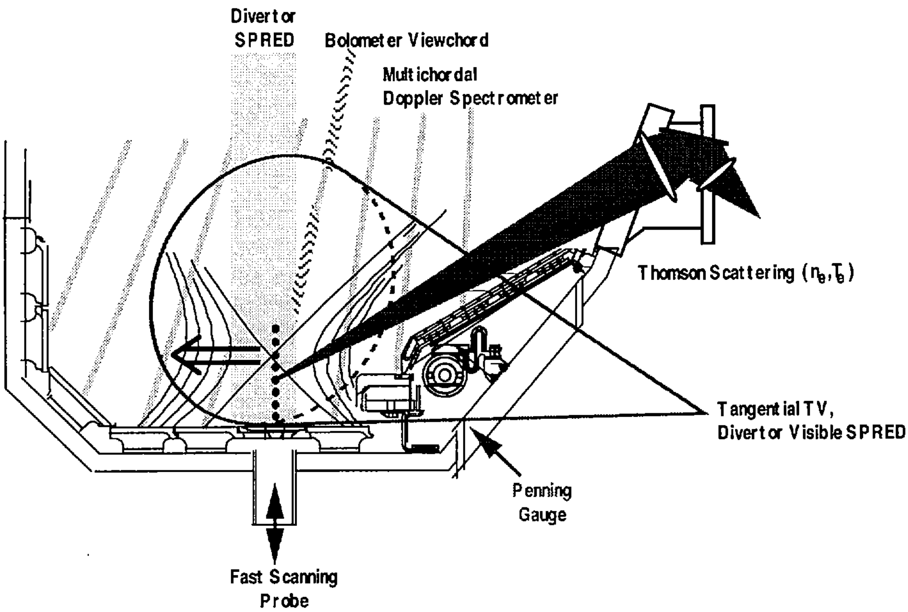

FIG. 1. Cross sectional view of the lower section of the DIII–D vessel showing the views of new divertor diagnostics. The plasma is swept radially to obtain a two dimensional map of the divertor plasma parameters.

Performance of a radiative divertor might be enhanced by divertor impurity enrichment. In a series of experiments simultaneous SOL gas puffing and divertor pumping were used to establish a SOL flow in order to preferentially concentrate the radiating impurities in the divertor plasma. In Section 4 we present the results of the so called "puff and pump" experiments where we have obtained direct evidence of plenum impurity enrichment.

Helium glow discharge cleaning (HeGDC) is one of the most effective wall conditioning tools in present day short pulse tokamaks. However, this technique is not applicable to long pulse devices. We have demonstrated that divertor pumping, which is applicable to long pulse operation, is an effective substitute for HeGDC (Section 4).

An overwhelming body of tokamak data agree roughly with the so called empirical Greenwald density limit scaling: $n_e < 10^{14} \times I_p/\pi a^2$ m^{-3}. In ITER, both to achieve a radiative divertor and ignition require operating at a line average density of ~1.5 times the Greenwald limit. We have shown that density profile control is a key to achieving high confinement at high densities. Using a combination of divertor pumping and pellet injection, we have obtained H–mode plasmas with a confinement of 1.8×ITER–89P at a regulated density of 1.5× Greenwald limit (Section 4).

A steady state model of the divertor plasmas might not be adequate for describing the divertor plasma behavior for calculating the life time of the divertor target materials. The divertor plasma properties can be inherently time dependent, as was seen in high density DIII plasmas [17], or be modulated by transient heat or particle pulses of ELMs and other events originating in the core plasma. In order to estimate divertor heat and particle fluxes due to ELMs in ITER we have measured ELM energy losses in the main plasma and the resulting heat and particle flux in the divertor (Section 5).

In a long pulse tokamak the life time of the divertor plate might be determined by the net erosion rate of the divertor material. We have measured erosion rates of several candidate divertor materials for ITER using the Divertor Material Evaluations Studies system (DiMES).

2. CHARACTERISTICS OF ATTACHED AND DETACHED PLASMAS

Here we will discuss the results and conclusions from a subset of the recent data containing moderate recycling and highly radiative detached plasmas induced by gas puffing [1–5,18]. Discharge parameters were in the following ranges: I_p = 0.9 to 1.5 MA, B_T = 2.1 T, P_{inj} = 1 to 10 MW, q_{95} = 3.7 to 6.6, and the $\nabla\mathbf{B}$ drift toward the divertor. Radial sweeps of the divertor plasma were used to allow diagnostics with vertical views to sample the entire divertor plasma. For this work it is assumed that conditions in the divertor remain nearly constant as the plasma is moved since the configuration is essentially an open divertor on horizontal targets without pumping throughout the sweep.

The divertor plasma parameters in the outer leg of moderate recycling ELMing H–mode plasmas display the classical characteristics of conduction limited heat flow in the SOL. The regions of significant radiated power are in the inner divertor leg and SOL. The radial profile and magnitude of the electron pressure remain roughly constant throughout the SOL while electron temperature decreases monotonically towards the plate. The radial profile and absolute values of n_e and T_e in the vicinity of the X–point are nearly the same as the corresponding midplane values. At the outer strike point, the density is ~3 times the X–point value, while T_e is reduced from the X–point value by the same factor. The transverse profiles of the electron density and temperature remain roughly invariant throughout the SOL. The parallel heat flux obtained from the gradient of the electron temperature along a flux surface corresponding to peak heat flux at the target plate is roughly constant along the field lines, which is consistent with low radiation in this region. At the separatrix however the conduction heat flux decreases by a factor of 2 from the X–point to the vicinity of the target plate, which is indicative of radial transport at the sharp boundary between the SOL and the private flux region.

The behavior of high recycling partially detached plasmas is qualitatively different from the previous case. The regions of significant radiated power shift to the vicinity of the X–point and outer leg, and the peak heat flux at the divertor target drops a factor of 3–5. Typical reconstructions of total radiated power from the bolometer arrays and IR measurement of divertor heat flux are shown in Fig. 2 at times before and during the partial detachment. In heavy puffing discharges the carbon emission coalesces outside the separatrix near the X–point although the core energy confinement is not affected. For very heavy puffing the peak in the visible carbon radiation appears inside the last closed flux surface above the X–point and the energy confinement of the core plasma is reduced.

In detached plasmas [18–32] the electron pressure is not constant along the field lines and parallel heat conduction does not always dominate heat transport down stream. Near the separatrix the pressure decreases by an order of magnitude from the midplane to the vicinity of the target plate; whereas, farther out radially pressure remains constant or increases towards the plate. Most of the pressure variation occurs below the X–point. The pressure profile at the target plate peaks outboard of the sepa-

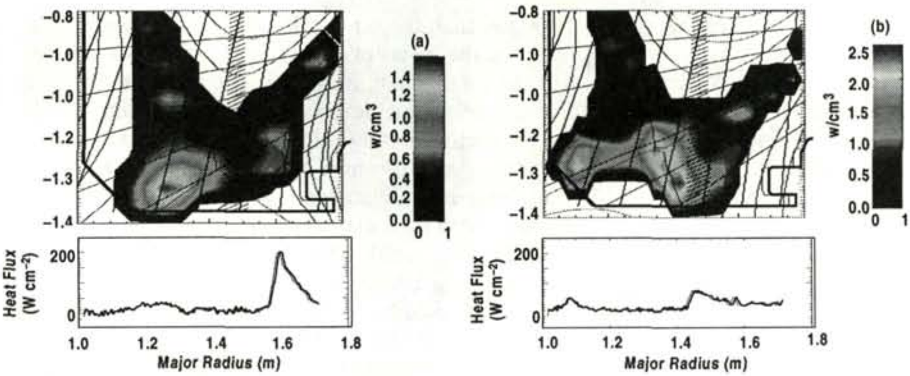

FIG. 2. Gray scale images of the plasma emissivity, before (a) and after detachment (b), reconstructed from the data from a 48 channel bolometer array. The figure also shows the corresponding profiles of heat flux to the divertor plate. After gas puffing the region of significant radiated power shifts from the inner divertor leg to the outer leg while the peak heat flux at the outer leg drops by a factor of three.

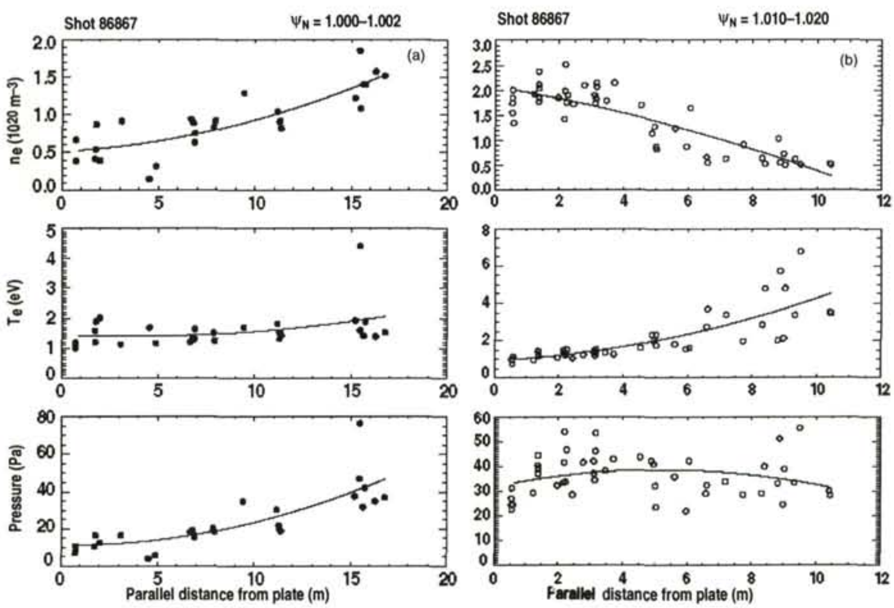

FIG. 3. Profiles of the electron temperature, density and pressure, along the field lines in a region between the X-point and the target plate, measured by the divertor Thomson scattering system during a detached L-mode shot. The solid circles represent data from vicinity of the separatrix (y = 1.001–1.003) and the open circles represent data from a flux surface within the SOL (y = 1.010–1.020). Near the separatrix, the electron pressure drops by a factor of five from the X-point to the plate, whereas the pressure is roughly constant farther out in the SOL.

ratrix where it is a factor of 3–5 greater than the separatrix value. In the vicinity of the separatrix, electron density increases at the X–point elevation to 10 times its midplane value , but then decreases towards the plate where it becomes comparable to the midplane value. Farther out in the SOL, electron density increases monotonically to ~5×10^{20} m^{-3} near target, 10 times the corresponding midplane value. In the vicinity of the separatrix, the electron temperature drops by more than an order of magnitude to 1–2 eV at the target plate. Most of the temperature drop occurs above the X–point. In the region below the X–point, parallel heat flux, estimated from the average gradient of the electron temperature is negligible compared to the moderate recycling case, discussed above. The same qualitative behavior is seen in lower power detached L–mode plasmas; except for lower densities in the cold areas. Profiles of electron density and temperature in a detached L–mode shot are shown in Fig. 3. There is an apparent discrepancy between this observation and observation of significant radiated power downstream. The resolution of this discrepancy is addressed in a later paragraph.

Spectroscopy data show that carbon and deuterium are the sources of almost all the divertor radiation[10,33,34]. Near the target plate carbon and deuterium radiation are roughly equal. However, total carbon radiation is three times greater than that of deuterium. The total power radiated per cm^2 deduced from spectroscopy agrees well with that detected from a bolometer with a slightly different field of view.

As an independent check on the effective electron temperatures derived from the ratios of XUV lines we have measured ion temperatures for C II and C III from Doppler broadening of visible lines taking into account the exact magnetic sub-level splitting caused by the Zeeman/Paschen-Bach effect. For C II, effective electron temperatures in the range 2–4 eV have been observed, with ion temperatures typically 1–2 eV lower. For C III, where the characteristic thermalization time can be much smaller than the ionization time, electron and ion temperatures are generally in good agreement, ranging from 6 to 15 eV depending on plasma conditions.

3. DISCUSSION AND MODELING

In general, the UEDGE code produces all experimentally observed divertor states [14,15] : fully attached, detached at the inner strike point, detached at both strike points, and ultimately a core MARFE. Detached states are produced at low power pure deuterium plasmas or at high power plasmas with impurity radiation. The code accurately simulates attached plasmas, with a good match of the SOL profiles at the midplane, near the X–point and in the divertor. In the following we will discuss in more detail a comparison of code results with the experimental data from a detached plasma. Although quantitative agreement between the simulation and experiment is not as good as for attached plasmas, the code solution identifies the physical processes which dominate the behavior of detached divertor plasmas.

The simulation which uses a fixed fraction impurity model and the measured core plasma parameters and input power, matches the midplane temperature profile well. The simulated SOL density profile is slightly broader than the experiment. These simulations show a target plate temperature of 1 eV, in agreement with the Thomson measurement. In the simulation, the 5 eV temperature contour (ionization front) is clearly upstream from the divertor plates by ~6 cm in the outer leg [Fig. 4(a)] and 14 cm in the inner leg; however, divertor Thomson scattering data for the outer leg shows this front to be 10 cm away from the plate on the outer leg. The UEDGE simulation produces

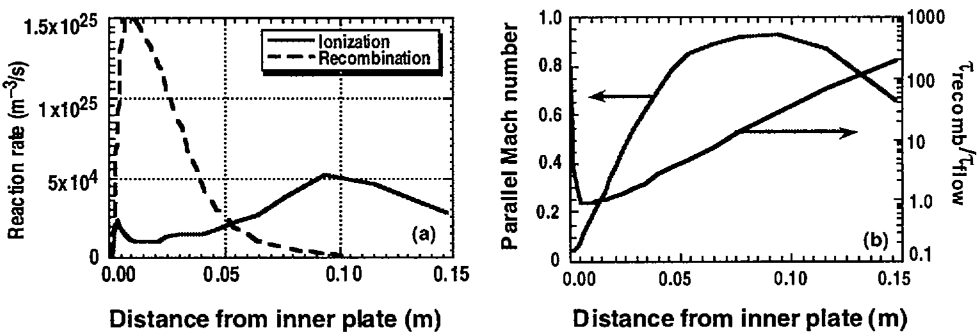

FIG. 4. UEDGE simulation results for a detached plasma using a fixed fraction impurity model. The code results show that the ionization is approximately 10 cm centimeters away from the plate and that a region of strong volume recombination has developed near the target plate(upper box). The upstream ionization causes a flow towards the plate that reduces the plasma pressure and convects heat(lower box).

more hydrogenic radiation than carbon radiation, whereas spectroscopy suggests that carbon radiation is twice the deuterium line emission.

In the simulation, plasma momentum loss occurs in two steps. First, in the region of 5–15 cm above the plate a large local particle source converts roughly one half of the upstream plasma pressure into parallel flow momentum [23] with the Mach number approaching unity [Fig. 4(b)]. Since most of the heat dissipation takes place at or above the X–point whereas most of the pressure drop occurs below the X–point, it seems that the mechanisms for the pressure drop and heat dissipation are not directly coupled, although a low temperature caused by radiation is a likely prerequisite for the momentum loss process. In the second step, ion neutral interactions transfer most of the directed flow momentum to the vessel walls. Volume recombination in this simulation is as high as 1.5×10^{25} m^{-3}/s near the plate with a volume integral which is 3 times the total plate ion current.

Hydrogenic radiation from this recombination offers a qualitative explanation for the apparent discrepancy between the observation of a region of high emissivity below the 5 eV ionization front and very low conduction heat flux based on the low electron temperatures (1–3 eV) and temperature gradient ($\lesssim$1 eV m^{-1}), measured by Thomson scattering. The near sonic flow towards the plate convects a substantial amount of thermal energy and a comparable or greater amount of ionization potential energy. In the regions where $T_e \sim 1$ eV and $n_e \sim 5\times10^{20}$ m^{-3}, the plasma recombines through three body recombination, since the three body recombination rate is an order of magnitude greater than the ionization and radiative recombination rates. Since the recombination is mainly into high n levels which subsequently decay to the ground state by line emission, most of the ionization potential is converted into hydrogenic line emission. This interpretation is consistent with the experimental observation that deuterium is the dominant radiating species near the plate.

Another possible explanation for the observed radiation in the cold plasma region is a burst of heat during ELMs. Since, presently, the Thomson data is taken between ELMs, the conduction heat flux during ELMs is not resolved. However, normally bolometric data is averaged over several ELMs.

4. DIVERTOR PERFORMANCE ENHANCEMENT

Feasibility of a radiative divertor depends critically on the achievable ratio of impurity concentration in the divertor relative to the core plasma and on the emissivity of the radiating impurity in the divertor plasma environment. SOL flows play a key role both in the process of divertor impurity enrichment and in the process of increasing impurity emissivities above the coronal equilibrium. In this section we present results of experiments on both impurity enrichment and spatial extension of the divertor radiative.

4.1. Divertor Impurity Enrichment by a Forced SOL Flow

A plasma flow in the direction of the target plate tends to drag impurities downstream, opposing the temperature gradient force [35,36] which tends to drive impurities upstream towards the core plasma. A sufficiently strong forced flow, established by simultaneous gas puffing in the SOL and divertor pumping, can thus increase the impurity concentration in the divertor plasma relative to the core. In the high recycling regime, a large plasma flow occurs naturally within an ionization mean free path of the recycling neutrals. The effect of this flow on impurity exhaust was demonstrated in the DIII device and ASDEX-U [35,37,38]. However, the range of recycling flows is normally limited to the vicinity of the divertor target, whereas it is desirable to have a significant flow throughout the radiating volume of the divertor plasma to oppose the forces which drive impurities upstream. A forced SOL flow, albeit smaller than the recycling flows, can be more effective upstream where recycling flux is low. Earlier DIII–D experiments [39] demonstrated that a forced SOL flow is compatible with a steady state constant density core plasma. The same experiments also showed that this 'puff and pump' approach was effective in reducing the argon content in the core plasma, but the results were somewhat inconclusive because the analysis was based on indirect measurements of the core argon content and there were no divertor argon measurements.

The experiments presented here [40] featured direct measurements of core plasma and exhaust gas impurity densities. Neon and argon concentrations in the core plasma are obtained from measurements of the charge-exchange excited transitions. A modi-

TABLE I. SUMMARY OF EXPERIMENTS ON IMPURITY ENRICHMENT BY A FORCED FLOW

D_2 Flow Location	Top	Divertor	Top	Divertor
Flow (Torr-l/s)	150	150	80	80
Line-Averaged Density	6.2×10^{19}	6.1×10^{19}	6.0×10^{19}	6.1×10^{19}
Plenum Pressure (mTorr)	4.0	3.5	1.6	1.5
ELM Frequency (Hz)	60	55	60	55
Neon Enrichment	1.4	1.0	1.2	1.0
Argon Enrichment (Relative)*	6.9	2.2	1.7	1.0

*Normalized to enrichment in 80 Torr-l/s divertor fueling.

fied Penning gauge provides simultaneous measurements of deuterium, helium, neon, and argon partial pressures in the divertor pumping plenum [41,42]. Divertor impurities are monitored by the divertor SPRED instrument that views through the main plasma and the lower divertor along a vertical chord. Trace impurity contents in the various reservoirs of two nearly identical discharges, one of which has D_2 injected from a single gas valve at the top of the machine and one with the same amount of D_2 injected into the divertor private flux region, are compared. The core and divertor plasma density are maintained the same in the two cases by controlled divertor pumping, so that the effect of other forces responsible for impurity transport in the SOL and divertor (e.g., divertor recycling, parallel temperature gradients. etc.) is maintained constant. This particular comparison allows one to distinguish the effect of SOL flow, since the top fueling case will have SOL flow and divertor recycling, whereas the divertor fueling case will mainly have divertor recycling. In all cases the impurity injected into the divertor private flux region. The results of such experiments are summarized in Table I. Two different deuterium flow levels, 80 and 150 torr-ℓ/s, were used for each of the impurities. For both impurities, the top fueling case consistently yields higher exhaust impurity enrichment than divertor fueling, showing that SOL flow indeed has an impact on divertor retention of impurities. The effect is particularly strong with argon where a relative enrichment of 7 is obtained. With argon, one also observes a factor of two relative enrichment with the increased level of D_2 injection even with divertor fueling.

4.2. Extension of Divertor Radiating Zone

Deviations from coronal equilibrium can increase impurity emission relative to coronal equilibrium several orders of magnitude [43]. Several authors [44,45] have suggested that it may be feasible to take advantage of such emissivity enhancements in a radiative divertor. Two processes contributing to radiation enhancement are charge exchange reactions with neutrals or rapid recycling of the impurities. The emissivity enhancement occurs mainly at temperatures above the first burnout temperature of the impurity. In a divertor plasma, enhanced non coronal radiation in essence would extend the high radiation zone upstream to areas of higher temperature where the radiative impurity is normally burned out. Both effects that lead to enhanced emissivity necessitate a large SOL flow. Furthermore, the convected heat flux due to this flow can limit the achievable heat flux reduction by non-coronal radiation [46]. However, heat convection can have a beneficial effect. Convection enhances heat transport along the field lines, thus would allow low temperature impurities to radiate from a larger volume than with pure conduction. A modest divertor heat flux reduction gained from these two effects combined might be sufficient for the success of a radiative divertor in ITER [45].

In a recent experiment [47] we have observed a radiative zone with a poloidal extent which is an order of magnitude greater than that expected from coronal radiation and conduction limited heat flow along the field lines. The experiment was performed in a configuration with a poloidal X–point-to-target plate distance of ~50 cm, which was six times the spatial resolution of the bolometer array diagnostic. The configuration has the additional advantage of providing a wide channel outside of the divertor plasma for the recycling particles to reach deep into the divertor volume. Deuterium gas was injected into the divertor of an ELMing H–mode plasma at a rate of 190 torr-ℓ/s to increase radiative losses and thereby decrease the divertor target heat flux. The radiative losses increased to 65% of the 10 MW of the input power. The 2D distribution of radiative losses is deduced from the bolometer array data. Over the entire outboard leg of the divertor, variation of the radiated power along the divertor channel is less than a factor of 2.

Assuming a one dimensional geometry and no convection, we have obtained the distribution of the parallel heat flux by integrating the radiated power density from the divertor plate to the X–point. Our results show that the parallel heat flux in the outboard divertor leg drops from an initial value of 100 MW/m^2 at the X–point to 45 MW/m^2 at the target plate, over a distance of 10 m. Furthermore, by substituting the heat flux into the heat conduction equation and integrating along the field lines, we have obtained an upstream electron temperature of 50 eV. Spectroscopic results show that carbon is the dominant radiative impurity in these plasmas. However, under these conditions, carbon radiation in coronal equilibrium would produce a radiation zone 10 times shallower than observed. This conflict could be resolved by allowing non-coronal radiation. A second possibility is that in a large segment of the SOL convection transports energy downstream faster than conduction, allowing a more extended radiating zone.

4.3. Wall Conditioning by Divertor Pumping

Divertor and vessel wall materials can absorb or release large quantities of particles, far greater than the plasma particle inventory [48]. In present day pulsed plasmas Helium Glow Discharge Cleaning (HeGDC) is commonly used to minimize the wall particle inventory and thereby uncontrolled plasma fueling by wall released particles. An experiment was conducted to evaluate the feasibility of continuous divertor pumping as a substitute for the transient HeGDC between plasma discharges to maintain a low recycling wall in steady state plasmas [49,50]. After obtaining reference discharges with HeGDC, a sequence of 12 discharges was conducted without HeGDC and with the divertor cryopump "off". Particle balance analysis shows that the net wall inventory was increased by 1250 torr-ℓ (9×10^{22} atoms) during this phase. Assuming uniform deposition of the particles over the 60 m^2 of (type?) graphite in the DIII–D, this quantity corresponds to an average of 60 monolayers or alternatively to a saturated layer (i.e. 0.4 deuterons per carbon atom) of 150 Å depth. The divertor cryopump was then activated for the next 10 discharges. Two separate estimates of the cryopump exhaust rate were made, based on pump plenum measurements from a fast time-response ionization gauge, and a slower time response capacitance manometer indicated that the wall inventory was reduced near to or below the reference level at the end of the of the first discharge sequence. Plasma stored energy measured during the steady ELMy phase of each discharge was reduced by 15% on the first discharge without HeGDC and was restored to the reference level on the first discharge with active pumping. Thus, continuous particle exhaust by the divertor cryopump is shown to maintain low recycling, good performance conditions in the absence of HeGDC.

4.4. Access to High Densities

We have embarked upon a series of experiments to understand the physics of density limit in tokamak plasmas and to devise a path for ITER to reach densities 50% above the Greenwald limit [51–54] ($n_{\max}^{\mathrm{GW}} \sim I_p / \pi a^2$) required for ignition and safe divertor operation. This density must be achieved in moderately high performance ITER plasmas [55] with H=2,q_{95} =3 , and β_N=2. The essential tools to accomplish this effort are a pellet injector, the Advanced Divertor cryopump, and arrays of high resolution diagnostics that measure profiles of electron density and temperature, ion temperature, impurity concentration and current profile. Up to this point in time, our highest quasi-steady (≥0.4 s) line-average density has been 50% above n_{max}^{GW}, with global energy confinement times of 1.8, normalized to the ITER89P scaling. The highest transient density obtained in L–mode discharges was 3 × n_{max}^{GW}. Analysis of the data shows that there is no fundamental obstacle to achieving line average densities above the Greenwald limit. However, there are numerous resolvable ones that make the path to high densities very difficult. In absence of divertor pumping, divertor density increases non linearly with line average density and ultimately results in the collapse of the divertor plasma. This obstacle was readily removed by divertor pumping to control the divertor plasma density. In contrast to ref.[51], it is found that the density relaxation time after pellets is largely independent of the density relative to the Greenwald limit; although, pellets generally trigger ELMs and in some regimes cause H– to L–mode transitions which eject most of the pellet particles.

Radiation driven instabilities, such as MARFE [56], within the core plasma can in principal prevent access to the desired densities. We have demonstrated that densities well above Greenwald can be reached with a modest heating power at q~3 without MARFE instability. Conversely, MARFEs were produced below the Greenwald limit at high q operation. Core radiation limits have been encountered at low auxiliary heating power and densities 1.5–3 × n_{max}^{GW}. In all such cases off axis absorption of the neutral beam power due to high density was the main factor leading to radiative collapse of the core plasma.

Large amplitude MHD modes frequently prevent access to desired densities. Analysis of Mirnov oscillations shows growth of rotating tearing-type modes (m/n = 2/1) when the injected pellets cause large density perturbations. These modes often reduce energy and particle confinement back to L–mode levels and occasionally lock and cause a disruption. These modes are normally observed at moderate to high densities. However, at times they are stabilized with further density increase.

5. ELMs

The difficult engineering of the plasma facing components of future high powered long pulse devices is further aggravated by the transient high heat and particle fluxes during ELMs [57-61]. In order to estimate divertor heat and particle fluxes due to ELMs in ITER we have measured ELM energy losses in the main plasma and the resulting heat and particle flux in the divertor [57]. These ELM measurements were made in single null plasmas during the quasi steady state phase of ELMing H–mode. The auxiliary heating power was varied from 2.5 MW to 12.0 MW at plasma currents of 1.0 to 1.8 MA. At a toroidal field of 2.1 T, the current scan yielded a q_{95} range of 3.6 to 6.4.

Loss of energy per ELM was determined from diamagnetic measurements. Over the entire parameter regime the average energy loss per ELM varies from about 20 kJ to 70 kJ with an ELM frequency varying proportional to the injected power at 10 to 100 Hz . Roughly, the energy loss per ELM is constant with injected power and increases with plasma current. The fractional ELM energy loss, the ELM energy divided by the main plasma stored energy, is found to scale inversely with the injected power normalized by a parameter related to the H–mode power threshold, the product of the toroidal field and the plasma surface area. For a given set of parameters individual ELM energy loss may vary by more than a factor of two. The standard density dependence to the H–mode power threshold scaling has been removed because it relates to the density before the H–mode transition, not the density the H–mode eventually achieves. An ELM energy scaling, derived from a combination of DIII–D and ASDEX-Upgrade data, predicts a 3% energy loss for ITER, or 35 MJ.

Divertor heat flux is measured by IR cameras at two toroidal positions. The ELM heat deposition profiles at the target plate are flatter and less peaked than the quiescent profiles, but remain localized to the same region of the divertor. The inboard divertor ELM energy deposition accounts for ~11% of the injected power and the outboard ~10%. One half to all of the main plasma energy loss measured by diamagnetism is deposited on the divertor plates as heat flux. Bolometric measurements indicate that ≤15% of the ELM energy is radiated away, mostly in the divertor. The scatter in energy accountability, 50%–100%, is in large part due to measurement limitations. A comparison of the data from the two IR cameras indicates that the toroidal peaking factor is usually less than 1.5 when integrated over the entire ELM heat flux. Previous measurements of divertor tile currents on DIII–D [62] have shown greater toroidal asymmetry than this, but on a faster timescale.

Divertor particle fluxes are deduced from the saturation current of an array of divertor floor Langmuir probes. The particle flux profile during the quiescent period between ELMs is seen to peak near the separatrix with a spatial width similar to the quiescent heat flux. During an ELM the instantaneous particle flux can increase a factor of 10–50. However, because of the short ELM duration the increase in time-averaged particle flux due to ELMs is of the same order as that of the background during the quiescent periods. The ELM particle flux spatial distribution is nearly centered on the quiescent profile and has a similar shape. The total integrated ELM particle flux should not be correlated with the number of particles lost from the main plasma as the ejected particles must certainly recycle a number of times.

6. DIVERTOR MATERIAL STUDIES

The Divertor Material Evaluations Studies (DiMES) hydraulic mechanism allows insertion and retraction of graphite samples into the divertor floor of DIII–D. The samples are implanted with a Si depth marker in order to measure the net erosion or redeposition of the graphite [63,64]. Thin (100 nm) metal films of beryllium, vanadium, molybdenum and tungsten are also deposited on the samples to study the erosion, transport and redeposition properties of these trace metals in the all carbon plasma-facing environment of DIII–D. Figure 5 shows that the net loss of the carbon increases with increasing incident heat flux. These results were obtained during ELM-free and ELMing plasmas using both depth-marking [65] and colorimetry [66]. The REDEP code [67,68] has been used to simulate the measured net erosion at 0.7 MW/m^2. The code results show a gross erosion rate 5 times higher than the net, indicating a redeposition rate of 80%. At higher heat flux the net erosion is larger than the extrapolated value using this redeposition rate, indicating that the redeposition rate could be decreasing. This is despite the expected increase in local redeposition due to the increased divertor plasma density at the higher heat flux. The reason for this decreased redeposition may be linked to the ELMing behavior and studies are currently underway to explain this effect. One of the current ITER calculations for carbon divertor plate lifetimes [69] (90% redeposition, no angular dependence, loss rate ≈ 2 nm/s at 2.5 MW/m^2) is more optimistic than these measured rates; however, a better understanding of the roles of ELMs, density and geometry (e.g. oblique incidence) is needed for a true comparison.

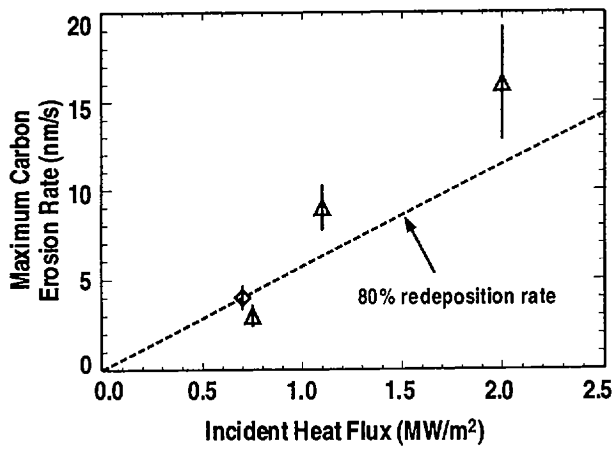

FIG. 5. Measured net carbon loss rate at DIII–D outer strike point versus incident heat flux measured by infrared thermography. Δ — ELMing H–mode, ◊ — ELM-free H–mode. The dashed line is the extrapolated net erosion rate from the REDEP calculated 80% redeposition rate of the ELM-free H–mode case.

The toroidal redeposited pattern of the metals has shown that the e-folding length of the metals decreases with increasing atomic number, and also ionization rate, as expected. A WBC code [70] Monte-Carlo simulation obtains good agreement with the experimental data indicating that an adequate understanding of the sputtering geometry, the ionization processes and the ion trajectories exists. The loss rates of the metal films are difficult to interpret due to the highly perturbing effect of the 1%–2% carbon background plasma depositing and eroding onto the metals. However, the measured trend of decreasing sputtering yield for increasing atomic number is in agreement with predicted sputtering yields for these materials [65].

7. SUMMARY

In summary, we have measured the plasma parameters over the entire cross section of the divertor plasmas which for the first time allow local transport studies in the divertor plasmas. It is found that detached plasmas display a complicated pattern of momentum and radiative heat loss along the field lines. Spectroscopic evidence, consistent with the measured plasma parameters and UEDGE modeling, shows evidence of copious volume recombination in detached plasmas. Furthermore, our analysis shows strong evidence of heat convection towards the divertor plate that in some cases greatly exceeds parallel electron heat conduction.

In several experiments we have utilized divertor pumping as an active tool for enhancing the plasma performance. A combination of gas puffing and divertor pumping was used to enrich impurity content of divertor plasmas and to obtain an extended divertor radiation zone. In the first experiment, based on direct measurements of neon and argon concentrations in the core plasma and pumping plenum, we have concluded SOL flows can increase divertor plenum impurity enrichment. In the second experiment we have observed nearly uniform radiation in the poloidal direction from the X–point to the target plate. This result is not consistent with purely classical parallel heat conduction and coronal equilibrium radiation. Thus we have concluded that convection and deviations from equilibrium must play a significant role in these plasmas. We also suspect the ELM heat pulse may transiently shift the radiative zone downstream. Divertor pumping in conjunction with pellet injection was used to overcome the divertor power balance limit and thus increase the core plasma density well beyond the Greenwald limit. We have achieved H–mode densities 1.5 times the Greenwald limit and L–mode densities as high as 3 times the limit. Finally, we have demonstrated that divertor pumping during the plasma shot can effectively replace He glow discharge cleaning (HeGDC), normally used between plasma shots to obtain high confinement.

From both our transport studies and performance enhancement experiments we conclude that SOL flows contribute significantly to the dynamics of heat and particle transport. Furthermore we have demonstrated that by a combination of gas puffing and divertor pumping forced flows can be generated which can be used to modify transport to our advantage, while maintaining the desired core plasma density. Taken together, these results show that the behavior of a divertor plasma near detachments departs from the conventional picture of a conduction limited heat flow and constant impurity fraction. The emerging picture appears far more favorable for the success of a radiative divertor.

REFERENCES

[1] FENSTERMACHER, M.E., et al., "Comprehensive 2D measurements of radiative divertor plasmas in DIII–D", Plasma–Surface Interactions (Proc. 12th Conf. St. Raphaël, 1996), to be published in J. Nucl. Mater.

[2] PETRIE, T.W., et al., "Investigation of electron parallel pressure balance in the scrape-off layer of deuterium-based radiative divertor discharges in DIII–D", ibid.

[3] ALLEN, S.L., et al., "Measurements of T_e and n_e with divertor Thomson scattering in radiative divertor discharges on DIII–D", ibid.

[4] WATKINS, J.G., et al., "Reciprocating and fixed probe measurements of n_e and T_e in the DIII-D divertor", ibid.

[5] JACKSON, G.L., et al., "Impurity control for enhanced divertor and edge radiation in DIII-D discharges", ibid.

[6] NILSON, D.G., et al., "Divertor Thomson scattering on DIII-D", to be published in Fusion Eng. Des.

[7] CARLSTROM, T.N., et al., "Initial operation of the divertor Thomson scattering diagnostic on DIII-D", High Temperature Plasma Diagnostics (Proc. 11th Int. Conf. Monterey, 1996) in press.

[8] LEONARD, A.W., et al., Rev. Sci. Instrum. **66** (1995) 1201.

[9] FENSTERMACHER, M.E., et al., "A tangentially viewing visible TV system for the DIII-D divertor", to be published in Rev. Sci. Instrum.

[10] WOOD, R.D., et al., "Measurement of divertor impurity concentrations on DIII-D", Controlled Fusion and Plasma Physics (Proc. 23rd Eur. Conf. Kiev, 1996), Vol. 20C, European Physical Society Geneva (1996).

[11] MOYER, R.A.., et al., "The role of turbulent transport in DIII-D scrape-off layer and divertor plasmas", Plasma–Surface Interactions (Proc. 12th Conf. St. Raphaël, 1996), to be published in J. Nucl. Mater.

[12] LASNIER, C.J., et al., "Characteristics of the scrape-off layer in DIII-D high-performance negative central magnetic shear discharges", ibid.

[13] ROGNLIEN, T., et al., A fully implicit, time dependent 2D fluid code for modeling tokamak edge plasmas, J. Nucl. Mater. **347** (1992) 196.
[14] PORTER, G.D., et al., "Divertor characterization experiments and modeling in DIII-D", Controlled Fusion and Plasma Physics (Proc. 23rd Eur. Conf. Kiev, 1996), Vol. 20C, European Physical Society, Geneva (1996); PORTER, G.D., et al., Simulation of experimentally achieved DIII-D detached plasmas using the EDGE code, Phys. Plasmas **3** (1996) 1967.
[15] FENSTERMACHER, M.E., UEDGE and DEGAS modeling of the DIII-D scrape-off layer plasma, J. Nucl. Mater. **220–222** (1995) 330.
[16] EVANS, T.E., et al., "Monte-Carlo impurity transport simulations in the edge of the DIII-D Tokamak using the *MCI* code", in Proc. *10th Int. Conf. on Stellarators, Madrid, in press.*
[17] OHYABU, N., et al., Density Oscillations in the Tokamak Plasma Boundary with an Expanded Divertor Channel, Rep. GA-A16484, General Atomics, San Diego, CA (1982).
[18] WEST, W.P., et al., "Divertor plasma studies on DIII-D: experiment and modeling", Controlled Fusion and Plasma Physics (Proc. 23rd Eur. Conf. Kiev, 1996), Vol. 20C, European Physical Society, Geneva (1996).
[19] PETRIE, T.W., et al., Contolled Fusion and Plasma Physics (Proc. 18th Eur. Conf. Berlin, 1991) Vol. 15C, Part III, European Physical Society, Geneva (1991) 237.
[20] HILL, D.N., et al., "Divertor plasma studies on DIII-D", Plasma Physics and Controlled Nuclear Fusion Research 1990 (Proc. 13th Int. Conf. Washington, 1990), Vol. 3, IAEA, Vienna (1991) 487.
[21] PETRIE, T.W., et al., J. Nucl, Mater. **196–198** (1992) 848.
[22] JANESCHITZ, G., et al., J. Nucl. Mater. **220–222** (1995) 73.
[23] WATKINS, M., REBUT, P., in 1992 International Conference on Plasma Physics (Proc. Conf. Innsbruck, 1992), Vol. 16C, Part II, European Physical Society, Geneva (1992) 731.
[24] JANESCHITZ, G., et al., J. Nucl, Mater. **220–222** (1995) 73.
[25] PETRIE, T.W., et al., "Radiative divertor experiments in DIII-D with deuterium injection", to be published in Nucl. Fusion.
[26] PETRIE, T.W., et al., Radiative divertor experiments in DIII-D with D2 injection, J. Nucl. Mater. **196–198** (1992) 848
[27] KALLENBACH, A., et al., Nucl. Fusion **35** (1995) 1231.
[28] MAHDAVI, M.A., et al., J. Nucl. Mater. **220–222** (1995) 13.
[29] MAINGI, R., et al., J. Nucl. Mater. **220–222** (1995) 320.
[30] GHENDRIH, P., et al., Phys. Plasmas **1** (1994)1929.
[31] SCHAFFER, M.J., et al., Nucl. Fusion **37** (1997) 83..
[32] STAMBAUGH, R.D., et al., in Plasma Physics and Controlled Nuclear Fusion Research 1994 (Proc. 15th Int. Conf. Seville, 1994), Vol. 1, IAEA, Vienna (1995) 83.
[33] ISLER, R., et al., Spectroscopic characterization of the DIII-D (in preparation).
[34] WEST, W.P., et al., "Modeling of impurity spectroscopy in the divertor and SOL of DIII-D using the 1-D multifluid model NEWT1D" (Proc. Int. Conf. Plasma Physics, Nagoya, 1996).
[35] MAHDAVI, M.A., et al., Phys. Rev. Lett. **47** (1982) 1062.
[36] NEUHAUSER, J., et al., Nucl. Fusion **24** (1984) 39.
[37] MAHDAVI, M.A., et al., J. Nucl. Mater. **111&112** (1982) 355.
[38] BOSCH, H.-S., et al., Phys. Rev. Lett. **76** (1996) 2499.
[39] SCHAFFER, M.J., et al., Nucl. Fusion **35** (1995) 1000.
[40] SCHAFFER, M.J., et al., "Direct measurement of divertor neon enrichment in DIII-D", Plasma–Surface Interactions (Proc. 12th Conf. St. Raphaël, 1996), to be published in J. Nucl. Mater.
[41] WADE, M.R., et al., Phys. Plasmas **2** (1995) 2357.
[42] WADE, M.R., et al., Phys. Rev. Lett. **74** (1995) 2702.
[43] CAROLAN, P.G., PIOTROWICZ, V.A., Plasma Phys. **25** (1983) 10.
[44] ALLEN, S.L., et al., J. Nucl. Mater. **196–198** (1992) 804.
[45] POST, D., et al., J. Nucl. Mater. **220–222** (1995) 1014.

[46] MAHDAVI, M.A., et al., "Stability of a radiative mantle in ITER", Plasma–Surface Interactions (Proc. 12th Conf. St. Raphaël, France, 1996), to be published in J. Nucl. Mater.
[47] LEONARD, A.W., et al., Distributed divertor radiation through convection in DIII-D, submitted to Phys. Rev. Lett.
[48] MAHDAVI, M.A., et al., in Controlled Fusion and Plasma Physics (Proc. 20th Eur. Conf. Lisbon, 1993), Vol. 17C, Part I, European Physical Society, Geneva (1993) 647.
[49] MAINGI, R., et al., "Comparison of wall/divertor deuterium retention and plasma fueling requirements on the DIII-D, TdeV, and ASDEX-Upgrade tokamaks", Plasma–Surface Interactions (Proc. 12th Conf. St. Raphaël, France, 1996), to be published in J. Nucl. Mater.
[50] MAINGI, R., et al., Nucl. Fusion **36** (1996) 245.
[51] GREENWALD, M., et al., Nucl. Fusion **28** (1988) 2199.
[52] BORRASS, K., Nucl. Fusion **31** (1991) 1035.
[53] PETRIE, T.W., et al., Nucl. Fusion **33** (1993) 929.
[54] GIBSON, A., Nucl. Fusion **16** (1976) 546.
[55] PERKINS, F., IAEA-CN-64/FP-24, these Proceedings, Vol. 2.
[56] BAKER, D.R., et al., Nucl. Fusion **22** (1982) 807.
[57] LEONARD, A.W., et al., "Divertor heat and particle flux due to ELMs in DIII-D and ASDEX-upgrade", Plasma–Surface Interactions (Proc. 12th Conf. St. Raphaël, 1996), to be published in J. Nucl. Mater.
[58] GOHIL, P., et al., Phys. Rev. Lett. **61** (1988) 1603.
[59] ZOHM, H., et al., Plasma Phys. Control. Fusion **36** (1994) 1307.
[60] ZOHM. H., et al., Nucl. Fusion **35** (1995) 543.
[61] DIETZ, K.J., et al., in Plasma Physics and Controlled Nuclear Fusion Research 1994 (Proc. 15th Int. Conf. Seville, 1994), Vol. 2, IAEA, Vienna (1995) 491.
[62] EVANS, T.E., et al., J. Nucl. Mater. **220–222** (1995) 235.
[63] BASTASZ, R., et al., J. Nucl. Mater. **220–222** (1995) 310.
[64] WAMPLER, W.R., et al., "Erosion and deposition of metals and carbon in the DIII-D divertor", Fusion Reactor Materials (Proc. 7th Int. Conf. Obninsk, 1995), to be published in J. Nucl. Mater.
[65] WHYTE, D.G., et al., "DIMES divertor Erosion Experiments on DIII-D", Plasma–Surface Interactions (Proc. 12th Conf. St. Raphaël, 1996), to be published in J. Nucl. Mater.
[66] WESCHENFELDER, F., et al., "In-situ measurement of erosion/deposition in the DIII-D divertor by Colorimetry", Controlled Fusion and Plasma Physics (Proc. 22nd Eur. Conf. Bournemouth, 1995), Vol. 19C, Part II, European Physical Society, Geneva (1995) 281.
[67] HUA, T.Q., BROOKS, J.N., J. Nucl. Mater. **220–222** (1995) 342.
[68] BROOKS, J.N., Nucl. Techol./Fusion **4** (1983) 33.
[69] JANESCHITZ, G., et al., J. Nucl. Mater. **220–222** (1995) 73.
[70] BROOKS, I.N., Phys. Fluids **8** (1990) 1858.

EDGE AND DIVERTOR PHYSICS IN ASDEX UPGRADE WITH EMPHASIS ON DENSITY LIMIT CHARACTERISTICS

V. MERTENS, A. HERRMANN, A. KALLENBACH, M. KAUFMANN, J. NEUHAUSER, J. SCHWEINZER, K. BEHRINGER, K. BÜCHL, A. CARLSON, R. DUX, G. HAAS, P.T. LANG, R. LANG, F. MAST, B. NAPIONTEK, M. WEINLICH, ASDEX UPGRADE and NBI TEAMS
Max-Planck-Institut für Plasmaphysik,
Euratom–IPP Association,
Garching and Berlin, Germany

Abstract

EDGE AND DIVERTOR PHYSICS IN ASDEX UPGRADE WITH EMPHASIS ON DENSITY LIMIT CHARACTERISTICS.

A large SOL database covering a wide range of ASDEX Upgrade plasma parameters embodying data measured at the outer midplane and divertor has been built up to support the development of reliable scalings necessary for ITER. Clear dependencies between the neutral particle flux in the divertor and, e.g., the midplane separatrix density could be established. Additionally, the density operational space in the vicinity of the Greenwald limit has been successfully investigated. In contrast to the power independent Greenwald scaling, the disruptive L-mode density limit in terms of global parameters has been found to increase moderately with heating power: $\bar{n}_e^{DL} \propto P_{heat}^{0.3}$. In terms of local edge parameters the dependencies become significantly stronger. Additionally, the Greenwald limit could be exceeded by up to 40%. Since the H-mode density limit is defined by the non-disruptive H $\rightarrow$ L-mode transition, the transition threshold has been studied for radiative mantle and/or very high recycling discharges. For impurity seeded plasmas the generally accepted threshold scaling $P \propto \bar{n}_e B_t$ with vanishing hysteresis is a good approximation. Very high recycling discharges are, however, characterized by a practically power independent threshold. In the vicinity of the Greenwald limit all discharges revert to the L-mode. In the gas refuelled H-mode the Greenwald limit could not be exceeded. However, controlled pellet injection into H-mode plasmas yields phases with $\bar{n}_e \approx 1.5\,\bar{n}_e^{Greenwald}$.

1. Introduction

The main topic of the research programme of ASDEX Upgrade is the investigation of the boundary and the divertor performance at high plasma densities and heating powers. Previous research has shown that the plasma edge behaviour can significantly influence the quality of the bulk plasma. Reactor designs like the ITER (EDA) concept aspire to operation in the high density and power range. High bulk density is needed for high fusion yield and high edge density for effective power removal by radiation. The expected power flowing towards the divertor plates in this concept can reach values which are too large to handle. Precise knowledge of scalings of edge parameters and detachment behaviour of the divertor is, therefore, of crucial importance. One possibility to attenuate this engineering power load problem might be the removal of energy by means of additional impurity radiation in the boundary. Furthermore, the ITER projected line averaged density [1] is significantly beyond the empirical Greenwald limit $\overline{n}_e^{GW} = I_p / (\pi a^2)$ $[10^{20} m^{-3}, MA, m]$, which describes quite successfully the density limit (DL), even on machines of different sizes [2]. Presently, the most probable methode to achieve long lasting phases with average densities $> \overline{n}_e^{GW}$ seems to be the repetitive injection of pellets. The maximum achievable density is restricted in the L-mode normally by a disruption and in the H-mode by an $H \rightarrow L$ mode transition (H-mode density limit). Both limits are of completely different physical nature. Moreover, a serious problem connected with high $\overline{n}_e$ is the deterioration of the energy confinement with rising edge density i.e. increasing recycling fluxes. Since the reactor concepts base on H-mode confinement, the accessibility of the H-mode at the desired high densities and the conservation of improved confinement have to be demonstrated. The related experimental data base is still not comprehensive enough for certain extrapolation to ITER (see Sect. 2). Especially the behaviour of the $L \leftrightarrow H$ mode transition threshold at high radiative and/or high recycling scenarios has to be investigated (see Sect. 3).

Our investigations cover lower single null discharges (R = 1.65 m, a = 0.5 m, $\kappa \approx 1.6$) with plasma currents up to 1.2 MA and NBI heating powers up to 10 MW. A centrifuge allows to inject strings of pellets with repetition rates up to 80 Hz and velocities up to 1.2 km/s. Highly radiative discharges are performed by injecting Ne, Ar or Nitrogen gas into the main chamber. ASDEX Upgrade is well equipped with diagnostics to measure boundary and divertor profiles. Much effort has been undertaken in the last years to improve the performance of these diagnostics like Lithium beam, edge ECE, Thomson scattering, Langmuir probes, thermography etc.

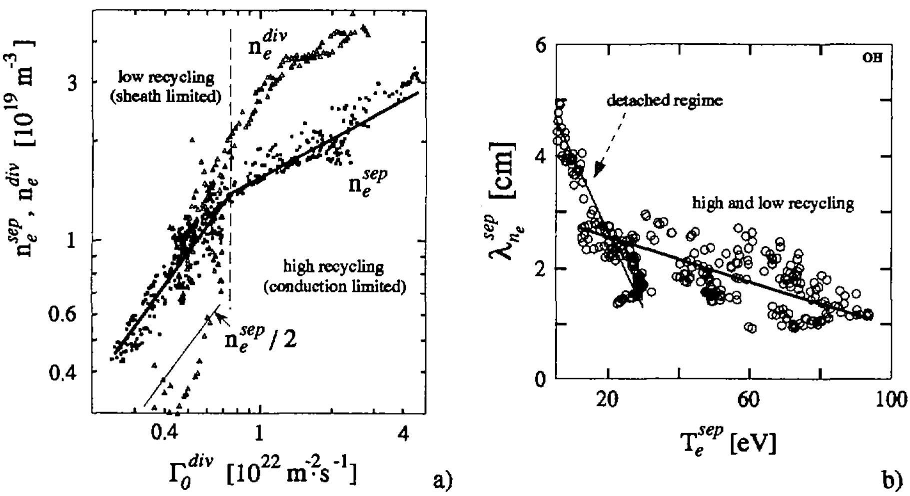

Figure 1: *a) Dependence of the divertor and separatrix density on the neutral gas flux density for the low and high recycling SOL-regime.*
b) SOL density fall-off lengths vs. midplane separatrix temperature for different SOL-regimes. Auxiliary heated discharges show the same behaviour.

2. Edge and Divertor Behaviour

2.1 *Characterization of Scrape-off Layer (SOL) Regimes*

The heat flux across the separatrix P_{sep} as well as the SOL conditions are varied over a wide range at ASDEX Upgrade resulting in different SOL regimes, whose features are presented in the following. The dependence of the divertor n_e^{div} and separatrix density n_e^{sep} on the neutral particle flux density Γ_0^{div} measured at the outer divertor branch is shown in Fig. 1 a). At low neutral flux densities, the separatrix density increases linearly. For higher values of Γ_0^{div} a weaker dependence follows from a regression analysis: $n_e^{sep} \propto {\Gamma_0^{div}}^{0.5}$. The point, where the separatrix density becomes nonlinear with the neutral flux marks the change from the low to the high recycling divertor regime. Below this point, the divertor density is about half of the separatrix density as it is expected for pressure balance. The temperature ratio between midplane and divertor is found to be about unity [3]. The electron temperature at the separatrix is between 50 and 100 eV and the heat transport is limited by the heat transport through the sheath. The change to the high recycling divertor starts when the divertor region becomes dense for recycled particles, because the mean free path for neutrals comes into the same order as the extension of the divertor region [4]. At higher densities the separatrix temperature decreases and the heat transport is limited by the temperature gradient between separatrix and divertor. This change from sheath limited to conduction limited heat transport already occurs in ohmic discharges with moderate densities, so that for most of the discharges performed in ASDEX Upgrade the heat transport is conduction limited. This is supported by a scaling of the H-mode electron temperature at the separatrix with the power crossing the separatrix showing a $T_e^{sep} \propto P_{sep}^{0.4}$ dependence [4]. A linear dependence is expected for convective heat transport and a 4/9 dependence for the conduction limited case [5]. For both regimes, the heat flux profile at the midplane and that measured at the divertor plate are comparable [3,6]. The density fall-off lengths in the midplane measured by the Lithium beam diagnostic and the reciprocating Langmuir probe show a moderate increase with

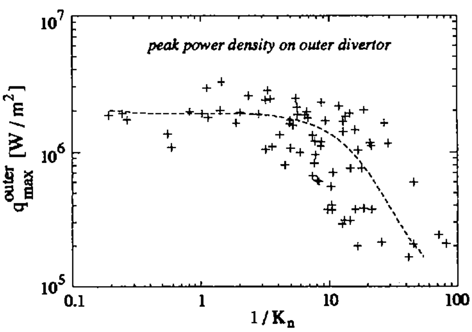

Figure 2: *Dependence of the peak power density measured by thermography at the outer plate on the collisionality ($1/K_n$) in the SOL.*

decreasing midplane temperature (see Fig. 1 b). At temperatures below about 30 eV the decay lengths increase strongly, due to the fact that the divertor operates in the detached regime and the perpendicular momentum transport broadens the power carrying sheath. In this regime the heat flux to the divertor is strongly reduced compared to midplane values [3,6] and a significant pressure drop occurs. The heat transport regimes discussed above may be described in terms of the collisionality in the SOL, expressed by the inverse Knudsen number ($1/K_n$ = *flux tube length*/λ_{ee}). Figure 2 shows the change of the maximum heat flux density with increasing $1/K_n$, i.e. collisionality. The inverse Knudsen number is about 10 when the mean free path of the high energy electrons λ_{ee}, which mainly contribute to the heat conduction, becomes comparable to the flux tube length. It marks the change from the sheath limited to the conduction limited regime. The decrease of the maximum heat load at $1/K_n > 10$ is due to radiation losses which increase at low temperatures, and a broadening of the power carrying sheath. The following investigations of the density limit concentrate on the detached regime with low target power load.

2.2 *Detachment Behaviour and L-mode Density Limit*

As a first example, in Figure 3 we describe the behaviour of a DL discharge during its density build-up. After the maximum heating power P_{heat} has been established at t = 1.7 s, one can clearly see the reduction of the divertor temperature with rising $\overline{n}_e$ by the decrease of the carbon C_{div}^{III} signal, which is measured closely above the outer divertor plate. This decrease indicates the begin of energy detachment. The quench of C_{div}^{III} is more pronounced than that of the ion saturation current I_{sat} measured at the target plate, since both carbon erosion and excitation rate of the observed transitions decrease rapidly with T_e^{div}. The slight drop at 2.1 s marks the formation of a small X-point Marfe. Towards higher densities, the Marfe expands into the region of closed flux surfaces, which is an unequivocal precursor of a density limit disruption. This growth can clearly be seen e.g. by a normalized bremsstrahlung signal viewing slightly above the X-point. All analyzed density limit disruptions are preceded by this Marfe and divertor detachment sequence.

The reduction of the particle flux is found to be strongly correlated to the onset of hydrogen recombination radiation in the divertor throat [7]. Figure 4 compares the spectra measured in the outer divertor branch exhibiting the hydrogen continuum radiation and Balmer lines at low and high $\overline{n}_e$. During the divertor temperature drop the brightness of the Balmer lines increases by up to two orders of magnitude, although, owing to the relatively high excitation threshold energy of > 10 eV, the excitation rate becomes significantly smaller. This observation can only be explained by an alternative population mechanism of excited neutral hydrogen atoms which becomes dominant at these low temperatures ($T_e^{div} < 5$ eV). This mechanism is obviously the recombination of hydrogen ions in the cold divertor plasma. Model calculations show that the quenching of the particle flux to the target can hardly be explained by ion-neutral collisions alone. Recombination in the divertor throat volume is essential to explain the main detachment characteristics [8].

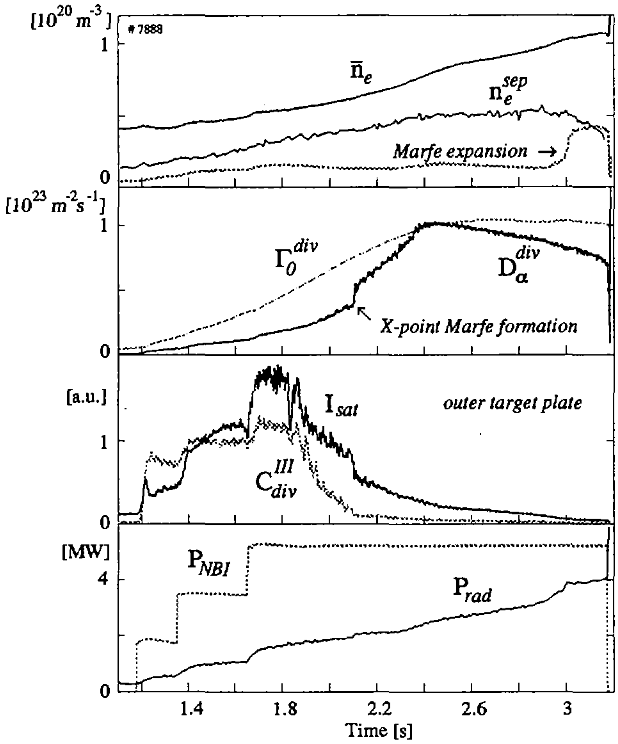

Figure 3: *Typical time traces of a L-mode DL discharge (I_p = 0.6 MA, q_{95} = 5). The 'Marfe expansion' indicating signal is a normalized bremsstrahlung line integral measured slightly above the X-point.*

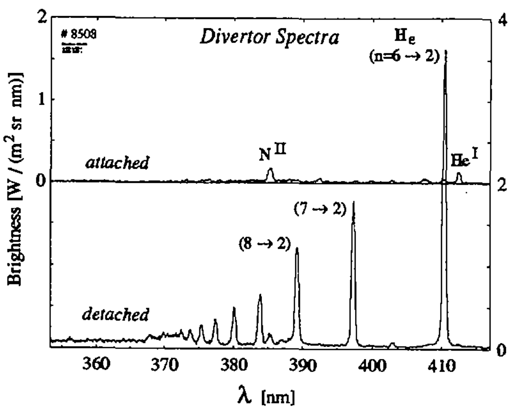

Figure 4: *Spectra measured in the outer divertor leg for an attached low density (upper spectrum) and a detached high density (lower spectrum) plasma.*

After detachment, further density increase triggers strong Marfe expansion and a subsequent density limit disruption. The Greenwald scaling proposes the density limit to be heating power independent. Experiments, however, have shown that in low Z_{eff} plasmas with only intrinsic impurities the DL can clearly be improved by increasing P_{heat}. Figure 5 a) shows the maximum achieved $\overline{n}_e$ versus heating power for NBI heated hydrogen and deuterium L-mode discharges. Hydrogen discharges at low plasma currents achieved the highest normalized densities $\overline{n}_e^{DL}/\overline{n}_e^{GW} \lesssim 1.4$. Hydrogen plasmas enable higher normalized densities than deuterium ones, since their radiation losses are systematically smaller. The limits scale like $\overline{n}_e^{DL} \propto P_{heat}^{0.3}$, except in the impurity driven HRL ('highly radiative L-mode') plasmas, which show nearly no power dependence. The corresponding $\overline{Z}_{eff}$ is of the order of 1.6 without impurity seeding and of about 3.5 with additional impurity injection.

The present understanding of the DL as an edge density limit focusses the view on the boundary parameters. Plotting the edge densities as function of P_{heat} or, more instructively, as function of P_{sep}, the power dependence is even more pronounced (see Fig. 5 b). The data are taken just before the strong Marfe expansion slightly below the DL. For H^+ and D^+ the separatrix densities increase approximately with $n_e^{sep} \propto P_{sep}^{0.6}$. Taking the net power flux into the divertor $P_{net} = P_{heat} - P_{rad}^{tot}$ instead of P_{sep}, a similar strong dependency results. Moreover, the separatrix density grows like $n_e^{sep} \propto \overline{n}_e^{\,2}$, reflecting the strong broadening of the electron density profile towards high $\overline{n}_e$. This may help in a reactor to radiate enough power at the boundary at moderate Z_{eff} values, since the additional radiation potential at a given Z_{eff} rises strongly with density [9]. A more detailed discussion of the boundary parameter behaviour is presented by [10, 11, 12]. The energy confinement in the L-mode is nearly independent of the recycling flux at low Z_{eff}, but rises in the HRL-mode with increasing $\overline{n}_e$ and P_{heat} up to H-mode values [13].

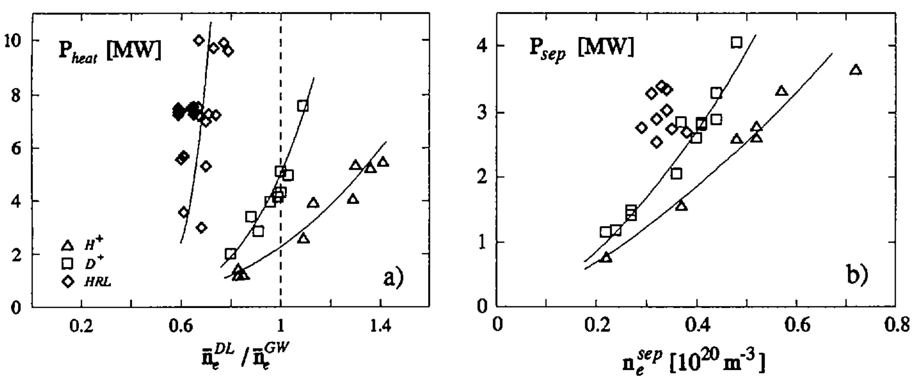

Figure 5: *L-mode density limit data plotted in global and local parameters.*

3. The L-H-L-mode Thresholds at High Densities

3.1 *Radiative Mantle Scenarios*

Since not only high density but also H-mode confinement is urgently desired in reactor operation, the accessibility of high quality H-modes (with or without auxiliary impurity injection) has to be demonstrated. The $H \rightarrow L$-mode threshold (as effective H-mode density limit) or equivalently the $L \rightarrow H$ threshold is generally accepted to depend mainly on the toroidal field B_t, $\overline{n}_e$ and, in a not well-established manner, on the edge recycling. Instead of the total heating power, P_{sep} is more conclusive in determining the threshold. The following equation (1) is a good approximation [14]:

$$P_{sep}^{L \rightarrow H} = P_{heat} - P_{rad}^{bulk} = 1.25 \cdot \overline{n}_e \cdot B_t \cdot (2/A_{plasma}) \; [MW, 10^{20} m^{-3}, T, amu]$$

The corresponding value for the $H \rightarrow L$ back transition is about a factor of 2 lower, known as the H-mode hysteresis [15]. Without strong additional impurity radiation and/or deuterium puffing the transitions between L- and H-mode only occur at rather low powers. For these conditions, also a clear difference between L- and H-mode energy confinement is observed.

If a discharge is in H-mode, its behaviour changes considerably when impurity injection is applied in combination with high heating powers. In the case of e.g. Ne seeding, 2/3 of the main chaimber Ne radiation is radiated close to but inside the separatrix [14]. Therefore, a considerable fraction of the power

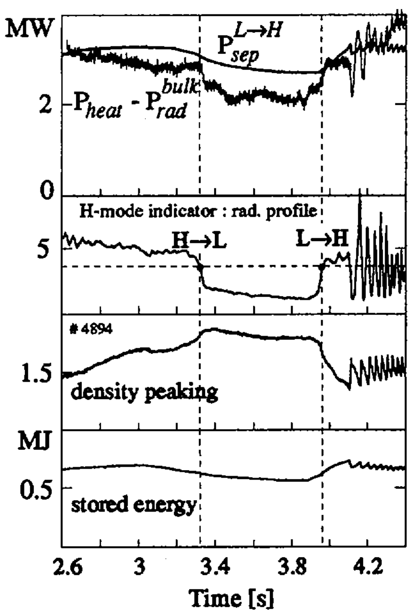

Figure 6: *Typical time traces for a Ne puff driven $H \rightarrow L$ and $L \rightarrow H$ transition demonstrating the loss of L-H-L hysteresis.*

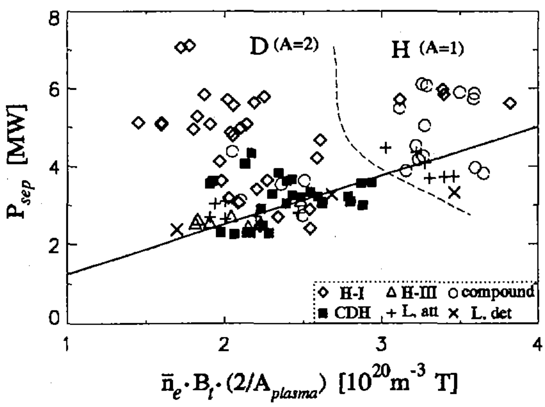

Figure 7: *Operational diagram of low and high radiative H^+ and D^+ discharges.*

flux is lost by radiation before being conducted across the separatrix. At very high radiation levels, when only a small amount of the heating power reaches the SOL, the H-mode degrades into an L-mode. Under these conditions, the otherwise pronounced difference in confinement and other properties between L- and H-mode becomes weak. Only e.g. peaking of the electron density profile and distinct changes in the radiation profile (see Fig. 6) mark the back transition. Furthermore, it is found that the L-H-L hysteresis seems to vanish. Fig. 6 compares the power flux into the SOL derived from P_{heat} and bolometer measurements with the prediction $P_{sep}^{L \to H}$. It is clearly seen that the usually low $H \to L$ threshold in increased up to the value of the $L \to H$ threshold, which is little or not affected. As an overview, figure 7 shows P_{sep} versus $\overline{n}_e \cdot B_t$ for discharges with low and high radiation levels. The solid line indicates the 'standard' $L \to H$ threshold. The H-mode threshold according to equation (1) and the assumption of the absence of the L-H-L hysteresis in these scenarios gives a proper description of the operational space of radiative scenarios. All densities in this figure stay below the Greenwald limit.

3.2 *Very High Recycling*

Since, in terms of global parameters, the Greenwald scaling imposes a heating power independent DL and the $L \to H$ mode operational limit is power dependent, both limits intersect. For ITER parameters the required operation density is beyond the Greenwald limit. There exists, however, only limited experience in this operational window. Especially the behaviour of the $L \leftrightarrow H$ threshold is not well known and deviations from the linear scaling might be possible. The strategy of the experiments presented in the following is guided by the aim to explore the $L \leftrightarrow H$ limit at high densities without impurity injection by approaching it from the low power L-mode and from the high power H-mode region, respectively. To combine the $L \to H$ threshold and the Greenwald scaling

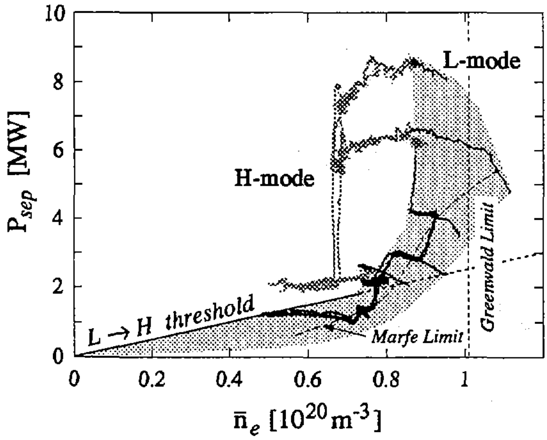

Figure 8: *Traces for low Z_{eff}, I_p = 0.8 MA, q_{95} = 4 deuterium discharges.*

a constant B_t has been chosen. Figure 8 exhibits the traces of several discharges in the P_{sep} versus $\overline{n}_e$ plane. The traces show that at low density equation (1) gives a good separation of the L/H operation space. At higher line averaged and neutral flux densities the discharges enter the operational space in the L-mode where the presently accepted scalings propose the existence of H-mode plasmas. Close below the Greenwald limit the threshold becomes practically independent of power and also the hysteresis is gone. The dashed-dotted line represents the start density for strong Marfe expansion. It is found that the discharges enter the region close below the Greenwald limit always in L-mode independent of their preceding confinement modes. The maximum densities in H-mode only reach 0.8-0.9 $\overline{n}_e^{GW}$. τ_E degrades gradually with increasing recycling towards L-mode level [16]. The region at $\overline{n}_e \approx 1 \cdot 10^{20}m^{-3}$ in Fig. 8 corresponds to $\approx 2 \cdot 10^{20}m^{-3}T$ in Fig. 7. The main difference is that in these cases the recycling reaches values significantly higher than those in the impurity radiative mantle scenarios presented above.

3.3 *High Densities with Pellet Injection*

To achieve densities beyond the Greenwald limit injection of solid pellets has been shown to be very successful. One reason is the very low fuelling efficiencies of gas puff scenarios can partly be overcome hereby. To obtain quickly and stationary reactor relevant densities, we combined moderate gas puffing and repetitive pellet injection into H-modes. With pellet injection alone $\overline{n}_e$ could not be successfully increased. Furthermore, as a special tool to maintain long lasting high density phases we performed a control circuit using a bremsstrahlung signal as a measure of $\overline{n}_e$ and inhibit the injection of pellets when the preprogrammed density is reached. Using this setup stationary phases of up to 1.5 $\overline{n}_e^{GW}$ have been achieved (see Fig. 9) [13,17]. A disadvantage of this scenario is a significant instantaneous mass loss due to the formation of an outward

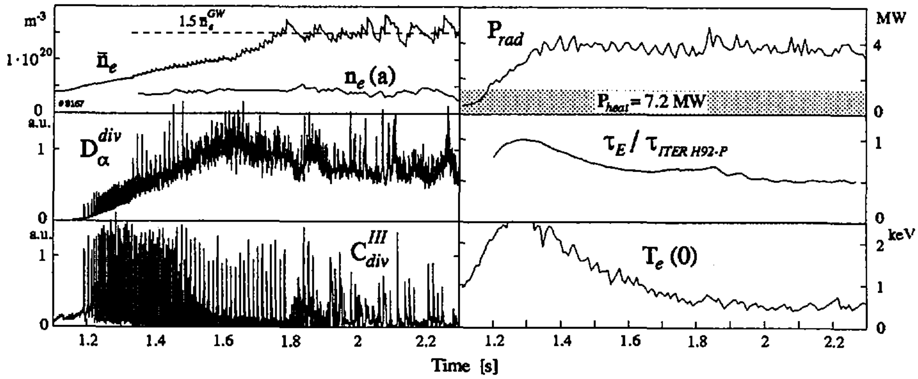

Figure 9: *Feedback controlled pellet refuelled discharge with preprogrammed* $1.5 \cdot \overline{n}_e^{GW}$. *After about 1.9 s the discharge falls from H-mode back into L-mode.*

drifting high-β plasmoid and additional ELM losses triggeredby each pellet. The corresponding fuelling efficiencies in H-mode are quite low [17]. Moreover, the discharges fall back into L-mode and do not develop improved confinement despite density peaking. However, recent experiments with pellet injection from the high toroidal field side into H-mode plasmas have shown dramatically enhanced fuelling efficiencies and preserved H-mode confinement up to $\lesssim \overline{n}_e^{GW}$ [10, 18].

4. Summary and Conclusions

A large SOL database covering a wide range of ASDEX Upgrade plasma parameters embodying data measured at the outer midplane and divertor has been built up to support the development of reliable scalings necessary for ITER. Clear dependencies between the neutral flux in the divertor and e.g. the midplane separatrix density could be established.

Towards high densities, the operational space in the vicinity of the Greenwald limit has been successfully investigated. In L-mode the DL is found to be always connected to the development of divertor detachment, Marfe expansion and disruption. Concomitantly, the Greenwald limit is exceeded by up to 40 %. In contrast to the Greenwald scaling, the L-mode density limit is found to clearly increase with power. On the other hand, gas refuelled H-mode plasmas do not exceed the Greenwald limit in either the low or high Z_{eff} cases. In radiative mantle scenarios, the $P^{L \to H} \propto \overline{n}_e \cdot B_t$ threshold scaling is still a good assumption, but the hysteresis is lost. At very high recycling the threshold, additionally, becomes practically independent of power close below the Greenwald limit. The experimental findings suggest that the loss of hysteresis is caused by the assimilation of the L- and H-mode confinement at high recycling levels.

As outlook, a promising possibility to reach densities beyond the Greenwald limit preserving H-mode confinement is the injection of pellets from the high toroidal field side. While the standard injection from the low field side into high density H-mode phases has been found to yield low fuelling efficiencies, degraded confinement and $H \to L$-mode back transitions, recent experiments from the high field side demonstrate very high efficiencies and unperturbed H-mode confinement up to $\overline{n}_e^{GW}$.

The problem for ITER to remove the power preferably uniformly in the boundary asks for high edge densities in order to keep bulk Z_{eff} low. The high recycling scenarios exihiting the $n_e^{sep} \propto \overline{n}_e^2$ scaling are clearly favourable in this respect. In contrast, additional impurity seeding leads to high Z_{eff} in present experiments. Obviously, optimization of the radiation profile e.g. by an optimal choice of the radiators is necessary for ITER.

REFERENCES

[1] JANESCHITZ, G., et al., Plasma Phys. Control. Fusion **37** (1995) 11A, A19.
[2] GREENWALD, M., et al., Nucl. Fusion **28** (1988) 2199.
[3] ROHDE, V., et al., in Controlled Fusion and Plasma Physics (Proc. 23rd Eur. Conf. Kiev, 1996), Vol. 20C, European Physical Society, Geneva (1996).
[4] SCHWEINZER, J., et al., ibid.
[5] KEILHACKER, M., et al., Phys. Scr. T2/2 (1982) 443.
[6] HERRMANN, A., et al., in Controlled Fusion and Plasma Physics (Proc. 22nd Eur. Conf. Bournemouth, 1995), Vol. 19C, Part III, European Physical Society, Geneva (1995) 241.
[7] NAPIONTEK, B., et al., (in preparation).
[8] BORRASS, K., et al., in Plasma-Surface Interactions (Proc. 12th Conf. St. Raphael, 1996) (in press).
[9] MATTHEWS, G.F., et al., ibid.
[10] KAUFMANN, M., et al., IAEA-CN-64/O1-5, this volume.
[11] SCHNEIDER, R., et al., IAEA-CN-64/D3-1, these Proceedings.
[12] SUTTROP, W., et al., in Controlled Fusion and Plasma Physics (Proc. 23rd Eur. Conf. Kiev, 1996), Vol. 20C, European Physical Society, Geneva (1996).
[13] MERTENS, V., et al., ibid.
[14] KALLENBACH, A., et al., Plasma Phys. Control. Fusion (in press).
[15] RYTER, F., et al., Plasma Phys. Control. Fusion **36** (1994) A99.
[16] RYTER, F., et al., IAEA-CN-64/AP1-5, this volume.
[17] LANG, P.T., et al., in Controlled Fusion and Plasma Physics (22nd Eur. Conf. Bournemouth, 1995), Vol. 19C, Part II, European Physical Society, Geneva (1995) 449.
[18] LANG, P.T., et al. (in preparation).

DISCUSSION

M. KEILHACKER: Let me first congratulate the ASDEX team on their very interesting work on the characteristics of the density limit.

Could you please elaborate a bit more on how far the pellets penetrated into the H mode plasma in the two cases of injection from the low and the high field side, respectively.

V. MERTENS: Pellet penetration was about 5–8 cm from the low field side, and about 17–19 cm from the high field side ($v_p \approx 130$ m/s). They are thus within the ELM region on the outer side, and also on the inner side, even taking the Shafranov shift into account.

Y. KAMADA: Regarding the P_{th} for back-transition at high recycling, have you observed I_p dependence or q dependence for P_{th}?

V. MERTENS: At very high recycling, where the transition threshold is independent of power, no difference or only a slight difference has been found between $3 < q_{95} < 4$. The experiments have been done only at one I_p value.

VARIATION OF THE DIVERTOR GEOMETRY IN ALCATOR C-MOD*

B. LIPSCHULTZ, J.A. GOETZ, I.H. HUTCHINSON,
B. LaBOMBARD, G.M. McCRACKEN[1], Y. TAKASE,
J.L. TERRY, P. BONOLI, S.N. GOLOVATO[2], P. O'SHEA,
M. PORKOLAB, R.L. BOIVIN, F. BOMBARDA[3], C.L. FIORE,
D.T. GARNIER, R.S. GRANETZ, M.J. GREENWALD, S.F. HORNE[4],
A.E. HUBBARD, J.H. IRBY, E.S. MARMAR, M. MAY[5],
A. MAZURENKO, J. REARDON, J.E. RICE, C. ROST,
J.M. SCHACHTER, J.A. SNIPES, P.C. STEK, R.L. WATTERSON[6],
J. WEAVER[7], B. WELCH[7], S.M. WOLFE
Plasma Fusion Center,
Massachusetts Institute of Technology,
Cambridge, Massachusetts,
United States of America

Abstract

VARIATION OF THE DIVERTOR GEOMETRY IN ALCATOR C-MOD.

The paper compares divertor characteristics of three different divertor geometries varying from a 'slot' through the standard Alcator C-Mod 'vertical-plate' to a more open 'flat-plate' configuration. Differences are primarily found in the density threshold for detachment, which is 50–80% higher for the flat-plate geometry. It is inferred that volumetric emission along a flux surface is higher in the case of vertical-plate operation, leading to lower temperatures at the plate and thus detachment. Other characteristics such as impurity screening, Z_{eff} and neutral pressures are unaffected.

1. Introduction

The ability to control divertor conditions is an important factor in determining the viability of the tokamak concept. Because of the very large parallel power flows envisaged for tokamak reactors (e.g. $q_{\|,SOL} \leq 1.0$ GW/m^2 in ITER) techniques must be developed to dissipate these power flows before they reach the plates. At the same time, any technique controlling divertor conditions must not adversely affect the core plasma. Divertor detachment is being studied as a method of achieving these goals [e.g. 1-4].

---

* Supported by US Department of Energy contract DE-AC02-78ET51013.

[1] Presently at JET Joint Undertaking, Abingdon, Oxfordshire, United Kingdom.

[2] Presently at Tokyo Electron America, Beverly, Massachusetts, USA.

[3] Associazione Euratom-ENEA sulla Fusione, Frascati, Italy.

[4] Presently at ASTeX, Woburn, Massachusetts, USA.

[5] Johns Hopkins University, Baltimore, Maryland, USA.

[6] Presently at CPClare Corporation, Lexington, Massachusetts, USA.

[7] University of Maryland, College Park, Maryland, USA.

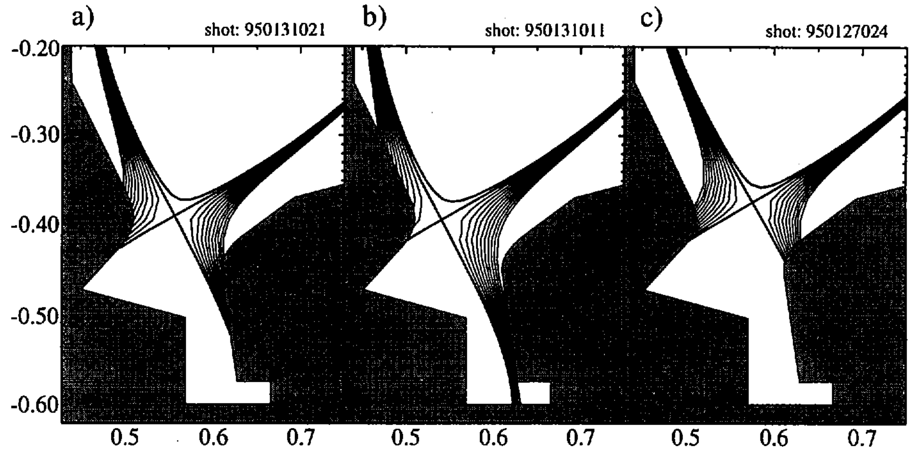

FIG. 1. Typical equilibria for (a) vertical-plate, (b) slot and (c) flat-plate equilibria. The break in slope between vertical and horizontal sections of the outer divertor plate ('nose') is indicated by an N.

Currently, the divertor geometry in a number of experiments is being modified to allow the normal to the wetted divertor area to be directed away from the confined plasma and the opening into the divertor from the main chamber to be narrower. These changes could lead to better neutral and impurity retention in the divertor and thus less adverse effects on the core plasma [3,5-7]. There is at present minimal experimental data to support these changes. We have explored this question by changing the equilibrium flux surfaces with fixed divertor hardware, effectively changing the divertor geometry. The plasmas used in these studies were all ohmically heated 0.8 MA plasma current, 5.3 T toroidal magnetic field and a single-null equilibrium (lower x-point). The toroidal magnetic field and current are both clockwise viewed from the top of the machine.

2. Experimental Results

Although the position of the C-Mod divertor surfaces is fixed in the vacuum vessel, the flux surface equilibria can be varied such that the separatrix strike point is located on different sections of the outer divertor plate. Different effective outer divertor configurations are produced in this manner. We concentrate on the outer divertor plate because the outer divertor leg is hotter and the equilibrium (effective divertor geometry) can be varied more easily. In figure 1 we show typical equilibria for a) the vertical-plate (the standard C-Mod and proposed ITER configuration) with strike points on vertical section; b) 'slot' with strike points at the bottom of a slot formed by the outer divertor and the parts of the vacuum vessel; and c) 'flat-plate' with strike point above the 'vertical' regions. The names used for these equilibria are not meant to be physically accurate, but only for reference.

2.1 Detachment threshold comparison

The detachment of plasma on a particular flux surface from the outer divertor plate is detected when the ratio of electron stagnation pressure at the

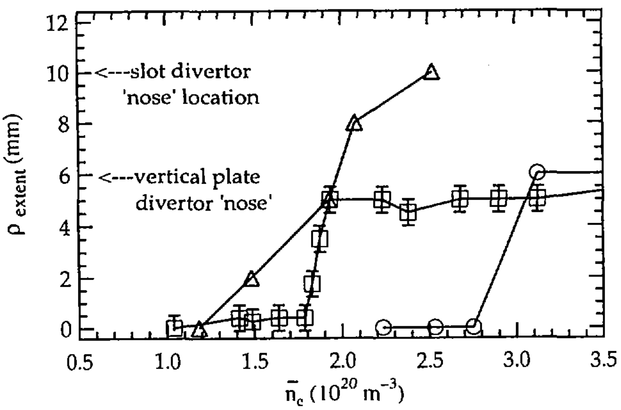

FIG. 2. Extent of detachment at the outer divertor plate for three different divertor geometries: squares — vertical-plate, circles — flat-plate, triangles — slot. ρ corresponds to the distance from the separatrix to the detachment front flux surface referenced to the midplane.

target to that upstream in the SOL, $2n_eT_{e,plate}/n_eT_{e,SOL} \leq 0.5$, indicating a pressure deficit. A set of Langmuir probes located at the divertor plates and upstream in the SOL are used for this assessment [8]. Figure 2 shows the typical radial extent of detachment into the common flux region from the separatrix. Each flux surface is labeled by its corresponding distance outside the separatrix at the plasma midplane (ρ in mm). For the standard vertical-plate geometry, the detachment extent is a stepwise function of $\bar{n}_e$, increasing rapidly until the divertor pressure deficit reaches the flux surfaces that intersect the juncture between the vertical and semi-horizontal sections of the outer divertor plate (herein designated the 'nose' of the outer divertor, see fig. 1). The detachment extent does not increase beyond the divertor nose even for densities 2.5 x the detachment threshold. Very large deficits in plasma pressure at the divertor surface compared to upstream in the SOL are typically found after detachment; $2n_eT_{e,plate}/n_eT_{e,SOL}$~.01. The values of the parallel heat flux in the SOL, $q_{||,SOL}$ (at the separatrix), at the detachment onset are 50-100 MW/m^2. The differences between vertical-plate and slot operation are minimal in the onset of detachment.

The flat-plate geometry resembles the open divertor geometries of earlier tokamaks. The angle of separatrix intersection with the plates in a poloidal plane is much closer to perpendicular. The surface normal over much of the plasma-wetted region points towards the core. The effect of switching the strike points to this configuration substantially increases the density threshold for detachment, figure 2. The $\bar{n}_e$ required for flat-plate divertor detachment is increased by 50-80% above that found for equivalent core conditions (input power, plasma current, etc.) with vertical-plate operation. In addition, the pressure deficit at the plate is typically smaller ($2n_eT_{e,plate}/n_eT_{e,SOL}$ ~ 0.1 compared to .01 for vertical-plate). It should be noted that the extent of detachment for the vertical-plate equilibrium shown (strike point ~ 1/2 way down the plate) does not extend around the divertor nose even for densities above the detachment threshold for the flat-plate.

2.2 Comparison of divertor plasma conditions

For all of these divertor geometries, detachment occurs when the electron temperature at the divertor surface falls below a value of ~ 5 eV. Figure 3 shows

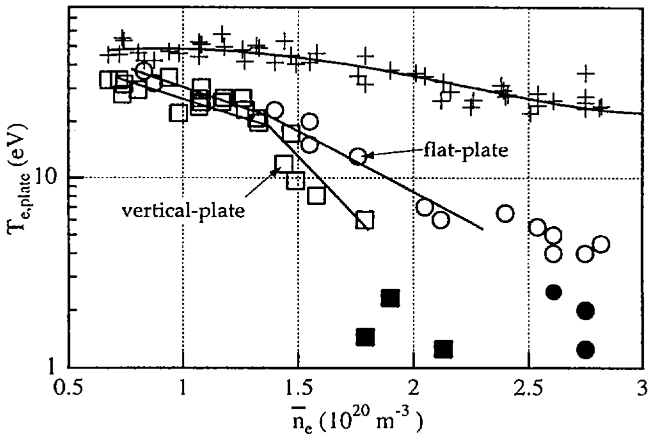

FIG. 3. Divertor plate electron temperature (r = 2 mm flux surface) versus $\bar{n}_e$; open squares — vertical-plate, open circles — flat-plate, full squares and full circles — detached. $T_{e,SOL}$ measured by the SOL probe is shown for reference (crosses).

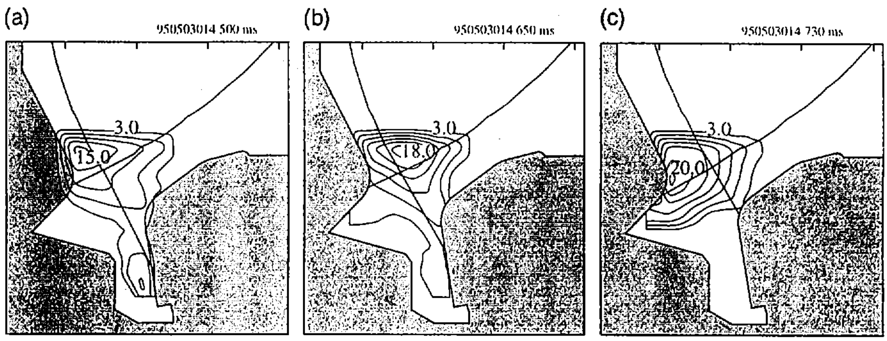

FIG. 4. Volumetric emissivity profile in the divertor region for (a) attached vertical-plate, (b) detached vertical-plate and (c) detached flat-plate operation.

$T_{e,plate}$ for the ρ = 2 mm flux surface as a function of $\bar{n}_e$ for the vertical- and flat-plate geometries. At low densities the divertor characteristics obtained with the two geometries are similar but as $\bar{n}_e$ is increased they diverge, with $T_{e,plate}$ dropping most rapidly for the vertical-plate. For vertical-plate operation, as $T_{e,plate}$ reaches 5 eV, detachment proceeds quickly and $T_{e,plate}$ drops abruptly to 1-2 eV. The drop in $T_{e,plate}$ with increasing $\bar{n}_e$ for the flat-plate case remains slow compared to the vertical-plate after detachment.

There are significant differences between flat- and vertical-plate operation in the volumetric emissivity profiles obtained from an array of bolometers viewing the divertor region. The brightnesses measured with the 12 detectors available for these discharges are tomographically inverted to provide local emissivities over an array of pixels 2.5 cm square [9]. That data is smoothed to provide the contour plots in figure 4. The three plots are from a single discharge. Figure 4a exhibits the typical non-detached vertical-plate emissivity profile. There is emission along the outer divertor leg with strong emission above the inner divertor nose as well. Later in the discharge after the density is raised, the divertor is detached, figure 4b. The emissivity peak has moved inside the separatrix. The strike point was then swept up the outer divertor plate to form the flat-plate equilibrium with a detached plasma, figure 4c. The emissivity peak moves back to the inner divertor but now to the inner strike point. The divertor geometry strongly affects the location of the divertor emissivity peak with respect to both the divertor plates and the separatrix.

There are also a number of similarities in divertor characteristics for the different geometries. It has previously been observed, for vertical-plate experiments, that the pressure can increase along a flux surface ($2n_eT_{e,plate}/n_eT_{e,SOL} > 1$) for a period just prior to detachment [10]. We have found that this is true for the flat-plate operation as well. This phenomenon was not observed during slot operation due to lack of diagnostic coverage. Vertical- and flat-plate operation also have similar characteristics with regard to Z_{eff}, impurity screening [11] and neutral pressure dependence on $\bar{n}_e$ [12]. Thus one concludes that modifying the divertor shape has little effect on neutral confinement in the divertor. However, because flat-plate divertor detachment occurs at higher densities than for the vertical-plate both the midplane and divertor pressures at detachment are correspondingly increased, figure 5.

The results shown in fig. 2 are surprising in that the extent of pressure loss at the outer divertor for vertical-plate operation is limited to below the divertor 'nose' even for densities above that required to detach the flat-plate divertor plasma. One obvious difference brought about by the geometry changes is that the parallel field line length *in the divertor* is varied. We define this 'divertor connection length', $L_{x,connect}$, to be the distance along a field line (ρ = 2 mm flux surface) from the separatrix intersection with the outer divertor plate (strike point) to a horizontal plane located at the x-point. In a series of discharges the strike point was moved to different locations along the outer divertor plate creating equilibria varying from slot to flat-plate. The resultant detachment onset densities are plotted vs. the divertor connection length in figure 6. The

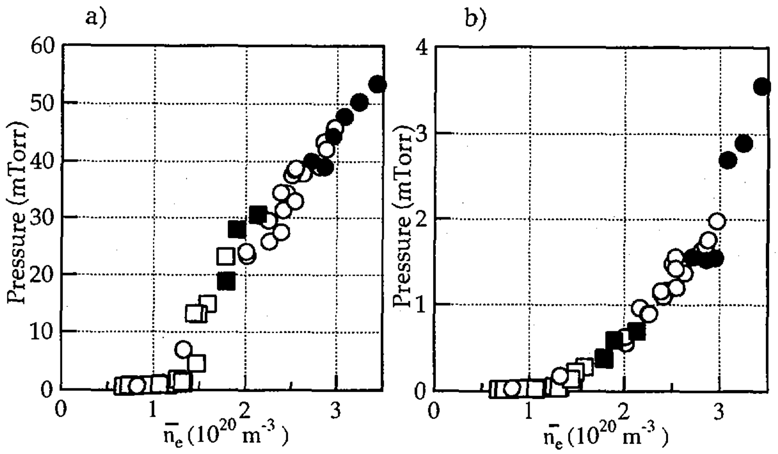

FIG. 5. (a) Divertor and (b) main chamber pressure versus $\bar{n}_e$: open squares — vertical-plate, open circles — flat-plate, full squares and full circles — detached.

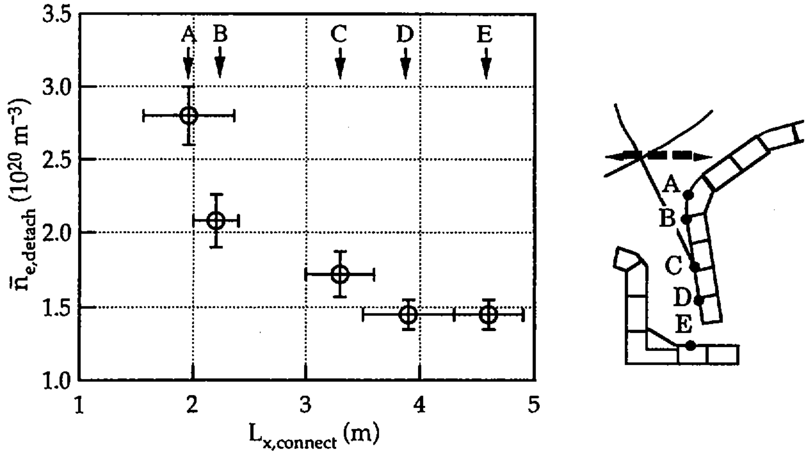

FIG. 6. Variation of the detachment threshold density with connection length inside the divertor (ρ = 2 mm). The length is measured from the horizontal plane indicated (dashed line) to the divertor plate along a field line.

corresponding location of the outer divertor strike point is also shown for each case. The dependence of $\bar{n}_{e,detach}$ on $L_{x,connect}$ is best fitted by an exponential or cubic function, much stronger than linear. We emphasize that the strongest variation in $\bar{n}_{e,detach}$ occurs for the shortest $L_{x,connect}$.

Operation with strike point at location B, shown in fig. 6, engenders characteristics of both the vertical and flat-plate. We find that detachment does extend beyond the vertical section of the plate to above the nose. However, the detachment threshold is significantly lower than the flat-plate The transition from vertical-plate to flat-plate operation is continuous, not a step function.

3. Discussion

3.1 Power balance

Although it is clear from the above data that there are marked differences in the detachment threshold correlated with variations in geometry, it is not clear why. To provide a framework within which to discuss the data we write down the relationship between the plasma parameters (in the SOL and divertor) and the power flowing into the SOL, $q_{||}$, based on simple 1-D fluid heat transport models [e.g. 13-15]. We assume that classical parallel electron heat transport (as opposed to convection) dominates the parallel transport. This treatment is only meant as a basis for discussion, not as a replacement for more thorough 2-D models. Assuming that radiation losses occur along a flux surface only in the region from the x-point to the plate we define f_{loss}, the fraction of parallel heat flux lost to radiation, charge-exchange and ionization of neutrals [16] by:

$$q_{||,x}(1 - f_{loss}) \equiv q_{||,plate} \qquad (1)$$

$q_{||,x}$ and $q_{||,plate}$ are the parallel power flow into the divertor region (from the SOL) and to the plate respectively. Further assuming that pressure is constant on a flux surface, one can then solve the heat transport equation for the dependence of $T_{e,plate}$ on the connection length, L, upstream and core parameters:

$$T_{plate} \propto \frac{q_{\parallel,x}^{10/7}(1 - f_{loss})^2}{L^{4/7} n_{upstream}^2} \tag{2}$$

Equation 2 thus expresses both a relationship of $T_{e,plate}$ to SOL parameters and volumetric losses along a given flux surface. We restrict our analysis to the ρ=2 mm flux surface hereafter. To generalize this expression still further we note that, for Alcator C-Mod discharges, $n_{upstream} \propto \bar{n}_e$.

It is intuitive that the upstream heat flux, $q_{\parallel}$ is not dependent on the divertor geometry. However, we need to make sure this is true. $q_{\parallel}$, on the ρ=2 mm flux surface, has been calculated by two methods:

$$q_{\parallel,x} = \frac{2}{7}\kappa_0 \frac{T_{SOL}^{7/2}(\rho = .002)}{L}; \tag{3}$$

$$q_{\parallel,x} = \frac{P_{SOL} B_{tot}}{4\pi(R_0 + a)\lambda_q B_{pol}} \exp\left(-{.002}/{\lambda_q}\right) \tag{4}$$

where P_{SOL} is the power flowing from the core plasma across the separatrix (= P_{IN} - $P_{Rad,main}$). λ_q is the e-folding length for $q_{\parallel}$ across flux surfaces measured with the SOL Langmuir probe. Both methods yield similar scalings. The results for the second method are shown in figure 7. The similarity of attached vertical- and flat-plate $q_{\parallel}$ confirms the independence of $q_{\parallel}$ on geometry. The detached vertical-plate data points have lower $q_{\parallel}$ values due to the shift of the peak in divertor radiation inside the separatrix after detachment (figure 4b) and the resulting drop in P_{SOL}.

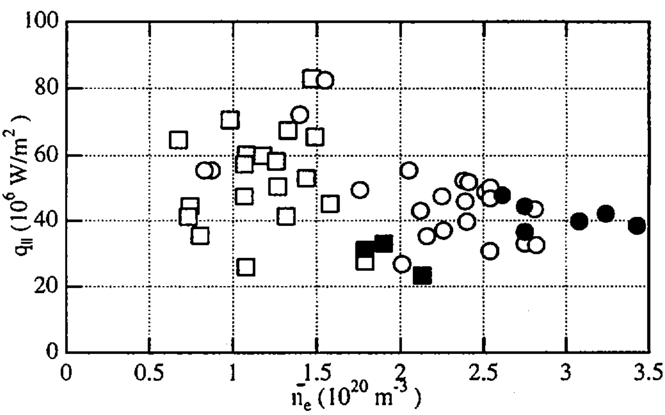

FIG. 7. $q_{\parallel}$ (ρ = 2 mm flux surface) versus $\bar{n}_e$: open squares — vertical-plate, open circles — flat-plate, full squares and full circles — detached.

On the basis of previous work and figure 3 we find that $T_{e,plate} < 5$ eV is a necessary condition for detachment onset [1,8-10,17]. From this and eq. 2 we expect that $\bar{n}_{e,detach} \propto q_{\parallel,x}^{5/7}(1 - f_{loss})L^{-2/7}$. This model is unable to explain the observed variation of detachment density threshold as an effect of connection length. The dependence on L is too weak (and $q_{\parallel}$ approximately the same). Thus a variation in f_{loss} with configuration may be responsible for the differences in detachment threshold.

3.2 Collisionality

There is another viewpoint from which to compare flat- and vertical-plate operation. The collisionality of the SOL can have an important effect on temperature gradients. Eq. 2 can be rewritten to include this:

$$\frac{(R_T^{3.5} - 1)}{R_T^{3.0}} \approx \frac{2.33 \cdot \nu_{epi}^*}{(1 - f_{loss})} . \qquad (5)$$

$R_T = T_{e,upstream}/T_{e,plate}$ and ν^*_{epi} is the dimensionless collisionality for epithermal electrons. The LHS of this equation can be approximated by $R_T^{0.5}$ for $R_T \geq 1.5$. R_T must be maximized in order to have large temperature ratios [15] and achieve detachment ($T_{e,plate}$ ~ 5eV). ν^*_{epi} is calculated based on the electron-electron momentum collision frequency for thermal electrons, ν_{ee}, and the electron thermal velocity, $v_{th,e}$:

$$\nu_{epi}^* \equiv \frac{L / v_{th,e}}{17 \cdot \nu_{ee}} = 417 \cdot \frac{n_e(10^{20} m^{-3}) L(m)}{T_e^2} \qquad (6)$$

The epithermal electrons (v_{epi} ~ 3.7 x v_{the}, $\nu_{epi}^* \approx \nu_{th}^* / 17$) are responsible for a large share of the parallel heat flux [18-19]. Therefore we examine the

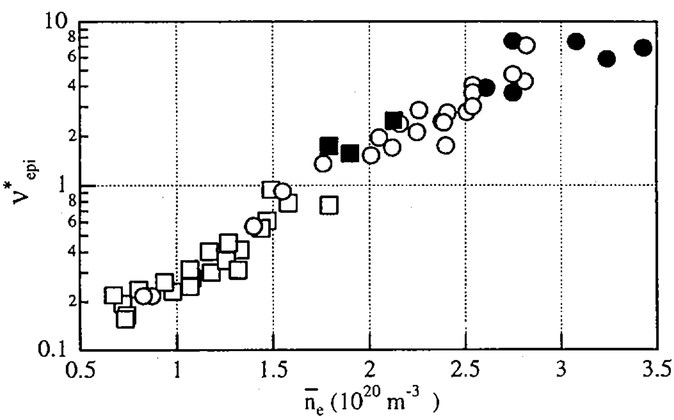

FIG. 8. Upstream, SOL collisionality (ρ = 2 mm flux surface) versus $\bar{n}_e$: open squares — vertical-plate, open circles — flat-plate, full squares and full circles — detached.

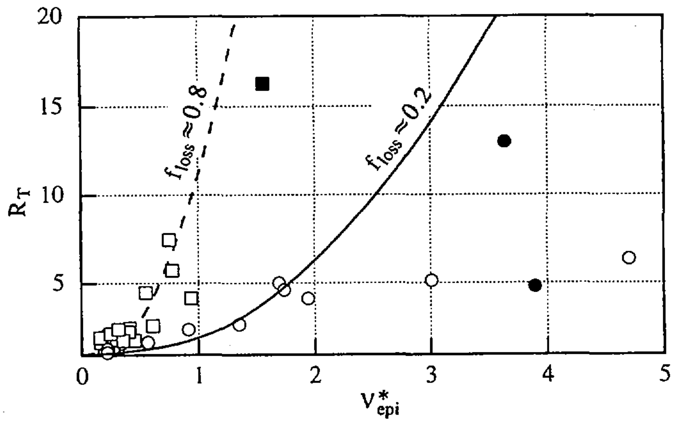

FIG. 9. R_T versus ν^*_{epi} (ρ = 2 mm flux surface): open squares — vertical-plate, open circles — flat-plate, full squares and full circles — detached. Fits from equation 5 are for f_{loss} = 0.2 and f_{loss} = 0.8.

functional dependence of their collisionality on geometry. We have evaluated this collisionality upstream in the SOL at the location of the SOL probe and, as expected, find no significant differences in the scaling of collisionality with $\bar{n}_e$ between the different operating geometries, figure 8. However, detachment of flat-plate discharges occurs at significantly higher collisionality than with the vertical-plate indicating that this parameter does not solely control the detachment threshold.

Referring to equation 6 we see that even in the absence of divertor radiation (we use this loosely to include all volumetric losses such as cx and ionization of neutrals), increasing collisionality leads to increases in temperature gradients and $T_{e,plate}$ falling to 5 eV. Neutrals are needed to remove momentum and finally achieve divertor detachment. Divertor radiation, through (1- f_{loss}), accelerates the drop in $T_{e,plate}$. The experimental values of R_T are plotted against collisionality in figure 9. In addition, equation 5 has been solved for R_T and plotted for 2 different values of f_{loss}. The non-detached vertical-plate data lie near to the line f_{loss} ~ 0.8. In comparison, the flat-plate data appear to have a lower f_{loss} that decreases with increasing R_T (increasing $\bar{n}_e$). Comparison of the integral of the bolometer emissivity profile (figure 4) across the outer divertor region for flat- and vertical-plate yields no significant differences within the experimental uncertainties. Therefore, one is led to conclude that the changes in f_{loss} must be more localized on flux surfaces than the spatial resolution of the emissivity profiles resulting from the bolometer tomography permits (2.5 cm).

The inference that volumetric losses along a flux surface are affected by geometry is also consistent with the dependence of $\bar{n}_{e,detach}$ on $L_{x,connect}$ seen in figure 5. That data indicates that small changes in connection length lead to large changes in $\bar{n}_{e,detach}$ (points A-C). This raises the question of whether differences in the flux surface volume below the x-point available for radiation (which is proportional to $L_{x,connect}$) are the cause of differences in f_{loss}. From equ. 2 (with T_e ~ 5 eV) $\bar{n}_{e,detach}$ ~ (1-f_{loss}) ~ ε x (1-$L_{x,connect}$) where ε is the local emissivity. If one assumes that ε is constant on a flux surface, then the predicted dependence of $\bar{n}_{e,detach}$ on $L_{x,connect}$ should be linear. This is not consistent with the data of figure 5. In order to fit the experimental dependence we must assume that the magnitude of ε drops below the divertor nose. It is reasonable that ε should not be constant on a flux surface because the cooling rate [20] for typical low-Z impurities not only has a peak (at around 10-15 eV), but T_e varies along a flux surface. The bolometer emissivity profile shown in figure 4a is consistent with this argument.

The drop in $(1-f_{loss})$ obtained by moving the strike point from above to below the nose is large . Further movement of the strike point down the plate leads to diminishing returns in reducing the detachment threshold. This is equivalent to saying that increasing the divertor depth beyond some value is of limited value for radiation.

3.3 Neutral effects

There is another factor which could affect the relative ease of detachment for different geometries: neutrals. The neutral atom density in the last several meters of field line length leading to the divertor plate plays an essential role in momentum removal (divertor detachment). There may be differences in this density between flat- and vertical-plate operation.

Previous analyses [12, 21-22] of the role of neutrals in momentum loss for Alcator C-Mod vertical-plate operation showed that: (1) The neutral density at the outer divertor surface, inferred from Langmuir probes and H_α measurements, continually decreased, moving from the bottom of the divertor plate to the nose and above. This is consistent with neutral pressure measurements in the private flux region and at the midplane, similar to that displayed in figure 5. (2) The neutral atom densities on the vertical sections of the outer divertor plate, and corresponding neutral pressures in the private flux region, are always more than sufficient (~ 4 mTorr through flux balance arguments) to explain the observed loss in ion-neutral momentum which is typically 4 x 10^{22} m^{-2}-sec.

Based on the work described above, the neutral density in the plasma fan for flat-plate operation will be significantly lower than for the vertical-plate geometry and may be more closely correlated with the midplane pressure. In that case, flat-plate divertor detachment may await the midplane pressure rising to ~ 4 mTorr.

Lower neutral density in the plasma fan for flat-plate operation is also consistent with the $T_{e,plate}$ data of figure 3. $T_{e,plate}$ (flat-plate) remains at ~ 5 eV for a wide range in $\bar{n}_e$. Detachment and the accompanying drop in $T_{e,plate}$ could be delayed to higher $\bar{n}_e$ and the higher neutral pressures (midplane pressures) which accompany it.

4. Summary

A comparison of the characteristics of different divertor geometries has been carried out in the Alcator C-Mod tokamak. A variety of geometries have been created by varying the placement of the outer divertor strike point at different locations. The principal difference between the different divertor geometries is in the divertor detachment threshold. The vertical-plate and slot geometries have significantly lower thresholds in $\bar{n}_e$ than the flat-plate for similar upstream conditions (e.g. $q_{||}$, ν^*). It is inferred that this difference in density threshold is due to differences in volumetric loss profiles in the divertor primarily in the region of the outer divertor nose. When the separatrix and common flux surfaces include this region (vertical plate) the losses are higher leading to lower $T_{e,plate}$ and detachment. This result argues that vertical-plate operation is useful for lowering the detachment threshold and large divertor lengths may be of marginal advantage in this regard.

Acknowledgments

We would like to thank the Alcator team and in particular the operations group, who were instrumental in achieving the required equilibria. We would also like thank Prof. Peter Stangeby and Dr. C.S. Pitcher for helpful discussions regarding the dependence of R_T on upstream parameters.

REFERENCES

[1] LIPSCHULTZ, B., et al., J. Nucl. Mater. 220-222 (1995) 50.
[2] MATTHEWS, G.F., J. Nucl. Mater. 220-222 (1995) 104.
[3] ALLEN, S., DIII-D TEAM, Plasma Phys. Control. Fusion 37 (1995) A191.
[4] NEUHAUSER, J., et al., Plasma Phys. Control. Fusion 37 (1995) A37.
[5] PICK, M., et al., J. Nucl. Mater. 220-222 (1995) 595.
[6] STEIBL, B., et al., in SOFE '95 (Proc. 16th IEEE/NPSS Symp. on Fusion Engineering, Champaign, 1995).
[7] NAGAMI, M., et al., J. Nucl. Mater. 220-222 (1995) 3.
[8] LaBOMBARD, B., Phys. Plasmas 2 (1995) 2242.
[9] GOETZ, J.A., et al., Phys. Plasmas 3 (1996) 1908.
[10] LaBOMBARD, B.L., in Plasma Surface Interactions in Controlled Fusion Devices (Proc. 12th Int. Conf. St. Raphael, France, 1996), paper I-11, J. Nucl. Mater. (in press).
[11] WANG, Y., A Study of Impurity Screening in Alcator C-Mod, PhD Thesis, Rep. PFC/RR-96-6, Plasma Fusion Center, Massachusetts Inst. of Technology, Cambridge (1996).
[12] NIEMCZEWSKI, A., Neutral Particle Dynamics in the Alcator C-Mod Tokamak, Rep. PFC/RR-95-8, Plasma Fusion Center, Massachusetts Inst. of Technology, Cambridge (1995).
[13] HOBBS, G.D., WESSON, J.A., Rep. CLM-R61, UKAEA, Culham (1966).
[14] MAHDAVI, A., et al., Phys. Rev. Lett. 47 (1981) 1602.
[15] STANGEBY, P.C., McCRACKEN, G.M., Nucl. Fusion 30 (1990) 1225.
[16] BORASS, K., JANESCHITZ, G., Nucl. Fusion 34 (1994) 1203.
[17] STANGEBY, P.C., Nucl. Fusion 33 (1993) 1695.
[18] CHODURA, R., Plasma flow in the sheath and presheath of a scrapeoff layer, NATO Ser. B: Physics 131 (1986) 99.
[19] HUTCHINSON, I.H., et al., Rep. PFC/RR-95-12, Plasma Fusion Center, Massachusetts Inst. of Technology, Cambridge (1995).
[20] POST, D.E., JENSEN, R.V., At. Data Nucl. Data Tables 20 (1977) 397.
[21] KURZ, C., et al., Rep. PFC/JA-96-34, Plasma Fusion Center, Massachusetts Inst. of Technology, Cambridge (1996).
[22] NIEMCZEWSKI, A., HUTCHINSON, I.H., LaBOMBARD, B., LIPSCHULTZ, B., McCRACKEN, G.M., Nucl. Fusion 37 (1997) 151.

DISCUSSION

K. LACKNER: Did you observe differences in the ohmic or L mode density limit between the different divertor plasma configurations?

B. LIPSCHULTZ: We did not study this.

F. WAGNER: Could you please characterize the role of molybdenum as a surface material in the geometrical studies you presented. Specifically, does the erosion change strongly with geometry, as it does for chemical sputtering in the case of carbon, and thus impact the SOL development?

B. LIPSCHULTZ: I can only comment on the Z_{eff} of the different configurations, which is the same. I don't know at this time if there were any differences in molybdenum levels.

D.N. HILL: Since the temperature at the target plates drops as $1/L_{\parallel}^{4/7}$, have you separately varied $L_{\parallel}$ (by a q scan) to isolate connection length from divertor volume effects on detachment density?

B. LIPSCHULTZ: In a separate work we have varied the safety factor for vertical target discharges. In that study we found the differences seen were completely accounted for by changes in $q_{\parallel}$ (different plasma currents). The effect of $L_{\parallel}$ was minor, as expected.

CONCEPT OPTIMIZATION 2

(Session A5)

Chairperson

T. TAMANA
Japan

STUDY OF H-MODE PHYSICS IN ASDEX UPGRADE

H. ZOHM, W. SUTTROP, H.J. DE BLANK, R.J. BUTTERY[1], D.A. GATES[1],
J.A. HEIKKINEN[2], W. HERRMANN, A. KALLENBACH, T. KASS,
M. KAUFMANN, T. KURKI-SONIO[2], B. KURZAN, M. MARASCHEK,
H. REIMERDES, F. RYTER, H. SALZMANN, J. SCHWEINZER,
J. STOBER, ASDEX UPGRADE, ECRH, ICRH, NBI TEAMS
Max-Planck-Institut für Plasmaphysik,
Euratom–IPP Association,
Garching, Germany

Abstract

STUDY OF H-MODE PHYSICS IN ASDEX UPGRADE.

H-mode physics in ASDEX Upgrade is studied with the help of fast diagnostics with high spatial resolution diagnosing the plasma edge. The power threshold for the L–H and H–L transitions is related to the edge plasma parameters. The edge temperature $T_{e,\,edge}$ at the transitions is the same for the L–H and H–L transitions at otherwise constant plasma parameters, indicating that the hysteresis in heating power is solely due to the reduced transport coefficients in the H-mode. The value of $T_{e,\,edge}$ necessary for the transition rises with increasing B_t and decreases with n_e, inconsistent with the parameter dependence predicted by theories based on ion orbit loss as the dominant nonambipolar radial loss current. Measurements of the radial electric field E_r reveal the well known large negative E_r at the plasma edge. Using a new method with high temporal resolution, the authors find that there is no 'jump'of the radial electric field before the transition within »100 ms. E_r can jump by »5 kV/m in less than 1 ms, but the full value of »20–40 kV/m is established on a slower time-scale associated with the buildup of $\tilde{N}p$. Edge localized modes of type III and I are clearly distinguished by the MHD characteristics of their precursors. In operational space, they are separated by a critical $T_{e,edge}$ above which type III ELMs are stabilized whereas type I ELMs occur when the edge pressure gradient reaches the ideal ballooning limit.

1 Introduction

The H-mode [1] with edge localized modes (ELMs) is considered the most promising regime of enhanced confinement for steady state operation in a future reactor-size magnetic fusion experiment. Although significant progress has been made in characterizing various H-mode phenomena [2], [3], there is still a lack of predictive theories for the H-mode operating regime (e.g. power threshold and ELM type). This is especially important as ITER will have to work at comparatively high density, whereas most of our experimental knowledge about H-mode

[1] UKAEA Government Division, Fusion, Culham, UK.

[2] VTT Energy, Helsinki University of Technology, Finland.

has been acquired at low to medium density. Therefore, dedicated experiments to study the H-mode at high density have been carried out in ASDEX Upgrade (further discussion of high density operation in ASDEX Upgrade in [4]).

With the development of new diagnostics and the improvement of temporal and spatial resolution of relevant measurements in ASDEX Upgrade, it is possible to gain new insight into the physical phenomena governing the behaviour of H-mode plasmas and to compare with predictions of H-mode theories. In this paper, we focus on the L-H and H-L transitions and ELMs whereas confinement properties are treated in [5].

2 L-H and H-L Transition Physics

The H-mode has been extensively studied in discharges with medium density ($\bar{n}_e/\bar{n}_{e,GW} \approx 0.3 - 0.6$, where $\bar{n}_{e,GW}$ refers to the Greenwald limit). Usually, the threshold power for the transition into the H-mode, P_{tot}^{LH}, is described as a function of global plasma parameters: $P_{tot}^{LH} \sim \bar{n}_e B_t / A_{Plasma}$ [6] where A_{Plasma} is the ion mass in atomic units. If the ion ∇B drift is directed away from the X-point ('unfavourable drift direction'), P_{tot}^{LH} is higher than with ∇B drift towards the X-point ('favourable drift direction') by a factor of roughly 2. In addition, a hysteresis with respect to heating power is found such that $f_{hyst} = P_{tot}^{LH}/P_{tot}^{HL} \approx 2$ in the favourable direction (the data for the unfavourable direction is less clear, but suggests an even bigger f_{hyst}). The factor f_{hyst} is especially important for ITER, because it determines the width of the H-mode operating region.

In order to explore the operational space at high density, a strong gas puff is applied. This also increases n_0, the neutral density which is believed to affect P_{tot}^{LH} and P_{tot}^{HL} [7]. In addition, we inject impurities such as Ne to control the energy flux across the separatrix. The effect of these experimental techniques on the L-H threshold can be summarized as follows [8]: With additional radiation, P^{LH} is still described by the $\bar{n}_e B_t$ scaling if the total heating power is replaced by $P_{sep} = P_{tot} - dW/dt - P_{rad}(core)$. Additional radiation itself does not significantly change f_{hyst}, but P^{HL} rises in scenarios with high density and consequently the highest n_0, leading to $f_{hyst} \rightarrow 1$, irrespective of the ion ∇B drift. However, it is at the moment not clear if n_0 itself or the associated change in edge plasma parameters determines the physics.

Since both theory and experiment suggest that L-H and H-L transitions are governed by the local edge plasma parameters and not by global plasma parameters [9], we correlate the L-H transition with local measurements of T_e (ECE radiometer and Thomson scattering) and n_e (Li-Beam and DCN interferometer). In most of the L-H transition theories, $T_{i,edge}$ plays a decisive role. This quantity can be evaluated from low energy neutral particle analysis [10]. Although these data are not generally available with high temporal resolution, for the cases we checked in the parameter range in which the L-H transition occurs ($\nu^* \geq 1$) we find $T_{i,edge} \approx T_{e,edge}$ within the error bars. Therefore, we will use this assumption in the following.

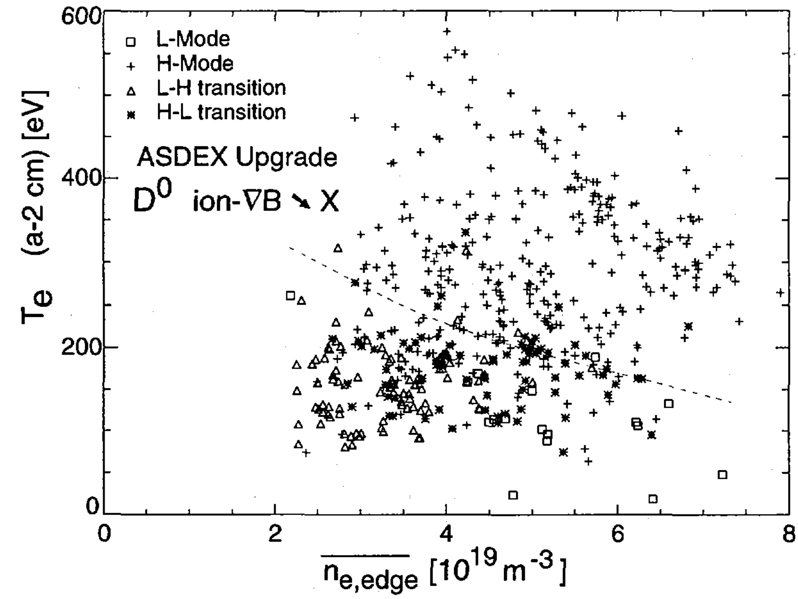

Figure 1: *$T_{e,edge}$ versus $\bar{n}_{e,edge}$ from 2 cm inside the separatrix at the L-H transition.*

Fig. 1 shows a plot of the edge electron temperature $T_{e,edge}$ taken 2 cm inside the separatrix (corresponding to $\rho_{pol} = 0.95$) versus $\bar{n}_{e,edge}$, the line-averaged edge electron density defined from a line integral of the DCN interferometer intersecting the plasma 5 cm inside the separatrix, for $B_t = 2.5$ T and favourable drift direction only. We use these quantities instead of the separatrix values, because the latter are dominated by the SOL physics rather than by the physics of the closed flux surfaces. Although there is significant scatter in $T_{e,edge}$ at the L-H transition, the general trend points towards decreasing $T_{e,edge}$ with $\bar{n}_{e,edge}$ at the transition. This is confirmed by inspecting the time history of single shots [11]: here, $T_{e,edge}$ roughly scales as $T_{e,edge} \sim \bar{n}_{e,edge}^{-0.5}$ as indicated by the broken line in Fig. 1. $T_{e,edge}$ is the same for the L-H as well as for the H-L transition, even in the high density scenarios. Thus, the hysteresis observed in the heating power is *not* due to a hysteresis in $T_{e,edge}$, but comes from the better energy confinement of the H-mode, allowing one to sustain the same $T_{e,edge}$ at lower heating power. Consequently, in the high density scenarios, the reduction of the hysteresis in power must be due to a decrease in the difference of the transport coefficients. This effect is indeed found for global confinement: τ_E in the H-mode decreases with n_0 [12], especially in the highly radiating scenarios with high n_0. Here, L- and H-mode confinement are more or less equal, the edge profiles do not show significant differences and, consequently, the hysteresis is absent [8], and it is only possible to define the H-mode through local signatures at the edge, (e.g. the occurrence of dithering cycles).

Another ingredient of the usual P^{LH} scalings is the dependence on B_t. The value of $T_{e,edge}$ necessary for the transition rises roughly linearly with B_t. With ion ∇B drift reversal, $T_{e,edge}$ at the transition is a factor of 2 higher. Finally, the isotope dependence of P_{thr}^{LH} also translates into the need for $T_{e,edge}$ to be higher by a factor 2 in H than in D to transit into H-mode. In all these cases, $T_{e,edge}$ is roughly the same at the L-H as well as at the H-L transition. The global scaling is recovered from these data taking into account that, in the L-mode, the power required to establish a certain $T_{e,edge}$ increases nearly linearly with $n_{e,edge}$.
With the knowledge of local parameters, a comparison between the measurements and the predictions of H-mode theories can be made. We estimate the torque resulting from ion orbit loss and balance it against the friction due to the presence of neutrals and the neoclassical return current that maintains ambipolarity of the radial fluxes. The resulting values for the radial electric field E_r can either be single- or multivalued; this is associated with stable L/H-phases or the transition region. The model qualitatively explains the loss of hysteresis with increasing n_0 due to increased CX friction [13]. However, none of the models balancing ion orbit loss and neoclassical current yields the observed parameter dependence: from these theories, the transition should happen at $T^{\alpha}/n = const.$ with $1 \leq \alpha \leq 5/2$, whereas, as pointed out above, $\alpha \leq 0$ in the experiment.

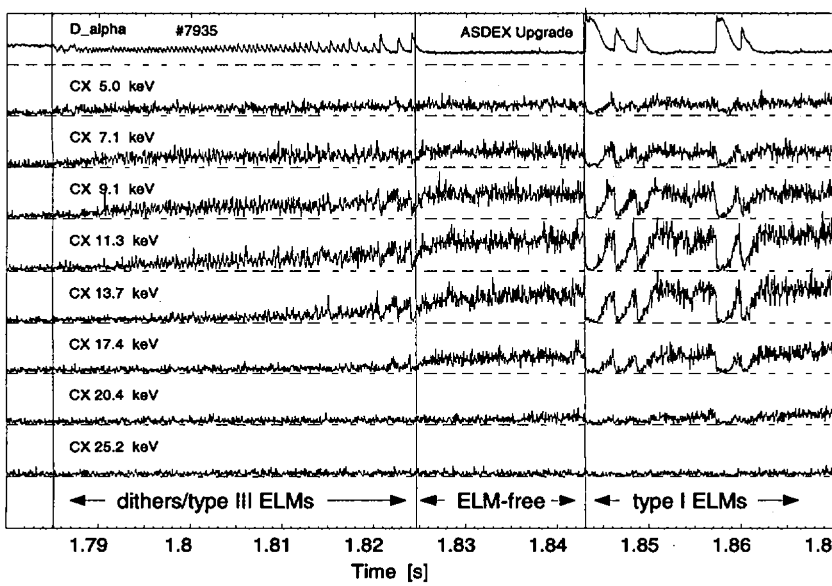

Figure 2: *The temporal evolution of different charge exchange fluxes (indicating the presence of E_r with $eE_rR_0 \geq$ the probed energy) during a slow L-H transition (B_t in the favourable direction).*

Also, in the experiment, the collisionality ν^* varies between $1.4 \leq \nu^* \leq 5$ at the transition 2 cm inside the separatrix, whereas the theories mentioned above rely on $\nu^* \approx 1$ for the transition [9]. This does not generally rule out ion orbit loss as an important effect for the L-H transition, but indicates that there are more physics elements to be considered.

Additional information on the physics of the L-H transition comes from the behaviour of E_r near the plasma edge. On ASDEX Upgrade, we infer E_r from changes in the flux of charge exchange neutrals due to a change in the orbit of ripple-trapped particles close to the separatrix when a substantial E_r exists [14]. This method can provide data with a time resolution of $\approx 50\mu$s for the decay of the field. The inherent time scale for particle flux changes is the scattering of beam ions into the ripple-trapped orbit confined by the radial electric field. The typical scattering angle for this process is only 2-3 degrees, so the typical time scale is not much longer than the decay time constant. In fact, fast changes in the fluxes suggest time constants of not more than a few hundred μs. The method does not have spatial resolution; however, the fluxes of the investigated slowing down ions originate from an area where the density of these ions and of the neutral background is high, i.e. close to the plasma edge.

Fig. 2 shows the temporal evolution of several charge exchange fluxes (here, an increase in the signals means that eE_rR_0 is of the order of the probed energy). Note that, with the usual definition of $dp/dr < 0$, our E_r is negative. Fig. 2 shows a slow transition: B_t is in the favourable direction and thus dithering cycles and type III ELMs occur. We find that E_r close to the separatrix has a typical magnitude of $E_r < 5$ kV/m in L-mode prior to the transition. At the transition ($t = 1.785$ s), E_r increases to about 10 kV/m within 5 ms and then continues to grow on a timescale of 100 ms up to its final value of 22 kV/m. However, the dithering cycles and type III ELMs in the early phase ($t \leq 1.825$ s) modulate E_r on the sub-ms timescale. During type III ELMs, E_r returns to near L-mode values, indicating at least a partial destruction of the transport barrier by this MHD event. Type I ELMs completely destroy the transport barrier. After an ELM, E_r begins to increase on a timescale of 1 ms, but the return to the maximum value may take several ms.

The transition in a discharge with B_t in the unfavourable direction is shown in Fig. 3: Here, a fast transition without any dithering cycles or type III ELMs occurs. Right at the transition, E_r increases by about 5 kV/m in less than 1 ms and then grows to its final value on a timescale of tens of ms. Thus, there are two mechanisms contributing to the build-up of E_r: a fast one (sub-ms timescale) that may lead to 'jumps' of E_r of approximately 5 kV/m and a slower one changing E_r on 10 ms timescale. Here, E_r in the fully developed H-mode reaches higher values than in the case shown in Fig. 2, mainly because the shot was heated by ctr-NBI (then, the contributions to E_r from v_{tor} and ∇p add up). Note that, in Fig. 3, E_r increases to substantial values before the transition. This is partly due to the higher $T_{e,edge}$ at the transition, leading to a bigger contribution via the ∇p term. In addition, at high heating power, in ASDEX Upgrade the L-mode also shows some improved confinement [5]. This phase starts at 1.695 s leading to the increase in the CX-signals at this time.

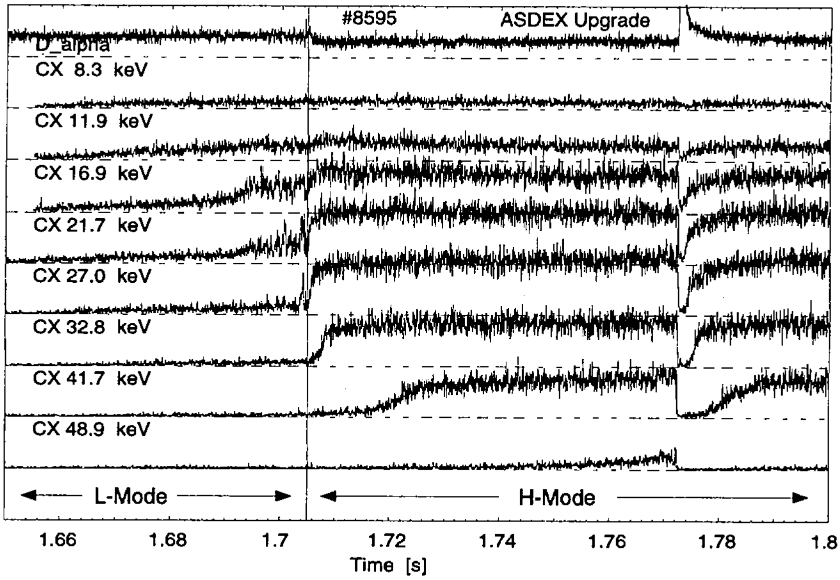

Figure 3: *The temporal evolution of different charge exchange fluxes (indicating the presence of E_r with $eE_r \geq$ the probed energy) during a fast L-H transition (B_t in the unfavourable direction). The vertical line indicates the L-H transition determined from the reduction of density fluctuations.*

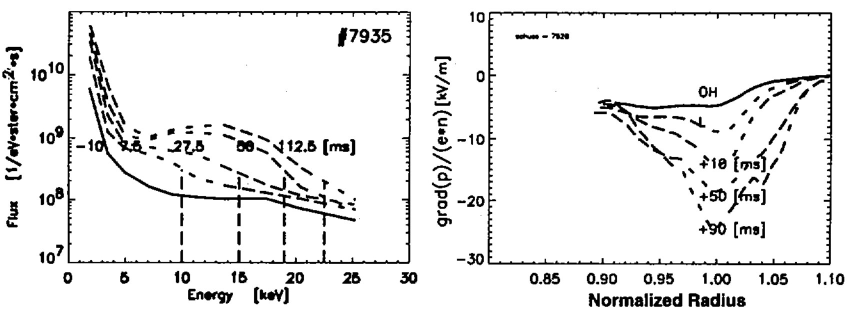

Figure 4: *Charge exchange energy spectra indicating the nonthermal distribution due to confined slowing down ions (left) and calculated contribution to E_r due to the pressure gradient term (right). Most of E_r can be ascribed to the steep pressure gradient.*

Aside from the D_α-signal, the time of L-H transition (vertical line in Fig. 3) can also be identified by the abrupt decrease in the power spectrum of density fluctuations measured by a reflectometer on both the high and the low-field side. Fig. 4 shows the energy spectra of charge exchange neutrals indicating the evolution of a nonthermal distribution due to the slowing-down ions trapped by the radial electric field. The nonthermal component extends to higher and higher energies, corresponding to increasing values of E_r. Also, $\nabla p/(en)$ calculated from $T_e(r)$ and $n_e(r)$ is shown. A major part of E_r can be ascribed to the radial pressure gradient of the main ions (assuming $T_e = T_i$, we evaluate $\nabla p_i/(en) \approx 25$ kV/m in the fully developed H-mode), similar to observations on DIII-D [15]. However, the fast changes in E_r in shots with a fast transition or after ELMs may be difficult to explain by the ∇p term alone. A possible candidate to contribute would be a poloidal rotation as measured in other experiments [15], indicating that right at the transition an additional torque, generated by a non-ambipolar loss current, could be active.

We cannot precisely evaluate the role of poloidal rotation at the transition as we have no direct measurement and in well-developed H-modes, the error bars of $\nabla p_i/(en_e)$ and E_r do not permit a calculation from the difference of the two terms (at the transition, the contribution of u_ϕ is small, $u_\phi B_\theta \leq 5$ kV/m, whereas in a fully developed H-mode it can contribute substantially).

Within our temporal resolution, we do *not* see an abrupt change of E_r prior to the transition as inferred from the drop in D_α although there is a steady increase of E_r during the L-mode prior to the transition in parallel to the pressure gradient. The 'jump' in E_r depends on the plasma parameters and occurs on a sub-ms time scale starting with the D_α-drop. Thus, the change in E_r seems to occur together with the build-up of the transport barrier.

3 ELM Physics

On ASDEX Upgrade, type I and type III ELMs are well distinguished by the power dependence of their repetition frequency. Also, clear differences between type I and type III magnetic precursors are found [16]: Type III precursor frequencies are typically 50-70 kHz with co-injection and 80-120 kHz with ctr-injection whereas type I precursors occur at very low frequencies (below 10 kHz in H-modes with co-injection and 15-25 kHz with ctr-injection). With co-injection, they are often hardly visible. Both precursor structures rotate in the electron diamagnetic drift direction.

From magnetic pick-up coils located in the midplane outside but close to the plasma we infer a toroidal mode number of $n = 10-15$ for type III whereas type I precursors normally have $n = 5-10$. Fig. 5 illustrates the difference between type I and type III precursors in a case with ctr-injection. Here, P_{rad} slowly increases so that P_{sep} decreases, leading to a drop of the repetition frequency of

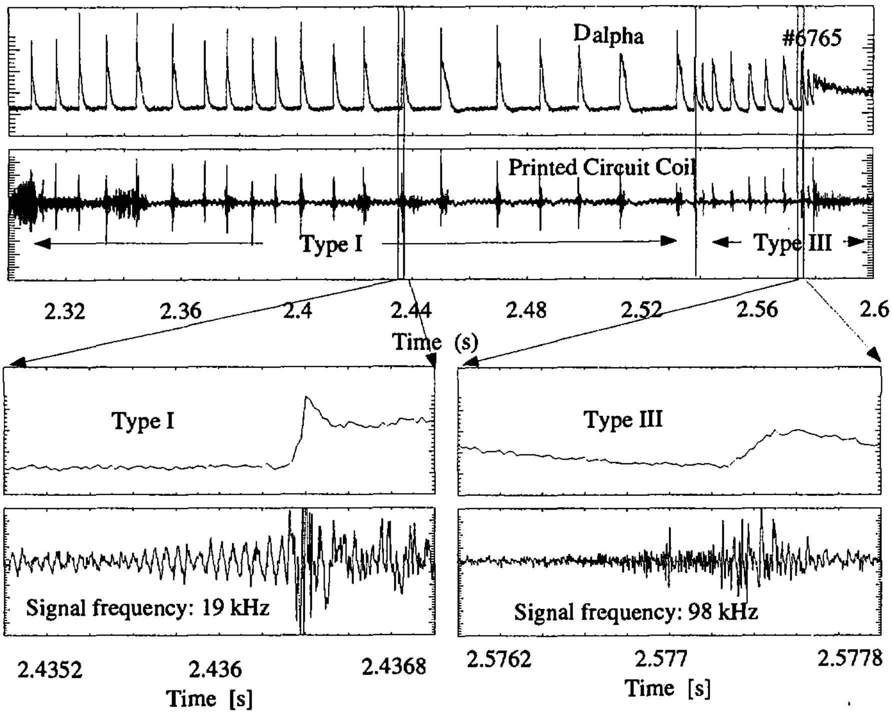

Figure 5: *Difference in MHD mode characteristics between type I (left) and type III (right) ELM precursors.*

the type I ELMs. At $t = 2.54$ s, the ELM type changes to type III, visible on the D_α trace by the higher repetition frequency. A further gradual decrease in P_{sep} leads to an H-L transition at $t = 2.58$ s.
The type III precursor is hardly seen on other coils further away from the plasma so that no reliable statement about the poloidal mode structure can be given yet. From the high n-number and the sharp radial decay of $\tilde{B}$, the mode must be located close to the plasma edge. Similar problems hold for type I, but as the mode is visible also on coils further away from the plasma, we conclude that m is lower than for type III, consistent with the lower n and the lower signal frequency. Thus, in addition to the dependence of the repetition frequency on heating power, we find a clear difference in the MHD signatures of type III and type I ELM precursors.

The differences in mode frequency can only partly be understood by the different spatial structure of the precursors. In the lab frame, MHD modes roughly rotate corresponding to E_r, i.e. with the sum of diamagnetic frequency ω^* and the frequency due to fluid rotation ω_{rot} [17]. With co-injection, the signal frequency is $\nu_{Mirnov} = n(\omega^* - \omega_{rot})/(2\pi)$, whereas for ctr-injection, $\nu_{Mirnov} = n(\omega^* + \omega_{rot})/(2\pi)$ holds, and therefore the mode frequencies are higher, consistent with the higher E_r in these discharges (see Fig. 2 and 3). However, the different n-number of the precursors cannot fully explain the different frequencies between type I and type III (a factor of 4-5 in frequency versus factor of 2-3 in mode number). This might point to a 'real frequency' of one of the modes in the fluid frame. In the case of type I ELMs with co-injection (the usual case in ASDEX Upgrade), ω^* and ω_{rot} almost cancel. Thus, the fact that type I precursors are often hardly visible under these circumstances is due to the low frequency, yielding a low Mirnov amplitude. Actually, the type I ELM precursors may also grow locked and therefore not be detected by magnetic probes at all. In these cases, they have a very high growth rate (on the sub-ms timescale), whereas the rotating precursors grow on a ms timescale. This may be due to the stabilizing effect of the wall on the rotating mode which is absent for the locked precursor.

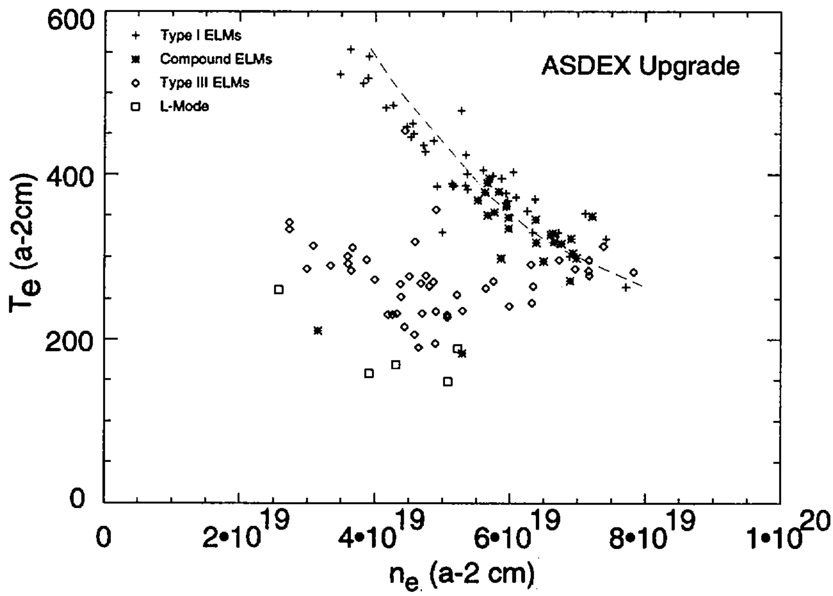

Figure 6: *Plot of $T_{e,edge}$ versus $n_{e,edge}$ prior to different ELM types for $I_p = 1$ MA. The broken line is the ideal ballooning limit to ∇p_e (see text).*

In co-injected cases, where there is a zero of E_r in the steep pressure gradient region, the mode will be most unstable at this position, whereas in ctr-injected discharges, no zero of E_r occurs in the region of high pressure gradient and thus a rotating precursor is observed. This difference in stability can explain that in ASDEX Upgrade, discharges with ctr-injection have a somewhat reduced ELM frequency as compared to co-injection.

With local measurements of T_e and n_e, we map the region where the different types occur [11]. Fig. 6 shows a plot of $T_{e,edge}$ versus $n_{e,edge}$, this time taken from a local measurement (Li-beam) for constant plasma current of 1 MA but various toroidal fields. Type I ELMs occur roughly at $T_{e,edge} \cdot n_{e,edge} = p_{e,edge} = const.$, which indicates a limit to ∇p_{edge}. Obviously, this limit is independent of the toroidal field. This is true for the ideal ballooning limit, where ∇p should roughly scale as I_p^2, which is indeed found from a current scan in ASDEX Upgrade [11]. A good quantitative agreement is found assuming $p_e = p_i$, magnetic shear $S = (r/q)(dq/dr) = 4$ (from equilibrium reconstruction) and pressure scale length $L_p = d(\ln p)/d(\ln r) = 0.03$ m, which leads to the broken line in Fig. 6. This observation is consistent with other experiments [18].

Independent of density, type III ELMs mainly occur at $T_{e,edge} \leq 300$ eV, whereas type I ELMs occur at $T_{e,edge} \geq 300$ eV, indicating that T_e plays a crucial role in determining the ELM type, possibly via resistivity as suggested in [3]. Here, the critical ∇p may depend on $T_{e,edge}$ itself and therefore, the type III ELM region is not defined by a $T_{e,edge} \cdot n_{e,edge} = const.$ line. This also explains why type III ELMs are normally absent with the unfavourable drift direction in ASDEX Upgrade: here, the L-H transition occurs at $T_{e,edge} \geq 300$ eV so that they should just be stabilized. In fact, there are cases with a slow power ramp in which we find some type III ELMs close to the transition even with the unfavourable drift direction. Also, in some of the L-mode phases with improved confinement as shown in Fig. 3, type III ELMs occur (identified by their magnetic precursor), indicating that here, ∇p is high enough for sufficiently low $T_{e,edge}$.

The region without data points corresponds to the ELM-free region. Here, $T_{e,edge}$ is too high for type III ELMs, but the ideal ballooning limit has not yet been reached and therefore no type I ELMs occur. The diagram qualitatively explains the experimental recipes to achieve long ELM-free phases: operation at low density, low q (and therefore high I_p) or shaping (to improve the ballooning limit) all open up a large ELM free region. In addition, small machines operating at low current, as e.g. the 'old' ASDEX device, operate in a region where the ideal limit is reached at low $T_{e,edge}$ due to the low current and therefore, type III ELMs can prevail even up to the ballooning limit as has been shown in [19].

Transport during type I ELMs is studied locally with the use of fast profile diagnostics. An ELM can be well described by enhanced transport coefficients ΔD and $\Delta \chi$ outside a radius r_{ELM} during the turbulent MHD phase [20]. Inside r_{ELM}, transport can even be described by the quiescent transport coefficients. Thus, the turbulent MHD phase greatly deteriorates confinement, but only outside r_{ELM}. This contradicts an analysis on JET, where changes in transport due to ELMs were found up to the $q = 1$ surface and connected to a global H-L transition during the ELM [21]. However, we cannot decide if transport due to a type I ELM is really diffusive, as no attempt was made to model the same experimental data with an outward drift.

Typical enhancements of transport during type I ELMs lie in the range of $\Delta D \approx 5-6$ m^2/s and $\Delta\chi \approx 10-12$ m^2/s; the direct influence of the ELM extends to $a - r_{ELM} \approx 2-4$ cm in the midplane outside. It has been stated before that in ASDEX Upgrade, the energy loss per ELM does not depend on P_{heat} (whereas the repetition frequency does); this is confirmed by the kinetic analysis that roughly finds $\Delta E_{ELM} = const.$ For fixed I_p, the transport enhancement and also r_{ELM} do not change with P_{heat}. In a current scan at fixed P_{heat} and B_t, we still find $r_{ELM} = const.$, but now the enhancement in transport coefficients scales like $1/I_p$. As $\nabla p_{edge} \sim I_p^2$ due to the ballooning limit, the energy loss per type I ELM roughly scales like $\Delta\chi\nabla p \sim I_p$. Therefore, the ELM frequency ('inverse reheat time') decreases roughly like $1/I_p$. As these experiments were carried out at $B_t = const.$, it is not clear if this is an I_p- or a q-scaling.

4 Conclusions

We have studied the H-mode operational space in ASDEX Upgrade in terms of $T_{e,edge}$ versus $n_{e,edge}$. The value of $T_{e,edge}$ at the L-H transition is the same as at the H-L transition at otherwise constant plasma parameters. Thus, the hysteresis in heating power comes from the reduced transport coefficients in the H-mode. The value of $T_{e,edge}$ necessary for the transition rises with increasing B_t and decreases with n_e. This is inconsistent with theories based on ion-orbit loss as the dominant nonambipolar radial loss current. Using a new method for measurement of E_r, we find that E_r can jump by ≈ 5 kV/m in less than 1 ms, but not prior to the reduction of transport (temporal resolution $\approx 100\mu$s). The full value of $\approx 20-40$ kV/m is mainly due to the build-up of ∇p.

ELMs of type I and type III show quite different magnetic precursor structures. In operational space, they are separated by a critical $T_{e,edge}$ above which type III ELMs are stabilized, whereas type I ELMs occur when the edge pressure gradient reaches the ideal ballooning limit. These observations suggest that type III ELMs are a resistive MHD phenomenon, whereas type I ELMs may be governed by ideal MHD.

REFERENCES

[1] WAGNER, F., et al., Phys. Rev. Lett. **49** (1982) 1408.
[2] GROEBNER, R.J., Phys. Fluids B **5** (1993) 2343.
[3] ZOHM, H., Plasma Phys. Control. Fusion **38** (1996) 105.
[4] MERTENS, V., et al., IAEA-CN-64/A4-4, this volume.

[5] RYTER, F., et al., IAEA-CN-64/AP1-5, this volume.
[6] RYTER, F., et al., Plasma Phys. Control. Fusion **36** (1994) A99.
[7] ITOH, S.-I., et al., J. Nucl. Mater. **220–222** (1995) 117.
[8] KALLENBACH, A., et al., in IPP Rep. 10/1, Plasma Phys. Control. Fusion (in press).
[9] ITOH, K., et al., Plasma Phys. Control. Fusion **38** (1996) 1.
[10] STOBER, J., et al., in Controlled Fusion and Plasma Physics (Proc. 23rd Eur. Conf. Kiev, 1996), European Physical Society, Geneva (1996).
[11] SUTTROP, W., et al., ibid.
[12] KALLENBACH, A., et al., Nucl. Fusion **35** (1995) 1231.
[13] DE BLANK, H.J., et al., in Controlled Fusion and Plasma Physics (Proc. 23rd Eur. Conf. Kiev, 1996), European Physical Society, Geneva (1996).
[14] HERRMANN, W., Phys. Rev. Lett. **75** (1995) 4401.
[15] KIM, J., et al., Phys. Rev. Lett. **72** (1994) 2199.
[16] SUTTROP, W., et al., Plasma Phys. Control. Fusion **38** (1996) 1407.
[17] KLÜBER, O., Nucl. Fusion **31** (1991) 907.
[18] GOHIL, P., et al., Phys. Rev. Lett. **61** (1995) 1603.
[19] ZOHM, H., Nucl. Fusion **35** (1995) 543.
[20] REIMERDES, H., IPP Rep. 1/300, submitted to Plasma Phys. Control. Fusion.
[21] PARAIL, V., et al., in Controlled Fusion and Plasma Physics (Proc. 23rd Eur. Conf. Kiev, 1996), European Physical Society, Geneva (1996).

DISCUSSION

K. TOI: You showed the jump in the charge exchange flux, which indicates the formation of an E_r (shear) layer, just after the transition. However, you mentioned that at the transition an additional torque may be active. Do you find any experimental evidence to suggest the possibility of additional torque at the transition?

H. ZOHM: In fast transitions, there may be cases where the increase in ∇p cannot fully account for the jump in E_r; this has, however, to be checked by measuring the poloidal rotation.

V. PARAIL: When you derived the pressure gradient at the onset of Type I ELMs, what kind of inhomogeneity length did you use and how does it depend on plasma current and temperature?

H. ZOHM: For the calculation of α, we have used a constant pressure scale length of 3 cm. We did not study the dependence on plasma parameters; this will be addressed in the future.

R.R. WEYNANTS: You see a gradual increase of E_r during the L mode leading up to the transition. Presumably, also the shear of E_r changes gradually. Do you then see a gradual improvement of confinement or is there evidence for a threshold?

H. ZOHM: The L–H transition always occurs as a 'jump', so there is evidence for a threshold. However, in some high power L modes, we can also observe a gradual improvement of confinement, but even in these discharges, the L–H transition itself is a jump.

S.I. ITOH: Could you explain again the sudden jump of the radial electric field, E_r, in relation to your previous work on dithering ELM.

H. ZOHM: The dithering phase can indeed be described by the ion orbit loss model, but any other bistable mechanism could do that, too. Experimentally, the dithering phase actually corresponds to jumps in E_r by ~5 kV/m.

MHD STABILITY STUDIES IN REVERSED SHEAR PLASMAS IN TFTR

J. MANICKAM, E.D. FREDRICKSON, Z. CHANG, M. OKABAYASHI,
M.G. BELL, R.V. BUDNY, W. PARK, G.L. SCHMIDT,
M.C. ZARNSTORFF, TFTR GROUP
Plasma Physics Laboratory,
Princeton University,
Princeton, New Jersey,
United States of America

F.M. LEVINTON, S.H. BATHA
Fusion Physics and Technology,
Torrance, California,
United States of America

T.C. HENDER, C.G. GIMBLETT, R.J. HASTIE
UKAEA–Euratom Fusion Association,
Culham, Abingdon, Oxfordshire,
United Kingdom

M. PHILLIPS, M.H. HUGHES
Northrop–Grumman,
Plainsboro, New Jersey,
United States of America

S.A. SABBAGH
Columbia University,
New York, N.Y.,
United States of America

Abstract

MHD STABILITY STUDIES IN REVERSED SHEAR PLASMAS IN TFTR.

MHD phenomena in reversed shear plasmas in TFTR are described for each of the three phases of the evolution of these discharges: the current ramp, high power neutral beam heating and after the beam power has been reduced. Theoretical analysis of discharges which disrupted in the high-β phase indicates that the β-limit is set by the ideal $n = 1$ infernal/kink mode. The mode structure of the disruption precursor reconstructed from the electron temperature data compares favorably with the predicted displacement vector from the ideal MHD model. In contrast, disruptions during the early and late phases are due to resistive instabilities, double tearing modes coupled to high-m edge modes. The resistive interchange mode, predicted to be unstable in reversed shear plasmas, is not seen in the experiment. Neo-classical tearing mode theory is shown to describe the non-disruptive MHD phenomena. A non-linear resistive MHD simulation reproduces off-axis sawtooth-like crashes during the post-beam phase. The dependence of the β-limit on the pressure peakedness and $q_{\min}$ is discussed, showing a path to stable higher-β regimes.

Tokamak plasmas having safety-factor profiles with shear reversal in the core are attractive for several reasons: a) improved stability to high-n ballooning modes[1], where n is the toroidal mode number, b) the potential for aligning the self-generated bootstrap currents with a stable current distribution[2], c) improved microstability which may result in improved confinement[2] and d) stabilization of neo-classical (bootstrap driven) instabilities in the reverse shear region[3].

This regime of reversed shear (RS) plasmas has been the subject of intense interest on many large tokamaks including the Tokamak Fusion Test Reactor, TFTR. In TFTR RS plasmas a spontaneous transition to improved confinement is often observed; this plasma regime is referred to as the Enhanced Reversed Shear (ERS) regime. This report will focus on the MHD properties of RS and ERS plasmas in TFTR.

1. Plasma Evolution

RS plasmas are produced by heating the plasma during the current rise phase of the discharge to slow the penetration of the current to the core. The resulting off-axis maximum of the current density results in a reversed shear q-profile. However it should be noted that the profile is not static and continues to evolve slowly as the current diffuses and as the pressure-driven bootstrap current is generated. The q-profile is mainly characterised by $q_{edge}, q_{axis}, q_{min}$ and r_{qmin}, the location of the q_{min}-surface. For the reasons outlined above, it is only possible to maintain q_{edge} at a constant value, q_{min} and $r_{\mathrm{q-min}}$ steadily decrease during the discharge. In most of the discharges q_{min} dropped to about 2 at the end of the heating phase. This aspect of RS operation plays a significant role in the context of MHD stability and will be discussed later. The pressure profile in RS plasmas is similar to those in supershots and is fairly peaked with a peakedness defined as PPF $\equiv$ $p_0/\langle p\rangle$ typically 4. Here p_0 represents the pressure on axis and $<>$ represents a volume average. In ERS plasmas the improved confinement causes the pressure profile to peak even more and results in PPF ≥ 6.

The RS and ERS discharges are limited in the achievable β by rapidly growing MHD instabilities, where $\beta \equiv 2\mu_0 < p > /B^2$, B is the vacuum toroidal field. It is often possible to prevent the disruptions by reducing the beam power after a prescribed period of high-power heating, *i.e.* by limiting the rise in β . In spite of this, some of the discharges disrupt after the beam power is reduced. Some even disrupt at very low β well after the beams have been turned off. A useful measure of the stored energy is the normalized β, $\beta_N \equiv \beta/(\frac{I}{aB})$ where I is the current in Mega Amps, a, the plasma minor radius in meters, and B is measured in Tesla. A better indicator of the fusion power achievable is $\beta^* \equiv 2\mu_0 < p^2 >^{\frac{1}{2}} /B^2$. Typically $\beta^* > \beta$ and β^* /β increases as PPF increases. In TFTR ERS discharges for PPF ~ 4, $\beta^*/\beta \sim 1.5$ and for PPF ~ 7, $\beta^*/\beta \sim 2$. An analogous expression to β_N, for the normalized β^* is $\beta_N^* \equiv \beta^*/(\frac{I}{aB})$. In TFTR, most of the experiments were conducted in plasmas with a current of either 1.6 MA or 2.2 MA. The highest β_N achieved at 1.6 MA was β_N ~2 and at 2.2 MA it was $\beta_N \sim 1.7$. The corresponding values of β_N^* are 3.8 and 2.9 respectively.

2. Observed MHD

The discharge has different forms of MHD activity in the three distinct beam heating phases. The early phase, referred to as the *prelude*, when low beam power is used to freeze the q–profile, the *high power* phase when the plasma β increases, and the post-beam phase, referred to as the *postlude*, when the beam power is reduced or even turned off. There is no significant difference in the MHD activity in *RS* and *ERS* plasmas, except that *ERS* plasmas reach higher values of β and may experience β -limiting disruptions.

The principal diagnostics for the MHD are the external Mirnov loops and the internal electron cyclotron emission, ECE, measurements of the electron temperature. Depending on the mode characteristics, internal and/or external, MHD events are observed on one or both of the diagnostics. The q profile is measured by the Motional Stark Effect, MSE, diagnostic.

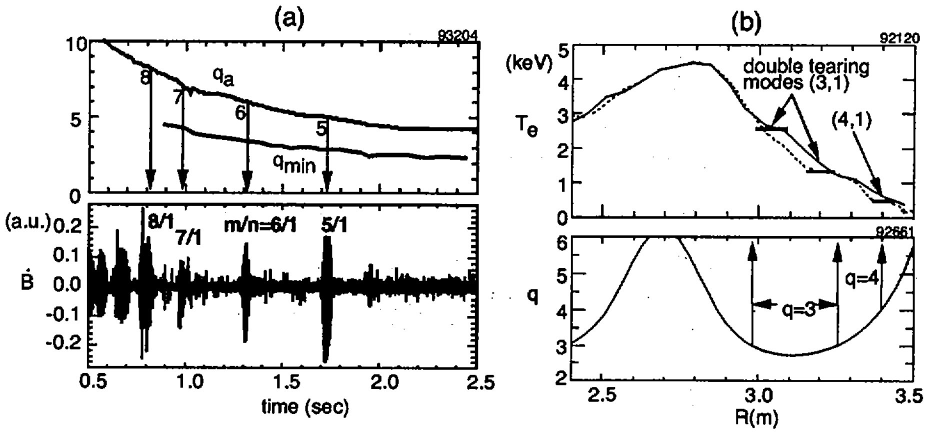

FIG. 1. MHD activity during the prelude phase includes (a) bursts associated with q_{edge} or q_{min} passing through integer values; (b) the flat spots in the temperature profiles indicate the presence of tearing modes localized near the rational surfaces.

In the *prelude* the MHD activity is seen on both Mirnov and ECE and is correlated with either $q_{\min}$ or q_{edge} passing through integer values. Figure 1a shows the evolution of q_{edge}, $q_{\min}$ and the signals from the Mirnov data. A clear correlation of the MHD activity with q_{edge} is observed. Figure 1b shows the electron temperature profile reconstructed from the ECE grating polychromator and the q profile from the MSE. A double tearing mode is observed localized near the two q =3 surfaces. The toroidal mode number, $n = 1$, and the poloidal mode number, m, is inferred to be 3. There is also a tearing mode at the q =4 surface. In some instances when the double tearing mode is coupled to the higher m edge modes, the plasma may disrupt.

During the main heating phase, there are two forms of MHD activity. There is continuous MHD activity as observed on the Mirnov loop signal. The ECE diagnosticis shows that this is usually located at and beyond the $r_{\text{q-min}}$ radius.As seen in Fig. 2 it has no apparent effect on the evolution of the discharge, and generally corresponds to a toroidal mode number, $n = 2$, and is determined to be co-rotating with the plasma. In some discharges a concurrent $n = 1$ or $n = 3$ mode is seen. As the stored energy rises an $n = 1$ mode may grow rapidly, also shown in Fig. 2, leading to a disruption. The mode is located in the vicinity of the $q_{\min}$ surface. In some disruptions a ballooning mode located in the positive shear region is observed, superposed on the $n = 1$ mode. This is similar to the observation in supershot plasmas[4]. Disruptions determine the β-limit in these plasmas.

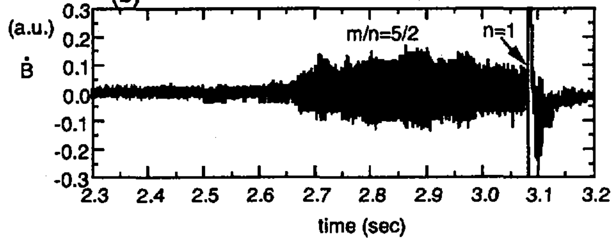

FIG. 2. (a) MHD during the high power heating phase does not affect the rise in stored energy. (b) Disruptions with an $n = 1$ precursor are observed at high β.

In the post-beam phase of ERS plasmas there is often a periodic drop in the core temperature in a manner similar to a sawtooth. However as $q_{\min}$ remains above unity, and the central temperature remains high, this is a different form of sawtooth-like collapse, see Fig. 3.

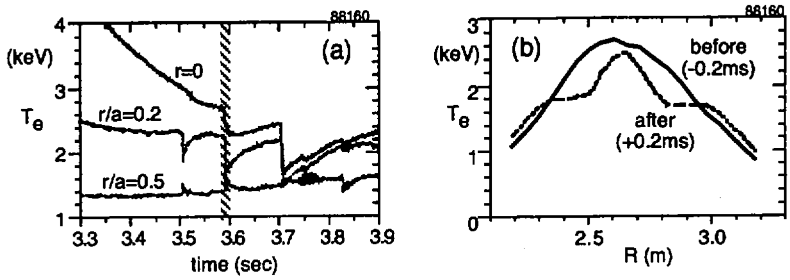

FIG. 3. Electron temperature profile shows an off-axis flattening as a result of a periodic sawtooth-like collapse. (a) Three chords showing an off-axis heat pulse, r/a = 0.2, 0.5, while the central chord, r/a = 0, is relatively unchanged; (b) $T_e(R)$ profiles 0.2 ms before and after the crash at 3.6 s, see the shaded region in (a). In some events the reconnection extends to the core, as seen at 3.7 s.

3. Analysis

The stability analysis of RS and ERS discharges has focussed mainly on the high power and postlude phases. It starts with a reconstruction of the plasma equilibrium profiles. The q -profile is determined by the Motional Stark Effect diagnostic, when it is available, or the data from a similar shot is used. It should be noted that the MSE diagnostic is not available during the high power phase. The evolution of the current profile in the high power phase is based on resistive diffusion, using the TRANSP code. The pressure profile is also determined by TRANSP based on the measured T_e, T_i, n_e profiles and other measured plasma parameters. To account for the uncertainity of the reconstruction, and to determine the sensitivity to the details of the profiles, equilibria with possible profile modifications are also considered. These equilibria are examined using a number of MHD stability codes as well as analytic methods.

Several high-β discharges which disrupted were examined and the predicted stability limit compared to the experimental value at the disruption. Table I shows the comparison of the β limit as well as some key plasma parameters at the time of disruption. The disruptive β limit is identified to be caused by an ideal $n = 1$ instability, an infernal/kink mode[5]. It is driven primarily by the pressure gradient in the low shear region, and consequently is sensitive to the location of rational surfaces. In the high current discharges it also has a large edge component. The high-n ballooning modes are stable across the plasma.

Table 1: Comparison of the theoretically predicted $\beta_N^{Crit.}$ with the maximum β_N observed in the experiment prior to the disruption. One non-disruptive case is included for comparison.

	1.6 MA			2.2 MA		
Shot No.	85693	85694	84011	91788	93260	93517
Expt. β_N	1.3	1.7	1.7	1.2	1.3	1.7
Theory $\beta_N^{Crit.}$	1.5	1.7	1.7	1.3	1.3	1.8
Disrupted	NO	YES	YES	YES	YES	YES
$q_{\min}$	2.2	2.0	2.0	1.8	2.0	1.9
$p_o/\langle p\rangle$	4.5	6.5	7.5	8.0	6.4	4.2

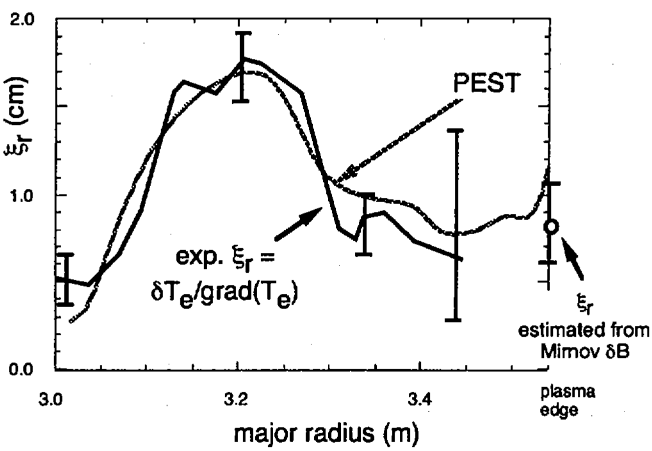

FIG. 4. Comparison of the predicted radial displacement vector along the outer mid-plane for a plasma at the β-limit with the reconstruction using the temperature data for a disruption precursor in a 2.2 MA discharge. Note that the maximum amplitude of the PEST ξ_r was scaled to match the maximum of the experimental ξ_r.

The predicted infernal/kink mode structure can be compared with a mode structure reconstructed from the ECE data. The contours of constant electron temperature are monitored and their displacement is used to determine the radial displacement of the flux surfaces. Figure 4 shows such a comparison for discharge number 93260. The ECE diagnostic is less reliable near the plasma boundary, however supplemental information is available by extrapolating the Mirnov signal back to the plasma edge assuming that $\xi_r \propto (r - r_{edge})^m$, where m is the poloidal mode number corresponding to nq_{edge}. The agreement between this reconstruction and the theoretical prediction from the PEST code is remarkable. A similar favorable comparison was made for discharge 84011 at 1.6 MA. This implies that the theoretical β -limit from ideal theory is a good guide to the stability properties of RS and ERS plasmas. Parametric dependence of the β -limits is discussed later in this report.

During the high power phase there is continuous MHD activity, which is inferred to be resistive in nature because the growth-times are on the resistive time scale and mode rotation is close to the plasma rotation. Theoretical analysis indicates that the resistive interchange criterion[6] is violated when the shear, q', is negative and the pressure gradient, p', is sufficiently large. In the experiment these conditions are often satisfied. However the mode is not seen at the rational surface in the negative shear region, rather the mode is seen at the rational surface in the positive shear region where the interchange mode is inherently stable, since $q' > 0$. Neo-classical tearing modes are a better candidate for this activity. In fact neo-classical theory indicates that the tearing and interchange modes are stabilized in the negative shear region and tearing modes are destabilized in regions with positive shear. Comparison of the evolution of the island width inferred from the Mirnov data agrees well with the predictions of analytic theory[3].

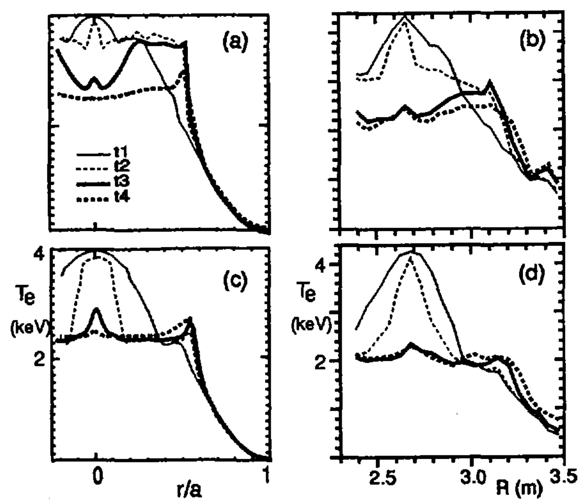

FIG. 5. Comparison of MH3D simulation (left) and experimental observation from two ECE systems (right) of a 2/1 sawtooth core reconnection. Four phases can be distinguished: (1) early growth phase (t_1), (2) double-tearing reconnection phase (t_2), (3) central temperature collapse phase (t_3), (4) final temperature equalization phase (t_4). The basic feature is the inner hot island moving out ((a) and (b)) and the outer cold island moving in ((c) and (d)).

The off-axis sawtooth observed in the post-beam phase is simulated with the non-linear resistive MHD code, MH3D[7]. A double tearing mode is shown to cause a magnetic reconnection and a thermal heat pulse. As the simulation evolves a hot island moves out and a cold island moves inwards. A comparison of the the T_e profiles from the experiment and the simulation is shown in Fig. 5.

4. Parameter dependence

The preceding analysis suggests that the β limit observed in TFTR discharges is governed by stability to the ideal $n = 1$ instability. It is largely an internal mode and is sensitive to various plasma parameters, including: $\beta, \beta^*, PPF, q_{min}, r_{qmin}, q'_{edge}$. A general study of these dependencies was reported in Ref. [8]. Details of a specific study using profiles from the experiment as a starting point are presented here. Figure 6a shows the dependence of the critical β_N and β_N^* for instability on the peakedness of the pressure profile, $p_o/\langle p\rangle$. After a modest increase there is a clear decline in the critical β_N as $p_o/\langle p\rangle$ increases, an optimal value is $p_o/\langle p\rangle =$ 3.5. It is interesting to note that while β_N declines as $p_o/\langle p\rangle$ is increased, β_N^* rises and is essentially independent of $p_o/\langle p\rangle$. This bodes well for the use of ERS type plasmas in an advanced tokamak. Figure 6b show the dependence on $q_{\rm min}$ at fixed $p_o/\langle p\rangle$. The variation in the critical values of β_N and β_N^* show a strong dependence on $q_{\rm min}$. The optimal value is $q_{min} \sim 1.2$. An analytic theory of the beta limit when the minimum in the q -profile lies just below a rational value has been developed [9]. In this limit the eigenfunction is adequately represented by three poloidal harmonics and a relatively low β-limit with $\beta_{crit} \propto \epsilon^{8/5}$ is found, ϵ is the inverse aspect ratio. The instability is described as a double kink.

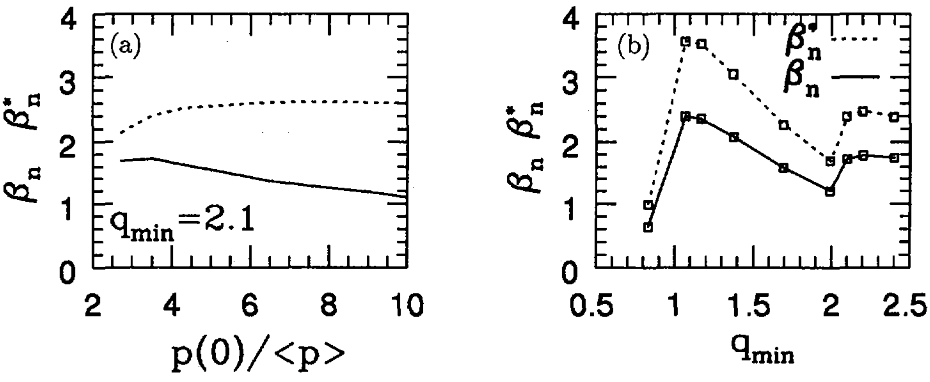

FIG. 6. (a) For large values of $p_0/\langle p\rangle$, the critical β_N^* is independent of the pressure peakedness. (b) There is a sudden drop in β_N and β_N^* when q_{min} is an integer.

5. Summary

This report describes the main experimental observations in RS and ERS plasmas in TFTR. Disruptions set a β-limit in these discharges. Detailed modelling of the experiment during the high power phase shows that the ideal $n = 1$, infernal/kink instability is responsible for the observed disruptions. The mode structure of the disruption precursor is shown to compare favorably with the prediction of ideal MHD theory. The role of resistive MHD in the RS and ERS plasmas is more complex. Resistive interchange modes, predicted to be unstable in the negative shear region of the plasma are not observed. Tearing modes are seen to play a role during the prelude and postlude phases. The resistive MHD observed during the high power phase is apparently benign and has been identified as neo-classical tearing modes. The absence of the better known resistive modes coupled with the strong agreement with ideal MHD theory, confirms that the TFTR plasmas are deep in the collisionless regime, a regime of particular relevance to tokamak reactors.

Analytic and numerical methods have been used to uncover the underlying physics of the instability. The peakedness of the pressure profile plays a key role in two ways. It is responsible for directly driving the instability, and is the source of the bootstrap current which modifies the q -profile leading to greater instability. $q_{\rm min}$ is shown to have a critical role. Specifically when nq_{min} is approximately an integer the probability of driving an instability increases. Careful tailoring of the q -profile can achieve improved stability limits.

This paper has concentrated largely on the performance limiting MHD issues. Several MHD stability issues remain to be addressed. In particular, analysis of the MHD activity in the prelude phase and some of the disruptions in the postlude phase remains to be studied.

Acknowledgement: This work was supported by the US Department of Energy under contract No. DE-AC02-76-CHO-3073. UKAEA authors were supported jointly by the UK Department of Trade and Industry and EURATOM.

REFERENCES

[1] GREENE, J.M., CHANCE, M.S., Nucl. Fusion **21** (1981) 453.
[2] KESSEL, C., et al., Phys. Rev. Lett. **72** (1994) 1212.
[3] CHANG, Z., et al., Phys. Rev. Lett. **74** (1995) 4663.
[4] PARK, W., et al., Phys. Rev. Lett. **75** (1995) 1763.

[5] MANICKAM, J., POMPHREY, N., TODD, A.M.M., Nucl. Fusion 27 (1987) 1461.
[6] GLASSER, A., GREENE, J.M., JOHNSON, J.L., Phys. Fluids 18 (1975) 875.
[7] CHANG, Z., et al., Phys. Rev. Lett. (in press).
[8] PHILLIPS, M., et al., Phys. Plasmas 3 (1996) 1673.
[9] GIMBLETT, C., et al., Phys. Plasmas 3 (1996) 3369.

DISCUSSION

D.C. MOREAU: Should we conclude that n = 2 infernal modes are not limiting β since you showed no drop in β at values of q_{min} = 1.5 or 2.5?

J. MANICKAM: This is a profile dependent issue. We have tested the profiles in TFTR reversed shear discharges for higher n modes. The stability limits for the higher n modes are above the limits for the n = 1 mode. With other profiles we do see drops in the stable β due to n = 2 when q_{min} = 1.5 or 2.5.

A.D. TURNBULL: You showed that in the postlude phase you drop the beam power and β drops. You also showed that the theory predicts that if β is reduced when $q_{min} \approx 2$, you should be able to get underneath the minimum in the β limit at $q_{min} \approx 2$. What actually prevents you (operationally) from getting under there and into the higher β region at $q_{min} \approx 1.2$?

J. MANICKAM: As shown earlier, q_{min} decreases with time and moves inward to a smaller radius. This means that since we start with $q_{min} > 2$, if we try to approach q_{min} = 1.2 at reduced β, the radius of q_{min} will probably go to zero long before we reach q_{min} = 1.2. The correct way to get there is to start with lower q_{min}. This requires different operational procedures, i.e. current ramp rate and beam timing. This will be attempted in the next run period.

R.J. HAWRYLUK: May I comment on this question? Most ERSs are successfully terminated without a disruption. Disruptions occur in the postlude when the values of q_{min} and $r(q_{min})$ decrease and the sharp pressure gradients grow into the positive shear region. As shown by Levinton et al. in paper IAEA-CN-64/A1-3, it is possible to obtain a back-transition by changing the neutral beam torque in the postlude phase. This relaxes the pressure gradients and reduces the disruption probability.

Y. KAMADA: Around the internal transport barrier we usually observe a strong rotational shear which may have a stabilizing effect. In your stability analyses, is the rotational effect included? If not, please comment on this point.

J. MANICKAM: In TFTR we use balanced injection of the neutral beams. Consequently, we do not have as strong a rotation as you do, and we do not need special consideration of this in our analysis. I believe that the principal role of the rotational shear would be to decouple resistive MHD activity at different rational surfaces, leading to some degree of stabilization.

LOCAL ANALYSIS OF CONFINEMENT AND TRANSPORT IN NEUTRAL BEAM HEATED DIII-D DISCHARGES WITH NEGATIVE MAGNETIC SHEAR*

D.P. SCHISSEL, C.M. GREENFIELD, J.C. DEBOO, L.L. LAO, E.A. LAZARUS[1], G.A. NAVRATIL[2], B.W. RICE[3], G.M. STAEBLER, B.W. STALLARD[3], E.J. STRAIT, H.E. ST. JOHN, M.E. AUSTIN[4], K.H. BURRELL, T.A. CASPER[3], D.R. BAKER, V.S. CHAN, E.J. DOYLE[5], J.R. FERRON, C.B. FOREST, P. GOHIL, R.J. GROEBNER, W.W. HEIDBRINK[6], R.-M. HONG, A.W. HOWALD, C.-L. HSIEH, A.W. HYATT, G.L. JACKSON, J. KIM, C.J. LASNIER[3], A.W. LEONARD, J. LOHR, R.J. LA HAYE, R. MAINGI[7], R.L. MILLER, M. MURAKAMI[1], T.H. OSBORNE, C.C. PETTY, C.L. RETTIG[5], T.L. RHODES[5], S.A. SABBAGH[2], T.C. SCOVILLE, R.T. SNIDER, R.D. STAMBAUGH, R.E. STOCKDALE, P.L. TAYLOR, T.S. TAYLOR, D.M. THOMAS, M.R. WADE, R.E. WALTZ, R.D. WOOD[3], D.G. WHYTE[8]
General Atomics,
San Diego, California,
United States of America

Abstract

LOCAL ANALYSIS OF CONFINEMENT AND TRANSPORT IN NEUTRAL BEAM HEATED DIII-D DISCHARGES WITH NEGATIVE MAGNETIC SHEAR.

High triangularity double-null discharges with weak or negative central magnetic shear and with both an L-mode and an H-mode edge have been produced on DIII-D. The L-mode edge cases are characterized by peaked toroidal rotation, ion temperature, and plasma density profiles with reduced ion transport in the negative shear region. The H-mode edge cases have broader profiles consistent with reduced ion transport, to the neoclassical level, over the entire plasma cross-section. The L-mode edge cases have a greater reduction in central ion diffusivity with stronger negative shear while the H-mode edge cases do not exhibit this dependence. Plasma fluctuation measurements show that a dramatic reduction in turbulence accompanies the improved ion confinement. Calculations of sheared $\mathbf{E} \times \mathbf{B}$ flow indicate that this mechanism can overcome the η_i mode growth rate in the region of reduced transport.

---

* Work supported by the US Department of Energy under Contract Nos DE-AC03-89ER51114, DE-AC05-96OR22464, DE-AC04-94AL85000, and Grant Nos DE-FG03-86ER53266 and DE-FG03-95ER54294.

[1] Oak Ridge National Laboratory, Oak Ridge, Tennessee, USA.
[2] Columbia University, New York, New York, USA.
[3] Lawrence Livermore National Laboratory, Livermore, California, USA.
[4] University of Maryland, College Park, Maryland, USA.
[5] University of California, Los Angeles, California, USA.
[6] University of California, Irvine, California, USA.
[7] Oak Ridge Associated Universities, Oak Ridge, Tennessee, USA.
[8] Institut national de la recherche scientifique, Energie et matériaux, Varennes, Quebec, Canada.

1. INTRODUCTION

An attractive, compact, economical fusion power plant requires the development of a plasma with both good energy confinement and MHD stability at high beta. Since the last IAEA meeting, a class of experiments with improved confinement and stability have been operated on the DIII–D tokamak by carefully tailoring the shape of the plasma current profile [1–3]. The shaping of the current profile in these discharges is such that a central region of weak or negative magnetic shear (NCS) [$s = (r/q)\, dq/dr \leq 0$] has been created. The inverted safety factor (q) profile of the NCS configuration is a robust regime that has reliably been obtained with both neutral beam heating and fast wave current drive. This paper reports on the confinement and transport properties of beam heated NCS discharges. NCS discharges with fast wave heating are presented at this conference in paper IAEA–CN–64/E–1. The high beta NCS operation results from the majority of the plasma volume being in the second stable regime for ideal MHD ballooning modes. Details of the MHD behavior of these plasmas will be presented in papers IAEA–CN–64/A1–2 and DP–1 at this conference.

2. NCS DISCHARGE EVOLUTION

NCS discharges are produced in DIII–D using codirectional neutral beam injection early in the initial current ramp [4]. This early beam injection typically started around 300–500 ms after plasma breakdown and with moderate 75 keV beam power (2–5 MW). Figure 1 shows the temporal evolution of a double–null NCS plasma with both an L–mode and H–mode phase. We will use the terminology NCS plasma with H–mode (L–mode) edge to indicate a plasma with weak or negative central magnetic shear combined with edge conditions characteristic of an ELM–free H–mode (L–mode). The toroidal field is 2.1 T and the gas and beam fuel is deuterium. The low beam target density ($n_e = 1–2 \times 10^{19}\ m^{-3}$) combined with the early neutral beam power yields central electron temperatures (T_e) around 3 keV early in the plasma current rise phase. Electron temperatures in this range create a central current diffusion time on the order of 5 s. The central current density is effectively frozen at this early low value, forcing a hollow current profile to develop as the plasma current ramps up. The hollow current profile results in negative shear since the q profile also has a minimum off axis [Fig. 1(b) plotted as $\Delta q = q(0) - q_{min}$]. In these experiments the q profile is directly determined from the profile of local field pitch angle measured by the 16 channel motional Stark effect (MSE) diagnostic [Fig. 1(f,g)], combined with information on the plasma shape as determined by EFIT from external magnetic measurements. By varying the early beam timing, the level of beam power, and the beam target density, some shot-to-shot control over the current profile shape has been possible.

The second phase of the NCS discharge begins with the initiation of high power neutral beam heating typically just after the plasma current has reached flattop; neutral beam power is incrementally increased at 2.0 s and 2.15 s in Fig. 1(a). Weak shear is maintained during the high power phase [Fig. 1(b)] and varies slowly in time. It is during this high power phase that this NCS discharge exhibits good confinement with the formation of an internal transport barrier. There is an increase in the core ion temperature (T_i) [Fig. 1(e)] relative to the middle part of the discharge indicating the formation of the transport barrier; a central value of approximately 17 keV is obtained. At this time the global confinement begins to improve until ultimately an H factor (against ITER89–P) of above 3.0 is obtained. The formation of a transport barrier can

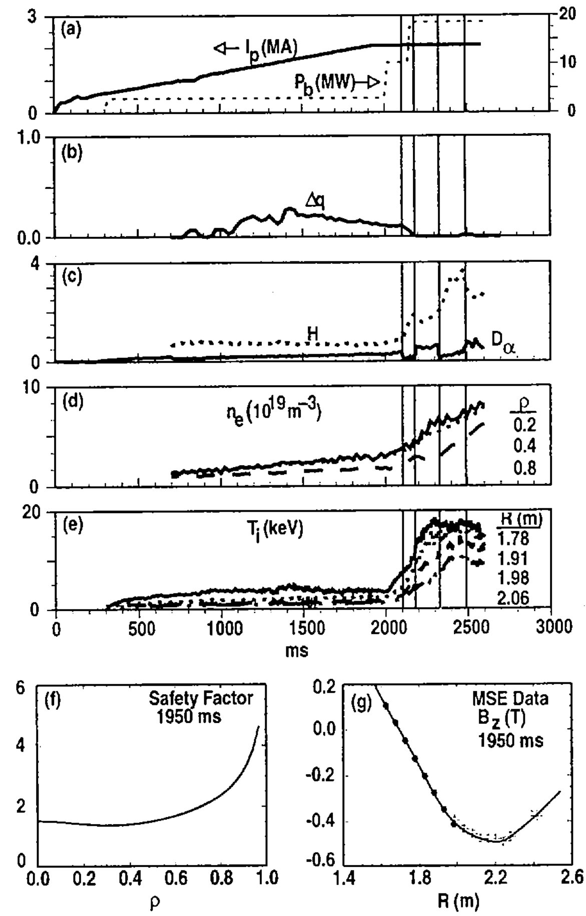

Fig. 1. (a) Early beam power during the current ramp produces the NCS configuration. (b) This double-null plasma (87935) has weak shear [$\Delta q = q(0) - q_{min}$]. (c) There are two H–mode edge phases (divertor D_α emission) in this discharge marked by the vertical lines. Enhancement (H) over ITER–89P exceeds 3. (d) Density profiles are peaked in L–mode edge and broad in H–mode edge. (e) Ion temperature is more peaked in L–mode edge. (f,g) The MSE diagnostic measures the local magnetic field pitch angle and, combined with magnetic probe measurements, results in a well determined q profile.

also be inferred directly from the increased ∇T_i when compared to discharges without NCS. Figure 2 compares both an H–mode and L–mode edge NCS plasma to an H–mode discharge with a monotonic q profile. The transport barrier formation near ρ = 0.5 is clearly evident by the increase in both T_i and toroidal rotation (Ω_ϕ) at that spatial location. NCS discharges with lower power during the second phase still have reversed shear but do not exhibit an increase in confinement. These low power NCS discharges have approximately the same confinement as an ordinary L–mode discharge with a monotonic q profile. This indicates that there is a power threshold for improved confinement in NCS discharges.

Transport has been studied in high triangularity ($\delta \approx 0.8$) double-null plasmas with plasma currents up to the 2.1 MA level. The ability to control the L– and H–mode transition in these plasmas has been made possible by the flexibility of the DIII–D digital plasma control system. The early level of beam heating in NCS discharges exceeds the H–mode power threshold for double–null diverted plasmas in DIII–D. For NCS plasmas to remain with an L–mode edge the plasma has been displaced toward the upper null which is opposite to the ion ∇B direction. At 2.1 s, the discharge in Fig. 1 is moved downward, balancing the two nulls, resulting in the H–mode transition 5 ms later. Interestingly, there is a transition back to L–mode 75 ms later even though the power has been increased to the 18 MW level. The speculation is that this return to L–mode results from the reduction in power flow near the edge due to the dramatic reduction in core energy transport inside the region of weak shear. Finally, at 2.33 s the discharge returns to an ELM–free H–mode until the first ELM occurs at 2.49 s.

3. TRANSPORT IN NCS DOUBLE–NULL DISCHARGES

L–mode edge NCS plasmas are characterized by a peaking of the density profile. This is evident from Fig. 1(d) where after the H to L transition at 2.18 s there is a larger increase in n_e at $\rho = 0.2$ than $\rho = 0.4$ with a decrease in density at $\rho = 0.8$. In general, the peaked density profile combined with the large core temperature gradients produce highly peaked pressure (p) profiles. The discharge in Fig. 1 reaches a value of $p(0)/\langle p \rangle = 4$ at 2.35 s but values up to 5 have been observed. The core of these discharges is in the second stable regime for ballooning modes due to the weak or negative magnetic shear. However, L–mode edge NCS discharges typically disrupt when normalized beta $\beta_N \equiv \beta\ (\%)/[I_p/aB_T\ (\mathrm{MA/mT})]$ exceeds 2.0–2.5. This disruption is believed to result from the plasma becoming unstable to a global resistive mode. The density peaking is direct evidence that a reduction in particle transport accompanies the reduction in energy transport in L–mode edge NCS plasmas. Typically, the rise rate in core density is approximately equal to the beam fueling rate with the inferred particle diffusivity dropping to near zero.

Density profile peaking in NCS H–mode edge plasmas has not been observed. Although the density continues to increase in Fig. 1 after the L to H transition at 2.33 s, the density profile begins to broaden. In general for H–mode edge NCS plasmas, the broad density profile results in a relatively broad pressure profile. This broader pressure profile leads to a broadening of the beam deposition profile which reduces the heating and fueling of the core plasma. The larger β_N value than the L–mode edge case is consistent with ideal MHD calculations with a broader pressure profile. Termination of the high performance phase in H–mode edge plasmas typically results from the onset of an edge kink mode.

The ability to time the L to H transition has led to the capability of combining the good confinement properties of the NCS L–mode core with the good confinement properties of the H–mode edge leading to NCS discharges with reduced ion transport over the entire plasma cross section [5]. It is this type of discharge that has resulted in record DIII–D performance. The L–mode phase allows for increased performance in the weak or negative shear region. The H–mode transition timed just prior to the L–mode phase disruption allows the discharge to continue by broadening the pressure profile before a stability limit is reached. Figure 2 illustrates the change in profile shape between an NCS L–mode edge and H–mode edge plasma. Ion temperature and rotation profiles rise linearly from the edge in the H–mode case in agreement with a global reduction in ion transport. Discharges with an early H–mode transition have

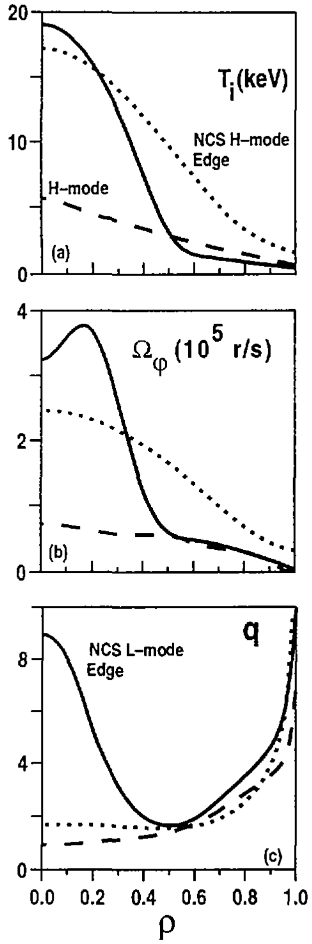

Fig. 2. (a,b) Ion temperature and rotation profiles for an H–mode with a monotonic q profile (82205) and two NCS discharges with an L– (83721) and H–mode (87977) edge. The NCS L–mode edge case has a clear transport barrier at ρ = 0.5 while the NCS H–mode edge plasma shows improved transport at all radii. (c) A variety of q profiles can be created in DIII–D.

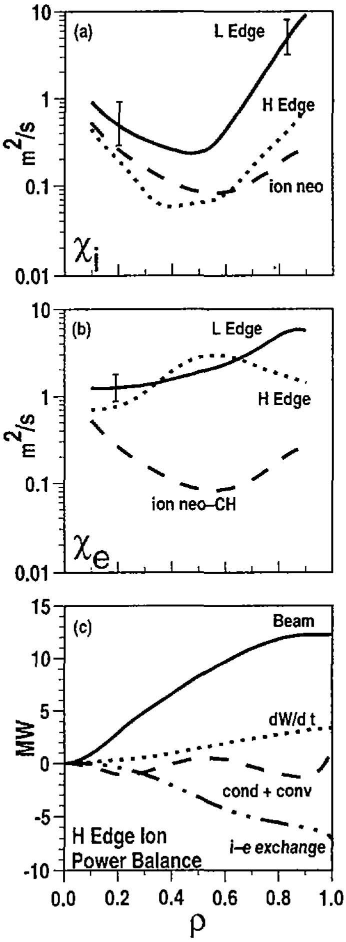

Fig. 3. (a, b) Ion and electron diffusivity for the NCS discharge (87935) of Fig. 1. The L–mode edge time is taken at 2.3 s and the H–mode edge time 2.45 s. The NCS H–mode edge χ_i is near neoclassical over the entire cross section. (c) The NCS H–mode edge ion power balance shows both conduction and convection are reduced to a negligible level.

lower performance than discharges with a later transition because the density rise at the edge reduces beam penetration and makes it difficult to obtain the enhanced central performance in the L–mode phase.

The detailed local study of the temporal evolution of NCS plasmas is made possible by the extensive array of DIII–D profile diagnostics [6] which measure T_i, Ω_φ, n_e, T_e, Z_{eff}, and radiated power. Local power balance energy transport analysis presented in this paper uses the computer codes ONETWO and TRANSP. Inputs into these codes include the temporal evolution of the kinetic plasma profiles and the detailed magnetic equilibrium reconstructions. The diffusivities (χ) are calculated from $q_{e,i} = n_{e,i}\,\chi_{e,i}\,\partial T_{e,i}/\partial r$, where $q_{e,i}$ is the radial energy flux due to conduction for each species, and $r = (\Phi/B_{T_0}\,\pi)^{1/2}$, where Φ is the toroidal flux. Uncertainties in χ are estimated by applying several different types of temporal smoothing to both transport input and output quantities. Classical electron–ion energy exchange is assumed and only diagonal transport coefficients are considered. The normalized radius ρ, used below and in the figures, is defined as r normalized to its maximum value.

Previous work [2,3] has demonstrated that both χ_i and χ_e are reduced after the formation of the internal transport barrier. Inside the region of negative shear χ_i drops by a factor of 10 after the transition to below Chang–Hinton neoclassical values while χ_e is reduced by approximately 50%. In general for all enhanced NCS plasmas, the overall power flow has the majority of beam power absorbed by the ion channel, the ions increasing their temperature and transferring power to the electrons via classical energy exchange and the power exiting the plasma via electron conduction.

A comparison between the L–mode and H–mode edge phases of the Fig. 1 NCS plasma is shown in Fig. 3. Inside the weak shear region ($\rho < 0.5$), both the L–mode and H–mode edge cases have low values of χ_i; the H–mode is near the neoclassical level [Fig. 3(a)]. Outside the weak shear region, the H–mode case continues to remain near the neoclassical level and is approximately a factor of 10 lower than the L–mode

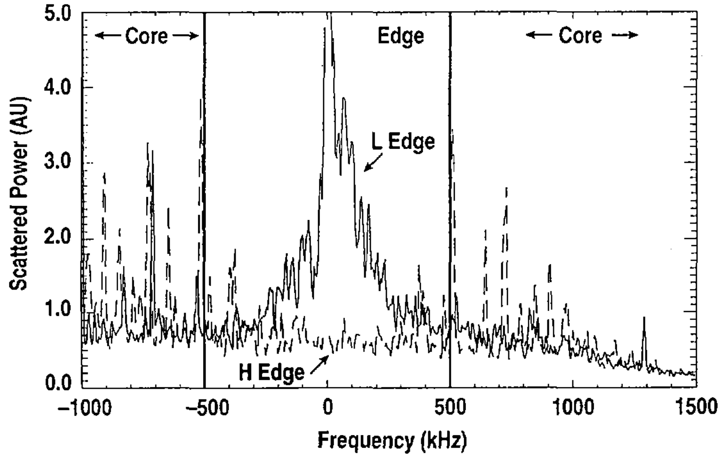

Fig. 4. Comparison of measured plasma fluctuations ($k_\theta = 2\ cm^{-1}$) for the L– and H–mode edge times in Fig. 3. The fluctuations in the NCS H–mode edge case are reduced over the entire cross section.

ion diffusivity. For both cases χ_e remains relatively unchanged [Fig. 3(b)], except at the plasma edge ($\rho > 0.8$), where there is a decrease of approximately a factor of 3–4 in the H–mode phase. In the H–mode phase the total conducted and convected ion power is reduced to negligible levels, so that in the ion channel the neutral beam power is balanced by the ion–electron exchange and the increase in stored energy [Fig. 3(c)].

In comparing pre–transport barrier formation to post–formation in NCS plasmas, there is both a temporal [7] and spatial [2] correlation between the reduction in transport and the reduction in electrostatic fluctuations as determined by far–infrared (FIR) scattering and beam emission spectroscopy. The spatial correlation can be illustrated with FIR measurements that compare NCS discharges with both an L–mode and H–mode edge. Recalling that the FIR diagnostic measures the frequency spectrum and relative magnitude of poloidally propagating density fluctuations, Fig. 4 compares the scattered power spectrum $\left(\propto \tilde{n}_e^2\right)$ for the L–mode and H–mode phases of the Fig. 3 plasma. The NCS L–mode edge case has low interior broadband turbulence that is comparable to the H–mode phase consistent with χ_i being reduced in the core. The spikes in the H–mode case represent low–n coherent MHD modes. The H–mode phase data demonstrates a reduction of the edge fluctuations resulting in low turbulence over the entire plasma cross section which is consistent with the global reduction in ion diffusivity.

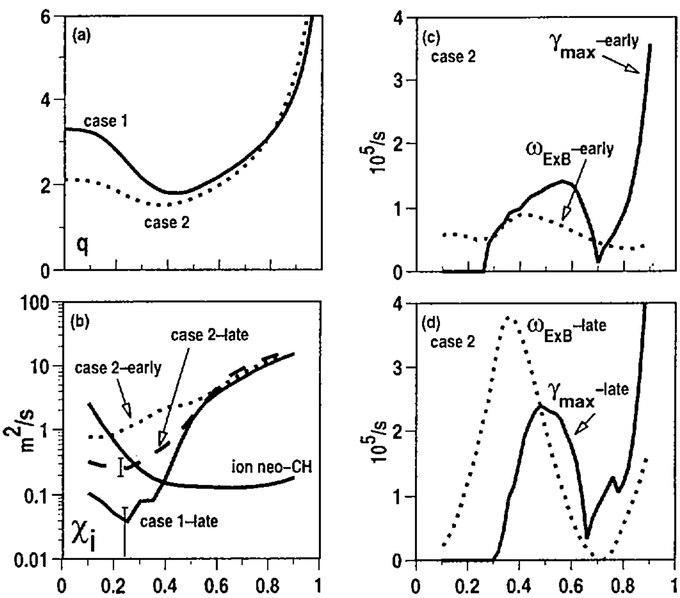

Fig. 5. (a) L–mode edge NCS plasmas with larger negative magnetic shear (Case 1 –87003) and weak shear (Case 2 – 87031). (b) χ_i is reduced from before (early at 5 MW) the transport barrier to after (late at 10 MW) the transport barrier formation. For fixed conditions χ_i is reduced for larger magnetic shear. (c) During the early formation of the transport barrier the turbulence growth rate (γ_{max}) exceeds the Doppler shift shear rate (ω_{ExB}). (d) After the transport barrier formation $\gamma_{max} < \omega_{ExB}$ in the region of reduced ion transport.

4. THE DEPENDENCE OF TRANSPORT ON SHEAR

Energy transport has been compared in two similar double–null NCS L–mode edge plasmas but with different core shear profiles [8]. The discharges differed by a 0.2 second delay in both the low and high power beam heating phases. The delayed beam timing results in a smaller Δq [Fig. 5(a)] of 0.56 versus 1.56 and a 20% higher electron density. Power balance analysis during the early formation of the transport barrier and after the full formation for the small Δq case shows the typical reduction in χ_i [Fig. 5(b)] inside the region of weak or negative shear. Note that the neutral beam power level during the early formation is at 5 MW compared to 10 MW after full formation. During the enhanced confinement phase, larger Δq results in a reduction in χ_i of about a factor of 5 inside the negative shear region; within experimental uncertainty χ_e remains unchanged. Temporally, the discharge with lower shear has approximately an 80 ms delay in the onset of reduced ion transport when compared to the discharge with higher shear. Although the larger Δq discharge has a larger improvement in central confinement, these discharges typically reach peak values sooner and at lower values of β_N and reactivity.

The FIR measured electrostatic fluctuations for these two discharges are similar with a behavior like that of the L–mode case in Fig. 4. These turbulence reductions in NCS discharges are, for example, consistent with the suppression of toroidal ion temperature gradient (ITG or η_i) driven transport. Data from the CER diagnostic also provides information on the **E**×**B** shear profile in DIII–D. It is generally observed that the reduction in electrostatic fluctuations and the reduction in diffusive transport occur in regions where the **E**×**B** flow shear $\partial/\partial\psi\,(E_r/RB_\theta)$ is the greatest. This large flow shear results from the strong peaking of toroidal rotation inside the region with weak or negative magnetic shear. The effects of the flow shear can be quantified [9] by comparing the change in flow shear, as determined by the Doppler shift shear rate

$$\omega_{ExB} = \frac{(RB_\theta)^2}{B}\frac{\partial}{\partial\psi}\left(\frac{E_r}{RB_\theta}\right)$$

to simulated turbulence growth rates (γ_{max}). When ω_{ExB} is greater than γ_{max}, **E**×**B** flow shear stabilization of turbulence is expected [10] resulting in the formation of a transport barrier [11].

The NCS configuration allows access to large ∇p since these plasmas are calculated to be MHD unstable with a forced positive magnetic shear profile. However, the NCS configuration alone is not sufficient for improved confinement. The existence of a power threshold for improved NCS confinement is consistent with the observation that to reduce turbulent fluctuations, a sufficient shear flow rate is required. We conclude from measurements and calculations that the stabilization of mircoturbulence by **E**×**B** flow shear is the prime candidate to explain the reduced transport.

The turbulence growth rates have been approximated by a linear growth rate calculated from a 3–D ballooning mode gyrokinetic stability (GKS) code in the electrostatic limit [12]. The maximum growth rate (γ_{max}) is calculated considering both the ITG and dissipative trapped electron modes. A comparison between γ_{max} and ω_{ExB} in the low magnetic shear L–mode discharge [Fig. 5, Case 2] during the low power beam phase is shown in Fig. 5(c); γ_{max} is equal to or exceeds ω_{ExB} for $\rho > 0.25$. During the high power phase [Fig. 5(d)], $\omega_{ExB} > \gamma_{max}$ inside the region of reduced ion transport ($\rho < 0.5$) consistent with turbulence suppression by **E**×**B** flow shear. The region of linear stability ($\gamma_{max} = 0$) for $\rho < 0.25$ in Fig. 5(c) results from a combination of negative shear and Shafranov shift and even more strongly from thermal ion dilution by fast ions and $T_i > T_e$. Changing the magnetic shear at zero Shafranov shift can at most move the linear stability boundary to $\rho = 0.15$ whereas setting $n_i = n_e$ and $T_i = T_e$ with the experimental magnetic shear extends the instability to the magnetic axis with γ_{max} exceeding ω_{ExB}. This suggests that the effects of low target density and neutral beam heating (i.e. thermal ion dilution and $T_i > T_e$) lower γ_{max} and thus lower the threshold ω_{ExB} for transport barrier formation.

Although our results indicate that **E**×**B** flow shear is a leading candidate to explain stabilization of mircoturbulence from non–NCS to NCS discharges, the further reduction in χ_i with larger shear can not be explained by the same mechanism. Qualitatively, Fig. 5(d) represents both the low and high shear discharges after the barrier formation. With no difference in the **E**×**B** shearing rates it is hard to understand how **E**×**B** flow shear can be playing a role in the further χ_i reduction. In addition to the unknown mechanism effecting ion transport with lower magnetic shear, for both cases at $\rho = 0.2$, calculations indicate that in the range $0.01 < k_\theta\rho_s < 100.0$ no linearly unstable electrostatic modes are present. Since χ_e does not change much upon entering the enhanced NCS regime, and certainly does not drop to electron neoclassical, there must be some instability effecting electron transport.

Energy transport has also been compared in two similar NCS H–mode edge plasmas [13] with different core shear profiles (Fig. 6). These different q profiles were created by different levels of early beam power; 3.5 MW for the lower Δq case

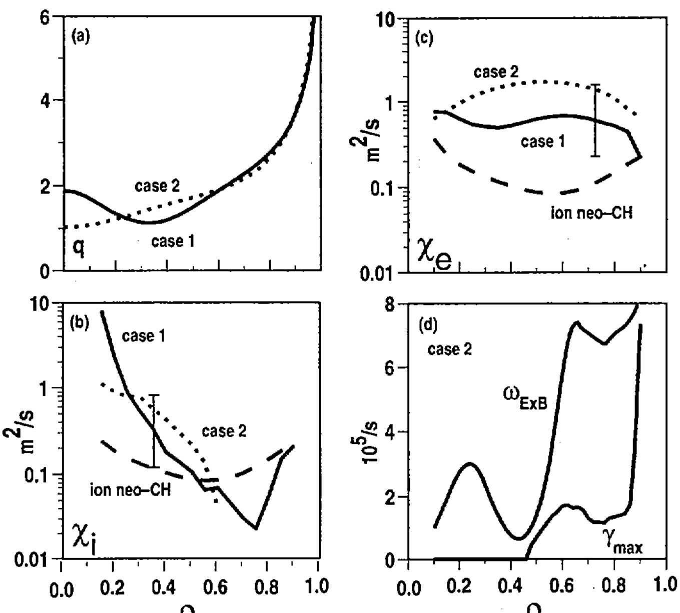

Fig. 6. (a) H–mode edge NCS plasmas with larger negative magnetic shear (Case 1 – 87953) and weak shear (Case 2 – 87937). (b, c) Ion and electron diffusivity does not change with magnetic shear. (d) The Doppler shift shear rate (ω_{ExB}) is greater than the turbulence growth rate (γ_{max}) at all radii for the NCS H–mode edge plasma.

compared to 5.5 MW for the larger Δq value. Prior to the termination of the high performance phases, both discharges have nearly identical evolution. FIR scattering measurements show no difference in density fluctuations between the two plasmas. As was demonstrated in Fig. 3(c), with the H–mode edge the plasma core basically behaves like an integrator of the applied heating power leaving no power to be diffusively conducted or convected away from the core. Based on transport analysis these two discharges have basically the same behavior [Fig. 6(b,c)]; negative values of χ are encountered at different times in the analysis but the calculated uncertainty includes positive values. A comparison of γ_{max} and ω_{ExB} in the enhanced confinement phase [Fig. 6(d)] shows $\omega_{ExB} > \gamma_{max}$ everywhere which is consistent with the neoclassical ion transport over the entire cross section as predicted by earlier simulations [14]. As in the L–mode edge case, the larger Δq discharge reaches its peak performance sooner but at a lower absolute value compared to the smaller Δq discharge. However, in contrast to the L–mode edge case, the H–mode edge cases show no further reduction of transport for the negative magnetic shear case compared to the weak shear case.

5. SUMMARY AND CONCLUSIONS

The beam heated, high triangularity, double–null NCS configuration has demonstrated enhanced confinement at high beta with robust and reliable operation. In general, NCS plasmas with enhanced confinement have a clear reduction in diffusive transport inside the region of negative shear. The reduced transport lowers the ion conductivity to the neoclassical level; the electron transport in comparison remains relatively unchanged. NCS discharges with an H–mode edge also have reduced ion transport in the outer region of the discharge resulting in neoclassical ion transport over the entire plasma cross–section. Larger values of negative shear further reduce the ion diffusivity in the L–mode edge discharges but not in the H–mode edge case. A reduction in particle transport also accompanies the reduction in energy transport in the NCS plasmas with an L–mode edge. Accompanying the reduced core transport in NCS discharges is the reduction in core fluctuations which is consistent with the suppression of η_i driven transport. Sheared $\mathbf{E}\times\mathbf{B}$ flow appears to play a key role in turbulence suppression. Future work will focus on understanding sources for anomalous core electron transport in the NCS regime as well as ion transport mechansims with low magnetic shear and an L–mode edge.

ACKNOWLEDGMENTS

This work was supported by the U.S. Department of Energy under Contract Nos. DE-AC03-89ER51114, DE-AC05-96OR22464, and DE-AC04-94AL85000 and Grant Nos. DE-FG03-86ER53266 and DE-FG03-95ER54294.

REFERENCES

[1] STRAIT, E.J., et al., Phys. Rev. Lett. **75** (1995) 4421.
[2] LAO, L.L., et al., Phys. Plasmas **3** (1996) 1951.
[3] RICE, B.W., et al., Phys. Plasmas **3** (1996) 1983.
[4] RICE, B.W., et al., Plasma Phys. Controlled Fusion **38** (1996) 869.
[5] LAZARUS, E.A., et al., Phys. Rev. Lett. **77** (1996) 2714.
[6] See references in SCHISSEL, D.P., et al., Nucl. Fusion **29** (1989) 185 for example.

[7] DOYLE, E.J., et al., paper IAEA–CN–64/A6–4, this volume.
[8] STALLARD, B., et al., Transport in negative central magnetic shear L–mode plasmas in DIII–D, submitted to Nucl. Fusion.
[9] HAHM, T.S., BURRELL, K.H., Phys. Plasmas **2** (1995) 1648.
[10] WALTZ, R.E., et al., Phys. Plasmas **1** (1994) 2229.
[11] HINTON, F.L., STAEBLER, G.M., Phys. Fluids B **5** (1993) 1281.
[12] KOTCHENREUTHER, M., Bull. Am. Phys. Soc. **37** (1992) 1432.
[13] GREENFIELD, C.M., et al., Transport in high performance weak and negative magnetic shear discharges in DIII–D, Controlled Fusion and Plasma Physics (Proc. 23rd Eur. Conf. Kiev, 1996), European Physical Society, Geneva (1996) (in press).
[14] STAEBLER, G.M., HINTON, F.L., et al., Phys. Plasmas **1** (1994) 909.

DISCUSSION

R.J. GOLDSTON: M. Zarnstorff at PPPL has been looking at the interesting effect that the radial electric field associated with plasma rotation can significantly affect the interpretation of MSE signals to determine q(r). Has this effect been taken into account in your calculations, and if so, how large an effect is it in your plasmas with strongly reversed shear?

D.P. SCHISSEL: B. Rice, one of our DIII-D collaborators at LLNL, has written a paper (Rep. GA-A22480) on the radial electric field correction of DIII-D MSE data and this effect has been accounted for in all the safety factor (q) profiles that I have shown. This effect becomes significant when the plasma radial electric field exceeds 25 kV/m.

Y. KISHIMOTO: In the reversed shear shot, the transport barrier usually forms around the q_{min} surface. However, in the theoretical model used in your paper, the growth rate and the related transport characteristics are continuous at the s = 0 surface, so there is no spatial reason for the transport barrier to form at the q_{min} surface. In the DIII-D experiments, is there a clear relation between the q_{min} surface and the location of the transport barrier?

D.P. SCHISSEL: In NCS discharges with an H mode edge there is reduced ion transport at all radii. Therefore in these cases there is no apparent relation between the location of the q_{min} surface and the decreased transport. What is significant for decreased transport is the relative magnitudes of $\omega_{E\times B}$ and γ_{max}. Reduced transport is observed in the region where $\omega_{E\times B} > \gamma_{max}$.

R.E. WALTZ: Turbulence simulations show the validity of the $\mathbf{E} \times \mathbf{B}$ shear stabilization rule. $\omega_E \approx \gamma_{max}$ holds at zero magnetic shear ($\hat{s} = 0$).

HIGH POWER DENSITY H-MODES IN ALCATOR C-MOD*

Y. TAKASE, R.L. BOIVIN, F. BOMBARDA[1], P.T. BONOLI, C.L. FIORE, D.T. GARNIER, J.A. GOETZ, S.N. GOLOVATO[2], R.S. GRANETZ, M.J. GREENWALD, S.F. HORNE, A.E. HUBBARD, I.H. HUTCHINSON, J.H. IRBY, B. LaBOMBARD, B. LIPSCHULTZ, E.S. MARMAR, M. MAY[3], A. MAZURENKO, G.M. McCRACKEN[4], P.J. O'SHEA, M. PORKOLAB, J. REARDON, J.E. RICE, C. ROST, J.M. SCHACHTER, J.A. SNIPES, P.C. STEK, J.L. TERRY, R.L. WATTERSON[5], B. WELCH[6], S.M. WOLFE
Plasma Fusion Center,
Massachusetts Institute of Technology,
Cambridge, Massachusetts,
United States of America

Abstract

HIGH POWER DENSITY H-MODES IN ALCATOR C-MOD.

Optimization studies of energy confinement in H-mode plasmas heated by ICRF waves were performed on the compact high-field tokamak Alcator C-Mod. Reduction of the radiated power from the main plasma by boronization of the molybdenum first wall made a major impact on improving the quality of H-mode, as characterized by the confinement enhancement factor over the ITER89-P L-mode scaling, $H_{\mathrm{ITER89\text{-}P}}$. Longer ELM-free periods became possible, and $H_{\mathrm{ITER89\text{-}P}} = 2.5$ was achieved transiently, but in this mode of operation impurity accumulation led to eventual termination of H-mode. More favorable high quality quasi-steady-state H-modes which led to steady-state levels of density ($\bar{n}_e = 4 \times 10^{20}$ m^{-3}), stored energy ($H_{\mathrm{ITER89\text{-}P}} = 2.0$, $\beta_N = 1.5$), and radiated power ($P_{\mathrm{rad}}^{\mathrm{main}}/P_{\mathrm{loss}} \leq 30\%$) were also achieved. This mode of operation is characterized by high levels of continuous D_α emission comparable to the L-mode level, with very little or no ELM activity. The H-mode behavior was affected by controlling the neutral pressure by wall conditioning and gas puffing.

* Work supported by US Department of Energy contract DE-AC02-78ET51013.

[1] Associazione Euratom–ENEA sulla Fusione, Frascati, Italy.
[2] Presently at Tokyo Electron America, Beverly, Massachusetts, USA.
[3] Johns Hopkins University, Baltimore, Maryland, USA.
[4] Presently at JET Joint Undertaking, Abingdon, Oxfordshire, United Kingdom.
[5] Presently at CPClare Corporation, Lexington, Massachusetts, USA.
[6] University of Maryland, College Park, Maryland, USA.

1. INTRODUCTION

Study of the high confinement mode known as H-mode [1] has been an area of active research on many tokamaks. Energy confinement in H-mode plasmas is often characterized by the confinement enhancement factor ($H_{\mathrm{ITER89-P}}$) over the well-established L-mode scaling [2]. Optimization of confinement enhancement in ICRF heated H-mode plasmas was a major research focus of the December 1995 – March 1996 operation campaign of the compact high-field tokamak, Alcator C-Mod [3] ($R = 0.67\,\mathrm{m}$, $a = 0.22\,\mathrm{m}$, $\kappa \leq 1.8$). Auxiliary heating was provided by radiofrequency (RF) waves in the ion cyclotron range of frequencies (ICRF). Unlike neutral beam heating, RF heating provides the additional input power without adding particles at the same time. Up to 3.5 MW of RF power at 80 MHz (extremely high power densities of 5 $\mathrm{MW/m^3}$ volume averaged, 0.6 $\mathrm{MW/m^2}$ surface averaged) was injected into the plasma during the course of this experiment using two "dipole" antennas, each with two current straps separated toroidally and excited out of phase [4]. With operational improvements such as plasma position feedback in combination with power feedback, it has become possible to maintain constant power through large load changes which occur during L-H transitions and ELMs.

Hydrogen minority heating in deuterium majority plasmas at 5.3 T was the main heating scenario, but a variety of other heating scenarios [5,6] was also used over the range $2.6 \leq B_{\mathrm{T}} \leq 8\,\mathrm{T}$ and $1 \lesssim \overline{n}_{\mathrm{e}} \lesssim 4 \times 10^{20}\,\mathrm{m^{-3}}$, essentially covering the entire operating space of C-Mod. To date, H-mode was observed in deuterium majority plasmas with second harmonic H (2.6 T), second harmonic ^{3}He (4 T), fundamental H (5.3 T), and fundamental ^{3}He (8 T) minority heating, and at intermediate fields with off-axis minority heating. H-mode was also observed in combination with the PEP (pellet enhanced performance) mode [5], but detailed studies remain a subject of future investigation.

Results from the previous campaign (up to June 1995) were reported in Ref. [5]. Details of the L-H transition and power threshold are described in Refs. [7] and [8]. In this paper, we report two types of H-mode observed in Alcator C-Mod: ELM-free H-mode and "enhanced-D_α" H-mode. The effect of controlling the radiated power from the main plasma, primarily by boronization, is also discussed. The enhanced-D_α H-mode is particularly interesting since it can lead to steady-state while maintaining high confinement. The absence of large amplitude ELMs is another attractive feature of this type of H-mode. A third type of H-mode with frequent Type-III ELMs [9] was observed prior to boronization, and after boronization when the radiated power fraction was high. This type of H-mode resulted in lower confinement enhancement relative to L-mode, and will not be discussed in detail in this paper. H-mode with detached divertor similar to the CDH mode [10] was also observed [11].

2. EFFECTS OF BORONIZATION

Operation during this campaign was different from the previous campaign in two ways: (1) The gas leakage path from the divertor chamber to the main plasma chamber was closed. This change has resulted in greatly enhanced neutral pressure in the divertor chamber [12]. The neutral pressure at the outer midplane of the main plasma chamber was reduced by a small amount. (2) Boronization was applied to the molybdenum first wall, typically on a weekly basis for most of this campaign. There was a short period of operation without boronization but with the divertor leakage closed.

Boronization of the molybdenum wall has significantly reduced the molybdenum content and the radiated power from the main plasma, particularly at the low end of the density range ($\bar{n}_e \lesssim 1.5 \times 10^{20}\,\mathrm{m}^{-3}$), and for low single-pass absorption heating schemes (e.g., ^{3}He minority heating at 8 T). Energy confinement of L-mode plasmas was found to follow the ITER89-P L-mode scaling regardless of the level of radiated power. In contrast, the quality of H-mode was improved dramatically (by up to a factor of two in $H_{\mathrm{ITER89-P}}$) by controlling the radiated power fraction to a low level, $P_{\mathrm{rad}}^{\mathrm{main}}/P_{\mathrm{loss}} \lesssim 30\%$. Here, $P_{\mathrm{rad}}^{\mathrm{main}}$ is the radiated power from the main plasma, $P_{\mathrm{loss}} = P_{\mathrm{in}} - dW/dt$ is the "loss power", P_{in} is the total input (not absorbed) power, and W is the total stored energy. H-mode plasmas are nearly thermal with $T_e \simeq T_i$. The high energy ion contribution to the total stored energy is typically 5% or less.

The confinement enhancement factor $H_{\mathrm{ITER89-P}}$ is plotted as a function of the radiated power fraction in Fig. 1. The low radiated power results in a larger fraction of the input power conducted to the plasma edge, which is believed to help establish and maintain the edge transport barrier. The presence of the edge transport barrier is indicated by the build-up of the edge temperature pedestal after the L-H transition (0.686 s), as shown in Fig. 2 for an ELM-free H-mode. The edge electron temperature $T_e(r/a = 0.9)$ increases after successive sawtooth heat pulses, with no decay observed until the edge temperature pedestal is fully established. In enhanced-D_α H-modes the edge temperature pedestal is somewhat lower than in ELM-free H-modes (Fig. 3), but the density is substantially higher.

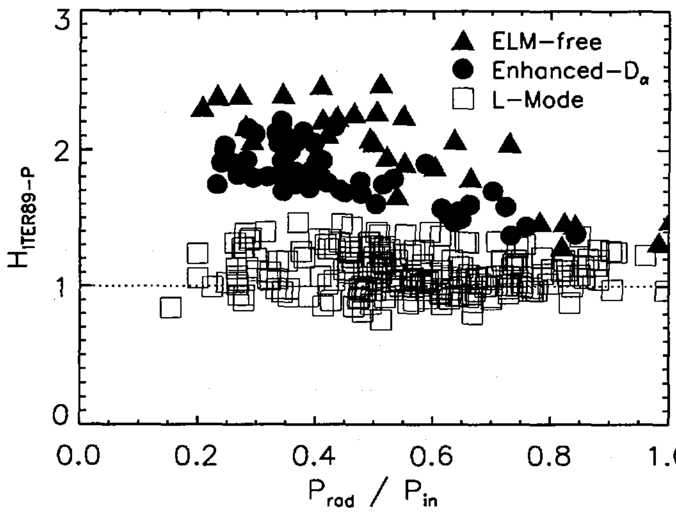

FIG. 1. Dependence of the H-factor on the radiated power fraction. Data were taken when $dW/dt \simeq 0$.

Lower radiated power fraction from the main plasma after boronization led to longer ELM-free H-modes with $H_{\rm ITER89-P} \lesssim 2.5$, compared to $H_{\rm ITER89-P} \lesssim 1.5$ observed in RF heated H-modes prior to boronization [5]. A quasi-steady-state high-quality H-mode ($H_{\rm ITER89-P} = 2.0$) with high levels of continuous D_α emission was also achieved. Very little variation in the stored energy increase was found as the power deposition layer (i.e., the minority resonance layer) was moved from $r/a = 0$ to 0.4 (just outside the sawtooth inversion radius) by changing the toroidal magnetic field. This is in contrast to pre-boronization L-mode results in which the stored energy increase during ICRF heating decreased by a factor of two as the resonance layer was moved out to $r/a = 0.4$ [5].

3. ELM-FREE H-MODE

ELM-free H-modes have the highest energy and particle confinement, but do not lead to steady state. An example of an ELM-free H-mode is shown in Fig. 2. The plasma pressure is expressed in terms of the normalized beta defined

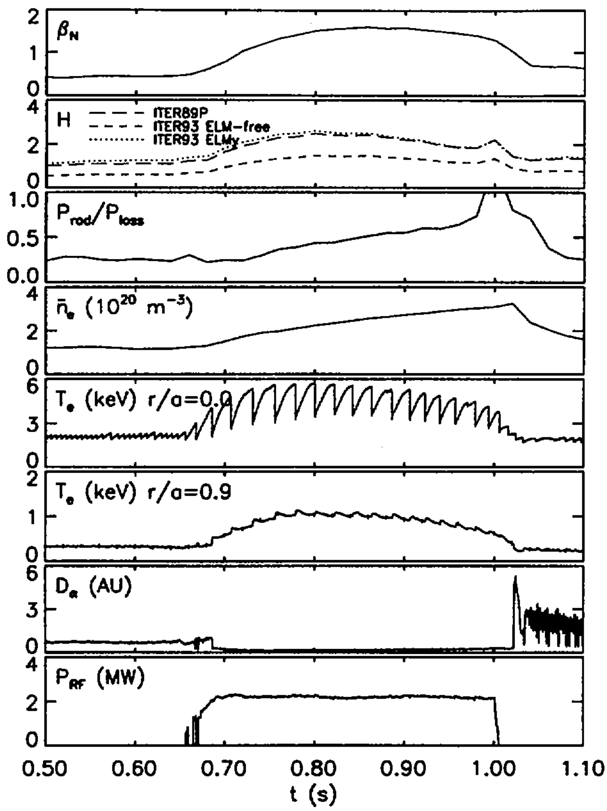

FIG. 2. ELM-free H-mode (shot 960116024), transiently reaching $H_{ITER89-P} = 2.5$ ($B_T = 5.3$ T, $I_p = 1.0$ MA).

as $\beta_N = \beta_T aB/I$ (% m T/MA), where β_T is the ratio of the volume averaged plasma pressure to the toroidal magnetic pressure. The energy confinement is characterized by the ratios of experimentally determined confinement time to the three empirical scaling laws, ITER89-P L-mode scaling [2] and ITER93 ELM-free and ELMy H-mode scalings for the total stored energy [13] (note that the ELMy scaling predicts virtually the same confinement as L-mode for C-Mod). The power used in evaluating the energy confinement (both experimental and scaling) is the "loss power" $P_{\rm loss} = P_{\rm in} - dW/dt$. The radiated power is not subtracted. The particle confinement time is extremely long in ELM-free H-mode. The density and the impurity content, and consequently the radiated power continue to increase throughout the ELM-free phase. As the radiated power increases, energy confinement starts to degrade when the radiated power fraction exceeds a value of $P_{\rm rad}^{\rm main}/P_{\rm loss} \simeq 0.5$, eventually leading to termination of the ELM-free H-mode as the radiated power fraction approaches 100%. The confinement enhancement factor reaches a value of $H_{\rm ITER89-P} = 2.5$ at $t = 0.8$ s. The corresponding volume averaged plasma pressure, plasma stored energy, and energy confinement time at the time of maximum stored energy were 0.15 MPa, 0.21 MJ, and 0.075 s. The energy confinement time during H-mode was 50% higher than that of the ohmic target plasma (0.050 s).

4. ENHANCED-D_α H-MODE

A more favorable type of H-mode, which can lead to steady state levels of density, stored energy, and radiated power while maintaining high confinement, was also observed. This type of H-mode is characterized by high levels of steady D_α emission (often exceeding the L-mode level), sometimes but not always accompanied by occasional small-amplitude ELMs. We will refer to this type of H-mode as "enhanced-D_α H-mode" in this paper. In some respects this type of H-mode has characteristics similar to quasi-steady-state ELMy H-modes [14], but the ELM behavior is qualitatively different. An enhanced-D_α H-mode with $H_{\rm ITER89-P} = 2.0$ and $\beta_N = 1.5$, which approaches a steady-state towards the end of the RF pulse, is shown in Fig. 3. After a brief period of ELM-free phase, the D_α emission increases gradually to a higher level. In this example, small isolated ELMs are visible as sharp upward spikes on the D_α signal, with corresponding downward spikes on the edge electron temperature. The slower modulation corresponds to the sawtooth heat pulse reaching the plasma edge. Energy confinement relative to ITER93 ELMy and ELM-free scalings [13] were 2.0 and 1.3, respectively. In more traditional ELMy discharges with frequent ELMs the confinement enhancement is lower, typically $H_{\rm ITER89-P} \lesssim 1.5$.

In enhanced-D_α H-modes, a region of intense D_α emission is observed in the scrape-off layer above the X-point adjacent to the inner divertor structure (the "inner nose"), in addition to a region of more faint emission below the X-point, as shown in Fig. 4. In ELM-free H-mode the intense D_α emission on the inner nose is absent, but the emission near the X-point is still observed, as shown in Fig. 5 (note the factor of 60 reduction in the maximum emissivity). The D_α

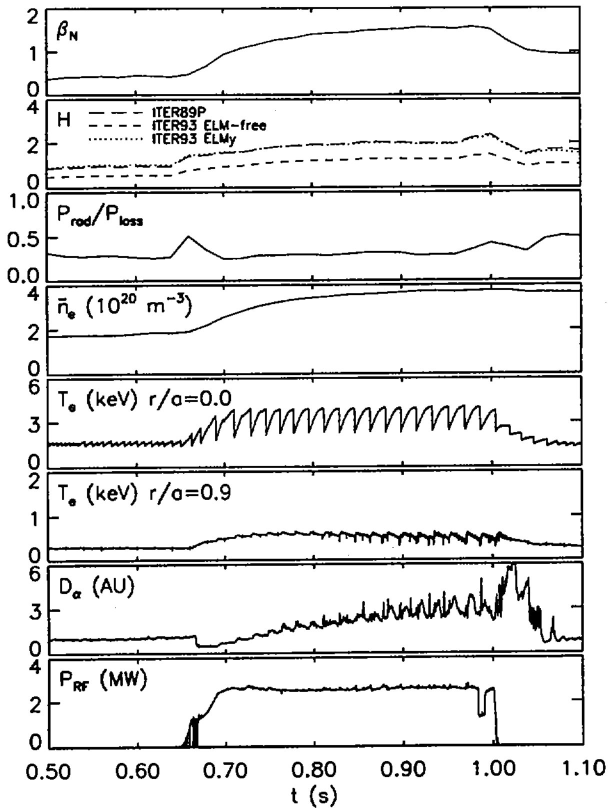

FIG. 3. Quasi-steady-state enhanced-D_α H-mode (shot 960116027) with $H_{ITER89\text{-}P}$ = 2.0 and β_N = 1.5 (B_T = 5.3 T, I_p = 1.0 MA).

signal plotted in Figs. 3 and 4 are from a view of the lower half of the inner wall, including the enhanced emission region on the inner nose. The D_α emission from the divertor region in enhanced D_α H-mode is higher than in ELM-free H-mode but usually not as high as in L-mode. The radiated power from the divertor region in enhanced-D_α H-mode is concentrated near the X-point, as shown in Fig. 6. In ELM-free H-mode it is less intense and is more distributed along the inner and outer legs of the separatrix below the X-point. The radiated power from the main plasma is greatly different. As shown in Fig. 7, the radiated power in the ELM-free plasma (at the end of a 0.3 s RF pulse) is much higher than in the enhanced-D_α H-mode across the whole profile.

The "enhanced-D_α" H-mode should not be confused with the "high-recycling" divertor discussed in Ref. [15]. The low radiated power from the main plasma, combined with steeper gradients in the scrape-off layer during H-mode, results in very high parallel heat flux into the divertor region, $q_\| \simeq 0.5\,\mathrm{GW/m^2}$ [11], comparable to the value expected for ITER. Results of initial attempts to reduce the heat flux to the divertor target plates are reported in Ref. [11].

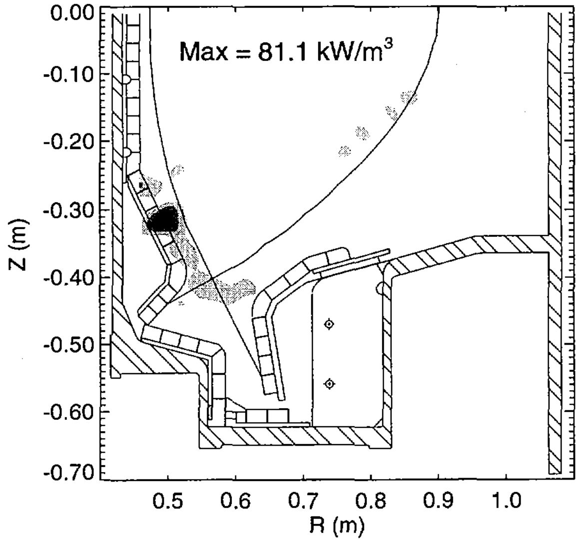

FIG. 4. Tomographic reconstruction of the D_α emission during an enhanced-D_α H-mode (shot 960116010 at 0.9 s).

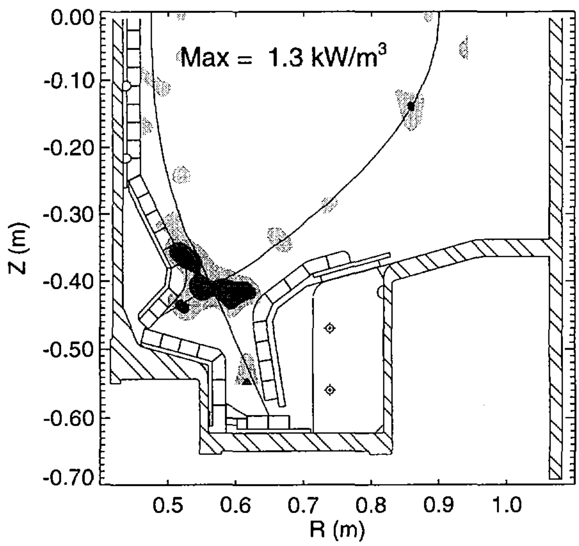

FIG. 5. Tomographic reconstruction of the D_α emission during an ELM-free H-mode (shot 960116024 at 0.8 s).

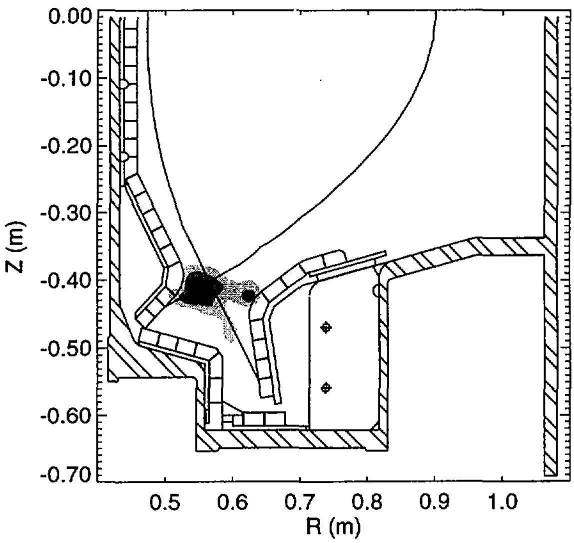

FIG. 6. Tomographic reconstruction of the radiated power from the divertor region during an enhanced-D_α H-mode (shot 960116010 at 0.9 s).

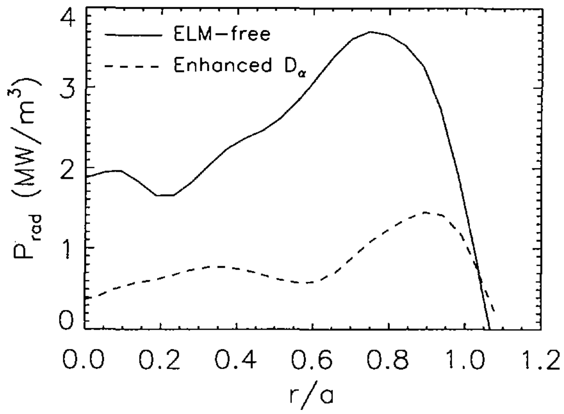

FIG. 7. Comparison of the radiated power profile for ELM-free H-mode (solid: 960116024 at 1.0 s) and enhanced-D_α H-mode (dashed: 960116027 at 1.0 s).

The enhanced-D_α H-mode was first observed during the early phase of this campaign with an unboronized molybdenum first wall. This mode was obtained using strong gas puffing during the H-mode phase. A quasi-steady-state condition was achieved with densities up to $\overline{n}_e = 3.7 \times 10^{20}\,\mathrm{m}^{-3}$. However, in these pre-boronization enhanced-D_α H-modes the radiated power fraction was high $P_{\rm rad}^{\rm main}/P_{\rm loss} \simeq 0.6$, and the confinement enhancement factor was low, typically $H_{\rm ITER89-P} = 1.2$–1.3.

The D_α behavior can be affected by controlling the particle source rate through wall conditioning and gas puffing. ELM-free H-modes can be obtained by outgassing the wall by He discharge cleaning and limiting the gas input to the plasma. As the divertor neutral pressure (measured before the H-mode transition) is increased, the H-mode character changes gradually from ELM-free to enhanced-D_α H-mode [16]. The transition usually occurs around several mtorr. However, enhanced-D_α H-mode has been observed with a divertor neutral pressure as low as 2 mTorr. For normal operating conditions, this corresponds to a target density of approximately $\overline{n}_e = 2 \times 10^{20}\,\mathrm{m}^{-3}$, but either type of H-mode can be produced at the same density depending on the neutral pressure. The level of D_α enhancement is higher when the power to the scrape-off layer $P_{\mathrm{SOL}} = P_{\mathrm{in}} - dW/dt - P_{\mathrm{rad}}^{\mathrm{main}}$ is higher. The best enhanced-D_α H-mode was observed slightly above the transition from the ELM-free H-mode regime to the enhanced-D_α H-mode regime. Excessive amounts of D_α emission resulted in poor H-factors.

Impurity particle confinement was studied using laser blow-off injection. In ELM-free H-modes the impurity confinement time is virtually infinite. The injected impurities remain in the plasma with no measurable decay, and intrinsic impurities (e.g., molybdenum) accumulate in the plasma core. The time histories of line emission from different charge states can be reproduced by a purely diffusive model in L-mode plasmas, but in enhanced-D_α H-mode a strong inward convection at the plasma edge is required in addition to an overall reduction of the diffusion coefficient. The impurity particle confinement time in enhanced-D_α H-modes was in the range 100–500 ms, much shorter than in ELM-free H-mode but still an order of magnitude longer than in L-mode plasmas (typically 20–30 ms). These H-modes had mild D_α enhancement (lower than the L-mode level) and good H-factors ($H_{\mathrm{ITER89-P}} \gtrsim 1.8$).

5. DISCUSSION

The quality of H-mode was substantially improved by reducing the radiated power from the main plasma using boronization. Longer ELM-free periods became possible, and high quality quasi-steady-state H-modes were obtained. This mode of operation is characterized by enhanced levels of continuous D_α emission localized on the "inner nose" of the divertor and very little or no ELM activity. The H-mode behavior (ELM-free, ELMy, or enhanced-D_α) was found to depend on the neutral pressure which can be controlled by wall conditioning and gas puffing.

The unique range of parameters obtainable in C-Mod (i.e., compact size, high magnetic field, and high density with $T_e/T_i \simeq 1$) provides critical tests of both empirical scaling laws and theoretical predictions. We note that H-mode confinement data points from C-Mod are found to lie well above the empirical scaling laws derived from larger tokamaks (ITER93H ELMy and ELM-free [13], JET–DIII-D [17], etc.), pointing out the necessity to re-examine the H-mode scaling laws. Such re-evaluation may have an important impact in extrapolating toward larger future devices such as ITER. C-Mod data have been added to the

ITER H-mode confinement database [13]. A more detailed description of the data contributed to the database, including comparison with various H-mode scaling laws, is reported in Ref. [18]. (Note that the enhanced-D_α H-mode is referred to as "ELMy" H-mode in Ref. [18].)

Hardware upgrades in the near future (1997–1998) include addition of 4 MW of tunable frequency (40–80 MHz) ICRF power and a current drive antenna to allow on-axis fast wave current drive and off-axis mode conversion current drive, modification of the inner divertor to enable higher triangularity operation, and addition of a divertor cryopump to control the density rise during H-mode. Planned experiments include investigation of VH-mode, the combination of PEP mode and H-mode, and when off-axis current drive becomes operational, the reversed shear enhanced confinement mode.

REFERENCES

[1] WAGNER, F., et al., Phys. Rev. Lett. **49** (1982) 1408.
[2] YUSHMANOV, P.N., et al., Nucl. Fusion **30** (1990) 1999.
[3] HUTCHINSON, I.H., et al., Phys. Plasmas **1** (1994) 1511.
[4] TAKASE, Y., et al., in Fusion Engineering (Proc. 14th IEEE/NPSS Symp. San Diego, 1991), Vol. 1, Inst. of Electrical and Electronics Engineers, Piscataway, NJ (1992) 118.
[5] TAKASE, Y., et al., in Controlled Fusion and Plasma Physics (Proc. 22nd Eur. Conf. Bournemouth, 1995), Vol. 19C, Part II, European Physical Society, Geneva (1995) 341;
TAKASE, Y., et al., Plasma Phys. Control. Fusion (in press).
[6] BONOLI, P.T., et al., IAEA-CN-64/EP-1, these Proceedings, Vol. 3.
[7] SNIPES, J.A., et al., Plasma Phys. Control. Fusion **38** (1996) 1127.
[8] HUBBARD, A.E., et al., IAEA-CN-64/AP2-11, this volume.
[9] SNIPES, J.A., et al., Phys. Plasmas **3** (1996) 1992.
[10] NEUHAUSER, J., et al., Plasma Phys. Control. Fusion **37** (1995) A37.
[11] LIPSCHULTZ, B., et al., "Modification of the divertor detachment onset density", Plasma Surface Interactions in Controlled Fusion Devices (Proc. 12th Int. Conf. St. Raphael, France, 1996), J. Nucl. Mater. (in press);
LIPSCHULTZ, B., et al., IAEA-CN-64/A4-5, this volume.
[12] LaBOMBARD, B., et al., "Experimental investigation of transport phenomena in the scrape-off layer and divertor", Plasma Surface Interactions in Controlled Fusion Devices (Proc. 12th Int. Conf. St. Raphael, France, 1996), J. Nucl. Mater. (in press).
[13] ITER H MODE DATABASE WORKING GROUP, Nucl. Fusion **34** (1994) 131.
[14] BURRELL, K.H., et al., Plasma Phys. Control. Fusion **31** (1989) 1649.
[15] LaBOMBARD, B., et al., Phys. Plasmas **3** (1996).
[16] HUTCHINSON, I.H., et al., IAEA-CN-64/O2-3, this volume.
[17] SCHISSEL, D.P., et al., Nucl. Fusion **31** (1991) 73.
[18] GREENWALD, M., et al., H Mode Confinement in Alcator C-Mod (in preparation).

DISCUSSION

K. LACKNER: Were your statements on energy confinement based on the 'launched' ICRF power?

Y. TAKASE: We do use the launched ICRF power. In the H minority heating presented in our paper, the absorbed power deduced from the slope change of the stored energy at RF power turn-off is typically 90–100% of the launched power.

Y.-K.M. PENG: The C-Mod ELM free confinement times are shown to have $H_{89P} \approx 2.5$, $H_{93ELMy} \approx 2$, $H_{DIIID-JET} \approx 2$. Would you comment on the significance of these results for the scaling laws.

Y. TAKASE: C-Mod has significantly different dimensional parameters (R, B_T, $\bar{n}_e$, etc.) from those of the tokamaks from which these scaling laws were derived. If the scaling exponents are wrong, predictions of these scaling laws for C-Mod can be off by a significant factor, and likewise when extrapolating to ITER. We have contributed our data to the ITER H mode database. The H mode scaling law may need to be revised by including data from C-Mod. We think the addition of C-Mod data provides important constraints on the scaling law, particularly on the size scaling.

O. KARDAUN: With respect to the energy content, what is your estimate of the contribution from fast particles?

Y. TAKASE: According to Fokker–Planck calculations, these high density H mode plasmas ($\bar{n}_e \approx 4 \times 10^{20}$ m^{-3}) have a fast particle (H minority) energy content of $\leq 5\%$.

O. KARDAUN: How large is the quantitative agreement between the various thermal energy measurements (based on W_{dia}, W_{MHD} and W_{kin}) you can routinely achieve?

Y. TAKASE: The total stored energies W_{dia} and W_{MHD} agree to within 5–10%. W_{kin} typically agrees with W_{dia} and W_{MHD} to within 10–20%.

OPTIMISATION OF JET PLASMAS WITH CURRENT PROFILE CONTROL

JET TEAM[1]
(Presented by C. Gormezano)

JET Joint Undertaking,
Abingdon, Oxfordshire,
United Kingdom

Abstract

OPTIMISATION OF JET PLASMAS WITH CURRENT PROFILE CONTROL.

Internal transport barriers extending up to r/a = 0.55 have been achieved on JET by tailoring the plasma current profile by proper current ramps up to 3 MA, with or without heating. The best performing discharges are produced when a long L-mode phase with high core confinement can develop before the onset of an H-mode. High central ion temperatures (32 keV) and electron temperatures (15 keV) are simultaneously produced, resulting in neutron rates comparable to the best Hot Ion H-mode in JET with a time duration (0.5 s) in excess of the energy confinement time.

1. INTRODUCTION

Operating a tokamak with higher confinement than predicted by the usual confinement scaling laws [1] has several advantages. One of them is to increase the fusion yield for a given input power allowing access in JET to regimes in DT operation where the alpha power can play a significant role. Another advantage is to operate a fusion reactor at lower plasma current. This opens the possibility of steady state operation, especially at high poloidal beta, high bootstrap current, by reducing the demand on non-inductive current drive. These so-called advanced tokamak scenarios require the demonstration of improved confinement not only transiently but for long duration.

Current profile control has proved to be an important technique to optimise confinement of tokamak plasmas. For example, in JET, current profile modification has produced high confinement with a reversed shear magnetic configuration in the pellet enhanced H-mode (PEP + H-mode) [2] and also in high β_p, high bootstrap current plasmas [3]. Ion minority current drive has been used to stabilise or destabilise sawteeth by local modifications of the current profile [4]. Lower Hybrid Current Drive (LHCD) has been used to modify the current profile before the formation of a Hot Ion H-mode [5], to raise the safety factor on axis q(o) above unity and provide sawtooth suppression during the high power heating phase resulting in an increase of the overall neutron rate. This technique has also allowed the addition of Ion Cyclotron Resonance Heating (ICRH) and Neutral Beam Injection (NBI) at high power levels in the Hot Ion H-mode which, in the absence of sawteeth, benefits from increased power deposition in the plasma core and a 30% increase in confinement [6].

Large efforts have been made to develop discharges with reversed shear either by using LHCD (Tore Supra) [7] achieving high confinement quasi steady-state discharges or by making use of heating in the current ramp phase to freeze

[1] See Appendix to IAEA-CN-64/O1-4, this volume.

the current profile to achieve an optimised q profile resulting in good central confinement [8-10].

In current ramp experiments in JET in the 1994/95 campaign, a few MW of LHCD power was applied during a fast current ramp (1MA/s). A substantial increase of the electron temperature (up to 10keV) was observed during the initial phase of the reversed shear. Transport analysis has shown that the electron thermal diffusivity during this phase was reduced by one order of magnitude to values close to the level of the neo-classical thermal conductivity. This phase of enhanced confinement was not maintained when heavy gas puffing was used to raise the density in order to allow NBI with low shine-through. A broad density profile resulted and an ELMy H-mode was produced with 12MW of NBI power.

New hardware has allowed operation of the JET NBI system at lower density. With proper current ramp and power waveforms, large Internal Transport Barriers (ITB) have been obtained with a combination of NBI and of ICRF resulting in high performance plasmas.

2. INTERNAL TRANSPORT BARRIER

In JET, the ITB is established when the main power waveform is applied during the current ramp phase of the plasma, with or without a preheating phase. The main evidence of an internal barrier can be seen from the evolution of the ion temperature profile as shown in Figs.1 and 2 for two different timings of the power application. With early power application (Fig.1), a barrier is formed very close to the plasma core, about 1.2 s after the start of the heating. This barrier then moves outwards to r/a = 0.45. The discharge remains in an L-mode during the whole development of the ITB and is generally terminated by a disruption, following high frequency core MHD.

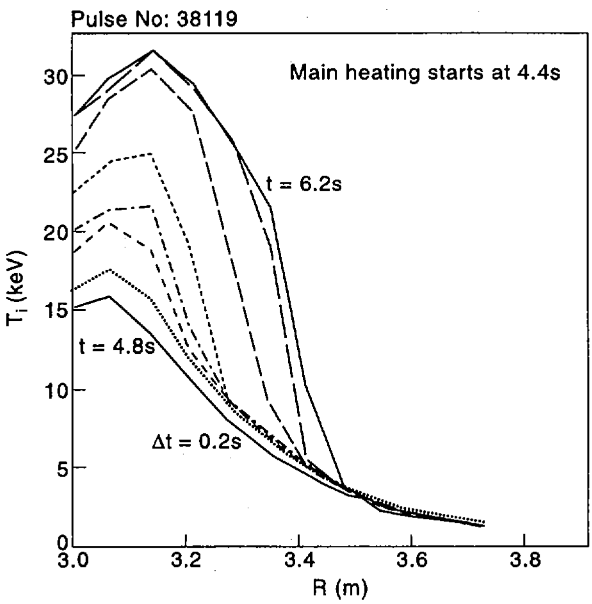

Fig.1 Evolution of ion temperature profile from charge exchange recombination (B_t = 3.4T; 2.5 < I_p < 3MA) with early power waveform and 1MW (ICRH) of preheating.

ITBs have also been established when power is applied later in time and with no preheating as shown in Fig.2. The barrier is established almost immediately with a slow expansion up to r/a ~ 0.55. In this case, the L-mode phase is followed by an H-mode with central pressure up to 2.5 bar. It can be noted that a pedestal is formed at the plasma periphery and the whole ion temperature profile is raised by about 2 keV. These profiles are quite different from profiles of equivalent Hot Ion H-modes with similar power and neutron yield which shows significantly lower central temperature and much higher edge temperature. Similar transport barriers can be seen on the electron temperature profiles and to a lesser extent on the density profiles.

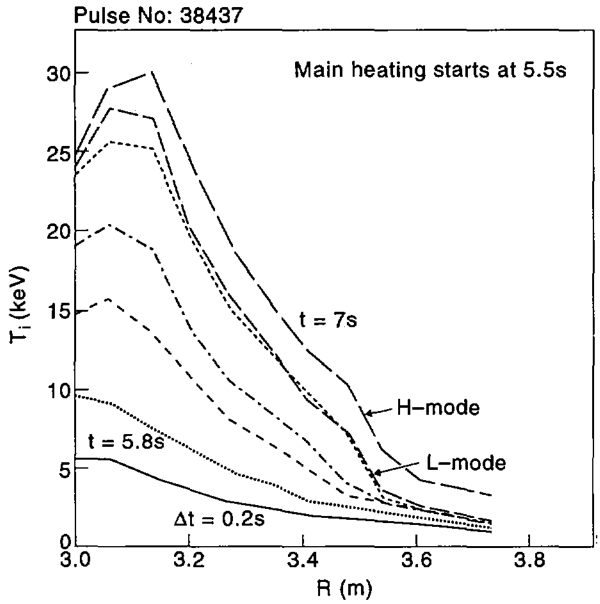

Fig.2 Evolution of ion temperature profile from charge exchange recombination (B_t = 3.4T; 2.5<I_p < 3MA) with late power waveform and no preheat.

ITBs are very sensitive to the timing of the high power waveform as illustrated in Fig.3. The ramp rate of the discharge to 2.5MA is adjusted to the highest rate compatible with the absence of MHD activity during the ramp. The second ramp in current is used to delay the onset of the H-mode. If H-modes appear too early, the L-mode peaked pressure profile is not yet fully established and NBI penetration is compromised by the formation of the edge pedestal. In addition, the strike points of the last closed surface are maintained close to the divertor pump entrance to prevent the edge density from forming quickly. This also delays the onset of the H-mode. The present configuration has low triangularity due to the mode of operation used for this campaign. As shown in Fig.4, early heating results in a late core transition. Late heating leads to an early H-mode which prevents the establishment of an ITB. The best performance (without disruption) has been obtained when the power is applied 5.5 s after the beginning of the discharge. Note that discharges with an ELMy H-mode obtained with late heating still have peaked density profiles because q(o) remains above unity and sawteeth are absent. The neutron yield is about 2 times higher than corresponding sawteething discharges with similar power. An optimisation of this mode of operation for high performance steady operation is still outstanding.

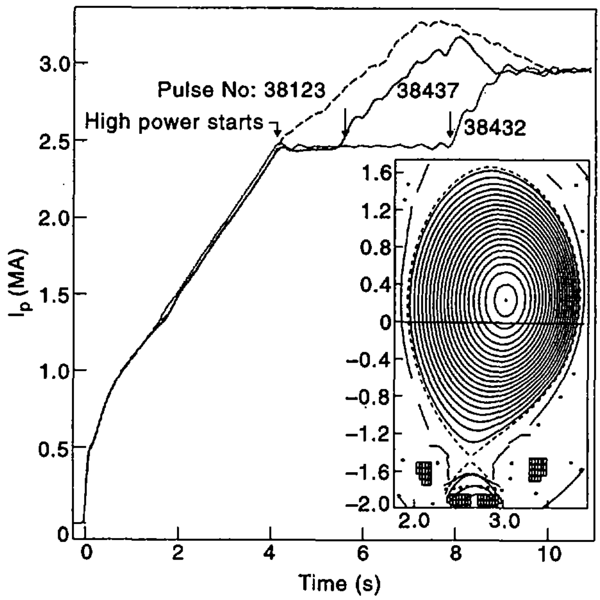

Fig.3 Typical current waveforms and flux contours for ITB. In the absence of heating, sawteeth appear at about t = 9 s.

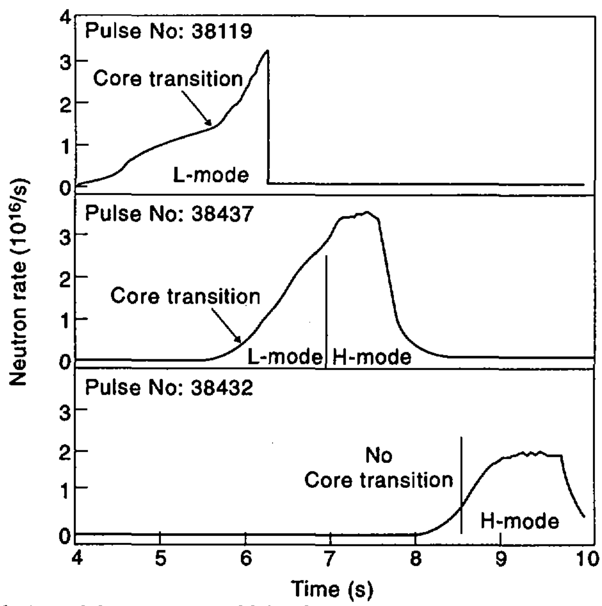

Fig.4 Time evolution of the neutron yield for different timing of the power waveform with a total power of 25MW. No ITB is observed when power is injected after 6 s from the start of the discharge.

3. HIGH PERFORMANCE DISCHARGES WITH SHEAR OPTIMISATION

An example of a high performance discharge where the L-mode phase is followed by an H-mode is shown in Fig.5. The H_{89} factor reaches 2 during the L-mode phase and 2.5 during the H-mode phase. These discharges have about 30% less stored energy than a comparable Hot Ion H-mode but a similar neutron yield because of the peaked profiles. There is no evidence of impurity accumulation on this time scale, Z_{eff} remaining constant at about 1.7. It is to be noted that in the case shown in Fig.5 the neutron yield remains about constant during the ELMs for as long as the power was applied, i.e. for times longer than the energy confinement time (0.4 s). However, in similar pulses a giant ELM often leads to a degradation of performance. The largest neutron yield which has been achieved in such discharges equals the highest yield in the Hot Ion H-mode achieved on JET in the present campaign.

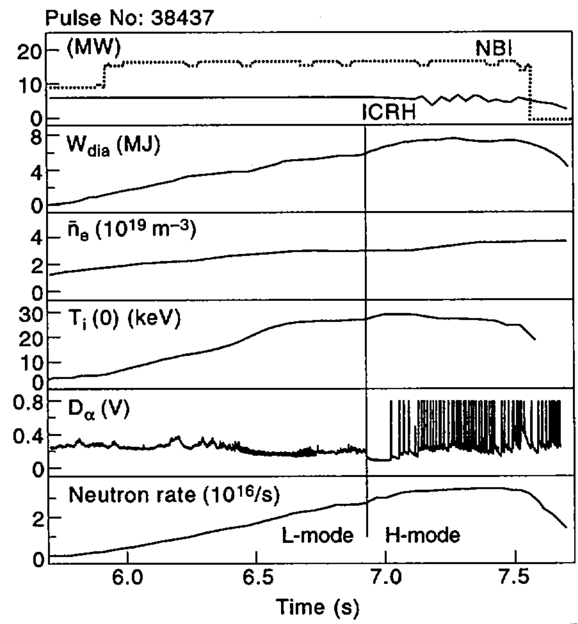

Fig.5 Time history of a high fusion yield pulse with shear optimisation (B_t = 3.4T; 2.5 < I_p 3MA). ICRH frequency (51MHz) corresponds to a resonance (H minority or 2nd harmonic D) close to the centre.

Several experimental observations (such as: no significant flux of gamma radiation, an increase of only 2 to 3 keV in electron temperature when comparing NBI only and combined heating shear optimised discharges), together with numerical simulations indicate that a substantial part of the Ion Cyclotron wave is coupled to fast deuterons at energies lower than a few hundred keV leading to ion heating, especially at high electron temperature.

In the absence of a proper simulation of the damping and heating of the Ion Cyclotron wave in such plasmas, a TRANSP simulation has been made for a discharge with shear optimisation where the ICRH power was off for 1 s. As shown in Fig.6, good agreement between experimental values and simulation is obtained with a significant thermal yield reaching more than 50% of the total yield. The current profile in JET can only be measured through a combination of polarimetry and magnetic measurements to reconstruct the equilibrium (EFIT). Unfortunately, only one polarimeter channel can reasonably be used. Consistency checks have been made between the equilibrium reconstruction and the calculated current profile in TRANSP. It is not yet possible to have a reliable q profile, but it appears that a strong reversed shear is not necessary to trigger an ITB, in agreement with observations on DIII-D. The location of the barrier at the onset of the H-mode appears to be in the vicinity of a q=2 surface.

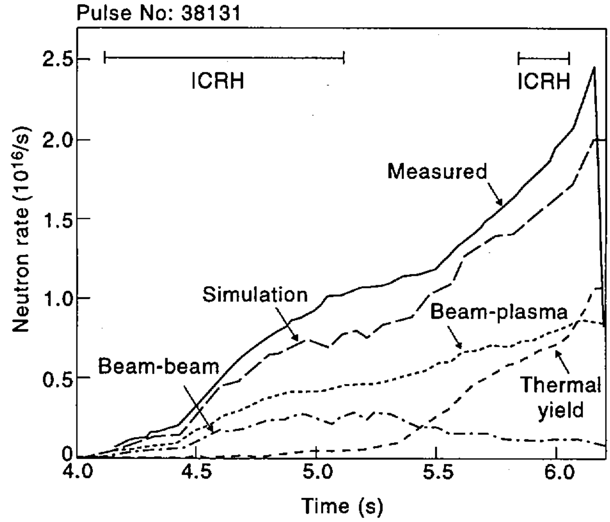

Fig.6 TRANSP simulation of pulse 38131. NBI (14MW) is on from 4 s ICRH (7MW) is off for 1 s.

4. POWER DEPENDENCE AND LIMITATIONS

A minimum power is required to obtain ITB in JET, as shown in Fig.7 where the data base of neutron rate versus total injected power is given for all discharges where a sustained core transition has been achieved. A substantial part of the data scattering is due to the large range of power, density and configuration waveforms investigated for shear optimisation, in particular neutron rate is very sensitive to target density. The low range of power corresponds to power step-down experiments, similar to Fig.6, where 6 to 8MW of ICRH power was switched off after about 1s when an ITB was already established. The dependence of this minimum power versus various parameters such as magnetic field and plasma current has not been done yet. The performance during the L-mode phase was often limited by low frequency, n =1 modes hardly rotating, sometimes locked, located near the q = 2 surface. These modes are very different from the modes appearing during pulses with early heating with an n = 1 structure rotating at very high frequency and leading to a disruption. The low frequency modes shown in Fig.8 are not disruptive, but limit the increase of neutron yield especially when these modes are locked. Their amplitude is variable which contributes to the scatter in the data and their dependence on plasma parameters is under investigation.

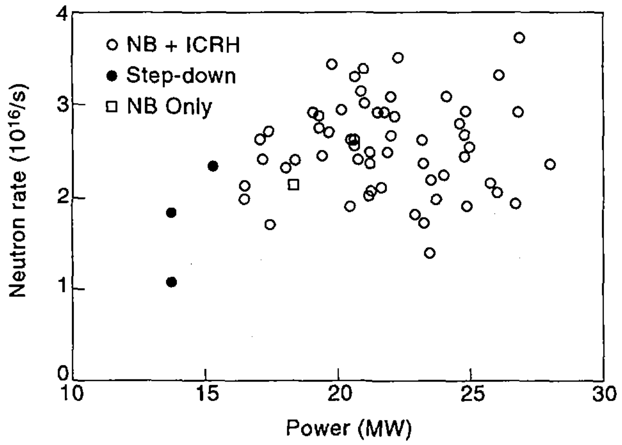

Fig.7 Neutron rate versus power for discharges with sustained core transitions .

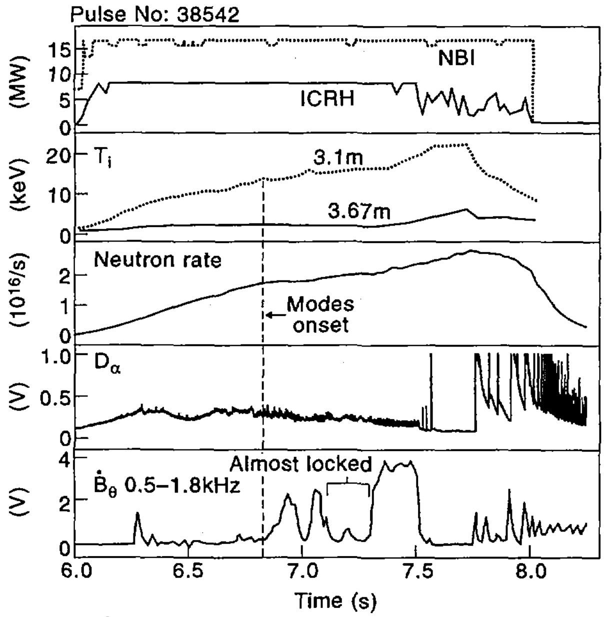

Fig.8 Time history of a discharge where low frequency MHD limits L-mode performance.

5. SUMMARY AND CONCLUSIONS

Internal Transport Barriers have been obtained on JET in low triangularity discharges with shear optimisation. The best performing discharges have a long L-mode phase followed by an H-mode phase which is deliberately delayed by a second current ramp. Up to 28MW of combined power has been used for discharges with I_p from 2.5 to 3MA and B_t = 3.4T with low target density. Internal barriers with r/a = 0.55 have been achieved, resulting in:

- high confinement L-modes (H_{89} = 2)
- simultaneous high T_i (32keV) and T_e (15keV)

- an ITB is only formed above a power level of about 17MW in these conditions
- high neutron yield (3.9 10^{16}/s) comparable to the best Hot Ion H-modes for times longer than an energy confinement time
- no apparent accumulation of impurities
- a high ratio of neutron yield to stored energy.

It should be noted that these are still early experiments. More development, including optimisation of pre-heat techniques, use of non-inductive current drive (LHCD and phased ICRH), use of higher triangularity, together with further optimisation of the ELMy H-mode phase, might lead to higher performance and/or extended duration. Extending the duration of the high performance phase is of obvious importance for reactor application.

ACKNOWLEDGEMENTS

Specific contributions from C. Greenfield, E. Lazarus, T. Luce, B. Rice, E. Strait (GA), M. Zarnstorff and G. Schmidt (PPPL) as well as from B. Lloyd, C. Warwick and C. Hunt are gratefully acknowledged.

REFERENCES

[1] JET TEAM (presented by J.C. Cordey), IAEA CN-64/AP1-2, this volume.
[2] TUBBING, B., et al., Nucl. Fusion **31** (1991) 839.
[3] CHALLIS, C., et al., Nucl. Fusion **33** (1993) 1097.
[4] BHATNAGAR, V.P., et al., Nucl. Fusion **34** (1994) 1579.
[5] EKEDAHL, A., et al., in Controlled Fusion and Plasma Physics (Proc. 23rd Eur. Conf. Kiev, 1996), Vol. 20C, European Physical Society, Geneva (1996).
[6] COTTRELL, G., et al., ibid.
[7] LITAUDON, X., et al., ibid.
[8] JET TEAM (presented by C. Gormezano), in Plasma Physics and Controlled Nuclear Fusion Research 1994 (Proc. 15th Int. Conf. Seville, 1994), Vol. 1, IAEA, Vienna (1996) 633.
[9] LEVINGTON, F.M., et al., Phys. Rev. Lett. **75** (1995) 417.
[10] STRAIT, E.J., et al., Phys. Rev. Lett. **75** (1995) 421.

DISCUSSION

S.A. SABBAGH: You state that the maximum neutron rates in your optimized JET discharges occur in plasmas which make a late transition from L to H mode. Similar results have been reported in DIII-D NCS high gain plasmas. In DIII-D, the L–H mode transition leads to improved performance because a *stability* limit of the L mode edge plasma is avoided. Why is the performance improved in your JET plasmas?

C. GORMEZANO: Our main aims in terminating the L mode phase by an H mode phase are (i) to avoid disruptions which are not good for high performance plasmas, and (ii) to further improve the yield. It is still premature to assess whether the L mode disruption phase is due to a β limit.

K. LACKNER: If you compare optimized shear discharges at a given heating power, but with different splitting between NBI and ICRH, do you see a systematic difference? I am referring to the discussion on the importance of toroidal velocity shear.

C. GORMEZANO: The driving terms for toroidal velocity shear are being analysed, computed or calculated and will be an essential ingredient in the analysis you are referring to. Unfortunately, this analysis is not yet completed.

A.E. HUBBARD: You show a steepening of T_e as well as T_i profiles. Do you infer that χ_e as well as χ_i is dropping inside the confinement barrier?

C. GORMEZANO: During our TRANSP analysis, we find that χ_i in the core drops rapidly. χ_e also drops but less rapidly. Both values are still above neoclassical values by a factor of 3 to 5.

TRANSPORT AND LOSS OF ENERGETIC IONS IN JT-60U

K. TOBITA, T. NISHITANI, H. HARANO[1], K. TANI, M. ISOBE[2],
T. FUJITA, Y. KUSAMA, G.A. WURDEN[3], H. SHIRAI, T. OIKAWA,
T. FUKUDA, K. HAMAMATSU, S. ISHIDA, M. NEMOTO,
T. KONDOH, A. MORIOKA, H. KIMURA, M. SAIGUSA,
S. MORIYAMA, O. DACOSTA[4], V.I. AFANASSIEV[5], JT-60 TEAM
Naka Fusion Research Establishment,
Japan Atomic Energy Research Institute,
Naka-machi, Naka-gun, Ibaraki-ken,
Japan

Abstract

TRANSPORT AND LOSS OF ENERGETIC IONS IN JT-60U.

The MeV ion confinement in reversed magnetic shear and the ripple loss of beam ions in up–down asymmetric ripple on JT-60U are presented. Triton burnup measurements showed a significant loss of energetic tritons from reversed shear plasmas. The loss dramatically increased with toroidal field ripple. A model calculation matched the experimental results, indicating that stochastic ripple loss as well as collisional ripple loss were responsible for the triton loss. The result suggests an imperative need to consider energetic ion loss in reversed magnetic shear research. An up–down asymmetric ripple experiment confirmed the earlier prediction for ITER that the ripple up–down asymmetry would not enhance energetic ion loss to a significant degree, and that the loss was independent of the ion drift (or B_T) direction. The result is encouraging with respect to flexible B_T reversal operation in next step fusion reactors with up–down asymmetric ripple from the point of view of ripple loss.

1. TRITON BURNUP IN A REVERSED MAGNETIC SHEAR PLASMA

Tritons produced at 1 MeV through the d(d,p)t reaction can undergo the secondary d(t,n)^{3}He reaction during slowing down, producing 14 MeV neutrons. By measuring 'triton burnup' from the 14 MeV neutron yield, we can explore energetic ion transport and loss in a DT plasma without directly handling tritium. For that reason, large tokamak experiments have been devoted to measuring triton burnup as well as other fusion products. In recent JT-60U experiments, triton burnup indicates an adverse aspect of reversed magnetic shear plasmas with regard to energetic ion losses.

[1] University of Tokyo, Bunkyo-ku, Tokyo, Japan.
[2] National Institute for Fusion Science, Nagoya, Japan.
[3] Los Alamos National Laboratory, Los Alamos, New Mexico, USA.
[4] STA Fellowship.
[5] A.F. Ioffe Physico-Technical Institute, St. Petersburg, Russian Federation.

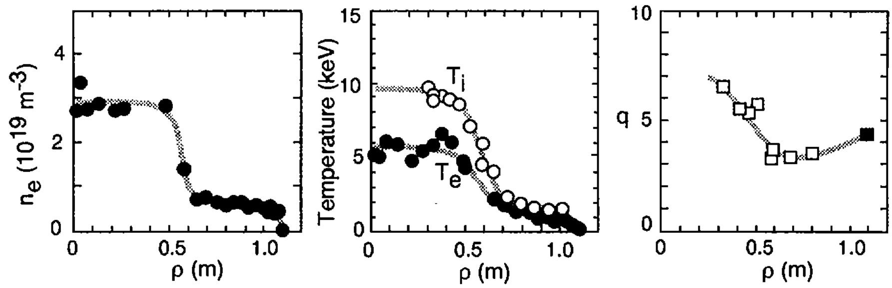

FIG. 1. Profiles in a reversed magnetic shear plasma: electron density and temperature profiles measured by Thomson scattering, ion temperature by charge exchange spectroscopy and safety factor by the motional Stark effect. ρ stands for the averaged minor radius.

1.1. Reversed magnetic shear plasma on JT-60U

The reversed shear configuration has demonstrated attractive plasma performance in several tokamaks [1, 2]. In JT-60U, ion and electron thermal transport is dramatically improved inside the internal transport barrier formed near the radius of q_{min} [3]. Figure 1 shows profiles of n_e, T_e, T_i and q obtained in a reversed magnetic shear discharge with I_p = 2 MA, B_T = 3.5 T and neutral beam power P_{NB} = 9.4 MW. Reversed magnetic shear is produced by early NBI during I_p ramp-up. The transport barrier seen in n_e, T_e and T_i at ρ = 0.5–0.6 m produces a wide core, which is characteristic of the reversed shear scenarios on JT-60U.

To confine MeV ions (such as fusion produced tritons) in a plasma with a ≈ 1 m, I_p should be as high as possible. Plasma parameters in the experiment were I_p = 2.0–2.5 MA (the high current regime achieved in JT-60U reversed shear operation), B_T = 3.5–4.0 T, safety factor at the surface q_{eff} = 4–4.5, and central safety factor q(0) = 3.5–8.

1.2. Triton burnup

In reversed shear operation, low rotational transform in the core expands energetic ion orbits vertically (Fig. 2), probably deteriorating the confinement of energetic ions and raising concern about first wall damage.

Comparisons of triton burnup between the experiment and the calculation assuming no triton diffusion, i.e. no triton loss, are shown in Fig. 3. Here triton burnup (14 MeV neutrons) is measured by a scintillation fibre detector [4] viewing almost the whole cross-section of the plasma. The reversed shear plasma in Fig. 3(b) has q_{min} = 2.1 at r/a = 0.65 and q(0) = 3.6. Early in time after the onset of NBI heating, the experimental burnup tends to be larger than the calculation. Yet the burnup in the early

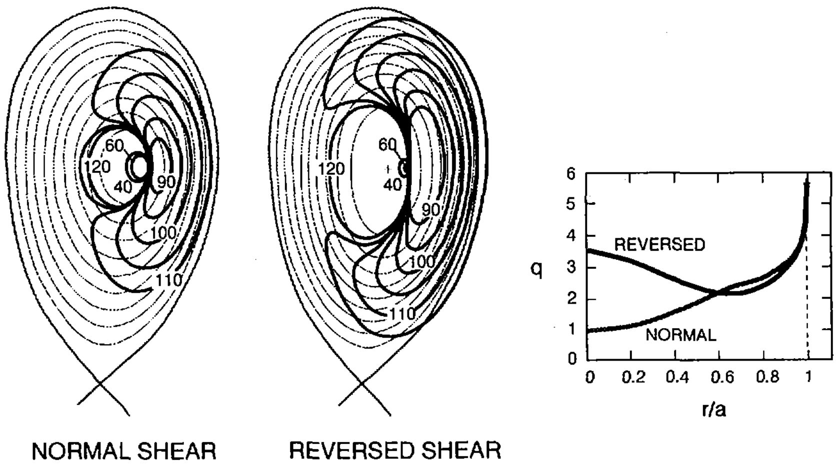

FIG. 2. Guiding centre orbits for a 1 MeV triton launched at r/a = 0.2, in a normal shear and a reversed shear plasma.

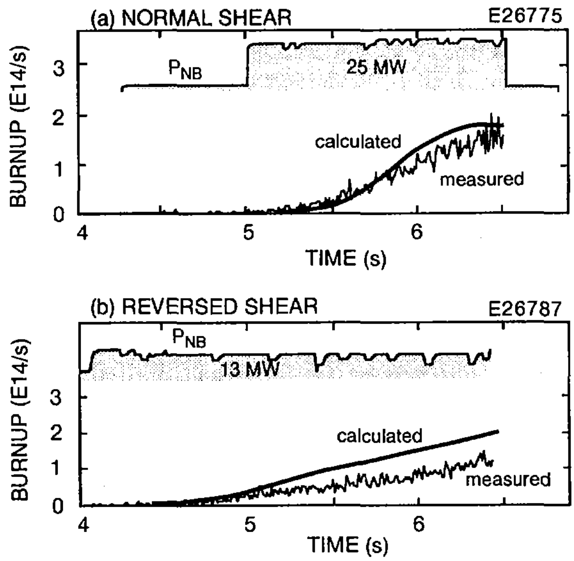

FIG. 3. Triton burnup in a normal shear plasma with monotonic positive shear and in a reversed shear plasma ($q(0) = 3.6$ and $q_{min} = 2.0$ at $r/a = 0.65$). The calculation assumes no triton losses with classical slowing down and does not include any orbit effects.

phase is a background, in that tritium accumulated in the vacuum vessel during the previous shots undergoes the D–T reaction as T_i rises. As time evolves, the burnup of tritons produced in the ongoing shot dominates and the background burnup contribution becomes relatively small. Except for the early phase, the measured burnup is 20% and 40% less than the calculation without triton losses in the normal shear and the reversed shear, respectively. This indicates that MeV ion confinement in reversed shear is inferior to that in normal shear. Here it should be noted that the depleted fraction of the experiment does not always mean 'triton loss from the plasma', but rather, to describe it prudently, 'excursion from the core plasma'. Suppose that tritons escape the core and stay in the plasma outside the transport barrier. Then triton burnup drops through lack of deuterium targets for the D–T reaction. Thus, the transport of tritons from a higher density region to a lower can reduce the burnup. The effect may be important especially in the reversed shear plasma exhibiting a dramatic density change across the internal transport barrier, as seen in Fig. 1. Yet a model calculation described below indicates that energetic tritons in the outer plasma are quickly diffused out by virtue of ripple transport and thus 'excursion from the core plasma' is considered to be 'loss from the plasma'.

By displacing the plasma position horizontally, the effect of toroidal field (TF) ripple on triton burnup was investigated. The fraction of confined tritons in particle number (Fig. 4(a)), which was determined by the experiment, falls as TF ripple rises in both magnetic shears, suggesting that TF ripple transport processes are responsible for the excursion of energetic tritons. An important finding is that the fraction confined for reversed shear is lower than that for normal shear at any ripple. The result indicates that reversed shear plasmas deplete energetic tritons more than normal shear plasmas.

An orbit following Monte Carlo (OFMC) calculation [5], which models all important processes related to ripple loss, matches the experimental data, as shown in Fig. 4(b). The successful match means that tritons are expelled by TF ripple

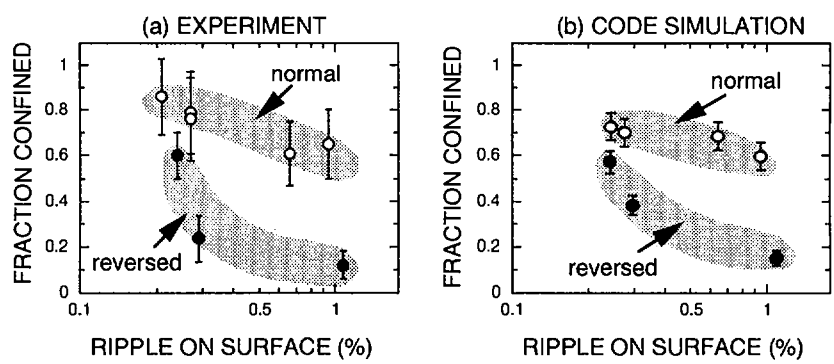

FIG. 4. (a) Experimental results on the fraction of confined tritons in particle number as a function of the ripple amplitude averaged over the plasma surface. (b) Fraction of confined tritons evaluated with the OFMC code with the inclusion of TF ripple effects and Coulomb collisions.

transport. In fact, a simulation assuming no TF ripple gives only 5% triton loss (2% lost by first orbit loss and 3% by neoclassical transport) for a reversed shear plasma, indicating an important contribution of ripple transport to the energetic triton loss.

1.3. Processes of triton loss in reversed shear

The causes of the larger triton loss in reversed shear are the birth profile of tritons and the value of q. Firstly, a broadened triton birth profile in reversed shear increases the fraction produced in the higher ripple region. The radius which most contributes to triton burnup is r/a = 0.4–0.5 for the reversed shear, whereas that for the normal shear is 0.3–0.4. Secondly, larger q in the core extends the ripple stochastic domain [6], approximately given by

$$\delta > 1\Big/\rho_L\left(\frac{\pi}{\sin\theta_b}\right)^{1/2}\left|2\theta_b q' + \frac{2q}{r}\frac{\cos\theta_b}{\sin\theta_b}\right|\left(\frac{Nq}{\varepsilon}\right)^{3/2}$$

with the ion gyroradius ρ_L, $q' \equiv dq/dr$, the number of TF coils N and the poloidal angle of the turning point θ_b. For the reversed shear plasmas considered, the stochastic domain prevails over the whole cross-section of the plasma for 1 MeV tritons. The essential effect to explain the enhanced loss in reversed shear is the value of q rather than the birth profile.

The time evolution of triton loss is helpful for understanding the loss processes. Figure 5 is an OFMC result on the temporal loss of tritons produced as an impulse at r/a = 0.45 at t = 0 s. The other conditions for the simulation are based on a shot with a ripple of 0.3% in Fig. 4(a). In the calculation, the initial pitch angle and the initial poloidal angle of each test particle are determined by random numbers. Within the bounce time, 2% of tritons are lost (first orbit loss). During the period 10^{-5} to ~10^{-2} s after birth, stochastic ripple loss dominates, determining most of the power loss.

After 10^{-1} s, when tritons are slowed down to ~100 keV, collisional ripple loss becomes important. This raises the particle loss but has little effect on the power loss. The particle fraction confined at ~10^{-1} s agrees with the experimental burnup. Several runs of the simulation also indicated that the power fraction confined was almost the same as the fraction of the particles born as trapped particles. Here the power fraction corresponds to [(the power that the confined energetic tritons have) + (the power transferred from tritons to the plasma)] / (the power of the tritons at birth). Even in the shot showing 12% of the particle fraction confined at a ripple of 1.1% in Fig. 4, the power fraction confined is as large as 50%.

From the results, the enhanced triton loss in reversed shear is concluded to be attributable to stochastic and collisional ripple losses. Such an enhanced loss of

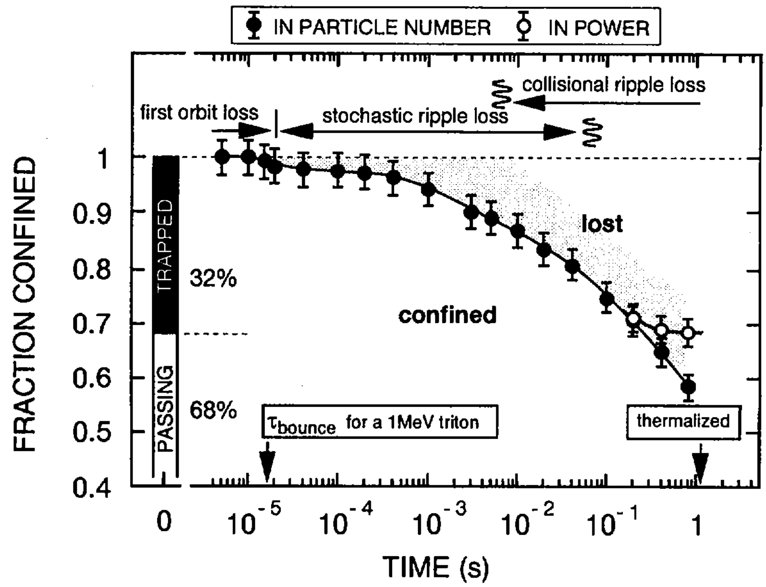

FIG. 5. Time evolution of triton loss simulated by the OFMC code for a reversed shear plasma. At r/a = 0.45, 1 MeV tritons are generated as an impulse at t = 0 s. Most initially trapped tritons are lost by collisionless processes, i.e. first orbit loss and stochastic ripple loss. After t ≈ 10^{-2} s, collisional ripple loss becomes operative. Among these loss processes, stochastic ripple loss determines most of the triton loss in power.

energetic ions would be a critical issue in terms of heat concentration on the first wall in a fusion reactor based on reversed shear. A possible solution to reduce the energetic ion loss is to lessen q values in the core, so that MeV trapped ions are kept out of the stochastic ripple loss domain. Thus the assessment of ripple losses of energetic ions will be necessary to find an appropriate q(r) leading to excellent confinement of both bulk plasma and energetic ions at the same time in reversed shear. Otherwise, TF coils will have to be designed oversized enough to reduce ripple loss to an acceptable level.

2. BEAM ION LOSS IN UP–DOWN ASYMMETRIC RIPPLE

TF ripple up–down asymmetry is of interest in the design of fusion reactors in terms of energetic ion loss. In particular, our major interest is to determine whether ripple loss is dependent on the ion ∇B direction in asymmetric ripple. This is necessary to assess the flexibility of B_T reversal operation for a reactor from the point of

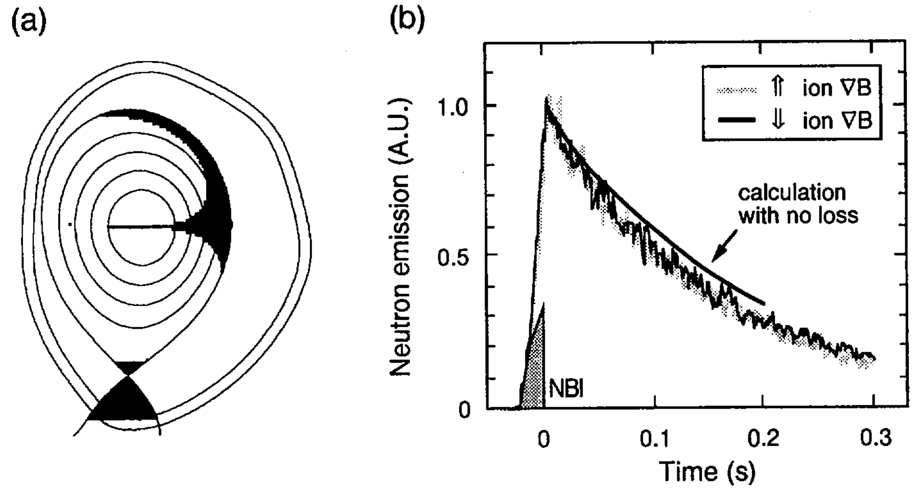

FIG. 6. (a) JT-60U plasma with an ITER-like ripple well (shaded area). (b) D-D neutron emission following short pulse NBI in upward and downward ion ∇B directions. The experimental decay is faster than the calculated decay because of ripple loss, and is independent of the ∇B direction.

view of localized ripple loss on the first wall. An earlier calculation of ripple loss for ITER showed no effect of the asymmetry on the total loss [7]. In JT-60U, the asymmetry effect was examined experimentally using neutral beam ions [8].

2.1. Experimental conditions

The experiment was carried out in the configuration with an ITER-like ripple well, as shown in Fig. 6(a). JT-60U's ripple asymmetry $\langle\delta^+\rangle - \langle\delta^-\rangle$ (the ripple difference between the upper half and the lower) for the configuration is 0.1% and 0.01% at r/a = 0.8 and 0.4, respectively, which is comparable with ITER's. The total ripple loss is estimated from the D–D neutron decay following a neutral beam blip [9]. The target plasma has I_p = 1.5 MA, B_T = 3.5 T, and $\bar{n}_e$ low enough (3×10^{18} m^{-3}) to lengthen the slowing down time of beam ions. The beams are injected perpendicularly and their loss from the plasma is related with TF ripple, as indicated in previous work [9].

2.2. Experimental results and analysis

Figure 6(b) shows that neutron emission evolves independently of the ion ∇B direction. Also shown is the calculated neutron decay assuming no beam ion loss with classical slowing down. The difference between the experiment and the calculation increases with time, because ripple transport of the beam ions becomes operative through collisions, thus exhibiting a slow loss. Around 0.15 s later, after the neutral beam is turned off, the loss comes to a saturation. From the difference in the decays late in time, the total loss fraction is determined to be 12 ± 3% for both drift directions: the diagnostic determines the total ripple loss arising from two partial losses, ripple trapped loss and banana drift loss. The result that the ion ∇B direction does not significantly affect the total loss fraction is consistent with the calculation done for ITER [7].

TABLE I. SIMULATED RIPPLE LOSS (%) OF NEUTRAL BEAM IONS IN THE CONFIGURATION SHOWN IN FIG. 6(a)

	Downward drift	Upward drift
Banana drift loss	7.7 ± 0.6	0.6 ± 0.2
Ripple trapped loss	1.8 ± 0.2	9.7 ± 0.6
Total loss	9.5 ± 0.6	10.3 ± 0.6

The experimental ripple loss in Fig. 5 was examined with the OFMC code. The result is shown in Table I. In the simulation, discrimination is made between the two partial ripple losses (banana drift and ripple trapped) of beam ions escaping from the plasma on the basis of their orbits just after leaving the plasma. The simulation result shows that the total loss is almost independent of the ion drift direction, and supports the experimental loss of 12 ± 3%. Interchange of the dominant loss process seen in Table I is not surprising, and is easily understood from particle trajectories in the given magnetic field. An important conclusion from the experiment and the simulation is that the ripple asymmetry has no significant effect on the total ripple loss, irrespective of the ion drift direction.

Theoretically, the up–down asymmetry gives rise to a net radial flux of the toroidally trapped particles, and the flux points inward or outward depending on the ion drift direction and the gradient of the ripple amplitude [10]. As in conventional ripple transport, the magnitude of the particle flux is determined by the energy of the particles, collisionality, the degree of asymmetry, etc. For that reason, the experiment using neutral beam ions does not necessarily guarantee the result obtained, i.e. the small effect of the ripple asymmetry on α particle transport in a reactor. As a matter of fact, the experiment did not identify the asymmetry effect itself, but the study in JT-60U is important in having confirmed experimentally that the prediction of energetic ion loss by the OFMC code is in agreement with the experiment for a plasma with a realistic up–down ripple asymmetry.

In conclusion, the experimental and simulated results are consistent with the earlier assessment of particle ripple loss on ITER, thus supporting the flexibility for B_T reversal operation.

REFERENCES

[1] LEVINTON, F.M., et al., Phys. Rev. Lett. **75** (1995) 4417.
[2] STRAIT, E.J., et al., Phys. Rev. Lett. **75** (1995) 4421.
[3] FUJITA, T., et al., IAEA-CN-64/A1-4, this volume.
[4] WURDEN, G.A., et al., Rev. Sci. Instrum. **66** (1995) 901.
[5] TANI, K., et al., J. Phys. Soc. Jpn. **50** (1981) 1726.
[6] GOLDSTON, R.J., et al., Phys. Rev. Lett. **47** (1981) 647.
[7] PUTVINSKI, S., et al., in Plasma Physics and Controlled Nuclear Fusion Research 1994 (Proc. 15th Int. Conf. Seville, 1994), Vol. 2, IAEA, Vienna (1995) 535.
[8] ISOBE, M., et al., Nucl. Fusion **37** (1997).
[9] TOBITA, K., et al., Nucl. Fusion **34** (1994) 1097.
[10] YUSHMANOV, P.N., et al., Nucl. Fusion **33** (1993) 1293.

DISCUSSION

G. BATEMAN: During the early 1980s, I wrote a series of papers showing how to reduce magnetic ripple to less than 1% using blocks of ferromagnetic iron or offset dipole coils. Why does JT-60U not use these ripple reduction techniques?

K. TOBITA: We don't think that JT-60U needs to reduce toroidal field ripple at the moment. As a matter of fact, the usual JT-60U operation is at ripple amplitudes of ~0.1%, comparable with other tokamaks. Recently, JFT-2M has started to use ferromagnetic iron on the first wall. The results will confirm whether or not the iron will work for the purpose without causing any ill effects.

TRANSPORT EXPERIMENTS

(Session A6)

Chairperson

P.K. KAW
India

TRANSPORT AND FLUCTUATIONS: MORE EVIDENCE ON TEXT*

G. CIMA, R.D. BENGTSON, X. BONNIN, R.V. BRAVENEC, R. CHATTERJEE, H. GASQUET, K.W. GENTLE, G. HALLOCK, P.D. HURWITZ, M. MEIER, P.E. PHILLIPS, D.R. ROBERTS, D.W. ROSS, W.L. ROWAN, D.L. WINSLOW, A.J. WOOTTON
Fusion Research Center,
University of Texas at Austin,
Austin, Texas

D. BROWER
University of California at Los Angeles,
Los Angeles, California

C.W. DOMIER, W.R. GECK, R.P. HSIA, F. JIANG, C. LIANG, B.H. DENG, N.C. LUHMANN, Jr.
University of California at Davis,
Davis, California

C. WATTS
Auburn University,
Auburn, Alabama

United States of America

Abstract

TRANSPORT AND FLUCTUATIONS: MORE EVIDENCE ON TEXT.

A small sample of recent findings at TEXT concerning heat and particle transport is given. Conventional and fluctuation techniques are applied to plasma edge and core. The experiments are mainly conducted in limiter TEXT-U plasmas with major and minor radii of 105 and 27 cm, an on-axis toroidal magnetic field of about $B_t = 2.1$ T, plasma currents between 100 and 300 kA and line average densities between 1 and 3×10^{13} cm^{-3}.

1. - Introduction

Experimental transport studies in fusion oriented magnetic confinement devices have been traditionally carried out by investigating the functional parametric dependencies of relevant fluxes. The dependencies of the obtained transport coefficients on the plasma parameters have then been compared to theoretical predictions.

---

*Work supported by the US Department of Energy under Contract Nos DE-FG03-86ER-53225 and W-7405-ENG-48.

This procedure has not provided us with satisfactory answers in many important cases. Most notably it has not uncovered the mechanisms which regulate the heat and particle transport in the hot core of tokamaks and stellarators.

To study the fluctuations of relevant plasma observables and identify the specific mode or instability responsible for a certain transport process is an alternative way to proceed. There is a substantial theoretical basis for linking the complete fluctuations spectra to the transport coefficients. The Kubo relations represent the best known example.

At the University of Texas at Austin, using the tokamak TEXT, we have attacked this fluctuation measurement approach to transport studies in a systematic way. Case by case we have considered which quantity and which characteristics of that quantity can be measured. In many cases to measure a specific observable (e. g. plasma density) with the needed accuracy in time and space may not even be theoretically possible. On the other hand, to measure the power spectrum of the fluctuations of a certain quantity, even with extreme frequency resolution, can be a possibility. An example is that of the temperature fluctuations of the plasma core of a tokamak, measured with the electron cyclotron radiation method (ECE). In this case one can demonstrate that the actual time history of the plasma temperature fluctuations is not measurable with the required time resolution, but it is comparatively simple to uncover the power spectrum of these fluctuations in the frequency range of interest.[1]

Thus fluctuation spectral measurements represent one way of finding the cause for a certain transport process, by first assessing its relevance with an estimate of the amplitude of the transport coefficient and then by identifying the main fluctuation modes through their dispersion relation. In what follows we will give a very small sample of what we have recently found at TEXT concerning heat and particle transport, applying the conventional and fluctuation techniques to the edge and the core of the plasma. The experiments described in this paper were conducted, unless otherwise stated, in limiter TEXT-U plasmas with major and minor radii of 105 cm and 27 cm, a toroidal magnetic field on axis around $B_t = 2.1$ T, plasma current in the range 100 to 300 kA, line average densities between 1 and 3 10^{13} cm^{-3}. Electron cyclotron heating (ECH) at the first harmonic, O-mode, was available at power levels between 100 and 300 kW.

2 - The Plasma Edge

We have made further measurements of edge and SOL plasma characteristics and related certain of them to the predictions of various proposed turbulence drive models. The average parallel wave vector $<\bar{k}_{\parallel}>$ of the turbulence has been measured using probes separated by 180° poloidally, 225° toroidally, @ 12 m along a field line with safety factor q = 4.2. The field line is first identified by an active probe technique, in which a biased probe is driven with an ac voltage, and the plasma current then swept in time (i.e. the safety factor q changed) until the signal on the probe @ 12 m away is correlated with the drive signal.

Figure 1a shows the cross power and coherence of the floating potential measured at the two probes, as a function of the poloidal distance around the flux surface. The peak correlation of the background turbulence at the two separated probes occurs at a different plasma current (i.e. different q) than the driven wave. The different poloidal location of the peak correlation then gives an average parallel wave vector. The results are that $0.03\ m^{-1} << \bar{k}_{\parallel}> < 0.1\ m^{-1}$, or $0.1 < qR<\bar{k}_{\parallel}> < 0.5$ and simultaneously measured parallel coherence lengths

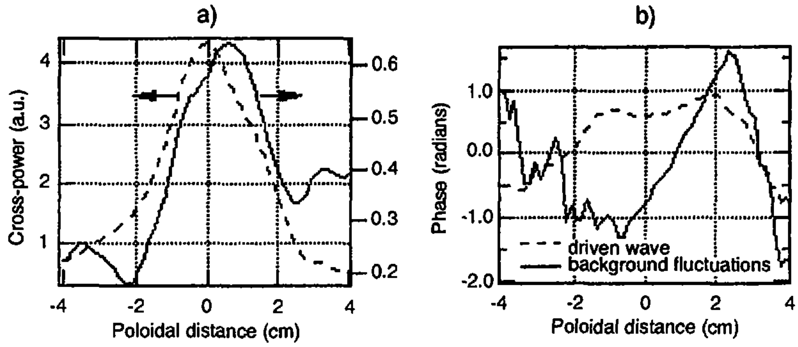

FIG. 1. Cross-power, coherence and phase shift for a driven wave and for the plasma turbulence for floating potential fluctuations measured on two probe arrays separated by 11.7 m along a magnetic field line.

are l_c = 15 & 3 m. The same result is obtained from a direct measurement of the phase shift (see *Figure 1b*) of the turbulence at the location of the field line. These results support the usual assumption of a small parallel wave vector.

Concerning possible drive mechanisms, the ionization drive[2] has been investigated first by seeking correlations between the ionization source strength $S = n_0 n_e \langle \sigma v \rangle_{ion} \propto IH_a$, the intensity of the H_a line, and the normalized density fluctuation level $\tilde{n}/n$ By varying the plasma density and the toroidal location of the measurements, IH_a is varied by a factor 4 while $\tilde{n}/n$ remains essentially unchanged. Second, using measured parameters in available theoretical expressions shows the predicted particle flux to be in the wrong direction and too small in magnitude by a factor > 10. Concerning the radiation drive[3], we have sought a direct measurement of the relationship between radiated power $P_{rad} \propto I_z(Te)$ and electron temperature T_e. 200 kW of ECRH was used to modulate the edge T_e, ECE used to measure T_e, and fast diodes used to measure the resulting changes to P_{rad}. The result is that in the plasma edge (r/a > 0.8) P_{rad} and T_e are in phase ($dI_z/dT_e > 0$), opposite to that required for any radiation drive. Concerning the condensation drive, we have developed a time domain triple probe technique which allows accurate measurements of $\tilde{T}_e$, $\tilde{n}$, $\tilde{\phi}_p$ and their respective phases. We find, in the region r/a < 1, $\tilde{T}_e$ and $\tilde{n}$ are in phase, and that $(\tilde{T}_e/T_e)/(\tilde{n}/n) \gtrsim 1$. That is, there is a significant pressure fluctuation, and there is no evidence for condensation.

We have found strong evidence for a poloidal asymmetry in the turbulence drive. H_a monitors are used to measure $R_A = (\tilde{n}/n)_{R+a}/(\tilde{n}/n)_{R-a}$, the ratio of the normalized density fluctuation levels at the outer to inner equator. $R_A = 1$ for limiter-bounded circular plasmas, in which the measured parallel coherence lengths of the turbulence (see above) would allow connection between outside and inside mid planes. However, for discharges in D-shaped separatrix-bounded plasmas $R_A > 2$; that is, the turbulence levels at the high field side are suppressed. The geometry of these discharges is shown in *Figure 2*, together with the power spectra. These discharges have very long connection lengths L_c along the field lines from outer to inner equator ($L_c = \infty$ in the SOL of a double null discharge) so that $l_c/L_c \ll 1$. Therefore under conditions in which the inner

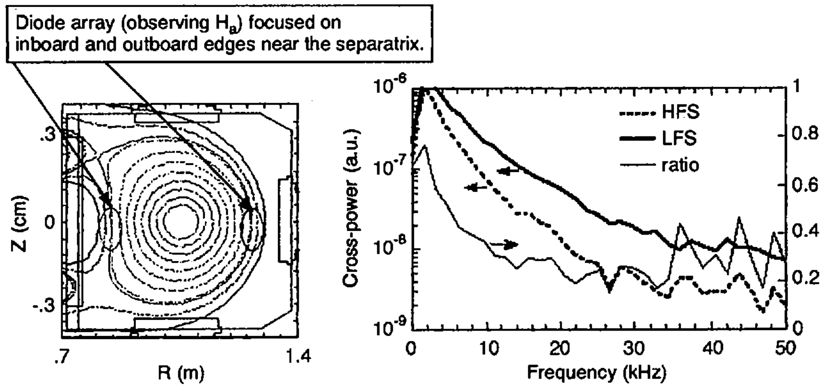

FIG. 2. Geometry of the D-shaped cross-section, and power spectra obtained for the turbulence at the two locations indicated.

and outer mid planes are separated we find the turbulence levels are different. The results suggest a role is being played by the curvature drive[4], as has been suggested by others[5].

3 - The Plasma Core

Essentially three parameters, n_e, T_e, ϕ (the electrostatic potential), and their fluctuations, have been measured in the plasma core on TEXT, with different degree of accuracy and completeness by 8 independent diagnostics (FIR, HIBP, BES, PCI, ECE fluct, ECE vert. viewing, ECE imaging, TS). Interesting and original measurements have been performed both on the stationary profiles and on the fluctuations. All diagnostics which were observing high frequency fluctuations showed a broad spectrum of high frequency fluctuations (~100 kHz). The various resolutions of the different diagnostic, often insufficient or marginal for drift wave-like turbulence measurements, remains the biggest obstacle to a quantitative assessment of the relevance of high frequency fluctuations for core transport.

4 - Phase Contrast Imaging

A Phase Contrast Imaging (PCI)[6] diagnostic with a vertical beam covering the central third of the plasma was successfully operated to study density fluctuations in the TEXT-U tokamak. The diagnostic has a bandwidth of 500 kHz and is sensitive to n_e fluctuations of about 10^{10} cm^{-3} with wavenumbers in the range of 0.5 cm^{-1} to 12 cm^{-1} along the major radial direction. It uses a 25 W CO_2 laser to illuminate the plasma and a focal plane filter to produce an image of the plasma electron density fluctuations on a detector array. Fourteen HgCdTe detectors in a linear array are used to achieve a spatial resolution of 2 mm across the beam.

Fig. 3 shows the auto-power spectrum of a single detector viewing along r/a=0.3 on the low field side. The spectrum shows two distinct peaks at about 75 kHz and 175 kHz. By comparison with other diagnostics making local fluctuation

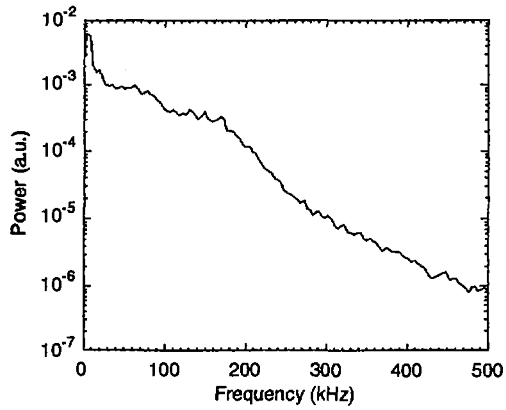

FIG. 3. Auto-power spectrum of a single detector.

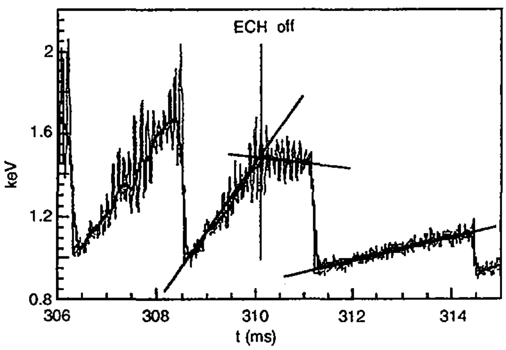

FIG. 4. T_e at $r/a = 0.13$.

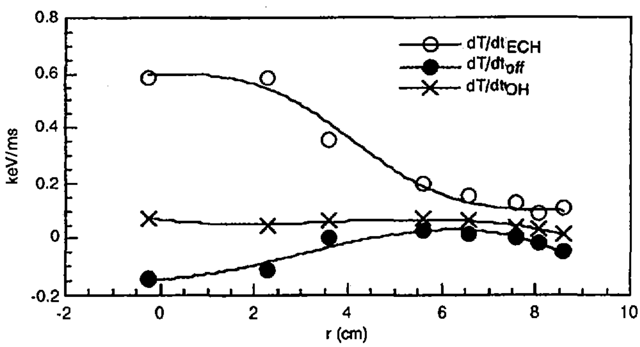

FIG. 5. Time derivative of core electron temperature.

measurements, these peaks can be associated with fluctuations in distinct parts of the plasma. The peak in the PCI spectrum at 75 kHz is due to the density fluctuations at the edge of the plasma and that at 175 kHz is due to fluctuations in the core of the plasma. Work is in progress to compare the dispersion relationship of the turbulence obtained from PCI with other diagnostics.

5 - Electron Core Confinement During ECH

A well focused ECH beam and a sufficiently large number of ECE diagnostic channels in the sawtoothing region of the plasma allowed to experiment with electron confinement within the sawtoothing region in between crashes.

Fig. 4 shows a typical ECE time history, measured within the inversion radius. Roughly 200 kW of ECH were turned off at t = 310ms. Eight ECE channels measured the evolution of the temperature profile inside the crashing region. In *Fig. 4*, just before and after ECH is turned off, one can distinguish three phases: the ECH on phase, the ECH off phase before a sawtooth crash, the ohmic heating phase during the following sawtooth. The temperature histories, averaged over the sawtoothing precursor activity, yield a very linear behavior in all phases and are completely characterized by their constant time derivative. The electron heat transport coefficient $\chi_e$is calculated in the second phase, when the profile produced with ECH starts to relax to the ohmic profile. The gaussian ECH beam from measurement and design is 4 cm wide, approximately half of the sawtoothing region in the case presented. *Fig.5* shows the electron temperature time derivatives in the three phases.

The problem of calculating heat diffusivity in this circumstance seems particularly simple, self consistent and is independent from the ECE calibration.

With the hypothesis of: absence of density gradients and convective losses, no electron/ion energy coupling, no radiation losses, in the ECHoff phase one can write:

$$\frac{3}{2}\frac{\partial T_{Relx}}{\partial t} = p_{OH} + \mathrm{div}(\chi_e \cdot \mathrm{grad}T)$$

where $p_{OH} = \frac{3}{2}\frac{\partial T_{OH}}{\partial t}$ is the ohmic heating power per particle.

In cylindrical symmetry, integrating once:

$$\chi_e(r) = \frac{\frac{3}{2}\int_0^r \left(\frac{\partial T_{Relx}}{\partial t} - \frac{\partial T_{OH}}{\partial t}\right) r\,dr}{r \cdot \mathrm{grad}T}$$

The resulting χ_e profile is shown in *Fig. 6*.

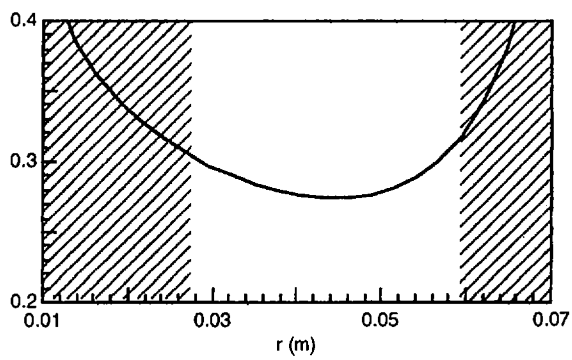

FIG. 6. Core electron thermal diffusivity.

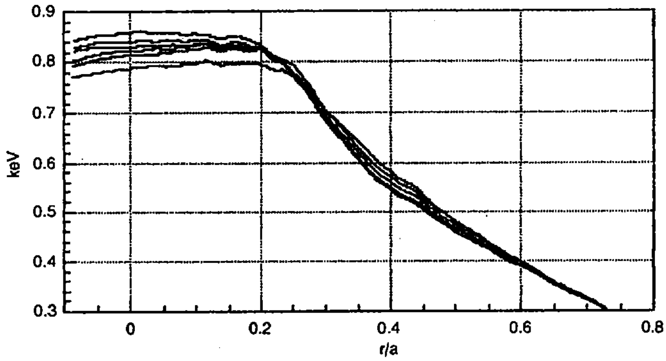

FIG. 7. T_e during sawteeth in the ohmic phase.

The result presented in Fig. 6 is the result of analizing analitic fits to the few experimental points and the evaluation of χ_e in the shaded regions of Fig. 6 is uncertain due to the smallness of gradT_e. This direct measurement seems to indicate that the electrons in the core plasma are remarkably well confined, on average roughly one order of magnitude better than in the rest of the plasma in this same discharge (Until the sawtooth crash occurs). The very flat temperature profiles measured during all sawteeth phases of purely ohmic discharges (*Fig.* 7.), are consistent with the good core electron confinement and uniformity of the ohmic power deposition (*Fig.4*).

The various traces of Fig. 7 have been obtained by stroboscopically analyzing a number of sawteeth pulses while the plasma, confined by top and bottom rail limiters, was gently shifted radially. The various curves correspond to evenly spaced phases of an averaged sawtooth.

One of the weakest assumptions in the evaluation of central χ_e is the one of cylindrical symmetry of the core. We have clear evidence from high resolution ECE that this is not the case. A very distorted configuration, which rotates with the plasma, sets in at an early phase in the sawtooth ramp. The following temperature profiles, *Fig. 8*, obtained with an array of ECE heterodynes[7], illustrate well the situation.

These features are most likely of the same nature of the previously reported plasma filamentation[8]. However our data demonstrates that the 'filaments' have a temporally cyclic nature, suggesting that they are a response to complicated central MHD structure interacting with very localized heating power deposition profile.

The highly structured rotating temperature profiles give rise to very noisy traces (see *Fig. 4*) in the time domain, sometimes described in the literature as sawteeth crash precursors. The precursors temperature fluctuation amplitude can reach, in the ECH cases on TEXT, 100% of the sawtooth amplitude.

High frequency fluctuation measurements[9] obtained with a stroboscopic variant of the intensity interferometry technique are shown in *Fig. 9*. There are no measurable high frequency fluctuations ($dT/T<10^{-3}$) in the plasma sawtoothing core, in between crashes. That is, we observe excellent core electron thermal confinement, high electron temperature gradients, and no evidence of fluctuations.

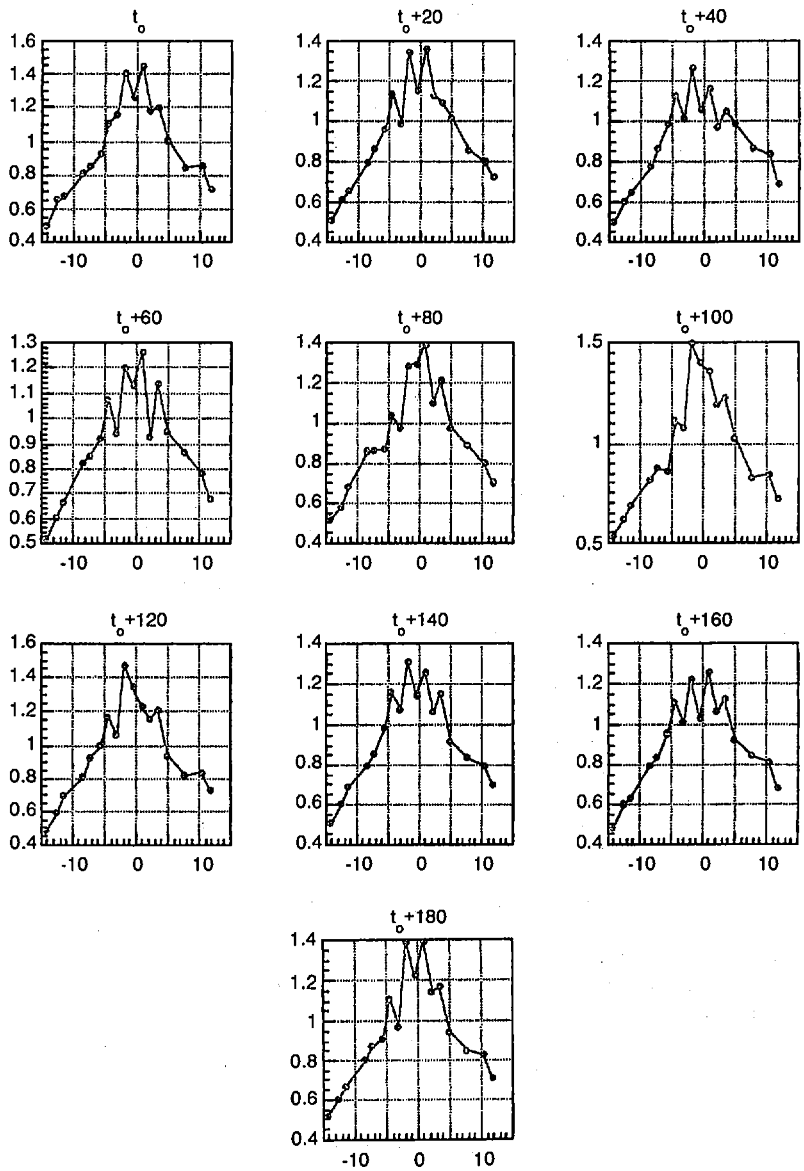

FIG. 8. Sequence of T_e profiles (keV against minor radius in cm) corresponding to a complete rotation period. The profiles repeat themselves as if the sequence rotated rigidly over many periods. The dominant mode number of the perturbation is $m = 1$, $n = 1$.

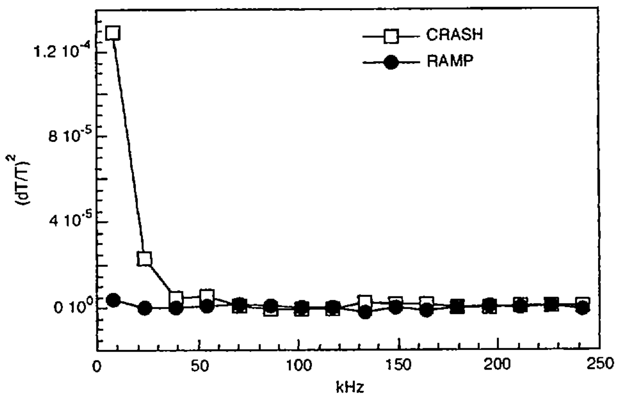

FIG. 9. T_e fluctuations at r/a = 0.1.

REFERENCES

[1] CIMA, G., Rev. Sci. Instrum. **63** (1992) 4630.
[2] WARE, A.S., et al., Phys. Fluids B 4 (1992) 877.
[3] THAYER, D.R., DIAMOND, P.H., Phys. Rev. Lett. **65** (1990) 2784.
[4] GARBET, X., et al., Nucl. Fusion **31** (1991) 967.
[5] ENDLER, M., et al., J. Nucl. Mater. **220–222** (1995).
[6] CHATTERJEE, R., et al., Rev. Sci. Instrum. **66** (1995) 457.
[7] HSIA, R.P., et al., Rev. Sci. Instrum. (in press).
[8] LOPEZ CARDOZO, N.J., et al., Phys. Rev. Lett. **73** (1994) 256.
[9] WATTS, C., CIMA, G., GANDY, R.F., REMPEL, T.D., Rev. Sci. Instrum. **66** (1995) 451.

DISCUSSION

A. FUJISAWA: Is your dispersion relation consistent with the data from the HIBP or from FIR scattering?

G.F. CIMA: It is consistent with the FIR scattering.

K. LACKNER: Referring to the T_e filaments which you also observe in ECH discharges, one way in which this would seem compatible with the very high parallel heat conduction would be that the whole region concerned would be very close to q = 1, with extremely low shear. The field lines would then proceed poloidally very slowly in subsequent toroidal transits and also stay together when at neighbouring flux surfaces. Do you have additional information regarding the shear in these regions?

G.F. CIMA: At these small radii, $\rho = 0.1$, the shear is bound to be low. The current profile measurements are sawtooth averaged and also show low shear.

DEPENDENCE OF CORE TURBULENCE ON THE DISCHARGE PARAMETERS IN T-10 AND ITS CORRELATION WITH TRANSPORT

V.A. VERSHKOV, S.V. SOLDATOV, D.A. SHELUKHIN
Institute of Nuclear Fusion,
Russian Research Center,
Kurchatov Institute,
Moscow, Russian Federation

Abstract

DEPENDENCE OF CORE TURBULENCE ON THE DISCHARGE PARAMETERS IN T-10 AND ITS CORRELATION WITH TRANSPORT.

Small scale turbulence was investigated on T-10 with multipin Langmuir probes and correlation reflectometry. In the entire plasma, six types of turbulence were distinguished, four of which were observed in the plasma core. A numerical computer model was developed to investigate the turbulence structure in detail. Three types of turbulence were simulated by the model. The measured turbulent radial particle flux is poloidally highly asymmetric. The absolute value of the flux agrees with the experimental value. The turbulence parameters depend strongly on the influx rate of the working gas. It is observed that a high level of quasi-coherent turbulence corresponds to high confinement regimes while a high level of low frequency turbulence corresponds to low confinement regimes.

1. INTRODUCTION

At present, the decrease of turbulent transport is a very important problem because improved confinement is needed for ITER operation. Several such regimes with enhanced confinement and suppressed turbulence were found experimentally but the physics of turbulence and its suppression is not clear. This paper continues previous studies of turbulence on the T- 10 tokamak [1–7]. The goals of investigation are to distinguish different types of small scale turbulence, to understand their properties, their dependence on the plasma parameters and their connection with transport.

2. EXPERIMENT

The T-10 parameters and the arrangement of diagnostics are described in Ref. [3]. OH and ECRH discharges with a current of 200 kA, a magnetic field of 2.5 T and an average density of (1.6–2.7) $\times$ 10^{19} m^{-3} were investigated. A special regime with deeply introduced rail limiter was investigated in order to approximate core plasma conditions and to compare reflectometry and probe data. Turbulent density fluctuations were investigated in the scrape-off layer (SOL) of T-10 with seven pin Langmuir probes at a minimum poloidal distance of 3 mm. The density fluctuations in the core plasma were measured with a T-10 three wave heterodyne reflectometer [1], using the ordinary mode in the frequency range of 25.5–56 GHz. This reflectometer is capable of measuring the radial and poloidal correlation lengths simultaneously. The probe and reflectometry signals were recorded with two analog–digital converters (ADCs) at a sampling rate of 1 MHz during 0.5 s.

3. IDENTIFICATION OF DIFFERENT TURBULENCE TYPES

Poloidal correlation analyses of frequency fluctuations of the probing wave reflected from R = 0.12 m and R = 0.17 m are shown in Figs 1(a) and (b), respectively. The time averaged amplitude Fourier spectrum of the first signal, the cross-phase and the coherence of both signals are presented in the first, second and third traces of each figure, respectively. Low and high frequency maxima are clearly seen from the coherence spectra, showing the presence of low and high frequency types of coherent turbulence. These turbulences are superimposed on a broad frequency band pedestal with low coherence. It is also seen from Fig. 1(a) that the high frequency maximum may significantly shift in frequency while the broadband pedestal does not change.

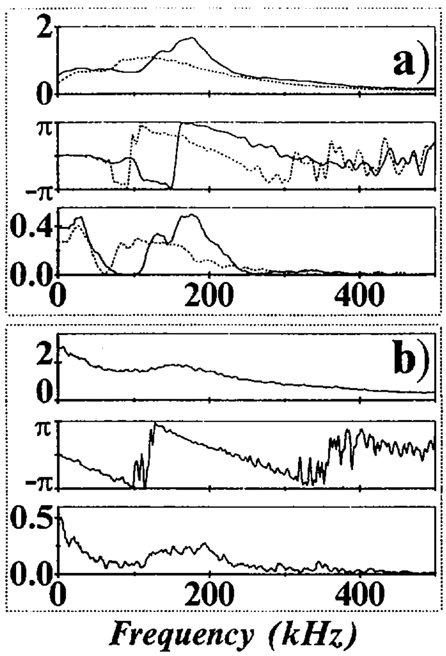

FIG. 1. Poloidal correlation measurements with reflectometry. Upper traces: Fourier amplitude spectrum; central traces: cross-phase of two signals; lower traces: coherence spectrum. a) Reflection from R = 0.12 m, solid line: after, dashed line: before neon puff; b) reflection from R = 0.17 m.

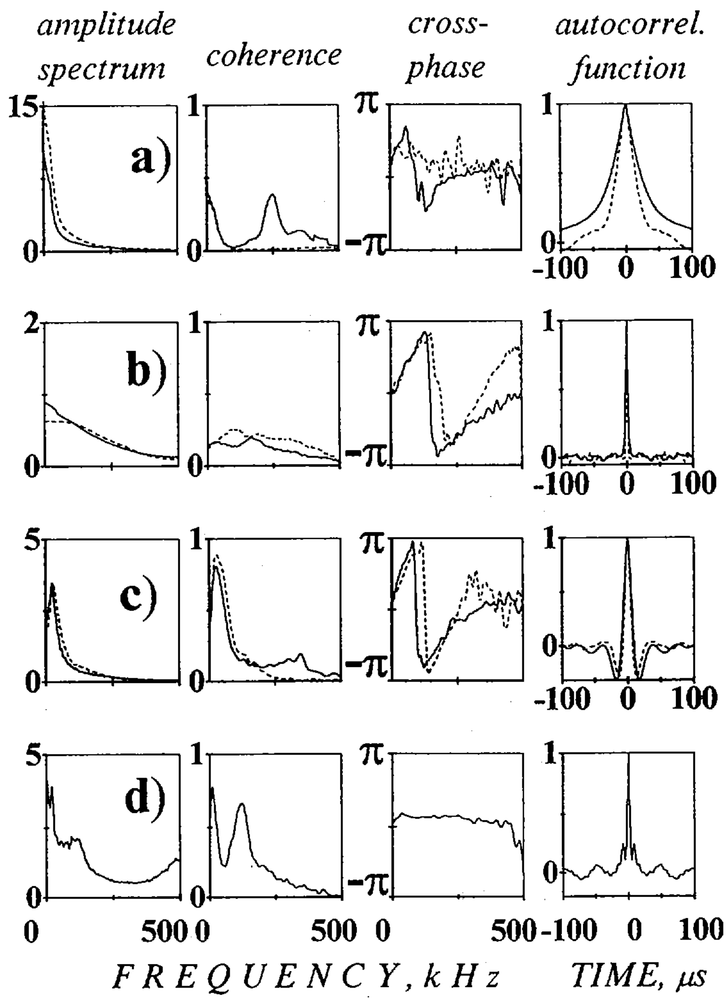

FIG. 2. Poloidal correlation measurements with multipin probe. Solid lines: experiment, dashed lines: computer simulations. Probe positions: (a) R = 0.305 m; (b) 0.235 m; (c) 0.255 m; (d) rail limiter probes.

This broad frequency band and the low coherent turbulence have been referred to as 'broadband' turbulence. Thus, three types of core turbulence were identified in the first experiments with correlation reflectometry [4]. Unfortunately, the interpretation of reflectometry results is difficult with respect to the radial localization and even the shape of the spectrum [8]. The experiments with multipin Langmuir probes have been performed to verify the reflectometry results and, in addition, to measure the potential fluctuations and particle turbulent fluxes.

Typical results of probe measurements are shown by the solid lines in Fig. 2. The ion saturation current of two probes spaced poloidally 0.6 cm apart was measured in

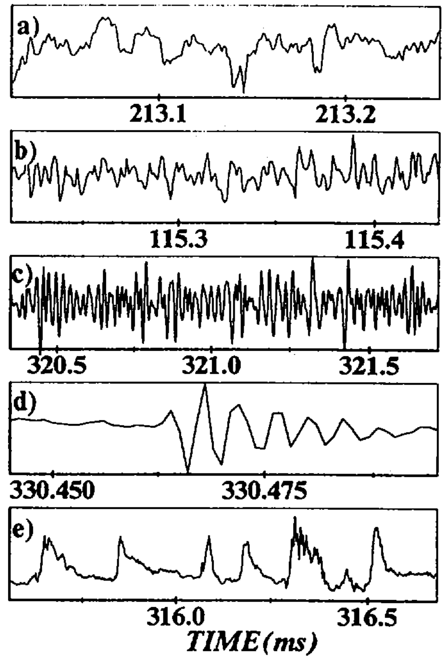

FIG. 3. Typical ion saturation current traces for different turbulence types: (a) low frequency stochastic turbulence; (b) broadband turbulence; (c) high frequency quasi-coherent turbulence; (d) edge quasi-coherent turbulence; (e) edge turbulence.

four radial positions. Figure 2(a) corresponds to the probe position at R = 0.305 m. We see that the peak of the Fourier spectrum is close to zero frequency. The autocorrelation time is 45 μs, and the poloidal dimension is about 0.05 m. The aperiodic relaxations are seen in the signal trace presented in Fig. 3(e), just like the 'events' observed on ASDEX [9]. This type of turbulence will be referred to as 'edge turbulence'. The second peak at 250 kHz is seen in the coherence spectrum. These fluctuations appear as multiperiod bursts of oscillations, shown in Fig. 3(d). They will be referred to as 'edge quasi-coherent' turbulence. The data shown in Fig. 2(b) were taken at a radius of 0.235 m. We see the increase of the high frequency tail in the Fourier spectrum and the low and flat coherence spectrum. The typical autocorrelation time is about 2 μs. These fluctuations look chaotic as is seen in Fig. 3(b). This wide frequency and low coherence type of turbulence is similar to the 'broadband' turbulence observed by reflectometry. The data of Fig. 2(c) taken at a radius of 0.255 m show a maximum at 30 kHz, which corresponds to the appearance of the 'quasi-coherent' bursts of oscillation. A typical trace of these fluctuations as shown in Fig. 3(c) reveals bursts with several periods at close frequencies. The wide Fourier spectral maximum results from averaging the bursts over the time. The position of the maximum shifts towards 120 kHz for the rail limiter probes (R = 0.22 m) as is seen in Fig. 2(d). In the same figure wee see the fourth type of turbulence, which corresponds to a zero frequency maximum in the coherence spectrum. The amplitude spectrum shows that these fluctuations include a 'quasi-coherent' component near 20 kHz. The trace in Fig. 3(a) shows that they also contain fast stochastic density jumps similar to the 'edge' relaxation. These fluctuations are typical for the hottest SOL part only and always occur in the core plasma. These two types will be referred to as 'LF quasi-coherent' and 'LF stochastic' turbulences. Thus, two specific types of edge turbulence and four types of core turbulence were observed with the probes in the SOL. This enables measurements of plasma density and potential fluctuations and of turbulence fluxes with a spatial resolution of 1 mm to be carried out.

4. NUMERICAL COMPUTER SIMULATIONS OF THE FLUCTUATIONS

The direct reconstruction of the spatial and temporal evolution of the fluctuation from the measurements at two fixed spatial positions is a difficult task. Therefore, a numerical model was developed [7] to simulate fluctuations. It was assumed that fluctuations could be described by stochastic local density increases. The perturbations have the shape of a Gaussian function with half-width Δ and move in the poloidal direction with velocity V. The fluctuations rise and decay exponentially with times τ_1 and τ_2. Aperiodic and oscillating spatial distributions are possible according to the expression:

$$n\,(X_p, X_1, t) = \exp\{-(X_p - X_1)^2/\Delta^2\}\{b + a\cos(2\pi\gamma(X_p - X_1)/\Delta\}$$

$$\times\{\exp - [(t - t_0)/\tau_2]^\alpha - \exp - [(t - t_0)/\tau_1]^\alpha\}$$

where $X_1 = X_0 + Vt$, X_p is the probe position, X_0 the initial position of the perturbation, X_1 the position of the perturbation at time t, γ the spatial period of the oscillation, and α the parameter that controls the time evolution. The parameters a and b determine the relative contributions of the aperiodic and oscillating parts. The local density enhancements are introduced, with a time period T, into the computational field, at random in space. The code generates the time realizations of the density evaluations at two probe positions with a step of 1 μs. Thus, the code output simulates the experimental data exactly.

A comparison of experimental and simulated turbulence characteristics for the cases of 'edge', 'broadband' and 'HF quasi-coherent' types of turbulence is shown by the dashed lines in Figs 2(a), (b) and (c), respectively. We see that in all three cases the computer model simulates experimental data satisfactorily. The results of the numerical model enable us to find the time and space structure of the turbulences; they will be presented below.

5. CHARACTERISTICS OF DIFFERENT TURBULENCE TYPES

Edge quasi-coherent turbulence is similar to the edge localized n = 0 mode in the Alfvén frequency range identified on TFTR [10]. Moreover, the maximum intensity and frequency (500 kHz) of this turbulence lies close to the rail limiter as is seen in Fig. 2(d). This agrees with the conclusions of Ref. [10].

Edge turbulence is characterized by relaxation bursts with spatial dimensions about 0.03–0.05 m and $k\rho_i = 0.03$, where k is the poloidal wavenumber and ρ_i is the ion gyroradius. It exists in the cold SOL regions and is poloidally highly asymmetric [5]. A possible physical mechanism responsible for it was discussed in Ref. [2], where a comparison with the resistive drift ballooning instability was presented. Unfortunately, this theory failed to explain the short rise-time. Moreover, the magnetic shear was not considered.

Broadband turbulence exists over the whole plasma column and has its maximum amplitude at the rail limiter [4]. It is characterized by a very broad amplitude and low and flat coherence spectra. The measured values of the poloidal and radial correlation lengths in the core [4] are about 0.005 m. The values of $k\rho_i$ for the cold and hot

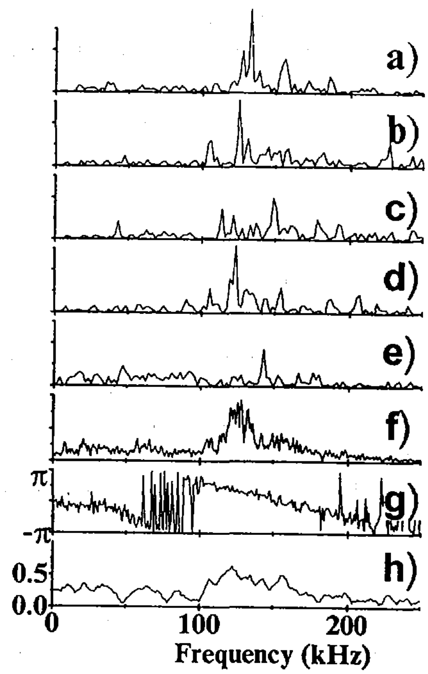

FIG. 4. Structure of high frequency quasi-coherent turbulence measured with reflectometry. (a) to (e) Fourier amplitude spectra of autocorrelation functions, calculated for 1 ms realization, sequentially in time; (f) Fourier amplitude spectrum of time averaged autocorrelation function; (h) coherence spectrum of two poloidally separated channels.

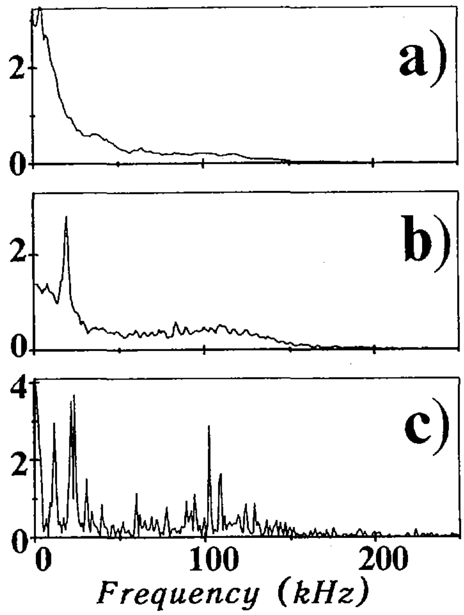

FIG. 5. Comparison of turbulence characteristics during density buildup and stationary discharge phase for rail limiter probes. Fourier amplitude spectrum of time averaged autocorrelation function during (a) buildup phase, (b) stationary phase, (c) Fourier amplitude spectra of autocorrelation functions taken for 1 ms realization.

parts of the SOL and for the core plasma are in the range of 0.5–1 [5]. This turbulence is poloidally highly asymmetric [5]. It rotates in the ion diamagnetic drift direction with respect to the plasma [5], thus indicating a possible ion origin. It was found that the relative potential fluctuations $(e\delta\varphi)/T_e$ are 1.7 times higher than the relative ion saturation current fluctuations $\delta I/I$ for edge and broadband turbulences. The broadband amplitude, typically, varies with the diffusive time and is possibly governed by the local plasma parameters. The ITG instability is one of the candidates for the broadband turbulence.

HF quasi-coherent turbulence has maximum amplitude in the core plasma [4]. The time evolution of the turbulence is analysed in Fig. 4. The traces (a) to (e) are the Fourier amplitude spectra of the autocorrelation functions of the reflectometer signals. The autocorrelation functions were calculated for time realizations of 1 ms, sequentially in time. Figure 4(f) shows the amplitude spectrum of the autocorrelation function averaged over the time. Figures 4(g) and (h) present averaged cross-phase and coherence. The presence of quasi-monochromatic oscillations is clearly seen for each 1 ms realization. The values of their frequencies vary in time from 110 to 160 kHz in a random way, resulting in the appearance of the maximum at 125 kHz in the spectra of averaged autocorrelation function and coherence. The poloidal velocity of the oscillations estimated from the slope of the cross-phase equals 2.7×10^3 m/s, which yields a wavelength of about 0.02 m and a poloidal number m $\approx$ 45. The measured radial correlation length is 0.03 m [4]. Thus, two physical mechanisms may be distinguished: the existence of a driving force over a frequency range of 110–160 kHz and the realization of this drive in a random excitation of high rational modes. The poloidal wavelength is sensitive to the impurity composition and decreases after Ne puffing (Fig. 1(a)). The poloidal velocity of this turbulence is close to the plasma rotation [3]. The Boltzmann relation $\delta I/I \approx e\delta\varphi/T_e$ holds for the HF quasi-coherent turbulence. The toroidal correlation measurements with the rail limiter probes show that the lines of constant phase are inclined by 4° with respect to the total magnetic field. They move along the field lines with a velocity of 6×10^4 m/s, which is about the ion sound speed; their longitudinal wavelength is 0.6 m, which is close to the ripple period. The radial correlation measurements reveal the phase shift of the fluctuations at two radial locations, which formally corresponds to a propagation towards the plasma centre with a velocity of 1.6×10^4 m/s. This is in agreement with a recent observation of electron temperature fluctuations in W7-AS [11]. The HF quasi-coherent turbulence amplitude in the plasma core may change at a time of 1 ms after strong edge cooling [4]. Thus, it may be involved in non-local transport processes.

LF quasi-coherent and LF stochastic turbulences. Figures 5(a) and (b) show the amplitude spectra of the time averaged autocorrelation functions of the ion saturation current of the rail limiter probes during and after gas puffing. We can see that, in the first case, the spectrum in the low frequency region is rather smooth while in the latter case the maximum near 20 kHz appears along with the HF quasi-coherent maximum near 120 kHz. The Fourier spectrum of the autocorrelation function, taken for a 1 ms time realization (Fig. 5(c)), shows the presence of quasi-coherent oscillations at low and high frequencies. Thus, we must conclude that the low frequency turbulence has two components: the first component is represented by the LF quasi-coherent fluctuations which appear simultaneously with the HF quasi-coherent turbulence and may have the same physical origin. These fluctuations resemble the net of filaments seen by visual plasma imaging [12–14]. The second component has a smooth spectrum peaking near zero frequency. A typical trace of this turbulence is shown in Fig. 3(a). The stochastic density jumps with a rise time of 2–5 μs is clearly seen. The rise time of the jumps is close to the period of 'edge quasi-coherent' oscillations, which equals 4 μs in the cold SOL (Fig. 2(a)) and 2 μs at the rail limiter (Fig. 2(d)). This may indicate a connection of the two phenomena. The Boltzmann relation $\delta I/I \approx e\delta\varphi/T_e$ holds for both types of turbulence. A typical feature of these fluctuations is the absence of rotation in the central part of the discharge, which is clearly seen from the constancy of the cross-phase in Fig. 1(a), for reflection from R = 0.12 m. At the same time, for R = 0.17 m, the LF fluctuations begin to rotate with the same velocity as the HF quasi-coherent turbulence (Fig. 1(b)). The estimated poloidal wavelength is about 0.18 m for 30 kHz at R = 0.17 m; such estimates are not possible for the central case. For the LF quasi-coherent oscillations near 20 kHz in the SOL, the poloidal wavelength is 0.065 m. Toroidal correlation measurements show that the constant phase lines of both types of turbulence are inclined by 8° with respect to the total magnetic field lines. The velocities along the field lines are 6×10^3 m/s for the LF stochastic and 1×10^4 m/s for LF quasi-coherent turbulences, which gives a longitudinal wavelength of 0.5 m for the last type. This value is equal to HF quasi-coherent fluctuation wavelength and is close to the ripple period (0.59 m). The wavelengths of about 1 m, observed in TFTR [14], are also close to the ripple period (0.77 m). Both velocities are directed along the main plasma current. The directions and the values of the velocities are close to the parameters of the toroidal plasma flow at the edge [15].

6. DIRECT CALCULATION OF PLASMA TURBULENT FLUXES

The radial particle turbulent flux was calculated as $G(r) = \langle \delta n \delta E \rangle / B$ from the ion saturation current δI and the poloidal electric field fluctuations δE, which were measured simultaneously. The angular brackets designate averaging over the time. The value of δE was measured by the difference in the floating potentials of two probes 0.6 cm apart, temperature fluctuations being neglected. The resulting particle flux was always outwards, at all poloidal angles. A high poloidal asymmetry of the flux was observed [5]. The values of the turbulent fluxes agree with the experimental values. The observed high radial flux asymmetry proves the previous results, where ballooning

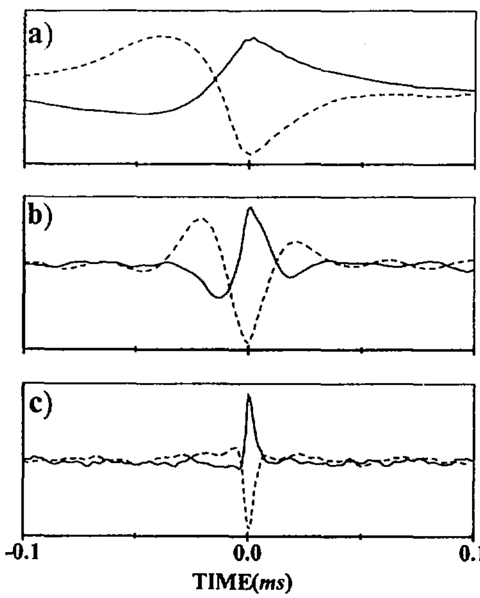

FIG. 6. Cross-flux functions for three types of turbulence. Solid lines: toroidal magnetic field counterclockwise; dashed lines: clockwise. (a) Edge turbulence; (b) high frequency quasi-coherent turbulence; (c) broadband turbulence.

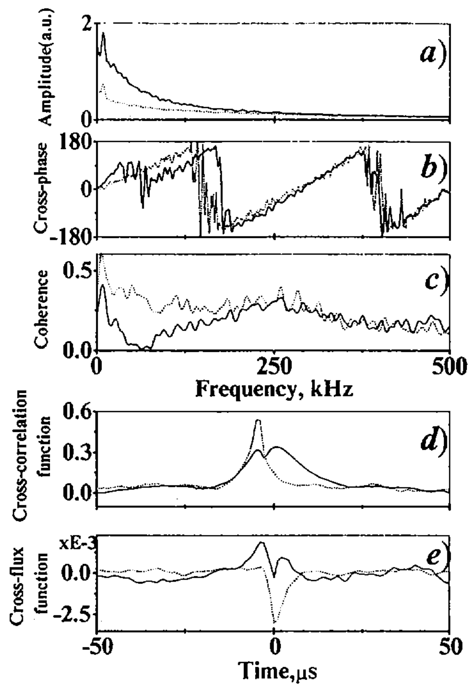

FIG. 7. Influence of MHD activity on turbulence characteristics measured with probes. Solid lines: high, dashed lines: low MHD level.

plasma flows along the magnetic field lines were found [15]. The cross-flux functions between the density and the electric field fluctuations are shown in Fig. 6 for three types of turbulence. They were calculated as the product of cross-correlation functions and the root mean squares values of the amplitudes of both signals. Thus, the value of these functions at zero argument gives the value of the turbulent particle flux. Solid and dashed lines correspond to the two opposite directions of the toroidal magnetic field. Figure 6(a) shows these functions for the edge, Fig. 6(b) for HF quasicoherent and Fig. 6(c) for broadband turbulence. We see that for all three cases the fluctuations are either in phase or out of phase, which always corresponds to the maximum outward particle flux. The correlation of density and electric field for the low frequency turbulence is presented in Fig. 7(e). A comparison of the cross-flux functions in the density buildup phase and in the stationary case is shown. We see that the high amplitude of the low frequency fluctuation in the first case makes the total flux decrease to zero. So it is possible that LF stochastic turbulence produces an inward pinch flux.

7. DEPENDENCE OF TURBULENCE ON DISCHARGE CONDITIONS

The *working gas influx rate* is the main parameter that strongly influences the turbulence. Figure 5 shows this dependence for the SOL case. It is seen that the LF stochastic turbulence is dominant during the density buildup phase (Fig. 5(a)). It decreases after the gas has been switched off (Fig. 5(b)), and both low and high frequency quasi-coherent turbulences appear. The same dependence is also valid for the plasma core as is seen in Fig. 8. The amplitude spectra and the autocorrelation functions of the reflected wave phase are presented during the density buildup phase (Fig. 8(a)) and after gas switch-off (Fig. 8(b)). The decrease of the low frequencies and increase of the quasi-coherent fluctuations are obvious after gas switch-off. The amplitude and the number of oscillations in the bursts decrease during the working gas puff as is also seen in Fig. 8. The decrease of the oscillation number in the bursts proves the increase of dissipation. The broadband turbulence is also sensitive to the gas puff rate. The experiments in SOL and core show the increase of poloidal correlation length and the decrease of the spatial dimensions of broadband after gas switch-off.

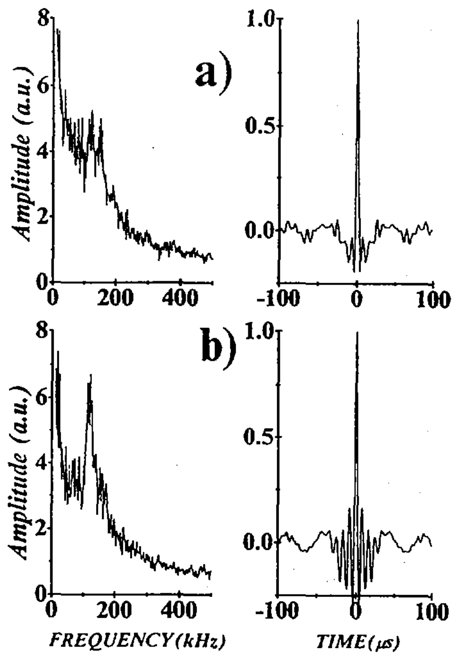

FIG. 8. Influence of working gas influx on turbulence measured with reflectometry. Left hand trace: amplitude Fourier spectrum, right hand trace: autocorrelation function. (a) During gas puff: (b) after gas puff switch-off.

Impurity puffing also affects the turbulence in two ways. The first is the frequency shift of the HF quasi-coherent turbulence, which is clearly seen in Fig. 1(a) after the neon puff (dashed line). In most cases, this frequency increase has to be explained by the decrease of the poloidal wavelength which implies that the impurity plasma composition determines the wavelength of the HF quasi-coherent turbulence. Secondly, the impurities reduce the plasma–wall interaction by an increase of radiation. Thus, this influence is similar to a reduction of working gas influx.

Fast periphery cooling may cause a change in the core plasma, with a delay that is much less than in the diffusive case [16]. The disappearance of all quasi-coherent turbulence in the core with a delay of 1–2 ms was observed in T-10 after strong cooling by a neon puff [4]. This reduced level was sustained for several milliseconds only. The broadband turbulence amplitude decreases in 5–10 ms. Such a phenomenon was never observed for reduced neon puffing rate. Thus, quasi-coherent turbulence may be involved in non-local transport.

MHD activity may also influence the plasma turbulence as is shown in Fig. 7 for the SOL turbulence. It is seen that during the MHD free stage (dashed lines) broad-

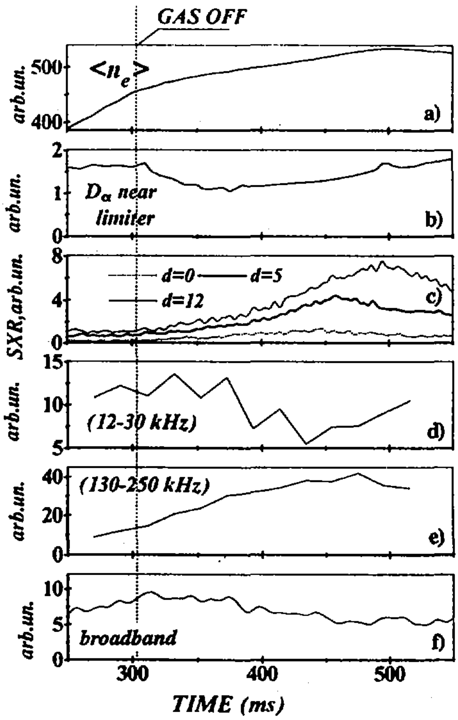

FIG. 9. Characteristics of discharge with impurity accumulation after gas switch-off. (a) Averaged density; (b) D_α intensity; (c) traces of soft X ray intensity of central chord and 0.05 m and 0.12 m away from it. Amplitudes of quasi-coherent turbulence: (d) for 12–30 kHz; (e) for 130–250 kHz; (f) broadband turbulence intensity.

band turbulence is dominant, and all plasma fluctuations rotate with the same velocity. The increase in MHD leads to the appearance of LF stochastic turbulence, which clearly rotates with different velocity and reduces the particle flux to zero. We may conclude that additional magnetic perturbations facilitate the appearance of stochastic density jumps.

Additional ECR heating affects turbulence virtually in the same way as the working gas puff. The case is that ECRH decreases the particle confinement and increases recycling substantially. Thus the main effect is the increase of LF core and the decrease of HF quasi-coherent turbulence.

8. CORRELATION OF TURBULENCE WITH PLASMA TRANSPORT

It is possible to measure directly the correlation of the particle fluxes with the turbulence and discharge parameters in a SOL as is done in Section 6. In most cases, the flux due to broadband turbulence is dominant. Unfortunately, however, this flux is

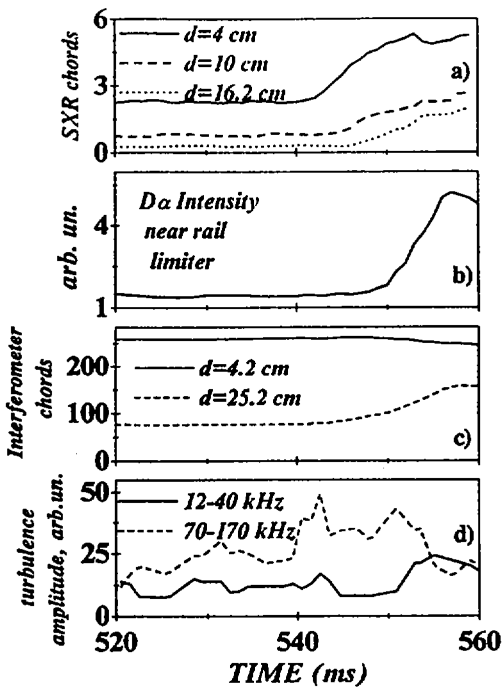

FIG. 10. Characteristics of discharge with central ECR heating. (a) SXR intensity for chords 0.04, 0.1 and 0.16 m away from the centre; (b) D_α intensity; (c) averaged density for chords 0.042 and 0.252 m away from the centre; (d) intensity of quasi-coherent turbulence. Solid line: 12–40 kHz; dashed line: 70–170 kHz.

measured with large errors when the correlation length becomes less than the probe distance (0.6 cm), which is practically always the case. There are a number of types of discharge in T-10 with distinctly different particle transport. Firstly, these discharges are called S and B regimes [17, 18]. They are similar to the ASDEX SOC and IOC regimes [19]. The transition from the S regime with low particle confinement to the B regime with improved particle confinement may be initiated either by the neon puff [17] or by switching off the working gas influx [18]. The backtransition may be caused either by switching on the working gas valve or by additional ECR heating. It was found that practically all cases of low confinement are associated with a high level of LF stochastic and broadband turbulences and a low level of LF and HF quasi-coherent turbulences. In contrast, high confinement regimes are associated with a low level of LF stochastic, and broadband turbulences and high level of quasi-coherent turbulences. The behaviour of the turbulence during S to B transition after the gas switch-off is shown in Fig. 9. The moment of gas switch-off is shown by the vertical dashed line. Observation of the argon impurity evolution shows strong accumulation in the centre, which begins 70 ms after the gas switch-off. The turbulence measured with reflectometry from the half-radius clearly shows the decrease of low frequency and broadband turbulences just at the time when the accumulation starts, while the HF quasi-coherent turbulence increases. The traces for the central ECR heating, which brings the discharge to an L mode with decreased confinement, are shown in Fig. 10. We see that the low frequency turbulence in the plasma core increases with a delay of 8 ms after the start of ECRH, while the high frequency decreases. This occurs simultaneously with the D_α line increase and the decay of the average density.

9. CONCLUSIONS

The six types of turbulence were observed in T-10 SOL by the multipin Langmuir probe, including four types that were identified previously by correlation reflectometry in the plasma core. This verifies the results of reflectometry and allows investigation of the structure of turbulence and particle fluxes. The simultaneous use of correlation reflectometry and Langmuir probes enables measurement of the radial, poloidal and toroidal correlation characteristics of the different turbulence types. The spatial and temporal fluctuation properties were successfully simulated by a numerical computer model. The fluctuation level and the turbulent radial particle flux are poloidally highly asymmetric. The turbulence parameters depend strongly on working gas influx rate, impurity puffing, MHD level and ECR heating. It was observed that a high level of high frequency quasi-coherent turbulence corresponds to high confinement regimes while a high level of low frequency turbulence is typical for low confinement regimes. The similarity of tokamak and stellarator turbulences may help us to understand the underlying physics.

ACKNOWLEDGEMENTS

The authors wish to acknowledge the support by the T-10 diagnostic and operational staffs. This work was supported by the Russian Foundation for Fundamental Research, Grant Nos 94-02-06521-a and 96-02-18807.

REFERENCES

[1] VERSHKOV, V.A., et al., in Controlled Fusion and Plasma Physics (Proc. 21st Eur. Conf. Montpellier, 1994), Vol. 18B, Part III, European Physical Society, Geneva (1994) 1192.
[2] VERSHKOV, V.A., et al., ibid., Part II, p. 886.
[3] VERSHKOV, V.A., et al., in Plasma Physics and Controlled Nuclear Fusion Research 1994 (Proc. 15th Int. Conf. Seville, 1994), Vol. 2, IAEA, Vienna (1995) 65.
[4] VERSHKOV, V.A., et al., in Controlled Fusion and Plasma Physics (Proc. 22nd Eur. Conf. Bournemouth, 1995), Vol. 19C, Part IV, European Physical Society, Geneva (1994) 5.
[5] VERSHKOV, V.A., et al., in Plasma–Surface Interactions in Controlled Fusion Devices (Proc. 12th Int. Conf. Saint Raphael, France, 1996).
[6] VERSHKOV, V.A., et al., in Controlled Fusion and Plasma Physics (Proc. 23rd Eur. Conf. Kiev, 1996), Vol. 20C, European Physical Society, Geneva (1996).
[7] SOLDATOV, S.V., et al., ibid.
[8] NAZIKIAN, R., et al., Rev. Sci. Instrum. **66** (1995) 392.
[9] ENDLER, M., et al., in Controlled Fusion and Plasma Physics (Proc. 20th Eur. Conf. Lisbon, 1993), Vol. 17C, Part II, European Physical Society, Geneva (1993) 583.
[10] CHANG, Z., et al., Nucl. Fusion **35** (1995) 1469.
[11] HARTFUSS, H.J., et al., invited talk at Controlled Fusion and Plasma Physics, 23rd Eur. Conf. Kiev, 1996, to be published in Plasma Phys. Control. Fusion.
[12] VINOGRADOVA, N.D., et al., in Plasma Physics and Controlled Nuclear Fusion Research 1965 (Proc. 2nd Int. Conf. Culham, 1965), Vol. 2, IAEA, Vienna (1966) 617.
[13] GOODALL, D.H.J., J. Nucl. Mater. **111&112** (1982) 11.
[14] ZWEBEN, S.J., et al., Phys. Fluids B **1** (1989) 2058.
[15] VERSHKOV, V.A., et al., J. Nucl. Mater. **162–164** (1989) 195.
[16] GENTLE, K., et al., in Controlled Fusion and Plasma Physics (Proc. 22nd Eur. Conf. Bournemouth, 1995), Vol. 19C, Part I, European Physical Society, Geneva (1995) 5.
[17] BAGDASAROV, A.A., et al., in Controlled Fusion and Plasma Physics (Proc. 12th Eur. Conf. Budapest, 1985), Vol. 9F, Part I, European Physical Society, Geneva (1985) 207.
[18] ALIKAEV, V.V., et al., Plasma Phys. Control. Fusion **30** (1988) 381.
[19] FUSSMANN, G., et al., in Plasma Physics and Controlled Nuclear Fusion Research 1988 (Proc. 12th Int. Conf. Nice, 1988), Vol. 1, IAEA, Vienna (1989) 145.

DISCUSSION

C. HIDALGO: Is there any correlation between the 'events' observed in the ion saturation current in the SOL region and the $\mathbf{E} \times \mathbf{B}$ turbulent transport?

V.A. VERSHKOV: The 'edge' turbulence, which I called 'events', is responsible for the plasma transport in the cold regions of the SOL.

LOCAL ANALYSIS OF TRANSPORT AND TURBULENCE IN TORE SUPRA

C. LAVIRON, F. CLAIRET, L. COLAS, P. DEVYNCK, X. GARBET,
F. GERVAIS[1], D. GRÉSILLON[1], L. GUIZIOU, P. HENNEQUIN[1],
G.T. HOANG, P. MOREAU, M. PAUME, A. QUÉMÉNEUR[1],
A. TRUC[1], X.L. ZOU
Association Euratom–CEA,
Centre d'études de Cadarache,
Saint-Paul-lez-Durance,
France

Abstract

LOCAL ANALYSIS OF TRANSPORT AND TURBULENCE IN TORE SUPRA.

Specific investigations have been carried out in Tore Supra — in ohmic and additionally heated plasmas — to locally analyse electrostatic and magnetic turbulence as well as transport, and to compare their variations with those of local parameters. On each side of the electric shear layer, the frequency of the density fluctuations and the wavenumber spectra are different in ohmic as well as in additional heating regimes, showing that turbulence has not the same characteristics in the gradient and the edge regions. For the first time, radial profiles of magnetic fluctuations have been obtained, showing that the level of fluctuations increases with the minor radius; this behaviour is well correlated with the radial shape of the electron heat diffusivity. In the L mode, there is also a good correlation of fluctuations and heat diffusivity with the local temperature gradient in the region $0.4 < r/a < 0.8$, with the evidence of a critical gradient threshold for magnetic fluctuations. In addition, improved confinement regimes, obtained by fast wave electron heating, show the stabilizing effect of increased magnetic shear on the density fluctuations, thus corroborating theoretical models. This shear effect can be used to explain the confinement time saturation at high density in the ohmic regime. A decrease of the density fluctuations in the vicinity of the electric shear layer is also observed. Finally, from dimensionally similar experiments and local analysis, the scaling law for the electron heat diffusivity, χ_e, is found to be gyroBohm-like, in agreement with theoretical expectations and other previous results.

1. INTRODUCTION

In thermonuclear plasmas, an important issue is the understanding of turbulence behaviour, which is well known to be the cause of anomalous transport in tokamaks. Many studies have been devoted to the different types of turbulence, according to different regimes of plasma operation, and great progress has been made up to now. An important point is, however, the fact that turbulence, as well as transport, is not similar over all the different regions of the plasma; we propose here to investigate this point.

[1] PMI-CNRS, Ecole polytechnique, Palaiseau, France.

In Tore Supra, turbulence is measured by three complementary diagnostics: density fluctuations by CO_2 laser scattering (named ALTAIR) [1] and reflectometry, and magnetic fluctuations by cross-polarization scattering (CPS) [2]. This powerful and unique combination allows not only the level of fluctuations but also their radial profile and their frequency and wavenumber spectra to be analysed. Specific investigations have been carried out, in ohmic and additionally heated plasmas, to locally analyse density and magnetic fluctuations, as well as transport, and to compare their variations with those of local parameters.

Central and edge density fluctuations are compared in Section 2, while Section 3 discusses the radial profile of magnetic fluctuations. Section 4 is devoted to the evolution of fluctuations and transport coefficients during RF application, and a comparison is made with the electron temperature gradient. The effect of magnetic shear on turbulence and transport is discussed in Section 5. Section 6 investigates the scaling of local transport and turbulence with normalized Larmor radius, ρ^*, and general conclusions are drawn.

2. CENTRAL AND EDGE DENSITY FLUCTUATIONS IN OHMIC PLASMAS

On Tore Supra and almost all large devices, it has been shown that the density fluctuation level is relatively low and constant in the plasma core but increases sharply near the edge [3, 4].

Although the scattering angle is very small, it has been shown [3] that ALTAIR has some spatial resolution within the vertical probing chord. When fluctuations are measured near the edge, the frequency spectra usually present two peaks (Fig. 1). This

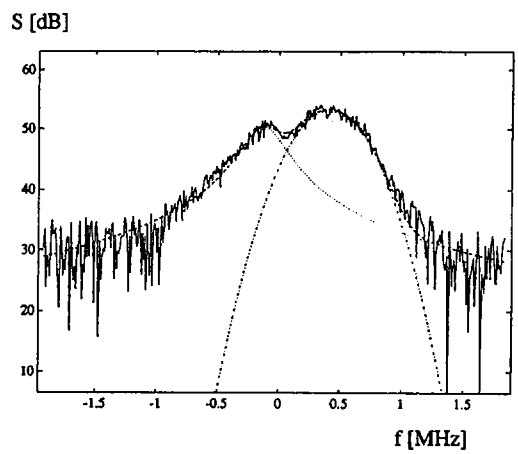

FIG. 1. Frequency spectrum in ohmic mode and best fit by Gaussian and Lorentzian functions.

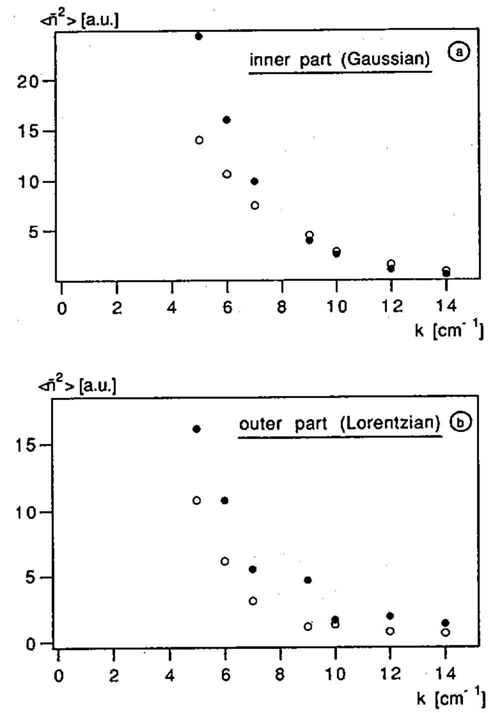

FIG. 2. k spectra in ohmic (open circles) and 2.3 MW additional heating (closed circles) regimes, on the two sides of the electric shear layer: (a) inner plasma for r/a < ρ_s; (b) outer plasma for r/a > ρ_s.

has been attributed to a Doppler shift effect, shifting the frequency spectra in opposite directions on the two sides of a radial electric shear layer. By separating these two components, an additional resolution is obtained with a spatial separation between both sides of the shear layer. In the ohmic mode, the electric shear layer is well inside the confined plasma, at a position of about $\rho_s \approx 0.92$ [5]. Moreover, the neat separation proves that the electric layer is very sharp (< ~1 cm).

An important difference between the outer and inner plasmas comes from the shape of these frequency spectra. Towards positive frequencies, corresponding to the electronic diamagnetic drift direction, and spatially to the inner part of the plasma (or to the electric shear layer, respectively), the spectrum is Gaussian. This is attributed to a turbulence correlation length that is greater than the probed wavelength, i.e. a large scale motion of the turbulence [6]. Conversely, towards negative frequencies, which correspond to the outer part and the scrape-off layer, the spectrum is Lorentzian, signature of a smaller correlation length and a small scale diffusive motion. In the Lorentzian case, a diffusion coefficient can be directly deduced from the width of the frequency spectra, in fair agreement with local transport analysis [6].

The k spectra have been analysed on the two sides of the shear layer, from 5 to 14 cm^{-1}, in ohmic and L mode regimes (Fig. 2). The variation of the fluctuation level induced by additional heating is not the same in the gradient and edge regions of the plasma. In the inner part (Fig. 2(a)), the increase of fluctuations is mainly concentrated at the lower values ($k \leq 7$ cm^{-1}), while in the outer part there is an increase for all k values probed (Fig. 2(b)). Moreover, their shape is not exactly the same for the two components: in the ohmic regime, there is a k^{-3} decay for the inner part, and a faster decay, of the order of k^{-4}, for the outer part. The relative amplitudes are difficult to compare between the two sides of the electric shear layer because each spectrum corresponds to a different sampling volume within which the fluctuation level is not the same: the inner part integrates fluctuations from $r/a \sim 0.5$ to ρ_s, while the outer part corresponds to a smaller volume (from ρ_s to the scrape-off layer), but with a higher relative fluctuation level ñ/n.

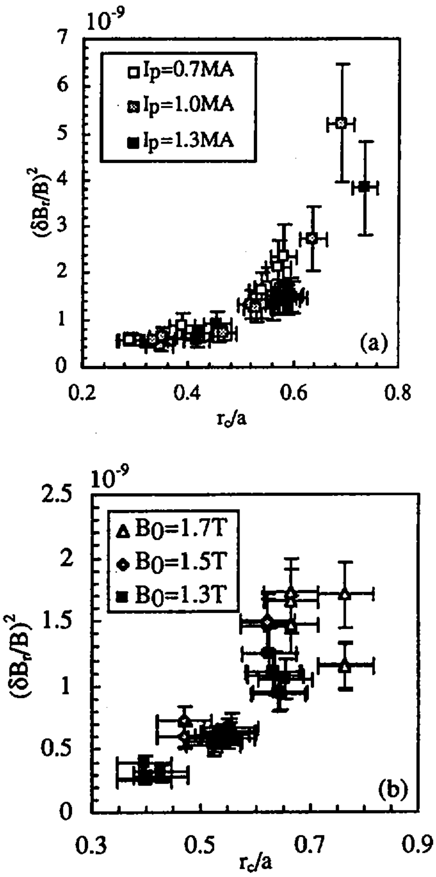

FIG. 3. Radial profile of magnetic turbulence obtained from CPS: (a) O → X (B_0 = 3.7 T), and (b) X → O (q_a = 3.5) scenario.

3. RADIAL PROFILE OF MAGNETIC FLUCTUATIONS

The original CPS diagnostic allows the internal magnetic fluctuations ($k_r \sim 12\ cm^{-1}$) with a spatial localization near the cut-off layer of the probing beam [2] to be measured. Radial profile analysis has been performed, using two techniques to scan the cut-off position between r/a = 0.3 and 0.75 [7]: either with a plasma density scan, or by changing the magnetic field. For the first case, using the O $\rightarrow$ X mode conversion scenario with $B_0 = 3.7$ T, a set of ohmic shots was carried out with three current plateaux ($I_p = 0.7$, 1.0 and 1.3 MA) at fixed volume average density $\langle n_e \rangle$. Shot by shot, $\langle n_e \rangle$ was scanned from 2.2×10^{19} to $5.2 \times 10^{19}\ m^{-3}$. Thus the O mode cut-off layer location (determined by a local density of $n_e = 4.47 \times 10^{19}\ m^{-3}$) was shifted from r/a = 0.3 to r/a = 0.75. In this density domain, the energy confinement time is constant, i.e. we are in the saturated ohmic confinement (SOC) regime.

Within instrumental error bars, the measured turbulence levels show no clear dependence on I_p and increase strongly with $\langle n_e \rangle$. This behaviour can be attributed either to a radial variation of $(\delta B/B)^2$ for different locations of the cut-off, or to a parametric dependence on $\langle n_e \rangle$. In the first case, a fluctuation radial profile in the gradient region can be derived from cut-off positions. Figure 3(a) shows that then $(\delta B/B)^2$ is a growing function of r/a, with a ninefold increase between r/a = 0.3 and 0.7.

To discriminate between radial and parametric dependences, experiments were conducted at low $\langle n_e \rangle$ and B_0 with the X $\rightarrow$ O CPS scenario. The incident X mode cut-off layer was moved by sweeping either B_0 and $\langle n_e \rangle$. The results are shown in Fig. 3(b). Note that, whatever B_0, the observed radial variations have similar features, consistent with those reported in Fig. 3(a). Therefore, these results cannot be interpreted in terms of a parametric dependence on B_0 or $\langle n_e \rangle$ and lead to attributing most of the observed $(\delta B/B)^2$ to the fluctuation radial profile. This profile, which increases sharply towards the edge, is consistent with the electron heat diffusivity profile χ_e.

4. HEATING EXPERIMENTS

The mechanisms driving the turbulence, such as the influence of the temperature gradient ∇T_e, have been investigated through additional heating experiments (lower hybrid and ion cyclotron resonance heating). The additional power has been varied up to 3.5 MW, inducing a temperature increase while all other plasma parameters remained unchanged. Figure 4 shows magnetic and density fluctuations compared to the local ∇T_e. For the CO_2 scattering measurements, the comparison is made at r/a = 0.7, corresponding to the maximum of the instrumental function. In the L mode, it can be observed that density and magnetic fluctuations are strongly correlated with ∇T_e in the region of $0.4 < r/a < 0.8$, with an increase of 60% for density fluctuations and a factor of four for magnetic fluctuations.

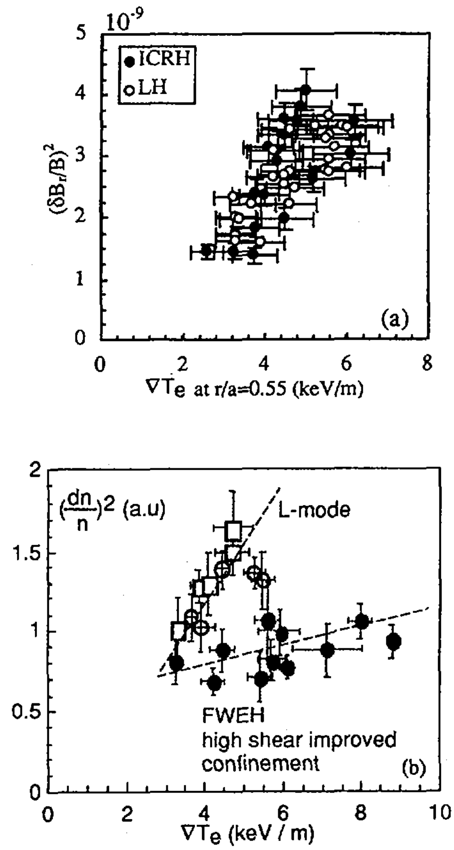

FIG. 4. (a) Magnetic fluctuations and (b) increase of density fluctuations relative to the ohmic level (squares: reflectometry; circles: CO_2 scattering) versus electron temperature gradient.

In addition, significant improvement of the confinement has been observed during fast wave electron heating (FWEH) experiments with a strong modification of the current density profile due to the high bootstrap current fraction [8]. Density fluctuations are strongly reduced (Fig. 4(b), closed symbols), as well as χ_e, in correlation with an increase of the magnetic shear in the gradient region. Therefore, the increase of ∇T_e inducing a development of the turbulence is here compensated for a stabilizing effect of the magnetic shear.

During additional ICRH power, the radial profile of the evolution of the density fluctuations obtained from reflectometry shows an increase of the fluctuations everywhere, except around r/a = 0.9 (Fig. 5). This local stabilization of the turbulence can be attributed to the presence of the electric shear layer (see Section 2), which locally prevents the development of additional fluctuations.

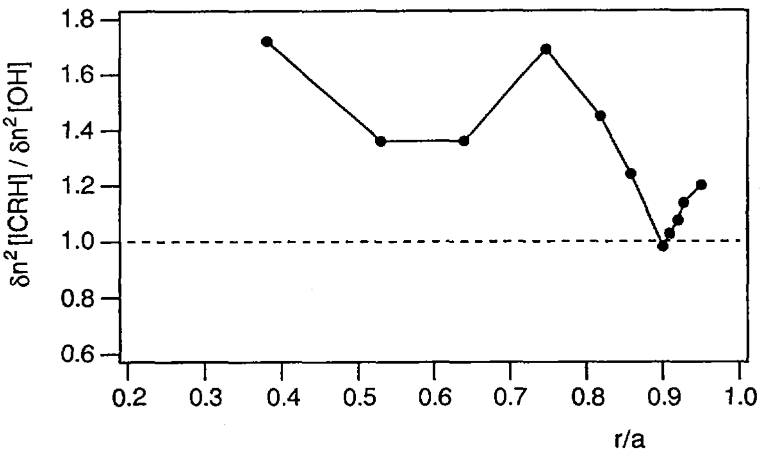

FIG. 5. Radial profile of density fluctuation increase from ohmic heating to ICRH (P_{add} = 2.3 MW), measured by reflectometry.

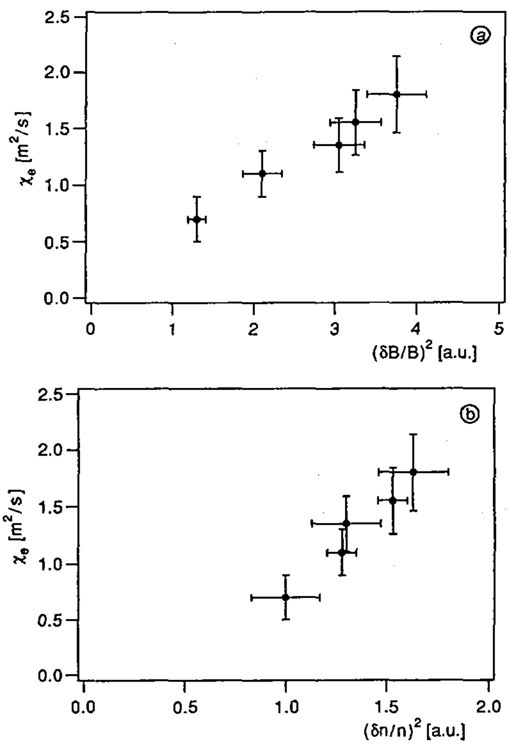

FIG. 6. Electron diffusivity, χ_e, versus (a) magnetic and (b) density normalized fluctuation levels at $\rho = 0.5$.

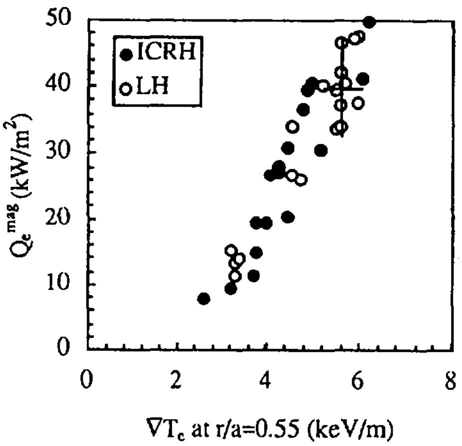

FIG. 7. Quasi-linear estimate of magnetic fluctuation induced heat fluxes, $Q_e = n_e \chi_e^{mag} \nabla T_e$, versus ∇T_e at the cut-off layer [7].

Figure 6 shows that the local electron heat diffusivity χ_e at $\rho = 0.5$ scales also linearly with both fluctuations, $\tilde{n}$ (from reflectometry) and $\tilde{B}$ (from CPS). While this result provides experimental support to the idea that turbulence is responsible for the increase in transport, it does not rule out any of the two components (magnetic or electric) of the fluctuations. As all plasma parameters except T_e were unchanged throughout the additional heating phase, the changes monitored on the fluctuations and on the electron heat diffusivity can only be attributed to ∇T_e changes (Fig. 4). This is also an indication that the global confinement properties of the plasma are strongly affected by the transport occurring in the gradient region, i.e. by the fluctuations in the same region.

From the magnetic fluctuation level, the heat diffusivity can be determined through the non-collisional formula $\chi_e^{mag} = \pi q R v_{th} (\delta B/B)^2$ [9]. The deduced heat flux is represented in Fig. 7 as a function of ∇T_e, proving the existence of a critical gradient threshold ∇T_c, as was previously seen on heat fluxes obtained from profile analyses [10]. This critical gradient is of some importance in explaining the resilience of the profiles as well as the difference found for χ_e calculated from heat pulse propagation experiments. A diffusivity behaving as $\nabla T_e - \nabla T_c$ is close to the expression proposed by Rebut–Lallia–Watkins [11]. However, the scaling of the actual critical gradient threshold does not agree [10] with the RLW prediction.

5. CORRELATION BETWEEN MAGNETIC SHEAR, TURBULENCE AND TRANSPORT

It is well known that, in ohmic plasmas, the confinement time increases with the density before saturating at a specific density. This has been shown to be correlated

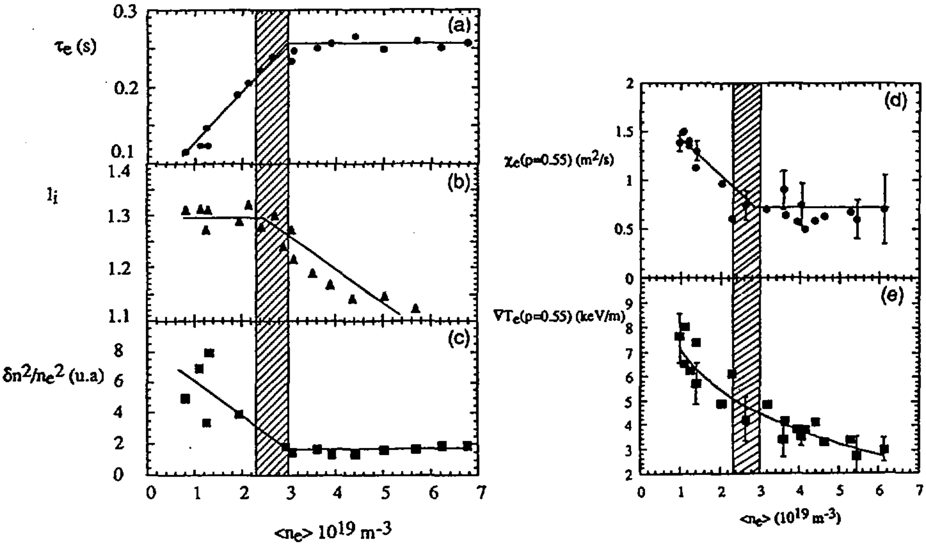

FIG. 8. (a) Confinement time; (b) internal inductance; (c) density fluctuations (at k_{obs} = 6 cm^{-1}); (d) electron heat diffusivity; (e) temperature gradient, as functions of density from a set of stationary helium discharges: I_p = 1.6 MA, B_T = 3.9 T and $q_\psi(a)$ = 3.5.

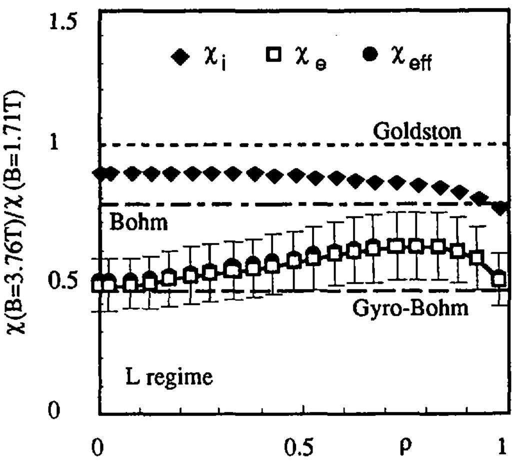

FIG. 9. Heat diffusivity ratio for the similarity experiments in the L mode.

with density fluctuations and transport coefficients (decrease, then saturation) [5]. The origin of this saturation is still not well understood; several explanations have been proposed, such as the development of an ionic turbulence at high density [12, 13], or the saturation of the electron confinement [5]. As was seen in the previous section, current profile and magnetic shear may be serious candidates. Figure 8 shows that when the confinement time saturates, above a critical density of the order of (2.5–3) $\times$ 10^{19} m^{-3}, the level of fluctuations and the heat diffusivity stop decreasing while the temperature gradient continues to decrease. In the linear ohmic confinement (LOC) regime, the internal inductance is constant, with a value of the order of 1.3, and the temperature gradient decreases with n_e, inducing lower fluctuations and a better confinement. For higher densities, the SOC regime is correlated with a decrease of the internal inductance, corresponding to a decrease of the current profile peaking and, as was carefully verified, of the magnetic shear. Although ∇T_e continues to decrease with n_e, the decrease in shear yields an inverse effect on the fluctuations. Therefore, the saturation of the ohmic confinement time at moderate density could be due to the modification of the current density profile.

6. LOCAL ANALYSIS OF SIMILARITY EXPERIMENTS

In Tore Supra, Goldston scaling does not work in the L mode, probably because heating is applied mainly on the electrons. For ohmic and L mode plasmas, the scaling law which fits the data can be expressed as:

$$\tau_E = 0.0199\, R^{2.00}\, I_p^{0.98}\, B_T^{0.2}\, \bar{n}^{\,0.43}\, P^{-0.75}$$

where τ_E, R (major radius), I_p (plasma current), B (toroidal magnetic field), $\bar{n}$ (line averaged density) and P (total injected power) are respectively expressed in units of s, m, MA, T, 10^{19} m^{-3} and MW. This density dependent scaling corresponds to a gyroBohm scaling, i.e. the heat diffusivity scales as $\chi \equiv (T/eB)\, \rho_*^{\alpha}\, f(\beta,\nu_*)$, with α of the order of 1, where ρ^* is the normalized Larmor radius, T is the temperature, $\beta \equiv nT/B^2$ is the plasma beta, and $\nu \equiv na/T^2$ is the collisionality.

In order to investigate the mechanisms driving this scaling, similarity experiments have been made where all non-dimensional parameters governing the plasma are kept constant, except for ρ^*. For two different magnetic fields (B = 3.76 and 1.71 T), the other engineering parameters are chosen so as to maintain q, β and ν^* constant, while ρ^* varies from 2.24 $\times$ 10^{-4} to 7.68 $\times$ 10^{-5}. A local transport analysis has been performed with the LOCO code [14]. The heat diffusivity ratio between the two series of experiments is computed and shows a rather gyroBohm type electron transport (Fig. 9). The effective transport, which takes into account ions and electrons, follows the same trend. These results confirm the global analysis.

7. CONCLUSIONS

In a large tokamak such as Tore Supra, the experimental observations made by several diagnostics seem to indicate that the mechanisms driving the turbulence are different in the gradient and the edge regions. In the gradient region, the turbulence is strongly correlated with the energy confinement and reacts to electron temperature changes, with additional shear effects (electric and magnetic) stabilizing the turbulence. In L regimes, the heat diffusivity is rather gyroBohm. In the edge region, the turbulence is mainly sensitive to other parameters, probably specific to the edge.

REFERENCES

[1] TRUC, A., et al., Rev. Sci. Instrum. **63** (1992) 3716.
[2] ZOU, X.L., et al., Phys. Rev. Lett. **75** (1995) 1090.
[3] DEVYNCK, P., et al., Plasma Phys. Control. Fusion **35** (1993) 63.
[4] FONCK, R.J., et al., Plasma Phys. Control. Fusion **34** (1992) 1993.
[5] GARBET, X., et al., Nucl. Fusion **32** (1992) 2147.
[6] HENNEQUIN, P., et al., in Controlled Fusion and Plasma Physics (Proc. 21st Eur. Conf. Montpellier, 1994), Vol. 18B, Part I, European Physical Society, Geneva (1994) 118.
[7] COLAS, L., et al., in Controlled Fusion and Plasma Physics (Proc. 23rd Eur. Conf. Kiev, 1996), Vol. 20C, European Physical Society, Geneva (1996).
[8] HOANG, G.T., et al., *ibid.*
[9] RECHESTER, A.B., ROSENBLUTH, M.N., Phys. Rev. Lett. **40** (1978) 38.
[10] GUIZIOU, L., et al., in Controlled Fusion and Plasma Physics (Proc. 22nd Eur. Conf. Bournemouth, 1995), Vol. 19C, Part I, European Physical Society, Geneva (1995) 37.
[11] REBUT, P.H., et al., Phys. Fluids B **3** (1991) 2209.
[12] BIGLARI, H., et al., Phys. Fluids B **1** (1989) 109.
[13] PEEBLES, W.A., et al., in Plasma Physics and Controlled Nuclear Fusion Research 1990 (Proc. 13th Int. Conf. Washington, 1990), Vol. 1, IAEA, Vienna (1991) 589.
[14] HARRIS, G.R., et al., Nucl. Fusion **32** (1992) 1967.

DISCUSSION

A.W. MORRIS: You present some impressive data on magnetic fluctuations in the confinement region and a transport coefficient assuming that the magnetic field structure is stochastic. Do you have evidence that the structure is indeed stochastic?

C. LAVIRON: Magnetic fluctuations do not present coherent modes, as the measured frequency spectra are broadband, extending from a few kilohertz to over 1 MHz. Moreover, a rough estimate of the island widths shows that the overlapping condition is fulfilled.

R.R. WEYNANTS: With the ergodic divertor you should be able to move the position of the electric shear layer. Did you do many experiments, and with what result?

C. LAVIRON: These experiments have been done: from the frequency spectra analysis of the CO_2 scattering diagnostic, we have been able to estimate the movement of the electric shear layer, from $r/a \approx 0.93$ to $r/a \approx 0.84$. This new position is consistent with theoretical predictions.

F. WAGNER: In hydrogen the transition from the ohmic linear to the saturated regime occurs at lower $\bar{n}_e$. I wonder whether this observation fits your analysis of the role of T_e' and shear in view of the fact that T_e' is smaller in H than in D (at constant $\bar{n}_e$) and shear would be larger in H than in D (judging from the radius of the $q = 1$ surface).

C. LAVIRON: The proposition that temperature gradient and magnetic shear give an inverse effect to fluctuations has not been tested for different gases such as hydrogen and deuterium. If they do, depending on the quantitative values of the temperature gradient and shear, this inverse effect could give a different saturation density.

R.E. WALTZ: There is a simple formula relating magnetic fluctuations to density fluctuations: $\tilde{B}/B \propto \beta\tilde{n}/n$. This formula does well on probe signal data. Have you checked this formula?

C. LAVIRON: This formula has not been explicitly checked, but magnetic and density fluctuations are correlated in additional heating experiments. This has been shown by the common correlation of magnetic and density fluctuations with the electron temperature gradient.

PHYSICS OF TURBULENCE CONTROL AND TRANSPORT BARRIER FORMATION IN DIII-D*

E.J. DOYLE, K.H. BURRELL[1], T.N. CARLSTROM[1], S. CODA[2], J.C. DeBOO[1], R.D. DURST[3], R.J. FONCK[3], P. GOHIL[1], C.M. GREENFIELD[1], R.J. GROEBNER[1], J. KIM[1], K.W. KIM, R.J. LA HAYE[1], L.L. LAO[1], E.A. LAZARUS[4], R.A. MOYER[5], G. NAVRATIL[6], T.H. OSBORNE[1], W.A. PEEBLES, C.L. RETTIG, T.L. RHODES, B.W. RICE[7], D.P. SCHISSEL[1], G.M. STAEBLER[1], E.J. STRAIT[1], T.S. TAYLOR[1], D.M. THOMAS[1], R.E. WALTZ[1]

Department of Electrical Engineering
and
Institute of Plasma and Fusion Research,
University of California,
Los Angeles, California,
United States of America

Abstract

PHYSICS OF TURBULENCE CONTROL AND TRANSPORT BARRIER FORMATION IN DIII-D.

The paper describes the physical mechanisms responsible for turbulence control and transport barrier formation on DIII-D as determined from a synthesis of results from different enhanced confinement regimes, including quantitative and qualitative comparisons to theory. A wide range of DIII-D data supports the hypothesis that a single underlying physical mechanism, turbulence suppression via $E \times B$ shear flow, is playing an essential, though not necessarily unique, role in reducing turbulence and transport in all of the following improved confinement regimes: H-mode, VH-mode, high-ℓ_i modes, improved performance counter-injection L-mode discharges and high performance negative central shear (NCS) discharges. DIII-D data also indicate that synergistic effects are important in some cases, as in NCS discharges where negative magnetic shear also plays a role in transport barrier formation. This work indicates that in order to control turbulence and transport it is important to focus on understanding physical mechanisms, such as $E \times B$ shear, which can regulate and control entire classes of turbulent modes, implying that it can also control transport. In the highest performance DIII-D discharges, NCS plasmas with a VH-mode like edge, turbulence is suppressed at all radii, resulting in neoclassical levels of ion transport over most of the plasma volume.

---

* Work supported by the US Department of Energy under Grant and Contract Nos DE-FG03-86ER53225, DE-AC03-89ER51114, DE-FG03-95ER-54294, DE-AC05-84OR21400, W-7405-ENG-48, DE-FG02-91ER54109, and DE-FG02-89ER53296.

[1] General Atomics, San Diego, California, USA.

[2] Massachusetts Institute of Technology, Cambridge, Massachusetts, USA.

[3] University of Wisconsin, Madison, Wisconsin, USA.

[4] Oak Ridge National Laboratory, Oak Ridge, Tennessee, USA.

[5] University of California, San Diego, California, USA.

[6] Columbia University, New York, New York, USA.

[7] Lawrence Livermore National Laboratory, Livermore, California, USA.

1. INTRODUCTION

Improved understanding and control of cross-field transport have long been primary objectives of the magnetic fusion research program — improved/controlled transport characteristics are essential for economical power plant operation. Over the years, a number of improved confinement regimes have been discovered each of which has distinct operational limits and characteristics. However, results from studies of turbulence and transport behavior in improved transport regimes on DIII–D indicate that a single underlying physical mechanism, turbulence suppression via **E**×**B** shear flow [1,2] is playing an essential, though not necessarily unique, role in reducing turbulence and transport in all of the following improved confinement regimes: H–mode, VH–mode, high-ℓ_i modes, improved performance counter-injection L–mode discharges and high performance negative central shear (NCS) discharges. From these results several conclusions can be drawn: (1) **E**×**B** shear decorrelation of turbulence and transport provides a unifying physical explanation for the improved transport observed in a wide range of confinement regimes. (2) Shear suppression of turbulence is a robust mechanism, with a demonstrated ability to control turbulence and transport at all radii. (3) Identification of the individual modes responsible for the observed turbulence is not as important as knowledge of turbulence drive and suppression mechanisms, which can provide a direct route to transport control.

E×**B** shear suppression of turbulence in a plasma is a mechanism akin to the interaction between sheared velocity fields and turbulence in fluids. In a plasma, however, the fundamental velocity is not the mass velocity, but rather the **E**×**B** velocity, the velocity at which turbulent eddies are convected [3]. Theoretically, shear (first derivative) in the **E**×**B** velocity can decorrelate turbulence, resulting in decreased radial correlation lengths and a significant reduction in turbulence and transport [4,5]. Fluctuation suppression is predicted to occur when the shearing rate associated with the **E**×**B** flow, $\omega_{\mathbf{E}\times\mathbf{B}}$, exceeds the decorrelation rate of the ambient turbulence $\Delta\omega_T$ [4]. An alternate criterion for turbulence stabilization can also be utilized: numerical simulations suggest that turbulence should be quenched if the shearing rate $\omega_{\mathbf{E}\times\mathbf{B}}$ equals or exceeds the linear growth rate γ of the most unstable mode present [6,7]. Other theoretical predictions are that **E**×**B** shear is a general mechanism which can control the saturation level of entire classes of turbulent modes [8], and that for some modes the curvature (second spatial derivative) of the **E**×**B** velocity can be important [9]. On DIII–D, reductions in turbulence levels, and decreased transport have been observed in all cases where the **E**×**B** shear is large enough to be theoretically significant.

E×**B** shear as a control mechanism for turbulence and transport has the major advantage of flexibility, in that the shear can be generated or enhanced in several different ways. The radial electric field E_r is determined from the lowest order radial force balance equation for a single ion species,

$$E_r = (Z_i e n_i)^{-1} \nabla P_i - v_{\theta i} B_\varphi + v_{\varphi i} B_\theta \qquad (1)$$

where i labels the ion species, Z_i is the charge of the ion, n_i the ion density, e is the electronic charge, P_i the ion pressure, $v_{\theta i}$ and $v_{\varphi i}$ are the ion poloidal and toroidal rotation velocities, and B_θ and B_φ are the poloidal and toroidal magnetic fields, respectively. In general toroidal geometry, it has recently been shown that the shearing rate $\omega_{\mathbf{E}\times\mathbf{B}}$ depends on E_r/RB_θ [10], explicitly

$$\omega_{\mathbf{E}\times\mathbf{B}} = \left| \left[(RB_\theta)^2/B\right] \partial/\partial\Psi (E_r/RB_\theta)\right| \qquad (2)$$

where Ψ is the radial flux coordinate. The significance of this latter result is that E_r/RB_θ behaves quite differently than the magnitude of the **E**×**B** velocity, E_r/B_φ, and is susceptible to modification by changing both E_r and the current profile distribution, which changes B_θ. Note that $\omega_{E\times B}$ is not a constant on a flux surface; the $(RB_\theta)^2/B$ term results in different shearing rates on the low and high field sides of a flux surface in a tokamak. Thus, E_r and **E**×**B** shear can be created and/or modified by poloidal and toroidal flows, pressure gradients, and by varying the current profile so as to modify B_θ.

The results presented in this paper have been obtained from a synthesis of results from a sustained multi-year program to investigate the turbulence and transport characteristics of enhanced confinement regimes on DIII–D. Emphasis has been placed on studying the physics of initial transport barrier formation as a high leverage route to understanding the underlying physical mechanisms responsible for the improved transport and confinement. A summary of the results from the different enhanced confinement regimes is given below, followed by conclusions drawn from the entire data set. Note that in this paper the term "transport barrier" is used in a generalized sense — in the highest performance DIII–D discharges, for example, transport is improved across the entire plasma radius.

2. EDGE L–H TRANSITION DATA

The edge region provides the largest data set for this study, and also the most advanced quantitative comparisons to theory. Early measurements in fast transitions (D_α drop time <1 ms) [11–15] and dithering transitions [16] demonstrated a spatial and temporal correlation between the creation of a region of sheared **E**×**B** flow inside the separatrix, suppression of turbulence levels, and improved transport. Shown in Fig. 1 are more recent Langmuir probe data showing the sheared edge E_r well created inside the separatrix in an Ohmic H–mode, and also showing the resulting change in density

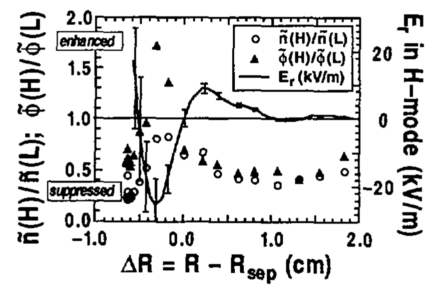

FIG. 1. Radial profile of the radial electric field E_r (solid line) and the ratios of the absolute root mean squares density and potential fluctuation levels in the H-mode (H) to the values in the Ohmic (L) phase. The density fluctuation data are represented by circles, and the potential by triangles.

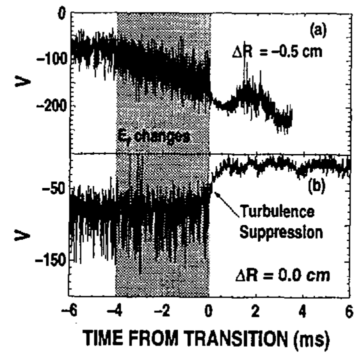

FIG. 2. Time evolution of floating potential φ_f across an L–H transition at locations (a) 0.5 cm inside the separatrix, and (b) at the separatrix. The potential values begin to change ~4 ms before the transition, consistent with a causal role for E_r.

and potential fluctuation levels across the transition [shown as a ratio of H–mode (H) to Ohmic (L) levels] [17]. As can be seen, density fluctuations are reduced at all radii shown by a factor of up to 10, while potential fluctuations are reduced everywhere except at the bottom of the E_r well structure, where the shear is approximately zero.

By operating close to the power threshold it has been possible to generate slow L–H transitions (D_α drop time a few ms), in which the time evolution of the edge parameters is sufficiently slow to demonstrate a sequence of events consistent with a causal role for E_r [17–19]. In Fig. 2, floating potential data from the Langmuir probe are shown from 5 mm inside the separatrix and at the separatrix radius. At a time 6 ms before the transition, the floating potentials are similar at the two radii, indicating that E_r is small. However, the difference between the dc floating potentials is observed to change ~4 ms *before* the transition, indicating an increase in the magnitude of E_r. At the transition, the dc potentials change more rapidly, while the fluctuating component of the floating potential signal is suppressed within 30–60 μs. Thus, the initial change in these plasmas occurs in E_r, followed by turbulence suppression, consistent with causality. As the fluctuations are unchanged during the period of the initial change in E_r, these results also indicate that there is a threshold shear level required to suppress turbulence.

Several quantitative comparisons have also been performed between the experimental results and simple, single fluctuating field theories. Measurements of edge turbulence characteristics across the L–H transition indicate that the edge **E**×**B** shear level generated on the low field side in H–mode is quantitatively more than sufficient to suppress turbulence ($\omega_{E\times B} > 5\Delta\omega_T$), as observed [15]. However, a spatial asymmetry in turbulence response is observed; fluctuations on the high field side of DIII–D are not suppressed at the L–H transition, consistent with the inboard/outboard variation in the **E**×**B** shearing rate as given by Eq. (2) [14,15]. The spatial profiles obtained from the Langmuir probe measurements shown in Fig. 1 can also be compared to theoretical predictions for turbulence reduction as a function of shear level [17]. Several models relate the change in relative fluctuation amplitude Θ across the transition to shear levels in the following way:

$$\Theta \equiv \langle\tilde{n}/n\rangle_H / \langle\tilde{n}/n\rangle_L = 1/(a + b|dE_r/dr|^c) \tag{3}$$

where a and b are parameters that depend upon L–mode turbulence characteristics, and c =2/3 in the high shear model of Biglari, et al. (BDT model) [4], c = 2 in the low shear model of Shaing, et al. [5], and c = 2 in the arbitrary shear model of Zhang and Mahajan [20]. A fit of these models to the data is shown in Fig. 3. As can be seen, the BDT model fits the data well in its range of validity ($|dE_r/dr| > 200$ V/cm^2), while the Zhang and Mahajan model works well at all shears. In the fit of the BDT model, data from regions of positive E_r shear were excluded since the amount of suppression observed differs depending on the sign of the shear (see Fig. 1). In general, the spatial dependence of the edge turbulence reduction is consistent with shear suppression for negative E_r shear, while for positive E_r shear the turbulence suppression is consistent with the effect of E_r shear plus curvature for modes for which an E_r well is destabilizing [17].

However, the experimental data also clearly demonstrate that simple, single field, theories such as [4,5,20] are inadequate to explain all the observed L–H transition phenomena: (1) the response of the density and potential fluctuations to the applied shear clearly differs (Fig. 1), while in the simple models their response should be identical. (2) The cross-phase between the density and potential fluctuations, which is not included in simple theories, plays a very important role in reducing turbulent driven transport in H–mode. For the same data as shown in Fig. 1, the turbulent driven particle flux is substantially reduced in H–mode at all radii, even though potential fluctuations increased in H–mode at some radii. This occurs because the cross-phase changed from ~π/2 in Ohmic to ~π in H–mode in the region of least turbulence suppression, reducing the turbulence induced particle flux to ~0, irrespective of fluctuation amplitude. The measured turbulent particle flux on the outboard midplane is large enough to account for the observed edge particle transport rates [21]. (3) Equation 2 contains no threshold for E_r shear effects on turbulence, while experimentally a threshold is observed. (4) The amount of turbulence suppression is observed to depend on the sign of the shear, while theory [Eq. (3)] is independent of sign. (5) The rapidity of the turbulence suppression observed in fast transitions (30–60 μs) [17,18], is inconsistent with the range for the exponent $2/3 < c < 2$, obtained from the spatial profiles described above. For the theoretical models to replicate such fast suppressions requires a much larger exponent, $c \sim 4$ [22]. The conclusion from these five points is that self-consistent theories (theories which account for the response of the turbulence and plasma parameters to the imposed **E×B** shear) are essential in modeling the L–H transition. Such theories have been developed, e.g., Refs. [9,23], but, predictably, they are much harder to test experimentally.

New aspects of the L–H transition mechanism still exist which require further study. For example, an additional type of "very slow" transition has been observed on DIII–D in which the edge D_α emission can take >50 ms to evolve from L– to H–mode levels. These very slow transitions occur at power levels close to threshold, such that at first they were thought to be possible examples of a slow phase transition. However, recent results indicate that these very slow transitions occur close to threshold in relatively high density plasmas where there is a MARFE and/or divertor detachment in L–mode. In H–mode, the MARFE dissipates. Thus, the time scale for very slow L–H

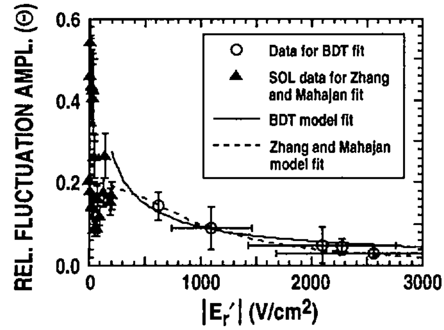

FIG. 3. Experimentally observed dependence of the relative fluctuation amplitude Θ on the magnitude of the E_r shear. The lines represent fits to theory, showing quantitative agreement.

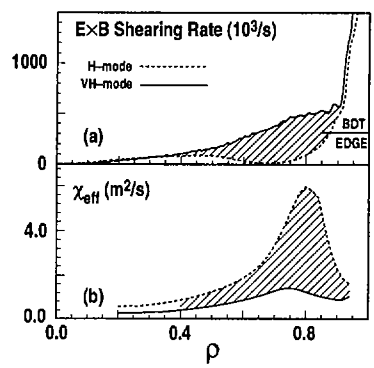

FIG. 4. Changes in the radial profiles of (a) the **E × B** *shearing rate $\omega_{E\times B}$ and (b) effective thermal diffusivity χ_{eff} from the H- to the VH-mode phase of a single discharge. The dashed lines are H-mode, the solid lines VH-mode. Also marked in (a) by the horizontal line and 'BDT EDGE' is an estimate of the shearing rate required to suppress edge turbulence based on DIII-D L-mode turbulence data.*

transitions may be governed by the time scale of the atomic physics processes involved in MARFE burn-through. Another difference between very slow and fast transitions is that in many very slow transition discharges the SOL profiles and turbulence levels remain unchanged from L– mode to the early H–mode phase, i.e., the turbulence suppression occurs only inside the separatrix.

3. VH–MODE DISCHARGES

VH–mode results from an inward expansion of the H–mode transport barrier to smaller major radius [24,25]. Increased confinement is attributed to increased **E**×**B** shear in the outer core region, due to an increase in core toroidal rotation rates – an example of a core transport bifurcation based on **E**×**B** decorrelation of turbulence as discussed in [26]. Illustrated in Fig. 4 are the changes in the **E**×**B** shearing rate $\omega_{\mathbf{E}\times\mathbf{B}}$ and effective thermal diffusivity χ_{eff} between the H– and VH–mode phases of a single discharge. As shown by the shaded regions, the shearing rate is substantially larger in VH–mode, with a marked decrease in transport in the same region. Shown in Fig. 4(a) by the horizontal line and inscription "BDT EDGE" is an estimate of the shearing rate predicted by the BDT model [4] to suppress edge turbulence, based on DIII–D L–mode edge turbulence data [17]. In VH–mode, the region where the shearing rate exceeds the level required for edge turbulence suppression expands inward to $\rho \sim 0.6$. Coincident with the increase in **E**×**B** shear, turbulence is reduced. Shown in Fig. 5 are time histories of the density fluctuations level at $\rho \sim 0.8$, and toroidal rotation velocities at several locations during the H– and VH–mode phases of a single discharge. The increased shear associated with VH–mode operation is shown directly by the divergence at ~2360 ms of the toroidal rotation traces at a radial location of $\rho \sim 0.8$. Density fluctuation levels at $\rho \sim 0.8$ decrease by a factor of ~2 in VH–mode compared with the H–mode phase, and short regular bursts in the fluctuation level disappear. These bursts of turbulence are associated with changes in the toroidal rotation profile in the same region, leading to the term "momentum transfer events" (MTEs) [25]. The repetitive nature of the fluctuation bursts associated with MTEs is similar to the limit-cycle behavior predicted for core turbulence in Ref. [27]. More complete details of the turbulence reduction observed in VH–mode have been published in Refs. [3,25,28]. Finally, magnetic braking experiments in VH–mode discharges have demonstrated a clear causal role for **E**×**B** shear in reducing turbulence and transport [3,28,29]. Similar magnetic braking experiments are described in more detail in the next section.

4. HIGH-ℓ_i DISCHARGES

In high-ℓ_i discharges, the plasma elongation is rapidly increased, thereby increasing the internal inductance ℓ_i and peaking B_θ [30]. The transport improvement observed in high-ℓ_i discharges is attributed to the modified current profile increasing the shear in E_r/RB_θ, resulting in increased toroidal rotation and consequent turbulence suppression. Magnetic braking of toroidal rotation in high-ℓ_i discharges reduces the **E**×**B** shearing rate, leading to an increase in turbulence and transport [31]. These braking experiments provide a direct demonstration that **E**×**B** shear plays a *causal role* in the reduced turbulence and transport normally observed in these plasmas. Shown in Fig. 6 are comparisons of the shearing rate $\omega_{\mathbf{E}\times\mathbf{B}}$ and single fluid χ_{eff} with and without magnetic braking in high-ℓ_i discharges. As shown by the shaded regions in Fig. 5, the application of the magnetic brake reduces the **E**×**B** shearing rate, resulting in a substantial increase in transport. Coincident with the application of the magnetic brake and increase in transport, fluctuation levels as monitored by the FIR scattering system increase by a factor of ~2–3. Turning off the brake allows the plasma rotation and confinement to return to unbraked levels.

5. COUNTER-INJECTION L-MODE DATA

Results from DIII–D [32] indicate that **E×B** shear suppression of turbulent fluctuations may also play a causal role in the improved confinement observed in counter-injection L-mode plasmas on several machines [33,34]. On DIII–D, counter-injection leads to significant changes in E_r as compared with Ohmic or co-injection plasmas. E_r in Ohmic discharges is typically positive across the entire plasma radius. Application of counter neutral injection changes both the magnitude and polarity of E_r, since E_r in the core is dominated by the toroidal rotation term in Eq. 1. Fluctuation data obtained during these discharges indicate a two-step turbulence response after the initiation of counter injection. First is a prompt (within 5–10 ms) reduction of about 30% in fluctuation levels for fluctuations with wavenumbers greater than approximately 2 cm^{-1}. On a longer time scale, the overall fluctuation level integrated over all wavenumbers decreases further by another factor of ~30%. That the changes in E_r and **E×B** shear consequent upon the initiation of counter injection are responsible for this reduction in turbulence levels is strongly suggested by the time coincidence of the observations and also by the lack of changes in other relevant profile parameters during this time.

6. NEGATIVE CENTRAL SHEAR (NCS) DISCHARGES

There are several reasons to believe that **E×B** shear effects are playing an essential role in controlling turbulence and transport in high performance NCS discharges [35–39]: (a) large central gradients in the toroidal rotation profile, combined with the modified current profile distribution, generate significant levels of **E×B** shear in the core of

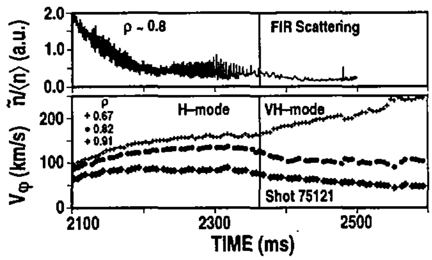

FIG. 5. Time evolution of density fluctuation levels, as monitored by an FIR scattering system, and impurity ion toroidal rotation velocities at several radial locations during the evolution of a single discharge from H-mode to VH-mode.

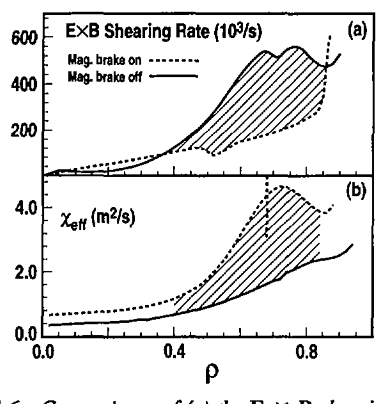

FIG.6. Comparisons of (a) the E × B *shearing rate $\omega_{E\times B}$, and (b) single fluid χ_{eff} radial profiles with and without magnetic braking in separate high-ℓ_i discharges. The dashed lines are with magnetic braking, solid lines without.*

NCS discharges. Shown in Fig. 7 is a comparison of E_r and **E**×**B** shearing rate profiles for an NCS plasma with an L–mode edge and a VH–mode discharge. The shearing rate is clearly higher in the core of the NCS plasma, while the VH–mode plasma has a superior shearing rate in the outer half of the plasma. After transport barrier formation in NCS plasmas the **E**×**B** shearing rate clearly exceeds the trapped electron η_i mode linear growth rate in the region of reduced transport, whereas the two rates are comparable immediately before barrier formation [36], i.e., $\omega_{E\times B}$ is quantitatively large enough to suppress turbulence such as η_i modes and, hence, reduce transport. (b) NCS is not necessary for the maintenance of high performance; performance is maintained in discharges where the current profile evolves such that the core magnetic shear becomes low or slightly positive [36]. However, high levels of **E**×**B** shear are maintained. (c) Negative magnetic shear is predicted to locally lower the threshold for turbulence suppression via **E**×**B** shear, further facilitating **E**×**B** shear suppression of turbulence in NCS discharges [40]. (d) A power threshold has to be exceeded before turbulence and transport are reduced, in agreement with **E**×**B** shear theory [26,40,41]. While this threshold seems to be sharp on TFTR [42], DIII–D data indicate a more gradual improvement in transport with increasing power.

In addition to **E**×**B** shear, negative magnetic shear also contributes to the formation of high performance NCS discharges. NCS enhances plasma stability and suppresses ballooning modes [35,43] and may also stabilize drift-type microinstabilities [44,45]. Thus, DIII–D data support a picture in which the enhanced performance in the NCS regime is obtained via a combination of *both magnetic and E×B shear effects.* As a result, very low levels of turbulence and transport are observed in NCS discharges; BES measurements indicate ñ/n levels of <0.1% in the core of NCS with an L–mode edge, as compared to 0.5-1.0% in conventional L–mode plasmas. The width of this core transport barrier region expands from the center outwards with additional power and collapses from the outside in when power is reduced. This latter observation is in accord with theoretical predictions, which typically contain a local transport bifurcation which is a function of local power density [26,40,41].

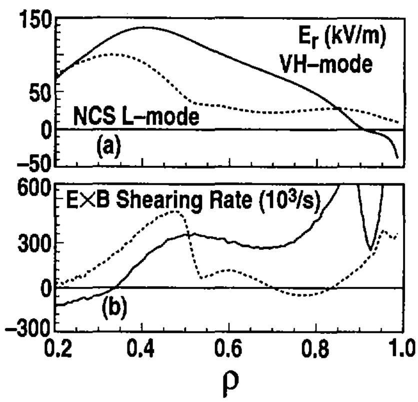

FIG. 7. Comparisons of (a) E_r profiles, and (b) the **E** × **B** *shearing rate $\omega_{E\times B}$, in NCS (L-mode edge) and VH-mode plasmas. The dashed lines are NCS data. Solid lines VH-mode.*

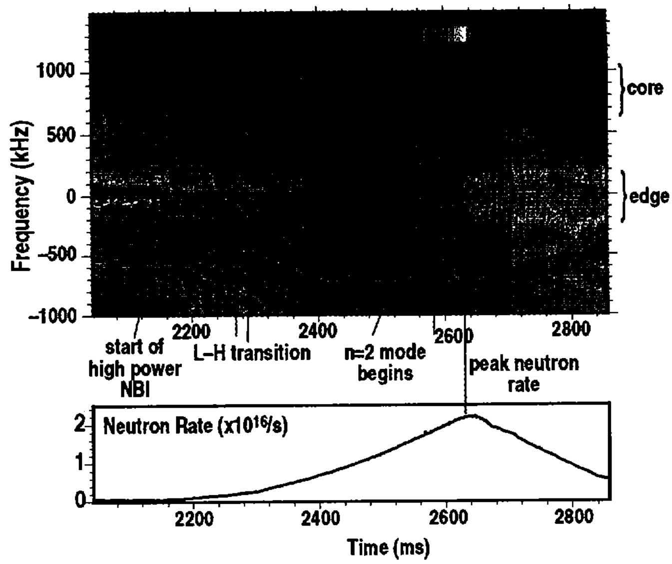

FIG. 8. Color contour plot at time evolution of density fluctuations in the highest performance DIII-D NCS discharge. Data are from FIR scattering system at a wavenumber of 2 cm^{-1}. Darker colors correspond to lower fluctuation levels (black lowest), brighter to higher (red highest). Also shown is the evolution of the neutron rate.

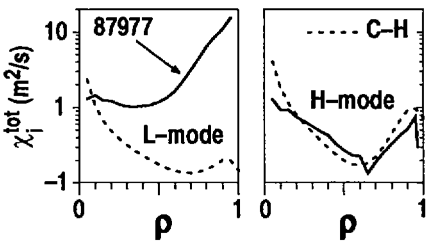

FIG. 9. Ion thermal diffusivity versus ρ for the same discharge as shown in Fig. 8. (a) L-mode phase at 2275 ms, and (b) H-mode at 2580 ms. The solid lines are the experimental values, the dashed lines calculated neoclassical values using the Chang-Hinton formula [46].

By inducing an edge L–H transition, the highest performance DIII–D NCS discharges combine the core turbulence suppression obtained in NCS discharges with an L–mode edge with the edge turbulence suppression of VH–mode discharges, resulting in turbulence suppression at *all* radii. An example of the time evolution of the density fluctuations as determined by FIR scattering in the highest performance DIII–D discharge (87977) is shown as a color coded contour plot in Fig. 8, with an additional plot showing the evolution of the neutron rate. While the inherent spatial resolution of the FIR scattering system is poor, the spatial variation of the E×**B** induced Doppler shifts, which dominate the scattered signal, allow us to associate frequency with position. Thus, large positive frequencies are associated with the plasma core on the low field side, frequencies close to zero correspond to the plasma edge and the magnetic axis, while large negative frequencies correspond to the plasma core on the high field side. Using this frequency/spatial mapping, Fig. 8 can be interpreted as follows: At the start of the high power beam phase at 2160 ms core turbulence is convected at increasing velocity (frequency) as plasma rotation increases. At the same time, the core fluctuation level decreases until it is entirely suppressed by 2300 ms. At 2300 ms the plasma edge transitions from L– to H–mode, and edge turbulence is rapidly suppressed. From 2400 to 2600 ms, *broadband density turbulence is suppressed across the entire plasma radius* during which period the neutron rate rises rapidly. At 2560 ms, coherent MHD is observed, leading to a slowing in the rate of increase of the neutron rate. The peak plasma neutron rate occurs at 2630 ms, coinciding with a return of broadband turbulence. As shown in Fig. 9, the high performance phase of this discharge achieved neoclassical levels of ion transport over most of the plasma volume [38,39]. This achievement of neoclassical ion transport and turbulence suppression across most of the plasma volume fulfills a longstanding goal of the magnetic confinement fusion research program.

Other significant observations in NCS plasmas include the following: A core transport barrier is often observed to form gradually in the initial low-power heating phase, before the main heating beams are applied. As shown in Fig. 8, the residual turbulence in high performance NCS plasma often exhibit a regular bursting character in time, reminiscent of the limit-cycle behavior predicted in Ref. [27] and of the turbulence bursts associated with MTEs in VH–mode. A spatial asymmetry in the turbulence suppression is also observed on occasion during periods in which the **E**×**B** shear is decreasing. As the shear decreases, turbulence and/or MHD are observed to increase preferentially on the high field side which, like the spatial asymmetry observed in the edge at the L–H transition, is thought to originate in the non-equal shearing rates on the high and low field sides, see Section 2 above. Finally, one remaining puzzle in these discharges is that the improvement in electron transport is much less dramatic than that in other channels [36,39].

7. CONCLUSIONS AND SUMMARY

A synthesis of results from DIII–D indicates that sheared **E**×**B** flow is playing an essential role in the formation and maintenance of a wide range of transport barriers and reduced transport regimes. The evidence for this conclusion can be summarized under the following headings: *1. Causality.* Edge measurements at the L–H transition provide evidence for a causal role for **E**×**B** shear, as do magnetic braking experiments in VH– and high-ℓ_i modes. *2. Quantitative tests of theory.* Edge turbulence measurements across the L–H transition show quantitative agreement with theory. The observed **E**×**B** shearing rates in all regimes are of sufficient magnitude that turbulence reduction can be expected. 3. *Qualitative tests of theory.* Measurements in all reduced transport regimes indicate a spatial and temporal correlation between the development of **E**×**B** shear and reduced turbulence and transport. Other processes such as magnetic shear effects are also important and can operate in parallel in a synergistic fashion. From these results, several conclusions can be drawn: (a) **E**×**B** shear regulation of turbulence and transport provides a unifying physical basis for the improved transport observed in a wide range of confinement regimes.(b) Shear suppression of turbulence is a robust mechanism, with a demonstrated ability to control turbulence and transport at all radii. (c) Identification of the individual modes responsible for the observed turbulence may not be as important as knowledge of turbulence drive and suppression mechanisms, which can provide a direct route to transport control. By combining the turbulence suppression features of NCS and VH–mode plasmas, the highest performance DIII–D discharges exhibit turbulence suppression at *all* radii, resulting in neoclassical levels of ion transport over most of the plasma volume [38,39].

REFERENCES

[1] GROEBNER, R.J., Phys. Fluids B 5 (1993) 2343.
[2] ITOH, K., ITOH, S.-I., Plasma Phys. Control. Fusion 38 (1996) 1.
[3] BURRELL, K.H., et al., Phys. Plasmas 1 (1994) 1536.
[4] BIGLARI, H., et al., Phys. Fluids B 2 (1990) 1.
[5] SHAING, K.C., et al., Phys. Fluids B 2 (1990) 1492.
[6] WALTZ, R.E., et al., Phys. Plasma 1 (1994) 2229.
[7] WALTZ, R.E., et al., Phys. Plasma 2 (1995) 2408.
[8] HASSAM, A.B., Comments Plasma Phys. Control. Fusion 14 (1991) 275.
[9] CARRERAS, B.A., et al., Phys. Fluids B 5 (1993) 1491.
[10] HAMN, T.S., BURRELL, K.H., Phys. Plasmas 2 (1995) 1648.
[11] GROEBNER, R.J., et al., Phys. Rev. Lett. 64 (1990) 3015.
[12] BURRELL, K.H., et al., Phys. Fluids B 2 (1990) 1405.
[13] DOYLE, E.J., et al., Phys. Fluids B 3 (1991) 2300.
[14] BURRELL, K.H., et al., Plasma Phys. Control. Fusion 34 (1992) 1859.
[15] DOYLE, E.J., et al., in Plasma Physics and Controlled Nuclear Fusion Research 1992 (Proc. 14th Int. Conf. Würzburg, 1992), Vol. 1, IAEA, Vienna (1993) 235.
[16] MATSUMOTO, H., et al., Plasma Phys. Control. Fusion 34 (1992) 615.
[17] MOYER, R.A., et al., Phys. Plasmas 2 (1995) 2397.
[18] BURRELL, K.H., et al., in Plasma Physics and Controlled Nuclear Fusion Research 1994 (Proc. 15th Int. Conf. Seville, 1994), Vol. 1, IAEA, Vienna (1995) 221.
[19] GROEBNER, R.J., et al., in Plasma Physics (AIP Conf. Proc. 345), ICPP 1994, AIP Press, New York (1995) 74.
[20] ZHANG, Y.Z., MAHAJAN, S.M., Phys. Fluids B 4 (1992) 1385.
[21] MOYER, R.A., et al., to be published in J. Nucl. Mater.
[22] STAEBLER, G.M., et al., Bull. Am. Phys. Soc. 39 (1994) 1616.
[23] DIAMOND, P.H., et al., Phys. Rev. Lett. 72 (1994) 2565.
[24] JACKSON, G.L., et al., Phys. Rev. Lett. 67 (1991) 3098.
[25] OSBORNE, T.H., et al., Nucl. Fusion 35 (1995) 23.
[26] STAEBLER, G.M., et al., Phys. Plasmas 1 (1994) 909.
[27] CARRERAS, B.A., et al., Phys. Plasmas 2 (1995) 2744.
[28] RETTIG, C.L., et al., Plasma Phys. Control. Fusion 36 (1994) A207.
[29] LA HAYE, R.J., et al., Nucl. Fusion 35 (1995) 988.
[30] LAO, L.L., et al., Phys. Rev. Lett. 70 (1993) 3435.
[31] LA HAYE, R.J., et al., In Local Transport Studies in Fusion Plasmas (CALLEN, J.D., et al., Eds), Editrice Compositori, Bologna (1993) 283.
[32] RETTIG, C.L., et al., Phys. Plasmas 3 (1996) 2374.
[33] GEHRE, O., et al., Phys. Rev. Lett. 60 (1988) 1502.
[34] IDA, K., et al., Phys. Rev. Lett. 68 (1992) 182.
[35] STRAIT, E.J., et al., Phys. Rev. Lett. 75 (1995) 442.
[36] LAO, L.L., et al., Phys. Plasmas 3 (1996) 1951.
[37] RICE, B.W., et al., Phys. Plasmas 3 (1996) 1983.
[38] LAZARUS, E.A., et al., Phys. Rev. Lett. 77 (1996) 2714; IAEA-CN-64/A1-2, this volume.
[39] SCHISSEL, D.P., et al., IAEA-CN-64/A5-3, this volume.

[40] DIAMOND, P.H., et al., submitted to Phys. Rev. Lett.
[41] DIAMOND, P.H., et al., Phys. Plasmas **2** (1995) 3685.
[42] LEVINTON, F.M., et al., Phys. Rev. Lett. **75** (1995) 4417.
[43] TURNBULL, A.D., et al., Phys. Rev. Lett. **74** (1995) 718.
[44] KADMOMSEV, B.B., POGUTSE, O.P., Sov. Phys. — JETP **24** (1967) 1172.
[45] KESSEL, C., et al., Phys. Rev. Lett. **72** (1994) 1212.
[46] CHANG, C.S., HINTON, F.L., Phys. Fluids **29** (1986) 3314.

STUDIES OF PERTURBATIVE PLASMA TRANSPORT, ICE PELLET ABLATION AND SAWTOOTH PHENOMENA IN THE JIPPT-IIU TOKAMAK

K. TOI, K.N. SATO, Y. HAMADA, S. OHDACHI, H. SAKAKITA[1],
A. NISHIZAWA, A. EJIRI, K. NARIHARA, H. KURAMOTO[2],
Y. KAWASUMI, S. KUBO, T. SEKI, K. KITACHI[1], J. XU, K. IDA,
K. KAWAHATA, I. NOMURA, K. ADACHI, R. AKIYAMA,
A. FUJISAWA, J. FUJITA, S. HIDEKUMA, N. HIRAKI[2],
S. HIROKURA, H. IDEI, T. IDO[1], H. IGUCHI, M. ISOBE[3],
K. IWASAKI[3], O. KANEKO, Y. KANO, M. KOJIMA, J. KOOG[3],
R. KUMAZAWA, T. KURODA, J. LI[4], R. LIANG[4], T. MINAMI,
S. MORITA, K. OHKUBO, Y. OKA, S. OKAJIMA[5], M. OSAKABE,
Y. SAKAWA[1], M. SASAO, K. SATO, T. SHIMPO, T. SHOJI[1],
H. SUGAI[1], T. WATARI, I. YAMADA, K. YAMAUTI
National Institute for Fusion Science,
Nagoya, Japan

Abstract

STUDIES OF PERTURBATIVE PLASMA TRANSPORT, ICE PELLET ABLATION AND SAWTOOTH PHENOMENA IN THE JIPPT-IIU TOKAMAK.

In the JIPPT-IIU tokamak edge cooling imposed by positive biasing of an inserted electrode and injection of a small ice pellet induces an almost instantaneous increase in the electron temperature near the centre. Rapid current ramp-up increases the electron temperature at the edge. The hot front thus produced quickly propagates towards the centre, although the toroidal current density increase produced by the ramp-up continues to be confined to the edge region of $r/a \geq 0.7$. Rapid current ramp-up also induces a small but sudden drop in the central electron temperature which takes place at a much earlier time than the current penetration. The results from cold pulse and current ramp-up experiments suggest non-local electron heat transport. A long helical shape ('tail') of ablation light is observed when an ice pellet is injected on-axis (horizontally) and slightly upwards or downwards off-axis. The direction of the tail is found to be closely related to plasma rotation. Plasma potential and density profiles are widely controlled by changing the pellet injection angle and size. Radial profiles of the particle diffusion coefficient and inward convection velocity are derived from the time evolution of density profiles produced by the pellet injection. A rapid potential change is observed during a sawtooth crash by a heavy ion beam probe (HIBP). This potential change is caused by a combination of an ambipolar electric field and rapid MHD motion across the magnetic field. However, the poloidal magnetic flux near the sawtooth inversion radius measured by the HIBP hardly changes at the crash. A multichannel motional Stark effect polarimeter has revealed that the safety factor at the plasma centre is well below unity, i.e. 0.7–0.8, during the sawtoothing phase. These results suggest that a partial reconnection takes place at the sawtooth crash.

[1] Nagoya University, Nagoya, Japan.
[2] Kyushu Institute of Technology, Iizuka, Japan.
[3] Graduate University of Advanced Studies, Nagoya, Japan.
[4] Institute of Plasma Physics, Academia Sinica, Hefei, Anhui, China.
[5] Chubu University, Kasugai, Japan.

1. INTRODUCTION

Experiments in JIPPT-IIU are dedicated to investigating fundamental processes in toroidal plasma confinement. The JIPPT-IIU device is a medium sized tokamak with major radius R = 91 cm, minor radius a = 23 cm and maximum toroidal field $B_t = 3$ T [1]. This paper summarizes the following three topics: (a) perturbative plasma transport, (b) ice pellet ablation and (c) sawtooth phenomena. In this experimental research several new plasma diagnostics as well as the usual diagnostics are effectively used, that is, a 28 channel YAG laser Thomson scattering system [2], a 500 kV heavy ion beam probe (HIBP) [3], a fast response Zeeman polarimeter [4], and a 15 channel motional Stark effect (MSE) polarimeter [5]. Moreover, a new pellet injection system has been developed, where the injection angle with respect to the horizontal plane and the pellet size can be easily and precisely controlled [6].

Anomalous plasma transport in a tokamak is very complicated and our understanding is still preliminary. Usually plasma transport is studied through steady state power and particle balances based on experimentally obtained radial profiles of various plasma parameters. On the other hand, the transient response of a plasma to various types of perturbation may give us some hints for elucidating anomalous transport. This perturbative transport study was initiated by the analysis of radial propagation of a heat pulse generated by sawteeth [7]. Modulated electron cyclotron heating power and gas oscillation are also used for the perturbative transport study. A cold pulse produced by sudden edge cooling is also used. Recently, strong non-local or non-diffusive electron heat transport has been observed in the cold pulse experiment [8]. In JIPPT-IIU we have carried out perturbative plasma transport using a cold pulse produced by electrode biasing and ice pellet injection and using edge heating by rapid current ramp-up. This topic is discussed in Section 2.

Ice pellet injection is considered to be a most promising fuelling technique for a reactor grade plasma. Therefore, ablation processes should be studied to understand anomalous plasma transport, and in particular particle transport. This paper describes detailed ablation processes at various injection angles and pellet sizes, and rapid potential change and density profile evolution associated with the pellet injection. Two CCD cameras arranged in the toroidal locations and a high speed framing camera are effectively used in the ablation study. This topic is discussed in Section 3.

Sawtooth phenomena are also an important subject to be understood clearly, because of their close connection with heat transport and energetic particle confinement. In this study the HIBP is effectively applied to detect the fast change of plasma potential and poloidal magnetic flux. The MSE polarimeter is also used to investigate whether or not the central safety factor q(0) is decreased to well below unity during sawtooth oscillations. This topic is discussed in Section 4.

2. PERTURBATIVE TRANSPORT STUDIES APPLYING A COLD PULSE AND RAPID CURRENT RAMP-UP

In JIPPT-IIU perturbative transport experiments are carried out by applying a cold pulse and rapid current ramp-up. The cold pulse is produced with a positively biased electrode inserted just inside the last closed flux surface. Fast electrons bombard the carbon electrode and release impurities and hydrogen. The electron temperature near the edge is slightly but suddenly reduced by the enhanced impurity influx and hydrogen recycling. Figures 1(a) and (b) show the time evolution of the plasma current, loop voltage, electron density, H_α/D_α emission and radiation power in an

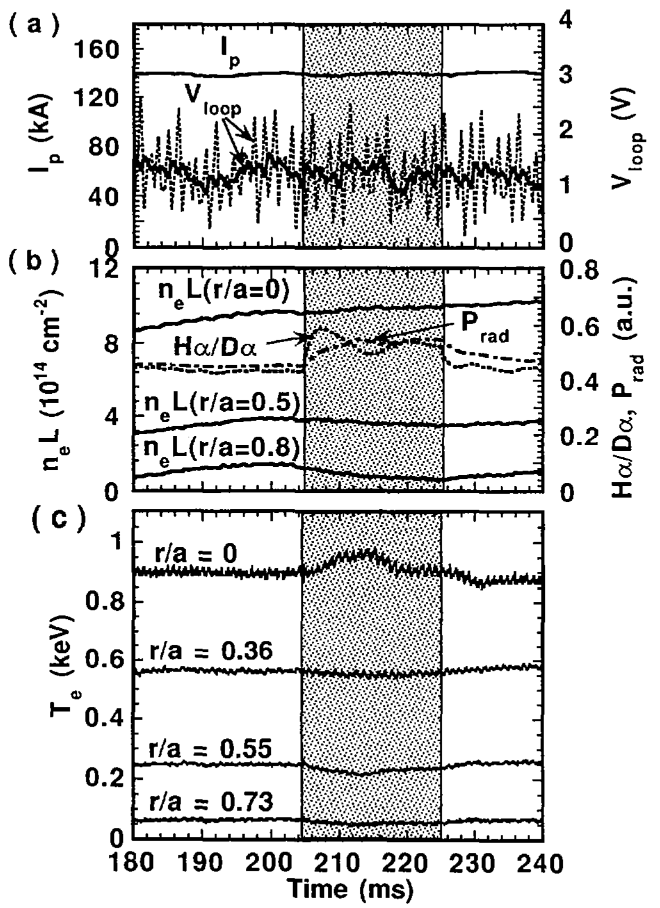

FIG. 1. Time evolution of plasma parameters in an ohmic discharge where a cold pulse is produced by positive biasing of an inserted electrode. Shaded area denotes the biasing phase. (a) Plasma current, loop voltage and smoothed loop voltage; (b) line integrated electron density, H_α/D_α emission and total radiation power; and (c) electron temperatures at various radial positions.

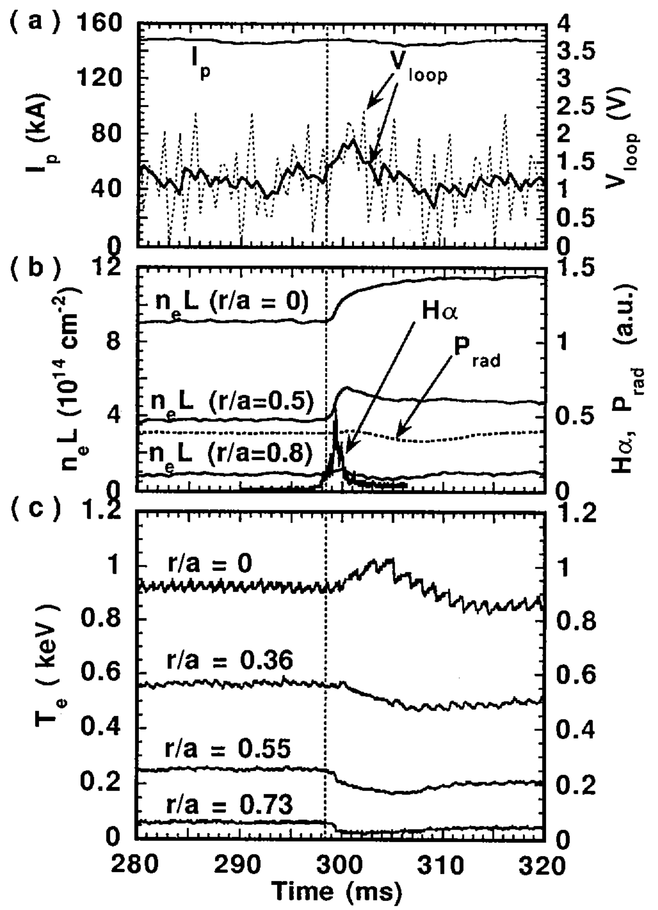

FIG. 2. Time behaviour of an ohmic discharge where a cold pulse is generated by ice pellet injection (horizontal injection). The vertical dotted line denotes the injection of the pellet, where the ablation is almost complete about 1 ms after the injection. Parameters shown are the same as those in Fig. 1.

ohmic discharge where electrode biasing is applied. The time evolution of the electron temperature in this discharge is shown in Fig. 1(c), where the electrode is inserted at $r/a \approx 0.8$. The electron temperature in the peripheral region ($r/a > 0.5$) is decreased and that in the region of $r/a = 0.30$–0.35 remains almost unchanged. A significant point is that the electron temperature near the centre ($r/a < 0.2$) rises without any long time delay with respect to the drop in the edge electron temperature. The loop voltage is kept almost constant or is slightly increased during the edge cooling, as seen from Fig. 1(a). This time behaviour of the electron temperature suggests a strong non-local (or non-diffusive) transport. The positive biasing of the electrode increases the ion saturation current in the scrape-off layer (SOL). This indicates enhanced transport due to the edge cooling induced by positive biasing. Incoherent magnetic fluctuations detected up to 100 kHz are enhanced during biasing. The amplitude of the coherent mode with m = 3/n = 1 remains unchanged, even if the coherent mode is already excited just before the biasing. The frequency of the coherent mode is also unchanged. It is thought that there is no obvious change of poloidal rotation in the area near the q = 3 surface predicted to be at $r/a \approx 0.7$. The inversion radius of sawteeth remains unchanged, although the normalized internal inductance ℓ_i is increased by about 0.1 in 10 ms. This suggests that the toroidal current density is appreciably modified near the edge by the edge cooling. The ohmic input near the edge is not enhanced because of edge cooling.

Similar phenomena are observed in an ohmic discharge just after ice pellet ablation where a small pellet is injected at a low speed. Figure 2 shows the time evolution of various plasma parameters in an ohmic discharge where a hydrogen pellet is injected horizontally. As seen from the interferometer and ECE signals shown in Fig. 2, the pellet is almost completely ablated at around half the plasma radius. The H_α signal obtained at the injection port rises rapidly and decays in less than 1 ms owing to completion of ablation (Fig. 2(b)). The electron temperature near the edge is suddenly reduced by the pellet ablation, and the cold pulse front propagates inwards (Fig. 2(c)). The electron temperature near the centre suddenly increases well before the arrival of the cold front produced by the pellet ablation. In this case the loop voltage is appreciably increased, as shown in Fig. 2(a). However, the loop voltage increase can be explained by the increase of the internal inductance, as described later. This behaviour of the electron temperature suggests a strong non-local transport. In contrast to the cold pulse experiment applying electrode biasing, the ion saturation current in the SOL is suddenly reduced by the pellet ablation. Magnetic fluctuations are also reduced just after the ablation. In particular, the coherent m = 3/n = 1 mode is clearly suppressed at the same time as the sudden drop in the edge electron temperature. This suggests an appreciable change of the toroidal current density profile near and outside the q = 3 surface (i.e. $r/a \geq 0.7$). The normalized internal inductance is increased by about 0.1 in 6 ms. As described above, the increase of the loop voltage is explained by the increase of the inductive voltage due to the change of ℓ_i. That is, the ohmic input near the edge estimated from the change of the loop voltage is almost unchanged. These data suggest that the current density profile is decreased near the edge and increased in the interior, because the total plasma current is kept constant. As seen from Fig. 2(c), the inversion radius of the sawteeth seems to expand slightly during the rise of the electron temperature near the centre. This electron temperature rise is interpreted as being due to either or both of the following causes: the reduction of heat diffusivity near the centre, and the increase in the ohmic heating power density near the centre. The former cause seems the more plausible from a consideration of the resistive diffusion of the poloidal magnetic field.

It is interesting to study the transient response of electron temperature to edge heating by rapid current ramp-up and to compare the results with those in the above mentioned cold pulse experiments. Figure 3 shows the time behaviour of an ohmic discharge with rapid current ramp-up. During the current ramp-up, H_α/D_α emission is

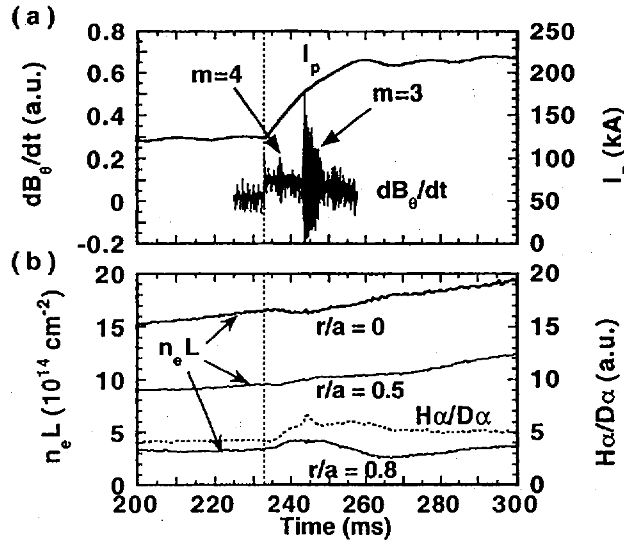

FIG. 3. Time behaviour of a discharge with rapid current ramp-up. (a) Plasma current and Mirnov coil signal, and (b) line integrated electron density and H_α/D_α emission. During the ramp-up, coherent modes with $m = 4/n = 1$ and $m = 3/n = 1$ are destabilized.

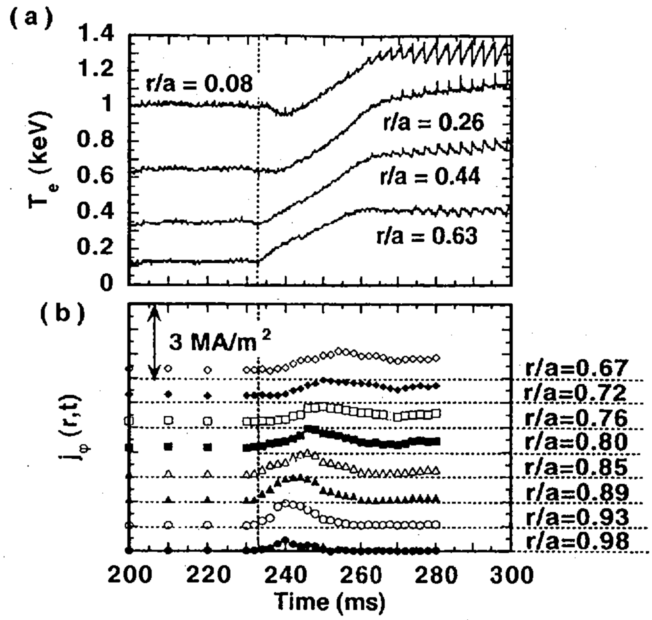

FIG. 4. Time behaviour of electron temperature and toroidal current density in the discharge shown in Fig. 3(a). (a) Electron temperatures obtained with ECE signals, and (b) time evolution of the toroidal current density obtained with a fast response Zeeman polarimeter, where each dotted horizontal line shows the zero level of the respective current density.

enhanced and the electron density near the edge is increased. However, the electron density near the centre ceases to increase or slightly decreases only a few milliseconds after the turn-on of the ramp-up (Fig. 3(b)). This enhanced particle loss seems to take place at the same time as the onset of $m = 4/n = 1$ magnetic fluctuations. The fast response Zeeman polarimeter has revealed that a skin effect of the toroidal current density produced by the ramp-up propagates to the region of $r/a = 0.7$ in about 20 ms after the turn-on of the ramp-up (Fig. 4). However, the electron temperature in the plasma interior, at $r/a < 0.4$, starts to rise well before the arrival of the increased toroidal current density produced by the ramp-up. Moreover, the electron temperature at the centre is suddenly decreased only about 4 ms after the turn-on of the ramp-up, which phenomenon also seems to correlate with the appearance of the $m = 4/n = 1$ mode. The results clearly show that electron heating in the interior takes place much faster than the radial diffusion of increased ohmic heating power at the plasma edge. This cannot be explained by the usual diffusive transport model. The non-local electron heat transport may correlate with coherent low mode number ($m = 4$ or 3) magnetic fluctuations that are enhanced during the ramp-up.

Off-diagonal terms in a transport matrix may play a role in the non-local electron heat transport discussed in this section. Electromagnetic fluctuations having a long radial correlation length should be taken into account, as well as electrostatic fluctuations such as drift waves.

3. STUDIES OF PELLET ABLATION CHARACTERISTICS AND PARTICLE TRANSPORT

The pellet ablation study is conducted by using a specially designed pellet injection system [6]. In this experiment an ablation cloud is measured with two CCD cameras and a fast framing camera, with attention given to plasma rotation. Rapid potential change is measured with an HIBP with high time resolution. Particle transport is intensively studied from an analysis of the time evolution of electron density profiles obtained with the YAG Thomson scattering system.

In the case of off-axis injection with an injection angle (θ, measured from the midplane of the plasma) larger than a certain value ($\theta \geq 4°$), a pellet penetrates straight into the plasma, creating a straight trace of ablation light, as predicted by the usual ablation theory. On the other hand, a long helical shape ('tail') of ablation light has been observed in the case of on-axis (horizontal) and upward or downward off-axis injection with a small angle ($\theta \leq 4°$). This is confirmed by time dependent measurement of the ablation cloud with the high speed framing camera. The direction of the tail is investigated for various injection angles by changing the directions of the toroidal magnetic field and the plasma current independently. These results show that the tail of the ablation cloud in ohmic discharges rotates poloidally in the electron diamagnetic direction, and toroidally in the direction counter to the current [6].

The local electron density and temperature in the ablation cloud have been obtained from the Stark broadening of the Balmer β (H_β) line (4861.3 Å) and from the ratio of the line intensity to the continuum intensity, respectively. Since the time resolution in this measurement is 0.5 ms, the obtained spectrum contains a whole time history of the pellet ablation. The spectrum is best fitted by a double Lorentzian. The FWHM of the two components of the spectrum is obtained as 10.0 and 60.0 Å, corresponding to an electron density of about 10^{16} and 10^{17} cm^{-3}, respectively. From the ratio of the H_β line intensity integrated over 4861.3 ± 100 Å and the continuum intensity integrated from 4550.0 to 4650.0 Å away from the H_β line, the electron temperature is estimated to be about 1 and 4 eV, for the two Lorentzians. The charge exchange equilibrium of protons and hydrogen atoms at extremely high density (10^{15}–10^{17} cm^{-3})

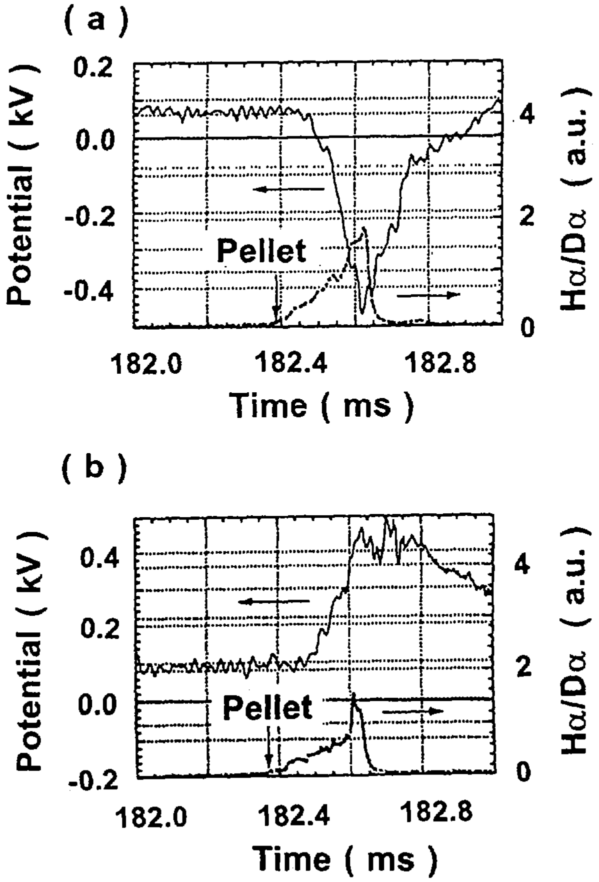

FIG. 5. Relative potential change measured by the HIBP during pellet ablation in the cases of (a) upward off-axis injection at z = 7 cm and (b) downward off-axis injection at z = −7 cm, where z indicates the chord radius of the injection line.

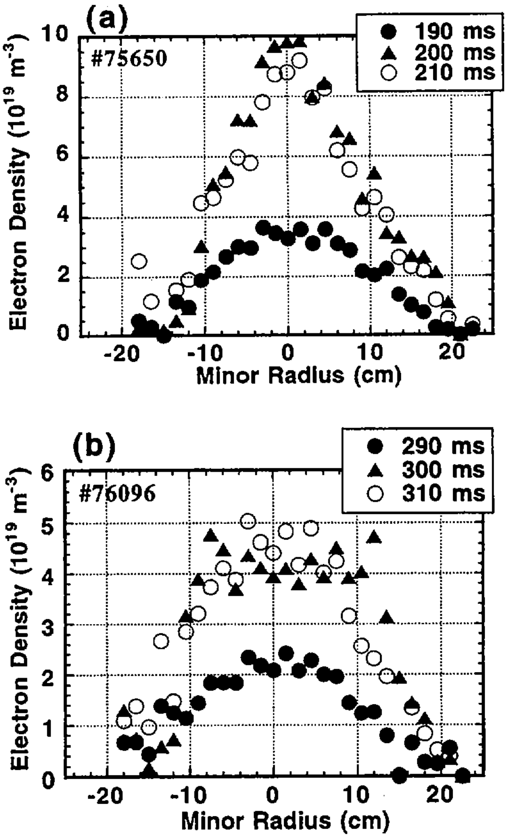

FIG. 6. Time evolution of electron density profiles obtained every 10 ms by the 28 channel YAG Thomson scattering system in ohmic discharges where an ice pellet is injected (a) on-axis at $t \approx 195$ ms (horizontal, $z = 0$ cm), and (b) upward off-axis at $t \approx 295$ms ($z = 7$ cm).

may be realized in the tail structure, since the charge exchange and elastic collision times are much shorter than the ionization time in this parameter range.

A rapid change of plasma potential during pellet ablation is measured for the first time with the HIBP, which has a high time response of more than 1 μs. Figure 5 shows the relative potential change observed near the plasma centre, r/a = 0.1, well inside the maximum ablation position for the two cases shown. In the case where a pellet is injected upwards off-axis, the potential change becomes negative, as shown in Fig. 5(a). In the case where a pellet is injected downwards off-axis, the potential change becomes positive, as shown in Fig. 5(b). This change is interpreted as being due to the toroidal drift of charged particles in the high density plasma of the ablation cloud, before the increased density due to ablation becomes uniform on the magnetic surface [9]. The rotation behaviour of the ablation cloud having the above mentioned

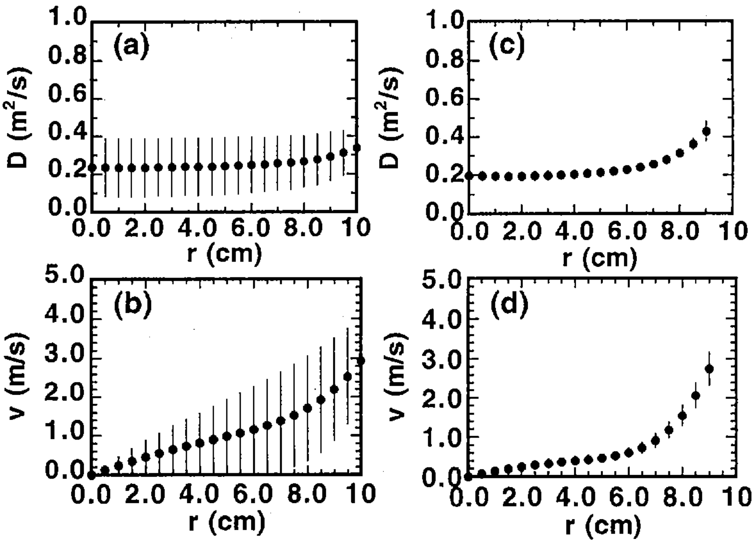

FIG. 7. Radial profiles of particle diffusion coefficient and inward convection velocity derived from time evolution of electron density profiles after ice pellet injection (a, b) in the case of on-axis injection, and (c, d) in the case of upward off-axis injection.

tail structure seems to be consistent with the relative potential change, as shown in Fig. 5.

The above mentioned pellet injection system can effectively control the electron density profile by changing the injection angle, as shown in Fig. 6. The on-axis (horizontal) injection produces the usual peaked profile (Fig. 6(a)). On the other hand, the (upward) off-axis injection produces a fairly flat density profile in the core region with a steep gradient at about half-radius just after the injection (Fig. 6(b)). In this case, the inward pinch effect is clearly observed from the time evolution of the density profile. From the time evolution of electron density profiles obtained for various injection angles, the particle diffusion coefficient D and inward convection velocity v are derived in the central plasma region of $r/a < 0.5$, where D and v are assumed to be kept constant for an analysed time window after the pellet injection (i.e. for 20 ms). The analysed results for the case of on-axis injection are shown in Figs 7(a) and (b). Figures 7(c) and (d) correspond to those in the upward off-axis injection. In the latter case D and v are estimated with relatively small analysed errors. This pellet injection system will provide an effective tool for the study of transport in a toroidal plasma.

4. STUDIES OF SAWTOOTH PHENOMENA WITH HIBP AND POLARIMETER

The HIBP is a very powerful tool to study the rapid change of plasma potential and poloidal magnetic field which may be induced by a sawtooth crash. Indeed, a

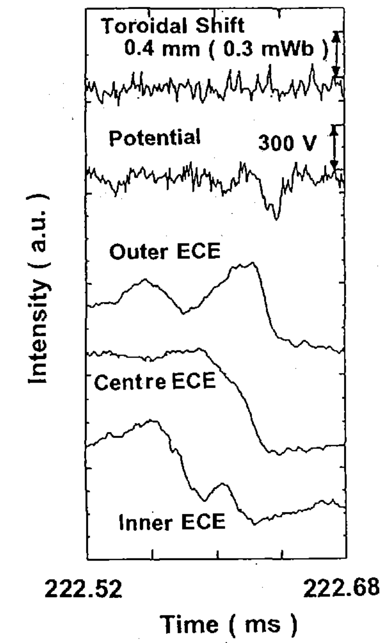

FIG. 8. Expanded time evolution of various plasma parameters during a sawtooth crash, where the toroidal shift of the secondary beam and plasma potential near the inversion radius are obtained with the HIBP, and three ECE signals obtained at outer (larger major radius), centre and inner (smaller major radius) locations inside the inversion radius.

rapid change in the plasma potential has been detected with an HIBP during a sawtooth crash [10]. The potential change with negative or positive polarity is observed inside the inversion radius (r_{inv}) of the sawtooth. Recently it has been clarified that the polarity of the potential change depends on the direction of the fast motion of the hot core (i.e. towards larger or smaller major radius R) at the reconnection. Figure 8 shows the expanded time evolution of the toroidal shift of the secondary beam and plasma potential measured with the HIBP near the inversion radius during the sawtooth crash, along with ECE signals obtained inside the inversion radius. When the hot core is shifted rapidly outwards (towards larger R) because of the MHD effect, as shown in the three ECE signals of Fig. 8, a negative potential pulse is observed, and vice versa. According to the MHD theory, a quick plasma motion perpendicular to the magnetic field ($v_\perp$) means generation of a radial electric field $E = -\nabla\Phi_{MHD}$. At $r < r_{inv}$ a nearly uniform electric field is predicted to be generated at the sawtooth crash, leading to one-directional quick motion towards the inversion radius [11]. The maximum of Φ_{MHD} which occurs at r_{inv} is estimated as $\Phi_{MHD} = v_\perp B_t r_{inv}$, and to be about 300 V. This magnitude and polarity are consistent with the above experimental results, when the HIBP is set 126° in the toroidal direction away from the ECE monitor and

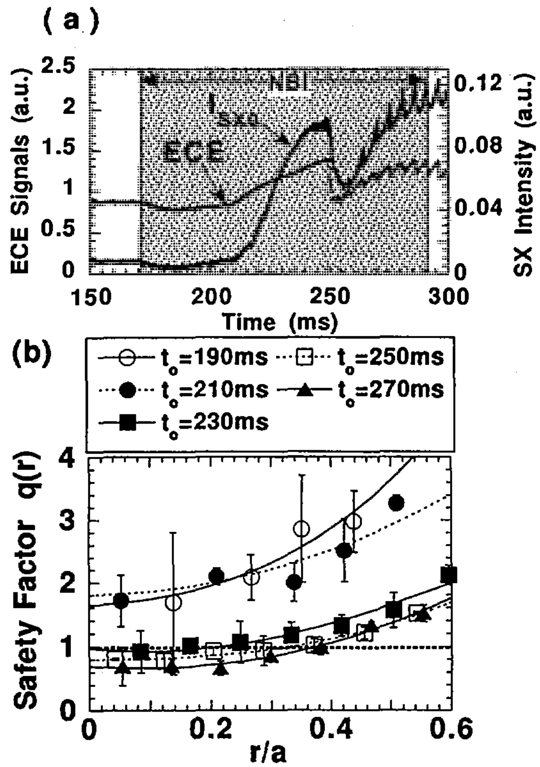

FIG. 9. (a) Time evolution of ECE and soft X ray signals in a current ramp-up discharge with neutral beam injection heating, and (b) radial profiles of the safety factor obtained with an MSE polarimeter. The profiles are obtained by averaging over each 20 ms time window from (t_0 – 10) ms to (t_0 + 10) ms, where the time t_0 specifies the centre of each time window given at the top of (b).

m = 1/n = 1 rapid motion is assumed. The toroidal shift of the beam is proportional to the local poloidal flux through the canonical momentum conservation law. The change of the flux at r < r_{inv} is found to be very small. This suggests that the change of q profile is small at the crash. This seems to be consistent with the fact that the safety factor at the magnetic axis q(0) measured with a 15 channel MSE polarimeter is decreased well below unity, i.e. to 0.7–0.8, even in the phase exhibiting obvious sawtooth oscillations, as shown in Fig. 9 [5]. These results are consistent with those of previous pellet injection experiments [12].

5. SUMMARY

In JIPPT-IIU, perturbative plasma transport experiments are carried out by using a cold pulse induced by electrode biasing and small ice pellet injection and also by using rapid current ramp-up. A strong non-local nature of the electron heat transport is observed in the perturbative transport study, but the mechanism is open for discussion. Upward or downward off-axis injection as well as on-axis injection of an ice pellet bring about interesting plasma behaviour related to particle transport in a tokamak plasma. Studies of sawteeth using an HIBP and MSE polarimeter suggest that only a partial reconnection of magnetic field lines takes place at the sawtooth crash.

ACKNOWLEDGEMENTS

The authors thank A. Iiyoshi and M. Fujiwara for their continuous encouragement.

REFERENCES

[1] TOI, K., et al., in Plasma Physics and Controlled Nuclear Fusion Research 1990 (Proc. 13th Int. Conf. Washington, DC, 1990), Vol. 1, IAEA, Vienna (1991) 301.
[2] NARIHARA, K., et al., Jpn. J. Appl. Phys. **35** (1996) 266.
[3] HAMADA, Y., et al., Plasma Phys. Control. Fusion **36** (1994) 1743.
[4] KURAMOTO, H., et al., Rep. NIFS-397, Natl Inst. for Fusion Science, Nagoya (1996).
[5] XU, J., et al., Rep. NIFS-419, Natl Inst. for Fusion Science, Nagoya (1996).
[6] SAKAKITA, H., et al., in Controlled Fusion and Plasma Physics (Proc. 21st Eur. Conf. Montpellier, 1994), Vol. 18C, Part I, European Physical Society, Geneva (1994) 310.
[7] CALLEN, J.D., JAHNS, G.L., Phys. Rev. Lett. **38** (1977) 491.
[8] GENTLE, K.W., et al., Phys. Rev. Lett. **74** (1995) 3620.
[9] HAMADA, Y., et al., Nucl. Fusion **36** (1996) 1047.
[10] HAMADA, Y., et al., in Plasma Physics and Controlled Nuclear Fusion Research 1994 (Proc. 15th Int. Conf. Seville, 1994), Vol. 1, IAEA, Vienna (1995) 349.
[11] BISKAMP, D., Phys. Fluids B **3** (1991) 3353.
[12] SAKAMOTO, M., et al., Plasma Phys. Control. Fusion **33** (1991) 583.

DISCUSSION

J.D. CALLEN: Similar non-local electron heat transport effects in TEXT and TFTR have been found, mostly only with ohmic heating or modest auxiliary heating and low density. Under what conditions are your non-local transport effects observed?

K.N. SATO: Although we have carried out studies under a wide variety of conditions, it seems this type of effect may occur mainly in ohmic discharges.

K. TOI: In JIPPT-IIU, studies on non-local electron heat transport were carried out in a relatively narrow parameter area, that is, with electron density $\bar{n}_e \approx (2\text{–}2.5) \times 10^{19}\ \mathrm{m}^{-3}$, $q_a \approx 5\text{–}6$ ($B_t \approx 2.9$ T, $I_p = 150\text{–}170$ kA) in ohmic plasmas.

ISOTOPE SCALING OF HEATING AND CONFINEMENT IN MULTIPLE REGIMES OF TFTR*

S.D. SCOTT, G.W. HAMMETT, C.K. PHILLIPS, E.J. SYNAKOWSKI,
S.H. BATHA[1], M.A. BEER, M.G. BELL, R.E. BELL, R.V. BUDNY,
C.E. BUSH[2], W. DORLAND[3], P.C. EFTHIMION, D. ERNST[4],
E.D. FREDRICKSON, J.C. HOSEA, S.M. KAYE,
M. KOTSCHENREUTHER[3], F.M. LEVINTON[1], Q.P. LIU[3],
R. MAJESKI, D.C. McCUNE, D.R. MIKKELSEN, H.K. PARK,
A.T. RAMSEY, J.H. ROGERS, S.A. SABBAGH[5], G. SCHILLING,
C.H. SKINNER, G. TAYLOR, S. VON GOELER, R.E. WALTZ[6],
J.R. WILSON, M.C. ZARNSTORFF
Plasma Physics Laboratory,
Princeton University,
Princeton, New Jersey,
United States of America

Abstract

ISOTOPE SCALING OF HEATING AND CONFINEMENT IN MULTIPLE REGIMES OF TFTR.

The isotope effect on confinement has been studied in a variety of TFTR plasma regimes comparing deuterium to deuterium–tritium performance. The strongly favorable isotope effect observed previously in the peaked-density supershot regime ($\tau_E \propto \langle A \rangle^{0.85}$) has been observed also in the *high* ℓ_i regime, with comparable strong increases in core ion energy confinement. In high-power beam-heated L-mode plasmas with broad density profiles, conditions which are more prototypical of ITER plasmas, deuterium–tritium plasmas attain 12–25% more thermal energy than comparable deuterium plasmas, corresponding to $\tau_E^{th} \propto \langle A \rangle^{0.5}$. ICRF-heated L-mode plasmas with 4 MW of heating show an 8–11% increase in total stored energy in *deuterium–tritium* plasmas, consistent with $\tau_E \propto \langle A \rangle^{0.35-0.5}$. In both the L-mode and supershot regimes, 30% more heating power is required to sustain the same temperature in the deuterium plasma than in tritium, which implies a transport scaling ($\chi \propto \chi_{Bohm} \rho_*^{-2}$) that differs qualitatively from the scaling inferred from B-field scans with fixed isotope. A model for the isotope effect is proposed based on shear-flow effects that explains most of the observed increase in temperature in the L-mode beam-heating experiments. No isotope effect on global τ_E is observed in ohmic plasmas, reverse shear discharges, or enhanced reverse shear discharges. More heating power is required for obtaining an ERS transition in tritium than in deuterium, which may provide a useful test of proposed models of ERS transition physics.

---

* Work supported by US Department of Energy contract DE-AC02-76-CHO3073.

[1] Fusion Physics and Technology, Torrance, California, USA.
[2] Oak Ridge National Laboratory, Oak Ridge, Tennessee, USA.
[3] Institute for Fusion Studies, University of Texas, Austin, Texas, USA.
[4] Massachusetts Institute of Technology, Cambridge, Massachusetts, USA.
[5] Columbia University, New York, N.Y., USA.
[6] General Atomics, San Diego, California, USA.

1. Introduction

Previous experiments in supershot plasmas [1,2] identified a strongly favorable isotope effect on energy confinement between deuterium and tritium. Despite achieving only modest tritium concentrations (~50%), supershots heated with tritium beams achieved 25% higher stored energy than comparable plasmas heated with deuterium beams, consistent with $\tau_E \propto \langle A \rangle^{0.85}$ at high power. The isotope effect was especially pronounced in the central ion thermal diffusivity, with $\chi_i \propto \langle A \rangle^{-1.8}$ at fixed ion temperature. A favorable isotope effect on τ_E between deuterium and DT has also been observed in peaked-density limiter H-mode plasmas[3,4]. Further isotope-scaling experiments have now been carried out on TFTR in DT plasmas to document the isotope effect in a variety of regimes, including broad-density L-mode regimes with $T_i \approx T_e$, regimes with significant electron heating (ICRF heating)[5], and ohmic heating. The observed energy confinement in broad-density plasmas with auxiliary heating is higher in tritium than in deuterium, and the improvement is consistent with $\tau_E \propto \langle A \rangle^{\sim 0.5}$.

From the ensemble of supershot and L-mode discharges it is possible to construct scans in which plasma beta and collisionality are held fixed while the normalized ion gyro-radius $\rho_* = \rho/a$ is changed through the isotope concentrations. These scans confirm that transport improves with increasing ion mass despite larger ρ_*, a trend that is contrary to the observed scaling of transport with ρ_* in magnetic-field scans. A theoretical model of the isotope effect is proposed based on shear-flow effects that reconciles these observations, and which explains most of the observed increase in temperature in the L-mode beam-heating experiments. Implications of this model for projecting the isotope effect to ITER will be discussed.

Finally, isotope effects have been studied in advanced-tokamak regimes with modified current profiles: high-ℓ_i[6], reverse shear (RS),and enhanced reverse shear (ERS)[7,8]. In high ℓ_i plasmas a robust isotope effect is observed similar to that in supershots. By contrast, little or no isotope effect on confinement is observed in reverse-shear or enhanced-reverse shear plasmas despite densities, temperatures, and heating profiles which are quite similar to those obtained in supershots. More heating power is required in tritium than in deuterium to generate an ERS transition, which may provide an interesting challenge to proposed theories of transition dynamics.

2. L-mode Regime with Neutral Beam Heating

To study the isotope effect in L-mode plasmas, we performed a beam power scan at constant $\overline{n}_e$ in deuterium ($D^o \rightarrow D^+$) and tritium ($T^o \rightarrow D^+ +$

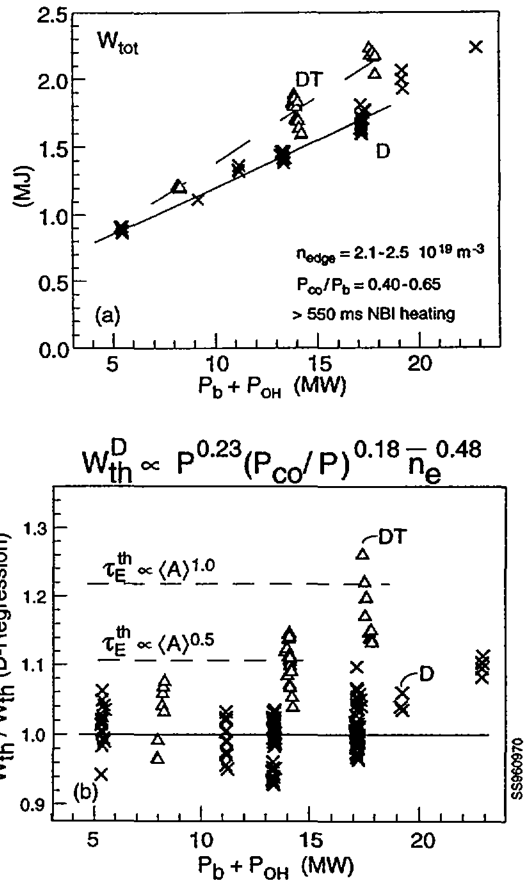

FIG. 1. (a) Total plasma energy as a function of heating power in L-mode plasmas heated with D-NBI versus T-NBI. Plasma conditions were $R = 2.52$ m, $a = 0.87$ m, $\bar{n}_{e19} = 4\text{–}5.5$, $T_{eo} = 3\text{–}7$ keV and $T_{io} = 3\text{–}12$ keV. Data points represent measurements at top of sawteeth ≥550 ms after start of beam injection. (b) Ratio of thermal stored energy to power-law regression fit to the deuterium data.

T^+) plasmas with high-recycling limiters. This generated sawtoothing discharges with broad density profiles ($F_{ne} = n_e(0)/\langle n_e \rangle = 1.4 - 1.8$), $T_i/T_e = 1.0 - 1.4$, and values of τ_E within 20% of the L-mode scaling values in deuterium. In order to achieve L-mode plasmas, the limiter was saturated with either deuterium or tritium gas. Only partial saturation of the limiter with tritium was accomplished due to the reservior of deuterium in the carbon tiles, yielding a tritium concentration of 32-40% in the hydrogenic influx from the limiter during beam injection. The core tritium concentration was larger (~45%) due to tritium beam fuelling.

The total plasma stored energy (Fig. 1) was larger in DT plasmas than in comparable deuterium plasmas. Using a power-law regression fit to the deuterium data, $W_{tot}^{D} \propto P_{inj}^{0.61}(P_{co}/P_{inj})^{0.1} n_{edge}^{-0.17}$, we see that global energy confinement in tritium increased 8-11% at low power (8 MW) and 10-25% at high power (13-18 MW). There was some tendency for the improvement ratio to decrease with time during the heating phase, with the lower range of 10-15% being obtained near the end of the 1.2-second T-NBI pulse. The plasma behavior in the first several hundred milliseconds of beam injection showed some indications of sliding into the supershot regime (with $T_i/T_e > 2$), so we consider the data late in the beam-heating phase to be most respresentative of the true effect in L-mode plasmas. The observed increase there was roughly consistent with the increase of 11% that would be expected from $\tau_E \propto \langle A \rangle^{0.5}$ scaling, given the modest increase in $\langle A \rangle$ from 1.9 to 2.4 in these plasmas.

DT L-mode plasmas attain $\sim$ 30% higher central temperatures and thermal energy densities than D plasmas with comparable density profiles and heating power (16-17 MW). This occurs despite somewhat broader power deposition by tritium beams, which deliver ~12% less power on-axis per incident MW than the deuterium beams. Due to preferential heating of the thermal ions, the volume-integrated beam heating power to ions $P_{bi}(r = a/2)$ remains about constant between deuterium and tritium, while P_{be} decreases ~24% in T-NBI. Thermal stored energy in the deuterium discharges can be well represented by the power-law expression $W_{th}^{D} \propto P_{inj}^{0.23} \overline{n}_e^{0.48} (P_{co}/P_{inj})^{0.18}$, similar to previous thermal scaling in TFTR L-mode plasmas[9]. Normalized to this scaling (Fig. 1b) the tritium discharges show increases in W_{th} of $-2\% \rightarrow +7\%$ at 8 MW, 4%-14% at 14 MW, and 12%-25% at 18 MW. Kinetic analysis indicates that, at high power, electron energy confinement $\tau_{Ee}(a/2)$ increases 10-20% in tritium, and ion energy confinement $\tau_{Ei}(a/2)$ increases 20-40%. Our confidence in this conclusion is weakened by an unresolved systematic discrepancy ($\leq$ 25%) in the ratio of kinetic to magnetic stored energy in these plasmas (comparable in size for D and DT). Momentum confinement during pure co-injection is approximately 15% better in tritium at high power, suggesting an improvement in the ion channel, if, as is typical, $\tau_\phi \approx \tau_{Ei}$.

3. Isotope and ρ_* Scaling

By varying the magnetic field and simultaneously adjusting the plasma density and heating power, gyro-radius scaling experiments can observe [10–13] the variation of heat transport with normalized ion gyro-radius, $\rho_* \equiv \rho/a$. In the L-mode regime, the *single-fluid* thermal diffusivity generally follows a simple Bohm-like scaling, $\chi_{fluid} \propto \chi_B \rho_*^{\sim 0}$ where $\chi_B = cT/eB$. Experiments on DIII-D have identified different gyro-radius scalings for the ions and electrons separately[11,12], with electrons having a gyroBohm scaling $\chi_e \propto \chi_B \rho_*^{1.1 \pm 0.3}$, and the ions having a Goldston-like

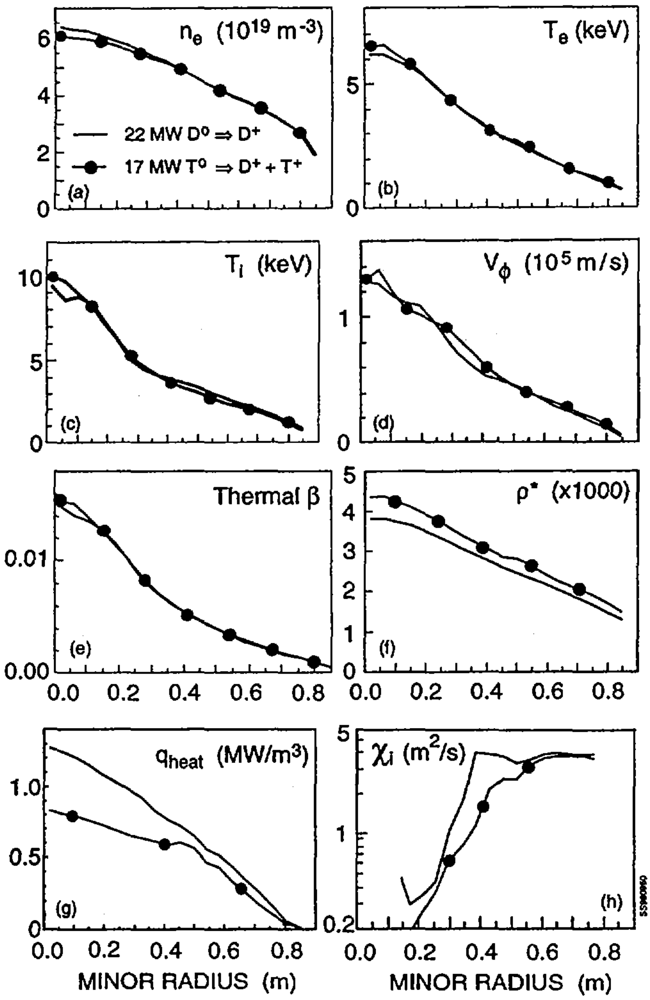

FIG. 2. Kinetic profiles in D and DT L-mode 'isotope ρ_*-scaling' plasmas matched in density, temperature, beta, ν^*, B_t, I_p, Z_{eff}, and ν_{*e}. Contrary to gyroBohm expectations, the D plasma with smaller ρ_* requires ~30% more heating power to sustain the temperature.

scaling, $\chi_i \propto \chi_B \rho_*^{-0.5\pm0.3}$. Alternately, ρ_* can be varied at constant beta and collisionality simply by comparing D and DT discharges matched in temperature and density (rather than at constant heating power). Such a comparison in supershot plasmas[14] showed that 25% less power was required to sustain the same temperature and density profiles in DT as compared to DD, while ρ_* was about 15% *larger* in DT due to tritium's larger mass.

A similar result is obtained in L-mode plasmas: the T-NBI discharge shown in Fig. 2 with ~12% larger ρ_* required 23% less total heating power (about 35% less power deposited on-axis) to sustain the temperature profile against thermal losses. A simple interpretation of these 'isotope ρ_* scaling' comparisons is that transport decreases with increased ρ_*, and viewed this way they imply $\chi_i \propto \chi_B \rho_*^{-2}$. However this result is incompatible with the Bohm-like ρ_* scaling inferred by varying the magnetic field with a single isotope. The isotope effect on χ_i is in the same direction as, but stronger than, the Goldston-like ρ_* scaling observed in DIII-D L-mode plasmas. In H-mode plasmas the apparent discrepancy is greater: the isotope τ_E scaling observed in the H-mode regime[15] implies a ρ_* scaling which is in the opposite direction to the observed gyroBohm scaling of both ions and electrons in that regime[12]. An alternate interpretation is that increased ion mass has an intrinsic and pronounced effect on transport whose full strength is obscured to some extent by the increased ρ_*.

4. Proposed Mechanism of the Isotope Effect

Figure 3 compares the measured T_i profiles for a pair of D and DT L-mode plamas at fixed heating power to the predictions of the original IFS-PPPL ITG-based transport model[16], and to predictions based on an extended model that includes sheared-flow effects:

$$\chi = \chi_{\text{IFS-PPPL}} \times (1 - \gamma_{ExB}/\gamma_{lin}) \tag{1}$$

where $\gamma_{E\times B}$ is the $E \times B$ shearing rate including general geometry effects[17] and neoclassical corrections to the impurity rotation measure-

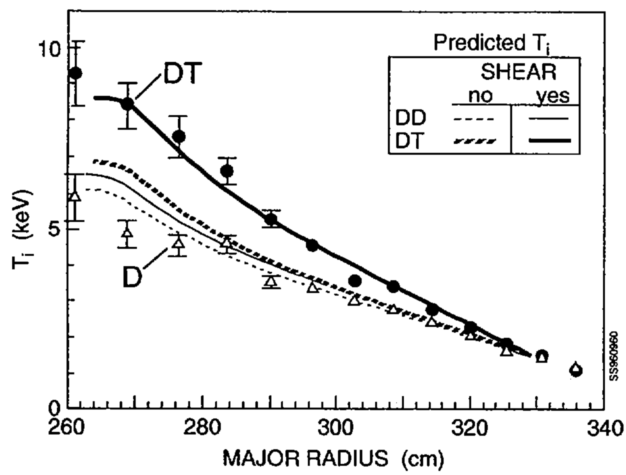

FIG. 3. Measured ion temperature in L-mode plasmas heated with comparable heating power (16.4 MW for D, 17.0 MW for DT) compared with predictions of the IFS–PPPL transport model with and without sheared-flow effects.

ments[18,19]. Here γ_{lin} is an approximate parameterization of the linear ITG growth rate maximized over k_θ. The basic mechanism underlying this shear-flow stabilization model was proposed by Biglari, Diamond, and Terry[20] for H-modes. The prescription of comparing $\gamma_{E\times B}$ with the linear growth rate is suggested by nonlinear ITG simulations[21,22]. As Waltz *et al.* have pointed out, this modified χ formula is of the form $\chi = \chi_{Bohm}\rho_*(1 - \alpha\rho_*)$, and thus one can get different ρ_* scalings in various regimes. Formally, the original IFS-PPPL transport model had a pure gyroBohm scaling which would give an unfavorable isotope scaling. This behavior is partially offset by marginal-stability features of the model which yield a fairly strong dependence on the boundary conditions (e.g. for these conditions, $T_i(0) \propto T_{i,r=0.85a}^{0.4}$).

The simulations use the measured density profile and calculated convective loss terms. Measured temperatures at r/a=0.85 were used as boundary conditions. Discrepancies between the predicted and measured temperature near the axis ($r/a \leq 0.15$) may be due to the lack of a sawtooth model in the present simulations. Figure 3 shows that much of the observed isotope effect on T_i can be modelled by the sheared-flow extension of the IFS-PPPL transport model. E_r shear has more stabilizing influence in the tritium shot than in the deuterium shot partly because γ_{lin} scales as v_{ti}/R, so a fixed amount of shearing will be more effective in tritium - because of its slower growth rate - than in deuterium. In this pair of discharges, another contributing factor is a slight mismatch in the net beam torque, with $P_{co}/P_{inj} = 0.50$ for deuterium versus 0.61 for tritium. A more powerful test of the shear-flow physics in the modified IFS-PPPL model is comparison against experimental heating results in TFTR toroidal rotation scans at fixed heating power. Preliminary analysis shows a level of consistency with theory similar to that shown in Fig. 3. Over a wider range of TFTR L-mode plasmas, variations between the transport model and measured temperatures of order 20% are typically obtained, indicating that further refinements are still needed. One known limitation is that the magnitude of $\gamma_{E\times B}/\gamma_{lin}$ needed for stabilization varies by a factor of two in some nonlinear simulations, depending on parallel shear flow destabilization[21] and on other parameters[22] in a way which has not yet been parameterized.

5. L-mode Regime with ICRF Heating

Isotope scaling experiments were also conducted using ICRF heating in the minority hydrogen (H) regime[23] with majority D or DT L-mode plasmas. The minority-H heating regime was chosen because its wave propagation, absorption, and fast-ion physics should remain similar in deuterium or deuterium-tritium plasmas and should provide comparable

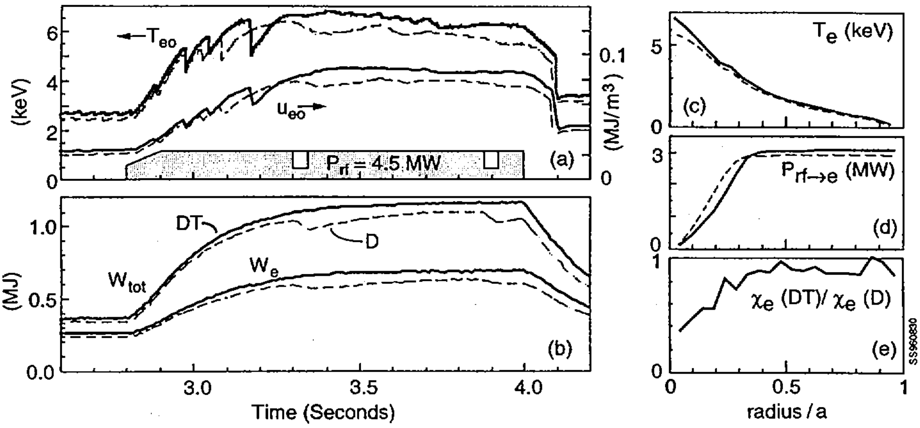

FIG. 4. (a) Central electron temperature measured by ECE and central electron pressure in matched D and DT plasmas with matched density profiles (n_{eo} = 5.9 × 10^{19} m^{-3}) with RF heating. (b) Total plasma energy and total electron energy. (c–e) Electron temperature profile, RF power deposition profile, and ratio of χ_e in the DT discharge to that in the DD discharge.

heating profiles for the two isotopes. These experiments complement the L-mode NBI experiments by avoiding possible effects associated with the isotopic mass of the energetic ion species. For these discharges the limiter was saturated with deuterium or tritium gas in ohmic plasmas similar to the sequence used for the L-mode NBI experiment. The experiments were conducted in moderate density ($\overline{n}_{e19} \approx 4$), broad-profile ($F_{ne}$=1.8) plasmas having roughly equal ion and electron temperatures.

The DT plasma attains 8-12% higher T_{eo}, 2-3% higher n_{eo}, and 10-15% higher central electron pressure (Fig.4). The volume-integrated increase in total electron energy content equals the increase in total plasma energy, suggesting little change in total ion energy content. This result provides clear evidence of a favorable isotope effect on χ_e in L-mode plasmas, which was difficult to demonstrate conclusively in the beam-heating experiments. Direct measurements of the RF-driven energetic H minority ions using a pellet charge-exchange diagnostic indicate that the peak tail temperatures are nearly identical for the D and D-T plasmas at a given RF power level. The tail temperatures are proportional to the RF power input, consistent with the Stix model[23]. Power deposition calculations indicate that virtually all of the RF power is absorbed within $r/a \leq 0.3$ (Fig. 4c) for both isotopes. In the region $r/a \geq 0.3a$, where the power input to the electrons is accurately known, χ_e is 10% lower in the DT plasmas. The kinetic analysis indicates a stronger isotopic effect on χ_e in the core ($r/a \leq 0.3$), although in this region the power deposition profile is more uncertain due to uncertainties in the minority hydrogen density and assumed antenna spectra.

The overall increase in W_{tot} in DT plasmas was 11% for $P_{rf} \leq 3.8$ MW and 8% at 4.5 MW, corresponding to $\tau_E \propto \langle A\rangle^{0.5}$ and $\tau_E \propto \langle A\rangle^{0.35}$ respectively.

6. Ohmic Confinement Scaling

In preparation for the L-mode beam-heating experiments, the inner bumper limiter was saturated with deuterium or tritium gas using a sequence of 3-6 ohmic plasmas with strong gas puffing. Two gas-up sequences were conducted in deuterium (19 ohmic discharges), followed by four sequences in tritium (30 discharges) and a partial change-over to tritium was achieved. Tritium concentration in the limiter influx measured by a Fabry-Perot interferometer [24] was typically ~30% at $\overline{n}_{e19}$=1.8, increasing to 40-45% at $\overline{n}_{e19}$=3.5. Thus these scans varied the plasma isotopic composition from H:D:T = 10:89:1 in the "deuterium" plasmas to 10:45:45 in the higher-density "tritium" plasmas, corresponding to increasing the average plasma mass $\langle A\rangle$ from 1.91 to 2.35.

The electron density profile measured just before sawteeth remained relatively broad throughout the scan, with F_{ne} varying over the range 1.3-1.7 and reaching a local maximum at about $\overline{n}_{e19}$=2.5. Similar trends

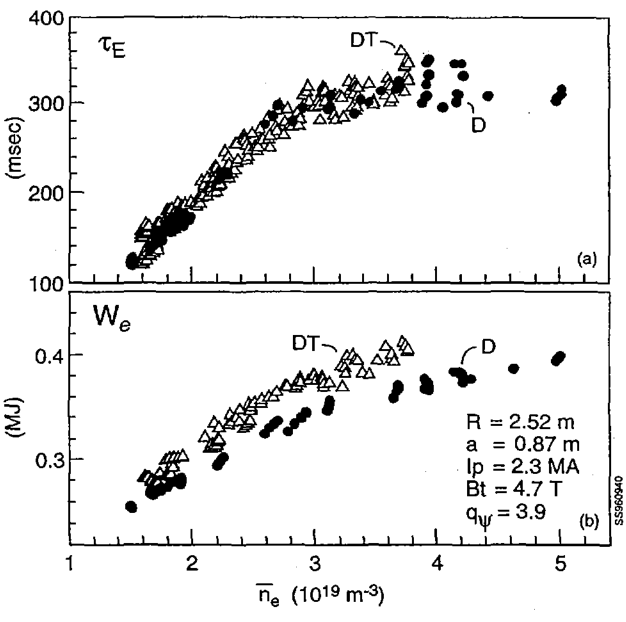

FIG. 5. (a) Global energy confinement time in ohmic D versus DT plasmas measured by magnetic diagnostics. (b) Total electron energy content from ECE T_e and interferometer n_e diagnostics.

in the density profile shape were observed previously in ohmic experiments comparing hydrogen to deuterium [25]. Z_{eff} inferred from visible bremsstrahlung decreased from 3.0 at low density to 1.3 at high density in deuterium. Central parameters ranged from $n_{eo} = 2 - 5 \times 10^{19}$ m^{-3}; $T_{eo} = 2.2 - 4.5$ keV; and $T_{io} \approx 2$ keV, independent of density, was inferred from neutron emission.

The radiated power fraction in deuterium followed the usual trend in ohmic plasmas, increasing from 30% at low density to 50% at high density. Both visible-bremsstrahlung emission and radiated power fraction were consistently higher in the tritium plasmas compared to deuterium plasmas at the same $\overline{n}_e$, with VB emission being about 11% higher, and the radiated power fraction about 15% higher (i.e. 58% vs 50% at high density). Total hydrogenic influx was about 25% less in the DT ohmic plasmas compared to D plasmas at the same $\overline{n}_e$ or edge density. A similar isotopic effect on radiated power and edge influx was also observed in previous TFTR ohmic experiments comparing ohmic hydrogen to deuterium[25] and in ASDEX[26].

Figure 5 shows the variation of global energy confinement time with $\overline{n}_e$ for deuterium and tritium. There is no observable difference in global τ_E between the two isotopes in ohmic plasmas. Statistical analysis indicates a ratio of τ_E^T/τ_E^D of 1.01 ± 0.05 at the low-density end ($\overline{n}_{e19}$=2.0-3.5), and a ratio of 1.02 ± 0.07 at the high-density end ($\overline{n}_{e19}$=3.5-5.0). A similar analysis of the total plasma energy also shows no isotope effect, with $W_{tot}^T/W_{tot}^D = 0.98 \pm 0.04$. The 1σ variation in deuterium τ_E for fixed density in this dataset is only 4%, so if the scaling $\tau_E \propto \langle A \rangle^{0.5}$ had been obeyed in this experiment, it should have been possible to resolve the "expected" increase of $\sqrt{1.23} = 11\%$. A less than 1% isotope effect on τ_E and W_{tot} was observed in the ohmic phase preceding the start of beam injection in the L-mode studies ($\overline{n}_{e19}$=1.6-3.3), which had a 1σ variation of about 4% for each species at fixed density. Previous studies of ohmic confinement in TFTR found $\leq 10\%$ higher τ_E in deuterium compared to hydrogen in the high-density saturated regime[25], however this difference was less than the variability in performance among various deuterium density scans.

Despite the absence of an isotope effect on global τ_E, there does appear to be a clear improvement in *electron energy* confinement. The core electron pressure is $10 \pm 4\%$ higher in the tritium plasmas for the same $\overline{n}_e$. As shown in Fig. 5b, the total stored electron energy, W_e, is $11 \pm 2\%$ larger in tritium at high density ($\overline{n}_{e19} \geq 2.5$), and the ratio of W_e to ohmic heating power is $17 \pm 6\%$ larger. The constancy of W_{tot} measured by the magnetic diagnostics in DT versus D plasmas, coupled with the increased W_e measured kinetically, implies that total ion energy must have decreased in tritium. Part of this decrease may be attributed to increased dilution in the tritium plasmas; Z_{eff} is 0.2 higher in tritium at high density and 0.1-0.7 higher at low density, corresponding to a change in dilution ($\Delta n_i/n_e$) of

8% at low density and 4% at high density. Lacking measured T_i profile measurements in the ohmic plasmas, we cannot determine whether local χ_i changed between D and DT ohmic plasmas.

7. High ℓ_i Regime

The "high-ℓ_i" plasma regime is created by a special plasma growth technique in the ohmic phase to increase the central current density followed by strong beam injection[6], and has density and temperature profile

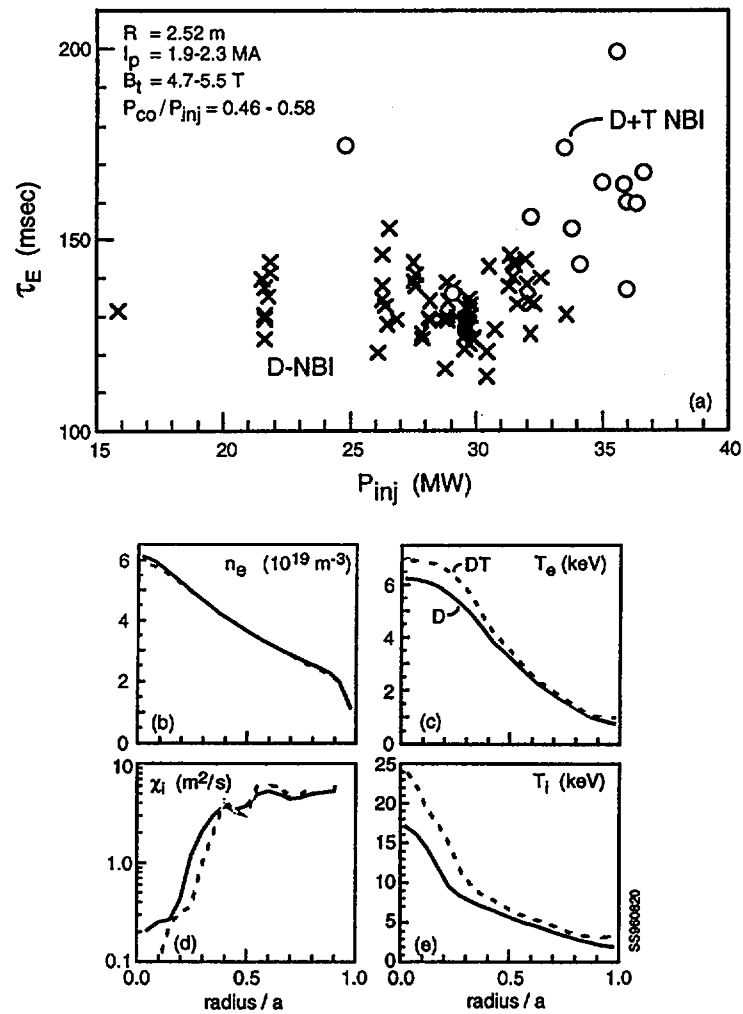

FIG. 6. (a) Energy confinement time at time of peak stored energy in the high-ℓ_i regime. Plasma conditions were R = 2.52 m, I_p = 2.25 MA, B_t = 5.1 T, q_ψ = 4.3, and P_{co}/P_{inj} = 0.48. (b–e) Measured density and temperature profiles and inferred χ_i for matched D and DT plasmas with P_{inj} = 26–29 MW.

shapes similar to supershots. A strong isotope effect has been observed in the high-ℓ_i regime: it occurs in high ℓ_i plasmas as a 20% increase in global τ_E, a 15% increase in central T_e, and a 40% increase in central T_i. For the comparison shown in Fig. 6, the density profiles are almost identical while the central ion temperature increases from 17 to 24 keV in the DT discharge, indicating significantly improved core ion confinement. Kinetic transport analysis by the TRANSP code indicates that χ_i is reduced 30-50% in the DT plasma over the core region $r/a \leq 0.35$. These features are similar to the isotope effect observed in supershot plasmas.

8. Reverse-Shear Regime

By contrast, there appears to be little or no isotope effect on confinement in plasmas with a reverse-shear q-profile (RS), at least as measured by global stored energy and τ_E. This is surprising, since the plasma conditions prevalent in RS plasmas are qualitatively similar to supershot plasmas: the density profile is peaked ($F_{ne} > 2$), and the central temperatures are high with $T_{io} > 20$ keV and $T_i/T_e \approx 3$.

Figure 7 plots the total stored energy as a function of heating power for RS plasmas heated with either pure D-NBI or mostly T-NBI. The 'NBI

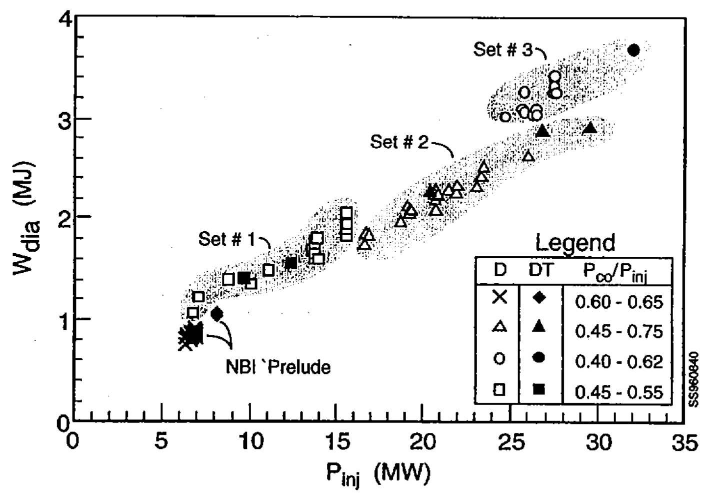

FIG. 7. Diamagnetic stored energy as a function of heating power in reverse-shear plasmas without an ERS transport barrier. All shots have I_p = 1.6 MA, B_t = 4.6 T, R = 2.59 m, with identical plasma growth and neutral beam 'prelude' [7] prior to the start of high-power beam heating. For the DT plasmas, the fraction of beam power in tritium is 100% for the 'NBI-prelude' discharges, 50–70% for Set 1, 60–100% for Set 2, and 55% for Set 3.

prelude' data points represent performance at the end of the beam prelude, when plasma conditions have reached thermal equilibrium. Set 1 comprises measurements taken 375 ms after the *end* of the high-power heating phase, during a 'postlude' of lower beam power. At this time, the plasma conditions are also nearly stationary. The higher-power data sets #2 and #3 represent measurements 275 ms and 325 ms, respectively, after the start of high-power injection, when the plasma conditions are still evolving rapidly but before any ERS transitions have occurred. There is no evidence for a significant isotope effect on confinement at *any* power in Fig. 7. Small increases in the total plasma energy during the first 100-200 ms of high-power beam heating in RS plasmas have been observed between D-NBI and T-NBI (see Fig. 9), but the plasma is strongly dominated by beam ions at that time, with $W_{beam}/W_{tot} \approx 0.7$.

The absence of an isotope effect on τ_E for RS plasmas is interesting primarily because it represents a challenge to proposed mechanisms of isotope effect in L-mode and supershot plasmas. It suggests that the q-profile or magnetic shear may be involved in the physics underlying the isotope effect.

9. Enhanced Reverse-Shear Regime

The absence of an isotope effect on confinement in reverse-shear plasmas appears to persist in plasmas which experience a transition to the enhanced reverse shear regime[7]. Figure 8 compares three identically prepared plasmas with reverse-shear q-profiles. Two of the shots had pure D-NBI throughout the discharge. The third had T-NBI+D-NBI in the ratio 3:1 during the high-power phase, then pure T-NBI during the reduced-power 'postlude' phase, when the plasma reached transport equilibrium. All three of the discharges experience an ERS transition early in the period of high-power beam injection, at about ~1.6 seconds, which persisted throughout the entire postlude phase. There is some difference in the total stored energy during the high-power phase owing to differences in heating power and onset time of the ERS transition. However in the postlude where all the plasmas have the same heating power (14.2 ± 0.1 MW), total stored energy is very similar and τ_E measured by magnetic diagnostics is virtually identical between the D and DT plasmas. The core tritium concentration in the T-NBI plasma calculated by TRANSP using particle transport models developed for supershot plasmas is approximately 40%. This tritium concentration would overpredict the measured DT neutron emission. A tritium concentration of $\geq$70% is implied by the measured DT neutron emission in the postlude.

Figure 8(c-e) shows the kinetic profiles obtained late in the postlude period. No significant differences are apparent in either the density or

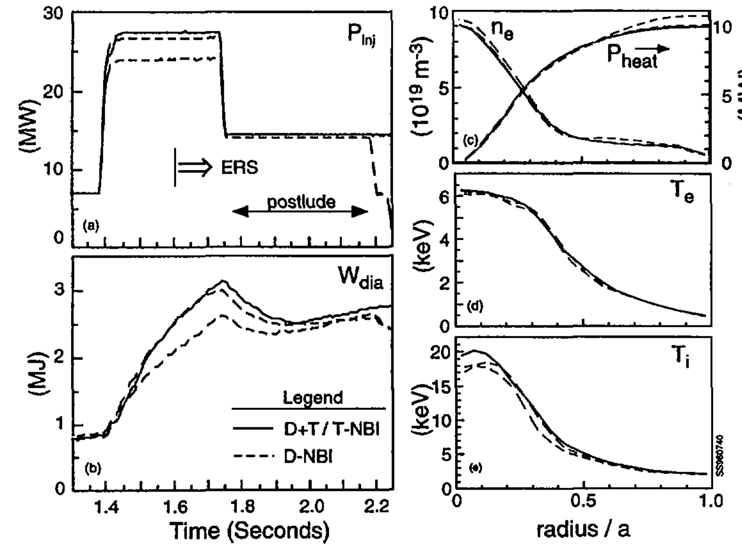

FIG. 8. (a, b) Time history of heating power and plasma energy in ERS plasmas heated with D-NBI versus T-NBI. ERS transition occurs at ~1.6 s and is sustained throughout the low-power postlude. (c–e) Profile measurements and heat deposition profile for the discharges at 2.15 s, when plasmas are nearly stationary.

temperature profiles. Since the heating profiles were also similar for these discharges, we infer that local transport is not materially changed by isotope in these plasmas. As is typical of the ERS regime, core ion energy confinement is very good in these plasmas, and it might be difficult to observe a further improvement due to isotope. The profiles do clearly indicate that the location of the transport barrier is the same between deuterium and tritium.

10. Isotope Scaling of the ERS Transition

In contrast to the negligible effect of isotope on energy confinement in ERS plasmas, there does appear to be a systematic trend in the conditions required to trigger an ERS transition. Under otherwise comparable conditions ERS transitions are reliably obtained at lower power in D-NBI than in T-NBI. Figure 9 plots the total plasma energy at 175 ms into the period of high-power heating and identifies plasmas which experience an ERS transition as a function of heating power with D-NBI versus T-NBI. The ensemble of plasmas illustrated in Fig. 9 was prepared with identical plasma-growth waveforms to produce a reverse-shear q-profile,

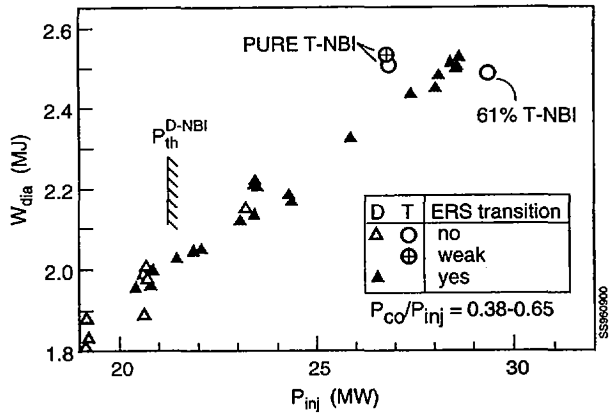

FIG. 9. Plasma stored energy as a function of beam power 175 ms after start of high power NBI in plasmas with a reverse-shear q-profile, shortly before transitions to ERS in the D-NBI plasmas. P_{th} is the threshold power for reliably obtaining an ERS transition.

near-balanced injection, similar limiter conditions, and the same timing of 'prelude' and high power neutral beams. ERS transitions were infrequent below 21 MW with D-NBI under these conditions but were reliably obtained above 23 MW. By comparison, a plasma with pure T-NBI at 27 MW had no ERS transition, another at the same power experienced a transition to ERS that was sustained for less than 200 ms. A third attempt with mixed 39%D-NBI and 61%T-NBI at a power level of 29 MW also failed to experience an ERS transition. The T-NBI plasmas fail to experience a transition despite having stored energy comparable to their companion D-NBI plasmas which do go into ERS. This behavior differs from the behavior in TFTR limiter H-modes, for which the H-mode threshold power appears insensitive to isotope[3].

By commencing high-power beam heating somewhat earlier in the plasma-growth startup, at 1.4 seconds versus the 1.7 seconds for the dataset considered above, robust and sustained ERS transitions were obtained with tritium beam concentrations up to 50-70% at power levels of 26-27 MW. Under these conditions the ERS power threshold with D-NBI was about 19 MW. Partial tritium injection with total power below 25 MW was not attempted.

The increased power threshold with T-NBI represents a useful test of proposed theories of the ERS transition mechanism based on shear-flow stabilization of microturbulence[27,28]. As shown in Fig. 10, the temperature and density profiles in the T-NBI shots do not differ markedly from the range of profiles obtained in the D-NBI plasmas, yet the D-NBI plasmas undergo a transition to ERS while the T-NBI plasmas do not. There is a tendency for slightly higher central carbon-ion temperature and higher ∇v_ϕ

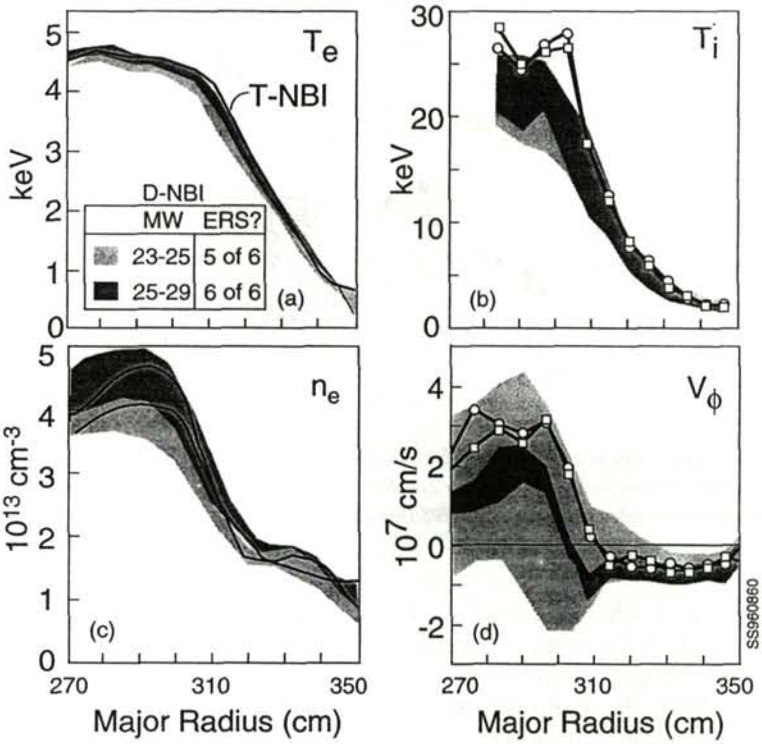

FIG. 10. Kinetic profiles for the discharges in Fig. 9. D-NBI data at 23–25 MW include two co-dominated shots ($P_{co}/P_{inj} = 0.65$) which experienced an ERS transition. Shaded regions represent range of variability in D-NBI profiles. The T-NBI plasmas with 27 MW experienced no or only weak ERS transitions.

in the T-NBI plasmas. Detailed shear-flow and growth-rate calculations are in progress to assess whether subtle differences in profile shapes could be reducing the E_r shear in the T-NBI discharges and thereby increasing the power threshold as predicted by theory.

11. Discussion

The TFTR experiments reported here comparing performance in deuterium versus deuterium-tritium operation have confirmed a favorable isotope effect on τ_E in a variety of plasma regimes, including regimes which at least superficially resemble proposed ITER plasmas: broad density profiles having $T_i \approx T_e$ with significant electron heating. On a purely empirical basis, these experiments provide experimental support for the ITER design assumption that τ_E will be larger in DT than D plasmas by a factor of order $\tau_E \propto \langle A \rangle^{0.5}$. Projections of the isotope effect to ITER would be less favorable if isotope scaling is indeed caused by sheared-flow effects, which get weaker in a large plasma. It is intriguing - and perhaps suggestive - that in both the L-mode and supershot regimes the isotope effect appears to be strongest at high heating power and high temperature. In this regard it is interesting to note that the maximum τ_E attained in quasi-stationary conditions (at the time of peak stored energy) in *any* deuterium plasma in TFTR is about 220 ms, whereas a confinement time of 330 ms, an increase of 50%, has been obtained with pure tritium-beam injection in a supershot plasma with a limiter well-conditioned with lithium pellets which attained a central ion temperature in excess of 40 keV.

But the TFTR experience has also confirmed the perplexing variability of the isotope effect that has been reported previously in other tokamaks: its strength appears to be sensitive to plasma conditions. The complete absence of an isotope effect on global τ_E in ohmic D versus DT plasmas is particularly surprising, in view of extensive studies on many other tokamaks which clearly demonstrate improved confinement in deuterium compared to hydrogen. The apparent absence of an isotope effect in reverse shear plasmas is also puzzling, given the overall similarity of the temperature and density profiles to supershot and high-ℓ_i plasmas, for which a strong isotope effect is observed. This trend suggests that the isotope effect is affected by the shape of the current profile, and represents a challenge for theoretical models of the isotope effect. Similarly, the larger heating power required to initiate an ERS transition in reverse-shear plasmas when heating with tritium beams should provide a potentially useful test of proposed models of the transition dynamics.

Identifying ρ_* scans from the L-mode and supershot isotope-scaling experiments which match all conditions except ρ_*, by varying the plasma isotope and heating power, clearly indicate improved confinement in the plasmas with larger ρ_*. This result fundamentally contradicts the scaling of transport with ρ_* observed by varying the magnetic field. Accepting the validity of the underlying Bohm or gyroBohm character of ρ_* scaling - since among other reasons it is roughly consistent with observed global τ_E scaling - one is led to conclude that the isotope effect must be governed by a fairly powerful, non-gyroBohm mechanism that leads to reduced transport for heavier isotopes *despite* their larger gyroradius. The proposed theoretical model of shear-flow modifications to ion-temperature-gradient turbulence, as embodied in the IFS-PPPL transport code, embodies such an intrinsic isotope effect through the ratio of linear growth rate to E_r shearing rate. Quantitatively, it reproduces the observed isotope effect in L-mode plasmas reasonably well. Interestingly, the model suggests that E_r-shear may affect transport scaling even in the L-mode regime, extending well beyond its previously appreciated role in controlling transport in enhanced confinement regimes such as H-modes, VH-modes and ERS plasmas.

Acknowledgements

We are grateful for the support of R. Hawryluk and K. McGuire, the dedicated performance of the TFTR technical staff, and for computational services by T. Gibney, M. Thompson, and R. Wieland. This work was supported by U.S. Department of Energy Contract NO. DE-AC02-76-CHO-3073.

REFERENCES

[1] ZARNSTORFF, M.C., et al., in Plasma Physics and Controlled Nuclear Fusion Research 1994 (Proc. 15th Int. Conf. Seville, 1994), Vol. 1, IAEA, Vienna (1995) 183.
[2] SCOTT, S.D., et al., Phys. Plasmas **2** (1995) 2299.
[3] BUSH, C.E., et al., Phys. Plasmas **2** (1995) 2366.
[4] BUSH, C.E., et al., Plasma Phys. Control. Fusion **38** (1996) 1353.
[5] ROGERS, J.H., et al., IAEA-CN-64/EP-2, these Proceedings, Vol. 3.
[6] SABBAGH, S.A., et al., IAEA-CN-64/AP2-17, this volume.
[7] LEVINTON, F.M., et al., Phys. Rev. Lett. **75** (1995) 4417.
[8] LEVINTON, F.M., et al., IAEA-CN-64/A1-3, this volume.
[9] JOHNSON, D., et al., in Controlled Fusion and Plasma Heating (Proc. 17th Eur. Conf. Amsterdam, 1990), Vol. 14B, Part I, European Physical Society, Geneva (1990) 114.
[10] PERKINS, F.W., et al., Phys. Fluids B **5** (1992) 477.
[11] PETTY, C.C., et al., Phys. Rev. Lett. **74** (1995) 1763.
[12] PETTY, C.C., et al., Phys. Plasmas **2** (1995) 2342.
[13] JET TEAM, in Plasma Physics and Controlled Nuclear Fusion Research 1992 (Proc. 14th Int. Conf. Würzburg, 1992), Vol. 2, IAEA, Vienna (1993) 161.
[14] SYNAKOWSKI, E.J., et al., in Controlled Fusion and Plasma Physics (Proc. 22nd Eur. Conf. Bournemouth, 1995), Vol. 19C, Part III, European Physical Society, Geneva (1995) 13.
[15] BURRELL, K., et al., Plasma Phys. Control. Fusion **31** (1989) 1649.
[16] KOTSCHENREUTHER, M., DORLAND, W., BEER, M.A., HAMMETT, G.W., Phys. Plasmas **2** (1995) 2381.
[17] HAHM, T., BURRELL, K., Phys. Plasmas **2** (1995) 1648.
[18] ERNST, D.R., et al., Notched velocity profiles, the radial electric field, and transport barriers in TFTR supershots (in preparation).
[19] HOULBERG, W.A., Oak Ridge Natl Lab., TN, personal communication.
[20] BIGLARI, H., DIAMOND, P., TERRY, P., Phys. Fluids B **2** (1990) 1.
[21] WALTZ, R., KERBEL, G., MILOVICH, J., HAMMETT, G., Phys. Plasmas **2** (1995) 2408.
[22] WALTZ, R., KERBEL, G., MILOVICH, J., Phys. Plasmas **2** (1995) 2687.
[23] STIX, T.H., Nucl. Fusion **15** (1975) 737.
[24] SKINNER, C.H., et al., in Plasma Surface Interactions in Controlled Fusion Devices (Proc. 12th Int. Conf. St. Raphael, France, 1996), J. Nucl. Mater. (in press) and Rep. PPPL-3188, Plasma Physics Lab., Princeton Univ., NJ.
[25] BARNES, C.W., et al., Phys. Plasmas **3** (1996) 4521.
[26] BESSENRODT-WEBERPALS, M., et al., Nucl. Fusion **31** (1991) 155.
[27] DIAMOND, P.H., et al., On the dynamics of transition to enhanced confinement in reversed magnetic shear discharges, Phys. Rev. Lett. (in press).
[28] HAHM, T.S., et al., IAEA-CN-64/D1-2, these Proceedings, Vol. 2.

DISCUSSION

K. LACKNER: How does your experience with hydrogen plasmas fit into your observations with deuterium and tritium?

S.D. SCOTT: Confinement scaling has been studied in NBI heated hydrogen versus deuterium L mode plasmas using deuterium beam injection of up to 6 MW (see Ref. [25]). Compared with the hydrogen plasmas, the deuterium plasmas achieve 20% higher total stored energy and 10% higher thermal energy, with most of the difference arising in the electron energy content. This represents a somewhat stronger isotope effect than observed in deuterium versus tritium L mode plasmas at comparable heating power.

G. BATEMAN: One of the explanations for the decrease of χ_i with increasing isotope mass has to do with the effect of impurities on ITG modes. Was there any change in the impurity profile in reversed shear discharges as the hydrogen isotope was changed?

S.D. SCOTT: The average Z_{eff} deduced from single-chord bremsstrahlung measurements is similar in deuterium and tritium reversed shear plasmas. Analysis of the radial profile of the impurity content is in progress.

CONFINEMENT
AND
WAVES, DISRUPTIONS AND INSTABILITIES

(Poster Session AP1)

TANGENTIAL CT INJECTION AND 1.5 CYCLE AC OPERATION EXPERIMENTS ON STOR-M

C. XIAO, O. MITARAI[1], A. HIROSE, W. ZAWALSKI, D. WHITE,
E. FURKAL, D. McCOLL, R. RAMAN[2], R. DÉCOSTE[3],
B.C. GREGORY[3], F. MARTIN[3]
Plasma Physics Laboratory,
University of Saskatchewan,
Saskatoon, Saskatchewan, Canada

Abstract

TANGENTIAL CT INJECTION AND 1.5 CYCLE AC OPERATION EXPERIMENTS ON STOR-M.

In the STOR-M tokamak, tangential injection of a low mass compact torus (CT) has resulted in doubling of the electron density and reduction in both the loop voltage and H_α radiation. Numerical calculation suggests that deeper penetration can be achieved if the initial CT magnetic dipole is aligned with the velocity. Successful AC operation with 1.5 cycles has also been achieved in STOR-M. It has been found that plasma position and density control is crucial to achieve a smooth reversal of ±18 kA plasma current.

1. Tangential CT Injection Experiments

1.1. Introduction

Conventional fueling methods (e.g., pellet injection) may be inadequate to fuel directly the core of a reactor-grade tokamak. Perkins *et al.* and Parks proposed to achieve controlled central fueling of a large tokamak by injection of accelerated compact tori [1]. This method has several advantages including a high fuel burn-up rate and feasibility of central density profile control. A disruption-free injection experiment was conducted on TdeV at 1.5 T toroidal magnetic field [2]. The goal of the University of Saskatchewan Compact Torus Injector (USCTI) project is to investigate and optimize interaction between CT and tokamak plasmas at various injection angles on the STOR-M tokamak.

1.2. CT Plasma Parameters

A CT is a high density plasmoid confined by embedded poloidal and toroidal magnetic fields of approximately equal strength. The USCTI has a coaxial configuration similar to the Marshall gun and consists of formation, compression, and acceleration sections. For disruption-free injection in the small

---

[1] Kyushu Tokai University, Kumamoto, Japan.

[2] Canadian Fusion Fuels Technology Project, Mississauga, Ontario, Canada.

[3] Centre canadien de fusion magnétique, Varennes, Quebec, Canada.

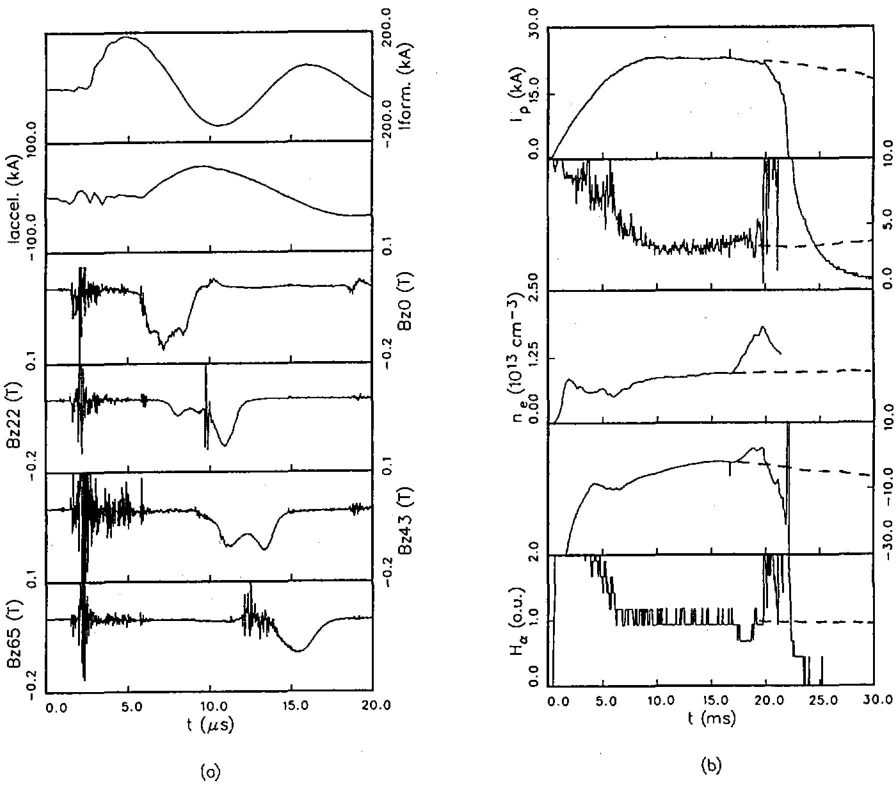

FIG. 1. (a) CT discharge currents and magnetic field signals. From top: formation current, acceleration current and poloidal magnetic fields at z = 0, 0.22, 0.43 and 0.65 m. (b) Tokamak discharge parameters after CT injection. From top: plasma current, loop voltage, electron density, horizontal position, and H_α radiation. Dashed lines indicate waveforms without CT injection.

STOR-M tokamak, low mass CTs of approximately 1 μg have been produced by fast formation and acceleration discharges and by careful control of gas puffing through-put. Measurements using magnetic probes and a He-Ne laser interferometer indicated the following typical CT parameters: $n_{\rm CT}$ (density) = $(1-4)\times 10^{21}$ m^{-3}, $B_{\rm CT}$ (magnetic field) = 0.1 T, and $V_{\rm CT}$ (velocity) = 120 km/sec. CT dimensions at the exit of the USCTI are: r_i (inner radius) = 0.018 m, r_o(outer radius) = 0.05 m, and L (length) $\sim$ 0.15 m. Figure 1(a) shows CT discharge current waveforms and poloidal magnetic fields measured at the axial locations $z = 0, 0.22, 0.43, 0.65$ m. The delay and width of the magnetic signals allow estimates of both the CT velocity and length.

1.3. Effects of CT Injection into STOR-M

The CT injection experiments were performed at a fixed injection angle of 27° with respect to the horizontal normal at the entrance to the tokamak vacuum chamber. The injection direction is along the plasma current. The discharge parameters of the STOR-M tokamak are: $R = 0.46$ m, $a = 0.12$ m, $\bar{n}_e = 1 \times 10^{19}$ m^{-3}, $I_p = 25$ kA, $V_l \sim 3$ V, and $B_t = 0.7$ T. Both the tokamak and injector were operated with hydrogen plasma.

Figure 1(b) shows the waveforms of a tokamak discharge with CT injection at $t = 16.5$ msec. The particle inventory in the CT is estimated to be 50% of the tokamak particle inventory during a normal discharge. After CT injection, the line averaged electron density, measured along the central vertical chord, increases immediately at a rate of $\sim 3 \times 10^{18}$ m^{-3}/sec from 9×10^{18} m^{-3} to 1.8×10^{19} m^{-3}. During the density rising phase, no significant change in plasma current (I_p) is observed. The loop voltage (V_l) remains intact immediately after CT injection and then exhibits a brief drop just before the onset of minor disruptions at $t = 20$ msec. The voltage drop suggests the signatures of current drive and/or plasma heating. The plasma horizontal displacement (ΔH) tends to be outward due to the increased poloidal beta value and a slow response

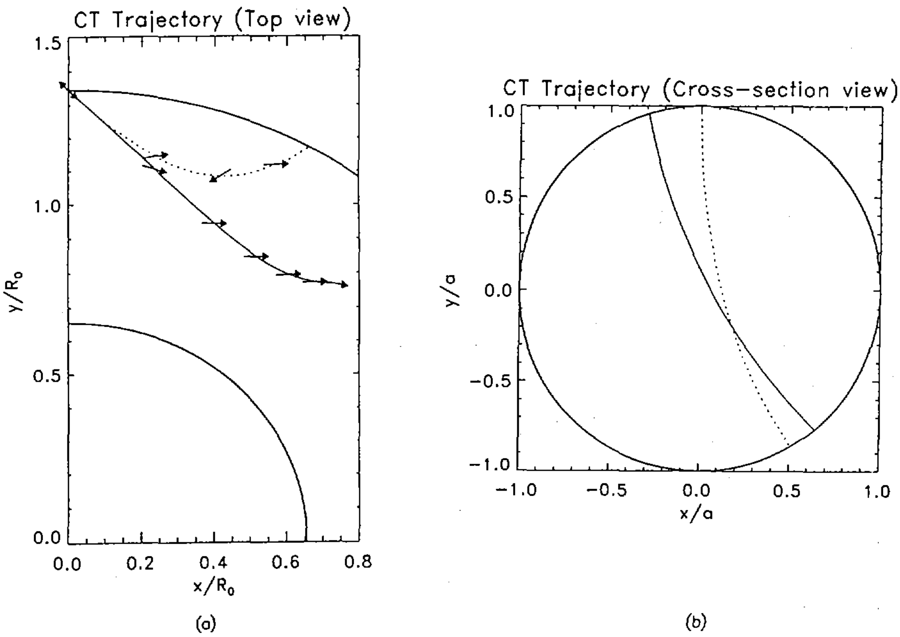

FIG. 2. (a) Horizontal parallel (solid line) and anti-parallel (dotted line) injection at an injection angle of $3\pi/4$ with respect to the tokamak normal direction. Arrows indicate the magnetic dipole orientations at normalized times separated by $\Delta t = 0.4$. (b) Center (dotted line) and off-center (solid line) vertical injection. R_0 in (a) is the major radius and a in (b) the minor radius.

of the position feedback control system. The H_α radiation level decreases for approximately 1.5 msec following CT injection and then returns to its nominal level. These observations are similar to the signatures associated with H-mode (improved confinement) operation induced by either a short current pulse or plasma biasing observed earlier in STOR-M [3].

1.4. Numerical Simulation of the CT Trajectory in a Tokamak

To determine optimum CT injection angle relative to the toroidal magnetic field, numerical simulations have been carried out to follow CT trajectories. In our simplified model, the Lagrangian associated with a CT [4] includes the following terms: a) CT translational and rotational kinetic energy, b) interaction between CT magnetic dipole and tokamak toroidal field, c) Alfvén wave drag, and d) retarding force due to the tokamak toroidal magnetic field gradient (not included in Ref. [4]). The result shown in Fig. 2(a) indicates that parallel injection (the angle between the initial CT magnetic dipole moment and the tokamak toroidal magnetic field is smaller than $\pi/2$, solid line) achieves deeper penetration than anti-parallel injection (dotted line) for horizontal injection (clockwise toroidal magnetic field direction is assumed in the calculation). In the case of vertical injection (Fig.2 (b)), off-diameter injection facilitates central penetration and the CT trajectory is independent of the initial magnetic dipole orientation (parallel or anti-parallel with respect to the initial velocity).

2. AC Operation Experiments

2.1. Introduction

Alternating current (AC) operation of a tokamak [5] is an attractive operating scenario, because the inductive current drive is highly efficient, reliable, technically simple and independent of the plasma density. Previous experiments [5-7] were limited to two half-cycle AC operation with one current reversal. For establishing feasibility of quasi-steady AC operation, experiments with multiple cycles are desired.

In the previous one cycle AC experiments on STOR-M, a smooth plasma current reversal with zero dwell time has been achieved. However, the negative plasma current phase suffered from disruption after the current peak due to limitations of the position feedback control system.

In recent experiments, a new ohmic heating circuit with two voltage reversible and one irreversible electrolytic capacitor banks was employed. The plasma position monitor and vertical field feedback control system were also modified to handle both the positive and negative plasma currents.

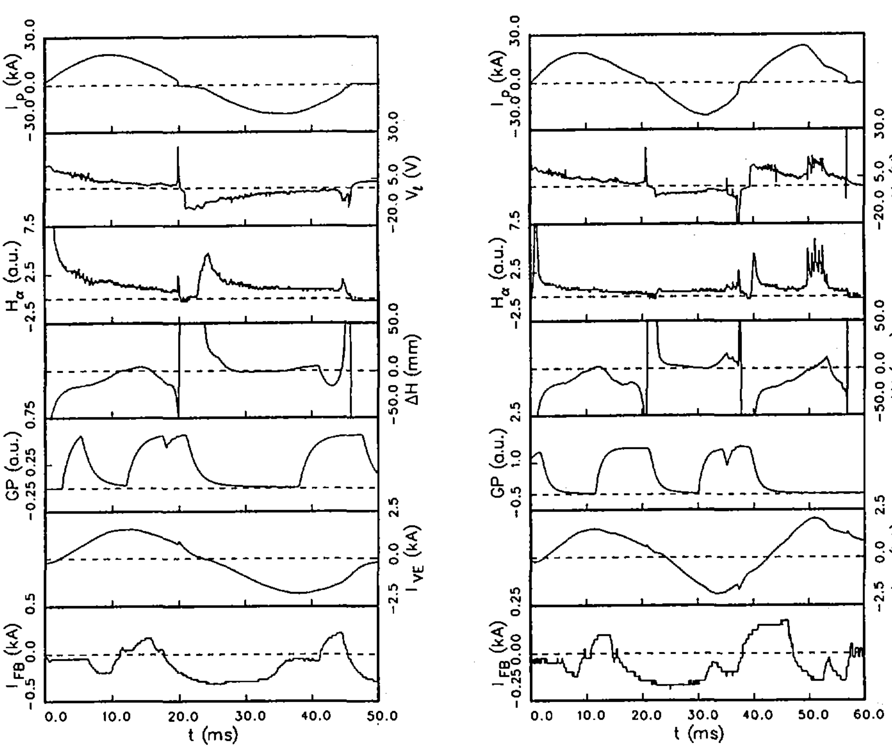

(a) (b)

FIG. 3. (a) Complete one cycle AC operation. From top: plasma current, loop voltage, H_α radiation, horizontal position, gas puffing control signal, vertical equilibrium field current, and feedback position coil current; (b) 1.5 cycle AC operation (same notation as in (a)).

2.2. Complete 1.0 Cycle AC Operation

In the one cycle AC operation experiments, additional bias voltage was added onto the plasma position monitoring circuit to optimize the plasma position during the negative plasma current phase. The disruption reported in Ref. [6] can now be avoided.

Figure 3 (a) shows waveforms of a one cycle AC discharge in which a plasma current (I_p) of +18 kA reverses its polarity to -18 kA. ΔH is proportional to the plasma position displacement with positive/negative signal indicating an outward/inward shift. A voltage pulse was added at 41.7 ms, just before the second current termination, corresponding to the peak in the feedback control current, I_{FB}, at the same time. The purpose of this pulse is to maintain a proper plasma position for a gradual current termination. Control of plasma density by preprogrammed gas puffing (GP) pulses is also crucial for smooth current reversal and termination.

The plasma current had a dwell time during the current reversal while the loop voltage (V_l) exhibited a positive spike before the current reversal. Further optimization of operating parameters, such as gas puffing and bias voltage pulse in the feedback control signal, is still needed. It is noted that the plasma has a soft current termination at the end of the second half-cycle, which is a prerequisite for 1.5 cycle AC operation.

2.3. 1.5 Cycle AC Operation

Figure 3 (b) depicts the temporal evolution of 1.5 cycle AC operation. Application of a voltage pulse at 37.1 msec is required to shift the plasma inward for soft landing of the negative current and to provide a correct vertical field for establishing the third half-cycle. During the third half-cycle, the plasma outward shift results in the plasma column scraping the limiter at $t = 50$ msec. The scraping causes minor disruptions evident from the bursts in both the loop voltage and H_α radiation. Further optimization of operation parameters will be attempted to remove the dwell time during the current reversal and to obtain a smooth current in the third half-cycle.

3. Conclusions

Tangential CT injection of a low-mass CT into the STOR-M tokamak is followed by prompt density increase at a rate of 3×10^{18} m^{-3}. The peak density after CT injection is twice the nominal density level. Loop voltage drop and reduction of H_α radiation level have also been observed. Numerical simulation suggests that the penetration depth of a CT in a tokamak is dependent (independent) of the initial CT magnetic dipole orientation in horizontal (vertical) injection. Successful 1.5 cycle AC operation with ± 18 kA plasma current has also been achieved in STOR-M by plasma position and density control.

ACKNOWLEDGEMENTS

Technical assistance provided by J. Ratzlaff, P. Balon, B. Chomyshen and G. Ehlert is acknowledged with gratitude.

This work was sponsored by the Natural Sciences and Engineering Research Council of Canada, Canadian Fusion Fuels Technology Project and the National Fusion Program of Canada. Supports for AC experiments from the Grant-in-Aid for Scientific Research from the Ministry of Education, Science, Culture and Sports, Japan, and Japan Society for the Promotion of Science are also acknowledged.

REFERENCES

[1] PERKINS, L.J., HO, S.K., HAMMER, J.H., Nucl. Fusion **28** (1988) 1365; PARKS, P.B., Phys. Rev. Lett. **61** (1988) 1364.

[2] RAMAN, R., et al., Phys. Rev. Lett. **73** (1994) 3101.

[3] XIAO, C., et al., in Plasma Physics and Controlled Nuclear Fusion Research 1992 (Proc. 14th Int. Conf. Würzburg, 1992), Vol. 1, IAEA, Vienna (1993) 417.
[4] BOZHOKIN, S.V., Sov. J. Plasma Phys. **16** (1990) 702.
[5] MITARAI, O., et al., Bull. Am. Phys. Soc. **29** (1984) 1337;
MITARAI, O., WOLFE, S.W., HIROSE, A., SKARSGARD, H.M., Nucl. Fusion **27** (1987) 604.
[6] MITARAI, O., et al., Nucl. Fusion **36** (1996) 1335.
[7] TUBBING, B.J.D., et al., Nucl. Fusion **32** (1992) 967.

ENERGY CONFINEMENT AND H-MODE POWER THRESHOLD SCALING IN JET WITH ITER DIMENSIONLESS PARAMETERS

JET TEAM[1]
(Presented by J.G. Cordey)

JET Joint Undertaking,
Abingdon, Oxfordshire,
United Kingdom

Abstract

ENERGY CONFINEMENT AND H-MODE POWER THRESHOLD SCALING IN JET WITH ITER DIMENSIONLESS PARAMETERS.

An account is given of recent experiments carried out on JET to determine the scaling of the L-H and H-L power threshold and the dependence of the energy confinement on the dimensionless parameters ρ^*, ν^* and β.

1. INTRODUCTION

In JET a series of ELMy H-mode experiments has been undertaken in which the values of the dimensionless physics parameters are close to ITER values. Two physics aspects have been studied. The first, described in Section 2, is the scaling of the H-mode power threshold where, in addition to the previously reported work on the L-H transition [1] also the H-L back transition is studied. In particular, it is found that there is little hysteresis in the two threshold powers. In the second series of experiments, described in Section 3, the dependence of the confinement scaling upon the dimensionless parameters, ρ^* (larmor radius $\equiv T^{1/2}/Ba$) , ν^* (collisionality $\equiv na/T^2$) and β ($\equiv nT/B^2$) is examined in turn. The dependence of energy confinement with the parameter ρ^* is obtained for a larger range of ρ^* and at higher β's than studied previously [2],[3]. The dependence of τ_ε is again found to be close to gyro-Bohm and in agreement with the ITERH93-P [4] scaling expression which is being used to predict the ITER confinement time. A similar behaviour was first found on DIII-D for low q ELMy H-modes [5]. The dependence of τ_ε with ν^*, the collisionality, is also found to be in agreement with the ITERH93-P expression, whilst the scaling with β is found to be very weak in contrast to the strong scaling with β of ITERH93-P. The reasons for this discrepancy and the implications of the results of Sections 2 and 3 are discussed in Section 4.

2. H-MODE THRESHOLD SCALING STUDIES

The studies reported in reference [1] have continued in the same ITER like JET geometry R = 2.9m, a = 0.92m, κ = 1.7, $q_{\psi 95}$ = 3.2, δ = 0.2. The current and toroidal fields ranged from 0.83MA/0.83T to 3MA/3T. The scaling of L-H power

[1] See Appendix to IAEA-CN-64/O1-4, this volume.

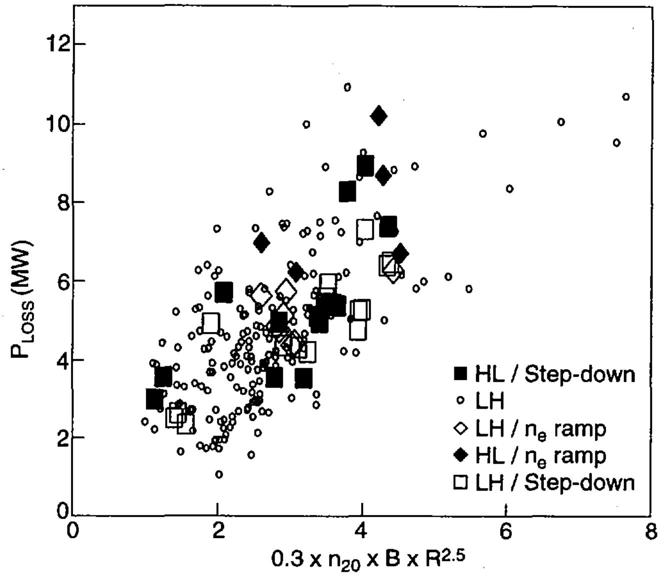

Fig.1 The loss power $P_{input} - \dot{W}$ versus $0.3\, n_{20} B R^{2.5}$ ($\times 10^{20}$ m^{-3} T $m^{2.5}$). The open symbols are for the L-H transition and the solid symbols are for the H-L transition, the rectangles are the power step down experiments, the diamonds are for the density ramp experiments, and the circles are power staircase experiments.

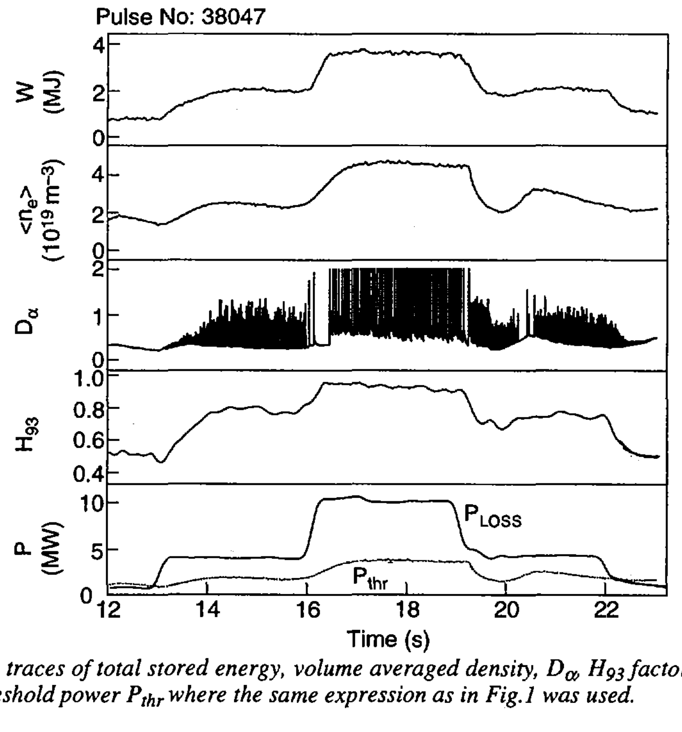

Fig. 2 Time traces of total stored energy, volume averaged density, D_α, H_{93} factor, and P_{loss} and the threshold power P_{thr} where the same expression as in Fig.1 was used.

threshold with density and toroidal field was found to be the same in the Mk IIA divertor as that of the Mk I divertor. However the range of density and field has been increased particularly at the low density end. The data obtained in Mk IIA is shown in Fig.1 versus one of the dimensionally correct forms of the threshold scaling used by F. Ryter and the ITER data base group [6]. As in Mk I there is a departure from linearity of the threshold with density at both low and high densities. However, at the low density end there is no increase in the threshold power at very low densities seen in some machines. Several different geometrical configurations have also been assessed and it has been found that there is no significant change in the threshold.

Two types of experiments have been performed on the H-L back transition: (a) power step-down experiments and (b) density ramp experiments. An example of a power step-down pulse is shown in Fig.2. The NBI input power level was varied in three steps. Soon after the onset of the first 4MW step, the D_α signal indicates the presence of an H-mode by the very high frequency transition ELMs (>100 Hz). One second after the start of the heating, the stored energy and density reach steady values and the confinement enhancement factor H_{93} relative to ITERH93-P has a value ~0.8. At t=16s the power is further increased to 10MW, and as a result the character of the ELMs changes to the type I with a frequency ~20 Hz. During this period H_{93} increases to 0.95. After a steady state is achieved the power is switched down to the starting value (4MW) and the nature of the ELMs then changes back to the transition type. As a consequence, H_{93} drops to around 0.8. Finally, when the NBI power is switched off the H-mode is lost at a similar loss power to that which was required to achieve the L-H transition.

Thus there is no hysteresis in the L-H/H-L threshold in these step-down pulses. The same is found to be the case for the density ramp experiments. As the density is increased eventually the transition ELMs appear and H_{93} drops. The H-mode then disappears at a power level close to that of L-H transition for the same density. The threshold power for the H-L transition is shown in Fig.1 for both methods of obtaining a back transition along with the L-H transition data for a whole series of fields and densities from the present campaign.

3. DEPENDENCE OF τ_E ON THE DIMENSIONLESS PARAMETERS ρ^*, ν^* AND β.

Three separate groups of experiments were carried out to determine the dependence of confinement on ρ^*, ν^* and β. The plasma geometry was the same as in Section 2 and only pulses with Type I ELMs are studied in this paper. To adjust the density, only moderate gas puffing was used, the main particle source being from NBI which was the main heating source also.

The results are compared with the ITERH93-P scaling expression which can be written in dimensionless form:

$$B\tau_{th} \propto \rho^{*-2.7}\,\nu^{*-0.28}\,\beta^{-1.2} \qquad (1)$$

where the parameters ρ^*, ν^* and β are defined in terms of their average values as $\rho^* \equiv W_{th}^{1/2}/n^{1/2}\,a^{3/2}$, $\nu^* \equiv n^3 a^7/W_{th}^2$ and $\beta \equiv W_{th}/B^2 a^3$, with W_{th} being the total thermal stored energy, n the volume averaged density and a the minor radius.

3.1 ρ^* scaling experiments

Three sets of experiments have been completed at different β's and collisionalities, close to those expected in ITER. These are listed in Table I. To keep ν^* and β fixed, the density should be proportional to $B^{4/3}$ and the stored

Table I. ρ^* scans

a) $\beta_{nth} \sim 2$ $\nu^*/\nu^*_{ITER} = 2.8$

Pulse No.	B	I	n	P	τ_{th}	$B\tau_{th}/\rho^{*-2.7}$
37380	1	1	2.2	7	0.14	1
37375	2	2	5.6	15	0.26	1.04

b) $\beta_{nth} \sim 1.6$ $\nu^*/\nu^*_{ITER} = 1$

Pulse No.	B	I	n	P	τ_{th}	$B\tau_{th}/\rho^{*-2.7}$
38429	1.5	1.5	2.5	10	0.20	1
38427	2.6	2.6	5.0	21	0.30	0.97

c) $\beta_{nth} \sim 1.5$ $\nu^*/\nu^*_{ITER} = 2.3$

Pulse No.	B	I	n	P	τ_{th}	$B\tau_{th}/\rho^{*-2.7}$
37379	1	1	2	4.4	0.19	1
38047	2	2	4.8	10	0.34	1.03
37944	2.6	2.6	6.8	12.5	0.43	1.05

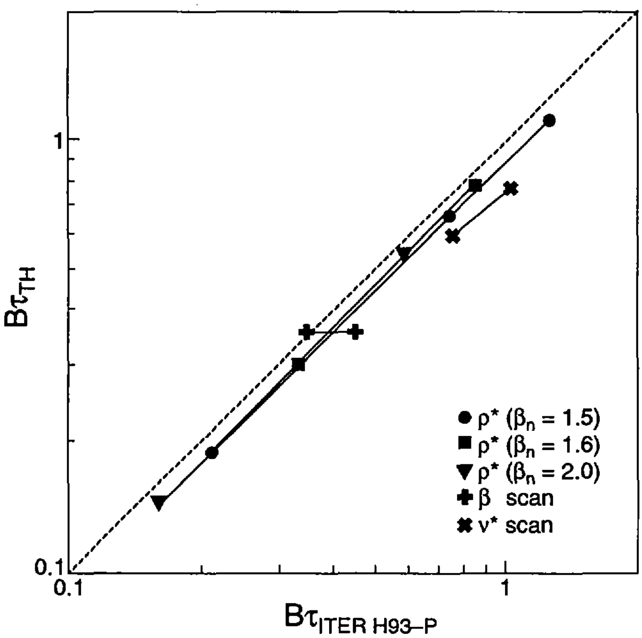

Fig.3 The normalised confinement time $B\tau_{th}$ versus $B\tau_{ITERH93\text{-}P}$. The three ρ^* scans are indicated by solid triangles, squares and circles. The β scan is indicated by the crosses and the ν^* scan by the diagonal crosses.

Table II. ν* and β scans

	ν* scan		β scan	
Pulse No.	37718	37728	38407	38415
B (T)	2	2.6	1.5	1.7
I (MA)	2	2.6	1.5	1.7
<n> ($10^{19}m^{-3}$)	5	5	2.7	4.1
P (MW)	10	16	6.5	16.5
W_{th} (MJ)	3.0	4.8	1.5	3.4
τ_{th} (s)	0.3	0.3	0.24	0.21
$B\tau_{th}$	0.6	0.78	0.36	0.35
ν^*/ν^*_{ITER}	3.4	1.3	2.1	1.5
β_{nth}	1	1	1.2	2.2

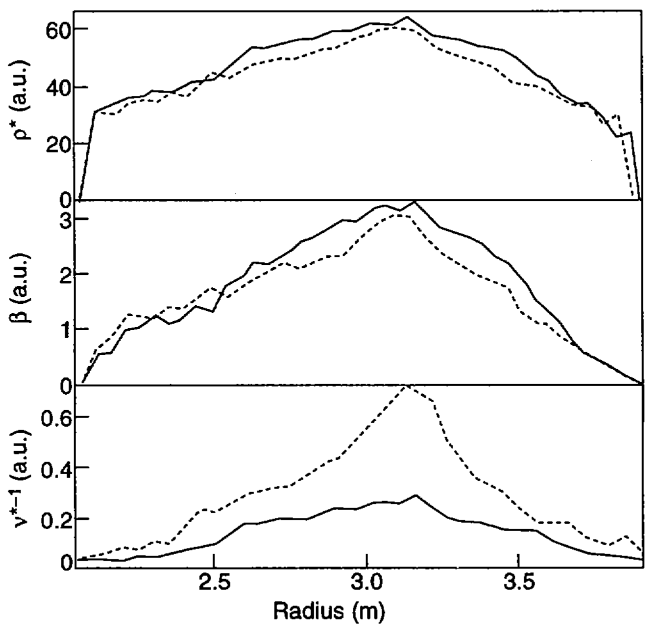

Fig. 4 Radial profiles of ρ, β and ν* for the pulses in the ν* scan.*

energy proportional to B^2. From Table I it can be seen that this has been approximately achieved and that the resulting dimensionless confinement $B\tau_{th}$ follows the $\rho^{*-2.7}$ scaling of ITERH93-P, that is the scaling is close to gyro-Bohm. The three ρ^* scans are shown against the scaling expression in Fig.3; H_{93} is greater than 0.9 for all of the pulses.

3.2 ν^* scaling experiments

Here β and ρ^* were kept fixed and this means that n = const. and $W_{th} \propto B^2$. The results are shown in Table II. The profiles of ρ^* and β are also well matched for these two pulses as can be seen in Fig.4. From Table II it can be seen that $B\tau_{th}$ scales as $\nu^{*-0.27}$ in close agreement with the ITERH93-P scaling.

3.3 β scaling experiments

Here ρ^* and ν^* were kept fixed. This means that $n \propto B^4$ and $W_{th} \propto B^6$. The results of these experiments are also given in Table II. A preliminary analysis of the data gives a very weak dependence of τ_ε upon β with $B\tau_\varepsilon \propto \beta^{-0.05}$, in marked contrast to the strong dependence of the ITERH93-P scaling expression. A similar result was recently found on DIII-D [7].

A comparison of both the ν^* and β dependence with the ITERH93-P scaling expression is given in Fig.3. The ν^* dependence follows the scaling expression whilst this is clearly not the case for the β dependence.

4. DISCUSSION

The main outcome of the threshold studies is that there are really two power thresholds. The first is the power requirement to reach steady state transition (or threshold) ELMs. There is a second power threshold for steady state periodic type I ELMs. In the transition ELM phase, the confinement improves continuously as the power is increased and the ELM frequency decreases. This phase is completely reversible and there is no hysteresis as the power is reduced. This is very similar to the situation in radiative divertors such as the CDH mode [8] where there is a smooth transition between the L and H states.

In the type I ELM phase, H_{93} reaches a higher value and is constant until the MHD β limit is reached. When the power falls significantly in the type I ELM phase, the transition ELM phase with lower confinement returns. Hence there is apparently no hysteresis in the type I ELM phase either. This latter behaviour may be different in JET to that of other devices due to the high temperature walls and high pumping which are very effective at controlling recycling in JET.

The dimensionless physics parameter scans in ρ^*, ν^* and β confirm the validity of the ITERH93-P scaling expression as far as its ρ^* and ν^* dependence is concerned. However, the β dependence seems not correctly described. There are several possible explanations for this discrepancy and these are currently being investigated. One obvious difference between determining the β scaling as compared with the ρ^* and ν^* scaling is that the range in β is much narrower than either the ρ^* or ν^* range. It is also possible that some data close to the MHD β limit has been included in the ITER data base from which ITERH93-P is derived.

If this lack of β scaling is confirmed by other experiments, the prediction of the ITER confinement time will be increased by about 10% at the β of the ignited ITER.

REFERENCES

[1] RIGHI, E., CAMPBELL, D.J., CORDEY, J.G., et al., in Controlled Fusion and Plasma Physics (Proc. 22nd Eur. Conf. Bournemouth, 1995), Vol. 19C, Part II, European Physical Society, Geneva (1995) II-073.
[2] BALET, B., CAMPBELL, D.J., CHRISTIANSEN, J.P., et al., Ibid., Part I, I-009.
[3] CORDEY, J.G., et al., Proceedings of the H-mode workshop PPPL (1995).
[4] ITER H-MODE DATABASE WORKING GROUP, in Controlled Fusion and Plasma Physics (Proc. 20th Eur. Conf. Lisbon, 1993), Vol. 17C, Part I, European Physical Society, Geneva (1993) 15.
[5] PETTY, C.C., et al., Phys. Plasmas **2** (1995) 2342.
[6] RYTER, F., et al., Nucl. Fusion **36** (1996) 1217.
[7] PETTY, C.C., et al., to be published in Controlled Fusion and Plasma Physics (Proc. 23rd Eur. Conf. Kiev, 1996).
[8] KALLENBACH, A., et al., in Controlled Fusion and Plasma Physics (Proc. 22nd Eur. Conf. Bournemouth, 1995), Vol. 19C, Part II, European Physical Society, Geneva (1995) II-005.

DISCUSSION

A. GIBSON: I notice that while some of your graphs show error bars, most do not. My question is: has there been a systematic sensitivity analysis of the effect of not exactly matching the quantities which are supposed to be held constant? Would such an analysis enable you to place error bars on the resulting predictions for ITER?

J.G. CORDEY: A full systematic analysis has been completed on each machine of the effect on the results of mismatches in the profiles. However, no estimate of the error on the ITER confinement time prediction has been made.

S.I. ITOH: I have a question about the discrepancy of the scalings — there may be at least two reasons for the scattering of data. One is the usual scattering, the other stems from the intrinsic plasma non-linearity.

For example, near the β limit a slight change in the parameter may cause a drastic change in the confinement. The phenomenon is thought of as a transition-like (catastrophic) event. If the database includes such data, it may be very difficult to obtain a correct prediction for the future. Is there a method for identifying such data in the database systematically?

J.G. CORDEY: Distinguishing data which had suffered a catastrophic loss of confinement would be very difficult once the data were in the database. However, the line traces of all the pulses are also available and by inspection of these time traces (such as the MHD signals) one could identify such time points and label them, so that they could be eliminated from the regressions.

W.D. DORLAND: The JET discharge used for the identity experiment with DIII-D appears to have $T_i = T_e$ exactly. Did you actually measure T_i, and therefore the toroidal rotation as well? If not, how does this influence the conclusions?

J.G. CORDEY: No, unfortunately neither T_i nor rotation profiles were measured on this pulse. However, recently the pulse has been repeated and both T_i and v_ϕ profiles measured. The T_i/T_e ratio is found to be very close to unity, as was assumed in the previous analysis, so I expect the conclusions to be unaffected.

O. KARDAUN: As far as I remember, the H mode confinement data set was checked during a working session at JET so as to exclude β limit confinement degraded discharges in the early days of its assemblage.

J.G. CORDEY: Yes, you are correct. The data in the ITER H mode database have been screened to exclude data with strong MHD fluctuations.

O. KARDAUN: According to your graph in Fig. 3, the difference between the observed and predicted $B\tau_E$ for the β scan is about 20–25%. In search of a physical reason behind this difference, not taking into account the offset effect from inverse regression, I would be particularly interested in (a) what the corresponding results would be if the ITER ELMy scaling (ITERH-92P(y)) were used instead of the ELM free scaling, and (b) whether you could state something about the ion–electron temperature ratio, T_i/T_e, and the density peakedness, $\langle n_e \rangle / \bar{n}_e$, for these two shots.

J.G. CORDEY: In answer to (a), the data have not yet been compared with the ITERH-92P(y) scaling expression; as to (b), the temperature ratio T_i/T_e is close to unity and the density profile is flat for both pulses.

IMPLICATIONS FROM DIMENSIONLESS PARAMETER SCALING EXPERIMENTS*

T.C. LUCE, C.C. PETTY, B. BALET[1], J.G. CORDEY[1]
General Atomics,
San Diego, California,
United States of America

Abstract

IMPLICATIONS FROM DIMENSIONLESS PARAMETER SCALING EXPERIMENTS.

The dimensionless parameter scaling approach is increasingly useful for predicting future tokamak performance and guiding theoretical models of energy transport. Expriments to determine the ρ_* (gyroradius normalized to plasma size) scaling have been carried out in many regimes. The electron ρ_* scaling is always "gyro-Bohm" ($\chi \propto \chi_B \rho_*$) while the ion ρ_* scaling varies with regime. The ion variation is correlated with both density scale length (L mode, H mode) and current profile. The ion ρ_* scaling in the low-q, H mode regime (where fusion power plants are expected to operate) is gyro-Bohm, which is the most favorable confinement scaling observed. New experiments in β scaling and collisionality scaling have been carried out in low-q discharges in both L mode and H mode. In L mode, global analysis shows that there is a slightly unfavorable β dependence ($\beta^{-0.1}$) and no ν_* dependence. In H mode, global analysis finds a weak β dependence ($\beta^{0.1}$) and an unfavorable dependence on ν_* ($\nu_*^{-0.35}$). The lack of significant β scaling spans the range of β_N from 0.25 to 2.0. The very small β dependence in L mode and H mode is in contradiction with the standard global scaling relations (ITER-89P: $\tau \propto \beta^{-0.52}$, ITER-93H: $\tau \propto \beta^{-1.23}$). This contradiction in H mode may be indicative of the impact on the H mode database of low-n tearing instabilities which are observed at slightly higher β_N in the β scaling expriments. For the low-q, H mode experiments, the observed scalings can be combined to yield a global scaling law $\tau_E \propto I^{6z/11} B^{(2-z)6/11} P^{-5/11} n^{3/11} a^{(31-6z)/11}$, where z is the yet unmeasured q scaling experiment. The measured β and ν_* scalings explain the weak density dependence observed in engineering parameter scans. This also shows the power of the dimensionless parameter approach, since it is possible to obtain a definitive size scaling from experiments on a single tokamak.

1. INTRODUCTION

Significant progress has been made in the last two years on applying dimensionless parameter scaling techniques to the problem of predicting and understanding tokamak energy transport. The value of this approach with respect to prediction of future machine performance is that present-day devices can operate at ignition-relevant values of the standard dimensionless parameters with the exception of ρ_*, which is the gyroradius normalized to the plasma linear size [1]. Therefore, the performance extrapolation is reduced to knowledge of a single parameter scaling which can be validated independently on many machines.

---

* This work was supported by the US Department of Energy under Contract No. DE-AC03-89ER51114.

[1] JET Joint Undertaking, Culham, Abingdon, Oxfordshire, United Kingdom.

Experiments to measure the ρ_* scaling of local transport in various operating regimes have been carried out on the DIII–D tokamak. In low-q H mode, the ρ_* scaling is "gyro-Bohm" [2], which means the net diffusivity χ scales like $\chi_B\ \rho_*$ where χ_B is the Bohm diffusivity. This gyro-Bohm scaling is qualitatively consistent with the H mode global regression scaling (ITER-93H) used by the ITER EDA for its confinement projections . For L mode plasmas, the measured global scaling lies near Bohm scaling (consistent with $\chi \propto \chi_B\ \rho_*^0$). This is consistent with the standard L mode regression scaling (ITER-89P). Two-fluid analysis showed the origin of the derivation from the expected gyro-Bohm scaling to be exclusively in the ion scaling [3,4]. Recently, high-q H mode discharges have also been shown to exhibit Bohm scaling in the ion channel [5]. The data clearly show that the deviation from gyro-Bohm scaling in the ion channel is correlated with shorter density scale length (L mode) or a current profile scale length (high-q). The physical mechanisms for this behavior are a topic of active research. Combining the most favorable confinement scaling regime (low-q H mode) and the H mode power threshold scaling, it is possible to construct a paradigm for minimizing the size of the plasma core for an ignition power balance point [6]. Extrapolating from DIII–D discharges, a plasma with 500 MW of fusion power could be sustained in the H mode against transport losses at $B = 5.7$ T, $I = 9.9$ MA, $\bar{n} = 2.0\times10^{20}\,\mathrm{m}^{-3}$, $R = 2.7$ m, and $\beta_N = 3.3$. This ignition power balance point is below the Troyon β limit and the Greenwald density limit.

In addition to ρ_* scaling experiments, scaling studies for the dimensionless parameters β and collisionality have also been carried out in both L mode and H mode. These experiments help clarify what physical processes are involved in the energy transport. In principle, a complete set of scaling experiments would define an empirical local scaling relation for transport. The experiments reported here represent a significant step in that direction, including the first reported β and collisionality scaling experiments in H mode.

2. PROOF-OF-PRINCIPLE EXPERIMENTS

A critical test of the dimensionless parameter scaling approach to transport studies is the realization of "identity" discharges — discharges on two tokamaks with widely different physical parameters, but exact matches of the dimensionless parameters. The first steps in this direction have been successfully carried out by comparing ELMing H-mode discharges on DIII–D and JET. The magnetic geometry of both machines was identical to 1% in aspect ratio, elongation, and q. The fluid dimensionless parameters ρ_*, β, and collisionality ν_* will be constant if na^2, $Wa^{-1/2}$, and $Ba^{5/4}$ are constant. The experimental match is 2%, 5%, and 3%, respectively. The proof of principle for the global confinement is whether the thermal confinement normalized to the cyclotron frequency is constant. This figure of merit agrees to within 2% for these discharges [5]. The next step is to show that the diffusivities scale appropriately ($\chi a^{-3/4}$ constant) across the plasma for both electrons and ions. Unfortunately, T_i is unavailable for the JET discharge, so it is assumed that $T_i = T_e$ and a one-fluid diffusivity $\chi \equiv (\kappa_e + \kappa_i)/(n_e + n_i)$ is used. The comparison is shown in Fig. 1. The scaled diffusivities agree to within 20% everywhere from $\rho = 0.2$–0.8. Recent JET discharges with ion temperatures will be analyzed in the near future. The present degree of agreement between the scaled JET and DIII–D plasmas provides confidence in the dimensionless scaling approach.

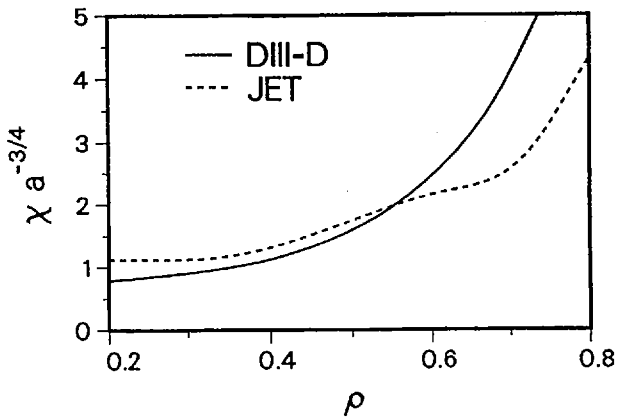

FIG. 1. Normalized one-fluid diffusivity for JET and DIII-D versus normalized radius.

3. β SCALING

Experimental results from the scaling of energy transport with β should differentiate between various proposed instability mechanisms. Most drift wave models show little enhancement or perhaps even slight reduction in transport with increasing β. On the other hand, transport models which invoke resistive MHD or magnetic fluctuations are generally expected to have strong β degradation. Standard regression analysis of global confinement databases would favor the latter. The ITER-89P L mode scaling gives $\beta^{-0.52}$, while the ITER–93H H mode scaling gives a very strong $\beta^{-1.2}$ dependence. In order to keep ρ_* and ν_* fixed while β varies, the following relations must be held for fixed plasma geometry: $n \propto B^4$, $T \propto B^2$, and $I \propto B$. This results in $\Delta\beta \propto (\Delta B)^4$. In the experiments reported here, a factor of 2 scan in β is made.

For the L mode experiment, the normalized confinement scales like $\beta^{-0.1}$. The global engineering parameters and the appropriate combinations proportional to the dimensionless parameters are shown in Table I. The density and stored energy matches are better than 10%. The normalized confinement time varies only slightly as β_N goes from 0.25 to 0.5. This is significantly weaker than the ITER–89P scaling. Preliminary two-fluid analysis shows that both fluids scale similarly.

In H mode, the normalized confinement time scales like $\beta^{0.1}$ as β_N is scanned from 1.0 to 2.0. Table I also shows the engineering and dimensionless variables for the H mode scan. The parameters were chosen to be in a regime where gyro-Bohm ρ_* scaling would be expected. The density and stored energy matches are better than 10%. This is significantly different from the β scaling in the ITER–93H scaling relation.

One speculation on the source of this difference for H mode plasmas is the effect of tearing modes at higher β_N. For the shots in the same sequence with slightly higher β_N, a $m = 3 / n = 2$ tearing mode is destabilized and the confinement can drop by up to 30%. This destabilization is attributed to neoclassical effects rather than classical $\Delta' > 0$ destabilization [7]. Since this effect depends on collisionality and aspect ratio, it would not be discriminated in the ITER regression database by windowing on β_N.

TABLE I. COMPARISON OF GLOBAL PLASMA PARAMETERS (β).

	L mode		H mode	
Parameter	Low-β	High-β	Low-β	High-β
B (T)	1.63	1.91	1.62	1.93
I_p (MA)	1.13	1.35	1.13	1.35
$\bar{n}$ ($10^{19}\,m^{-3}$)	1.8	3.7	3.4	7.2
W_{th} (kJ)	93	246	260	830
P_{tot} (MW)	0.91	2.91	1.75	6.2
τ (s)	0.102	0.084	0.150	0.134
R/a	2.68	2.67	2.76	2.77
κ	1.72	1.73	1.81	1.83
q_{95}	3.66	3.64	3.67	3.85
$\bar{n}/B^4$	0.25	0.28	0.49	0.52
W_{th}/B^6	5.0	5.1	14.4	16.1
β (%)	0.28	0.54	0.87	1.90
$B\tau$	0.17	0.16	0.24	0.26

A similar effect is unlikely in the L mode database. The source of the apparent β scaling there may be fast ion losses due to beam-driven instabilities (*e.g.*, fishbones) in the highest β_N shots.

4. COLLISIONALITY SCALING

The theoretical expectations for scaling with collisionality are less clear. Neoclassical theory gives normalized confinement inversely proportional to collisionality in the banana regime. Drift wave transport is expected to be roughly independent of collisionality in the banana regime. Both the ITER–89P L mode scaling and the ITER–93H mode scaling have a $\nu_*^{-0.28}$ dependence. In order to keep ρ_* and β fixed as collisionality varies, the following relations must hold: $n \propto B^0$, $T \propto B^2$, and $I \propto B$. This implies $\Delta\nu_* \propto (\Delta B)^{-4}$. The experiments reported here vary ν_* by a factor of 8.

For the L mode scan, the normalized confinement is almost independent of ν_*. The engineering parameters and the effective global dimensionless parameters are shown in Table II. Because of the large scan in ν_*, the effect of mismatches in ρ_* and β are minimized. The density and stored energy matches are within 10%.

For the H mode ν_* scan, the normalized confinement time drops as the collisionality increases, consistent with a $\nu_*^{-0.35}$ scaling. The H mode ν_* parameters are also given in Table II. The experiments were carried out in the low-q H mode regime

TABLE II. COMPARISON OF GLOBAL PLASMA PARAMETERS (ν_*).

Parameter	L mode		H mode	
	Low-ν_*	High-ν_*	Low-ν_*	High-ν_*
B (T)	1.91	1.14	1.91	1.14
I_p (MA)	1.37	0.81	1.35	0.8
$\bar{n}$ ($10^{19}\,m^{-3}$)	2.7	2.4	6.3	6.2
W_{th} (kJ)	228	82	930	340
P_{tot} (MW)	3.55	0.72	3.6	1.61
τ (s)	0.064	0.113	0.26	0.21
R/a	2.69	2.70	2.74	2.77
κ	1.73	1.73	1.7	1.7
q_{95}	3.56	3.60	3.84	4.055
$\sqrt{W_{th}/\bar{n}}/B$	4.9	5.1	6.4	6.5
β (%)	0.52	0.52	2.2	2.2
$B\tau$	0.12	0.13	0.50	0.24

where gyro-Bohm ρ_* scaling would be expected. The β values are similar to the ITER demonstration discharges. It is not yet clear whether this ν_* scaling is observed in both channels. The observed scaling is close to the ρ_* scaling in the ITER–93H scaling relation.

5. DISCUSSION

Converting from dimensionless variables back to engineering variables for a global confinement scaling is a straightforward algebraic manipulation. Assuming a standard power law form for the scaling relation, the power degradation and density scaling are completely determined by the ρ_*, β, and ν_* scaling. [In this paper, the collisionality ν_* is defined without q; this is the collision frequency normalized to the transit time rather than the bounce time.] For the H mode scans, the conversion to a global scaling law in engineering variables is clear because the experiments are carried out in a regime where both the electron and ion ρ_* scaling are expected to be the same. Taking the observed scalings: ρ_*^{-3} (gyro-Bohm), β^0, and $\nu_*^{-1/3}$, the following relation is obtained:

$$\tau_E \propto I^{6z/11} B^{(2-z)6/11} P^{-5/11} n^{3/11} a^{(31-6z)/11} \qquad (1)$$

where $-z$ is the q scaling in the dimensionless parameter formalism. Note that the weak density dependence observed in engineering variable scans [8] is recovered from the combination of three different scans. The rather weak power degradation is surprising. A weaker collisionality scaling than $\nu_*^{-1/3}$ would give more density scaling and more power degradation. It is important to point out that Eq. (1) also demonstrates that the dimensionless parameter scaling approach yields a definitive prediction for the size scaling from single machine experiments. By verifying the dimensionless parameter scalings independently on several machines, confidence in the size scaling can be gained while avoiding the inevitable systematic effects in multiple machine databases. If $z \equiv 11/6$ to give the standard linear current scaling, then Eq. (1) becomes

$$\tau_E \propto I^{1.0} B^{0.09} P^{-0.45} n^{0.27} a^{1.82} \qquad (2)$$

The next step is to compare these inferred engineering scaling relations with the larger set of discharges taken to find the dimensionless parameter matches to see if the experimental deviations can be described by the derived scaling relation.

The same exercise for the L–mode scans is not very straightforward, due to the variable ion ρ_* scaling. Without knowing the physical mechanism for this variation or at least an empirical characterization of it, scaling of ion transport is uncertain. Also, various heating schemes deposit power in electrons and ions in differing proportions and the exchange term is not ''dimensionally correct,'' so the fraction of power lost in electrons and ions is uncertain.

In conclusion, great progress toward the prediction and understanding of energy transport has been made by applying the dimensionless parameter scaling approach. In the next few years, it may be possible to derive a complete scaling rule by means of this approach.

6. ACKNOWLEDGMENTS

This is a report of work supported by the U.S. Department of Energy under Contract No. DE-AC03-89ER51114. We gratefully acknowledge the work of R.J. Groebner, P. Gohil, D.M. Thomas, and D.R. Baker in analyzing the CER data.

REFERENCES

[1] WALTZ, R.E., DeBOO, J.C., ROSENBLUTH, M.N., Phys. Rev. Lett. **65** (1990) 2390.

[2] PETTY, C.C., et al., Phys. Plasmas **2** (1995) 2342.

[3] PETTY, C.C., et al., Phys. Rev. Lett. **74** (1995) 1763.

[4] LUCE, T.C., PETTY, C.C., in Controlled Fusion and Plasma Physics (Proc. 22nd Eur. Conf. Bournemouth, 1995), Vol. 19C, Part III, European Physical Society, Geneva (1995) 25.

[5] PETTY, C.C., et al., in Controlled Fusion and Plasma Physics (Proc. 23rd Eur. Conf. Kiev, 1996), Vol. 20C, European Physical Society, Geneva (1996).

[6] PETTY, C.C., LUCE, T.C., Projections of Gyroradius Scaling Experiments to an Ignition Tokamak, Rep. GA-A22271, General Atomics (1996), to be published in Nucl. Fusion.

[7] LA HAYE, R.J., IAEA-CN-64/AP1-21, this volume.

[8] SCHISSEL, D.P., et al., Nucl. Fusion **34** (1994) 1401.

STATISTICAL PROPERTIES OF TURBULENT TRANSPORT AND FLUCTUATIONS IN TOKAMAK AND STELLARATOR DEVICES

C. HIDALGO, M.A. PEDROSA, B. VAN MILLIGEN, E. SANCHEZ,
R. BALBIN, I. GARCIA-CORTES
Euratom–CIEMAT Association,
Madrid, Spain

J. BLEUEL, L. GIANNONE, H. NIEDERMEYER
Euratom–IPP Association,
Garching, Germany

Abstract

STATISTICAL PROPERTIES OF TURBULENT TRANSPORT AND FLUCTUATIONS IN TOKAMAK AND STELLARATOR DEVICES.

The statistical properties of fluctuations and turbulent transport have been studied in the plasma boundary region of stellarator (TJ-IU, W7-AS) and tokamak (TJ-I) devices. The local flux probability distribution function shows the bursty character of the flux and presents a systematic change as a function of the radial location. There exist large amplitude transport bursts that account for a signifiicant part of the total flux. There is a strong similarity between the statistical properties of the turbulent fluxes in different devices. The value of the radial coherence associated with fluctuations and turbulent transport is strongly intermittent. This result emphasizes the importance of measurements with time resolution in understanding the interplay between the edge and the core regions in the plasma. For measurements in the plasma edge region of the TJ-IU torsatron, the turbulent flux does not, in general, show a larger radial coherence than the one associated with the fluctuations.

1. INTRODUCTION

For improving our understanding of the mechanisms underlying anomalous turbulent transport it is important to measure not only the fluctuation induced transport, which can account for most of the particle transport in the plasma edge region of tokamak and stellarator devices, but also the statistical properties of the time resolved turbulent flux.

The statistical properties of turbulent transport have recently been investigated in the plasma edge region of the TJ-I tokamak and TJ-IU [1, 2] and W7-AS [3] stellarator devices. These experiments have shown that a significant fraction of the local particle flux can be attributed to the presence of large and sporadic transport bursts.

In this paper, we investigate the statistical properties and the radial structure of fluctuations and particle flux in the plasma edge region of stellarator and tokamak devices. These studies could provide a useful criterion for distinguishing between different mechanisms proposed to explain fast (non-local) transport effects in tokamak and stellarator plasmas.

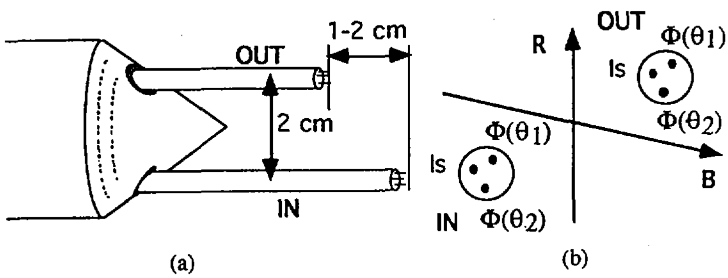

FIG. 1. Experimental set-up for radial correlation measurements: (a) design of probes; (b) location of probes in the plasma (top view).

2. EXPERIMENTAL SET-UP

Measurements of fluctuations and turbulent flux have been carried out by means of Langmuir probes in the ohmically heated TJ-I tokamak ($R = 0.3$ m, $a = 0.1$ m, $\bar{n}_e \approx (1\text{–}3) \times 10^{19}$ m^{-3}, $B_t \approx 1$ T, $I_p \approx 30$ kA) [4], in the TJ-IU torsatron ($P_{ECRH} = 200$ kW, $\iota \approx 0.23$, $R = 0.6$ m, $\bar{a}_e \approx 0.1$ m, $\bar{n}_e \approx 0.5 \times 10^{19}$ m^{-3}, $B_t = 0.67$ T) [5] and in the W7-AS stellarator [6] ($P_{ECRH} = 400$ kW, $\iota \approx 0.34$, $R = 2.0$ m, $\bar{a} \approx 0.2$ m, $\bar{n}_e \approx 3 \times 10^{19}$ m^{-3}, $B_t = 2.5$ T).

The time resolved radial turbulent flux, $\Gamma = \tilde{n}_e\tilde{E}_\theta/B_t$ (where $\tilde{n}_e$ and $\tilde{E}_\theta$ are the fluctuating density and the poloidal electric field, respectively) has been measured by means of Langmuir probes both neglecting the influence of electron temperature fluctuations (TJ-I, TJ-IU) and taking into account the effect of $\tilde{T}_e/T_e$ fluctuations (W7-AS).

A Langmuir probe with three tips is used in these measurements in the TJ-I and TJ-IU devices. One tip of the probe array is biased at a fixed voltage in the ion saturation current regime. Two of the tips, aligned perpendicularly to the magnetic field and poloidally separated by $\Delta = 2$ mm, are used to deduce the poloidal electric field ($\tilde{E}_\theta \approx [\Phi(\theta_1) - \Phi(\theta_2)]/\Delta$) from the measured floating potential, Φ. Fluctuations in the poloidal electric field have been deduced from the floating potential fluctuation measurements, and electron density fluctuations are given by $\tilde{n}_e \approx \tilde{I}_s$, where I_s is the ion saturation current. To determine the radial scale-length of fluctuations and turbulent fluxes, we have designed a specific experimental set-up. Two arrays of Langmuir probes radially separated 1 to 2 cm allow simultaneous measurements of fluctuations and turbulent transport at two radial positions. The probes were oriented with respect to the magnetic field direction to avoid shadows between them (see Fig. 1).

The influence of electron temperature fluctuations on the computation of the particle transport due to fluctuations has been investigated in the W7-AS stellarator. The fast sweeping Langmuir probe method has been used to determine the spectra of the electron temperature fluctuations and their correlation with electron density fluctuations (see Ref. [7] and references therein).

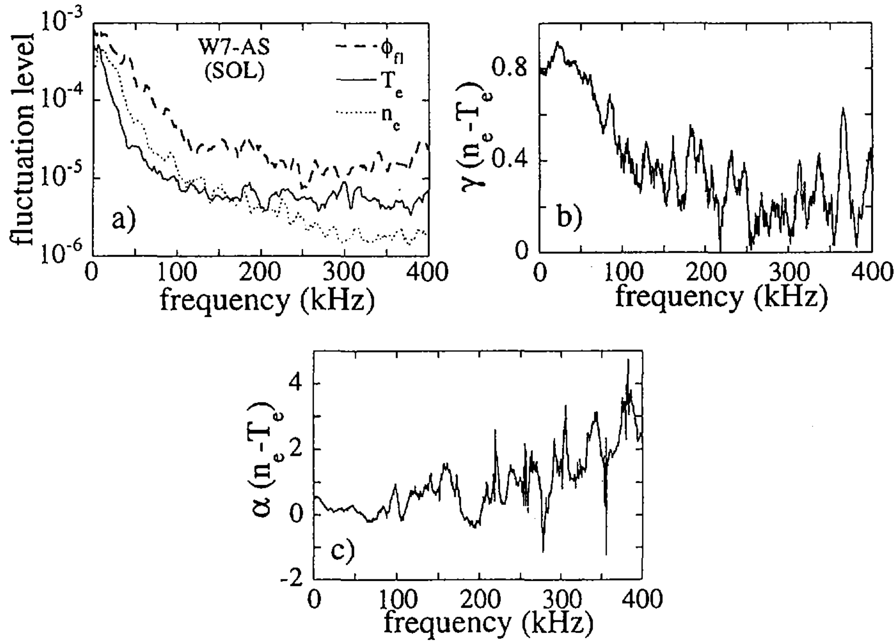

FIG. 2. Frequency spectra for (a) density, floating potential and electron temperature fluctuations, (b) coherence and (c) phase between density and temperature fluctuations in the SOL region in W7-AS stellarator [8].

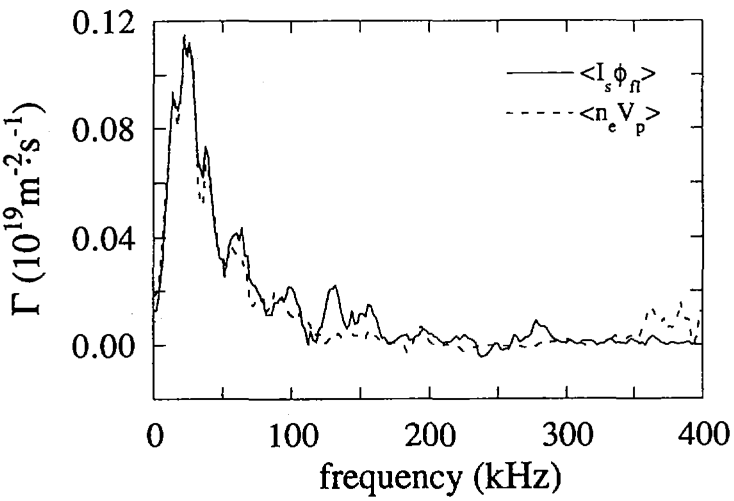

FIG. 3. Particle flux induced by fluctuations calculated by considering the influence of temperature fluctuations and calculated under the assumption $\tilde{T}_e/T_e \approx 0$.

3. STATISTICAL PROPERTIES OF TURBULENT TRANSPORT

3.1. Measurements in the W7-AS stellarator

Figure 2 shows the power spectrum of density, temperature and floating potential fluctuations and the correlation between density and electron temperature fluctuations measured at the radial position $r/a_s \approx 1.1$, where a_s is the location of the velocity shear layer. Fluctuations are dominated by frequencies below 100 kHz, and the level of temperature fluctuations is in the range of 15–25% with $\tilde{T}_e/T_e \approx \tilde{n}_e/n$.

The coherence between $\tilde{n}$ and $\tilde{T}_e$ is significant for frequencies below 100 kHz, and the relative phase between density and temperature fluctuations is close to zero in the scrape-off layer (SOL) region of W7-AS. Although there is evidence for substantial electron temperature fluctuations in the plasma boundary region, in W7-AS the resulting turbulent transport is strikingly similar to that calculated on the assumption of $\tilde{T}_e/T_e \approx 0$ (Fig. 3). This result is due to the negligible phase difference between $\tilde{n}$ and $\tilde{T}_e$ [8].

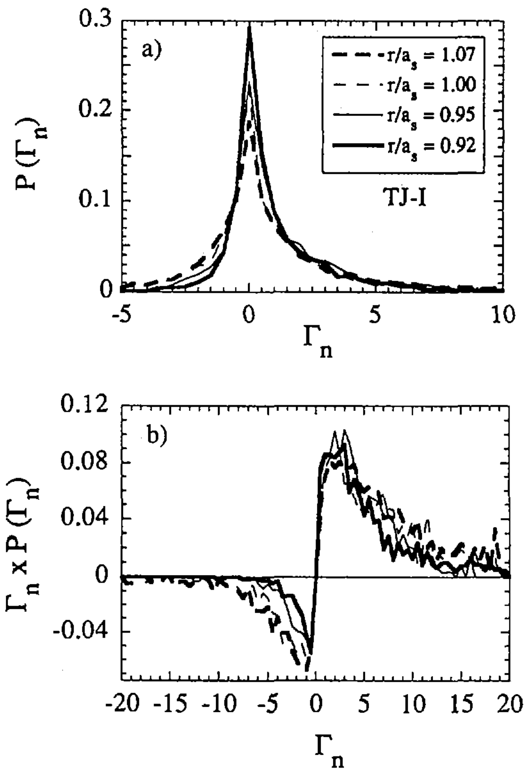

FIG. 4. (a) Local flux PDF and (b) flux fraction function in the TJ-I tokamak at different radial positions.

3.2. Measurements in the TJ-I and TJ-IU devices

The statistical properties of fluctuations and turbulent transport are different on the plasma bulk and the SOL sides of the velocity shear layer. In particular, in the TJ-I tokamak, both the ion saturation current (I_s) and the potential (Φ_f) signals have a near Gaussian distribution function in the edge region of the plasma ($r < a_s$), whereas the I_s fluctuations deviate from the Gaussian distribution in the SOL region of the plasma [2]. The local flux power distribution function (PDF) presents a systematic variation as a function of the radial location (Fig. 4). The local turbulent flux PDF is not symmetric. The non-Gaussian character of the PDF is clearly seen: there exist large amplitude transport bursts that account for a significant part of the total flux.

This asymmetry provides a measure for the average outward flux compared to the maximum instantaneous fluxes. In most cases, the local particle flux is, on the average, outward. However, under some conditions a fluctuation induced inward particle transport has been observed. The origin of this turbulent inward 'pinch' is under investigation at present.

To study changes in the statistical properties of the turbulent transport related to the global characteristics of the plasma (i.e. heating, plasma current, electric field), the local flux PDFs for TJ-I and TJ-IU plasmas have been compared. The structures of the local flux PDF look very similar in the two devices, which supports the hypothesis that the plasma turbulence in magnetic confinement devices has a universal character.

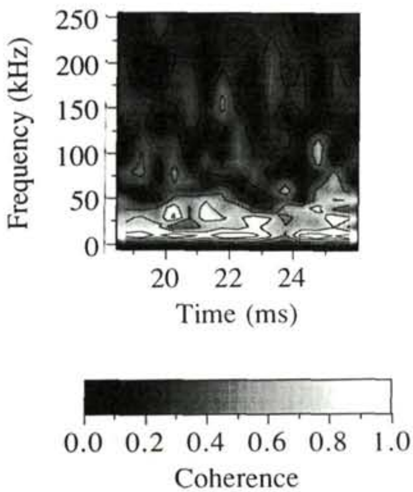

FIG. 5. Time resolved wavelet coherence versus time for the floating potential. The coherence is measured between two radially separated probes (Δr = 1 cm) in the plasma boundary of TJ-IU. During several time intervals and at various frequencies, the coherence assumes values far above the time average value.

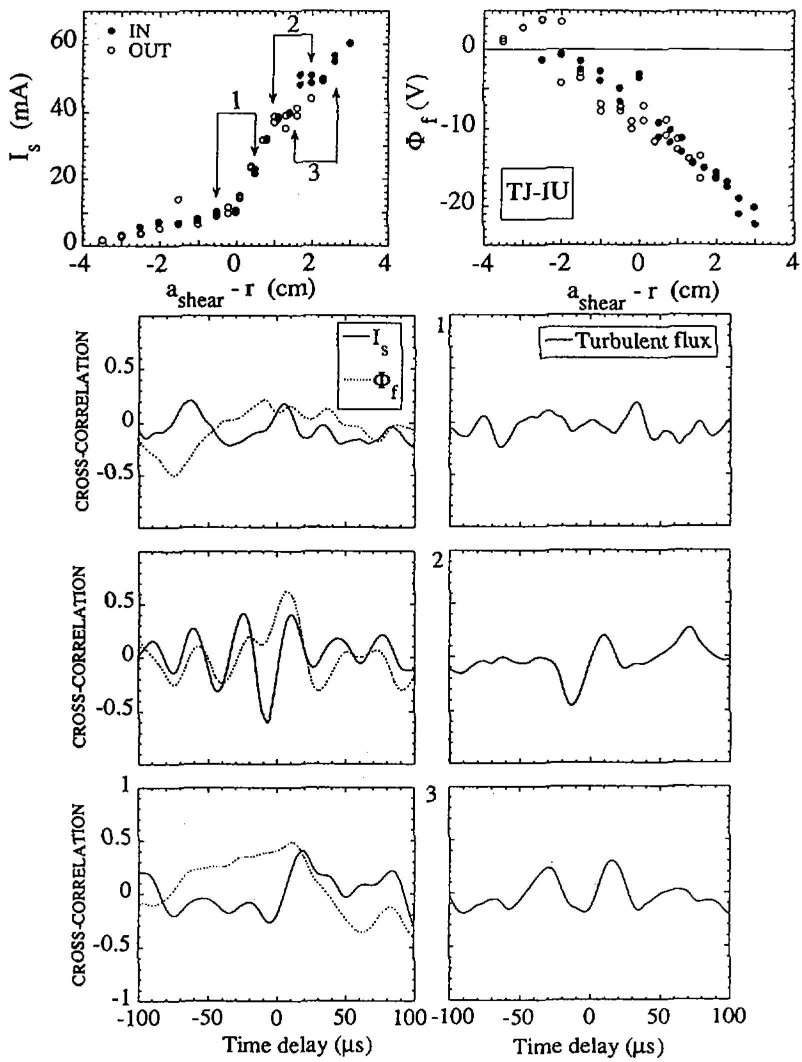

FIG. 6. Radial profiles of ion saturation current (I_s) and floating potential (Φ_f) and radial cross-correlation calculated for fluctuating signals ($\tilde{I}_s$–$\tilde{I}_s$, $\tilde{\Phi}_f$–$\tilde{\Phi}_f$) and turbulent transport ($\tilde{\Gamma}$–$\tilde{\Gamma}$) measured at different probe positions in the TJ-IU torsatron. Probes are radially separated by 1 cm.

4. RADIAL SCALE-LENGTH OF FLUCTUATIONS AND TURBULENT FLUXES

Comparative studies between the radial correlation of turbulent fluxes and fluctuations have been carried out in the TJ-IU torsatron [9]. We have simultaneously measured the levels of fluctuation ($\tilde{I}_s$ and $\tilde{\Phi}$), and the turbulent fluxes have been computed (neglecting the influence of electron temperature fluctuations) at two different radial locations ($\Delta r \approx$ 1–2 cm) in the TJ-IU plasma boundary region. Wavelet analysis techniques have been used to characterize the fluctuations [10].

The frequency spectra of the fluctuations are dominated by frequencies below 50 kHz for density and potential and by frequencies below 100 kHz for the turbulent transport.

The value of the radial coherence length associated with fluctuations and transport is strongly intermittent (Fig. 5). For probes located on the plasma bulk side of the velocity shear layer, the radial correlation is highly bursty, achieving occasionally values that are much higher than the time average value.

The radial profiles of the ion saturation current and floating potential magnitudes, along with the radial cross-correlation calculated for fluctuating signals and turbulent transport, are shown in Fig. 6. This figure shows the correlation at three radial probe locations (marked by arrows in the profile). Significant correlation between signals measured with Langmuir probes located radially apart up to 1 cm on the plasma bulk side of the velocity shear layer has been observed for the low frequency range (<50 kHz). For measurements taken at a radial distance of $\Delta r \approx 1$ cm, the radial coherence associated with turbulent transport is in general not stronger than the corresponding correlation of the fluctuations. It is interesting to note that in some cases a double peak in the cross-correlation calculated for turbulent fluxes has been obtained (see Fig. 6).

The level of radial correlation for fluctuations and time resolved fluxes decreases with increasing radial distance between probes up to 2 cm. However, in some conditions, a significant radial coherence associated with turbulent flux has been observed at $\Delta r \approx 2$ cm.

At low density plasmas ($\bar{n}_e \approx 1 \times 10^{12}$ m^{-3}), a very high radial coherence length between potential fluctuations has been observed. This effect is less remarkable for ion saturation current fluctuations. Further investigations are in progress in order to quantify the relevance of such processes.

5. CONCLUSIONS

The statistical properties of fluctuations and turbulent transport change from the scrape-off side to the plasma bulk side of the velocity shear layer. Fluctuations in the ion saturation current clearly deviate from the Gaussian distribution in the SOL region of the plasmas. The local flux probability distribution function shows the bursty character of flux and presents a systematic change as a function of the radial location. Although the level of electron temperature fluctuations is significant in the plasma boundary region of the W7-AS stellarator, the statistical properties of the particle flux can be investigated by neglecting their effect. There is a strong similarity between the statistical properties of the turbulent fluxes in different devices, supporting the hypothesis of the universal character of plasma turbulence in magnetic confinement devices.

The value of the radial coherence associated with fluctuations and turbulent transport is strongly intermittent. This result emphasizes the importance of measurements with time resolution for understanding the interplay between the edge and the core regions in the plasma. For measurements taken at a radial distance of $\Delta r \approx 1$–2 cm in the plasma edge region of the TJ-IU torsatron, the radial coherence associated with the turbulent flux turns out to be not stronger than that associated with the fluctuations. However, in some conditions, the radial coherence of the particle flux can be significant. Further investigations are needed to quantify the relevance of such processes. These studies could provide a useful criterion for distinguishing between different mechanisms proposed to explain fast (non-local) transport effects in tokamak and stellarator plasmas [11–14].

ACKNOWLEDGEMENTS

The authors thank B.A. Carreras for illuminating discussions. This research was sponsored in part by DGICYT (Dirección General de Investigaciones Científicas y Técnicas) of Spain under Project No. PB93-0231-C02-02.

REFERENCES

[1] HIDALGO, C., Plasma Phys. Control. Fusion **37** (1995) A53.
[2] CARRERAS, B.A., HIDALGO, C., SANCHEZ, E., Plasma Phys. **3** (1996) 2664.
[3] ENDLER, M., et al., Nucl. Fusion **35** (1995) 1307.
[4] GARCIA-CORTES, I., et al., Phys. Fluids B **4** (1992) 4007.
[5] ASCASIBAR, E., et al., in Plasma Physics and Controlled Nuclear Fusion Research 1994 (Proc. 15th Int. Conf. Seville, 1994), Vol. 1, IAEA, Vienna (1995) 749.
[6] WELLER, A., et al., Plasma Phys. Control. Fusion **33** (1991) 1559.
[7] GIANNONE, L., et al., Phys. Plasmas **1** (1994) 3614.
[8] BALBIN, R., et al., in Stellarators (Proc. 10th Int. Conf. 1995), EUR-CIEMAT **30** (1995) 93.
[9] PEDROSA, M. A., et al., Plasma Phys. Control. Fusion **38** (1996) 365.
[10] VAN MILLIGEN, B.Ph., et al., Phys. Plasmas **2** (1996) 3017.
[11] GENTLE, K., et al., Phys. Rev. Lett. **74** (1995) 3620.
[12] CONNOR, J.W., Phys. Rev. Lett. **70** (1993) 180.
[13] ROMANELLI, F., ZONCA, F., in Controlled Fusion and Plasma Physics (Proc. 20th Eur. Conf. Lisbon), Vol. 17C, Part IV, European Physical Society, Geneva (1993) 1387.
[14] CARRERAS, B.A., NEWMAN, D., LYNCH, V.E., DIAMOND, P.H., Phys. Plasmas (in press).

CONFINEMENT AND TRANSPORT STUDIES IN ASDEX UPGRADE

F. RYTER, M. ALEXANDER, O. GRUBER, O. VOLLMER,
G. BECKER, O. GEHRE, K.W. GENTLE[1], K. LACKNER,
F. LEUTERER, A.G. PEETERS, H.D. MURMANN,
S. DE PEÑA HEMPEL, G. PEREVERZEV, H. SALZMANN,
J. SCHWEINZER, W. SUTTROP, ASDEX UPGRADE,
ECRH and NBI TEAMS
Max-Planck-Institut für Plasmaphysik,
Euratom–IPP Association,
Garching and Berlin, Germany

Abstract

CONFINEMENT AND TRANSPORT STUDIES IN ASDEX UPGRADE.

The global confinement studies in ASDEX Upgrade indicate that in the high density regimes required for ITER, confinement degradation occurs in the H mode (from $f_H \approx 2.0$ down to 1.2), but not in the L mode ($f_H \approx 1$). In scenarios including edge radiation, density peaking counterbalances the degradation of the H mode (up to $f_H \approx 1.6$) and improves the L mode to values close to the H mode. Transport studies associate an inward drift to this effect. Improved L modes are also observed just below the H mode threshold when the latter is high. The thermal electron diffusivity inferred from ECRH modulation is close to that of power balance, whereas results from sawteeth are generally larger, the latter seeming essentially determined by the sawtooth amplitude. Dimensionless similar ρ_* scans in the L mode yield Bohm scaling, whereas H mode scans exhibit a gyro-Bohm behaviour. The H mode is sensitive to the neutral gas pressure and therefore the required profile matching at the plasma edge is difficult to achieve.

1. GLOBAL CONFINEMENT

Confinement is an essential issue for ITER which will probably require the improved confinement of the H mode, compared to the L mode. Therefore, in ASDEX Upgrade, the L and H mode confinement properties were compared, in particular, at high density, with and without radiative edge.
Under usual operational conditions, i.e. with low H mode power threshold, the H mode exhibits higher confinement than L mode by a factor $f_H = 1.6 - 2$, compared to the ITER89-P L mode scaling. However, with a high threshold, provided by either reversing the ion ∇B drift or using hydrogen instead of deuterium, the L mode confinement gradually improves with power and approaches that of the H mode just below the threshold: in terms of confinement, the L-to-H transition becomes a smooth phenomenon [1]. Transition physics in these cases is discussed in [2].

[1] Department of Physics, University of Texas, Austin, Texas, USA.

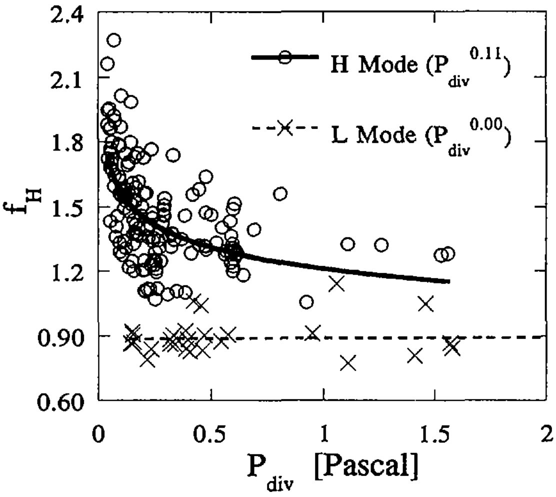

FIG. 1. Enhancement factor versus divertor pressure (lines are fits).

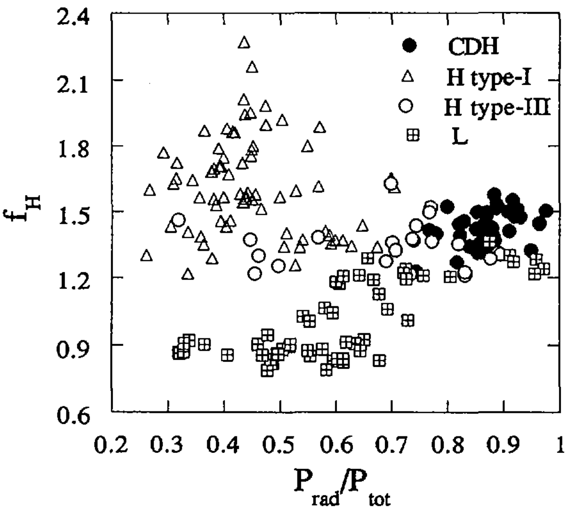

FIG. 2. Enhancement factor versus fractional radiation.

High density operation in ASDEX Upgrade was performed with gas puffing or pellet injection [3]. Figure 1 shows the reaction of the L and H modes to density increase by gas puffing. In such experiments, the neutral pressure in divertor seems to be a useful technical parameter for the analyses. Physical reasons might be changes of density, closely coupled to neutral gas pressure [3], temperature, β and/or ν_* at the edge. Whereas the L mode is not influenced by the neutral gas pressure, the H mode confinement is degraded. The highest H mode points (f_H = 2.0 - 2.2) are from discharges with somewhat higher averaged triangularity (0.2 instead of 0.1). However, the plasma shape in these cases simultaneously causes particularly low pressure and the influence of each effect could not be separated so far. The difference between L and H mode is attributed to the fact that the H confinement is governed by the edge transport barrier, which is sensitive to conditions in this region.
Operation at high density with radiative edge provided the Completely Detached H-mode, [4]. In such discharges, f_H reaches 1.6 (Fig. 2) because the degrading effect caused by the necessary high neutral pressure is compensated by a peaking of the electron density profile, as shown by transport simulations [5]. In L modes with edge radiation density peaking increases and there also L confinement approaches that of the H mode, as indicated by Fig. 2.

2. PERTURBATIVE TRANSPORT STUDIES

The comparison of transport coefficients obtained from power balance and perturbative experiments, which are per definition different [6], is expected to improve the understanding of transport physics. We report here on studies of the electron heat conductivity (χ_e) using sawtooth (χ_e^{ST}) and ECRH modulation (χ_e^{ECRH}) heat pulse propagation.
The recently installed ECRH system (140 GHz, up to 400 kW) allows for modulation experiments with on-axis or off-axis deposition, generally performed with 100% on/off power modulation, duty-cycle of 50% and frequencies between 10 Hz and 1 kHz. The sawtooth and ECRH modulation studies were made in Ohmic and NBI-heated L mode plasmas. Plasma current, magnetic field, density and working gas (H^+ or D^+) were varied to achieve a wide range in χ_e.
Two analysis methods were used: a time-dependent code (TDC) and a Fourier transform (FT) interpreted with a slab model including geometrical corrections from [7], as they apply to our experiments. In the TDC analysis the diffusion equation is solved in cylindrical geometry using a forced boundary method [8]. Damping terms (electron-ion exchange, modulation of P_{OH}) are calculated. The density perturbation, generally small, is not included. The calculated time evolution of the electron temperature pulses agrees well with the experimental one for r/a $\leq$ 0.7 using flat χ_e profiles, having however larger values than χ_e^{PB} from power balance, as discussed below. The not gradient-driven outward heat flux at the plasma edge allows to reproduce the experiment for r/a $\geq$ 0.7.

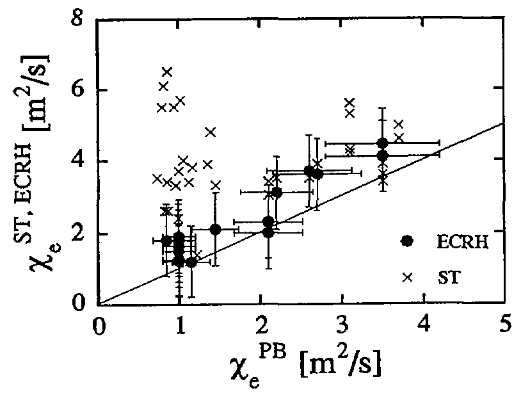

FIG. 3. χ_e^{ST} *or* χ_e^{ECRH} *versus* χ_e^{PB} *for Ohmic and L mode discharges.* ($\chi_e^{PB} \geq 2$ m^2/s *from discharges in hydrogen; the line is the 1 to 1 line).*

The FT analysis was applied to both sawtooth and ECRH modulation data. TDC and FT give the same χ_e values within the uncertainties. For our modulation scheme (50% duty-cycle), the Fourier frequency spectrum of the temperature shows the odd harmonics and no even harmonics, *suggesting the absence of non-linear reaction of the plasma to the modulation.* We also observed that, *both for sawteeth and ECRH,* χ_e *does not depend on the modulation frequency, excluding a temperature dependence of* χ_e [9].

In Fig. 3 we compare χ_e^{ST} and χ_e^{ECRH} with χ_e^{PB}. The analysis of sawteeth yields $\chi_e^{PB} \leq \chi_e^{ST} \leq 6\chi_e^{PB}$ and shows no correlation at all between χ_e^{ST} and χ_e^{PB}. In contrast, for the ECRH modulation experiments Fig. 3 clearly shows that χ_e^{ECRH} is at most 2 times larger than χ_e^{PB}. This is in agreement with the assumption $\chi_e \propto \nabla T_e^{\alpha}$ with $\alpha \leq 1$, [9].

Generally, χ_e^{ST} is larger than χ_e^{ECRH}. This is attributed to the size of the perturbation which can be large (up to 400 eV) for sawteeth compared to at most 70 eV for ECRH modulation, as shown in Fig. 4. This is related to the fact that the maximum modulated ECRH power was 400 KW, whereas the power liberated within a sawtooth crash (duration $\approx$ 100 μs) can reach 10 MW in NBI-heated plasmas, in which the largest χ_e^{ST} values are observed. Figure 4 also indicates a clear correlation between χ_e^{ST} and the amplitude of the perturbation for sawteeth, but no correlation for ECRH, as also specifically examined in ECRH power scans (50 kW to 400 kW). *We therefore conclude that the results from ECRH modulation are closely related to the steady-state transport, according to [6]. This is generally not the case for the sawteeth for which other phenomena, seemingly linked with the sawtooth amplitude, probably play a role.*

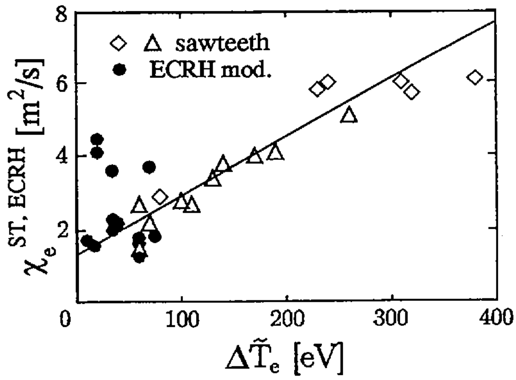

FIG. 4. χ_e^{ST} versus amplitude of temperature perturbation, for sawteeth at mixing radius, for ECRH at deposition radius (the line is the fit for sawteeth).

ECRH modulation experiments were modelled with the ASTRA code [10]. Similarly to the results from TCD for sawteeth, the best agreement with the data is obtained with flat χ_e profiles with values higher than χ_e^{PB}. However, power balance and ECRH modulation can be simultaneously well simulated by introducing a ∇T_e dependence of χ_e. Here also, a good agreement at the plasma edge (r/a $\geq$ 0.7) requires outward heat flux. The edge behaviour may be caused by non-local transport as well, [9], as also indicated by our ASTRA simulations. It was, however, not possible so far to differentiate between the two possibilities.

3. TRANSPORT IN DIMENSIONLESS SIMILAR DISCHARGES

Using the scale invariance approach to confinement scaling [11] the thermal diffusivity can be expressed as a power law of the normalised gyro-radius, ρ_*, in a dimensionally correct form as

$$\chi = \chi_B \rho_*^\alpha F(\nu_*, \beta, q, \text{shape}, \ldots) \qquad (1),$$

with $\rho_* = \rho_g/a \sim (A_i T)^{1/2}/(Ba)$, Bohm diffusivity $\chi_B \sim T/B_t$, collisionality $\nu_* \sim qn/T^2$ and normalised pressure $\beta \sim nT/B_t^2$ (minor radius a, safety factor q, plasma density n, electron or ion temperature T, magnetic field B_t). If the scaling with ρ_* is known, then the transport behaviour of existing experiments can be scaled to larger ignition devices having similar q, ν_* and β, even without a complete understanding of the process of turbulent diffusion [12]. The exponent α of ρ_* can be interpreted as an indication for the characteristic turbulence wavelength λ, assuming $v_{\text{phase}} \approx v_{\text{drift}}$: a) $\alpha = 1$ ($\lambda \sim \rho_g$ gyro-Bohm); b) $\alpha = 0$ ($\lambda \sim a$ Bohm); c) $\alpha = -1$ ($\lambda \gg a$ stochastic); d) $\alpha = -1/2$ (Goldston).

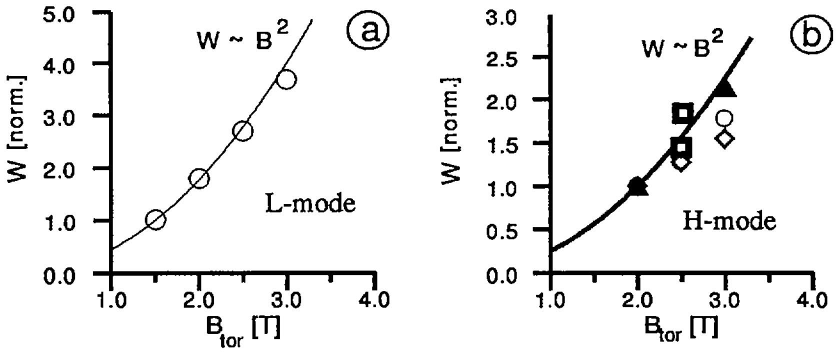

FIG. 5. Normalised plasma energy versus toroidal field in ρ^* scans (a for L mode in H^+, b for H mode in D^+). Diamonds: gyro-Bohm; circles: Bohm; triangles: Goldston; squares: same power and density (see text).

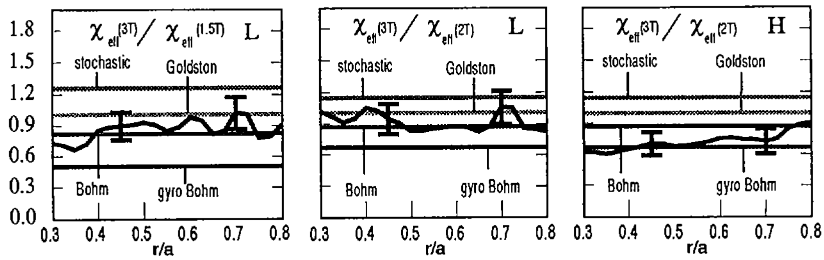

FIG. 6. Profiles of χ_{eff} ratios for L and H mode ρ^* scans.

The confinement scaling with ρ_* has been examined in ASDEX Upgrade in L and H modes with "dimensionless similar" discharges by varying just ρ_* while keeping all other dimensionless parameters fixed. To keep q, ν_* and β constant the relations $I_p \sim B_t, n_e \sim B_t^{4/3}$ and $T \sim B_t^{2/3}$ have been fulfilled in these ρ_* scans (single-null, $\kappa = 1.7$, $\delta = 0.1$) at densities between 4 and $10 \times 10^{19}\mathrm{m}^{-3}$. The power demand was scaled as $B_t^{(5-2\alpha)/3}$ depending on the transport model. The q profiles should be similar because the edge q ($q_{95} \approx 4$) and the sawtooth inversion radius (r/a ≈ 0.3) were constant. We kept the NBI power deposition profiles as self-similar as possible by adapting the beam energy to the density.
A dimensionless ρ_* scan in the L mode (H^+ discharges) was outlined such that the discharge with the lowest values of $\bar{n}_e$ ($4 \times 10^{19}\mathrm{m}^{-3}$) and B_t (1.5T) was just below the L-to-H threshold. As we performed the scan assuming a Bohm-like behaviour the heating power was increased as $P_{\mathrm{heat}} \sim B^{5/3}$ and the discharges at higher toroidal fields were deeper in the L mode. The global analysis of the L mode series showed the expected behaviour of $W \sim B_t^2$ (Fig. 5.a), resulting in

a slight increase of $\tau_{E,th}$ with B_t. Local analysis revealed the constancy of the β and ν_* profiles ($\nu_* \approx 0.3$ at r/a = 0.5) over a large part of the cross section. Local thermal diffusivities, χ_{eff}, were calculated with the ASTRA code and their ratios for different discharges are compared in Fig. 6 with scaling predictions according to Eq. 1. Due to the high density, electron and ion channels could not be resolved and χ_{eff} was used. *It is concluded that confinement scales as Bohm-like for this L mode series ($f_H \approx 1.2$).*

The H mode scans (steady-state with type-I ELMs) were performed in H^+ and D^+ for both isotopes either reaching the H-to-L threshold at the highest field of 3T or with higher heating power staying deep in the H mode. It was not possible in any of these scans to exactly achieve the $W_{th} \sim B_t^2$ dependence by applying the power demanded by either gyro-Bohm, Bohm or Goldston assumptions, illustrated in Fig. 5.b for deuterium.

The local demands on β and ν_* for dimensionless similarity were achieved for only one pair (3T/2T) in D^+ (Figs. 5.b, triangles), out of 18 discharges. The local analysis of this pair reveals the constancy of β and ν_* profiles ($\nu_* \approx 0.1$ at r/a = 0.5) over a large range of the plasma cross section. *Comparing χ_{eff} yields a gyro-Bohm behaviour of local thermal transport* (Fig. 6), as found in other Tokamaks [13, 14]. The heating power for this pair was between the Bohm and Goldston scalings.

The apparent discrepancy between the global and local results for this pair is caused by the differences in the heating profiles, despite the attempt to keep the heating profiles constant by varying the acceleration voltage. The influence of the heat deposition was demonstrated by a simulation of the 3T discharge using as starting point the shot at B_t = 2T. The χ_{eff} profiles from the 2T case were fitted with a gyro-Bohm expression:

$$\chi_{eff} = \frac{T^{3/2}}{B^2} \times F(r/a) \tag{2}$$

where F(r/a) is a profile factor accounting for the gross radial variation of χ_{eff} due to the unknown dependence of transport on $\nu_*, \beta, q, \ldots$. Taking the density profile of the B_t = 3T discharge, the temperature profile was simulated with ASTRA for the experimentally applied heating power, with deposition profiles calculated for this shot. The resulting temperature and χ_{eff} profiles of the simulation are in very good agreement with the experimental ones.

The confinement deterioration caused by gas puffing described in section 1 also affects the ρ_* experiments. Comparing discharges with B_t = 2.5T at the same heating power, line-averaged density and plasma current, distinct differences in confinement are found (Fig. 5.b, squares). No additional loss channels or other hidden parameters influencing the confinement in the whole set of scaling experiments could be identified. Radiation, ELMs and differences in rotation can be excluded. The increasing neutral density causes lower temperature and higher density at the edge, which obviously leads to degraded confinement both at the edge [2] and in the core. This runs counter to the demands of dimensionless scaling.

The Bohm and gyro-Bohm behaviours obtained in the L and H modes respectively are in agreement with the results from DIII-D and JET [13, 14]. Our experiments were performed at $\nu*$ values about 10 times higher (higher density, lower temperature) than in the two other experiments. *Therefore, the recent results in ASDEX Upgrade reveal that the Ansatz given by Eq. 1 is justified over such a wide ν_* range. They also suggest that the enhancement factor depends on edge profile variations caused by the neutral gas pressure.*

REFERENCES

[1] RYTER, F., et al., in Controlled Fusion and Plasma Physics (Proc. 22nd Eur. Conf. Bournemouth, 1995), Vol. 19C, Part IV, European Physical Society, Geneva (1995) 89.
[2] ZOHM, H., et al., IAEA-CN-64/A5-1, this volume.
[3] MERTENS, V., et al., IAEA-CN-64/A4-4, ibid.
[4] GRUBER, O., et al., Phys. Rev. Lett. **74** (1995) 4217.
[5] BECKER, G., et al., in Controlled Fusion and Plasma Physics (Proc. 22nd Eur. Conf. Bournemouth, 1995), Vol. 19C, Part I, European Physical Society, Geneva (1995) 25.
[6] LOPES-CARDOZO, N.J., Plasma Phys. Control. Fusion **37** (1995) 799.
[7] JACCHIA, A., et al., Phys. Fluids B **3** (1991) 3033.
[8] RIEDEL, K.S., et al., Nucl. Fusion **28** (1988) 1509.
[9] STROTH, U., et al., Plasma Phys. Control. Fusion **38** (1996) 611.
[10] PEREVERZEV, G.V., et al., Rep. 5/42, Max-Planck-Institut für Plasmaphysik, Garching (1991).
[11] CONNOR, J.W., et al., Nucl. Fusion **17** (1977) 1047.
[12] WALTZ, R.E., et al., Phys. Rev. Lett. **65** (1990) 2390.
[13] PETTY, C.C., et al., Phys. Rev. Lett. **74** (1995) 1763.
[14] BALET, B., et al., in Controlled Fusion and Plasma Physics (Proc. 22nd Eur. Conf. Bournemouth, 1995), Vol. 19C, Part I, European Physical Society, Geneva (1995) 9.

ICRF ASSISTED LOW VOLTAGE START-UP IN TEXTOR-94

R. KOCH[1], A.I. LYSSOIVAN[1], B. GIESEN[2], P. HÜTTEMANN[2], O. NEUBAUER[2], A.M. MESSIAEN[1], G. VAN OOST[1], J.A. BOEDO[3], F. DURODIÉ[1], G. FUCHS[2], H.G. ESSER[2], H.R. KOSLOWSKI[2], L. KÖNEN[3], H.T. LAMBERTZ[2], J. ONGENA[1], J. RAPP[2], H. REIMER[2], G. TELESCA[1], M. VERVIER[1], H. WEBER[2]

[1]Laboratoire de physique des plasmas — Laboratorium voor Plasmafysica, Association Euratom–Belgian State, Ecole royale militaire — Koninklijke Militaire School, Brussels, Belgium

[2]Institut für Plasmaphysik, Forschungszentrum Jülich, Association Euratom–KFA, Jülich, Germany

[3]University of California, San Diego, California, United States of America

Abstract

ICRF ASSISTED LOW VOLTAGE START-UP IN TEXTOR-94.

Successful ICRF assisted low voltage start-up was demonstrated for the first time on TEXTOR-94. Plasma current ramping up to 400 kA during ≈ 0.25 s was achieved with $E \approx 0.5$ V/m. ICRF pre-ionisation, target plasma production and preheating have been performed in the standard second harmonic ICRH regime at $P_{RF} \approx 350$–500 kW by using the existing two double loop antennas, one without and the other with Faraday screen. Reproducible low voltage start-up was possible in the presence of a compensated stray (error) magnetic field of the order of $|\bar{B}_v| \le 10$ G and a gas pressure of (2–4) $\times 10^{-5}$ mbar. Without ICRF pre-ionisation ($\bar{n}_{e0} \approx 0.2$–$0.8) \times 10^{12}$ cm^{-3}), no start-up at low loop voltage was achieved. ICRF assisted start-up at conventional electric field operation ($E \approx 1.09$ V/m) gives $\sim 10\%$ reduction in the volt-second consumption, evaluated at the beginning of the current flat-top.

1. INTRODUCTION

Low loop voltage tokamak start-up will be required in reactor scale fusion devices. Such a scenario is envisaged for ITER, where the inductive electric field at start will be limited to values of $E \sim 0.3$ V/m. To perform reliably start-up at such low electric field, non-inductive pre-ionisation, target plasma production and preheating are desirable.

Theory [1] predicts and a number of experiments on start-up assisted by electron cyclotron heating (ECH) [2-3] confirmed reductions of the loop voltage when pre-ionisation is used. The non-inductive pre-ionisation and target plasma preheating also lead to savings in poloidal magnetic flux (volt-seconds) during the starting phase of the discharge, thus increasing the tokamak pulse length. Another potential of non-inductive pre-ionisation assistance to tokamak start-up is the control over the localisation of the initial breakdown, thereby reducing plasma-wall interaction and the energy losses arising from low-Z impurity line radiation [4]. Non-inductive pre-ionisation may also be considered as a means to obtain reliable start-up without extreme sensitivity to such factors as prefill gas pressure and stray magnetic field value [2].

An alternative to plasma production by ECH is the use of radio-frequency power in the ion cyclotron range of frequencies (ICRF). This has been successfully applied earlier to stellarator "currentless" operation [5] and was proposed for pre-ionisation in tokamaks [6]. Like ECH pre-ionisation, this method is based on RF energy absorption by electrons in the presence of a toroidal magnetic field. However in the case of ICRF plasma production, the RF power is expected to be dissipated mostly collisionally either directly or through conversion to the ion Bernstein wave (IBW) ($\omega > \omega_{ci}$) or to the slow wave (SW) ($\omega < \omega_{ci}$). Absorption and coupling by non-linear mechanisms is also possible [7]. The existence of absorption mechanisms different from direct cyclotron absorption mechanisms gives an additional attractiveness to the method, i.e. a low sensitivity of the plasma production efficiency to the value of the toroidal magnetic field B_T [6].

ICRF plasma production using conventional double-loop screened and screenless antennas has been successfully achieved in the tokamak TEXTOR-94 [8-9]. Helium plasma with central line-averaged density up to $\bar{n}_{e0} \approx 3\times10^{12}$ cm^{-3} was reliably produced in a wide range of toroidal magnetic field $B_T \approx 0.36$-2.24 T ($2\omega_{CHe} \leq \omega \leq 12\omega_{CHe}$) without any change in RF frequency (f=32.5 MHz). Multi-ion species RF plasma ($\bar{n}_{e0} \approx (1 - 2)\times10^{12}$ cm^{-3}) in a gas mixture of He with reactive gases at different concentrations (deuterated silane up to 50%) was also produced in a wide range of B_T (1.0 - 2.25 T, $2\omega_{CHe} \leq \omega \leq 4\omega_{CHe}$). The lower and upper limits of B_T for the production of RF plasma have not been reached so far. Typically, the RF-plasma density is proportional to the base gas pressure and to the RF power and the density profile is broadly peaking near the centre. The electron temperature (deduced from spectroscopic and electric probe measurements) was in the range 10 - 40 eV, increasing in the low gas pressure case. Such results have been achieved in pure toroidal magnetic field operation (V_{loop}=0). This method of plasma production provides in particular a means of wall cleaning and conditioning in the presence of toroidal magnetic field [10-12] that is relevant to superconducting devices. It also provides potential for current start-up assistance. However, this had never been tested in tokamaks.

2. EXPERIMENTAL RESULTS AND ANALYSIS
2.1 EXPERIMENTAL CONDITIONS

Studies of ICRF assisted start-up have been carried out in TEXTOR-94 (major radius 1.75 m, minor radius 0.46 m) using the existing ICRH system. This comprises two double loop antennas, optimised for heating and not for plasma production, one without (A1) and the other with Faraday screen (A2). The antennas are positioned at the low magnetic field side of the tokamak (LFS) and at toroidally opposite locations. The antenna straps are at the minor radius locations $r_{A1} = r_{A2} = 0.52$ m. The current straps in the screenless antenna A1 were fed either out of phase (π-phasing) or in phase (*zero*-phasing). The screened antenna A2 was fed out of phase only. The power was applied to both antennas from separate RF generators in overlapping pulses. The RF pulse lengths were varied from 0.6 s up to 1.0 s. It is started at $t \leq -0.2$ s thereby providing ICRF pre-ionisation and target plasma production before application of the loop voltage ($t \geq 0$ s) and afterwards providing plasma preheating during the start-up phase and the whole current ramp-up phase ($0 \leq t \leq 0.6$ s).

The start-up experiments with ICRF pre-ionisation have been performed in helium (gas puffing or continuous gas filling regimes) because it was generally observed that RF discharges are more reproducible with a high recycling gas than with deuterium or hydrogen [8].

The experiments were performed in the standard 2nd harmonic ICRH regime (f=32.5 MHz, B_T=2.25 T), with the $\omega=2\omega_{CHe}$ layer positioned at $r \approx +10$ cm from the vessel centre. During the pre-ionisation and plasma production phase, in this frequency range, the slow wave is strongly evanescent and the power is expected to be mostly collisionally dissipated in the ion Bernstein wave (IBW). Coupling with IBW may take place by direct excitation at the antenna or by conversion at the 2nd cyclotron harmonic layer of the evanescent FW to an IBW. It is to be noted that in the absence of poloidal magnetic field, for not too low pressure, the cyclotron layer appears as a bright vertical line in the RF-produced plasma [9]. This could be an indication either of IBW excitation or of ion cyclotron heating.

The typical RF power at generators was $P_{RF} \approx 350 - 500$ kW, coupled to the plasma with an efficiency $\eta = R_{pl} / (R_{pl}+R_v) \leq 60\%$. (Here R_{pl} is the antenna-plasma loading resistance, R_v is the antenna resistance in vacuum). The presence of inhomogeneous poloidal stray fields (even though compensated by programmed currents in poloidal field coils) tends to destabilise the strongly interlinked RF power coupling and plasma production processes. Besides, antenna coupling decreased in the low gas pressure range ($p_{He} \approx (2 - 4)\times10^{-5}$ mbar) which is required to cause more rapid "burn-through" of the impurity radiation barrier [4] and to perform start-up at low loop voltages [2]. These circumstances resulted in a lower plasma density ($\bar{n}_{e0} \approx (0.2 - 0.8)\times10^{12}$ cm^{-3}) achieved during the ICRF pre-ionisation phase as compared with ICRF plasma production in the case of pure toroidal magnetic field operation [9].

2.2 ICRF ASSISTED START-UP AT CONVENTIONAL ELECTRIC FIELD (E ≈ 1.09 V/M)

To study the influence of ICRF pre-ionisation on the behaviour of the OH discharge, the first start-up experiments have been performed at normal loop voltage (V_{loop}). Conventionally, a loop voltage of the order of ~12 V is employed for ohmic start in TEXTOR-94, corresponding to an electric field at the vacuum vessel centre (R=1.75 m) of ~1.09 V/m.

Preliminary results show that with the assistance of ICRF power start-up at such a loop voltage may be significantly improved. This is illustrated in Fig.1, where ohmic and ICRF assisted start-up are compared. On applying the RF power to both antennas simultaneously, target RF plasma was produced with $\bar{n}_{e0} \approx 0.2\times10^{12}$ cm^{-3}. The presence of the pre-ionisation phase (typically, -50 ms < t < -100 ms) leads to a prompt initiation of both plasma density and current (I_p) without any delay. With ICRF assistance, the plasma density during initial start-up phase (before initiation of the plasma position feedback control) was lower. Two factors, at least, may lead to the observed phenomena: inadequate base pressure values at the onset of the loop voltage and/or off-axis plasma formation. The latter factor will be discussed below. During the ramp-up phase, the plasma current in ICRF assisted discharges was typically higher (by ~5-7%) with higher current ramp rate (by > 10%). ICRF power gives also rise to a noticeable reduction in the

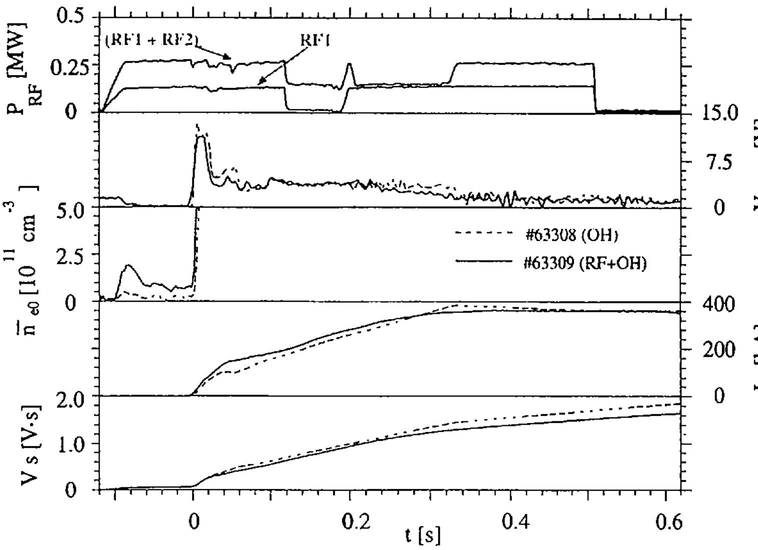

FIG. 1. Comparison of plasma parameters during OH (No. 63 308, dotted lines) and ICRF assisted (No. 63 309) start-up (V_{loop} = 12 V).

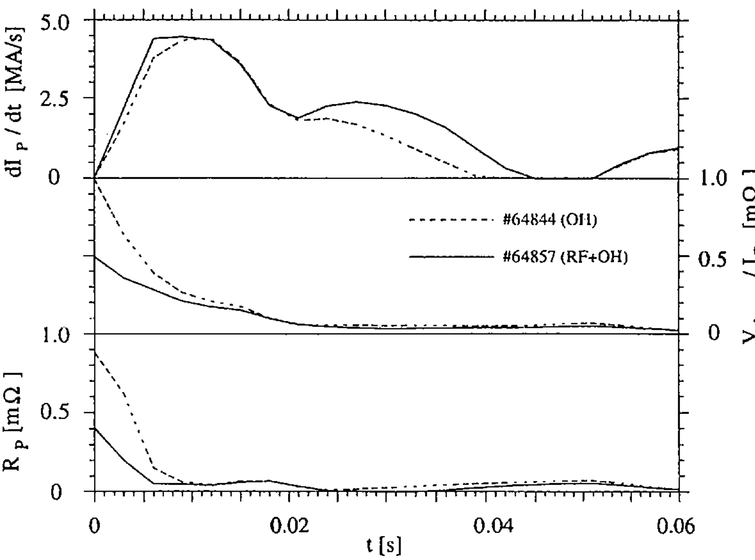

FIG. 2. Time evolution of current derivative, total resistance and plasma resistance during OH (No. 64 844, dotted lines) and ICRF assisted (No. 64 857) start-up phase (V_{loop} = 12 V).

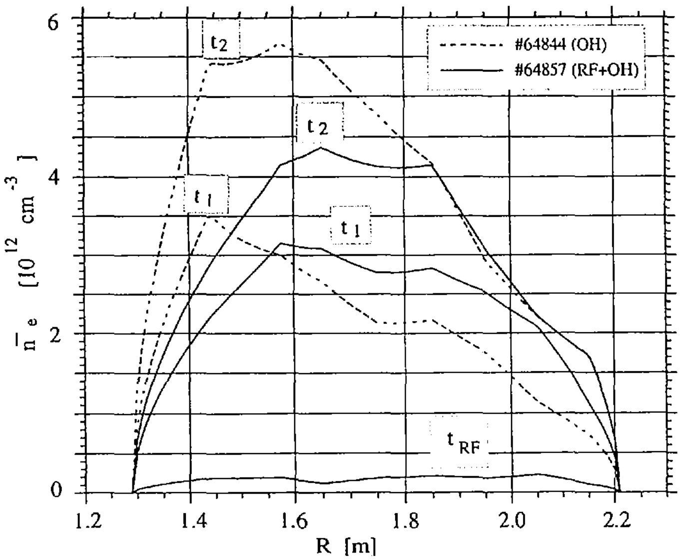

FIG. 3. Comparison of plasma formation during start-up (V_{loop} = 12 V) before plasma position control (t_{RF} = −0.08 s, t_1 = 0.013 s, t_2 = 0.026 s) for two discharges shown in Fig. 2.

volt-second (V·s) consumption. For example , this amounts to 10% when evaluated at the beginning of the current flat-top (see Fig.1). However, more experimental data is needed to refine this estimate.

To understand the effects of the ICRF power on the dynamics of the discharge, we take into account that the loop voltage has both an inductive and a resistive component

$$V_{loop} = d/dt\,(L_{pp}I_p) + R_pI_p \quad (1)$$

with $$L_{pp} = \mu_0 R\,[\ln(a_{pol}/a) + 0.25]\ \ (H) \quad (2)$$

where I_p is the plasma current, R_p is the plasma resistance, and L_{pp} is the plasma-poloidal coil inductance. The latter is given by the approximate formula Eq.(2) [13] which, in particular, does not take the real current profile into account. μ_0 is the free-space permeability, R is the tokamak major radius and a_{pol}/a is the ratio of the poloidal coil radius to the plasma minor radius.

Figure 2 shows the time evolution of the plasma resistance estimated from Eqs. (1-2) for both ohmic (dashed lines) and ICRF assisted discharges (solid lines). As can be seen, the plasma resistance in the ICRF assisted discharge is considerably lower during early phases (t < 20 ms), when the RF power is comparable with the OH one, and goes back to the ohmic value at later times when the ohmic power largely dominates. Similarly, the current ramp rate is higher in the ICRF assisted case during this early phase. This initial difference in discharges is expected since the RF power (P_{RF}) coupled to plasma heats electrons causing a reduction in the plasma resistivity similar to the case of ECH pre-ionisation [2]. An increase in P_{RF} leads to modest additional increase in current ramp rate and decrease in R_p.

An important concern in the start-up study is plasma formation during the initial phase of the discharge (before plasma position control sets in). Analysis of the line-averaged density profiles, from the 9-channel HCN-interferometer, is illustrated in Fig.3 and indicates that during pure ohmic start-up the plasma formation occurs initially at low major radius, where the inductive electric field is highest. With ICRF pre-ionisation, plasma formation is clearly more central with additional broadening of the profile to LFS (antenna location). However, this does not lead to any reduction in radiated power, like for ECH pre-ionisation [2]. Spectroscopic measurements of the oxygen (OI) and carbon (CI) line radiation near the plasma edge also show no difference.

2.3 LOW LOOP VOLTAGE START-UP (E ≈ 0.5 V/M) ASSISTED WITH ICRF POWER

Start-up at low loop voltage generally requires a more careful control of gas pressure and stray (error) magnetic fields produced by OH transformer itself and by the image currents flowing through the tokamak vessel. However, ECH assisted low voltage start-up demonstrated improved reliability of tokamak operation over an extended range of prefill pressures and error magnetic fields [2].

The first attempts at low voltage start-up experiments on TEXTOR-94 with ICRF pre-ionisation also gave promising results. Plasma current ramping up to 400 kA during ≈ 0.25 s was achieved with E ≈ 0.5 V/m. Figure 4 shows time traces of the RF power, the loop voltage, the current and the central line-averaged density. The loop voltage is applied at t=0. One should notice (i) the presence of RF-produced plasma prior to application of the loop voltage, (ii) the ≈ 130 ms plateau in plasma current starting at t = 0, (iii) the normal ramping up of the current and of the density. The abrupt termination of the discharge is due to the choice of an OH programming for indefinite ramp-up of the current. Figure 5a

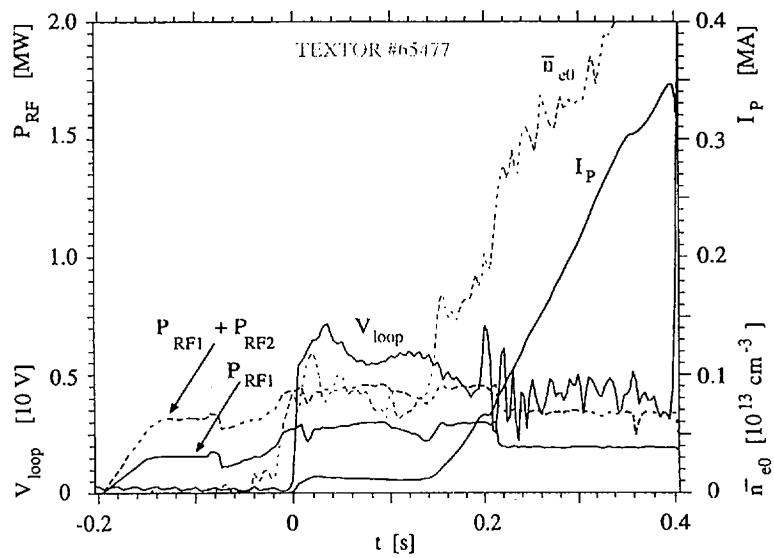

FIG. 4. ICRF assisted low loop voltage start-up (No. 65 477, V_{loop} = 5 V).

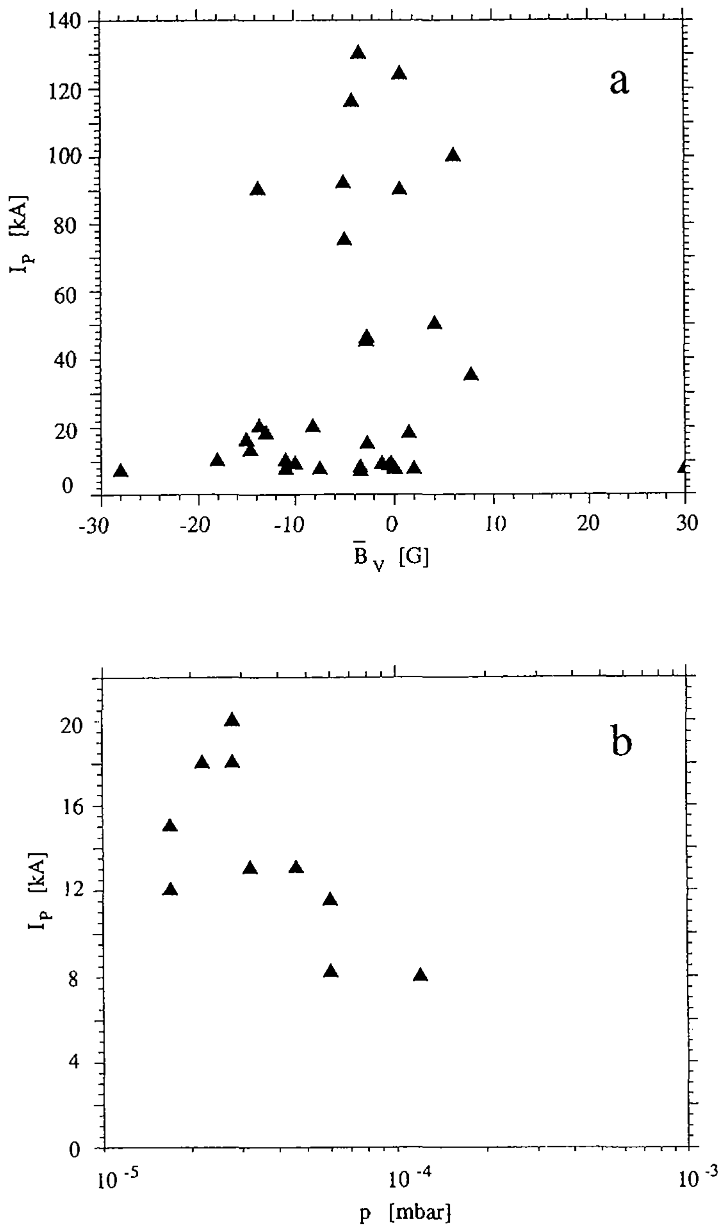

FIG. 5. Influence of tokamak vertical magnetic field B_v on plasma current start and low current plateau dependence versus gas pressure (V_{loop} = 5 V).

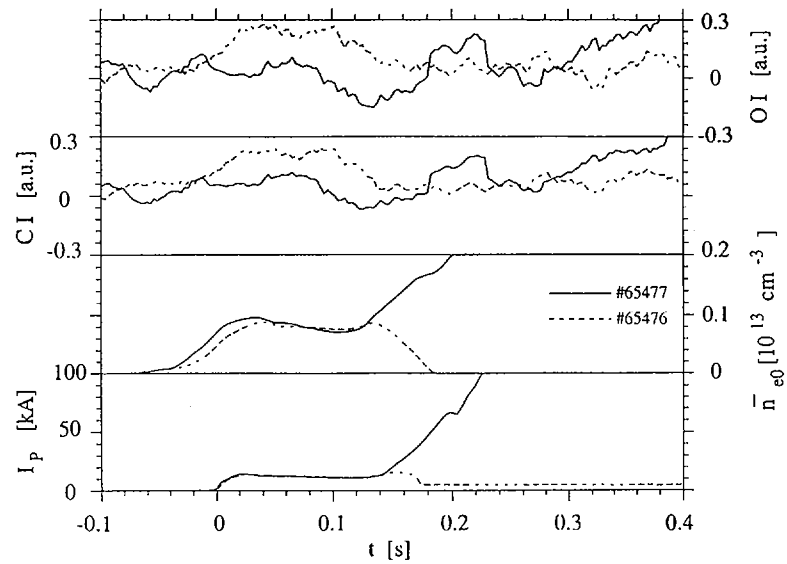

FIG. 6. Effects of low Z impurities on plasma current evolution at low voltage start-up assisted by ICRF power.

shows a statistics of the maximum current achieved in the low loop voltage RF-assisted start-up, in the absence of plasma position feedback, and for different values of the averaged vertical magnetic field $|\bar{B}_V|$ estimated from two equatorial pick-up coils. The cancellation of $|\bar{B}_V|$ is obtained by adjustment of the currents in compensating coils. It is clear that relatively minor stray field values can prohibit current ramping. When ramp-up is not obtained, the low-current plateau subsists for longer times. In this case, the total measured current is made up of ≈6 kA of current flowing in the liner and ≈5 kA in the plasma. Fig.5b illustrates the dependence of this plateau current (plasma + liner) versus gas pressure. The increase of the plasma current when the pressure is lowered reflects the lower plasma resistance and is an indirect indication of higher temperature. This inverse dependence of temperature on plasma pressure (and hence density) is corroborated by other indications from probe and spectroscopic measurements [9]. However, the lower plasma density resulting from the lower pressure is conflicting with the RF requirement to go to higher density to get better coupling. Thus, reproducible low voltage start-up was possible in the presence of (compensated) stray field of the order of $|\bar{B}_V| < 10$ G and gas pressure $(2\text{-}4)\times10^{-5}$ mbar. Both choices of the vertical field and of the pressure are critical for current start-up. Without ICRF pre-ionisation start-up at low loop voltage was not achieved. Difficulties encountered in reproducing current ramp-up in a polluted machine also point to the sensitivity of low loop voltage RF start-up to the low Z impurity content. Figure 6 shows that for discharges with identical density and identical plateau current ($t \leq 0.13$ s) (i.e. same plasma resistance in the initial phase) the discharge with a larger impurity content does not achieve current ramp-up while the other one does.

3. CONCLUSIONS

Initial start-up experiments on TEXTOR-94 point to a positive effect of plasma pre-ionisation and target plasma formation by ICRF on current start-up. Like for ECH, a reduction in the volt-second consumption is observed when ICRF is applied in the standard high V_{loop} scenario. RF start-up assistance also allowed to achieve current ramp-up at low loop voltage, so far never achieved with OH only. Further experiments are necessary to investigate the sensitivity of RF start-up to various parameters and to improve reproducibility. These experiments demonstrate the potential of ICRF systems for pre-ionisation and plasma production in tokamaks and provide a strong indication of the usefulness of ICRF power for low voltage start-up assistance.

REFERENCES

[1] PENG, Y.-K.M., et al., Nucl. Fusion **18** (1978) 1489.
[2] LLOYD, B., et al., Nucl. Fusion **31** (1991) 2031.
[3] ALIKAEV, V.V., et al., in Controlled Fusion and Plasma Heating (Proc. 17th Eur. Conf. Amsterdam, 1990), Vol. 14B, Part II, European Physical Society, Geneva (1990) 1084.
[4] HAWRYLUK, R.J., SCHMIDT, J.A., Nucl. Fusion **16** (1976) 775.
[5] SHVETS, O.M., et al., in Heating in Toroidal Plasmas (Proc. 4th Int. Symp. Rome, 1984), Vol. 1 (1984) 513.
[6] LYSSOIVAN, A.I., et al., Nucl. Fusion **32** (1992) 1361.
[7] KORZH, A.F., STEPANOV, K.N., Sov. J. Plasma Phys. **13** (1987) 164.
[8] LYSSOIVAN, A.I., et al., in Controlled Fusion and Plasma Physics (Proc. 22nd Eur. Conf. Bournemouth, 1995), Vol. 19C, Part III, European Physical Society, Geneva (1995) 341.
[9] LYSSOIVAN, A.I., et al., in Controlled Fusion and Plasma Physics (Proc. 23rd Eur. Conf. Kiev, 1996), Vol. 20C, European Physical Society, Geneva (1996).
[10] NAZAROV, N.I., et al., Sov. J. Plasma Phys. **13** (1987) 871.
[11] ESSER, H.G., et al., in Plasma-Surface Interactions (Proc. 12th Int. Conf. St. Raphael, 1996) to be published in J. Nucl. Mater.
[12] GAUTHIER, E., et al., ibid.
[13] SHEFFIELD, J., in Tokamak Start-Up (KNOEPFEL, H., Ed.), Plenum Press, New York (1986) 7.

INFLUENCE OF THE SHAPE ON TCV PLASMA PROPERTIES

J.-M. MORET, H. WEISEN, S. FRANKE, M. ANTON, R. BEHN,
B.P. DUVAL, F. HOFMANN, B. JOYE, Y. MARTIN, C. NIESWAND,
Z.A. PIETRZYK, W. VAN TOLEDO
Centre de recherches en physique des plasmas,
Association Euratom–Confédération Suisse,
Ecole polytechnique fédérale de Lausanne,
Lausanne, Switzerland

Abstract

INFLUENCE OF THE SHAPE ON TCV PLASMA PROPERTIES.

The energy confinement time of ohmic L-mode plasmas was observed to depend strongly on the shape, improving slightly with elongation and degrading strongly at positive triangularity. This dependence can be explained by geometrical effects on temperature gradient combined with power degradation, without invoking a poloidal variation or a shape dependence of the transport coefficients. The variation with the shape of the sawtooth and Mirnov activity of these plasmas may be the consequence rather than the cause of the change in the confinement.

1. INTRODUCTION

TCV has the unique capability of creating a wide variety of plasma shapes, controlled by 16 independent coils. This opens a new domain in Tokamak operation which has been explored to investigate the influence of the shape on plasma properties. In limited ohmic L-mode stationary discharges ($R = 0.88$ m, $a = 0.25$ m, $B_T = 1.4$ T), the following parameters have systematically been scanned: elongation: $\kappa = 1.1 \rightarrow 1.9$; edge safety factor: $q_a = 2 \rightarrow 6$; triangularity: $\delta = -0.45 \rightarrow 0.75$; line average density: $n_e = 2.5 \rightarrow 8.5 \times 10^{19}$ m^{-3}. The confinement properties of these plasmas are quantified by the electron energy confinement time, $\tau_{Ee} = W_e/P_{oh}$, where P_{oh} is the ohmic input power. The total electron energy, W_e, is obtained by volume integration of Thomson scattering measurements at 10 spatial positions. For a given plasma shape, τ_{Ee} exhibits the usual increase with q_a and the usual linear dependence on the density. In all conditions a strong dependence of τ_{Ee} on the plasma shape was found: a slight improvement with elongation and a marked degradation with positive triangularity, both at fixed value of q_a (fig. 1a, ○-symbols). The degradation factor over the scanned triangularity range is

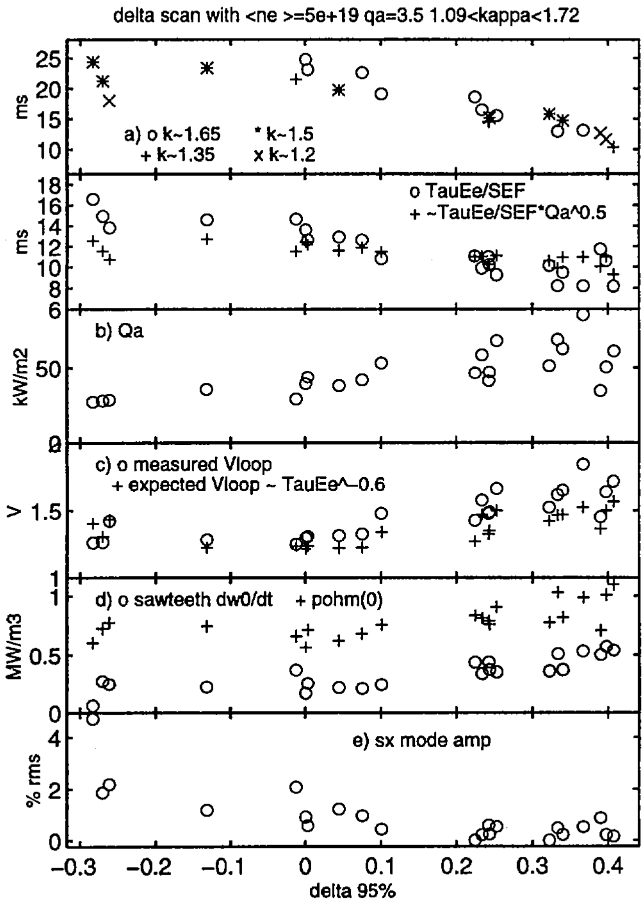

FIG. 1. Shape dependence of relevant parameters.

typically 2 and reaches 3 at the highest density [1]. Variation in P_{rad}/P_{oh} is small and cannot account for the change in confinement [2].

2. TRANSPORT

A direct consequence of the shaping is a modification of the flux surface separation and incidently of the gradients. This will influence the conducted energy fluxes $q = -n\chi\, \nabla T$. The density n, the thermal diffusivity χ and the temperature T of both the ions and the electrons are assumed constant on a poloidal flux (ψ) surface. Because the normalised flux coordinate depends on the current distribution, the profiles were mapped on to the equatorial plane.

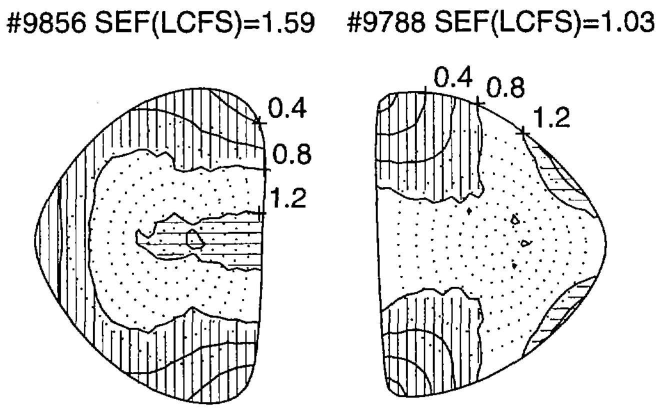

FIG. 2. Distribution of the gradient geometrical factor for negative (left) and positive (right) triangularity. Vertical and horizontal hatching shows the reduced and increased gradient regions, respectively.

The energy flux becomes $-n\chi$ (dT/dr) (dr/dψ) $\nabla\psi$ where r is the distance from the magnetic axis measured on the outer equatorial plane and normalised such that it equals the minor radius on the last closed flux surface (LCFS). The spatial distribution of the geometrical factor (dr/dψ) $\nabla\psi$ is plotted in figure 2 for two shapes. This shows how the compression of flux surfaces toward the outer tip of a positive triangularity shape creates an extended region with increased gradients. At negative triangularity, this region shrinks due to increasing separation of the flux surfaces away from the equatorial plane, so that a large part of the plasma can benefit from favorable shaping.

To quantify this geometrical effect on the confinement time, one can compare the thermal energy of a shaped plasma with that of a circular plasma with the same thermal conduction and the same power deposition. From $\langle q\rangle = -n\chi$ (dT/dr) (dr/dψ) $\langle\nabla\psi\rangle$ = P/S, where P is the power crossing a flux surface and S its area, the temperature profile and the corresponding thermal energy can be derived. It is then convenient to define a Shape Enhancement Factor as the ratio of this energy to that of a similar circular plasma (indexed o):

$$H_S = \frac{\displaystyle\int_0^a \left(\int_r^a \frac{P}{n\chi} \frac{\langle\nabla\psi\rangle^{-1}}{S} \frac{d\psi}{dr} dr' \right) dV}{\displaystyle\int_0^a \left(\int_r^a \frac{P}{n\chi} \frac{1}{S_o} dr' \right) dV_o}$$

where flat density profile was assumed. The weighting function $P/n\chi$ was chosen as $(-dT_0/dr)\ S_0$ where T_0 is the average of the normalised temperature profile over all conditions. This function is essentially zero up to mid-radius and constant outside, so that gradient geometrical effects are effective in the outer region. Correcting the electron energy confinement time with the H_s factor cancels all dependence on elongation and largely reduces the triangularity dependence (fig.1a, ×-symbols).

This residual variation can be attributed to power degradation. The heat flux at the LCFS decreases with triangularity (fig.1b). This is due in part to the lower average current density for fixed q_a at low δ and in part to the improved confinement which leads to a reduction of the ohmic power necessary to sustain the chosen plasma current. Assuming Spitzer conductivity $\eta \sim T_e^{1.5}$, an ohmic plasma is expected to respond to a change in confinement mainly by dropping its power requirement $P_{oh} \sim (n_e/\tau_{Ee})^{3/5}$, with only a modest increase in stored energy, $W_e \sim (\tau_{Ee}/n_e)^{2/5}$. A drop in P_{oh} and loop voltage in accordance with this expectation is indeed observed as δ is reduced (fig.1c). In fig.1a (+ symbols) a degradation with an exponent of 1/2 was assumed in addition to the geometrical correction. Note that the pertinent parameter for the degradation reconciling all shapes is the power flux $Q_a = P_{oh}/S$, not the total power; in the latter case high elongations would have a lower confinement time.

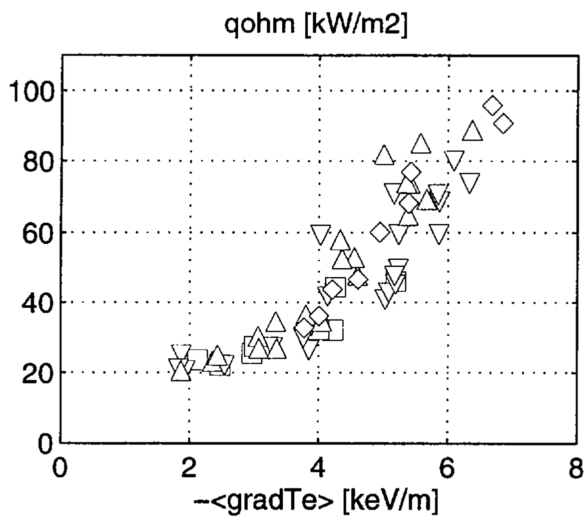

FIG. 3. Power flux versus electron temperature gradient for all shapes and all currents at n_e = (4.0–5.5) × 10^{19} m^{-3}. Symbols represent the triangularity: □ [–0.45, –0.15], ▽ [–0.15, 0.15], △ [0.15, 0.45], ◇ [0.45, 0.75].

Another approach is to set up a simplified radial power balance in which: (i) the radiated power, localised near the plasma edge [2], has been neglected; (ii) in the absence of an adequate measurement of the ion temperature profile T_i, ion and electron channel losses were not separated. Combining the power balance of both species leads to the definition of an effective thermal diffusivity χ_{eff} such that $q_{oh} = -n_e\chi_{eff} \langle\nabla T_e\rangle$ and $\chi_{eff} = \chi_e + \chi_i (\nabla T_i/\nabla T_e)$, where q_{oh} is the input energy flux. In figure 3 the usual plot of the power flux versus the temperature gradient is drawn for the gradient region. Given the rough assumptions made and the poor accuracy of a local power balance, no significant influence of the shape on the effective thermal diffusivity can be detected. A heat flux degradation effect or alternatively a temperature gradient dependence of the thermal conductibility however appears clearly.

3. EFFECT OF SHAPE ON MHD BEHAVIOUR

Sawtooth amplitudes are strongly dependent on triangularity (fig.1d), being largest at positive triangularity and sometimes vanishing at negative triangularity. The sawtooth ramp power density estimated from an X-ray measurement is smaller than the central ohmic power density by typically 0.5 MW/m^3. This is also the minimum ohmic power density necessary to sustain sawteeth in this set of experiments. This power density is believed to correspond to power lost from within the inversion radius by conduction and radiation. MHD mode activity is present as brief bursts at the time of the sawtooth collapses for $\delta > 0$. As δ is reduced the duration of the bursts of modes increases until they merge into continuous mode activity for $\delta < 0$, often resulting in locked modes and disruptions (fig.1e). The reduction of sawtooth amplitudes at low δ is not due to a significant change of the inversion radius. It can be explained in part by a reduction of the central heating by about 0.2 MW/m^3 due to the improved confinement at low δ. The additional power drained by strong MHD modes at $\delta < 0$ can lead to total suppression of sawteeth as seen for $\delta = -0.28$ in fig.1. The dependence of mode activity on δ may be due to strong reduction of the heat flux at the LCFS at low δ, leading to reduced edge temperatures which may destabilise resisitive modes. An intrinsic dependence of mode stability on plasma shape may also play a role.

4. CONCLUSION

In summary, the large variation in global energy confinement time within the domain of explored shapes can be explained by direct geometrical effects combined with heat flux degradation, without the need to invoke a poloidal variation or a shape dependence of the transport coefficients. Changes in MHD activity may largely result from confinement changes rather that being their cause. These conclusions may not apply to other operational regimes, such as auxiliary heated plasmas or near stability limits, as suggested by DIII–D results [3]. This work however indicates that a global confinement optimisation can be achieved by tuning the plasma shape. Negative triangularity, which may exhibit poor MHD or vertical stability [4], is not the only option. More general shapes can be envisaged which could result from a compromise between the benefits of the geometry and other constraints.

ACKNOWLEDGEMENTS

We thank the entire TCV team for their technical effort. This work was partly supported by the Fonds National Suisse de la Recherche Scientifique.

REFERENCES

[1] MORET, J.-M., et al., "How the shape influences the plasma properties of TCV", Controlled Fusion and Plasma Physics (Proc. 23rd Eur. Conf. Kiev, 1996), Vol. 20C, European Physical Society, Geneva (1996).

[2] WEISEN, H., et al., "Measurement and modelling of light impurity behaviour in TCV", ibid.

[3] HYATT, A.W., LAZARUS, E.A., OSBORNE, T.H., in Controlled Fusion and Plasma Physics (Proc. 21st Eur. Conf. Montpellier, 1994), Vol. 18B, Part I, European Physical Society, Geneva (1994) 14.

[4] DUTCH, M.J., et al., in Controlled Fusion and Plasma Physics (Proc. 22nd Eur. Conf. Bournemouth, 1995), Vol. 19C, Part IV, European Physical Society, Geneva (1995) 77.

MODELLING AN RLC CIRCUIT FOR THE INVESTIGATION OF DISRUPTION INSTABILITIES IN TOKAMAKS

R. AMROLLAHI, E. FARSHI
Plasma Physics Department,
AEOI, Tehran,
Islamic Republic of Iran

Abstract

MODELLING AN RLC CIRCUIT FOR THE INVESTIGATION OF DISRUPTION INSTABILITIES IN TOKAMAKS.

A study of the plasma current time derivative in disruption instabilities is reported. Several experiments with the Damavand tokamak are performed, resulting in the observation of underdamped oscillations of the plasma current time derivative during the disruption instabilities. An RLC model was adopted in order to describe the presence of underdamped oscillations of a frequency of ~100 kHz. In this model, the plasma produced inside the tokamak chamber shows capacitance as well as ohmic resistance and inductance properties. After the calculation of R, L, and C, it is seen that the present RLC model satisfies the condition of underdamped oscillations during the disruption instabilities.

1. TOKAMAK CHARACTERISTICS AND EXPERIMENTAL CONDITIONS

The principal data of the present experiment related to the Damavand tokamak are as follows:

Discharge time: 15 ms; R = 36 cm; a = 7 cm; $B_T = 1.2$ T; $n_e = 3 \times 10^{13}$ cm^{-3}; $I_p = 40$ kA; $T_i = 150$ eV; $T_e = 300$ eV.

In the present disruption experiment, a discharge time of 9 ms was measured. The discharge current before the rise was 22 kA and afterwards (and before the first spike) was 28 kA. The loop voltage was 4 and 11 V, respectively (Fig. 1). The toroidal field was about 0.8 T [1]. Visible radiation of D_β (λ = 4860 Å), C III (λ = 4647 Å), O V (λ = 2781 Å) and C V (λ = 2271 Å) was measured by using an MDR-2 monochrometer. The dI_p/dt of the plasma was measured by using a Rogowski coil. In order to avoid elimination of high frequency oscillations of the signal, no attempt was made to measure the plasma current, I_p, by using the usual integrator circuit where it works as a low pass filter.

2. EXPERIMENTAL RESULTS

Figure 1 shows plasma current and loop voltage. As is shown in Figs 2(a, b), in the negative spiking of the loop voltage, where the disruption instability shows up, dI_p/dt has underdamped oscillations. These oscillations are of a frequency of ~100 kHz. Figures 2(c, d), show the radiation spectrum of D_β, C III, O V and C V lines before and during the disruption in the edge and central portions of the plasma.

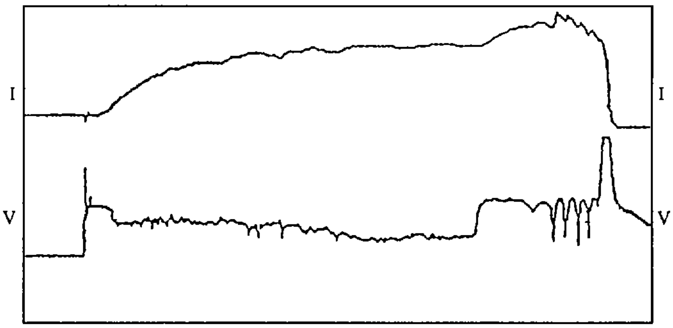

FIG. 1. Loop voltage and plasma current (relative units).

3. RLC MODEL

To explain the underdamped oscillations related to the plasma current time derivative, an RLC circuit was used to model the tokamak plasma. In fact, we assume that a dielectric medium (diluted plasma) exists between the plasma and the tokamak chamber, where it leads to a capacitance C. It is well known that the plasma also has ohmic and induction properties. This is exactly analogous to the transmission lines used in engineering [2]. Figure 3(a) shows the model used for the transmission lines. Since the tokamak plasma follows a closed path, with some approximations the circuit shown in Fig. 3(b) can be simulated. In this approximation, the plasma resistance has been neglected since it is low compared to the other plasma parameters. To analyse the circuit, the quantities L, G and C should be evaluated.

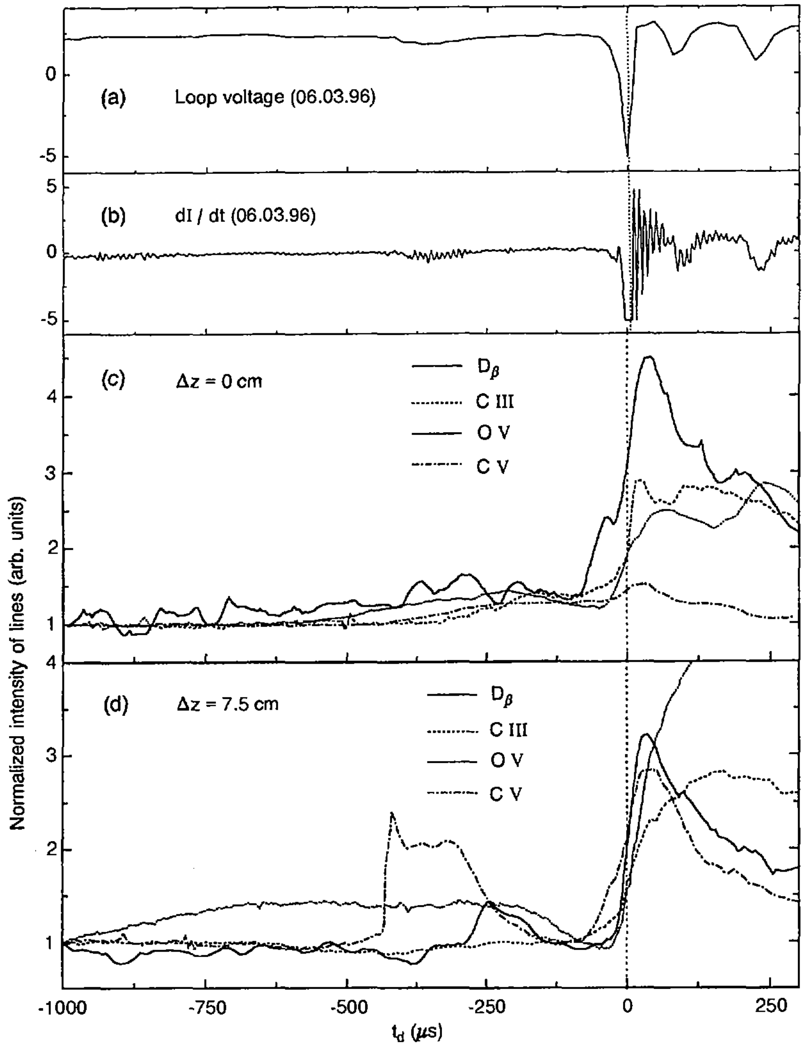

FIG. 2. (a) Loop voltage (the spike is seen to be related to the disruption); (b) dI/dt oscillation (after the disruption underdamped oscillations appear); (c, d) behaviour of light radiation in the visible range at plasma centre and edge (t_d = 0: start of disruption).

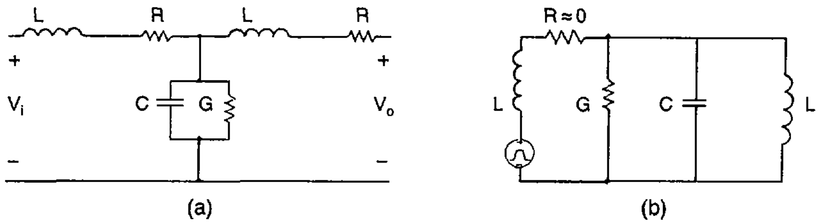

FIG. 3. RLC circuit model for (a) transmission line; (b) a tokamak plasma.

4. CALCULATION

The capacitance, C, of a coaxial cable is given by [3]

$$C = \frac{\pi \epsilon \ell}{\ln(b/a)} \tag{1}$$

where a and b are the internal and external radii of the cable, ϵ is the permittivity of the dielectric material, and ℓ is the cable length. For the Damavand tokamak, we have $a = 7$ cm, $b = 8.2$ cm, and $\ell = 2\pi R = 2.375$ m. To evaluate the dielectric constant, ϵ, the tensorial relationship is neglected for simplicity; instead, the following relation is used:

$$\epsilon_r = \frac{\epsilon}{\epsilon_0} = 1 + \frac{\mu_0 \rho c^2}{B^2} \tag{2}$$

where **B** is the toroidal magnetic field, μ_0 the permeability of free space, ρ the specific mass and c the velocity of light. Following relations (1) and (2) [3], values of 3.7×10^{-8} F/m and 1.8×10^{-6} F are obtained for ϵ and c, respectively. To evaluate the inductance, L, we have [4]

$$L = \mu_0 R\left[\ln\left(\frac{8R}{a}\right) - 2\right] + L_i \tag{3}$$

where L_i is the internal inductance. This leads to a value of $L = 9.6 \times 10^{-7}$ H. In an RLC circuit, using $\omega_0 = 1/\sqrt{LC}$, we have $\omega_0 \sim 7.8 \times 10^5$ rad/s or $f \sim 1.2 \times 10^5$ Hz, consistent with Fig. 2(b). For our further calculations, we use the following relations [2, 5]:

$$G = \frac{2\pi\sigma}{\ln(b/a)} \text{ (mho/m)} \tag{4}$$

$$\sigma = \frac{\pi\epsilon_0^2\,(3kT_e)^{3/2}}{Ze^2 m_e^{1/2} \log \Lambda}\ (\text{mho/m}) \tag{5}$$

where ϵ_0 is the free space dielectric constant, k the Boltzmann constant, T_e the electron temperature, Z the ion charge, e the electron charge, and m_e the electron mass. Log Λ is a constant coefficient. Using the corresponding values of the above quantities, we obtain $G \sim 10^{-1}$ mho and, consequently, $\alpha = G/2C \sim 10^4$. During the disruption due to the presence of the impurities, the value of G will drop to a lower value (Fig. 2(c, d)). In fact, for the value of G, impurities will play an important role in the edge region of the plasma.

The plasma current can also be obtained by solving the RLC circuit, which yields [6]:

$$i_L = Ke^{-\alpha t} \sin \omega_d t \tag{6}$$

where $\omega_d = \sqrt{\omega_0^2 - \alpha^2}$. In our experimental conditions, we have $\omega_d \sim \omega_0$, where we have obtained $\omega_d \sim 7.8 \times 10^5$ rad/s. The value of α is of the order of 10^4, which causes current damping, consistent with Fig. 3(b).

For the current passing through the dielectric G, we have

$$i_G = LG \frac{di_L}{dt} \tag{7}$$

$$(i_G)_{rms} = G\sqrt{L/C}\,(i_L)_{rms} \tag{8}$$

where $G\sqrt{L/C} \sim 0.2$, and it can be concluded that the current passing through G is about 0.2 times the plasma current. This current is also known as the halo current [7, 8].

5. CONCLUSIONS

RLC modelling leads to the assumption of the existence of some structures causing underdamped oscillations of the RLC circuit. These structures can be related to temperature variations, changes and increases in the impurities, charge exchange flux changes, etc. The structures, for a tokamak plasma with disruption instabilities, show a behaviour similar to that appearing in an RLC circuit. The current damping and the frequency of the oscillations are clear indications that our assumption is basically correct. Further studies are needed to elucidate the reason for the underdamped condition in an RLC circuit during the disruption.

REFERENCES

[1] AMROLLAHI, R., in Controlled Fusion and Plasma Physics (Proc. 23rd Eur. Conf. Kiev, 1996), Vol. 20C, European Physical Society, Geneva (1996).

[2] HAYT, W.H., Engineering Electromagneticcs, McGraw-Hill, New York (1981).

[3] CHEN, F., Introduction to Plasma Physics, Plenum Press, New York (1974).

[4] KAMMASH, T., Fusion Reactor Physics, Ann Arbor Science Publishers (1975).

[5] NIU, K., Nuclear Fusion, Cambridge University Press (1989).

[6] DESOER, C., Basic Circuit Theory, McGraw-Hill, New York (1984).

[7] CASTLE, G.G., in Controlled Fusion and Plasma Physics (Proc. 23rd Eur. Conf. Kiev, 1996), Vol. 20C, European Physical Society, Geneva (1996).

[8] GRANETZ, R.S., "Disruptions and halo currents in Alcator C-MOD", paper presented at the APS Plasma Physics Conference (1995).

HEAT TRANSPORT IN THE RTP TOKAMAK

G.M.D. HOGEWEIJ, N.J. LOPES CARDOZO, M. DE BAAR,
C.J. BARTH, M.N.A. BEURSKENS, F.M.A. BOX, C.C. CHU,
D.F. DA CRUZ, F. DE LUCA[1], A.J.H. DONNÉ, P. GALLI[1],
J.F.M. VAN GELDER, G. GORINI[1], B.J.J. GROBBEN, B. DE GROOT,
J.M. HERRANZ[2], C.A.J. HUGENHOLTZ, A. JACCHIA[3], F.A. KARELSE,
J. DE KLOE, O.G. KRUIJT, S. KUYVENHOVEN, J. LOK, P. MANTICA[3],
H.J. VAN DER MEIDEN, F.G. MEIJER, A. MONTVAI, A.A.M. OOMENS,
T. OYEVAAR, M. PETERS, F.J. PIJPER, R.W. POLMAN,
J.H. ROMMERS, M. DE ROVER, F. SALZEDAS, F.C. SCHÜLLER,
P.H.M. SMEETS, C.J. TITO, G.C.H.M. VERHAAG, E. WESTERHOF
FOM Instituut voor Plasmafysica 'Rijnhuizen',
Association Euratom–FOM,
Nieuwegein, Netherlands

Abstract

HEAT TRANSPORT IN THE RTP TOKAMAK.

Transport studies in the RTP tokamak are reported. The topics covered are: (1) generation of steady state hollow electron temperature profiles with negative central shear, and the effects on heat transport; (2) measurements of transport phenomena during the flight of a pellet through the plasma; (3) demonstration of transport barriers; (4) dependence of the diffusivity on q_a, density, temperature and temperature gradient; (5) possibility to describe transient transport by a local mode; (6) test particle transport in chaotic magnetic fields.

GENERAL

The research programme of the Rijnhuizen Tokamak Project RTP (R=0.72 m, a=0.164 m, boronized vessel, $B_T \leq 2.5$ T, $I_p \leq 150$ kA, pulse duration ≤600 ms) concentrates on two issues: i) physics of transport processes in tokamak plasmas and ii) the interaction of millimeter waves with tokamak plasmas. For this purpose, the device is equipped with 0.9 MW Electron Cyclotron Heating (ECH), a pellet injector and a comprehensive set of electron diagnostics including a 20 channel heterodyne ECE receiver, a 19 ch. interfero/polarimeter and a 120 ch. Thomson scattering system with a spatial resolution of 2.6 mm.

1. NEGATIVE CENTRAL SHEAR

With strong off-axis second harmonic ECH, steady state hollow T_e profiles have been achieved reproducibly in medium to high density plasmas at low plasma current (f_{ECH}=110 GHz, P_{ECH}=350 kW, P_Ω~75 kW, $n_e(0) \geq 4\times10^{19}$ m^{-3}, q_a>5) [1]. The

[1] Dipartimento di Fisica, Università degli Studi di Milano, Milan, Italy.
[2] Asociación Euratom–CIEMAT, Madrid, Spain.
[3] Istituto di Fisica del Plasma, Associazione Euratom–CNR, Milan, Italy.

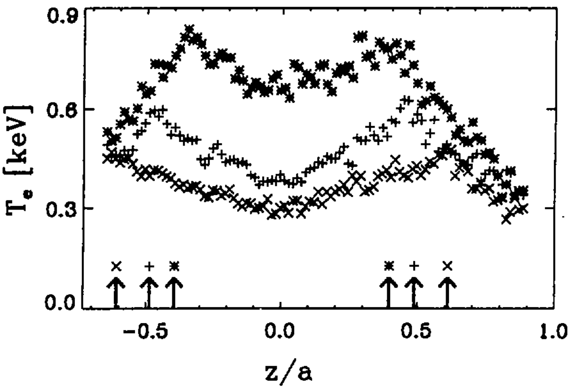

FIG 1. T_e profiles measured with Thomson scattering during off-axis ECH, with absorption positions as indicated ($n_e(0) \approx 4 \times 10^{19}$ m^{-3}).

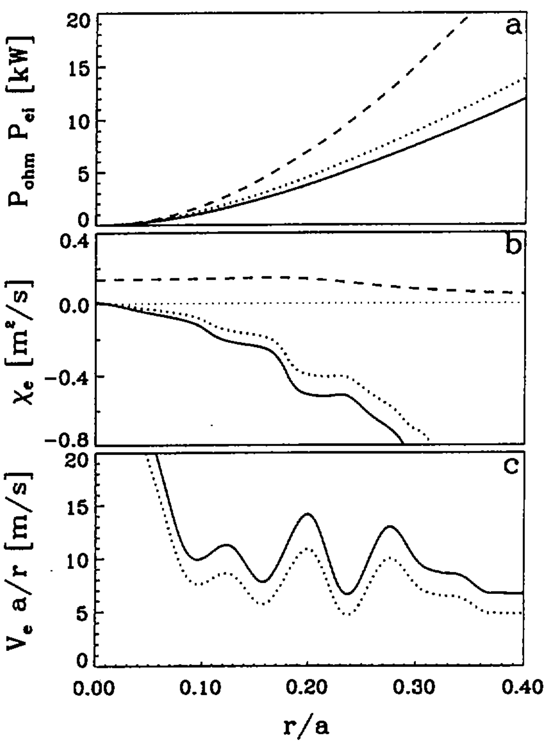

FIG. 2 LPB results for r/a = 0–0.4, for r_{res}/a = 0.5, middle profile in Fig. 1. (a) P_Ω (volume integrated ohmic power density (p_Ω), dashed line) and P_{e-i} (volume integrated electron–ion exchange (p_{e-i})) under two assumption for T_i (see text, full and dotted line); (b) corresponding χ_e^{eff} (full and dotted line) and neoclassical prediction of χ_e (dashed line); (c) outward heat convection velocity V_e, needed to sustain the measured T_e profile, assuming $\chi_e = \chi_e^{neo}$, with the same assumptions for T_i as before.

resonance position (r_{res}) was varied from r/a = 0.3 to 0.7; examples for various r_{res} are shown in Fig.1. The hollow T_e profile leads to reversed magnetic shear from r=0 out to $r=r_{res}$, and to a value of the safety factor q well above 1 everywhere, reaching q>4 on axis. Some of these discharges show MHD activity which has been attributed to double-tearing modes [2].

A local power balance (LPB) analysis has been performed for these discharges. Bolometry showed that radiation losses could be neglected. Since no measurements of the ion temperature (T_i) were available, an assumption for the T_i profile had to be made in order to assess the e-i exchange term (p_{e-i}). We assumed T_i profiles such that the ion thermal diffusivity (χ_i) fulfilled $\chi_i = \lambda\ \chi_i^{neo}$, with λ = 1 or 3. The LPB analysis shows that in the region of reversed magnetic shear the net electron heat flux is very small and in some conditions even directed outward, i.e. **up** the gradient of T_e. As a result the effective electron diffusivity $\chi_e^{eff} = -q_e / n_e \nabla T_e$ is very low (below neo-classical), and comes out negative for discharges with $n_e(0)\approx 4\times 10^{19}$ m^{-3}; see Fig.2a,b. This points to the existence of an electron heat flux not driven by ∇T_e. Even when assuming T_i=0 everywhere ($\lambda=\infty$) such a flux is required. Writing the difference between the neoclassical and measured flux as a convective term,

$$q_{e,conv} = n_e V_e T_e \qquad (1)$$

results in $V_e \times a/r \approx 10$ m/s; see Fig.2c. Note that in this experiment both ∇T_e and the shear are reversed, and that this convective flux is directed outward.

Modulated ECH has been applied to plasmas with hollow T_e profiles. The 110 GHz gyrotron was modulated at a high duty cycle (85-90%) in order to sustain the hollow T_e profile and to generate heat pulses at the same time. In this scheme, the heat pulses propagate inward from r_{res} towards the centre.

Preliminary analysis shows that, if a simple diffusive model is adopted, the amplitude decay of the inward propagating pulses is too strong compared to the phase delay. This again points towards the existence of a convective term counteracting the inward propagation, i.e. outward heat convection. The incremental convective velocity V_e^{inc} required to explain the asymmetry of the pulse amplitude was quite large, at several tens of m/s. Moreover, the heat pulse data show that inside r_{res} the incremental diffusion coefficient χ_e^{inc} has a 'normal' value (~1 m^2/s). Therefore, heat pulse data confirm that the good confinement in the region with reversed shear is not due to a reduction of the (diagonal) heat conduction, but to the fact that the off-diagonal fluxes become more pronounced. This is partly due to the fact that ∇T_e and therefore the diagonal heat flux is so small, that the outward, off-diagonal flux gains in relative importance. However, it is important to realise that the off-diagonal flux is directed outward, hence has changed direction with respect to the normal discharge conditions. The only gradients that have changed direction are ∇T_e, ∇j and the shear. The n_e profile does not become hollow; we have no information on the velocity shear.

2. ENHANCED TRANSPORT DURING PELLET ABLATION

Pellet ablation was studied by injecting a single pellet (~5×10^{18} atoms/pellet, ~700 m/s) radially into ohmic target plasmas (B_T=1.7-2.25 T, q_a=4.1-5.3), and taking Thomson scattering profiles **during** the ablation of the pellet, measuring T_e and n_e at ≈120 positions simultaneously in a 15 ns snapshot. The ablation was monitored by the H_α and H_β lines, measured viewing the ablation cloud along the pellet trajectory. Also photographs of the ablation cloud (seen from above) were taken.

It was found that the ablation, and concomittant dramatic perturbations of T_e and n_e, hardly affect the plasma pressure (p_e) until the pellet reaches the sawtooth inversion radius (r_{inv}). As soon as r_{inv} has been passed, a rapid collapse of the core pressure takes place, brought about by a collapse of T_e without a compensating increase in n_e (see Fig. 3). At the same time, within 40 μs a large fraction of the

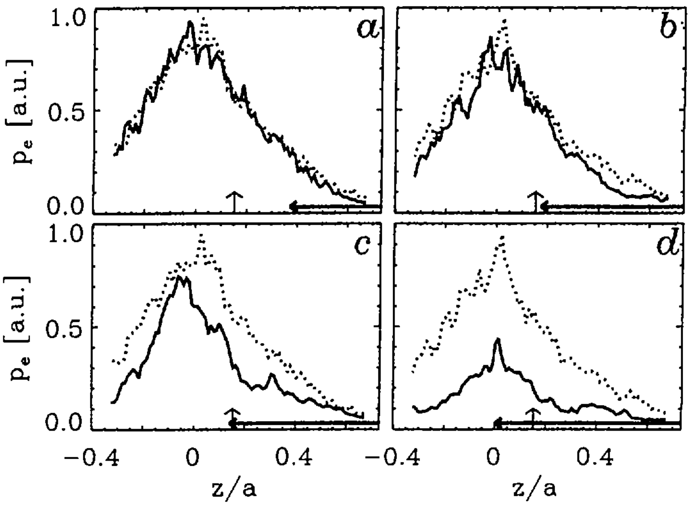

FIG. 3. Electron pressure profiles of 4 RTP discharges during pellet ablation, with the same plasma conditions (full lines). For comparison a pre-pellet profile in a similar discharge is plotted for each case (dotted lines). The region passed by the pellet is indicated by a horizontal arrow; a vertical arrow indicates $r_{inv}/a \approx 0.15$ for all discharges. Note the collapse of p_e inside the pellet position in the two latter cases.

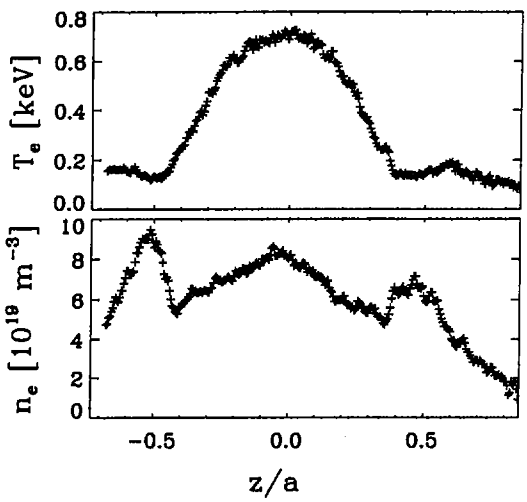

FIG. 4. Example of T_e and n_e profiles measured with Thomson scattering during pellet ablation with oblique injection. The profiles were taken at the moment the pellet has come closest to the magnetic axis (at $r/a = 0.35$, where $q \approx 1.4$) in a discharge with $n_e(0) \approx 8 \times 10^{19}$ m^{-3}, $q_a = 5.1$.

plasma pressure is lost from the entire plasma [3], corresponding to an effective diffusivity of $\approx$100 m^2/s. It is hypothesized that when the pellet crosses r_{inv} a temporary strong ergodization of the magnetic field is induced through the rapid growth of an m=1 island, which overlaps with islands already formed at larger radii. Recently the pellet injector was modified such as to allow the injection of pellets under a vertical angle of up to 8 degrees. In this way it is possible to tune the pellet trajectory such that it either just misses r_{inv}, or hits it tangentially. In a first measuring campaign, many interesting T_e and n_e profiles were measured; their analysis is under way. As an example, Fig.4 shows T_e and n_e measured at the moment that the pellet has come closest (r/a=0.35) to the magnetic axis.

3. TRANSPORT BARRIER

Various types of experiments in RTP point towards the existence of a strong thermal transport barrier near r_{inv} [4]. Firstly, when intense centrally localized additional heating is applied, a narrow region with an extremely steep T_e gradient is found near r_{inv} [5]. Secondly, this transport barrier has been made visible with off-axis modulated heating: placing the modulated heat source just inside or outside the barrier yields dramatic different phase and amplitude profiles of the induced heat pulse [6]. Thirdly, the pellet ablation experiments described above can be interpreted in terms of a transport barrier near r_{inv} which is temporarily destroyed by the ablating pellet.

4. DIFFUSIVITY: DEPENDENCE ON q_a, T_e, ∇T_e AND n_e

Dedicated experiments were carried out to measure the incremental heat diffusivity χ_e^{inc} by means of modulated ECH, in discharges in which T_e and ∇T_e were varied independently. This was achieved by strong off-axis continuous ECH, leading to a very flat T_e profile, and simultaneous application of on-axis modulated ECH. By varying the duty cycle, and thus the average power, of the modulated source, ∇T_e could be varied from $\approx$0 to 10 keV/m at a very modest variation of T_e. (Fig.5) [7].

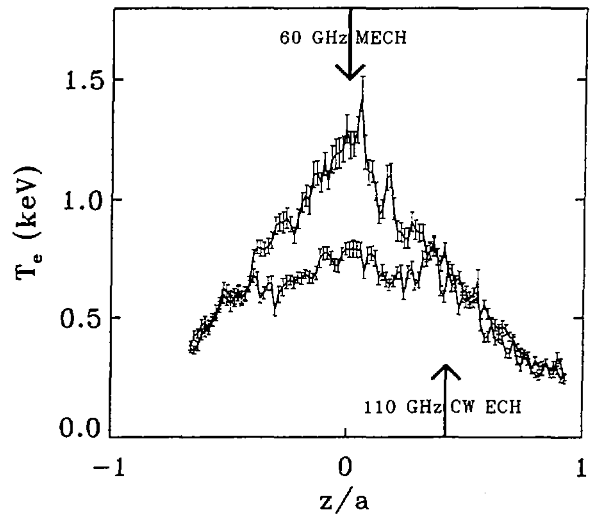

FIG. 5. Application of strong off-acis ECH is used to establish broad, flat-top T_e profiles. On-axis deposition of modulated ECH is used for heat pulse propagation studies. By varying the average power of the modulated ECH, ∇T_e was varied independdently of T_e.

Modulated ECH was also used to measure the profile of χ_e^{inc} in a series of discharges in which q_a was varied from 3.2 to 5 [6]. Furthermore, sawtooth heat pulse propagation was studied in discharges with different heating power, yielding measurements of χ_e^{inc} for a variation of both T_e and ∇T_e. Moreover, a scan of n_e was carried out [7].

Despite the single parameter scans over significant ranges, no significant parameter dependence could be demonstrated. All data could be described using a single χ_e^{inc}-profile. This features a transport barrier near r_{inv}. Outside this barrier χ_e^{inc} increases from ≈ 2 m^2/s to ≈ 10 m^2/s at the edge, while inside the barrier $\chi_e^{inc} \approx 4$ m^2/s. Outside r_{inv} χ_e^{inc} exceeds the power balance value by a factor 2-3 everywhere. Dependences on q_a, T_e, ∇T_e or n_e stronger than a power 0.5 could be rigourously excluded. A strong T_e dependence as reported from TFTR [8] ($\chi_e \propto T_e^{1.5\text{-}2.5}$) is not compatible with the RTP measurements.

5. TRANSPORT: LOCAL OR NON-LOCAL?

Dedicated experiments were carried out to shed light on the question whether heat transport can be described as a local phenomenon or not [7]. Experiments in which the ECH power was switched (from off to on) were used for this purpose. A detailed analysis of the evolution of the T_e profile was made, based on ECE and a sequence of Thomson scattering profile measurements. On the basis of similar experiments in the W7-AS stellarator Stroth proposed a non-local model in which the local value of χ_e depends directly on the input power [9]. A similar model did provide a satisfactory description of the RTP data. However, a local model could match the RTP data equally well, provided that the heat flux is described as the sum of two components (an outward diagonal term and an inward off-diagonal term) with different associated time constants. Experiments with modulated ECH corroborate this picture.

6. TRANSPORT IN A CHAOTIC MAGNETIC FIELD

Detailed measurements of the T_e profile in RTP have revealed that small scale magnetic structures are generally present in the plasma [5,10]. This was an incentive to study thermal transport in stochastic magnetic fields. Such a study generally involves two steps: i) finding the radial field line displacement as a function of the toroidal angle, and ii) constructing the random walk of test particles by invoking some mechanism that decorrelates the particles from the field lines.

Numerical studies were carried out in which as a first issue different types of perturbations to the magnetic field were compared. In particular, global perturbations such as generally used in the literature were compared to local perturbations due to current filaments. It was shown that with the latter type a lower level of magnetic perturbation is needed to reach the same level of stochasticity (as determined by the widths of stochastic layers and other quantifiers). This can be understood since the global perturbations contribute to the field perturbation also in regions where they are not resonant and thus do not contribute to field stochastization [11].

Secondly, the study of field line transport revealed that under no realistic circumstances the field line excursions can be considered as a Gaussian random process. In fact, the field line transport starts out as a superdiffusive process, but it saturates and is subdiffusive in the long run, with the displacement proportional to (path length)$^{0.25}$ [11].

Thirdly, it was shown that at all realistic perturbation levels the effect of magnetic shear remains a very important aspect of the fanning out of field lines with increasing toroidal angle. Rather than the exponential divergence of neighbouring field lines resulting from the field stochasticity, the linear field line separation due to shear determines the decorrelation of field lines. The evolution (for increasing toroidal

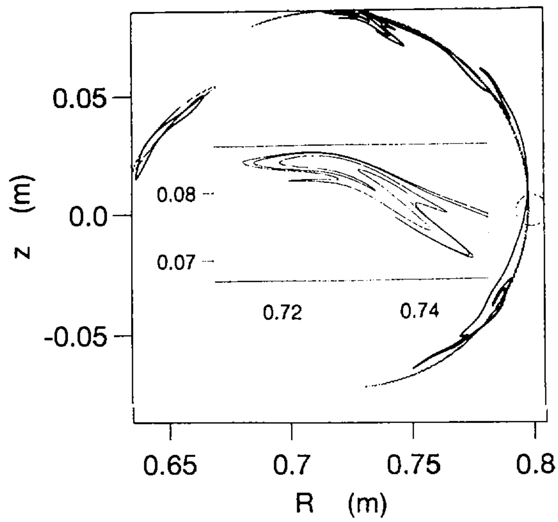

FIG. 6. A computation of the evolution (for increasing toroidal angle) of the shape of a bunch of field lines that initially has a circular cross-section, in a stochastic tokamak field with turbulence level $b/B = 10^{-3}$. Plotted are the initial circle and the cross-sections after one and five revolutions around the torus. The light grey curve shows the effect of shear only. Note that the stretching due to the magnetic shear dominates over the stochastic motion of the field lines. The combined effect of stretching and stochastic radial motion leads to an intricate folding process.

angle) of a bunch of field lines with an initially circular cross section, under the combined influence of shear and field stochasticity, leads to extremely intricate patterns within a few revolutions around the torus; see Fig 6. These patterns differ essentially from the isotropic patterns assumed in the standard treatments of stochastic fields (e.g.[12]), and lead to different (smaller) test particle transport [11].
Using the numerical results for the field line displacement, test particle transport was computed for a number of different decorrelation mechanisms. Apart from collisions and temporal field fluctuations one new mechanism is introduced, namely the synergy of electrostatic and magnetic turbulence. In this case the magnetic turbulence provides the radial step, while the electrostatic fluctuations determine the decorrelation of the test particle from the field line. This leads to an effective transport that is much larger than would result from either the magnetic or the electrostatic fluctuations alone. The test particle transport coefficient increases weakly with particle velocity [11].

Finally, a Hamiltonian description of the drift orbits of strongly relativistic (passing) particles in unperturbed and perturbed magnetic fields was given [13].

GENERAL DISCUSSION

The large number of different experiments carried out to uncover aspects of electron heat transport lead to the following general conclusion. Firstly, it is found that there is a pronounced transport barrier near the sawtooth inversion radius. This has been demonstrated by various experimental techniques, and under a variety of plasma conditions. Secondly, it was shown that off-diagonal heat fluxes (i.e. not driven by

∇T_e) play an important role in the power balance. Such a flux is particularly pronounced with negative central shear, in which case it is directed outward. The off-diagonal flux can be influenced significantly by the ECH. In experiments in which the ECH power was switched from 0 to 350 kW, the response of the plasma could be described by a local, diffusive transport model provided it accounted for the off-diagonal flux. Also the experiments in which T_e and ∇T_e were varied independently gave evidence for the existence of a significant off-diagonal flux which varies depending on the ECH power. A conclusive model has not yet been constructed.
Thirdly, the diagonal electron heat diffusivity as measured in perturbative experiments of various kinds turned out to vary very little between different plasma conditions. In particular, the parameters T_e, ∇T_e, n_e and q_a have very little influence on χ_e^{inc}. The good confinement in the region of negative shear is in RTP attributed to the off-diagonal flux rather than a change in χ_e^{inc}.

ACKNOWLEDGEMENTS

This work was performed under the Euratom-FOM, the Euratom-ENEA-CNR and Euratom-Ciemat Association agreements, with financial support from NWO, CNR, Ciemat and Euratom.

REFERENCES

[1] HOGEWEIJ, G.M.D., et al., Phys. Rev. Lett. **76** (1996) 623.
[2] DONNÉ, A.J.H., et al., IAEA-CN-64/EP-8, these Proceedings, Vol. 3.
[3] DA CRUZ, D.F., Jr., et al., Phys. Rev. Lett. **75** (1995) 3685.
[4] HOGEWEIJ, G.M.D., et al., Nucl. Fusion **36** (1996) 535.
[5] LOPES CARDOZO, N.J., et al., Phys. Rev. Lett. **73** (1994) 256.
[6] MANTICA, P., et al., Nucl. Fusion **36** (1996) 1317.
[7] PETERS, M., PhD Thesis, Eindhoven University of Technology (1996).
[8] EFTHIMION, P.C., et al., Phys. Rev. Lett. **66** (1991) 421.
[9] STROTH, U., et al., Plasma Phys. Control. Fusion **38** (1996) 611.
[10] LOPES CARDOZO, N.J., et al., ICPP 1994 (Foz do Iguaçu), AIP Conf. Proc. **345** (1995) 135.
[11] DE ROVER, M., PhD Thesis, Eindhoven University of Technology (1996).
[12] RECHESTER, A.B., ROSENBLUTH, M.N., Phys. Rev. Lett. **40** (1978) 38.
[13] DE ROVER, M., LOPES CARDOZO, N.J., MONTVAI, A., Phys. Plasmas (in press).

WARE PINCH EFFECT IN TORE SUPRA

H. CAPES, P. LAPORTE
Association Euratom–CEA,
Centre d'études de Cadarache,
Saint-Paul-lez-Durance,
France

Abstract

WARE PINCH EFFECT IN TORE SUPRA.

Particle transport in low β_p plasmas is investigated. Emphasis is placed on the correlation between central particle density and toroidal electric field. For two types of Tore Supra discharge, with LH current drive or in the PEP mode, the loop voltage profile deduced from an equilibrium reconstruction is used to calculate the velocity of the Ware pinch. A particle transport analysis for the plasma centre shows that a transport model assuming both a Ware pinch velocity and low, but anomalous diffusivity, allows the electron density evolution to be modelled correctly. In the outer part of the plasma, the transport coefficients remain anomalous.

1. INTRODUCTION

The role of particle transport is fundamental for understanding anomalous transport and improving fusion reactor performance. One of the most important questions concerns the origin of convective particle flux. Indeed, in contrast to the electron temperature, the electron density does not show high profile resiliency, and, in general, the particle flux does not exhibit strong non-linearity in its dependence on the density gradient [1]. The particle transport is modelled in terms of two transport coefficients: particle diffusivity and pinch velocity. These two transport coefficients, identified from an analysis of transient density profiles, are generally reported to scale with density and power, similarly to the electron heat diffusivity obtained from an equilibrium power balance analysis [2]. However, the mechanism of the observed particle pinch is not understood nor are the thermodynamical forces driving the convective part of the particle flux known accurately. Indeed, the particle pinch can be modelled by off-diagonal elements in the transport matrix related either to the gradient of the temperature [3] (during sawteeth), or the safety factor [4] (in steady state), or the parallel electric field [5] (after the onset of electron cyclotron heating). The goal of this paper is to analyse the link between the observed pinch velocity and the neoclassical prediction in experiments, where a strong density perturbation is associated with a strong variation of the loop voltage. Here, low β_p plasmas are investigated for which the Ware pinch effect is the dominant part of the neoclassical velocity. The selected discharges, with LH current drive or in the PEP mode, exhibit strong density profile perturbations mainly localized in the central part of the plasma, allowing accurate transport analysis.

2. EXPERIMENTS AND TRANSPORT ANALYSIS

Since the analysis of density perturbations induced by a gas puff does not provide accurate information on transport near the plasma centre, density perturbations generated either by LH current drive or on-axis pellet injection are analysed in terms of a transport model including both anomalous and neoclassical contributions. With LH current drive, a flattening of the density profile is generally observed when the average density can be kept constant during LH wave launching. In contrast, in the PEP mode, an increase of the central density during the relaxation phase following on-axis pellet sublimation has been reported [6]. In order to calculate the neoclassical contribution to the flux, the parallel electric field must be known. It is usually deduced by solving the current diffusion equation, which can lead, for non-stationary plasmas, to large error bars. This is mainly due to the MHD activity and to uncertainties on the source values of the central Z_{eff} and the non-inductive current. Instead of solving the resistive current equation, the parallel electric field can be deduced by computing the time derivative of the poloidal magnetic flux ψ obtained from a time sequence of equilibria [7, 8]. Here, the IDENTD equilibrium code [7] is used, and the loop voltage E is calculated at a fixed radial position from the relation $E = -(\psi(t + \Delta t) - \psi(t))/\Delta t$. Equilibrium identification is constrained by measured values of poloidal field and flux. Different time intervals Δt are used (Δt = 50, 75, 100 ms), which leads to an estimated error of the time derivative of ±35%, larger than the uncertainties on the

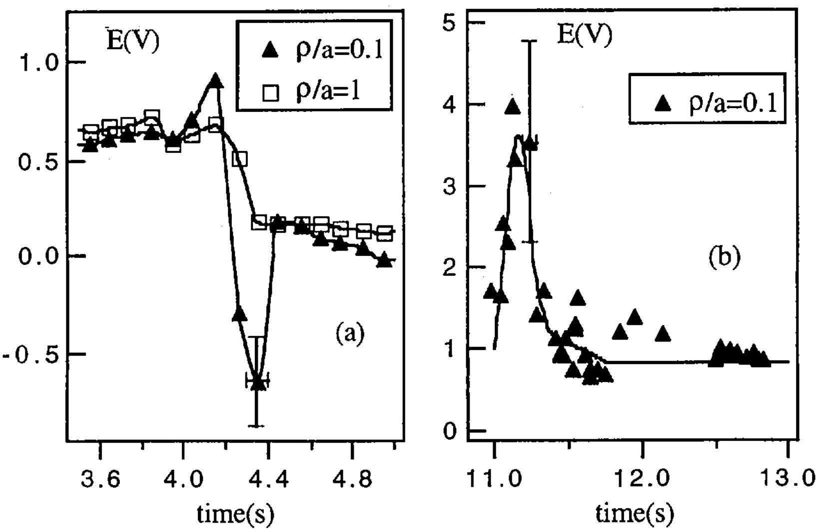

FIG. 1. Loop voltage E, in volts, calculated (a) during LH heating and (b) in the PEP mode. The LH wave is coupled to the plasma at t = 4.2 s, and pellet sublimation occurs at t = 10.8 s, with ICRH heating applied at t = 11.25 s. The uncertainties arising from time derivative evaluation reach ±35%. The fitted curves (—) result from a least squares calculation.

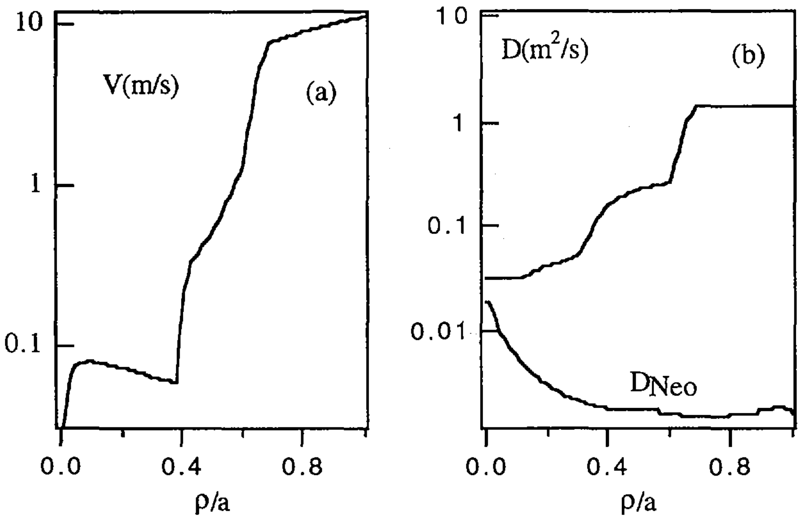

FIG. 2. Profile of transport coefficients (a) V and (b) D. The inward pinch velocity is neoclassical inside $\rho/a < 0.4$.

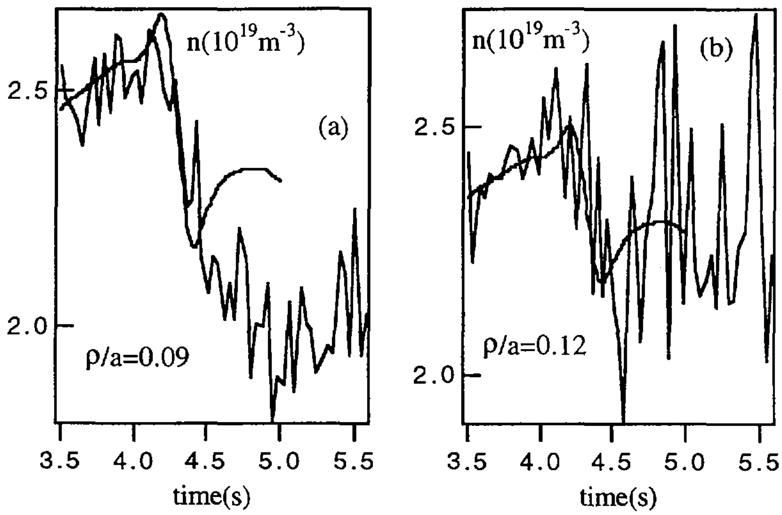

FIG. 3. Time evolution of calculated central density (—) compared to Thomson data for two radial positions: (a) $\rho/a = 0.09$ and (b) $\rho/a = 0.12$.

poloidal flux identification (±15%). Finally, the temporal and spatial electric field profiles are obtained by fitting the values deduced from the IDENTD analysis with a least squares method (Fig. 1). In the following, the fitted loop voltage profile is used to calculate the neoclassical particle flux, and the anomalous particle flux is adjusted in order to reproduce the interferometer and Thomson scattering signals.

2.1. LH current drive experiments

During LH current drive experiments, the loop voltage plotted in Fig. 1(a) decreases strongly at the plasma edge and reaches negative values in the centre, indicating local reversal of the ohmic current circulation. The best agreement between modelling and experiment is obtained when the pinch velocity V is neoclassical in the plasma centre. Indeed, for $\rho/a < 0.4$, the inward pinch velocity calculated just after the onset of the LH heating (Fig. 2(a)) follows the neoclassical expression, which is dominated by the Ware pinch contribution. However, the particle diffusivity D remains anomalous even in the centre, about ten times greater than the neoclassical value calculated at $\rho/a = 0.2$ (Fig. 2(b)). In the outer part of the plasma ($r/a > 0.4$), the anomalous values shown in Fig. 2 are consistent with those identified in standard low density ohmic plasmas. In Fig. 3, the time variation of the central density, calculated with the previously depicted transport coefficients, is compared to the Thomson scattering signals. The negative parallel electric field in the central region of the plasma, which induces an outward Ware pinch, allows the flattening of the density profile to be reproduced, except very close to the magnetic axis ($\rho/a = 0.09$), where larger negative values of the electric field (50%) would be needed to reproduce the Thomson data correctly. Such negative values are slightly outside the estimated error bars.

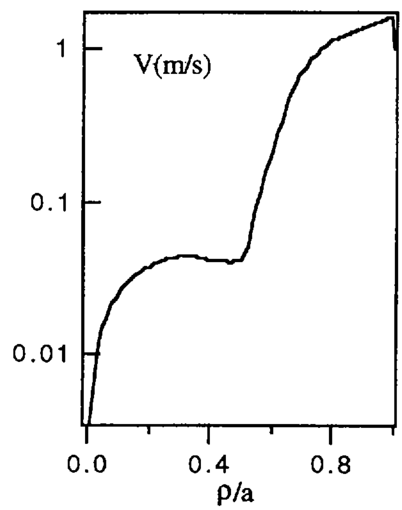

FIG. 4. Pinch velocity profile at t = 11 s. V is neoclassical inside ρ/a = 0.5.

Nevertheless, very localized spatial variations of the electric field cannot be excluded near the plasma centre since no experimental data have been used to constrain the equilibrium identification in this region.

2.2. PEP discharges

In the PEP mode, the loop voltage plotted in Fig. 1(b) increases strongly after pellet injection, mainly because of plasma cooling, and decreases again when ICRH heating is applied (t = 11.25 s). As in the previous case, good agreement is obtained when the neoclassical pinch is used in the central part of the plasma ($\rho/a < 0.5$). The inward pinch velocity used in the simulation at t = 11 s is shown in Fig. 4. It must be emphasized that the central pinch is not only similar in magnitude to the neoclassical prediction, but is also correlated to the parallel electric field, as is predicted by neoclassical theory. Indeed, the particle transport analysis reveals that the Ware pinch calculated with the loop voltage displayed in Fig. 1(b) allows the time variation of the central density to be reproduced (Fig. 5). In particular, improvement in the particle confinement that follows pellet sublimation is correctly modelled by the enhancement of the inward Ware pinch induced by the growth of the parallel electric field. The particle diffusivity still remains anomalous across the plasma ($D(\rho/a = 0.1) = 0.1\ m^2/s$). As in Section 2.1, the anomalous transport coefficients D and V for $\rho/a > 0.5$ agree with those identified in gas fuelled ohmic discharges with comparable densities. In ohmic post-pellet plasmas, the magnitude of the inward pinch velocity has often been reported to be consistent with the neoclassical prediction [9, 10]. However, there was no statement of a strong correlation of the central density with the loop voltage, such as the one presented here.

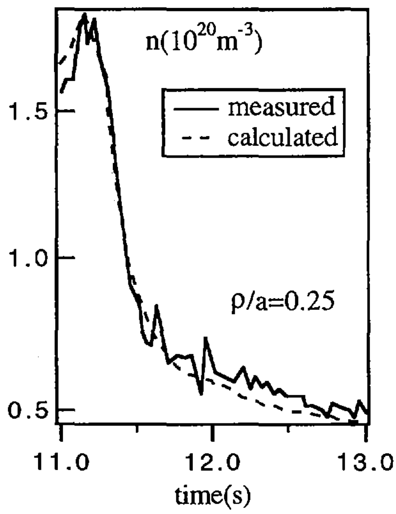

FIG. 5. Time evolution of calculated density compared to Thomson data.

3. CONCLUSIONS

A simulation of low β_p Tore Supra discharges exhibiting strong central particle density and toroidal electric field variations has shown that the plasma turbulence responsible for anomalous transport in the central part of the discharge mainly affects the particle diffusivity. The central pinch velocity remains at a neoclassical level and appears to be correlated with the parallel electric field, as is predicted by neoclassical theory. The fact that the Ware pinch has no anomalous contribution is in agreement with the quasi-linear theory for electrostatic turbulence [11]. Indeed, this theory does not predict an anomalous contribution to off-diagonal elements which couple, in the transport matrix, the radial (parallel) flux to the parallel (radial) thermodynamical force, such as the Ware pinch velocity or the bootstrap current. In contrast to the inner plasma, both diffusivity and inward pinch velocity are anomalous in the outer part of the plasma (typically, $\rho/a > 0.5$), with values close to those obtained in standard ohmic discharges. It is interesting to remember that the anomalous pinch velocity is usually higher in small devices than in large ones. This suggests that atomic physics or plasma edge turbulence could play a specific role in the origin of anomalous convective particle flux at the edge. Further dedicated experiments could be useful in investigating the influence of the Ware pinch. In particular, analysis of perturbed density profiles resulting from modulations of the parallel electric field induced, for example, by modulations of the LH current drive could be promising. Indeed, such experiments where the Ware pinch would be alternatively inward and outward could allow the influences of temperature gradient and parallel electric field on the electron density profile to be studied. Of course, two contraints must be satisfied for accurate transport analysis: first, the particle recycling must not be affected by LH waves, and, then, the LH pulse period must be lower than the central particle confinement time. In addition, the consequences of the neoclassical behaviour of the central particle confinement for the current profile analysis must also be taken into consideration, since part of the bootstrap current depending on the density gradient could be driven by the toroidal electric field, because of the Ware pinch effect. Therefore, a current transport analysis requires performing, in addition, a particle transport analysis.

REFERENCES

[1] O'ROURKE, J., et al., Plasma Phys. Control. Fusion **35** (1993) 585.

[2] EFTHIMION, P.C., et al., Phys. Fluids B **3** (1991) 2315.

[3] CAPES, H., MERCIER, C., in Plasma Physics and Controlled Nuclear Fusion Research 1982 (Proc. 9th Int. Conf. Baltimore, 1982), Vol. 1, IAEA, Vienna (1983) 337.

[4] BOUCHER, D., et al., Rep. JET-P(92) 23, Jet Joint Undertaking, Abingdon (1992).

[5] DNESTROVSKII, Y.N., et al., Sov. J. Plasma Phys. **10** (1984) 137.

[6] GERAUD, A., et al., in Controlled Fusion and Plasma Physics (Proc. 21st Eur. Conf. Montpellier, 1994), Vol. 18B, Part I, European Physical Society, Geneva (1994) 298.

[7] BLUM, J., et al., Nucl. Fusion **30** (1990) 1475.

[8] FOREST, C.B., et al., Phys. Rev. Lett. **73** (1994) 2444.

[9] STROTH, U., et al., Nucl. Fusion **31** (1991) 2291.

[10] GIANNELLA, R., et al., Plasma Phys. Control. Fusion **34** (1992) 687.

[11] HEGNA, C.C., et al., Phys. Fluids B **12** (1991) 3263.

MODELING OF TORE SUPRA EXPERIMENTS AND IMPLICATIONS FOR THE CONTROL OF AN 'ADVANCED' STEADY STATE REACTOR

X. LITAUDON, D. MOREAU, I. VOITSEKHOVITCH, V. BASIUK,
A. BÉCOULET, G.T. HOANG, F. KAZARIAN-VIBERT, Y. PEYSSON
Département de recherches sur la fusion contrôlée,
Association Euratom–CEA,
Centre d'études de Cadarache,
Saint-Paul-lez-Durance, France

Abstract

MODELING OF TORE SUPRA EXPERIMENTS AND IMPLICATIONS FOR THE CONTROL OF AN 'ADVANCED' STEADY STATE REACTOR.

A comprehensive and detailed modeling of the current profile control experiments performed on Tore Supra is reported. A non-linear functional dependence of the local electron heat diffusivity on the local magnetic shear value has been inferred from Tore Supra experiments and has to be included in the transport modeling to reproduce the observed electron temperature profile evolution in a large variety of non-inductive plasmas. Implications of Tore Supra experiments for current profile control scenarios in ITER are studied. In the standard (21 MA) ITER case, current profile optimisation can be achieved to avoid sawteeth throughout the discharge. In 'advanced' ITER operation (13 MA), practical means of controlling the plasma evolution are studied for achieving steady state high performance discharges.

1. Introduction

Experiments in different tokamaks (DIII-D, JET, JT-60U, TFTR, Tore Supra) have shown that optimization of the magnetic shear configuration may contribute to the enhancement of the tokamak performances. The required current density profile modifications are generally the result of a rapid change of the plasma parameters and are transient in nature. A future challenge is to determine a strategy with the combined use of various heating and current drive schemes to access, maintain and ultimately control the required q-profile in steady state tokamak operation.

In this context, non-inductive plasma regimes have been obtained in Tore Supra with various stationary current profile shapes (peaked, flat and hollow current profiles). In part 2 of this paper we report a comprehensive and detailed modeling of the steady state lower hybrid current drive (LHCD) experiments performed on Tore Supra. In particular, the non-linear coupling between the heat diffusivity and the magnetic shear is discussed within the framework of both interpretative and predictive local transport analyses. Then implications of Tore Supra experiments on current profile control scenarios in ITER are presented in part 3. Pulsed (10^3 s) and "advanced" steady state ITER discharges are simulated.

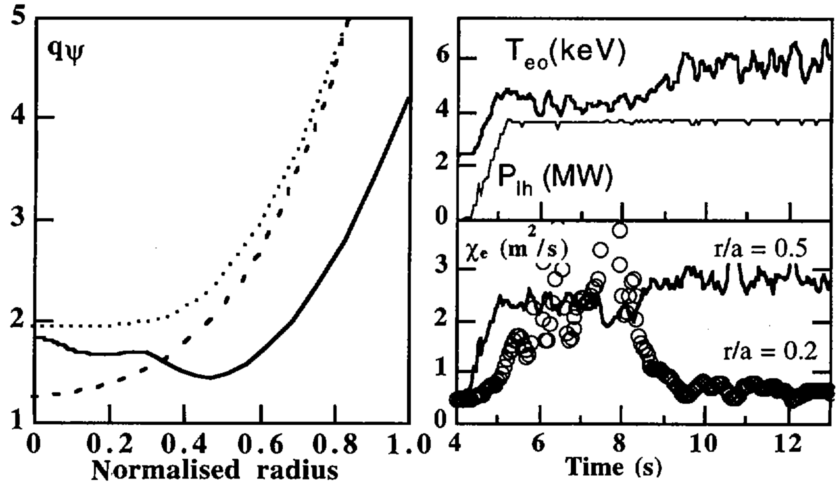

FIG. 1. (left) Stationary q-profiles obtained during various LHCD experiments in Tore Supra; (right) time evolution of T_{e0}, $\chi_e(r/a = 0.2)$ and $\chi_e(r/a = 0.5)$ during the weak central magnetic shear discharges (dotted line). q-profiles and χ_e values are deduced from CRONOS.

2. Modeling of Tore Supra LH non-inductive operation

Using an original current density profile shaping method with the LH waves in the weak damping regimes (multi-pass wave absorption), various stationary q-profiles have been obtained in Tore Supra, for which the magnetic shear, $s_m = r/q\ dq/dr$, in the central region is either positive, close to zero or negative, Fig. 1 (left) [1]. These experiments allow to compare the local confinement properties of plasmas with different current profiles. In particular, spontaneous central electron temperature transitions to an improved core confinement LHEP [LH enhanced performance] phase are reported to occur when the magnetic shear vanishes or is even negative due to the off-axis character of the LH power and current deposition, Fig. 1 (right) [1-4].

Both interpretative and predictive local transport analyses were performed with the 1-D CRONOS code [4] to assess the dependence of electron thermal diffusivity χ_e on the local magnetic shear.

2.1 Interpretative local electron transport analysis

For the present analysis, we restrict the data set to discharges where all the experimental data (hard x-ray bremsstrahlung emission measurements, magnetic and polarimetric data, experimental determination of the non-inductive current) are consistent with independent simulations of the LH wave propagation and absorption ray-tracing/Fokker-Planck [5] or wave-diffusion/Fokker-Planck (WDFP) models [6]. The final assessment of the power deposition and non-inductive current profiles is made by comparing the time traces of the full set of magnetic measurements (loop voltage V_l, internal inductance l_i, Faraday rotation angles, $\alpha_{Far.}$, and toroidal safety factor profiles) with their calculated counterparts (CRONOS) using the experimental electron temperature (T_e) and density (n_e) profiles. The sensitivity analysis of the time evolution of various signals with

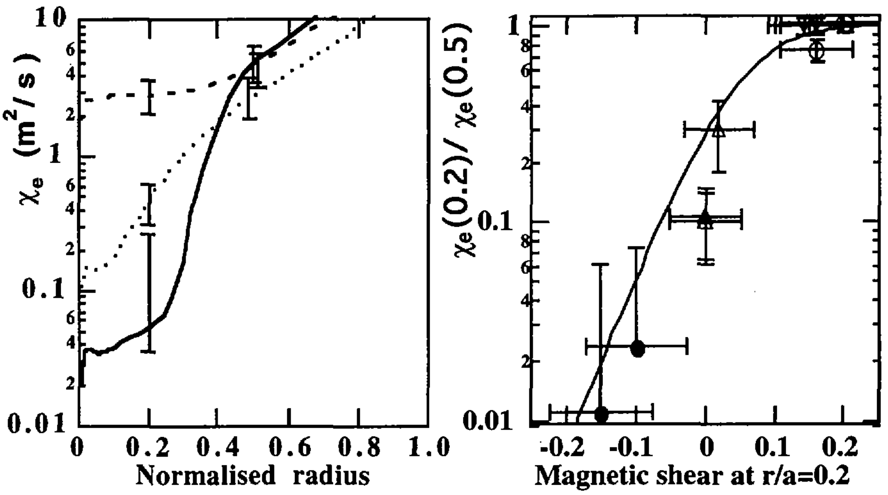

FIG. 2. (left) Various electron heat diffusivity profiles corresponding to plasma discharges performed with the q-profiles shown in Fig. 1 (same legend); (right) $\chi_e(r/a = 0.2)$ normalised to $\chi_e(r/a = 0.5)$ versus magnetic shear at $r/a = 0.2$ for various non-inductive LHCD regimes; the full line is the shear function $F(s_m)$. The error bars on χ_e come from the uncertainties concerning both the determination of the T_e gradient and the power deposition profile.

respect to the LH absorption profile is based on a least square fit parameter between the measured and the calculated data. Then, from the knowledge of the ohmic and LH electron heating sources and of the measured density and temperature profiles, the χ_e radial profiles are deduced. The consistency between various methods for determining the LH current density and power deposition profiles has been carefully checked before drawing conclusions about χ_e.

The results of such systematic and consistent calculations for various LH power deposition and q-profiles are depicted in Fig. 2 (left) when a stationary plasma state (flat toroidal electric field profiles as calculated by CRONOS) is reached. This study exhibits the strong dependence of χ_e on the local magnetic shear : (i) for the monotonic (ohmic-like) q-profile ($s_m > 0$), χ_e is practically constant in the plasma core with a value close to that at mid-plasma radius, (ii) for the weak central magnetic shear configuration χ_e decreases by a factor 5 to 10 at the center of the discharge when the T_{eo} transition is observed, (iii) for the non-monotonic q-profiles produced with off-axis LH power deposition, χ_e is two orders of magnitude smaller in the negative magnetic shear region than in the outer one and becomes close to its neoclassical value [4].

In Fig. 2 (right), χ_e in the internal plasma region ($r/a = 0.2$) has been normalised to its value at $r/a = 0.5$ which approximately corresponds to the standard L-mode value. This ratio has been plotted versus the central magnetic shear (s_m at $r/a = 0.2$) for various non-inductive and ohmic discharges. Such a normalisation of χ_e, which is required since different plasma conditions (toroidal field, plasma current and density, LH power...) are compared, allows to infer a possible functional dependence of the local electron heat diffusivity on the local magnetic shear value. The following filter-like function :

$$F(s_m) = \left[1 + \exp\left(\frac{s_c - s_m}{s_d}\right)\right]^{-1}$$

where s_c and s_d are constant coefficients, provides a fairly good fit to the data shown in Fig. 2. The parameter s_c represents a critical shear value for which $F(s_m)$ starts to decrease significantly below unity, while $1/s_d$ determines dF/ds_m at the critical shear value. $F(s_m)$ has been plotted versus s_m in Fig. 2 (right) with $s_c = s_d = 0.05$ to best reproduce the interpretative results. $F(s_m)$ represents a reduction of χ_e compared to L-mode values in the region of weak or reversed magnetic shear and will be used in predictive modeling with $s_c = s_d = 0.05$.

2.2 Electron transport model and predictive simulations

For predictive simulations we have used the mixed Bohm and gyro-Bohm electron transport model which has been successful in simulating ohmic, L-mode and H-mode regimes in JET [7]. To link the electron heat diffusivity to the magnetic shear, the Bohm term is reduced in the region of flat or negative magnetic shear by the shear function $F(s_m)$ with $s_c = s_d = 0.05$ (see § 2.1).

To simulate the present LHCD experiments, the location of the LH power deposition and the LH current profiles have been deduced from the WDFP code [6] previously validated through hard x-ray emission data and complete ray-tracing simulations [4-5]. The time-dependent bootstrap current is calculated with the self-consistent pressure profiles and plasma equilibria using the NCLASS code [8] previously validated on Tore Supra experiments [1].

We have simulated fully non-inductive LHCD discharges in which the loop voltage was maintained exactly zero through a feedback loop while the plasma current evolved freely to its equilibrium value [9]. This operation mode offers the possibility of decoupling the current density and the electron temperature profiles in a reproducible manner. The set of experiments chosen for the predictive simulations is characterized by the following parameters : central density $n_{eo} = 3\text{-}4 \times 10^{19} m^{-3}$, toroidal magnetic field $B_t = 4T$, plasma current $Ip = 0.6\text{-}0.8$ MA, and edge safety factor $q_a = 6.5\text{-}8.5$, LH power $P_{lh} = 3\text{-}4$ MW.

We first reproduce the time evolution of experiments in which the q-profile was monotonic (ohmic-like). Fig. 3 (left) shows the agreement between the simulated time evolution of the safety factor on axis q_o, V_l, T_{eo}, and their experimental counterpart. The simulation shows that the pressure and current profiles reached a stable state within 3s with T_{eo} = 4-5 keV, q_o = 1.4 while the central magnetic shear values are kept above the critical shear parameter s_c, i.e. $F(s_m) \approx 1$. Furthermore, the calculated electron temperature profiles fit correctly the Thomson scattering data during the whole discharge (Fig. 3 right).

Other discharges corresponding to different conditions (e.g. different LH phasing or initial ohmic conditions) have been realised with flat or hollow current density profiles and peaked electron temperature profiles. One of the most interesting characteristics of these discharges is the observed transition to the "so-called" hot core LHEP phase when the electron temperature profile peaks in the plasma core (see Fig. 1 right). Fig. 3 shows the predictive time evolution of the central electron temperature and of the temperature profiles performed by including or not the magnetic shear function $F(s_m)$ in the electron thermal diffusivity model. A better agreement with the experimental temperature profiles is obtained when the transport is reduced close to the gyro-Bohm term only, in the weak magnetic shear region. Furthermore, the improvement of the electron confinement due to the magnetic shear effect plays a major role in reproducing the slow transition ($\approx$ 10 confinement times) of the central temperature from 6 keV to 8 keV which is triggered when s_m at r/a = 0.2-0.3 decreases below s_c.

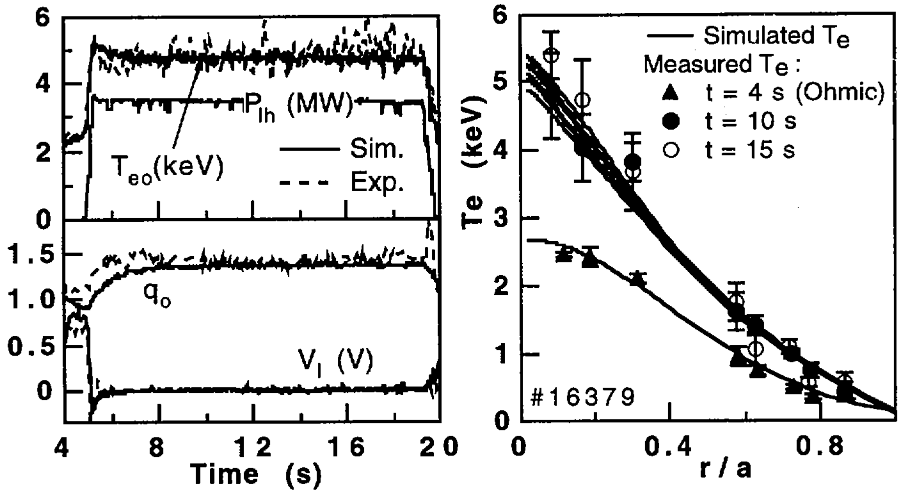

FIG. 3. Time dependent transport simulation (CRONOS) of steady state Tore Supra experiments with monotonic q-profile: (left) the experimental (dashed line) and the simulated (full line) T_{eo}, q_o, V_l time evolution; (right) the experimental and the simulated T_e profiles.

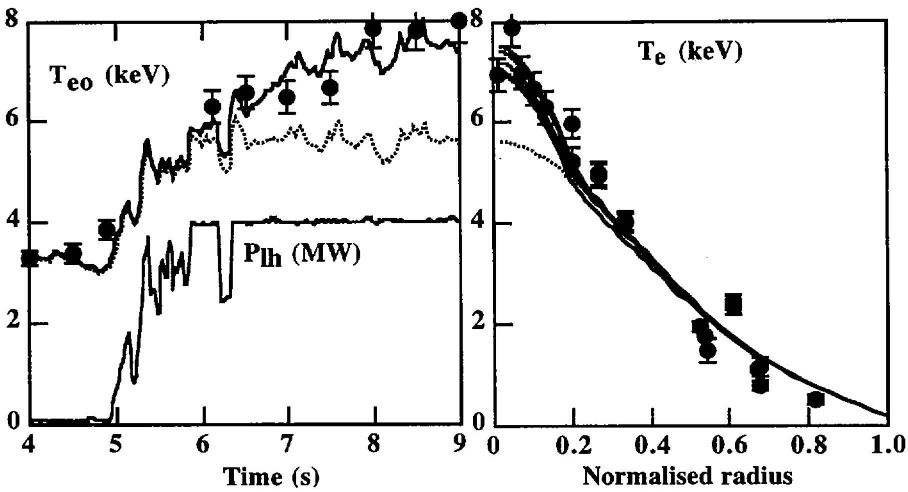

FIG. 4. Time dependent transport simulation (CRONOS) of steady state Tore Supra experiments with weak central magnetic shear and improved core confinement: (left) the experimental (dark circles) and the simulated (full line) T_{eo}; (right) the experimental and the simulated T_e profiles (full lines). The dashed lines correspond to a simulation performed without including the magnetic shear dependence, $F(s_m)$, in the transport model.

From these simulations, we conclude that the non-linear coupling between the heat transport and the magnetic shear has to be included in our modeling to reproduce the electron temperature profile evolution in a large variety of non-inductive Tore Supra plasmas. Transport simulations performed by reducing the electron thermal diffusivity to the gyro-Bohm term with the functional shear dependence $F(s_m)$ in regions of weak or reversed magnetic shear are able to reproduce the emergence of different possible thermal steady states during the current profile evolution.

3. Plasma control in standard and "advanced" steady state ITER operation

Two possible ITER scenarios have been studied with the transport codes ASTRA and CRONOS : i) the stabilization of sawteeth in the 21 MA standard ignition case and (ii) plasma control in "advanced" steady state operation. The proposed scenarios use the attractive plasma confinement regimes obtained through modifications of the current profile (shear optimization). The same Bohm and gyro-Bohm expressions as before have been used in all simulations and the transport model links the heat conductivity to the magnetic shear through $F(s_m)$ as for simulating Tore Supra experiments in section 2. In order to carry out numerous time-dependent simulations over the ITER discharge duration and to study steady state scenarios and possible control scheme, a fast LHCD model has been implemented in both codes. It reproduces the main features of the LH wave absorption and current drive physics both in the low temperature phase [10] before or during current ramp-up (multi-pass damping as in Tore Supra experiment) and in the high-beta burning phase in which LH single-pass damping will occur well off-axis.

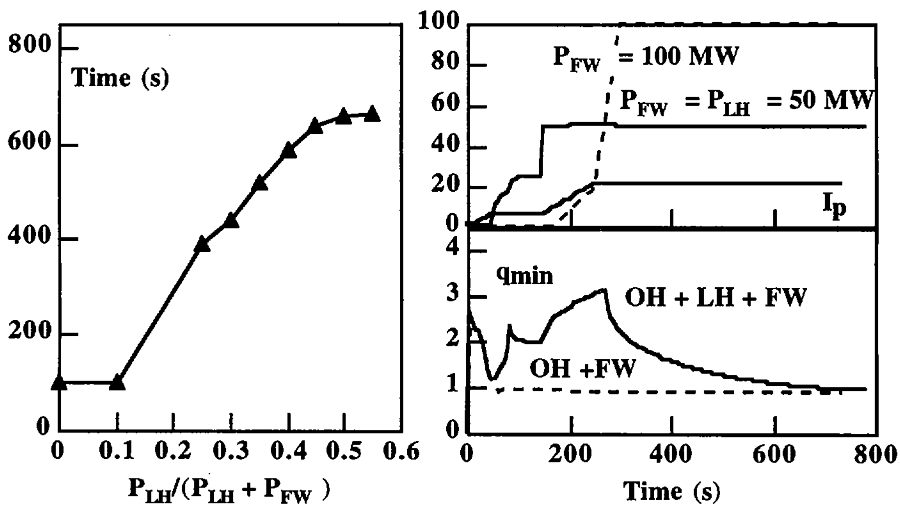

FIG. 5. Sawtooth stabilization in the 21 MA standard ignition case (ASTRA): (left) time in seconds when $q_{min} = 1$ versus relative available amount of LH power; (right) time evolution of plasma current (I_p), heating powers and minimum safety factor (q_{min}) with FW + LH heating and with FW heating only. In the FW + LH case, the FW power waveform is the same as in the FW only case but is limited at 50 MW.

In the standard ITER case with pulsed operation at 21 MA, current profile optimisation can be achieved by non-inductive LH current drive and sawteeth can be avoided. The LH waves are first used during the low current and low beta phase of the discharge in the aim of reversing the magnetic shear when the bootstrap component is still low. Central fast wave power is then added in order to reach ignition while the density is increased. In the burning phase the magnetic shear zone shrinks slowly and the q-profile reverts to a monotonic shape, but q-values can be kept above 1 during the long resistive diffusion time. Simulations have been performed with ASTRA with various ratios between the LH and FW heating powers for a given maximum power of 100 MW while the alpha-particle heating power is maintained at 300 MW by adjusting the fuel density. The result of this scan is shown in Fig. 5 (left) where the time during which the minimum value of the safety factor (q_{min}) is larger than 1 is plotted. With 50 MW of LH and FW powers, the q-profile could be maintained above 1 throughout the discharge for more than 600 s. Fig. 5 (right) shows the time evolution of q_{min}, for the optimised case with 50 MW available for both the LH and FW systems and for a case with 100 MW available as central FW heating only. Too low values of the LH power do not allow to produce a wide negative shear region whereas increasing the LH power can be made only at the expense of central heating which is needed for ignition. The most efficient operation is produced with about equal LH and FW powers.

Practical means of controlling the plasma evolution in "advanced" steady-state operation (Ip ≈ 13 MA) have been investigated with CRONOS. Because of the non-linear dependence of the transport coefficients on pressure and magnetic shear profiles, strong coupling loops exist between the q-profile, heat transport, alpha-particle heating, bootstrap current and resistive diffusion, which in turns determines the q-evolution. Thus, access to optimized MHD-stable profiles and prescribed fusion yields will require simultaneous control of the off-axis (LH)

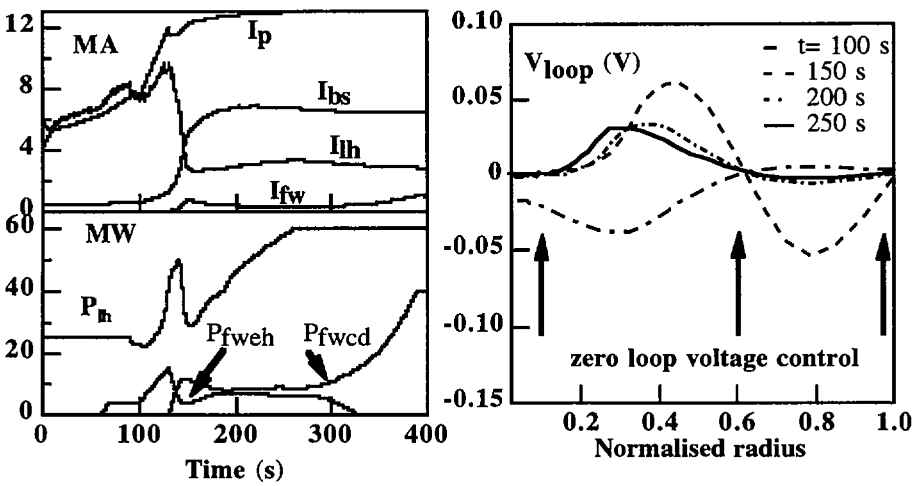

FIG. 6. Plasma control in 'advanced' steady state operation (CRONOS): (left) time evolution of the plasma current, non-inductive currents and RF powers which control the plasma evolution towards steady state; (right) evolution of the loop voltage profiles. Arrows indicate the radii where the loop voltage is controlled.

current generation, of the central heating and current drive power, and of the D-T fuel density. Appropriate feedback schemes will therefore be necessary to control the discharge and maintain it in the desired high-Q steady state equilibrium [11]. It was found that real-time estimates, on a slow resistive time scale, of the ohmic current density or of the internal loop voltage from magnetic reconstructions would be advantageous for control purposes and could allow to maintain a stable reversed shear configuration during a continuous thermonuclear burn. In Fig. 6, a steady state ITER scenario is shown in which the electric field profile was controlled by two independent sources of non-inductive current (LH and FWCD) and the voltage applied on the primary circuit. During the formation of the initial hollow profiles at low current ($\approx$ 6 MA) and just after the 0.15 MA/s rampup phase up to $I_p \approx 13$ MA, the loop voltage is maintained exactly zero (i.e. the plasma current evolves freely to its equilibrium value) while the off-axis LH and central FW driven currents maintain a zero loop voltage at r/a = 0.6 and r/a = 0 respectively. During the burning phase, the alpha-particle heating power (300 MW) is controlled by adjusting the fuel density ($n_e \approx 1.2\text{x}10^{20}$ m^{-3}).

REFERENCES

[1] EQUIPE TORE SUPRA, in Controlled Fusion and Plasma Physics (Proc. 23rd Eur. Conf. Kiev, 1996); Plasma Phys. Control. Fusion (in press).
[2] HOANG, G.T., et al., Nucl. Fusion **34** (1994) 75.
[3] MOREAU, D., Rep. EUR-CEA-FC-1586, in Strong Microwaves in Plasmas (Proc. 3rd Int. Workshop, 1996).
[4] LITAUDON, X., et al., Plasma Phys. Control. Fusion **38** (1996) 1603.
[5] PEYSSON, Y., et al., Phys. Plasmas (in press).
[6] KUPFER, K., MOREAU, D., LITAUDON, X., Phys. Fluids **5** (1993) 4391.
[7] ERBA, M., et al., Rep. JET-P (96) 10, JET Joint Undertaking, Abingdon, Oxfordshire, UK (1996).
[8] HOULBERG, W. A. Oak Ridge Natl Lab., TN, personal communication, 1996.
[9] KAZARIAN, F., et al., Plasma Phys. Control. Fusion (in press).
[10] KUPFER, K., MOREAU, D., Nucl. Fusion **32** (1992) 1845.
[11] MOREAU, D., in Tokamak Concept Improvement (Proc. Int. Workshop Varennes, 1994) 259.

TRANSIENT DENSITY FLUCTUATIONS RELATED TO THE SAWTOOTH CRASH IN THE TORE SUPRA TOKAMAK

P. HENNEQUIN, F. GERVAIS, A. QUÉMÉNEUR, A. TRUC
Ecole polytechnique,
Palaiseau

C. LAVIRON, P. DEVYNCK, A.L. PECQUET
Association Euratom–CEA,
Centre d'études de Cadarache,
Saint-Paul-lez-Durance

France

Abstract

TRANSIENT DENSITY FLUCTUATIONS RELATED TO THE SAWTOOTH CRASH IN THE TORE SUPRA TOKAMAK.

Transient density fluctuations appearing during the sawtooth crash were studied in detail on the Tore Supra tokamak via collective scattering of CO_2 laser light. Their spatial and temporal temporal evolution is strongly correlated with the spatial structure which develops at the outset of the internal disruption (fast hot core motion m = 1, n = 1) inferred from a large set of diagnostics. A simulation of the measurements has been made to account for these results, and a spatial distribution of the sawtooth turbulence related to the topology of this mode is derived.

1. INTRODUCTION

Tokamak sawteeth are still a puzzle. Indeed, the complexity and the diversity of this phenomenon that has been observed for many years and, above all, the fast crash time-scale (100 μs) that is constant over tokamak sizes and performance changes are not yet satisfactorily accounted for by major theories.

The onset of turbulence during the process has been suggested theoretically [1] as a possible mechanism and has been observed experimentally on TFR [2], TFTR [3] and Tore Supra [4].

Transient density fluctuations related to the sawtooth crash have been measured on the Tore Supra tokamak to address both the problems of spatial localization of turbulence and its propagation.

2. SUMMARY OF OBSERVATIONS

About one hundred sawteeth have been studied during identical and stationary ohmic discharges in the Tore Supra tokamak. The experimental context and preliminary results were reported in Refs [4, 5] so that we can restrict ourselves to a summary here.

Each sawtooth was synchronously recorded by a larger set of diagnostics (temperature, density, soft X ray, MHD activity, etc.) on a fast acquisition rate; thus, a detailed observation of the spatial and temporal plasma evolution was possible through the crash, particularly of the fast hot core displacement (lasting about 50 μs), followed by a poloidally asymmetric temperature collapse (50–70 μs). The initial kink-like motion is an m = 1, n = 1 mode, whose direction in a poloidal cross-section is statistically evenly distributed over all poloidal directions for our set of ohmic shot sawteeth.

Density fluctuations ñ(k, t) were measured for different locations of the vertical measurement volume: along a nearly central chord (X = 7 cm from the centre of the q = 1 surface), near the q = 1 surface (X = 23 cm) and outside this surface (X = 30 cm). The half-width of the scattering volume (2.7 cm) is rather small compared to $r_{q=1}$(≈25 cm). The probed fluctuation wave vector **k** was directed horizontally towards the low field side in the poloidal plane of the scattering experiment. Moreover, the direction of the propagation of density fluctuations can be determined by heterodyne detection, and fluctuations propagating (or convected) in the **k** direction appear on the negative frequency side of the spectrum.

A first burst of high frequency density fluctuations is detected synchronously with the fast displacement of the hot core at the beginning of the crash (referred to as 'first phase'). A stronger burst appears when the central temperature collapses and heat flows outside the inversion surface ('second phase'). These fluctuations are superimposed over the quasi-stationary turbulence (QST) usually associated with anomalous transport. The enhancement of the turbulence spectral density during the

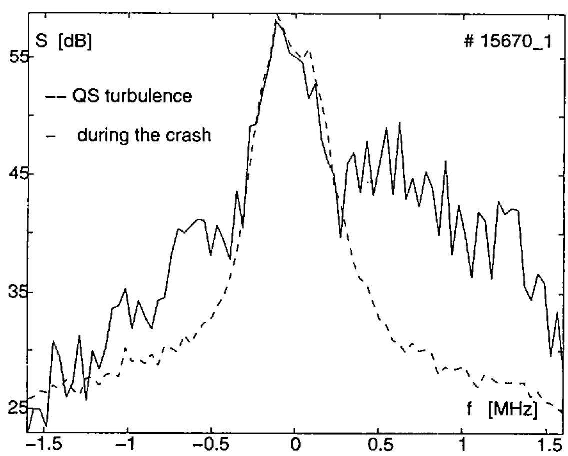

FIG. 1. Enhancement of fluctuation spectral density S(ω) in the high frequency range during the sawtooth crash (phase I, k = 4 cm^{-1}).

crash is noticeable mainly in a frequency range (0.3 to 1.6 MHz) that is higher than the QST one, as can be seen in Fig. 1.

The enhanced power level in this range can reach 18% of the QST level for the first phase, and up to 70% for the second phase ($k = 4\ cm^{-1}$). The turbulence associated with the internal disruption is localized within the $q = 1$ surface as no enhanced turbulence has ever been observed when the measurement chord is set outside the $q = 1$ surface. These fluctuations are, in fact, two orders of magnitude larger than the local quasi-stationary ones, which have been shown to be small in this central zone of the plasma. This could explain the high value of heat diffusivity during the collapse.

3. SPATIAL LOCALIZATION

Nevertheless, beyond these very general features, there is a great dispersion of power levels and frequency spectrum shapes from one sawtooth to another, under otherwise identical experimental conditions.

The measurement chord being static, this has been ascribed [5] to a spatial localization linked with the spatial structure of the MHD mode, which undergoes an arbitrary poloidal rotation from one sawtooth to another. The most natural parameter for an analysis of the data is then the poloidal direction of hot core motion, θ, inferred from SXR emissivity maps reconstructed by tomography.

The case shown in Fig. 1 corresponds to inward propagation, the positive frequency shift of the spectrum being representative of the direction of the fluctuation mean velocity as a Doppler shift. Both positive and negative shifts of the 'sawtooth' spectrum have been observed, depending on the individual sawtooth. A systematic analysis of this shift has shown [5] that fluctuations mainly propagate in the direction opposite to the initial kink-like motion of the hot core as if they flowed away from the hot core compression zone.

Although the power levels also show a strong correlation with the poloidal cartography, an ambiguity remains in deriving a spatial poloidal distribution of the sawtooth turbulence [5]. Indeed, the observations must be interpreted carefully.

4. INTERPRETATION OF THE OBSERVATIONS

Two main effects may bias the observations:

(a) Poor spatial resolution: the scattering signal is integrated all along a vertical measurement chord so that a central phenomenon may be masked by QST, whose level is much higher at the edge than at the centre.

(b) The way the 'sawtooth' fluctuation spectrum is extracted from QST: the 'sawtooth'power level reported is not the exact mean squares value of the fluctuations related to the crash since it only accounts for fluctuations outside the QST frequency range. In fact, they are evaluated by integrating the 'sawtooth' fluctuation spectral density over frequencies after subtracting the QST spectrum; thus, an enhancement in the QST range is not taken into account as it is largely hidden in the QST spectrum.

A simulation of the measurements based on a cinematic model is used to simultaneously account for spatial localization and frequency shift effects. The aim of a comparison between experimental results and such a simulation is to provide a more precise description of the turbulence associated with the sawtooth crash, where spatial localization and velocity distribution are involved.

5. SIMULATION OF THE MEASUREMENTS

5.1. Spectral modelling

The first step is to model the frequency spectrum of the scattered light. It can be related to the plasma flow characteristics through the Doppler shift effect [6]. The frequency shift of the observed spectra is then $\mathbf{k}\cdot\mathbf{v}_0$, where $\mathbf{v}_0$ is the mean plasma flow velocity over the scattering volume. The frequency spectrum may also be formed of other fluctuation modes such as propagating waves.

If the plasma flow is not uniform, the local velocity $\mathbf{v}$ is considered, and the local characteristics of the fluctuation spectral density are assumed to vary slowly along the measurement chord. Observed frequency spectra can then be simulated by adding local contributions over the scattering volume, each of them shifted by $\mathbf{k}\cdot\mathbf{v}$ and balanced by the fluctuation amplitude and the instrumental function (local amplitude of the laser beam).

Power levels (ΔS) are evaluated after integration over frequencies outside the QST frequency range. A low value of power levels may, therefore, be explained either by a low value of the density fluctuation form factor or by a value of the scalar product $\mathbf{k}\cdot\mathbf{v}_0$ comparable with the QST frequency range.

5.2. Amplitude and velocity distributions

The computation of these simulated spectra requires the existence of a particular set of both amplitude and velocity spatial distributions along the scattering chord. Analysis of the experimental observations has previously suggested [5] that a turbulent flow runs along $q = 1$ from both sides of the compression zone, because of kink-like motion of the hot core. The corresponding distributions of turbulence amplitude and mean velocity are shown in Fig. 2.

Figure 3 shows two examples of computed frequency spectra, in the case where the measurement chord is set at $X = 23$ cm (tangential to the $q = 1$ surface).

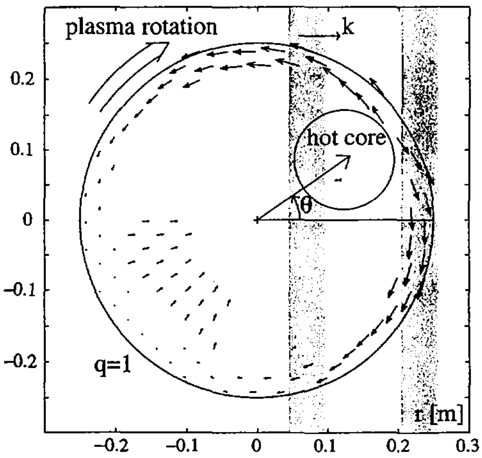

FIG. 2. Phase I turbulence distribution.

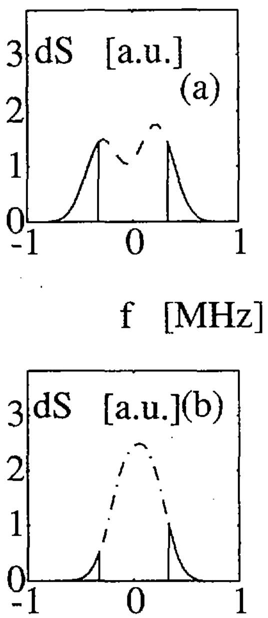

FIG. 3. Simulated spectra.

The additional Doppler effect due to the poloidal plasma rotation, shown by an arrow in Fig. 2, is taken into account in this computation.

This shows that the two flows, on both sides of the hot spot, make different contributions to the simulated spectra, leading to different frequency shifts: the Doppler shift for the co-rotating flow is enhanced by the poloidal plasma rotation.

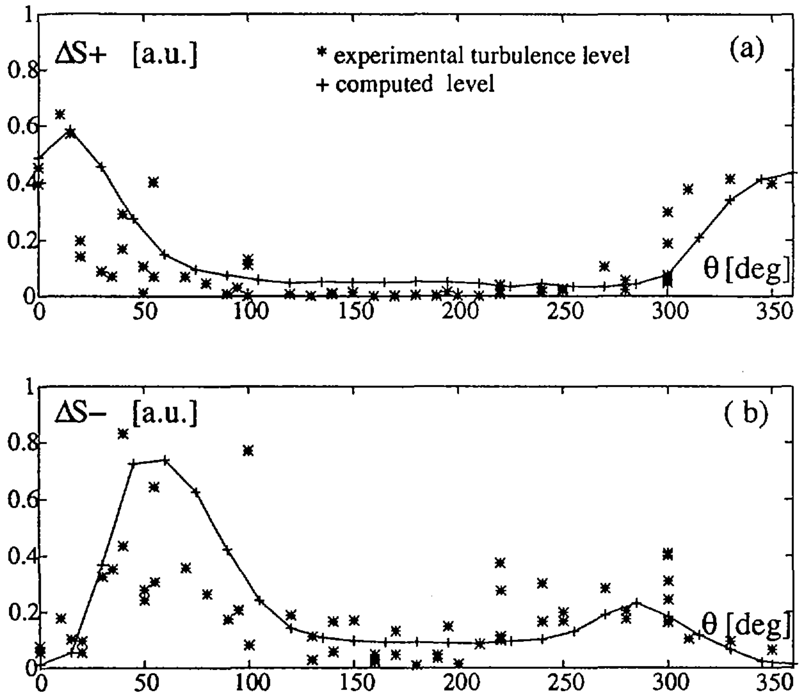

FIG. 4. Comparison of experimental and simulated turbulence levels (phase I) for a measurement chord nearly tangential to the q = 1 surface with X = 23 cm.

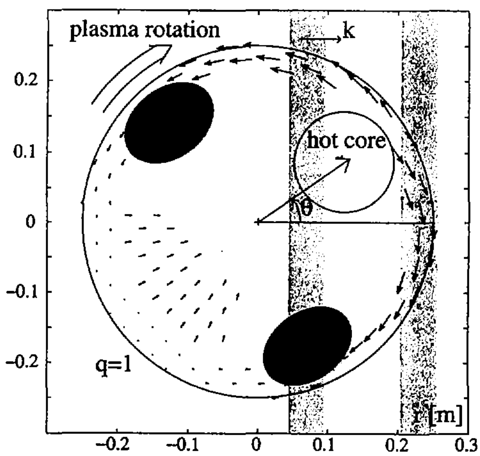

FIG. 5. Phase II turbulence distribution.

On the other hand, the Doppler shift for the counter-rotating flow is set off by plasma rotation to low frequency values, and the specific spectrum is partly hidden in the QS spectrum. For $\theta = 30°$, Fig. 3(a), the co-rotating flow crosses the upper part of the scattering chord in the **k** direction and the lower part in the opposite direction. The two corresponding components are well separated in the spectrum (a), owing to the enhanced velocity. In contrast, when the counter-rotating flow crosses the scattering chord ($\theta \approx 30°$), these two components are not separated (Fig. 3(b)).

5.3. Phase I

A fit of phase I experimental results is represented in Fig. 4, separating positive and negative frequency contributions. These results concern measurements with X = 23 cm, where only the turbulence around the q = 1 surface can be detected, as well as a simulation with the distribution shown in Fig. 2.

Quantitatively, the model accounts for the strong in–out asymmetry observed. The 'up–down-like' asymmetry ($\theta = 30°$ and 330°) comes from the poloidal plasma rotation, which is taken into account by the model, as was discussed above: when the hot core crosses the upper part of the measurement chord ($\theta = 30°$) the Doppler shift is outside the frequency range of QST, while it is hidden by the QST spectrum when it crosses downwards ($\theta \approx 330°$).

When fluctuation measurements are made along the scattering chord which passes through the q = 1 surface closer to the magnetic axis (X = 7 cm), the dissymmetry between kink-like motions crossing the upper and lower parts of the measurement chord ($\theta = 70°$ and 290°) is enhanced. Some turbulence distributed more closely to the plasma centre is detected. The experimental results are well simulated by the return flow shown in Fig. 2.

The flow used for the simulation is partly similar to the one appearing at the outset of the internal kink (ideal or resistive model). The flow velocity along q = 1 is five to ten times higher than that of the hot core motion (1 km/s).

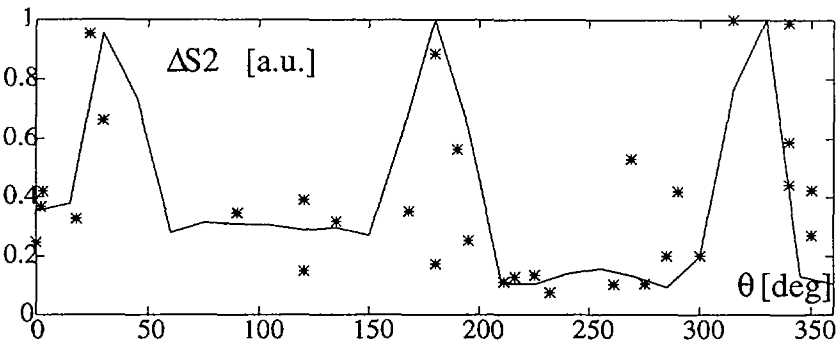

FIG. 6. Comparison of experimental and simulated turbulence levels (phase II) for a central chord X = 7 cm.

5.4. Phase II

During the crash (phase II), the direction of propagation has similar characteristics, but the location of the maximum level versus θ reveals a different localization of the turbulence. Experimental results can be simulated by the configuration shown in Fig. 5, where the location of the turbulence maximum is indicated in grey, located in the wake of the phase I flow on both sides of the cold temperature zone seen in the SXR tomography. Such a comparison is shown in Fig. 6.

6. CONCLUSIONS

The systematic analysis of the turbulence during ohmic sawteeth in Tore Supra has shown that transient density fluctuations appearing synchronously with the sawtooth crash are localized within the q = 1 surface. During phase I, the experimental data are well simulated by fluctuations flowing along the q = 1 island separatrix from the hot core compression zone. During the collapse phase, the location of the maximum turbulence seems to be displaced towards both sides of the colder zone seen in the SXR tomography.

Theoretical models, involving an onset of stochasticity [7], have predicted some turbulence near the destroyed q = 1 separatrix, but a detailed dynamic description of the turbulence behaviour for experimental confrontation is still lacking.

REFERENCES

[1] DUBOIS, M.A., SAMAIN, A., Nucl. Fusion **20** (1980) 1101.

[2] GERVAIS, F., et al., in Controlled Fusion and Plasma Physics (Proc. 16th Eur. Conf. Venice, 1989), Vol. 13B, Part II, European Physical Society, Geneva (1989) 497.

[3] NAZIKIAN, R., et al., in Controlled Fusion and Plasma Physics (Proc. 18th Eur. Conf. Berlin, 1991), Vol. 15C, Part I, European Physical Society, Geneva (1991) 265.

[4] GERVAIS, F., et al., in Controlled Fusion and Plasma Physics (Proc. 20th Eur. Conf. Lisbon, 1993), Vol. 17C, Part I, European Physical Society, Geneva (1993) 223.

[5] HENNEQUIN, P., et al., in Controlled Fusion and Plasma Physics (Proc. 22th Eur. Conf. Bournemouth, 1995), Vol. 19C, Part III, European Physical Society, Geneva (1995) 61.

[6] GRESILLON, D., et al., in Controlled Fusion and Plasma Physics (Proc. 21st Eur. Conf. Montpellier, 1994), Vol. 18B, Part I, European Physical Society, Geneva (1994) 118.

[7] LICHTENBERG, A.J., et al., Nucl. Fusion **32** (1992) 495.

HT-7 SUPERCONDUCTING TOKAMAK AND ITS OPERATION*

HT-7 GROUP
(Presented by J.K. Xie)

Institute of Plasma Physics,
Academia Sinica,
Hefei, Anhui, China

Abstract

HT-7 SUPERCONDUCTING TOKAMAK AND ITS OPERATION.

The superconducting tokamak HT-7 was recently put into operation. Its main objectives are to investigate reactor relevant issues such as advanced operation modes and plasma-wall interaction in the near steady state condition. HT-7 is reconstructed from the former T-7 tokamak at the Kurchatov Institute in Moscow. Many major new design features have been implemented and the machine has been totally reassembled. High power LHCD and ICRF systems have been installed for quasi-steady-state operation. The vacuum chamber was modified with a changeable liner facing the plasma. It can be heated or cooled and also coated with different materials in order to keep a good condition for long pulse discharges. The main parameters are: major radius 1.22 m, minor radius 0.3 m, toroidal field 2.5-3 T, plasma current 0.3-0.4 MA and discharge duration 3-5 s, which will be extended to several tens of seconds after modification. The iron core transformer and poloidal coil system provides ~2.2 V·s magnetic flux with a bias field. The poloidal coils are charged by a flywheel AC motor-generator with a silicon controlled rectifier system which is controlled by a three grade computer system for programming or feedback operation. After test and discharge operation the HT-7 tokamak showed very good properties for carrying out experiments. In an ohmic discharge the plasma parameters reached $I_p \approx 160$ kA, loop voltage ≈ 1 V, with Z_{eff} below 2, and the plasma reached 1.5 s in the ohmic regime. The mean electron temperature ≈ 1 keV and the ion temperature ≈ 0.3-0.5 keV in the ohmic regime. The lower safety factor at the limiter radius reached ~2 without disruption.

After the successful demonstration of the D–T reaction in the JET and TFTR tokamaks, more attention has been given to the feasibility of a tokamak reactor. The key characteristics of a tokamak reactor which have to be fulfilled are steady state operation and high performance of the fusion plasma, along with favourable economic and safety characteristics. These characteristics make up what is called the advanced tokamak operation mode. The HT-7 superconducting tokamak programme is an important step in this direction at the Institute of Plasma Physics of the Academia Sinica. The main efforts are made for the investigation of steady state superconducting operation and advanced operation modes relevant to a reactor.

* This project was supported by the Academia Sinica, the National High Technology Programme of China and the ICSC World Laboratory, and was carried out with the collaboration of the Kurchatov Institute, Moscow, Russian Federation.

1. HT-7 TOKAMAK DEVICE

HT-7 is the first superconducting tokamak in China. It is reconstructed from T-7, the first superconducting tokamak in the world, built by the Kurchatov Institute, Moscow, at the beginning of the 1980s. The purpose of the reconstruction is to improve the accessibility to the plasma, and to provide the possibility to assemble more diagnostics and install wave launchers for high power lower hybrid wave current drive and ion cyclotron resonance heating. Modifications have also been made for long pulse operation with higher plasma parameters. Reconstruction of HT-7 was completed at the end of 1994. Since then testing of the superconducting magnet and other subsystems has been carried out and plasma discharges have been conducted.

The torus of HT-7 (Fig. 1) has a five layer structure, including the cryostat and vacuum vessel, outer and inner copper shell screens with liquid nitrogen cooling, and superconducting magnet with forced flow helium cooling. Four units of rigid and bellows segments make up the vacuum vessel, with 34 ports for diagnostics, wave launchers and other experimental equipment. The toroidal resistance of the discharge chamber is 2.3 mΩ. A changeable stainless steel liner is assembled inside the vessel as the plasma facing first wall for improving the capabilities for heating, cooling and wall conditioning. It also protects the bellows from the plasma bombardment. The vessel can be baked by poloidal field induced current and cooled by water flow. The electrical heating wire in ceramic tubes is assembled on the back of the liner for baking and hot wall operation. The toroidal field coils, which consist of 48 NbTi–Cu

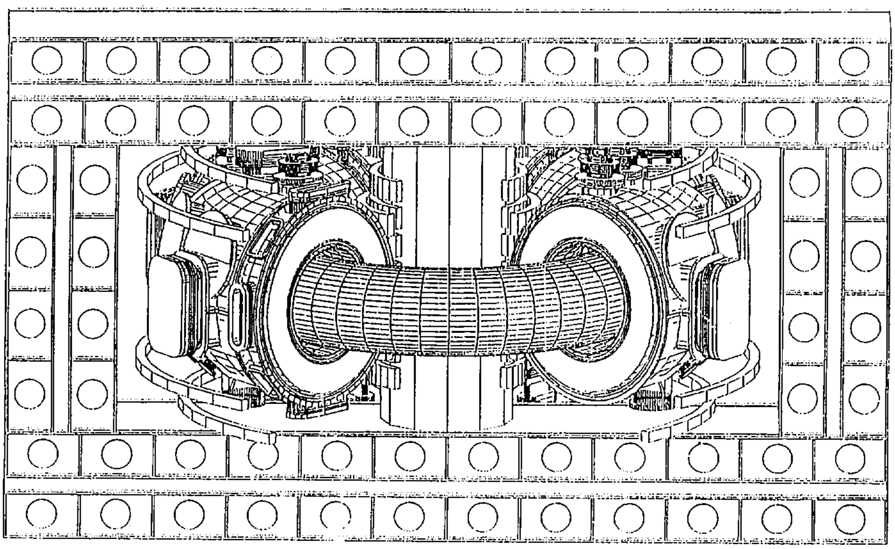

FIG. 1. Torus of the HT-7 superconducting tokamak.

superconducting windings with nine coolant channels, are rearranged into 24 coils for the improvement of accessibility. Two layers of copper screen with 15 mm thickness and the cryostat were remade to increase the number and size of the ports, and the current lead was reconstructed to minimize the cryogenic dissipation.

The designed parameters of HT-7 are:

Major radius (plasma), R	1.22 m
Minor radius	
Plasma, a	0.26–0.30 m
Liner	0.326 m
Vessel	0.372 m
Toroidal field strength, B_t	2.5 T
Magnet temperature, T_m	~4.5 K
Copper screen temperature, T_s	~80 K
Baking temperature	
Liner, $T_{b,l}$	>576 K
Vessel, $T_{b,v}$	>400 K
Plasma current, I_p	~300 kA

Systems on the periphery of the HT-7 device include: the nitrogen liquefier system with 500 L/s liquefying capability and 80 m^3 liquid nitrogen tank capacity; the helium refrigeration system with 100 L/s of liquefying capability and 250 W of refrigeration at 4.5 K; power supply systems for toroidal and poloidal fields with an AC flywheel generator and grid; RF and microwave sources; control and diagnostics systems, data acquisition and processing systems, electrical and water supply systems, and vacuum and technical diagnostics systems.

2. MAIN PHYSICS OBJECTIVES

2.1. Issues to be investigated

The main objective of using a complicated superconducting tokamak is to investigate the issues important for attaining a desirable tokamak reactor. These are:

- Long pulsed LHCD discharge with a duration of more than 10 s;
- AC operation with/without LHCD;
- Plasma current modulation for changing the profile and plasma parameters;
- Profile control by RF power;
- Fuel gas control during steady state discharge;
- Testing of first wall treatment and edge condition handling;
- Improved confinement in different regimes;
- Measurements and investigation of fast electrons and ions;
- Testing of new RF launchers.

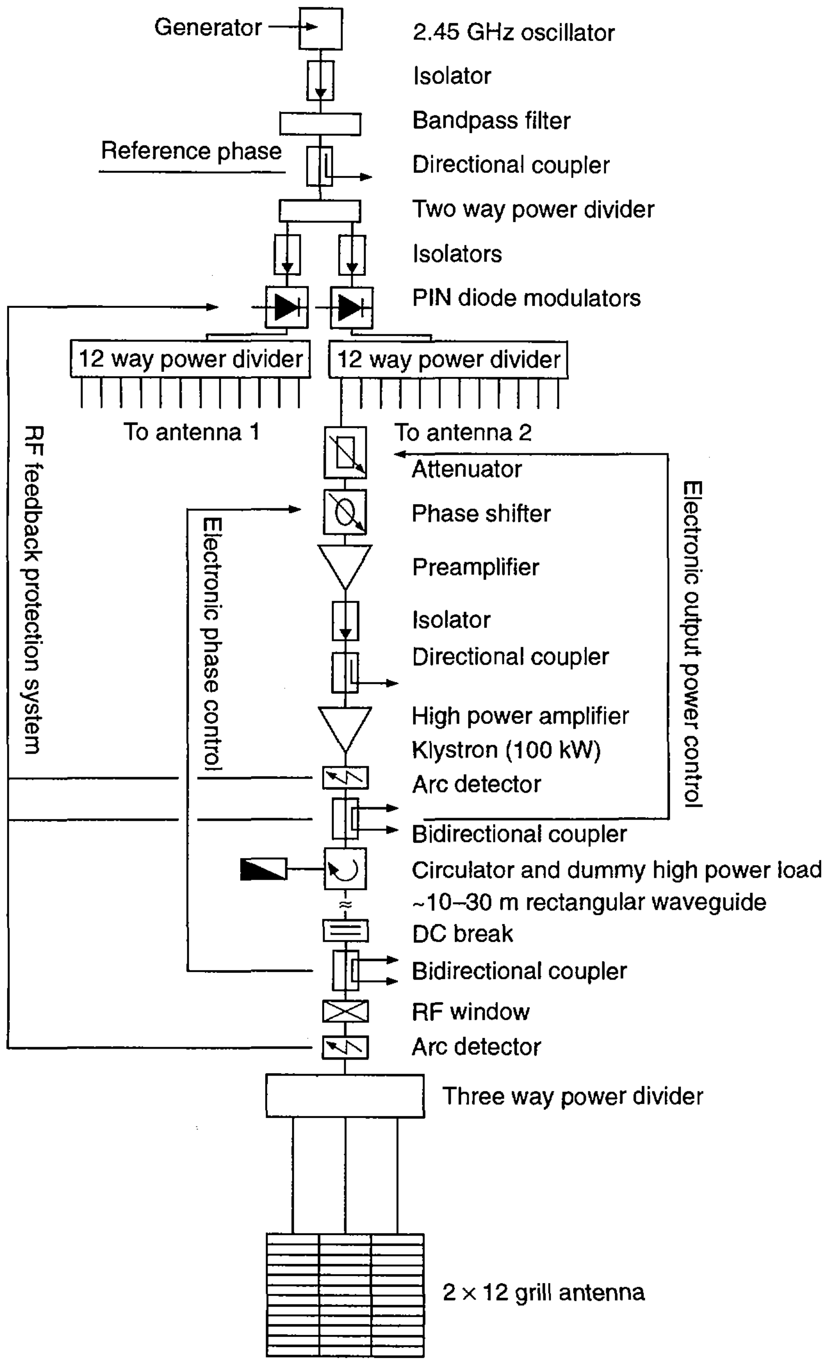

FIG. 2. LHCD system.

2.2. Current drive and heating for steady state operation

LHCD is designed for maintaining steady state operation. The two microwave sources are composed of 12 klystrons, a transmission line and a 2 × 12 grill launcher. Each klystron has 110 kW output power and the phase shift between adjacent waveguides can be rapidly adjusted from −180 through +180 degrees (see Fig. 2). This allows good flexibility in the LHCD experiment for investigating optimized penetration, current drive efficiency, density limit and wave heating. The klystrons are capable of continuous wave operation and the limit on maximum launching duration is mainly determined by the cooling of the BeO ceramic windows.

The ICRH system has 2 MW output power in the frequency range 20–40 MHz. Minority heating and second harmonic heating, as well as direct electron heating

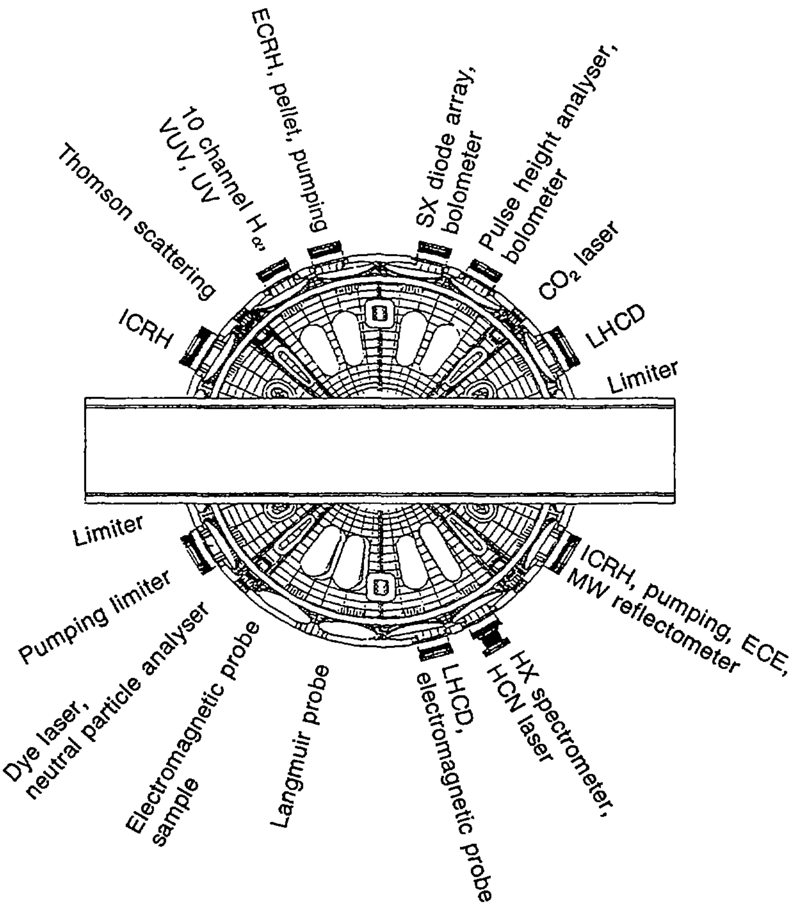

FIG. 3. Diagnostics on the HT-7 tokamak.

methods, are to be applied for investigation of heating, fast ion confinement and synergetic effects with LHCD.

The RF system has been connected to the tokamak and is being conditioned to a higher power level.

2.3. Diagnostics

The diagnostics are arranged to make the parameter measurements needed for the above mentioned experiments (Fig. 3). They include:

— Electromagnetic measurements, such as I_p, V_f, displacement, magnetic fluctuations, diamagnetic signal and flux surfaces;
— Langmuir probes;
— Spectroscopy with UV and VUV optical spectroscopy multichannel analyser systems;
— HCN interferometer;
— Soft X ray pulse height analyser;
— Neutral particle analyser;
— Bolometer array;
— Soft X ray diode array;
— Continuous spectrum measurement for Z_{eff};
— Fabry–Pérot interferometer;
— Scanning ECE measurement;
— CCD camera;
— Thomson scattering measurement;
— CO_2 laser collective scattering measurement;
— H_α/D_α emission measurement;
— Material probes.

Besides the diagnostics for standard plasma parameter measurements, we are also interested in obtaining information about fast particles, perturbation with respect to confinement and profile relaxation.

3. MACHINE TEST AND DISCHARGE OPERATION

The superconducting coils have been tested successfully with a toroidal field of 1–2 T. Two phase (liquid and gaseous) forced flow helium is used as the coolant. The operation parameters are: magnet temperature 4.5–6 K, magnet lead temperature <4.5 K, copper screen temperature 80–90 K, vessel temperature without heating and water cycle −20 to −40°C, temperature on the liner ~200°C normally during the discharge, vessel temperature ~ 100°C during the experiment, pressure in the cryostat 2×10^{-4} Pa and in the vessel 8×10^{-6} Pa, the heat removal rate of liquid nitrogen is 7–10 kW (with or without vessel baking) and the heat removal rate

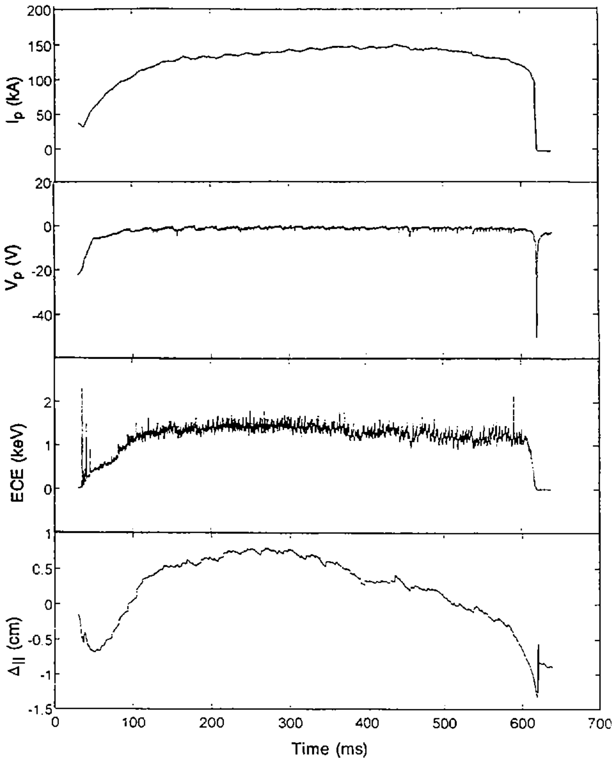

FIG. 4. Typical ohmic discharge (HT-7 shot 3371).

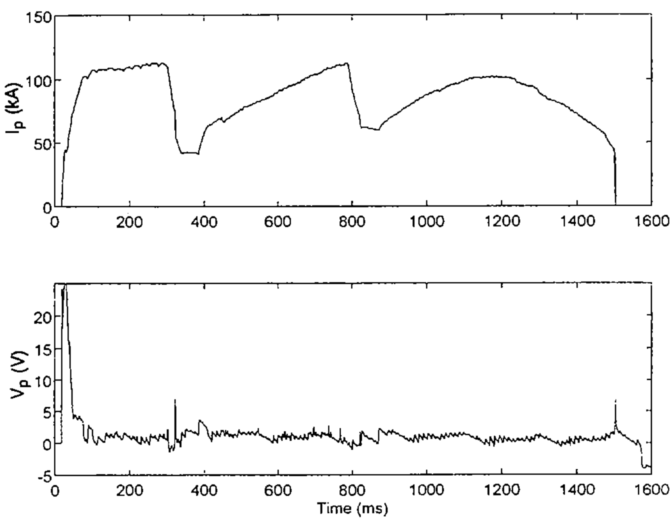

FIG. 5. Discharge with plasma current modulation (HT-7 shot 3526).

of liquid helium is less than 100 W for the magnet. The cooling down period is about 70 h from room temperature to 100 K and ~ 20 h from 100 K to the magnetized condition.

The discharge is initiated by a capacitor bank and is ramped up to a plateau by a flywheel generator and thyristor rectifier. The plasma parameters for test operation are: plasma current 120–150 kA with 600 to > 1000 ms of current plateau, loop voltage < 1 V, mean electron temperature ~ 1 keV, ion temperature 0.3–0.4 keV, electron density $> 1 \times 10^{19}$ m^{-3}. The plasma displacement remains smaller than 1 cm (Fig. 4).

With careful conditioning of the first wall (only stainless steel), the discharge became rather clean, and Z_{eff} is about 2 as measured by the spectroscopy. The main impurities are light materials such as oxygen and carbon.

A discharge of current modulation with programmed loop voltage has been obtained (Fig. 5). The plasma current drops from 120 to 45 kA with a slow rate of 1–4 MA/s. Several modulation cycles can be made in one discharge. The modulation changes the plasma profile. A high ramp-down rate causes minor disruptions and a lower rate does not disturb the equilibrium and MHD stability. This transient process is under investigation, which may provide important information on the parameters of field penetration and energy relaxation.

RECENT EXPERIMENTS AND CONFINEMENT STUDIES ON THE HL-1M TOKAMAK

HL-1M TEAM
(Presented by E.Y. Wang)

Southwestern Institute of Physics,
Chengdu, Sichuan,
China

Abstract

RECENT EXPERIMENTS AND CONFINEMENT STUDIES ON THE HL-1M TOKAMAK.

In 1993 and 1994, HL-1 was modified to HL-1M by replacing the vacuum chamber. HL-1M is a circular cross-section tokamak with $R = 1.02$ m, $a = 0.26$m, $B_t < 3$ T, $I_p < 350$ kA, a pulse duration of up to 2 s, $\bar{n}_e = (1\text{–}7) \times 10^{19}$ m^{-3} and $T_e(0) = (0.5\text{–}1)$ keV. In recent HL-1M experiments, a pellet injector (with up to eight pellets), lower hybrid current drive (LHCD) (with a power of up to 0.5 MW) and a biased electrode were employed to study confinement and current drive. The goal of the HL-1M programme is to conduct high power auxiliary heating (NBI power of ~1 MW, ICRH power of ~1 MW and ECRH power of 0.5 MW) and current drive (LHCD power of >1 MW) experiments. A simple boronization technique was used in HL-1M. An H mode induced by the biased electrode with boronization appears via the formation of an internal transport barrier at r/a ~ 0.5, which is followed by the edge transport barrier formation at r/a ~ 0.9. In the HL-1 and HL-1M experiments, improved confinement has been observed during combined ohmic and LHCD discharges. These results indicate a significant decrease in the edge density fluctuations in the improved particle confinement mode during LH wave injection. The HL-1M experiments show that suppression of density fluctuations is related to poloidal rotation produced by LH wave injection. A distinct poloidal asymmetry was observed in the response of the density fluctuations at ohmic, H mode and LHCD discharges on HL-1M. During ohmic discharges on the outboard midplane, the fluctuations are higher than inboard. On the outboard midplane, the fluctuations decrease significantly in the case of H mode and LH wave injection, while the fluctuations inboard generally show little or no reduction.

1. INTRODUCTION

In 1993 and 1994, HL-1 was modified to HL-1M by replacing the vacuum chamber. The plasma minor radius was increased from 0.2 to 0.26 m, and the number of windows was increased from 23 to 54. HL-1M is a circular cross-section tokamak with $R = 1.02$ m, $a = 0.26$ m, $B_t < 3$ T, $I_p < 350$ kA and two full poloidal graphite limiters located at a distance of 180° from each other toroidally [1].

The goal of the HL-1M programme is to conduct high power auxiliary heating (NBI power of ~1 MW, ICRH power of ~1 MW and ECRH power of ~0.5 MW) and current drive (lower hybrid current drive (LHCD) power of >1 MW) experiments in order to develop the physics and technology basis for the next tokamak, HL-2A, which is a modification of the ASDEX machine of the Max-Planck-Institut at Garching, Germany.

Experiments with ohmic heating started in autumn 1994. LHCD at a power level of <0.5 MW was added in summer 1995. In recent HL-1M experiments, boronization using $C_2B_{10}H_{12}$ vapour was employed. Plasma current and position (horizontal and vertical) are feedback controlled in order to improve the machine conditions. Significant progress was made on the plasma performance of HL-1M. Typical parameters of ohmically heated hydrogen plasmas are: $\bar{n}_e = (1-7) \times 10^{19}$ m^{-3}, $T_e(0) = (0.5-1)$ keV, $I_p = 100-320$ kA, and a pulse duration of up to 2 s.

2. PROGRESS IN PLASMA PERFORMANCE

Operation with I_p of up to 320 kA ($q_a < 3$, pulse duration ~ 0.3 s) and a pulse duration of up to 2 s ($I_p \sim 100$ kA) have been achieved. The plasma discharges are highly stable and reproducible.

The plasma position control over the major radius was partly programmed and partly produced by a fast feedback system; it provided variation of the horizontal displacement within a few millimetres during the flat-top of I_p. Plasma current and vertical position were feedback controlled.

A simple chamber boronization technique using $C_2B_{10}H_{12}$ vapour was employed in HL-1M [2]. The most radical effects of boronization in HL-1M have proven to be a three to six times reduction in the total radiated plasma power and a decrease of the loop voltage by 60%. A spectroscopic survey of the radiation in the VUV region showed total decrease of all spectral lines of high Z impurity atoms. Suppression of oxygen and carbon lines was observed. The intensity of radiation in the soft X ray region has been also drastically reduced. With boronization, the energy confinement time improved by 30–40% in HL-1M.

3. INTERNAL CONFINEMENT IMPROVEMENT

An H mode induced by a biased electrode [3] with wall boronization in HL-1M appears via the formation of an internal transport barrier at $r/a \sim 0.5$, which is followed by edge transport barrier formation at $r/a \sim 0.9$. In the central region, the electron temperature measured by an ECE heterodyne receiver rises by about 10–20%, and its profile becomes steepened as is shown in Fig. 1. The largest temperature gradient lies in the region of $r/a \sim 0.4$–0.6 and $dT_e(r)/dt$ increases by 30% during L–H transition. A transport barrier with reduced local thermal diffusivity was formed in the internal region, as is shown in Fig. 2.

Across the edge transport barrier at $r/a \sim 0.9$, the density fluctuations are reduced by about 50%, and the poloidal plasma rotation speed, measured by a Mach probe array, increases from 1 to 8 km/s [4]. Small quantities of high Z impurities (Al, Fe) have been injected into the HL-1M plasma by laser blow-off in order to study impurity transport. The penetration of the impurities into the plasma was monitored, temporally resolved by using the VUV spectrum, and was simulated by an

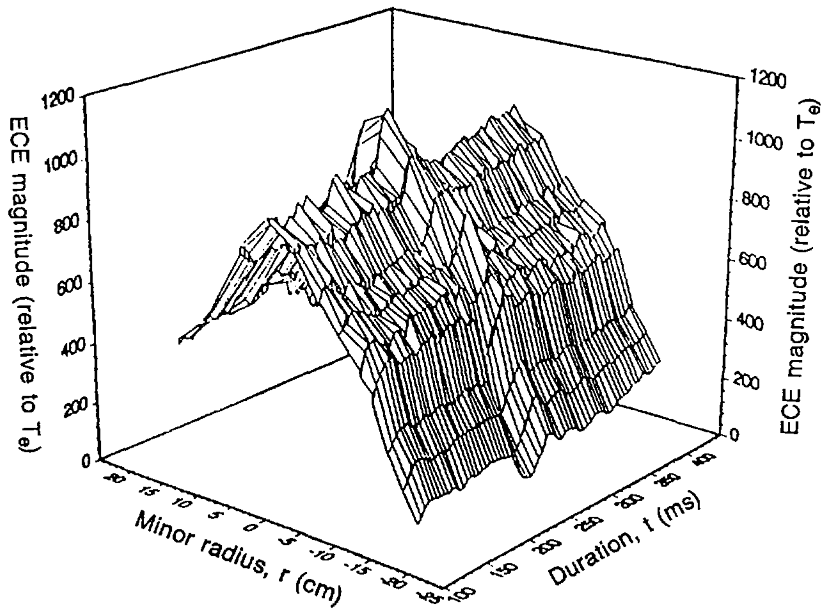

FIG. 1. Time evolution of electron temperature measured by an ECE heterodyne receiver. In the central region, T_e rises, and its profile becomes steepened during L–H transition.

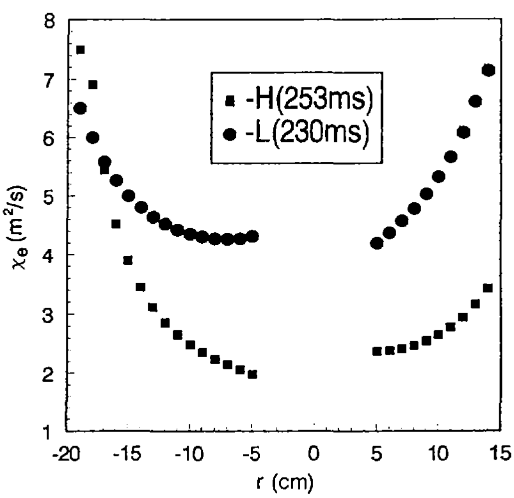

FIG. 2. Thermal diffusivity profiles in L and H mode phases.

impurity transport code yielding values for the transport diffusion coefficient, D, and the convection velocity, V. The impurity transport simulated by the STARTAHL transport code [5] shows that a particle diffusion coefficient D outside the $q = 1$ surface is reduced from 1.2 m^2/s in the L mode to 0.8 m^2/s in the H mode and a transport barrier exists for $r/a \sim 0.8$–0.9, in which $D \sim 0.2$ m^2/s, i.e. much smaller than outside this barrier [5]. The radial position of this calculated transport barrier is roughly consistent with the measured poloidal rotation speed changes at the edge [4].

4. IMPROVED CONFINEMENT DURING LHCD

Significant density increase (up to a factor of two) has been observed in the HL-1 and HL-1M experiments during combined ohmic and LHCD discharges. In these experiments, a decrease in the H_α signal by $\sim$40–60% and a slight decrease in the impurity emission have been observed for $\bar{n}_e < 1 \times 10^{19}$ m^{-3}. An estimate of the particle confinement time, τ_p, has shown that it increases by a factor of $\sim$2.5

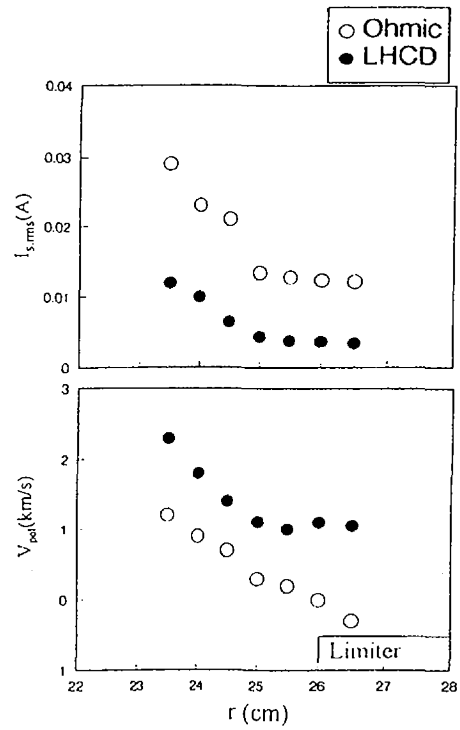

FIG. 3. Radial profiles of probe ion saturation current fluctuation, $I_{s\text{-}rms}$, and poloidal velocity, V_{pol}, for ohmic and LH current drives.

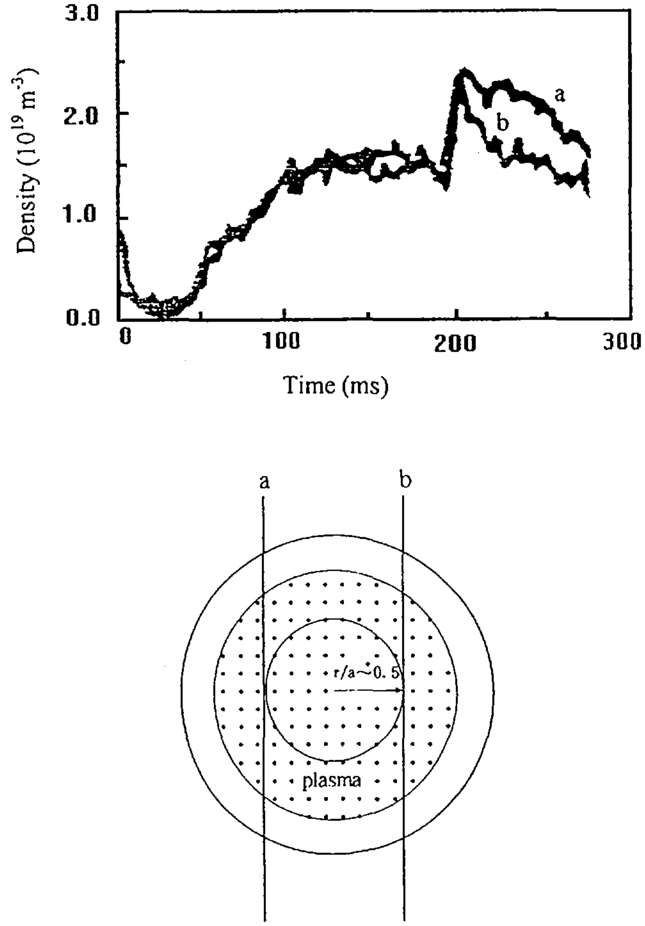

FIG. 4. Time evolution of line average electron density measured along (a) inboard and (b) outboard chord as shown by the lower part of the figure.

for normal current drive and by a factor of ~ 1.5 for anticurrent drive during wave injection [4]. These results indicate a decrease in the edge density fluctuations in improved particle confinement mode during lower hybrid (LH) wave injection. The HL-1M experiments have shown that the suppression of density fluctuations is related to the poloidal rotation produced by LH wave injection. The radial profiles of the ion saturation current fluctuations of the Langmuir probe and the poloidal rotation speed measured by a Mach probe during ohmic and LH current drives are given in Fig. 3.

5. POLOIDAL ASYMMETRY

For a more detailed investigation of the poloidal asymmetry of the edge plasma, a poloidal array of H_α detectors was installed on HL-1M. Moreover, such an arrangement allows a poloidal picture of the density fluctuations to be obtained, which may be responsible for the particle transport, as well. A distinct poloidal asymmetry was observed in the response of the density fluctuations for OH, H mode and LHCD on HL-1M [1]. During ohmic discharges on the outboard midplane, the fluctuations are higher than inboard. On the outboard midplane, the fluctuations decrease significantly upon H mode and LH wave injection, whereas the fluctuations inboard generally show little or no reduction.

In the pellet injection experiments, the density decay time constant related to confinement is 2.5 times shorter outboard than inboard after pellet injection, as is shown in Fig. 4. The thermal diffusivity also appears as a poloidal asymmetry during OH and becomes more symmetric during L–H transition, as is shown in Fig. 2.

6. CONCLUSIONS

HL-1M shows very good performance as compared with HL-1. Plasma current and position (horizontal and vertical) are feedback controlled so as to follow prescribed programs. The plasma discharges are highly stable and reproducible.

An H mode induced by a biased electrode with wall boronization in HL-1M appears via the formation of an internal transport barrier at $r/a \sim 0.5$, which is followed by edge transport barrier formation at $r/a \sim 0.9$. In the LHCD experiments in HL-1M, the suppression of edge density fluctuations in the improved particle confinement mode is related to the poloidal rotation produced by LH wave injection.

A distinct poloidal asymmetry in the response of density fluctuations and thermal diffusivity to L–H transition has been observed in the HL-1M tokamak. These observations are consistent with a poloidal symmetrization of the fluctuations and thermal diffusivity at the L–H transition. This H mode transition behaviour of the fluctuations was found to be similar to that of the improved confinement mode during LH wave injection.

REFERENCES

[1] WANG, E.Y., "Recent HL-1M results", paper presented at an IAEA Tech. Comm. Meeting on Research Using Small Tokamaks, Gandhinagar, India (1995).

[2] BUZHINSKY, O.I., et al., A simple boronization technique for T-3M and T-11M tokamak chambers, J. Nucl. Mater. **191–194** (1991) 1413.

[3] WANG, E.Y., et al., Biased H-mode experiments in Phaedrus-T, Nucl. Fusion **35** (1995) 457.

[4] HONG, W.Y., WANG, E.Y., RAN, L.B., YANG, S.K., PAN, Y.D., CHEN, L.Y., QIAN, S.J., "The fluctuations and flow velocities measured with a Mach probe array on the HL-1M tokamak", Plasma-Surface Interactions in Controlled Fusion Devices (Proc. 12th Int. Conf. Saint Raphael, France) (1996).

[5] FENG, X.Y., WANG, Z.X., WANG, E.Y., CHEN, J., CHEN, H., YU, Z.R., QIN, Y.W., "Laser blow-off system for studies of impurity transport in the HL-1M tokamak", in Plasma Physics and Controlled Nuclear Fusion (Proc. 7th Int. Toki Conf. Toki-City, Japan, 1995) (book of abstracts).

ION CYCLOTRON EMISSION: A COLLECTIVE ALPHA-PARTICLE EFFECT IN DEUTERIUM–TRITIUM PLASMAS IN TFTR AND JET

R.O. DENDY, K.G. McCLEMENTS, C.N. LASHMORE-DAVIES
UKAEA Fusion,
UKAEA–Euratom Fusion Association,
Culham, Abingdon, Oxfordshire,
United Kingdom

R. MAJESKI, S. CAUFFMAN, C.Z. CHENG, N.N. GORELENKOV
Princeton Plasma Physics Laboratory,
Princeton, New Jersey,
United States of America

G.A. COTTRELL
JET Joint Undertaking,
Abingdon, Oxfordshire,
United Kingdom

Abstract

ION CYCLOTRON EMISSION: A COLLECTIVE ALPHA-PARTICLE EFFECT IN DEUTERIUM–TRITIUM PLASMAS IN TFTR AND JET.

Ion cyclotron emission (ICE) is the first collective alpha-particle effect observed in TFTR and JET deuterium–tritium (DT) plasmas. The links between the observed spectral characteristics of ICE and the underlying properties of the fusion alpha-particle population responsible for its excitation are well understood theoretically, and ICE has emerged as a mainstream diagnostic for fusion alpha-particles in TFTR and JET. The primary alpha-particle parameters at the outer midplane that enter the theoretical model and can be inferred from ICE observations are: local number density; parallel drift velocity; mean perpendicular velocity normalised to the local Alfvén velocity; and velocity spread about the mean.

1 Experimental overview

Ion cyclotron emission (ICE) spontaneously generated by deuterium-tritium (DT) plasmas in JET and TFTR [1-7] has been successfully interpreted in terms of a collective instability driven by centrally born fusion alpha-particles whose drift orbits carry them close to the outer mid-plane edge. The ICE spectra of interest (Fig 1), in the range of a few tens to a few hundreds of MHz, typically display well-defined sequential peaks at multiple harmonics of the alpha-particle cyclotron frequency at the outer midplane. The intensity of the spectral peaks is strongly suprathermal, but the detected signal has negligible impact on the

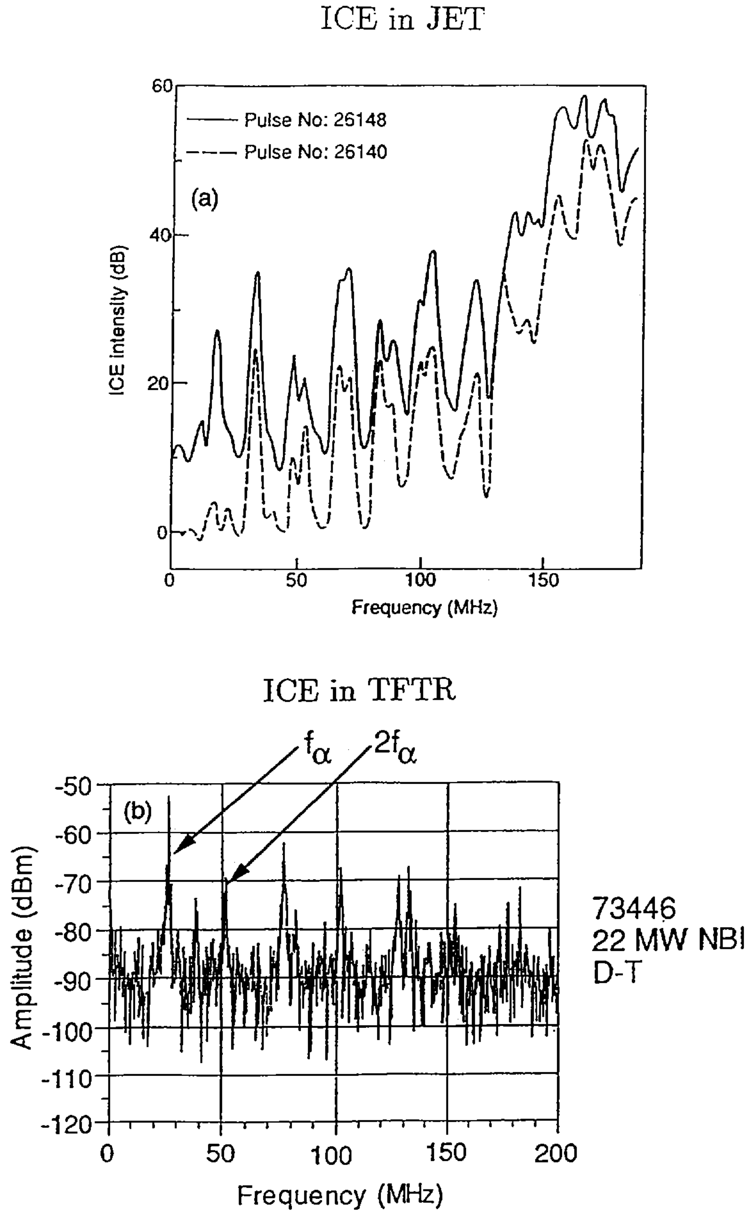

FIG. 1. Ion cyclotron emission spectra displaying peaks at sequential alpha-particle cyclotron harmonics in (a) JET and (b) TFTR. For JET, two spectra are shown corresponding to (upper curve) a high power DT discharge and (lower curve) a similar pure D discharge [3].

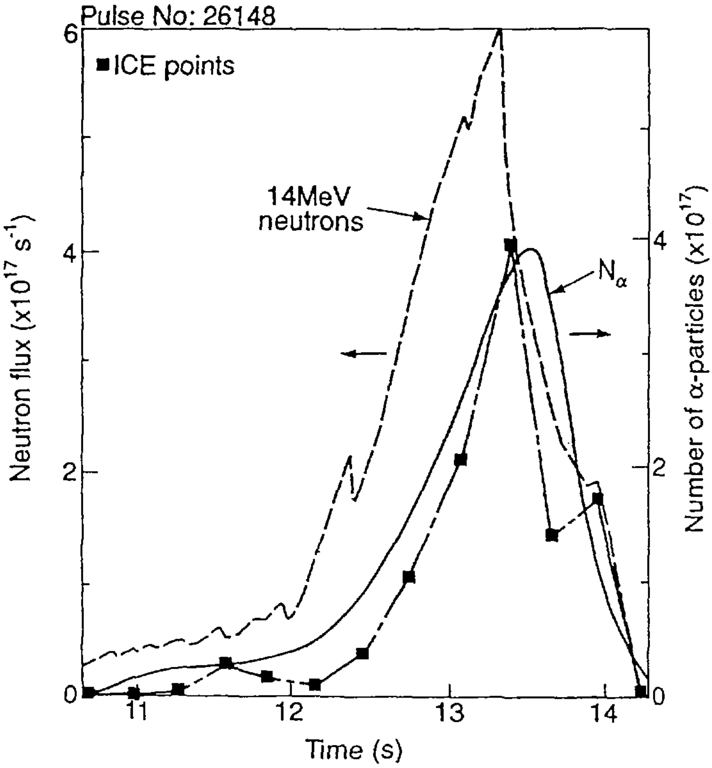

FIG. 2. Time evolutions during a high power JET DT discharge at the 14 MeV neutron emission (dashed line), the integrated ICE signal (squares) and the calculated edge population of alpha-particles (solid line) [1].

overall power balance. In JET [1], ICE intensity scales approximately linearly with the neutron source rate from shot to shot, while its time evolution during a single DT discharge follows that of the calculated edge density of alpha-particles (Fig 2). Repeated termination of the ICE signal by strong ELMs was observed during the termination phase of a high-power DT discharge in JET. Detection of ICE has been carried out with antennas located at the outer (and, recently, inner [8]) mid-plane in JET and with probes located above and below the magnetic axis in TFTR. In all cases, the observed spectral peak frequencies uniquely match cyclotron harmonics at the outer mid-plane. Thus, fusion ICE emerged experimentally as a suprathermal cyclotronic phenomenon, strongly correlated with the edge alpha-particle population and with an emitting region strongly localised radially and poloidally to the outer midplane.

TFTR observations [2, 3, 5, 6, 9] of ICE from DT supershot and L-mode discharges have confirmed, and greatly extended, this picture and our understanding of the emission mechanism. In supershots, ICE driven by alpha-particles typically lasts for 100ms to 200ms, before being replaced by a different signal [9] at injected beam ion cyclotron harmonics. In L-modes, alpha-particle ICE typically lasts throughout and, when a supershot is tripped into L-mode, alpha-particle ICE can reappear [2]. As we shall describe, these effects are explicable in terms of fundamental properties of the emission mechanism and of fusion alpha-particle dynamics.

2 Emission mechanism

The distinctive velocity-space structure of the alpha-particle population at the outer mid-plane edge appears to be the key to the emission mechanism and its localisation. Calculations for both JET [1] and TFTR [2] show that the drift orbit excursions of certain newly-born alpha-particles from the plasma centre, strongly localised in pitch angle near the trapped-passing boundary, are responsible for the dominant alpha-particle population at the outer mid-plane, where local fusion reactivity is negligible. Collective instability of this highly non-Maxwellian local population, which can be approximated by a finite-thickness drifting ring in velocity-space, is responsible for ICE. The specific mechanism appears to be the magnetoacoustic cyclotron instability, originally introduced theoretically [10,11] long before ICE was observed, and subsequently extended to the JET [4] and TFTR [6] regimes. It leads naturally to the excitation of fast Alfvén waves at alpha-particle cyclotron harmonics, for the distributions that we have discussed. The linear growth rate of this instability calculated for JET parameters matches key features of the observations, including simultaneous excitation at multiple cyclotron harmonics (Fig 3) with doublet splitting of spectral peaks [3,4], and it scales linearly with alpha-particle density. The magnetoacoustic cyclotron instability operates more strongly when the alpha-particles are super-Alfvénic in the edge plasma and is less susceptible to termination by collision-induced spreading of the alpha-particle velocity distribution than in the sub-Alfvénic regime. These considerations have been shown [6] to underly the observational differences between ICE driven by fusion products in JET and TFTR, as follows.

Alpha-particle ICE was observed throughout the JET DT H-mode discharges, where the driving particles in the edge region were super-Alfvénic. In contrast, the corresponding population in TFTR supershots is sub-Alfvénic, and the relatively short-duration rise and fall of alpha-particle ICE has been matched by theory. Figure 4 shows [6] the time-evolution of the ICE intensity averaged over six TFTR supershots, together with the theoretically computed linear growth rate of the sub-Alfvénic magnetoacoustic cyclotron instability. The latter is constrained by experimental parameters, notably the measured time-evolving fusion

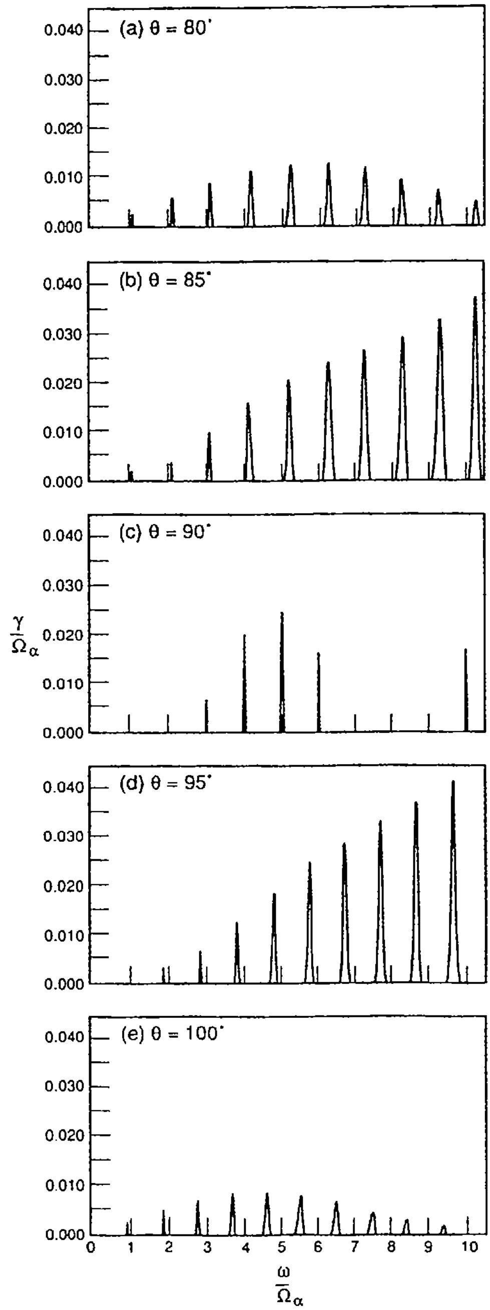

FIG. 3. Calculated growth rate [4] of the magnetoacoustic cyclotron instability showing excitation of the fast Alfvén wave at multiple alpha-particle cyclotron harmonics, under conditions appropriate to the outer midplane in JET DT plasmas. The plasma beta is 1.6×10^{-3}, the alpha-particle concentration is 10^{-4}, and θ denotes the propagation angle with respect to the magnetic field.

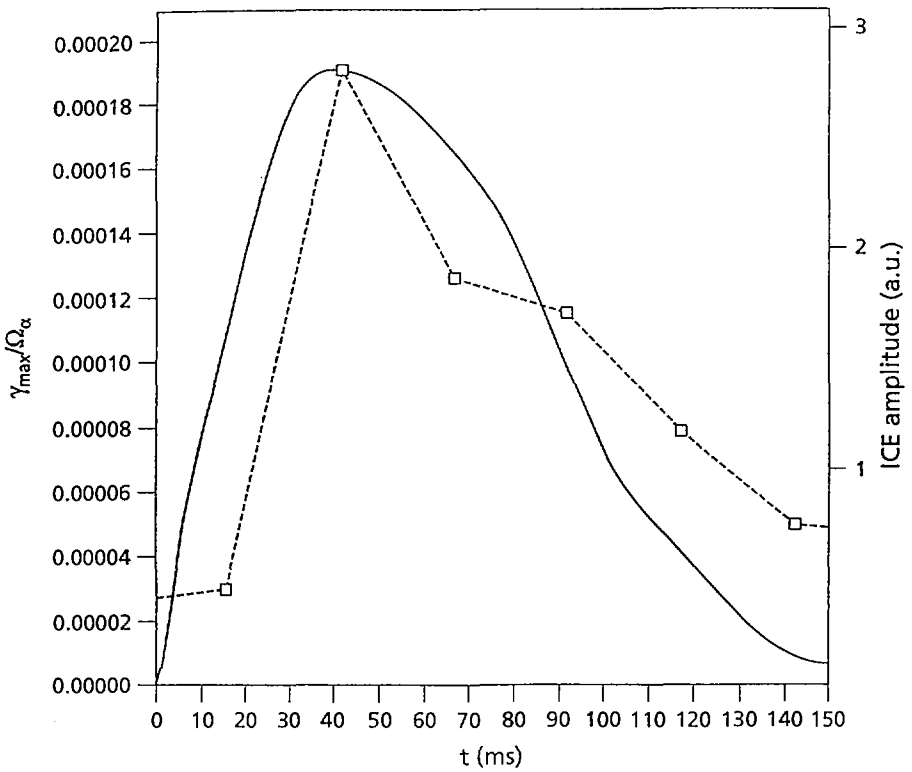

FIG. 4. ICE intensity time evolution (squares) and computed linear growth rate (solid line) [6].

reactivity, and by Sigmar's simple analytical model [12] for collisional slowing-down. Figure 5 shows [2] alpha-particle driven ICE during a supershot-to-L-mode transition in TFTR. The neutron source rate (a), edge electron density (b), and ICE power in the Ω_α fundamental (c) are plotted as functions of time. The Ω_α fundamental is excited briefly at the onset of neutral beam injection, but reappears in accord with theory [6] after a He puff, once the local Alfvén velocity falls significantly below the alpha-particle birth velocity.

The linear growth rates obtained from the locally uniform theory reflect the balance of non-Maxwellian alpha-particle drive against thermal and energetic ion cyclotron damping and electron transit time damping, and are typically a few per cent of the cyclotron frequency [3,4]. We have already described how the ICE signal is detected at all poloidal angles, while its excitation region is strongly localised radially and poloidally. This has motivated a study [5] of the two-dimensional eigenmode structure and stability of compressional Alfvén waves, which includes non-local effects such as gradients of cyclotron frequency

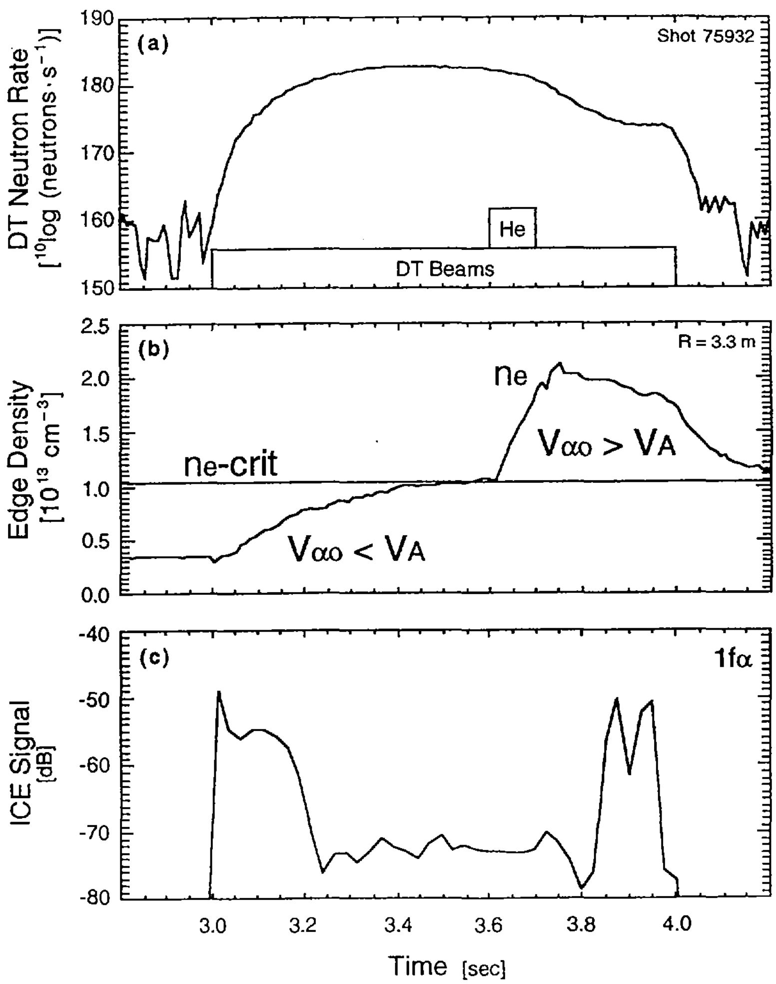

FIG. 5. ICE intensity with He gas puffing [2].

along fast-particle trajectories. While the growth rates obtained are lower than in the local theory, the overall picture is similar and, in addition, explanations for further aspects of the observations emerge. These include the transition to a broad-band spectrum observed at higher harmonics in TFTR, and the spectral peaks seen at odd deuteron harmonics in the earliest JET observations [13,14] of ICE from pure deuterium plasmas, where protons are the most energetic charged fusion product.

3 Conclusions

The theory and interpretation developed for JET DT plasmas [1,4] has proved applicable to the recently acquired and more extensive TFTR DT ICE database [2, 3, 5-7]. We can explain the following observational features of ICE: the wave mode excited; the localisation of its source; spectral peaks at sequential multiple cyclotron harmonics of the alpha-particles; doublet splitting of spectral peaks; the linear scaling of ICE with fusion reactivity observed in the JET database; correlations between the time-evolution of ICE intensity and mhd activity such as ELMs; the relative resilience of fusion product-driven ICE in JET H-modes compared to TFTR supershots; the time-evolution of ICE intensity in relation to measured neutron flux in the course of discharges in JET and TFTR; and the differing time-evolution of ICE observed in TFTR L-modes and supershots. The primary alpha-particle parameters at the outer mid-plane that enter the theoretical model and can be inferred from ICE observations are: local number density; parallel drift velocity; mean perpendicular velocity normalised to the local Alfvén velocity; and velocity spread about the mean.

ACKNOWLEDGEMENTS

This work was supported by the UK Department of Trade and Industry and Euratom, and the US Department of Energy under Contract No. DE-AC02-76-CH03073.

REFERENCES

[1] COTTRELL, G.A., et al., Nucl. Fussion 33 (1993) 1365.
[2] CAUFFMAN, S., et al., Nucl. Fusion 35 (1995) 1597.
[3] DENDY, R.O., et al., Nucl. Fusion 35 (1995) 1733.
[4] DENDY, R.O., et al., Phys. Plasmas 1 (1994) 1918.
[5] GORELENKOV, N.N., CHENG, C.Z., Nucl. Fusion 35 (1995) 1743.
[6] McCLEMENTS, K.G., et al., Phys. Plasmas 3 (1996) 543.
[7] JOHNSON, D.W., et al., Plasma Phys. Control. Fusion 37 (1995) A69.
[8] SADLER, G.J., et al., Nucl. Fusion 35 (1995) 1609.
[9] DENDY, R.O., et al., Phys. Plasmas 1 (1994) 3407.
[10] MIKHAILOVSKII, A.B., Rev. Plasma Phys. 1 (1975) 77.
[11] BELIKOV, V.S., KOLESNICHENKO, Ya.I., Sov. Phys.-Tech. Phys. 20 (1976) 1146.
[12] SIGMAR, D.J., in Physics of Plasmas Close to Thermonuclear Conditions (Proc. Conf. Varenna, 1979), Vol.1, Editrice Compositori, Bologna (1979) 271.
[13] COTTRELL, G.A., DENDY, R.O., Phys. Rev. Lett. 60 (1988) 33.
[14] SCHILD, P., et al., Nucl. Fusion 29 (1989) 834.

HALO CURRENTS AND VDEs IN COMPASS-D

G.G. CASTLE, A.W. MORRIS, D.A. GATES,
C.G. GIMBLETT, M. VALOVIČ
UKAEA Fusion,
Culham Laboratory,
Abingdon, Oxfordshire,
United Kingdom

Abstract

HALO CURRENTS AND VDEs IN COMPASS-D.

A series of experiments were performed on COMPASS–D in a single null ITER-like configuration ($R = 0.557\ m$, $a = 0.232\ m$, $b = 0.385\ m$) to investigate the properties of poloidal and toroidal halo currents flowing in the vacuum vessel during vertical displacement events, or VDEs. Both poloidal and toroidal halo currents are induced during a disruption and these currents can produce large forces on the vacuum vessel; these forces are a design consideration for ITER and also have serious consequences for in-vessel components and the vacuum vessel on devices such as JET. The toroidally symmetric ($n = 0$) portion of the poloidal halo currents produces vertical forces on the vacuum vessel, while the asymmetric portion produces torques, lateral forces, and locally high pressures. Scans of elongation κ, predisruption plasma current $I_p(0)$, and toroidal field B_ϕ were performed. Different disruption types such as high β_p, H-mode, $\overline{n}_e$ limit, ELM-induced and control failures were investigated. The results of experiments performed on COMPASS–D indicate that the symmetric portion of the halo current is bounded by $\sim 1.2\, I_p(0)/q(95)$, and that it flows in a paramagnetic sense. The toroidally asymmetric portion of the halo current is fixed spatially in COMPASS–D, and although the asymmetry can be quite large, no reversal of the halo current direction is observed. Attempts to change the halo currents by means of external helical fields are described.

1 Introduction

When a tokamak plasma is vertically unstable and position control is lost, it moves vertically and contacts the vessel wall, causing the plasma current to terminate and large vessel currents to flow [1, 2, 3, 4, 5, 6]. These vessel currents are the sum of eddy currents (the inductive response of the vessel wall to changes in plasma current or position) and halo currents (currents that flow from the plasma into the vessel wall and complete a circuit back through the plasma). The vessel currents possess both toroidally symmetric ($n = 0$) and asymmetric ($n \geq 1$) components. The study of the asymmetries in the halo currents is important for the design of machines like ITER [7] because both the maximum global stresses like torques and lateral forces and the maximum local stresses are produced by these asymmetries. What follows is a description of experiments performed on COMPASS–D to investigate both the symmetric and asymmetric halo currents. The evolution of a typical VDE is shown in Fig. 1.

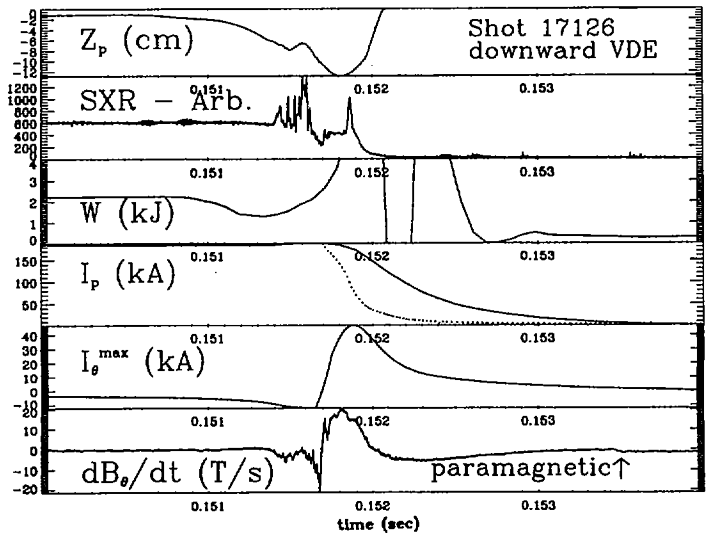

Figure 1: *Summary of diagnostics traces during a VDE showing Z_p from magnetic diagnostics, the central chord Soft X-Ray emission, stored energy from magnetic diagnostics, traces of the sum of the vessel and plasma current (solid line) and the plasma current alone (dashed line), the poloidal halo current, and $\dot{B}_\phi$ for a coil near the maximum halo current density.*

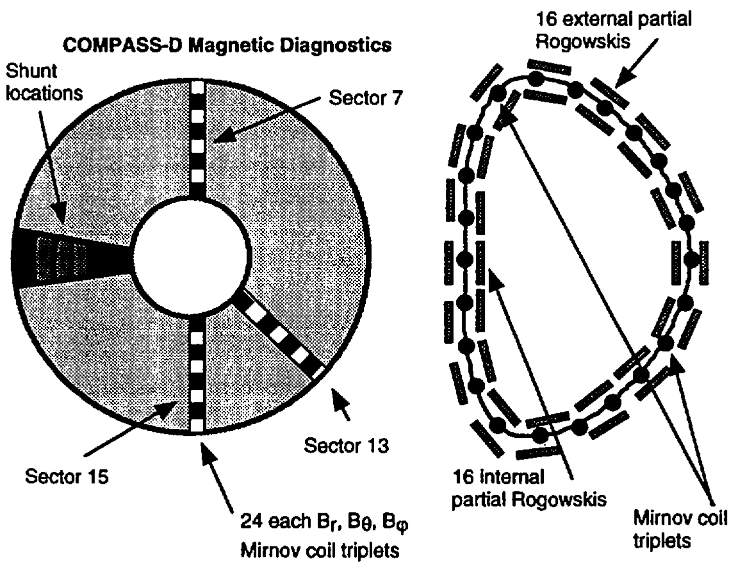

Figure 2: *Diagram indicating COMPASS-D magnetic diagnostic coil locations. Sectors 7, 13, and 15 correspond to toroidal angles of $\phi = \pi$, $\frac{\pi}{4}$, and 0, respectively, while the shunts are located at $\phi = -\frac{\pi}{2}$.*

2 Halo Diagnostics

The poloidal halo current is derived from magnetic measurements of the local changes in toroidal field during a disruption. At each of three toroidal locations ($\phi = 0$, $\frac{\pi}{4}$ and π) there is an array of 24 $\dot{B}_\phi$ coils (see Fig. 2). To determine the poloidal current distribution at each toroidal angle, we assume that the current distribution is toroidally symmetric. We then use the simple formula

$$I_\theta(\theta_i) = \frac{2\pi R(\theta_i)\tilde{B}_\phi(\theta_i)}{\mu_o} \tag{1}$$

to determine the poloidal halo current $I_\theta(\theta_i)$ flowing at location θ_i. Since the halo currents complete their circuit through the vessel, the signal is only non-zero when there are currents flowing in the vessel by the coils, and therefore $I_\theta(\theta_i)$ is just this local vessel current. If the vessel current distribution were toroidally symmetric, the poloidal current distribution deduced would be exact; however, if the distribution contains an asymmetric component, then the currents deduced from a single poloidal array of $\dot{B}_\phi$ coils will not accurately reflect the net poloidal current. This problem can be overcome (for an $n = 1$ asymmetry) with coils at three toroidal locations (although aliasing from even-$n \geq 2$ components remains a possibility). The toroidal geometry acts to attenuate spatially the $n = 1$ component somewhat; that is, each coil detects contributions from the toroidally opposite side of the vacuum vessel as well as the local fields. For COMPASS–D this effect is on the order of a few percent and is a function of the aspect ratio of the plasma during the VDE. Therefore, an approximation to the toroidally symmetric poloidal halo current is determined as follows: we obtain the poloidal halo current distributions at angles $\phi = 0$ and $\phi = \pi$, then average them:

$$\overline{I}_\theta(\theta) = \frac{I_\theta(\phi = 0) + I_\theta(\phi = \pi)}{2}. \tag{2}$$

COMPASS–D is also equipped with 3 resistive shunts installed between X-point tiles and the vessel. The 3 tiles are separated poloidally and occupy in total a poloidal extent of approximately 42° and a toroidal extent of 22.5°. The shunt currents are deduced from the voltages across the shunts, and the maximum shunt current is I_{shunt}.

3 Toroidally symmetric poloidal halo currents

Vertical disruptions were induced both away from and towards the X–point and scans of B_ϕ ($B_\phi = 1.1 - 1.85\ T$, $I_p(0) = 180\ kA$) and $I_p(0)$ ($I_p(0) = 115 - 240\ kA$, $B_\phi = 1.2\ T$) were performed to determine the scaling of halo current magnitudes and to investigate any differences due to conducting structures in the vessel or asymmetries in VDE direction. The predisruption plasma current, $I_p(0)$, is measured 20 ms before the current has dropped to half of its steady-state value. Single parameter scans ($I_p(0)$ or B_ϕ) show that the maximum magnitude of the poloidal halo current scales like $I_p(0)^2/B_\phi^\alpha$ with typically $\alpha = 0.6 - 0.9$. However, the whole COMPASS–D database indicates that the maximum poloidal halo current is bounded by the line $I_{halo}^{max} \simeq 1.2\, I_p(0)/q(95)$ (see Fig. 3). Scalings of plasma elongation ($1.1 \leq \kappa \leq 1.6$) were performed which verified that I_{halo} increases with κ. Increasing the triangularity δ from 0.25 to an ITER-like $\delta \sim 0.4$ (at constant $I_p(0)$ and B_ϕ) reduced I_{halo} by about 50 % and also slightly reduced the asymmetric halo currents for downward (towards the X-point) VDEs. VDEs were

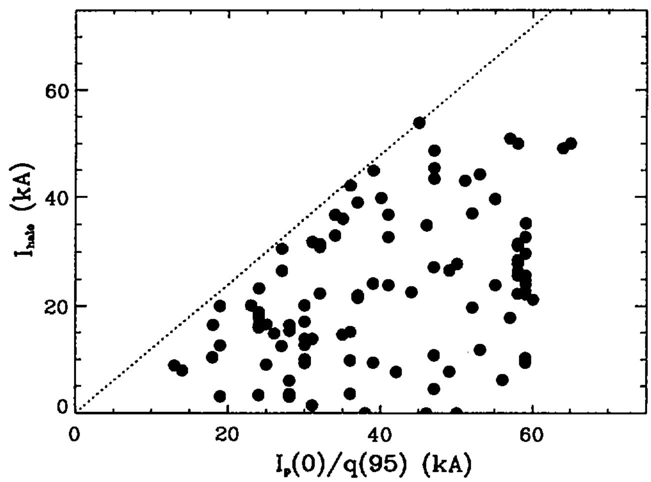

Figure 3: *I_{halo}^{max} as a function of $I_p(0)/q(95) \sim I_p^2(0)/B_\phi$ for a large range of disruptions in COMPASS-D with various $I_p(0)$, $q(95)$, and B_ϕ values, different configurations, elongation, etc. The worst-case boundary appears to be approximately $I_{halo}^{max} \sim 1.2\, I_p(0)/q(95)$ (dashed line).*

also observed in disruptions triggered by high β_p, high $\overline{n}_e$, low $q(95)$ and ELMs during H-mode discharges. The symmetric halo currents measured during ELM-induced VDEs during H-mode discharges indicate no difference between those observed in forced VDEs with identical $I_p(0)$ and B_ϕ, implying that forced VDEs are a valid means of determining halo current behaviour. The energy quench phase tends to induce poloidal halo currents that flow in such a sense as to preserve the diamagnetic portion of the toroidal flux (tending to pull plasma facing components from the vessel wall), while during the current quench phase the poloidal halo currents flow paramagnetically (tending to compress plasma facing components) and reach maximum amplitude. Reversing I_p has no effect on the direction of the poloidal halo currents, but reversing the toroidal field causes the halo current direction to reverse. This behaviour is consistent with the poloidal halo current being driven by the toroidal electric field due to the large $\dot{I}_p$ and by the poloidal electric field generated by the tendency of the plasma to try to conserve the linked toroidal flux as it decreases in size.

4 Toroidally asymmetric poloidal halo currents

One measure of the degree of toroidal asymmetry is the peak-to-average ratio of the poloidal halo currents, the Toroidal Peaking Factor (TPF). We can compute this quantity with some assumptions about the toroidal variation of the halo currents; if one imagines the poloidal halo current to be distributed as

$$I_\theta(\theta,\phi) = I_0(\theta) + I_1(\theta)\cos(\phi - \phi_o) \tag{3}$$

then the TPF is

$$\mathcal{P} = 1 + \frac{|I_1|}{|I_0|}. \tag{4}$$

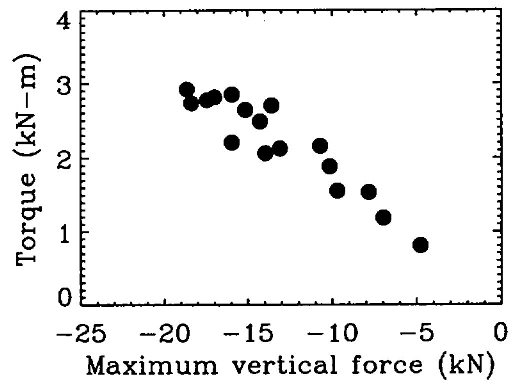

Figure 4: *Maximum torque on vacuum vessel as a function of maximum vertical force due to poloidal halo currents for a set of forced downward VDEs (COMPASS-D SND discharges, shots 17110-17137,* $1.12 \leq B_\phi\,(T) \leq 1.86$, $107 \leq I_p(0)\,(kA) \leq 189$, $\kappa = 1.6$*).*

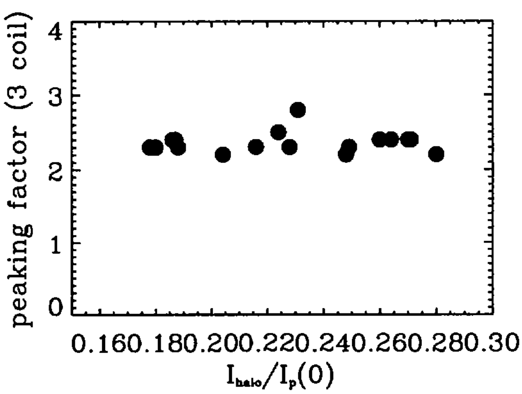

Figure 5: *Toroidal peaking factor* $\mathcal{P}_3$ *as a function of* $I_{halo}/I_p(0)$ *for a set of forced downward VDEs (COMPASS-D SND discharges, shots 17110-17137,* $1.12 \leq B_\phi\,(T) \leq 1.86$, $107 \leq I_p(0)\,(kA) \leq 189$, $\kappa = 1.6$*).*

The TPF as determined by three coils located at a single poloidal angle θ and three different toroidal angles is referred to as $\mathcal{P}_3$. The phase ϕ_o and magnitudes I_0 and I_1 are obtained at the time of peak halo current (peak I_0) from the three measurements at the same poloidal angle and use of Equation 3. Measurements of the toroidal phase ϕ_o of the halo currents indicated that I_{shunt} and I_{halo} were in good agreement. Frequently $\mathcal{P}_3$ is around $\sim 2 - 4$ or so. This does not mean the measured halo current reverses at any toroidal location (it always has the same sign in practice), only that the fit used for the asymmetry predicts a change in sign where the halo current is not actually measured.

In Fig. 4 one can see how for a series of discharges (mostly a B_ϕ scan, but some $I_p(0)$ variation as well) the maximum torque increases proportionally with the maximum vertical force, implying a constant peaking factor $\mathcal{P}_3$ (Fig. 5). However, when the full COMPASS–D dataset (which covers a much larger parameter space) is examined, considerable scatter in $\mathcal{P}_3$ is found. The vertical force on the vessel was calculated by integrating $\vec{j}_\theta \times \vec{B}_\phi \cdot \hat{e}_z$ over the vessel wall volume at each of two toroidally opposing angles and averaging the result. The torque was calculated by taking the difference of the two vertical forces and multiplying by the effective moment length.

In contrast to Alcator C-Mod and DIII-D [1, 6] (but in agreement with some other machines), on COMPASS–D it is observed that there is very little (if any) toroidal rotation of the $n = 1$ poloidal halo currents during a VDE. In fact, the phase of the $n = 1$ component is fixed in the $\phi \sim -(70 - 90)^\circ$ range for the subset of data examined. One possible explanation is that during a VDE the current density anisotropies due to the vessel port structures produce large enough error fields to lock the phase of the $n = 1$ component of the poloidal halo currents with respect to the vessel, another is non-uniformities in plasma-facing components. The large currents flowing in the vessel ($I_{vessel} \sim 0.5 I_p(0)$) are forced to flow *around* the ports and the resultant non-uniformities in the vessel current distribution produce magnetic fields normal to the vessel surface. Near each port these fields are of order $B_\perp \sim \mu_o j_\phi a_p$ where j_ϕ is the toroidal current density and a_p is the port radius. If one sums the contributions from each port on COMPASS–D, one finds that the $m/n = 1/1$ component of the field normal to the vessel wall is expected to be small ($\sim 7 \times 10^{-5}\,T$), but the $m/n = 2/1$ field at the vessel wall is around $1.9\ mT$ for the same conditions (field strengths of this size are several times larger than those necessary to produce locked modes in quiescent plasmas of low density on COMPASS–D). Resonant Magnetic Perturbation (RMP) coils with a dominantly $m/n = 2/1$ structure at a level of $\leq 1\,mT$ (at the plasma surface) were employed to try to modify either the phase or the amplitude of the asymmetric halo current by creating locked modes of various phases then turning off the vertical position feedback to produce a VDE. It was found that the creation of locked modes prior to the VDE had no effect on the magnitude or phase of either the $n = 0$ or the $n = 1$ halo components. No consistent mechanism has been found that explains both the generation of the asymmetric component and its rotation or lack thereof; however, these experiments suggest that the asymmetry is driven during the quench phase and is independent of the cause of the disruption.

5 Conclusions

The results of the COMPASS–D experiments have several implications for ITER and other large tokamaks. It was found during independent scans of $I_p(0)$ and B_ϕ that the symmetric portion of the halo current scales as $I_p(0)^2/B_\phi^\alpha$ ($\alpha \sim 0.6 - 0.9$), and (perhaps more importantly) that the maximum symmetric halo currents appear to be bounded by $I_{halo}/I_p(0) \simeq 1.2/q(95)$. The asymmetric part of the halo current was found to be fixed in phase on COMPASS–D, perhaps due to machine non-uniformities. Similar results were obtained from calculations of the forces due to $\vec{j} \times \vec{B}$ interactions in the vacuum vessel. The creation of locked modes of various phases prior to the VDE had no effect on the halo currents, suggesting that the initial conditions of the disruption are less important than the dynamics during the quench phase.

This work was funded jointly by the UK Department of Trade and Industry and Euratom.

REFERENCES

[1] GRANETZ, R.S., et al., Nucl. Fusion **36** (1996) 545.
[2] GRUBER, O., et al., Plasma Phys. Control. Fusion **35** (1993) B191.
[3] YOSHINO, R., et al., Nucl. Fusion **33** (1993) 1599.
[4] PAUTASSO, G., et al., Nucl. Fusion **34** (1994) 455.
[5] CASTLE, G.G., et al., in Controlled Fusion and Plasma Physics (Proc. 23rd Eur. Conf. Kiev, 1996), Vol. 20C, European Physical Society, Geneva (1996).
[6] HYATT, A.W., ibid.
[7] WESLEY, J., et al., IAEA-CN-64/FP-25, *these Proceedings*, Vol. 2.

BETA LIMIT STUDIES AND THE EFFECT OF ERROR FIELDS AT LOW COLLISIONALITY ON COMPASS-D

D.A. GATES, B. LLOYD, A.W. MORRIS, G. McARDLE,
M.R. O'BRIEN, M. VALOVIČ, C.D. WARRICK, H.R. WILSON,
COMPASS-D and ECRH TEAMS
UKAEA Fusion,
Culham Laboratory,
Euratom–UKAEA Fusion Association,
Abingdon, Oxfordshire,
United Kingdom

Abstract

BETA LIMIT STUDIES AND THE EFFECT OF ERROR FIELDS AT LOW COLLISIONALITY ON COMPASS-D.

Recent experiments to determine the operational limits on β at low collisionality on COMPASS-D (R_0 = 0.557 m, a = 0.17 m, $B_\phi(max)$ = 2.1 T, $I_p(max)$ = 320 kA, κ = 1.0–1.7) in ITER-like single null divertor (SND) plasmas have shown deviations from standard ideal MHD β-limits. This is an important issue for ITER since ITER will operate at lower collisionality than most high β tokamak experiments to date and has a design point with a normalised β ($\beta_N \equiv aB_\phi\beta/I_p$) of ~2.5. The source of this deviation from the ideal β-limit is neoclassical bootstrap driven islands. Data are presented which demonstrate that the observed dynamics of the instability are well modelled by neoclassical theory. An important issue is the mechanism that determines the onset of the instability since the purely neoclassical theory predicts instability at all values of β_p. Data from a density scan are compared to two theories which predict a critical island width for instability. A theory based on the effects of ion polarisation currents compares well with the available measurements. The results of a q-scan show that the parametric dependence of the operational β limit is not linear in I/aB and appears to have a peak value when I_p ~ 150 kA (which corresponds to a q_{95} of ~4.3). A model based on neoclassical tearing modes is presented that reproduces the general trend of the data as a function of q_{95}. Experiments intended to demonstrate the sensitivity of neoclassical islands to applied error fields show that these modes can be triggered for values of β and n_e that are stable in the absence of such magnetic perturbations. Data are presented showing that the scaling of the error field amplitude required to trigger an island is consistent with the predictions of the ion polarisation current threshold model.

1. Introduction

Much attention has been focused recently upon tokamak operational pressure limits imposed by neoclassical MHD instabilities, in particular the effects of bootstrap current driven magnetic islands. This is primarily due to the observation on several divertor tokamaks that the β limit at low density (and hence low collisionality) is often determined by rotating low m/n magnetic islands. This effect has been observed on COMPASS-D [1], DIII-D [2], and ASDEX-U [3]. Initial calculations of the stability of bootstrap driven islands [4,5] indicated that these modes were unstable for all values of β_p with $\nu^* < 1$. More recent calculations, motivated by the observation of a critical island width for instability on TFTR [6], suggest that other stabilising mechanisms are important in determining the onset of these modes. At present, there are two proposed mechanisms for stabilisation: one based on a model of the transport through the island [7], called the $\chi_{\perp}/\chi_{\parallel}$ model, the other on the effect of ion polarisation currents [8]. This paper will summarise the experimental evidence on COMPASS-D and compare this evidence to the existing theories.

2. Island Dynamics

Detailed modelling of the dynamics of the measured MHD instabilities (using global plasma parameters) demonstrates that the neoclassical island evolution equation accurately describes the growth of the observed island. Figure 1a shows the fluctuating poloidal magnetic field amplitude of the observed 2/1 mode as measured by a Mirnov coil during a power ramp-down experiment. Figure 1b shows the time history of the applied ECRH power and β_p for the same discharge. Figure 1c shows that the time history of the island width as calculated using the cylindrical formula from the measured Mirnov amplitude gives good agreement with the output of a code which solves the neoclassical island evolution equation, which is given by:

$$\frac{dw}{dt}=\left(\frac{1.22\eta_{nc}}{\mu_0}\right)\left[\Delta'+a_1\varepsilon^{1/2}\beta_p\frac{L_q}{L_p}\left(\frac{w}{w^2+w_c^2}\right)-a_2\frac{\rho_{\theta i}^2\beta_p g(\varepsilon)}{w^3}\left(\frac{L_q}{L_p}\right)^2\right] \qquad (1)$$

where w = island width, η_{nc} = the neoclassical resistivity, Δ' = the jump in logarithmic derivative of the perturbed flux, ε = the inverse aspect ratio, β_p = the local poloidal β, and L_p and L_q are, respectively, the scale lengths of the pressure and q (all quantities to be evaluated at the rational surface of interest, $r=r_s$ where $m = nq(r_s)$). Here a_1 and a_2 are coefficients which depend on the details of the

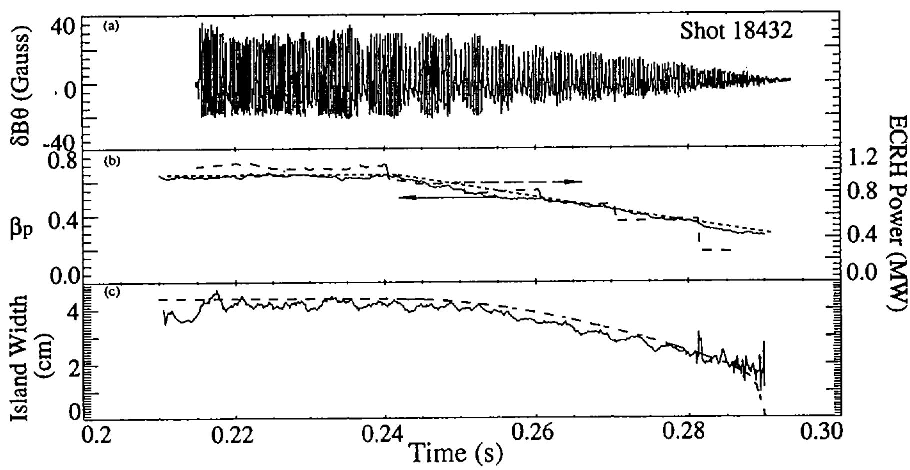

Figure 1: a)Perturbed poloidal field as measured by Mirnov coil, b) time history of applied ECRH power and β_p (measured and fit), c) measured island width (solid line) and island width as calculated from Eqn 1 (dashed line).

equilibrium parameters. The second term on the right is the bootstrap island term modified to include the effects of transport, with w_c parameterising the magnitude of the contribution of the $\chi_\perp/\chi_\parallel$ model and given by the relation:

$$w_c = 1.8 r_s \sqrt{\frac{8 R_0 L_q}{r_s^2 n}} \left(\frac{\chi_\perp}{\chi_\parallel}\right)^{1/4} \tag{2}$$

The third term in Eqn. (1) is the contribution due to ion polarisation currents, with $\rho_{\theta i}$= the poloidal ion Larmor radius, and $g(\varepsilon)$ defined by:

$$g(\varepsilon) = \begin{cases} \varepsilon^{3/2} & for\ v_i/\varepsilon\omega_{*e} < 1 \\ 1 & for\ v_i/\varepsilon\omega_{*e} > 1 \end{cases}$$

The ratio L_p/L_q is unmeasured, so it is assumed fixed and = 1.0 during the discharge. $\Delta' = -2/r_s$ also by assumption. The coefficients are taken to be $a_1 = a_2 = 7$ (for discussion of coefficients see Refs [7] and [8]).

3. Instability Thresholds - Scalings and Magnitude

The implications of the threshold models will be discussed and the predictions compared to a series of high β discharges for which the density was varied between $3.2\times10^{18}m^{-3}$ and $1.1\times10^{19}m^{-3}$ while all other externally controllable parameters were held fixed. The typical equilibrium parameters for the discharges are I_p = 150kA, B_ϕ = 1.2Tesla, a = 17.0cm, R_0 = 56.0cm, q_{95} = 4.3, κ = 1.6. The ECRH power was turned on and ramped to its maximum value (~1.2MW). The individual gyrotrons were turned on at 20ms (~ $3\tau_E$) intervals.

Figure 2 shows the Mirnov activity as measured by the outboard midplane Mirnov coil for four of the shots in the scan. The values of density and β_p at the onset of MHD (or at maximum if no MHD) are also shown. As the density is raised the onset of the MHD is delayed progressively until it ceases to appear.

The symbols in Figure 3 represent the measured values of β and density at which MHD activity is observed to begin for the density scan aforementioned. The shaded region and the hashed region in Figure 3 represent the solutions of the equation:

$$w_{crit} = \varepsilon^{-1/4} \sqrt{g(\varepsilon) L_q / L_p}\, \rho_{\theta i} \sim \begin{cases} 1cm & v_i/\varepsilon\omega_{*e} < 0.3 \\ 3cm & v_i/\varepsilon\omega_{*e} > 0.3 \end{cases} \tag{3}$$

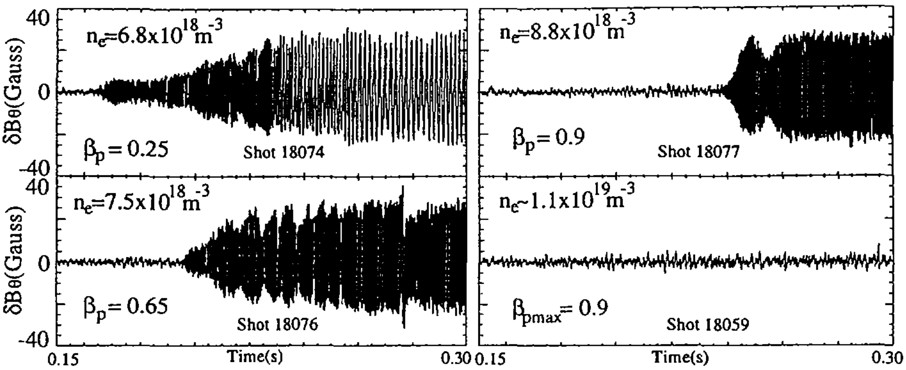

Figure 2: Progressive delay of the onset of MHD as density is raised

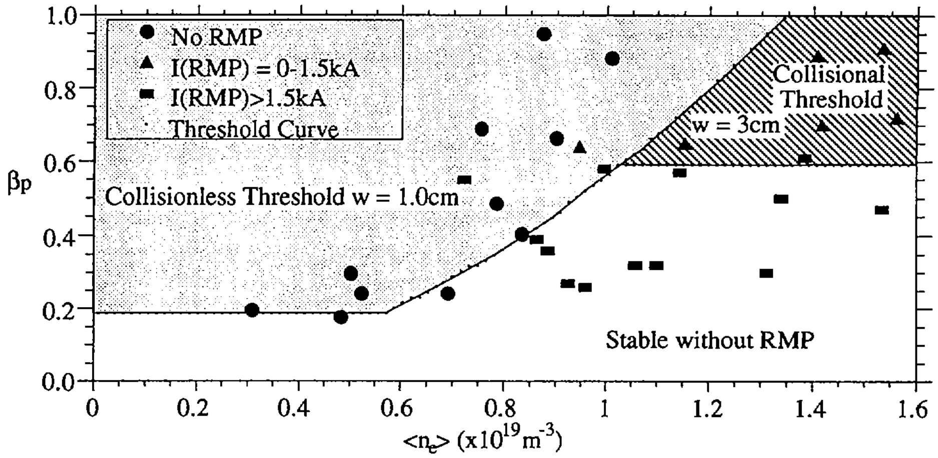

Figure 3: β_p and density at the point of onset of MHD activity for cases with no RMP (circles) with I_{RMP} < 1.5kA (triangles) and I_{RMP} > 1.5kA (rectangles). The solid curve bounds the regions of varying w_{crit} as from Equations (3) and (4)

with $g(\varepsilon)$ as above with $T_i = 130$eV (in agreement with Neutral Particle Analyser measurements), subject to the condition:

$$\beta_p > \beta_{pcrit} \equiv -\frac{3\sqrt{3}}{2\varepsilon^{3/4}}\left(\frac{g(\varepsilon)L_p}{L_q}\right)^{1/2}\Delta'\rho_{\theta i} \sim \begin{cases}0.2 & \nu_i/\varepsilon\omega_{*e} < 0.3\\ 0.6 & \nu_i/\varepsilon\omega_{*e} > 0.3\end{cases} \quad (4)$$

as predicted by the ion polarisation current model.

The shape of the regions in Figure 3 can be understood in terms of the behaviour of Equations (3) and (4). There is a critical β_p below which the modes are always stable because Δ' is negative and the other terms are all proportional to β_p. The ion polarisation term predicts this "critical β_p" is a strong function of collisionality (through $g(\varepsilon)$). These two critical values of β_p are the straight lines in Figure 3. The connecting curve represents the transition from the high to low collisionality regime (collisionality here meaning the collisionality-like parameter $\nu_i/\varepsilon\omega_{*e}$).

It is not possible to construct such a graph for the $\chi_\perp/\chi_\parallel$ model since the scaling of $\chi_\perp$ with density and β_p inside an island is unknown. However, one can calculate the absolute value seed island width required for instability for typical COMPASS-D parameters and one finds that the size of the required seed island is predicted to be quite small, in particular, assuming $\chi_\perp \sim 1\mathrm{m}^2/\mathrm{s}$ and $\chi_\parallel = v_{the}\lambda_\parallel = v_{the}R_0qL_q/(mw)$ and using Equation 126 from Ref. [7]:

$$w_{crit} = 31.3\left(\frac{\Delta' r_s}{\varepsilon\beta_p}\right)^2\left(\frac{\chi_\perp}{r_s v_{th_e}}\right)\left(\frac{L_p^2}{r_s L_q}\right) < 2.9\times10^{-5}\frac{\chi_\perp}{\beta_p^2\sqrt{T_e(keV)}} < 0.36mm \quad (5)$$

Figure 4a shows the typical early time evolution of a mode, while Figure 4b shows the observed threshold island width as a function of plasma density for

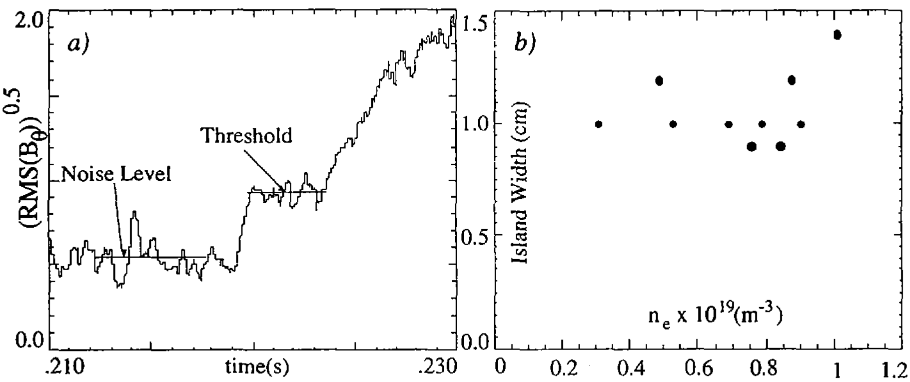

Figure 4: a) Typical early time history of MHD activity showing presence of threshold, b) threshold island width as a function of n_e for shots without RMPs

the shots with naturally occurring MHD modes in Figure 3. The value (which is independent of density) is much larger than that predicted by the $\chi_\perp/\chi_\parallel$ model and in good agreement with that predicted by the ion polarisation current model.

4. Error Field Experiments

An important distinction between the ion polarisation current model and the $\chi_\perp/\chi_\parallel$ model is the prediction that the critical β_p for instability for the ion polarisation current model, as given in Equation (4), has a strong collisionality dependence. The critical β_p for the $\chi_\perp/\chi_\parallel$ model is given by:

$$\beta_{pcrit} = -\frac{w_c \Delta'}{3.5\sqrt{\varepsilon}} \frac{L_p}{L_q} \sim 10 w_c \sim 0.2 \tag{6}$$

(with w_c in meters) which is roughly constant if w_c is constant.

In order to probe the regions of β_p-n_e space where neoclassical islands are naturally stable on COMPASS-D, a series of experiments were performed using the extensive set of quasi-helical windings on COMPASS-D. The power was quickly ramped and the plasma pressure was allowed to reach a steady state value for plasmas with densities in the range $8\times10^{18}m^{-3} < n_e < 1.6\times10^{19}m^{-3}$. The error field or Resonant Magnetic Perturbation (RMP), which was configured to have a large 2/1 component, was then ramped slowly to a maximum value of ~ 4kA. The different plot symbols in Figure 3 distinguish levels of applied error field current required to induce a 2/1 mode, with circles indicating naturally occurring modes, triangles indicating a level of 0-1.5kA and squares indicating a value greater than 1.5kA. Note that the predicted value of the collisional β_{pcrit} from the polarisation current corresponds well with the drop in the amplitude of the applied error field required to induce an island. Since the islands can appear naturally for only slightly reduced densities this implies a β_{pcrit} which is a strong function of collisionality.

If a correlation can be made between the magnitude of error field required to induce an island and the value of β_p/β_{pcrit}, the RMP experiment can be considered good evidence for the ion polarisation current model. However, there is no theory (as of yet) that is capable of describing the complex interaction of the static error field with the rotating island and how this affects the various drive terms in the neoclassical island equation. A series of experiments were carried out where

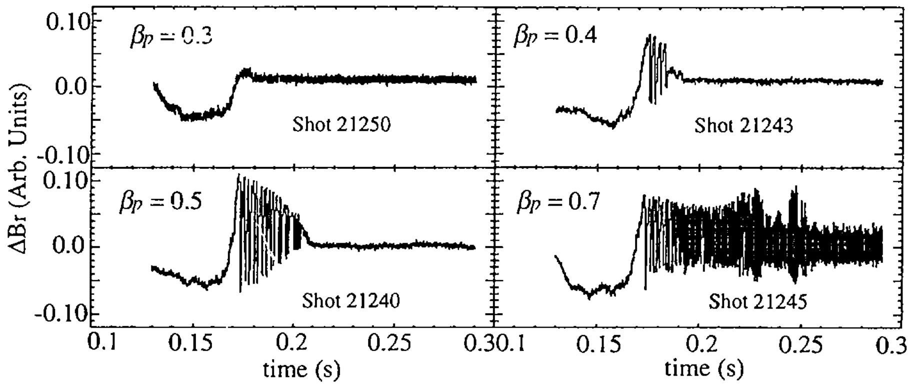

Figure 5: Error field experiment demonstrating the existence of a critical β_p for instability. All four discharges have the same density and magnitude of applied error field. The steady state value of β_p is shown in each frame.

the RMP was ramped to full value, then turned off for a series of shots with varying steady state values of β_p and a fixed density of $n_e = 1.2 \times 10^{19} m^{-3}$. The n=odd radial magnetic perturbations are shown in Figure 5, along with the value of β_p for that discharge. As the pressure is raised, the mode decays more slowly, until it remains in steady state when the critical β_p is exceeded. This confirms that the value of β_p previously correlated with the critical β_p is in fact the value below which modes are stable. In order for this result to be explained by the $\chi_\perp/\chi_\parallel$ model w_c would have to change by a factor of 3 for a factor 2 change in density.

5. q-scaling of the neoclassical island β-limit

The q-scaling of the β-limit is very different than that predicted by ideal instability calculations if the limit is instead determined by neoclassical magnetic islands, as is the case for COMPASS-D low collisionality discharges. The simple model proposed here is that the β limit is determined by the saturated bootstrap driven island interacting either with the $q=1$ surface or with the plasma edge. This can be simply stated as:

$$\frac{w_{sat}}{r_s} = min\left[\alpha_1\left(1-\frac{r_{q=1}}{r_s}\right), \alpha_2\left(\frac{a}{r_s}-1\right)\right] \tag{7}$$

where the α's are the fractional island widths required for interaction. Substituting the definition of $\beta_N (\equiv 20\beta_p(a)/Aq_a,\ A \equiv R/a)$ and the expression for the saturated island width, which is given by:

$$w_{sat} = \frac{a_1 \varepsilon^{1/2} \beta_p}{\Delta'}\left(\frac{L_q}{L_p}\right) \tag{8}$$

independent of threshold mechanism, one finds:

$$\beta_N < \frac{20\sqrt{\varepsilon}}{a_1}\left(\frac{n}{m}\right)^3 q_a(-r_s\Delta')\left[\langle p\rangle\frac{dq}{dp}\right]\left(\frac{r_s}{a}\right)^{3/2} min\left[\alpha_1\left(1-\frac{r_{q=1}}{r_s}\right), \alpha_2\left(\frac{a}{r_s}-1\right)\right] \tag{9}$$

where $\langle p \rangle$ is the volume averaged pressure.

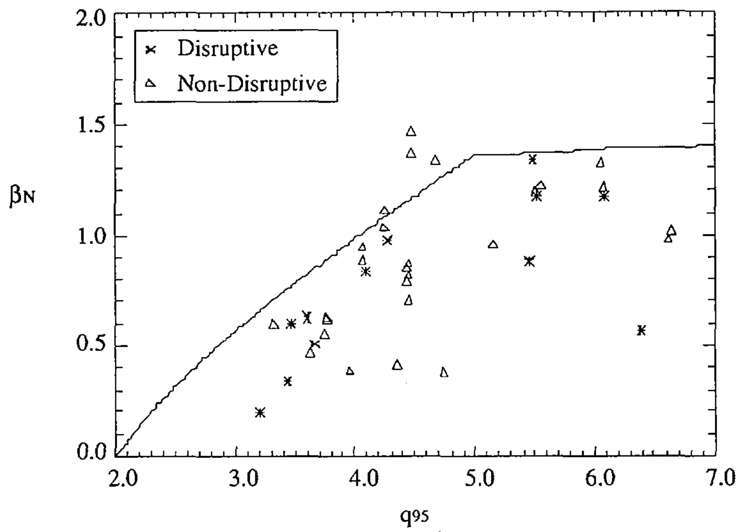

Figure 6: Comparison between measured β-limit and scaling predicted by Equation (9)

A simple scaling of the β-limit with q is obtainable by assuming a specific form for the q-profile. As an illustration we assume a form,

$$q = q_a x^2 / \left[1 - \left(1 - x^2 \right)^{q_a/q_0} \right] \tag{10}$$

Figure 6 shows the curves predicted by Equations (9) and (10) as calculated with data from COMPASS-D. The agreement between the prediction and the observed β limit is remarkable, particularly in light of the simplicity of the model.

6. Conclusions

An extensive series of experiments has been carried out to identify and characterise neoclassical islands on COMPASS-D. Also, the factors that determine the threshold for the onset of these modes have been identified and compared to two existing theories which predict a value for the magnitude of the required critical island width. The data is found to be supportive of the "ion polarisation current model" put forward in Ref. [8], while the $\chi_\perp/\chi_\parallel$ model of Ref. [7] is found to predict too small a critical island to explain observations. The predictions of a simple model for the β-limit based on the assumption of a critical maximum island width are compared to the results of a q-scan and found to be in reasonable agreement with observations. Neoclassical islands are an important issue for any future reactor. There are particularly serious implications if the observed maximum β_N on COMPASS-D at q_{95} = 3 scales to ITER. There are outstanding issues as regards how these results can be scaled to an ITER like device: a) the scaling of seed islands with machine size, b) the lack of observation of these low *m/n* modes on present large divertor experiments such as JET and JT-60U, c) uncertainty in the theory (e. g. the effects of energetic particles and rotation). It has also been demonstrated in this paper that the onset of these modes depends on several conditions being met, so that they are by no means inevitable and higher values of β_N have been achieved on COMPASS-D [1]. These matters require further investigation so that the extrapolation of the effect of these modes on ITER can made with confidence.

References

[1] GATES, D. A., et al., in Controlled Fusion and Plasma Physics (Proc. 22nd Eur. Conf. Bournemouth, 1995) **19C**, Part IV, EPS, Geneva, (1995) 117.
[2] LAHAYE, R., et al., submitted to Nucl. Fus. (1996).
[3] ZOHM, H., et al., Plas. Phys. Cont. Fus. **37** (1995) A313.
[4] See National Technical Information Service Document No. DE6008946 (W. Q. XU and J. D. CALLEN, University of Wisconsin Plasma Report No. UWPR 85-5, 1985).
[5] CARRERA, R., et al., Phys. Fluids **29** (1986) 899.
[6] CHANG, Z. et al., Phys. Rev. Lett. **74** (1994) 4663.
[7] FITZPATRICK, R., Phys. Plasmas **2** (1995) 825.
[8] WILSON, H. R., et al., Phys. Plasmas **3** (1996) 248.
[9] GORELENKOV, N. N., et al. to be published in Phys. Plasmas
[10] WILSON, H. R., et al., UKAEA Fusion report 336, to be published in Plas. Phys. Cont. Fus. (1996)

This work is jointly funded by the UK Department of Trade and Industry and EURATOM.

DISRUPTIONS AND VERTICAL DISPLACEMENT EVENTS IN JET

JET TEAM[1]
(Presented by A. Tanga)

JET Joint Undertaking,
Abingdon, Oxfordshire,
United Kingdom

Abstract

DISRUPTIONS AND VERTICAL DISPLACEMENT EVENTS IN JET.

Major disruptions and vertical displacement events (VDEs) represent a serious problem for the integrity of large devices such as ITER and a reactor. This arises from the localised power deposition on the divertor target and first wall, the production of runaway electrons in the post-disruptive plasma and the substantial forces transmitted to the vacuum vessel by eddy and halo currents. Extensive experiments have been performed in JET to characterise the phenomena associated with disruptions and VDEs and to investigate the underlying physics. In addition, the installation of a disruption feedback stabilisation system based on a set of four internal saddle coils driven by high power (3 kA/1.5 kV), high frequency (0–10 kHz) amplifiers has allowed initial experiments on the control of disruptions by suppression of the n=1 mhd precursor. This system has also been used to study fundamental aspects of the physics of error field induced modes, which is of direct application to ITER.

1. VERTICAL DISPLACEMENT EVENT (VDE)

For the Pumped Divertor phase of JET, an improved vertical stabilisation system designed to stabilise vertical instability growth rates of up to $1000s^{-1}$ was installed. Under quiescent conditions, this has proven capable of stabilising all plasma equilibria used at elongations of up to 1.9. Whilst disruptions are rather frequent (40 - 60% of the total pulses) high current disruptions and VDE events are relatively rare occurrences (< 10%) of the total number of disruptions. However these kinds of disruption which produce the largest forces and halo current are of the highest interest. A major problem relating to control of the vertical position was encountered at disruptions, as was observed in the original JET configuration, and at edge localised modes (ELM's). This loss of control was generally experienced at singular giant ELM's in highly shaped plasmas, which often terminated the long ELM-free H-modes in high fusion performance experiments. At such ELM's, a rapid displacement of the plasma occurred, generally inwards and upwards, and as a result the plasma usually made contact with the upper inner wall region. The sudden plasma movement led to a rapid rise in the radial field current to the limiting value of 2.5kA on a timescale of ~ 5ms, the upper level of the radial field amplifier was exceeded, and a VDE resulted. Typical traces for a VDE event are shown in Fig.1.

[1] See Appendix to IAEA-CN-64/O1-4, this volume.

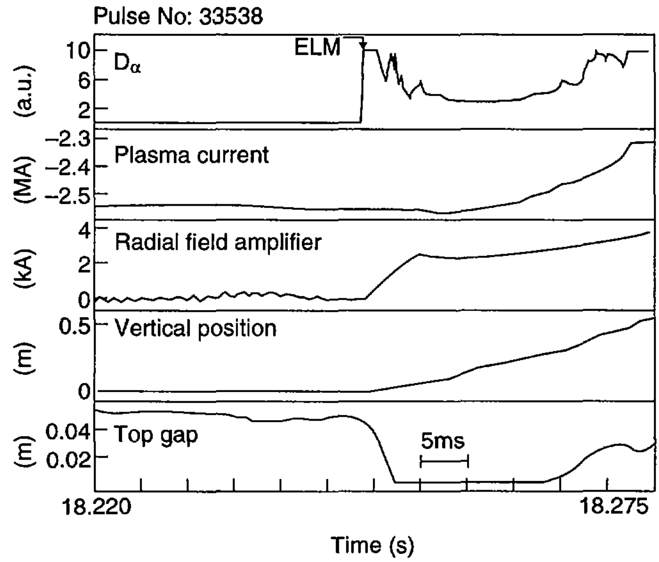

Fig.1 Time evolution of an upward VDE event following a giant ELM. Pulse number 33538.

Within a timescale of ~ 100μs the thermal energy is deposited on the target plates as shown by infrared fast camera observations and the plasma moves vertically as shown by magnetic signals (n=0). Langmuir probe observations support the hypothesis of a toroidal SOL current of the order of 10kA, intercepted by the divertor target during ELM's.

Using a simplified model of the vertical stabilisation it can be shown that such SOL current could produce a sufficiently large amplitude impulse to cause the loss of control with the subsequent VDE.

2. DISRUPTION FORCES

Plasma disruptions produce forces primarily on the vacuum vessel. The study of the dynamic stresses on the vessel for a plasma disruption is performed by a FE shell model representing 180° of the vessel. The input for a disruption is obtained from the strain gauge data taking into account the plasma position signals.

In order to evaluate the forces produced by the plasma in a given configuration an estimate of the disruption dynamics is necessary. However, for the same plasma configuration the disruption dynamics changes considerably leading to a large variation of the forces produced.

2.1 Vertical forces

The vertical forces are generated by the plasma vertical movement during a disruption. They scale with the square of the plasma current as shown in Fig.2. The value of the vertical force therefore depends on the plasma configuration, on the plasma current and on the plasma dynamics. An empirical estimate of the maximum vertical force which can be generated in a given configuration (F number) is calibrated against the forces measured in disruptive plasma pulses [1].

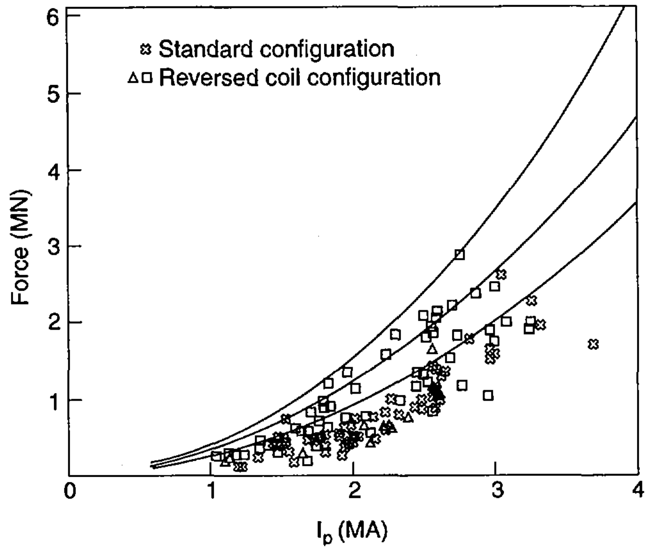

Fig.2 Measured vertical vessel force versus the plasma current prior to disruption.

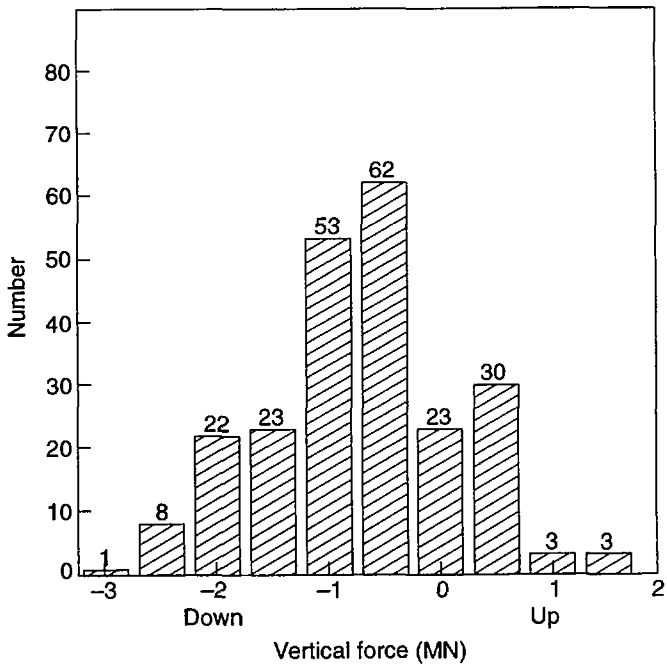

Fig.3 Distribution of the measured vertical vessel force for all the disruptions which occurred in 1996 (up to September 1996).

At a comparable plasma current the disruptions which produce the large vertical forces are those caused by VDE, with loss of the vertical stabilisation in which the current movement product $I_p.\Delta Z$ is larger. On the other hand, disruptions in which the control of the vertical position is maintained during the decay of the plasma current produce small or negligible vertical forces.

The frequency distribution of the vessel forces in the last 2 years of JET operations is shown in Fig.3. The distribution shows the higher forces produced by the downward disruptions despite the stabilisation effects of the currents induced in the divertor coils.

2.2 Halo currents

The halo current sensitive diagnostics have been installed in the vacuum vessel: a pair of toroidal field pick up coils located on the top and bottom of the vessel, poloidal current shunts at 2 toroidal positions, a number of poloidally and toroidally distributed shunts on the earthing connections of certain in-vessel components [2]. It has been found that the integrated estimated halo current scales with the measured vertical force.

The total average halo currents was found to be ≤ 20% of the initial plasma current, as shown in Fig.4.

3. LATERAL DISPLACEMENTS

The vacuum vessel displacements are measured at the ports and the radial displacements are available on four octants at the upper and lower main vertical ports (MVP's) and all eight octants at the main horizontal port (MHP), where also the tangential displacements are measured.

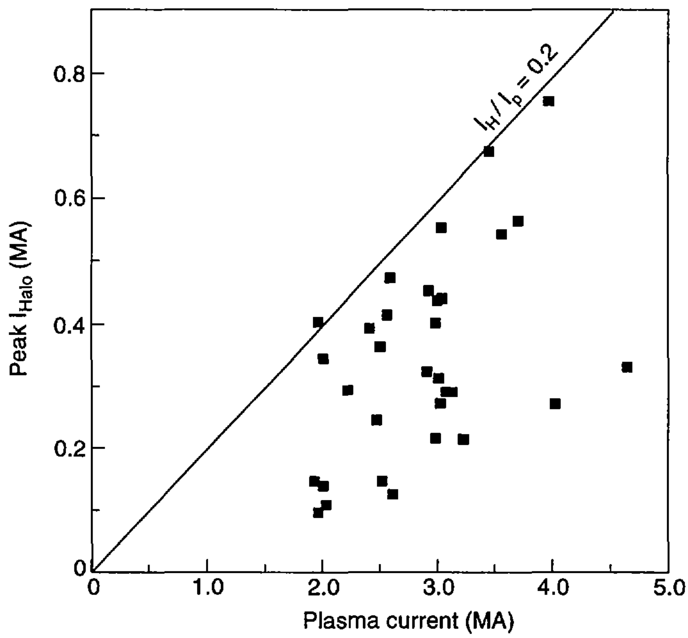

Fig.4 Integrated halo current versus plasma current prior to the disruption.

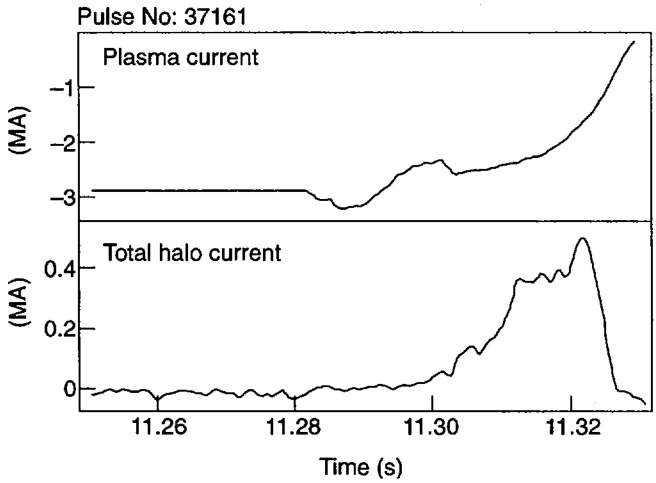

Fig.5 Time evolution of VDE and measured halo current for pulse 37161.

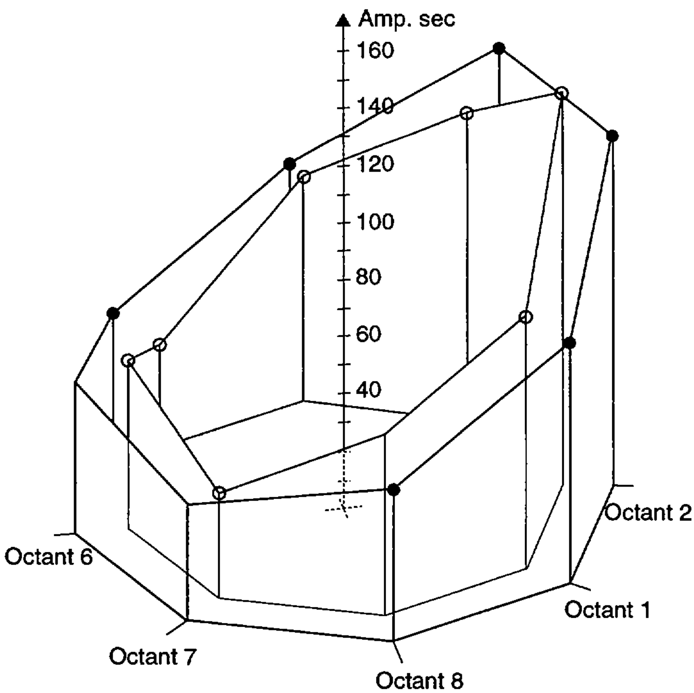

Fig.6 Time integrated mushroom tile current for pulse 34078 highly asymmetric disruption.

The toroidal distribution of the halo current is given only for upwards disruptions.

Local measurements of intercepted halo currents and measurements of forces on the vessel supports indicate large time fluctuations and toroidal asymmetries of the halo current density in the presence of toroidal asymmetries of the global vertical forces acting on the JET vessel as measured from the 8 instrumented tiles in 8 locations at the top of the vessel. The typical trends are shown in Fig.5.

In the presence of the measured toroidally asymmetric halo currents a net lateral movement of the vacuum vessel was observed. The toroidal distribution of the time integrated halo currents peak was as high as twice the average as shown in Fig.6. The observed lateral movement of the vessel is associated with an apparent asymmetry of the measured plasma current centred at two different toroidal locations. The inferred m=1, n=1 island would be equivalent to a tilting of the plasma with a resulting force which needs to be balanced by other asymmetric toroidal forces such as induced or halo current forces. From the movement of the position of the plasma current centroid the apparent edge safety factor could be evaluated. A correlation has been found between large sideways movements and an estimated value of the safety factor between 1.0 and 1.3. From the vector sums of the average octant displacements, it appears the whole vessel moved approximately by 5.6mm in the direction between octant 5 and 6.

4. SADDLE COILS

Experiments on the influence of external error fields on mhd stability have been pursued using the internal saddle coil set [3]. n=1 'locked' modes induced by intrinsic error fields are considered to be significant for ITER since the critical error field threshold is predicted to be very low, $B_r/B_t \sim 2\times10^{-5}$.

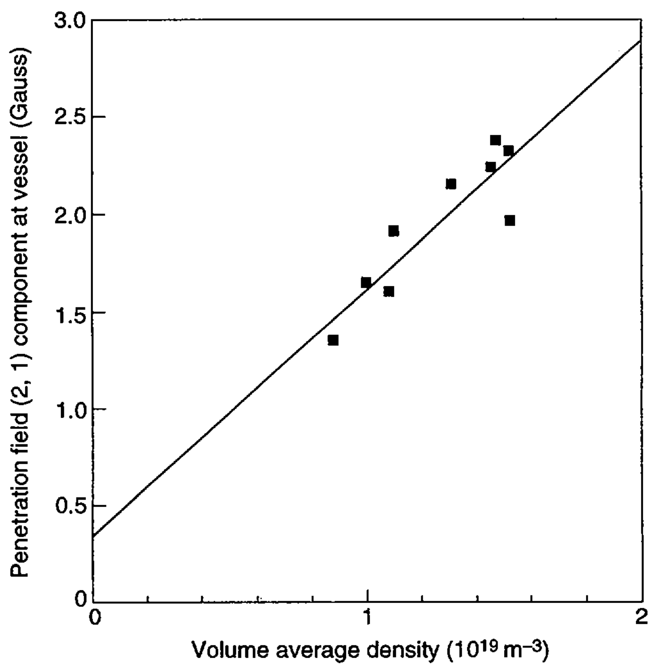

Fig.7 Penetration threshold ($I_{SC} \cdot B_{r21}$) as a function of the average electron density n_e.

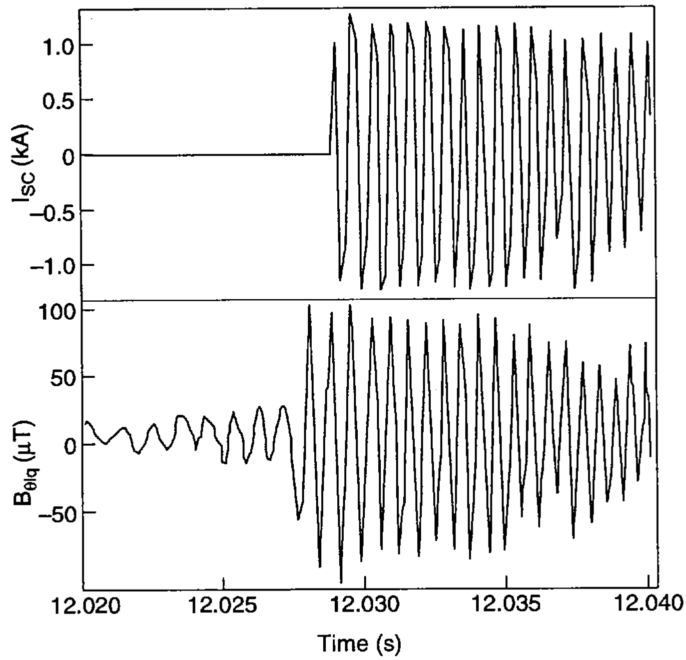

Fig.8 Modification of a tearing mode growth rate at the sudden application of the feedback current (I_{SC}). Feedback started by a trigger on mode amplitude at a field level of ~ 50μT. $B_{\theta lq}$= field at the poloidal limiter (n=1).

Initial experiments have investigated the threshold for the static error field modes. In JET n=1 fields B_r as small as 0.12 mT (B_r/B_t~5 10^{-5}) are sufficient to penetrate (with n_e=1-1.4$10^{19}$m^{-3} q_{95}~3, I_p=1-1.5MA) and generate tearing modes. Figure 7 shows the linear dependence of the penetration threshold with the plasma electron density.

Rotating tearing modes have also been generated with the application of a small n=1 field rotating at a frequency close to the plasma rotation frequency.

The considerable scatter of the data shown in Fig.7 appears to depend on the details of the plasma equilibrium.

Magnetic feedback control has been applied in JET to saturated tearing modes. The amplitude and the position of the modes have been measured by four fast pickup coils. The spurious pickup due to the feedback vacuum field and to the ideal MHD plasma response to this field has been measured and compensated in the digital controller. The plasma ideal response is independent of the field frequency and strongly dependent on the plasma configuration and q value. Upon the application of the feedback AC field a modification of the growth rate of the tearing mode has been observed in a few pulses as shown in Fig.8.

It has not yet proved possible to stabilise tearing mode precursors of density limit disruptions because their high instability parameter Δ' and the low feedback gain applied.

CONCLUSIONS

The analysis of the disruption dynamics and vessel forces in JET has shown that the large vertical forces produced by the elongated plasma cause both halo current forces localized on in-vessel components and stresses on the main vacuum vessel. VDE events producing the highest vertical forces cause sideways vessel displacements associated with a tilting of the plasma column. Experimental evidence shows that this event occurs when the limit q is in the region 1-1.3. Loss of control of vertical stabilisation associated with ELM's in shaped plasma produce upward VDE's. Experiments with the lower saddle coils set have measured the threshold for the static error field mode and have been applied to the saturated tearing modes. Systematic measurements of vessel displacements and forces have been carried out.

REFERENCES

[1] NOLL, P., et al., Fusion Technol. **15** (1989) 259.

[2] ANDREW, P., et al., in Fusion Engineering (Proc. 16th IEEE/NPSS Symp. Champaign, 1995), Vol. 1 (1995) 770.

[3] SANTAGIUSTINA, A., et al., in Controlled Fusion and Plasma Physics (Proc. 22nd Eur. Conf. Bournemouth, 1995), Vol. 19C, Part IV, European Physical Society, Geneva (1995) 461.

EDDY-CURRENT CHARACTERIZATION AND PLASMA ROTATION CONTROL IN WALL-STABILIZED TOKAMAK DISCHARGES

M.E. MAUEL, E. EISNER, A. GAROFALO, T.H. IVERS,
R. KOMBARGI, D. MAURER, D. NADLE, G.A. NAVRATIL,
A. SAINZ, M.K.V. SANKAR, M. SU, E. TAYLOR, Q. XIAO
Department of Applied Physics,
Columbia University,
New York, N.Y.

W.A. REASS, G.A. WURDEN
Los Alamos National Laboratory,
Los Alamos, New Mexico

United States of America

Abstract

EDDY-CURRENT CHARACTERIZATION AND PLASMA ROTATION CONTROL IN WALL-STABILIZED TOKAMAK DISCHARGES.

Measurements of eddy-currents flowing on the surfaces of a segmented, adjustable, and close-fitting conducting wall are used to identify MHD instabilities which precede plasma disruptions and to characterize the eddy-currents present during wall stabilization. The eddy-currents on the plasma side of the wall are measured to be similar to those predicted for an ideal axisymmetric wall and account for the effectiveness of segmented walls for wall-stabilization. Dynamic control of slowly growing internal instabilities which persist during wall stabilization is investigated by energizing a small number of highly localized saddle-coils. The toroidal rotation frequency of the resonant mode is strongly modulated by the application of both oscillating single-phase and rotating two-phase saddle-coil currents. When the toroidal phase of a rotating magnetic perturbation is advanced by 180°, the growth of the phase-instability associated with tearing mode stabilization is detected in preparation for active feedback experiments.

1. INTRODUCTION

Critical elements of plans to improve the economic potential of steady-state tokamak power sources [1] and to achieve high-beta, steady-state operation of spherical tokamaks [2] are the use of passive wall-stabilization to suppress external kink instabilities and plasma rotation control and/or active feedback to stabilize resistive wall modes [3,4] and neoclassical tearing modes [5,6].

The High Beta Tokamak-Extended Pulse (HBT-EP) experiment (R = 0.92 m, a = 0.15 m, B = 0.35 T) was built to investigate these phenomena [7]. HBT-EP uses an internal, movable conducting wall and a high-power, modular saddle-coil system to provide passive and active control of long wavelength MHD instabilities. The conducting wall consists of 20 segments (made from 0.012 m thickness aluminum) having plasma-to-wall separations which can be independently adjusted between discharges. As reported previously, fast-growing instabilities appear when the wall is retracted, and they are suppressed when the conducting wall is moved near the plasma's edge [8,9]. Although wall-stabilization is effective in stabilizing external kinks in plasmas with relatively broad current profiles, as the current profile evolves and becomes more highly-peaked, slowly-growing internal instabilities are observed. Application of resonant magnetic perturbations is one approach to control these instabilities [10]. In the HBT-EP device, both single-phase and two-phase resonant magnetic perturbations are applied to the plasma using four to ten highly-localized saddle-coils placed at toroidal gaps of the conducting wall. Modulation of the oscillation frequency of the saddle-coil current decelerate or accelerate resonant modes in the plasma in a controlled manner. Furthermore, both the phase-instability [11] and the frequency modulations associated with single-phase magnetic feedback of internal modes are detected by measuring the plasma's temporal response to resonant saddle coil currents.

2. WALL STABILIZATION

Wall-stabilization of external kink instabilities is investigated with discharges having high beta or high edge currents. Discharges with high edge

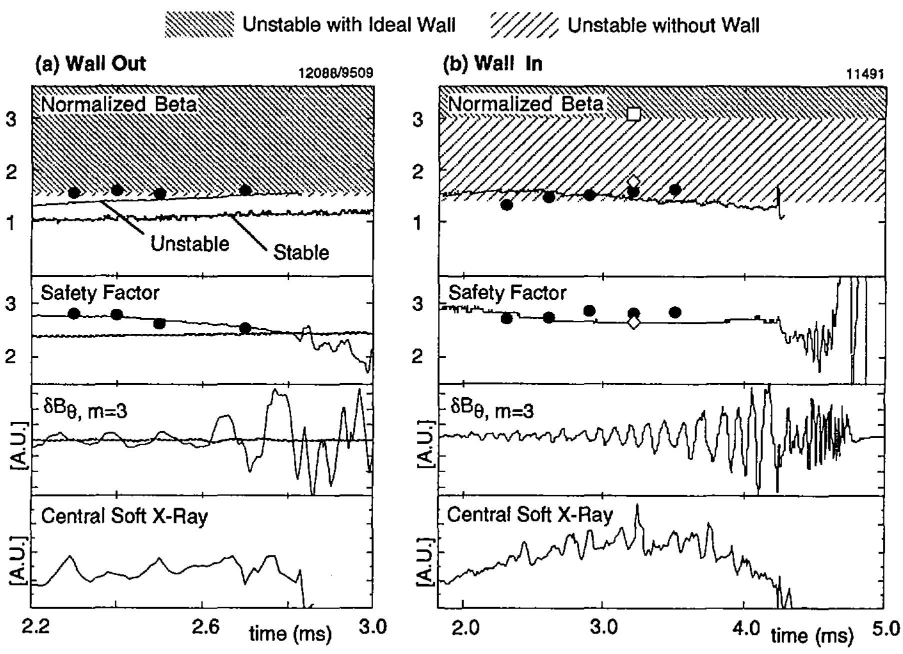

FIG. 1. Disruptions induced by MHD instabilities observed when (a) the adjustable wall was retracted and when (b) the wall was fully inserted. For each discharge, the ideal stability boundaries with and without an ideal wall are indicated by cross-hatching. The time evolution of β_N, q(a), the perturbed magnetic field, and the central chord of the soft x-ray array are shown.

currents are created with sustained, 6 MA/s, current ramps. When the wall is retracted, b/a = 1.52, rapidly growing kink instabilities result in current disruption immediately after the edge safety factor, $q(a)$, decreases below 3. When the wall is inserted, b/a = 1.07, brief instability bursts are observed when the resonant $q = 3$ surface approached the plasma edge from within, but long quiescent periods occur when $q(a)$ decreases below 3. Discharges with a more conventional current profile and a higher Troyon-normalized beta, $\beta_N > 1.3$, are produced using a rapid formation technique, $dI_p/dt \sim 100$ MA/s, followed by a weak current ramp, ±0.5 MA/s, to modify the current profile. Fig. 1a illustrates an $n = 1$ external kink observed near marginal instability for a plasma with β_N = 1.6 and a relatively low internal inductance, $l_i = 0.85$, when the conducting wall was retracted. A $(m, n) = (3, 1)$ kink grows to large amplitude within 200 μs, and a global disturbance seen by a soft x-ray detector array leads to a thermal collapse and current disruption [9]. Fast growing kinks are not present in similar discharges with reduced β_N, and this demonstrates that these discharges operate near the β_N-limit for $n = 1$ ideal modes.

Detailed comparisons of observations with theory are made possible by reconstructing high β_N equilibrium consistent with (1) measured soft x-ray profiles, (2) measurements from several arrays of external magnetic loops, and (3) the poloidal fields measured with an internal magnetic probe at the plasma's edge ($0.8 < r/a < 1.2$). The measurements are sufficient to specify equilibria for discharges exhibiting sawtooth oscillations. By constraining $q(0)$ to near unity, the plasma current profile and the equilibrium components of the eddy currents flowing in both the segmented wall and the vacuum chamber are determined by least-squares minimization. The solid circles in Fig. 1 represent global parameters from the full reconstruction procedure, and open symbols represent parameters from equilibria modified to exceed the ideal beta limit when the wall is inserted.

The PEST/VACUUM ideal MHD stability codes [12] are used to analyze discharges with the conducting wall retracted (Fig. 1a) and with the conducting wall fully inserted (Fig. 1b). With the wall retracted, the plasma is found to be marginally unstable, and the wall has little effect on stability. However, with the wall inserted, the plasma is predicted to be ideally stable, and wall stabilization doubles the ideal beta limit. For the discharge shown in Fig. 1b, a magnetic perturbation with reduced growth rate was still present during wall-stabilization. This mode was dominated by the $(m, n) = (3, 1)$ vacuum resonance and may represent a resistive kink or a resistive wall mode [3].

The toroidal components of the eddy-currents flowing at the toroidal centers of both the plasma-facing and the vacuum sides of two wall segments are measured in HBT-EP. This enables a detailed comparison between the measured eddy-currents and the currents computed by the PEST/VACUUM codes [13]. Since the PEST/VACUUM codes compute the eddy-currents which flow on an idealized wall having no toroidal gaps, this comparison helps to quantify the effects of wall segmentation and identify the observed MHD instabilities. Fig. 2 illustrates the measured and predicted eddy-current patterns for the discharges shown in Fig. 1. The eddy-currents measured on the plasma-facing side of the wall closely resemble the ideal computations. The measurements demonstrate that toroidal gaps do not distort the stabilizing helical eddy currents on the wall's plasma-facing side. In contrast, the toroidal gaps do affect the eddy-current return

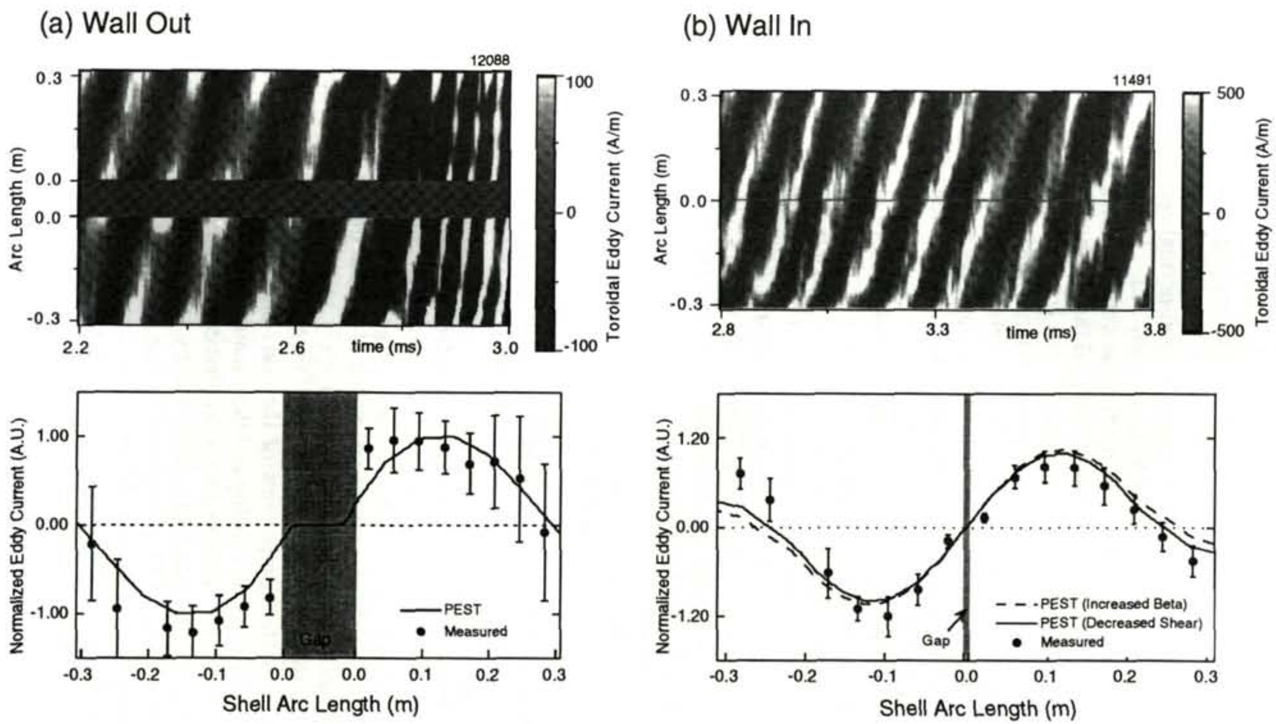

FIG. 2. Measurements of the eddy-currents induced on the modular conducting wall by unstable $n = 1$ external kink modes. When the wall is removed (a), the PEST/VACUUM code can be directly compared with measurements. When the wall is inserted (b), PEST/VACUUM predicts stability. However, the measured eddy-current patterns resemble those induced by an unstable companion equilibrium having either elevated β_N or reduced magnetic shear.

path. Measurements show the helical currents close on the wall's vacuum side to a greater extent than calculated in the axisymmetric ideal codes. Nevertheless, the correspondence between the measured and predicted eddy-currents on the plasma-facing surface accounts for the effectiveness of segmented conducting walls for wall-stabilization.

3. ROTATION CONTROL WITH SADDLE COILS

Plasma stability on an extended time-scale is being investigated using compact saddle-coils driven by two high-power linear amplifiers (10 MW each). For the studies reported here, each saddle-coil pair imposes a magnetic perturbation dominated by poloidal mode number $m = 2$ and toroidal mode number $n = 1$. Two to five saddle-coil pairs are connected to produce a non-rotating, single-phase resonant magnetic perturbation over only 3% to 8% of the plasma's surface. Similarly, two saddle-coil pairs are connected as a two-phase, quadrature winding to produce a rotating magnetic perturbation.

Fig. 3a illustrates the response of a wall-stabilized discharge when a single-phase, perturbation with linearly increasing frequency is applied to the plasma using only two saddle-coil pairs. Prior to switching on the saddle-coil current, the discharge contains a saturated $(m, n) = (2, 1)$ internal instability with

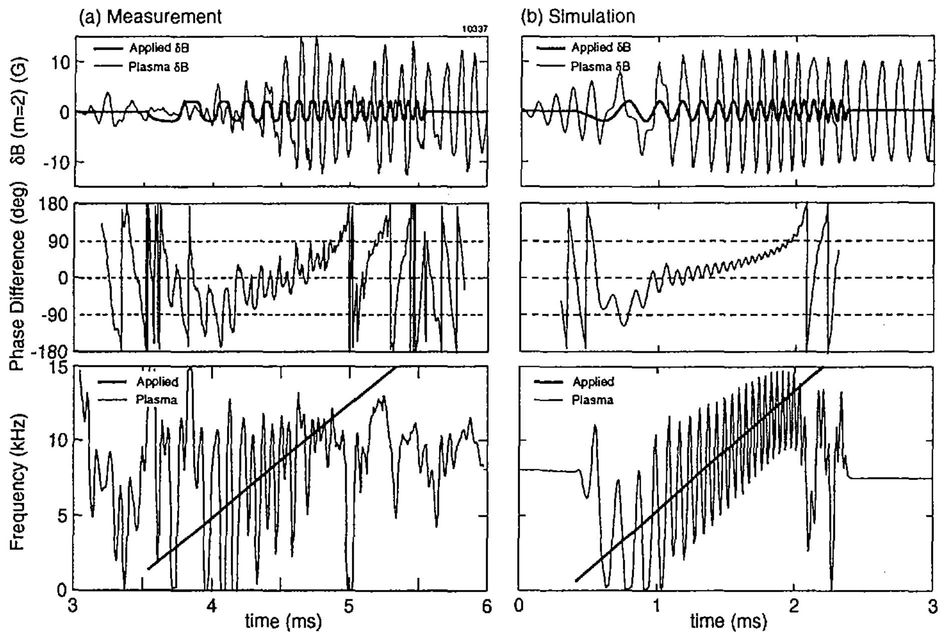

FIG. 3. Measurement of the dynamic response of $(m,n) = (2, 1)$ magnetic fluctuations acted upon by oscillating current in a single-phase pair of saddle-coils with a linearly increasing frequency. The observed mode frequency is strongly modulated. The measured phase dynamics (a) resembles a non-linear, single-helicity simulation (b).

a natural toroidal rotation frequency between 5 and 10 kHz. The oscillating saddle-coil current (± 500 A) is swept in frequency from 1 to 16 kHz. The $(m, n) = (2, 1)$ plasma response is measured both by Fourier decomposition of the wall eddy-currents and by Fourier-analyzing Rogowski coils. The measured magnitude and phase of the plasma perturbation determines the toroidal component of the electromagnetic torque on the mode from the saddle-coils. This torque is proportional to the sine of the phase difference between the applied field and the resonant plasma perturbation, $\Delta\varphi$. The increasing phase slippage between the saddle coil field and the mode indicates an increasing applied torque. At 4.3 ms, $\Delta\varphi \sim 90°$, the maximum average torque is attained, and further acceleration of the mode stops. A wider frequency range of rotation control is obtained by increasing the number of saddle coils with the same current level. With five saddle-coil modules, the rotation frequency of the resonant helical mode more than doubles, exceeding 20 kHz. Rotating magnetic perturbations applied with the two-phase saddle coil configuration produces similar changes in mode rotation. Additionally, the two-phase saddle-coil is used to maintain mode rotation in the direction opposite to the normal electron-diamagnetic-drift direction of rotation.

Single-phase rotation control also illustrates the dynamic response of internal perturbations to resonant external magnetic fields. In Fig. 3a, the phase of the mode with respect to the phase of the saddle-coil current oscillation undulates as a result of plasma viscosity and the amplitude modulation of the applied torques. The phase undulations produce non-sinusoidal distortions of the detected magnetic signals. The phase dynamics of these large perturbations are well-modeled using a single-helicity, large-aspect ratio description for the nonlinear growth of driven resistive modes [11,14]. Fig. 3 shows a comparison between the nonlinear simulation and the measured dynamic response to single-phase rotation control.

4. PHASE INSTABILITY ASSOCIATED WITH TEARING MODE STABILIZATION

The unstable growth of the phase-difference, $\Delta\varphi$, between a rotating synchronous external perturbation and an internal resonant mode is referred to as the "phase-instability" [11]. The growth of the phase-instability is measured in HBT-EP using a technique described in Ref. 9. Midway during a 1.5 ms long application of a rotating magnetic perturbation, the phase is rapidly advanced by 180°. Before the phase advance, the phase of the plasma mode "locks" to the applied perturbation, and the mode amplitude increases as the "O-points" of the $(m, n) = (2, 1)$ mode align with the positive phase of the saddle-coil current. When the rotation frequency of the applied field coincides with the plasma's natural rotation frequency, $\Delta\varphi$ approximately vanishes, indicating an absence of externally-applied torque. Immediately after the phase-flip, the "X-point" of the internal mode is aligned with the positive conductor of the saddle coil, $\Delta\varphi \sim \pi$, and this reduces the mode amplitude. However, small deviations in phase grow rapidly, as the torque applied by the saddle coils realigns the mode, and $\Delta\varphi \to 0$.

Fig. 4 illustrates measurement of the rate of phase-growth following a rapid phase-flip of an otherwise constantly rotating 10 kHz, $(m, n) = (2, 1)$, large amplitude resonant magnetic perturbation. As shown in the figure, the phase

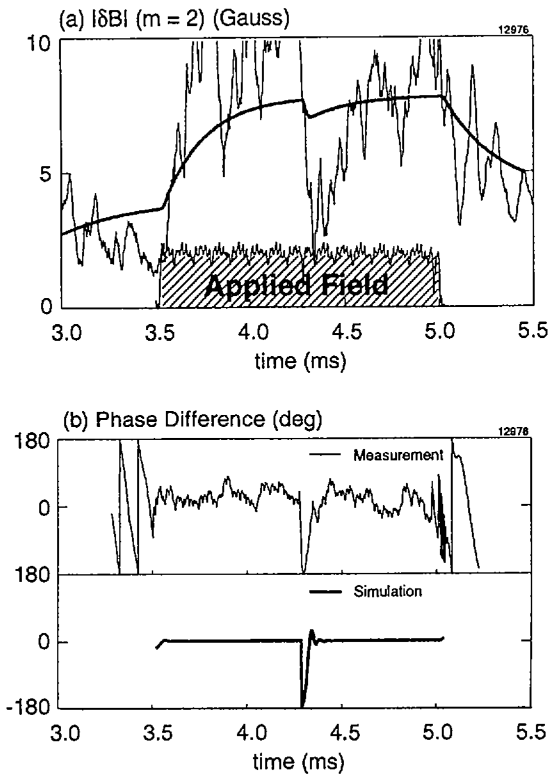

FIG. 4. Measurement of phase-instability when the toroidal phase of a rotating magnetic perturbation is advanced by 180°. Immediately following the phase-flip, the amplitude of the resonant magnetic fluctuations decreases (a) as the measured phase-difference between the plasma mode and the applied field realigns (b).

instability grows rapidly with $\Delta\varphi/\Delta t \sim \omega$. This is consistent with the predictions of the nonlinear single-helicity model, although the mode amplitude responds more rapidly to the applied feedback than expected from the nonlinear model. Since the bandwidth of the stabilization amplifiers at HBT-EP exceeds 30 kHz, the phase-instability should not prevent active feedback control of these internal modes [15].

5. SUMMARY

Experiments with the HBT-EP device demonstrate the effectiveness of wall stabilization with a conducting wall consisting of individually adjustable and electrically disconnected segments. Direct measurements of the eddy-current patterns induced by kink instabilities show the currents which flow on the plasma-facing surface of the wall closely resemble those predicted by ideal MHD for a conducting wall without toroidal gaps.

Application of single-phase and two-phase magnetic fields strongly modifies the toroidal rotation of resonant plasma modes. Significant mode rotation control is possible even for saddle coils covering only 3% of the plasma surface. The dynamic response of the plasma to a time-varying applied field is observed, including the response to single-phase rotation control (generating strong phase undulations) and rapid phase-flips of rotating perturbations (generating unstable phase-growth).

Experiments planned in the near future include active feedback of slowly-growing plasma instabilities and the application of multiple-helicity and multiple-frequency perturbations in order to study the effects of sheared plasma rotation.

ACKNOWLEDGMENTS

The research reported here is supported by DOE Grant DE-FG02-86ER53222. The authors would also like to acknowledge J. Manickam and M. Chance for their assistance with the PEST/VACUUM codes, T. Jensen for discussions relating to the interpretation of plasma rotation measurements, and the technical support of N. Rivera, E. Rodas, M. Cea, and H. Alvestad.

REFERENCES

[1] THOMASSEN, K.I., et al., in Plasma Physics and Controlled Nuclear Fusion Research 1994 (Proc. 15th Int. Conf. Seville, 1994), Vol. 2, IAEA, Vienna (1995) 625.

[2] BUTTERY, R., et al., ibid., p. 633.

[3] STRAIT, E.J., et al., Phys. Rev. Lett. **74** (1995) 2483.

[4] FITZPATRICK, R., JENSEN, T.H., Phys. Plasmas **3** (1996) 2641.

[5] CHANG, Z., et al., Phys. Rev. Lett. **74** (1995) 4663.

[6] SMOLYAKOV, A.I., et al., Phys. Plasmas **2** (1995) 1581.

[7] SANKAR, M.K.V., et al., J. Fusion Energy **12** (1993) 303.

[8] IVERS, T.H., et al., in Plasma Physics and Controlled Nuclear Fusion Research 1994 (Proc. 15th Int. Conf. Seville, 1994), Vol. 2, IAEA, Vienna (1995) 287.

[9] IVERS, T.H., et al., Phys. Plasmas **3** (1996) 1926.

[10] MORRIS, A.W., et al., Phys. Rev. Lett. **64** (1990) 1254.

[11] LAZZARO, E., NAVE, M.F.F., Phys. Fluids **31** (1988) 1623.

[12] CHANCE, M.S., personal communication;
MANICKAM, J., GRIMM, R.C., DEWAR, R.L., Comput. Phys. Commun. **24** (1981) 355.

[13] GAROFALO, A., et al., Interpretation of eddy currents induced by MHD instabilities in a segmented wall (in preparation).

[14] D'ANTONA, G., IEEE Trans. Nucl. Sci. **41** (1994) 216.

[15] BOSIA, G., LAZZARO, E., Nucl. Fusion **31** (1991) 1003.

DISRUPTION STUDIES IN DIII-D*

A.G. KELLMAN, J.W. CUTHBERTSON[1], T.E. EVANS,
D.A. HUMPHREYS, A.W. HYATT, G.L. JAHNS[2],
T. JERNIGAN[3], C.J. LASNIER[4], R.L. LEE, J.A. LEUER,
S. LUCKHARDT[1], M.J. SCHAFFER, P.L. TAYLOR,
D.G. WHYTE[5], D. WROBLEWSKI[2], J. ZHANG[1]
General Atomics,
San Diego, California,
United States of America

Abstract

DISRUPTION STUDIES IN DIII-D.

Characteristics of disruptions in the DIII-D tokamak including the current decay rate, halo current magnitude and toroidal asymmetry, and heat pulse to the divertor are described. Neon and argon pellet injection is shown to be an effective method of mitigating the halo currents and the heat pulse with a 50% reduction in both quantities achieved. The injection of these impurity pellets frequently gives rise to runaway electrons.

1. INTRODUCTION

Disruptions represent a serious obstacle to the successful realization of a commercially viable tokamak power plant. In addition to the high thermal and electromagnetic loads resulting from the rapid loss of both thermal and magnetic energy, disruptions can generate large, toroidally asymmetric poloidal "halo" currents in the scrapeoff layer. These currents strongly influence tokamak design because they can give rise to large forces on the vessel and internal components. This paper describes work on the DIII–D tokamak on the characterization of these different disruption phenomena, successful reduction of the heat pulse and halo currents using neon and argon pellets, and the development of a real time disruption avoidance system for high beta discharges using a neural network.

2. DISRUPTION CHARACTERIZATION

Disruptions in DIII–D fall into two basic classes, major disruptions and vertical displacement events (VDEs). In a major disruption, an MHD mode grows, leading to a loss of thermal energy (thermal quench) and the resulting cold plasma suffers a rapid

---

* Work supported by the US Department of Energy under Contract Nos DE-AC03-89ER51114, DE-AC05-96OR22464 and W-7405-ENG-48, and Grant No. DE-FG03-95ER54294.

[1] University of California, San Diego, California, USA.

[2] ORINCON Corporation, USA.

[3] Oak Ridge National Laboratory, Oak Ridge, Tennessee, USA.

[4] Lawrence Livermore National Laboratory, Livermore, California, USA.

[5] INRS-Energie et matériaux, Varennes, Quebec, Canada.

decay of the plasma current (current quench). In single null divertor discharges, a loss of vertical position in the direction of the X–point typically follows the thermal quench. In a VDE, the loss of vertical position precedes the thermal quench. As the plasma moves vertically against the first wall, the cross section and edge q decrease until the shrinking plasma disrupts, losing its thermal energy, typically when the edge q approaches two.

For both disruption types, a rapid decay in the plasma current is observed following the thermal quench. Although there is a large variation in the current decay rate for a given plasma current, for full aperture discharges (volume>$19m^3$) the fastest current decays have a characteristic decay time, $I_{po}/(dI/dt) \sim 4$ ms, where I_{po} is the pre-disruption current and dI/dt is the average decay rate from 90% to 10% of the current. VDEs have the shortest decay times because the dual effects of the reduced cross section and the high resistivity of the cold plasma increase the plasma resistance. Discharges with low plasma current, small volumes (<15 m^3) and large distances to the conducting wall exhibit even shorter decay times, approaching 2 ms. The post-thermal quench equilibria for these discharges are so vertically unstable that they exhibit extremely rapid loss of vertical position and have shorter decay times than full-aperture VDEs.

Heat flux measurements during disruptions show that the relative importance of two energy loss mechanisms, conduction to the divertor floor and radiation, depend on the type and phase of the disruption. In three different disruptions, the fraction of the total energy lost during the thermal quench (primarily the thermal energy) that was conducted to the floor varied considerably: 85% for a VDE, 50% for a major disruption at high beta and 22% for a discharge terminated by a large argon puff. During the thermal quench, radiation plays a very small role in a VDE while it dominates the energy loss in the argon puff disruption. In all cases, the role of radiation increases in the current quench phase and is the major energy loss mechanism. In the VDE and the argon puff disruptions, radiation accounts for 85%–90% of the energy lost during the current quench with a value of 65% for the high beta disruption. Detailed heat flux measurements and a complete energy balance during DIII–D disruptions have been reported earlier by Lee [1] and Hyatt [2].

One of the more significant disruption-related problems for future machines is the development of large poloidal currents that flow on the open field lines surrounding the plasma and return poloidally through the vessel. These poloidal "halo" currents interact with the toroidal field resulting in large, poloidally localized forces on the vessel and internal components [3]. In order to better understand the driving mechanism and dependence of the halo current on plasma properties, we have conducted a series of experiments in which a VDE is initiated by disabling the vertical feedback system. The poloidal and toroidal structures of the poloidal halo currents are measured with an extensive array of detectors in the lower divertor region referred to as the tile current array (TCA) [4].

The basic phenomenology of the VDE is shown in Fig. 1. As the plasma drifts vertically downward [Fig. 1(a)], its cross section shrinks, the edge safety factor decreases, and the plasma disrupts, losing its thermal energy [Fig. 1(b)]. During the VDE, two mechanisms drive the halo current. Following the thermal quench, the core plasma current (that contained within the last closed flux surface) begins to decay, inducing toroidal current in the cold "halo" plasma on the open field lines surrounding the last closed flux surface [Fig. 1(c)]. Flux contours and toroidal halo current are determined using an array of distributed current elements to represent the plasma and calculating the best distribution of currents in the plasma region and vessel to fit magnetic diagnostics. Because the halo region is essentially force free ($j \times B = \nabla p \sim 0$), the current flows along the field lines. Thus by driving a toroidal halo current, a poloidal

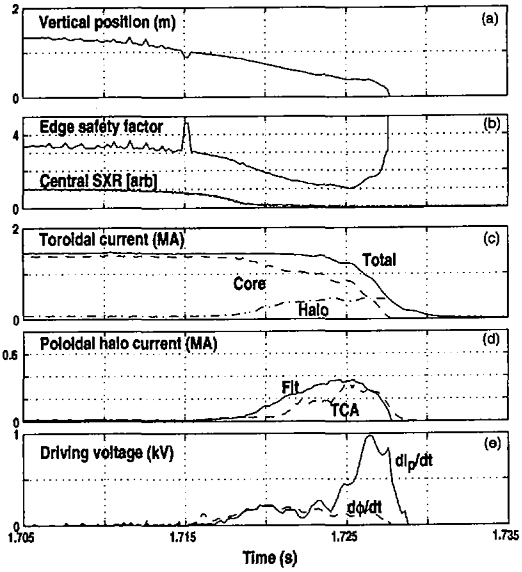

FIG. 1. Time evolution of a VDE ($\beta_n = 1.1$, shot 90 219). Poloidal halo current reaches 370 kA (23% of the pre-disruption I_p). The peak poloidal halo current determined by a magnetic fitting code (FIT) agrees well with that measured by the tile current array (TCA).

current is also driven that is related to the toroidal component by $I_{halo}(pol) = I_{halo}(tor)/q_{edge}$ [Fig. 1(d)]. A second mechanism that directly drives poloidal halo current is the reduction in the toroidal flux linked by the plasma as the cross section shrinks. Comparison of the two driving terms shows that at the time of maximum poloidal halo current the driving voltage from the current decay, $V_{dI/dt}$, is considerably larger than that from toroidal flux compression, $V_{d\phi/dt}$, although the terms are comparable earlier in the buildup of the poloidal current [Fig. 1(e)]. The halo width increases as the plasma moves downward and at the time of the peak poloidal halo current the halo width is typically 10–15 cm, measured on the plasma midplane. During the final stage of the current decay, there are no closed flux surfaces and all the toroidal current is carried on open field lines. Despite the finite toroidal halo current (I_{halo}(toroidal)=420 kA at 1.7275 s), the poloidal halo current is very small during this stage because the edge q is very high.

Poloidal halo currents of up to 30% of the pre-disruption current, I_{po}, have been measured during VDE's when the data is averaged over ± 0.5 ms (Fig. 2). Values up to 40% have been observed with shorter averaging (± 0.1 ms). The scaling proposed by Granetz [5], $I_{halo}/I_{po} \sim 1/q_{950}$, ($q_{950}$ is the pre-disruption q at the 95% flux surface) does not explain the DIII–D data in which large variations in halo current are observed at fixed I_{po}/q_{950} and the highest halo current is observed at high q_{95}. Examination of two discharges with the same I_{po} and q_{950} but a factor of two difference in I_{halo}/I_{po} (23% vs. 10%) is useful to understand the underlying physics determining the magnitude of the halo current:

I_p=1.48MA, q_{950}=3.4	I_{halo}/I_{po}	dI_p/dt(core)	I_{halo}(tor)	$q_{edge\text{-}min}$
low βn=1.1	0.23	150 MA/s	0.46 MA	1.00
high βn=3.2	0.10	670 MA/s	0.62 MA	2.05

Because $I_{halo}(pol)=I_{halo}(tor)/q_{edge}$, if a sufficiently high edge q is maintained during the VDE evolution, a low poloidal halo current will result even if a large toroidal halo current is driven by the current decay in the plasma core. An analytic model shows that a key parameter determining the evolution of the edge q and thus the halo current evolution is the quantity γ_p/γ_z where γ_p is the initial plasma current decay rate and γ_z is the vertical instability growth rate. Since $q_{edge}{\sim}a^2/I_p$ (a is the minor radius), a rapid current decay relative to the instability growth rate ($\gamma_p/\gamma_z>1$) results in a high edge q because the current decays while the plasma cross section is still large ($q_{edge-min}=2.05$) This is the case for the high beta discharge shown in the table. In the opposite regime, $\gamma_p/\gamma_z<1$, a slow current decay relative to the vertical motion allows the edge q to get small ($q_{edge-min}=1.0$) and thus even for lower toroidal halo current the poloidal halo current is larger. This is the case for the low beta discharge. This implies that a successful technique to reduce poloidal halo currents is to induce a rapid current decay while the plasma is still far from the floor and large enough to have a high edge q. The impurity pellet injection described in the next section follows this approach.

The critical consequence of the poloidal halo currents is the resulting vertical force on the vessel. On DIII–D, the force is inferred from direct measurement of the vertical vessel displacement. This is shown to scale linearly with poloidal halo current magnitude as expected since the duration of the halo current is short compared to the characteristic mechanical times of the vessel.

In addition to the large amplitude of the halo currents, large toroidal asymmetries are observed in the halo current. Toroidal peaking factors (peak-to-average value) as high as 3 are observed at the time of peak halo current with values as high as 5 for shorter averaging times, ±0.1 ms (Fig. 2). As shown in the figure, a value of I_{halo}/I_{po}

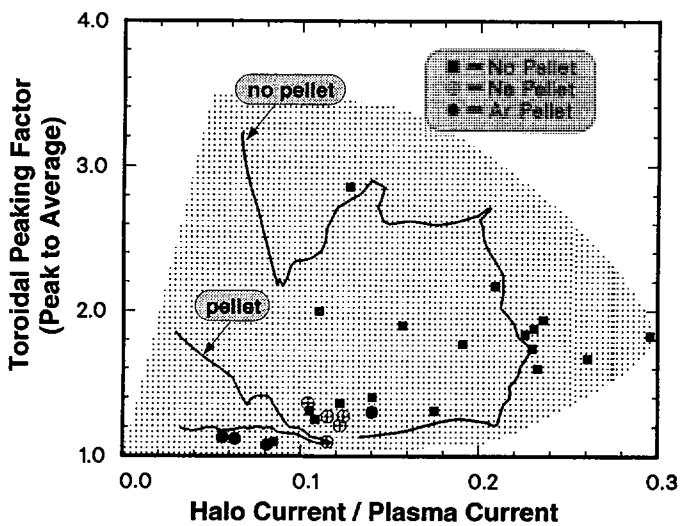

FIG. 2. Toroidal peaking factor and halo current normalized to the pre-disruption plasma current for VDEs. Points show the values at the time of peak halo current. The two solid lines show the trajectory of a pellet and non-pellet discharge with identical pre-disruption equilibria. The shaded region is the boundary of the trajectories of all discharges.

of 30% with a 2:1 toroidal peaking factor represents the highest combination obtained simultaneously at the time of the peak halo current. Typically, the maximum halo current occurs near the minimum peaking factor for a given discharge. Often however, at only slightly reduced halo current, the peaking factor is considerably higher. This is shown by the curve in Fig. 2 (labeled no pellet) which represents the trajectory of one discharge (I_{halo}/I_{po} vs. peaking factor). The shaded region represents the boundary of the trajectories for all discharges studied.

The toroidal structure of the halo current can be highly localized with a non-sinusoidal perturbation that is less than 100° in toroidal extent. However, asymmetries are also observed that more closely resemble an n=1 sinusoidal structure. Rotation of the asymmetry is always observed during the initial phase of the VDE when the discharge is drifting vertically prior to the thermal quench. Typical rotation frequencies are 200–400 Hz and the structure generally rotates opposite to the bulk plasma rotation. The asymmetry typically continues to rotate following the thermal quench, however, locking has been observed. When the asymmetry locks, there is no preferred toroidal location for the locking. The implication of the locking is that toroidally discrete components in the vessel effectively see higher poloidal currents than if the asymmetry rotated and the force was averaged over a large toroidal extent.

3. DISRUPTION MITIGATION AND AVOIDANCE

The combined effects of high halo currents, toroidal asymmetries in the halo currents, and the intense heat pulse during the disruption make mitigation of disruptions imperative. In DIII–D we have explored the use of both neon and argon pellet injection and have shown that both are effective at significantly reducing these effects. In our experiments, these pellets were injected both into VDEs and into centered, well controlled discharges in order to test pre-emptive termination of discharges. The pellet injector uses high pressure He gas as a propellant and two different size pellets (1.7 mm and 2.8 mm) were tested in these experiments. The 2.8 mm Ne pellets contained 3×10^{20} Ne atoms which represented approximately 35% of the electron content of the discharges. Depending on the vertical position of the plasma at the time of injection and the pellet size and speed, penetration varied from ρ/a of 0.55 to 0.25, where ρ/a is the normalized flux coordinate.

The basic phenomenology of pellet injection into a VDE is shown in Fig. 3. In this discharge, a 2.8 mm argon pellet is injected after the beginning of the vertical instability when the discharge is 15 cm below its nominal equilibrium position [Fig. 3(a)]. The duration of the ablation is 600 μs and the current decay begins within 200 μs of the end of the ablation. The stored energy loss begins promptly with the pellet injection and is complete within 100–200 μs of the end of the ablation [Fig. 3(b)]. During the 600 μs ablation, the internal inductance of the current profile increases from 0.75 to 1.0. The pellet causes the growth of large n = 1 and n = 2 modes [Fig. 3(d)] which may play a role in the loss of the remaining thermal energy and the subsequent profile flattening indicated by the drop in ℓ_i.

Both the Ne and Ar pellets were successful at significantly reducing the halo current magnitude and toroidal asymmetry during a VDE (Fig. 2). Typical reduction of the halo current was 30%–50% with the largest percentage reductions for the highest halo currents. The peaking factors were reduced to below 1.4 on all pellet discharges with typical values of 1.1–1.2. Moreover, the reductions in both magnitude and peaking factor are observed throughout the entire disruption, not just at the time of peak

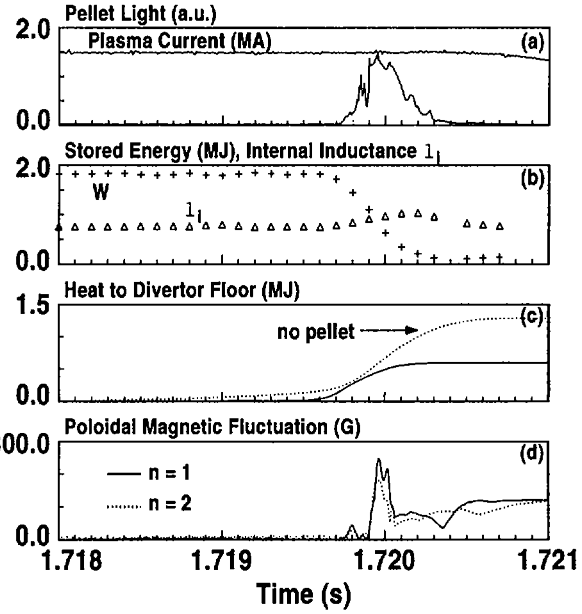

FIG. 3. Argon pellet injection into a VDE (β_n=3.2, q=3.4, shot 90 206) causes an immediate loss of stored energy and rapidly initiates the current quench. The heat conducted to the floor is reduced by 50% with the injection of a pellet. Large MHD activity develops within 250 μs of pellet injection.

halo currents, as shown by the trajectory curves for the pellet and the non-pellet discharges in Fig. 2. Mitigation was successful over the full range of q_{95} values tested, 2.7 to 4.0, and with both small and large pellets. For both Ne and Ar pellets, injecting pellets into a well centered discharge led to the lowest halo currents and lowest vessel displacement with 65% lower halo current than a comparable VDE. There are two primary reasons for the effective halo current reduction with pellet injection. The higher current decay rate due to the higher resistivity with the pellet injection and the early injection of the pellet combine to make the current decay while the plasma has a larger cross section. This keeps the q high and, as described earlier, results in a low poloidal halo current.

Analysis of IR camera data from the Ne and Ar killer pellet experiments has clearly shown at least a 50% reduction of the disruption heat pulse to the divertor floor. Using an Ar pellet injected into a VDE, the total energy conducted to the divertor region during the thermal quench was only 30% of the thermal energy compared to 62% for the comparable VDE [Fig. 3(c)]. Similarly, when the combined thermal and current quench phases are considered, only 16% of the total energy available (thermal and magnetic energy) was conducted to the divertor compared with 38% for the comparable VDE. Heat flux mitigation has also been observed with neon injection where less than 20% of the energy lost during the thermal quench was conducted to the divertor region.

Although the heat flux mitigation to the divertor is not complete, the discharge shown in Fig. 3 (β_n=3.2, q_{95}=3.4) demonstrates that the use of pellet injection is a viable method for high beta discharges near the stability limit. In this discharge, both the n=1 and n=2 modes grow to ~200 G within 250 μs after the start of pellet injection. Despite this, the energy loss due to radiation from the pellet is so large and rapid that the plasma stored energy has decreased by ~50% before the MHD grows. In lower β discharges, the impurity radiation decreases the stored energy by more than 75% of its initial value before any MHD activity grows. Although we have no measurements of the energy conducted to the divertor on these discharges, the prompt loss of the thermal energy before the rise of MHD activity indicates that the heat flux mitigation due to radiation is more complete at lower β when the plasma is farther from the stability boundary.

The rapid and effective loss of thermal energy with the pellet injection is confirmed by a 1-D model of the plasma including pellet ablation and impurity radiation (conduction is not included). The model predicts that at ρ/a =0.7, the peak radiated power occurs within 20 μs after the Ne pellet is ablated and within 150 μs, both the electron and ion temperatures at that radius are at 10 eV ($T_{initial}$ ~ 2 keV). The high electron density following the pellet injection accounts for the effective coupling of the ion and electron temperature (T_e). Measurements of T_e using a multi-pulse Thomson scattering system confirm model predictions of 5–10 eV for $0.5 < \rho/a < 0.9$ with slightly higher temperatures near the plasma edge because the neon is deposited predominantly inside ρ/a=0.9. Both the model and measurements of the Ne spectrum show that the plasma cools so rapidly that no charge states above Ne^{+8} are produced.

Despite the successful mitigation of halo current and heat flux, a critical problem created by the pellet injection is the formation of runaway electrons. Evidence of runaway electrons was observed as single or repeated bursts of hard X–rays and by nonthermal ECE emission following the pellet ablation and often throughout the current decay phase. Runaways were observed on every discharge with Ar pellets and many Ne pellets. No runaway electron signatures were observed on any of the non-pellet VDEs.

A critical part of the DIII–D program is identification of the disruption boundary so that either the disruption can be avoided or a mitigation technique can be implemented. To accomplish this, an artificial neural network, combining a large set of plasma diagnostic signals has been implemented on DIII–D to estimate the high β disruption boundary [6]. A sensitivity analysis was used to reduce the set to 33 signals of importance, including poloidal field and flux, diamagnetic flux, magnetic fluctuations, D_α, soft X–ray, visible bremsstrahlung, and neutron emission, and line averaged density. The system has been implemented in real-time on the DIII–D control system and is operated routinely. The network more accurately predicts the disruption boundary than the usual formulation (β_{max}~I/aB) and can correctly predict the disruption boundary more than 100 ms in advance of the disruption.

4. SUMMARY

The current decay rate, heat flux to the divertor, and halo current magnitude and structure have been measured during disruptions in DIII–D. Halo currents up to 30% of the pre-disruption plasma current with a toroidal peaking factor of 2:1 have been observed during VDEs and the magnitude depends on the current decay rate relative to the vertical instability growth rate. Neon and argon pellet injection into these VDEs has been effective at reducing the halo currents by 50%, almost eliminating the toroidal asymmetry, and reducing the heat flux conducted to the divertor by at least 50% in reactor relevant discharges (q=3.4, β=3.2). A serious consequence of this impurity pellet injection technique is the formation of runaway electrons. A real-time neural network technique has been developed that predicts the high β disruption boundary sufficiently in advance of the disruption to make mitigation or avoidance schemes feasible.

REFERENCES

[1] LEE, R.L., et al., "Thermal deposition analysis during disruption on DIII-D using infrared scanners", Fusion Engineering (Proc. 16th Symp. Champaign, 1995), Vol. 2 (1996) 902.

[2] HYATT, A.W., et al., "Magnetic and thermal energy flow during disruptions in DIII-D", Controlled Fusion and Plasma Physics (Proc. 23rd Eur. Conf. Kiev, 1996), European Physical Society, Geneva (1996).

[3] STRAIT, E.J., LAO, L.L., Nucl. Fusion **31** (1991) 527.

[4] EVANS, T.E., et al., "Measurements of non-axisymmetric halo currents with and without 'killer' pellets during disruption in the DIII-D tokamak", Plasma-Surface Interactions in Controlled Fusion Devices (Proc. 12th Int. Conf. St. Raphael, 1996), J. Nucl. Mater. (in press).

[5] GRANETZ, R.S., et al., Nucl. Fusion **36** (1996) 545.

[6] WROBLEWSKI, D., et al., Tokamak disruption alarm based on a neural network model of the high beta limit, Nucl. Fusion (in press).

DISCUSSION

R. YOSHINO: In which direction does a plasma move during plasma current quench in the double null operation in DIII-D? In JT-60U, plasma vertical displacement is very small when the vertical plasma position is placed at the 'neutral point'.

A.G. KELLMAN: There is no preferred direction of vertical motion in double null divertor disruptions.

R.J. TAYLOR: In the paper presented by P.R. Thomas (IAEA-CN-64/A3-2), irreversibility was mentioned as a very difficult issue. Do you see that in the future we could have sufficient control so as not to get into irreversible operating regimes? What is your outlook on requirements (flows or randomization)?

A.W. MORRIS: There has been good progress recently in developing 'proximity detectors' for disruptions on DIII-D, JET and COMPASS-D (see, for example, paper IAEA-CN-64/AP1-20 by A.G. Kellman et al.). These use multivariable databases and neural networks to improve on the traditionally separate density, q_{95} and β operational limits. There seems to be no reason why such techniques should not be extended to other 'irreversible' regimes. It is of course also necessary to learn how to adjust the plasma, in real time, to move further from the irreversible regime. The recent progress, on many tokamaks, in sophisticated plasma control, advanced diagnostics and analysis techniques gives grounds for optimism.

PRACTICAL BETA LIMIT IN ITER SHAPED DISCHARGES IN DIII-D AND ITS INCREASE BY HIGHER COLLISIONALITY

R.J. LA HAYE, J.D. CALLEN[1], M.S. CHU, S.DESHPANDE[2], T.A. GIANAKON[1], C.C. HEGNA[1], S. JARDIN[2], L.L. LAO, J. MANICKAM[2], D.A. MONTICELLO[2], A. PLETZER[3], A.H. REIMAN[2], O. SAUTER[3], E.J. STRAIT, T.S. TAYLOR, A.D. TURNBULL, H.R. WILSON[4]
General Atomics,
San Diego, California,
United States of America

Abstract

PRACTICAL BETA LIMIT IN ITER SHAPED DISCHARGES IN DIII-D AND ITS INCREASE BY HIGHER COLLISIONALITY.

The maximum beta that can be sustained for a long pulse in ITER shaped plasmas in DIII-D with $q_{95} \gtrsim 3$, ELMs and sawteeth is found to be limited by resistive tearing modes, particularly m/n = 3/2 and 2/1. At low collisionality comparable to that which will occur in ITER, the beta limit is a factor of two below the usually expected $n = \infty$ ballooning and $n = 1$ kink ideal limits.

Successful steady-state tokamak operation requires operating at the highest possible beta while avoiding both ideal and resistive MHD instabilities which reduce confinement and induce disruption. Experimental results from a large number of tokamaks indicate that the high beta operational envelope of the tokamak is well defined by ideal magnetohydrodynamic (MHD) theory [1] and is given by $\beta(\%) \lesssim 4\ell_i I/aB$ MA/m/T for a large range of conditions. The maximum beta values experimentally obtained, consistent with the ideal limit, are more than sufficient for the goals of long pulse burning experiments, such as ITER. The highest beta values achieved have historically been obtained in fairly short pulse discharges, often <1–2 sawteeth periods and <1–2 energy replacement times. In these discharges, the current profile is not fully relaxed. It is well recognized that the ideal limit depends on the details of the current density profile and pressure profile and it is expected that the bootstrap current from the pressure gradient at high beta can lead to lower MHD stability limits. Furthermore, in some previous experiments, the instabilities limiting the achievable beta are very clearly pressure driven resistive modes and significantly below the threshold predicted for ideal instabilities [2]. It is of interest to determine the maximum beta in discharges of sufficient length to have fully penetrated profiles and for opportunities for resistive modes to play a role.

[1] University of Wisconsin, Madison, Wisconsin, USA
[2] Princeton Plasma Physics Laboratory, Princeton, New Jersey, USA.
[3] CRPP-EPFL, Lausanne, Switzerland.
[4] UKAEA Fusion, Culham, Abingdon, Oxfordshire, United Kingdom.

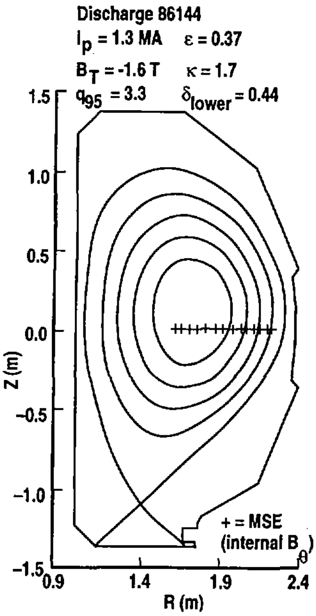

Fig. 1. Equilibrium cross section in DIII–D similar to that proposed for ITER. The 16 radial positions of the MSE diagnostic of poloidal field profile are also shown.

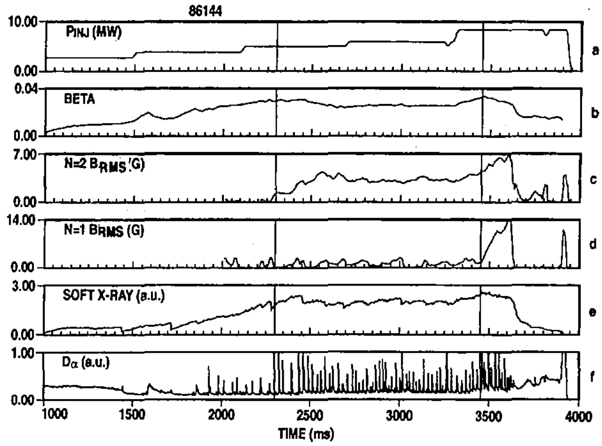

Fig. 2. Discharge #86144. (a) Injected beam power, (b) β from MHD reconstruction code EFIT, (c) rms amplitude of n = 2 rotating tearing mode (m = 3, n = 2), (d) rms amplitude of n = 1 rotating tearing mode (m = 2, n = 1), (e) central soft x-ray chord showing periodic sawteeth, and (f) D_α photodiode signal at divertor showing frequent edge localized modes. Note onset of 3/2 mode at 2250 rms and 2/1 mode at 3450 ms.

The maximum operational beta in single-null divertor (SND), long-pulse discharges in DIII–D with a cross-sectional shape similar to the proposed ITER tokamak (Fig. 1) is found to be limited significantly below the threshold for ideal instabilities by the onset of resistive MHD instabilities. [A hard disruptive beta limit is usually considered to be due to ideal MHD instabilities, either the n=1 kink or the n=∞ ballooning mode where n is the toroidal mode number.] The temporal evolution of a typical discharge is shown in Fig. 2; the beam power is increased gradually. There is a "soft" beta limit due to the onset of an m/n = 3/2 rotating tearing mode which saturates at an amplitude that decreases energy confinement by $\Delta\tau_E/\tau_E \approx -20\%$ [Fig. 2(b,c)] and a "hard" beta limit at slightly higher beta due to the onset of an m/n = 2/1 rotating tearing mode which grows to an amplitude that destroys the confinement and induces a disruption [Fig. 2(b,d)]. (Plasmas are neutral beam heated ELMing H–mode with sawteeth; the safety factor q_{95} is just above 3.)

Higher stable beta in these long-pulse discharges is successfully run by operating at either higher density $\bar{n}$ and/or lower field and thus higher collisionality which suppresses both the 3/2 and 2/1 mode onsets. By long pulse, we mean that beta is evolving on a time scale long compared to the ELM and sawteeth periods and the energy replacement time τ_E. At fixed field, density $\bar{n}$ is the control parameter varied by gas puffing with the normalized beta $\beta_N \equiv \beta$ (%)/[I_p/aB_T (MA/mT)] and the normalized density $G \equiv \bar{n}$ (10^{14} cm^{-3}) $\pi a^2/I_p$. The onset of the 2/1 mode approaches the expected ideal limit of $\beta_N \approx 4\, l_i \approx 3.8$ at $G \approx 1$ at high field (Fig. 3) where l_i is the internal inductance. As shown in Fig. 3, there is a 2/1 tearing mode beta limit which increases with density and thus collisionality below which the plasma is stable. Successful quasi-steady-state operation without limiting modes at $\beta_N \approx 3$ was achieved with $G \approx 0.65$ as shown in Fig. 4 in comparison to a lower density discharge with reduced confinement due to an $n = 2$ tearing mode which further degrades at higher power due to an $n = 1$ tearing mode which leads to disruption. The ideal stability for the stable $\beta_N = 3$ discharge was analyzed by the code GATO. With $\beta_N = 3.2$ and $4\ell_i = 3.6$, $n = \infty$ ballooning is stable on all surfaces, the $n = 1$ external kink is stable and the $n = 1$ internal kink is stable only if $q(0) > 1$.

Two possible means have been evaluated as the cause of the onset of these instabilities. Resistive tearing modes that occur at rational surfaces q = m/n cause reconnection into islands of full width w. The island onset and growth can be due to either free energy from an unstable current J_ϕ profile ($\Delta' > 0$) or to a helical bootstrap current which amplifies a seed island ($\Delta' < 0$). These mechanisms are tested using accurate MHD equilibria reconstructions with the code EFIT [3] using the external magnetics, local measurements of the internal poloidal field with the 16 channel motional Stark effect diagnostic and the measured pressure profile.

Resistive MHD analysis of Δ' and stability is linearly computed from EFIT by analytical formulas [4,5] and by the PEST-III [6] and MARS [7] codes. Resistive non-linear MHD analysis is computed on these equilibria with the PIES code [8]. Any changes to Δ' with beta and/or density may be due to current density profile modification by central beam-driven current and edge bootstrap and inductive currents.

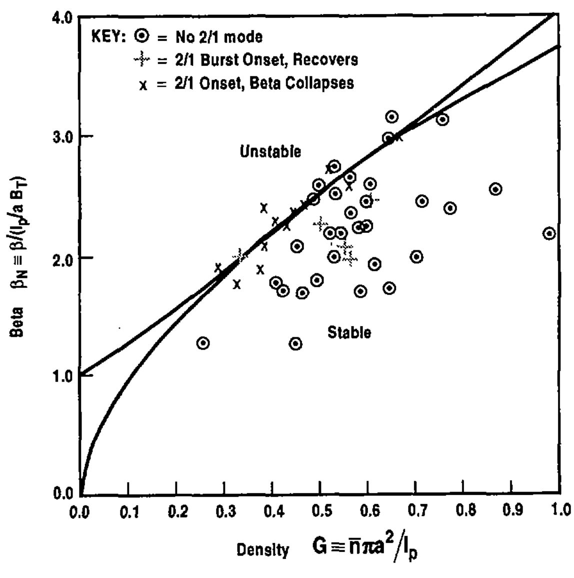

Fig. 3. $\beta_N \equiv \beta/(I/aB_T)$ versus $G \equiv \bar{n}\pi a^2/I_p$. X are onset of 2/1 mode, + are onset of a transient 2/1 mode from which the plasma recovers and O are discharges with no 2/1 mode. The curves are the 2/1 stability boundary determined by either a power law fit or to an offset linear fit. (The range of SND discharges is narrowed to $q_0 \approx 1$, $q_{95} < 4$ with $I_P \approx 1.3$–1.6 MA and $B_T = -1.3$ to -1.9 T.)

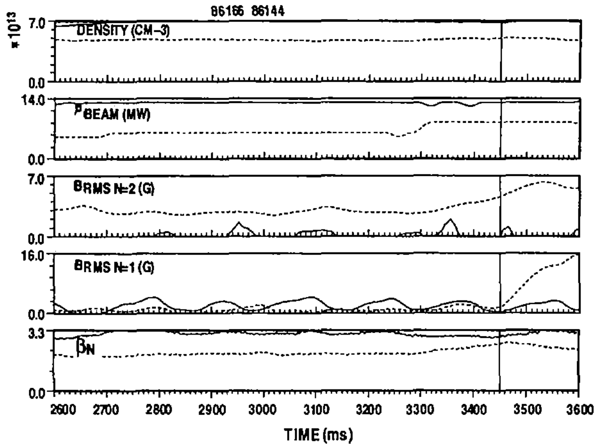

Fig. 4. Successful quasi-steady state operation without limiting modes at $\beta_N \approx 3$ is achieved (#86166, solid lines) by raising density/collisionality (as compared to #86144, dashed lines).

To explain the onset of both the 3/2 and 2/1 rotating resistive modes at higher beta and/or lower density (collisionality) would require steepening of the local grad J_ϕ at both q = 3/2 and 2/1 in a plasma where the current profile is tightly constrained; sawteeth keep the axial $q \approx 1$ and the edge q_{95} is held fixed. Changes in grad J_ϕ are not clearly supported by the data. As an example, the reconstructions of matched discharges with similar beta ($\beta_N \approx 2.1$) but with different density and thus collisionality are shown in Fig. 5. The current density and q profiles are very similar. However, while both have a small saturated 3/2 mode, the lower density/collisionality discharge (#77968) is at the onset of the growth of a 2/1 mode which eventually collapses beta and produces a disruption. Conventional analysis does not clearly explain the difference in stability. The comparison of the m/n=2/1 unstable and stable discharge parameters of Fig. 5 and the linear and non-linear codes is given in Table I: note that $8\,\bar{n}_{14}^3 R/\beta^2(\%)B^4$ is an effective collisionality parameter. The high m and cylindrical linear approximations agree with each other as to the relative stability but neither agrees with the experimental stability. The PEST-III and MARS linear codes which do not use approximations also agree with each other but not with the experimental stability and the non-linear PIES code disagrees with the linear codes. There is a strong ∇P stabilization in the linear theory (sometimes called the "Glasser effect") that goes away when the pressure gradient is non-linearly flattened near the rational surface by the formation of a small but finite island.

A variety of cases are under calculation by all of the codes which include β_N = 1.7–3.2, G = 0.3–1.0 and with 3/2 onset, 3/2 saturated, 2/1 onset, 2/1 saturated and no 3/2 or 2/1 modes. Of the six different cases analyzed so far, the non-linear PIES code gets 3/2 islands in the five experimental cases which are unstable and no 3/2 islands in the stable case. PIES finds 2/1 islands in agreement with three of six experimental cases, in disagreement with two stable experimental cases, and no 2/1 island in agreement in one case which is experimentally stable. Sensitivity of both the linear and nonlinear code results to details of the current and q profiles makes comparison with experiment problematic.

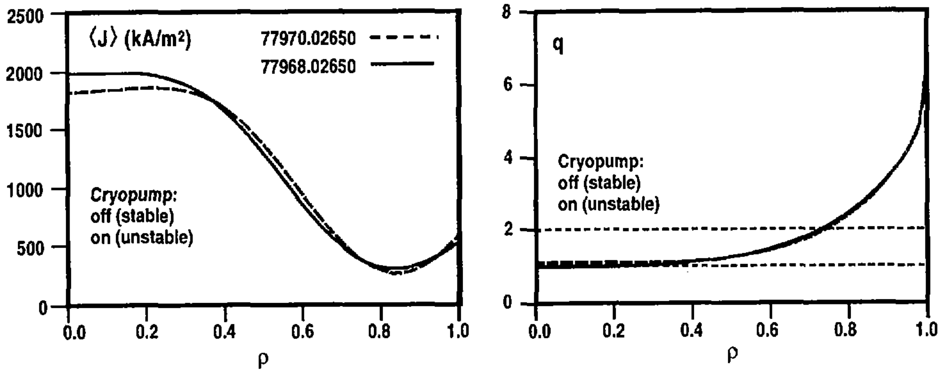

Fig. 5. Kinetic EFIT MHD reconstructions with internal poloidal field profile from MSE of a stable higher density discharge (77970.02650, dashed line) and an unstable cryopumped lower density discharge (77968.02650, solid lines). Measured internal pressure and B_θ profiles are used in the fits. At t = 2650 ms in the lower density higher temperature discharge, a 2/1 tearing mode begins to grow.

Table I. Comparison of m/n=2/1 Stability, Experiment, and Codes

	77968.02650	77970.02650
$\beta_N = \beta(\%) / (I_p/aB)$	2.0	2.3
$G = \bar{n}^{14}\pi a^2/I_p$	0.39	0.48
$\nu_{eff} = 8\,\bar{n}_{14}^3 R/\beta^2(\%)B^4$	0.018	0.027
2/1 ? (in experiment)	Onset, unstable	Stable
High m	Stable, $\Delta' r_s/2m = -0.5$	Stable, $\Delta' r_s/2m =$ 0.0
Cylindrical	Unstable, $\Delta' r_s/2m = 1.1$	Unstable, $\Delta' r_s/2m = 2.0$
PEST-III	Stable	Stable
MARS	Stable	Stable
PIES	Unstable	Unstable

An explanation of the experimental results can be made using the neoclassical bootstrap current destabilization of a seed island for $\Delta' < 0$, i.e. otherwise stable. This effect is increasingly more destabilizing with beta as the modified Rutherford equation for island growth is given by

$$\left(\frac{\mu_0}{1.22\eta_{nc}}\right)\frac{dw}{dt}=\Delta'+\varepsilon^{1/2}\beta_\theta\left(\frac{L_q}{L_p}\right)\left[\frac{w}{\left(w^2+w_c^2\right)}\right]-\rho_{\theta i}^2\beta_\theta g(\varepsilon,\nu_i)\frac{\left(L_q/L_p\right)^2}{w^3}$$

where the second term on the RHS is usually ($L_q/L_p > 0$) destabilizing. Other MHD events such as sawteeth or ELMs often trigger the onset of the resistive modes, supporting the idea that they are neoclassically destabilized by a seed perturbation. The neoclassical destabilization of tearing modes requires the conditions to be right, i.e., high beta and low collisionality, and a seed island. The collisionality can enter (for $\Delta' < 0$) in either of two ways. In the "$\chi_\perp/\chi_\parallel$" model [9], the pressure is not equilibrated on the perturbed flux surface when perpendicular transport $\chi_\perp$ across a seed island dominates over that along the island $\chi_\parallel$, so that the critical island width w_c is an increasing function of collisionality. In the "$\omega*$" model [10], the toroidally enhanced ion polarization drift response of the plasma to the seed island due to inertial effects adds a stabilizing term to the modified Rutherford equation (the third term on the RHS) which dominates at small w. It has a collisional factor $g(\varepsilon, \nu_i) = \varepsilon^{3/2}$ for $\nu_i/\varepsilon\omega_{*e} \ll 1$ and $g(\varepsilon, \nu_i) = 1$ for $\nu_i/\varepsilon\omega_{*e} \gg 1$ that can increase the critical island size a factor of 2–3 since our density scan causes $\nu_i/\varepsilon\omega_{*e}$ to range from 0.05 to 4. (ν_i/ε is the effective ion collision frequency and ω_{*e} is the electron drift frequency.)

The ITER-like discharges in DIII–D have both sawteeth and ELM perturbations with the sawteeth period 10 to 20 times that of the ELMs. Examination of the databases of the onset of m/n=3/2 and 2/1 modes shows: (1) in 14 of 17 cases of the onset of the 3/2 mode, the mode clearly starts on a sawtooth crash with 1 case on what may be an impurity burst, (2) in only 4 of 18 cases of the onset of the 2/1 mode does the mode start on a sawtooth crash and this may be coincident with an ELM or an ELM triggered by a sawtooth (as the ELMs are frequent, the causality with ELMs is not definitive). Further evidence of neoclassical destabilization as seen in Fig. 2, (b) and (c), for the 3/2 mode is: (1) the initial growth is $|\tilde{B}_\theta| \sim \Delta t$ not Δt^2 ($dw/dt \sim w^{-1}$ not $dw/dt \sim \Delta'$), and (2) the saturated mode amplitude $|\tilde{B}_\theta| \sim \beta^2$ ($w \sim \beta$ not $w \sim \Delta'$).

If $\Delta' < 0$, the neoclassical stability depends on the size of the seed perturbation w relative to critical islands $w_c = (L_s/k_\theta)^{1/2} (\chi_\perp/\chi_\parallel)^{1/4}$ and/or $w_g = [g(\varepsilon, \nu_i)(L_q/L_p)/\varepsilon^{1/2}]^{1/2} \rho_{\theta i}$. This is shown in Fig. 6 for the mode growth rate as a function of w for increasing β_θ. As beta is increased there is a critical beta and w for $dw/dt \geq 0$. If this beta is exceeded, a small island can grow to a large size [11]. The critical point is for $w_c^2 \gg w_g^2$, $\beta_\theta = -2\,\Delta' w_c/[\varepsilon^{1/2}(L_q/L_p)]$ and for $w_g^2 \gg w_c^2$, $\beta_\theta = -3\,\Delta' w_g/2/[\varepsilon^{1/2}(L_q/L_p)]$. For typical DIII–D parameters, $w_c \approx 0.5$ cm and $w_g \approx 2$ cm compared to a $\approx$

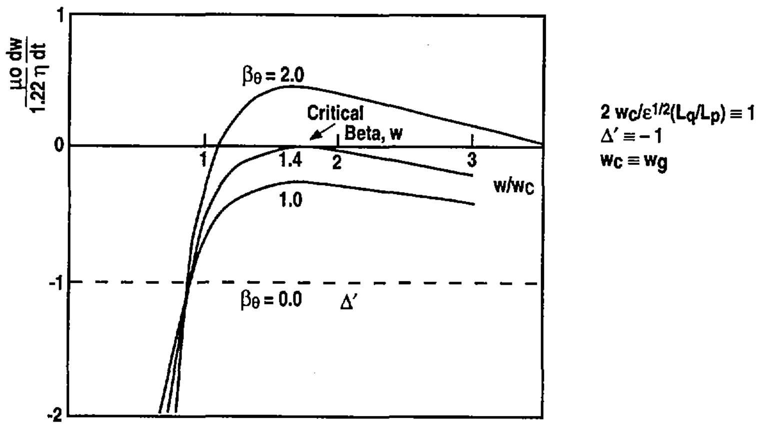

Fig. 6. Neoclassical model for island growth rate versus island size w for $\Delta' < 0$ and increasing values of beta. The critical beta, w for $\dot{w} \geq 0$ is indicated.

62 cm. As both w_c and w_g depend on beta, a self-consistent scaling is needed. For the $\chi_\perp/\chi_\parallel$ model taking $\chi_\parallel = \chi_{BOHM} (\rho_*\nu_*)^{-1}$ and $\chi_\perp = \chi_{BOHM} * \beta$, one gets critical $\beta \sim (-\Delta' a)^{4/3} (L_p/L_q)^{4/3} \nu_*^{1/3} \rho_*^{1/3}$ with $\nu_* \equiv [(m_e/m_i)^{1/2} \nu_{ei}/\varepsilon]/\omega_{bi}$ and $\rho_* \equiv \rho_i/a$ dimensionless parameters. For the ω_* model, $\beta_{crit} \sim -\Delta' a\ (L_p/L_q)\ g(\varepsilon, \nu_i)^{1/2}\ \rho_*$ yielding a different dependence upon collisionality and gyroradius. Of course, if Δ' or profiles vary with beta and/or collisionality, the scaling would be yet different.

As the neoclassical destabilization with beta depends on collisionality in different ways, empirical fits of critical beta for onset of 3/2 or 2/1 tearing were made to ν_*, ρ_*, etc. for as wide a range of variables as possible. The database of discharges at the onset of 3/2 tearing or 2/1 tearing scans B_T = 0.9–2.1 T at I_p = 0.65–1.5 MA with $q_{95} < 4$, $\bar{n}_{14}$ = 0.26–0.82, with critical β = 1.73–5.16%. The radial scale lengths at q=m/n for q, T_e, and T_i at the 3/2 and 2/1 mode onsets, respectively, do not vary significantly. [The H–mode core density profile is fairly flat in all cases.] For the 3/2 mode onset, the mean $L_q/a = 0.55 \pm 0.05$, $L_{Te}/a = -0.39 \pm 0.06$, and $L_{Ti}/a = -0.33 \pm 0.03$. The mean Δ' using the high m approximation is -9.4 ± 1.5 m^{-1}. For the 2/1 mode onset, the mean $L_q/a = 0.40 \pm 0.03$, $L_{Te}/a = -0.41 \pm 0.08$, and $L_{Ti}/a = -0.38 \pm 0.10$. The mean Δ' using the high m approximation is -8.0 ± 1.8 m^{-1}. Thus the principal experimental variables for the tearing mode destabilization are beta, collisionality and to a much lesser extent gyroradius. A fit to $\beta_{crit} \sim \nu_*^x \rho_*^y$ was done in two ways. For global parameters, one expects for $T_e = T_i \sim \beta B^2/\bar{n}$, $\nu_* \sim \bar{n}^3 R/B^4 \beta^2$, $\rho_* \sim \beta^{1/2}/n^{1/2} a$ and $a \sim R$ at fixed q_{95} so that

$$\beta \sim \nu_*^x \rho_*^y \sim \bar{n}^{\frac{3x-y/2}{1+2x-y/2}} R^{\frac{x-y}{1+2x-y/2}} \Big/ B^{\frac{4x-y/2}{1+2x-y/2}}$$

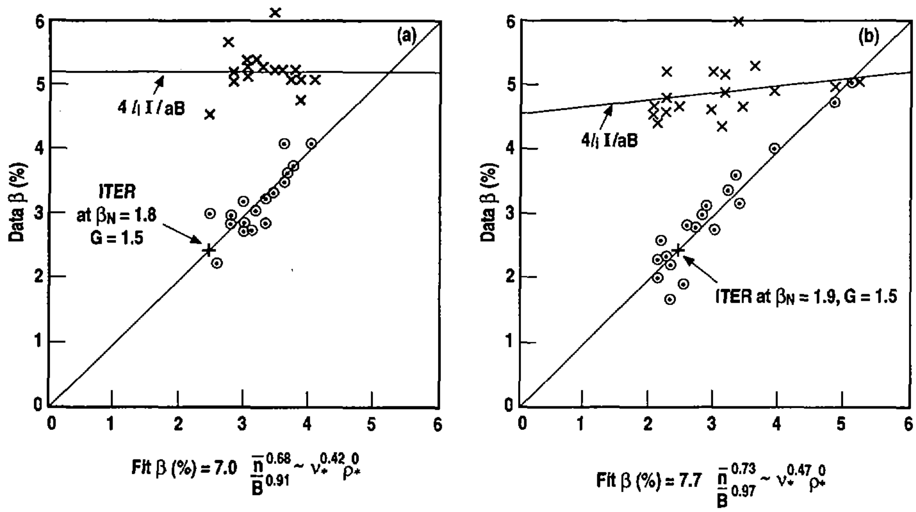

Fig. 7. (a) Onset of 3/2 tearing (⊙) in DIII–D fitted to global parameter combinations. (b) Onset of 2/1 tearing (⊙) in DIII–D fitted to global parameter combinations. Expected ITER beta limit is also shown (+) as well as expected ideal limit (×).

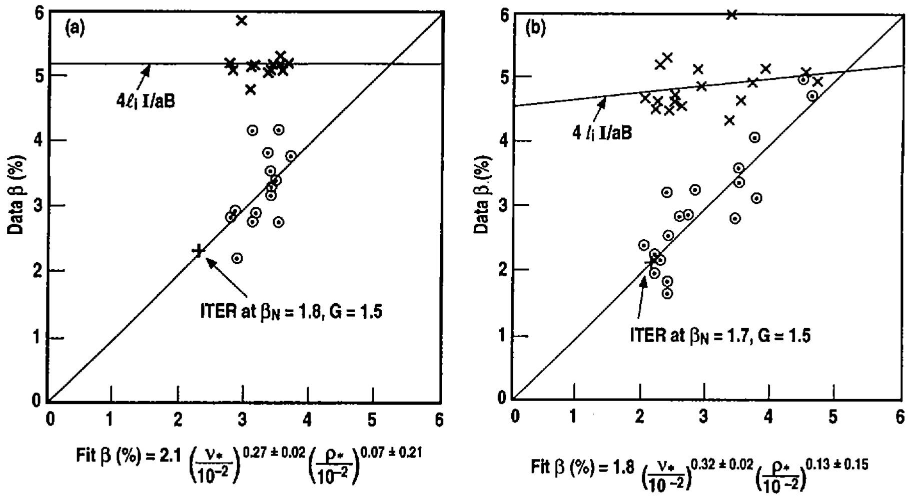

Fig. 8. (a) Onset of 3/2 tearing (⊙) in DIII–D fitted to <u>*local*</u> *parameters. (b) Onset of 2/1 tearing (⊙) in DIII–D fitted to* <u>*local*</u> *parameters. Expected ITER beta limit is also shown (+) as well as expected ideal limit (×).*

This global scaling allows a survey of the gross parameters under direct control of the physics operator. For the onset of the 3/2 mode, the best fit gives x = 0.42 with no significance to y. The result (⊙) is shown in Fig. 7(a) with the expected ideal limit (×) of 4 l_i (I/aB) for comparison and the expected ITER limit ($\bar{n}_{14}$ = 1.3, R = 8.0 m, a = 2.8 m, B = 5.7 T, I = 21 MA) if G = 1.5 can be achieved. The soft 3/2 tearing limit is as much as a factor of 2 below the ideal limit. For the onset of the 2/1 mode, the best fit gives $x = 0.47$ with again no significance to y. The results are shown in Fig 7(b). At high density, low field, the 2/1 tearing occurs at a beta near the expected ideal limit. The dependence on the <u>local</u> parameters of the soft 3/2 tearing mode beta limit was also fitted and is shown in Fig. 8(a). For the 3/2 mode, the range in ν_* is only 3.1 and in ρ_* only 1.4 as at low B, the 2/1 mode turns on first and the discharges disrupt. The dependence on the <u>local</u> parameters of the hard 2/1 tearing mode beta limit was also fitted and is shown in Fig. 8(b). ν_* varies a factor of 16 while ρ_* varies a factor of 1.6. The ρ_* dependence may be anything from 0 ~ 1/3 within the uncertainty. A fit using $\nu_i/\varepsilon\omega_{*e}$ (which is more relevant for the ω^* model) instead of ν_* was almost as good.

As the higher field, larger ITER device is expected to have both lower ν^* and ρ^*, extrapolation to ITER requires knowing what Δ' really is or will be, understanding of which of the neoclassical threshold mechanisms dominates, how β_{crit} scales with ν^* (and ρ^*), and how the necessary seed perturbation island (particularly from sawteeth and ELMs) for the neoclassical destabilization scales. An interesting possibility is whether a higher stable beta can be obtained by operating at q > 1 to eliminate sawteeth perturbations or with negative magnetic shear which is neoclassically stabilizing for modes inside the negative shear reversal region ($L_q/L_p < 0$).

ACKNOWLEDGMENTS

Work supported by the U.S. Department of Energy under Contract Nos. DE-AC03-89ER51114, W-7405-ENG-48, DE-AC05-84OR21400, DE-AC05-96OR22464, DE-AC04-76DP00789, Grant Nos. DE-FG03-89ER51121, DE-FG03-86ER53225, and in part by the Swiss National Science Foundation and the U.K. Department of Trade and Industry and EURATOM. Cylindrical delta prime calculations by Frank Waelbroeck of the IFS are appreciated.

REFERENCES

[1] STRAIT, E.J., et al., Phys. Plasmas **1** (1994) 1415.
[2] STRAIT, E.J., et al., Phys. Rev. Lett. **62** (1989) 1282.
[3] LAO, L.L., et al., Nucl. Fusion **25** (1985) 1611.
[4] HEGNA, C.C., CALLEN, J.D., Phys. Plasmas **1** (1994) 2308.
[5] FURTH, H.P., et al., Phys. Fluids **16** (1973) 1054.
[6] PLETZER, A., et al., J. Comput. Phys. **115** (1994) 530.
[7] BONDESON, A., et al., Phys. Fluids B **4** (1992) 1889.
[8] REIMAN, A.H., GREENSIDE, H.S., J. Comput. Phys. **87** (1990) 349.
[9] FITZPATRICK, R., Phys. Plasmas **2** (1995) 825.
[10] WILSON, H.R., et al., Phys. Plasmas **3** (1995) 248.
[11] CHANG, Z., et al., Phys. Rev. Lett. **74** (1995) 4663.

DISRUPTIONS, HALO CURRENTS AND KILLER PELLETS IN ALCATOR C-MOD*

R.S. GRANETZ, I.H. HUTCHINSON, J. SORCI, D.T. GARNIER,
J.H. IRBY, B. LaBOMBARD, E.S. MARMAR, ALCATOR GROUP
Plasma Fusion Center,
Massachusetts Institute of Technology,
Cambridge, Massachusetts,
United States of America

Abstract

DISRUPTIONS, HALO CURRENTS AND KILLER PELLETS IN ALCATOR C-MOD.

During the current quench phase of disruptions in Alcator C-Mod, large poloidal 'halo' currents flow in the conducting vacuum vessel and internal structures. In order to better understand these halo currents and the stresses arising from the resulting $J \times B$ forces, Alcator C-Mod has been fitted with a comprehensive set of sensors to measure their magnitude, temporal evolution and spatial distribution. It is found that these halo currents are toroidally asymmetric, with peaking factors (i.e. peak/average) typically of about 2, although extreme cases can go well above 3. The asymmetric pattern usually rotates toroidally at a few kilohertz, thus ruling out first-wall non-uniformities as the cause of the asymmetry. Analysis of information compiled in the C-Mod disruption database indicates that the maximum halo current during a disruption scales roughly as either I_p^2/B_ϕ or I_p/q_{95}, but that there is a large amount of variation which is not yet understood. Attempts have also been made to reduce the magnitude of halo currents flowing in the divertor region of the vacuum vessel by injecting high-Z doped pellets to greatly speed up the current quench.

1. INTRODUCTION

Disruptions are of great concern for tokamaks, primarily because of the potential for damaging the divertor, first wall, and/or other plasma facing components. Disruption damage can be caused by localised thermal deposition on the first wall, as well as structural failure due to $J \times B$ forces arising from induced currents. Alcator C-Mod, by virtue of its high magnetic field, high plasma current, compact size, and shaped plasmas is particularly well-suited for studying fast disruption current quenches (instantaneous dI_p/dt up to 1.4 MA/ms). Due to its highly conducting first wall, very large eddy currents, with a significant poloidal component due to halo currents[1–4], can be induced in the structure. Disruption research on Alcator C-Mod has concentrated on measuring the temporal behavior and spatial distribution of these halo currents, characterising the scaling of their magnitude with plasma current, dI_p/dt, κ, etc., and identifying ways of reducing their magnitude, including injection of killer pellets.

* Supported by US Department of Energy contract DE-AC02-78ET51013.

Most of the results presented in this paper have been obtained using an extensive set of Rogowski current sensors specifically designed for measuring halo currents. Two Rogowski coils completely encircle the inboard cylindrical wall of the vacuum vessel at the top and at the bottom, and measure the *total* halo current flowing in the vessel wall. The lower coil is situated close to the inboard half of the divertor structure. An additional coilset is also located at the position of the lower full Rogowski, but its length is segmented into 10 'partial' sensors. (Alcator C-Mod has a ten-fold toroidal symmetry, i.e. 10 sets of ports, 10 divertor modules, etc.) This array provides information on the toroidal structure of halo currents in the vicinity of the inboard divertor. The outboard half of the C-Mod divertor is functionally toroidally continuous, but is actually comprised of 10 discrete modules. Each module is mechanically and electrically attached to gussets welded to the vacuum vessel. An array of 10 'gusset' Rogowski sensors measure the currents through the contact points, providing information on the toroidal structure of halo currents in the vicinity of the outboard divertors. Additional sensors for determining the vertical distribution of halo current in the inboard wall, as well as instrumentation to directly measure mechanical strains, have also been installed.

2. HALO CURRENT CHARACTERISTICS

In Alcator C-Mod virtually all disruptions are either caused by, or result in fast vertical displacement of the plasma (~80% move towards the x-point), eventually terminating in contact with internal hardware at the top or bottom of the vacuum vessel. For downward-going disruptions, large halo currents flow in the bottom of the machine, while very little is seen at the top, as shown in

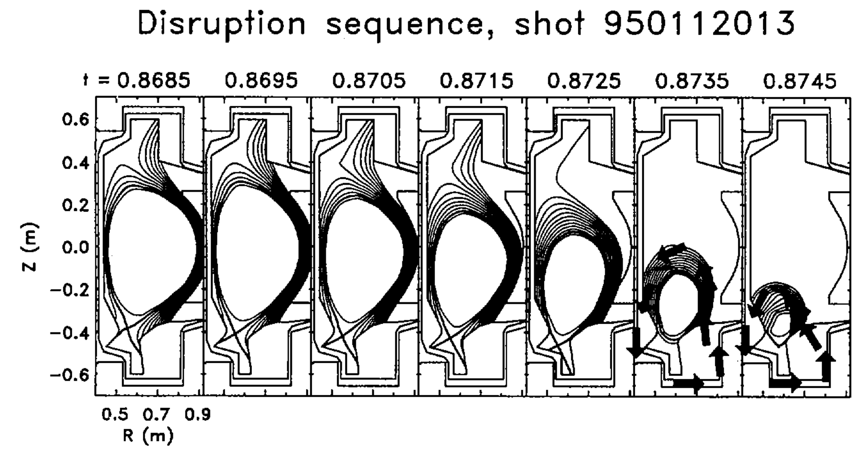

FIG. 1. Magnetic flux reconstructions at 1 ms intervals of a typical disruption. The arrows show the poloidal projection of halo current flow. The current path in the plasma SOL must actually be helical, in order to be force-free.

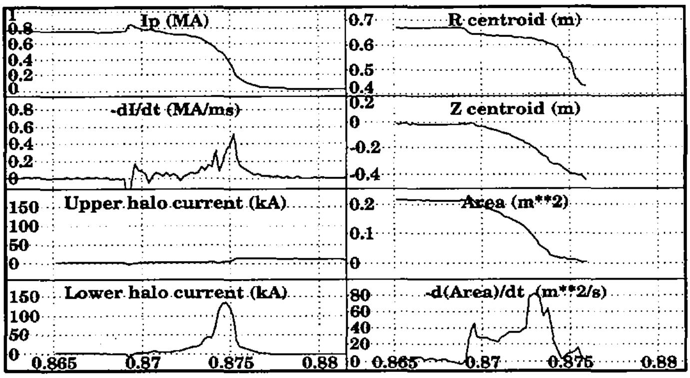

FIG. 2. Evolution of plasma current, upper and lower halo currents, etc., for the disruption shown in Fig. 1. Note that for a downward disruption, appreciable halo current only flows in the lower portion of the vacuum vessel.

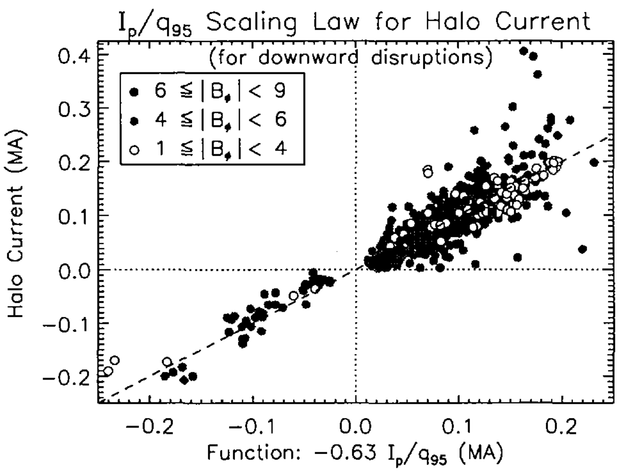

FIG. 3. Peak halo current at the bottom of the vessel for downward-going disruptions. Scalings of the form I_p^2/B_ϕ or I_p/q_{95} fit the data equally well. (The values of I_p and q_{95} are taken just prior to the disruption.)

Figs. 1 and 2. For upward-going disruptions this behavior is reversed. The *direction* of the poloidal current flowing in the inboard wall of the vacuum vessel is independent of the direction of plasma vertical motion. For the normal configuration (B_ϕ and I_p in the clockwise direction when viewing down on the torus from above), the halo currents in the inboard wall flow downward. When the toroidal field and plasma current are reversed, the poloidal halo current reverses direction as well. Thus, in all cases the total poloidal halo current in the plasma SOL flows in the direction which generates a $J_{\rm pol} \times B_\phi$ force tending to oppose the vertical motion of the plasma. Measurements of the halo current magnitude over a wide range of operating parameters ($0.2 \leq |I_p| \leq 1.2$ MA, $1.5 \leq |B_\phi| \leq 8.0$ T) indicate that the peak current scales as either I_p^2/B_ϕ or I_p/q_{95}, as seen in Fig. 3, with a large degree of scatter, not all of which is understood. No independent variation with elongation is observed.

3. TOROIDAL STRUCTURE OF HALO CURRENTS

Spatially resolved measurements of halo currents reveal significant toroidal asymmetry, which is usually well characterised as an $n = 1$ component superimposed on an $n = 0$ background (although a few examples having $n = 2$ structure have also been seen). The amplitudes of the two harmonics are comparable, resulting in toroidal peaking factors (i.e. peak/average) of order 1.5–2. Furthermore, this asymmetric pattern usually rotates toroidally at a few kHz, as shown in Fig. 4, thus ruling out first-wall non-uniformities as the cause of the asymmetry. When I_p and B_ϕ are reversed, the halo rotation also reverses. The $J \times B$ force due to halo current is locally exacerbated by the toroidal peaking.

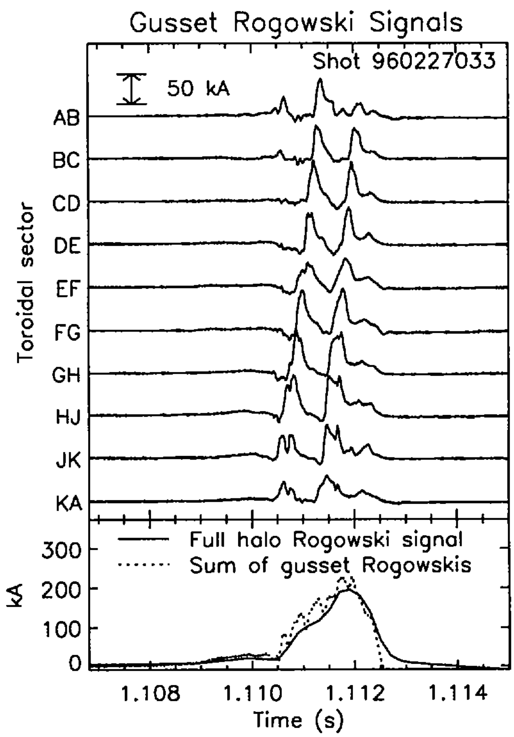

FIG. 4. Halo currents flowing through the outboard divertor modules, as measured by the toroidal array of 'gusset' Rogowski coils, during a disruption. A rotating $n = 1$ structure is clearly seen.

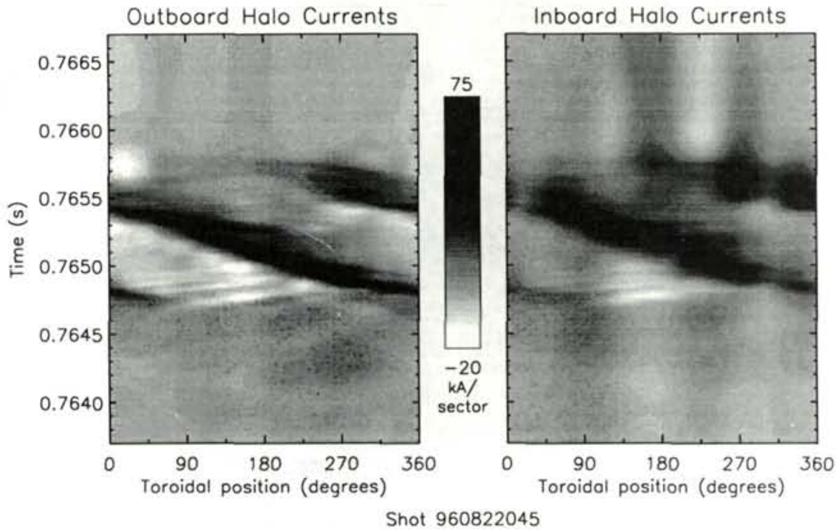

FIG. 5. Comparison of the toroidal structure and rotation of halo currents flowing through the outboard divertor (measured with the 'gusset' Rogowskis) and the inboard divertor (measured with the 'partial' Rogowski segments). The two sets of measurements, from two different poloidal locations, show nearly identical toroidal structure and phase.

However, for the few disruptions with unusually high halo current fractions, the peaking factors have all been relatively low.

Comparison of the halo currents flowing through the outboard divertor (measured with the array of 'gusset' Rogowskis) and through the inboard divertor (measured with the array of 'partial' Rogowski segments) reveals nearly identical toroidal structure *and* toroidal phase, as shown in Fig. 5. This implies that the halo current path through the bottom portion of the vessel wall is purely poloidal. Since the halo current must form a closed circuit between first wall contact points by flowing around the plasma periphery, and since this flow must be helical in order to satisfy force-free constraints, a resonance condition on the field-line helicity may be involved in the development of halo currents and perhaps in the current quench as well. Axisymmetric reconstructions of the plasma equilibrium suggest that this is true, however, full 3-D MHD reconstructions may be necessary to properly describe the plasma configuration when significant halo currents have developed.

4. KILLER PELLET RESULTS

Experiments aimed at reducing the deleterious effects of disruptions on the divertor have been carried out using "killer" pellets, as proposed by ITER[5]. The goal is to eliminate both the stored thermal and magnetic energy by enhanced radiation before the plasma has time to move a significant distance

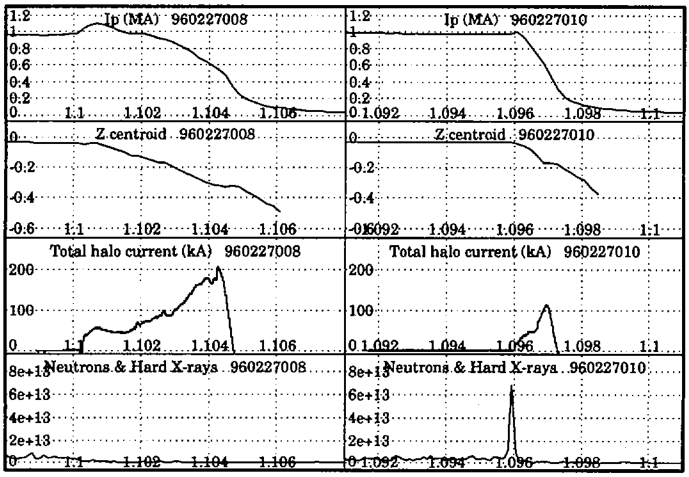

FIG. 6. Comparison between typical current quench (on left) and killer pellet accelerated quench (on right). Owing to the shorter quench time, the vertical displacement is reduced, resulting in less halo current in the lower part of the vessel.

downwards. In Alcator C-Mod, this requires the dissipation of about 1 MJ in 500 μs. In principle this can be accomplished with a few milligrams of any high-Z metal. An additional requirement is that the electron temperature must be reduced to $\leq$ 10 eV in order to increase the plasma resistance enough to give a sufficiently fast L/R time for the current quench. The best results to date have been obtained by injecting plastic pellets impregnated with 2.5 mg of silver powder. The disruption quench time has been reduced from $\sim$5 ms to 1 ms, resulting in a two-fold reduction of halo current in the divertor region, as shown in Fig. 6. These accelerated quench disruptions also exhibit a short burst of hard x-rays at the time of pellet ablation, indicating probable generation of runaway electrons.

REFERENCES

[1] JENSEN, T.H., CHU, M.S., Phys. Fluids B **1** (1989) 1545.

[2] PICK, M.A., NOLL, P., BARABASCHI, P., MARCUS, F.B., ROSSI, L., in Proc. 14th Symp. on Fusion Engineering, San Diego, 1991, p. 87.

[3] GRUBER, O., LACKNER, K., PAUTASSO, G., SEIDEL, U., STREIBL, B., Plasma Phys. Control. Fusion **35** (1993) B191.

[4] GRANETZ, R.S., et al., Nucl. Fusion **36** (1996) 545.

[5] JANESCHITZ, G., ITER JOINT CENTRAL TEAM, ITER HOME TEAMS, Plasma Phys. Control. Fusion **37** Suppl. 11A (1995) A19.

POSITIVE CURRENT SPIKE GENERATION DURING MAJOR DISRUPTIONS AND ICRF HEATING EXPERIMENTS UNDER CONDITIONS OF L-H TRANSITION ON THE T-11M TOKAMAK

S.V. MIRNOV, I.A. KOVAN, A.M. BELOV,
I.A. MONAKHOV, Yu.V. PETROV, I.B. SEMENOV,
V.N. AMOSOV, E.A. AZIZOV, O.I. BUZHINSKIJ,
A.P. CHERNOBAI, A.V. KRASILNIKOV, V.B. LAZAREV,
I.N. MAKASHIN, S.G. MALTSEV, A.I. MARKIN,
M.V. MOROZOV, A.A. PETROV, V.G. PETROV,
V.V. PITERSKIJ[1], V.I. POZNIAK[1], A.N. ROMANNIKOV,
Yu.M. SEMENETS, S.M. SOTNIKOV, S.N. TUGARINOV,
L.E. ZAKHAROV[2]
State Research Center TRINITI,
Troitsk, Moscow Region,
Russian Federation

Abstract

POSITIVE CURRENT SPIKE GENERATION DURING MAJOR DISRUPTIONS AND ICRF HEATING EXPERIMENTS UNDER CONDITIONS OF L-H TRANSITION ON THE T-11M TOKAMAK.

The paper combines two different sets of work performed on the T-11M tokamak: disruption and ICRF heating investigations. Positive current spike generation is a main feature of major disruptions on a tokamak. It is attempted to use the method of magnetic perturbation visualization, which was suggested earlier to study the phase of positive current generation during disruption. On the visualization maps ($B_j(t, \theta)$) it is seen that the moment of current generation coincides with the turbulent disruption phase. The main added current begins to generate near-positive current filaments of m = 3,4/n = 1 perturbations near the inner side of the plasma column. Before the turbulization stage only the n = 1 perturbation is seen, but after turbulization n = 1 and 2 (m = 3-5) show up. Ion heating with an efficiency of up to $\eta_D = \Delta T_D n_e \times 10^{-13}/P_{RF} = 15\ \mathrm{eV \cdot cm^{-3}/kW}$ was recorded during ICRF heating of D^+-H^+ plasma in conditions of L-H-like mode transitions on the T-11M tokamak. The efficiency attained is 4-5 times higher than the typical values for hydrogen minority ICRF heating regimes, which were observed earlier on a variety of tokamaks including T-11M. New results were obtained after vacuum chamber wall boronization and coating of the main limiter and the antenna Faraday screen with boron containing films. Under these conditions, the evident presence of a small boron admixture in a D^+-H^+ plasma can lead to strong cyclotron damping of ion Bernstein waves near the layer of second harmonic cyclotron resonance of fully ionized boron with subsequent efficient energy transfer to the bulk ion component. An important role in this case is played by the choice of the optimum hydrogen content, which makes it possible to locate the FW-IBW conversion layer in the vicinity of the B^{+5} second harmonic layer as well as to avoid IBW electron damping.

---

[1] Russian Research Center, Kurchatov Institute, Moscow, Russian Federation.
[2] Plasma Physics Laboratory, Princeton University, Princeton, New Jersey, USA.

1. DISRUPTION INVESTIGATIONS

The disruption instability is a main natural obstacle to the creation of a tokamak. Energy deposition and halo currents are very dangerous to the construction of tokamaks.

The subject of our investigations is the dynamics of the most dangerous major disruption phase — the fast thermal quench (or second thermal quench) — , during which the positive current spike (PCS) and the negative voltage spike (NVS) are generated. As is well known, this disruption phase is preceded by pressure and current flattening in the plasma centre [1–3] due to internal $m = 1/n = 1$ disruption [4] or locked mode activity [3] (slow thermal quench). The following fast thermal quench looks like a magnetic explosion of the outer plasma column region with strong energy deposition on the first wall. It is clear that the main energy reservoir of the disruption is the internal magnetic energy of the plasma column.

The real mechanisms of energy losses and wall deposition are, however, not clear. These mechanisms are important for predictions of plasma–wall interaction during the disruption.

On the T-11M tokamak ($R = 0.7$ m, $a = 0.2$ m), an experimental programme of nearly 50 major disruption pulses with long rotating precursors, short precursors and locked mode precursors (LMPs) for $q(a) = 2.5$–3, $n_e < n_{ecr}$, $I_p = 80$–100 kA, $B_t = 0.8$–1 T was carried out. Our first aim was to define the PCS localization region during the disruption.

We used the new method of visualization of magnetic field recording, which was suggested earlier [5]. Magnetic perturbations are recorded by arrays of B_p probes (coils), which are located around the torus in the poloidal and toroidal directions. The number of probes in one array was really 24, and in the second array, it was 7; therefore, interpolation (smoothing) of probe signals is required, as we need to have a continuous function along the direction of the array. After approximation, we have a continuous perturbation function along the probe array, from 0 to 360° of the poloidal angle. This function was used for brightness and colour modulation of the display screen glow. At times, on the screen a complete picture of the perturbation behaviour in space during the whole measurement window could be seen. The regions with high brightness corresponded to the maximum positive perturbations and the dark regions to negative perturbations. In Fig. 1(a), a visualization picture of a typical major disruption is shown, which was received on T-11M (time resolution: 5 μs). The vertical dimension corresponds to poloidal angles from 0 to 360° (inner side of the plasma column). The middle line corresponds to the outer side (angle: 180°). The time window (horizontal direction) corresponds to 300 μs. The major disruption has a typical precursor in the oscillation mode $m = 2, 3$. Apparently, during the disruption, it is transformed to $m = 3, 4$.

In Fig. 1(b) the PCS (dotted) and NVS oscillograms and soft X ray (SX) behaviour are presented. We see that (SX) drop (flattening) in the centre, connected, as is well known, with internal MHD activity, begins 100 μs before the PCS. At this

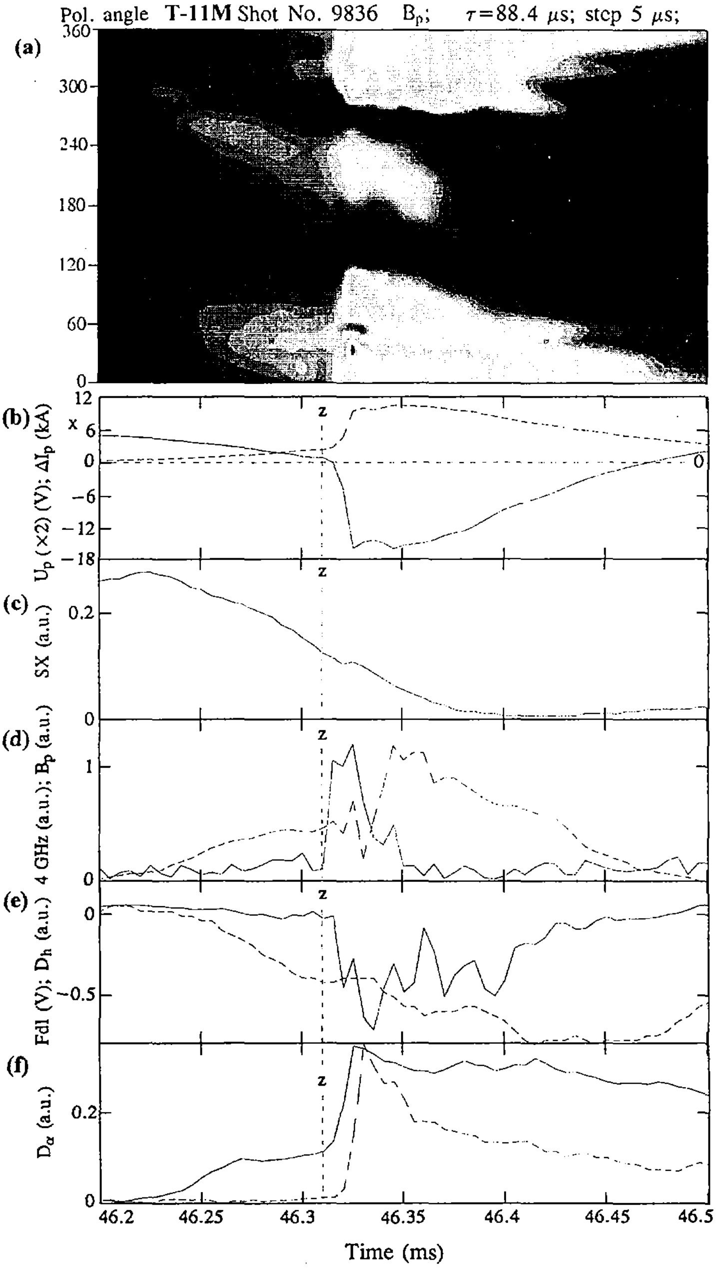

FIG. 1. (a) Map showing $B_p(t,\theta)$; (b) negative voltage pulse U_p (full line) and positive current spike ΔI_p (broken line) of 10 kA or $0.1I_p$; (c) soft X ray intensity (from centre); 4 GHz signal, B_p (broken line): typical signal of single magnetic probe; (e) diamagnetic flux Fdℓ, D_h (broken line): Shafranov shift (near 1 cm); (f) deuterium spectral line emission, D_α, indicative of plasma-limiter (chord − 16 cm, full line) and plasma-wall (chord + 4 cm, dotted line) interactions.

time, the m = 2 magnetic activity, going to m = 3, begins to increase. Simultaneously, as we can see from the Shafranov shift behaviour (Fig. 1(e), D_h (dotted)), the internal magnetic energy of the plasma column begins to drop. The plasma energy (from diamagnetic flux, Fig. 1(e), $Fd\ell$), however, remains nearly constant almost up to the PCS. With the SX drop the D_α emission near the limiter (Fig. 1(f), chord − 16 cm) — a measure of the plasma–limiter interaction — begins to increase. This interaction correlates with the magnetic perturbation increases (Fig. 1(d), B_p (dotted)) and probably corresponds to some plasma column expansion.

At time z, however, the fluent behaviour of all these processes is interrupted. At first, the sharp increase of the 4 GHz emission signal begins, measured by the antenna near the first wall [6]. 1–4 GHz emission corresponds to the L–H domain. We can expect that this emission will be a measure of the high energy electrons in the plasma. We remark that on T-10 [6] and T-11M a GHz emission pulse accompanied all major disruptions. After the start of the GHz emission sharp increase of PCS, NVS, paramagnetic flux and the indicator of plasma–wall interaction, D_α emission far from the limiter (Fig. 1(f), chord + 4 cm) begins. Simultaneously, we can see a sharp start of the magnetic perturbations. This start is accompanied by a short (10–20 μs) pulse of HF activity ($\nu > 1$ MHz), accompanied by short scale perturbations [7], typical for all major disruptions. It is clear that at this time the boundary plasma starts becoming turbulent. The new MHD structure, which appears after the start of turbulence, has higher m (3 + 4) than before [8]. On the basis of all our information we can draw some preliminary conclusions.

2. CONCLUSIONS

(a) PCS generation, in general, takes place in the turbulent phase of disruption which precedes a short scale high frequency burst (HFP). The localization regions of PCS are mainly in the positive current filaments of m = 3, 4 and on the inner side (on R) of the plasma column. This is partly (to 40%) the result of poloidal flux conservation between plasma and first wall. During the incipient turbulence phase the main energy flux goes to the wall.

(b) During the LMP, the disruption structure is fixed in space. The development of disruptions destroys the primary LMP structure. In the case of rotating precursors, no strong phase connection between primary and disruption structure is present. Major disruptions develop in the incipient phase, and the new structure joins the primary one. This is perhaps the reason for the inequality of the plasma–wall interaction during the disruption. During the LMP, the plasma–wall interaction, as is well known [9], is more localized.

(c) In all probability the reason for the plasma becoming turbulent is reconnection of magnetic regions with different helicity by analogy with the internal disruption. In this situation, we can expect runaway electron production during reconnection. This is proven by the GHz signal behaviour.

(d) A comparison of MHD measurements in different cross-sections of the T-11M (24 + 7 probes over 180° of the toroidal angle) shows that in the preliminary phase of the disruption the main helical perturbations m = 2, 3 have n = 1. But during the disruption stage perturbations with n = 2 (m = 2, 3, 4, 5) appear. It is clear that for a full analysis of disruption magnetics, for example, for a correct reconstruction of the magnetic island, we need to have simultaneous magnetic structure measurements in different toroidal cross-sections.

3. ICRF HEATING

3.1. Experimental observations

ICRF heating experiments were performed under conditions of the L–H transition which came to occur spontaneously after vacuum chamber wall boronization and main limiter and antenna screen coating by boron containing dielectric layers [10].

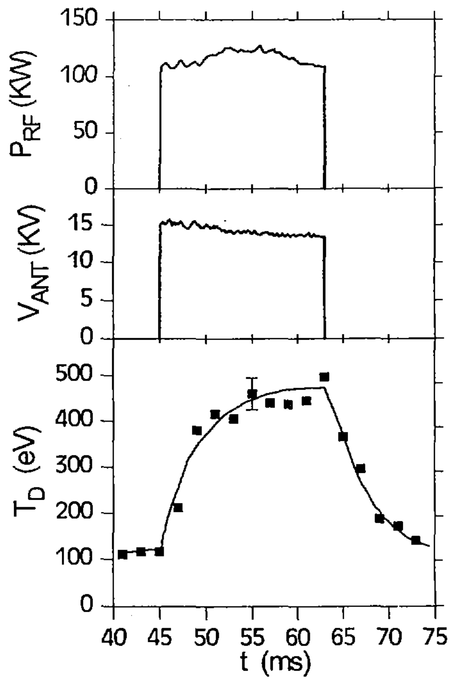

FIG. 2. Temporal behaviour of RF injected power, P_{RF}; antenna voltage, V_{ANT}, and central deuterium temperature, T_D, during ICRF heating ($\bar{n}_e = 4.7 \times 10^{13}$ m^{-3}).

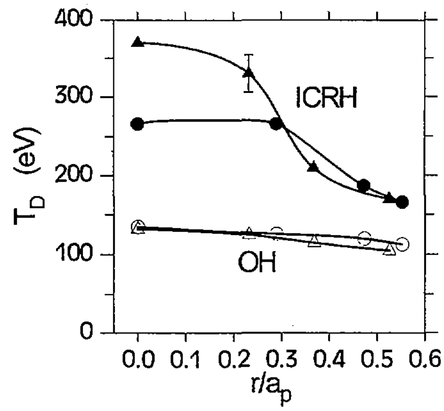

FIG. 3. Typical core plasma deuterium temperature profiles during ICRF (full symbols) and ohmic (open symbols) heating. Circles: L mode; triangles: L–H mode transition.

Experiments were carried out with a D^+–H^+ plasma: $R_p/a_p = 0.7/0.19$ m, $B_t = 1.15$ T, $I_p \approx 100$ kA, $\bar{n}_e \leq 7 \times 10^{13}$ cm^{-3}, $T_{e0}(OH) \approx 400$ eV, $T_{i0}(OH) \approx 130$ eV, $n_H/n_D \approx 0.1$–0.15; fast waves (FWs) of f = 17.5 MHz were injected from the low field side (LFS) of the tokamak by a poloidal loop antenna. The ion heating efficiency recorded in experiments with $P_{RF} \leq 150$ kW (Fig. 2), $\eta_D = \Delta T_D \bar{n}_e 10^{13}/P_{RF} = 15$ eV·cm^{-3}/kW, was four to five times higher than the typical values for hydrogen minority ICRF heating regimes observed earlier on a variety of tokamaks including T-11M [11]. Owing to poor horizontal equilibrium control of the plasma column at higher levels of injected RF power, strong interaction between the plasma and the antenna Faraday screen took place, which led to a reduction of heating efficiency and caused major disruptions at $P_{RF} \geq 300$ kW.

The spatial distribution of the deuterium temperature measured by a charge exchange neutral particle analyser in high efficiency ICRF heating regimes appeared to be more peaked in the central plasma regions than in previous observations during ICRF experiments on T-11M (Fig. 3).

3.2. Discussion and calculations

The enhanced ion heating efficiency can be explained by strong cyclotron damping of ion Bernstein waves (IBWs) near the layer of the second harmonic cyclotron resonance of fully ionized boron (A = 11, Z = 5, ionization potential 340 eV) with subsequent efficient energy transfer to the bulk ion component [12]. It is assumed that IBWs arise in the central regions of the T-11M plasma as a result of FW–IBW conversion near D^+–H^+ hybrid resonance. Recent theoretical analysis of FW–IBW

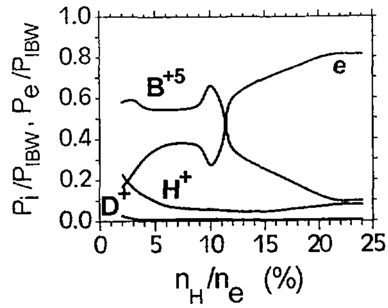

FIG. 4. Calculated fraction of IBW power transmitted to different plasma species versus relative hydrogen concentration for T-11M experimental conditions.

conversion taking into account high magnetic field side (HFS) FW cut-off (cut-off-resonance-cut-off-triplet treatment) has shown that the conversion coefficient can reach high values for certain values of wavenumbers $K_\parallel$ of LFS excited fast waves (e.g., Ref. [13]).

With boron entering into the composition of the first wall, limiter and antenna screen coatings of T-11M, B^{+5} ions should exist inevitably in central plasma regions, their additional accumulation in the plasma core during L–H transition being possible. According to our analysis, the fact that the concentration of B^{+5} is small is not critical for IBW damping.

A important role in examining the scenario of ion heating is played by the choice of the optimum hydrogen content, which makes it possible to locate the FW–IBW conversion layer near the B^{+5} second harmonic layer and to avoid strong IBW electron damping. Figure 4 shows the calculated dependence of the fraction of IBW power absorbed by the plasma species on the relative hydrogen content. The calculations are based on a 3-D ray tracing code with 15 IBW rays ($K_\parallel = 1/R_0$–$15/R_0$) excited in the tokamak midplane. This approach underestimates the power absorption by hydrogen and deuterium at low n_H/n_e due to their direct cyclotron interaction with FWs; nevertheless, it is clear that at $n_H/n_e \approx 10\%$ the power input to B^{+5} ions can significantly exceed the power input to other plasma species. Numerical simulations also predicted a very sharp profile of power absorbed by boron in the vicinity of $\omega = 2\omega_{cB}^{+5}$, which can explain the peaked T_D profile recorded in the experiments (Fig. 3). The fraction of IBW power absorbed by B^{+5} appeared to be almost independent of the boron concentration for $n_B^{+5}/n_e = 0.3$–3%; it rises with the electron concentration and is inversely proportional to $K_\parallel$. Numerical analysis of the thermalization characteristics of RF accelerated B^{+5} ions [12] has also shown that they can deliver energy mainly to the bulk ion component without large 'tail' formation for quite high values of injected RF power density.

4. FINAL CONCLUSIONS

Cyclotron acceleration of a small fraction of totally stripped boron (beryllium) ions by IBWs, converted from FWs in the vicinity of the D–H hybrid resonance, seems to be a quite promising method of efficient central ion heating, even for low magnetic field side FW excitation. The inevitable B^{+5} (Be^{+4}) ion content in the plasma of a tokamak with boron (beryllium) contained in the first wall coating seems to be sufficient for successful heating. The examined scenario also implies an easy way of transition between electron or ion heating regimes by variation of the hydrogen ion content in the plasma.

REFERENCES

[1] MIRNOV, S.V., SEMENOV, I.B., in Plasma Physics and Controlled Nuclear Fusion Research 1976 (Proc. 6th Int. Conf. Berchtesgaden, 1976), Vol. 1, IAEA, Vienna (1977) 291.
[2] KARGER, F., et al., ibid., p. 267.
[3] WESSON, J.A., et al., Nucl. Fusion **29** (1989) 641.
[4] MIRNOV, S.V., SEMENOV, I.B., in Controlled Fusion and Plasma Physics (Proc. 8th Eur. Conf. Prague, 1977), Part I, European Physical Society, Geneva (1977) 45.
[5] SEMENOV, I.B., et al., in Controlled Fusion and Plasma Physics (Proc. 22nd Eur. Conf. Bournemonth, 1995), Vol. 19C, Part I, European Physical Society, Geneva (1995) 421.
[6] POZNIAK, V.I., et al., in Plasma Physics and Controlled Nuclear Fusion Research 1994 (Proc. 15th Int. Conf. Seville, 1994), Vol. 2, IAEA, Vienna (1995) 169.
[7] MIRNOV, S.V., SEMENOV, I.B., At. Ehnerg. **30** (1971) 20.
[8] MEREJKIN, V.G., Sov. J. Plasma Phys. **4** (1988) 275.
[9] JANOS, A.C., in Plasma Physics and Controlled Nuclear Fusion Research 1992 (Proc. 14th Int. Conf. Würzburg, 1992), Vol. 1, IAEA, VIenna (1993) 527.
[10] LAZAREV, V.B., et al., in Plasma Physics and Controlled Nuclear Fusion Research 1994 (Proc. 15th Int. Conf. Seville, 1994), Vol. 2, IAEA, Vienna (1995) 45.
[11] AZIZOV, E.A., et al., in Controlled Fusion and Plasma Physics (Proc. 19th Eur. Conf. Innsbruck, 1992), Vol. 16C, Part I, European Physical Society, Geneva (1992) 47.
[12] KOVAN, I.A., et al., in Controlled Fusion and Plasma Physics (Proc. 23rd Eur. Conf. Kiev, 1996), Vol. 20C, European Physical Society, Geneva (1996).
[13] MAJESKI, R., PHILLIPS, C.K., WILSON, J.R., Phys. Rev. Lett. **73** (1994) 2204.

EVOLUTION OF THE TEARING MODE DURING LHCD INDUCED MODE LOCKING IN WT-3

T. MAEKAWA[1], Y. TERUMICHI, M. ASAKAWA,
S. YOSHIMURA, Y. YOSHIZAWA, M. SUKEGAWA,
K. MATSUNAGA, A. YAMAZAKI, K. UNO,
T. IZUHARA, M. NAKAMURA[2]
Department of Physics,
Faculty of Science,
Kyoto University,
Kyoto, Japan

Abstract

EVOLUTION OF THE TEARING MODE DURING LHCD INDUCED MODE LOCKING IN WT-3.

Through the application of lower hybrid current drive, toroidal rotation of the tearing mode excited in OH plasmas is slowed down, and finally mode locking is artificially induced. The time evolution of the plasma internal structure during mode locking is investigated by using soft X ray (SX) cameras, and it is found that SX bursts appear intermittently at the plasma periphery in accordance with overlapping of the m = 1 and m = 2 structures in the inner part of the plasma before disruption. Through the application of second harmonic electron cyclotron heating, the mode locking comes untied, the toroidal rotation frequency increases and no disruption takes place.

1. INTRODUCTION

Mode locking of low mode number MHD activity is an interesting subject related to major disruption. Neutral beam injection (DIII-D, JET, JT-60U) and AC saddle coil current (COMPASS-D) were effective for controlling the toroidal rotation of the plasma and avoiding mode locking. In our experiments on the WT-3 tokamak (R_0 = 65 cm, a = 20 cm, B_0(max) = 1.75 T), lower hybrid current drive (LHCD) is effective for slowing down the toroidal rotation of the tearing mode and inducing mode locking, while electron cyclotron heating (ECH) is effective for recovering the rotation. Thus we can artificially obtain mode locking of the tearing mode and investigate the internal structure of the plasma by using soft X ray (SX) computerized tomography (CT).

[1] Department of Fundamental Energy Science, Graduate School of Energy Science, Kyoto University, Kyoto, Japan.

[2] Osaka Institute of Technology, Osaka, Japan.

2. TEARING MODE ACTIVITY [1]

In WT-3, tearing mode activity (Mirnov oscillations) is steadily excited in OH plasmas with the safety factor at the limiter $q_a = 2.7$–3.2. Measurements with magnetic probes show that the poloidal and toroidal mode numbers are $m = 2$ and $n = 1$, respectively. The frequency is in the range $f_T = 8$–13 kHz. The mode structure is investigated with five SX cameras viewing a poloidal cross-section at the same toroidal position and two cameras at different toroidal positions. By using CT, we can resolve poloidal mode numbers up to $m = 4$, and we find that the activity has an $m = 1$ mode structure in the inner area ($r/a \simeq 0.35$) and an $m = 2$ mode structure in the outer area ($r/a \simeq 0.75$). Both modes have the same toroidal mode number $n = 1$ and rotate poloidally in the electron diamagnetic direction, with the rotation frequency of the $m = 1$ mode being just twice that of the $m = 2$. Furthermore, the mutual phase of rotation in the poloidal section of both modes is such that the mutual inductance of two helical current filaments located at the $q = 1$ and $q = 2$ surfaces for producing $m = 1/n = 1$ and $m = 2/n = 1$ magnetic islands, respectively, is at a maximum. These results indicate that the modes are coupled and the whole structure rotates toroidally in the direction counter to the plasma current with an angular velocity $\omega_T = 2\pi f_T$, suggesting that the radial electric field is negative.

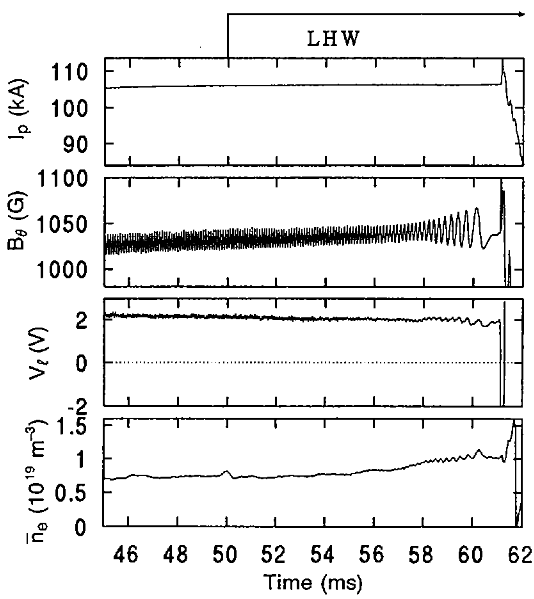

FIG. 1. Time evolution of plasma current, poloidal magnetic field, loop voltage and line averaged electron density before and after LH power is turned on.

3. LHCD INDUCED MODE LOCKING

When LH power in the range P_{LH} = 70–120 kW from a klystron (2 GHz, 350 kW max.) is applied to the OH plasmas at a line averaged density $\bar{n}_e \simeq 0.7 \times 10^{13}$ cm^{-3}, the frequency of oscillations of the Mirnov and SX signals decreases, while the amplitude is first slightly decreased and next increased with a further decrease of the frequency, and finally the mode is locked, as shown in Fig. 1 and Figs 2(a) and (b). Disruption always follows the mode locking. In the case of

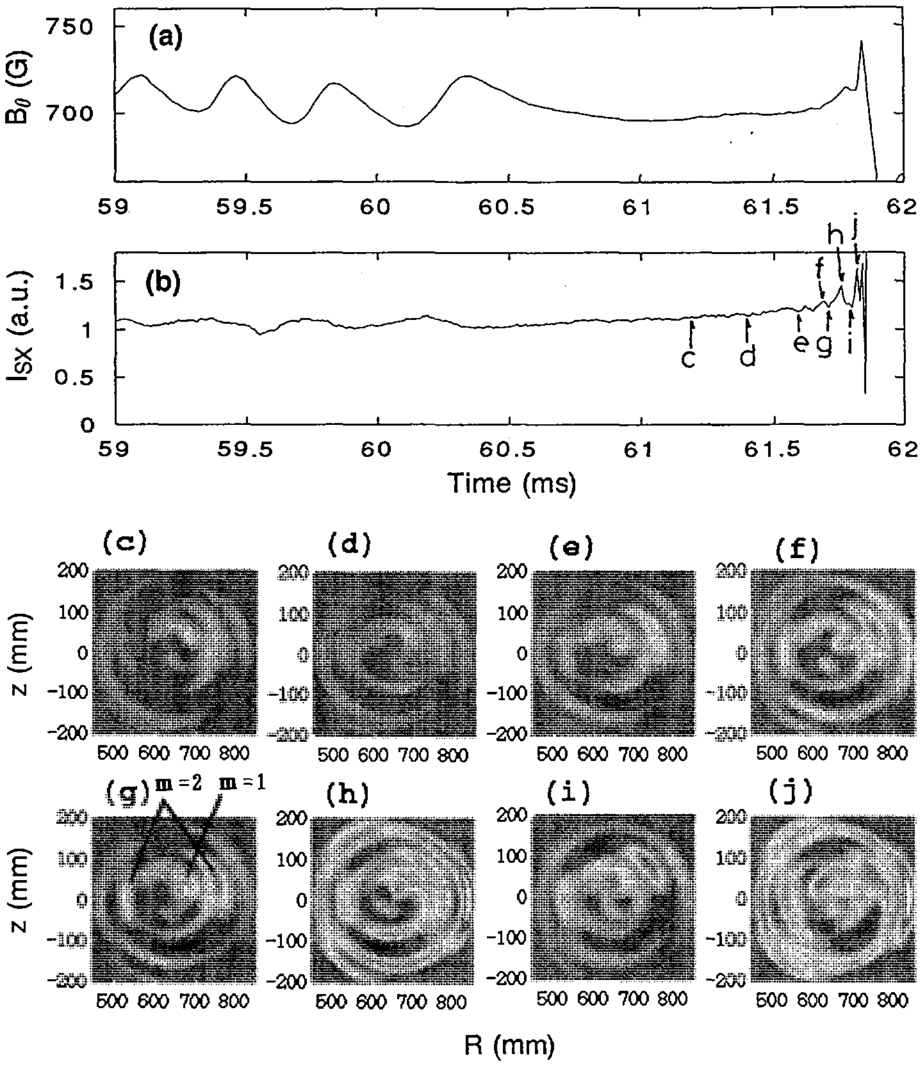

FIG. 2. Time evolution of (a) poloidal magnetic field, (b) SX intensity just before and during mode locking, and (c–j) SX CT images at the times denoted in (b).

$\bar{n}_e < 0.6 \times 10^{13}$ cm^{-3}, where the injected LH waves with Brambilla spectra $N_\parallel \simeq 1$–4 gain access to the central part of the plasma, both the frequency and the amplitude decrease, and finally the mode is completely suppressed. In the case of $\bar{n}_e > 0.8 \times 10^{13}$ cm^{-3}, where the LH waves cannot gain access to the central region, the frequency decreases while the amplitude increases, and finally disruption takes place without mode locking. In any case the toroidal rotation frequency of the mode is decreased by LHCD, which is possibly explained by the reduction of the negative radial electric field due to the enhanced loss of fast electrons by the tearing instability.

Thus we can artificially obtain mode locking by the use of LHCD and investigate the evolution of the plasma during mode locking. In Figs 2(c)–(j), the CT image at t = 61 ms is subtracted so that the successive images show the differences between the emission at the times indicated and that at 61 ms. In accordance with the mode locking appearing in the magnetic signal in Fig. 2(a), the SX CT images in Figs 2(c)–(j) show that the m = 1 and m = 2 islands do not rotate and continuously grow, and strong bursts appear intermittently at the plasma periphery in accordance with the overlapping of the m = 1 and m = 2 islands in the inner part of the plasma just before disruption ((f), (h) and (j)). These bursts may suggest that the magnetic islands of m = 2 and m = 1 overlap intermittently before disruption.

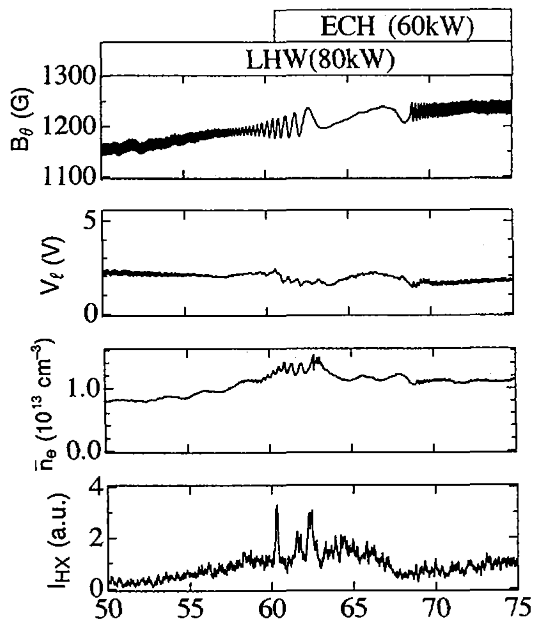

FIG. 3. Time evolution of poloidal magnetic field, loop voltage, line averaged electron density and hard X ray intensity before and after ECH is turned on.

4. UNLOCKING BY ECH

When EC power from a gyrotron (56 GHz, 200 kW max.) is injected nearly perpendicular to the toroidal field from the low field side in the extraordinary mode just before the mode locking takes place, the mode locking comes untied, the toroidal rotation frequency increases and no disruptions take place, as shown in Fig. 3. Untying of mode locking is obtained as far as the second harmonic electron cyclotron resonance layer is located within the plasma. The causes of the recovery and increase of the toroidal rotation by ECH are unknown. It is noted that LHCD and ECH exert opposite effects on particle confinement as well as on toroidal rotation; that is, during LHCD (ECH) on WT-3 the density decreases (increases) at the scrape-off layer, while the density of the main plasma increases (decreases) [2]. These effects are possibly related.

5. SUMMARY

(1) Through the application of LHCD, toroidal rotation of the tearing mode excited in OH plasmas is slowed down, and finally mode locking is artificially induced.
(2) SX CT shows that during mode locking SX bursts appear intermittently at the plasma periphery in accordance with overlapping of the m = 1 and m = 2 islands in the inner part of the plasma before disruption.
(3) Through the application of second harmonic ECH, the mode locking comes untied, the toroidal rotation of the tearing mode recovers and no disruptions take place.

REFERENCES

[1] TERUMICHI, Y., et al., in Plasma Physics and Controlled Nuclear Fusion Research 1994 (Proc. 15th Int. Conf. Seville, 1994), Vol. 2, IAEA, Vienna (1995) 189.
[2] NAKAMURA, M., et al., Nucl. Fusion 31 (1991) 1485.

AN ATTEMPT TO MITIGATE DISRUPTIVE PLASMA CURRENT DECAY IN RELATION TO VACUUM VESSEL ELECTRICAL ASPECTS

M. ABE, A. DOI, T. TADOKORO
Hitachi Research Laboratory, Hitachi Ltd.

M. OTSUKA
Hitachi Works, Hitachi Ltd.

Omika-sho, Hitachi-shi, Ibaraki,
Japan

Abstract

AN ATTEMPT TO MITIGATE DISRUPTIVE PLASMA CURRENT DECAY IN RELATION TO VACUUM VESSEL ELECTRICAL ASPECTS.

In order to search for techniques to mitigate disruptions, the characteristics of disruptive I_P decays were tested for (1) low and high vacuum vessel loop resistance Ω_V conditions, and (2) scrape-off layer (SOL) plasma to vessel current (halo current) control. These tests were to manipulate the SOL current. Case (1) had the advantage of lower loop voltage V_l without an increase of the force due to the eddy current, in comparison with high Ω_V conditions. In case (2), the I_P decay rate was reduced by suppressing the SOL current. The core plasma current and the shell effect during the first phase, in which magnetic axis and core plasma still exist within the closed flux surfaces, were enhanced, which is effective in mitigating disruptive I_P decay.

1. INTRODUCTION

The next step in magnetic fusion research will be experiments on large scale fusion devices such as ITER [1]. An important point for such a large machine is the design of a device that is able to withstand strong electromagentic forces, which implies that the maximum electromagnetic force should be taken into account. A high electromagnetic force acts on the vacuum vessel during disruptive plasma current (I_P) decay due to a disruption or a vertical displacement event (VDE). Attempts have been undertaken to identify a relevant mechanism and to mitigate the disruptive I_P decay in order to reduce the forces in question [2, 3].

Experiments aiming at an understanding of the characteristics of a disruptive I_P decay have been carried out in the Hitachi Tokamak HT-2 [4], based on a magnetic analysis that reconstructs the poloidal magnetic field from measured magnetic data [5, 6]. Some results suggested the possibility of an I_P decay rate modification [7, 8]. Hence, a search was undertaken for techniques to mitigate the disruptive I_P decay. Decay characteristics were tested for: (1) low and high vacuum vessel loop resistance Ω_V conditions, and (2) scrape-off layer (SOL) plasma to vessel current (SOL current or halo current) control. The low Ω_V condition of case (1) had the advantage of a low loop voltage V_l, probably with a small halo current; in case (2), the I_P decay rate was reduced by suppressing the SOL current.

This paper discusses the characteristics of disruptive I_P decay in relation to Ω_V control and SOL current control.

2. THE HITACHI TOKAMAK HT-2

The small tokamak HT-2 has the following parameters: major radius $R_P = 0.42$ m, minor radius $a_p = 0.11$ m, toroidal field $B_T = 0.6$ to 1.1 T (capability 2.5 T), $I_P \leq 55$ kA and elongation $\kappa = 0.9$ to 1.4 [9]. Figure 1 shows the poloidal cross-section. There are two types of poloidal field coils (PFCs). One is the HY coils (HY1 to HY8). Each HY coil has an independently controlled transistor chopper power supply and is used for poloidal field control and I_P drive. The other coils are single functional PFCs of two horizontal field coils, the DH coil and the AH coil (for rapid control), iron core biasing coils, the B coils and the OH coils. The DH and OH coils are rather supplementary and are not used in this study.

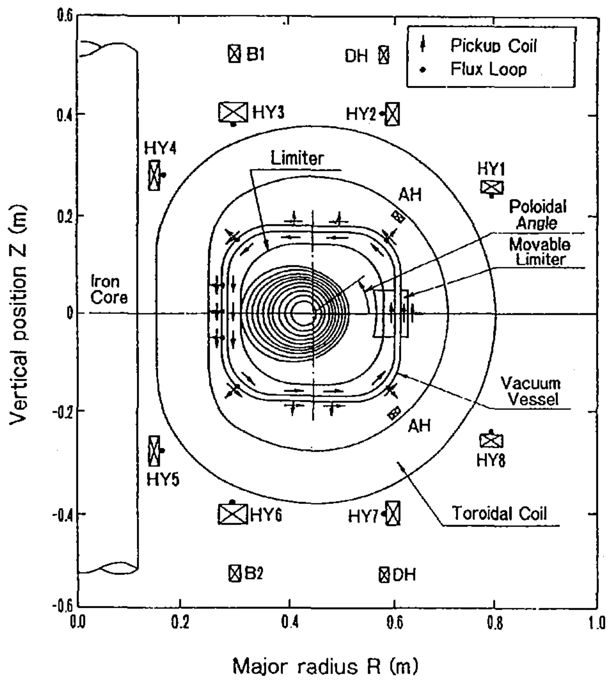

FIG. 1. Poloidal cross-section of HT-2.

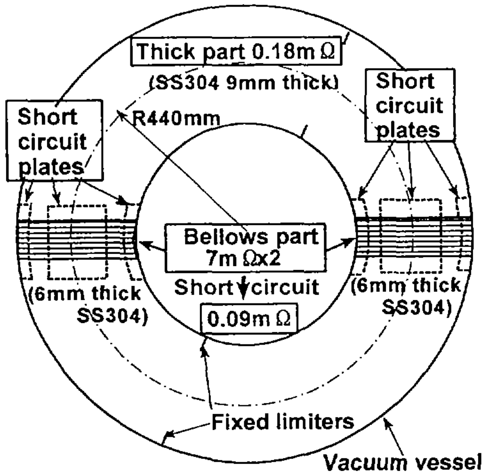

FIG. 2. HT-2 vacuum vessel with two bellows shortcircuited for the low Ω_V experiment.

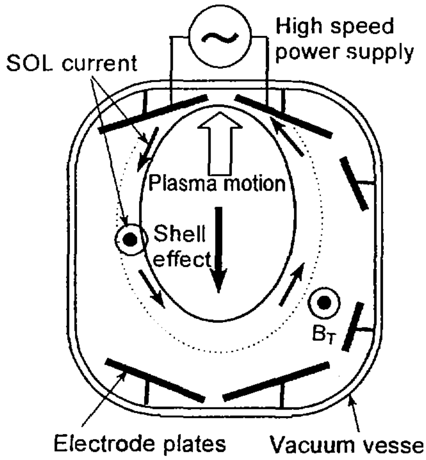

FIG. 3. Schematic figure showing positions of electrode plates and power supply.

The features of this device are: (1) accurate poloidal field control even during the breakdown phase [4], which allows discharges with low Ω_V [9], and (2) sufficient magnetic sensors to carry out a magnetic analysis, even during disruptive I_P decay. We have two techniques for the magnetic analysis: one [5] is based on an algorithm developed by Swain et al. [10] and the other one [6] uses an MHD equilibrium computation algorithm developed by Lao et al. [11]. However, our algorithm contains fields due to eddy current and an error field of toroidal field coils (TFCs). The latter is the 5×10^{-4} T radial field in HT-2 at $B_T = 1.0$ T. The iron core produces a magnetic field, which we calculate analytically on the assumption of an iron core of infinite length. We have experimentally confirmed its accuracy in the former Hitachi Tokamak HT-1 [12].

The HT-2 vacuum vessel has two bellows, shortcircuited for the low Ω_V experiment as shown in Fig. 2. The vessel current disturbs the plasma startup. However, a low V_l startup is possible with accurate magnetic field control. The change of Ω_V did not affect the shell effect. The high Ω_V (14 mΩ) was higher than that of cold plasmas during breakdown and disruptive I_P decay phase (electron temperature T_e = 5–10 eV, $\Omega_P(T_e)$ = 2–6 mΩ). The low Ω_V (0.3 mΩ) was lower than Ω_P (5–10 eV). This situation of Ω_V in comparison with Ω_P is similar to that prevailing in ITER.

A power supply (600 V, 2 kA) is connected to electrode plates that are placed in the vacuum vessel, facing the plasma as is shown in Fig. 3. The SOL current flowed through the electrodes, and the power supply was able to control it.

3. EXPERIMENTS AND RESULTS

Three kinds of experiment were carried out. The first and the second experiment made use of a high Ω_V of 14 mΩ and a low Ω_V of 0.3 mΩ, respectively, without SOL current control. The third experiment used SOL current control and Ω_V = 14 mΩ. Disruptive I_P decays were triggered by terminating the poloidal field control system.

3.1. Experiments with original setup

3.1.1. *Characteristics of I_P decay*

Figure 4 illustrates out understanding of the disruptive I_P decay [8]: the magetic axis moves towards the vacuum vessel wall, all mangetic flux surfaces become open and the plasma current flows on the open flux surfaces with very low T_e. The time evolution of I_P, the poloidal field B_P at a poloidal angle of 270° (bottom), Z_P as the current centre, and the forces on the plasma and the vacuum vessel F_Z^P, F_Z^V are plotted in Fig. 4(a), and Fig. 4(b) shows flux contours for two time slices. The forces (F_Z^{PT}, F_Z^{VT}) of the solid lines are obtained by magnetic analysis, and the dotted lines are estimated actual forces, as will be discussed later. The plasma current flows in the dotted area.

The disruptive I_P decay can be divided into two phases according to the position of the magnetic axis. During the first phase, the magnetic axis and the hot core plasma on the closed flux surfaces still exist as shown in the upper time slice of Fig. 4(b), while the SOL area is developing. Entering the second phase, the magnetic axis moves on the vacuum vessel wall, and all magnetic surfaces in the plasma are open (SOL area), as is shown in the lower time slice. Then, the plasma is instantaneously cooled to several eV, and I_P decays with a simple resistive decay time constant of τ_2 = L_P/Ω_P. We think that it is not possible to manipulate the second phase.

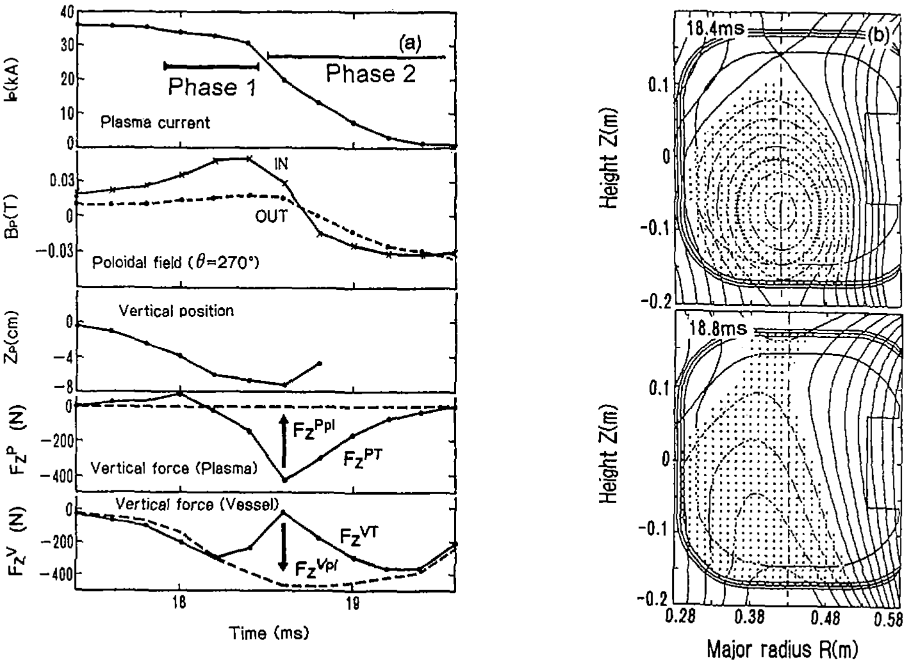

FIG. 4. Typical VDE and disruption in HT-2: (a) Time evolutions of plasma current I_P, poloidal field B_P, Z_P as current centre, forces on plasma and vacuum vessel F_Z^P, F_Z^V. (b) Flux contours for two time slices. Upper figure: first phase; lower figure: second phase.

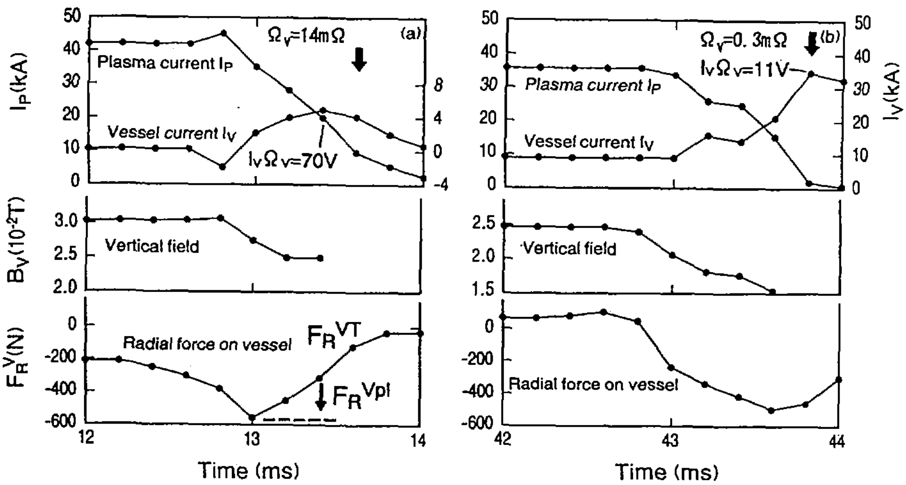

FIG. 5. Waveforms of radial disruptive I_P decay for two Ω_V. The loop voltage was for the low Ω_V condition, with insignificant increase of the electromagnetic force. Bold arrows show the start of the second phase.

However, since the movement of the magnetic axis depends on the poloidal magnetic field in the first phase, we expect that there is a possibility for modification of I_P decay by changing the external conditions. For example, the decay rate dI_P/dt of the first phase depended on the configuration of the poloidal magnetic field [8].

3.1.2. Consideration of plasma force balance during I_P decay

The tokamak plasma experiences a vertical electromagnetic force, F_Z^{Ppl}, due to interaction between B_T and the SOL current poloidal component (halo current), F_Z^{PE}, due to the eddy current on the vacuum vessel, and F_Z^{PPFC}, due to PFCs. The magnetic analysis treats the toroidal current only, and F_Z^{Ppl} cannot be obtained directly. However, since the forces are balanced on the plasma, F_Z^{Ppl} can be calculated from $F_Z^{Ppl} = -(F_Z^{PE} + F_Z^{PPFC}) = -F_Z^{PT}$. The reaction force acts on the vacuum vessel. The total force on the vessel F_Z^V is $F_Z^{VT} - F_Z^{Ppl}$, where F_Z^{VT} is a force due to the toroidal current only. The arrows in Fig. 4(a) are F_Z^{Ppl} calculated from Eq. (1). The estimated total forces on the plasma and the vacuum vessel are plotted by the dotted lines. When F_Z^{Ppl} is strong at the start of the scond phase, F_Z^{VT} is weak, showing that the shell effect is not working. This is due to the development of the SOL and the reduction of current in the core plasma, while only the latter is effective for the shell effect. At the start of the second phase, the plasma is supported by F_Z^{Ppl} against the Z_P destabilizing force,F_Z^{PPFC}.

The starting point of our attempt is to increase the stabilizing forces, F_Z^{Ppl} and F_Z^{PE}. To increase F_Z^{Ppl}, we decrease Ω_V in order to reduce the resistance of the SOL (halo current) current path. In order to increase the shell effect, we control the SOL current, expecting a rise of the plasma current on the closed flux surfaces.

3.2. Experiments with low loop resistance vacuum vessel

Figure 5 compares I_P decay waveforms for two Ω_V conditions on a linear scale, showing the time evolutions of I_P, vessel current I_V, vertical field B_V and radial

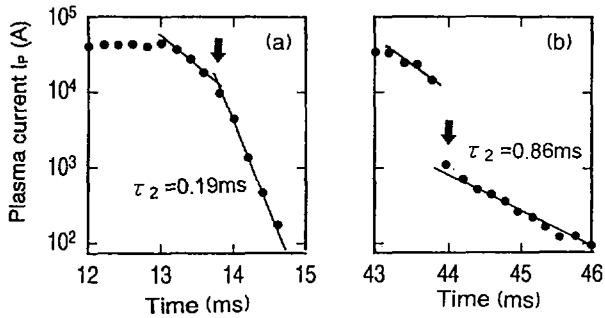

FIG. 6. Waveforms of disruptive I_P decay for two Ω_V on logarithmic scales. Arrows show the start of the second phase.

force on the vessel, $F_R{}^V$. Figure 6 shows I_P decay waveforms on a logarithmic scale. The periods of 0.8 ms before the arrows have equivalent dI_P/dt for the two conditions. With low Ω_V, I_P decays rapidly at the time labelled by the bold arrows, as is clearly seen on the log scale plot. I_V is large but V_l, which roughly equals $I_V\Omega_V$, is quite low. This is an advantage, especially for superconducting coils.

The rapid decrease of I_P at the arrow for low Ω_V can be explained as follows: Entering the second phase, the magnetic axis reaches the vessel wall. The plasma has only a SOL area with no closed magnetic surfaces. T_e decreases to below 10 eV, as estimated from V_l, and Ω_P becomes larger than $\Omega_V = 0.3$ mΩ. This situation makes the toroidal current migrate from the plasma to the vessel, rather than enhancing the SOL current, and decreases the ohmic heating power in the plasma. This mechanism enhances the I_P decay at the start of the second phase. During the first phase (before the arrow), the magnetic axis still exists in the plasma, moving towards the vessel wall. The dI_P/dt values are roughly the same because the shell effect and the characteristics of magnetic axis movement are similar for both Ω_V conditions and dI_P/dt depends on the plasma movement [7].

As the replacement of the current is enhanced, we can expect the SOL current to be low in low Ω_V conditions. We confirm this from the B_V plot. The B_V values decrease in the disruptive I_P decay phase because of the shell effect. The drop is about 10×10^{-3} T for low Ω_V and 5×10^{-3} T for high Ω_V, at the end of the first phase, with $I_P = 16$ kA. $I_P{}^0$ is about 40 kA for both conditions. Then, for high Ω_V, the excess radial force is about 200 N with a loop length of $2\pi R_P = 2.5$ m. We estimate that, for high Ω_V, the halo current is larger by a quantity equivalent to about 200 N radial force at the end of the first phase. On entering the second phase, the difference becomes even larger, because the SOL current is less than 2 kA for low Ω_V, while it is 15 kA for high Ω_V.

Although there is an eight times larger I_V, we have confirmed that the increase in the electromagnetic force is insignificant, as is shown in the bottom graphs of Figs 6(a) and (b), which plot the total radial force on the vessel. In our view, the reason for this is as follows: The inward radial force is due to the vertical field which is balanced by the plasma pressure before the disruption. The destabilizing force during I_P decay is due to the loss of pressure, which is considered to be roughly the same, and, as a consequence, the force has roughly the same magnitude for the two conditions.

From the experiments with low Ω_V, we have concluded that low resistance is not effective in slowing down the I_P decay, but has the advantage of low V_l during disruption by increasing I_V. The increase of the electromagnetic force is insignificant, and the halo current is estimated to be small.

3.3. Experiments with SOL current control

Figure 7 shows that I_P decays with biasing ± 500 V between the electrodes during VDE. The open circuit voltage between the electrodes during disruptive I_P decay was measured in advance of the control experiments. The maximum voltage

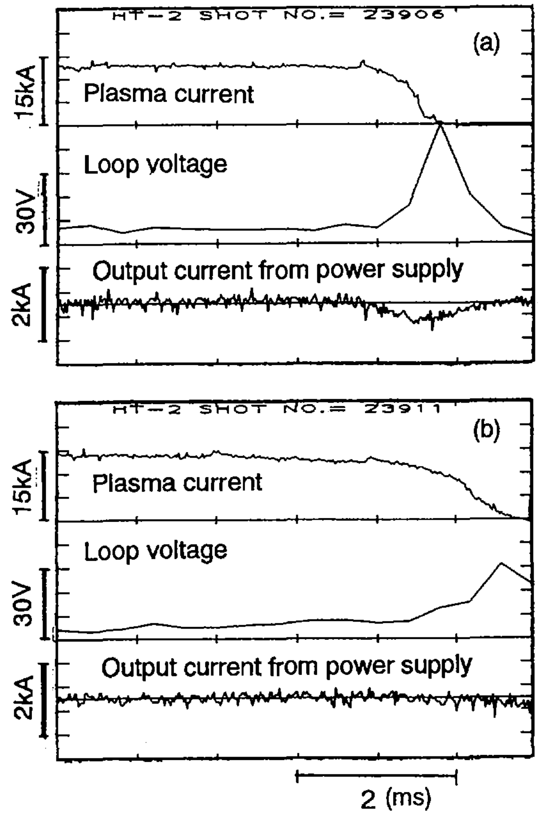

FIG. 7. Waveforms of I_P decay with control of voltage between electrode plates: applied voltage (a) to enhance the SOL current; (b) to suppress the SOL current.

observed during the VDE was about 250 V with I_P^0 = 15 to 25 kA. The applied voltage directions were to enhance the SOL current (Fig. 7(a)) and to suppress it (Fig. 7(b)). The low Ω_V cases of Figs 5(b) and 6(b) were intended to enhance the SOL current, but there was also an enhancement of dI_P/dt due to the change of the toroidal current path from SOL to vessel. However, Fig. 7(b) has no such replacement of the SOL current so that we could expect that a pure SOL current effect was observed.

Suppressing the SOL current results in a slower I_P decay and a lower V_l. We think that the SOL current is reduced by the voltage and the core current is increased. This results in an enhancement of the shell effect to slow down the plasma movement and to reduce the decay rate. From these experiments, we concluded that SOL current control with biasing appears to be effective in mitigating the I_P decay, and preservation of the core plasma current is important in softening this decay.

4. SUMMARY

The HT-2 experiments on disruptive I_P decay showed that this decay could be divided into two phases: In the first phase, the plasma had a magnetic axis, the core plasma area had closed flux surfaces and dI_P/dt depended on the external conditions. In the second phase, the plasma had only the SOL area and I_P decayed with a resistive decay time constant. Then we expected that the first phase could be controlled. As techniques of mitigating the disruptive I_P decay or controlling the first phase, we tested the characteristics of disruptive I_P decays for (1) low and high vacuum vessel loop resistance Ω_V conditions, and (2) scrape-off layer (SOL) plasma to vessel current control. These tests referred to SOL current enhancement and suppression, respectively. Case (1) had the advantage of low V_l without increase of the electromagnetic force, compared to the high Ω_V case. In case (2), the I_P decay rate was reduced by suppressing the SOL current. We also claim here that preservation of current on the closed flux surfaces could be a key point in mitigating the I_P decay and that low Ω_V would be a favourable condition for low halo current.

REFERENCES

[1] INTERNATIONAL ATOMIC ENERGY AGENCY, ITER Poloidal Field System, ITER Documentation Series, No. 27, IAEA, Vienna (1991).

[2] YOSHINO, R., J. Plasma Fusion Res. **70** (1994) 1081.

[3] YOSHINO, R., et al., in Plasma Physics and Controlled Nuclear Fusion Research 1994 (Proc. 15th Int. Conf. Seville, 1994), Vol. 1, IAEA, Vienna (1995) 685.

[4] ABE, M., TAKEUCHI, K., Fusion Technol. **29** (1996) 277.

[5] ABE, M., et al., J. Plasma Fusion Res. **70** (1994) 671.

[6] ABE, M., TAKEUCHI, K., Kaku Yugo Kenkyu (Nuclear Fusion Research) **67** (1992) 257 (in Japanese).

[7] ABE, M., et al., Jpn. J. Appl. Phys. **29** (1990) 395.

[8] ABE, M., et al., J. Plasma Fusion Res. **69** (1993) 352.

[9] ABE, M., et al., "Plasma startup characteristics in the Hitachi tokamak HT-2 with modified low loop resistance", submitted to Fusion Technol.

[10] SWAIN, D.W., NEILSON, G.H., Nucl. Fusion **22** (1982) 1015.

[11] LAO, L.L., et al., Nucl. Fusion **30** (1990) 1035.

[12] ABE, M., et al., in Engineering Problems of Fusion Research (Proc. 9th Symp. Chicago, 1981) Vol. 1 (1981) 916.

DIVERTOR EXPERIMENTS
AND
TOKAMAK CONCEPT OPTIMIZATION

(Poster Session AP2)

ACTIVE CONTROL OF HELIUM ASH EXHAUST AND TRANSPORT CHARACTERISTICS IN JT-60U

A. SAKASAI, H. KUBO, K. SHIMIZU, T. FUJITA, N. ASAKURA,
K. ITAMI, S. HIGASHIJIMA, S. SAKURAI, H. TAKENAGA,
N. HOSOGANE, JT-60 TEAM
Naka Fusion Research Establishment,
Japan Atomic Energy Research Institute,
Naka-machi, Naka-gun, Ibaraki-ken,
Japan

Abstract

ACTIVE CONTROL OF HELIUM ASH EXHAUST AND TRANSPORT CHARACTERISTICS IN JT-60U.

In–out asymmetry of the He flux in the divertor during ELMy H mode was observed. The in–out asymmetry has been successfully controlled by changing neutral beam power and plasma current. Asymmetry control and solid target boronization permitted effective He ash exhaust. Helium transport in reversed shear plasmas has been investigated using He beam injection and He gas puffing. Helium particle confinement was improved inside the internal transport barrier (ITB). The He density profile depends on the strength of the ITB. When a partial collapse eliminated the ITB, He particles inside the ITB were expelled.

1. INTRODUCTION

Control of He ash is one of the key issues for future tokamak reactors, such as ITER and SSTR (Steady State Tokamak Reactor). ITER is designed to operate in H mode or some other enhanced confinement regime. A detailed experimental database related to He level regulation and He ash removal should be developed for the decision on the device size and the margin of ignition achievement. ELMy H mode is attractive because of its capability for steady state operation and particle exhaust by MHD relaxation in the plasma peripheral region.

By using a neutral beam of He atoms for central He fuelling and a short pulsed He gas puff for peripheral fuelling, He exhaust characteristics (He flux and neutral particle pressure in the divertor) have been studied to simulate He ash in ELMy H mode on JT-60U [1, 2] and DIII-D [3, 4]. The previous study on JT-60U with He beam fuelling indicated that He ash could be easily exhausted in ELMy H mode and L mode discharges. The in–out asymmetry of the D flux in the divertor was studied in L mode and ELMy H mode on JT-60U [5]. The D flux is larger on the inner target than on the outer target. However, the asymmetry in the He flux has not yet been investigated in JT-60U or in other devices. Its characteristics are an important issue for He ash control.

In reversed shear mode, the electron density in the central region is peaked and the confinement is greatly enhanced inside the internal transport barrier (ITB), which is formed near the position of minimum q. Electron density, electron temperature and ion temperature profiles ($n_e(r)$, $T_e(r)$ and $T_i(r)$) inside the ITB are peaked in JT-60U [6]. Because of its improvement of particle and energy confinement in the core region, reversed shear mode is attractive as a new operation scenario for ITER. Helium ash exhaust from the reversed shear plasma is a matter of concern. It is very important to clarify the He transport characteristics of the reversed shear plasma because of the issue of enhancement of He particle confinement.

2. EXPERIMENTAL ARRANGEMENT

JT-60U is a single null open divertor tokamak with a major radius of 3.2 m, a minor radius of 1 m, a plasma current of up to 6 MA and a toroidal field of up to 4 T. A tangential viewing charge exchange recombination spectroscopy (CXRS) system provides radial density profiles of fully ionized He. CXR emission of He II (468.52 nm, n = 4–3) is led to 0.5 m and 1.0 m Czerny–Turner spectrometers through 80 m pure quartz optical fibres. The detection system consists of image intensified double linear photodiode arrays that have high sensitivity and are used for He density profile measurement. Instrument calibration of the CXRS system was performed by the use of an integrating sphere.

A set of spectrometers, a Langmuir probe array and an infrared television camera are used to measure the divertor characteristics. Recycling influx profiles of D and He ions were derived from the measured line intensities of D_α and He I (728.1 nm or 667.8 nm) with a 60 channel optical fibre array coupled to visible spectrometers. These diagnostics permitted measurements in ELMy H mode discharges with a high X point configuration (X_p = 20 cm). The measured electron temperature at the divertor target is used to calculate the He influx.

3. ACTIVE CONTROL OF He ASH

The in–out asymmetry of the He flux in the divertor was investigated by changing NB power and I_p. Recycling influx profiles of D and He in the divertor region were measured with spectroscopic diagnostics of a 60 channel optical fibre array viewing a wide divertor area. A He exhaust experiment was carried out in ELMy H modes with H factor ($\equiv \tau_E/\tau_E^{ITER\text{-}89P}$) = 1.4–1.7.

The discharge conditions were I_p = 1.0 MA/B_t = 2.5 T (q_{eff} = 6.2), 1.4 MA/3.5 T (q_{eff} = 6.0), 1.7 MA/2.5 T (q_{eff} = 3.5), 1.5 MA/2.5 T (q_{eff} = 3.9), 1.7 MA/3.5 T

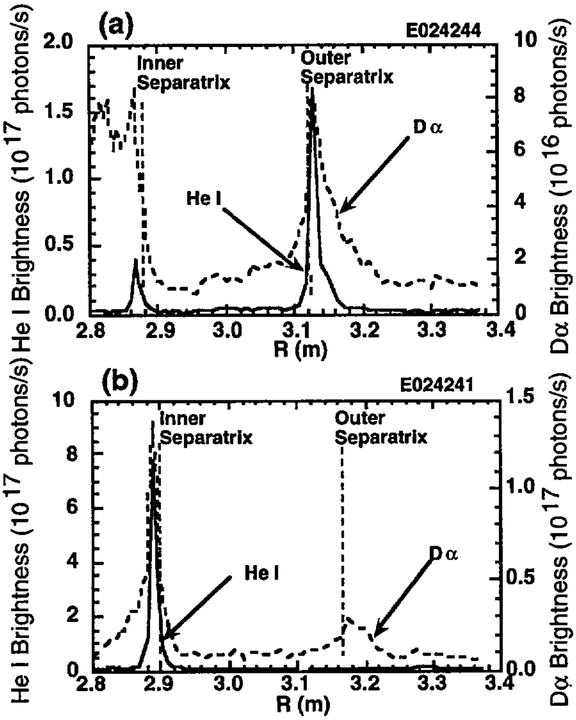

FIG. 1. Comparison of He I brightness (He flux) and D_α brightness (D flux) profiles in the divertor with (a) I_p = 1.0 MA, B_t = 2.5 T, P_{NB} = 18 MW; and (b) I_p = 1.7 MA, B_t = 3.5 T, P_{NB} = 18 MW in ELMy H mode.

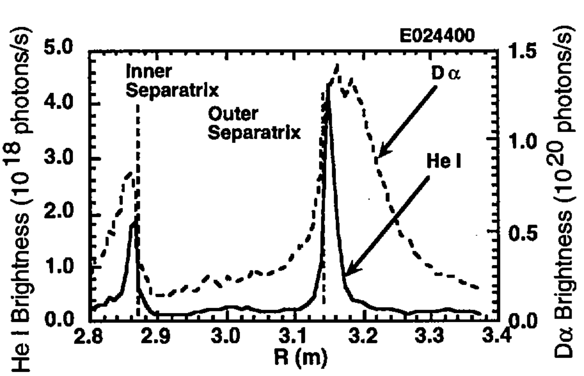

FIG. 2. He I brightness and D_α brightness profiles in the divertor in the case of I_p = 1.0 MA, B_t = 2.5 T, P_{NB} = 18 MW with reversed B_t and I_p.

(q_{eff} = 4.8), vol. = 60 m^3 and P_{NB} = 18 MW with He gas puffing of 5 Pa·m^3/s for 0.2 s to obtain the dependence of q_{eff}, I_p and B_t. The He exhaust experiment was also carried out in L mode with the same configuration and high n_e under the condition of 1.7 MA/3.5 T (q_{eff} = 4.8) and P_{NB} = 10 MW. Figure 1 shows the He I (728.1 nm) brightness (He flux) and D_α brightness (D flux) profiles in the divertor in the cases of: (a) I_p = 1.0 MA, B_t = 2.5 T, P_{NB} = 18 MW; and (b) I_p = 1.7 MA, B_t = 3.5 T, P_{NB} = 18 MW with He gas puffing. In the case shown in Fig. 1(a) the He flux is larger on the outer target than on the inner target. The central ion temperature is 10 keV, the central electron temperature is 3.5 keV and the central electron density is (2.5–3) × 10^{19} m^{-3}. The He gas puff started at t = 6.0 s. In contrast, the He flux was larger on the inner target than on the outer target in the case of high I_p, as shown in Fig. 1(b). The outboard enhanced He flux was obtained under the condition of I_p = 1.7 MA, B_t = 3.5 T if high power NBI of 23 MW was applied. The in–out asymmetry of the outboard enhanced He flux is very large in ELMy H mode with high NB power heating and low I_p.

The effect of the ion ∇B drift direction on the in–out asymmetry of the He flux was investigated under the condition of reversed B_t and I_p with He gas puffing. Figure 2 shows the He I brightness and D_α brightness profiles in the divertor in the case of I_p = 1.0 MA, B_t = 2.5 T, P_{NB} = 18 MW, with the ion ∇B drift away from the divertor (reversed B_t and I_p). The outboard enhanced He flux was also observed under these conditions. On the other hand, the inner He flux was less than the outer flux under the other conditions. The reversed effect on the in–out asymmetry of the He flux profiles was not observed. This result indicates that the asymmetry in the He flux profiles does not depend on the ion ∇B drift direction.

However, the in–out asymmetry in the D flux is changed in the case of reversed B_t and I_p. The outer D flux is larger than the inner flux under all conditions in ELMy H mode. The reversed effect on the in–out asymmetry in the D flux was clearly observed [5]. The He flux profiles were very narrow as compared with the D flux profiles. This result of B_t and I_p reversal is interesting with respect to its causality and mechanism.

The in–out asymmetry of the He flux was investigated using 60 keV ^{4}He beams ($P_{He\text{-}NB}$ = 2.1 MW, for an equivalent fuelling of 0.9 Pa·m^3/s) with normal B_t (the ion ∇B drift towards the divertor) in ELMy H mode. The ^{4}He beam injection started at t = 6.0 s and lasted for 3.0 s. It is evident that the He I intensity in the divertor increased linearly with time during the ^{4}He beam injection. The I_p scan was performed under the conditions of 1.0 MA/2.5 T, 1.2 MA/3.0 T, 1.3 MA/3.25 T and 1.4 MA/3.5 T to clarify the dependence of I_p on the asymmetry with the same q_{eff}. The He flux towards the outboard target is gradually decreased and the He flux towards the inboard target is gradually increased in the case of I_p higher than 1.0 MA. The scan of NB power was also carried out under the conditions of P_{NB} = 18, 14, 12 and 10 MW (1.0 MA/2.5 T) to clarify the dependence of P_{NB} on the asymmetry.

Figure 3 shows a comparison of He I brightness and D_α brightness profiles in the divertor in the cases of: (a) I_p = 1.0 MA, B_t = 2.5 T, P_{NB} = 18 MW; (b) I_p = 1.3 MA,

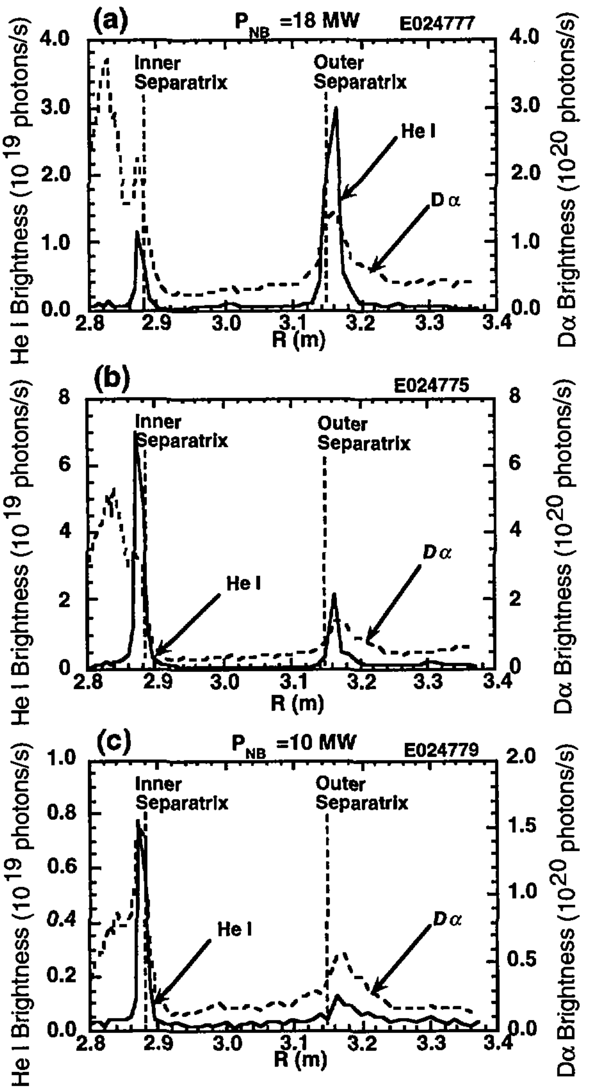

FIG. 3. Comparison of He I brightness and D_α brightness profiles in the divertor with (a) I_p = 1.0 MA, B_t = 2.5 T, P_{NB} = 18 M; (b) I_p = 1.3 MA, B_t = 3.25 T, P_{NB} = 18 MW; and (c) I_p = 1.0 MA, B_t = 2.5 T, P_{NB} = 10 MW in ELMy H mode.

B_t = 3.25 T, P_{NB} = 18 MW; and (c) I_p = 1.0 MA, B_t = 2.5 T, P_{NB} = 10 MW in ELMy H mode with He beam injection. The asymmetry of the outboard enhanced He flux was observed with P_{NB} = 18 MW, as shown in Fig. 3(a). In the case of P_{NB} = 10 MW, the inboard He flux was enhanced, as shown in Fig. 3(c). The He flux towards the outer target is gradually decreased with the lower NB power, from the result of the NB power scan.

The I_p and B_t scan shows that the outboard He flux is enhanced near the condition of $I_p = 1.0$ MA, $B_t = 2.5$ T, $P_{NB} = 18$ MW and $\beta_p = 1.8$. The asymmetry seems to depend on β_p (including edge parameters n_e, T_e, T_i, etc.). Under the condition of $\beta_p < 1.8$, the asymmetry is reversed and the He flux is enhanced on the inboard side. Large periodic pulses of He I (667.8 nm) emission in the divertor region and the edge region of the main plasma were observed to synchronize with pulses of D_α emission at ELM pulses, using new spectroscopic measurement with a fast sampling time (50 μs). The behaviour of He at ELM pulses might be related to the in–out asymmetry of the He flux.

4. HELIUM TRANSPORT IN THE REVERSED SHEAR PLASMA

Helium transport characteristics of the reversed shear plasma were investigated using a ^{4}He beam (central fuelling) and a short pulse He gas puff (edge fuelling). Figure 4 shows the time evolution of a typical reversed shear discharge ($I_p = 1.2$ MA,

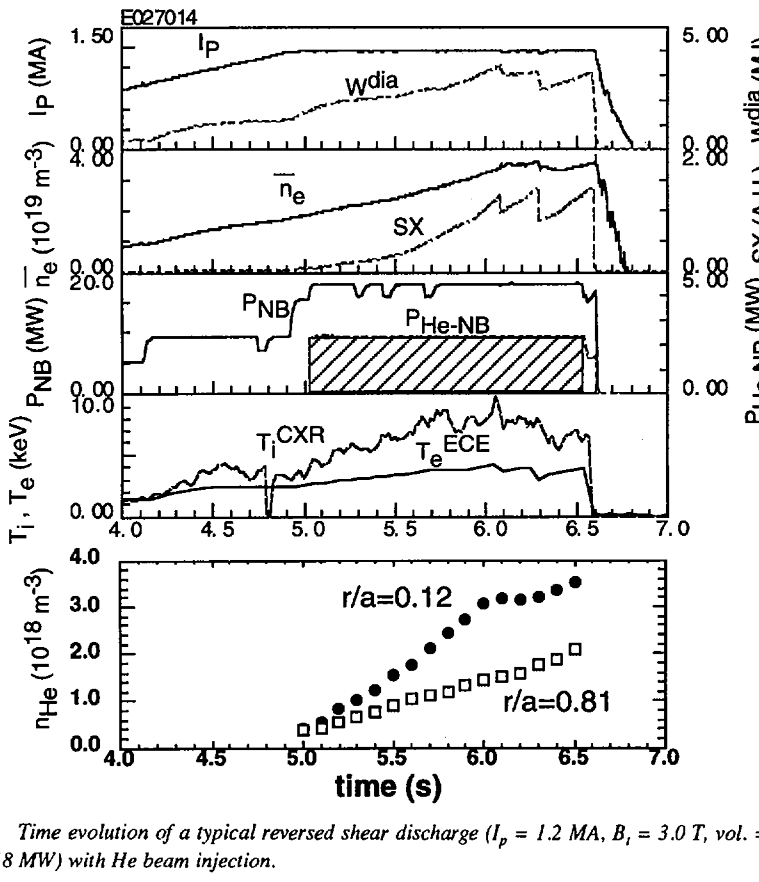

FIG. 4. Time evolution of a typical reversed shear discharge (I_p = 1.2 MA, B_t = 3.0 T, vol. = 65 m^3, P_{NB} = 18 MW) with He beam injection.

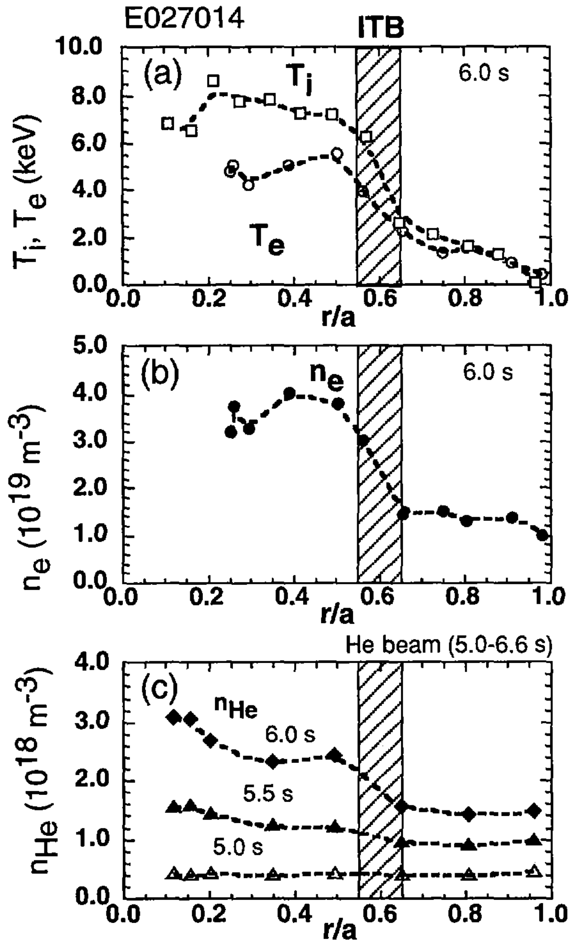

FIG. 5. (a) Ion and electron temperature profiles, (b) electron density profile and (c) He density profiles in reversed shear mode with He beam injection.

B_t = 3.0 T, vol. = 65 m^3 and P_{NB} = 18 MW) with He beam injection of $P_{He\text{-}NB}$ = 2.3 MW. The formation of the ITB started at t = 5.4 s. The increase of the He density in the core plasma (r/a = 0.12) is much faster than that in the peripheral region (r/a = 0.81). The He density in the core plasma is very peaked with the formation of the ITB. Two partial collapses occurred at t = 6.1 s and t = 6.3 s. In this discharge, the ITB was not eliminated and it re-formed. The He density in the core plasma was greatly reduced by these partial collapses. However, the He density in the peripheral region was not affected by the collapse and it linearly increased.

Figure 5 shows (a) ion and electron temperature profiles, (b) electron density profile and (c) He density profiles in reversed shear mode with He beam injection. In reversed shear mode, the electron density in the central region is peaked and the

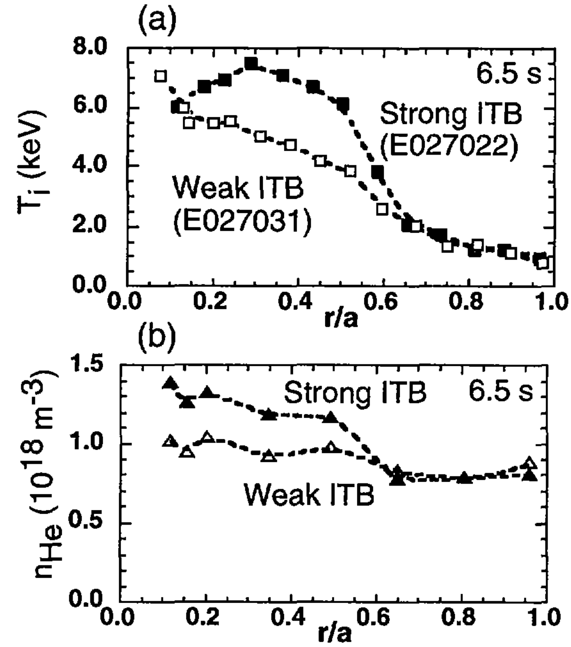

FIG. 6. Comparison of (a) ion temperature profiles and (b) He density profiles with a weak ITB and a strong ITB in reversed shear mode with He gas puffing.

confinement is greatly enhanced inside the ITB, which is formed near the position of minimum q. The profiles of $n_e(r)$, $T_e(r)$ and $T_i(r)$ inside the ITB are peaked. The ^{4}He beam injection started at t = 5.0 s and lasted for 1.5 s. The H factors are 1.5 at t = 6.0 s and 2.0 at 6.5 s. The central ion temperature is 8 keV, the central electron temperature is 5 keV and the central electron density is 4×10^{19} m^{-3}.

In the case of He beam injection, the He density is higher inside than outside the ITB, and the He density increase is much faster inside than outside the ITB. In the case of He gas puffing, the He density profile is almost flat for 0.5 s after the start of the puff. Then the He density inside the ITB continuously increases and reaches 1.4×10^{18} m^{-3} regardless of the He source. On the other hand, the He density outside the ITB reaches a saturation level of 0.8×10^{18} m^{-3} at t = 0.5 s after the start of the He gas puff.

To summarize, He accumulation was observed inside the ITB. This result indicates that it is difficult to purge He particles from inside the ITB. This behaviour of He in reversed shear mode is clearly different from that in ELMy H mode and L mode [1]. However, the profile of He concentration in the reversed shear plasma is almost flat because the $n_e(r)$ profile has almost the same shape as the He density profile.

The peaking factors of $n_e(r)$, $T_e(r)$ and $T_i(r)$ profiles inside the ITB depend on the strength of the ITB and the profiles become more peaked if a strong ITB is formed. Figure 6 shows (a) ion temperature profiles and (b) He density profiles with a strong

ITB and a weak ITB in reversed shear discharges with He gas puffing. The He gas puff of 5 Pa·m^3/s for 0.1 s started at t = 5.6 s. In the case of a strong ITB formation, the He density profile is very peaked inside the ITB, while it is almost flat in the case of a weak ITB formation. It is found that the peakedness of the He density profile depends on the strength of the ITB. This result indicates that He particle confinement is enhanced by ITB formation.

An enhancement of He particle confinement is not desirable for He exhaust. However, it was observed that He particles inside the ITB were expelled when a partial collapse occurred, as in the case of particle exhaust due to ELMs. The He flux in the divertor is three times larger after a partial collapse than before a partial collapse. Because a partial collapse terminates the ITB, He particle confinement is degraded. The partial collapse and safety factor q(r) control in reversed shear mode are expected to reduce He ash content in the core plasma.

Helium transport coefficients are determined by comparing the evolution of the measured He density profiles with calculated results using a 1-D transport code. The time evolution of the warm component intensity from the CXRS measurement is treated as the source term. In reversed shear mode with He gas puffing, He density profiles were peaked inside the ITB with time. The values of the transport coefficient were found to be $D_A = 1$ m^2/s and $V_A = -1.0$ m/s (inside the ITB), -10 m/s (near the ITB) and -2 m/s (outside the ITB), where D_A is the radial diffusion coefficient and V_A is the convective velocity. Before the formation of the ITB, the He density profile was almost flat, with $D_A = 1$ m^2/s and $C_V \approx 0.5$, which is comparable to L mode plasmas, where C_V is a dimensionless peaking parameter defined by $V_A(r) = -C_V D_A(r) 2r/a^2$ (a is the plasma minor radius). This result indicates that the He transport coefficients of reversed shear plasmas are very much different from those in L mode. The He transport in reversed shear plasmas is characterized by a large inward velocity near the ITB.

5. HELIUM REMOVAL BY SOLID TARGET BORONIZATION

The He concentration, He flux and He pressure were reduced to 1/2, 1/10 and 1/3, respectively, by solid target boronization (STB) wall pumping in ELMy H mode. In STB, the outer divertor channel hits 300 μm thick B_4C-converted CFC (carbon fibre composite) tiles, evaporating and redepositing B_4C layers on the divertor plates during a discharge. Helium and deuterium recycling is greatly reduced by STB [2].

Asymmetry control and STB permitted active He ash exhaust. Divertor operation with higher He pressure in the outboard divertor is advantageous for its good accessibility to the pumping system.

The effective He particle confinement time in the system τ^*_{He} is defined from the global He particle balance equation $dN_{He}/dt = -N_{He}/\tau^*_{He} + S_{He}$, where N_{He} is the total number of He ions in the plasma and S_{He} is the external He particle source rate (He beam or He gas puff). τ^*_{He} was evaluated during high β_p ELMy H mode from the He gas puffing experiment because $S_{He} = 0$ after the initial He gas puff; $\tau^*_{He} = 0.95$ s in an

STB discharge and $\tau^*_{He} \approx 10$ s without STB. The ratio of τ^*_{He} to the energy confinement time τ_E was τ^*_{He}/τ_E = 6–8 in an STB discharge [7]. This result is within the range generally considered to be necessary for successful operation of future reactors such as ITER [7].

6. CONCLUSIONS

The in–out asymmetry of the He flux in the divertor during ELMy H mode has been successfully controlled by changing NB power and plasma current. The effect of the ion ∇B drift direction, I_p and B_t (q_{eff}) dependence on He exhaust was investigated in ELMy H mode and L mode. The in–out asymmetry of the He flux profiles does not depend on the ion ∇B drift direction. The asymmetry seems to be determined by β_p (including edge parameters n_e, T_e, T_i, etc.). It does not explicitly depend on NB power and I_p. Helium could be effectively exhausted in combination with the control of the asymmetry and the He removal due to STB. This result suggests that selective exhaust, for example He ash removal from the outboard and fuelling particle removal from the inboard, is possible for controlling the burning of the core plasma in future reactors.

The He transport characteristics of reversed shear plasmas have been studied using He beam injection and He gas puffing. The improvement of the He particle confinement was found inside the ITB. The He density profile depends on the strength of the ITB. Helium particle confinement is enhanced by ITB formation. The He transport in reversed shear plasmas was found to be characterized by a large inward velocity near the ITB. When partial collapse occurred, He particles inside the ITB were expelled at the same time as the disappearance of the ITB. Therefore the partial collapse and safety factor q(r) control in reversed shear mode are expected to reduce He ash content in the core plasma.

ACKNOWLEDGEMENTS

The authors would like to thank the members of the Japan Atomic Energy Research Institute who have contributed to the JT-60 project.

REFERENCES

[1] SAKASAI, A., et al., J. Nucl. Mater. **220–222** (1995) 405.

[2] SAKASAI, A., et al., in Plasma Physics and Controlled Nuclear Fusion Research 1994 (Proc. 15th Int. Conf. Seville, 1994), Vol. 2, IAEA, Vienna (1995) 95.

[3] WADE, M.R., et al., J. Nucl. Mater. **220–222** (1995) 178.

[4] HILLIS, D.L., et al., in Plasma Physics and Controlled Nuclear Fusion Research 1994 (Proc. 15th Int. Conf. Seville, 1994), Vol. 2, IAEA, Vienna (1995) 87.

[5] ASAKURA, N., et al., ibid., Vol. 1, p. 515.

[6] FUJITA, T., et al., IAEA-CN-64/A1-4, this volume.

[7] REITER, D., WOLF, G.H., KEVER, H., Nucl. Fusion **30** (1990) 2141.

DISCUSSION

F. ENGELMANN: Do you have a number for the ratio τ^*_{He}/τ_E in the helium exhaust experiments on JT-60U with reversed shear and if so, how does it compare with the value in the ELMy H mode?

A. SAKASAI: Helium exhaust has not been applied in reversed shear plasmas yet, so we cannot obtain a good value of τ^*_{He}/τ_E in the reversed shear plasma.

EXPERIMENTAL EVIDENCE FOR THE SUITABILITY OF ELMing H-MODE OPERATION IN ITER WITH REGARD TO CORE TRANSPORT OF HELIUM*

M.R. WADE[1], D.L. HILLIS[1], K.H. BURRELL, T.C. LUCE, R. MAINGI[2],
P.K. MIODUSZEWSKI[1], C.C. PETTY, W.P. WEST, R.-M. HONG,
D.H. KELLMAN, J.C. PHILLIPS, DIII-D TEAM
General Atomics,
San Diego, California,
United States of America

Abstract

EXPERIMENTAL EVIDENCE FOR THE SUITABILITY OF ELMing H-MODE OPERATION IN ITER WITH REGARD TO CORE TRANSPORT OF HELIUM.

Studies have been conducted in DIII-D to assess the viability of the ITER design with regard to helium ash removal, including both global helium exhaust studies and detailed helium transport studies. With respect to helium ash accumulation, the results are encouraging for successful operation of ITER in ELMing H-mode plasmas with conventional high-recycling divertor operation. Helium can be removed from the plasma core with a characteristic time constant of ~ 8 energy confinement times, even with a central source of helium. Furthermore, the exhaust rate is limited by the pumping efficiency of the system and not by transport of helium within the plasma core. Helium transport studies have shown that $D_{He}/\chi_{eff} \sim 1$ in all confinement regimes studied to date and there is little dependence of D_{He}/χ_{eff} on the normalized gyroradius in dimensionless scaling studies, suggesting that D_{He}/χ_{eff} will be ~ 1 in ITER. These observations suggest that helium transport within the plasma core should be sufficient to prevent unacceptable fuel dilution in ITER. However, helium exhaust is also strongly dependent on many factors (e.g. divertor plasma conditions, plasma and baffling geometry, flux amplification, pumping speed) that are difficult to extrapolate. Studies have revealed that the helium diffusivity decreases as the plasma density increases, which is unfavorable to ITER's extremely high density operation.

1. INTRODUCTION

The fusion power generated in the plasma core of a fusion reactor such as the International Thermonuclear Experimental Reactor (ITER) is integrally linked to the level of helium ash remaining in the core plasma, which for a given plasma density determines the number of fuel ions available for fusion processes. Hence, improvements in energy confinement (e.g., H–mode, VH–mode, and negative central shear (NCS) regimes) that are accompanied by even larger improvements in helium confinement are not necessarily favorable when extrapolating to a reactor. Studies on

[1] Oak Ridge National Laboratory, Oak Ridge, Tennessee, USA.

[2] Oak Ridge Associated Universities, Oak Ridge, Tennessee, USA.

* Work supported by the US Department of Energy under Contract Nos DE-AC03-89ER51114, DE-AC05-96OR22464 and DE-AC04-94AL85000, and Grant Nos DE-FG03-86ER53266 and DE-FG03-95ER54294.

DIII–D in a variety of confinement regimes (including L–mode, H–mode, and VH–mode) have assessed whether helium buildup poses substantial problems in these regimes. The majority of these studies have been conducted in H–mode plasmas with edge localized modes (ELMs). The results obtained to date are encouraging for the successful operation of ITER in ELMing H–mode plasmas with conventional high-recycling divertor operation.

2. ITER REQUIREMENTS

Because the specific ITER requirements are difficult to scale to a present-day device due to differences in geometry, exhaust capacity, etc., this discussion will primarily concentrate on physics requirements, not specific engineering requirements. The helium exhaust problem is truly global in nature since the helium ash is generated in the plasma core and can only be removed from the system via pumping at the plasma edge. Since the source of thermal energy and the source of helium ash are the result of alpha particle thermalization, the energy and helium particle continuity equations (either the 0-D or 1-D forms) are coupled. Global transport studies have shown that in order to prevent unacceptable fuel dilution, the characteristic He removal time must be less than 7–15 energy confinement times, (i.e., $\tau^*_{He}/\tau_E < 7$–15), depending on the impurity content of the plasma [1]. Here, τ^*_{He} is the global helium confinement time and τ_E is the energy confinement time. In terms of local transport, one can combine the thermal and helium continuity equations (assuming that the alpha particles thermalize completely on the flux surface on which they were generated) to get the following equation for the helium density profile [2]:

$$\frac{dn_{He}}{dr} - \frac{V_{He}}{D_{He}} = -n\frac{\chi_{eff}}{E_\alpha D_{He}}\frac{dT}{dr} \tag{1}$$

where V_{He} is the convection velocity for helium, D_{He} is the helium diffusivity, χ_{eff} is the single-fluid thermal diffusivity, E_α = 3.5 MeV is the alpha particle energy, and n and T are the plasma electron density and temperature, respectively. Note that this equation is only valid in regions where the recycling source is negligible. The primary parameters determining the helium density profile are the ratios V_{He}/D_{He} and D_{He}/χ_{eff}. Simulations of helium exhaust in ITER have shown that the helium content is extremely sensitive to the value of D_{He}/χ_{eff} with values of $D_{He}/\chi_{eff} \leq$ 0.5 being unacceptable [3].

3. HELIUM EXHAUST WITH A CENTRAL SOURCE OF HELIUM

Previous experiments on DIII–D with helium introduced via gas puffing at the plasma edge have shown that sufficient helium exhaust can be achieved ($\tau^*_{He}/\tau^*_E \approx 8$) simultaneously with good energy confinement in an H–mode plasma with ELMs [4]. To extend these results to a case with a central source of helium, as would be expected in a reactor, experiments with continuous helium neutral beam injection have been conducted on DIII–D. This central helium source coupled with simultaneous divertor exhaust provides a full simulation of the situation in a burning device. The DIII–D neutral beam system now includes the capability of 2.0 s steady-state He neutral beam injection (NBI). Divertor exhaust of helium is facilitated by condensing an argon (Ar) frost layer (~1.5 μm thick) on the liquid helium surface of the DIII–D divertor cryopump.

These experiments were carried out in a single-null divertor configuration with the ion grad-B drift towards the lower divertor, a plasma current of 1.0 MA, magnetic field of 2.1 T, and a major radius of 1.67 m. In these discharges (Fig. 1), the plasma density and temperature are held approximately constant during the period of interest through feedback control of plasma density via deuterium gas injection. Helium beam injection (3.0 MW at 75 keV) is initiated at 2.0 s and maintained for 1.4 s. The helium density in the plasma core, as measured by charge-exchange recombination (CER) spectroscopy, responds immediately to the initiation of helium NBI. Throughout the He NBI phase, the divertor outer strike point (OSP) is maintained in the optimal location for divertor exhaust. The time behavior of both the helium density and total core inventory of helium [Fig. 1(c)] is observed to follow the expected temporal evolution given by:

$$N_{He}(t) = N_{He}(t_o) + \left[S_{He}\tau^*_{He} - N_{He}(t_o)\right]\left\{1 - \exp\left[-\frac{(t-t_o)}{\tau^*_{He}}\right]\right\} \qquad (2)$$

where N_{He} is the total number of He ions in the plasma and S_{He} is the instantaneous He source rate. Least-squares fitting of the evolution of the helium inventory to Eq. (2) and standard energy balance analysis give $\tau^*_{He}/\tau_E \approx 8.5$, well within the range necessary for ITER. The shape of the helium density profile remains essentially the same during the He beam injection phase after a brief transient. This observation and the flat profiles even in the presence of a central He source indicate high core transport rates and that transport does not limit the helium exhaust rate. This observation is corroborated by particle balance calculations based on CER and Penning gauge measurements, which show that the removal rate is determined by the equilibration time between the divertor plasma and the pumping plenum, which is observed to be on the order of 1.0 s, whereas the core-to-divertor equilibration time is ~ 100 ms. The enrichment factor γ (defined as ratio of the helium fraction in the pumping plenum to the helium fraction in the core) is in the range $0.2 \le \gamma \le 0.6$, meeting the present ITER design criterion that $\gamma \geq 0.2$.

4. HELIUM TRANSPORT STUDIES

Helium transport studies on DIII–D are carried out by injecting a small amount (~3%–5% of the electron density) of helium gas during an otherwise steady-state portion of the discharge. The helium density profile evolution subsequent to this puff is monitored by CER with a minimum time resolution of 5 ms. The local helium transport coefficients are then determined via regression analysis of the inferred local helium particle flux and the measured helium density gradients, assuming the flux takes on the general form $\Gamma_{He} = -D_{He}\nabla n_{He} + V_{He}n_{He}$ [5].

As discussed in Section 2, the primary parameters of interest in helium transport studies are the ratios D_{He}/χ_{eff} and V_{He}/D_{He}. In general, the helium density profiles in ELMing H–mode plasmas are nearly flat in the inner regions of the plasma core (ρ ≤ 0.5) . Hence, the parameter V_{He}/D_{He} is typically very small (≤0.01 m^{-1}). In all confinement regimes studied to date, the steady-state helium density profile has the same shape as the electron density shape, suggesting that preferential helium accumulation will not be a problem in ITER [5]. Studies on DIII–D have shown that

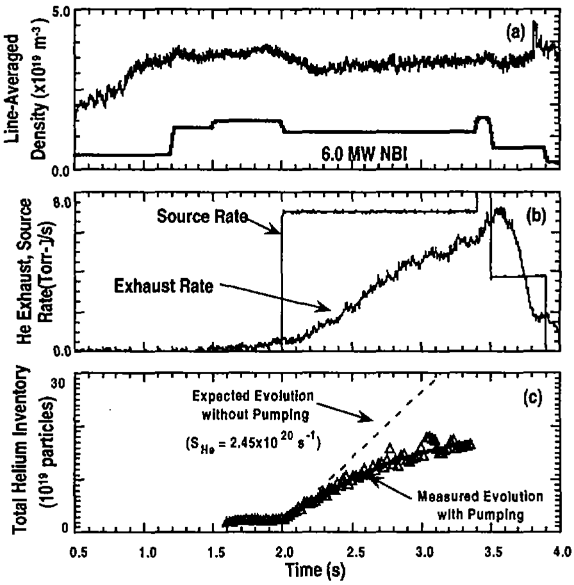

FIG. 1. Time evolution of the (a) line-averaged density, injected power, (b) helium source and exhaust rates, and (c) total helium inventory within the core plasma for a typical discharge with helium NBI. Helium NBI is applied starting at 2.0 s and maintained until 3.5 s. The predicted helium density and inventory if no helium exhaust were present are plotted as dotted lines in (c).

D_{He}/χ_{eff} ~ 1 for all confinement regimes studied to date including L–mode, ELM-free H–mode, ELMing H–mode, and VH–mode (Fig. 2). This suggests that the helium transport within the plasma core of ITER should not pose significant problems. However, helium transport and energy transport may scale quite differently from present-day devices to ITER. To address this issue on DIII–D, nondimensional scaling studies, which have primarily emphasized energy transport in the past, have been expanded to include helium transport studies. The premise in these studies is that the diffusivity (either thermal or particle) can be written in the form:

$$\chi = \chi_B(\rho_*)^{\alpha} F(\beta, \nu_*, q, R/A, \kappa, \ldots) \tag{3}$$

where F is an arbitrary function of all of the relevant dimensionless parameters except ρ_*, the gyroradius normalized to the machine size. The diffusivity is normalized to the Bohm diffusion coefficient, $\chi_B \equiv cT/eB$, for convenience. The primary unknown in extrapolating from present-day devices to ITER is the dependence of transport on ρ_* since present-day experiments can operate at ITER-like values for all the other dimensionless quantities. Experimentally, one can determine the exponent α in Eq. (3) by varying ρ_* while holding F (or equivalently all the other dimensionless quantities) constant. Energy transport experiments of this kind in ELMing H–mode plasmas in the ITER shape and ITER-like dimensionless parameters on DIII–D have shown the scaling to be "gyro-Bohm"-like, with the characteristic transport scale lengths being on the order of a gyroradius [6, 7].

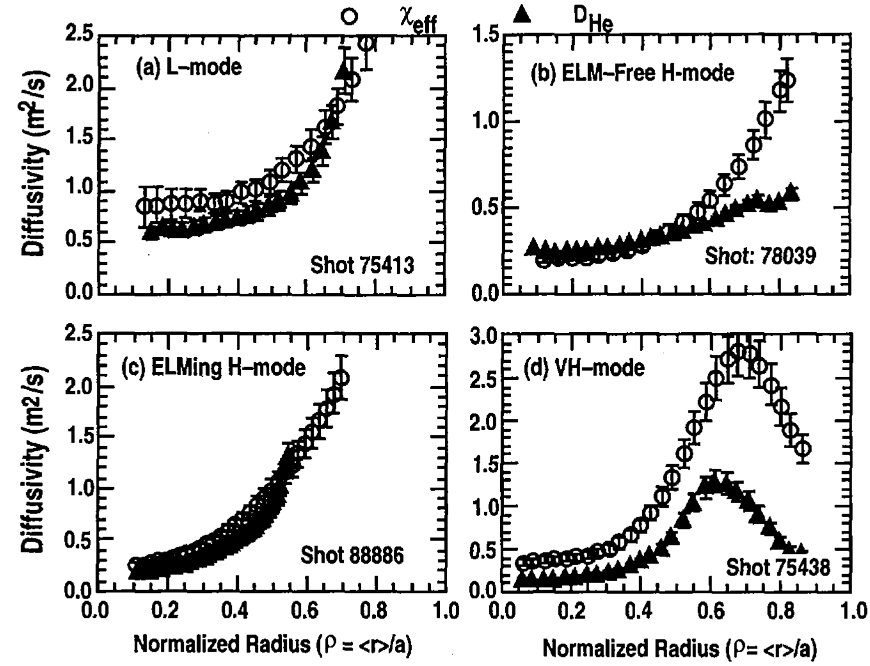

FIG. 2. Helium diffusivity (solid triangles) and single-fluid thermal diffusivity (circles) for an (a) L-mode, (b) ELM-free H-mode, (c) ELMing H-mode, and (d) VH-mode discharge. Note that this data is from discharges with different plasma current, injected power, etc., so care should be taken in comparing the magnitudes of the diffusivities.

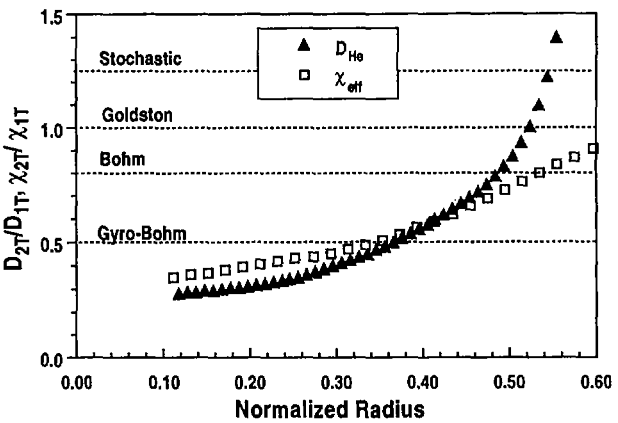

FIG. 3. Ratio of the helium and single fluid diffusivities inferred for the dimensionally similar discharges described in the text. See Ref. [7] for a more detailed description of the labels.

For the experiments discussed here, both the plasma shape (lower single-null divertor with κ = 1.68 and δ = 0.36) and the expected ITER parameters were approximately matched - β^{th} = 1.72 %, β_N^{th} = 1.67 % (MA/m-T), $\nu_{*i,min}$ = 0.01, and q_{95} = 3.8. To obtain a variation in the gyroradius of 1.5 while the other dimensionless parameters were held nearly constant, measurements were made in two cases: (1) B_T = 2.1 T, I_p = 1.14 MA, n_e = 6.26×10^{19} m^{-3}, P_{input} = 5.9 MW, and (2) B_T = 1.05 T, I_p =0.57 MA, n_e = 2.74 × 10^{19} m^{-3}, P_{input} = 1.2 MW . The helium diffusivity is inferred from analysis of the evolution of the helium density profile subsequent to a helium gas puff during an otherwise steady-state portion of the discharge. Note that because the propagation of the helium perturbation to ρ = 0.6 in the B_T = 1.05 T case is too rapid (~70 ms) to be followed accurately by the CER system, transport analysis of this discharge is limited to the interior regions of the plasma ($\rho \leq 0.5$). Using the premise of Eq. (3), the scaling of helium diffusivity with ρ_* is found to be approximately gyro-Bohm-like (Fig. 3). The transport analysis further suggests that inward convection (i.e., particle pinch) is considerably larger in the 2.1 T case outside ρ = 0.4. This would have the effect of decreasing the net transport rate in the 2.1 T case relative to the 1.05 T case. Therefore, if one considered the ratio of the net helium transport rate instead of simply the helium diffusivity, the scaling for $\rho \geq 0.4$ would be adjusted closer to gyro-Bohm. Energy transport analyses of the same discharges have shown the thermal diffusivity to scale with ρ_* in a similar manner as the helium diffusivity. Hence, D_{He}/χ_{eff} has at most a weakly linear dependence on ρ_*, which is favorable in the extrapolation to ITER.

Scaling studies of the dependence of the helium transport coefficients with various parameters in ELMing H–mode plasmas have also been done. Studies in which the injected power was varied have shown that D_{He} and $|V_{He}|$ increase as the injected power is increased [5]. Both of these trends are favorable in terms of extrapolation to future, high-power devices. To assess the density dependence, helium transport data has been obtained during a density scan in ELMing H–mode in DIII–D in a lower, single-null diverted discharge with I_p = 1.0 MA, B_t = −2.1 T, q_{95} = 5.5. In the first case, the plasma density was maintained at 4.9 × 10^{19} m^{-3} (0.53 n_{GW}, where $n_{GW} = I_p/\pi a^2$ (10^{20} m^{-3}, *MA, m*) is the Greenwald density limit [8]) with 6.5 MW of neutral beam power. In the second case, the density was reduced by approximately 40% to 3.2 × 10^{19} m^{-3} (0.34 n_{GW}) using the divertor cryopump on DIII–D, and the neutral beam injection power was reduced to 4.1 MW in order to maintain similar plasma temperatures in the two cases. Transport analysis shows that the helium diffusivity is approximately 50% lower in the higher density case. Energy transport analysis has shown that χ_{eff} changes only slightly in these cases, which is consistent with previous studies that have shown little dependence of global energy confinement on density [9]. No attempt was made in these experiments to maintain similarity in the dimensionless quantities. Therefore, it is possible that this variation is simply due to the parametric dependence of helium diffusivity on one (or even several) of the dimensionless quantities in Eq. (3), most notably collisionality. However, this data does present a concern because ITER seeks to operate at densities significantly above the Greenwald limit.

5. SUMMARY AND CONCLUSIONS

The results presented here are promising as far as helium ash removal in ITER is concerned. The successful demonstration of helium exhaust with a central source of helium in an ELMing H–mode plasma is encouraging, especially considering that the estimated exhaust efficiency is ~5%. An equally encouraging result is that D_{He}/χ_{eff} is found to be ~1 and there appears to be a weak dependence of D_{He}/χ_{eff} on normalized gyroradius, making the extrapolation less uncertain as far as core transport rates are concerned. These observations suggest that core transport rates for helium will be sufficient for ITER in ELMing H–mode plasmas.

However, helium exhaust is strongly linked to the exhaust capabilities of a particular device. The exhaust efficiency is dependent on plasma and baffling geometry, flux amplification, pumping speed, etc., which makes the extrapolation from present-day devices to ITER design dependent. Because of this reason, this review has not addressed the extrapolation of the results from detailed divertor studies of helium in DIII–D [10]. Also, the divertor plasma in ITER is expected to be in a detached state, characterized by low temperature and high density such that the mean free path against ionization of the helium neutrals recycling from the divertor surface will be quite long. Since this could lead to a reduction in the retention of helium in the divertor plasma, the helium exhaust results presented in Section 2 may not be nearly as favorable if done with a detached divertor plasma. In this regard, detailed studies of helium transport in the plasma edge and divertor plasma in combination with two-dimensional modeling are required to make a better assessment of the extrapolation of the present set of results to the specific ITER design.

REFERENCES

[1] REITER, D., WOLF, G.H., KEVER, H., Nucl. Fusion **30** (1990) 2141.

[2] SYNAKOWSKI, E.J., et al., Phys. Fluids B **5** (1993) 2215.

[3] REDI, M.H., COHEN, S.A., SYNAKOWSKI, E.J., Nucl. Fusion **31** (1991) 1689.

[4] WADE, M.R., et al., Phys. Rev. Lett. **74** (1994) 2702.

[5] WADE, M.R., et al., Phys. Plasmas **2** (1995) 2357.

[6] PETTY, C.C., et al., Phys. Plasmas **2** (1995) 2342.

[7] LUCE, T.C., et al., in Plasma Physics and Controlled Nuclear Fusion Research 1994 (Proc. 15th Int. Conf. Seville, 1994), Vol. 1, IAEA, Vienna (1995) 319.

[8] GREENWALD, M., et al., Nucl. Fusion **28** (1988) 2199.

[9] SCHISSEL, D.P., et al., Nucl. Fusion **34** (1994) 1401.

[10] WADE, M.R., et al., J. Nucl. Mater. **220-222** (1995) 178.

IMPURITY TRANSPORT AND EXHAUST IN RADIATIVE EDGE EXPERIMENTS IN ASDEX UPGRADE

H.-S. BOSCH, A. KALLENBACH, D.P. COSTER,
R. DUX, G. HAAS, M. KAUFMANN,
K. LACKNER, J. NEUHAUSER,
S. DE PEÑA HEMPEL, R. SCHNEIDER,
ASDEX UPGRADE, NBI and ICRH TEAMS
Max-Planck-Institut für Plasmaphysik,
Euratom-IPP Association,
Garching und Berlin, Germany

Abstract

IMPURITY TRANSPORT AND EXHAUST IN RADIATIVE EDGE EXPERIMENTS IN ASDEX UPGRADE.

For continuous burn of an ignited fusion plasma, helium exhaust is a critical issue because helium accumulation would lead to plasma dilution and to a radiation collapse. In addition, radiative plasma scenarios, as envisaged for ITER, depend strongly on the controllability of the injected impurities, i.e. on scrape-off layer transport and exhaust of these gases on a sufficiently fast time-scale. The paper discusses transport and exhaust of helium and neon as well as general features of radiative H mode discharges (CDH mode) in ASDEX Upgrade.

Introduction

To sustain a burning plasma in ITER or any fusion reactor, the impurity concentration in the bulk plasma has to be kept very low. Apart from the minimization of the influx of impurities from divertor target plates and wall, there are special problems with He, as it is produced intrinsically by the fusion process, and with Ne, here discussed as one example of rare gases which may be used to decrease the power flow onto the target plates by radiation in the plasma edge and/or in the divertor.

Both ion species have to be exhausted at a rate which in the case of He prevents intolerable plasma dilution, and for Ne guarantees radiation control on time-scales short compared to the relevant inherent energy balance time-scales. Exhaust of recycling gases depends strongly on particle transport in the plasma core, but it is primarily controlled by scrape-off layer (SOL) transport and pumping.

In this paper first scrape-off layer transport and pumping is discussed for both He and Ne, then we discuss details of He transport in the core and fimally radiation losses from Ne and the establishment of the CDH mode in ASDEX Upgrade.

1 Scrape-off layer transport and exhaust

To optimize particle exhaust, the neutral density in front of the pump duct has to be maximized. In parallel, the concentration of the minority gases (He or Ne) has to be high in order to keep the hydrogen isotopes gas throughput as low as possible. This requires a compression of the minority particles in the scrape-off layer (SOL) and divertor, i.e. a large ratio of He or Ne neutral gas density in the divertor region compared to the edge ion density of the respective species. As local measurements of the impurity density in the divertor neutral gas are not (yet) available in ASDEX Upgrade, we derive the compression factor in decay experiments from the temporal variation of recycling fluxes (line radiation of low ionization stages) at the plasma edge, using a simplified two-chamber model [1] and the known (calibrated) external pumping efficiency.
An overview of experimental data for He and Ne is shown in figure 1, where recycling decay rates and the compression ratios derived from them are shown

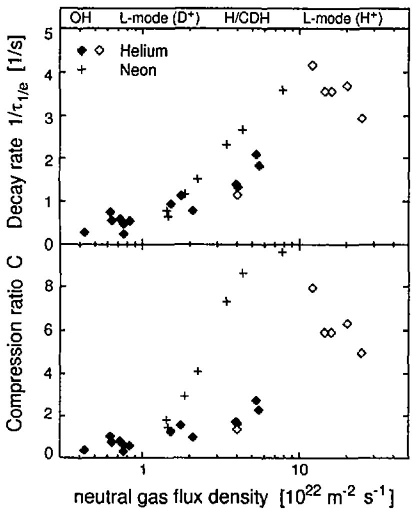

Figure 1: Decay rates of recycling signals for He and Ne in deuterium (solid data points) and hydrogen plasmas (light squares). The bottom graph shows the corresponding compression factor, derived with a two-chamber model, demonstrating better compression of Ne as compared with He. For both species, however, the compression increases with $\phi_{0,div}$.

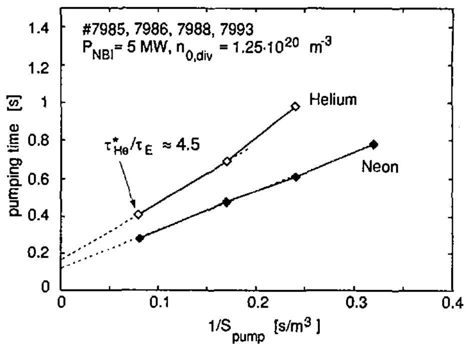

Figure 2: Extrapolation of HeII- and NeVII-line radiation decay rates, which are a measure for the global particle confinement time τ_p^*, to infinite pumping speed allows the determination of τ_p . The x-axis shows the inverse pumping speed which is varied by switching off turbomolecular pumps via gate valves.

as a function of the divertor neutral flux density $\phi_{0,div}$ which is a measure for the deuterium background neutral density. Although these data are taken in very different plasma regimes and have large scatter, they show a strong increase of divertor retention with $\phi_{0,div}$ [1, 2]. This increase is thought to be due to the neutral gas reservoir in the divertor chamber which is proportional to $\phi_{0,div}$. The neutrals in this rather large chamber in ASDEX Upgrade (reaching up to the height of the X-point) can be reionized in the outer part of the SOL and then introduce a recirculating flux which entrains the impurities and keeps them in the divertor [3].

At a given, constant pumping speed, the increase in divertor neutral pressure is achieved by increasing the external gas throughput which also increases the particle flow everywhere in the scrape-off layer, and in principle it could also be this externally induced particle flux which is responsible for the improvement in divertor retention [4]. However, varying the pumping speed (number of active turbomolecular pumps) for constant neutral pressure at the pump duct and hence varying the net particle throughput, demonstrates that it is not entrainment of the impurities by the externally induced deuterium flux (from the main chamber), but rather the recirculating flux from neutrals in the divertor chamber which provides the divertor retention[5]. This simple model has been confirmed by 2D-modelling of the SOL and divertor plasma [6].

Figure 1 also shows that the He compression is lower than that of Ne for most conditions, and usually He is even de-enriched, i.e. the He fractional density in the pumped gas is smaller than at the plasma edge, mainly because of its longer mean free path compared with Ne. But in discharges with high divertor neutral gas pressure, the enrichment factor of He is larger than about 0.3 [3], which is consistent with the ITER requirement of a value of 0.2 [7].

2 He transport in the bulk plasma

Experimentally, from the decay of short, external gas puffs one determines the effective particle confinement time τ_p^*, which is determined both by the bulk plasma particle confinement time τ_p and by the internal recycling and external pumping. Varying the pumping speed for constant divertor parameters allows a separation of these different confinement times by extrapolation to infinite pumping. An analytical model shows that τ_p^* should vary linearly with the pumping time constant (proportional to the inverse pumping speed), the extrapolated value for infinite pumping speed being τ_p [8]. Such an experiment in an H mode discharge is shown in figure 2 for He and for Ne. It can be seen that again $\tau_{Ne}^* < \tau_{He}^*$, but the two relations converge to a common central confinement time $\tau_{Ne} = \tau_{He}$ which is considerably lower. This shows that in these H mode discharges impurity transport in the core plasma is rather fast, and impurity exhaust is limited by transport in the SOL and by the available pumping, not by core particle confinement.

Concerning He exhaust, the value of $\tau^*_{He}/\tau_E \simeq 4.5$ with the regular pumping speed available in ASDEX Upgrade indicates exhaust compatible with ignition conditions [9]. In H mode and radiating boundary discharges values as between about 4 and 8 have been achieved [2]. This has been found to be independent of the scrape-off layer plasma being attached to or detached from the divertor target plates [3], presumably due to the large height of the divertor baffle.

3 Ne exhaust and feedback control of radiation

As discussed above, the exhaust rate of Ne is usually much higher than that of He, and increases with divertor neutral density. This allows feedback control of Ne puffing to keep the radiation losses from the plasma constant and has led to a scenario with a large radiated power fraction and a detached divertor plasma, while preserving H mode confinement, the so-called CDH-Regime (Completely Detached H Mode)[1, 10]. Time traces of a CDH discharge are shown in figure 3.

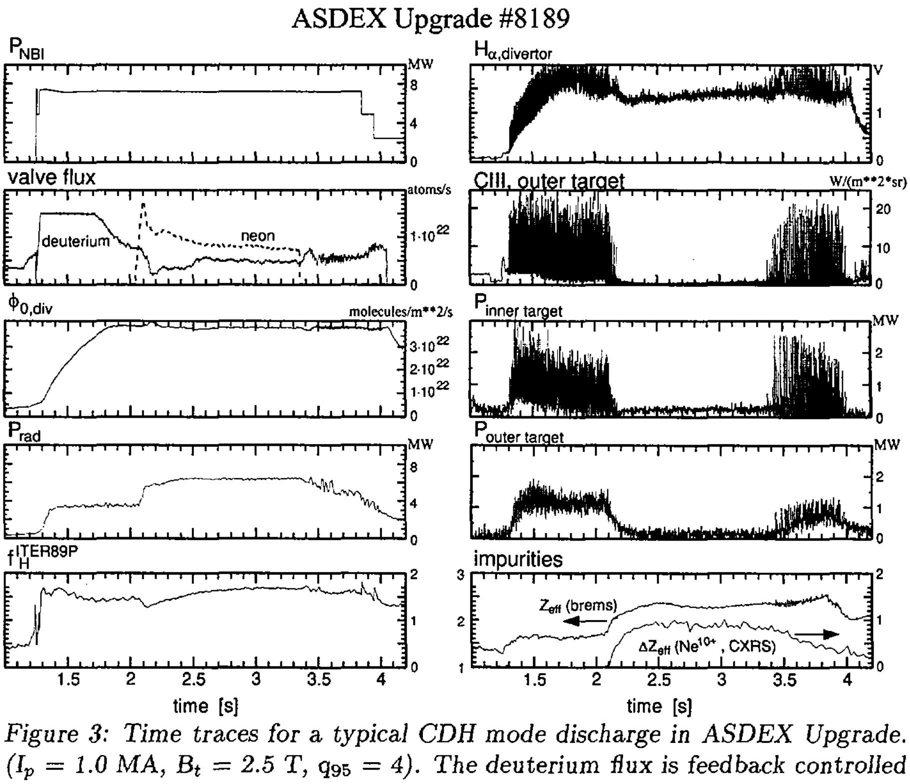

Figure 3: Time traces for a typical CDH mode discharge in ASDEX Upgrade. (I_p = 1.0 MA, B_t = 2.5 T, q_{95} = 4). The deuterium flux is feedback controlled to keep the divertor neutral flux density constant, and the neon puff is feedback controlled on the total radiation loss (about 90 % of the input power). During the CDH mode the power flow to the target plates is strongly reduced and the ELMs change from type-I to type-III.

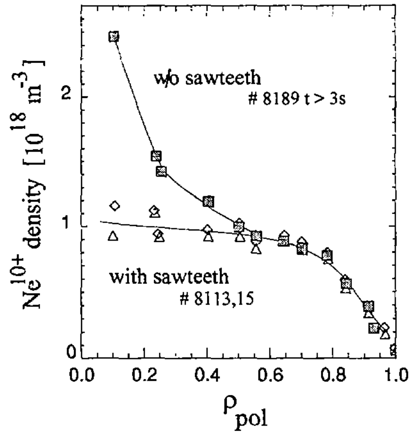

Figure 4: Radial profiles of fully ionised neon from CXRS for standard CDH discharges with and without sawtooth activity. Both discharges have the same radiation loss in the bulk plasma, where the neon density is rather similiar, but the central plasma dilution is strongly improved with sawteeth.

The external deuterium puff (in the midplane) is feedback controlled on the divertor neutral flux density, and a Ne puff is feedback controlled on the total radiated power. With the beginning of the neon puff the plasma detaches, as is monitored by the strong drop in CIII light in front of the outer target plate (very close to the plate), and in the total power to the target plates (measured with thermography). With the increase in radiation losses, the power flow over the separatrix drops to a value just above the L-H back-transition threshold, and the large type-I ELMs change to small, tolerable type-III ELMs, as one can see in the H_α or CIII light or in the target power load. During the CDH mode the energy confinement increases slightly (compared to the value without radiation, but high neutral gas density in the vacuum vessel), and $\tau_E \simeq 1.7 \cdot \tau_{ITER89P}$. The strong reduction in the target plate power load makes this operational mode one possible scenario for the operation of ITER, as has been discussed in more detail in [11].

It has been found, however, that the Ne concentration at the edge, which is needed to radiate about 90% of the input power (both by Ne and intrinsic impurities), leads to too high concentrations in the plasma, as can be seen by the increase in Z_{eff} due to Ne, shown in the bottom trace of figure 3. In this discharge no sawteeth are present as is usually the case for this q-value (q_{95} = 4) in ASDEX Upgrade. However, these discharges are only marginally stable against sawteeth, and in some cases sawteeth appear, improving the impurity situation considerably, as is seen in figure 4. The two discharges shown here have the same power radiated by neon at the plasma edge, but the central dilution differs by more than a factor of 2.

Detailed analysis of the spatial distribution of the Ne radiation shows that a considerable fraction of this power loss occurs inside the separatrix. This loss in the bulk is responsible for the beneficial change in ELM type, as it lowers the power flow over the separatrix to values close to the L-H threshold. On the other hand, the power flow must not fall below the threshold to retain H mode. Therefore increased radiation in theSOLand divertor would be preferable. To explore this problem in more detail, experiments with other gases (i.e. N_2 and Ar) have been compared with our neon seeded discharges. Argon with its maximum of the radiation characteristics at higher electron temperature than neon radiates an even larger fraction inside the bulk plasma, while nitrogen shows the largest fraction of radiated power in the divertor among the three elements. However, the N_2 seeded discharges show compound ELMs and short L mode phases and no good stationary CDH mode could be established [12]. Also strong wall pumping of nitrogen has been observed, excluding it as a seed impurity for stationary long pulse operation.

4 Conclusion

Helium exhaust in ASDEX Upgrade has been found to improve with increasing divertor neutral flux density, and in H mode discharges and radiative CDH mode discharges the helium enrichment in the divertor chamber is sufficient when compared with the ITER requirements, i.e. the enrichment factor $\eta > 0.2$, or if expressed in global particle confinement times, $\tau^*_{He}/\tau_E \simeq 4.5$. However, this depends strongly on the pumping capacity, and therefore these numbers cannot be directly projected to ITER. The helium core confinement time τ_{He} has been determined by an extrapolation to infinite pumping speed, and for high neutral divertor density it is of the order of $2 \times \tau_E$, certainly sufficient for ITER.

Highly radiating plasmas with Ne puffing at high divertor density show good confinement with detachment from the divertor plates (CDH mode). However, without sawteeth these plasmas show too high Z_{eff}. If sawteeth can be maintained, the impurity profile stays rather flat and Z_{eff} in the plasma center is sufficiently low.

Experiments with N_2 and Ar have demonstrated some potential to tailor the radiation profile which might be necessary to fulfil simultaneously different requirements concerning ELM type, power threshold and density limit.

REFERENCES

[1] KALLENBACH, A., et al., Nucl. Fusion 35 (1995) 1231.

[2] BOSCH, H.-S., et al., Particle exhaust studies in ASDEX Upgrade (in preparation).

[3] BOSCH, H.-S., et al., Particle exhaust in radiative divertor experiments, J. Nucl. Mater. (in press).

[4] SCHAFFER, M., et al., Direct measurement of divertor neon enrichment in DIII-D, J. Nucl. Mater. (in press).
[5] BOSCH, H.-S., et al., Phys. Rev. Lett. **76** (1996) 2499.
[6] SCHNEIDER, R., et al., IAEA-CN-64/D3-1, these Proceedings, Vol. 2.
[7] JANESCHITZ, G., et al., Plasma Phys. Control. Fusion **37** (1995) A19.
[8] BOSCH, H.-S., et al. (in preparation).
[9] REITER, D., et al., Nucl. Fusion **30** (1990) 2141.
[10] GRUBER, O., et al., Phys. Rev. Lett. **74** (1995) 4217.
[11] NEUHAUSER, J., et al., Plasma Phys. Control. Fusion **37** (1995) A37.
[12] KALLENBACH, A., et al., Radiative boundary discharges and the H–L transition, Plasma Phys. Control. Fusion (in press).

EROSION AND TRANSPORT OF TUNGSTEN IN ASDEX UPGRADE

K. KRIEGER, K. ASMUSSEN, R. NEU, V. ROHDE,
J. ROTH, R. SCHWÖRER, A. THOMA,
ASDEX UPGRADE, NBI and ICRH TEAMS
Max-Planck-Institut für Plasmaphysik,
Euratom-IPP Association,
Garching and Berlin,
Germany

Abstract

EROSION AND TRANSPORT OF TUNGSTEN IN ASDEX UPGRADE.

To prove the suitability of tungsten as a material for divertor target plates, tungsten coated divertor tiles were mounted in the ASDEX Upgrade tokamak. Under normal discharge conditions, the W-concentrations in the confined plasma were found to be in the range of 10^{-5} and below, with negligible influence on the overall plasma parameters. Tungsten net erosion yields were determined from ion beam surface analysis of test tiles exposed at the outer target plate. The observed net yields were lower than the total yields obtained in ion beam sputtering experiments, owing to the effect of prompt local redeposition of W^+ ions. The deposition pattern of tungsten at target plates, limiters and wall elements was determined by analysis of long term sample probes and by analyzing collector probes exposed in single discharges. Combining the erosion and deposition measurements, it was possible to establish a global migration pattern for tungsten.

1 INTRODUCTION

The choice of plasma facing materials, in particular for divertor components, is an important design issue for the construction of next step fusion devices like ITER. Beryllium or graphite are used as divertor materials in most of present day tokamaks due to their low atomic charge. Both materials, however, show deficiencies, which might be unacceptable for use in a future fusion device. Graphite has a large hydrogen retention capability, which might lead to an unacceptable tritium inventory and there is evidence for unfavorable chemical erosion. Beryllium suffers from a high physical sputtering yield (3.5% for a D^+ plasma with T_i=10eV [1]) as well as from a low melting point and a high vapor pressure.

Tungsten, on the other hand, exhibits much more favorable properties with respect to erosion, hydrogen retention and other physical properties. However, the high self-sputtering yield makes the use of tungsten only feasible for low T_e ($\lesssim$ 75eV [2]), high n_e divertor conditions. Additionally, due to the high radiation power of W, its fractional abundance in the main plasma must be kept below 10^{-5}.

To investigate the feasibility of tungsten in a divertor tokamak under reactor relevant conditions, W-coated divertor tiles were mounted in the ASDEX Upgrade divertor. The major points of interest were the investigation of erosion processes, the transport of eventually sputtered W atoms into and in the bulk plasma and finally the deposition in main chamber and divertor. Tungsten behavior was investigated mainly by observation of spectral lines in the main plasma and the divertor [3, 4] and by analyzing material erosion and deposition of exposed probes using ion beam techniques [5, 6].

2 THE TUNGSTEN DIVERTOR EXPERIMENT

The tungsten divertor in ASDEX Upgrade was established as two toroidal belts of tungsten coated graphite tiles covering the radial extent of the inner and outer strike point location (Fig. 1). A few customized graphite tiles covering approximately 10% of the total area were left for Langmuir probe arrays and the divertor thermography diagnostic. The tungsten coating with a thickness of 0.5mm was produced by plasma spray deposition onto graphite substrate with a W/Re-multilayer as diffusion barrier to prevent formation of tungsten carbide [7]. To avoid excessive heat loads by plasma streaming onto leading edges, the tiles were mounted with a slight tilt. As a consequence the plasma discharges were restricted to operation with the direction of I_p antiparallel to B_t. Apart from this boundary condition, the discharges covered almost the full accessible range of plasma current ($0.6\text{MA} \leq I_p \leq 1.2\text{MA}$), density ($2\times10^{19}\text{m}^{-3} \leq \bar{n}_e \leq 1.5\times10^{20}\text{m}^{-3}$) and heating power ($P_{aux} \leq 10\text{MW}$). The resulting power load of the target plates reached 6MW/m^2 under stationary conditions and peak loads of up to 15MW/m^2 during ELMs in low density H-mode discharges.

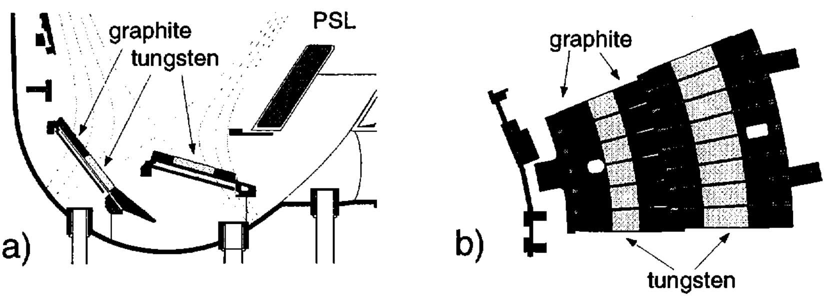

Figure 1 *Schematic view of the tungsten divertor in ASDEX Upgrade. Fig. 1a shows the poloidal cross-section of the lower half of the vessel with the divertor region; figure 1b shows a view from top onto one of the 16 toroidal segments.*

3 TUNGSTEN INFLUX AND PLASMA CONCENTRATION

The time evolution of the tungsten flux at the divertor tiles was monitored by spectroscopic observation of a WI line at 400.8nm using a spectrometer, which is viewing approximately perpendicular onto the target plates [8].

In discharges with density ramps the WI intensity decreases with increasing plasma density, reflecting the strong dependence of the W-sputtering yield on the temperature of the plasma particles, which drops in the divertor with rising density. Accordingly, in high density discharges with neon seeding, no enhanced sputtering by neon could be observed [3, 4]. In low density discharges, however, neon seeding resulted in increased W-sputtering.

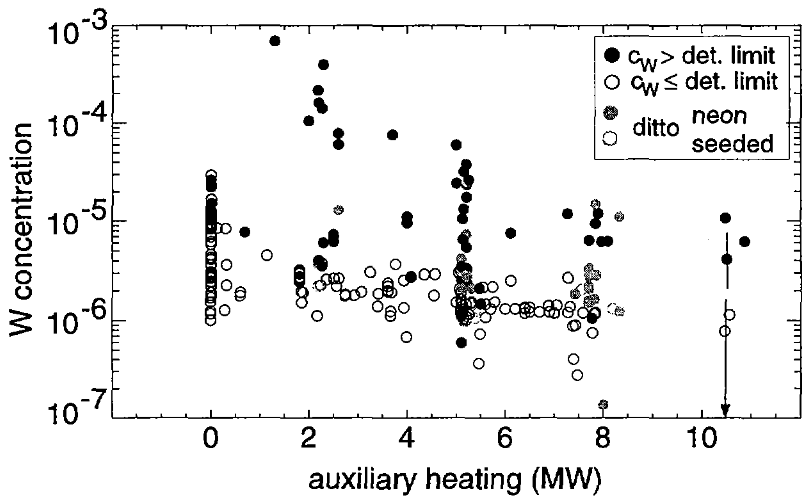

Figure 2 *Tungsten concentration obtained from analysis of the spectral line array at 5nm plotted as a function of auxiliary plasma heating power. Open plot symbols denote upper limits for c_W in the respective discharges.*

The tungsten content of the central plasma was monitored by spectroscopic observation of a line-array at 5 nm emitted by ionization states around WXXX using a grazing incidence spectrometer viewing in the equatorial plane[9]. The spectrometer was cross-calibrated by comparing the measured radiation from discharges with W-laser ablation to the radiation power expected from theoretical models [10]. The detection limit corresponds to a concentration $c_W = n_W/n_e$ of approximately 0.5×10^{-5} for a plasma density of $\bar{n}_e = 4 \times 10^{19}\mathrm{m}^{-3}$ and scales $\propto 1/\bar{n}_e^2$. In most of the investigated discharges — Ohmic as well as L- and H-Mode — the tungsten level was below 2×10^{-5}. Figure 2 shows the W-concentration plotted versus auxiliary heating power. For a given heating power, the data scatter over two orders of magnitude, which reflects the influence of varying plasma conditions and corresponding changes in impurity transport. However, the maximal concentrations decrease with increasing auxiliary heating power, which can be attributed at least partly to the degradation of the particle confinement with increasing power and to the generally higher densities in discharges with high input power, which lead to better shielding of the neutral particle influx.

In a few discharges with low auxiliary heating power, accumulation of W to concentrations above 10^{-4} occurred without enhanced tungsten flux from the target plates (Fig. 2). These discharges are characterized by strong MHD-mode activity and the absence of sawteeth [3]. However, even this discharge scenario with the highest observed tungsten concentrations did not lead to a disruption of the discharge.

4 TUNGSTEN EROSION MEASUREMENTS

Tungsten plasma surface interaction in the divertor was studied using a probe manipulator system, which allows to expose test tiles in the outer divertor plate

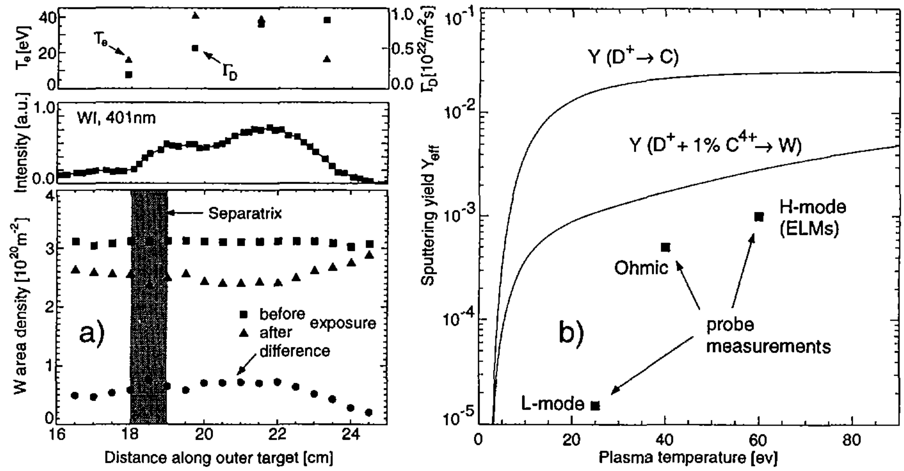

Figure 3 *(a) Radial profile of tungsten marker erosion along the outer target plate surface with WI spectral line emission above the target and T_e and Γ_D measurements by flush-mounted target Langmuir probes for a series of low density ($\bar{n}_e = 2.5 \times 10^{19}\mathrm{m}^{-3}$) Ohmic discharges with 18.7s divertor plasma. (b) Measured net erosion yields compared to total sputtering yields of tungsten and carbon from ion beam experiments and TRIM simulations.*

for single discharges [5]. Net erosion, i.e. the difference between erosion and subsequent redeposition, was determined by exposing graphite probes covered with a thin (1–100nm) W-marker stripe oriented in radial direction and measuring the thickness of the marker before and after exposure using Rutherford backscattering. Tungsten deposition and implantation on low-Z substrate materials like graphite was determined by exposure of pure graphite probes and subsequent ion beam surface analysis.

For the interpretation of the results, both the particle flux to the target plates and the energy of the incident ions must be known. Direct measurement of these quantities is performed by a set of flush mounted Langmuir probes [11].

Figure 3a shows erosion results from a probe exposure in a series of low-density Ohmic discharges representing an operating regime with high temperature — low density conditions in the divertor. The marker erosion pattern is clearly correlated with the spatial distribution of the WI spectral line emission. The effective erosion yield reaches a value of $Y_{\mathrm{eff}} \simeq 5 \times 10^{-4}$ near the strike point location.

Figure 3b shows a comparison of the measured effective erosion yields for the described scenarios with results from ion beam measurements and from TRIM sputtering simulations taking into account the energy and angular distribution of an isotropic Maxwellian distribution accelerated in the sheath potential [12, 13]. In Ohmic and L-mode discharges, the energy of the deuterium ions is too low to result in significant sputtering of tungsten, while it contributes to 50% in H-mode discharges. Carbon, which is still the dominant plasma impurity, is ionized in the charge state C^{4+} at these temperatures. The resulting impact energy $E_{C^{4+}} \simeq 14kT_e$ is sufficient to cause significant sputtering. However, as seen in Fig. 3b, the calculated effective sputtering yield assuming a C-concentration of 1% is by a factor 4–40 higher than the measured values. A plausible explanation for this observation is the effect of prompt local redeposition of W^+ ions within their first gyro orbit after ionization, which occurs because of the small ratio of ionization length to gyro orbit radius of W^+ [14].

5 LONG TERM EVOLUTION OF TUNGSTEN TILES

The contamination of the tungsten spray coating with low-Z impurities, in particular carbon from the graphite wall elements and boron from the boronization procedure, was determined by Auger electron spectroscopy (AES) and X-ray photoelectron spectroscopy (XPS) [5]. To monitor the long term evolution of the built in target tiles, a probe with a similar tungsten coating was exposed routinely to discharges. In addition, tiles from the outer divertor plate were removed after the first half of the experimental period. Analysis of both the long term probe and the target tiles showed significant dilution of the tungsten with surface concentrations of carbon and boron adding up to nearly 60% and decreasing to 20–30% in a depth of 500nm [5].

Further, the deuterium inventory of the target tiles from the outer target plate was determined by ion beam induced nuclear reaction analysis using the reaction ^{3}He(D, p)α. The resulting area density of deuterium rises from $0.3 \times 10^{20}\mathrm{m}^{-2}$ at the inner edge of the tile to $2.5 \times 10^{20}\mathrm{m}^{-2}$ at the average strike point location near the outer edge, which is significantly smaller than typical values for carbon.

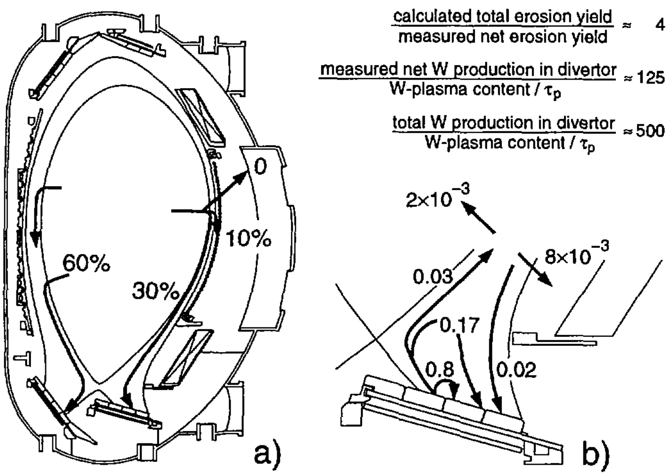

Figure 4 *Migration pattern of tungsten in the ASDEX Upgrade vessel estimated for low density Ohmic discharges with a core W-concentration of* $\simeq 10^{-5}$ *and a tungsten confinement time of* $\simeq$ *80ms determined in similar discharges by W-laser ablation. Fig. 4a shows the fraction of tungsten from the confined plasma deposited on inner and outer target plates and on main chamber limiters and vessel walls. Fig. 4b shows the migration pattern for tungsten eroded at the outer target plate.*

6 TUNGSTEN MIGRATION

Using the results of the erosion measurements described above and comparing these results with deposition measurements at various vessel locations, it is possible to establish a global pattern for the migration of tungsten in ASDEX Upgrade [6]. Tungsten deposition at surfaces in the ICRH antenna limiter shadow was determined from probes exposed by a manipulator system in the midplane, similar to the system in the divertor. Wall deposition of tungsten was measured by analysis of long term sample probes exposed for a whole experimental period, however, no tungsten was found above the detection limit of 1/100 monolayers of W-atoms. The ratio of inner target versus outer target tungsten deposition was estimated by analysis of graphite tiles removed after the previous experimental period, where only a few tungsten test tiles were mounted in the graphite divertor.

Combining all these measurements, one obtains a migration pattern as shown in Fig. 4 for the low-density Ohmic discharge type described above. Comparison of the W-flow pattern with results obtained for Cu on ASDEX [15] shows as main difference the much better divertor retention of tungsten, which must, however, be attributed to a large extent to the effect of prompt local redeposition.

7 SUMMARY

Results of the operation with tungsten divertor plates in ASDEX Upgrade are reported. The discharges of this experimental campaign cover almost the full parameter space of ASDEX Upgrade operation.

The tungsten concentration in the main plasma remained below 2×10^{-5} in over 90% of the discharges. The peak concentrations above this level decrease with increasing heating power, which might be correlated to the corresponding degradation of particle confinement. Even at high W-concentrations, no disruptions were triggered by the presence of tungsten in the plasma. A strong dependence of tungsten WI line radiation on the divertor temperature was found, with vanishing WI line emission for detached plasma operation as well as for high density radiating edge scenarios with impurity seeding.

Effective sputtering yields drop to an almost negligible level below plasma temperatures of about 20eV and are reduced compared to total sputtering yields due to the beneficial effect of prompt local redeposition. The low erosion combined with the high divertor retention of tungsten leads to negligible deposition of tungsten at the main vessel walls. On the other hand, significant contamination of the tungsten tile surface with low-Z impurities developed within the course of the experimental campaign.

Analysis of tungsten production and transport in ASDEX Upgrade is still in progress, however, the presented first results encourage the use of high-Z divertor materials, in particular for operating scenarios with high plasma densities and heating powers.

REFERENCES

[1] ECKSTEIN, W. et al., Physical Sputtering and Radiation-Enhanced Sublimation, in *Physical Processes of the Interaction of Fusion Plasmas with Solids*, edited by HOFER, W. et al., pages 93–133, Academic Press, New York, 1996.

[2] ROTH, J., J. Nucl. Mater. **176 & 177** (1990) 132.

[3] NEU, R. et al., The tungsten divertor experiment at ASDEX Upgrade, accepted for publ. by Plasma Physics and Contr. Fusion, 1996.

[4] NEU, R. et al., The tungsten divertor experiment at ASDEX Upgrade, Jour. Nucl. Mat., in press.

[5] KRIEGER, K. et al., Study of gross and net erosion in the ASDEX Upgrade divertor, J. of Nucl. Mat., in press.

[6] KRIEGER, K. et al., Migration of tungsten eroded from divertor tiles in ASDEX Upgrade, J. of Nucl. Mat., in press.

[7] GARCÍA-ROSALES, C. et al., High heat flux loading of tungsten coatings on graphite deposited by plasma spray and physical vapour deposition, accepted for publication in Nucl. Fusion Technology, 1996.

[8] FIELD, A. R. et al., Rev. Sci. Instrum. **66** (1995) 5433.

[9] NEU, R. et al., in *Europhysics Conference Abstracts (Proc. of the 22th EPS Conference on Controlled Fusion and Plasma Physics, Bournemouth, 1995)*, edited by KEEN, B. et al., **19C**, part I, pages 65–68, Geneva, 1995, EPS.

[10] ASMUSSEN, K., Untersuchungen zum Verhalten von Wolfram in Tokamakplasmen, Rep. IPP 10/2, Max-Planck-Institut für Plasmaphysik, Garching, 1996.

[11] WEINLICH, M. et al., Contr. to Plasma Physics **36** (1996) 53.

[12] ECKSTEIN, W. et al., Sputtering Data, Rep. IPP 8/82, IPP, Garching, 1993.

[13] NAUJOKS, D. et al., J. Nucl. Mater. **230** (1996) 93.

[14] NAUJOKS, D. et al., Nucl. Fusion **36** (1996) 671.

[15] ROTH, J. et al., Nucl. Fusion **29** (1989) 915.

TRANSPORT STUDIES IN THE SCRAPE-OFF LAYER AND DIVERTOR OF ALCATOR C-MOD*

B. LaBOMBARD, J.A. GOETZ, I.H. HUTCHINSON, D. JABLONSKI, J. KESNER, C. KURZ[1], B. LIPSCHULTZ, G.M. McCRACKEN[2], A. NIEMCZEWSKI[3], J.L. TERRY, A. ALLEN, R.L. BOIVIN, F. BOMBARDA[4], P.T. BONOLI, C. CHRISTENSEN, C.L. FIORE, D.T. GARNIER, S.N. GOLOVATO[5], R.S. GRANETZ, M.J. GREENWALD, S.F. HORNE[6], A.E. HUBBARD, J.H. IRBY, D. LO, D. LUMMA, E.S. MARMAR, M. MAY[7], A. MAZURENKO, R. NACHTRIEB, H. OHKAWA, P. O'SHEA, M. PORKOLAB, J. REARDON, J. RICE, J.C. ROST, J. SCHACHTER, J.A. SNIPES, J. SORCI, P. STEK, Y. TAKASE, Y. WANG, R.L. WATTERSON[8], J. WEAVER[9], B. WELCH[9], S.M. WOLFE
Plasma Fusion Center,
Massachusetts Institute of Technology,
Cambridge, Massachusetts,
United States of America

Abstract

TRANSPORT STUDIES IN THE SCRAPE-OFF LAYER AND DIVERTOR OF ALCATOR C-MOD.

Parallel and cross-field heat and particle transport in the divertor and scrape-off layer (SOL) of Alcator C-Mod have been systematically studied using an extensive aray of divertor/SOL diagnostics. Some key results include: (a) Classical parallel heat transport is obeyed with ion–neutral momentum coupling effects. (b) Cross-field heat transport is proportional to local gradients. (c) Cross-field heat diffusivity is found to scale with local density, n, electron temperature, T_e, and magnetic connection length, L, aproximately as $\chi_\perp \sim T_e^{-0.6}\, n^{-0.6}\, L^{-0.7}$ in ohmic L-mode discharges, insensitive to toroidal field strength. (d) $\chi_\perp$ depends on divertor neutral retention. (e) H-mode transport barrier effects partially extended into the SOL. (f) Thermoelectric currents in the SOL may play a role in forming inside/outside divertor asymmetries. (g) Reversed parallel flows in the SOL depend on inside/outside divertor asymmetries and may be caused by ionization source imbalances in the divertor legs.

---

* Work supported by the US Department of Energy under Contract No. DE-AC02-78ET51013.

[1] Presently at University of California, San Diego, California, USA.
[2] Presently at JET Joint Undertaking, Abingdon, UK.
[3] Presently at McKinsey & Company, Inc., London, UK.
[4] Associazione Euratom–ENEA sulla Fusione, Frascati, Italy.
[5] Presently at Tokyo Electron America, Beverly, Massachusetts, USA.
[6] Presently at Applied Science and Technology, Inc., Woburn, Massachusetts, USA.
[7] Johns Hopkins University, Baltimore, Maryland, USA.
[8] Presently at CPClare Corporation, Lexington, Massachusetts, USA.
[9] University of Maryland, College Park, Maryland, USA.

1. PARALLEL HEAT TRANSPORT

Three different parallel heat transport regimes are routinely observed in the divertor/SOL which can coexist in the same discharge [1]: low-recycling, high-recycling (Fig.1a), and detached divertor (Fig.1b). The existence of low- and high-recycling regimes is consistent with classical parallel heat transport and localized volumetric losses in the divertor. As the divertor plasma density is increased, an accompanying increase in Coulomb collisionality and divertor radiation occurs while T_e gradients form along magnetic field lines, particularly near the strike point (0 mm in Fig.1) where radiation is high, field line lengths are long and power is additionally lost to the private flux zone.

Plasma detachment (pressure loss on a flux surface) is detected in regions in the divertor where the electron temperature at the divertor plate drops below ~ 5 eV. Neutral pressure measurements in the private flux zone and D_α emissivity measurements over the outer divertor surface confirm this region to be one of low ionization fraction (< 50%) where ion-neutral collisions become effective in removing and redistributing parallel plasma momentum. Fig. 1b shows an example of plasma detachment near the separatrix. The peak parallel heat flux at the entrance to the divertor region for this discharge is ~ 400MW·m^{-2}.

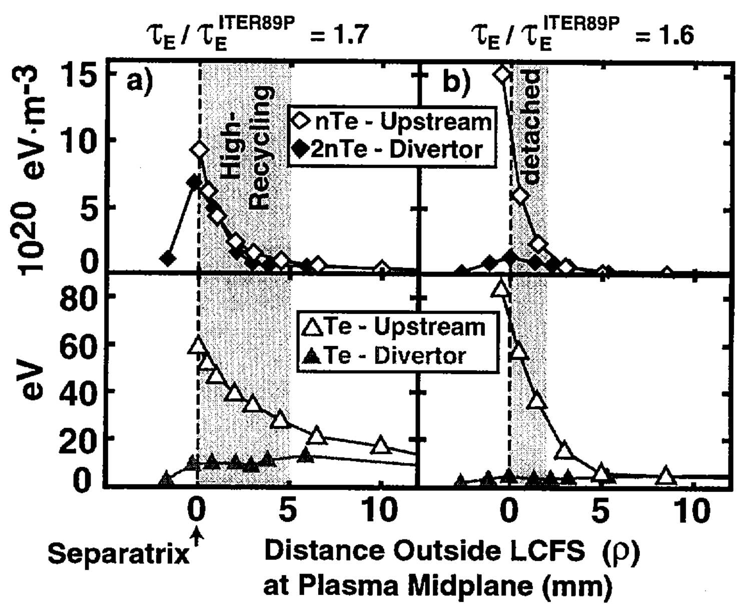

FIG. 1. Electron stagnation pressure and temperature profiles in H-mode plasmas recorded by a fast-scanning Langmuir-Mach probe upstream of the divertor throat and by divertor plate probes, mapped onto flux surface coordinate, ρ. a) Example of parallel T_e gradients forming in a high-recycling divertor discharge. b) Example of parallel T_e and nT_e gradients forming in a detached divertor discharge.

2. CROSS-FIELD SOL PROFILES

Figure 2 shows representative cross-field profiles of density, temperature, and electron pressure for three ohmic (L-mode) discharges with $\bar{n}_e$ = 1.3, 1.9, 2.5 x10^{20} m^{-3}, and one ELM-free H-mode discharge with $\bar{n}_e$ = 3.0x10^{20} m^{-3} (I_p = 1.0 MA, B_T= 5.3 tesla). All profiles display a non-exponential dependence on flux surface coordinate, i.e., the slope on the logarithmic plot varies substantially with location. The local pressure gradient scale lengths in ohmic (L-mode) plasmas can vary by a factor of ~ 4 across the profile and generally exhibit the smallest values at low density and largest values at high density. In contrast, despite the higher core densities, H-mode plasmas exhibit the shortest pressure gradient scale lengths at the separatrix with over a factor of 10 variation across the profile (~1 mm at ρ = 0 to ~ 14 mm at ρ = 15 mm).

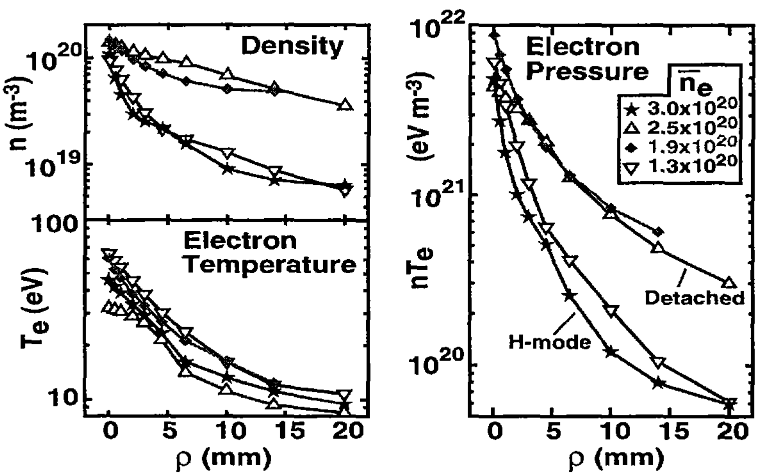

FIG. 2 Cross-field density and temperature profiles inferred from fast-scanning probe for different core line-averaged densities ($\bar{n}_e$). The steepest SOL pressure gradients appear near the separatrix in H-mode discharges.

3. DEPENDENCE OF SOL GRADIENTS ON CORE CONFINEMENT

Pressure gradient scale lengths in the SOL are inversely correlated with the quality of the global energy confinement. Figure 3 plots the "H-factor" (global energy confinement time normalized to that from the ITER89P L-mode scaling law) versus the local electron pressure gradient scale length (λ_p) at the last closed flux surface (LCFS). Data are shown from a set of ohmic L-mode [2] and ICRF heated H-mode plasmas with a wide range of densities, currents and magnetic fields. These discharges were specially prepared for diagnosis with the scanning probe and therefore do not include the full range of H-factors accessible to Alcator C-Mod (up to ~2.5) [3]. The shortest pressure gradient scale lengths for any confinement regime tend to occur when the H-factor is highest. Ohmic H-modes exhibit a similar trend, having λ_p < ~ 1mm.

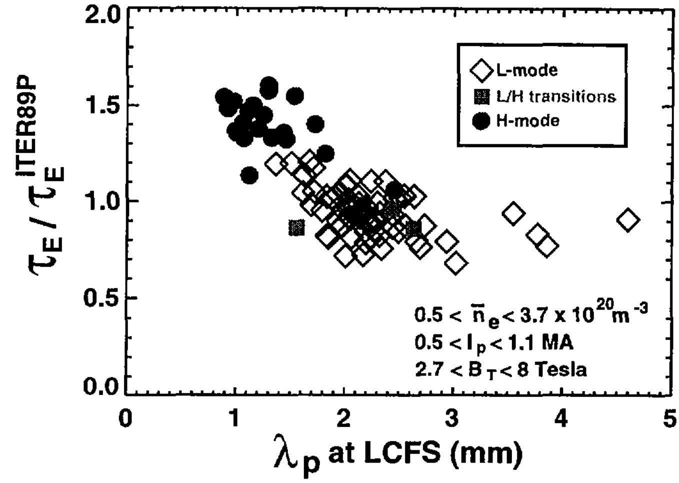

FIG. 3 Correlation between global confinement H-factor and electron pressure gradient scale length at the LCFS.

4. SCALING OF LOCAL GRADIENT SCALE LENGTHS

For ohmic L-mode discharges, local cross-field pressure e-folding lengths in the SOL are found to scale with local plasma parameters over a wide range of discharge conditions ($0.5 < \bar{n}_e < 2.8 \times 10^{20}$ m^{-3}, $0.4 < I_p < 1.1$ MA, $2.8 < B_T < 7.8$ tesla, attached/detached divertor). A power law formula for the perturbation of local λ_p about a mean value, λ_p^*, has been investigated [4],

$$\lambda_p = \lambda_p^* (T_e/50)^{\alpha} (n/10^{20})^{\beta} (L/12.5)^{\gamma} (B_T/5)^{\delta} \quad (1)$$

where T_e, n - electron temperature (eV) and density (m^{-3}) at the scanning probe location, L - 1/2 of total connection length (m), B_T - toroidal magnetic field on axis (tesla). Results of regression analysis from a set of 130 dischargesare shown in Table 1. The statistics of the data set is sufficient to separately resolve the dependence of λ_p on B_T and L. There is essentially no sensitivity of λ_p to the magnitude of B_T, despite the factor of 2.5 variation of B_T in the data set.

*Table 1 - Regression analysis using Eq. (1). Multiple correlation coefficient (**R**) and sample variance (χ_R^2) determine the statistically best representation (gray column).*

λ_p^* (mm)	2.36 ±.04	2.37 ±.04	2.48 ±.04	2.34 ±.04	2.48 ±.04
α	-1.04 ±.03	-1.13 ±.04	-1.49 ±.06	-1.15 ±.04	-1.49 ±.06
β	_	0.14 ±.04	0.25 ±.04	0.15 ±.04	0.25 ±.04
γ	_	_	0.72 ±.09	_	0.73 ±.09
δ	_	_	_	0.13 ±.07	-.02 ±.07
R	.877	.880	.899	.881	.899
χ_R^2	1.43	1.38	1.14	1.38	1.14

The strong inverse dependence of local λ_p on local T_e is consistent with a model that balances classical parallel heat conduction with a level of anomalous cross-field transport that is proportional to the local pressure gradient ($\lambda_p \sim T_e^{-5/4}$) [1]. Based on this model, these data suggest that local cross-field heat diffusivity scales approximately as $\chi_\perp \sim T_e^{-0.6}\, n^{-0.6}\, L^{-0.7}$, with no explicit dependence on B_T.

5. ESTIMATES OF CROSS-FIELD HEAT DIFFUSIVITY PROFILES

A neutral leakage pathway (bypass) in the divertor structure was closed during the summer of 1995. The result was an increase in the divertor/midplane neutral pressure ratio from ~70 to ~ 250 in otherwise similar discharges. $\chi_\perp$ profiles (Fig. 4) deduced from an "onion skin" transport model [4] show a factor of ~3 variation over the SOL in L-mode discharges with the absolute level decreasing by a factor of ~3 when the bypass was closed. H-mode discharges show a large variation in $\chi_\perp$ across the SOL with values near the separatrix falling to ~0.1 $m^2 \cdot s^{-1}$, perhaps indicative of the H-mode transport barrier extending partly into the SOL.

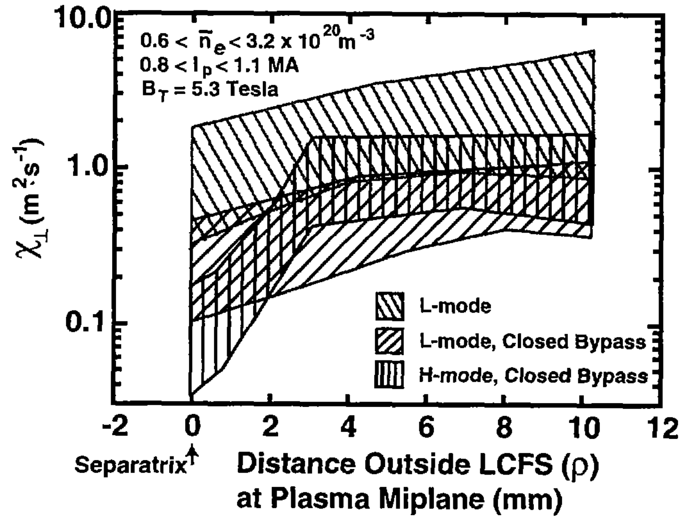

FIG. 4 Envelope of cross-field thermal diffusivity profiles, $\chi_\perp$, estimated from heat transport modeling of 93 diverted discharges.

6. ASYMMETRIC HEAT AND PARTICLE TRANSPORT

6.1 Heat Transport Asymmetries

Low density discharges with a hot SOL (low collisionality) exhibit a large divertor asymmetry, having outside/inside electron temperature ratios approaching ~10 with negative B_T ($B \times \nabla B$ towards x-point) and ~0.2 with positive B_T (Fig.5a). The density and temperature asymmetry preserves nT_e ~ constant on a flux surface and suggests that a heat flux asymmetry which reverses (inside-outside) on reversal of B_T is responsible [5]. As the collisionality in the SOL increases, the magnitude of the asymmetry decreases, vanishing in the highest density (lowest edge temperature) discharges.

Measurements suggest that parallel heat fluxes arising from currents in the SOL significantly contribute to the total heat flux arriving at divertor surfaces. A large component of the current is thermoelectric in nature, i.e., consisting of parallel currents driven by the inside/outside temperature asymmetry and obeying classical conductivity. A runaway situation can occur: thermoelectric currents drive asymmetric inside/outside parallel heat fluxes which, in turn, cause an increased temperature asymmetry. This mechanism, which scales with SOL collisionality, may play an important role in forming divertor asymmetries [4].

6.2 Parallel Particle Flows

Reversed parallel plasma flows (away from the divertor surface) in the outer divertor leg are detected near the separatrix under conditions when the divertor temperature asymmetry favors a higher T_e in the outer divertor leg (case "A" with negative B_T in Fig. 5b). An imbalance in the ionization rate of neutrals in the private flux zone near the inner and outer strike points may influence the magnitude of flow at the Mach probe location and be responsible for the flow reversal [4]. Such an ionization imbalance may drive divertor-to-divertor parallel convection loops that encircle the entire core plasma.

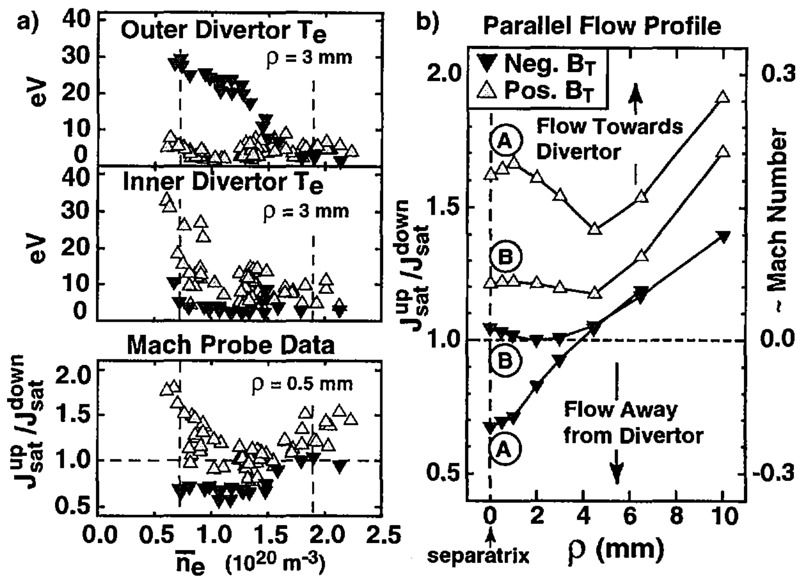

FIG. 5 (a) Outer and inner divertor T_e and ratio of ion saturation currents (J_{sat}) from a Mach probe (upstream of outer divertor leg) versus line-averaged density. Positive and negative field directions and flux surface location, ρ, indicated. (b) Mach probe deduced parallel flow profiles for: (A) large in-out asymmetry, $\bar{n}_e = 0.7x10^{20}\ m^{-3}$ and (B) no asymmetry, $\bar{n}_e = 1.9x10^{20}\ m^{-3}$.

REFERENCES

[1] LaBOMBARD, B., et al., Phys. Plasmas **2** (1995) 2242.
[2] GREENWALD, M., et al., Phys. Plasmas **2** (1995) 2308.
[3] TAKASE, Y., et al., IAEA-CN-64/A5-4, this volume.
[4] LaBOMBARD, B., et al., Experimental investigation of transport phenomena in the scrape-off layer and divertor, Plasma–Surface Interactions in Controlled Fusion Devices (Proc. Int. Conf. St. Raphael, 1996), to be published in J. Nucl. Mater.
[5] HUTCHINSON, I.H., et al., Plasma Phys. Control. Fusion **37** (1995) 1389.

IMPURITY SCREENING STUDIES IN THE ALCATOR C-MOD TOKAMAK

G.M. McCRACKEN, R.S. GRANETZ, B. LIPSCHULTZ,
B. LaBOMBARD, J.L. TERRY, F. BOMBARDA[1],
J.A. GOETZ, D. JABLONSKI, S. LISGO[2], H. OHKAWA,
J.E. RICE, P.C. STANGEBY[2], ALCATOR GROUP
Plasma Fusion Center,
Massachusetts Institute of Technology,
Cambridge, Massachusetts,
United States of America

Abstract

IMPURITY SCREENING STUDIES IN THE ALCATOR C-MOD TOKAMAK.

Screening experiments have been undertaken in both limited and diverted discharges with a range of gaseous impurities in ohmic discharges. Measurements have been made as a function of plasma density and of the poloidal position of gas injection. It has been found that for recycling impurities such as neon and argon the number of impurities in the core plasma is proportional to the number injected. For non-recycling impurities (carbon and nitrogen) the number in the core is a function of the rate of injection. For discharges limited on the inner wall the screening is a function of the poloidal position of injection, with the injection at the inner wall giving the poorest screening. In diverted discharges with recycling impurities the position of injection does not significantly affect the screening. For non-recycling impurities the screening is typically a factor of 3 better when impurities are injected from the divertor rather than from the outside midplane. However, the best screening occurs when the impurities are injected at the inner midplane. Screening is typically a factor of 10 better for diverted than for limited discharges. Impurity transport has been modelled using the Monte Carlo code DIVIMP with a background plasma derived from experimental measurements of plasma parameters at the target and in the scrape-off layer (SOL). It is found that the code can reproduce the experimental measurements within a factor of 2.

1. Introduction

An understanding of impurity transport is important in order that the location and level of radiation in the boundary can be controlled without significant cooling or dilution of the fusion fuel in the confined plasma. A series of experiments has been carried out to investigate the screening effect of the divertor and SOL plasma by injecting recycling (Ne and Ar) and non-recycling (CH4 and N2) gases into the high density edge conditions in diverted and limited discharges in the Alcator C-Mod tokamak [1]. Compared with studying intrinsic impurities, the use of injected gaseous impurities has the advantage of giving unambiguous knowledge of the source rate and location under a range of operating conditions.

---

[1] Associazione Euratom-ENEA sulla Fusione, I-00044 Frascati, Italy.

[2] Institute for Aerospace Studies, University of Toronto, Downsview, Ontario, Canada M3H 5T6.

2. Experiment

The details of the experimental arrangement have been described previously [1,2]. The impurity gas is injected through a number of capillary tubes entering the vessel at different poloidal and toroidal locations. The carbon, nitrogen and neon radiation in the core plasma is measured with a single spatial channel, scannable VUV spectrometer [3] and the argon with a crystal spectrometer [4] viewing Ar XVII at up to 5 chords simultaneously. The MIST code [5] is used to calculate the charge state distribution, including transport, and hence the total impurity content. The results are calibrated by the measured brightness of a core impurity line.

The impurity flux in the divertor is monitored with a visible spectrometer using a 2-D CCD detector viewing up to 14 locations at both the inner and outer divertor simultaneously and with a 12 chord bolometer array [6]. In addition there are core measurements of n_e, T_e, total radiation profiles, Z_{eff} and other spectroscopic diagnostics. The n_e and T_e profiles in the SOL and at the target plates are measured with a scanning probe and an array of Langmuir probes in the tiles [7]. The impurity injection experiments have been carried out both under conditions where the effect on plasma parameters is small and also where the injection of the impurity has been a serious disturbance, causing the plasma to detach from the divertor target [6]. Typical conditions at the divertor plate vary from T_e=20 eV, n_e=1x10^{19} m^{-3} for the non-perturbative studies to T_e=2 eV, n_e=2x10^{20} m^{-3} for the detached conditions.

3. Results

3.1 Diverted discharges

(a) Recycling gases

The number of argon atoms inside the separatrix at any given time during the discharge is proportional to the total number injected. Gas has been injected

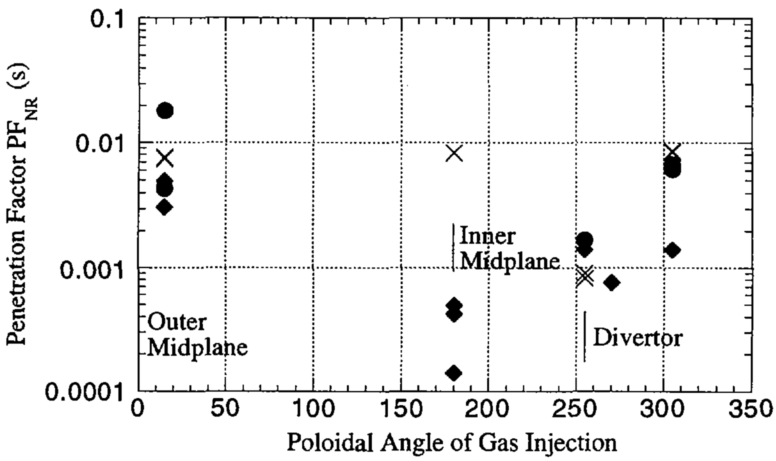

FIG. 1. Variation of the penetration factor of nitrogen for different poloidal injection positions in attached plasmas at different densities. The injection rate is in the range (2-4) × 10^{20} atoms/s. Circles: n_e = (1.3-1.5) × 10^{20} m^{-3}; diamonds: n_e = (1.6-1.9) × 10^{20} m^{-3}; crosses: calculated value using DIVIMP, all experimental values of n_e.

via the capillary tubes into the private flux zone in the divertor, at the inner wall midplane and into the outer SOL. Within the scatter in the data the number of confined atoms is independent of the gas puffing position. The fraction of argon getting into the confined plasma is a decreasing function of density varying from 4% down to 1.5% as the density n_e increases from 1 to 2.5×10^{20}. The dependence on divertor geometry has been studied. There is little effect due either to variation of the outer gap or to varying the position of the strike point on the vertical targets [8].

(b) Non-recycling gases

In contrast to the rare gases, nitrogen or methane puffs result in an impurity concentration in the confined plasma which decays with a time constant of ~ 30 ms at the end of the injection pulse. The time constant is comparable to that measured for impurities injected by laser ablation and indicates an impurity recycling coefficient ≤ 0.3. For a long impurity injection pulse the impurity concentration rises to a constant value. The total number of impurities in the plasma is proportional to the impurity *injection rate* rather than being proportional to the integrated amount, as is the case for the recycling gases. The penetration factor (PF_{NR}), defined as the impurity number in the confined plasma normalized to the influx (i.e. the impurity particle confinement time) is a characteristic time which varies from < 10^{-4} s to 10^{-2} s, depending on species and conditions. Carbon has a lower PF_{NR} than nitrogen [1].

The screening of the non-recycling impurities (both CH4 and N2) is dependent on the poloidal position of gas injection. Screening is best for those impurities injected at the inner wall and in the divertor and poorest for those injected at the outer midplane, fig 1.

Using a fixed nitrogen injection pulse the effect of varying the plasma density in ohmic diverted discharges has been investigated. It is found that PF decreases slowly with increasing density in a similar way to argon. However at densities above about $n_e = 1.8 \times 10^{20}$ m^{-3} the nitrogen injection results in sudden detachment at the outer target. This leads to an increase in the PF by a factor of 2 to 3.

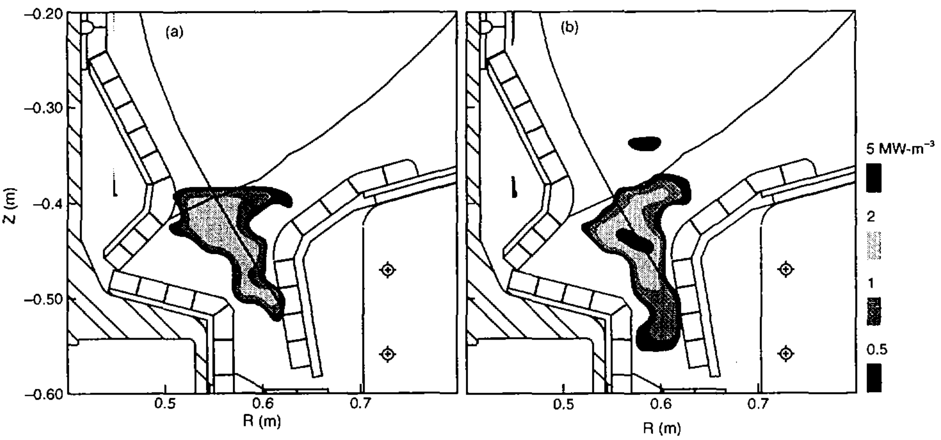

FIG. 2. Distribution of radiation in the divertor from bolometer tomography during nitrogen injection. Injection rate 2 × 10^{20} atoms/s (a) into the outer SOL, (b) into the private flux region. The radiation before the nitrogen injection has been subtracted.

In order to follow the transport of the injected impurities the visible impurity radiation in the divertor has been studied using a visible spectrometer. The charge states NI (868.0), NII(463.0 nm), NIII (451.5 nm) and ArII (442.6 nm) have been examined. When the N_2 gas is injected from either the inside or the outside midplane the NII and NIII signals increase. The spatial distributions of the line brightness of NII and NIII are peaked just above the inner strike point, near the inner divertor "nose". The spatial distribution of the total radiation is obtained from the bolometer array by tomographic reconstruction. It is found that the radiation is below the X-point distributed along the separatrix, fig 2. The distribution before the nitrogen injection is subtracted from that obtained during injection. The peak radiation is ~5 MW m^{-3}.

Evidence of impurity flow in the SOL has been obtained through directly viewing low charge states of carbon and nitrogen at various points of injection [9]. The impurity particle flow is always towards the divertor target, independent of the direction of the toroidal field, even for injection at the inner wall mid-plane.

3.2 Limited discharges

The screening of both non-recycling and recycling impurities has been studied for ohmic discharges limited on the inner Mo wall [10]. The limiter plasmas have a slightly smaller elongation (κ=1.3) than the diverted plasmas (κ=1.6) in order that there is a significant SOL connected to the inner wall limiter. Only limiter plasmas with at least 15mm thick SOL connecting to the inner wall (ie several e-foldings) have been used for the present comparison.

The time behavior of each impurity type is similar to that in diverted discharges, with the impurity density being proportional to the integrated gas injected for recycling impurities and to the injection rate for the non-recycling impurities. Impurities injected into limiter plasmas had a factor 10 to 20 higher probability of penetrating into the core than in attached divertor discharges with as much as 45% of the recycling injected atoms appearing in the confined

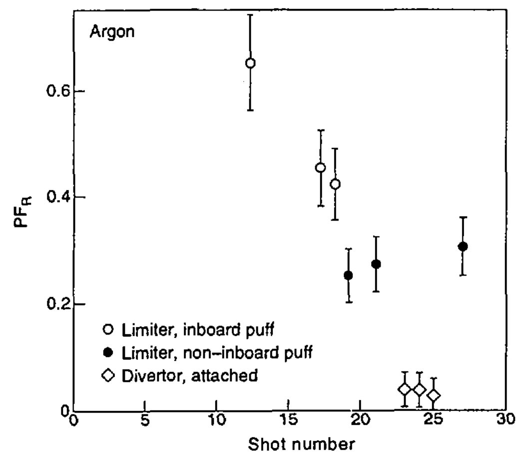

FIG. 3. Comparison of argon screening in limiter and divertor plasmas. Limiter plasmas with argon injection at the outer midplane have a factor of 10 worse screening than divertor plasmas. $I_p \approx 0.8$ *MA,* $n_e = (0.7\text{-}2.1) \times 10^{20}\ m^{-3}$. *Run set 950218.*

plasmas. Compared to detached divertor discharges they were only a factor of 3 times worse. These findings were the same for both recycling and non-recycling gases. Results for argon are shown in fig 3. Screening in limiter plasmas was found to vary with the poloidal location of the gas puff. Inboard midplane puffing which bypasses the SOL typically results in a factor 2 to 3 greater penetration than puffing from locations well outside the SOL.

4. Modelling

The impurity injection has been modelled using the 2-D Monte Carlo code, DIVIMP, in combination with the neutral Monte Carlo code NIMBUS [11]. Cross-field transport, parallel transport, ionization and heating are included. So far only non-recycling impurities have been modelled since this does not require assumptions about the energy and angular distribution of the recycling species. The experimental n_e and T_e profiles are used as input to an onion-skin model to calculate the n_e and T_e distribution in the SOL for each discharge. The impurities are launched as atoms with an energy of 0.5 eV, taken as an estimate of the energy resulting from the dissociation of the injected molecular species. Results of the PF are compared to experimental data in fig 1. For a cross field diffusion coefficient $D = 1.0\ m^2\ s^{-1}$, agreement between model and experiment is within a factor of 2 except at the inner wall. Less dependence on n_e is observed in the model than in the experiment. This low PF may be due to the fact that ionization is taking place far from the separatrix and some of the ions are lost to the wall even before they get to the divertor. Limitations of the present grid prevent these ions being followed.

Using the code, the parallel forces on the impurities have been calculated at different radii in the SOL. Near the target the friction force dominates as expected. Further from the target the ion temperature gradient force drives the impurities away from the target along a field line towards the separatrix. From there they diffuse radially outwards and return to the target [12].

5. Discussion and Conclusions

There is good screening for both recycling and non-recycling gases in diverted discharges; this is attributed to the high plasma density and high power density in the C-Mod SOL. However while the core density of a recycling species is proportional to the total number of injected atoms and is independent of the poloidal position of injection, the density of a non-recycling species is proportional to the rate of injection and is dependent on the injection position. The screening of both recycling and non-recycling species is significantly reduced when the plasma detaches from the divertor target. The radial location of ionization is, in all cases, in the SOL. This is partly due to the low energy of the injected gas species.

Screening of non-recycling impurities is best when impurities are injected in the divertor or at the inner wall. The good screening at the inner wall is tentatively ascribed to the sink action of the toroidally continuous wall. Modeling with DIVIMP generally gives good agreement with experiment showing much better screening for impurities injected in the divertor than at the outer midplane. However it does not at present explain the good screening of impurities injected at the inner mid-plane. Spectroscopic and bolometric measurements of the impurities in the divertor indicate that the radiation is concentrated along the separatrix below the x-point.

The screening of impurities in diverted discharges is about a factor of 10 better than in limiter discharges. However when considering overall performance one must take into account both production of impurities and screening. The lower impurity production of intrinsic impurities at the divertor, when the plasma temperature at the target is reduced below the value corresponding to the sputter threshold, is an additional advantage of divertor operation.

Acknowledgments: The authors are grateful to the whole Alcator team and in particular to the operations group, for the excellent operation of the machine. This work is sponsored by the US Department of Energy under contract No DE-AC02-78ET51013.

REFERENCES

[1] McCRACKEN, G.M., LIPSCHULTZ, B., LaBOMBARD, B., in Controlled Fusion and Plasma Physics (Proc. 22nd Eur. Conf. Bournemouth, 1995), Vol. 19C, European Physical Society, Geneva (1995) 313.

[2] McCRACKEN, G.M., et al., J. Nucl. Mater. (1997).

[3] GRAF, M.A., et al., Rev. Sci. Instrum. **66** (1995) 636.

[4] RICE, J.E., MARMAR, E.S., Rev. Sci. Instrum. **61** (1990) 2753.

[5] HULSE, R.A., Nucl. Technol./Fusion **3** (1983) 259.

[6] LIPSCHULTZ, B., et al., J. Nucl. Mater. **220–222** (1995) 50.

[7] LaBOMBARD, B., et al., Phys. Plasmas **2** (1995) 2242.

[8] WANG, Y., PhD Thesis, Plasma Fusion Center, Massachusetts Inst. of Technology, Cambridge (1996).

[9] JABLONSKI, D., et al., J. Nucl. Mater. (1997).

[10] GRANETZ, R.S., et al., J. Nucl. Mater. (1997).

[11] STANGEBY, P.C., ELDER, D., J. Nucl. Mater. **196–198** (1992) 258.

[12] STANGEBY, P.C., ELDER, D., Nucl. Fusion **35** (1995) 1391.

CONTROL OF BOUNDARY POWER FLUX WITH ERGODIC DIVERTOR ON TORE SUPRA

P. GHENDRIH, A. GROSMAN, T. HUTTER, B. MESLIN,
A. BÉCOULET, C. GRISOLIA, D. GUILHEM, T. LOARER,
J.-C. VALLET, TORE SUPRA TEAM
Association Euratom-CEA,
Centre d'études de Cadarache,
Saint-Paul-lez-Durance,
France

Abstract

CONTROL OF BOUNDARY POWER FLUX WITH ERGODIC DIVERTOR ON TORE SUPRA.

Recent investigations of the power handling capability of the stochastic boundary generated by the ergodic divertor of Tore Supra are characterized by (a) control of the radiative boundaries in the detached divertor regime, (b) assessment of the prototype of vented target plates to be implemented on the ergodic divertor and (c) high power operation. Detached divertor operation is shown to be stable but sensitive to the wall particle content. Investigation of the power deposition patterns with the prototype target plate has shown that these patterns are related to the temperature modulations which are found in the stochastic boundary. High power operation (~ 8 MW) with the ergodic divertor is characterized by standard L mode confinement and a factor of two lowering of the peaking factor of the power flux to the target plate.

1. INTRODUCTION

The ergodic divertor aims at providing an efficient means of controlling the plasma-wall interaction on Tore Supra [1]. Similarly to the poloidal divertor configuration, the interaction volume is radially withdrawn from the closed flux surfaces [2]. The connection between core volume and divertor volume is then determined by long parallel connection lengths. It is therefore governed by the strong parallel transport, together with a small contribution from the transverse transport [3]. While the poloidal divertor is characterized by a strong modification of the magnetic equilibrium, the ergodic divertor destroys the outermost flux surfaces via small resonant perturbations [1]. Transport throughout the divertor volume to the target plates is then twofold: there is an ergodic region with a balance between parallel and transverse transport, and a laminar region governed by parallel transport to the wall [4]. The latter region is reminiscent of the standard divertor and, similarly, one has to handle here large parallel power fluxes. Since the target plates are actively cooled, with a thermal time constant much smaller than the shot duration, there is an absolute upper limit to the power handling capability [5]. As in ITER, high power operation can only be achieved with controlled power deposition. Recent progress in the operation of the ergodic divertor has been devoted to testing a vented target plate [5] and to high power operation and hence the means of increasing the radiated power [6]. These results are reported in the present paper. In Section 2, the divertor detachment scenario with the ergodic divertor is described. The heat deposition on the prototype vented target plate is addressed in Section 3. Finally, large power operation, $P_{total} \sim 8$ MW with fast wave electron heating (FWEH) is presented in Section 4.

2. RADIATIVE AND DETACHED DIVERTOR OPERATION

The ergodic divertor, in contrast to most divertor experiments, refers to the case of a radiative divertor in an open configuration with respect to neutral recirculation. Owing to the design of the divertor coil, one finds that almost all wall components are placed within a density e-folding length from the divertor plasma. In particular, a maximum gap of 0.02 m exists between the diverted plasma and the inner 10 m^2 of graphite wall. Gradual deuterium trapping and subsequent release from this large graphite surface are shown to lead to an increasing particle flux on a shot to shot basis [7]. In a series of ohmic shots at given magnetic equilibrium, $I_p = 1.4$ MA, $B_\varphi = 3$ T, $\beta_p + \ell_i/2 = 0.75$, R = 2.38 m (a = 0.8 m), a gas injection lasting 2.75 s increases the volume averaged density from $0.56\langle n_e\rangle_{max}$ to $\langle n_e\rangle_{max} = 2.9 \times 10^{19}\, m^{-3}$. This density ramp does not drive any change in the radiated fraction which remains large, $f_R \sim 0.75$. However, a significant change in the radiated pattern is observed (Fig. 1). The most important response is observed for the bolometer chords probing the high and low field regions of the divertor volume, i.e. the volume of stochastic open field lines generated by the ergodic divertor. As shown in Fig. 1, a rather complex sequence of events occurs [8]. During the first and last seconds of the shot, i.e. in the limiter configuration when the ergodic divertor is not resonant, the radiation pattern has the characteristic features of a marfe [9]. This high field radiation observed during current ramp-up and ramp-down is a signature of a wall particle content close to saturation [7].

Let us concentrate on the transition from the attached divertor regime, from t = 1.7 s to t = 3.4 s, to the detached divertor regime from t ~ 5 s to t = 8 s. The swing in the radiation profile which characterizes the transition between these two regimes, Fig. 1, is slow: $\Delta t_{swing} \sim 1.6$ s. This transition time is much longer than any transport time-scale in the plasma boundary. In the series of shots, the behaviour of the bolometer signals, i.e. the radiation pattern at constant radiated fraction f_R, exhibits a standard dependence on the density. Three critical densities govern the evolution of the low field side bolometer chord as shown in Fig. 1 for shot TS 21816 (fifth shot in the series): At t = 3.4 s, $\langle n_e\rangle_{swing} = 2.15 \times 10^{19}\, m^{-3}$, the low field radiation starts decreasing. This slow decrease changes to a fast decrease at t = 4.7 s $\langle n_e\rangle_{detach} = 2.8 \times 10^{19}\, m^{-3}$, which ends when a steady state is reached at t = 4.97 s $\langle n_e\rangle_{steady} = 2.94 \times 10^{19}\, m^{-3}$. A similar sequence is observed for the neutral behaviour, e.g. a D_α chord viewing the top of the machine and a fast neutral analyser chord viewing the midplane (Fig. 1). Slightly different behaviour is

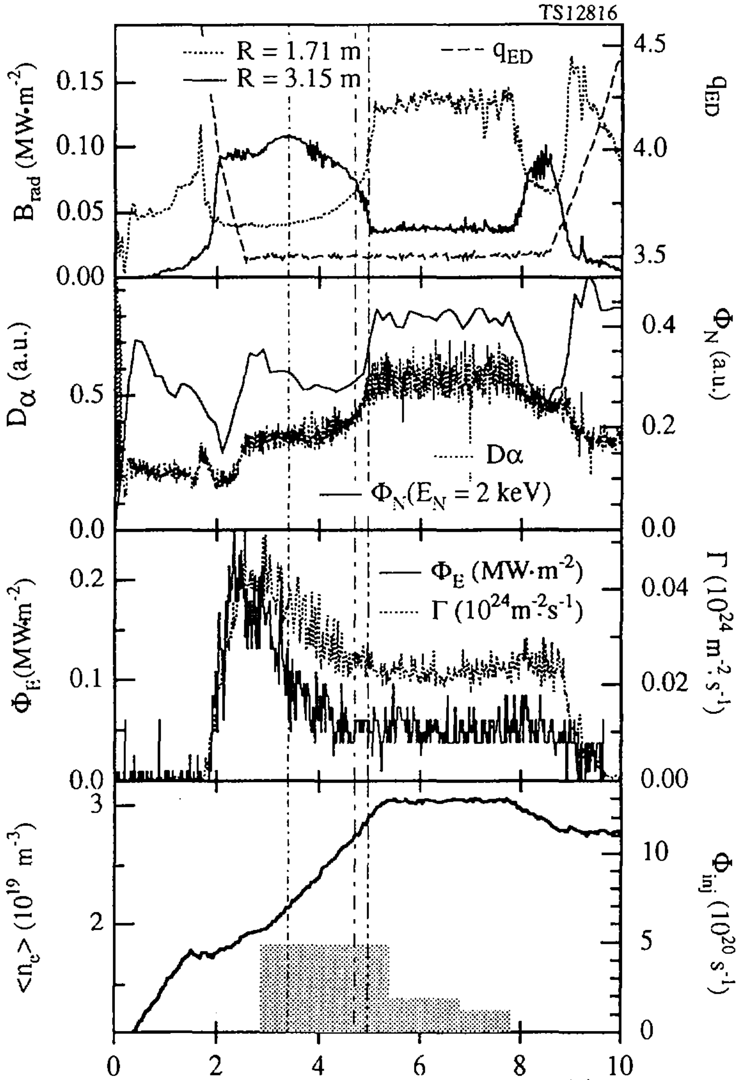

FIG. 1. Divertor detachment with the ergodic divertor (ohmic regime). Top diagram: bolometer chord from the high (R = 1.71 m) and low (R = 3.15 m) fields. The vertical lines correspond to the critical densities governing the decrease of the low field radiation. The divertor resonance is determined by $q_{ED} \leq 4$. Second diagram: modification of neutral behaviour exemplified by D_α and fast CX neutral analyser signals. Third diagram: energy flux (IR data) and particle flux (Langmuir probe) to the target plate. Bottom diagram: volume averaged density and gas injection rate driving the detachment.

observed for the plasma parameters at the target plate. The gas injection immediately leads to a decrease in the heat and particle fluxes to the divertor target plate (Fig. 1). By using Langmuir probe data, this flux decrease to the target plates can be analysed as being due to a factor of two decrease in the temperature from $T_e \sim 10$ eV at $t \sim 2$ s to $T_e \sim 5$ eV at $t \sim 4$ s, with a density rise followed by a density plateau lasting until $t \sim 3.4$ s before a small decrease of the density into the detached regime. In terms of the plasma pressure, one finds a plateau until $t \sim 3$ s, followed by a decrease governed by the temperature decrease up to $t \sim 4$ s. The detachment thus occurs in two steps: a gradual detachment of the radiation front from the divertor from $\langle n_e \rangle_{swing}$ to $\langle n_e \rangle_{detach}$, until a more sudden transition occurs, from $\langle n_e \rangle_{detach}$ to $\langle n_e \rangle_{steady}$, which leads to a marked change in the location of particle recycling. Similar sharp transitions have been reported for the DIII-D partially detached divertor scenario [10].

Let us now analyse the variation of the critical densities on a shot to shot basis. We find that these critical values decrease from shot to shot while the total amount of gas injected to reach the density plateau exhibits a factor of two decrease. This indicates that the density threshold of the various steps in this divertor detachment is sensitive to the location of the particle injection. Upstream particle fuelling, due to wall particle outflux and recycling, lowers the threshold to detachment and finally results in divertor plugging. The radiation swing and the shift of the recycling location are also correlated to a temperature drop which reduces the deuterium screening in the divertor volume, hence increasing the fuelling efficiency [11]. These effects may open the way to several deleterious properties, such as the loss of the divertor pumping capability due to the decrease of the ionic flux to the pumping throat [12], or confinement degradation as a marfe forms on the core side of the separatrix as reported for axisymmetric divertors [13]. The ability to operate detached divertor plasmas during long shot operation will therefore rely on the capability of controlling the wall status during high density operation. Furthermore, the required edge plasma density to achieve fast wave heating and therefore high power radiative divertor experiments on Tore Supra [14] has led to an increased investigation of the wall particle content. A wall saturation criterion has been derived from the analysis of premagnetization plasmas [15]. As underlined by the present analysis of divertor plasma detachment, this control of the wall status will enable progress towards steady state radiative divertor operation.

3. POWER DEPOSITION ON THE VENTED TARGET PLATE

Following the successful test of a vented limiter [16], vented target plates have been designed for the ergodic divertor. A prototype has been installed with dedicated diagnostics. Such a target plate is designed to sustain large power flux while allowing for pumping of deuterium (with in situ titanium gettering) [5]. Investigation of the energy deposition on this element indicates that significant shadowing by the divertor coils themselves takes place at low values of the normalized magnetic perturbation $\delta B_r/B_\varphi$, where δB_r is the radial magnetic perturbation induced by the divertor coil.

This effect is illustrated inn Fig. 2, where the energy flux is plotted against the distance d_φ along the target plate (aligned close to the magnetic field direction). The energy flux to the water cooled copper tube covered with a 0.1 mm thick B_4C layer is readily computed from the temperature increase measured with infrared imaging [17]. The test of the prototype target plate reported in Fig. 2 has been performed at low toroidal field, $B_\varphi = 2$ T, ohmic heating and two values of the perturbation current, $I_{ED} = 22$ kA and $I_{ED} = 42$ kA (maximum perturbation current: $I_{ED} = 45$ kA).

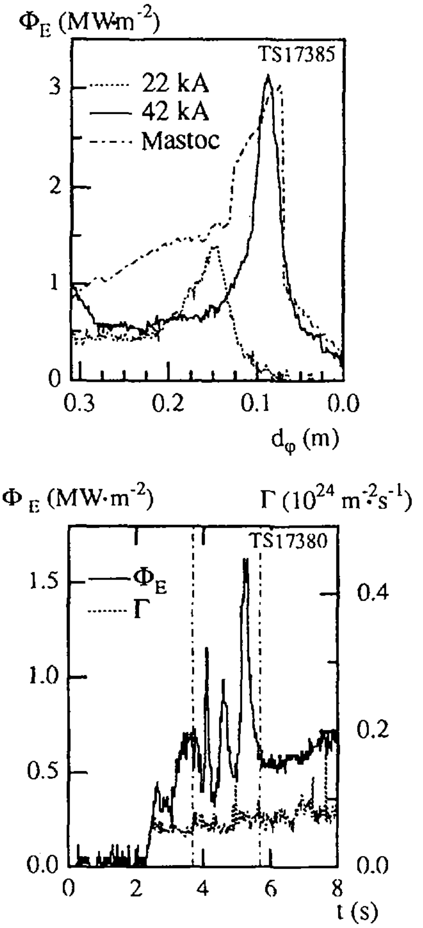

FIG. 2. Top: energy flux Φ_E (IR data) to the prototype vented target plate along a direction close to that of the magnetic field d_φ; $d_\varphi = 0$ is located in the poloidal symmetry plane of the divertor coil. The two values of the radial perturbation are labelled by the divertor current. The deposition profile computed with the Mastoc code is also reported. Bottom: Energy flux Φ_E (IR data) and particle flux Γ (Langmuir probe) during a plasma current ramp (between the vertical lines); the divertor resonance at $t \sim 2$ s governs the deflection to the target plate.

We find that the wetted fraction of the vented target plate exhibits a square root dependence on $\delta B_r/B_\varphi$. The total target extent is wetted at 42 kA ($\Delta d_\varphi \sim 0.31$ m), while $(42/22)^{1/2} \sim 72\%$ of the target plate is wetted at 22 kA ($\Delta d_\varphi \sim 0.23$ m). This dependence has since been recovered with calculations from the Mastoc code (field line tracing with a bounded parallel excursion governed by transport balance [3]). The whole set of target plates which will be operational during the forthcoming experimental campaign has therefore been modified according to this result. The angle of the vented structure with the toroidal field has been reduced from 14° to 8° in order to allow for operation at 4 T with no shadowing of the vented structure. This change in the design is especially important with respect to neutral collection by the vents and therefore the pumping capability. It is interesting to note that the reduced but non-vanishing flux to the target plate and the large neutral population which characterize the detached regime described in Section 2 will allow for pumping due to neutral backscattering through the vents, even during detached operation where the efficiency of standard ionic flux pumping strongly decreases [12].

Another striking feature of the heat deposition pattern on the target plates is the strong peaking found in these low field ohmic shots. Calculation of the energy deposition pattern with the Mastoc code and a theoretical analysis of the energy flux transmission for a given field line [3] have led to qualitative agreement in the deposition profile. It seems, however, that the cross-field transport has been overestimated in this calculation, $\chi_\perp = 2.5\ m^2 \cdot s^{-1}$, thus leading to a reduced peaking of the deposition pattern (Fig. 2). However, the shadowing effect due to the divertor and the location of the peak heat deposition are in excellent agreement with the experimental pattern. The location of this pattern is a sensitive function of the equilibrium parameters. This effect is illustrated in Fig. 2, where a current ramp from $t = 3.7$ s to $t = 5.7$ s linearly decreases the boundary safety factor from $q_{ED} = 3.4$ to $q_{ED} = 2.75$. During this 20% variation of the safety factor, four consecutive peaks pass at the location of the divertor Langmuir probe. A 2% variation of the plasma current is thus sufficient to provide sweeping of the peak energy deposition. The particle flux measured with the Langmuir probe does not exhibit such deposition patterns. The latter can therefore be regarded as a signature of temperature modulations observed experimentally in stochastic boundaries with radially [18] and poloidally [19] resolved Langmuir probe measurements.

4. HIGH β_p, HIGH POWER OPERATION

In view of long pulse operation with the ergodic divertor, experiments have been carried out in order to increase β_p and therefore the fraction of bootstrap current. Fast wave direct electron heating at $B_T = 2$ T has been used to increase the localization of the deposited power. These experiments require a precise adjustment of the magnetic equilibrium in order to expel the main ion cyclotron resonances from the plasma [20], while ensuring resonant and MHD stable conditions for the ergodic divertor [21].

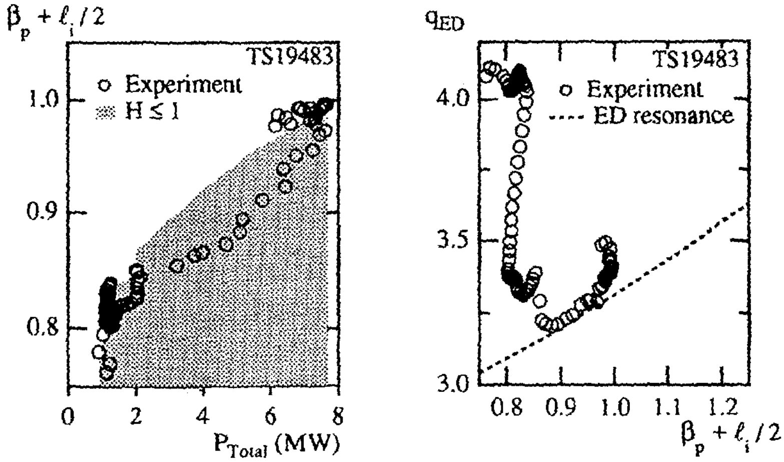

FIG. 3. Left: dependence of Shafranov parameter $\beta_p + \ell_i/2$ versus total power for a given shot with FWEH. The upper bound of the shaded region, $H = 1$, is computed with the experimental value of $\ell_i/2$. Right: experimental safety factor achieved versus $\beta_p + \ell_i/2$, compared to the theoretical resonance criterion (dashed line).

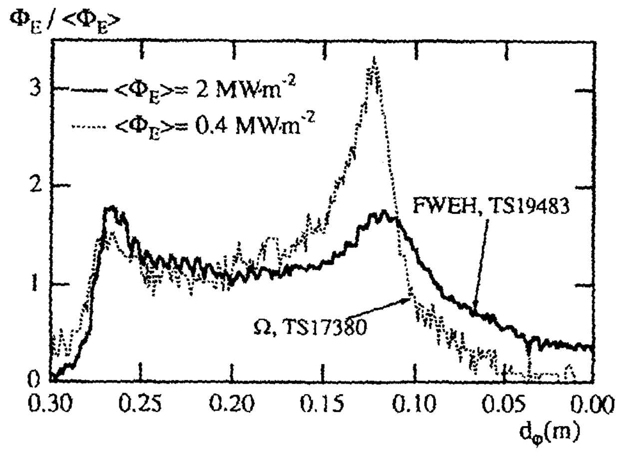

FIG. 4. Peaking factor of the power flux Φ_E to the vented target plate versus distance along the plate d_φ. Ohmic heating (dashed line) and FWEH (full line).

Operation with 7.6 MW total power has been achieved in a configuration based on a reduced divertor volume (R = 2.39 m) and a main hydrogen cyclotron resonance layer localized at $\rho \sim 0.84$ on the high field side of the divertor volume. This high power level includes ohmic power, 5.5 MW of FWEH and 0.75 MW of lower hybrid heating. The small increase of the energy content to $\beta_p \sim 0.3$ follows a typical L mode scaling, $\beta_p \propto P_{total} \sim 0.25\ nl^{-0.5}$. The increase of $\beta_p + \ell_i/2$ requires a larger safety factor to achieve the ergodic divertor resonance (Fig. 3). This effect is predicted by the theoretical analysis of the perturbation spectrum [22]. It should allow one to decrease the plasma current as β_p increases, hence further increasing β_p and eventually generating a meaningful fraction of bootstrap current. Such a favourable trend will be further investigated in order to open the way to long pulse operation with the ergodic divertor.

Operation at high power has also provided a test of the prototype target plate in conditions close to those to be achieved in the forthcoming experimental campaign. Comparing a low density ohmic shot to the present FWEH shot, both at low radiated power, we find that the factor of six increase in the total power leads to a factor of five increase of the mean power flux (Fig. 4). The factor of ~ 1.8 decrease in the peaking factor, i.e. the ratio of the peak energy flux to the average power flux, ensures a more favourable power removal regime in the L mode regime (FWEH discharge) when compared to the ohmic regime. The further tilting of the target plate should further reduce the peaking factor and hence improve the power handling capability of the ergodic divertor. This would allow steady state operation of the ergodic divertor at power levels in the range of 10 MW and a low fraction of radiated power.

5. CONCLUSIONS

Investigation of the power handling capability of the ergodic divertor has been carried out along three main lines. Standard radiating divertor operations have been pursued. Divertor detachment triggered by deuterium injection exhibits a modification of the radiating front in steps as reported for the axisymmetric divertor. A specific effort dedicated to improving the power exhaust of the target plate has been initiated with the testing of a prototype vented target plate. This actively cooled element will allow an increase of the total power up to the 10 MW range. Neutral instead of ionic collection will provide a means of active pumping in the detached or partially detached divertor regime. Finally, high power tests have been performed with FWEH up to 7.6 MW. These indicate a lowering of the peaking factor by a factor of 1.8, which agrees very well with the confinement degradation governed by the power dependence of the L mode scaling. The improvement in the power removal efficiency with the ergodic divertor described in this paper should allow one to address the issues of improved core confinement [23] in a divertor configuration.

REFERENCES

[1] SAMAIN, A., et al., J. Nucl. Mater. **111&112** (1982) 408.

[2] GHENDRIH, P., GROSMAN, A., CAPES, H., to be published in Plasma Phys. Control. Fusion.

[3] GHENDRIH, P., et al. in Plasma-Surface Interactions (Proc. 12th Conf. St. Raphael, 1996), to be published in J. Nucl. Mater.

[4] NGUYEN, F., et al., J. Nucl. Mater. **176&177** (1990) 499.

[5] DOCEUL, L., et al., paper presented at 19th SOFT, Lisbon, 1996.

[6] MONIER-GARBET, P., et al., in Plasma Physics and Controlled Nuclear Fusion Research 1992 (Proc. 14th Int. Conf. Würzburg, 1992), Vol. 1, IAEA, Vienna (1993) 317.
[7] GRISOLIA, C., et al., J. Nucl. Mater. **196–198** (1992) 281.
[8] VALLET, J.-C., in Controlled Fusion and Plasma Physics (Proc. 20th Eur. Conf. Lisbon, 1993), Vol. 17C, Part II, European Physical Society, Geneva (1993) 611.
[9] LIPSCHULTZ, B., J. Nucl. Mater. **145–147** (1987) 15.
[10] PETRIE, T.W., et al., J. Nucl. Mater. **196–198** (1992) 842.
[11] LOARER, T., et al., in Plasma-Surface Interactions (Proc. 12th Conf. St. Raphael, 1996), to be published in J. Nucl. Mater.
[12] LOARER T., et al., J. Nucl. Mater. **220–222** (1995) 183.
[13] PETRIE, T.W., et al., in Plasma-Surface Interactions (Proc. 12th Conf. St. Raphael, 1996), to be published in J. Nucl. Mater.
[14] GROSMAN, A., et al., J. Nucl. Mater. **220–222** (1995) 188.
[15] GRISOLIA, C., et al., in Plasma-Surface Interactions (Proc. 12th Conf. St. Raphael, 1996), to be published in J. Nucl. Mater.
[16] PÉGOURIÉ, B., ibid.
[17] GUILHEM, D., et al., in Controlled Fusion and Plasma Physics (Proc. 21st Eur. Conf. Montpellier, 1994), Vol. 18B, Part II, European Physical Society, Geneva (1994) 254.
[18] FÉRON, S., et al., in Plasma-Surface Interactions (Proc. 12th Conf. St. Raphael, 1996), to be published in J. Nucl. Mater.
[19] TAKAMURA, S., et al., J. Nucl. Mater. **162–164** (1989) 643.
[20] EQUIPE TORE SUPRA, Plasma Phys. Control. Fusion **36** (1994) B123.
[21] TURLUR, S., et al., in Plasma-Surface Interactions (Proc. 12th Conf. St. Raphael, 1996), to be published in J. Nucl. Mater.
[22] GHENDRIH, P., Résonance du Divertor Ergodique, Rep. EUR-CEA-FC-1537, Association Euratom-CEA, Centre d'études nucléaires de Cadarache, Saint-Paul-lez-Durance (1995).
[23] EQUIPE TORE SUPRA, IAEA-CN-64/O2-2, this volume.

INFLUENCE OF LIMITER BIASING ON CONFINEMENT AND STABILITY OF ISTTOK PLASMA

J.A.C. CABRAL, H. FERNANDES, P. MALINOV, P. BELO, A. SOARES, M.P. ALONSO, A. MALAQUIAS, R. CANARIO, A.F. VARANDAS
Associação Euratom–IST,
Centro de Fusão Nuclear,
Instituto Superior Técnico,
Lisbon, Portugal

Abstract

INFLUENCE OF LIMITER BIASING ON CONFINEMENT AND STABILITY OF ISTTOK PLASMA.

Experimental results on the response of the ISTTOK plasma column to the sudden biasing of tokamak stainless steel limiters, with special emphasis on the modification of confinement and stability, are reported.

1. INTRODUCTION

The study of the influence of externally applied electric and magnetic fields on plasma confinement and stability is a very important issue in tokamak plasma physics [1]. Limiter biasing is currently used to model the scrape-off layer radial profiles and to achieve better plasma confinement. Biasing experiments may provide better understanding of radial plasma currents and radial particle transport [2], of the poloidal and toroidal velocities of plasma rotation [3], and of the transition to high confinement [4]. Improved plasma stability during biasing is also to be expected because of the stabilization of small scale turbulence by the increase in velocity shear [5].

2. EXPERIMENTAL CONDITIONS

ISTTOK is a small tokamak with the following external parameters: $R = 0.46$ m, $a = 0.085$ m, $B_T = 0.48$ T, $p_H = 4 \times 10^{-4}$ torr, $V_{pre} = 2000$ V, $V_{dis} = 200$ V, $N = 40$ turns. The experiments were performed in typical ISTTOK flat-top discharges [6] characterized by $\tau_D \sim 60$ ms, $I_p \sim 7$ kA, $n_e \sim 8 \times 10^{18}$ m^{-3}, $T_e \sim 200$ eV, $\tau_E \sim 1.5$ ms, $\beta \sim 0.6\%$ and $q(r = a) \sim 4$. The instant of limiter biasing, t_B, lies in the range of 20 to 26 ms after the start of the discharge, t_0. Usually, only one limiter (horizontal external) was biased but also the other, diametrically opposed (vertical up) limiter was used, either simultaneously with the first one or replacing it.

3. EXPERIMENTAL RESULTS

Starting from a well stabilized reference discharge (REFD) showing a flat-top in the evolution of I_p, we studied the modifications of the plasma column behaviour in a limiter biasing regime in which the applied voltage changed from –300 to +300 V, in steps of 100 V. In this paper, unless otherwise specified, the biasing voltage V_B was either –250 V (No. 2455), 0 V (No. 2473) or +250 V (No. 2454). Other voltages have led to similar parameter behaviour, with only quantitative variations.

3.1. Main Rogowski coil

In the REFD the plasma current exhibits a plateau (Fig. 1(b)). With positive (PBIAS) or negative (NBIAS) bias, the plasma current shows a large increase in its fluctuations (Figs 1(c) and (a)). The peak to peak amplitude is about 300 A for the REFD, 1200 A for NBIAS and 3000 A for PBIAS.

Digital filtering, reducing the noise level of I_p, permits the observation that, after t_B, PBIAS leads to an initial rise of the mean plasma current, a few milliseconds later followed by a disruption or by the crash associated with the sawtooth instability (I_p = 8 kA leads to $q_{(r=0)}$ = 0.95). NBIAS leads to an initial decrease followed by a

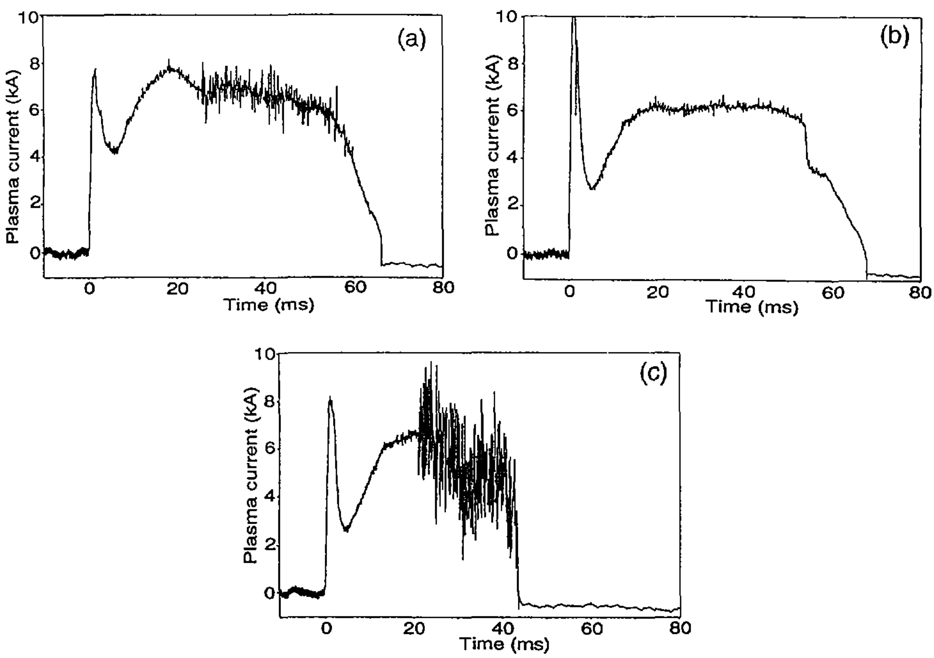

FIG. 1. Temporal variation of plasma current: (a) NBIAS (No. 2455), (b) REFD (No. 2473), (c) PBIAS (No. 2454).

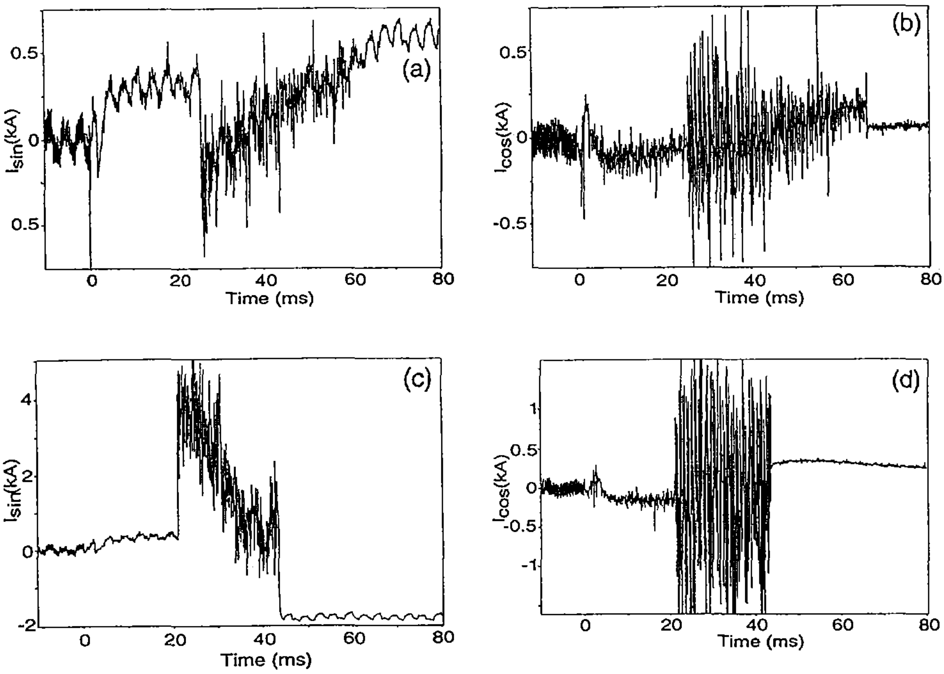

FIG. 2. Temporal variation of sin and cos coil signals for: (a) NBIAS sin (No. 2455), (b) NBIAS cos (No. 2455), (c) PBIAS sin (No. 2454), (d) PBIAS cos (No. 2454).

smooth and continuous rise of the mean plasma current. The REFD, at the usual biasing times, has already attained a current plateau that is almost free of slow fluctuations.

3.2. Sin and cos coils

The signals of the sin and cos position coils also show strong fluctuations after t_B. The cos (sin) coil is associated with plasma column displacements in the horizontal (vertical) direction. PBIAS gives rise to a strong horizontal oscillation (Fig. 2(d)) and a large transitory upward vertical displacement of the plasma column, showing smaller fluctuations (Fig. 2(c)). NBIAS leads to a much weaker horizontal oscillation (Fig. 2(b)) and to a smaller downward vertical displacement of the column, exhibiting also small fluctuations (Fig. 2(a)).

3.3. Toroidal loop

Dividing the loop voltage by the plasma current, we obtain the temporal variation of the plasma resistance. For the REFD, this parameter takes values which show the progressive heating of the plasma electrons. In the plateau region, the resistance decreases from 0.5 to 0.375 mΩ, corresponding, for example, to an increase of T_e from 100 to 265 eV (Spitzer resistivity).

Limiter biasing produces the following modifications: with PBIAS, the plasma resistance increases suddenly after t_B and afterwards shows strong fluctuations with a mean value of around three times the unbiased level. This would correspond to a decrease in T_e from 200 to 50 eV; with NBIAS, the plasma resistance decreases also rapidly after biasing and shows fluctuations with an average value of three quarters of the unbiased level, indicating an increase of T_e, for example, from 200 to 500 eV.

3.4. Mirnov coils

The ISTTOK Mirnov coils are positioned in the poloidal plane at –90°, –60°, –45°, –30°, 45°, 90° and 120° with respect to the equatorial axis. The magnetic coils at –45° and –30° have an acquisition frequency of 333 kHz while all other coils have a frequency of 100 MHz. After biasing, the MHD activity decreases for NBIAS, has a smooth variation for the REFD and shows a temporary increase from t_B = 21 to 30 ms, followed by a strong decrease up to the end of the discharge, for PBIAS.

3.5. Microwave interferometer

ISTTOK has a 100 GHz microwave interferometer, with heterodyne detection at 850 MHz. The line average plasma density along the central vertical chord shows, for the REFD, a continuous decrease in time. With NBIAS (PBIAS), a small (a great) decrease (increase), in comparison with the unbiased case, is observed. These average density changes appear 1 ms after t_B and last for about six confinement times.

3.6. Photodiode

With a fast photodiode, provided with a special H_α interference filter, we followed the intensity of this radiation line at the plasma edge during the entire discharge. The REFD has a more or less continuous decrease of the H_α radiation, probably due to the decrease of n_e with time. With PBIAS we note, after t_B, a large increase (+50%) of the H_α radiation level. With NBIAS this level is diminished strongly (–50%).

3.7. Heavy ion beam diagnostics

The ISTTOK heavy ion beam diagnostics (HIBD) is based on the injection into the plasma of a 22 keV, 1 μA Cs^+ beam, following an almost vertical trajectory, and on two multiple cell detectors, one for the primary beam position and attenuation measurements and the other one for the doubly ionized ions [7]. With the HIBD we have observed that the central value of n_e was in some cases increased by some 20% (No. 2319: V_D = –200 V), but in most cases it remained practically unchanged for

NBIAS. With PBIAS there is evidence of a sudden increase in plasma density (+40%) in the plasma core and of its decrease (–20%) at the plasma edge (No. 2454). However, these results may not be generalized since, in the majority of the discharges, the total detector cell currents show, after t_B, a very strong noise signal due to the impact on the detector cells of energetic photons and fast particles coming from the plasma, which completely masks the currents associated with the Cs^{++} ions. In these cases, not even strong digital filtering can lead to reliable results.

4. INTERPRETATION OF THE RESULTS

4.1. Plasma column displacement

The vertical and horizontal displacements of the plasma column can be calculated from the signals of the two plasma position Rogowski coils. The expressions relating the vertical (ΔV) and horizontal (ΔH) column deviations to the sin and cos coil currents (Isin and Icos) are well known. The expression for ΔH has a Shafranov correction factor, involving beta poloidal and the internal inductance. For these discharges ($\beta_\theta = 0.61\%$ and $\ell_i = 0.724$), this correction factor is of the order of 0.07% of ΔH/b, where b is the vessel radius. Therefore, the sin (cos) current is proportional to I_p and to the vertical (horizontal) displacements, and inversely proportional to twice the vessel radius. The temporal variation of ΔV (ΔH) is then simply obtained by multiplying Isin (Icos) by $2b/I_p$.

Using a digital low pass filter (0–200 Hz), we suppressed the high frequency fluctuations and thus obtained the slow evolution of ΔH and ΔV during the biasing regime. In an X–Y plot (Figs 3(a) and (b)) we present, for NBIAS and PBIAS, the slow motion of the plasma current centre in the transverse plane. The plasma column movements start with a rapid vertical jump, positive for PBIAS and negative for NBIAS. We note that for both cases the plasma column moves clockwise for most of

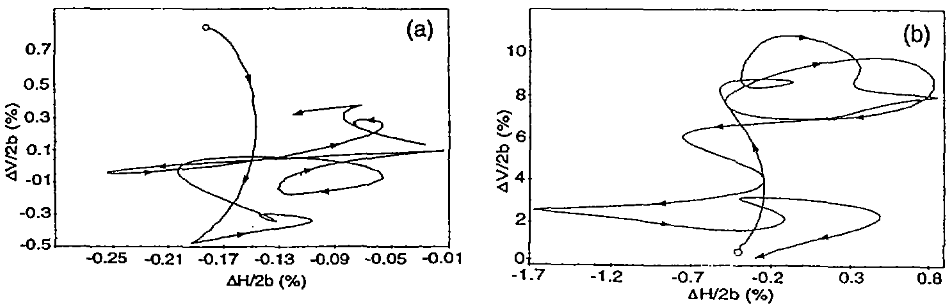

FIG. 3. Displacement of plasma current centre in the transverse plane for (a) NBIAS (No. 2455) and (b) PBIAS (No. 2454).

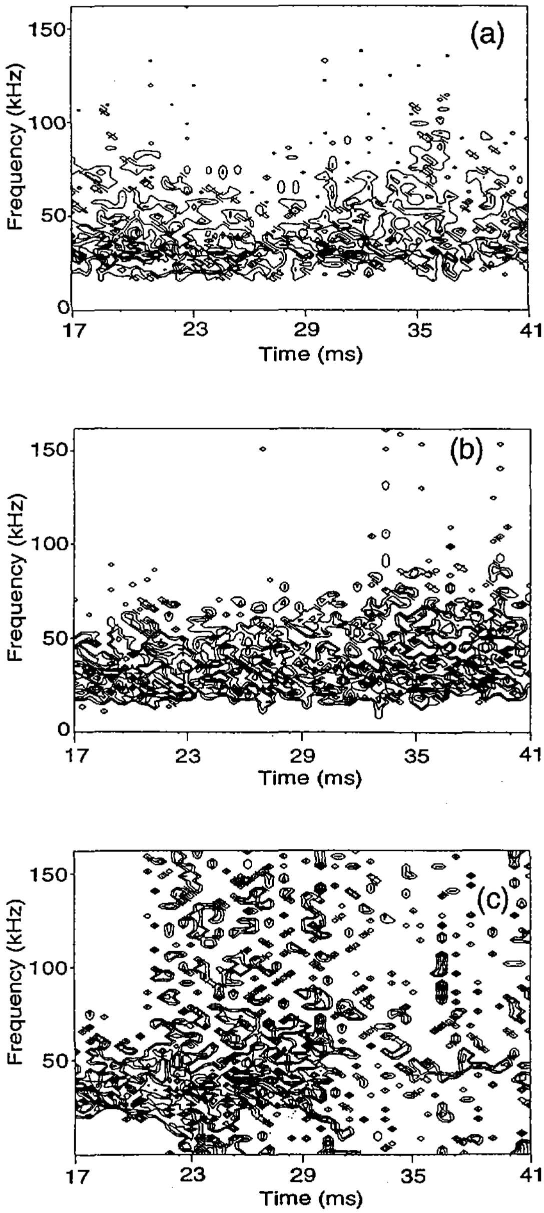

FIG. 4. Temporal evolution of magnetic fluctuation spectrum: (a) NBIAS (No. 2455), (b) REFD (No. 2473), (c) PBIAS (No. 2454).

the time. The use of identical vertical and horizontal scales would reveal that the current centre displacement is mostly in the vertical direction ($\Delta V_{max} - \Delta V_{min}$) ~ 5.5 ($\Delta H_{max} - \Delta H_{min}$) for both PBIAS and NBIAS. Further, PBIAS causes displacements that are typically seven to eight times higher than those created by NBIAS. This may have to do with the difference in the values of the limiter currents, which reached 40 A for NBIAS and –300 A for PBIAS.

The fast vertical displacements of the plasma column are not directly related to a local plasma drift, because of the horizontal E field (horizontal limiter) and the toroidal magnetic field. Indeed, these rapid displacements always maintained a vertical direction even when we replaced the horizontal by the vertical limiter, which should lead to a local horizontal drift velocity. Therefore, the vertical shift of the plasma column is only determined by the value of the applied radial electric field and its polarity, independently of its location in the poloidal plane.

4.2. Analysis of MHD activity

To analyse in greater detail the MHD activity under limiter biasing conditions, with the help of a numerical code, we have obtained, for the three typical discharges, amplitude contour graphics in the time–frequency domain.

For the REFD this contour plot is shown Fig. 4(b). The spectrum shows a smooth temporal variation, showing a bandwidth increase from 20–50 kHz at t = 17 ms to 20–80 kHz at t = 41 ms, but keeping a high amplitude spectral band at 20–40 kHz.

For NBIAS (Fig. 4(a)), we observe a decrease of the main spectral peak amplitudes mostly in the 20–40 kHz band. The spectrum enlarges from the initial 20–75 kHz to 20–100 kHz at t ~ 36 ms. For PBIAS (Fig. 4(c)), at t_B we note an extraordinary broadening of the bandwidth from 20–65 kHz to 3–160 kHz, which remains populated up to the end of the discharge. After t_B and until t = 30 ms, when both the plasma current and the magnetic fluctuations suddenly drop, we note that the domain of the high amplitude spectral peaks is enlarged from 20–40 kHz to 20–80 kHz, revealing an increase of the MHD activity. At t = 30, 36 and 40 ms, there are fast plasma current drops, associated either with partial disruptions or the sawtooth instability, each one creating a relatively large amplitude broad spectrum which lasts less than one confinement time. The lowering of the magnetic fluctuation level between the occurrences of these fast events is typical of the sawtooth instability of ISTTOK [6]. From this analysis, we may conclude that after biasing, and at least during six confinement times, the MHD activity increases (decreases) for PBIAS (NBIAS).

5. CONCLUSIONS

Concluding, we note that the results presented above suggest that PBIAS, although increasing the fluctuation level of most of the plasma parameters, leads to an increase of the central plasma density and to the peaking of the n_e profile which, typically, follows the crash of the sawtooth instability in ISTTOK [6]. NBIAS improves plasma confinement as n_e initially rises and afterwards decreases only slightly and T_e has an important increase, probably leading to a kind of edge controlled H mode. Indeed, the lowering of the MHD activity and the decrease of the H_α radiation level are well known signatures of the L–H mode transition. The plasma column stability is also increased by NBIAS since we have observed the decrease of the amplitude of the most important tearing modes.

REFERENCES

[1] WEYNANTS, R.R., VAN OOST, G., Plasma Phys. Control. Fusion **35** (1993) B177.
[2] CORNELIS, J., et al., Nucl. Fusion **34** (1994) 171.
[3] ROZHANSKY, M.V., TENDLER, M., Phys. Fluids B **4** (1992) 1877.
[4 MOYER, R.A., et al., Phys. Plasmas **2** (1995) 2397.
(5] HUGILL, J., Plasma Phys. Control. Fusion **36** (1994) B173.
[6 CABRAL, J.A.C., et al., Plasma Phys. Control. Fusion **38** (1996) 51.
[7] CABRAL, J.A.C., et al., IEEE Trans. Plasma Sci. **22** (1994) 350.

H MODE TRANSITION AND POWER THRESHOLD IN JT-60U

T. FUKUDA, M. SATO, T. TAKIZUKA,
K. TSUCHIYA, Y. KAMADA, H. TAKENAGA,
JT-60 TEAM
Naka Fusion Research Establishment,
Japan Atomic Energy Research Institute,
Naka-machi, Naka-gun, Ibaraki-ken,
Japan

Abstract

H MODE TRANSITION AND POWER THRESHOLD IN JT-60U.

The impact of neutral particles on the H mode transition power threshold is addressed in this paper. The fact that the compiled threshold database from various tokamaks has not yet been successful in providing a unique and reliable threshold power scaling is mainly ascribed to the ambiguities due to size and density dependences. In particular, the density dependence is regarded as the most crucial issue, which is, however, also most difficult to analyse, because of its sensitivity to the wall conditions. On the basis of the results of experimental investigations on JT-60U, it was established, first, that the edge neutral particle density determines the degree to which the threshold power depends on the density, and, second, that the density boundary below which the H mode transition cannot occur may also be governed by the edge neutrals. Therefore, information on the edge neutral particles can integrate the different density dependences observed in various tokamaks, and thereby a firm basis for size scaling may also be established, which may, to an adequate accuracy, also be extrapolated to a fusion reactor.

1. INTRODUCTION

The establishment of the H mode transition power threshold scaling, together with a thorough understanding of the physics of transition, is, at present, regarded as one of the urgent issues of research. However, the threshold database compiled from various tokamaks has not yet provided a unique and reliable scaling that can be extrapolated to a fusion reactor such as ITER. The so-called dimensionally correct $0.03n_e^{1.0}B_T^{1.0}R^{2.5}$ scaling [1] predicts a minimum threshold power (P_{th}^{min}) of 160 MW at 5×10^{19} m^{-3} for ITER. Here, units are 10^{19} m^{-3}, T and m. However, the prediction of other scalings suggested so far ranges from 60 MW. In order to reduce the ambiguity due to the size dependence, as suggested in Ref. [1], a more reliable assessment of the n_e and B_T dependences in a single device was called for. It should be emphasized here that the decisive element in modifying P_{th}^{min} in various scaling laws, in addition to the size scaling, is the n_e dependence. Furthermore, on the basis of a vague assumption of the n_e dependence, it is anticipated to induce the transition at low density and resort to the fusion power to sustain the H mode at higher density [2]. However, the low density boundary below which the transition cannot occur has not yet been scaled.

We have thereupon carried out an experimental campaign at JT-60U to address the feasible density scaling including the description of the low density transition limit. JT-60U has the capablity of operating at a highest magnetic field of ≥ 4 T and a highest neutral beam (NB) heating power of ≥ 40 MW among the large divertor tokamaks, which is suitable for threshold power scaling studies.

Theories had predicted the possible influence of neutral particles [3] in terms of either ion–neutral friction or a charge exchange process. However, the quantitative treatment was recently first carried out by Shaing [4]. The role of neutrals was interpreted there in terms of the paradigm of a large number of trapped ions experiencing charge exchange in a region where neutrals are abundant, and losing their energy to result in a reduced number of orbit loss ions. Hence, larger heating power is required to induce the transition when neutrals are abundant.

2. IMPACT OF DENSITY DEPENDENCE ON THE THRESHOLD SCALING

The threshold power database that comprises 118 data was compiled from 71 consecutive pulses produced in a single series of experiments with fixed equilibrium configuration, i.e. a single null X point open divertor configuration with the ion ∇B drift direction towards the X point. As will be shown in the next section, indiscriminate accumulation of transition data obtained at different times under the various wall conditions obscures the intrinsic parametric dependence. The ranges of I_p and B_T scanned are, respectively, 0.9–2.4 MA and 1.5–4.0 T. Systematic q scan as well as I_p/B_T scans at fixed q_{eff} of 3.8 and 4.7 were performed. Here, $q_{eff} = 0.5 \times (5\, a_p^2 B_T/R_p I_p)\,(1 + \kappa^2)\,[1 + (a_p/R_p)^2\,(1 + 0.5 \times (\beta_p + \ell_i/2)^2)]\,[1.24 - 0.54\,\kappa + 0.3(\kappa^2 + \delta^2) + 0.13\delta]$ and $q_{eff} \approx q_{95}/0.8$. Also, the density was scanned in the range $(0.7\text{–}2.8) \times 10^{19}$ m^{-3}.

The time derivative fraction of the diamagnetic stored energy normalized by the NB absorption power was $<36\%$, and the radiation power was $(11 \pm 7)\%$. The net absorbed power is defined as $P_{abs} + P_{OH} - \dot{W}$. Here, P_{abs} neither includes the radiation power nor the ripple loss fraction which was $(24 \pm 9)\%$, including the first orbit and charge exchange losses. As a result of having compiled the database from consecutive pulses with a fixed equilibrium profile, Z_{eff} decreased from ≥ 4 to <2, and its average was 2.8.

The NB power was varied stepwise with a step size of 1–2 MW during the discharge to define the heating power right above and below the threshold. The waveforms of a typical discharge are shown in Fig. 1. The NB injection power and the diamagnetic stored energy are shown in Fig. 1(a), while Fig. 1(b) represents the divertor D_α signal. Here, concomitantly with the reduction of the divertor D_α intensity at 9.86 s, an increase of $\bar{n}_e$ and W^{dia} is observed in the middle of the second NB power step, whilst these quantities saturate at the end of the prior NB power step. It is worth noting that the quantities at 99% poloidal flux respond to the transition, but not those at 95% poloidal flux as is ubiquitously demonstrated in various tokamaks. Here, we define P_{net} 'right above threshold' and 'right before the transition'

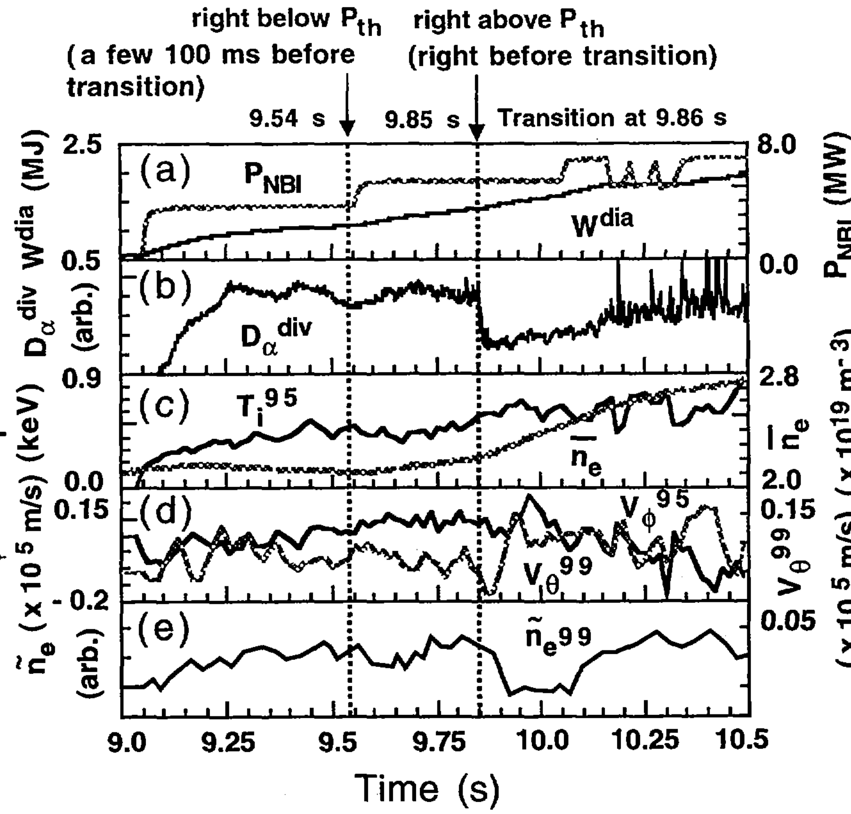

FIG. 1. Typical waveforms of the data compiled in the database: (a) NB injection power and diamagnetic stored energy; (b) divertor D_α signal; (c) edge ion temperature and averaged electron density; (d) edge toroidal flow velocity at 95% poloidal flux and edge poloidal flow velocity at 99% poloidal flux; (e) edge density fluctuations at 99% poloidal flux. Apparently, the H mode transition occurs at 9.86 s.

at 9.85 s (indicated by a dotted line in Fig. 1), and P_{net} 'right below threshold' and 'a few 100 ms before the transition' at 9.54 s, which is the very end of the prior NB power step (broken line). Therefore, all compiled data in our database belong to the L mode phase. The actual threshold, presumably lying between these two values, i.e. the threshold power (P_{th}), was estimated with an accuracy of 0.3 MW to < 1 MW.

Figure 2 shows the result of threshold power scaling, which can be written as

$$P_{th}\ [\mathrm{MW}] = 1.1\ n_e^{0.5}\ [10^{19}\ \mathrm{m}^{-3}]\ B_T^{1.0}\ [\mathrm{T}] \qquad (1)$$

Here, open circles and crosses represent, respectively, P_{net} right above and right below the threshold. The scaling factor was obtained by least squares fitting of the

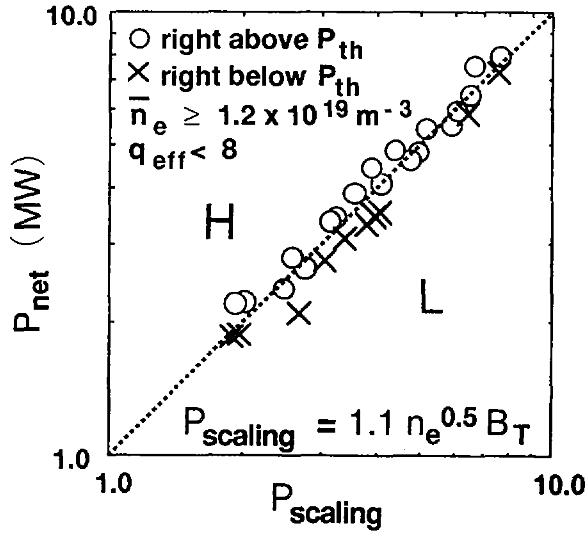

FIG. 2. Threshold power scaling evaluated under the constraints of $\bar{n}_e \geq 1.2 \times 10^{19}\ m^{-3}$ and $q_{eff} < 8$. Open circles and crosses denote P_{net} right above and below the threshold, respectively.

selected data, where values 'well above' and 'well below' the threshold were disregarded. The significance of the $n_e^{0.5}$ dependence is discussed in detail in our previous paper [5]. In the above scaling, the radiation power and ripple loss fraction are not yet taken into account. It should be noted here that our scaling was obtained under the restriction that low density data below $1.2 \times 10^{19}\ m^{-3}$ were excluded. Implications of this constraint are discussed in detail in Section 3.

Among the various 'dimensionally correct' scalings suggested by the ITER H mode database Working Group mentioned in Ref. [1], the new JT-60U scaling is approximately 1.7 times higher in absolute values than the $n_e^{0.75} B_T^{1.0} S$ scaling. However, it does not look compatible with the $n_e^{1.0} B_T^{1.0} R^{2.5}$ scaling. Therefore, P_{th} does not seem to depend so strongly on density as $n_e^{1.0}$ in our database. Here, Fig. 3 was produced by superimposing the new JT-60U results on the figures published in Ref. [1], where only the lower points represent the power threshold suggested by the solid lines. It is also worth noting that the JT-60U results lie in the same region as JET, which has similar dimensions as JT-60U. The factor of 1.7 difference may be lower if one takes the radiation and ripple loss fractions into account, having in mind that JT-60U has a relatively large ripple loss fraction among the operating tokamaks included in the ITER database. However, it also implies the different forms of scaling law. On the assumption that the aspect ratio ($A = R/a$) might be involved as well, which is directly relevant to the banana orbit width [$\Delta_b = F(A^{0.5})$] and the resulting number of trapped-ion losses, possible alternative size scalings, e.g., $n_e^{0.5} B_T^{1.0} R^{1.0} \times a^{0.5}$, are under investigation at present.

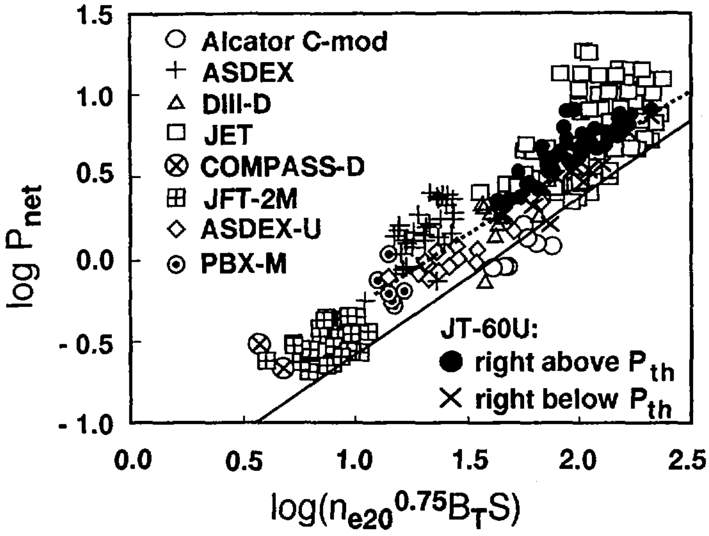

FIG. 3. JT-60U H mode transition power threshold results superimposed on the $n_e^{0.75}B_TS$ scaling suggested by the ITER H mode database Working Group [1].

Provided that the density dependence of $n_e^{0.5}$ is correct (indeed, the $n_e^{0.5}$ dependence was reconfirmed after one year in the second campaign, where the threshold database was compiled with exactly the same experimental procedures) and that size scaling obeys the non-dimensional constraint, i.e. if a

$$P_{th}\,[\mathrm{MW}] = 0.18 n_e^{0.5}[10^{19}\ \mathrm{m}^{-3}]\ B_T^{1.0}[\mathrm{T}]\ R^{1.5}[\mathrm{m}] \tag{2}$$

scaling is assumed, an extrapolation of P_{th} to the ITER EDA design yields 53 MW at $5 \times 10^{19}\ \mathrm{m}^{-3}$. Here, it should be stressed again that, with the assumption of a non-dimensional constraint, the density dependence can easily modify the value of the threshold power by a factor of two. The non-dimensional constraint assumes that P_{th} depends explicitly on engineering variables such as n_e, B_T, R, and treats neither the critical edge temperature nor edge physics phenomena, where atomic processes may play a crucial role. This is the major motivation of our work on the neutral effect described in Section 4. Furthermore, the new JT-60U results are quite inconsistent with the previous scalings published in Refs [6, 7], which claimed weak or no density dependence. It should be noted here that all previous results indicate a P_{th} higher than that predicted by our new scaling, and only the early pulses of our database agreed well with the previous scaling.

3. RELATION BETWEEN THRESHOLD SCALING AND EDGE ION COLLISIONALITY

We will now proceed to the cases where conditions imposed to influence the scaling are removed. P_{net}/B_T is plotted against $\bar{n}_e$ in Fig. 4(a). It is evident that the threshold power is minimum in the region of $\bar{n}_e \approx 1.2 \times 10^{19}$ m^{-3}. Substantial increase of the threshold power appears in the range of $\bar{n}_e < 1.2 \times 10^{19}$ m^{-3},

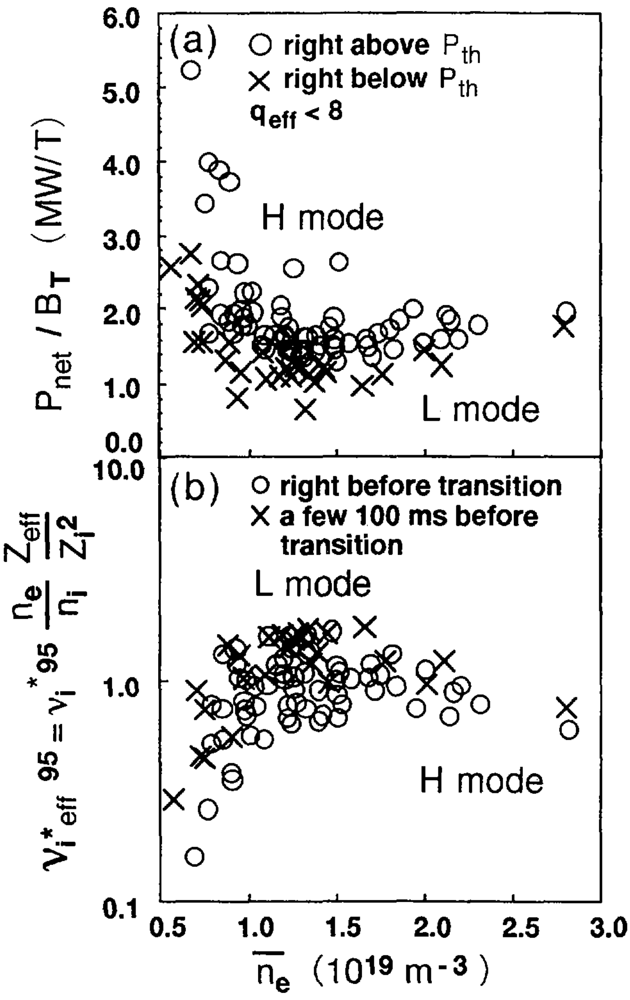

FIG. 4. (a) P_{net}/B_T versus averaged density, $\bar{n}_e$. The constraint $q_{eff} < 8$ is retained. (b) Density dependence of effective edge ion collisionality, $\nu^{*95}_{i\,eff}$, at 95% poloidal flux. Open circles and crosses correspond, respectively, to right before and a few 100 ms before the transition.

where the necessary NB injection power inducing the transition exceeds 20 MW even at 2 T. It should be emphasized that the threshold power increases moderately also in the range of $\bar{n}_e \geq 1.5 \times 10^{19}$ m^{-3}. Figure 4(b) shows the $\bar{n}_e$ dependence of the effective edge ion collisionality written in the form:

$$\nu^{*95}_{i\,eff} = \nu_{ii} R q_{eff}/\epsilon^{2/3}\ v^{95}_{th}(n_e/n_i)\ (Z_{eff}/Z_i^2) \tag{3}$$

where v^{95}_{0} is the ion thermal velocity at 95% poloidal flux; the impurity contribution is included [8]. No constraints are imposed on the database to produce Fig. 4(b); open circles and crosses correspond to the data right before and a few 100 ms before the transition, respectively. It can readily be seen that $\nu^{*95}_{i\,eff}$ is around unity only near the limited region of the minimum threshold, whilst conventional theory requires unconditional unity [9] at >95% poloidal flux. In the range of $\bar{n}_e < 1.2 \times 10^{19}$ m^{-3}, $\nu^{*95}_{i\,eff}$ decreases significantly, corresponding to an increase of the threshold power, while it decreases moderately in the range of $\bar{n}_e > 1.5 \times 10^{19}$ m^{-3}, which is relevant to an increase of the threshold power ascribed to the n_e dependence. It was also found that the reduction of $\nu^{*95}_{i\,eff}$ is directly relevant to an increase of T^{95}_i in both density ranges. Therefore, our hypothesis is that lower collisionality requires higher edge temperature to induce the transition, which is practically realized by applying a higher heating power.

4. EFFECT OF EDGE NEUTRALS ON THRESHOLD SCALING

In order to elucidate the cause of increased threshold power at low density and the physics of the density dependence as well as to resolve the inconsistency with our previous results, we have evaluated the edge neutral density (n^{95}_0) with the DEGAS code [10]. n^{95}_0 was evaluated by averaging over the meshes on a flux surface at ≥95% poloidal flux. Here, as is indicated by the calculated results, we emphasize that the value of n^{95}_0 is mainly determined in the region near the X point.

Figure 5 depicts the relationship between the edge neutral density and the ion collisionality, where open circles and crosses, respectively, refer to right before and a few 100 ms before the transition, for $\bar{n}_e \geq 1.2 \times 10^{19}$ m^{-3}. The open squares and plus signs are, similarly, related to $\bar{n}_e < 1.2 \times 10^{19}$ m^{-3}. With due account for the role of non-dimensional quantities, the ratio of n^{95}_0 and n^{95}_e was plotted against $\nu^{*95}_{i\,eff}$. It is evident that $\nu^{*95}_{i\,eff}$ starts to decrease right before the transition, above a fixed boundary of n^{95}_0/n^{95}_e ((2–3) $\times 10^{-5}$, in this work), regardless of the density range. However, the low density data extend further into the low $\nu^{*95}_{i\,eff}$ range. This feature is quite consistent with the characteristic density dependence of P_{th} and $\nu^{*95}_{i\,eff}$ in Fig. 4, i.e. both the low density boundary and the apparent density dependence of P_{th} scaling can be ascribed to n^{95}_0/n^{95}_e. As a consequence of increased n^{95}_0/n^{95}_e, which occurs when $\bar{n}_e$ takes an excursion in either direction away from the minimum P_{th}

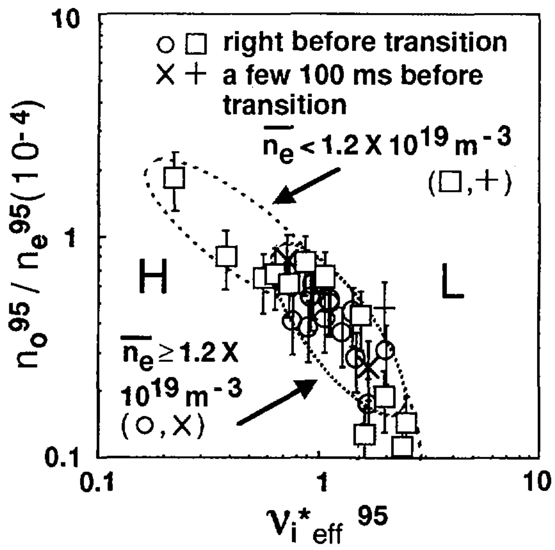

FIG. 5. Relation between edge neutral density normalized with edge electron density and edge ion collisionality, all evaluated at r/a = 0.95. Open circles and crosses refer, respectively, to times right before and a few 100 ms before the transition for $\bar{n}_e \geq 1.2 \times 10^{19}$ m^{-3}. Open squares and plus signs similarly refer to $\bar{n}_e < 1.2 \times 10^{19}$ m^{-3}.

region, higher critical edge T_i and heating power are required to induce the transition; its degree is moderate when $\bar{n}_e \geq 1.5 \times 10^{19}$ m^{-3} and substantial when $\bar{n}_e < 1.5 \times 10^{19}$ m^{-3}. The increased threshold power at higher neutral density is consistent with the theoretical prediction in Ref. [4]. Therefore, it may be speculated that the reduction of n_0^{95} at a given n_e^{95} substantially reduces the low density constraints. In addition, we can also reduce P_{th} by a decrease of n_0^{95}/n_e^{95}, at a given density.

In order to elucidate the principal mechanism of the neutral effect, the charge exchange frequency, ν_{cx}^{95}, was evaluated. Here, $\nu_{i\,eff}^{*95} = n_0^{95}\langle\sigma v\rangle_{cx}$, and $\langle\sigma v\rangle_{cx}$ represents the cross-section for the charge exchange reaction. Similar to the definition of $\nu_{i\,eff}^{*95}$, the ratio of ν_{cx}^{95} and ν_b (bounce frequency given by $\epsilon^{1/2}v_{th}^{95}/R_p q_{eff}$), which is again a non-dimensional parameter, was considered. Although the size of the error bars is large, ν_{cx}^{95}/ν_b increases monotonically as the ion collisionality is reduced, and the absolute value of ν_{cx}^{95}/ν_b, where the transition becomes hardly attainable [a value of $\nu_{i\,eff}^{*95}$ of 0.05 was conjectured from Fig. 4(b)], is approximately 9.6×10^{-3} in this work. Reference [4] introduces the value of 1.4×10^{-2} for the ν_{cx}^{95}/ν_b limit, which is within a factor of two of our estimate. Therefore, the charge exchange process remains one of the potential candidates.

5. H TO L BACKTRANSITIONS

In the second series of the experimental campaign, where the scaling of the H to L backtransition was highlighted, 45 consecutive discharges in parametric ranges similar to these of the L to H transition experiment were performed, again with a fixed equilibrium configuration. Here, NB power was stepped down with a step size of 1–2 MW during the discharge, and we have applied barely enough heating power to attain the H mode, in order to reduce the impurity influx as well as to exclude the ELM induced backtransitions, which occasionally move the plasma back into the L mode at relatively high NB power. Instead, we have focused on spontaneous backtransitions caused by reduction of the heating power.

Contrary to the theoretical predictions [11], P_{net} at the backtransition was similar to that for the L to H transition, and no apparent hysteresis was observed. As the radiation loss at the backtransition was considerably larger than that for the L to H transition, it was subtracted from P_{net}. In addition, the value of Z_{eff} was higher at the backtransition by a factor of 1.3, and so was the D_α intensity, by a noticeable amount, in spite of the significant reduction of n_0^{95} right after the L to H transition. As our result is in contradiction with ASDEX work [12], a detailed analysis of the edge neutral density and other parametric dependences is under way.

6. CONCLUSIONS AND DISCUSSION

As a result of the intensive experimental campaign at JT-60U, where the H mode transition threshold power database was compiled from consecutive pulses produced in a single series with a fixed equilibrium configuration, we have: (1) The L to H mode threshold power scaling of $P_{th}\,[\mathrm{MW}] = 0.18\, n_e^{0.5}\,[10^{19}\ \mathrm{m^{-3}}]\, B_T^{1.0}\,[\mathrm{T}] \times R^{1.5}\,[\mathrm{m}]$ was obtained, on the assumption of non-dimensional constraints. Extrapolation of this result to the ITER EDA design yields 53 MW at $5 \times 10^{19}\ \mathrm{m^{-3}}$. In the second campaign, where the same experimental procedure was repeated one year after the initial experiment, the $n_e^{0.5}$ dependence was reconfirmed. (2) The newly established scaling indicates a substantially lower threshold power than the previous results at JT-60U, whose database was indiscriminately accumulated at different times under various discharging and wall conditions. (3) Possibly because of an increase in the impurity concentration and edge neutral density, the hysteresis of the backtransition power threshold was obscured in our work.

Although the density range was limited to below $3 \times 10^{19}\ \mathrm{m^{-3}}$ in this work, what is fundamental in evaluating the density contribution to the threshold power scaling seems to lie in how much the neutral density is involved in the variations of density and not in the absolute value of density itself. The low density boundary below which the transition cannot occur, as well as the origin of the density dependence, was investigated quantitatively in terms of the neutral particle density with the DEGAS code for the first time. It was demonstrated that (4) the ratio of edge neutral density and electron density increases significantly below the minimum threshold density range, which induces a higher critical edge temperature right before the transition as well as an increase in the threshold power. In other words, the reduction of n_0^{95}/n_e^{95} can potentially reduce the low density constraints. (5) n_0^{95}/n_e^{95} also increases moderately above the minimum threshold density, which suggests that the density dependence may be an intrinsic n_0^{95} dependence. Therefore, the manipulated threshold power scaling in this work can be correct only under the limited conditions of n_0^{95}/n_e^{95} ($\bar{n}_e$). As to the principal mechanism of the neutral particle effect, charge exchange was suggested as one of the potential candidate processes.

Thus, this work has first introduced the significance of atomic processes in threshold scaling studies, suggesting that information on the edge neutral density may integrate the different density dependences observed in various tokamaks. Accordingly, a firm basis for size scaling may be established; it can, with adequate precision, be extrapolated to a fusion reactor.

ACKNOWLEDGEMENTS

One of the authors (T.F.) would like to acknowledge Dr. K.C. Shaing at the Institute of Fusion Studies, University of Texas at Austin, United States of America, for stimulating and productive discussions. The results described in this paper were obtained with substantial contributions of the JT-60 Team. The authors are also indebted to Drs H. Kishimoto and M. Azumi for continuous support and encouragement.

REFERENCES

[1] RYTER, F., H MODE DATABASE WORKING GROUP, Nucl. Fusion 36 (1996) 1217.

[2] ITER CONFINEMENT DATABASE AND MODELING GROUP, in Plasma Physics and Controlled Nuclear Fusion Research 1994 (Proc. 15th Int. Conf. Seville, 1994), Vol. 2, IAEA, Vienna (1995) 525.

[3] SHAING, K.C., HOULBERG, W.A., CRUME, F.C., Comments Plasma Phys. Control. Fusion 12 (1988) 69.

[4] SHAING, K.C., HSU, C.T., Phys. Plasmas 2 (1995) 1801.

[5] SATO, M., FUKUDA, T., TAKIZUKA, T., et al., Threshold power for H-mode transition in JT-60U plasmas, to be published in Plasma Phys. Control. Fusion.

[6] KIKUCHI, M., et al., in Plasma Physics and Controlled Nuclear Fusion Research 1992 (Proc. 14th Int. Conf. Würzburg, 1992), Vol. 1, IAEA, Vienna (1993) 189.

[7] SATO, M., KIKUCHI, M., FUKUDA, T., et al., in Plasma Physics and Controlled Nuclear Fusion Research 1994 (Proc. 15th Int. Conf. Seville, 1994), Vol. 1, IAEA, Vienna (1995) 265.

[8] FUKUDA, T., KIKUCHI, M., KOIDE, Y., et al., Plasma Phys. Control. Fusion 36 A (1994) 87.

[9] SHAING, K.C., CRUME, E.C., Jr., Phys. Rev. Lett. 63 (1989) 2369.

[10] TAKENAGA, H., ASAKURA, N., SHIMIZU, K., et al., J. Nucl. Mater. 220–222 (1995) 429.

[11] ITOH, S.-I., ITOH, K., Phys. Rev. Lett. 60 (1988) 2276.

[12] RYTER, F., et al., in Controlled Fusion and Plasma Physics (Proc. 21st Eur. Conf. Montpellier, 1994), Vol. 18B, Part I, European Physical Society, Geneva (1994) 330.

STUDY OF H-MODE THRESHOLD CONDITIONS IN DIII-D*

R.J. GROEBNER, T.S. CARLSTROM, K.H. BURRELL, S. CODA[1], E.J. DOYLE[2], P. GOHIL, K.W. KIM[2], R. MAINGI[3], R.A. MOYER[4], Q. PENG, C.L. RETTIG[2], T.L. RHODES[2], D.P. SCHISSEL, G.M. STAEBLER, R.D. STAMBAUGH, D.M. THOMAS, J.G. WATKINS[5]
General Atomics,
San Diego, California,
United States of America

Abstract

STUDY OF H-MODE THRESHOLD CONDITIONS IN DIII-D.

Studies have been conducted in DIII-D to determine the dependence of the power threshold P_{lh} for the transition to the H-mode regime and the threshold P_{hl} for the transition from H-mode to L-mode as functions of external parameters. There is a value of the line-averaged density n_e at which P_{lh} has a minimum and P_{lh} tends to increase for lower and higher values of n_e. Experiments conducted to separate the effect of the neutral density n_0 from the plasma density n_e give evidence of a strong coupling between n_0 and n_e. The separate effect of neutrals on the transition has not been determined. Coordinated experiments with JET made in the ITER shape show that P_{lh} increases approximately as $S^{0.5}$ where S is the plasma surface area. For these discharges, the power threshold in DIII-D was high by normal standards, thus suggesting that effects other than plasma size may have affected the experiment. Studies of H–L transitions have been initiated and hysteresis of order 40% has been observed. Studies have also been done of the dependence of the L–H transition on local edge parameters. Characterization of the edge within a few milliseconds prior to the transition shows that the range of edge temperatures at which the transition has been observed is more restrictive than the range of densities at which it occurs. These results suggest that some temperature function is important for controlling the transition.

* Work supported by US Department of Energy contracts DE-AC03-89ER51114, DE-AC05-96OR22464 and DE-AC04-94AL85000, and grants DE-FG03-86ER53266 and DE-FG03-95ER54294.

[1] Massachusetts Institute of Technology, Cambridge, Massachusetts, USA.
[2] University of California, Los Angeles, California, USA.
[3] Oak Ridge Associated Universities, Oak Ridge, Tennessee, USA.
[4] University of California, San Diego, California, USA.
[5] Sandia National Laboratories, Livermore, California, USA.

1. INTRODUCTION

The H–mode discharge provides one of the most important regimes of improved confinement in both the present generation of tokamaks and in designs of future machines, particularly ITER. Study of the transition to H–mode (L-H transition) provides a high leverage route to obtain a basic understanding of the physics of the tokamak boundary layer, particularly edge transport, and is needed to provide reliable predictive capability for future machines. A two-part approach has been used in DIII–D to study H–mode transition physics. Primarily in support of the design of ITER, which must operate in the H–mode regime to be successful, studies have been done of the dependence of the H–mode power threshold P_{lh} on global parameters. These parameters include density, neutrals and machine size. In addition, studies have been initiated of the power P_{hl} at which back (H-L) transitions occur. The second part of the approach to H–mode studies involves determining the local edge conditions which are required for transition to the H–mode to occur. This latter work is required in order to obtain a more fundamental understanding which is required for the development of quantitative predictive models for the transition.

2. DEPENDENCE OF TRANSITION ON GLOBAL PARAMETERS

The candidate scaling relationship for P_{lh} in terms of global (or control) parameters proposed for ITER [1] is $P_{lh} \propto n_e B\, S$, where n_e is the line-averaged electron density, B is the toroidal magnetic field and S is the surface area of the plasma. Because this relationship leads to predictions of high values of P_{lh} (~150 MW) in ITER, improved confidence in this scaling is needed. During the last two years, DIII–D has studied the dependence of P_{lh} on n_e and S. One improvement in analysis techniques is that P_{lh} is now based on improved measurements of P_{sep}, the power flowing through the separatrix [2,3]. $P_{sep} = P_\Omega + P_{aux} - dW_p/dt - P_{rad}$ where P_Ω is the ohmic heating power, P_{aux} is the auxiliary heating power, dW_p/dt is the rate of change of the stored energy in the plasma and P_{rad} is the radiated power from inside the last closed flux surface. This approach is consistent with the power flux through the plasma boundary controlling edge parameters which probably control the transition.

The range in n_e over which the H–mode can be obtained in DIII–D is not controlled by fundamental limits to H–mode accessibility but rather by operational constraints [4]. At low densities, locked modes can inhibit or raise P_{lh} for the H–mode; when locked modes are removed with coils to correct error fields, the H–mode is obtained at low n_e. At high densities, achieving the H–mode is limited by MARFE activity associated with high values of neutral pressure due to gas puffing.

Threshold studies performed in DIII–D in 1993 indicated that P_{lh} increased approximately linearly with n_e [5]. New data for the density scaling of the threshold were taken in 1994 and some of these data examined P_{lh} at lower values of n_e than obtained in 1993. The analysis of the 1994 data [Fig. 1(a)] indicates that there is a value of n_e at which P_{lh} tends to increase for higher values of n_e [4], consistent with the 1993 results, and also to increase for lower values of n_e. Thus, over the entire density range, the variation of P_{lh} with n_e is weaker than linear with P_{lh} having a range of factor of two and n_e a range of a factor of four. The actual values of P_{lh} for the 1994 data are somewhat less than for the 1993 data. This change may be due partially to gradual improvements in vessel conditioning. However, part of the change is due to the fact that P_{lh} for the 1994 data was adjusted by P_{rad} whereas earlier data had not been corrected in this way.

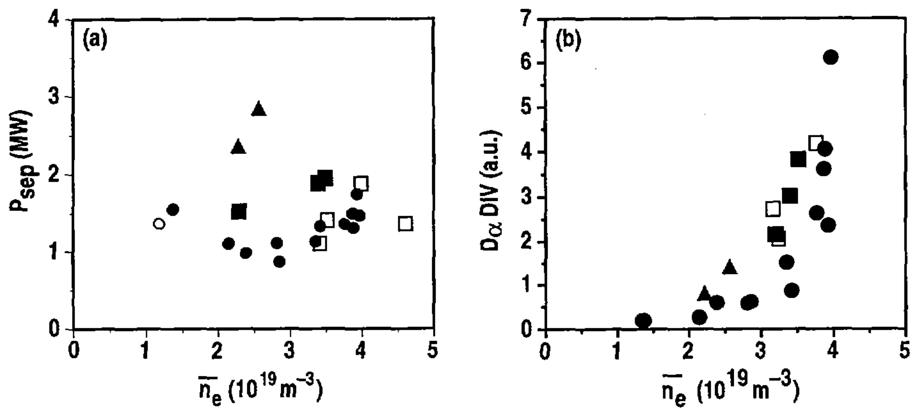

FIG. 1. (a) P_{th} (P_{sep}) required to produce H-mode versus line averaged density n_e (I_p = 1.35 MA, B_T = 2.1 T). Data from 1994 with (open circles) and without (solid circles) error field correction coil show that P_{th} is at a minimum for n_e in the range (2–3) $\times$ 10^{19} m^{-3} and increases for lower and higher values of n_e. Data from the neutrals experiment are shown for positive density ramp (open squares), no gas puff (solid squares) and negative density ramp (triangles). (b) Divertor D_α emission, assumed to be an indicator for neutral density, as a function of n_e. The 1994 n_e scan (circles) shows that D_α increases nonlinearly with n_e. D_α values obtained from the experiment which attempted to break the correlation of neutral density and n_e are comparable to values from the 1994 scan, evidence that neutral density is strongly correlated with n_e. Symbols have the same meaning as in (a).

It has long been suspected that neutrals play a hidden role in the H–mode transition. In order to examine this issue, an experiment was performed in DIII–D to measure P_{lh} at a fixed value of n_e as the ratio of neutral density n_0 to n_e was changed by ramping the density up with a large gas puff and by ramping the density down with the aid of the DIII–D cryopump. A serious impediment to studies of neutrals is that no direct measurements of the neutral density at the separatrix are readily available. Under the assumption that the neutral pressure and D_α emission are reasonable indicators of n_0, this experiment showed that n_e and n_0 are tightly coupled and that the original goals of the experiment were not achieved. For example, Fig. 1(b) compares the D_α emission from the divertor for the 1994 density scan, in which the time rate of change of the electron density *dn/dt* was 0, and for the neutrals experiment in which *dn/dt* was varied from negative to positive. The D_α signals are more strongly correlated with the value of n_e than with the value of *dn/dt*. Study of neutral pressure provides the same result. However, the power threshold values obtained from this experiment show a different trend than expected from the 1994 n_e scaling data. Figure 1(a) shows that the values of P_{lh} obtained with a negative density ramp (using the cryopump) were about a factor of two higher than observed in the 1994 data, P_{lh} without a ramp was moderately higher than the 1994 data and P_{lh} with a positive density ramp was comparable to the 1994 data. These effects are not yet understood. One possibility is that the correlation between n_0 and n_e was actually broken, particularly with the aid of the cryopump, and that P_{lh} does have a dependence on n_0. Perhaps this result is due to some unknown divertor or scrape-off layer effect. Further analysis and further experiments are required to study this result.

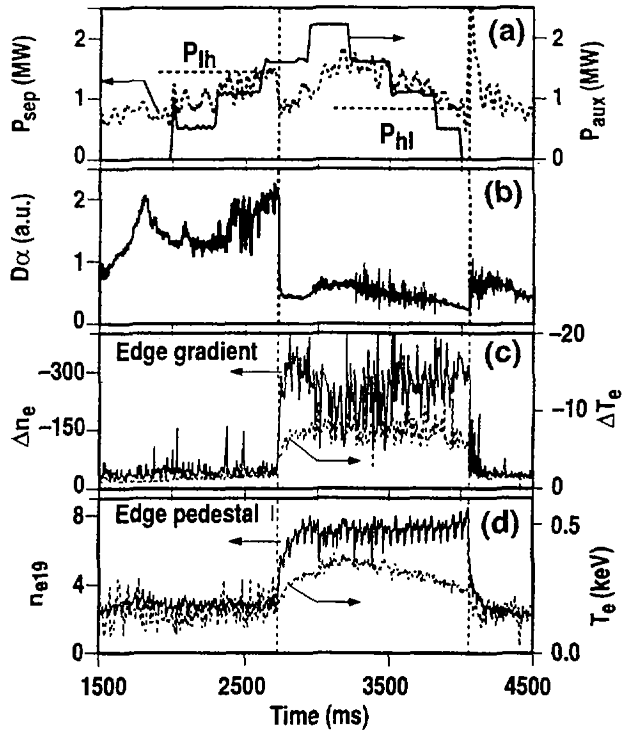

FIG. 2. (a) Solid line shows injected neutral beam power P_{aux} which was ramped up and then ramped down in stairstep fashion. Dashed line shows P_{sep}. H-L transition occurred after beam power was turned off. Nevertheless, H-mode was sustained with P_{sep} of about 60% of P_{lh} (I_p = 1.35 MA, B_T = 2.1 T). (b) D_α as a function of time. Dashed vertical lines mark time of L-H transition (about 2700 ms) and H-L transition (4100 ms). (c) Gradients of T_e (keV/m) and n_e ($10^{19}m^{-4}$) in the transport barrier show similar time behavior. They rise rapidly after the L-H transition and drop abruptly at the H-L transition. (d) Pedestal values of T_e and n_e, determined from hyperbolic tangent fit, show that T_e starts to decrease as P_{sep} is decreased. In contrast, n_e remains unchanged until the back transition.

The dependence of P_{lh} on surface area has been studied with coordinated discharges in JET and in DIII-D which were performed in the ITER shape and with similar control parameters [6]. These experiments indicate that P_{lh} is proportional to $S^{0.5}$, a dependence which is much more favorable for ITER than the scaling relationship shown above. However, the measured P_{lh} in DIII-D was high by normal DIII-D standards and work is required to determine if this result is due to systematic effects related to shape or neutral pressure. In particular, discharges in DIII-D which have the ITER shape have a large outer gap, and perhaps effects related to neutrals were different than for more conventional discharges with smaller gaps.

It is well known that the H-mode exhibits significant hysteresis; that is, it is possible to sustain a discharge in the H-mode with less heating power than is required to produce the transition to H-mode. This effect is of interest both because of its implications regarding the basics physics of the H-mode and because the design for

ITER plans to operate in a regime where the hysteresis will be used to maintain the H–mode. Quantitative studies of the hysteresis in DIII–D have been initiated. Data have been obtained by increasing the heating power in small increments to assess P_{lh} and then decreasing the power in small steps to measure P_{hl}, the power level at which the transition from H– to L–mode occurs. These studies are somewhat inhibited because the L-H threshold is low in DIII–D and discharges tend to remain in H–mode even when auxiliary heating is turned off. As with studies of P_{lh}, it is very important to account for P_{rad} in assessing the net loss power required to sustain the H–mode. Systematic studies of the hysteresis in DIII–D have not yet been completed. However, it is clear that significant hysteresis is observed in DIII–D H–mode discharges, as is illustrated in Fig. 2. In this example, the back transition occurs at a loss power which is about 60% of the loss power required to produce the L-H transition.

3. DEPENDENCE OF TRANSITION ON LOCAL EDGE PARAMETERS

A major goal of L-H studies is to obtain a fundamental physics understanding which will provide the basis for quantitative predictive models of the transition. For this goal to be obtained, improved knowledge of local edge conditions required for the transition must be obtained. The DIII–D diagnostic set, routinely providing measurements of edge T_e, n_e, and T_i profiles with sub-centimeter spatial resolution and temporal resolution of 6 milliseconds or better can make such measurements and is being used to construct a database of these edge quantities and their gradients just prior to the transition to H–mode. This database is being used to assess the range of edge conditions present at the L-H transition and the ultimate goal is to search for a critical edge parameter which must be achieved so that the H–mode transition can occur.

Local edge parameters are evaluated with the aid of a non-linear least squares algorithm which is used to fit spline functions [7] to the measurements which have been mapped to a magnetic coordinate system. In this paper, the "edge" of the plasma is defined as the center of the region which becomes the transport barrier in H–mode. For the data examined so far, it appears that $\rho = 0.95$ (where ρ is the normalized toroidal flux) is close to being in the center of many H–mode transport barriers, so the L–mode profiles have been evaluated at this ρ value.

The range of edge parameters observed just prior to the transition to the H–mode is summarized in Table I. This table indicates that the database contains discharges whose control parameters cover a wide range of the DIII–D operating space. The most salient feature of the local edge parameters is that the transition occurs for a fairly wide range of density but for a relatively small range of temperature. This result is obtained even though the power threshold varies by more than an order of magnitude, and suggests that the threshold condition is some function of temperature. If the transition is related to the ion collisionality ν_{i*}, it is more complex than the requirement to achieve a fixed value of ν_{i*}, which varies by a factor of eight in the database. The scale lengths for T_e, n_e, and T_i are in the range of one to a few times the ion poloidal gyroradius $\rho_{\theta i}$ which in turn is nearly constant at 0.5–0.8 cm.

A weakness of this approach is that some scatter is introduced into the results because the chosen ρ value is somewhat arbitrary and is probably not correct for all plasma conditions and because there is an uncertainty of about ±0.5 cm in the location of the separatrix obtained from the equilibrium fit. An improved analysis for H–mode transport barriers has been developed which uses a hyperbolic tangent plus a linear term to fit edge profiles as functions of space in physical coordinates. An advantage of this approach is that edge profiles can be conveniently parameterized in terms of a few

Table I
Range of Machine Control Parameters and Edge Parameters in Transition Database. All Edge Data are Evaluated in L–Mode <10 ms Before Transition to H–Mode

Control parameters	Edge parameters (ρ = 0.95)
$1.3 < B_T < 2.1$ (Tesla)	$0.034 < T_e < 0.13$ keV
$1.0 < I_p < 2.0$ (MA)	$0.11 < T_i < 0.22$ keV
$1.2 < n_e < 4.0 \times 10^{19}$ m^{-3}	$0.5 < n_e < 4.4 \times 10^{19}$ m^{-3}
$1.0 < P_{lh} < 14.0$ (MW)	$2 < \nu_{i*} < 17$ (n_i assumed equal to n_e)
	$0.5 < \rho_{\theta i} < 0.8$ (cm)
	$1 \times \rho_{\theta i} < L_{n_e} < 6 \times \rho_{\theta i}$
	$1 \times \rho_{\theta i} < L_{T_e} < 4 \times \rho_{\theta i}$
	$1 \times \rho_{\theta i} < L_{T_i} < 12 \times \rho_{\theta i}$

fit parameters, including the symmetry point of the hyperbolic tangent and a pedestal value, and the evolution of these parameters during a discharge can be readily obtained by fitting a time series of edge profiles. The usefulness of this technique for studying L–mode edge plasmas is under study.

4. SUMMARY AND CONCLUSIONS

In summary, H–mode studies have been conducted in DIII–D to examine the dependence of P_{lh} on external control parameters, to examine the hysteresis of the H–mode and to characterize the local edge parameters at the time of the transition. One improvement in the power threshold studies is that P_{lh} is being defined as P_{sep} where P_{sep} is the power flowing through the plasma boundary and is obtained by adjusting the heating power for radiation and the time rate of change of the plasma stored energy. Although this approach may provide better insights into the true scaling of P_{lh}, extrapolations of such values of P_{lh} to ITER tend to underestimate the actual heating power needed to overcome line radiation and transient effects.

The dependence of P_{lh} on n_e is weak when constraints to the normal operating space are avoided. More precisely, P_{lh} has a minimum for densities in the middle of this operating space and tends to rise for lower or higher values of n_e. Coordinated experiments performed with JET indicate that P_{lh} scales as $S^{0.5}$. This result is favorable for ITER, but further work is required to determine if the large gaps required to produce the ITER-shaped plasmas tend to produce a high power threshold in DIII–D. Both the studies of density and of size scaling here have produced results which are different than those indicated by the ITER scaling relationship [1].

Initial studies of the effects of neutrals on P_{lh} suggest that it is very difficult to decouple neutral density from electron density. These studies are also hampered by lack of direct measurements of the neutral density inside the plasma. Modeling of the neutral density is required to help overcome these problems. Studies of H–mode hysteresis in DIII–D have been initiated. Significant hysteresis has been observed with P_{hl} being of the order of half of P_{lh}. However, significant variation in the amount of hysteresis has been observed and the relation between P_{lh} and P_{hl} in DIII–D remains to be determined.

A systematic study of the local edge conditions required to obtain H–mode has been initiated with the establishment of a database of edge T_e, T_i and n_e observed just prior to the transition. This database shows that the range of edge temperatures observed just prior to the transition is relatively narrow. These observations suggest that the transition condition is some function of temperature, a hypothesis originally suggested by sawtooth-triggered transitions in ASDEX [8] and supported by a significant amount of data from several machines. This idea is also supported by some observations of H-L transitions in DIII–D. For instance, Fig. 2 shows that as the heating power was decreased, the pedestal value of T_e also decreased and the back transition occurred as T_e approached the level it originally had before the L-H transition. However, there are counter-examples which show that the pedestal value of T_e remains high and unchanged until the H-L transition. Such transitions may be triggered by ELMs, but this is not yet known for certain. It can also be argued that the database reflects boundary conditions imposed by the scrape-off layer (SOL) rather than any fundamental H–mode physics. In particular, electron heat conduction along the open field lines in the SOL is very large and ensures that T_e at the last closed flux surface will be low. In turn, the electron-ion equilibration will tend to keep T_i relatively low and possibly in a small range. Thus, it is necessary to develop further experimental tests which will reveal unambiguously whether or not the threshold condition is some function of edge temperature.

REFERENCES

[1] RYTER, F., ITER H-MODE DATABASE WORKING GROUP, Controlled Fusion and Plasma Physics (Proc. 21st Eur. Conf. Montpellier, 1994), Vol. 18B, Part I, European Physical Society, Geneva (1994) 334.

[2] RYTER, F., et al., Plasma Phys. Control. Fusion **36** (1994) 99.

[3] CARLSTROM, T.N., Plasma Phys. Control. Fusion **38** (1996) 1149.

[4] CARLSTROM, T.N., GROEBNER, R.J., Phys. Plasmas **3** (1996) 1867.

[5] CARLSTROM, T.N., et al., Plasma Phys. Control. Fusion **36** (1994) 147.

[6] CARLSTROM, T.N., et al., Plasma Phys. Control. Fusion **38** (1996) 1231.

[7] GROEBNER, R.J., et al., Plasma Phys. Control. Fusion **38** (1996) 1249.

[8] ASDEX TEAM, Nucl. Fusion **29** (1989) 1959.

LOCAL PLASMA PARAMETERS AND H-MODE THRESHOLD IN ALCATOR C-MOD*

A.E. HUBBARD, J.A. GOETZ, M.J. GREENWALD,
I.H. HUTCHINSON, Y. IN, J.H. IRBY, B. LaBOMBARD,
P.J. O'SHEA, J.A. SNIPES, P.C. STEK, Y. TAKASE,
S.M. WOLFE, ALCATOR GROUP
Plasma Fusion Center,
Massachusetts Institute of Technology,
Cambridge, Massachusetts,
United States of America

Abstract

LOCAL PLASMA PARAMETERS AND H-MODE THRESHOLD IN ALCATOR C-MOD.

Local plasma conditions in the outer region of the Alcator C-Mod tokamak are studied at the transition between L- and H-mode. Both controlled parameter scans and a database of H-mode discharges are examined. It is found that a minimum edge temperature, as measured by electron cyclotron emission diagnostics, must be exceeded in order to enter and remain in H-mode. This condition is not always sufficient, however. Density, and therefore pressure, appear to play a less important role. Comparison of 5.3 T and 8 T discharges shows that the threshold temperature increases with B_T. The ion Larmor radius thus remains in a narrow range at the transition, while beta and collisionality show a very wide variation. Discharges with the ion grad-B drift away from the x-point have L-mode temperatures similar to those with the usual direction toward the divertor. Both the global power threshold and local edge temperature at the L-H transition are approximately doubled.

1. INTRODUCTION

The role of the local temperature and density in the transport barrier region in determining the transitions between the L-mode and H-mode confinement regimes has been examined on the Alcator C-Mod tokamak. C-Mod is a high field, compact device, with R=0.67 m and a=0.21 m. H-mode is routinely obtained with ICRF heating, at toroidal fields up to 8 T. Ohmic and RF H-modes have also been seen at B_T as low as 2.6 T. These parameters are quite different from those of other divertor tokamaks, making C-Mod an interesting device for H-mode threshold studies. Most operation has been with molybdenum walls, but improved H-modes have been obtained in 1996 experiments following boronization [1].

Scalings for the H-mode power threshold on C-Mod in terms of global quantities show that the power required to obtain an L-H transition is P_{thresh}(MW) = 0.02-0.04 $n_e B_T S$, where n_e is the line averaged density (10^{20} m^{-3}) and S the surface area (m^2) [2]. Wall conditions appear to play a role and after boronization thresholds tend to lie at the lower end of this range (Fig. 1). Below a density of ~0.9 x

* Supported by US Department of Energy contract DE-AC02-78ET51013.

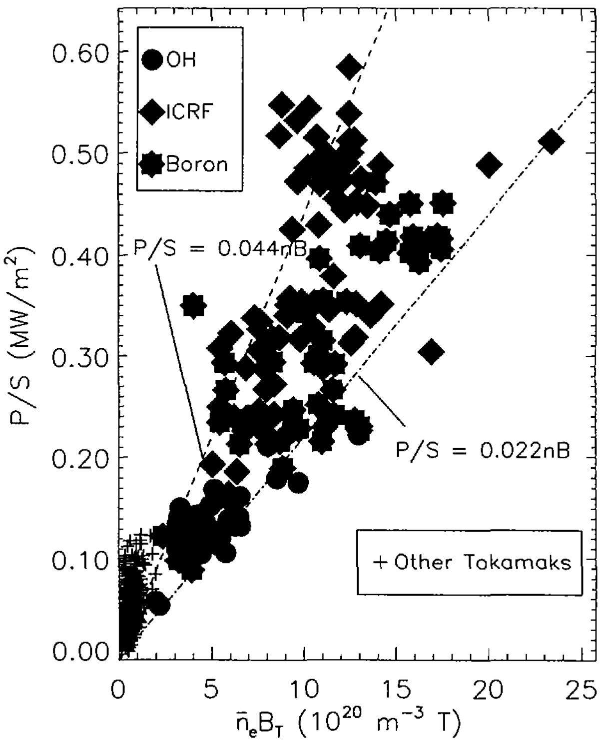

FIG. 1. Global H-mode power threshold for C-Mod, showing scaling with the product of density and magnetic field.

$10^{20}m^{-3}$, the threshold power increases sharply. The low density limit on C-Mod has recently been lowered to 0.66 x $10^{20}m^{-3}$. Multi-machine global parameter scalings, which include C-Mod data, are used to predict power requirements for ITER [3]. However, with any present scaling, there is typically variation of a factor of two or more in the threshold power on a given machine, and nearly an order of magnitude when comparing different machines. A lower threshold is generally found for the H-L transition, and the scaling of this hysteresis is even less well established. A further limitation of global power scalings is that they provide little insight into the physical mechanisms responsible for the transitions in confinement.

The limitations in our understanding and predictive capability motivate the search for more local threshold conditions. It has been observed since the earliest H-modes on ASDEX [4,5] that edge parameters appear to play a role. In particular, the transition was often correlated with a sawtooth heat pulse, and H-mode could be delayed by cooling the edge. Recent experiments on DIII-D [6] and ASDEX Upgrade [7] also point to a role for edge electron or ion temperature.

2. DIAGNOSTICS

The study of local parameters on C-Mod concentrates on the region just inside the separatrix. Since this is where temperature and density gradients are observed to steepen and fluctuation levels to drop in H-mode, it is likely that this is an important region for the threshold. The primary edge diagnostics are electron cyclotron emission (ECE) for $T_e(R)$ and reflectometry for $n_e(R)$. ECE diagnostics consist of a Michelson interferometer, which is absolutely calibrated, and a nine channel grating polychromator, which gives higher time and radial resolution and is cross-calibrated against the Michelson. Estimated systematic errors are $\pm$ 10% on T_e, with radial resolutions approximately 1 cm. The random noise level is typically ~ 20 eV. Density profiles are measured by an interferometer with 10 vertical chords. For some discharges, these are supplemented by edge profiles from a 5-channel o-mode amplitude-modulated reflectometer. A scanning Langmuir probe is used to measure profiles outside the separatrix, where the ECE becomes optically thin. Probably the biggest source of uncertainty for all of these measurements, given the steep gradients characteristic of the edge region, is the mapping of data to a given surface of normalized poloidal magnetic flux, ψ. The mapping is done using the EFIT magnetic reconstruction package [8] and its estimated accuracy is 3 mm at the horizontal midplane. The effects of these uncertainties can be minimized by keeping magnetic equilibria similar while doing controlled threshold scans.

The time behaviour of plasma parameters during a typical ELM-free H-mode with boronized wall conditions is shown in Fig. 2. In the RF-heated L-mode, electron temperature increases throughout the plasma cross-section while the density is unaffected. Once the H-mode transition occurs, as evidenced by a drop in D_α,

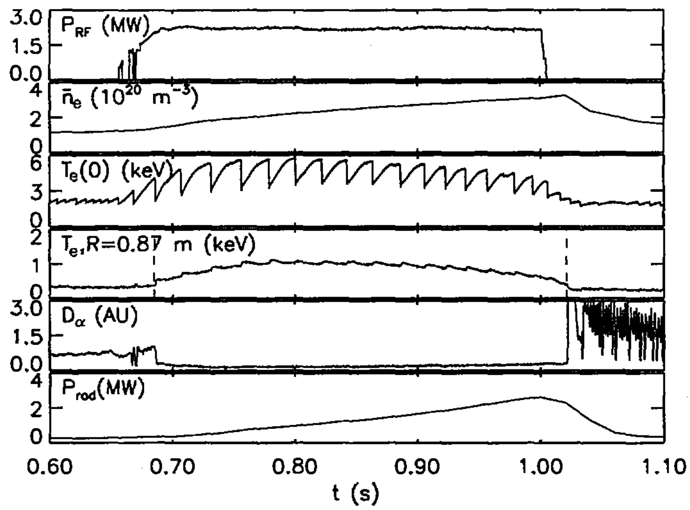

FIG. 2. Time evolution of plasma parameters during an ELM-free H-mode with I_p=1.0 MA and B_T=5.3 T. The vertical lines show the L-H and H-L transitions.

there is a rapid formation of an edge pedestal in both density and temperature. The central T_e and n_e also increase, as does the radiated power due to an improvement in impurity confinement. This gradually erodes the edge T_e pedestal, and an H-L transition occurs at 1.02 seconds. ELMy and enhanced D_α H-modes are also observed on C-Mod. For threshold studies, it is the conditions just before the L-H and H-L transition, rather than the details of H-mode behaviour, which are of interest.

3. RESULTS

The most striking result to date is that for a given magnetic configuration, ie. constant I_p, B_T and grad-B drift direction, the L-H transition occurs at a nearly constant edge T_e over a wide range of plasma densities and input powers. This is most clearly evident in a controlled parameter scan such as that summarized in Fig. 3, which shows results at 0.8 MA and 5.3 T. For each discharge, the power was stepped up and the temperature at the ψ=0.95 surface increased correspondingly. In each case the L-H transition (solid symbols) occurred when $T_e(\psi=0.95)$ reached 0.12 keV. At the lowest densities in this scan, the optical depth of the ECE at this radius is becoming marginal. However, the same trend is observed further in the plasma (ψ=0.85), where T_e and n_e are higher. The power required to reach the threshold temperature generally increases with density, consistent with the global power scaling. The exception is near the low density limit, when the edge is much cooler and where more power is required to reach H-mode. In other low n_e discharges of this scan, the edge remained below 0.1 keV even at maximum available power and H-mode was not achieved.

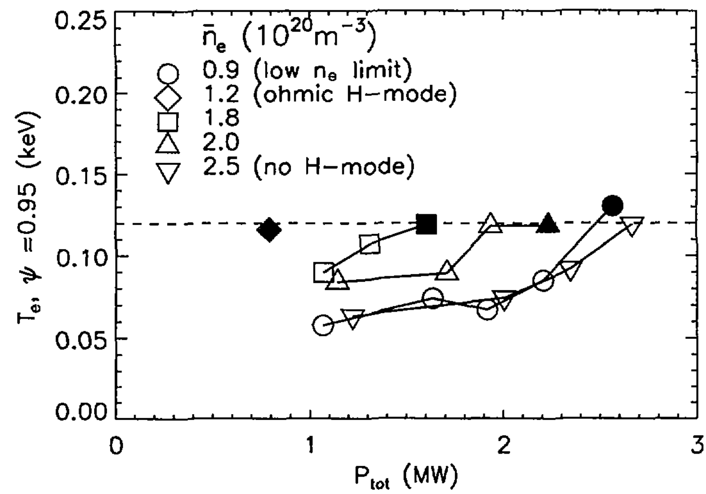

FIG. 3. Dependence of T_e at ψ=0.95 on total input power in L-mode, for a series of discharges with different densities. The solid symbols indicate conditions just prior to the L-H transition.

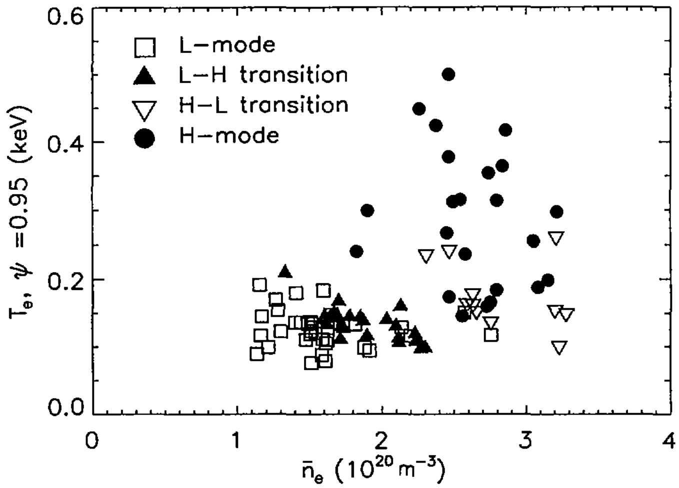

FIG. 4. Edge T_e versus line averaged density for discharges with I_p=1.0-1.2 MA and B_T=5.3 T. Note the large increase in T_e during H-mode, and the clustering of values at the L-H transition.

The trend of a minimum edge temperature for achieving H-mode is also seen in the wider database of C-Mod shots. Figure 4 shows a number of discharges from the post-boronization run period, with I_p=1.0-1.2 MA and B_T = 5.3 T. While, not unexpectedly, there is more scatter in the data, all the L-H transitions (solid triangles) occur at T_e > 100 eV and most are at T_e < 150 eV, independent of density. A few discharges are found to have higher temperature at the transition, in particular those with n_e approaching the low density limit. This implies that the edge temperature threshold may be a necessary but not always sufficient condition for entering H-mode. Similar trends were found in the 1995 data [2]. The lower threshold T_e quoted here is a result of more accurate calculation of the location of ECE channels with respect to flux surfaces; there is not a systematic change due to boronization.

Scalings of local discharge parameters with global parameters show that the strongest dependence is on toroidal field. The L-H transition temperature increases with B_T (Fig. 5), with a power between 1.2 and 1.5, depending on the dataset used and the other parameters included in regression fits. This is consistent with a global power threshold which increases with B_T, as seen on C-Mod and in multi-machine databases. No significant dependence on I_p is seen. There is a weak dependence of the average threshold temperature on n_e, due mainly to the increased scatter at low density. The minimum T_e at which H-modes have been seen is, however, nearly independent of density.

The behaviour at the H-L transition is more complicated, and depends on the type of H-mode and radiation conditions. After the H-mode edge temperature pedestal is formed, it tends to decrease as density and P_{rad} increase due to improved particle confinement, especially in ELM-free H-modes. If the edge temperature is reduced below the L-H threshold temperature, the plasma reverts to L-mode. This

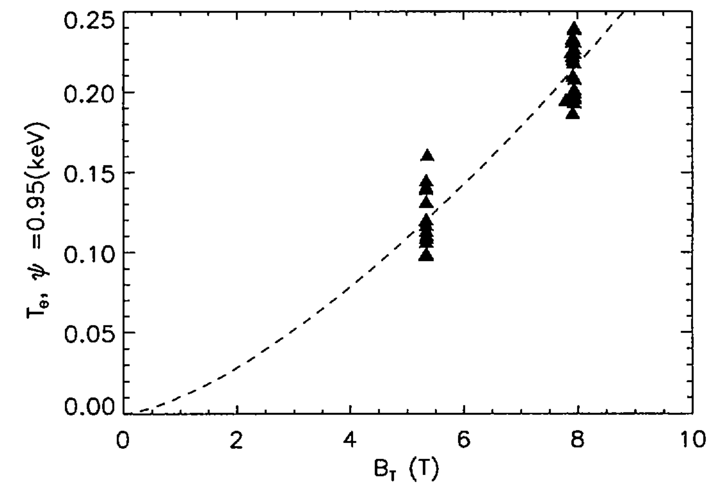

FIG. 5. Dependence of T_e threshold on toroidal field, for a group of 1996 discharges with I_p=1.0-1.1 MA and density well above the low density limit. Dashed line is best fit, proportional to $B_T^{1.46}$.

was the typical behaviour in pre-boronization experiments, and leads to a relatively slow loss of confinement. On many boronized discharges, particularly ELMy H-modes, the edge T_e remains well above the L-H threshold throughout a long H-mode. When the H-L transition occurs, there is a rapid collapse of the edge pedestal. At least some of these discharges, which typically have very steep edge pressure gradients, are computed to be unstable to ballooning and low n ideal modes. MHD activity is sometimes seen prior to such H-L transitions. It again appears that the edge temperature threshold is a necessary but insufficient condition for remaining in H-mode, and that this local condition, unlike global power thresholds, does not show hysteresis. In this context, the lower H-L power threshold may be seen as a result of the improved confinement in H-mode, ie. for a given P/n_e, an H-mode plasma will have a hotter edge. Given the wide variation in H factors which is seen under various conditions and on different experiments, it is not surprising that the H-L global power threshold shows a wide variation. The added requirement for MHD stability further complicates this power threshold.

An interesting and often-observed feature of the H-mode is that approximately twice as much power is required when the ion grad-B drift direction is away from instead of towards the active divertor. In the context of a local threshold, it is thus of interest to compare the edge plasma conditions in the two configurations. While most C-Mod operation, including all of the results quoted above, has been with the favourable drift direction, a few days were devoted to operation with 're-verse' B_T and I_p. It was found that in L mode, edge temperatures follow the same scaling with total power per particle as in discharges with 'normal' field direction (Fig. 6). The main difference is that they remained in L-mode with much more

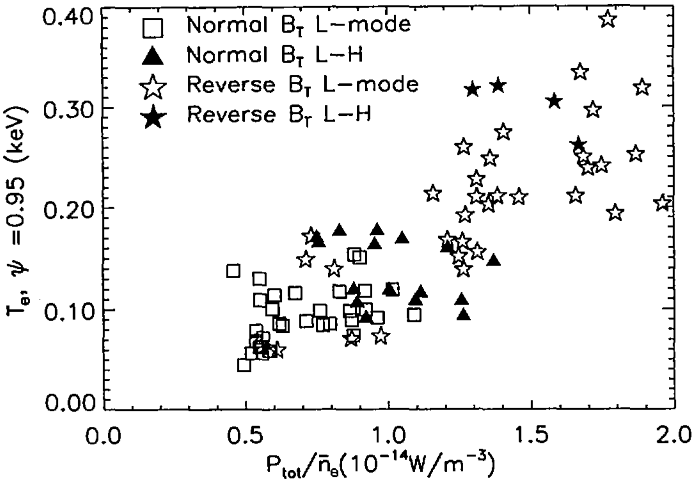

FIG. 6. Comparison of T_e (ψ=0.95) versus P_{tot}/n_e for similar groups of discharges with ion grad-B drift towards and away from the divertor. Parameters are B_T=5.3-5.6 T, I_p=0.8-1.0 MA, n_e=(1.8-3.0) × 10^{20} m^{-3}, and RF power 0-3.1 MW.

power, and correspondingly higher edge temperatures. In the few discharges which did briefly enter H-mode, the temperatures at the L-H transitions were in the range 260-320 eV, approximately twice the threshold values with the more favourable drift direction. A similar observation has been mentioned on ASDEX Upgrade [9]. This shows that the reason for higher global thresholds with reverse field is *not* that the edge is cooler. Whatever the mechanism for the H-mode transport improvement, it clearly is affected by field direction, either via drift or other flows.

4. DISCUSSION

Thresholds based on local parameters offer a basis for comparison with H-mode transition theories. Most prevalent theories involve stabilization of turbulence via ExB shear, though there is debate as to the mechanism for the shear [10]. It should be noted that the measured ECE temperatures inside the separatrix are indicative of the temperature gradient in the transport barrier region. Measured gradient scale lengths are typically 1 cm or less, limited by diagnostic resolution. At the high densities on C-Mod we expect $T_i \sim T_e$, but are presently lacking spatially resolved measurements of T_i in the edge region. It will thus be difficult to distinguish a threshold in T_e from one in T_i or dT/dR. Similar thresholds and scalings to those shown are found plotting dT_e/dR, or T_e at the 85% or 90% flux surface, so ψ=0.95 is not necessarily the critical location for H-mode transitions. However, since up-down asymmetries mainly affect the region outside or just inside the separatrix, the results of reverse field experiments imply that the extreme edge region plays an important role in H-mode physics.

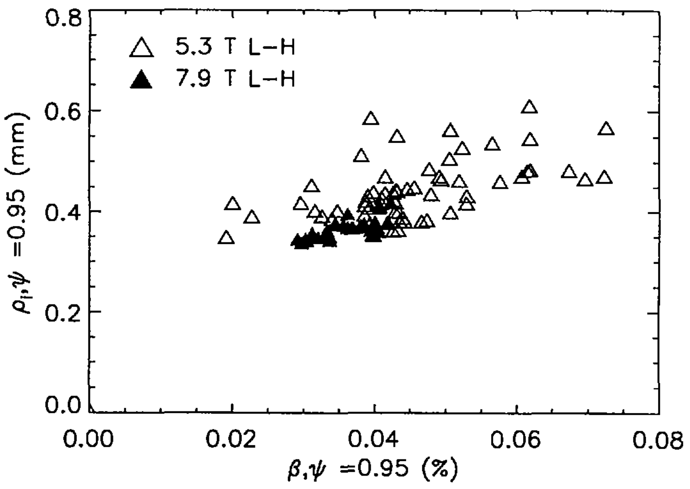

FIG. 7. Variation of β and ion gyroradius at ψ=0.95 for L-H transitions with a wide range of plasma parameters, B_T=5.3-8 T, I_p=0.7-1.23 MA, n_e=(0.9-3.5) × 10^{20} m^{-3}, and P_{RF}=0-2.8 MW.

The threshold scalings can be used to help identify which dimensionless variables may be important for H-mode transitions. The observed temperature threshold is not strongly dependent on n_e, as is most evident in the controlled scan. This implies either that ν* and β are not important variables, or that their functional dependences are such as to cancel out the density dependence. Given the positive dependence of threshold T_e with field, the ion gyroradius ρ emerges as a possibly important parameter. Figure 7 shows ρ vs β at the 95% flux surface, calculated using B_T at the outer midplane and assuming that T_i=T_e, for all L-H transitions in the database for the spring 1996 campaign. While there is scatter in both parameters, the ion gyroradius shows less variation at the transition than does β and is nearly independent of B_T. The standard deviation is 15% of the mean for ρ and 25% for β. The calculated ρ ~ 0.4 mm is to be compared with gradient scale lengths of 1-2 mm typical of the C-Mod SOL near the separatrix. The normalized ion collisionality ν_i* at ψ=0.95 varies from 2.1 to 32 at the L-H transition, with 55% standard deviation, making it an unlikely candidate for a dimensionless threshold.

Comparing the observed local and dimensionless parameters on machines of different sizes and global parameters may provide further opportunities for scalings and tests of theory. Planned experiments on C-Mod include H-mode threshold scans at 8 T and more systematic study of the H-L transition and low density limit.

REFERENCES

[1] TAKASE, Y., et al., IAEA-CN-64/A5-4, this volume.
[2] SNIPES, J.A., et al., Plasma Phys. Control. Fusion **38** (1996) 1127.
[3] RYTER, F., H MODE DATABASE WORKING GROUP, Nucl. Fusion **36** (1996) 1217.

[4] WAGNER, F., et al., Phys. Rev. Lett. **53** (1984) 1453.
[5] ASDEX TEAM, Nucl. Fusion **29** (1989) 1959.
[6] CARLSTROM, T.N., GROEBNER, R.J., Phys. Plasmas **3** (1996) 1867.
[7] SUTTROP, W., et al., in Controlled Fusion and Plasma Physics (Proc. 23rd Eur. Conf. Kiev, 1996), Vol. 20C, European Physical Society, Geneva (1996).
[8] LAO, L.L., St. JOHN, H., STAMBAUGH, R.D., KELLMAN, A.G., PFEIFFER, W.W., Nucl. Fusion **25** (1985) 1611.
[9] ZOHM, H., Plasma Phys. Control. Fusion **38** (1996) 105.
[10] GROEBNER, R.J., Phys. Fluids B **5** (1993) 2343.

INVESTIGATION OF CAUSALITY IN THE H–L TRANSITION ON THE JFT-2M TOKAMAK

K. HANADA, K. SHINOHARA, M. HASEGAWA, S. SHIRAIWA,
H. TOYAMA, K. YAMAGISHI, S. OHDACHI[1], T. OIKAWA[2],
H. TOTSUKA, E. ISHIYAMA, N. SHINODA, H. SAITO,
T. YOSHIDA, I. NAKAJIMA, M. USHIGOME
Department of Physics,
School of Science,
University of Tokyo,
Tokyo

Y. MIURA, T. SHOJI, H. KAWASHIMA, K. HOSHINO, K. NAGASHIMA,
H. TAMAI, N. SUZUKI, M. MAENO, T. YAMAUCHI, Y. ISHIGE,
H. OGAWA, S. SENGOKU, K. UEHARA, M. SATO, T. SHIINA,
M. SASAKI, T. OGAWA, K. OASA, T. KAWAKAMI, S. KASAI,
Y. ASAHI, M. MAEDA, K. HASEGAWA, K. ITOH, Y. KASHIWA,
K. KIKUCHI, T. KOIKE, M. KOMATA, Y. OHUCHI, F. OKANO,
M. SAITO, M. SAWAHATA, N. SEKI, T. SHIBATA, S. SUZUKI,
H. TAKEUCHI, T. TANI, Y. TOMIYAMA, K. UMINO
Naka Research Establishment,
Japan Atomic Energy Research Institute,
Naka-machi, Naka-gun, Ibaraki-ken

Japan

Abstract

INVESTIGATION OF CAUSALITY IN THE H–L TRANSITION ON THE JFT-2M TOKAMAK.

The causality of the H–L transition is investigated. Fluctuations, radial electric field and particle flux are measured by probes immersed inside the separatrix. The particle flux in the H mode plasma is less than half of that in L mode. The particle diffusion coefficient is about 0.25 m^2/s in the edge region of the H mode plasma, and its value is significantly less than the value in the L mode plasma (4 m^2/s). The particle flux in the H mode plasma is dominantly caused by coherent turbulence with a frequency of 80–120 kHz, and poloidal and radial wavelengths of 1.2–1.8 cm and 2 cm, respectively. The transition at the local position is triggered by the change of the radial electric field and the enhancement of fluctuation. The time delay between the change of the radial electric field and the enhancement of fluctuation is not observed. The shear layer of the radial electric field vanishes within 300 μs from the start of the change in the radial electric field. Before the temperature and density collapse, the flux increases up to eight times that in the H mode transiently. The estimated diffusion coefficient becomes 2 m^2/s and is comparable to the value in the L mode. The change of the radial electric field due to the H–L transition propagates outward. The viscosity estimated from the propagation of the potential is approximately 0.3 m^2/s,

---

[1] National Institute for Fusion Science, Nagoya, Japan.
[2] Japan Atomic Energy Research Institute, Naka, Japan.

which is similar to the value (1 m^2/s) derived from the response of the toroidal momentum when the direction of the injected NBI changes from co- to counter- and from counter- to co- with respect to the direction of the plasma current.

1. INTRODUCTION

An improvement in energy confinement is a key issue in nuclear fusion research. It is predicted that the $\mathbf{E} \times \mathbf{B}$ sheared flow plays an essential role in turbulence suppression in many improved confinement models [1–3]. The causality of sheared flow formation, turbulence suppression and reduction of flux are the crucial points in understanding the mechanism of improved confinement. However, this causality has not really been studied so far although it was reported that the formation of a radial electric field (E_r) precedes the reduction of the density fluctuation level in the slow L–H transition case on DIII-D [3].

This paper reports the details of the time evolution of flux, radial electric field and fluctuation during the H–L transition.

2. EXPERIMENTAL SET-UP

The probe head made of boron nitride is a rectangular parallelepiped with the top surface (20 mm × 20 mm) facing the centre line of the torus and the side surface (20 mm × 40 mm). Four electrodes made of molybdenum, 1 mm in diameter and 2 mm in length, to be used as a triple probe, are arranged every 3 mm along the toroidal direction and three more electrodes to measure the poloidal electric field are located on the top surface. On the side surface, seven electrodes are located to measure the potential on the different four radial positions. The output signals from the probes have been acquired with 1 MHz sampling.

The probe head is located 2 cm outside the separatrix at the start of the discharges. The insertion of the probe inside the separatrix is carried out such that the plasma moves outward and then returns to its previous position by coil current control. In fact, the plasma moves outward 3 cm radially without H–L transition. The plasma contamination due to probe insertion cannot be removed, and the H–L transition occurs during the insertion of the probe. To check the effect of the insertion, a microwave reflectometer is used. The level of density fluctuation does not differ whether the probe is inserted into the separatrix or not, except for the H–L transition. In L mode, the value measured by probes by way of insertion is the same as that measured by way of extraction. This suggests that the insertion of the probe does not seriously affect the condition of the plasma, except for the H–L transition.

3. EXPERIMENTAL RESULTS

3.1. Comparison of plasma parameters of H and L modes

Radial plasma parameter profiles are shown in Fig. 1. The probe is inserted 5 mm inside the separatrix without H–L transition in H mode. The space potential decreases just inside the separatrix as shown in Fig. 1(c). This indicates that an E_r shear layer is formed in the H mode plasma and the fluctuation level is reduced in the E_r shear layer.

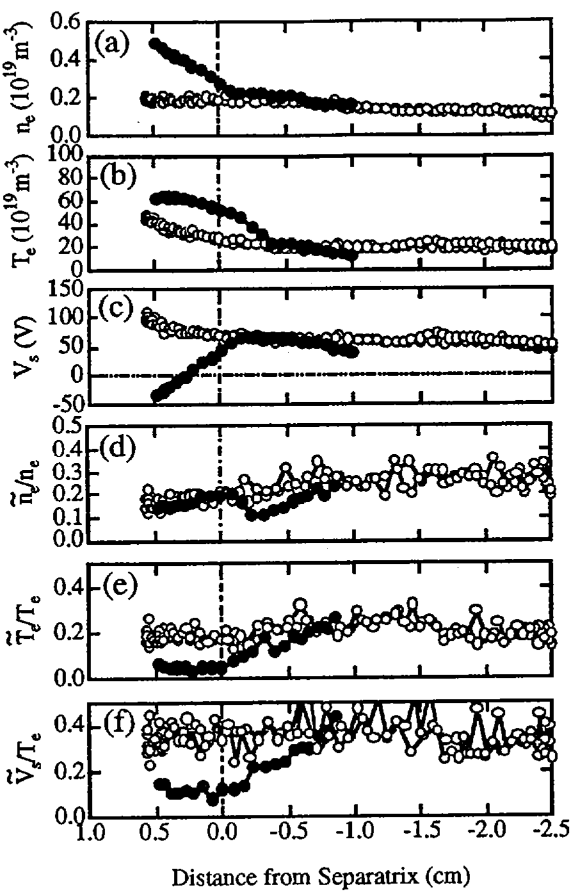

FIG. 1 Comparison of radial profiles of (a) density, (b) temperature, (c) space potential, (d) density fluctuation level, (e) temperature fluctuation level and (f) potential fluctuation level in the H mode (closed circles) and L mode (open circles). The vertical line in (a)–(f) shows the position of the separatrix estimated by magnetic measurement. The data on the L mode measured by way of insertion and extraction are plotted in the same figure.

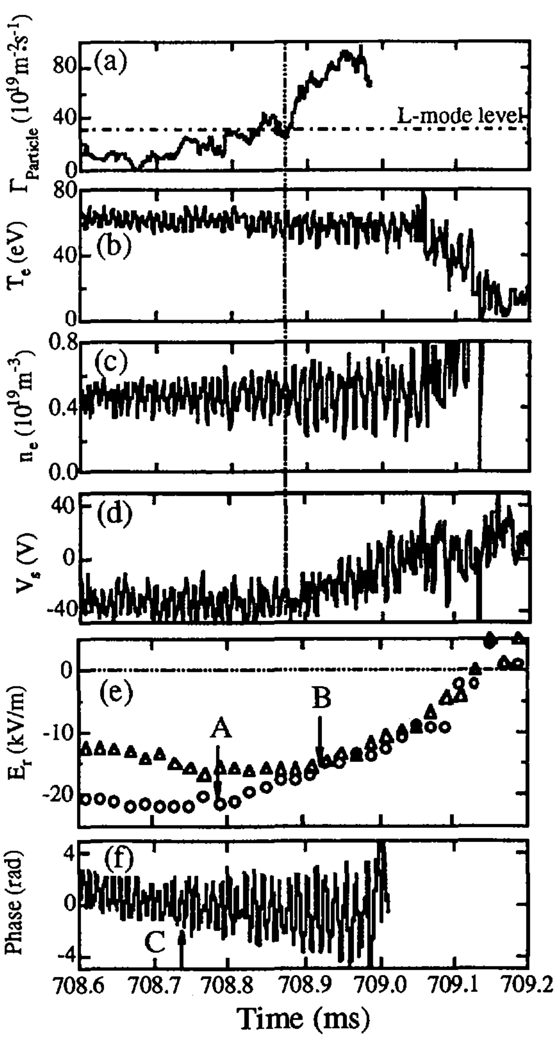

FIG. 2 Time evolutions of (a) particle flux induced by electrostatic turbulence within 128 μs, (b) density, (c) temperature, (d) space potential at D_{sep} = 6 mm, (e) radial electric field derived from the potentials at D_{sep} = 9.2 mm and 6.0 mm (open circles) and radial electric field derived from the potentials at D_{sep} = 6.0 mm and −1 mm (open triangles), where D_{sep} is the distance from the separatrix, (f) phase signal measured by microwave reflectometer with 38 GHz, which shows the fluctuation at D_{sep} = 14 mm. The vertical line shows the starting time of the transition at D_{sep} = 6 mm. The arrows A, B show the time when the radial electric field starts changing, and arrow C shows the starting time of fluctuation enhancement.

A spectral analysis for the fluctuation in that E_r shear region shows that a remarkable peak around 80–120 kHz appears. Poloidal and radial wavelengths of 1.2–1.8 cm and 2 cm are estimated by the cross-phase of two V_f signals which are 3 mm away from each other along the poloidal and radial directions. The particle flux is mainly caused by this turbulence. The spectrum of the fluctuation in the L mode has no remarkable peak, and the main part of the flux lies in the range of 10–50 kHz.

3.2. Causality in the H–L transition

The H–L transition occurs when the probes are immersed into the H-mode plasma. The time evolution of the plasma parameters around the H–L transition is shown in Fig. 2. The flux in the H mode is about 10×10^{19} $m^{-2} \cdot s^{-1}$ before the H–L transition, which is about one third of that in L mode. The density gradient in the H mode is large and the calculated particle diffusion coefficient, D = 0.25 m^2/s, is significantly less than that in the L mode plasma (4 m^2/s). This shows that the transport barrier is formed in the E_r shear region of the H mode plasma.

The particle flux increases strongly from 708.88 ms (see the vertical line in Fig. 2) and reaches 80×10^{19} $m^{-2} \cdot s^{-1}$. This value corresponds to eight times the flux in the static H mode. As the radial profile does not change so much, the particle diffusion coefficient becomes 2 m^2/s and is comparable to that in the L mode. The E_r shear at this position vanishes, as is shown in Fig. 2(e). This implies that the transition of the transport coefficient at D_{sep} = 6 mm occurs at the time shown by the vertical line, where D_{sep} shows the distance from the separatrix. After the transition of the transport coefficient, the large density gradient is almost kept constant with the help of the large flux.

The enhancement of the fluctuation level and the change of V_s at the same radial position are synchronized as shown in Figs 2(c) and (d). No time delay is observed. The change of the potential due to the H–L transition propagates from inside to outside in the poloidal cross-section; as a result, the change of E_r derived from the potential at D_{sep} = 9.2 mm and 6 mm (see arrow A in Fig. 2(e)) precedes that derived from the potential at D_{sep} = 6.0 mm and –1 mm (see arrow B in Fig. 2(e)). The fluctuation level at D_{sep} = 14 mm measured with the reflectometer (see arrow C in Fig. 2(f)) increases earlier than that at D_{sep} = 6 mm measured with the probe (see the vertical line in Fig. 2). This means that the transition does not occur simultaneously in the whole shear region.

The absolute value of E_r becomes zero at 709.1 ms, and the E_r shear layer vanishes at this time. The change of E_r starts from 708.8 ms, and it takes 300 μs to extinguish the E_r shear layer. This observation shows that it is possible to estimate the value of the viscosity during the H–L transition as follows:

$$\mu \approx \frac{(9.2 \times 10^{-3})^2}{300 \times 10^{-6}} \approx 0.3 \ m^2/s$$

This value is similar to the value (1 m^2/s) derived from the response of the toroidal momentum when the direction of the injected NBI changes from co- to counter- and from counter- to co- with respect to the plasma current [4].

4. CONCLUSIONS

These observations show that (1) the transport barrier is formed in the E_r shear region; (2) the H–L transition starts before 300 μs from the large change of n_e and T_e and the transport coefficient increases up to the L mode level before the large change of n_e and T_e; (3) the changes of E_r and fluctuation level occur simultaneously at the local position, and the time delay between them cannot be observed; (4) the change of E_r and the fluctuation level do not occur simultaneously in the whole E_r shear region, and the change propagates outward; (5) the viscosity estimated from the propagation of the potential during the H–L transition is approximately 0.3 m^2/s.

REFERENCES

[1] TOYAMA, H., et al., in Plasma Physics and Controlled Nuclear Fusion Research 1994 (Proc. 15th Int. Conf. Seville, 1994), Vol. 1, IAEA, Vienna (1995) 575.

[2] OHDACHI, S., et al., Plasma Phys. Control. Fusion **36** (1994) 201.

[3] BURRELL, K.H., et al., in Plasma Physics and Controlled Nuclear Fusion Research 1994 (Proc. 15th Int. Conf. Seville, 1994), Vol. 1, IAEA, Vienna (1995) 221.

[4] IDA, K., et al., Phys. Rev. Lett. **74** (1995) 1990.

IMPROVED PLASMA CONFINEMENT IN THE TUMAN-3M AND FT-2 TOKAMAKS

M.V. ANDREJKO, L.G. ASKINAZI, V.N. BUDNIKOV,
V.V. BULANIN[1], V.V. DYACHENKO, L.A. ESIPOV,
V.E. GOLANT, E.R. ITS, V.A. KORNEV, S.V. KRIKUNOV,
S.I. LASHKUL, S.V. LEBEDEV, L.S. LEVIN, B.M. LIPIN,
A.V. PETROV[1], K.A. PODUSHNIKOVA,
V.V. ROZHDESTVENSKY, A.I. SMIRNOV, A.Yu. STEPANOV,
O.N. SHCHERBININ, V.Yu. SHORIKOV, A.S. TUKACHINSKY,
A.V. VERS[1], S.P. YAROSHEVICH
A.F. Ioffe Physico-Technical Institute,
Russian Academy of Sciences,
St. Petersburg, Russian Federation

Abstract

IMPROVED PLASMA CONFINEMENT IN THE TUMAN-3M AND FT-2 TOKAMAKS.

In 1994 a new vacuum vessel was installed in TUMAN-3M. During the first experimental run, the device was operated in the ohmic regime. The purpose of the experiments was to check the possibility of achieving ohmic H mode, found previously in TUMAN-3, and to study the conditions of the L-H transition and parametric dependences of the energy confinement time in both OH and ohmic H mode. The plasma parameters were R_0 — 0.53 m, a_l — 0.22 m, I_p — 80–150 kA, B_t — 0.5–0.9 T, n_e — (0.8–1.8) × 10^{19} m^{-3}, T_{e0} — 0.4–0.8 keV and T_{i0} — 0.1–0.2 keV. A clear τ_E dependence on plasma current and no dependence on density are found in OH discharges with a circular limiter configuration. Ohmic H mode was obtained after boronization. Discharges enter H mode operational space from the low density margin. The threshold density slightly increases with plasma current and toroidal field. Input ohmic power substantially exceeds the threshold power derived from the ITER database. The transition time increases with plasma current from 0.5–1 ms at I_p = 80 kA up to 5–7 ms at I_p = 150 kA. The reduction of τ_E in ohmic H mode under poor vacuum conditions was observed, indicating the direct influence of plasma purity on confinement. In FT-2 tokamak experiments (R_0 = 0.55 m, a_l = 0.08 m, I_p = 20–40 kA, B_t = 2.2 T, n_e = (1.0–3.0) × 10^{19} m^{-3}, T_{e0} = 0.5 keV, T_{i0} = 0.1 keV, P_{RF} = 150 kW, f_{RF} = 920 MHz), improved plasma confinement has been found in three discharge scenarios: lower hybrid heating (LHH), OH alone and current ramp-up (CRU) combined with LHH. Improved confinement was shown by an increase in the particle confinement time, an increase in the energy confinement time (LHH scenario) and an increase in the ion thermal energy confinement (CRU + LHH scenario). Different mechanisms are discussed as possible causes of confinement improvement: electron heating by RF waves, formation of a broadened or a hollow current density profile, an increase in the plasma rotation velocity and damping of plasma microturbulence.

[1] State Technical University of St. Petersburg, St. Petersburg, Russian Federation.

1. STUDY OF ENERGY CONFINEMENT AND CONDITIONS OF L–H TRANSITION IN OHMICALLY HEATED PLASMAS IN TUMAN-3M

In 1994 a new vacuum vessel was installed in TUMAN-3M. During the first experimental run, the device was operated in the ohmic regime. The purpose of the experiments was to check the possibility of achieving ohmic H mode, found previously in TUMAN-3 [1], and to study the conditions of the L–H transition and parametric dependences of the energy confinement time in both OH and ohmic H mode. The plasma parameters were R_0 — 0.53 m, a_l — 0.22 m, I_p — 80–150 kA, B_t — 0.5–0.9 T, n_e — (0.8–1.8) $\times 10^{19}$ m^{-3}, T_{e0} — 0.4–0.8 keV and T_{i0} — 0.1–0.2 keV.

1.1. OH confinement results

Before the experimental run, the machine was boronized using carborane deposition in a He glow [2]. As a result, relatively low recycling was observed in the experiments. The OH regime was obtained in a wide plasma current range: 80–150 kA, with q^{cyl} values from 2.4 to 3.5. Energy confinement time parametric dependences were studied using diamagnetic measurements of the stored energy. Data from the density scan for OH with two different values of plasma current are given in Fig. 1. The data show a weak density dependence for a given current and a strong increase in τ_E with I_p. At lower densities the experimental energy confinement time exceeds Neo-Alcator predictions by a factor of 2. These results are in

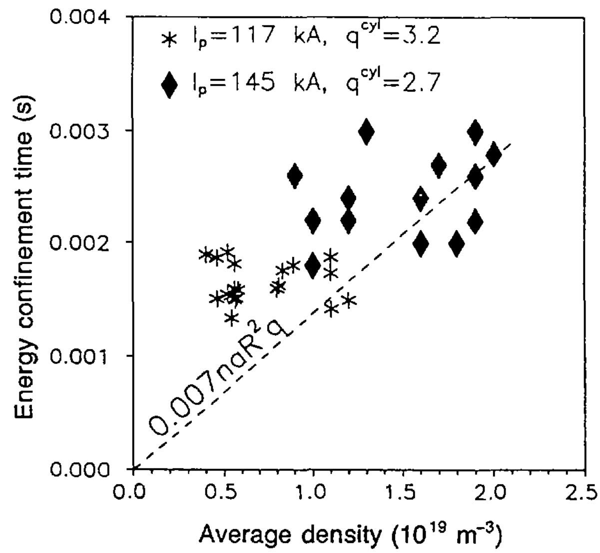

FIG. 1. Energy confinement time as a function of density for OH regimes with I_p = 117 and 145 kA.

qualitative agreement with observations in Alcator C-Mod [3]. Note that typical B_t and n in our experiments are a factor of 10 lower than in Ref. [3]. It seems the contradiction with Neo-Alcator scaling could be explained by the lower recycling provided by divertor operation in Alcator C-Mod and the boronization in TUMAN-3M. Low recycling may result in a diminished influence of atomic processes on confinement and corresponding changes in the scaling law.

1.2. Conditions of L–H transition in ohmically heated plasmas

Transition into H mode has been found in ohmically heated plasmas in TUMAN-3M. Ohmic H mode appears spontaneously or could be triggered by an increase in deuterium puffing rate, as was the case in previous TUMAN-3 experiments [1]. Discharges enter H mode operational space from the low density margin. As is shown in Fig. 2, the position of the margin slightly changes with plasma current. In the I_p scan the safety factor value was approximately constant and therefore the influence of I_p and B_t on the density margin position could not be distinguished. Figure 2 also illustrates that input ohmic power substantially exceeds the threshold power derived from the ITER database [4].

The transition time increases with plasma current from 0.5–1 ms at I_p = 80 kA up to 5–7 ms at I_p = 150 kA. Typical waveforms of plasma parameters in the 150 kA ohmic H mode are shown in Fig. 3. The transition starts at 51 ms and continues till 57 ms. During this period D_α and U_p are decreased, indicating a

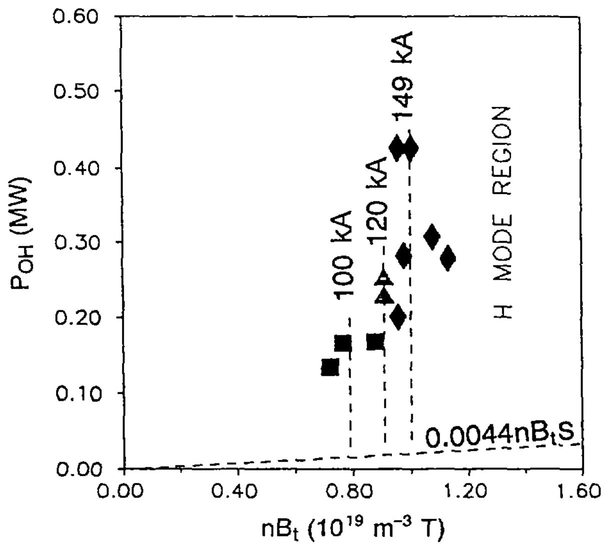

FIG. 2. H mode operational region. Symbols show input power before transition into ohmic H mode.

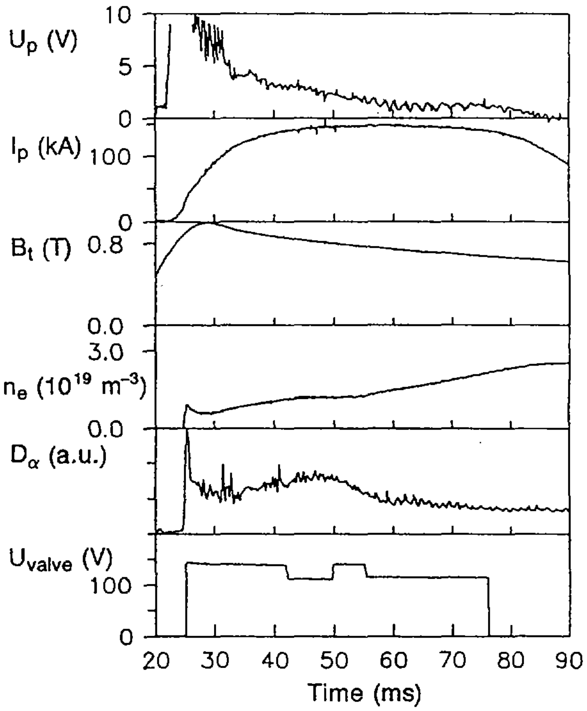

FIG. 3. Temporal evolution of plasma parameters in the 150 kA ohmic H mode.

gradual reduction of the particle flux in the periphery and broadening of the current density profile. The ohmic H mode is ELM free and is characterized by a continuous density increase. After the transition, SXR emission from the plasma centre (not shown in Fig. 3) increases owing to an increase of the electron temperature.

1.3. Ohmic H mode confinement studies

In order to check the strong τ_E dependence on I_p previously observed [5], experiments in a wide I_p range were performed in ohmic H mode plasmas. Plasma current was scanned from 80 to 150 kA. The limited number of points does not allow the exact τ_E dependence on I_p to be derived; nevertheless, a significant influence of I_p on τ_E can be concluded.

The I_p scan was performed in a boronized vessel, but the quality of the coating was worse than in previous experiments, because only one source of carborane was used instead of the two in Refs [2, 5]. Spectroscopic data show a decrease of oxygen concentration by a factor of 2–3, while a factor of 4–8 reduction was observed in Ref. [2]. Under these conditions we found that τ_E was a factor of 1.5 lower. This

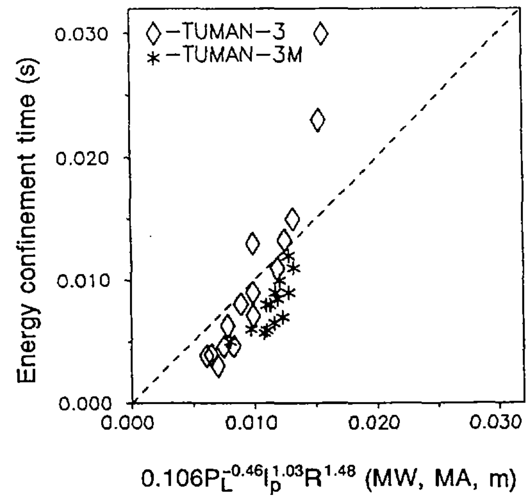

FIG. 4. Energy confinement time in ohmic H mode as a function of JET/DIII-D H mode scaling.

can be seen in Fig. 4, which shows a comparison of the JET/DIII-D H mode scaling predictions with experimental energy confinement time in ohmic H mode. The reduction of τ_E under poor vacuum conditions indicates a direct influence of plasma purity on confinement. Note that the longest energy confinement time in the old machine (30 ms) was observed after successful boronization. In TUMAN-3M we found a τ_E dependence similar to the scaling prediction, but the values were slightly lower than in TUMAN-3.

2. IMPROVED PLASMA CONFINEMENT IN THE FT-2 TOKAMAK

In FT-2 tokamak experiments, improved confinement has been found in three discharge scenarios. First, it was found during lower hybrid heating (LHH). An abrupt drop in H_β radiation and MHD activity, an increase in the plasma density and stored energy, and a broadening of the ion temperature profile were observed after RF pulse switch-off [6]. After the transition the energy confinement time increased by a factor of 2–3. The analysis of microturbulence by microwave enhanced scattering and reflectometry in the frequency range 0–500 kHz showed that after the transition, fluctuations in the plasma were essentially suppressed at the periphery, $r \approx 7$ cm [7]. The observed phenomena allow this regime to be identified with H mode. The H_β emission, Mirnov probe and reflectometer signals throughout the L–H transition are shown in Fig. 5. The suppression of plasma oscillations and the abrupt drop of the reflectometer signal at 29 ms indicate the transition. The pronounced spikes on the H_β emission represent ELM activity. Before each H_β burst, coherent magnetic precursor oscillations with frequency $\nu_{prec} \approx$ 24–32 kHz

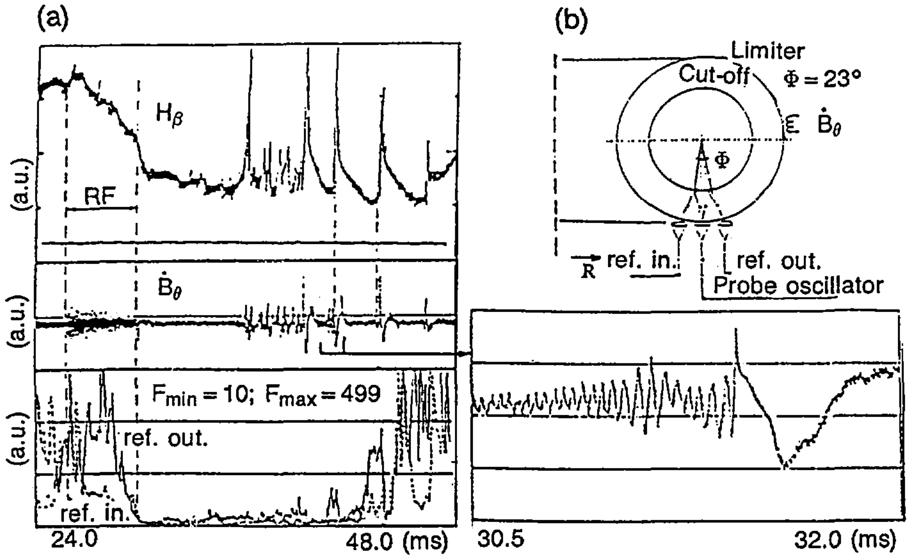

FIG. 5. (a) Temporal behaviour of H_β intensity, Mirnov probe signal ($\dot{B}_\theta$) and reflectometer signal measured by inner (ref. in.) and outer (ref. out.) antennas during the L–H transition. (b) Arrangement of the diagnostics.

were found. Cross-correlation analysis of magnetic probe signals of the precursors gives poloidal mode m $\approx$ 9 at the resonance magnetic surface q = 4.5. The appearance of precursors is explained by the resistive ballooning mode growth at the outside plasma toroidal boundary [8]. As detailed analysis showed, the improved confinement begins during the RF pulse and is sustained after the RF switch-off because of L–H and H–L transition hysteresis, $P^{L-H}_{thresh} > P^{H-L}_{thresh}$. Broadening of the current density profile and slowing of the hydrogen recycling at the discharge periphery seem to be causes of the hysteresis.

Recently the L–H transition has been obtained with OH alone. In order to trigger the transition, the plasma was shifted to the outside of the torus. In this case the plasma temperature as measured by a Langmuir probe in the outside SOL increases and causes the decrease of both H_β line emission and turbulence. The preprogrammed plasma shift (of the order of 1 cm) resulted in an increase of the average density and ion temperature. It was supposed that because radiative losses are decreased the energy flow through the plasma separatrix, $P_{sep} = P_{OH} - P_{rad}$, achieves the threshold value for L–H transition. Note that heating of the outside SOL leads to a longer ELM free period in the H mode [8].

The third method of triggering improved confinement is the combination of a fast current ramp-up (CRU) with LHH. In this case the plasma current was ramped from 20 to 30 kA during 0.5 ms, which might result in a broadened or a hollow current profile. The following conclusions have been drawn from the first CRU + LHH experiments: (1) the central density rises substantially as a result of an increase in the particle confinement; (2) there is a considerable (factor of 2–3) decrease in the high energy charge exchange neutral flux during CRU, while the ion temperature remains unchanged; (3) a factor of 2–3 increase in the rotational velocity was found from cross-correlation processing of the MHD signals; (4) there is a substantial increase in the ion energy confinement time. The last conclusion is based on an analysis of the central ion temperature buildup and decay. In the CRU + LHH scenario the characteristic time increases by a factor of 3 compared with the case of pure LHH. The ion energy confinement time becomes comparable with the particle confinement time (~ 5 ms).

In these experiments the collective CO_2 laser scattering [9] has been used to study the microturbulence behaviour. This diagnostic allowed the investigation of electron density fluctuations with wavenumbers $k_\perp$ from 12 to 30 cm^{-1} and in a frequency band from 60 to 800 kHz. For small scattering angles the scattered power spectrum P_s has been regarded as an integral of the local power spectrum of fluctuations along the laser beam. The waveforms of scattered power P_s integrated over the 100–800 kHz frequency range for central chord probing are shown in Fig. 6 for the

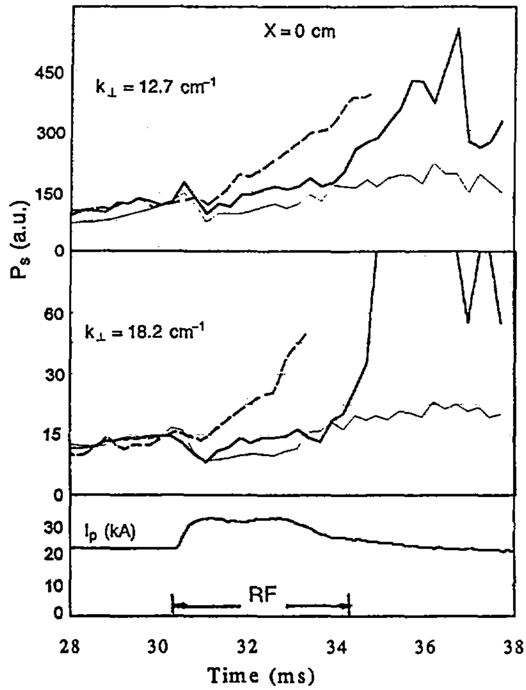

FIG. 6. Waveforms of scattered power P_s integrated over the 100–800 kHz frequency range along the central chord X = 0 for three experimental cases: CRU only (thin solid line), CRU + LHH (thick solid line) and LHH only (dashed line).

three experimental cases. One can see the significant suppression of plasma oscillations both during the CRU without LHH and during CRU + LHH. In the case of LHH alone the oscillations were not suppressed. The data obtained under the different incident laser beam positions suggest that the suppression of small scale fluctuations during CRU takes place mainly in the plasma core.

ACKNOWLEDGEMENTS

The work on TUMAN-3M was supported by the Russian Foundation for Basic Research (grant 96-02-17958) and by the Ministry of Science of the Russian Federation (index number 01-06). The work on FT-2 was supported by the Russian Foundation for Basic Research (grants 95-02-04072 and 94-02-04759).

REFERENCES

[1] ARBUZOV, A.N., et al., in Controlled Fusion and Plasma Heating (Proc. 17th Eur. Conf. Amsterdam, 1990), Vol. 14B, Part I, European Physical Society, Geneva (1990) 299.
[2] ASKINAZI, L.G., et al., in Controlled Fusion and Plasma Physics (Proc. 20th Eur. Conf. Lisbon, 1993), Vol. 17C, Part IV, European Physical Society, Geneva (1993) 1517.
[3] HUTCHINSON, I.H., et al., Plasma Phys. Control. Fusion **36** (1994) B143.
[4] RYTER, F., et al., in Controlled Fusion and Plasma Physics (Proc. 21st Eur. Conf. Montpellier, 1994), Vol. 18B, Part I, European Physical Society, Geneva (1994) 334.
[5] ANDREJKO, M.V., et al., Plasma Phys. Control. Fusion **36** (1994) A165.
[6] BUDNIKOV, V.N., et al., JETP Lett. **59** (1994) 685.
[7] BUDNIKOV, V.N., et al., Plasma Phys. Rep. **21** (1995) 817.
[8] BUDNIKOV, V.N., et al., in Controlled Fusion and Plasma Physics (Proc. 23rd Eur. Conf. Kiev, 1996), Vol. 20C, European Physical Society, Geneva (1996) paper d028.
[9] BUDNIKOV, V.N., et al., ibid., paper e003.

NEW FEATURES OF THE L–H TRANSITION IN H MODES IN HT-6M

B.N. WAN, Y.X. WAN, J.G. LI, J.R. LUO,
J.K. XIE, HT-6M GROUP
Institute of Plasma Physics,
Academia Sinica,
Hefei, China

Abstract

NEW FEATURES OF THE L-H TRANSITION IN H MODES IN HT-6M.

The H mode achieved by applying an edge ohmic heating pulse in HT-6M shows some new features. The floating potentials and their fluctuations at different radial positions are comparable to the ohmic phase levels before and during the L–H transition and increase after the H–L transition. The time-scale of the L–H transition is of the order of 1 ms, which is unusual. During the H confinement regime the plasma current becomes peaked. The MHD instabilities terminate the H mode or cause discharge disruption. Analyses show that edge current and relevant magnetic shear play a decisive role in establishing the transport barrier. The time-scales of the L–H transition and current penetration are governed by the resistive diffusion time.

1. INTRODUCTION

H mode confinement improvement occurs in many configurations and has been achieved by many means. The sheared edge radial electric field or the poloidal rotation is thought to be the cause for the universal mechanism of the L–H transition [1]. The sheared **E** × **B** flow can reduce the radial extent of the turbulence in the plasma and hence also reduce the transport. However, one key question in the assessment of theories of the L–H transition based on the sheared **E** × **B** flow, when the transport barrier is formed, is still unsolved: Does the fluctuation decrease first, followed by a change in the profiles, or does everything change simultaneously? Some experimental evidence, however, indicates that the formation of the edge sheared E_r does not precede the transition. Measurement of the fluctuation spectra obtained with fairly good time resolution (≤ 100 μs) in the ASDEX tokamak confirms that the radial E field does not change before or during the transition [2], although the levels of fluctuation both in the scrape-off layer and in a narrow region inside the separatrix drop on a 100 μs time-scale. The investigation of the H mode confinement in the CHS heliotron/torsatron indicates that the increase in E_r and its shear near the edge are not a necessary cause of H mode transition [3]. The observed dramatic change in the edge electric field may be only a consequence of the transition. Thus, the sheared **E** × **B** flow or the poloidal rotation might, at least, not be the unique mechanism for the L–H transition.

On the other hand, an investigation of coherent magnetic oscillations such as $m = 4/n = 1$ or $m = 3/n = 1$ on ASDEX and JIPP-IIU suggests an alternative model of the L–H transition [4, 5], i.e. that the toroidal current profile at the edge can significantly influence the radial profiles (for example, T_e, n_e, p) at the plasma edge and may govern the L–H transition. The analyses of the L and H mode data on JET suggest that the transitions are marked by rapid changes in J_ϕ within a narrow boundary layer, typically at $0.8 < r/a < 1$ [6]. After the transitions, J_ϕ relaxes on the time-scale governed by resistive diffusion. Changes in J_ϕ are associated with the non-inductive part, including bootstrap and beam driven currents. This conclusion is confirmed in JT-60U [7] and JIPP-IIU [5], which show that the plasma performance is affected by the shape of the current profile at the edge, in particular for the bootstrap dominated discharges. The effect of local magnetic shear on the L–H transition is clearly seen. Theory predicts that high edge magnetic shear can suppress the turbulence and trigger the H mode transition [8].

The current density profile near the edge can be modified simply by inducing a short voltage pulse in the HT-6M tokamak. The resulting current increase is mainly located at the plasma edge, because of the skin effect causing edge ohmic heating (EOH). This is of advantage in studying the role of current density shape and magnetic shear at the edge of L–H transition.

2. CHARACTERISTICS OF THE H–L AND L–H TRANSITIONS

HT-6M is an air core tokamak operated in circular limiter configuration with $R = 65$ cm, $a = 20$ cm, $B_t \sim 0.9$ T and $I_p \sim 60$ kA. The H mode is achieved on the HT-6M tokamak by applying EOM [9]. A voltage pulse with an 18 V peak and 0.4 ms duration is induced on the plasma current plateau, causing fast current ramp-up to the second steady stage. The plasma current increase ($\sim 10\%$ I_p) is mainly located at the plasma edge of about 0.95a, estimated according to the Spitzer resistivity on the resistive diffusion time-scale. The sequence of the OH–L–H–L phases is observed after applying EOH. The H phase of the discharge is characterized by: reduced H_α radiation, increased central chord averaged electron density, suppressed fluctuation levels, increased n_e and T_e gradients at the edge, etc. However, some new features are typically observed as shown in Fig. 1. The EOH pulse is induced at 194 ms (Fig. 1(a)) and causes current ramp-up (Fig. 1(b)) simultaneously. The H_α radiation (Fig. 1(f)), floating potentials (Figs 1 (c, d, e)) and their fluctuation levels increase with the EOH pulse. Floating potentials and their fluctuation levels decrease immediately after the EOH pulse and are gradually reduced to the levels of the ohmic phase at about 196 ms. The decrease of the H_α radiation begins at about 197 ms. The radial edge electric field, which is inferred from the relative change of V_f at different radial positions, is comparable to the level in the ohmic phase before and during the L–H transition. However, the photofluctuation of the H_α radiation remains unchanged until the H_α radiation decreases.

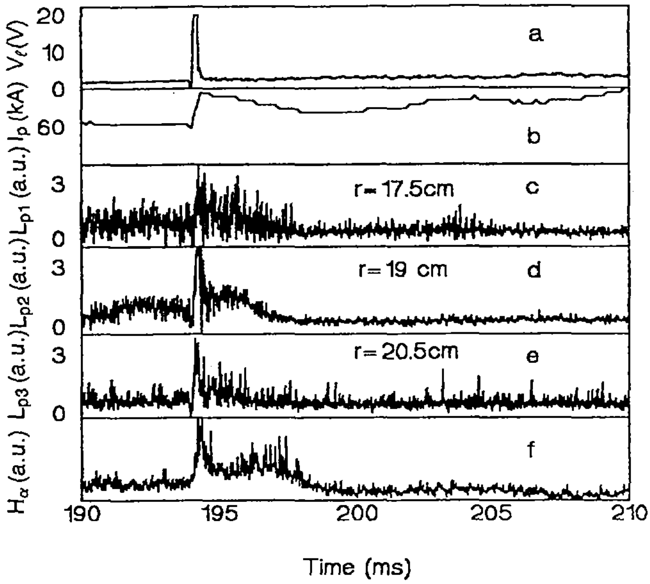

FIG. 1. Typical waveforms of EOH discharge.

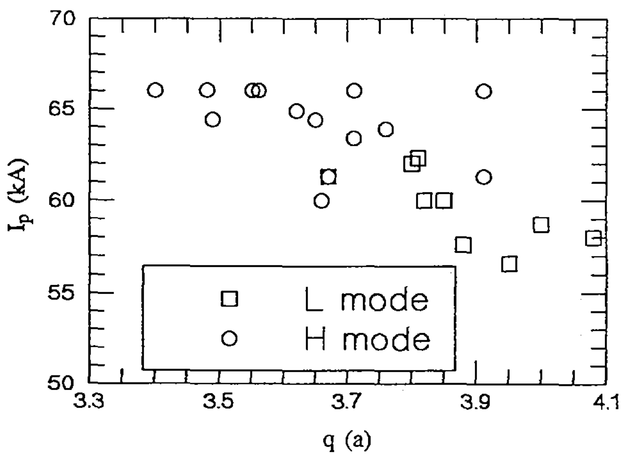

FIG. 2. I_p versus $q(a)$ for L and H modes.

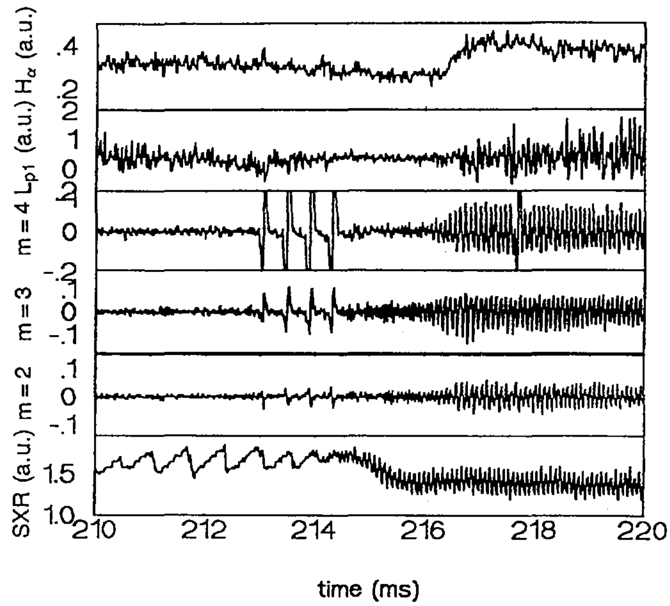

FIG. 3. Waveforms of H mode termination.

The H_α radiation drops on the time-scale of a millisecond, which is longer than the typical time-scale of 100 μs of the L–H transition. To the first approximation, the photofluctuation in H_α traces the n_e fluctuation [10]. This means that the edge n_e fluctuation level is not suppressed until the L–H transition sets in. This fact suggests that the increased E_r field shear near the edge and the reduction of the fluctuation in the transport barriers may not necessarily be the cause of the L–H transition.

By scanning the plasma parameters, T_{eb} and n_{eb} are found to be not related to the L–H transition. However, most of the L–H transitions are observed in large plasma current and low q(a), as is shown in Fig. 2. The high plasma current implies a large ohmic power because the induced voltage of EOH is fixed at 18 V. The appearance of an H mode in the EOH discharge implies that the H mode power threshold scales as $P_{tot} \propto B_T$. Low q values yield the maximum ohmic power for a given B_T. The high plasma current is also beneficial in suppressing the energy and particle losses because of small λ_{ne}, λ_{Te} and diffusion coefficient D [11].

The current induced by EOH is primarily located at the edge and gradually penetrates inwards. This characteristic feature is indicated by the decay sequence of V_f at different radial positions, as is shown in Figs 1(c, d, e). After the L–H transition, the current penetration continues and causes a peaked current density profile [9]. The sawtooth inversion radius expands from 3 cm to about 7.5 cm on a time-scale of ten milliseconds, followed by the MHD instability. This time is of the order of the resistive diffusion time over this radial extent. Termination of the H mode or discharge disruption occurs when the m = 1/n = 1 mode couples with external modes ($m = 2, 3, 4/n = 1$) and their amplitudes increase as is shown in Fig. 3. The temporal sequence of the MHD instabilities from $m = 1$ to $m = 4$ can be clearly seen, and then the termination of the H mode occurs. It is also obvious that the fluctuations in V_f and H_α radiation increase after the H–L transition. These facts again suggest that the variation in E_r near the edge and the fluctuation in the transport barrier may not be the cause but rather the consequence of the H–L transition in the HT-6M tokamak.

3. ANALYSES

The appearance of an H mode in low q(a) is related to the current density profile at the edge when EOH is applied. By assuming a parabolic plasma current profile, the $m = 3/n = 1$ rational surface is located at $r/a \sim 0.9$ for $q(a) = 3.6$. The current caused by EOH is mainly located at $r/a \sim 0.95$ and near the rational surface of $q = 3 (m = 3/n = 1)$. The induced plasma current is high enough to modify the current profile around the $m = 3/n = 1$ surface to form a locally reversed profile. This configuration is, however, unstable with respect to the linear tearing mode and may be responsible for the L phase of the discharge. If the current increase penetrates to the location of the resonant $m = 3/n = 1$ surface, causing $dJ_\phi/dr \approx 0$, the $m = 3/n = 1$ tearing mode becomes stable. The magnetic shear increases outside the resonant surface. The turbulence can be suppressed under the increased magnetic shear, together with a stabilized tearing mode. If the magnetic turbulence plays a decisive role in anomalous transport, it determines the time-scale on which the transport barrier is established. The resistive diffusion time is estimated to be of the order of 1 ms, by assuming the island width of the $m = 3/n = 1$ mode to be 0.1a. This time is in fairly good agreement with the time-scale of the H_α radiation decrease in the L–H transition. Indeed, the estimated radius of the high magnetic shear coincides approximately with the location of the transport barrier which is marked by a steep n_e gradient. The conclusion that the current relaxes on a time-scale that is governed by the resistive time [6] is verified by the time evolution of the sawtooth inversion radius. The current caused by EOH does not significantly influence the $m = 3/n = 1$ mode for higher q(a), because the rational surface is located farther inside the plasma ($r/a \sim 0.8$ for $q(a) = 4$). A calculation assuming a parabolic current density profile shows that the current profile near the $m = 3/n = 1$ rational surface is only slightly modified for $q(a) = 4$. Hence, the increased magnetic shear does not significantly suppress the fluctuation and thus reduce the relevant transport. This conclusion agrees fairly well with the results of an analysis of JET data, which demonstrates the significant role of the edge current density in $0.8 < r/a < 1$ in the L–H transition [6].

Because of the increased gradient of the current density profile (peaked current profile) in the core plasma, the $m = 1/n = 1$ mode becomes unstable. The $m = 1/n = 1$ mode develops and then couples with other modes, because of the reduced radial extent between the rational surfaces. The mode coupling causes rapid energy and particle transport, terminating the H mode or causing disruption. The fluctuation in V_f and H_α radiation increases after the H–L transition. This fact supports the conclusions drawn from an analysis of the L–H transition.

Measurements of the fuel ion rotation in the DIII-D tokamak indicate that a negative well of the radial electric field in the sheared region is mainly the result of an increased pressure gradient [12]. The increased edge pressure gradient may be relevant with a large bootstrap current. In fact, an appreciable amount of bootstrap current can be generated at large radii by high power heating [13]. The J_ϕ profile may have a steep gradient at the edge where the magnetic shear increases rapidly. This modification of the edge current profile may stabilize tearing modes whose resonant surfaces are located nearby. Turbulence can be suppressed by increased high magnetic shear. The H mode confinement achieved by high power heating is also correlated with the J_ϕ modification at the edge and with relevant high magnetic shear. Thus, the negative well in E_r at the edge may be a consequence of the increased pressure of the current density gradients.

4. SUMMARY

The edge plasma current density profile and the relevant magnetic shear can play a decisive role in establishing the transport barrier. No significant changes in floating potentials and their fluctuations at different radial positions appear before or during L–H and H–L transitions. These facts suggest that the edge E_r and its shear may, at least, not be the unique mechanism for transitions in the HT-6M tokamak.

ACKNOWLEDGEMENTS

The authors are grateful to the HT-6M team for continuous support in experiments and to A.L. Yao for data acquisition.

REFERENCES

[1] BURRELL, K.H., Plasma Phys. Control. Fusion 36 (1994) A291.
[2] HOLZHAUER, E., et al., Plasma Phys. Control. Fusion 36 (1994) A3.
[3] TOI, K., et al., Plasma Phys. Control. Fusion 36 (1994) A117.
[4] TOI, K., et al., Phys. Rev. Lett. 62 (1989) 430.
[5] TOI, K., et al., Phys. Rev. Lett. 64 (1990) 1895.
[6] CHRISTIANSEN, J.P., Nucl. Fusion 30 (1990) 599.
[7] KAMADA, Y., USHIGUSA, K., NAITO, O., Plasma Phys. Control. Fusion 36 (1994) A123.

[8] HAHM, T.S., DIAMOND, P.H., Phys. Fluids **30** (1987) 133.
[9] LI, J., et al., in Plasma Physics and Controlled Nuclear Fusion Research 1994 (Proc. 15th Int. Conf. Seville, 1994), Vol. 1, IAEA, Vienna (1995) 249.
[10] KALLENBACH, A., et al., Plasma Phys. Control. Fusion **36** (1994) 1229.
[11] STANGEBY, P.C., Nucl. Fusion **30** (1990) 1225.
[12] KIM, J., et al., Phys. Rev. Lett. **72** (1994) 2199.
[13] JET TEAM, Plasma Phys. Control. Fusion **36** (1994) A23.

FORMATION AND EVOLUTION OF INTERNAL TRANSPORT BARRIERS IN ALCATOR C-MOD*

D.T. GARNIER, E.S. MARMAR, C.L. FIORE, J.A. GOETZ,
S.N. GOLOVATO, M.J. GREENWALD, A.E. HUBBARD,
J.H. IRBY, P.J. O'SHEA, J.J. RAMOS, J.E. RICE,
J.M. SCHACHTER, P.C. STEK, Y. TAKASE,
R.L. WATTERSON, S.M. WOLFE
Plasma Fusion Center,
Massachusetts Institute of Technology,
Cambridge, Massachusetts,
United States of America

A. MARTYNOV
Keldysh Institute of Applied Mathematics,
Moscow, Russian Federation

Abstract

FORMATION AND EVOLUTION OF INTERNAL TRANSPORT BARRIERS IN ALCATOR C-MOD.

Central fueling of Alcator C-Mod plasmas with lithium and deuterium pellets often leads to a strong reduction of core energy and particle transport. These transient modes, which typically persist for a few energy confinement times, are characterized by the development, during the post-pellet reheat, of a very steep pressure gradient (scale length $l_p \leq a/5$) in the inner third of the plasma. Inside the transport barrier, the ion thermal diffusivity drops to values close to those predicted from neoclassical theory. The global energy confinement time shows an increase of about 30% relative to L-mode scaling. Sawtooth suppression is typical, but is not observed in all cases. The addition of up to 3 MW of ICRF auxiliary heating, shortly after the pellet injection, leads to high fusion reactivity, with D-D neutron rates enhanced by a factor of about 10 over L-mode discharges with similar input powers. The measured current density profile shows that a region of reversed magnetic shear exists at the plasma core. The change in current profile is consistent with the calculated bootstrap current created by the pressure gradient. MHD stability analysis indicates that these plasmas are near both the $n = \infty$ and the $n = 1$ marginal stability limits.

1. INTRODUCTION

Pellet-fueling induced confinement enhancement was first seen in ohmic discharges on Alcator C [1] and was subsequently observed on other experiments. More recently, on JET, shear reversal in ICRF heated, pellet fueled, current-ramped discharges was reported [2,3], and the acronym, PEP, for Pellet

* Work supported by US Department of Energy contract DE-AC02-78ET51013.

Enhanced Performance, was coined to describe them. With 80 MHz fixed-frequency sources, ICRF heated PEP modes have been obtained, without current ramping, in two regimes on Alcator C-Mod: at 5.3 tesla, hydrogen minority deuterium majority heating has been used, while at 7.9 tesla, heating with ^{3}He minority in deuterium majority plasmas was used.

2. EXPERIMENTAL OBSERVATIONS

Typical plasma parameters for a 7.9 tesla case are illustrated in figure 1. Time histories of the key core parameters for this $I_p = 1$ MA case clearly show the peaking of density profile following the injection of a lithium pellet at 0.76 seconds.

Figure 2 compares the total plasma pressure profiles at 3 times in a discharge: during the pre-pellet ohmic phase; near the peak of the PEP mode

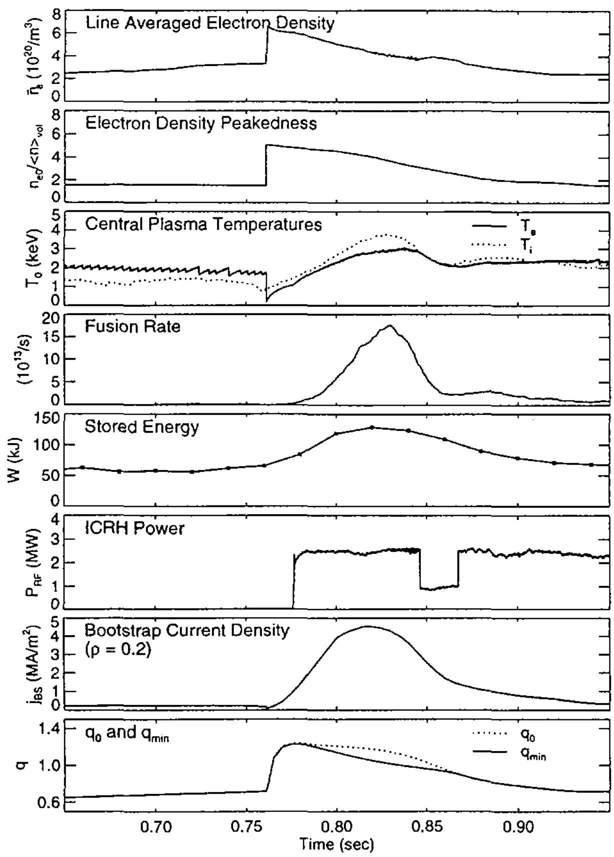

FIG. 1. Time histories of plasma parameters for an 8 T, 1 MA PEP-mode shot. The lithium pellet was injected at 0.76 s. The time histories of bootstrap current density and q are calculated with TRANSP.

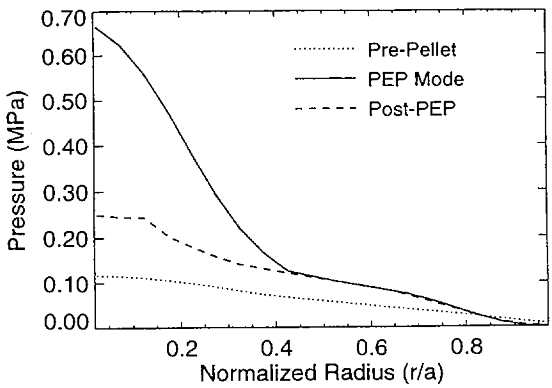

FIG. 2. Pressure profiles at three times: pre-pellet, shortly after the peak in the neutron rate, and after the collapse to L-mode.

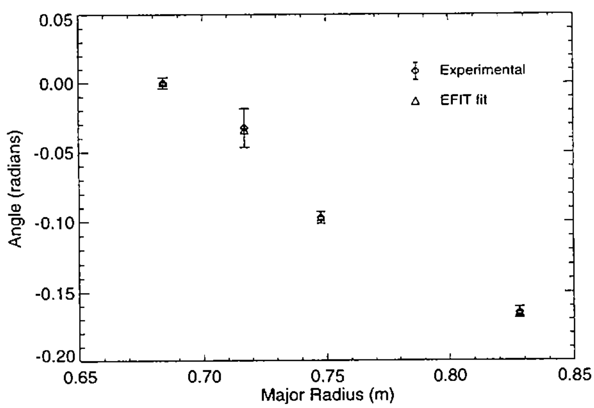

FIG. 3. Comparison of measured magnetic field angle midplane profile with the fitted profile from the EFIT equilibrium reconstruction. The measurements are taken from a series of similar 5 T, 0.8 MA discharges, into which two lithium pellets were injected: the first to induce PEP-mode, the second to make the internal field measurements.

phase; and following the collapse of the core and return to L-mode. It is apparent that the transport improvement is restricted to the inner half of the profile. With the measured temperature and density profile time histories, along with calculated ICRF power deposition and measured bolometric radiation profiles as inputs, the TRANSP [4] code is used to calculate the evolution of transport coefficients as well as current density profiles. According to these calculations approximately 30% of the current density at $\rho = 0.2$ is due to the pressure gradient driven bootstrap current, whose time history is shown in the second last panel of figure 1. The final panel of this same figure illustrates the time histories of q_0 and q_{min}, consistent with the notion that the observed region of reversed shear is due to the increased bootstrap fraction.

Internal poloidal magnetic field profiles are measured in Alcator C-Mod, at a single time point in a discharge, using a lithium pellet ablation trail imaging technique [5]. Figure 3 compares the measured total magnetic field angle, obtained in this fashion on a sequence of 4 similar discharges, to the resulting EFIT [6] derived angles; the measured internal angles have been added as constraints for the EFIT reconstruction of the equilibrium. Figure 4 illustrates the corresponding current density and q profiles. The measurements were taken 75 ms after the injection of the pellet which induced the PEP transition, 10 ms after the peak in the fusion neutron rate. The hollow q profile is apparent, with $q_0 = 2$ and q_{min} just larger than 1. This was a 5.3 tesla, 0.8 MA case. TRANSP calculations indicate that the current density profile is roughly consistent with that expected when bootstrap effects are included, with 1/4 of the current density at $\rho = .3$ driven by the bootstrap current.

All PEP modes are observed to be transient. On C-Mod, they typically last from 50 to 100 ms. This is comparable to the resistive time scale for the current profile to relax from reverse to normal shear, but cause and effect cannot be established without measurements of the current profile time evolution. Several phenomena can apparently be ruled out as the cause of the transition out of PEP mode. As seen on ECE and soft x-ray tomography diagnostics, there is often low m/n coherent MHD activity observed near the time of the transition back to L-mode; however, in many cases this activity appears to saturate long before the collapse, and in some cases it is absent. The resumption of sawtoothing does not always correlate with the end of the PEP phase; often, the pressure profile has relaxed back to those typical of L-mode, as much as 100 ms before sawtoothing resumes.

3. MHD STABILITY

To explore the ideal stability of C-Mod PEP mode discharges, the 7.9 tesla shot already described was analyzed using the CAXE and KINX [7] set of

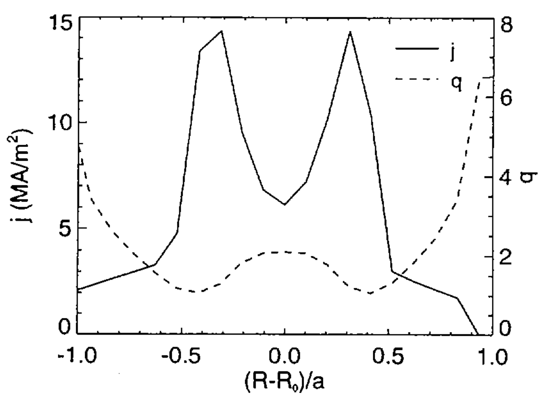

FIG. 4. Current density and q profiles inferred from the midplane poloidal field profile measurements shown in Fig. 3. The measurements are made 10 ms after the peak neutron rate is reached.

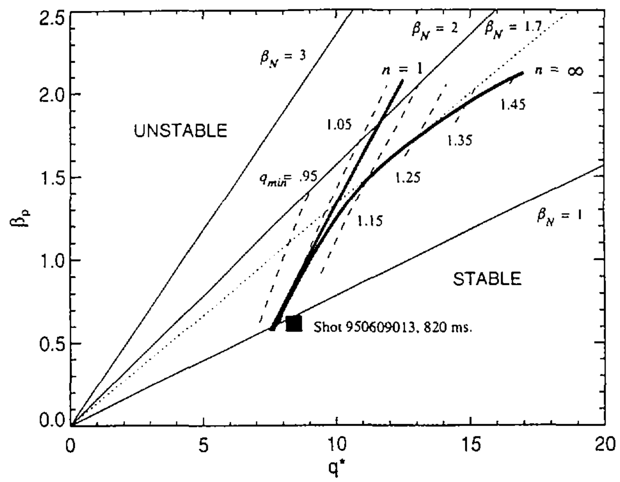

FIG. 5. Ideal stability of an 8 T, 1 MA PEP-mode discharge, and discharges with similar equilibria. Those equilibria falling to the left or above the heavy lines are unstable to ideal modes.

codes for equilibrium reconstruction and ideal MHD stability. Using q^* and β_p scalings, the stability of discharges over a range of these parameters, but with similar pressure and current density profiles, can be examined. Figure 5 shows the results of such an investigation, which indicate that the basis equilibrium is stable, but is very close to the marginal stability limits both for the $n = 1$ kink and $n = \infty$ ideal ballooning modes, as shown by the heavy lines. In all cases it is assumed that there is no conducting wall present. Thus a modest increase in the plasma β, or a slight drop in q_{min} could be expected to drive the discharge unstable. These results further indicate that, for this current density profile, a β limit exists for the $n = \infty$ modes for $\beta_N \gtrsim 1.7$; discharges with higher normalized β should be unstable to the high-n ballooning modes for values of q_{min} up to 1.5. Discharges with $q_{min} > 2$ and small or negative central shear enter the region of "second stability" and are stable to high-n ballooning modes even with large values of β.

4. DISCUSSION

There has recently been much attention focussed on reverse shear configurations and resultant improvements in confinement [8,9]. Typically, these NCS/ERS discharges have many, if not all, of the macroscopic characteristics of PEP mode discharges; NCS/ERS is accessed by tailoring the initial growth of the plasma to freeze in a hollow current profile, followed by strong neutral beam heating. The relative importance of the central fueling from the beams in accessing NCS/ERS is not known; however, this fueling cannot be separated from the central heating when NBI is the main auxiliary heating source. It is well established that reverse shear alone is not sufficient to achieve the transition.

Other modes of enhanced core confinement have also been identified, including the high β_p modes on JT-60U [10] and JET [11], and the CH-Mode on PBX-M [12]. In all of these cases, areas of commonality include enhanced particle and energy confinement, with highly peaked core pressure profiles. In most, if not all cases, core fueling appears to play an important role, either through pellet or beam particle deposition. If it turns out that central particle fueling is one of the necessary conditions to access these enhanced core confinement modes, then extrapolation to future devices, such as ITER, may be very difficult.

REFERENCES

[1] GREENWALD, M., et al., Phys. Rev. Lett. **53** (1984) 352.
[2] HUGON, M., et al., Nucl. Fusion **32** (1992) 33.
[3] SMEULDERS, P., et al., Nucl. Fusion **35** (1995) 225.
[4] HAWRYLUK, R., in Physics of Plasmas Close to Thermonuclear Conditions (COPPI, B., et al., Eds), Vol. 1, Commission of the European Communities, Brussels (1980) 19.
[5] TERRY, J.L., et al., Rev. Sci. Instrum. **63** (1992) 5191.
[6] LAO, L.L., et al., Nucl. Fusion **30** (1990) 1035.
[7] MEDVEDEV, S., et al., in Controlled Fusion and Plasma Physics (Proc. 20th Eur. Conf. Lisbon, 1993), Vol. 17C, Part III, European Physical Society, Geneva (1993) 1279.
[8] STRAIT, E.J., et al., Phys. Rev. Lett. **75** (1995) 4421.
[9] LEVINTON, F.M., et al., Phys. Rev. Lett. **75** (1995) 4417.
[10] NISHITANI, T., et al., Nucl. Fusion **34** (1994) 1069.
[11] STALLARD, B.W., et al., Bull. Am. Phys. Soc. **40** (1994).
[12] PBX-M GROUP, Fusion Eng. Des. **26** (1995) 83.

TURBULENT FLUCTUATIONS IN THE MAIN CORE OF TFTR PLASMAS WITH NEGATIVE MAGNETIC SHEAR

E. MAZZUCATO, S.H. BATHA[1], M.A. BEER,
M.G. BELL, R.E. BELL, R.V. BUDNY, C.E. BUSH[2],
P.C. EFTHIMION, T.S. HAHM, G.W. HAMMETT,
B. LeBLANC, F.M. LEVINTON[1], R. NAZIKIAN,
H.K. PARK, S.F. PAUL, G. REWOLDT,
G.L. SCHMIDT, S.D. SCOTT, E.J. SYNAKOWSKI,
W.M. TANG, G. TAYLOR, M.C. ZARNSTORFF
Plasma Physics Laboratory,
Princeton University,
Princeton, New Jersey,
United States of America

Abstract

TURBULENT FLUCTUATIONS IN THE MAIN CORE OF TFTR PLASMAS WITH NEGATIVE MAGNETIC SHEAR.

Turbulent fluctuations in plasmas with reversed magnetic shear have been investigated in TFTR. Under intense auxiliary heating, these plasmas are observed to bifurcate into two states with different transport properties. In the state with better confinement, it has been found that the level of fluctuations is very small throughout most of the region with negative shear. By contrast, the state with lower confinement is characterized by large bursts of fluctuations which suggest a competition between the driving and the suppression of turbulence. These results are consistent with the suppression of turbulence by the $\mathbf{E}\times\mathbf{B}$ velocity shear.

1. Introduction

Recent results [1-4] point to the beneficial effects of negative magnetic shear on plasma performance in tokamaks. In these experiments, magnetic configurations with a non-monotonic safety factor q have been obtained using a variety of techniques. The common result is a strong peaking of the pressure profile, which indicates a reduction of plasma transport in the central region with negative shear. Since short scale turbulence is considered to be the source of anomalous losses in tokamaks, these results appear to be consistent with theoretical predictions that negative shear can suppress geodesic curvature driven instabilities, such as trapped particle modes [5], the toroidal ion temperature gradient mode [6], and high-n ballooning modes [7].

In order to study the effects of negative magnetic shear on plasma turbulence in tokamaks, we have conducted an experimental study of turbulent fluctuations in plasmas with reversed magnetic shear on the Tokamak Fusion Test Reactor (TFTR) [8]. These are deuterium plasmas with a major radius R=2.6 m, a minor radius

[1] Fusion Physics and Technology, Torrance, California, USA.

[2] Oak Ridge National Laboratory, Oak Ridge, Tennessee, USA.

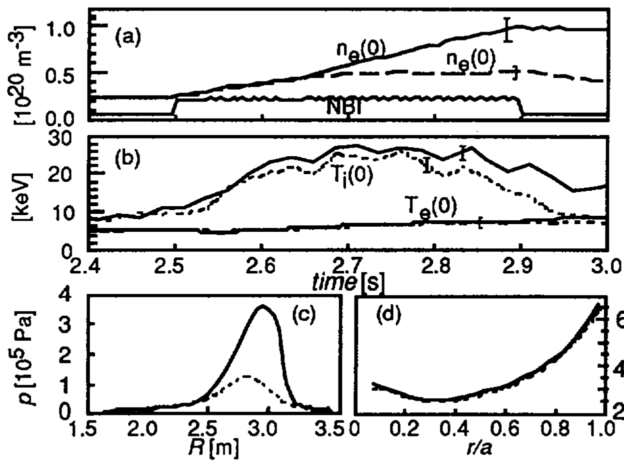

FIG. 1. Time evolution of central electron density (a) and of temperatures (b) in ERS (solid line) and RS (dashed line) plasmas with 29 and 27 MW of balanced NBI, respectively. The bottom graphs show the radial profile of the plasma pressure (c) at t=2.9 s and the safety factor (d) at the bifurcation time.

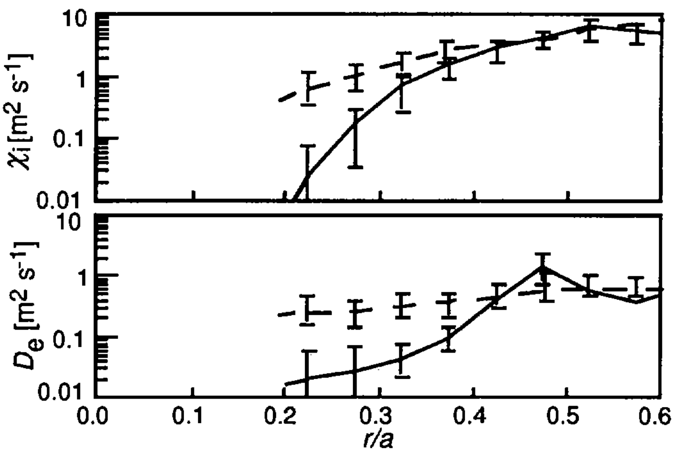

FIG. 2. Ion thermal conductivity (χ_i) and electron particle diffusivity (D_e) in the ERS (solid line) and RS (dashed line) plasmas of Fig. 1 (t=2.75 s).

a=0.94 m, a toroidal magnetic field B=4.6 T, and a plasma current I_p=1.6 MA. The central plasma region with negative shear is created early in the discharge by a combination of heating and current drive. Under intense auxiliary heating with neutral beam injection (NBI), these plasmas are observed to bifurcate into two different states [3], the reversed shear (RS) and the enhanced reversed shear (ERS) mode (Fig. 1). While the RS mode is similar to the *supershot regime* which is normally observed in TFTR with monotonic q-profiles, the ERS mode is characterized by highly peaked

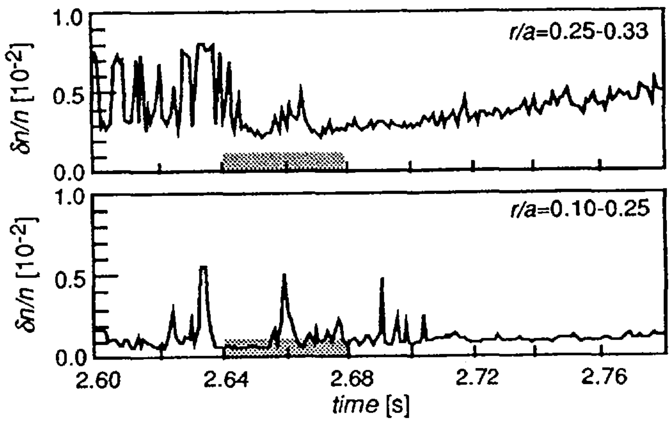

FIG. 3. Time evolution of density fluctuations in the ERS mode. The shaded area represents the time of bifurcation.

density and plasma pressure profiles (Fig. 1). Since at the time of bifurcation the q-profiles are very similar in the two regimes, the observed phenomenon cannot be ascribed solely to the negative magnetic shear.

A transport analysis, ignoring particle pinches, shows a greatly reduced plasma transport in the ERS mode (Fig. 2). In particular, the precipitous drop of the ion thermal conductivity inside the reversed shear region to values below those of conventional neoclassical theory [3] reveals the formation of a transport barrier.

2. Turbulent Fluctuations

Short scale turbulent fluctuations have been studied with X-mode microwave reflectometry in the frequency range 123-142 GHz [9]. Figure 3 shows the time evolution of density fluctuations at two radial locations inside the negative shear region of an ERS plasma. From these results, it appears that large bursts of turbulence, initially present in the discharge, disappear after the transition into the ERS mode.

By using the displacement of the reflecting point of the probing wave, caused by the plasma density rise, we get the amplitude of density fluctuations shown in Fig. 4 as a function of the normalized minor radius r/a. The abscissas in this figure are the

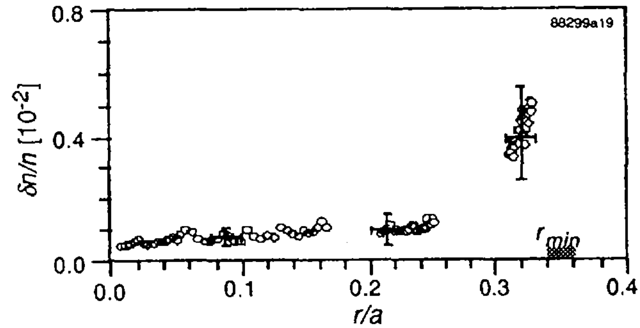

FIG. 4. Amplitude of density fluctuations in the ERS mode of Fig. 1 at $t=2.72$–2.78 s; r_{min} is the radial position with minimum q.

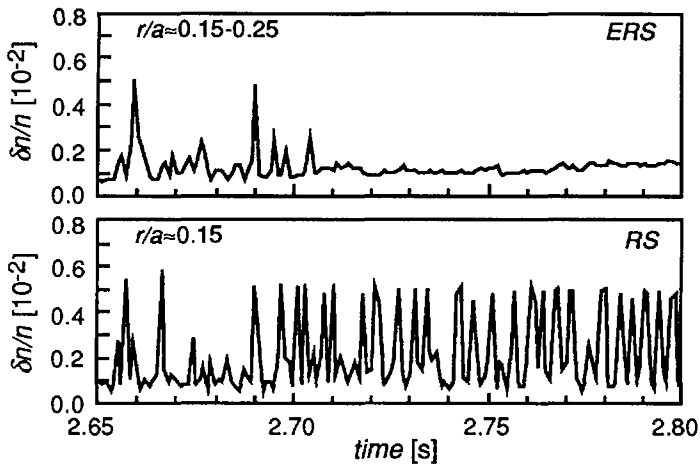

FIG. 5. Time evolution of density fluctuations in ERS and RS modes.

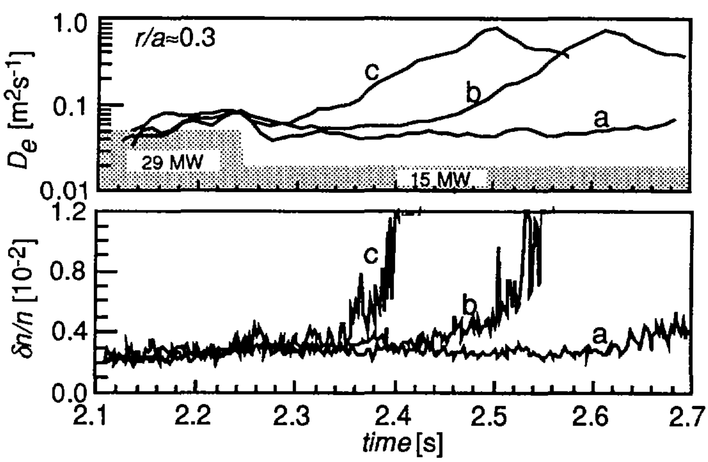

FIG. 6. Electron particle diffusivity and amplitude of density fluctuations at $r/a \approx 0.3$. a: Balanced injection; b: co/counter=5/1; c: co/counter=6/0.

calculated positions of the reflecting cutoff on the low field side of the equatorial plane, including a relativistic correction [10] which ranges from 2 to 6 cm. As described elsewhere [9], to obtain the amplitude of density fluctuations from reflectometry measurements requires the knowledge of the shape of the radial spectrum of fluctuations. Unfortunately, in the rapidly evolving plasmas of the present experiment, this is difficult to obtain with radial correlation measurements. Fortunately, all previous theoretical and experimental studies of short scale fluctuations in large tokamaks indicate that the bulk of the turbulent activity occurs at wavelengths larger than the ion Larmor radius (ρ_i), typically in the range of radial wave numbers $0.2 < k_r\rho_i < 1$. Accordingly, the values in Fig. 3 and 4 have been obtained assuming $k_r = 1$ cm^{-1}, which corresponds to $k_r\rho_i \approx 0.5$, and we have calculated the error bars by taking the extreme values of $k_r\rho_i = 0.2$ and 1, respectively. In spite of these uncertainties, we draw the conclusion that the level of fluctuations is very small in the main core of ERS plasmas, and that it rises near the point where q reaches its minimum value. Both of these phenomena are reminiscent of the radial dependence of the plasma transport coefficients (Fig. 2).

Turbulent fluctuations in the RS mode are substantially different from those in the ERS mode, as illustrated in Fig. 5 which shows the time evolution of the fluctuation amplitude in the middle of the negative shear region. From these data, it appears that bursts of turbulence, reaching the maximum detectable level, persist throughout the entire plasma pulse. Closer to the plasma center ($r/a<0.1$), this phenomenon disappears and the measured level of fluctuations becomes similar to that in the ERS mode. This indicates that a central quiescent region exists in the RS mode as well, but with a much smaller radial extent than in the ERS mode.

The observed correlation between the decrease in fluctuations and the transition into the ERS mode implies that a surge of turbulence must occur at the back-transition from the ERS to the RS mode. This is indeed what is observed, as illustrated in Fig. 6 which shows the time evolution of the electron particle diffusivity and the level of turbulence across a back-transition. The latter occurs when, for achieving steady state conditions, the NBI power is lowered from 29 to 15 MW. The three cases shown in Fig. 6 differ on the co-counter NBI power ratio. It has been found [11] that, while balanced (case a in Fig. 6) and counter-dominated injection produces plasmas which remain in the ERS mode until the end of NBI, co-dominated injection causes a back-transition into the RS mode (cases b and c in Fig. 6). Figure 6 illustrates very clearly that the loss of ERS confinement, which is represented by the rise in the value of D_e, coincides with a sharp increase in the level of turbulent fluctuations.

3. Discussion

We have compared the experimental observations with the theoretical predictions for toroidal electrostatic drift-type modes. Figure 7 shows the linear growth rate of the most unstable mode (γ) which was calculated with a kinetic toroidal eigenvalue code [12]. Surprisingly, we find the largest values of γ in the ERS mode, which provides further evidence that shear reversal is not the only cause of turbulence suppression in these plasmas. Furthermore, the size of the central stable region is the same in both plasma regimes. These results, which were confirmed by those obtained with a toroidal gyrofluid code [13], demonstrate that other phenomena, besides the reversed shear, play a role in the ERS/RS dynamics.

A possible mechanism for the suppression of turbulence is the decorrelation of turbulent fluctuations by a large **ExB** velocity shear which may exist in regions of large pressure gradient [14-22]. This mechanism, which in the past has been invoked for explaining the reduction in the level of fluctuations at the edge of plasmas in the H-mode [14-18], might also be at work in the central plasma region with negative magnetic shear [19-22]. The numerical simulations in Ref. [19] indicate that turbulence is suppressed when the linear growth satisfies the condition $\gamma \leq \omega_s$, where ω_s is the characteristic **ExB** shearing rate which was derived in Ref. [20]. On the tokamak midplane, we obtain $\omega_s \approx |(RB_\theta/B)\partial(E_r/RB_\theta)/\partial R|$, where B_θ is the poloidal magnetic field, and E_r is the radial electric field. The latter can be obtained from the radial component of the force balance equation, using measured quantities

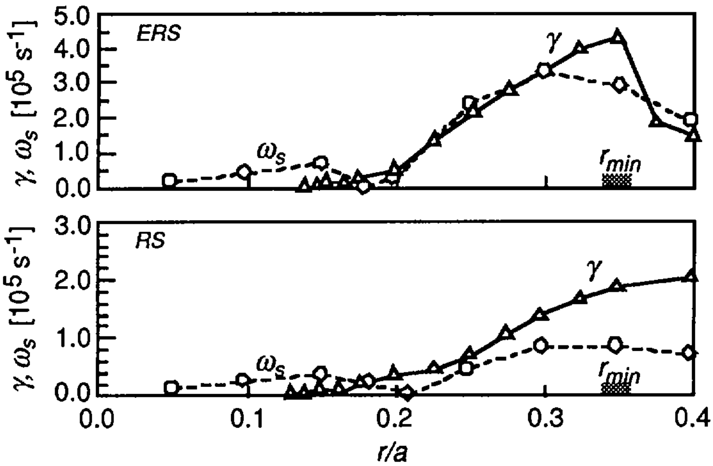

FIG. 7. Maximum linear growth rate γ (triangles) and shearing rate ω_s (circles) for the ERS and RS plasmas of Fig. 1 at t=2.75 s.

and the neoclassical poloidal velocity. In the unstable part of the reversed shear region, where $\gamma>0$, we obtain $\gamma\leq\omega_S$ for the ERS mode, and $\gamma>\omega_S$ for the RS mode (Fig. 7). Similarly, we find that the ERS relaxation in Fig. 6 is caused by a decrease in the shearing rate below the calculated value of γ [11]. The observed difference in the co/counter NBI injection is, then, explained by the sign of the term containing the toroidal velocity in the force balance equation, which in the case of co-injection causes a reduction in E_r.

From these results, we draw the conclusion that the observed reduction of fluctuations in ERS plasmas is consistent with the suppression of turbulence by the ExB velocity shear.

4. Conclusion

In conclusion, the results presented in this paper provide the first experimental evidence of a correlation between the low level of turbulent fluctuations and the improved confinement in the main core of plasmas with reversed magnetic shear (ERS). We have also detected large bursts of fluctuations in plasmas with similar magnetic shear but with a poorer confinement (RS), suggesting a competition between the driving and the suppression of turbulence.

These observations are consistent with the suppression of turbulence by a decorrelation of turbulent fluctuations from the ExB velocity shear.

Acknowledgment

The authors are grateful to the TFTR group for the operation of these experiments, and to R. J. Hawryluk for his constant encouragement. This work was supported by U.S. Department of Energy Contract No. DE-AC02-76-CHO3073.

REFERENCES

[1] HUGON, M., et al., Nucl. Fusion **32** (1992) 33.
[2] LAZARUS, E.A., et al., Phys. Fluids B **4** (1992) 3644.
[3] LEVINTON, F.M., et al., Phys. Rev. Lett. **75** (1995) 4417.
[4] STRAIT, E.J., et al., Phys. Rev. Lett. **75** (1995) 4421.
[5] KADOMTSEV, B.B., POGUTSE, O.P., Sov. Phys. — JETP **24** (1967) 1172.
[6] COPPI, B., et al., Phys. Fluids **10** (1967) 582.
[7] CHANCE, M.S., GREENE, J.M., Nucl. Fusion **21** (1981) 453.
[8] MAZZUCATO, E., et al., Phys. Rev. Lett. **77** (1996) 3145.
[9] MAZZUCATO, E., NAZIKIAN, R., Phys. Rev. Lett. **71** (1993) 1840.
[10] MAZZUCATO, E., Phys. Fluids B **4** (1992) 3460.
[11] SYNAKOWSKI, E.J., et al. (in preparation).
[12] REWOLDT, G., et al., Phys. Fluids **30** (1987) 807.
[13] BEER, M.A., PhD Thesis, Princeton Univ., NJ (1994).
[14] BIGLARI, H., DIAMOND, P.H., TERRY, P.W., Phys. Fluids B **2** (1989) 1.
[15] SHAING, K.C., et al., Phys. Fluids B **2** (1990) 1492.
[16] BASU, B., COPPI, B., Phys. Fluids B 4 (1992) 2817.
[17] DONG, J., HORTON, W., Phys. Fluids B **5** (1992) 1581.
[18] HINTON, F.L., STAEBLER, G.M., Phys. Fluids B **5** (1993) 1281.
[19] WALTZ, R.E., et al., Phys. Plasmas **1** (1994) 2229.
[20] HAHM, T.S., BURRELL, K.H., Phys. Plasmas **2** (1995) 1648.
[21] LAO, L.L., et al., Phys. Plasmas **3** (1996) 1951.
[22] LEBEDEV, V.B., et al., IAEA-CN-64/D1-3, these Proceedings, Vol. 2.

DEUTERIUM-TRITIUM TFTR PLASMAS WITH HIGH INTERNAL INDUCTANCE*

S.A. SABBAGH[1 **], E.D. FREDRICKSON[2], D.K. MANSFIELD[2], M.G. BELL[2], S.H. BATHA[3], R.E. BELL[2], R.V. BUDNY[2], C.E. BUSH[2], Z. CHANG[2], R.J. HAWRYLUK[2], D.W. JOHNSON[2], F.M. LEVINTON[3], J. MANICKAM[2], K.M. McGUIRE[2], D. MUELLER[2], F. PAOLETTI[1 **], H.K. PARK[2], A.T. RAMSEY[2], C.H. SKINNER[2], E.J. SYNAKOWSKI[2], H. TAKAHASHI[2], G. TAYLOR[2], L.E. ZAKHAROV[2], M.C. ZARNSTORFF[2]

[1] Department of Applied Physics,
Columbia University,
New York, N.Y.

[2] Plasma Physics Laboratory,
Princeton University,
Princeton, New Jersey

[3] Fusion Physics and Technology, Inc.,
Torrance, California

United States of America

Abstract

DEUTERIUM-TRITIUM TFTR PLASMAS WITH HIGH INTERNAL INDUCTANCE.

Deuterium-tritium plasmas with increased plasma internal inductance, l_i, have been produced in TFTR to investigate stability limits at high l_i, I_p, and B_0, and to assess fusion power production in these plasmas. A novel technique of plasma initiation at low edge safety factor, q_a, has allowed operation at I_p up to 2.3 MA and l_i up to 1.5. These plasmas exhibit larger sawtooth inversion radii than plasmas with lower l_i at the same I_p. The sawteeth are stabilized at sufficiently large injected neutral beam heating power, P_b, consistent with a model of ω^*-stabilization. The stability limit due to disruption is consistent with a scaling of the maximum $\beta_N \equiv 10^8 \langle\beta_t\rangle aB_0/I_p$ being proportional to l_i. Increased energy confinement, attained by lithium conditioning of the limiter, has exceeded that of supershot plasmas at heating power levels above 30 MW. Fusion powers of up to 8.7 MW have been generated in these plasmas. At the maximum attempted I_p and B_0, the plasmas are no longer limited by gross plasma instability, but rather by limiter power handling. Plasmas with reversed central shear and increased l_i due to increased edge magnetic shear have also been created. The stability limit for these plasmas also exhibits an increase in the maximum β_N with increased l_i.

---

* Supported by US Department of Energy contracts DE-FG02-89ER53297, DE-AC02-76-CHO3073, and DE-FG02-90ER54084.

** Present address: Plasma Physics Laboratory, Princeton University, P.O. Box 451, Princeton, NJ 08543, USA.

I. Introduction

Plasma instability driven by the plasma pressure is presently the most restrictive constraint on plasma performance in large tokamaks [1,2]. Understanding the dependence of the beta limit on plasma equilibrium parameters is therefore crucial to improving fusion power production in tokamak plasmas. Experiments in several machines including DIII-D [3,4], JT-60U [5], and TFTR [6] have shown that increasing the peakedness of the equilibrium current profile (i.e., increasing internal inductance, l_i) can lead to improvements in the normalized beta, $\beta_N \equiv 10^8 \langle\beta_t\rangle aB_0/I_p$, attainable in these machines. Here, a is the minor radius and B_0 is the toroidal magnetic field at the geometric center. This result agrees with ideal MHD stability calculations [7,8] that show a linear increase of the β_N limit with increasing l_i for equilibrium pressure profiles that are not excessively peaked.

A demonstration of increased plasma stability at maximum absolute parameters is a logical continuation of these experiments. The fusion power output, P_f, in high temperature tokamak plasmas heated by neutral beam injection scales approximately as the square of the plasma stored energy, W_{tot} [9].Therefore, if the maximum achievable normalized beta, β_{Nmax}, increases linearly with l_i, an increase in the maximum P_f can be obtained by increasing the product of $l_i I_p B_0$.

Technical aspects of generating the high l_i plasma in previous experiments, including TFTR [10], had limited operation to reduced I_p. Recently, deuterium-tritium plasmas with increased internal inductance have been produced in TFTR with monotonic q profiles at high I_p. A novel approach has been developed to create plasmas with both high $l_i \leq 1.5$ and high $I_p = 2.0$ - 2.3 MA with $B_0 = 4.8$ - 5.6 T ($q^* \equiv 5(a^2B_0/R_pI_p(\mathrm{MA}))(1+\kappa^2)/2 = 3.4$ - 3.6) to investigate beta limit physics at increased $l_i I_p B_0$ product, as well as to develop a test-bed for alpha physics studies at high fusion power.

Increasing the gross stability of plasmas with reversed magnetic field shear in the plasma core [11] has also been investigated in high poloidal β D-T plasmas with $I_p = 0.8$ - 1.0 MA and increased l_i created by rapidly decreasing I_p. We find that β_{Nmax} is also increased as l_i is increased in these plasmas.

The peak D-T fusion power output as a function of I_p for the recent high l_i plasmas created with $I_p \geq 2$ MA, as well as for supershots, reversed shear [11], weak shear plasmas [12], and previously reported high β_p, high l_i plasmas utilizing a rapid decrease in I_p to produce increased l_i [10] is shown in Fig. 1. Fusion powers of up to 8.7 MW have been generated in high l_i plasmas. The fusion power output and stored energy of the recent high l_i D-T plasmas at $I_p = 2.3$ MA and $B_0 = 5.6$T are presently not limited by plasma instability. Instead, they are limited by the occurrence of large density influxes from the limiter which occur at $W_{tot} \geq 6$ MJ and $P_b \geq 33$ MW. These "density bloom" events rapidly decrease τ_E. If this limiter power handling constraint could be removed, the increased stability margin of the high l_i plasmas should allow fusion power production in excess of 14 MW at the $l_i I_p B_0$ product already produced. The P_f for a given W_{tot} is also greater in high $l_i I_p$ plasmas, exceeding 10% of the power normally generated by lower l_i supershots.

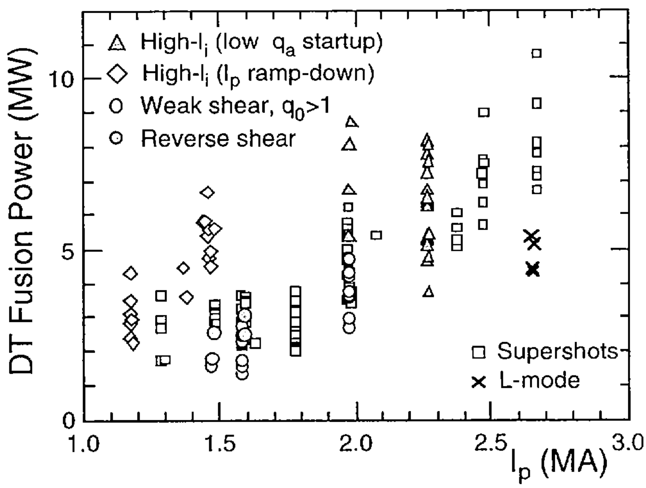

Figure 1 Fusion power output vs. I_p for several TFTR operational regimes.

II. Generation of high l_i plasma at high current

Details of the technique used to produce TFTR plasmas at both high l_i and high I_p are shown in Fig. 2. A peaked current profile was produced by initiating a deuterium ohmic plasma on the outer RF limiter with reduced minor radius, a_p = 0.46 m (about 53% of the final minor radius), and q_a = 2.3. The discharge was subsequently moved to the inner belt limiter (plasma major radius, R_p = 2.3 m), and I_p raised to 2.4 MA. This configuration formed the core of the subsequent high l_i plasma, which was created by expanding the minor radius to 0.87 m in 100 ms. Neutral beam injection power, P_b, up to 36 MW was used to heat the plasma. In this case, 70% of P_b is supplied by tritium neutral beams.

Several variants of this plasma growth scheme have been used to minimize MHD activity while retaining the high $l_i I_p$ product by modifying the plasma growth evolution and using mild decreases in I_p. Also, q_a was sometimes raised to an intermediate value of 3.3 to allow injection of Li pellets without disruption. Pellet injection during this phase increases τ_E during NBI. Such a variation is indicated by the dashed trace in Fig. 2(a-c). Both the increase in l_i and $l_i I_p$ generated in an equivalent ohmic plasma are shown in Fig 2(d-e). A typical value of l_i reached in supershot plasmas is shown for reference. In high l_i plasmas, l_i and $l_i I_p$ have reached peak values of 1.5 and 3.4 MA respectively. Additional details of the plasma growth, and increased τ_E through lithium conditioning can be found in the papers of Fredrickson *et al.* [13], and Mansfield *et al.* [14].

Fusion power, plasma stored energy, and line-integrated edge density are shown in Fig. 2(f-g). A density bloom occurs in the plasma shortly after 4 s

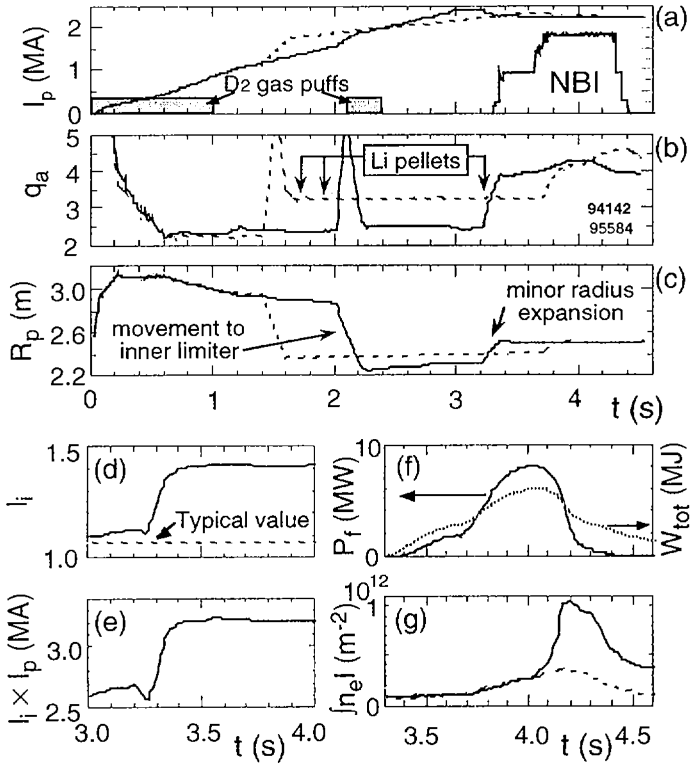

Figure 2 Time evolution of plasma parameters for high l_i *plasmas. Frames (a - c) show plasma current, edge safety factor, and major radius. Frames (d - g) show plasma internal inductance,* $l_i \times I_p$ *product, D-T fusion power and plasma total stored energy, and line integrated edge density. For comparison, frame (g) includes the evolution of an equivalent plasma (dashed trace) in which a density bloom does not occur.*

which reduces both the stored energy and fusion power output. The density evolution of a plasma which does not have a bloom is shown for comparison. The P_f and W_{tot} typically decrease after the edge density increases sharply. Central electron and ion temperatures of 8.3 keV and 42 keV, respectively, with central electron densities of up to 7×10^{19} m^{-3} and peaking factor $F_{ne} \equiv n_e(0)/\langle n_e \rangle \leq 2.9$ have been reached. Non-inductively driven current of greater than 30% has been computed by TRANSP at I_p = 2 MA with a 27% contribution from the bootstrap current.

The q profile has been measured in plasmas with high l_i using a motional Stark effect (MSE) diagnostic [15]. Compared to plasmas with standard (lower) values of l_i at the same I_p, high l_i I_p plasmas have greater core current density and reduced edge current density. The on-axis safety factor, q_0 varies from 0.75 - 0.8 with an error of 0.04 during the NBI phase.

Unlike TFTR high β_p, high l_i plasmas created by ramping down I_p, the recent discharges did not make a transition to a limiter H-mode. Reducing the edge current density and increasing the edge shear is therefore more effective in reducing the H-mode power threshold than the present techniques used to increase l_i.

III. Beta limit scaling with l_i and pressure peakedness

A general increase in β_N with increasing l_i for TFTR plasmas with monotonic q profiles and $I_p > 1$ MA is demonstrated in Fig. 3. The maximum β_N for high l_i plasmas at $I_p \geq 2$ MA follow the trend established by plasmas with $I_p = 1$-2 MA. Pressure profile peaking factors, $F_p \equiv P(0)/\langle P\rangle$ range from 3 - 6.2 in high l_i plasmas. At greater values of F_p, the β_{Nmax} can be reduced substantially. For example, Fig. 3 shows supershot plasmas produced with a lithium conditioned limiter have reached $F_p \sim 8$ and disrupted at low $\beta_N \sim 1.2$.

High l_i plasmas with $l_i > 1.3$, $I_p \geq 2$ MA and $B_0 \geq 5.1$T and $F_p \sim 5$ have exceeded $\beta_N = 2$ without disruption. These plasmas were limited in performance by density blooms. Only one high l_i plasma has disrupted at high β_N. This disruption, which had $\beta_N = 2.38$, was generated in a high l_i plasma with $I_p = 2$ MA, $B_0 = 4.8$ T specifically designed to reach β_{Nmax} before the onset of a bloom. This can be compared to a supershot disruption with $I_p = 2.5$ MA, $B_0 = 5.1$ T, equivalent F_p, and $\beta_{Nmax} = 1.85$. The ratio of l_i between these plasmas is 1.29 and the ratio of the beta limits also 1.29, consistent with a linear scaling of β_{Nmax} with l_i.

This general behavior of the β limit can be modelled by ideal MHD theory. A study of the instability threshold β_N and $\beta_N^* \equiv 2\mu_0\langle p^2\rangle^{0.5}a/B_0I_p$, as

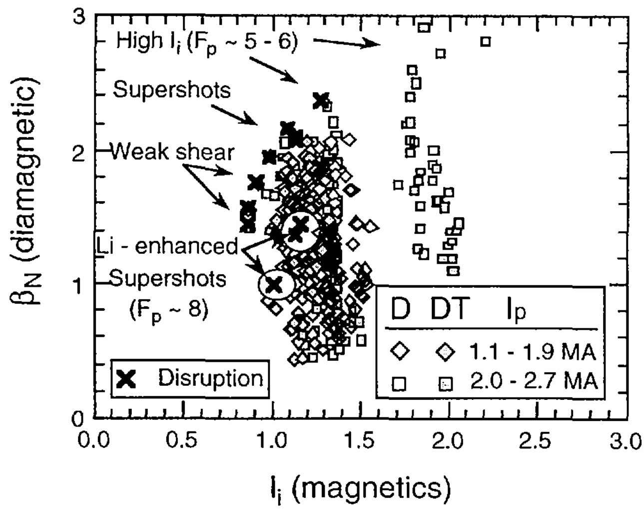

Figure 3 Increase of β_N as a function of l_i for several TFTR plasma operating regimes.

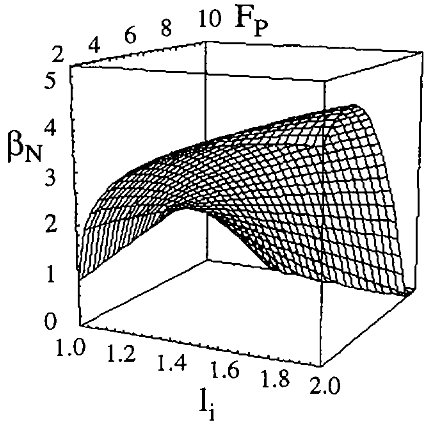

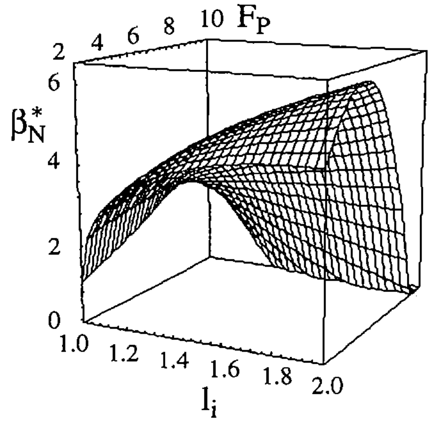

Figure 4 Dependence of stability to ideal low-n modes as a function of l_i *and* F_p.

a function of l_i and F_p for ideal low-n modes ($1 \le n \le 4$) using the PEST code is shown in Fig. 4. High-n modes were also tested, but do not set the stability limit for $2.5 \le F_p \le 6$. The equilibrium pressure and q profiles, and boundary shapes used for the study are taken from TRANSP runs of experimental discharges which exhibit extreme values of F_p and l_i. The profiles for these actual plasmas are then used to produce phantom equilibria with interpolated, and slightly extrapolated values of the profile peaking parameters. The q_0 has also been scaled to be slightly greater than one in order to eliminate the robust $m = 1$, $n = 1$ instability, computed by ideal MHD stability codes for experimentally stable plasmas which are measured to have $q_0 < 1$. The q_a was held constant (4.9) in this study, and no conducting wall was used.

At sufficiently low l_i, β_{Nmax} decreases rapidly due to a purely current-driven kink mode. The decrease of β_{Nmax} shown at high values of $F_p \sim 8$ and higher l_i is similar to that observed in lithium-enhanced supershots (Fig. 3). A local maximum stable operating value of $\beta_N{}^*$ is found as a function of F_p for a given l_i. The maximum l_i that can be reached will either be constrained by technical considerations, or by the occurrence of internal mode destabilization. Therefore, an optimized operating point with a given (l_i, F_p) can be reached. In the range of l_i created in the present experiments, the $\beta_N{}^*$ is optimized at $F_p \sim 5$. The modelled instability is normally a global kink/ballooning mode.

Experimentally, there is a positive correlation observed between increased F_p and τ_E in supershots and high l_i plasmas. Thus, maximizing $\beta_N{}^*$ or P_f for a given l_i can occur at greater F_p than the computed optimally stable value when operating at maximum $l_i\, I_p\, B_0$ due to insufficient τ_E. In this case, τ_E may be increased by operating at a higher F_p thereby optimizing against combined stability and τ_E constraints.

Further stability analyses were performed for TRANSP reconstructions of the high l_i experimental plasmas. The q profiles varied depending on the exact low q_a startup technique used. Pressure profiles were varied by considering different discharges with F_p in the range 3.6 - 5.1. In cases using $F_p > 5$, the computed stability limit β_{Nmax} varies from 2.3 - 2.6 consistent with the intentional high l_i disruption at β_{Nmax} = 2.38 and F_p = 6.2 created experimentally. Both low and high-n modes were computed to be unstable. This is above the limit for high I_p > 2.3 MA supershot plasmas of $\beta_N \leq 2$. The β_{Nmax} for equilibria with F_p = 3.6 varied from 2.8 - 3.3 depending on the q profile considered. Low-n kink/ballooning modes set the limit in this case.

IV. MHD instabilities and impact on confinement

Stationary magnetic perturbations (SMPs) [16] (also referred to as quasi-stationary modes (QSMs) in JET [17] and JT-60U [18]), have occurred at several distinct phases of the high l_i plasma evolution. These modes typically caused disruption during the ohmic phase. During beam heating, performance is limited by a reduction in τ_E due to an increase in particle recycling and edge plasma density that occurs after the onset of the SMP.

In all cases, techniques have been developed to stabilize SMPs. A combination of D_2 gas puffing, plasma initiation on a higher-recycling outer limiter, and a rapid initial decrease of q_a has stabilized the mode during the initial second of the discharge evolution. Additional gas puffing during the transition to the inner limiter has eliminated SMPs during this phase. SMPs have also been observed after the minor radius expansion, perhaps due to eddy currents generated in the vacuum vessel. Plasma rotation, generated by a 200-300 ms initial period of co-injected neutral beams has stabilized the mode,

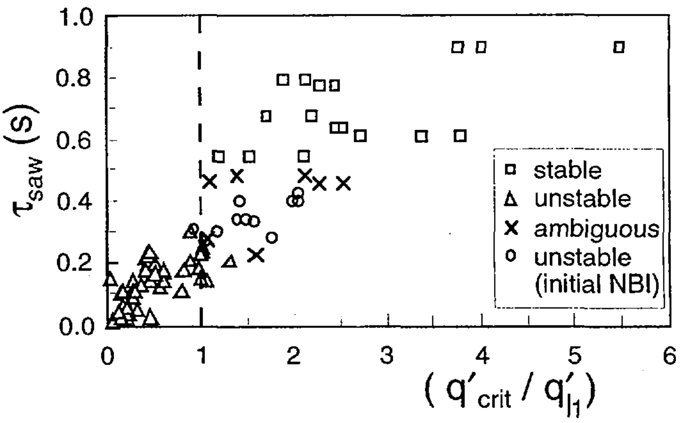

Figure 5 Sawtooth period vs. the ratio of the Zakharov-Rogers critical shear model of sawooth stabilization to the TRANSP computed shear at q = *1 in high* l_i *plasmas. Squares indicate stability; triangles instability. Circles indicate that a sawtooth occurred during the inital phase (*$\Delta t \sim 3\ \tau_E$*) of NBI. Crosses indicate that a crash occured at NBI termination.*

similar to results in JT-60U[18]. Injection of a lithium pellet 50 ms after the expansion has also suppressed the mode. Pellet injection has also been used to suppress SMPs during the decrease of I_p during normal discharge termination.

Low order rational MHD tearing modes, which have been modelled as neoclassical ∇p driven modes in TFTR [19] have been absent from the recent high l_i plasmas, similar to supershots with $I_p > 2$ MA. Fishbones and sawteeth have been observed. The $q = 1$ radius of these plasmas occurs at $r/a = 0.35$, which is larger than the value 0.25 typically observed in supershot plasmas. This result is based on the sawtooth inversion radius as measured by an electron cyclotron emission (ECE) diagnostic. Plasmas with larger $q = 1$ radii do not suffer a reduction in τ_E as long as sawteeth are stabilized during NBI.

Sawtooth stabilization in these plasmas is analyzed in terms of the Zakharov-Rogers two-fluid collisionless m=1 reconnection model [20]. Data points in Fig. 5 represent time points chosen at the half-maximum rise and fall of W_{tot}, at the maximum stored energy, and at maximum critical shear for 20 experimental discharges. The sawtooth period, τ_{saw}, which was determined from electron temperature fluctuations as measured by ECE, increases with the ratio of the critical shear to the TRANSP computed shear, q'_{crit}/q', at the $q = 1$ surface. Experimentally, plasmas are found to be unstable when $q'_{crit}/q'|_1 \leq 1$ and stable when $q'_{crit}/q'|_1 \geq 2.1$ in agreement with theory. During the initial heating phase of the plasma, the stability criterion is met $(1 \leq q'_{crit}/q'|_1 \leq 2.1)$ yet sawteeth are typically observed while the pressure gradient builds. The criterion is therefore not strictly applicable during dynamic heating phases.

When the modes considered above are stabilized, techniques to raise τ_E in standard supershot plasmas have been used to improve performance. The established technique of lithium conditioning of the limiter has produced τ_E up to 240 ms in D-T plasmas, which slightly exceeds that of supershot plasmas with $P_b > 30$ MW. Also, a positive isotopic mass dependence of τ_E in D-T plasmas has been observed, typically yielding an increase of greater than 20% in high $l_i\, I_p$ plasmas. Details of the isotope effect in these and other TFTR plasmas can be found in a companion paper by Scott, *et al.* [21].

V. Reversed shear plasmas with increased l_i

Plasmas with reversed shear (RS) and high l_i were created by using NBI during the initial rise of I_p [11], and then rapidly decreasing I_p during NBI. In these plasmas, $\varepsilon\beta_p$ reached 1.1, $\beta_N = 2.6$, and $H \equiv \tau_E/\tau_{E\ ITER-89P} = 3.5$. The measured (using MSE) $q_0 = 3.5 \pm 0.5$ and $q_{min} = 2.5 - 3$. These plasmas are computed to have robust stability to high-n modes over 65-80% of the plasma minor radius and access to the second stability region in the core (Fig. 6). The computed low-n mode stability limit increases at high l_i compared to standard RS plasmas and agrees with the experimental disruption limit. For example, RS plasmas with $l_i = 0.9$ and $I_p = 1.6$ MA have disrupted at $\beta_N = 1.6$, in agreement with an ideal $n = 1$ mode becoming unstable at this

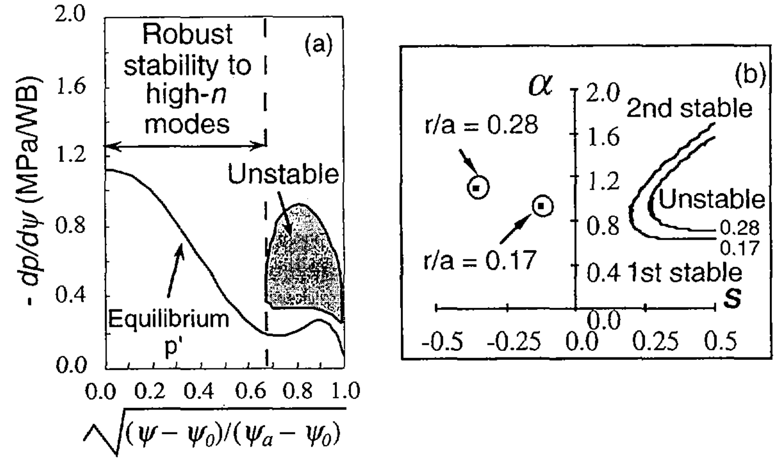

Figure 6 High-n stability for $\varepsilon\beta_p = 1$ plasma with reversed shear in the plasma core and increased edge shear. Frame (a) shows the equilibrium p' vs. the square root of the normalized poloidal flux, and the unstable region to high-n ballooning modes. Frame (b) shows an (α, S) diagram for two minor radial positions, r/a = 0.17 and, r/a = 0.28.

value. The high l_i RS plasmas at l_i = 1.25 and I_p = 0.9 MA disrupted at $\beta_N = 2.9$, also in agreement with the computed n = 1 ideal instability threshold.

VI. Conclusion

A new technique of low q_a plasma initiation in TFTR has allowed plasmas with increased l_i to be generated at I_p up to 2.3 MA. With sawteeth stabilized, the increased q = 1 radius in these plasmas does not degrade confinement. Rather, the increased l_i I_p product has yielded an increase in $\beta_{N\,max}$. Consequently, peak DT fusion power levels which rival the highest attained in TFTR have been generated. At the highest values of $l_i I_p B_0$, performance in these plasmas is no longer limited by stability, but by a reduction in τ_E caused by large density blooms generated by the increased power load to the limiter. Future experiments including a radiative mantle of krypton are planned to eliminate this constraint. High l_i plasmas with reversed shear in the core have also been created, and have demonstrated an increase in $\beta_{N\,max}$ as l_i is increased by increasing the edge magnetic shear.

REFERENCES

[1] McGUIRE, K.M., et al., Phys. Plasmas 2 (1995) 2176.

[2] TAYLOR, T., et al., in Proc. Workshop on Tokamak Concept Improvement, Varenna, Italy, 1994, Vol. 1, Editrice Compositori, Bologna (1995) 111.

[3] FERRON, J.R., et al., Phys. Fluids B 5 (1993) 2532.
[4] LAO, L.L., et al., Phys. Rev. Lett. 70 (1993) 3435.
[5] KAMADA, Y., et al., in Plasma Physics and Controlled Nuclear Fusion Research 1994 (Proc. 15th Int. Conf. Seville, 1994), Vol. 1, IAEA, Vienna (1995) 651.
[6] SABBAGH, S.A., et al., Phys. Fluids B 3 (1991) 2277.
[7] MAUEL, M.E., et al., in Plasma Physics and Controlled Nuclear Fusion Research 1992 (Proc. 14th Int. Conf. Würzburg, 1992), Vol. 1, IAEA, Vienna (1993) 205.
[8] HOWL, W., et al., Phys. Fluids B 4 (1992) 1724.
[9] BELL, M.G., et al., in Plasma Physics and Controlled Nuclear Fusion Research 1994 (Proc. 15th Int. Conf. Seville, 1994), Vol. 1, IAEA, Vienna (1995) 171.
[10] SABBAGH, S.A., et al., ibid., p. 663.
[11] LEVINTON, F.M., et al., Phys. Rev. Lett. 75 (1995) 4417.
[12] NAZIKIAN, R., et al., IAEA-CN-64/A2-4, this volume.
[13] FREDRICKSON, E.D., et al. (in preparation).
[14] MANSFIELD, D.K., et al., Phys. Plasmas 3 (1996) 1892.
[15] LEVINTON, F.M., et al., Phys. Rev. Lett. 63 (1989) 2060.
[16] TAKAHASHI, H., et al., "Interpretability of magnetic diagnostics in tokamaks — Search for a locked mode in TFTR", paper presented at 7th Int. Conf. on Plasma Physics and Controlled Nuclear Fusion, Toki, 1995.
[17] SNIPES, J.A., et al., Nucl. Fusion 28 (1988) 1085.
[18] YOSHINO, R., et al., in Plasma Physics and Controlled Nuclear Fusion Research 1994 (Proc. 15th Int. Conf. Seville, 1994), Vol. 1, IAEA, Vienna (1995) 685.
[19] CHANG, Z., et al., Phys. Rev. Lett. 74 (1995) 4663.
[20] ZAKHAROV, L., ROGERS, B., Phys. Fluids B 4 (1992) 3285.
[21] SCOTT, S., et al., IAEA-CN-64/A6-6, this volume.

CHAIRPERSONS OF SESSIONS

Session O1	A. GIBSON	European Community
Session O2	R. PARKER	ITER
Session A1	H. KISHIMOTO	Japan
Session A2	D.M. MEADE	United States of America
Session A3	D. ROBINSON	United Kingdom
Session A4	M. SHIMADA	Japan
Session A5	T. TAMANA	Japan
Session A6	P.K. KAW	India

SECRETARIAT OF THE CONFERENCE

T.J. DOLAN	Scientific Secretary
U. SCHNEIDER	Scientific Secretary
E. PILLER	Conference Organizer
J. WEIL	Editor
M. SPAK	Editor
I. WARDELL	Records Officer

HOW TO ORDER IAEA PUBLICATIONS

No. 4, October 1996

☆ ☆ **In the United States of America and Canada**, the exclusive sales agent for IAEA publications, to whom all orders and inquiries should be addressed, is:

Bernan Associates, 4611-F Assembly Drive, Lanham,
MD 20706-4391, USA

☆ ☆ **In the following countries** IAEA publications may be purchased from the sources listed below, or from major local booksellers. Payment may be made in local currency or with UNESCO coupons.

AUSTRALIA	Hunter Publications, 58A Gipps Street, Collingwood, Victoria 3066
BELGIUM	Jean de Lannoy, 202 Avenue du Roi, B-1060 Brussels
BRUNEI	Parry's Book Center Sdn. Bhd., P.O. Box 10960, 50730 Kuala Lumpur, Malaysia
CHINA	IAEA Publications in Chinese: China Nuclear Energy Industry Corporation, Translation Section, P.O. Box 2103, Beijing
CZECH REPUBLIC	Artia Pegas Press Ltd., Palác Metro, Narodni tř. 25, P.O. Box 825, CZ-111 21 Prague 1
DENMARK	Munksgaard International Publishers Ltd., P.O. Box 2148, DK-1016 Copenhagen K
EGYPT	The Middle East Observer, 41 Sherif Street, Cairo
FRANCE	Office International de Documentation et Librairie, 48, rue Gay-Lussac, F-75240 Paris Cedex 05
GERMANY	UNO-Verlag, Vertriebs- und Verlags GmbH, Dag Hammarskjöld-Haus, Poppelsdorfer Allee 55, D-53115 Bonn
HUNGARY	Librotrade Ltd., Book Import, P.O. Box 126, H-1656 Budapest
INDIA	Viva Books Private Limited, 4325/3, Ansari Road, Darya Ganj, New Delhi-110002
ISRAEL	YOZMOT Literature Ltd., P.O. Box 56055, IL-61560 Tel Aviv
ITALY	Libreria Scientifica Dott. Lucio di Biasio "AEIOU", Via Coronelli 6, I-20146 Milan
JAPAN	Maruzen Company, Ltd., P.O. Box 5050, 100-31 Tokyo International
MALAYSIA	Parry's Book Center Sdn. Bhd., P. O. Box 10960, 50730 Kuala Lumpur
NETHERLANDS	Martinus Nijhoff International, P.O. Box 269, NL-2501 AX The Hague Swets and Zeitlinger b.v., P.O. Box 830, NL-2610 SZ Lisse
POLAND	Ars Polona, Foreign Trade Enterprise, Krakowskie Przedmieście 7, PL-00-068 Warsaw
SINGAPORE	Parry's Book Center Pte. Ltd., P.O. Box 1165, Singapore 913415
SLOVAKIA	Alfa Press Publishers, Hurbanovo námestie 3, SQ-815 89 Bratislava
SPAIN	Díaz de Santos, Lagasca 95, E-28006 Madrid Díaz de Santos, Balmes 417, E-08022 Barcelona
SWEDEN	Fritzes Customer Service, S-106 47 Stockholm
UNITED KINGDOM	The Stationery Office Books, Publications Centre, 51 Nine Elms Lane, London SW8 5DR

☆ ☆ Orders (except for customers in Canada and the USA) and requests for information may also be addressed directly to:

Sales and Promotion Unit
International Atomic Energy Agency
Wagramerstrasse 5, P.O. Box 100, A-1400 Vienna, Austria

Telephone: +43 1 2060 22529 (or 22530)
Facsimile: +43 1 2060 29302
Electronic mail: SALESPUB@ADPO1.IAEA.OR.AT